Juan Caicedo · Shamim Pakzad   *Editors*

Dynamics of Civil Structures, Volume 2

Proceedings of the 33rd IMAC, A Conference and Exposition on Structural Dynamics, 2015

SEM

Springer

Conference Proceedings of the Society for Experimental Mechanics Series

Series Editor

Tom Proulx
Society for Experimental Mechanics, Inc.,
Bethel, CT, USA

Juan Caicedo • Shamim Pakzad
Editors

Dynamics of Civil Structures, Volume 2

Proceedings of the 33rd IMAC, A Conference and Exposition on Structural Dynamics, 2015

 Springer

Editors
Juan Caicedo
University of South Carolina
Columbia, SC, USA

Shamim Pakzad
Department of Civil and Environmental Engineering
Lehigh University
Bethlehem, PA, USA

Preface

Dynamics of Civil Structures represents one of ten volumes of technical papers presented at the 33rd IMAC, A Conference and Exposition on Balancing Simulation and Testing, 2015, organized by the Society for Experimental Mechanics, and held in Orlando, Florida, February 2–5, 2015. The full proceedings also include volumes on Nonlinear Dynamics; Model Validation and Uncertainty Quantification; Sensors and Instrumentation; Special Topics in Structural Dynamics; Structural Health Monitoring & Damage Detection; Experimental Techniques, Rotating Machinery & Acoustics; Shock & Vibration Aircraft/Aerospace, Energy Harvesting; and Topics in Modal Analysis.

Each collection presents early findings from experimental and computational investigations on an important area within Structural Dynamics. Dynamics of Civil Structures is one of these areas.

The Dynamics of Civil Structures Technical Division serves as a primary focal point within the SEM umbrella for technical activities devoted to civil structures testing, monitoring, and assessment. This volume covers dynamic testing and analysis of all kinds of civil engineering structures such as buildings, bridges, stadiums, dams, etc. Over the last few years, there has been an interest in input and output modal analysis, as well as output only, ambient vibration testing of bridges. In addition to the material in this volume, a number of technical contributions devoted to new methods, non-linear dynamics, wind turbine dynamics, and monitoring related to civil structure dynamics may be found in other volumes of these proceedings.

The organizers would like to thank the authors, presenters, session organizers, and session chairs for their participation in this track.

Columbia, SC, USA   Juan Caicedo
Bethlehem, PA, USA   Shamim Pakzad

Contents

Chapter 1
Determination of Modal Properties of an Irregular 20-Story Concrete Shear Wall Building

Ferya Moayedi, Salman Soleimani-Dashtaki, and Carlos E. Ventura

Abstract This paper presents the results obtained from the ambient vibration measurements done on a 20 story tall building, with reinforced concrete core, located in Vancouver, British Columbia, Canada. The experiment reveals the dynamic characteristics of the investigated building by advanced system identification methods using enhanced signal processing techniques and the fundamentals of frequency domain decomposition. The results include the natural frequencies and the mode shapes of the building obtained from the ambient vibration measurements. The dynamic characteristics of interest in this study are the lateral and torsional natural frequencies and the corresponding mode shapes. A total of 11 modes of vibration, up to the fourth translational and torsional modes, were successfully identified. This paper uses the Enhanced Frequency Domain Decomposition (EFDD) and the Curve-fit Frequency Domain Decomposition (CFDD) methods to identify the modes and utilizes the Frequency Domain Operating Deflection Shapes (FDODS) technique for modal validation. The experimental results were then compared to the analytical estimations from the ETABS models of the building created at the time of the structural design phase and model validation and calibration is performed.

Keywords System identification • Experimental techniques • Ambient vibration measurement • Modal estimation • Model validation

1.1 Introduction

Ambient vibration measurements have been made on a 20 story tall building located in downtown Vancouver. The tests performed on the building provide information on the dynamic characteristics of the structure including the mode shapes and natural frequencies. Those dynamic characteristics of interest in this study are the lateral and torsional natural frequencies and the corresponding mode shapes. In order to investigate the dynamics of the building, transducers have been used to record vibrations in terms of velocity and acceleration at each floor level. The data were then analyzed and the building was modeled in order to extract the modal properties of the structure. These properties include the natural frequencies of the building and their modes of vibration in the translational and torsional modes, as well as their respective modal damping ratios.

The investigated structure has two reinforced concrete cores, each one with a set of stairs from the basement all the way up to the roof. Of the two concrete cores, one also contains an elevator shaft which continues throughout the height of the building. The shape of the building in plan-view is mainly a rectangle with some minor extrusions at some levels. The size of the building in the three lower floors is approximately 36 m by 30 m and in the upper floors it reduces to 30 m by 20 m.

Typical storey height is approximately 3.7 m. Figure 1.1 below demonstrates an overview of the building, by presenting an overall photo of the building as well as a typical floor plan for this structure. The building was in the final stages of construction at the time ambient vibration measurements were made, tests were done while the floor tiles were being placed and the cabinets being installed.

F. Moayedi (✉)
University of British Columbia, 6250 Applied Science Lane, Vancouver, BC V6T 1Z4, Canada
e-mail: ferya@civil.ubc.ca

S. Soleimani-Dashtaki
University of British Columbia, Room 1012 D – 6250 Applied Science Lane, Vancouver, BC V6T 1Z4, Canada

C.E. Ventura
University of British Columbia, Room 2018 – 6250 Applied Science Lane, Vancouver, BC V6T 1Z4, Canada
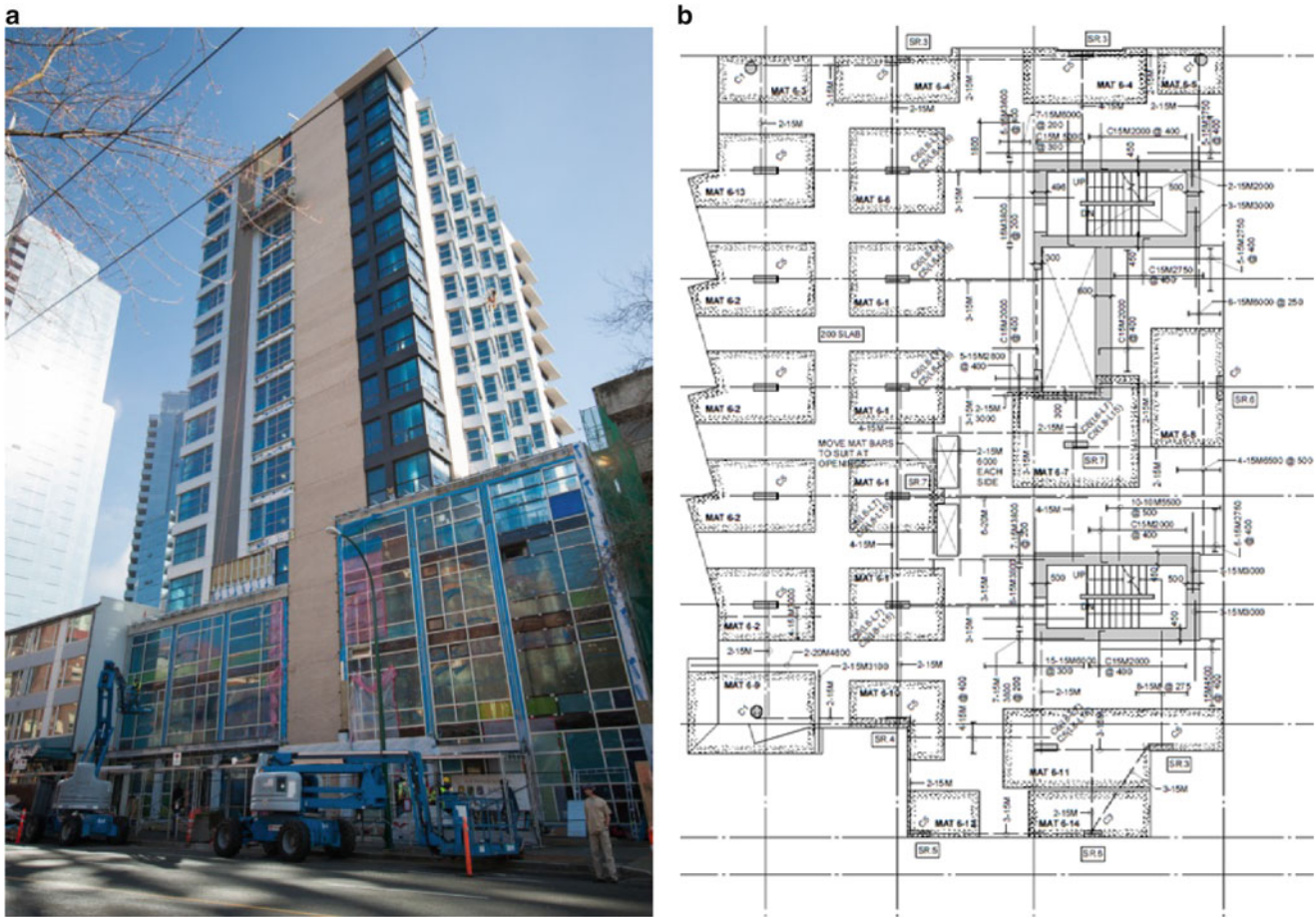
Fig. 1.1 Photo of the investigated building (**a**) and typical floor plan (**b**)

1.2 Experimental Phase

The natural modes of vibration of the building are captured by performing ambient vibration measurements on the building structure. Ambient vibration test is preferable to forced vibration measurement for different reasons. In order to obtain the modal parameters of large structures, there is adequate excitation from wind, traffic, and human activity forces. Hence, there would be no need for exciting devices to be used and the risk of damaging the structure can be avoided [1]. In order to perform the ambient vibration measurements on the structure and capture the natural modes of vibration, the velocity and acceleration of the structure, TROMINO® (Micromed) accelerometers were utilized to capture the characteristics of the building.

In order to capture the behavior of the structure, measurements were made in different setups. In each setup one transducer was always kept at the highest floor of the building as a reference sensor, recording motions for the entire duration of the test, and a number of transducers were moved around to different floors; having two sensors placed at every single floor at a time, usually at opposing corners. All floors of the building were measured using five transducers, and in total, ten setups were needed to complete the building measurements.

Illustrative diagram of the test setups for the building is shown below in Fig. 1.2. Each setup was recorded for a period of 32 min with a sampling rate of 128 Hz.

The duration of the measurements and the location of the data recordings were predetermined by looking at the structural drawings and the ETABS model of the building prior to the test. In this study, transducers in each setup recorded data for a minimum duration of 30 min with a minimum sampling rate of 128 Hz. It is recommended to have longer recording time in order to capture the lower frequency content including the lowest modes of vibration. What this paper would like to suggest, to be used as a rule of thumb, is that the measurement duration of 1,000 times the fundamental period of the building, in units of seconds, would result in sufficient data to capture the frequency content of interest with a decent resolution.

Fig. 1.2 Typical sensor locations
inside building
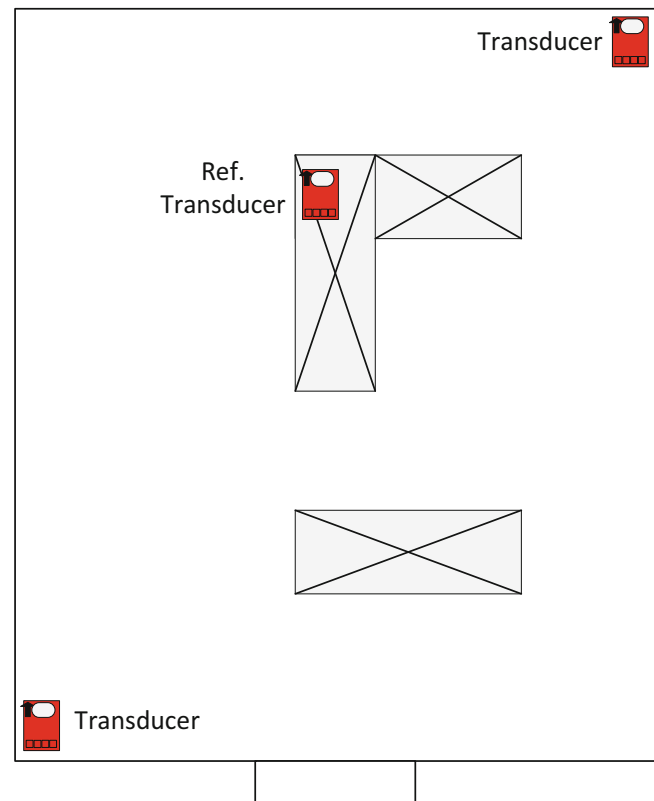
1.3 System Identification and Test Results

After testing, the recorded data need to be extracted from the TROMINO®s onto a computer using the Grilla® Software. The same software is then used in order to convert the data to ASCII format and a series of basic and preliminary signal processing is performed on the data in order to check the validity of the recorded signals. It is recommended that the time history plots for all the recorded signals are developed and investigated for any possible spikes and outliers, prior to any type of analysis.

Data validation and pre-processing of the data was done using MATLAB at the preliminary stages. MATLAB codes were generated in order to view the time history plots, take them into the frequency domain, and verify the data. Signal processing was performed in order to identify as many modes of vibration as possible. The data was decimated in different ways and data filtering with different orders was done to zoom into specific frequency bands in order to minimize the noise and identify the structural modes of vibration at each frequency range.

Further processing, filtering, and modeling were done using ARTeMIS Modal Pro (SVIBS). As further explained in detail throughout the paper, the software ARTeMIS Modal Pro was utilized in order to perform the main signal processing, modal identification, and mode shape validation for the structure studied. Other software used in conjunction with the mentioned programs, would be MATCAD, EXCEL, and ConTEXT which were used for data handling, cleanup, and preliminary processing of the raw data.

The Frequency Domain Decomposition (FDD) technique which decomposes the spectral density matrix at every frequency line using Singular Value Decomposition (SVD) was utilized in order to estimate the mode shapes and the natural frequencies based on the set of single degree of freedom (SDOF) systems for each mode. It is evident that the estimated modes can be grouped into the following types: structural modes, harmonics, and noise modes [2]. Investigation was done on the Singular Value Decomposition (SVD) graphs in order to identify the modes of the mentioned types and peak-picking method was performed in order to distinguish and select only the structural modes of vibration from the rest of the plotted frequency content.

It was realized that the noise to signal ratio is much higher at higher frequencies such that distinguishing between the structural and noise modes becomes extremely difficult at frequencies higher than 16 Hz. Thus, the decimation and filtering algorithms were optimized to give the highest resolution possible up to 16 Hz and frequencies higher than 16 Hz were eliminated from the modal estimation.

Initially, Frequency Domain Operational Deflection Shapes (ODS) technique was used in order to scan the frequency domain for possible mode shapes. Then FDD, EFDD, and CFDD techniques were utilized in order to identify the specific natural frequencies by the peak-picking method. Finally, the same ODS method was performed in order to validate the deflected mode shapes. The following sections would present the results obtained using each mentioned technique.

1.4   Frequency Domain Decomposition (FDD)

This technique approximately decomposes the response into a set of independent single degrees of freedom systems and performs singular value decomposition of the spectral density matrices. Table 1.1 summarizes the identified modal frequencies using this technique.

The peak-picking process which resulted in the presented graph of the FDD technique is illustrated in Fig. 1.3.

Table 1.1 Identified frequencies using the FDD technique

Mode no.	Mode descriptions	Frequency (FDD) Hz	Mode complexity %
1	First translational mode in the Y-direction	1.08	2.16
2	First translational mode in the X-direction	1.27	6.33
3	First torsional mode	1.83	10.14
4	Second translational mode in the X-direction	4.46	9.71
5	Second translational mode in the Y-direction	4.97	2.07
6	Second torsional	6.72	27.08
7	Third translational mode in the X-direction	9.68	74.47
8	Third torsional mode	11.45	21.23
9	Third translational mode in the Y-direction	12.03	30.95
10	Fourth translational mode in the Y-direction	15.01	56.68
11	Fourth translational mode in the X-direction	15.57	61.33
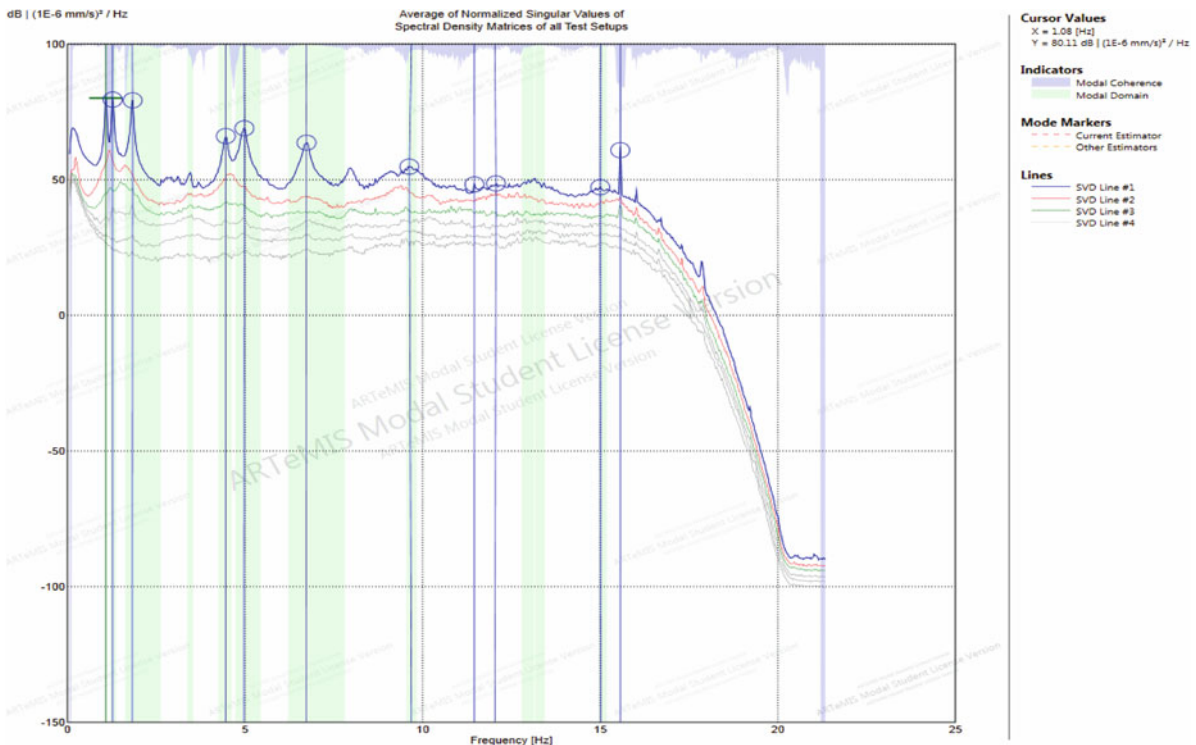
Fig. 1.3 Singular values of spectral density matrices of all test setups (FDD technique)

As it can be interpreted from the plot some of the peaks are not very well distinct. Thus, it might be almost impossible to identify them in one shot signal processing from the scratch. Therefore, some of the picked frequencies had been pre-identified by zooming into smaller frequency ranges through filtering and decimation.

Moreover, Frequency Domain ODS plots are developed and the "Toggle Cursor Mode" of ARTeMIS was activated in order to scan all the possible peaks in the frequency domain to identify building deformations representing any of the familiar mode shapes; frequencies of the specific peaks are recorded for further investigations through FDD techniques.

The authors would like to suggest targeted investigations in each frequency band in order to pre-determine some of the possible natural frequencies, and then peak-picking becomes much easier when finalizing the results.

1.5 Enhanced Frequency Domain Decomposition (EFDD)

The enhanced FDD adds a modal estimation layer which is divided into two steps. The first step is to perform the FDD Peak Picking, and the second step is to use the FDD identified mode shapes to identify the Single-Degree-Of-Freedom (SDOF) Spectral Bell functions and from these SDOF Spectral Bells estimate both the frequency and damping ratio.

Table 1.2 contains the calculated frequencies and damping percentages for the identified modes of vibration from peak-picking done using the EFDD plot presented in Fig. 1.4 followed.

Table 1.2 Identified frequencies using the EFDD technique

Mode no.	Mode descriptions	Frequency (EFDD) Hz	Mode complexity %	Damping ratio %
1	First translational mode in the Y-direction	1.08	1.91	1.49
2	First translational mode in the X-direction	1.27	6.21	1.43
3	First torsional mode	1.83	9.73	1.07
4	Second translational mode in the X-direction	4.46	9.64	1.28
5	Second translational mode in the Y-direction	4.96	2.68	1.34
6	Second torsional	6.73	23.12	1.28
7	Third translational mode in the X-direction	9.63	64.85	0.00
8	Third torsional mode	10.90	36.11	0.00
9	Third translational mode in the Y-direction	12.04	36.29	0.00
10	Fourth translational mode in the Y-direction	15.01	56.68	0.00
11	Fourth translational mode in the X-direction	15.56	68.12	0.06
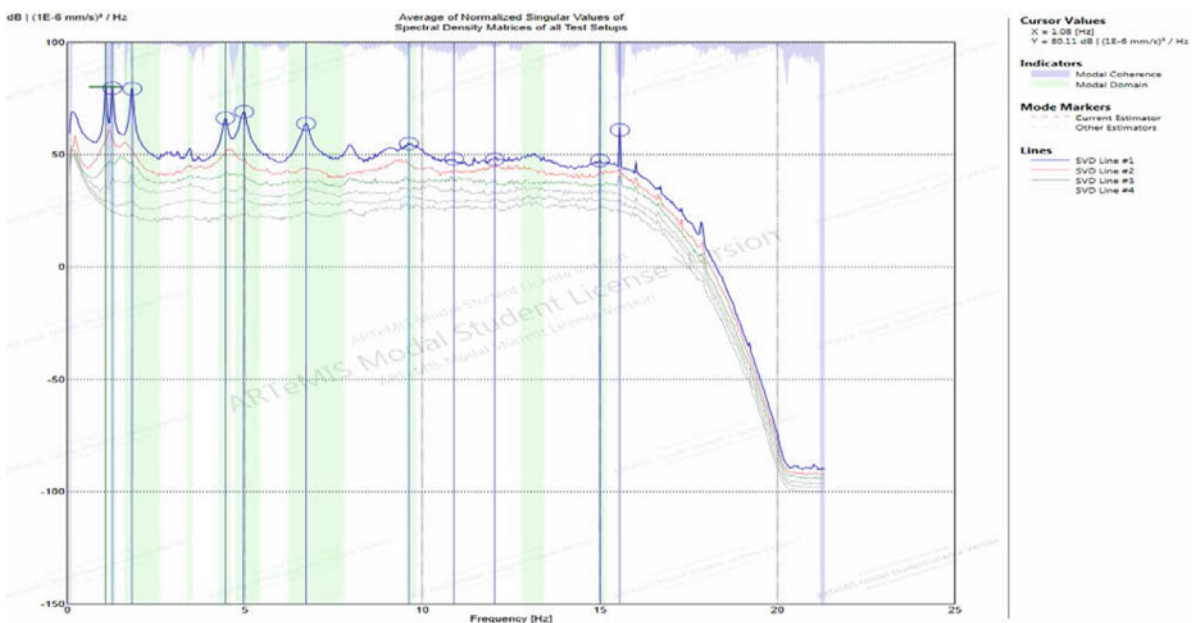
Fig. 1.4 Singular values of spectral density matrices of all test setups (EFDD technique)
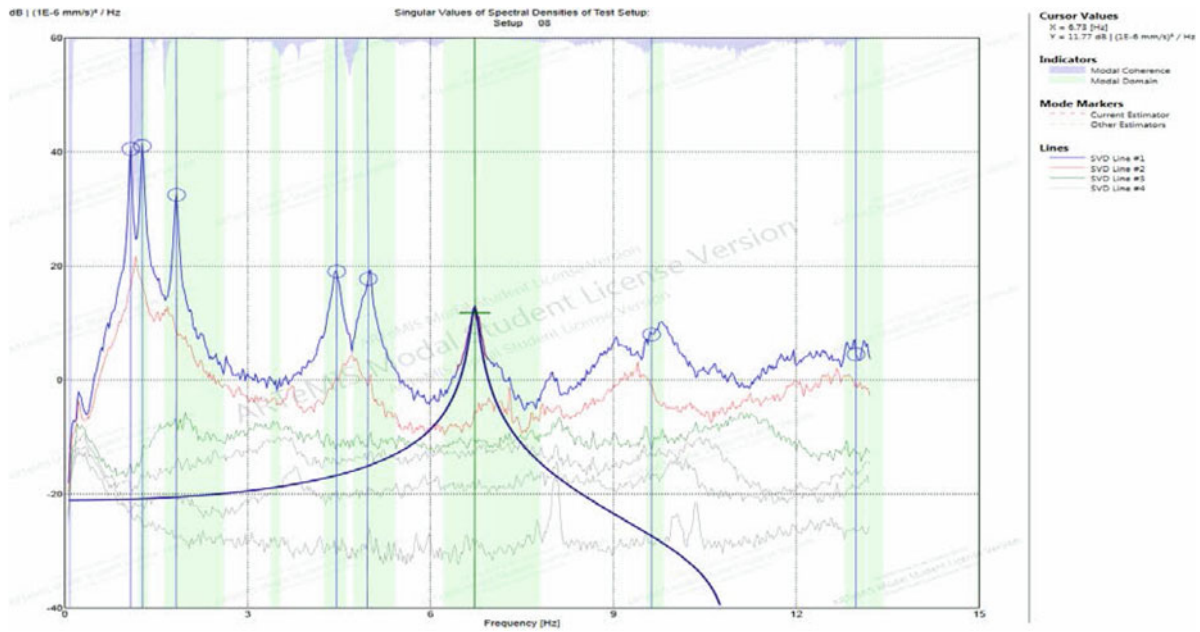
Fig. 1.5 Singular values of spectral density matrices of all test setups (CFDD technique)

Table 1.3 Identified frequencies using the CFDD technique

Mode no.	Mode descriptions	Frequency (CFDD)	Mode complexity	Damping ratio
		Hz	%	%
1	First translational mode in the Y-direction	1.082	1.909	1.708
2	First translational mode in the X-direction	1.274	6.212	1.295
3	First torsional mode	1.825	9.729	0.912
4	Second translational mode in the X-direction	4.454	9.635	0.733
5	Second translational mode in the Y-direction	4.960	2.677	0.814
6	Second torsional	6.724	23.117	0.837
7	Third translational mode in the X-direction	9.625	64.847	0.000
8	Third torsional mode	11.635	50.371	0.347
9	Third translational mode in the Y-direction	11.958	26.685	0.000
10	Fourth translational mode in the Y-direction	15.000	60.562	0.000
11	Fourth translational mode in the X-direction	15.563	61.428	0.000

1.6   Curve-Fit Frequency Domain Decomposition (CFDD)

The curve-fit FDD is similar to the EFDD estimation. The natural frequency and the damping ratio of the modes are estimated by curve fitting the SDOF Spectral Bell using frequency domain least-squares estimation, shown graphically in Fig. 1.5.

Since the SDOF spectral bell is free of influence of other modes there is only a single eigenvalue and residue to fit. The natural frequency as well as the damping ratios are then extracted from the eigenvalues and are presented in Table 1.3.

1.7   Frequency Domain Operating Deflection Shapes (ODS)

An Operating Deflection Shape or ODS is the deflection of a structure at a particular frequency relative to a specific point, also known as the driving point, on the structure. ODS analysis is used for determination of the vibration pattern of a structure under given operating conditions.
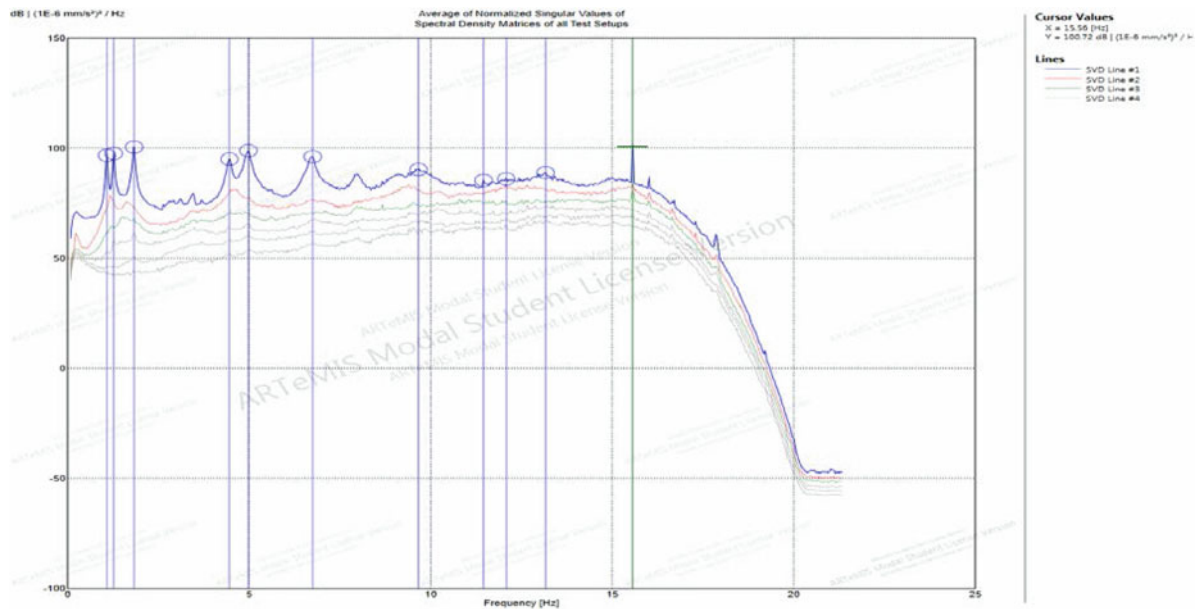
Fig. 1.6 Singular values of spectral density matrices of all test setups (FDODS technique)

Table 1.4 Identified frequencies using the frequency ODS shape technique

Mode no.	Mode descriptions	Frequency (FDODS) Hz	Mode complexity %
1	First translational mode in the Y-direction	1.08	2.16
2	First translational mode in the X-direction	1.27	6.40
3	First torsional mode	1.83	9.78
4	Second translational mode in the X-direction	4.46	8.51
5	Second translational mode in the Y-direction	4.98	1.90
6	Second torsional	6.75	28.10
7	Third translational mode in the X-direction	9.67	47.72
8	Third torsional mode	11.46	23.07
9	Third translational mode in the Y-direction	12.08	28.63
10	Fourth translational mode in the Y-direction	13.17	39.70
11	Fourth translational mode in the X-direction	15.56	49.23

Before any modal estimation and after each modal identification, the ODS was done to confirm the validity of the deflected shape at the identified frequency. The final plot is shown in Fig. 1.6 and a summary of the frequencies identified by the FDODS technique is presented in Table 1.4.

1.8 Summary of Results

The frequencies identified using the above techniques are all summarized in Table 1.5. As evident, the three methods are fairly similar in all of the identified modes of vibration.

The frequencies, and their corresponding periods, of the structural modes of vibration identified using the FDD technique are compared against the values obtained from the ETABS model of the building. Table 1.6 summarizes the first ten modes from the ambient vibration measurements to the modes extracted from the ETABS model.

1.9 Mode Shapes

The following mode shapes have been exported from ARTeMIS after the analysis of the data (Figs. 1.7, 1.8, 1.9 and 1.10).

Table 1.5 Summary of the natural frequencies from different FDD techniques

Mode no.	Mode descriptions	Frequency (FDD) Hz	Frequency (EFDD) Hz	Frequency (CFDD) Hz
1	First translational mode in the Y-direction	1.08	1.08	1.08
2	First translational mode in the X-direction	1.27	1.27	1.27
3	First torsional mode	1.83	1.83	1.83
4	Second translational mode in the X-direction	4.46	4.46	4.46
5	Second translational mode in the Y-direction	4.97	4.96	4.98
6	Second torsional	6.72	6.73	6.75
7	Third translational mode in the X-direction	9.68	9.63	9.67
8	Third torsional mode	11.45	10.90	11.46
9	Third translational mode in the Y-direction	12.03	12.04	12.08
10	Fourth translational mode in the Y-direction	15.01	15.01	13.17
11	Fourth translational mode in the X-direction	15.57	15.56	15.56

Table 1.6 Modal periods and frequencies

Mode no.	FEM period s	Measured period s	FEM frequency Hz	Measured frequency Hz
1	1.956	0.93	0.511	1.08
2	1.396	0.79	0.716	1.27
3	0.873	0.55	1.145	1.83
4	0.334	0.22	2.996	4.46
5	0.284	0.20	3.519	4.97
6	0.193	0.15	5.174	6.72
7	0.134	0.10	7.446	9.68
8	0.124	0.09	8.085	11.45
9	0.118	0.08	8.440	12.03
10	0.091	0.07	10.950	15.01
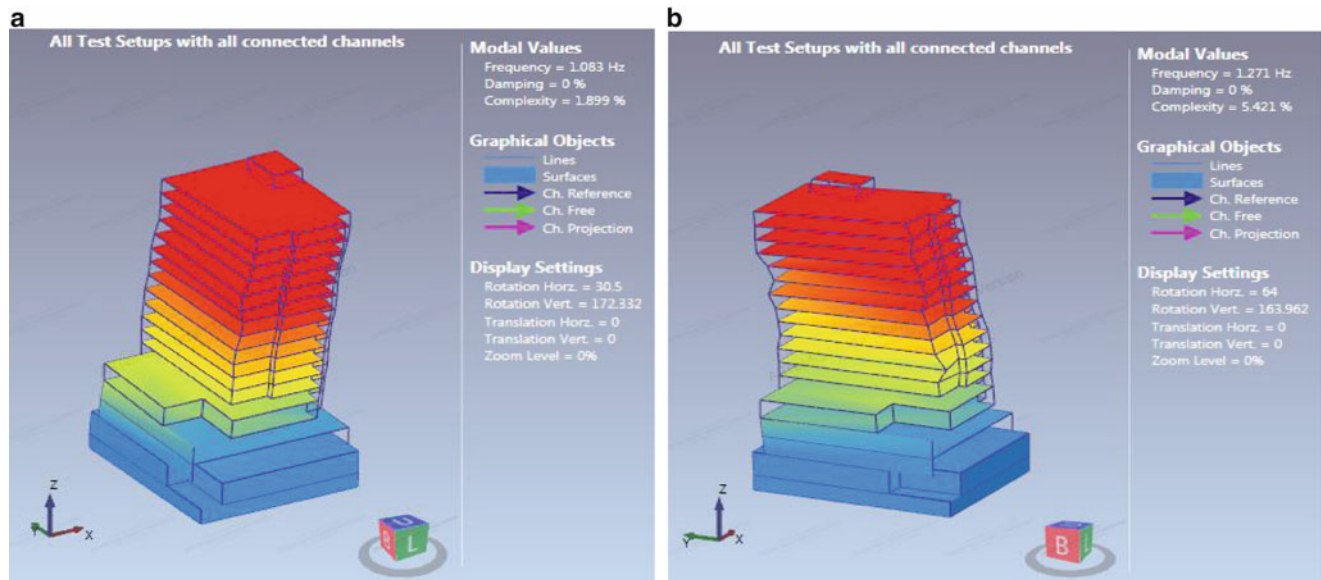
Fig. 1.7 Mode 1 – X direction (**a**) and Y direction (**b**)
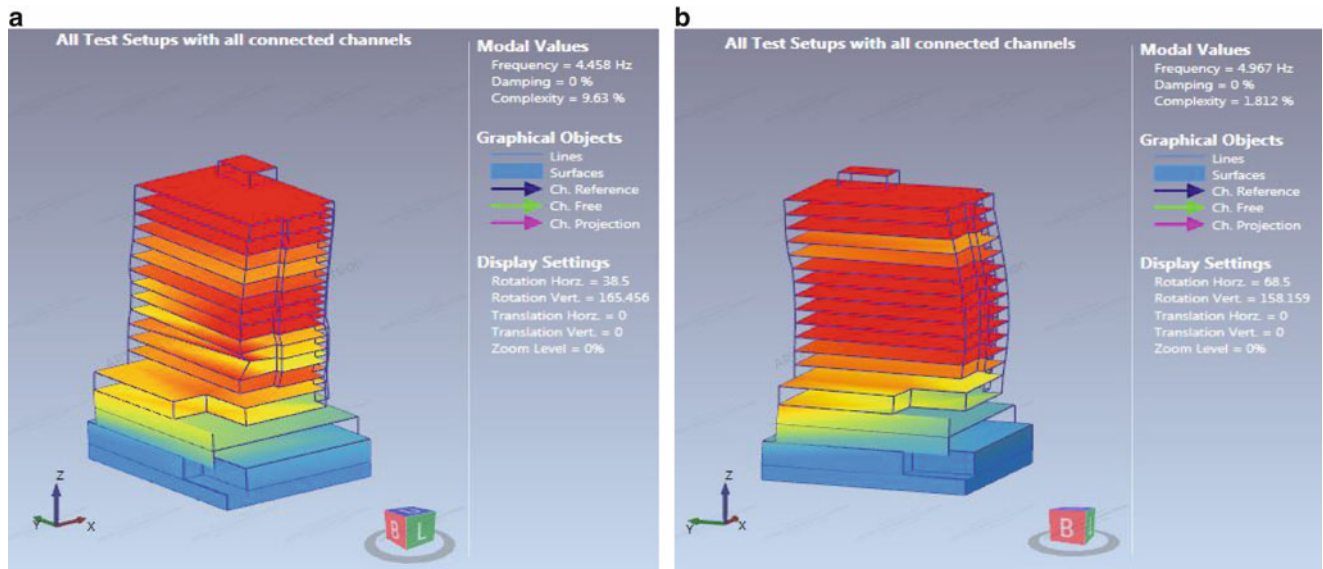
Fig. 1.8 Mode 2 – X direction (**a**) and Y direction (**b**)
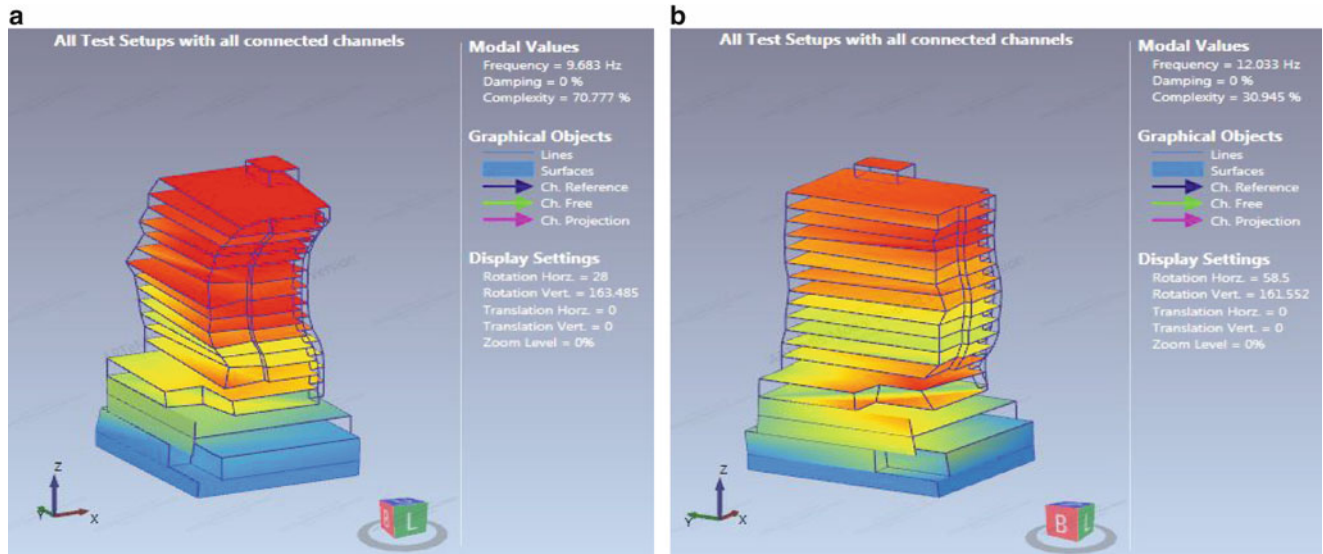
Fig. 1.9 Mode 3 – X direction (**a**) and Y direction (**b**)

1.10 Discussion of Results

System identification and modal characteristics of the reinforced concrete core building is determined by performing ambient vibration measurement tests using TROMINO® tri-axial transducers. As expected, the frequencies identified using the above techniques which are all summarized in the previous sections indicate that the measured natural periods of the building are approximately half the calculated natural periods derived from the ETABS model. This difference between the measured and the calculated results is due to the assumptions made in creating the FEM model such as not considering the effects of non-structural components on building stiffness.

The modal properties of the building obtained from this experiment can be potentially used in FEM model updating. The authors of this paper would like to conclude that the utilized testing strategy would work very well for the building tested. The number of modes identified was beyond the expectation.
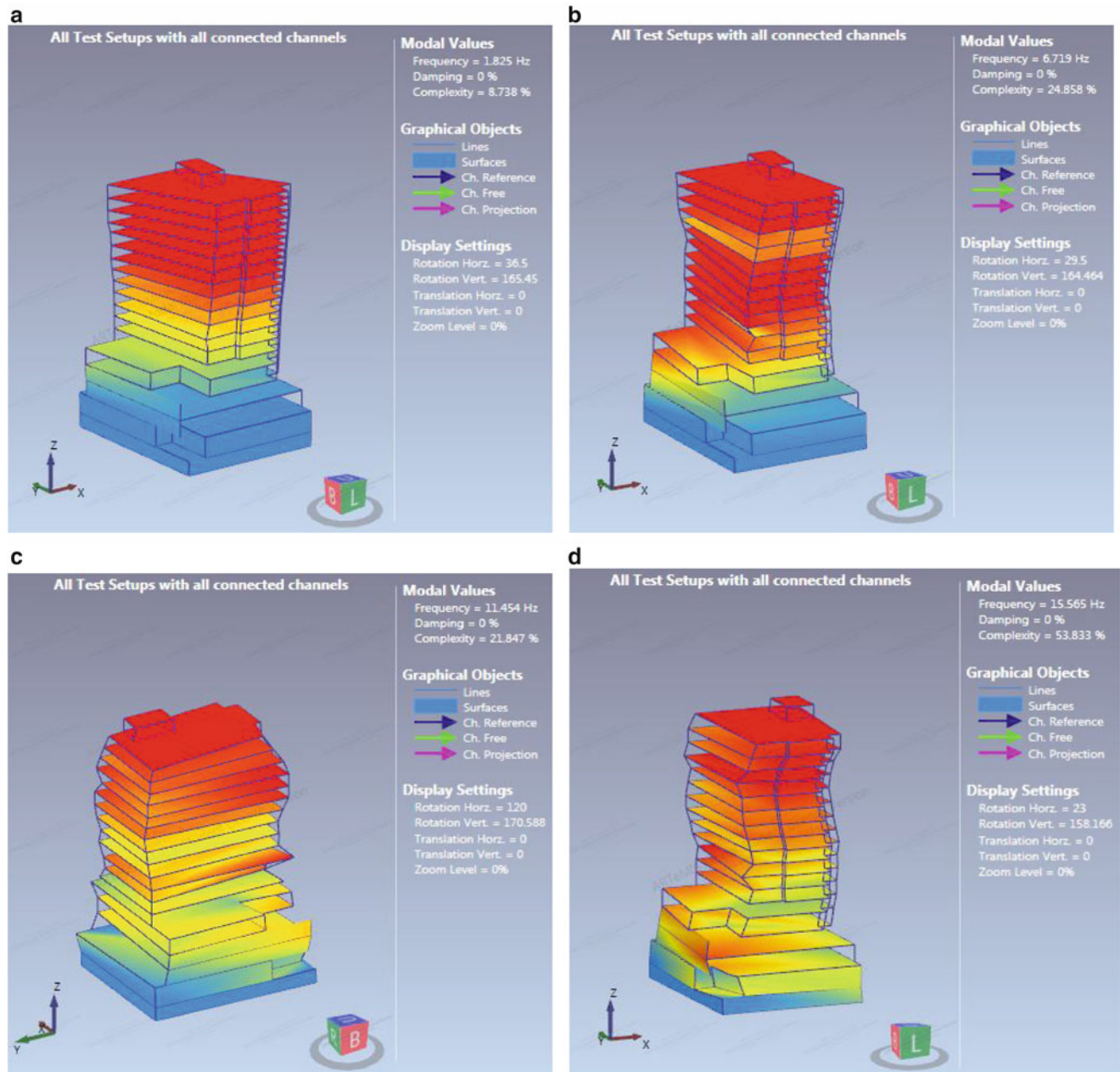
Fig. 1.10 Torsional modes – 1 (**a**), 2 (**b**), 3 (**c**) and 4 (**d**)

References

1. Ventura C, Schuster N (1996) Structural dynamic properties of a reinforced concrete high-rise building during construction. CJCE 23 pp. 950–972
2. Brincker R, Anderson P, Moller N (2006) An indicator for separation of structural and harmonic modes in output-only modal testing. IMAC XXIV
3. Brüel & Kjær (2013) Operating deflection shapes analysis. Struct Dyn

Chapter 2
Effect of Foundation Rocking on the Dynamic Characteristics of a 30-Story Concrete Shear Wall Building

Salman Soleimani-Dashtaki, Ferya Moayedi, and Carlos E. Ventura

Abstract The dynamic characteristics of a structure after the completion of its construction phase can be determined using ambient vibration measurement techniques. A newly constructed 30 stories tall reinforced concrete building in Burnaby, British Columbia, Canada, is tested using this technique. The experimental results reveal the dynamic characteristics of the investigated building including the building rocking and sliding at the foundation level. The method used is the advanced system identification using enhanced signal processing techniques based on the fundamentals of frequency domain decomposition. The paper expands on the technique, from the basics of the test setups to the details of the analysis.

A total of 15 natural periods of vibration are successfully identified including the translational and torsional modes (up to mode 5). The modal estimation is performed using the techniques such as the Enhanced Frequency Domain Decomposition (EFDD), the Curve-fit Frequency Domain Decomposition (CFDD), and the Frequency Domain Operating Deflection Shapes (FDODS); and the outcomes are compared against each other. The modes found from the analytical ETABS models of the building at the structural design phase are then compared and calibrated against the obtained experimental results.

Keywords Experimental techniques • Ambient vibration measurement • Modal estimation • System identification • Foundation rocking modes

2.1 Introduction

The selected building for this experiment is a 30-storey concrete tower structure which sits on top of four levels of reinforced concrete underground parking. The building has a huge central core with four elevator shafts and staircases all the way from the parkade level up to the roof. There are concrete reinforced columns of 60 in. in diameter extending from the foundations all the way up to level 29. Columns get narrower with the height of the building, and at level 25 they reach a diameter of 30 in. The building in plan has a complex geometry with one round corner and straight edges at all other corners. This geometry is introducing some torsional irregularity to the tower, so the instrumentation is optimized to also capture the torsional modes to a good extent.

The height of the parking levels are 2.9 m each, the height of the lobby is 4.9 m, and the height of all the other levels is approximately 3.7 m. The building is under the final stages of construction at the time when measurements are made; therefore construction noises are evident throughout the recorded signals.

Figure 2.1 below shows an overview of the building and its typical floor plan. The dynamic characteristics of the building including its lateral and torsional mode shapes and natural periods of vibration are determined through ambient vibration measurements.

S. Soleimani-Dashtaki (✉)
University of British Columbia, Room 1012 D – 6250 Applied Science Lane, Vancouver, BC V6T 1Z4, Canada
e-mail: salman@civil.ubc.ca

F. Moayedi • C.E. Ventura
University of British Columbia, Room 2018 – 6250 Applied Science Lane, Vancouver, BC V6T 1Z4, Canada
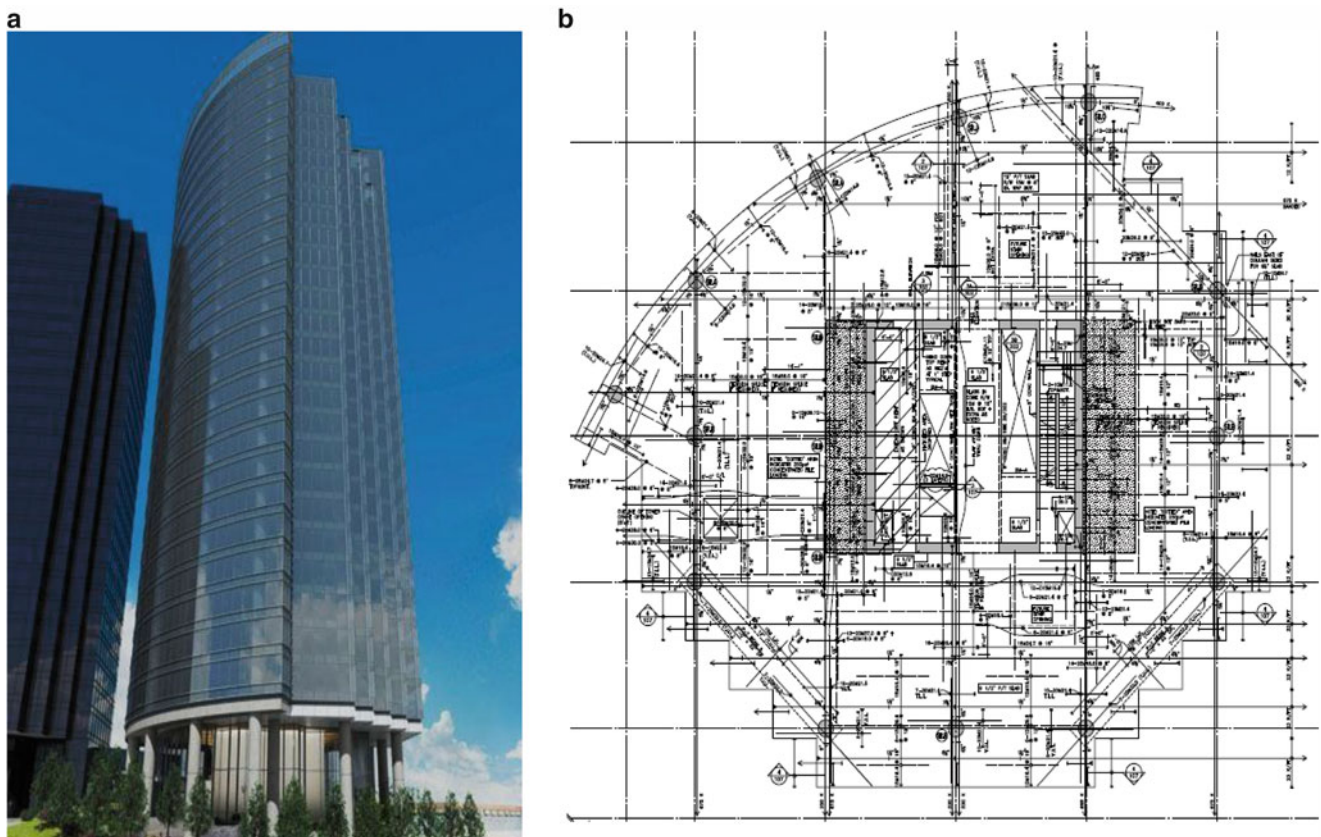
Fig. 2.1 Photo of the investigated building (**a**) and one of its typical floor plans (**b**)

2.2 Experimental Phase

By having a minimum of two transducers at each floor, most of the natural modes of vibration of the building are captured. In fact, having two sensors is required for identification of the torsional modes. In order to capture the dynamic characteristics of the building, a reference transducer is placed on the roof, located closely to the core of the building, and kept recording for the duration of the test, while the other transducers are moved around and relocated to different floors of the building.

To monitor the velocity and acceleration of the structure, TROMINO® (Micromed) accelerometers were utilized to capture the characteristics of the building. The building is measured using 9 transducers, and in total, 10 setups were required to complete the measurements on all the floors. Each setup records for a duration of 40 min with the sampling rate of 128 Hz. It is worth mentioning that all transducers were set to record at 10 channels while connected to minimum 3 GPS satellites at a time during the measurements in all of the setups. Having the transducers acquire date, time, and location stamps from the GPS satellites allows for precise time synchronization between the devices, with accuracy of ± 0.001 ms.

Transducers are generally placed at opposing corners of the floor and record the movements in the X, Y, and Z directions. In this study, the translational modes in the NS and EW directions as well as the torsional modes of the building are of interest. Also, the building was instrumented all the way down to the foundation level, in order to detect the natural modes associated with the foundation rocking and sliding. The sketch shown in Fig. 2.2 illustrates the typical location of the transducers.

2.3 System Identification and Test Results

The extraction of the data from the TROMINO®s is through the software Grilla®. The software converts the binary data recorded by the transducers to ASCII format which is preferable for data analysis. Prior to any extensive analysis, the time history plots are developed in order to check the validity of the recorded data and point out any outliers or spikes which may later manipulate the results. In general, data validation is done through a series of developed MATLAB codes.

Fig. 2.2 Sensor locations in a
typical test setup
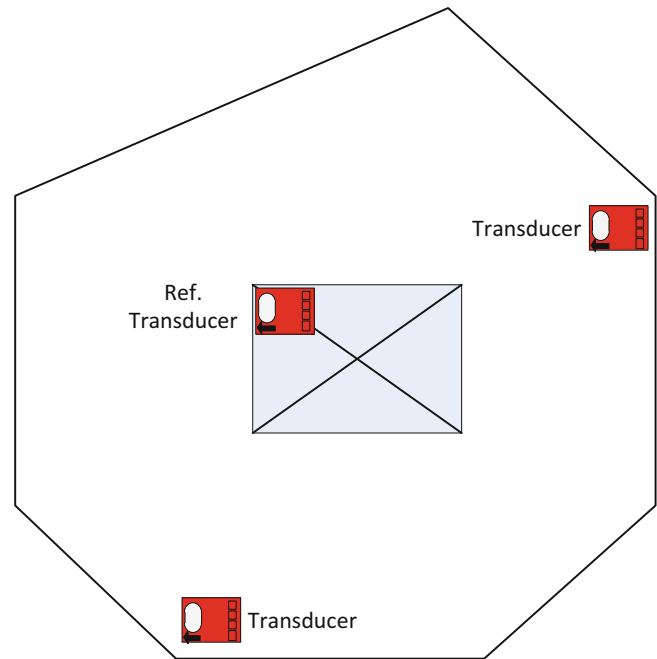
The ARTeMIS Modal Pro (SVIBS) software is used in order to perform the main signal processing, modal identification, and the mode shape validation for the structure studied. Data is filtered and decimated to decrease the noise to signal ratio and increase resolution. Additionally, the Band Pass type Butterwort filters are used to zoom into specific frequency bands in order to investigate the peaks one by one and distinguish the structural modes of vibration at each frequency range. The results are finally combined into one optimized SVD plot containing the outstanding structural natural frequencies.

The noise to signal ratio is greater in higher frequencies such that distinguishing between the structural and noise modes becomes extremely difficult at frequencies higher than 12 Hz. Thus, the decimation and filtering algorithms are optimized to give the highest resolution possible up to 12 Hz and frequencies higher than 12 Hz are eliminated from the modal estimation.

Initially, Frequency Domain Operating Deflection Shapes (ODS) technique is used in order to scan the frequency domain for possible mode shapes. Then FDD, EFDD, and CFDD techniques are utilized to identify the specific natural frequencies by the peak-picking method. Finally, the ODS method is again performed in order to validate the deflected mode shapes.

In addition to the mentioned techniques used in the system identification process, the modes considering rocking and sliding of the building foundation have been investigated using only the FDD method. The results obtained using each mentioned technique are compared and discussed in this paper, followed by a more extensive analysis presentation for the foundation rocking and sliding for the building. Also, the appendix of the paper includes a series of photos and diagrams illustrating the test setups as well as the identified mode shapes for the buildings.

2.4 Frequency Domain Decomposition (FDD)

This technique approximately decomposes the response into a set of independent single degrees of freedom systems and performs singular value decomposition of the spectral density matrices [1]. The results of the processed data using the FDD technique are provided in Table 2.1.

Table 2.1 Identified frequencies using the FDD technique

Mode no.	Mode descriptions	Frequency (FDD) Hz	Mode complexity %
1	First translational mode in the Y-direction	0.50	0.30
2	First translational mode in the X-direction	0.53	1.87
3	First torsional mode	0.94	4.26
4	Second translational mode in the X-direction	1.95	5.97
5	Second translational mode in the Y-direction	2.28	31.80
6	Second torsional	2.58	14.99
7	Third translational mode in the X-direction	3.73	28.23
8	Third torsional mode	4.61	14.35
9	Third translational mode in the Y-direction	5.19	42.21
10	Fourth translational mode in the Y-direction	5.61	27.35
11	Fourth torsional mode	6.63	50.98
12	Fifth translational mode in the X-direction	7.29	36.66
13	Fourth translational mode in the Y-direction	8.20	46.67
14	Sixth translational mode in the X-direction	8.41	60.90
15	Fifth torsional mode	10.04	78.28
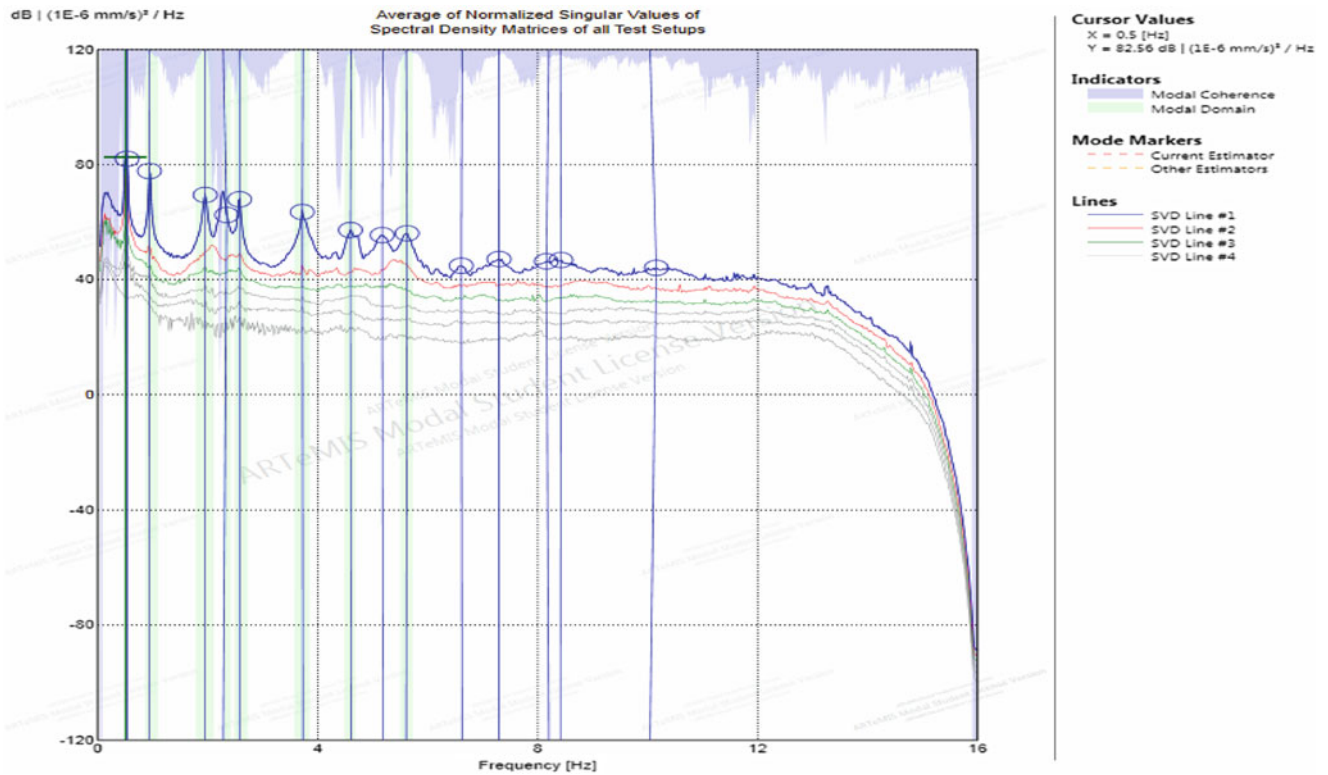
Fig. 2.3 Singular values of spectral density matrices of all test setups (FDD technique)

The singular values of the spectral density matrices of all test setups using the Frequency Domain Decomposition (FDD) technique are shown in the plot represented in Fig. 2.3.

2.5 Enhanced Frequency Domain Decomposition (EFDD)

The Enhanced FDD adds a modal estimation layer which is divided into two steps. The first step is to perform the FDD Peak Picking, and the second step is to use the FDD identified mode shapes to identify the Single-Degree-Of-Freedom (SDOF) Spectral Bell functions and from these SDOF Spectral Bells estimate both the frequency and damping ratio. The following

Table 2.2 Identified frequencies using the EFDD technique

Mode no.	Mode descriptions	Frequency (EFDD) Hz	Mode complexity %	Damping ratio %
1	First translational mode in the Y-direction	0.50	1.03	1.84
2	First translational mode in the X-direction	0.53	1.87	0.00
3	First torsional mode	0.94	2.26	1.08
4	Second translational mode in the X-direction	1.95	6.33	1.37
5	Second translational mode in the Y-direction	2.28	21.96	1.13
6	Second torsional	2.57	11.59	0.74
7	Third translational mode in the X-direction	3.74	25.43	1.27
8	Third torsional mode	4.61	8.81	1.32
9	Third translational mode in the Y-direction	5.18	30.11	1.15
10	Fourth translational mode in the Y-direction	5.60	23.28	1.13
11	Fourth torsional mode	6.61	48.69	0.00
12	Fifth translational mode in the X-direction	7.28	37.13	0.82
13	Fifth translational mode in the Y-direction	8.31	6.64	0.00
14	Sixth translational mode in the X-direction	8.44	53.22	0.00
15	Fifth torsional mode	10.14	76.44	0.00
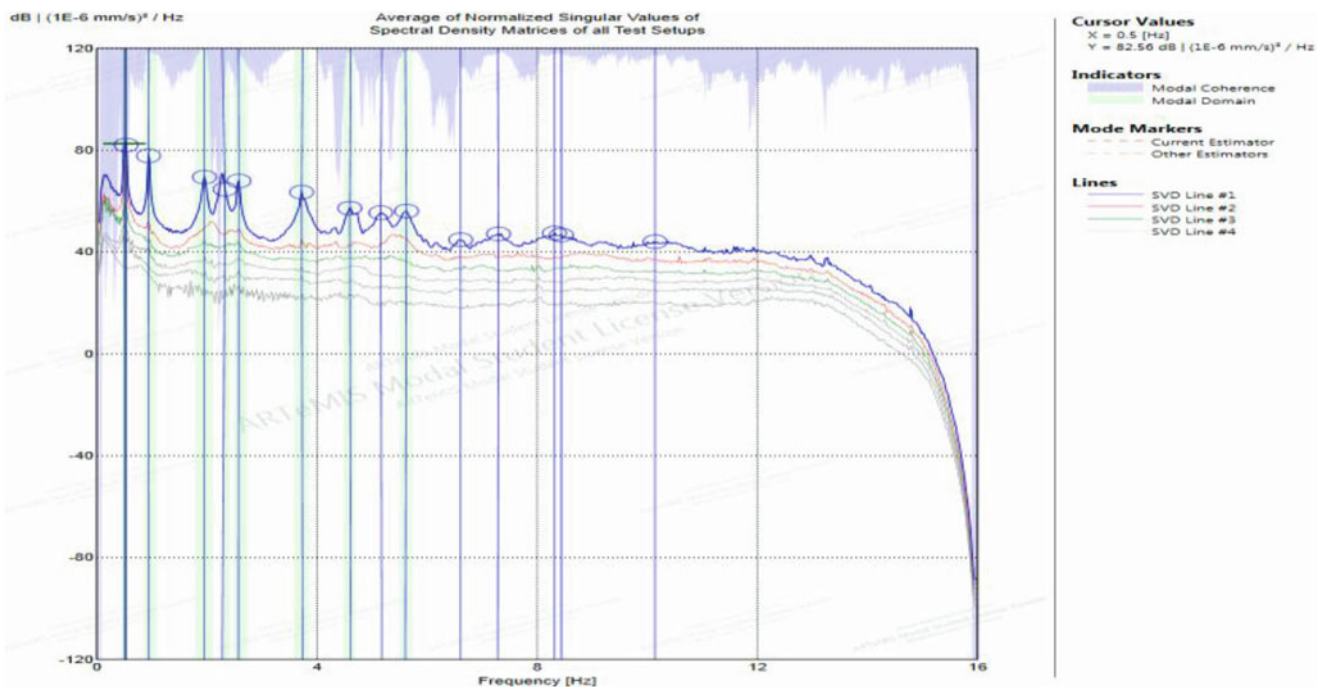
Fig. 2.4 Singular values of spectral density matrices of all test setups (EFDD technique)

table contains the calculated frequencies and damping percentages for the identified modes. The results of the processed data using the EFDD technique are provided in Table 2.2.

The singular values of the spectral density matrices of all test setups using the Enhanced Frequency Domain Decomposition (EFDD) technique are shown in the plot represented in Fig. 2.4.

2.6 Curve-Fit Frequency Domain Decomposition (CFDD)

The Curve-fit FDD is similar to the EFDD estimation. The natural frequencies and the damping ratios of the modes are estimated by curve fitting the SDOF Spectral Bell using frequency domain least-squares estimation.

Table 2.3 Identified frequencies using the CFDD technique

Mode no.	Mode descriptions	Frequency (CFDD) Hz	Mode complexity %	Damping ratio %
1	First translational mode in the Y-direction	0.50	0.30	0.00
2	First translational mode in the X-direction	0.53	1.87	0.00
3	First torsional mode	0.94	2.26	1.74
4	Second translational mode in the X-direction	1.95	6.33	0.96
5	Second translational mode in the Y-direction	2.28	21.96	0.85
6	Second torsional	2.57	11.59	0.46
7	Third translational mode in the X-direction	3.74	25.43	0.84
8	Third torsional mode	4.61	8.81	0.69
9	Third translational mode in the Y-direction	5.16	47.55	0.00
10	Fourth translational mode in the Y-direction	5.60	23.28	0.65
11	Fourth torsional mode	6.61	48.69	0.00
12	Fifth translational mode in the X-direction	7.28	37.13	0.44
13	Fourth translational mode in the Y-direction	8.31	6.64	0.00
14	Sixth translational mode in the X-direction	8.44	53.22	0.00
15	Fifth torsional mode	10.14	76.44	0.00
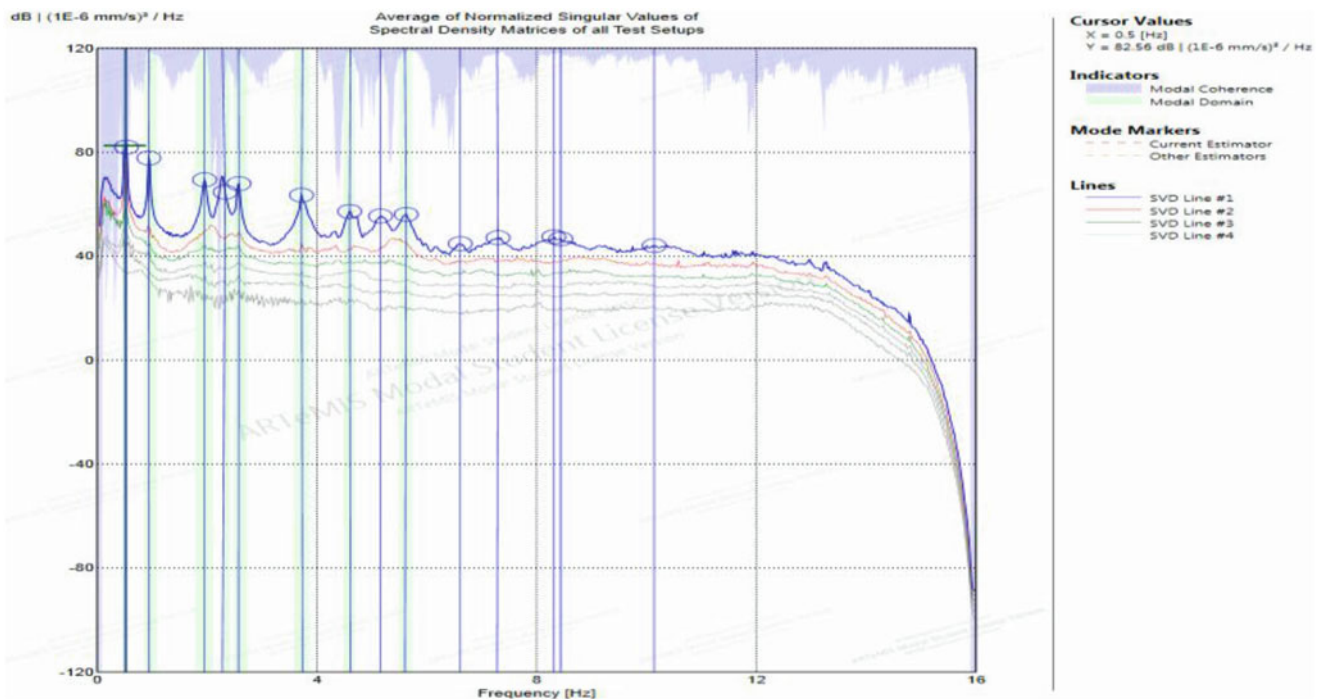
Fig. 2.5 Singular values of spectral density matrices of all test setups (CFDD technique)

Since the SDOF spectral bell is free of influence of other modes, there is only a single eigenvalue and residue to fit. The natural frequencies as well as the damping ratios are then extracted from the eigenvalues and are presented in Table 2.3.

The singular values of the spectral density matrices of all test setups using the Curve-fit Frequency Domain Decomposition (CFDD) technique are shown in the plot represented in Fig. 2.5 above.

2.7 Frequency Domain Operating Deflection Shapes (ODS)

An Operating Deflection Shape or ODS is the deflection of a structure at a particular frequency relative to a specific point, also known as the driving point, on the structure. The results of the processed data using the ODS technique are provided here in Table 2.4 below.

The singular values of the spectral density matrices of all test setups using the Frequency Domain Operating Deflection Shapes (ODS) technique are shown in the plot represented in Fig. 2.6 below.

Table 2.4 Identified frequencies using the frequency ODS shape technique

Mode no.	Mode descriptions	Frequency (ODS) Hz	Mode complexity %
1	First translational mode in the Y-direction	0.50	10.52
2	First translational mode in the X-direction	0.53	1.87
3	First torsional mode	0.94	2.54
4	Second translational mode in the X-direction	1.95	6.32
5	Second translational mode in the Y-direction	2.28	26.47
6	Second torsional	2.58	12.03
7	Third translational mode in the X-direction	3.72	27.58
8	Third torsional mode	4.61	9.88
9	Third translational mode in the Y-direction	5.17	50.11
10	Fourth translational mode in the Y-direction	5.63	32.13
11	Fourth torsional mode	6.61	31.02
12	Fifth translational mode in the X-direction	7.30	41.94
13	Fourth translational mode in the Y-direction	8.31	84.50
14	Sixth translational mode in the X-direction	8.44	64.68
15	Fifth torsional mode	10.14	58.32
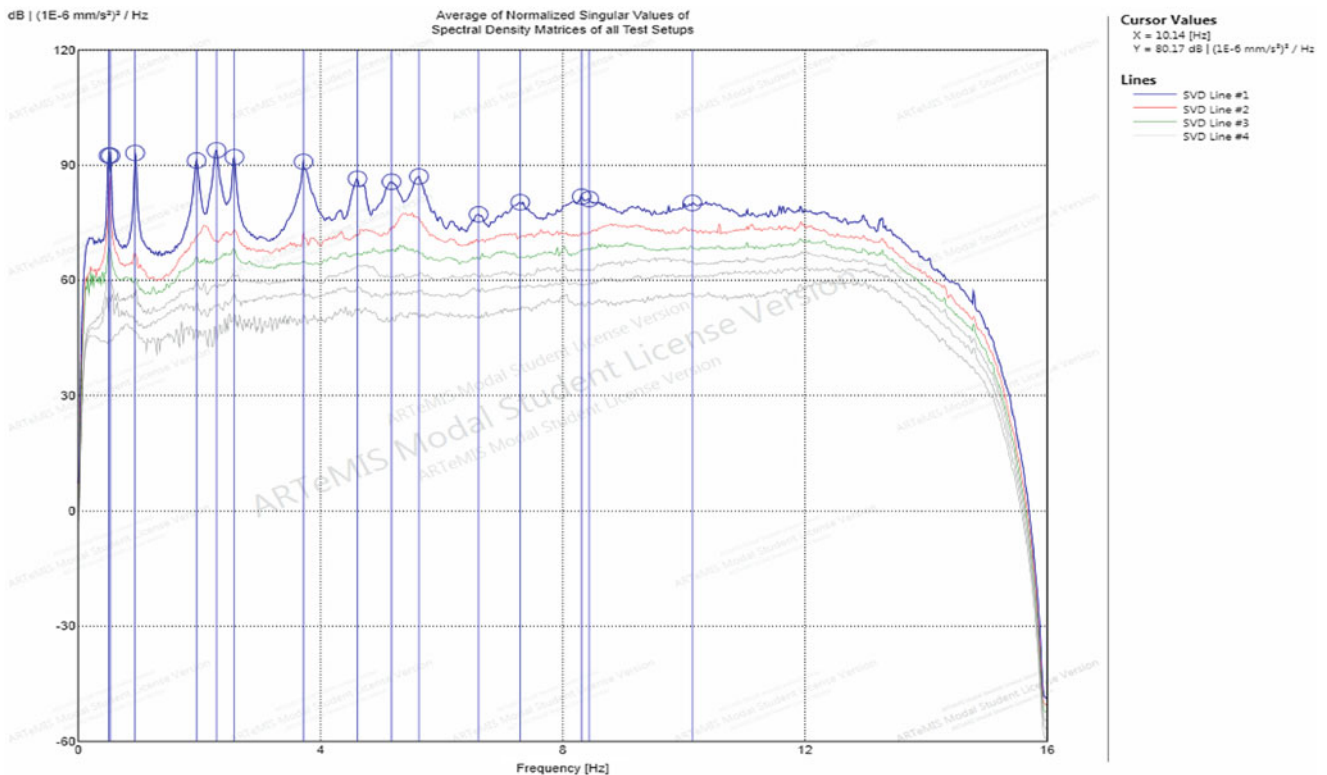
Fig. 2.6 Singular values of spectral density matrices of all test setups (FDODS technique)

2.8   Detecting the Foundation Rocking Components of the Modes

An enhanced modal estimation was performed using the frequency domain decomposition technique in order to identify the frequencies at which the vibration modes represent foundation rocking. Since considerable rocking components are expected to be detected in the very first fundamental modes at lower frequency ranges, a different filtering and decimation approach is utilized in order to identify these specific mode shapes.

For this purpose, only one of the measured test setups for this tall building is considered. Indeed, the only setup considered in this part of the study is a modified version of the test "Setup 8" which was recorded by 8 transducers all sitting on top of different foundations at the lowest parking level of the building. The locations of the main foundations are determined prior to the test, from the structural drawing sets.

The FDD plot shown in the Fig. 2.7 below is obtained after passing a series of *Band Pass* type *Butterworth* filters, in increasing orders, over the data, with no decimations. Then the peak-picking method was performed again in order to identify the modal frequencies for the rocking and sliding of the foundation.

In order to identify the proper mode shapes, the equations driving the building model in the ARTeMIS had to be modified such that a rigid body motion can be assumed throughout the height of the building. The data was filtered in different orders to minimize the noise content at the high frequency range. Table 2.5 below presents the modal frequencies obtained.
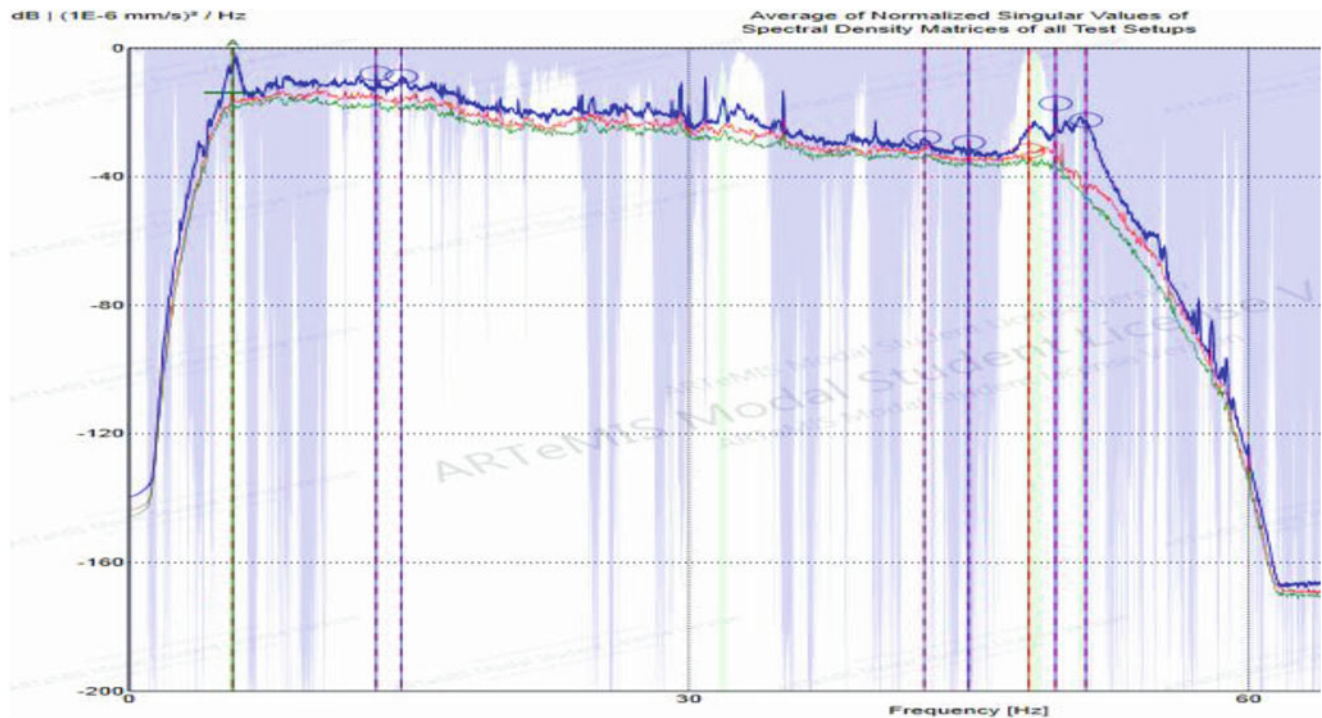
Fig. 2.7   Singular values of spectral density matrices of the rocking test setup

Table 2.5 Foundation rocking and sliding modes

		Frequency (FDD)	Rocking Component
Mode no.	Rocking Component	Hz	Y/N
1	Foundation rocking in the Y direction	0.51	Yes (strong)
2	Foundation rocking in the X direction	0.53	Yes (strong)
3	Foundation rocking in the X-Y direction	0.93	Yes
4	Foundation rocking in the Y direction	1.94	Yes
5	Foundation rocking in the X direction	2.26	Yes
6	Foundation rocking in the X-Y direction	2.60	No
7	Foundation rocking in the X direction	3.72	Yes (weak)
8	Foundation rocking in the X-Y direction	4.60	No
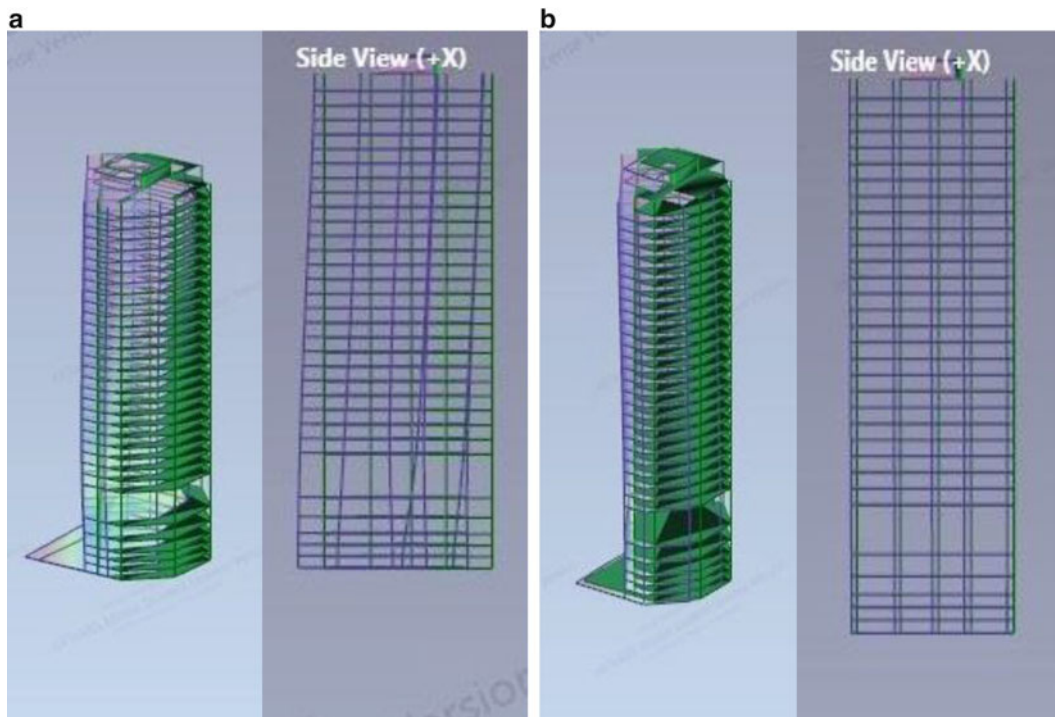
Fig. 2.8 Sliding (**a**) and rocking (**b**) mode shapes

Fig. 2.9 MAC values for the rocking and sliding modes of vibration
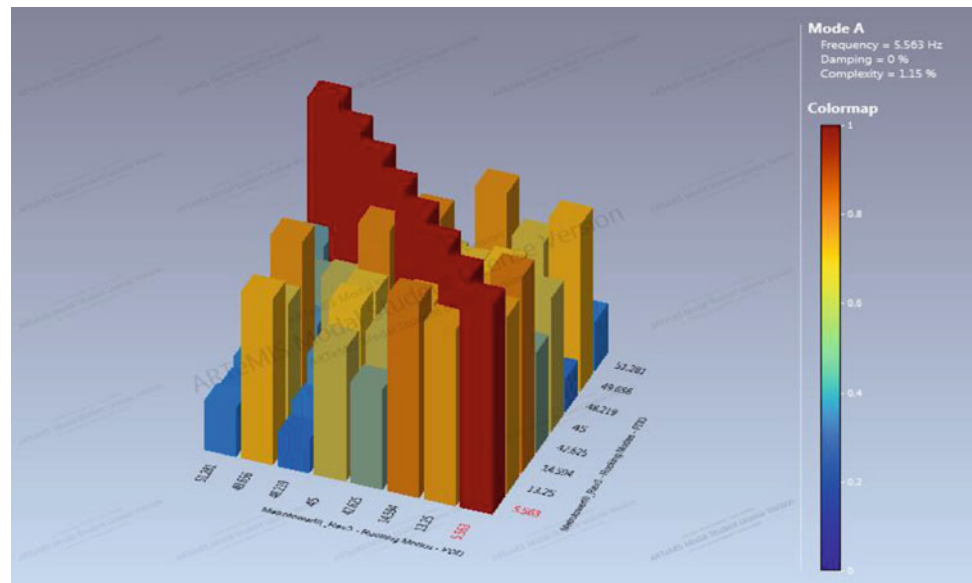
Typical rocking components of the structural mode shapes are presented in Fig. 2.8. Also, all of the mode shapes from the identified frequencies are presented in the appendix of the paper.

It is worth mentioning that when dealing with higher frequencies, identifying the modes become much more complex. Thus the reliability of the results might become lower. Therefore, Modal Assurance Criterion (MAC) values are also calculated for modal validation. Figure 2.9 represents the 3D graph of the MAC values calculated for these higher identified modes.

2.9 Summary of the Results and Discussion

The frequencies associated with the structural modes of vibration, obtained by the FDD, EFDD, and CFDD techniques, are summarized in Table 2.6. As it can be observed from the tabulated values, the results from the different modal analysis methods are very similar, increasing the confidence interval for the methodology.

It should be noted that there are always degrees of coupling between the modes, especially when dealing with higher frequency modes of vibration. For instant, the foundation rocking modes are observed to have significant coupling degrees with the first translational modes of vibration. Thus, in order to accurately identify the frequencies at which the foundation rocks, the ambient vibration records in the translational directions had to be deactivated in the model so that the vertical components of the records can be isolated and investigated separately, to confirm the rocking frequencies on the FDD plots. Also, the Stochastic Subspace Identification (SSI) can be strategically used in such sophisticated modal estimations.

The frequencies, and their corresponding periods, of the structural modes of vibration identified using the FDD technique are compared against the values obtained from the ETABS model of the building, created at the structural design phase. Table 2.7 summarizes the first 13 measured vibration modes along with the calculated modal periods and frequencies from the ETABS model of the structure.

As evident, the three methods are fairly similar in all of the identified modes of vibration. Also, the comparison between the frequencies, and their corresponding periods, from the test results with the ETABS model of the building reveals that generally the actual building has a much higher stiffness than the designed structure. Indeed, the ETABS values for the period are almost double their corresponding values from the test results. In general, this sort of difference holds true for most of the structures, but it can be justified by considering that the poured concrete usually has a higher mean strength than the specified minimum compressive strength which the structural designer prescribes for the main structural elements;

Table 2.6 Summary of the natural frequencies obtained using different FDD techniques

Mode no.	Mode descriptions	Frequency (FDD) Hz	Frequency (EFDD) Hz	Frequency (CFDD) Hz
1	First translational mode in the Y-direction	0.50	0.50	0.50
2	First translational mode in the X-direction	0.53	0.53	0.53
3	First torsional mode	0.94	0.94	0.94
4	Second translational mode in the X-direction	1.95	1.95	1.95
5	Second translational mode in the Y-direction	2.28	2.28	2.28
6	Second torsional	2.58	2.57	2.57
7	Third translational mode in the X-direction	3.73	3.74	3.74
8	Third torsional mode	4.61	4.61	4.61
9	Third translational mode in the Y-direction	5.19	5.18	5.16
10	Fourth translational mode in the Y-direction	5.61	5.60	5.60
11	Fourth torsional mode	6.63	6.61	6.61
12	Fifth translational mode in the X-direction	7.29	7.28	7.28
13	Fourth translational mode in the Y-direction	8.20	8.31	8.31
14	Sixth translational mode in the X-direction	8.41	8.44	8.44
15	Fifth torsional mode	10.04	10.14	10.14

Table 2.7 Modal periods and frequencies

Mode no.	FEM period s	Measured period s	FEM frequency Hz	Measured frequency Hz
1	4.471	2.00	0.224	0.50
2	4.205	1.89	0.238	0.53
3	2.43	1.06	0.411	0.94
4	1.096	0.51	0.912	1.95
5	0.792	0.44	1.263	2.28
6	0.757	0.39	1.321	2.58
7	0.563	0.27	1.776	3.73
8	0.398	0.22	2.512	4.61
9	0.357	0.19	2.800	5.19
10	0.316	0.18	3.166	5.61
11	0.259	0.15	3.864	6.63
12	0.242	0.14	4.129	7.29
13	0.192	0.12	5.203	8.20

this results in a higher building stiffness. Furthermore, based on most of the building codes, an *effective moment of inertial,* representing the cracked value for the concrete section, is used in the design phase. Thus, the designed structure is generally expected to show higher ductility, compared to what the test results show.

2.10   Concluding Remarks

System identification and modal characteristics of the reinforced concrete core building is determined by performing ambient vibration measurement tests using TROMINO® tri-axial transducers. Pre-processing of the data is performed using the MATLAB software, by transferring the time domain data into the frequency domain via Fast Fourier Transform algorithm. The data verification in the frequency domain is achieved by analyzing the data using different FDD techniques.

This paper would like to conclude that the utilized testing strategy would work very well for this tested tall building. The number of modes identified was beyond the expectation. However, recording at higher sampling rates, such as 256 Hz or higher, would have increased the resolution of the data. This could facilitate looking for specific information, especially at the higher frequency ranges. For example, modal estimation for foundation rocking and sliding would certainly be improved by an increased sampling rate. Also, taller buildings need to be recorded for longer durations of time in order to capture the low frequency contents with higher resolution [2]. Generally, longer signals are processed longer, but they reveal much more distinct information about the dynamics of the tested structure.

Appendix

This appendix, with respect to the order of presence of Figs. 2.10, 2.11, 2.12, 2.13, 2.14, 2.15, 2.16, 2.17, 2.18, 2.19, 2.20, 2.21, and 2.22, shows the ARTeMIS model of the building, all of the test setups, the deflected translational mode shapes, the torsional mode shapes, and the foundation rocking/sliding modes.
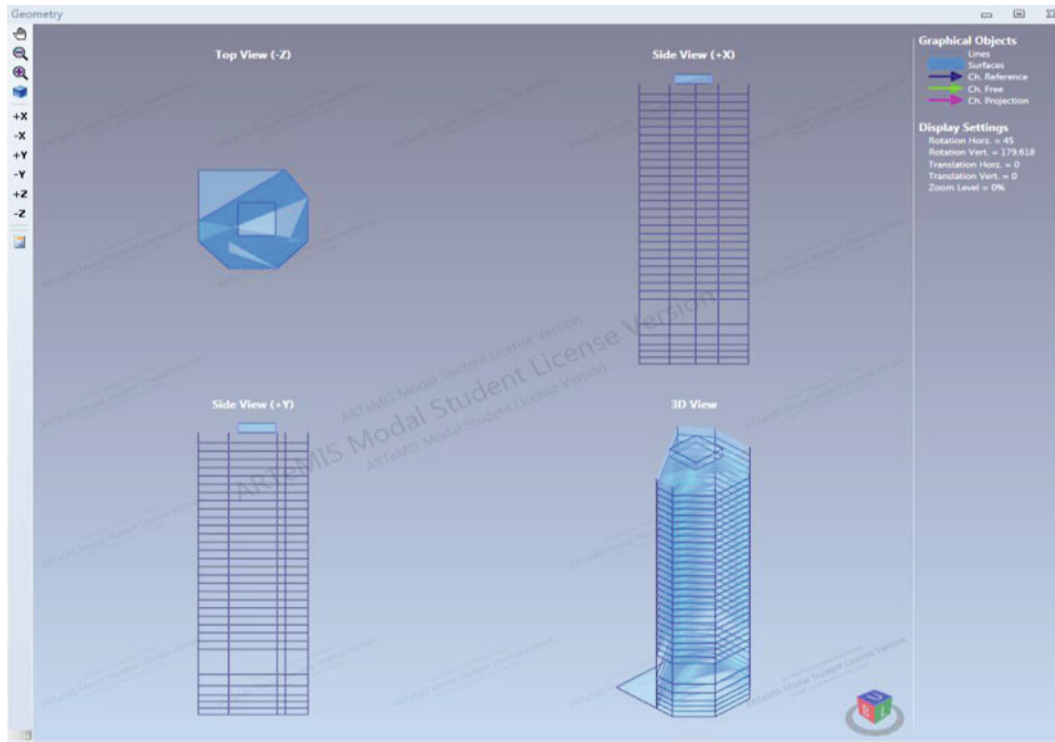
Fig. 2.10 ARTeMIS model of the tested building
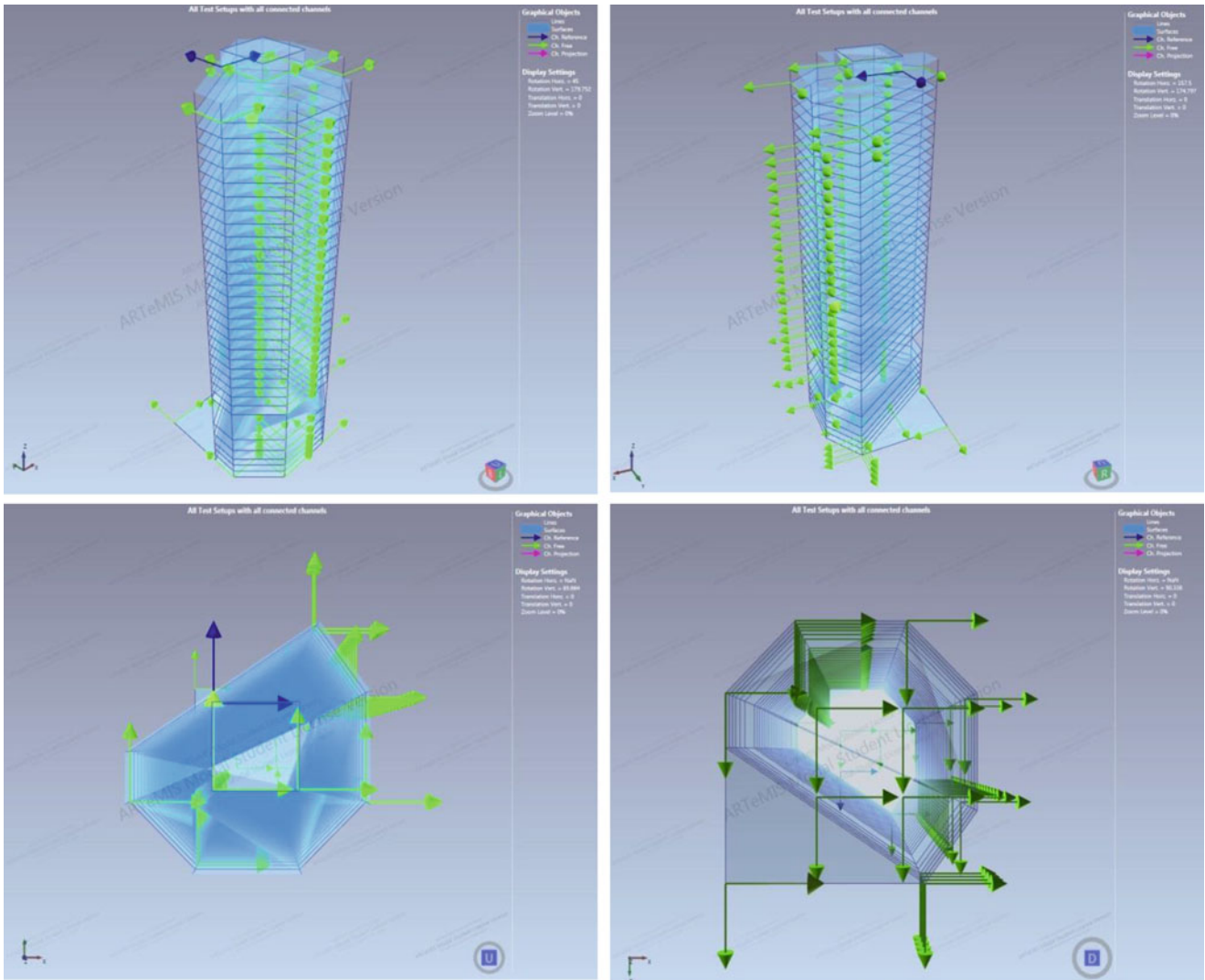
Fig. 2.11 Sensor locations and instrumentation for all the test setups
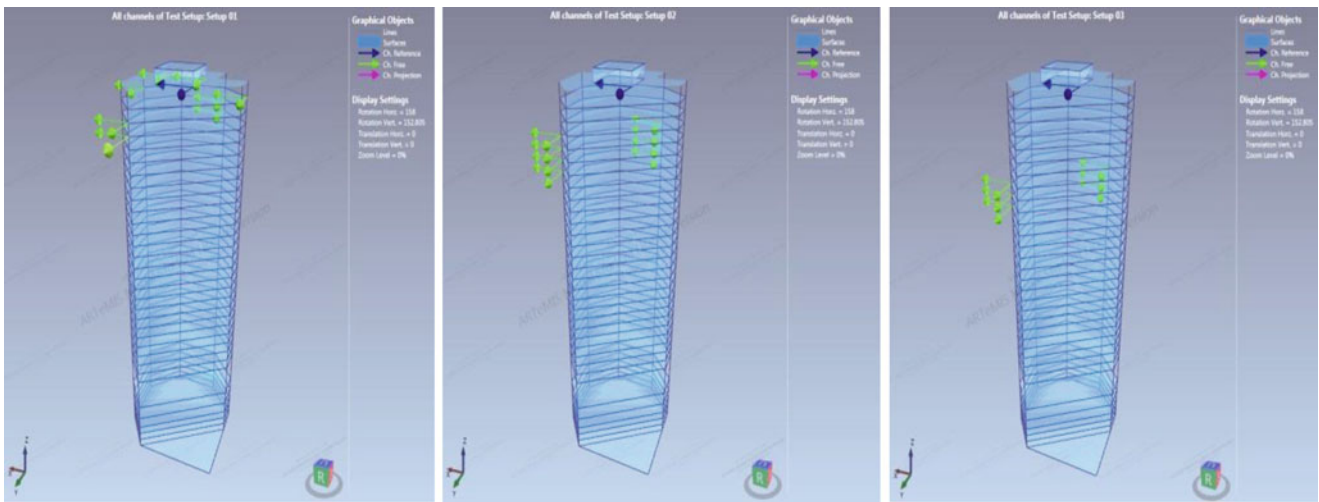
Fig. 2.12 Setup 01, 02, and 03
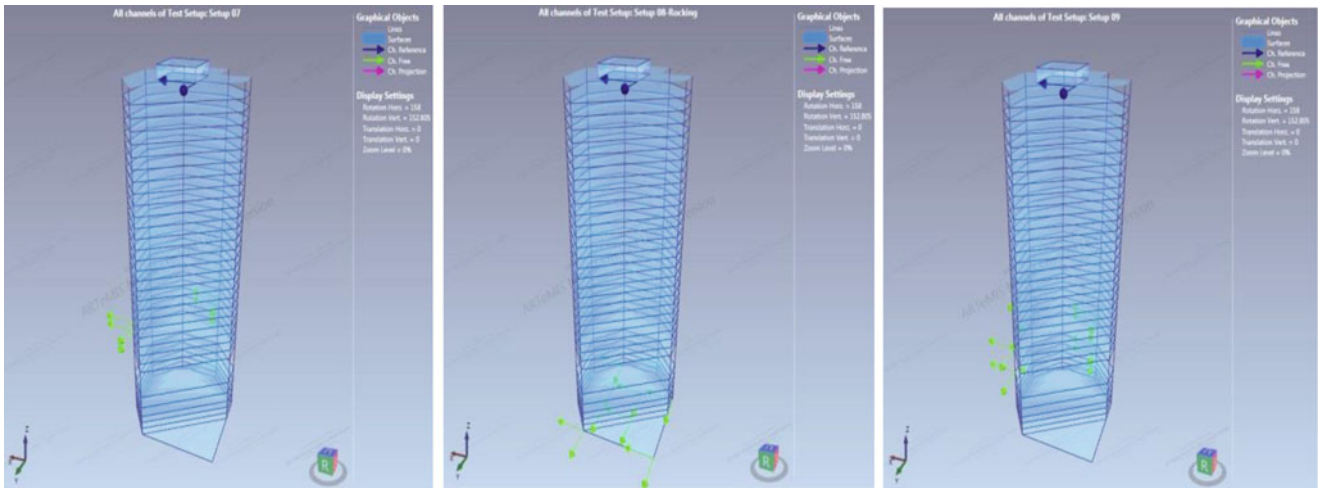
Fig. 2.13 Setup 04, 05, and 06
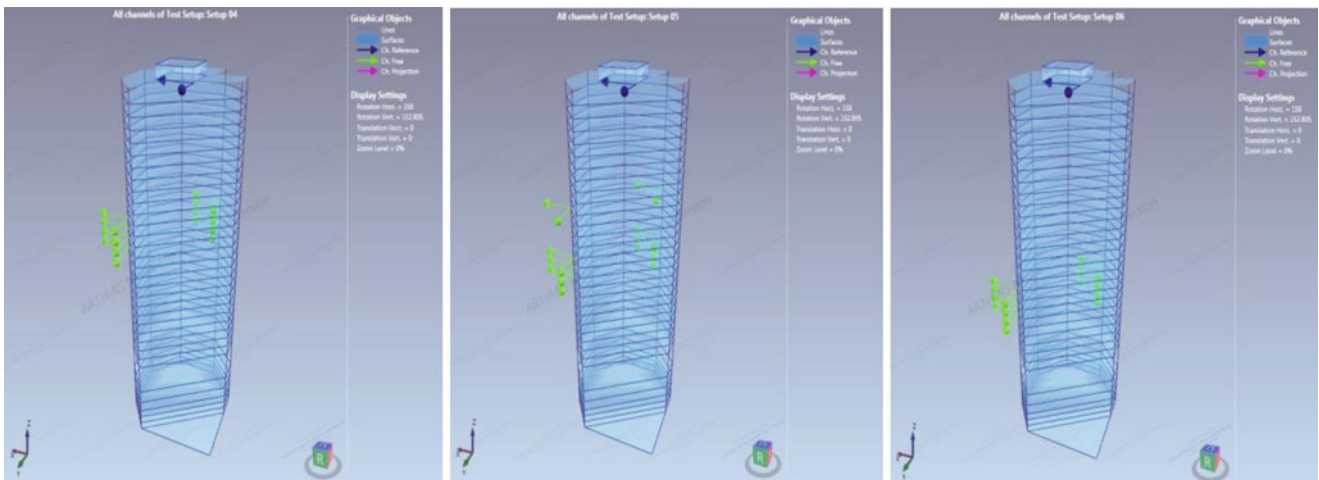
Fig. 2.14 Setup 07, 08, and 09

Fig. 2.15 Setup 10 – the specific setup for capturing the foundation rocking and sliding
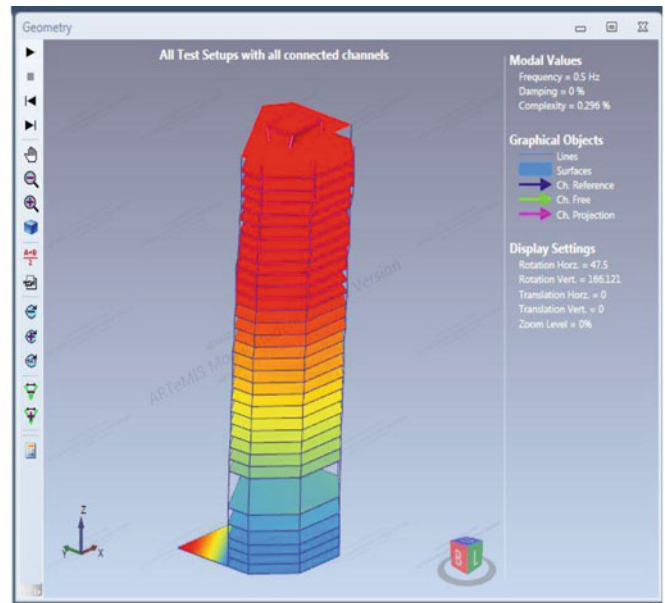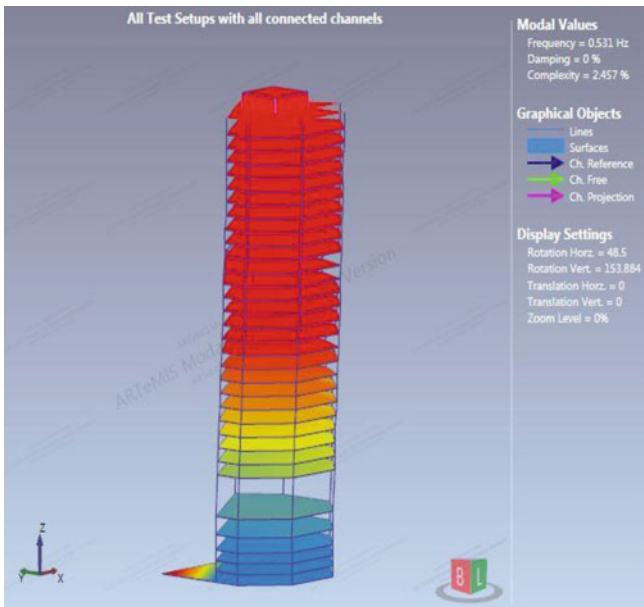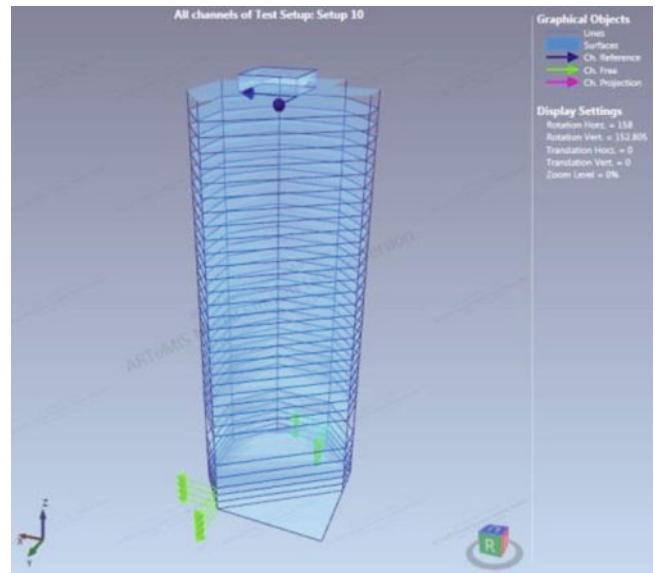
Fig. 2.16 Mode 1 – X and Y directions
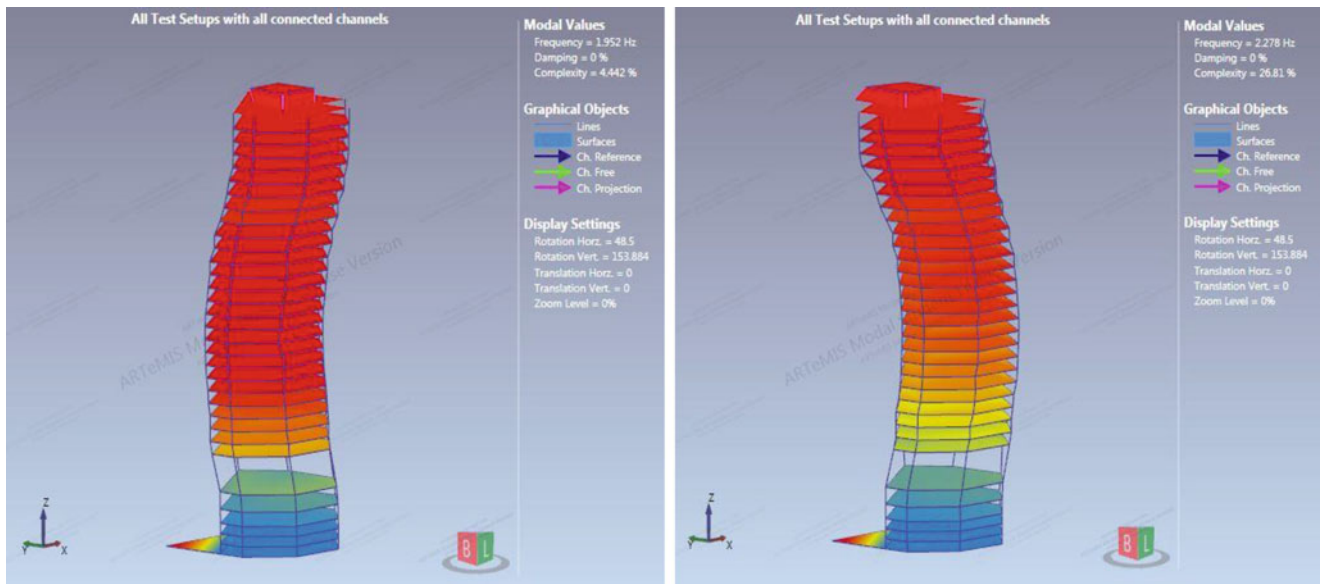
Fig. 2.17 Mode 2 – X and Y directions
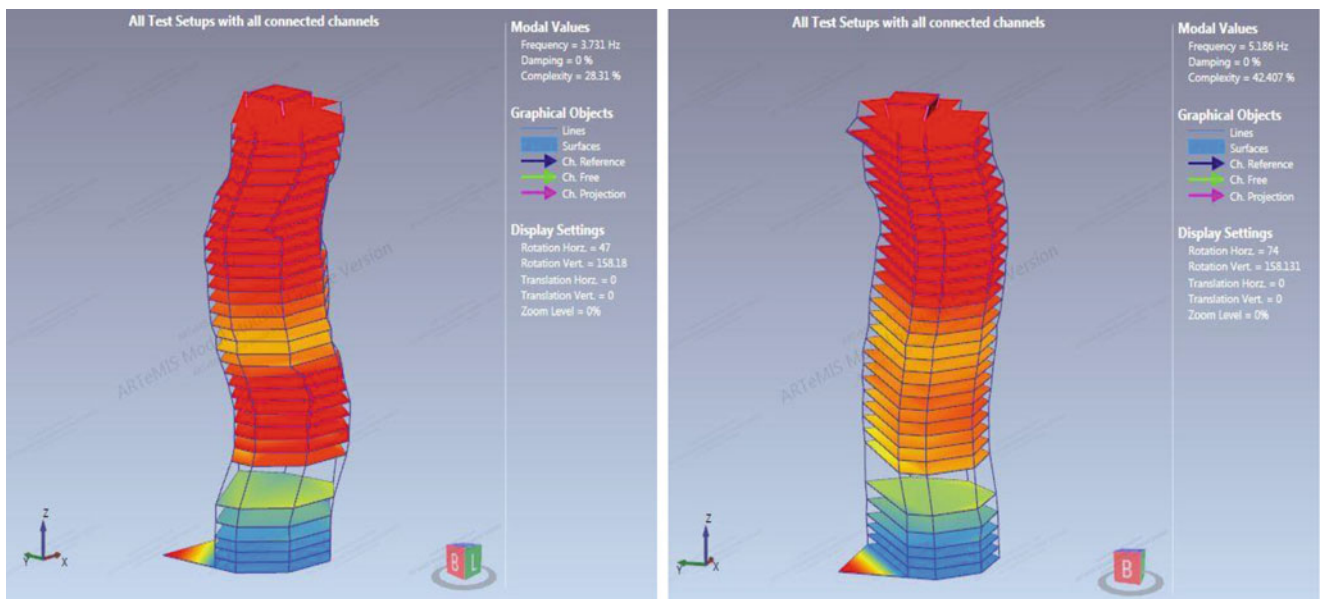
Fig. 2.18 Mode 3 – X and Y directions
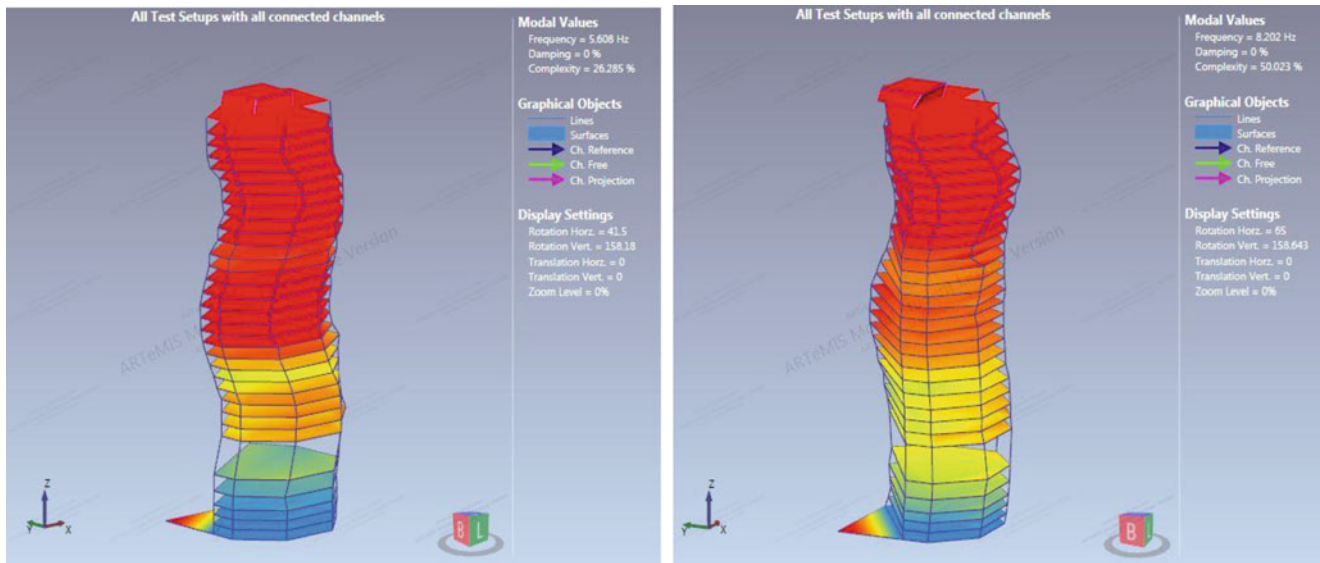
Fig. 2.19 Mode 4 – X and Y directions
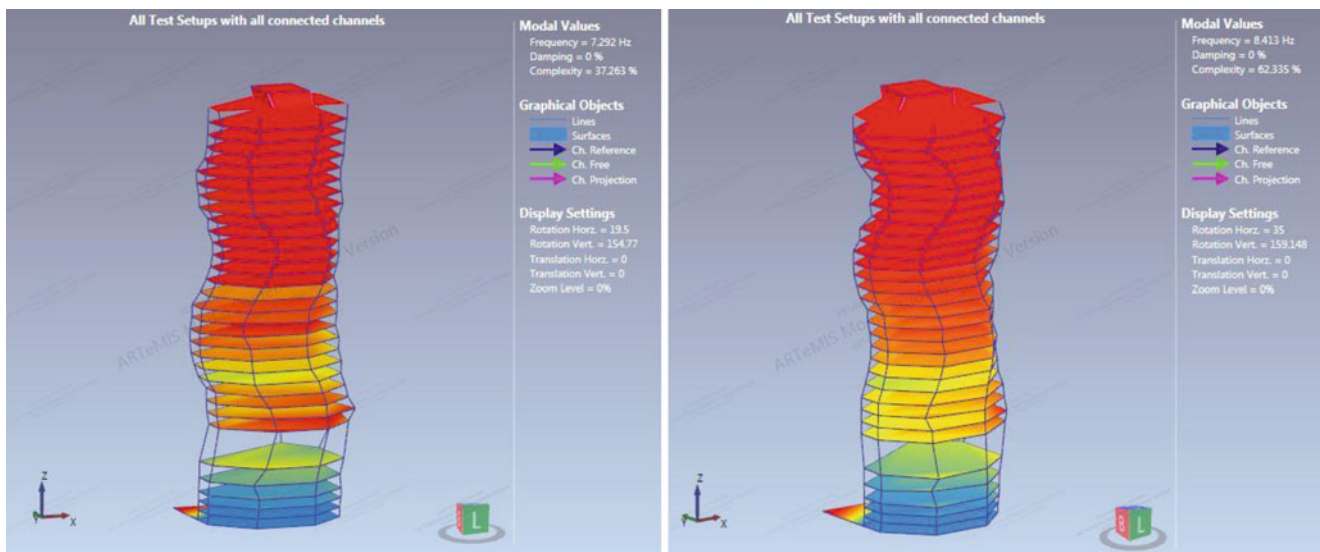
Fig. 2.20 Mode 5 and 6 – X directions
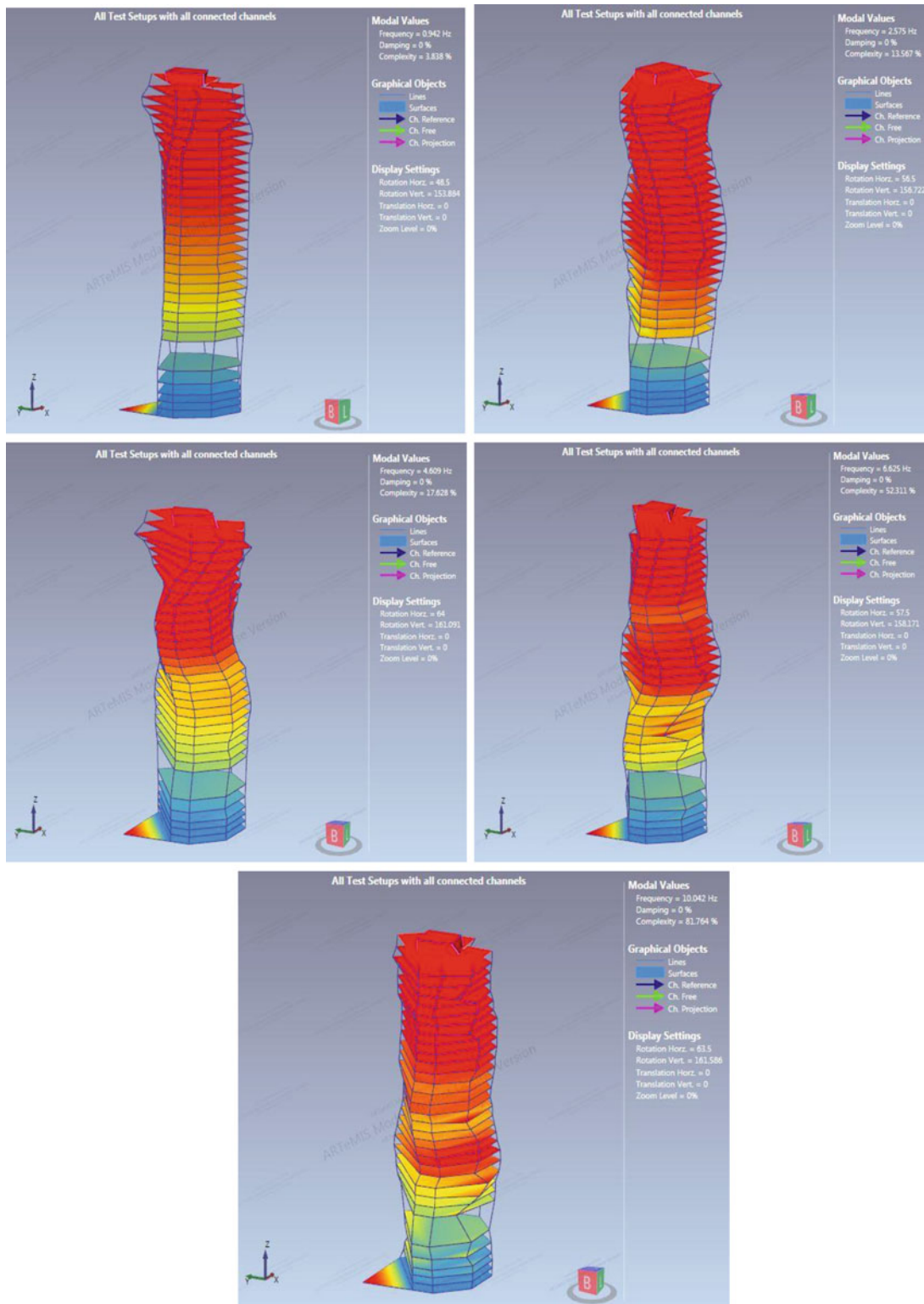
Fig. 2.21 Torsional mode 1, 2, 3, 4 and 5
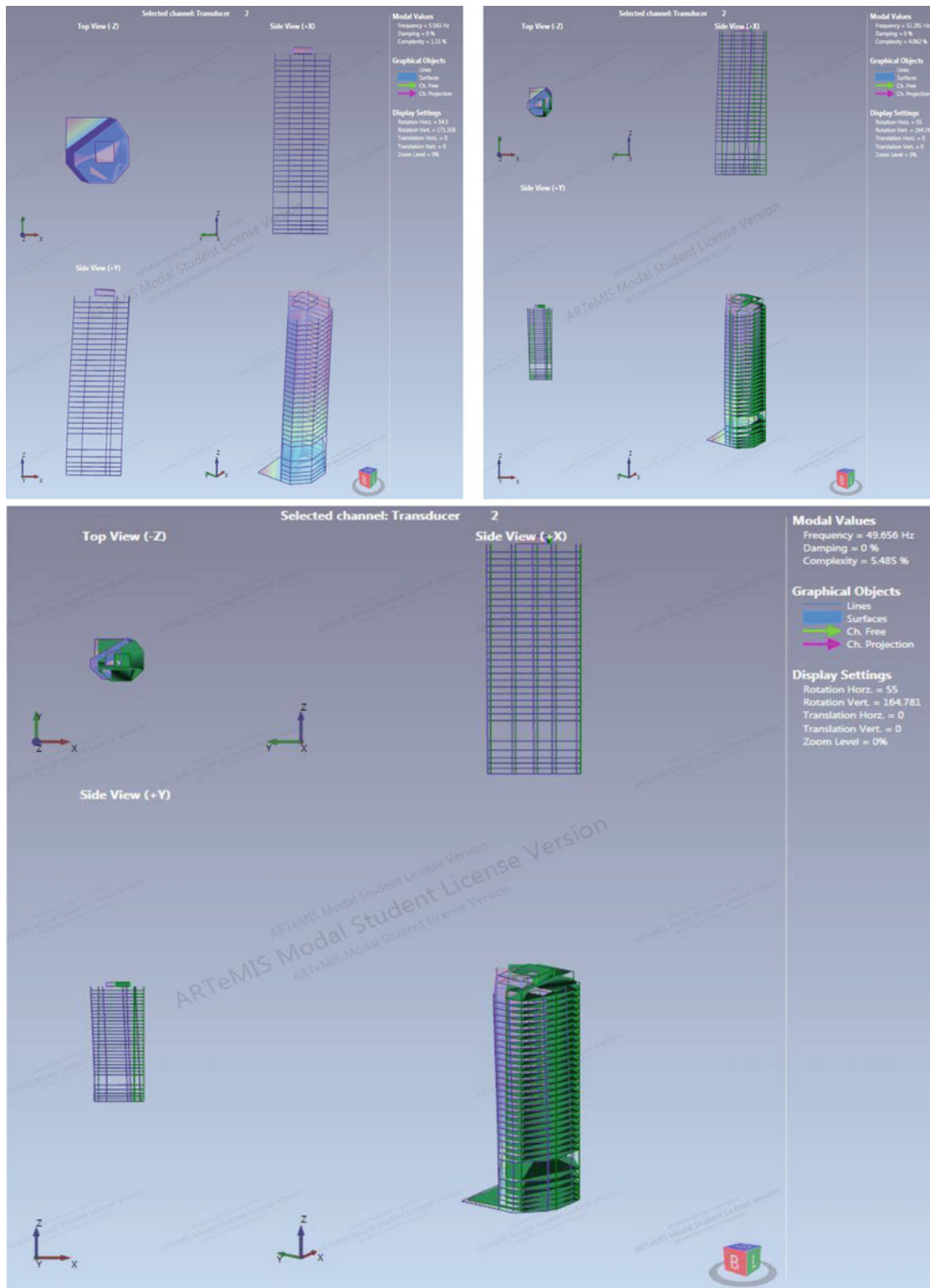
Fig. 2.22 Foundation rocking, sliding, and combined modes

References

1. Ventura CE, Brinker R (2001) FEM updating of the heritage court building structure. In: 19th international modal analysis conference (IMAC), Kissimmee, pp 324–330
2. Brinker R, Anderson P (2000) An indicator for separation of structural and harmonic modes in output-only modal testing. Struct Vibr Solut. www.svibs.com

Chapter 3
Ambient Vibration Testing of a 4-Storey Parking Garage

Ilaria Capraro, Yuxin Pan, Kieran Rollins, Wu Gao, and Carlos E. Ventura

Abstract This paper presents the results of ambient vibration tests performed on the 4-storey reinforced concrete Health Sciences Parkade at the University of British Columbia in Vancouver, Canada. Two tests were conducted in March 2014 under different operational conditions: for the first test, a detailed ambient vibration test, was conducted during normal operating conditions while in the second test, the data was acquired when the Parkade was almost empty, but only at a few locations.

The comparison between the results of the two tests shows that the frequency values are quite similar, even if the levels of vibration during the first test were much higher than those from the almost empty case. The vertical component of vibration was found to be predominant motion, showing a strong amplification of the vibrations due to traffic. The results also show that the "added" mass due to the presence of the cars did not significantly affect the modal frequencies.

The Frequency Domain Decomposition (FDD) and the Stochastic Subspace Identification (SSI) were used to estimate the dynamic parameters of the structure. A total of six modes were identified within the frequency range of 2–8 Hz, and all showed a significant 3D response. The natural frequencies and mode shapes from each technique have been compared and the similarities and differences are further discussed in the paper.

Keywords Ambient • Vibration • Modal • Analysis • Operational

3.1 Introduction

In this paper, the results of ambient vibration testing on the Health Science Parkade at the University of British Columbia (UBC) in Vancouver, Canada, are presented. The main purpose of this experimental work was to determine the dynamic properties of the structure, including natural frequencies, mode shapes and modal damping, in order to investigate the possible seismic behavior of the Parkade and evaluate the potential necessity for seismic retrofit. The experimental tests were conducted by graduate students of the Department of Civil Engineering of the University of British Columbia in Vancouver, Canada.

The Health Sciences Parkade is essentially formed by two 4-storey reinforced concrete buildings which are connected by sets of three parking ramps at each level. The north building also has a basement level, which is used as a storage area by UBC Parking Services. The lateral force resisting system is composed primarily of shear walls and a moment resisting frame system. The shear walls extend from the ground level to the top floor. At the basement level there are additional internal and external shear walls that provide increased lateral stiffness at that level. Moreover, the height of the external shear walls is only about half of the available storey height, which leads to potentially detrimental short column effects. This stiffness irregularity in elevation can be clearly appreciated in Fig. 3.1. This figure shows the north elevation of the Parkade at the intersection between East Mall and Hospital Lane streets.

I. Capraro (✉) • Y. Pan • K. Rollins • W. Gao • C.E. Ventura
Department of Civil Engineering, The University of British Columbia, 6250 Applied Science Lane, Vancouver, BC V6T 1Z4, Canada
e-mail: icapraro@civil.ubc.ca

Fig. 3.1 North elevation of the
Parkade taken from East Mall
and Hospital Lane intersection

3.2 Ambient Vibration Tests

The first set of ambient vibration test on the Health Science Parkade was obtained on Friday March 14th 2014 by a group
of three UBC graduate students. The test was performed from 9 a.m. until 5 p.m. During this period, the Parkade was
experiencing a high level of traffic, typical of normal operational conditions.

A total of nine Tromino recorders were available to perform the test. One was kept as reference sensor and positioned at the
northwest corner on the second floor. The remaining instruments were roving sensors and were relocated from floor to floor.
The test setup configuration remained constant throughout. At each level, a consistent vertical alignment was maintained in
combination with a consistent orientation according the construction north provided in the structural drawings. The location
and orientation of the sensors during the complete ambient vibration test are shown in Fig. 3.2. The sensors were equipped
with short spikes to be leveled at each position and the time synchronization between each other was done using by the
internal GPS built-in into each sensor.

The data was recorded for each setup for duration of 40 min at a sampling rate of 256 samples per second (sps) and stored
in the internal memory of the Tromino in binary form.

3.3 Data Processing

The recorded data was processed and analyzed using the commercial computer program ARTeMIS Modal, Version 3.0 [1].
A test model was built according to the geometry of the building. Due to the complex geometry of the structure and in order
to better identify the form of the mode shapes, the height of each story in the test model was doubled with respect to the
actual dimensions. The test model is shown in Fig. 3.3. Given the high amplitude of vertical vibrations, and because the focus
of this study was on the lateral vibration, the data from the vertical channels was not included in the analysis.

In order to evaluate natural frequencies, mode shapes and modal damping, the analysis was performed with two different
techniques: Frequency Domain Decomposition (FDD) for the frequency domain and the Unweighted Principal Component
Stochastic Subspace Identification (UPC-SSI) for the time domain.

The data acquired from the ambient vibration tests was transferred via USB cable to a pc. Using the Software Grilla [2],
provided by the supplier of the Tromino instruments, the data was then re-sampled to 128 Hz, and then synchronized using
the software package GEOPSY V 2.7.4 [3] and then saved in ASCII format files. This re-sampling was necessary due to
synchronization issues inherent in the program Grilla.
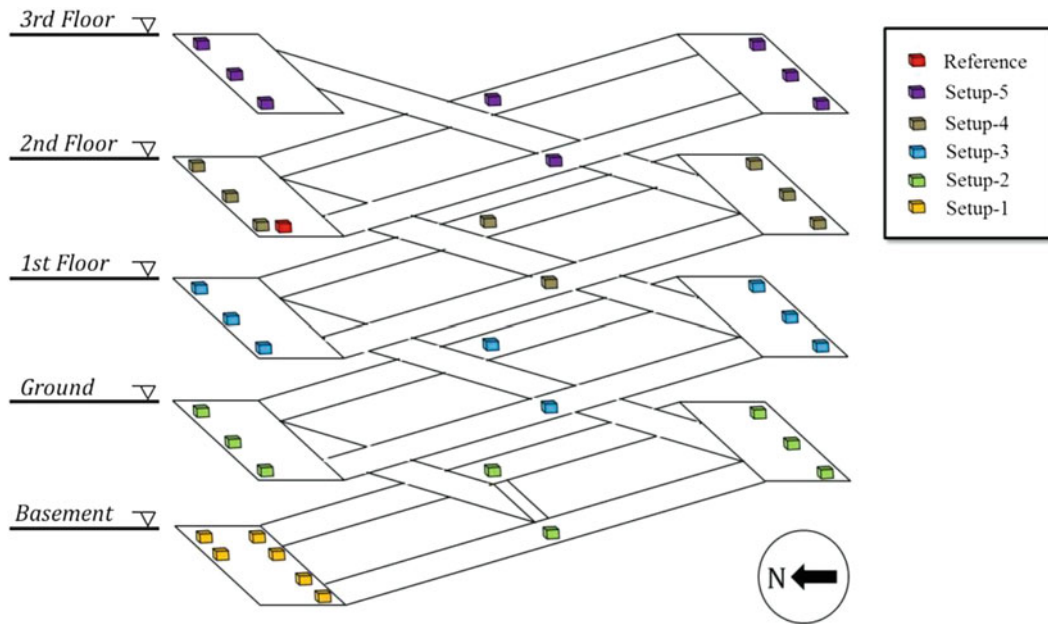
Fig. 3.2 Setups configuration of the ambient vibration test
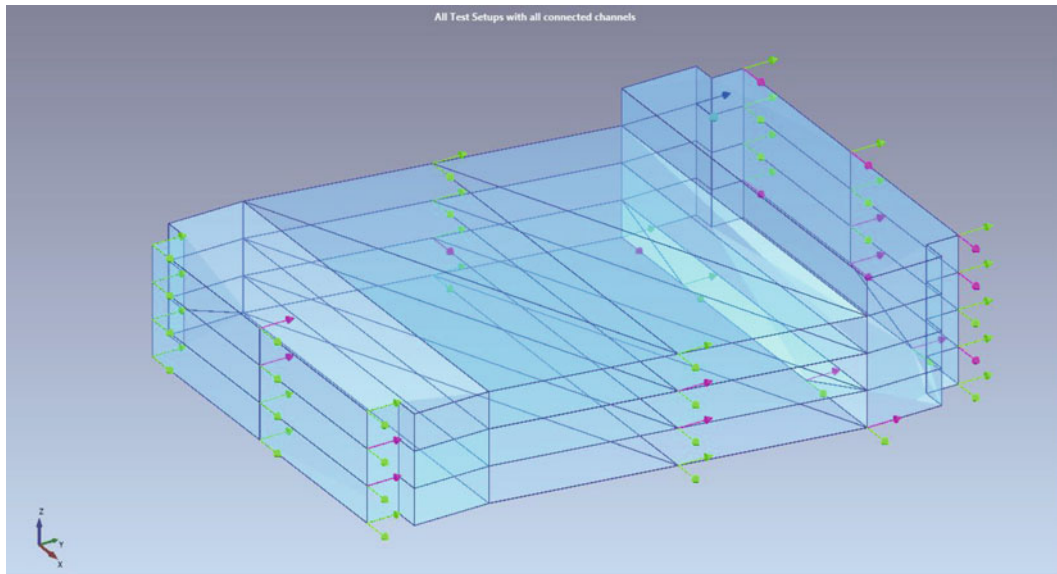
Fig. 3.3 All setups with horizontal channels connected

The analysis was performed first using the FDD technique setting the number of frequency lines to 1,024 and selecting a total of six projection channels. Decimation was applied to focus on a frequency range from 0 to 32 Hz. The plot of the average of Normalized Singular Values of the Spectral Density Matrices of all setups is given in Fig. 3.4. The natural frequencies were estimated first through the peak picking of the average normalized values of the spectral density matrices.

A total of six modes were identified with confidence up to a frequency of 8 Hz. The fundamental mode corresponds to a longitudinal mode in the N-S direction at a frequency of 2.756 Hz; and the first torsional mode has a frequency of 3.894 Hz. The first transversal mode in the E-W direction has a frequency of 4.413 Hz and the fourth mode, a second mode in torsion, has a frequency of 5.781 Hz.

Fig. 3.4 FDD, average of normalized singular values of spectral densities matrices of all setups
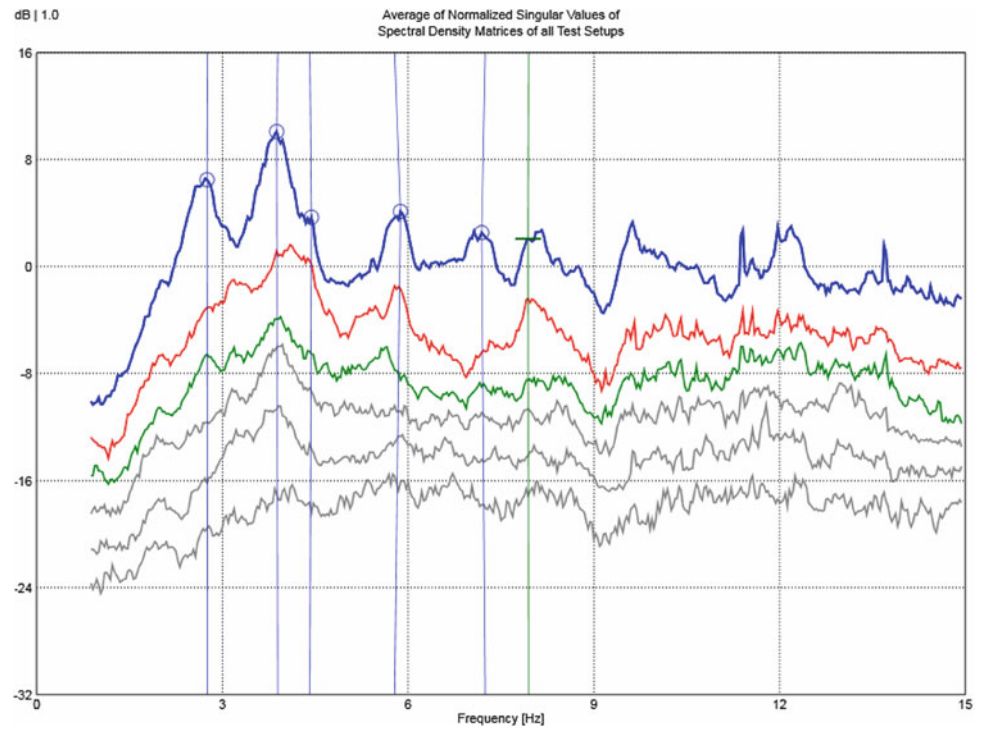
Fig. 3.5 First longitudinal mode, N-S direction, at 2.756 Hz
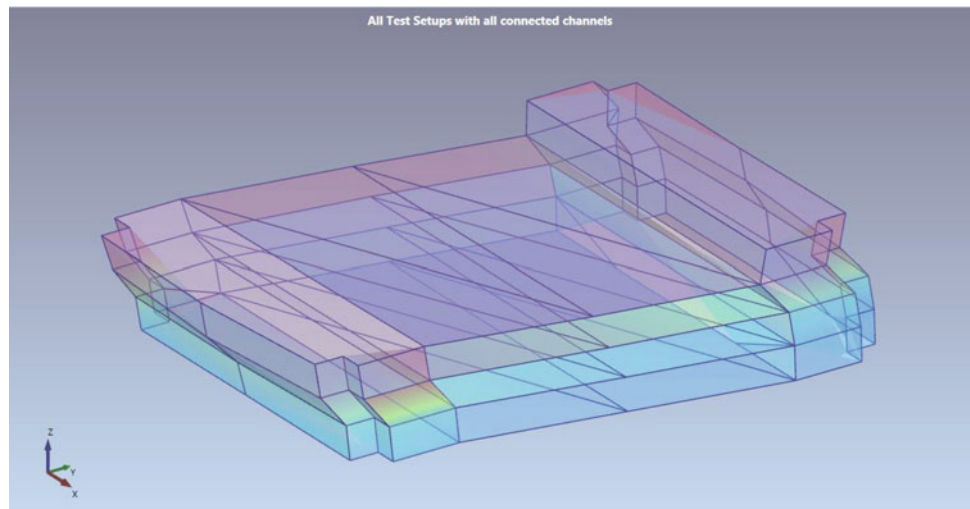
In Figs. 3.5, 3.6, 3.7 and 3.8 the first four mode shapes are represented.

The six modes identified with the FDD were also identified with the SSI-UPC technique. As a reference, a plot of the Stabilization Diagram of the estimated State Space Model for Setup 4 is given in Fig. 3.9. For each mode, natural frequency as well as modal damping was evaluated.

Table 3.1 presents a comparison between the frequencies obtained using the two different techniques. Damping estimates resulted in unusually high numbers, but these are not presented here as further analysis of the data may be required to confirm if these values are indeed that high. Other analysis techniques will be used to verify these numbers.

Fig. 3.6 Second mode, torsional, at 3.894 Hz
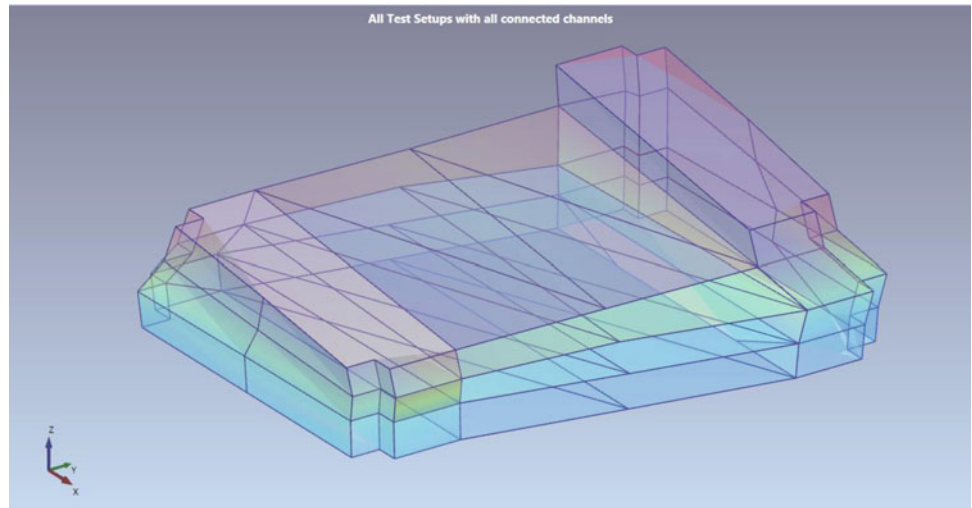
Fig. 3.7 Third mode, transversal in E-W direction, at 4.413 Hz
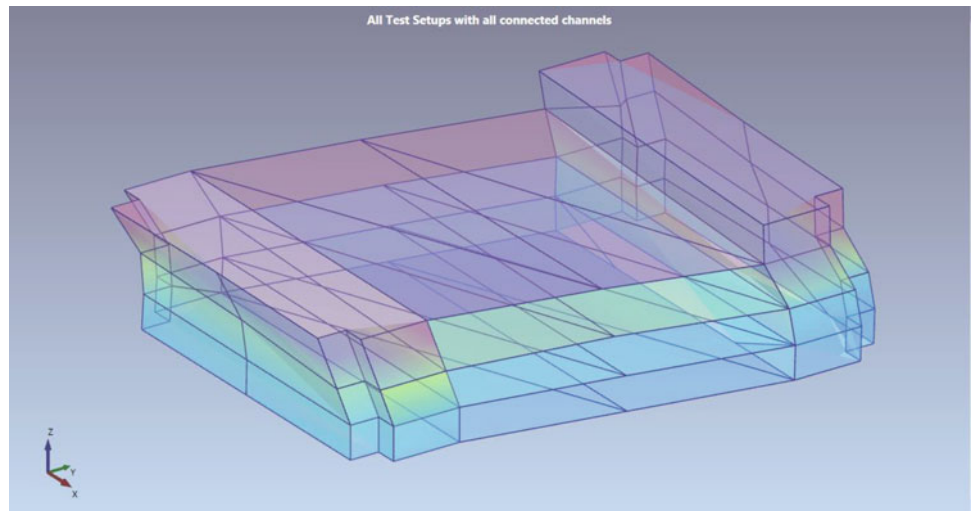
Fig. 3.8 Fourth mode, second torsional, at 5.781 Hz
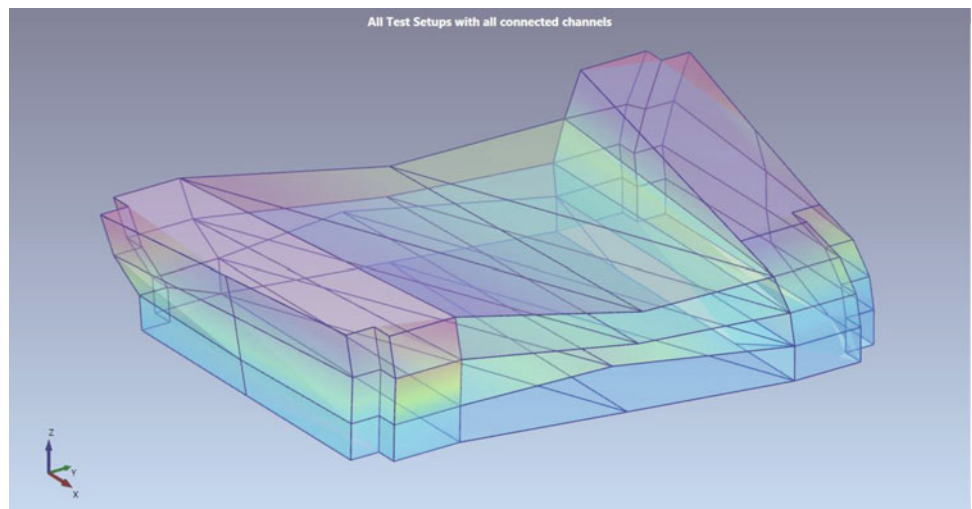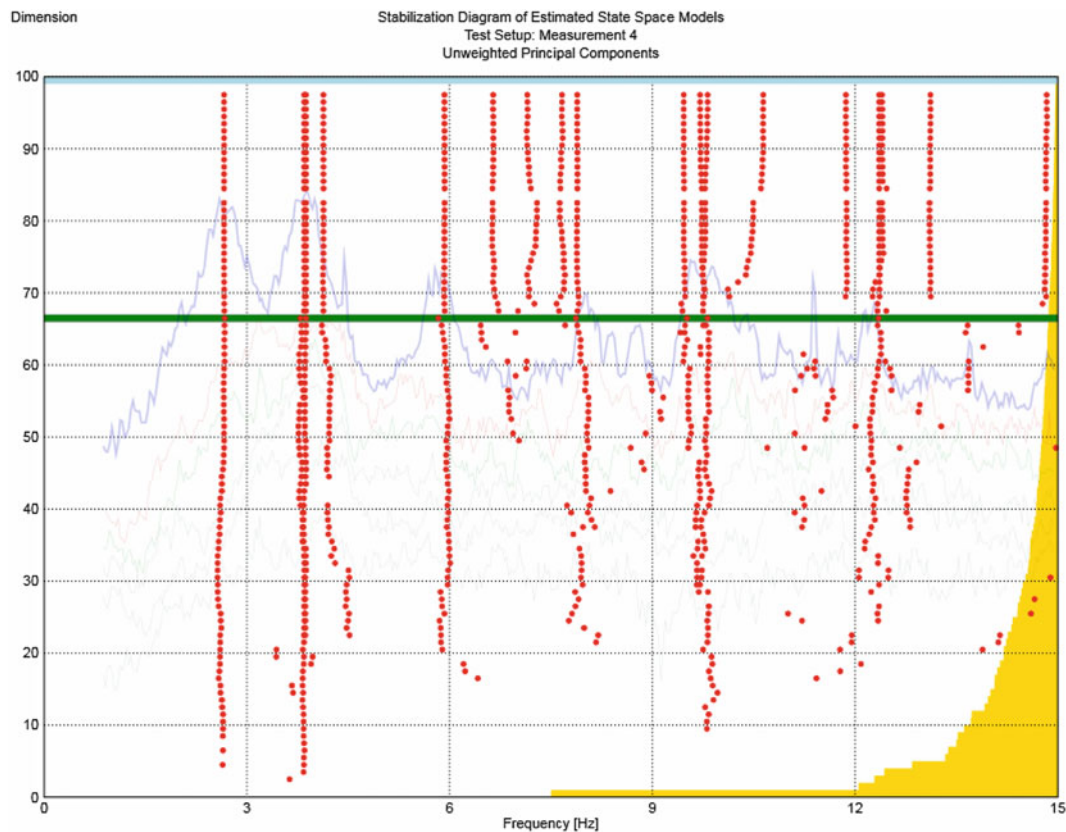
Fig. 3.9 SSI-UPC, stabilization diagram of estimated state space models for setup 4

Table 3.1 Comparison of the results obtained with FDD and SSI-UPC

| Mode # | Frequency [Hz] | | Comment |
	FDD	SSI – UPC	
1	2.756	2.607	First N – S longitudinal
2	3.894	3.863	First torsional
3	4.413	4.132	First E – W transversal
4	5.781	5.923	Second torsional
5	7.244	7.148	Second N – S longitudinal
6	7.944	7.891	Third N – S longitudinal

3.4   Effect of Mass of Vehicles

The second ambient vibration test was conducted on March 17th 2014 late in the day when very few cars were using the Parkade. During the test, a single Tromino sensor was placed at the same location and orientation as the reference Tromino in the first ambient vibration test. The data was acquired at a sampling frequency of 256 sps and the duration of the recording was also 40 min.

The spectra for the recorded velocities were computed with a Fast Fourier Transform (FFT) implemented using MATLAB [4]. Figure 3.10 shows the comparison between the spectra for each different channel: N-S direction, E-W direction and Vertical channel, respectively.

From the FFT comparison it can be seen that the frequency spectrum obtained from the reference sensor during the complete ambient vibration test is quite similar to the one obtained with the test conducted when the Parkade is almost empty. The first natural frequency is about 12 % higher and was obtained in a noisy environment when the traffic was present. As confirmed in past studies [5], the vertical component of vibration was predominant at frequencies between 10 and 20 Hz, showing a strong amplification of the vibration due to traffic load. The change in mass on the structure between the two tests due to the presence of the cars didn't affect significantly the lateral frequencies of the structure.
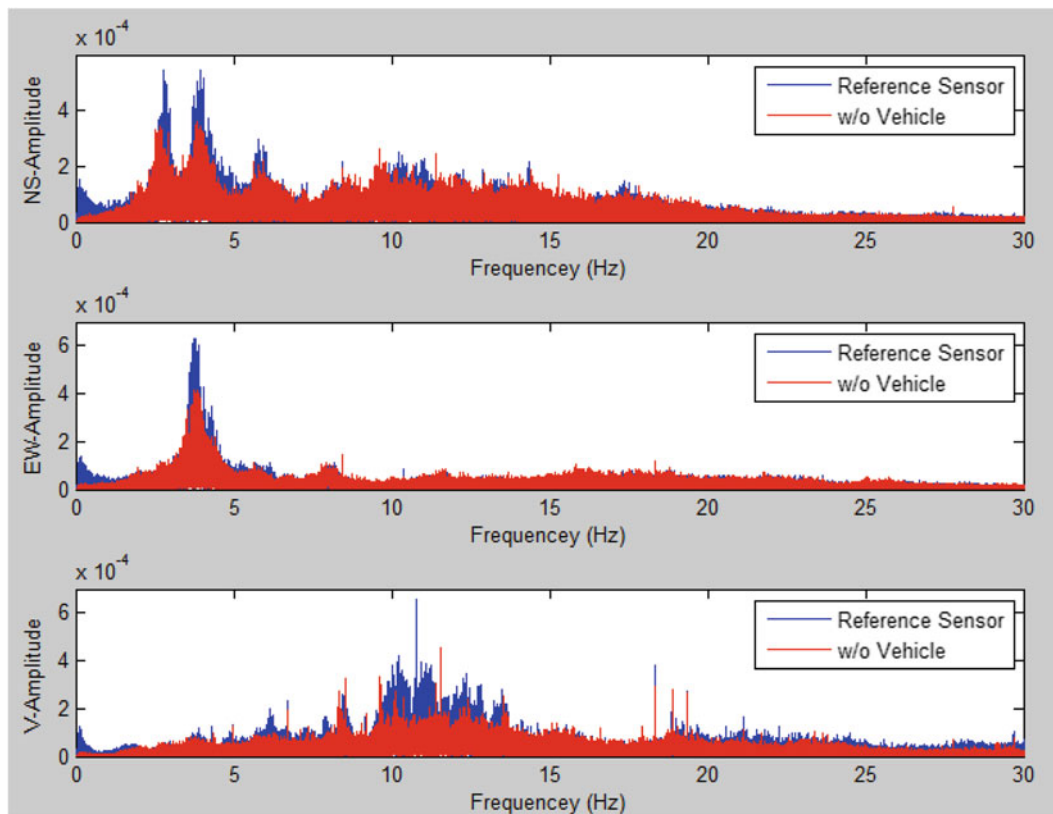
Fig. 3.10 FFT comparison between NS-EW and vertical channel records during the two AVT

3.5   Conclusions

Within a range of frequencies up to 8 Hz, a total of six modes have been identified with confidence. The first natural frequency of the Health Sciences Parkade has been identified at 2.756 Hz and corresponds to a fundamental longitudinal mode in the N-S direction. The first torsional mode has a frequency that is just about 1 Hz higher than the fundamental mode. This indicates that during a seismic event, the building is likely to experience both strong lateral and torsional responses.

The comparison between results obtained with FDD and SSI-UPC shows in general good agreement between frequency values, with a variation within 0 % and 9 %. Modal damping values were obtained through the SSI-UPC analysis but were unrealistically high and the data needs to be further analyzed to determine these values with confidence.

Because of the limited number of sensors located on the lateral ramps, just two on each floor, little information could be obtained from those parking ramps. As for the central ramps, no sensors were used to record its vibrations (due to safety issues), thus it was not possible to evaluate how the central ramp contributes to the overall dynamic behavior of the Parkade.

The comparison between the two ambient vibration tests shows almost no significant difference in frequency values, indicating that the presence of the cars does not greatly affect the dynamic parameters of the Parkade – in the lateral direction of motion, of course. However, the amplitude of the recorded data is, as expected, much higher than in the case of almost empty Parkade, confirming a strong amplification of the response due primarily to traffic loads.

References

1. Structural Vibration Solutions [Online]. http://www.svibs.com/. Last accessed 20 Oct 2014
2. Micromed SPA (2011) Tromino, portable ultra-light acquisition system for seismic noise and vibration. Treviso, p 137
3. GEOPSY (2011) Geophysical signal database for noise array processing, V 2.7.4. Grenoble, France
4. The MathWorks, Inc. (2014) MATLAB, Natick
5. Folchi R, Ferraglio EL (2004) La misura delle vibrazioni indotte dal traffico [Online]. http://www.euexcert.it/wp-content/uploads/2011/10/2004.
   10-LA-MISURA-DELLE-VIBRAZIONI-INDOTTE-DAL-TRAFFICO.pdf
6. Computer & Structures, Inc. (2014) [Online]. http://www.csiamerica.com/products/sap2000. Last accessed 20 Oct 2014

Chapter 4
Blind Source Separation: A Generalized Modal Identification Tool for Civil Structures

Ayan Sadhu

Abstract Over the last decade, Blind Source Separation (BSS) has evolved as a powerful tool for system identification of flexible structures. Several numerical and experimental studies have been proposed to demonstrate its effectiveness in dealing with noisy full-scale data. The author has recently developed a suite of methods that enhance the capabilities of BSS in addressing issues associated with decentralized implementation, autonomous processing, nonstationary excitations, and the presence of narrowband excitations in ambient vibration measurements. The basic idea of the algorithms proposed by the author is to cast the problem of identification within the framework of underdetermined BSS invoking sparsifying transforms. The resulting partial mode shape coefficients are combined to yield complete modal information. The transformations are undertaken using Stationary Wavelet Packet Transform (SWPT), yielding a sparse representation in the wavelet domain. Both numerical and experimental studies demonstrate the potential of these methods. The speaker will introduce this suite of methods and some examples where these methods have successfully been applied.

Keywords Decentralized modal identification • Narrowband excitation • BSS • Wavelet Transforms • PCA

4.1 Introduction

Blind Source Separation (BSS) methods have recently emerged as a powerful class of signal processing methods capable of modal identification for a large class of linear structural problems. The application of BSS methods to flexible structures have been reported for a large number of numerical and experimental cases, e.g., [1–6]. These results clearly demonstrate the potential of using the principle of BSS for a wide range of structural engineering problems. Originally proposed for a fairly restrictive class of problems involving broadband excitations, static mixtures, and relatively large sensor densities, BSS extensions to decentralized [7–10], nonstationary [11], autonomous processing [12], convolutive mixing [13] and for narrow band excitation case [9, 14] have also been reported in recent studies.

The basic principle of BSS methods is primarily related to the most popular BSS tools, Second-Order Blind Identification (SOBI) [15] and Independent Component Analysis (ICA) [16]. Both SOBI and ICA aim to estimate the modal parameters from a set of measurements that are assumed to be a superposition of modal responses. ICA methods assume that the sources are non-Gaussian (SOBI methods do not have this restriction), and the objective of ICA algorithms is to estimate the linear transformation which assures that the sources are as independent as possible. Whereas ICA methods use higher-order statistics (e.g., kurtosis), SOBI methods use second-order statistics and assume that the sources have a temporal structure. The exploitation of the time structure by introducing several time-lagged co-variance matrices in SOBI enables better handling of sources with different spectral contents [5].

In BSS methods, two keys assumptions are, (1) the number of measurements (n_m) to be more than the number of sources (n_s), (2) the excitation is generally assumed to be broadband [1, 4, 5]. If the former assumption is violated (e.g., $n_m < n_s$), it leads to the underdetermined problem which is frequently occurred in decentralized system where only fewer measurements are available at any particular measurement set-up. On the other hand, if the later assumption is violated, and there are unknown harmonics present in the excitation, the excitation harmonics are also identified along with the structural modes. Due to the permutation ambiguity in BSS methods [1, 5, 15], delineating structural harmonics from excitation harmonics is a challenge. The presence of excitation harmonics in structural vibration measurements occurs in mechanical systems with rotating machineries, [17–19], in civil structures such as gravity dams comprising of turbines and generators [20],

_____

A. Sadhu (✉)

Department of Civil Engineering, Lakehead University, Thunder Bay, ON, Canada P7B 2X9

e-mail: ayansadhu.civil@gmail.com; asadhu@lakeheadu.ca

human-induced narrowband vibrations in pedestrian bridges [9, 14, 21–24], and when dynamic interactions with surrounding structures exist in buildings [25]. In the present paper, the above two shortcomings are addressed in the framework of decentralized ambient modal identification.

The advantage of a decentralized architecture stems from the fact that the recent trends in ambient modal identification have been towards using wireless sensors and algorithms that can harness the decentralized data acquisition and processing architecture of wireless sensors [6, 9, 26–31]. As well, unlike centralized algorithms that require access to a relative large number of simultaneous measurement channels, decentralized algorithms can achieve significant savings in the cost of performing system identification by limiting the number of sensors used in the identification process. Recently, the author proposed a BSS architecture requiring only two measurement channels at-a-time [8]. However the wireless sensors have very limited processing and transmission capabilities, which restrain the implementation of any particular modal identification algorithm with longer processing requirements. Considering the fact that the transmission rates are strongly affected by the signal length, a compressed sensing scheme is recently pursued in the framework of decentralized BSS algorithm [12].

The main objective of this paper is to present a series of algorithm based on sparse BSS that are recently proposed [6] in conjunction with (1) decentralized modal identification [8, 10, 32], (2) presence of narrow-band excitation case [9, 14, 24]. The key steps in the proposed method are as follows. First, a sub-set of raw vibrations are transformed using SWPT. This results in a sparse transformation of the signal (dense representation in the frequency domain) in the individual sub-bands in the decomposition. For decentralized modal identification, Principal Component Analysis (PCA) is employed to identify partial mode shape coefficients in each intermediate step. When the excitation harmonics are present, a novel bootstrap-based statistical characterization is used to identify modal parameters.

4.2 Background

The methodology presented here builds on the key concepts of sparse BSS. A brief background on sparse BSS is presented first, before going into the details of the algorithm.

4.2.1 Sparse BSS

The basic elements of sparse BSS are presented here, and the readers are referred elsewhere for more detailed discussion on this topic [8]. Consider the problem of standard BSS for the static mixtures case in discrete matrix form:

$$\mathbf{x}(k) = \mathbf{A}\mathbf{s}(k) \tag{4.1}$$

where, $\mathbf{A}$ is the mixing matrix and $\mathbf{s}$ represents the sources. Both $\mathbf{A}_{n_m \times n_s}$ and s are to be determined, and is the essence of the BSS problem. Assuming that the system is linear and time-invariant, and the excitation is white, $\mathbf{A}$ can be viewed as the matrix of mode shapes and $\mathbf{s}$ the corresponding modal responses [17]. Non-sparse BSS Methods such as ICA [16] and SOBI [15] exploit the higher-order statistics and second-order statistics of the sources respectively, to determine the mode shapes and the modal responses. While these methods yield good results for the over-determined case (i.e., $n_m \geq n_s$), they are not directly applicable to the decentralized case where only partial sensor information (i.e., $n_m < n_s$) is used for intermediate processing, which does not satisfy the full rank condition.

The essence of sparse separation is to perform identification in a transformed signal space (e.g., Fourier, wavelet) such that the sources are rendered sparse by the transformation, with at most one source active at any time. This can easily be understood through an example. Consider two measurement channels represented by x_1 and x_2:

$$\begin{bmatrix} x_1(k) \\ x_2(k) \end{bmatrix} = \begin{bmatrix} a_{11} & a_{12} \\ a_{21} & a_{22} \end{bmatrix} \begin{Bmatrix} s_1(k) \\ s_2(k) \end{Bmatrix} \tag{4.2}$$

Now, if only one of the sources s_1 is present, then Eq. 4.2 can be written as:

$$\begin{bmatrix} x_1(k) \\ x_2(k) \end{bmatrix} = s_1(k) \begin{bmatrix} a_{11} \\ a_{21} \end{bmatrix} \tag{4.3}$$

Fig. 4.1 SWPT binary tree indexing of $\psi^{j,v}$
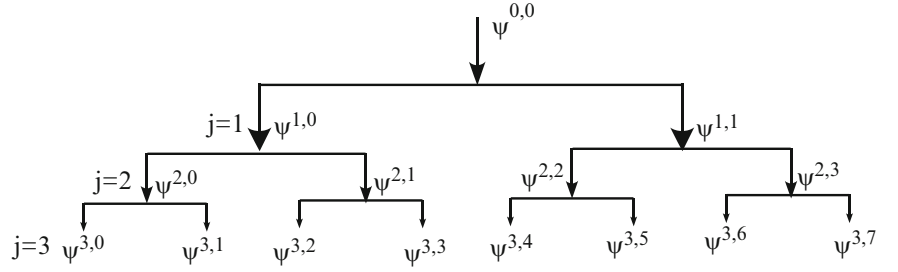
Under such conditions, the plot of x_1 versus x_2 yields the direction vector of partial mixing matrix coefficients. Generally, sparsity is difficult to obtain directly from raw vibration data. However, it is possible in the frequency or in the time-frequency domain. This is the basic idea of sparse transformation. Recently, the author presented a methodology to achieve sparse transformations using Stationary Wavelet Packet Transform (SWPT) [8].

WPT is an extension of the WT and can be implemented by a generalization of the pyramidal algorithm [33, 34]. A wavelet packet is a triple-index function $\psi_k^{j,v}(t)$, where j, k and v can be interpreted as scale, shift and frequency parameter [35, 36], and a SWPT basis is defined as [34]:

$$\psi_k^{j,v}(t) = \frac{1}{2^j} \psi^v \left(\frac{t-k}{2^j} \right) \tag{4.4}$$

where, $\psi^{1,0}(t) = \phi(t)$ and $\psi^{1,1}(t) = \psi(t)$ represent the scaling (father) and wavelet (mother) functions, respectively. For a given scale level j, a binary tree as shown in Fig. 4.1 can be formed using the basis functions, $\psi_k^{j,v}(t)$, whose nodes are indicated by the scale level, j and the frequency parameter, $v = 0, 1, 2, \ldots, (2^j - 1)$.

The wavelet packet coefficients at each node (j, v) are written as:

$$w_k^{j,v}(y) \triangleq \left\langle y(t) \, \middle| \, 2^{-j/2} \psi^v \left(\frac{t-k}{2^j} \right) \right\rangle = \frac{1}{2^{j/2}} \int_{-\infty}^{\infty} y(t) \psi^v \left(\frac{t-k}{2^j} \right) dt \tag{4.5}$$

The wavelet packet component signal $y^{j,v}(t)$ at each node can be expressed as a linear combination of wavelet packet basis functions $\psi_k^{j,v}(t)$:

$$y^{j,v}(t) = \sum_k w_k^{j,v} \psi_k^{j,v}(t). \tag{4.6}$$

For the jth level of decomposition, the original signal $y(t)$ can be expressed as a summation of all the wavelet packet component signals, $y^{j,v}$ [8]:

$$y(t) = \sum_{v=0}^{2^j - 1} y^{j,v} = \sum_{v=0}^{2^j - 1} \sum_k w_k^{j,v} \psi_k^{j,v}(t) \tag{4.7}$$

Thus, the WPT is a generalization of SWT in that each frequency band of the wavelet spectrum is further sub-divided into finer frequency bands, repeatedly.

4.3   Details of the Algorithm

Consider a linear, classically damped, and lumped-mass n_s degrees-of-freedom (DOF) structural system, subjected to a broad-band random input force, $\mathbf{F}(t)$:

$$\mathbf{M}\ddot{\mathbf{x}}(t) + \mathbf{C}\dot{\mathbf{x}}(t) + \mathbf{K}\mathbf{x}(t) = \mathbf{F}(t) \tag{4.8}$$

where, $\mathbf{x}(t)$ is a vector of displacement coordinates at the DOF. The solution to Eq. 4.8 for those of broad-band $\mathbf{F}(t)$ can be written in terms of an expansion of vibration modes. In matrix form,

$$\mathbf{x} = \boldsymbol{\Psi} \mathbf{q} \tag{4.9}$$

where, $\mathbf{x} \in \Re^{n_m \times N}$ is the trajectory matrix composed of the sampled components of $\mathbf{x}$, $\mathbf{q} \in \Re^{n_s \times N}$ is a matrix of the corresponding modal coordinates, $\boldsymbol{\Psi}_{n_m \times n_s}$ is the modal transformation matrix, and N is the number of data points in each measurement. The measurement at the ith degree-of-freedom ($i = 1, 2, \ldots n_m$) of Eq. 4.9 can be expressed as

$$x_i(t) = \sum_{r=1}^{n_s} \psi_{ir} q_r(t) \tag{4.10}$$

Consistent with the notation of BSS for the static mixtures case in Eq. 4.1, we can write the measurement at the ith location:

$$x_i(t) = \sum_{l=1}^{n_s} A_{il} s_l(t) \qquad i = 1, 2, \ldots, n_m \tag{4.11}$$

Where A_{il} is the mode shape coefficient corresponding to the ith location for the lth source (mode), and s_l is the lth modal response at time t.

Considering the wavelet packet coefficients of the sensor responses and sources at any specific node (j, v), and finally applying the orthogonality condition for wavelets, we get [8]:

$$f_{k,i}^{j,v}(t) = \sum_{l=1}^{n_s} A_{il} e_{k,l}^{j,v}(t) \qquad i = 1, 2, \ldots, n_m \tag{4.12}$$

Where $f_{k,i}^{j,v}$ and $e_{k,l}^{j,v}$ represents the wavelet packet coefficient of the ith sensor and lth source at a specific node (j, v) respectively. At the last scale level ($j = s$), assuming only one source is active in each sub-band after decomposition, Eq. 4.12 can be written as:

$$f_{k,i}^{s,v}(t) = A_{il} e_{k,l}^{s,v}(t) \qquad i = 1, 2, \ldots, n_m \tag{4.13}$$

Equation 4.13 relates the SWPT coefficients of ith measurement with the SWPT coefficients of the sparse lth source. Therefore, following the same logic for $i = q$ and $i = r$ in Eq. 4.13, the partial mixing matrix coefficients of qth sensor measurement normalized with the rth measurement is:

$$\frac{f_{k,q}^{s,v}}{f_{k,r}^{s,v}} = \frac{A_{ql} e_{k,l}^{s,v}(t)}{A_{rl} e_{k,l}^{s,v}(t)} = \frac{A_{ql}}{A_{rl}} = a_{ql}; \qquad l = 1, 2, \ldots, n_s \tag{4.14}$$

Then, $a_{ql} = \frac{A_{ql}}{A_{rl}}$ represents the estimated normalized mixing matrix coefficient of the lth mode at the qth DOF. Therefore, we get:

$$f_{k,q}^{s,v} = a_{ql} f_{k,r}^{s,v} \tag{4.15}$$

4.3.1 Decentralized Case

Due to the imperfect filtering, the wavelet coefficients at last scale level may not be mono-component. However, any coefficient containing more than one source should not be treated as a modal response. Assuming a mode mixing of n_m sources, Eq. 4.13 can be expressed as [8]:

$$\mathbf{R_f}(0) = \mathbf{A} \mathbf{R_e}(0) \mathbf{A}^T \tag{4.16}$$

PCA is an orthogonal transformation in which $\mathbf{R_f}(0) = (^1/_N)(\sum_{k=1}^{N} \mathbf{f}_\alpha^{s,v}(k)\mathbf{f}_\alpha^{Ts,v}(k))$ is diagonalized using singular value decomposition, $\mathbf{R_f}(0) = \mathbf{V}_{\mathbf{f}_\alpha^{s,v}}\mathbf{\Lambda}_{\mathbf{f}_\alpha^{s,v}}\mathbf{V}_{\mathbf{f}_\alpha^{s,v}}^T$, where $\mathbf{V}_{\mathbf{f}_\alpha^{s,v}}$ are the eigenvectors of the co-variance matrix of $\mathbf{f}_\alpha^{s,v}$. Then, the standard linear transformation expressed as under:

$$\mathbf{f}_\alpha^{s,v_p}(k) = \mathbf{V}_{\mathbf{f}_\alpha^{s,v}}^T \mathbf{f}_\alpha^{s,v} \tag{4.17}$$

PCA gives the major and minor principal components (PC), principal directions (PD) and their respective variances (σ_1^2 and σ_2^2). The ratio of major and minor variances is defined as the condition number (CN). In the present study, the reciprocal of the conditional number (RCN) as defined below is used as the parameter to identify the mono-component coefficients and the corresponding major PCs and PDs are used to estimate the modal parameters [8].

4.3.2 Presence of Narrowband Excitation

When there is a presence of narrowband excitation, the PCA-based characterization is not sufficient to delineate the structural sources with the excitation sources. Therefore, a novel statistical characterization is introduced herein [24]. If we pre-multiply both side with $f_{k,q}^{Ts,v}$ and take the expectation both sides, Eq. 4.15 can be simplified as:

$$\sigma_{f_{k,q}^{s,v}} = |a_{ql}|\sigma_{f_{k,r}^{s,v}}$$
$$|a_{ql}| = \frac{\sigma_{f_{k,q}^{s,v}}}{\sigma_{f_{k,r}^{s,v}}} \tag{4.18}$$

where, $\sigma_{f_{k,i}^{s,v}}$ is the standard deviation of $f_{k,i}^{s,v}$. In order to estimate the sign of a_{ql}, the cross-correlation coefficient (ρ) between $f_{k,q}^{s,v}$ and $f_{k,r}^{s,v}$ can be used. We know that

$$\rho_{f_{k,q}^{s,v},f_{k,r}^{s,v}} = \frac{E[f_{k,q}^{s,v} \cdot f_{k,r}^{Ts,v}]}{\sigma_{f_{k,q}^{s,v}} \times \sigma_{f_{k,r}^{s,v}}} = \frac{a_{ql}.\sigma_{f_{k,r}^{s,v}}^2}{|a_{ql}|\sigma_{f_{k,r}^{s,v}}.\sigma_{f_{k,r}^{s,v}}} = \pm 1 \tag{4.19}$$

Thus the cross-correlation coefficient with a value of ± 1.0 indicates the presence of a mono-component source. Further, the absolute value of the mixing coefficient a_{ql} can be estimated using Eq. 4.18 and the sign of ρ (i.e., $\frac{|\rho|}{\rho}$) in Eq. 4.19 can be used to estimate the true value of a_{ql}.

$$a_{ql} = \frac{|\rho_{f_{k,q}^{s,v},f_{k,r}^{s,v}}|}{\rho_{f_{k,q}^{s,v},f_{k,r}^{s,v}}} \frac{\sigma_{f_{k,q}^{s,v}}}{\sigma_{f_{k,r}^{s,v}}} \tag{4.20}$$

Using this procedure, the normalized partial mixing matrix coefficients can be estimated using SWPT coefficients of partial sensor measurements at the highest scale level. A thresholding criteria based on average root-mean-square (RMS) value of the coefficients can be used to retain coefficients with significant energy [8].

Kurtosis contains information regarding the nature of the underlying density of the identified sources. For a sample realization, this is given by:

$$\kappa_x = E\left[\left(\frac{x-\mu}{\sigma}\right)^4\right] \tag{4.21}$$

A value close to 3 indicates modal sources, while lower values indicates the presence of harmonic excitation frequency. Once a source containing modal response is detected, then Eq. 4.20 employing the standard deviations is utilized to estimate the partial mode shape matrix. However, in order to estimate the statistical measures such as kurtosis and standard deviation of the underlying density function, a sufficiently large sample size is required. In order to circumvent this issue, several bootstrapped samples are generated using the residual bootstrap method [37]. The 98 % confidence interval of kurtosis obtained from bootstrapping is used to delineate the excitation harmonics from modal harmonics.

4.3.2.1 Modal Information Synthesis from Partial Mode Information

Calculating the partial mixing coefficients from two sensors (corresponding to the qth and rth measurement channels) has been explained so far. This process can be repeated using a fixed or movable common reference sensor location, which is the essence of the decentralized sensing concept [8, 28, 30]. If $\hat{\phi}_{i,j}^{Si}$ represents the estimated mode shape coefficient at the ith DOF of jth mode ϕ_j in the Sith setup, then $\hat{\phi}_j$ is simply the union of the partial mode shape coefficients, $\hat{\phi}_{i,j}^{Si}$ from each group (Si):

$$\hat{\phi}_j = \bigcup_{i=1}^{Sg} \hat{\phi}_{i,j}^{Si} \tag{4.22}$$

where, Sg is the total number of groups. Finally the complete mode shape matrix is obtained using $\Phi = [\hat{\phi}_1|\hat{\phi}_2|\ldots|\hat{\phi}_j|\ldots|\hat{\phi}_{n_s}]$.

4.4 Numerical Study

In order to present an application of the proposed modal identification technique, simulations are performed on a 5-storey shear-beam structure model [8]. For the example building, the natural frequencies are 0.91, 3.37, 7.11, 10.66 and 12.73 Hz. The 5-DOF building ($n_s = 5$) is excited by a zero mean unit variance Gaussian white noise at all floor levels. In addition to the white noise, a harmonic of frequency 5.1 Hz is added to the excitation (well-separated from the natural frequencies).

The SOBI method [15] is first employed to extract the mixing matrix using all the floor responses. Due to presence of harmonics, SOBI, which is based on the assumption of white noise input, is unable to separate out the sources. Figure 4.2 shows a significant amount of mode mixing in the separated sources using SOBI, which leads to significant estimation errors in the mixing matrix (modes).
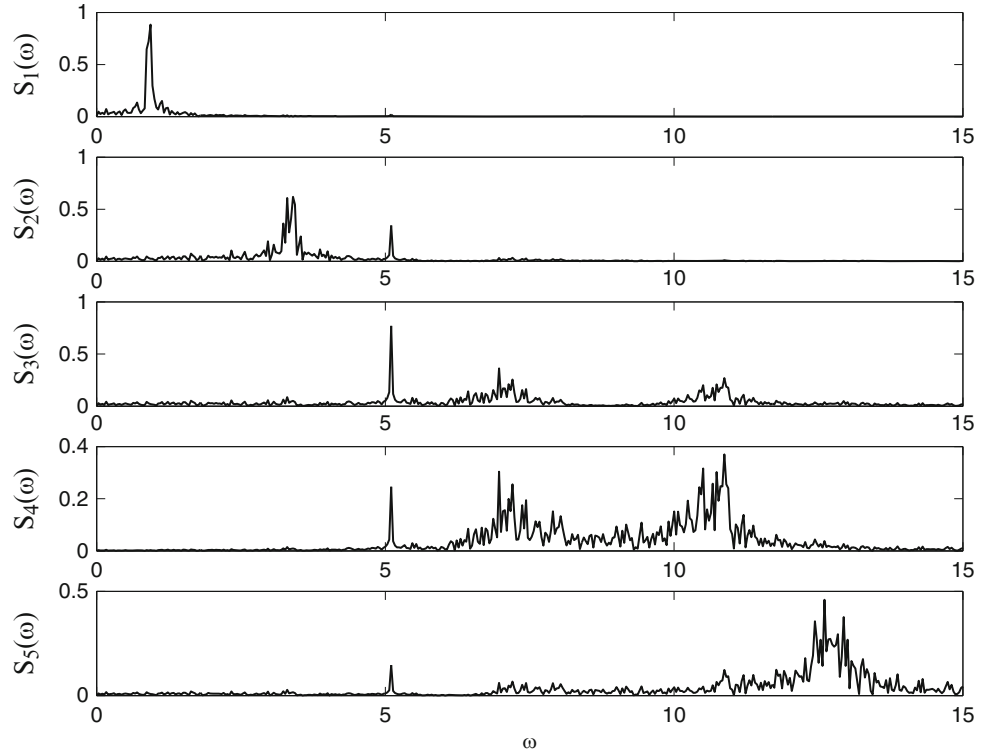
Fig. 4.2 Fourier spectrum of the separated sources using SOBI
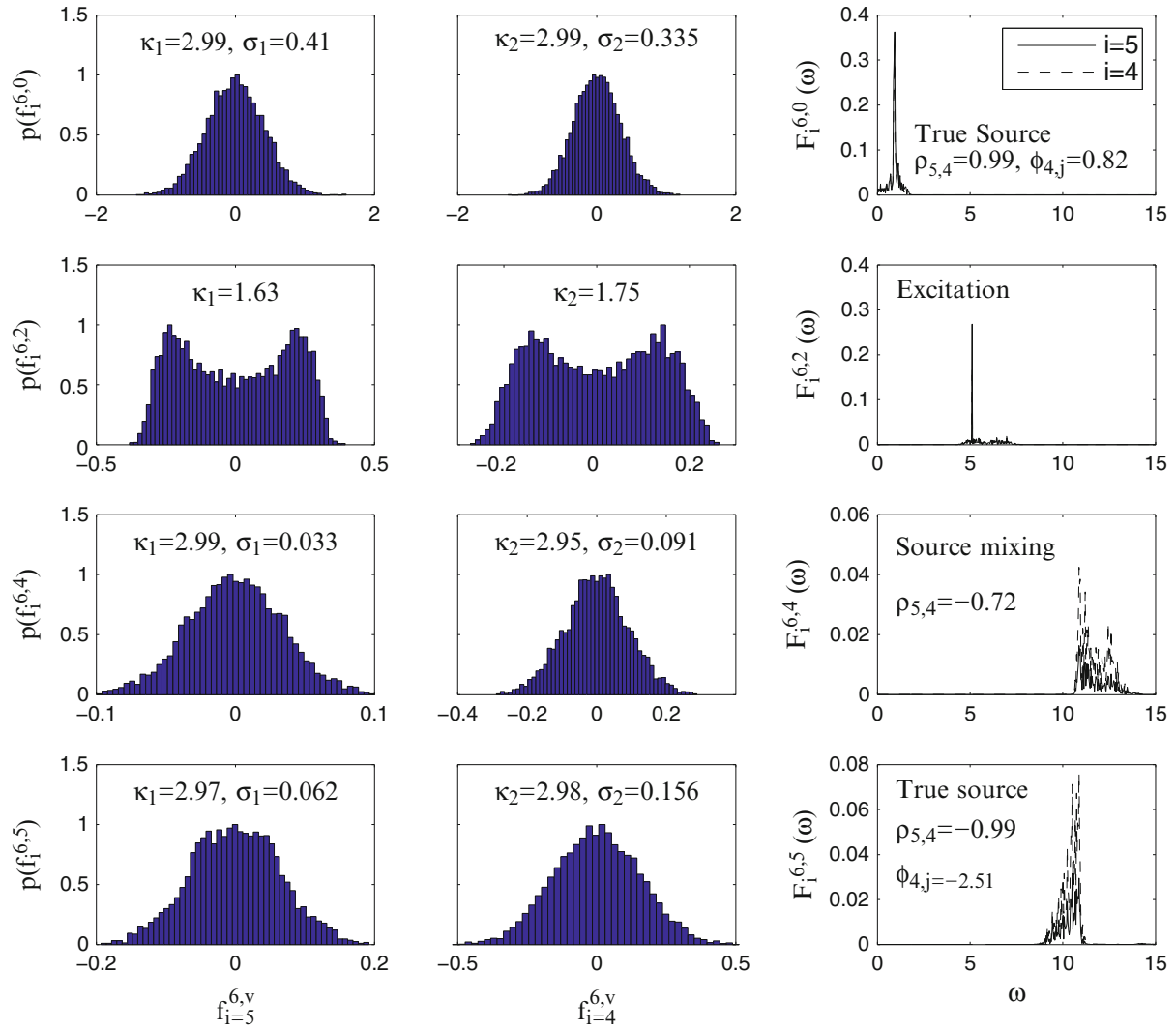
Fig. 4.3 Details of identification using the PDF of $f_5^{6,v}$ and $f_4^{6,v}$

The proposed method is then applied to the partial measurements. Two response measurements at the fifth and the fourth floors are processed using SWPT up to scale level $s = 6$. In order to identify the modal parameters from SWPT coefficients, the sample probability density of the selected coefficients are used. Figure 4.3 shows the details of the identification using the information of PDF of $f_5^{6,v}$ and $f_4^{6,v}$. The first two columns of Fig. 4.3 show the PDF of SWPT coefficients $f_i^{6,v}$ for $v = 0, 2, 4$ and 5, where $i = 4, 5$. The third column shows the Fourier spectra of the coefficients. It can be seen that the PDF of $f_i^{6,v}$ with $v = 0$ and 5 have the value of κ close to 3.0, which corresponds to belonging to a system mode. The absolute value of cross-correlation $\rho_{5,4}$ for those coefficients close to 1.0 implies a mono-component source, which can be considered as a modal response. The ratio of their standard deviation yields the mode shape coefficient and the sign of ρ determines the sign of the mode shape coefficients. In this fashion, the mixing coefficients can be estimated repeatedly using Eq. 4.20. For example, $f_5^{6,0}$ and $f_4^{6,0}$ has a ρ value of 0.99, for which $\phi_{4,j}$ is $+0.82$. On the other hand, $f_5^{6,5}$ and $f_4^{6,5}$ has a ρ value of -0.99, for which $\phi_{4,j}$ is -2.51.

Although the PDF of $f_i^{6,4}$ has the value of κ close to 3.0, the cross-correlation between $f_5^{6,4}$ and $f_4^{6,4}$ is -0.72 ($|\rho| \neq 1$). It implies that the coefficients contain mode mixing which is evident from the associated Fourier spectrum. The PDF of $f_i^{6,2}$ has the value of $\kappa \ll 3.0$, which implies that the source is an excitation harmonic which is then discarded from further analysis. It can be seen that the coefficient $f_i^{6,2}$ accurately separates the excitation harmonic with a frequency of 5.1 Hz. The results are finally summarized for all coefficients containing the modal response in Table 4.1.

Table 4.1 Details of the identification results

j	$\rho_{5,4}^{6,v}$	ω_j	ξ_j	$a_{4,j}^v = \frac{\sigma_4^{6,v}}{\sigma_5^{6,v}}$	$A_{4j} = (+/-)a_{4,j}^v$	Φ_{4j}	% error
1	0.999	0.91	2.07	0.82	0.82	0.82	0.0
2	−0.997	3.39	1.99	0.093	−0.093	−0.087	5.8
3	−0.991	7.10	1.97	1.288	−1.288	−1.29	0.16
4	−0.992	10.65	1.96	2.51	−2.51	−2.52	0.8
5	−0.993	12.77	1.97	3.32	−3.32	−3.39	2.1

Table 4.2 Effect of noise level in MAC numbers

j	SNR = 100	SNR = 20	SNR = 10
1	1.0	1.0	1.0
2	0.99	0.984	0.98
3	1.0	0.99	0.99
4	0.99	0.99	0.99
5	1.0	0.99	0.99

4.4.1 Construction of the Full Mixing Matrix from Partial Mixing Coefficients

Calculating the partial mixing coefficients from two sensors (corresponding to the fifth and fourth floor responses) has been explained so far. This process can be repeated using a fixed or movable common reference sensor location, which is the essence of the decentralized sensing concept. Partial mixing matrix coefficients so obtained can be concatenated using Eq. 4.22. The MAC numbers for the full mixing matrix obtained are greater than 0.98 for all the five modes. The calculated mode shapes are relatively insensitive to noise (reflected by the relatively high MAC values) even for SNR as high as 10 (as shown in Table 4.2). This can be attributed to the inherent de-noising capability of the wavelet filter-bank implementation.

4.5 Conclusions

A suite of decentralized ambient modal identification methods that can satisfactorily delineate the modal sources even when narrow band harmonics are present in the excitations is presented. The algorithm is based on the principle of sparse blind source separation using stationary wavelet packet transforms. The main advantage of the proposed approach is in its decentralized architecture, with as few as two sensors at a time used for mode shape construction. Due to filter bank implementation, the proposed method is robust to measurement noise and other extraneous frequencies. Through numerical and experimental studies, it is shown that the method works well when single or multiple harmonics are present, as long as the disturbance frequencies are well separated from the structural modes.

References

1. Antoni J (2005) Blind separation of vibration components: principles and demonstrations. Mech Syst Signal Process 19(6):1166–1180
2. Poncelet F, Kerschen G, Golinval JC, Verhelst D (2007) Output-only modal analysis using blind source separation technique. Mech Syst Signal Process 21:2335–2358
3. Hazra B, Sadhu A, Lourenco R, Narasimhan S (2010) Retuning tuned mass dampers using ambient vibration response. Smart Mater Struct 19(11):115002
4. Hazra B, Sadhu A, Roffel AJ, Paquet PE, Narasimhan S (2012) Underdetermined blind identification of structure by using the modified cross-correlation method. J Eng Mech 138(4):327–337
5. Hazra B, Sadhu A, Roffel AJ, Narasimhan S (2012) Hybrid time-frequency blind source separation towards ambient system identification of structures. Comput Aided Civ Infrastruct Eng 27(5):314–332
6. Sadhu A (2013) Decentralized ambient modal identification of structures. Ph.D. Thesis, Department of Civil Engineering, University of Waterloo
7. Sadhu A, Hazra B, Narasimhan S (2011) Decentralized modal identification using wavelet transforms. In: Proceedings of engineering mechanics institute conference (ASCE/ASME), Boston, USA
8. Sadhu A, Hazra B, Narasimhan S, Pandey MD (2011) Decentralized modal identification using sparse blind source separation. Smart Mater Struct 20(12):125009

9. Sadhu A, Narasimhan S, Goldack A (2014) Decentralized modal identification of a pony truss pedestrian bridge using wireless sensors. J Bridg Eng 19(6):04014013
10. Sadhu A, Hazra B, Narasimhan S (2013) Decentralized modal identification of structures using parallel factor decomposition and sparse blind source separation. Mech Syst Signal Process 41(1–2):396–419
11. Sadhu A, Hazra B, Narasimhan S (2012) Blind identification of earthquake-excited structures. Smart Mater Struct 21(4):045019
12. Sadhu A, Hu B, Narasimhan S (2012) Blind source separation towards decentralized modal identification using compressive sampling. In: Proceedings of the 11th IEEE conference on information science, signal processing and their applications: special sessions, Montreal, Canada, pp. 1184–1189
13. Sadhu A, Narasimhan S (2012) Blind source separation of convolutive mixtures towards modal identification. In: Proceedings of the society for experimental mechanics series, vol 26, pp 209–220
14. Sadhu A, Goldack A, Narasimhan S (2014) Ambient modal identification using multi-rank parallel factor decomposition. Struct Control Health Monit. doi:10.1002/stc.1706
15. Belouchrani A, Abed-Meraim K, Cardoso J, Moulines E (1997) A blind source separation technique using second-order statistics. IEEE Trans Signal Process 45(2):434–444
16. Hyvarinen A (1999) Fast and robust fixed-point algorithm for independent component analysis. IEEE Trans Neural Netw 10(3):626–634
17. Antoni J, Garibaldi L, Marchesiello S, Sidhamed M (2004) New separation techniques for output-only modal analysis. Shock Vib 11(3-4):227–242.
18. Peeters B, Cornelis B, Janssens K, Auweraer HV (2007) Removing disturbing harmonics in operational modal analysis. IOMAC, Copenhagen
19. Pintelon R, Peeters B, Guillaume P (2008) Continuous-time operational modal analysis in the presence of harmonic disturbances. Mech Syst Signal Process 22:1017–1035
20. Andersen P, Brincker R, Ventura C, Cantieni R (2008) Mode estimation of civil structures subject to ambient and harmonic excitation. In: Proceeding of the 26th international modal analysis conference, Orlando
21. Fujino Y, Pacheco BM, Nakamura SI, Warnitchai P (1993) Synchronization of human walking observed during lateral vibration of a congested pedestrian bridge. Earthq Eng Struct Dyn 22(9):741–758
22. Newland DE (2003) Vibration of the London millennium bridge: cause and cure. Int J Accoust Vib 8(1):9–14
23. Ingolfsson ET, Georgakis CT (2011) A stochastic load model for pedestrian-induced lateral forces on footbridges. Eng Struct 33(12):3454–3470
24. Sadhu A, Narasimhan S (2014) A decentralized blind source separation algorithm for ambient modal identification in the presence of narrowband disturbances. Struct Control Health Monit 21(3):282–302
25. Rainieri C, Fabbrocino G, Manfredi G, Dolce M (2012) Robust output-only modal identification and monitoring of buildings in the presence of dynamic interactions for rapid post-earthquake emergency management. Eng Struct 34:436–446
26. Gao Y, Spencer Jr BF, Ruiz-Sandoval M (2006) Distributed computing strategy for structural health monitoring. Struct Control Health Monit 13:488–507
27. Lynch JP (2007) An overview of wireless structural health monitoring for civil structures. Philos Trans R Soc A 365:345–372
28. Zimmerman AT, Shiraishi M, Swartz RA, Lynch JP (2008) Automated modal parameter estimation by parallel processing within wireless monitoring systems. J Infrastruct Syst 22:102–113
29. Bocca M, Eriksson LM, Mahmood A, Jantti R, Kullaa J (2011) A synchronized wireless sensor network for experimental modal analysis in structural health monitoring. Comput-Aided Civ Infrastuct Eng 26:483–499
30. Sim SH, Carbonell-Marquez JF, Spencer BF, Jo H (2011) Decentralized random decrement technique for efficient data aggregation and system identification in wireless smart sensor networks. Probab Eng Mech 26(1):81–91
31. Yun GJ, Lee SG, Carletta J, Nagayama T (2011) Decentralized damage identification using wavelet signal analysis embedded on wireless smart sensors. Eng Struct 33(7):2162–2172
32. Sadhu A, Hazra B, Narasimhan S (2014) Ambient modal identification of structures equipped with tuned mass dampers using parallel factor blind source separation. Smart Struct Syst 13(2):257–280
33. Coifman RR, Wickerhauser MV (1992) Entropy-based algorithms for best basis selection. IEEE Trans Inf Theory 38(2):713–718
34. Pesquet JC, Krim H, Carfantan H (1996) Time-invariant orthonormal wavelet representations. IEEE Trans Signal Process 44(8):1964–1970
35. Wickerhauser M (1994) Adapted wavelet analysis from theory to software. AK Peters, Wellesley
36. Mallat SG (1998) A wavelet tour of signal processing. Academic Press, San Diego
37. Efron B, Tibshirani R (1993) An introduction to the bootstrap. Chapman and Hall, New York

Chapter 5
Developments with Motion Magnification for Structural Modal Identification Through Camera Video

Justin G. Chen, Neal Wadhwa, Frédo Durand, William T. Freeman, and Oral Buyukozturk

Abstract Non-contact measurement of the response of vibrating structures may be achieved using several different methods including the use of video cameras that offer flexibility in use and advantage in terms of cost. Videos can provide valuable qualitative information to an informed person, but quantitative measurements obtained using computer vision techniques are essential for structural assessment. Motion Magnification in videos refers to a collection of techniques that amplify small motions in videos in specified bands of frequencies for visualization, which can also be used to determine displacements of distinct edges of structures being measured. We will present recent developments in motion magnification for the modal identification of structures. A new algorithm based on the Riesz transform has been developed allowing for real-time application of motion magnification to normal-speed videos with similar quality to the previous computationally intensive phase-based algorithm. Displacement signals are extracted from strong edges in the video as a basis for the data necessary for modal identification. Methodologies for output-only modal analysis applicable to the large number of signals and short length signals are demonstrated on example videos of vibrating structures.

Keywords Computer vision • Non-contact • Modal identification • Mode shape • Motion magnification

5.1 Introduction

Non-contact techniques for measuring structures have only recently been available as a serious option. Laser vibrometers provide an accurate way of measuring the surface velocity of an object and are now widely used as the gold standard for non-contact vibration measurement [1]. For large structures, scanning laser vibrometers have the capability of measuring a large number of points in succession, however for phased measurements they require another stationary laser vibrometer to serve as a reference, or they must be continuously scanning systems [2]. Laser vibrometer arrays consisting of multiple laser vibrometers measuring simultaneously are also an option [3]. However in general, laser vibrometers may be prohibitively expensive for many applications.

Video cameras collect light from a scene of interest onto a sensor consisting of an array of pixels and can obtain data with high spatial density. Interpretation of this data can be complex, especially to translate a video into quantitative measurement of the vibration and displacements of a structure. Computer vision techniques and digital image correlation have been successfully used to measure displacements of structures and quantify vibrations in structures [4–8].

This paper presents developments in structural modal identification in videos using the family of algorithms called motion magnification [9–11]. These algorithms can visualize operational deflections shapes (ODS) in a vibrating structure by magnifying motions in a video in a particular frequency band [12]. The most recent development of interest is the development of a Riesz transform based method that allows for fast or real-time processing for phase-based Motion Magnification [13]. This will be demonstrated by visualizing the ODS of a cantilever beam by using a subsampling technique in real time. The other development is expanding the use of the previously developed displacement extraction algorithms to obtain a displacement at many pixels in a video of interest at any strong edges of a structure [12]. Two different methods of identifying ODS from the many signals extracted from the video are demonstrated: peak picking and frequency domain

J.G. Chen • O. Buyukozturk (✉)
Department of Civil and Environmental Engineering, Massachusetts Institute of Technology, 77 Massachusetts Avenue, Cambridge, MA 02139, USA
e-mail: ju21743@mit.edu; obuyuk@mit.edu

N. Wadhwa • F. Durand • W.T. Freeman
Computer Science and Artificial Intelligence Laboratory, Massachusetts Institute of Technology, 77 Massachusetts Avenue, Cambridge, MA 02139, USA

decomposition. For these two developments, real-time Motion Magnification and ODS identification with numerous signals from video, some theory on the underlying methodologies is presented, followed by experimental results, and a conclusion offering directions for future work.

5.2 Derivation

5.2.1 Real-Time Motion Magnification

Recently, Wadhwa et al. [13] showed that Motion Magnification can be done in real-time. They decompose frames of a video into spatially-bandpassed subbands that correspond to different spatial scales. They then use the Riesz transform to compute an oriented local phase that approximately corresponds to the motion in the direction of the dominant orientation at every point, in every scale. This motion signal can be temporally filtered and amplified. More details about this technique can be found in their paper, but some of the key ideas are summarized here.

Subbands of an image are spatially bandpassed versions of that image. For example, the Fourier transform can be viewed as a way of decomposing an image $I(x)$ into a linear combination of complex sinusoids, each of which is a subband of that image. The phase of these subbands is linked to the global motion of the image $I(x)$ via the Fourier shift theorem

$$I(x) = \sum_{n=0}^{N} A_n e^{inx} \Rightarrow I(x - \delta) = \sum_{n=0}^{N} A_n e^{inx} e^{-in\delta}. \tag{5.1}$$

However, the Fourier transform is only able to decompose the image into global subbands that can only characterize global motions, while most motions in a video are local. Therefore, it is better to decompose the image into localized subbands using one of a variety of transforms like the Laplacian or steerable pyramids [14, 15]. Rather than decompose the image using filters that correspond to a single sinusoid like the Fourier transform, these transforms have filters that correspond to a wider range in the frequency domain making them more local in space.

In case of the Laplacian pyramid and the steerable pyramid, the produced subbands are real-valued signals, which are missing the corresponding imaginary part. In one dimension, the Hilbert transform, specified by transfer function

$$-i \frac{\omega}{|\omega|}, \tag{5.2}$$

can be applied to a real subband to yield a 90° phase-shifted version of it, which corresponds to the imaginary part. For example, the Hilbert transform of $\cos(x)$ is $\sin(x)$. These two signals can be combined to form a complex signal, which can be phase-shifted arbitrarily

$$\text{Real}((\cos(x) + i \sin(x))e^{i\delta}) = \cos(x - \delta) \tag{5.3}$$

In two dimensions, the Hilbert transform must be applied along a specific orientation. This is problematic as images do not have a preferred orientation. One solution used in Wadhwa et al. [11] was to first decompose the image into multiple scales and then further decompose each scale into several orientations using a complex steerable pyramid. This results in a large number of subbands, with 21× the total number of pixels of the original image. In addition, the filters required to divide the image into many orientations are often non-separable making their evaluation inefficient. All of this makes the processing unable to run in real-time. A second solution, allowing for real-time Motion Magnification, proposed in Wadhwa et al. [13] was to instead use the Riesz transform, the two dimensional generalization of the Hilbert transform [13, 16, 17].

The Riesz transform is defined by a pair of filters with transfer functions

$$-i \frac{\omega_x}{\|\vec{\omega}\|}, -i \frac{\omega_y}{\|\vec{\omega}\|}. \tag{5.4}$$

The direction invariance follows from the fact that the Riesz transform can be steered to an arbitrary orientation. For example, the Riesz transform of each frame of the image sequence $I(x, y, t) := \cos(\omega_x x + \omega_y y + \delta(t))$ is

$$R_1 := \sin(\omega_x x + \omega_y y + \delta(t)) \frac{\omega_x}{\sqrt{\omega_x^2 + \omega_y^2}} \text{ and } R_2 := \sin(\omega_x x + \omega_y y + \delta(t)) \frac{\omega_y}{\sqrt{\omega_x^2 + \omega_y^2}} \tag{5.5}$$

This can be steered to an arbitrary direction θ via the matrix multiplication

$$\begin{pmatrix} \cos(\theta) & \sin(\theta) \\ -\sin(\theta) & \cos(\theta) \end{pmatrix} \begin{pmatrix} R_1 \\ R_2 \end{pmatrix}. \tag{5.6}$$

giving a Hilbert transform in the specified direction. Of particular interest is if the Riesz transform is steered to the dominant orientation θ_0, given by $\tan^{-1}(R_2/R_1)$. The result of the matrix multiplication in Eq. 5.6 is a vector with only one non-zero entry, which in our case is

$$\sin(\omega_x x + \omega_y y + \delta(t)), \tag{5.7}$$

the Hilbert transform along the dominant orientation of the input image sequence. Like in 1D, this can now be combined with the original image sequence to form a complex signal which has phase

$$\omega_x x + \omega_y y + \delta(t). \tag{5.8}$$

This can be temporally filtered to remove the DC component $\omega_x x + \omega_y y$. The remainder $\delta(t)$ can be amplified and used to phase shift the complex signal, whose real part will be a motion magnified version of the original image sequence $I(x, y, t)$. That is,

$$\text{Real}((\cos(\omega_x x + \omega_y y + \delta(t)) + i \sin(\omega_x x + \omega_y y + \delta(t)))e^{i\alpha\delta(t)}) = \cos(\omega_x x + \omega_y - (1 + \alpha)\delta(t)). \tag{5.9}$$

More details about this processing can be found in Wadhwa et al. [13]. In practice, on a standard laptop, this processing runs at about 35 frames per second.

So far, we have described processing that amplifies small motions in videos. However, many ODS occur at temporal frequencies that are too fast to see at 35 frames per second. To handle these faster vibrations, we stroboscopically sample the scene by choosing a sampling rate that will alias the ODS frequencies to approximately 2.5 Hz. In particular, for an ODS frequency F, we choose a frame rate f, such that

$$2.5\,\text{Hz} \approx |\text{mod}(F + f/2, f) - f/2|. \tag{5.10}$$

We automatically choose f by finding the f between 17 and 25 Hz that minimizes the difference between the right and left sides of Eq. 5.10.

5.2.2 Operational Deflection Shape Extraction Methods Adapted to Camera Data

In previous work displacements were extracted from a cropped region of a video and processed to give a displacement signal that was representative of that region [12]. The details are given in [12] but the general procedure is to downsample the video to average out noise, use a quadrature pair of filters to extract the local phase information in the video, determine the locations of the strong edges, obtain displacement signals from the local phase information, and then use a weighted average to obtain a single displacement signal for the whole video. In this procedure, once the displacement signals are obtained from the local phase, each pixel in the video at the location of a strong edge has a displacement signal associated with it. These displacement signals may be somewhat noisier than the averaged result, however the benefit is high spatial sampling over the strong edges of structures in the video. We can extract high spatial resolution ODS from the displacement signals obtained from the videos. For a typical video this may result in 500–3,000 displacement signals, which is many more than the typical accelerometer-based measurement. This presents a special challenge when performing mode shape identification, as some methods may not scale well with increasing numbers of signals. Two methods were implemented in an output only manner with use of a broadband excitation, peak picking from fast Fourier transform (FFT) spectra and frequency domain decomposition.

Peak picking to obtain ODS from a collection of signals involves taking the FFT of the displacement time signals and picking out peaks in the frequency domain that correspond to potential resonant modes. Cross power spectral densities (PSD) are taken with reference to a single signal to determine the phase difference between the displacement signals at different frequencies. This information combined with the normalized magnitudes of the FFT at the picked frequencies create the ODS. The downside to this method is that it does not work well with closely spaced modes and it is difficult to identify non-physical harmonics in the response [18].

Frequency domain decomposition (FDD) is a method used for modal identification of output-only systems which addresses some of the drawbacks of the peak picking method [18]. It involves first calculating the spectral matrix, a matrix containing the cross PSD between all the output signals. The singular value decomposition (SVD) of the spectral matrix at each frequency is taken to decompose the spectral matrix into a set of auto spectral density functions as singular values, where strong resonant peaks in the singular values correspond to possible resonant modes and the singular vectors are the corresponding ODS. The benefit is that this algorithm performs than peak picking when signals are noisy and there is better discrimination for closely spaced resonant modes and the possible identification of non-physical harmonics [18, 19].

5.3 Results

5.3.1 Real-Time Motion Magnification

The real-time motion processing in Wadhwa et al. [13] can run at 35 frames per second for a 640×400 image. As mentioned in Sect. 5.2.1, vibrations occurring over the Nyquist frequency of 17.5 Hz can be visualized by subsampling the video at a rate to alias the modal frequencies to approximately 2.5 Hz. This sampling requires low exposure times to reduce motion blur. We use a bright light to provide sufficient illumination for an exposure time of 0.3 ms. The camera is a color Point Grey Grasshopper 3 (GS3-U3-23S6M-C) that is connected to a laptop with a quad-core 2.7 GHz Intel i7-3820QM processor. The processing only uses a single core of this processor.

We use the processing to visualize two of the ODS of a damaged cantilevered beam when it is struck by a hammer near the support in the flexible direction. The results are shown in Fig. 5.1. The camera is set to sampling rates of 21.2 Hz for the one node ODS and 24.5 Hz for the two node ODS. The modal frequencies are 87 and 248 Hz respectively and they get aliased to 2.5 and 2.9 Hz. However, the spatial shape of the motions at these frequencies still correspond to the original operational deflection shape.
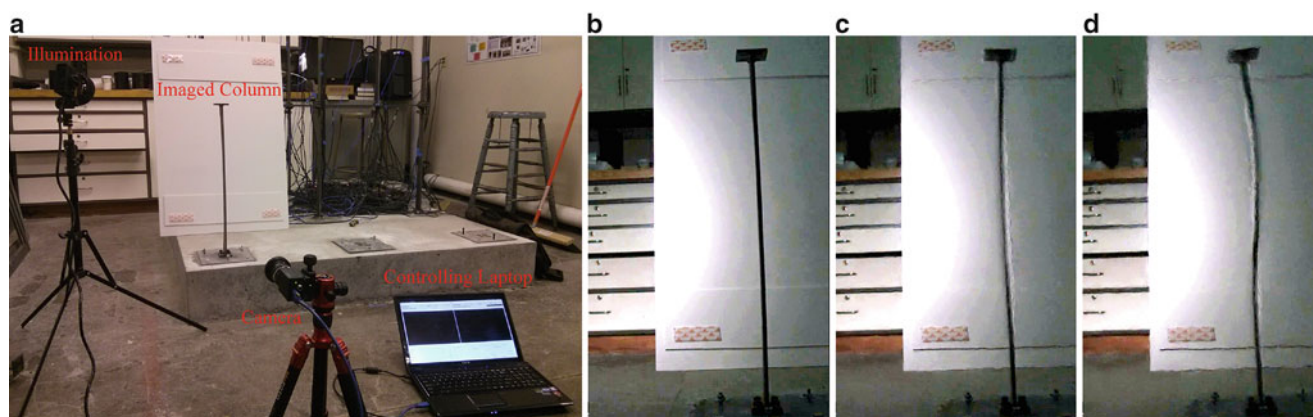
Fig. 5.1 Real-time motion magnification is used to visualize the second and third bending operational deflection shapes of a cantilevered beam. The experimental setup is shown in (**a**). An ordinary laptop processes data from the camera in real-time. An unprocessed frame from the camera is shown (**b**) and two frames from processed videos are shown in (**c**) and (**d**). In (**b–d**), the frame has been rotated 90° counter-clockwise and the contrast has been enhanced

Fig. 5.2 Setup for ODS identification of a cantilever beam: (**a**) a picture of the experimental setup, (**b**) a frame from the camera video, and (**c**) the mask showing pixels with extracted displacements
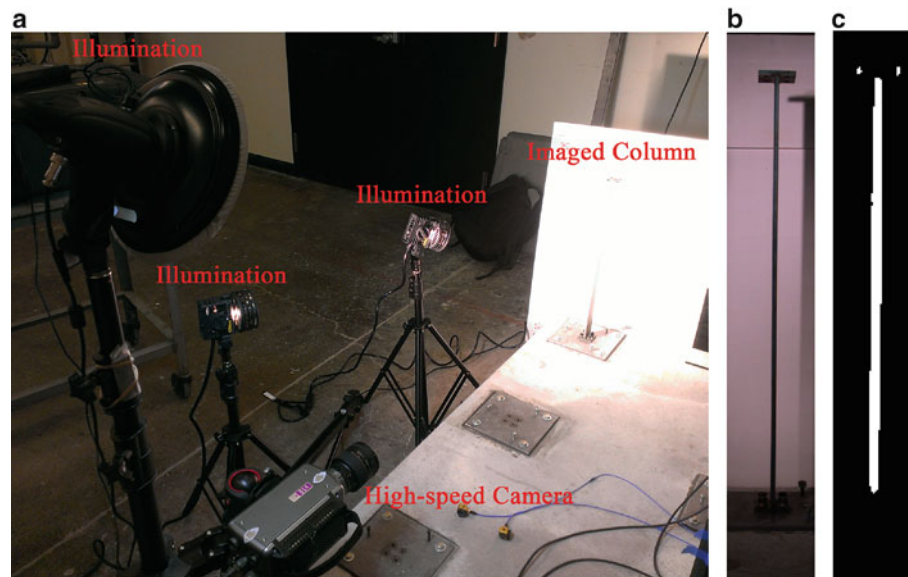
5.3.2 Quantitative ODS Extraction from Camera Video

The experimental setup used to test the ODS identification methods involved a high-speed camera, cantilever beam, and sources of illumination as shown in Fig. 5.2a. The column was struck with an impact hammer on the bottom third to induce vibrations in as many bending modes as possible. Video was recorded at 2,000 frames per second with a full frame resolution of $1,248 \times 200$ using the high speed camera with a frame shown in Fig. 5.2b . The video was downsampled by a factor of two such that after the processing, the valid frame was 304×42 (12,768) pixels in the video and from that, edges were strong enough to obtain signals for 1,234 pixels in the image. The mask shown in Fig. 5.2c has in white the pixels where displacement signals were obtained.

From the displacements the ODS were identified using the two methods described in the derivation section, peak picking from FFT spectra, and frequency domain decomposition. The spectra obtained from the displacement signals are shown in Fig. 5.3 with the one used for the peak picking technique in (a) and the singular values given in (b) and (c). The frequencies determined to be candidates for resonant modes are the same for both methods, which makes sense as the FDD method uses the same FFTs of the displacement signals to generate the singular values. The results of the ODS identification are shown in Fig. 5.4, with 2D plots showing the normalized magnitude of the ODS at each identified frequency and the phase relationships between the signals.

The resulting identified ODS for both cases end up being the first five bending modes at 14, 88, 248, 490, and 812 Hz and the first two torsional modes at 294 and 896 Hz. Comparing the two methods the results are almost identical for the five bending modes. They are also similar for the torsional modes, albeit with the phase information more varied in the case of the peak picking method. A more detailed comparison of the identified ODS is given in Fig. 5.5 where the ODS magnitudes are averaged in horizontal rows to give a single value for each vertical sample which results in a more visually interpretable 1D mode shapes for the column. The ODS are shown in blue for the result from the FFT peak picking method and red for FDD. For the bending modes, the results are almost identical, but for the torsional modes the differences are more clear, especially with the second torsional mode where the peak picking ODS is much noisier than the FDD ODS. The MAC values comparing the identified ODS are given in Table 5.1 with the bending and torsional modes denoted by either B or T. The MAC values quantitatively match the qualitative observations previously described.
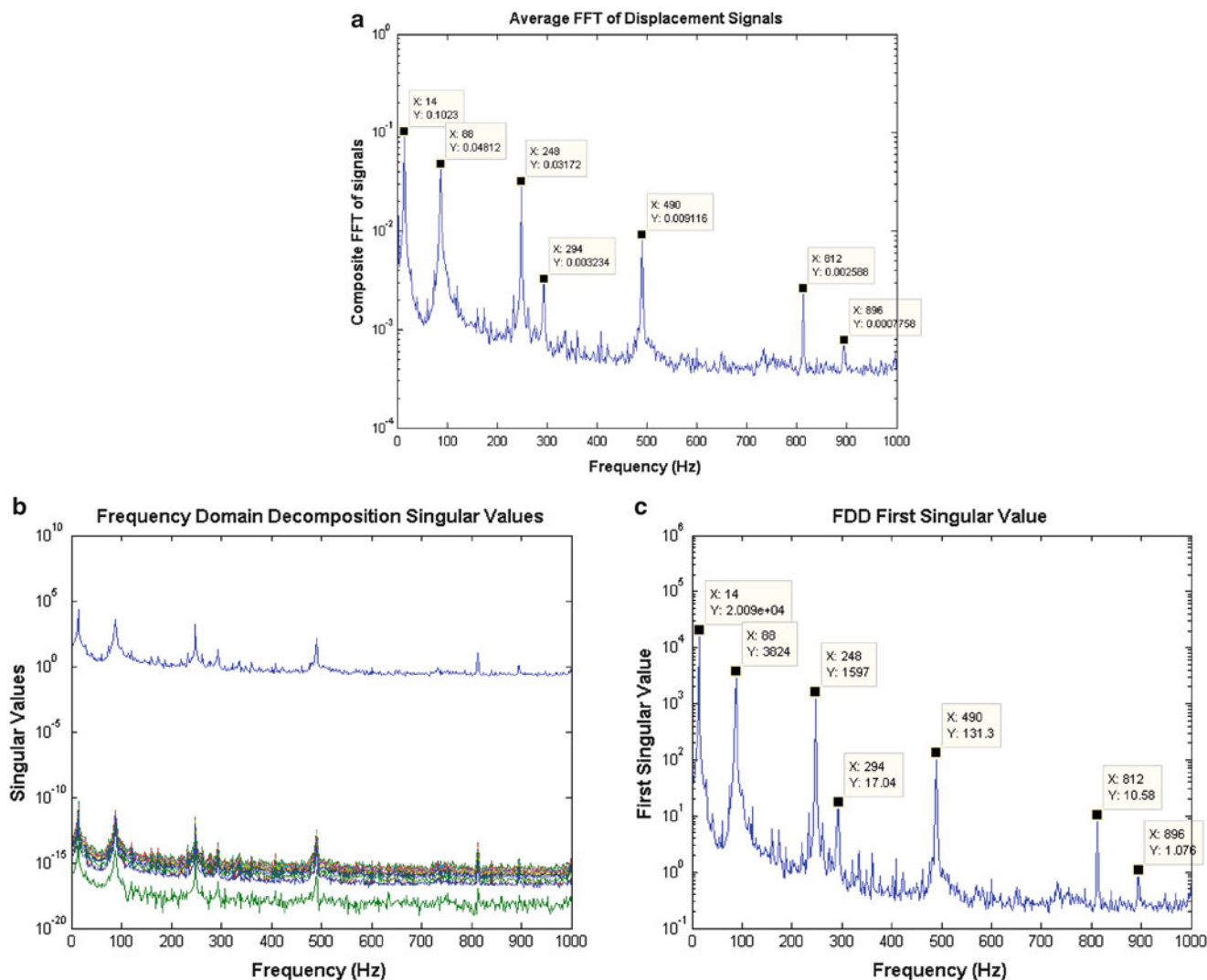
Fig. 5.3 Spectra used to determine potential resonant modes of interest, (**a**) average FFT of displacement signals and selected frequencies of interest, (**b**) singular values as a result of FDD, and (**c**) first singular value and selected frequencies of interest

5.4 Conclusion

In this paper we have presented two developments in the use of motion magnification algorithms with video for structural model identification. The first development is the demonstration of real-time Motion Magnification of a cantilever beam using a new technique involving Riesz pyramids for video processing. Using a sub sampling technique, the second and third vibrational mode are visualized in real-time. The second development is the application of modal identification techniques to the large number of displacements extractable from video of a cantilever beam. Upwards of 1,000 displacement signals are extracted from video of a cantilever beam and they are processed with both the peak picking and frequency domain decomposition techniques to identify the first five bending modes and first two torsional modes. The techniques provide comparable results except in the case of the second torsional mode which has less signal than the other modes. The hope is that these developments bring closer the reality of using cameras for modal inspection of structures.

Fig. 5.4 Identified ODS using the (**a**) peak picking method and the (**b**) frequency domain decomposition method
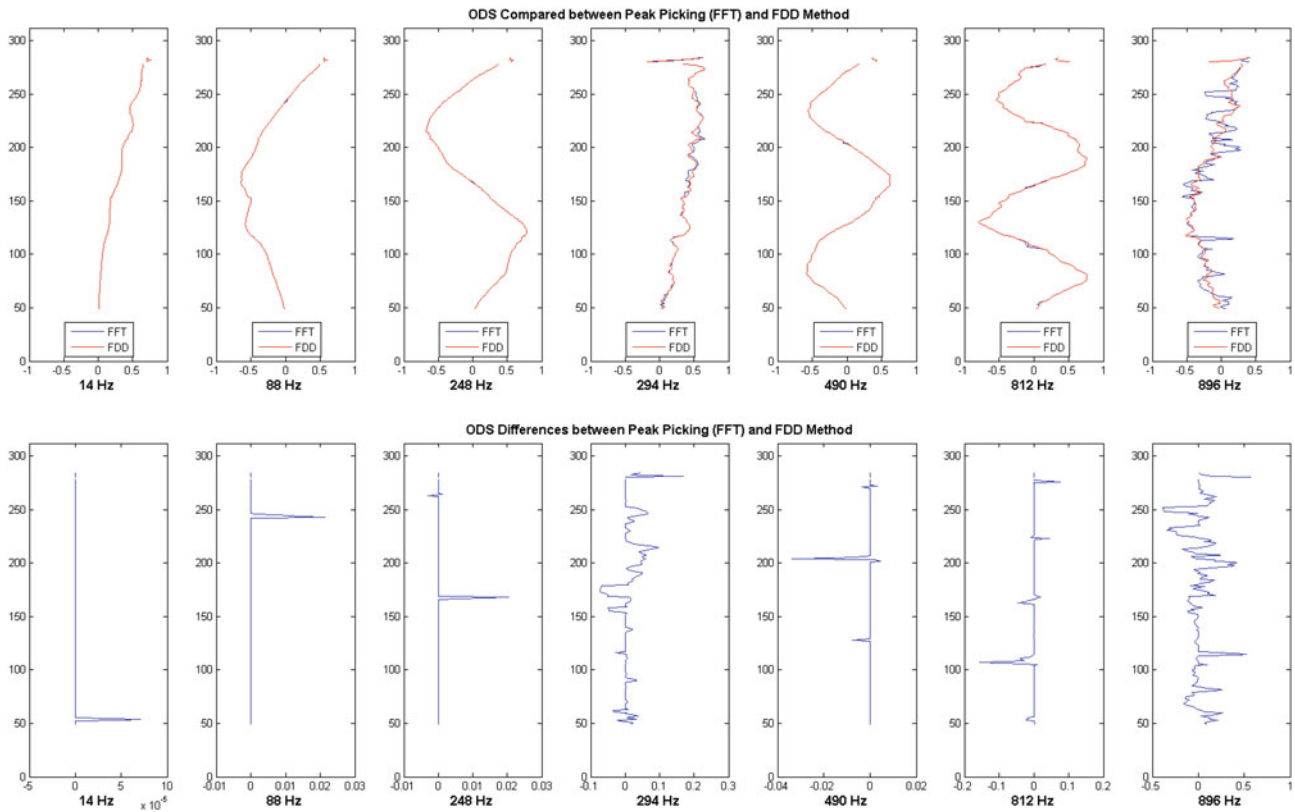
Fig. 5.5 Comparison of video identified ODS

Table 5.1 MAC values comparing ODS identified with FDD with peak picking (FFT) techniques for the various bending (B) and torsional (T) modes

ODS	FFT B1 (%)	FFT B2 (%)	FFT B3 (%)	FFT B4 (%)	FFT B5 (%)	FFT T1 (%)	FFT T2 (%)
FDD B1	100.00	7.75	4.38	1.17	0.00	84.50	0.41
FDD B2	7.78	100.00	1.56	2.53	1.19	33.61	63.21
FDD B3	4.38	1.56	100.00	0.19	5.07	1.38	20.33
FDD B4	1.15	2.57	0.19	100.00	0.09	1.96	1.03
FDD B5	0.00	1.30	4.85	0.12	99.91	0.18	0.54
FDD T1	83.34	34.91	1.07	1.58	0.09	99.52	13.48
FDD T2	1.08	78.09	25.88	3.34	0.10	14.37	76.41

References

1. Castellini P, Martarelli M, Tomasini E (2006) Laser Doppler vibrometry: development of advanced solutions answering to technology's needs. Mech Syst Signal Process 20(6):1265–1285
2. Stanbridge A, Ewins D (1999) Modal testing using a scanning laser Doppler vibrometer. Mech Syst Signal Process 13(2):255–270
3. Aranchuk V, Lal A, Sabatier JM, Hess C (2006) Multi-beam laser Doppler vibrometer for landmine detection. Opt Eng 45(10):104302–104302
4. Caetano E, Silva S, Bateira J (2011) A vision system for vibration monitoring of civil engineering structures. Exp Tech 35(4):74–82
5. Lee JJ, Shinozuka M (2006) A vision-based system for remote sensing of bridge displacement. NDT&E Int 39(5):425–431
6. Wahbeh AM, Caffrey JP, Masri SF (2003) A vision-based approach for the direct measurement of displacements in vibrating systems. Smart Mater Struct 12(5):785
7. Patsias S, Staszewskiy W (2002) Damage detection using optical measurements and wavelets. Struct Health Monit 1(1):5–22
8. Ferrer B, Espinosa J, Roig AB, Perez J, Mas D (2013) Vibration frequency measurement using a local multithreshold technique. Opt Express 21(22):26198–26208
9. Liu C, Torralba A, Freeman WT, Durand F, Adelson EH (2005) Motion magnification. ACM Trans Graph 24:519–526
10. Wu H-Y, Rubinstein M, Shih E, Guttag J, Durand F, Freeman W (2012) Eulerian video magnification for revealing subtle changes in the World. ACM Trans Graph (Proc SIGGRAPH) 31:65

11. Wadhwa N, Rubinstein M, Durand F, Freeman WT (2013) Phase-based video motion processing. ACM Trans Graph (Proc SIGGRAPH 2013) 32(4):80
12. Chen JG, Wadhwa N, Cha Y-J, Durand F, Freeman WT, Buyukozturk O (2014) Structural modal identification through high speed camera video: motion magnification. In: Topics in modal analysis I, vol 7. Springer, Cham, Switzerland, pp 191–197
13. Wadhwa N, Rubinstein M, Durand F, Freeman WT (2014) Riesz pyramids for fast phase-based video magnification (2014) IEEE International Conference on Computational Photography (ICCP), IEEE
14. Burt P, Adelson E (1983) The Laplacian pyramid as a compact image code. IEEE Trans Commun 31(4):532–540
15. Simoncelli EP, Freeman WT (1995) The steerable pyramid: a flexible architecture for multi-scale derivative computation. In: Proceedings of the 1995 international conference on image processing, ICIP '95, vol 3. IEEE Computer Society, Washington, pp 3444–3452
16. Felsberg M, Sommer G (2001) The monogenic signal. IEEE Trans Signal Process 49(12):3136–3144
17. Unser M, Sage D, Van De Ville D (2009) Multiresolution monogenic signal analysis using the Riesz–Laplace wavelet transform. IEEE Trans Image Process 18(11):2402–2418
18. Brincker R, Zhang L, Andersen P (2001) Modal identification of output-only systems using frequency domain decomposition. Smart Mater Struct 10(3):441
19. Brincker R, Andersen P, Møller N (2000) An indicator for separation of structural and harmonic modes in output-only modal testing. In: International modal analysis conference (IMAC XVIII), San Antonio. Society for Engineering Mechanics, Bethel, pp. 1649–1654

Chapter 6
Interactive Platform to Include Human-Structure Interaction Effects in the Analysis of Footbridges

Daniel Gomez, Christian E. Silva, Shirley J. Dyke, and Peter Thomson

Abstract An increasing number of structures, such as pedestrian bridges, are affected by excessive vibration when they are dynamically excited. The development of new materials and improvements in guidelines have given rise to designs with longer spans and slender structural elements, which in turn cause such structures to be more susceptible to vibration problems. However, serviceability guidelines do not address the changes of the dynamic properties of pedestrian bridges nor do they accurately predict their dynamic response. In order to improve the structural analysis and design, a new computational tool is developed using an intercommunication platform between MATLAB and SAP2000 application programming interface (API) to consider different human walking models, including user-defined models, directly on the footbridge to take into account human-structure interaction effects. Details of the application are presented in this paper and results of the analysis for some walking models and their effects on the dynamic parameters of the bridge are given.

Keywords Pedestrian excitation • Vibration serviceability • Human-structure interaction • Dynamic response • Vertical footbridge vibration

6.1 Introduction

In recent years, an increasing number of pedestrian bridges have been reported of presenting problems with excessive vibration induced by human activities. Some of the causes are: more flexibility, less mass, and use of large spans between supports. This has caused that footbridges are more sensitive to dynamic loads causing excessive vibrations and in the worst case causing the structure to collapse. As a result, the conditions of serviceability load due to walking people are controlling the design criteria for this type of structures [1]. Unfortunately, some design and construction codes ignore this problem by assuming the pedestrian load as static, ignoring the interaction between human activities and structure. As a consequence, architects and engineers are concerned for the serviceability of footbridges, making sure that they are beautiful, safe and comfortable.

Specifically in pedestrian bridges, the use of large spans implies that the vibration modes are generally associated with low frequencies, from 1 to 8 Hz [2]. For walking, the gait of people has a pace frequency between 1.7 and 2.3 Hz in the 90 % of the population [3]. This show the potential risk of such structures to fall in resonance. Resonance occurs when the natural frequency of the bridge matches the excitation frequency, in this case the gait frequency of the people, or one of its harmonics [1].

The loads generated by human activities change in time and space, varying considerably the dynamic properties of slabs, pedestrian bridges, stairs and grandstands [4]. Some aspects of the Human-Structure Interaction (HSI), such as synchronization, have been extensively studied mainly in the lateral direction. Unfortunately, the effects that people produce on the dynamic properties of the structure in the vertical direction are commonly ignored because the methods to predict vertical vibration responses of bridges are still often inaccurate [5]. Even with the recent advances in load models and response prediction, measured footbridge responses often deviate from those predicted. The main reason for this lack of correlation is that experimental tests of HSI in the vertical direction as well as analytical models of the load produced by people are unable to adequately simulate the dynamic interaction between the two systems [6].

D. Gomez (✉) • C.E. Silva • S.J. Dyke • P. Thomson
Department of Mechanical and Civil Engineering, Purdue University, West Lafayette, IN 47906, USA

School of Civil Engineering, Universidad del Valle, Cali, Colombia
e-mail: dgomezp@purdue.edu; silva15@purdue.edu

In particular, pedestrian loading models from human walking generally considerer the dynamic loading to be an external force to the structure [4], with no feedback to the pedestrian. However, the motion of the structure can affect the human behavior changing the gait frequency, thus modifying the dynamic properties of the human-structure system. Also, other sources of uncertainties are changes in mass and damping that a pedestrian might introduce to a bridge affecting the dynamic response.

However, a more simple and reliable model should be developed to include both exciter and structure in the response, to create a credible model capable of capturing the underlying relations between the two dynamic systems. The goal of this paper is obtained a realistic structural behavior due to human walking using a commercial software like SAP2000. To do this, an application is developed to include the structural response in a loop at the same time that the mass source is changing to simulate the movement of the pedestrian.

6.2 Problem Formulation

Some effects of walking pedestrians on dynamic properties of structures in the vertical direction are mostly ignored. This is mainly due to the lack of reliable HSI experimental data in the vertical direction as well as models capable of representing the interaction between the two dynamic systems [6]. The general approach in HSI establishes that the pedestrian moving load can be assumed as a mass body moving in the bridge, based in the d'Alembert's principle its effects are: the weight, or gravitational effect of the moving load, and the inertial effects of the load mass on the deformed structure [7]. A first case arises when only the weight effect of the pedestrian is considered, and the mass of the moving load neglected against the mass of the structure, the computations of responses (acceleration, velocity, displacement, strain or stress) of the structure is an easy and well known procedure. The other extreme case is when the structure mass is assumed to be negligible against the load mass, and only the mass of the pedestrian is considered in the analysis. The third case is both, the gravitational and the inertial action of pedestrian loads, interact with the mass of the structure (See Fig. 6.1).

The first approach, when the pedestrian mass is negligible, is the procedure widely used by structural engineers to design pedestrians bridges. Specific commercial software based on finite element analysis describe a methodology to bring the user the possibility to get the response of pedestrian bridge due to human loads. Unfortunately, this procedure does not include the inertial effect of the pedestrian mass and only use the modal mass of the structure in the analysis. This analysis can be describe by (Eq. 6.1) in an Euler-Bernoulli's simple supported beam, i.e. a beam with zero deflection and zero bending moment at both ends, with constant cross-section and mass per unit length $\bar{m}$. The pedestrian moving load is represented by $P(t)\,\delta(x - ct)$ with constant speed c and the beam damping ratio ζ is proportional to the velocity of the vibration.

$$EI\frac{\partial^4 u(x,t)}{\partial x^4} + \bar{m}\frac{\partial^2 u(x,t)}{\partial t^2} + 2\zeta\omega_n\frac{\partial u(x,t)}{\partial t} = P(t)\,\delta(x - ct) \tag{6.1}$$

The boundary conditions are

$$u(0,t) = 0; \qquad\qquad u(0,t) = 0$$

$$\left.\frac{\partial u^2(x,t)}{\partial x^2}\right|_{x=0} = 0; \qquad\qquad \left.\frac{\partial u^2(x,t)}{\partial x^2}\right|_{x=l} = 0$$
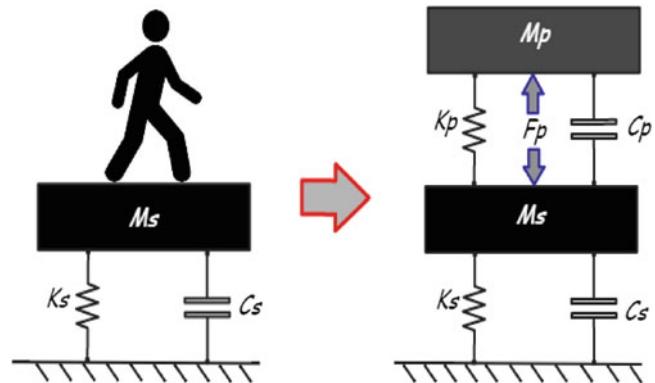
Fig. 6.1 Conceptual 2DOF model of coupled (bridge-pedestrian) system

The initial conditions are

$$u(x, 0) = 0; \qquad \frac{\partial u(x, t)}{\partial t} = 0$$

Where ω_n is natural frequency of the beam, E is the Young's modulus and I is the second moment of area of the cross-section.

To include the effect of a moving mass over the beam, [8] introduced an assumption according to which the gravitational effects of the load may be separated from the inertial ones while the moving mass (in this case the pedestrian mass) acts at a definite constant point x_0.

$$EI \frac{\partial^4 u(x, t)}{\partial x^4} + \bar{m} \frac{\partial^2 u(x, t)}{\partial t^2} + 2\zeta \omega_n \frac{\partial u(x, t)}{\partial t} = \left[P(t) - m \frac{d^2 u(ct, t)}{dt^2} \right] \delta(x - ct) \qquad (6.2)$$

The pedestrian load in (Eq. 6.2) acts on the beam by force $P(t)$ and by inertial force $-m \frac{d^2 u(ct,t)}{dt^2}$ which is dependent of the vertical acceleration at point $x = ct$ where the load is situated at time t. The mass of the pedestrian is denoted with m in the right-hand side of this expression. This equation describes the case in which a moving load is idealized by a single mass point. However, due to the complexity to solve (Eq. 6.2), some authors made a study of the motion of a sprung mass along a beam, and applied the solution to vibrations issues of highway bridges [7].

Due to complexity of simulate human dynamic effects on structure, a simple procedure is proposed using a well-know FEM software package. Dynamic properties of the pedestrian are include in the analysis changing the position in each step. To simulate the human-structure behavior the linear response is assumed in order to apply superposition in the total response. In order to validate the procedure, experimental data due to human walking in a small bridge is compared with the SAP2000 results.

6.3 Experiment Design and Data Collection

In order to keep focus on the primary mechanism for investigation in this paper, it is chosen to employ a simplistic bridge for the investigation. Therefore, a simple support bridge with four steel box girders and an aluminum deck was built. The bridge length was set to 4.56 m to include exactly five steps every 0.76 m each (See Fig. 6.2). This length correspond to the average of the stride cycle of a pedestrian.

The fundamental flexural mode for the bridge has natural frequency of 4.63 Hz and damping ratio of about 0.68 % and were obtained experimentally by several free vibration tests in the empty structure. One item to notice is that it is a bridge, which can resonate as a result of a pedestrian load, in that the first mode can be excited by the second harmonic component of the stride cycle (with a mean step frequency close to 2 Hz as suggested in the literature). Also, the steel structure is very

Fig. 6.2 Experimental bridge
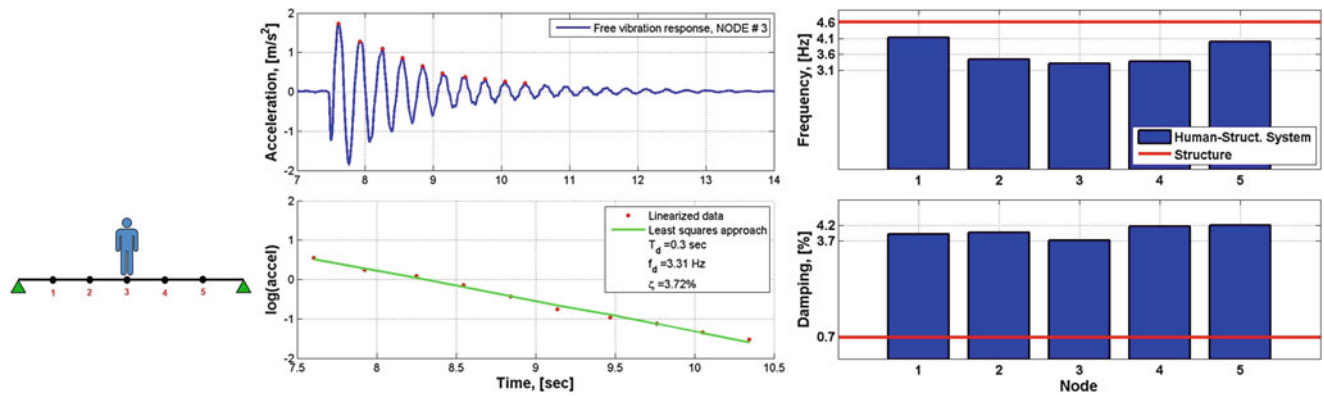
Fig. 6.3 Free vibration responses of the bridge with passive person and change in dynamic parameters (Mode 1)
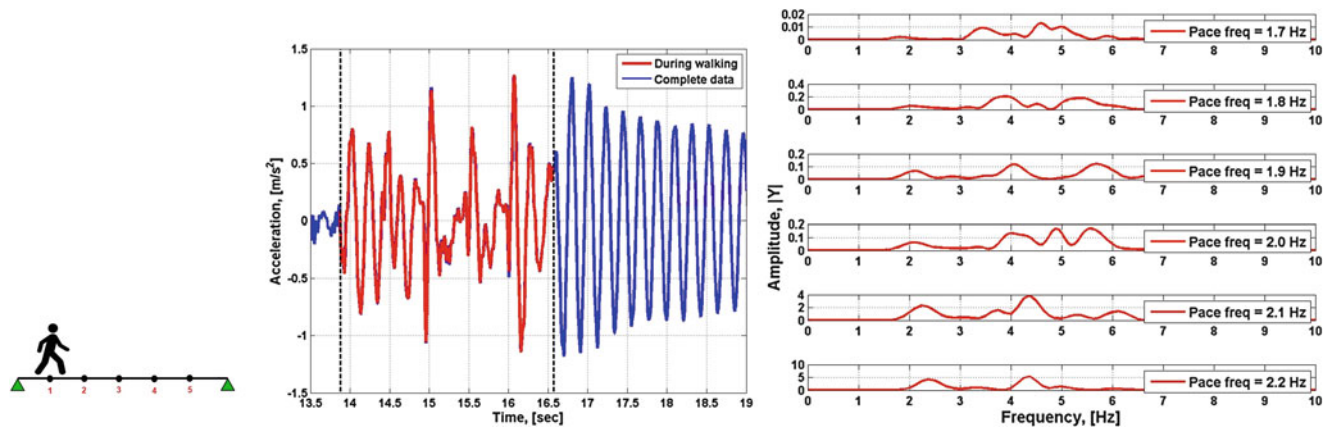
Fig. 6.4 Time history response due to pedestrian (pace freq. $= 2$ Hz) and PSD for different pace frequency

lightly damped which can be problematic in the serviceability limit state of the bridge. To compare the natural frequency and the damping ratio for the first mode in the human-bridge system, several free vibration tests were conducted with a person placed in a passive mode over each node of the structure (See Fig. 6.3).

Such tests were performed in order to get the changes in dynamic properties due to a person standing on the bridge with a mass equal to 74 kg. The results in Fig. 6.3 show the natural frequency of the empty bridge (red line) compared with the natural frequency of the coupled system, described by the blue bars. The difference between the natural frequency of the empty structure and the natural frequency when the person is on the bridge is an evidence that Eq. (6.1) is not a good model for the coupled problem, even when the load is static over the structure.

Moreover with the same person but in different positions of the beam, the participating modal mass in the response changed, resulting in different natural frequency even with the same person (the same mass) over the bridge. For that reason, the lowest frequency obtained in the analysis was produced when the person was in the middle of the bridge, and his/her total mass was involved in the structural response. Furthermore, the damping increased its value from 0.7 % in the empty structure to around 3.9 % for the human-bridge system, however any conclusion can be extracted from that preliminary data.

On the other hand, several test were conducted using a pedestrian over the bridge. The person walked at different pace rates (1.7–2.2 Hz) follow the hearing aid of a metronome. The metronome was used to coordinate the pace of the pedestrian around a specific value. The pace frequencies were chosen close to the average frequency for the stride of a person, which is around 2 Hz. The forced vibration response in acceleration was recorded in every node in the same place that the free-vibrations tests, but only the response in the middle of the span (node 3) is shown (see Fig. 6.4).

In order to get the signal analysis in frequency domain, the power spectral density (PSD) was used. To analyze only the response of the pedestrian-bridge system the red part in Fig. 6.4 was considered, which indicates when the person walked in the structure. The PSD for each pace frequency is shown in Fig. 6.4. The frequency domain analysis show that the first frequency recorded is due to the pedestrian pace frequency. Also, its second harmonic, which is close to the first natural frequency of the pedestrian-bridge system, produced higher amplitudes in the structural response. This phenomenon is due to the interaction between the pace frequency of the pedestrian and the natural frequency of the structure, and it is not possible to represent this interaction with a traditional procedure in any FEM software package.

6.4 Sap2000 Application Programming Interface

The need for computational power and the subsequent requirement to embrace edge technology tools and resources are demanding and expensive. The necessity to increase productive computational systems motivates researchers to investigate more advanced and optimized tools for the analysis and design of structures, leading to develop new software capabilities. In this direction, the computational tool that accesses SAP2000 through its Application Programming Interface (API), has come to significantly expand the usage of more sophisticated procedures for the needs of structural engineering.

SAP2000 API is a programming tool that allows users to automate many of the processes required to build, analyze and design models and to obtain customized results. It allows users to link SAP2000 with third-party software, as MATLAB, providing a path for two-way exchange of model information. In terms of computer programming, the API consists of a software library that offers access to a collection of objects and functions capable of controlling the way that the SAP2000 behaves, thus, overriding the standard procedures. For this specific problem, API is very helpful to improve the structural analysis due to pedestrian load, allowing include the human weight like a moving load that produce a force that change as function of time.

The analysis is controlled through an interactive graphical user interface (GUI), which consists of a main window that contains all the components necessary to load the SAP2000 model, load or define the human load, the step position, and choose the analysis procedure (See Fig. 6.5). In such way, the user can interact entirely with the GUI interface provided, while SAP2000 runs hidden in the background. All of the required actions related to the characteristics of the Human load model are transferred to SAP2000 finite element model via the API from MATLAB directly.

The results of the procedure proposed in this paper are shown in Fig. 6.6. In order to use a input load for simulation, the ground reaction force shape was obtained from [9], and divided by the pedestrian mass to obtain a time-history acceleration to be used in the analytical model. With this acceleration function, the response of the structure is compared with two experimental data response in the middle of the bridge. These data were recorded for the same pedestrian walking with a metronome at 2 Hz.
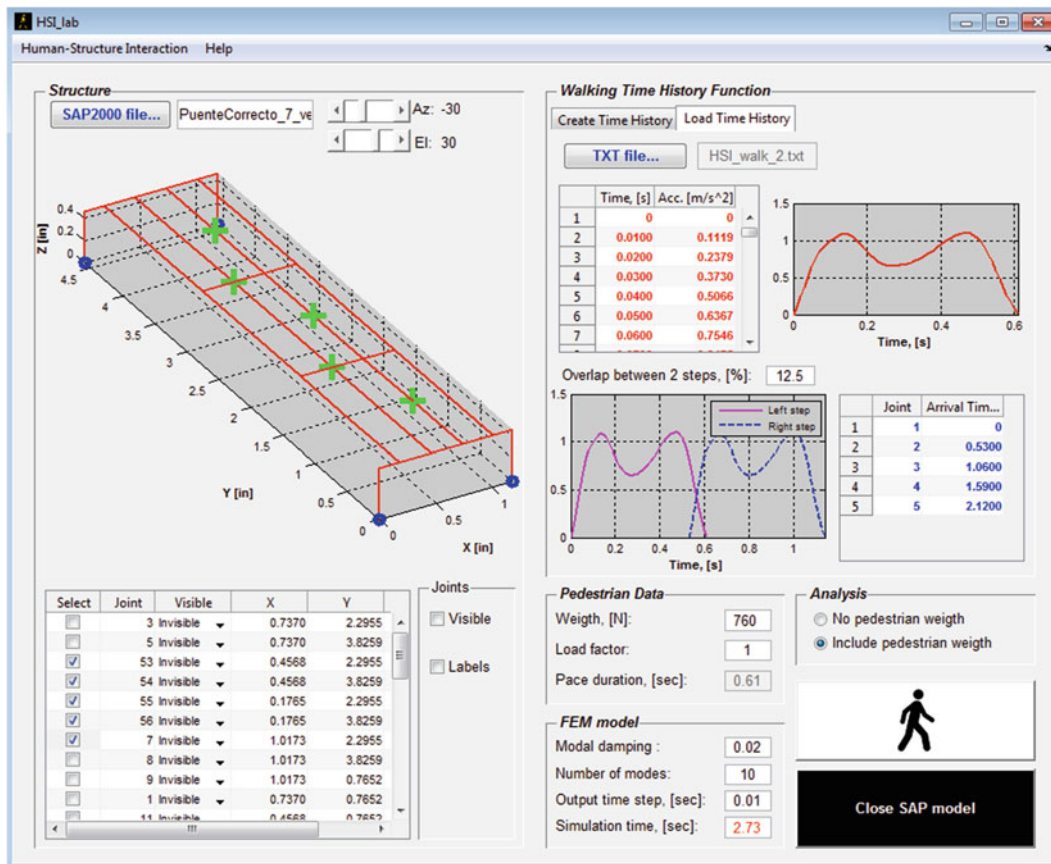
Fig. 6.5 GUI main window

Fig. 6.6 Structural response comparison
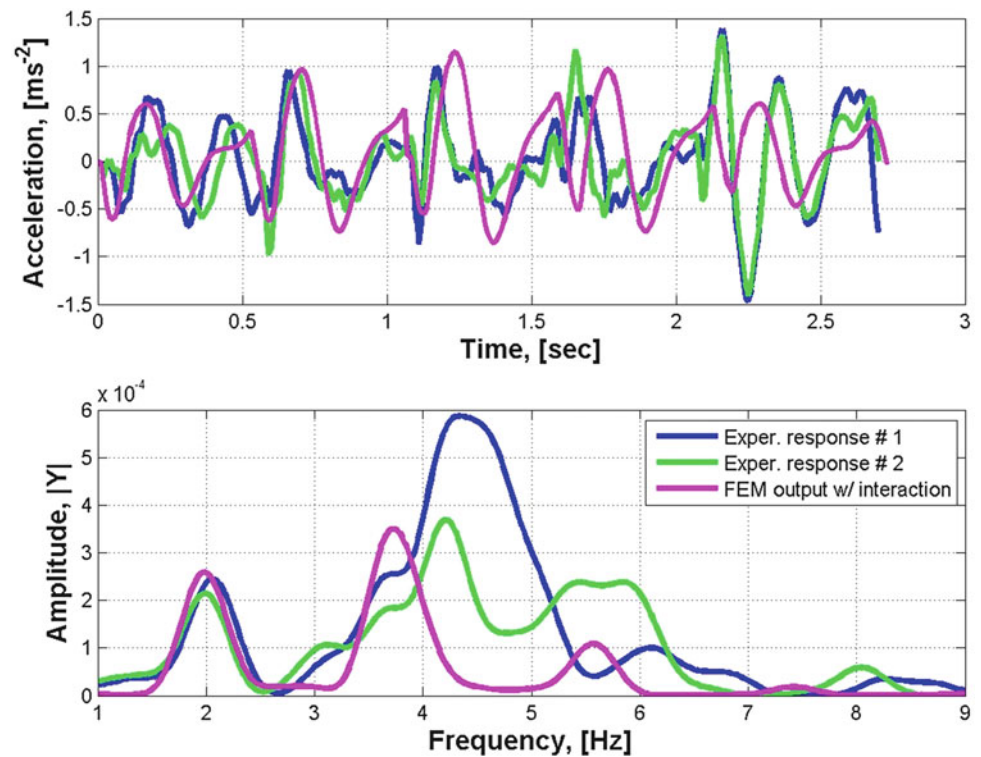
The analytical model response of the system showed that the pedestrian-bridge interaction is captured in both, time and frequency domain, even when the ground reaction force does not correspond to the forces due to pedestrian. In a future work, the researchers will measure the ground reaction force due to a subject, in order to use it directly in the platform. This is expected to improve the response of the system.

6.5   Conclusions

The problem of influence of walking people on pedestrian bridges vibration properties, such as natural frequency and damping is not well understood, let alone quantified. The complexity of this problem is mainly related to couplings between varying loading and transient structure response. Therefore proper understanding of structural response due to human loads is necessary for a successful analysis and design. However, there is not a guideline that specifies how to include pedestrian load to get a realistic structural response. That imply that designing major footbridge assuming the pedestrian load as static, ignoring the interaction between subject and structure. Thus, a simple methodology for establishing an accurate procedure for predicting the structural behavior in a FEM model has been developed to include HSI, coupling with the SAP2000 analysis method.

The aim here was to develop a new application to connect SAP2000, through its API, with MATLAB. This app is capable of controlling the SAP2000 FEM model to include extra information that is necessary for HSI analysis. This new application allow an intuitive data flow that can be used to facilitate both pre- and post-processing procedures. To emulate the HSI in the analysis, an iterative process is used in order to change the position of the mass source in each analysis. This unique iterative load structure procedure allows us to estimate a realistic behavior due to human load.

References

1. Sánchez J, Gomez D, Thomson P (2013) Analysis of human-structure interaction in footbridges in Santiago de Cali. Dyna 80(177):86–94
2. Živanović S, Pavic A, Reynolds P (2005) Vibration serviceability of footbridges under human-induced excitation: a literature review. J Sound Vib 279(1):1–74
3. Newl D (2004) Pedestrian excitation of bridges. Proc Inst Mech Eng C J Mech Eng Sci 218(5):477–492

4. Racic V, Pavic A, Brownjohn J (2009) Experimental identification and analytical modelling of human walking forces: literature review. J Sound Vib 326(1):1–49
5. Bocian M, Macdonald J, Burn J (2011) Modelling of self-excited vertical forces on structures due to walking pedestrians. In: Proceedings of the 8th international conference on structural dynamics (Eurodyn 2011), Leuven, Belgium, pp. 1110–1117
6. Shahabpoor E, Pavic A, Racic V (2013) Using MSD model to simulate human-structure interaction during walking. In: Topics in dynamics of civil structures, vol 4. Springer, Berlin, pp 357–364
7. Frỳba L (1999) Vibration of solids and structures under moving loads. Thomas Telford, London
8. Inglis SCE (1934) A mathematical treatise on vibrations in railway bridges, vol 25. Cambridge University Press, Cambridge
9. Winter DA (2009) Biomechanics and motor control of human movement. Wiley, New York

Chapter 7
Comparing Closed Loop Control Models and Mass-Spring-Damper Models for Human Structure Interaction Problems

Albert R. Ortiz-Lasprilla and Juan M. Caicedo

Abstract The interaction between human and structure can produce significant dynamic effects. This has been demonstrated in several occasions including the closing of the Millennium bridge in London shortly after being open to traffic. Models based on springs, dampers and lumped masses have been widely accepted by the scientific community to model the human in human-structure interaction (HSI) problems. Recently, models of the human body based on control theory have been proposed. This paper provides a comparison between two traditional models using spring, dampers and lumped masses and those using control theory. The models are updated in a probabilistic sense using Bayesian inference. The experimental data used for the comparison is obtained from a laboratory test structure specially designed for HSI studies.

Keywords Human-structure interaction • Closed loop control • Human loads • Feedback • Vibration induced by people

7.1 Introduction

The interest in human-structure interaction (HSI) has increased during the last two decades due to the number of reports of structures with vibration problems due to crowds. During the design process it is common to model the human loads as static force depending only on the mass of the occupants [1]. However, this does not correctly represent the interaction between humans and structure.

The effects of human loads in structures are difficult to predict because they depend on the type of activity people are performing. However, models for typical activities such as standing, sitting, and jumping have been proposed in the literature. Traditional models represent the human body as a system of lumped masses, dampers and springs when people do not jump [2–6]. Arguably, these models might not fully represent the human body because lumped masses, dampers and springs cannot add energy to the overall system. Furthermore, people could react differently at different levels of excitation and other environmental conditions.

Ortiz et al. [7] proposed a new type of model for human-structure interaction. The new model uses a close loop control from systems theory. This model is able to add energy to the system, and could be a more representative way to model the human in HSI problems. The controller parameters could change depending on the characteristics of the human body and how it reacts to the changing environments [8]. Although control theory concepts have been applied to structural engineering, closed loop control systems have not been widely studied for HSI problems [9–12].

This paper compares HSI models using a closed loop control system with the traditional models based on lumped masses, dampers and springs (MDS) systems. The control theory based models are a Proportional and Derivative controller (PD), and a Proportional, Integrative and Derivative controller (PID). These controllers use information about the present, past and future errors (in case of PID), or present and future errors (if PD is used), calculated as the difference between the real and desired value. MDS systems are modeled using the human body as a single and two degree of freedom systems [2]. All models have been developed for a single occupant in a standing position with straight knees. The structure is modeled as a single degree of freedom system.

The paper is organized as follows. Section 7.2 gives an overview of the models and the model updating process to estimate the model parameters. The description of the tests as well as the method to compare the performance of each model are discussed in Sect. 7.3. In Sect. 7.4, tests results are compared with experimental tests. Finally, some conclusions about the similarities and constraints of these models is discussed. All work was carried out in accordance with the Code of Ethics of the World Medical Association [13].

A.R. Ortiz-Lasprilla (✉) • J.M. Caicedo
Department of Civil and Environmental Engineering, University of South Carolina, Columbia, SC 29208, USA
e-mail: aro@email.sc.edu; caicedo@cec.sc.edu

7.2 Background

7.2.1 HSI Modelling

The dynamic behavior of structures occupied by humans has been widely studied in recent years. A literature review published by Zivanovic et al. [9] indicates that there are two different types of models for the human body. The first, and more general, are called mass models. These models only use the mass of the human and do not model any HSI. The second type are based on mass-damper-stiffness (MDS) systems, which are likely used in problems related to human-structure interaction. Many authors have developed MDS models ranging from single degree of freedom to multiple degree of freedom models in order to represent the dynamics of the human body [2, 5, 14–17].

7.2.2 Mass-Spring-Damper (MDS) Models

Many authors have proposed MDS models for modeling the human body. The mechanical representation of the models considered on this paper are given in Fig. 7.1.

The SDOF model was proposed by Matsumoto and Griffin [2], Falati [14], Brownjohn [16] in a deterministic fashion. The model parameters are described by single values of mass (m_1), stiffness (k_1) and damping constant (c_1). Equation (7.1) shows the response of the system for an excitation $p(t)$.

$$m\ddot{x}(t) + c\dot{x}(t) + kx(t) = p(t) \tag{7.1}$$

The equation describing the dynamics of a 2DOF is the same (Eq. 7.1) but the terms are replaced by matrices of mass, damping and stiffness (Eq. 7.2), and a vector of forces for each degree of freedom:

$$M = \begin{bmatrix} m_1 & 0 \\ 0 & m_2 \end{bmatrix}, \quad C = \begin{bmatrix} c_1 + c_2 & -c_2 \\ -c_2 & c_2 \end{bmatrix}, \quad K = \begin{bmatrix} k_1 + k_2 & -k_2 \\ -k_2 & k_2 \end{bmatrix} \tag{7.2}$$

7.2.3 Controller Models

The controller system for modeling the human structure interaction follows two concepts: (i) the human does not have constant parameters of stiffness and damping and, (ii) these values depend on the interaction with the structure. The term closed-loop control always implies the use of feedback control action in order to reduce the system error. Figure 7.2 shows the block diagram of a close loop control system where G(s) is the structural system and H(s) is the controller. The terms R(s) and C(s) represent the forces acting on the structure and outputs of the system. B(s) is the force used to control the structure.
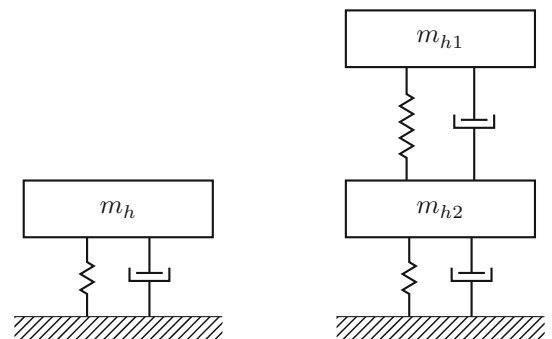
Fig. 7.1 Single and two degree of freedom models commonly used for modeling human dynamics
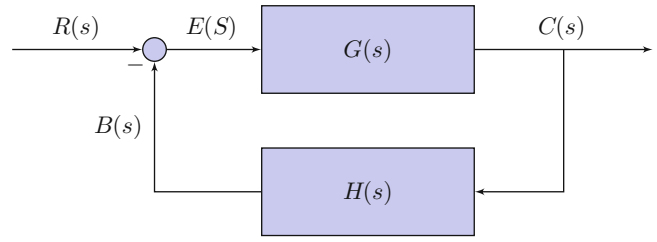
The transfer function TF(s) for a closed loop control system as shown in Fig. 7.2 is defined as (Eq. 7.3):

$$TF(s) = \frac{G(s)}{1 + G(s)H(s)} \tag{7.3}$$

Where the terms G(s) and H(s) are the mathematical representations of the structure and the transfer function of the controller in the Laplace domain. For simplicity the structure $G(s)$ is modeled as a single degree of freedom (SDOF) system, even though modeling errors are expected. The values of mass and stiffness of the SDOF are expected to be different than the actual mass and stiffness of the structure due to these modeling errors. For a single degree of freedom, the term G(s) is defined as (Eq. 7.4):

$$G(s) = \frac{\frac{1}{m}}{s^2 + \frac{c}{m}s + \frac{k}{m}} \tag{7.4}$$

The transfer function of $H(s)$ depends on the controller. In this paper, the common PID (Proportional, Integrative and Derivative) and PD (Proportional and Derivative) are used, then the transfer function for the PID is (Eq. 7.5):

$$H(s) = K_p(1 + T_d s + \frac{1}{T_i s}) \tag{7.5}$$

Where K_p, T_d and T_i are the proportional, derivative and integrative terms of the controller. For a PD controller the transfer function can be represented as (Eq. 7.6):

$$H(s) = K_p(1 + T_d s) \tag{7.6}$$

7.2.4 Model Updating

The dynamic behavior of mechanical and controller systems presented in the previous section depends on parameters that can be updated. In this paper Bayesian inference is used to update the parameters of the models based on experimental data [18, 19]. Bayes inference is based on the use of conditional probability (Eq. 7.7):

$$P(\Theta|D) \propto P(D|\Theta)P(\Theta) \tag{7.7}$$

Where $P(\Theta|D)$ is the posterior probability density functions (PDF) of the parameters Θ given the observation D. $P(\Theta)$ is the prior PDF of the parameters θ and it represents the knowledge that we have about the parameters before updating. $P(D|\Theta)$ is the likelihood of the occurrence of the measurement D given the vector of parameters Θ.

The process is performed in two steps. First, the parameters of the structure ($\Theta_e = k_s, c_s, m_s$) are estimated using experimental data of the empty condition. Then, the parameters of the system created by the human and the structure are estimated using data from the occupied structure (Θ_o). Table 7.1 shows the variables to update for each of the models presented in the previous section.

The information gained in the first model for the empty condition is then used as prior information for the human-structure interaction models. Therefore the parameters of the structure are updated using

$$P(\Theta_e|D_e) \propto P(D_e|\Theta_e)P(\Theta_e) \tag{7.8}$$

Table 7.1 Variables used for each model

Model	Variables
Empty	c_s, k_s, m_s
2DOF	c_h, k_h, m_h
3DOF	$c_{h1}, k_{h1}, m_{h1}, c_{h2}, k_{h2}, m_{h2}$
PD controller	K_p, T_d
PID controller	K_p, T_d, T_i

And the parameters of the structure and the HSI models are estimated using

$$P(\Theta_o|D_e, D_o) \propto P(D_o|\Theta_o)P(\Theta_e|D_e)P(\Theta_h) \tag{7.9}$$

Where Θ_h are the prior of the variables used by HSI models showed by the Table 7.1. The previous equation indicates that our prior considers that the parameters of the structure are not dependent on the parameters of the HSI models. This is $P(\Theta_o) = P(\Theta_h)P(\Theta_e|D_e)$.

The prior distributions for the structural parameters (k_s, m_s, and c_s) are defined based on the measurements of the structure. The prior PDF for the mass (m_s) is considered as a Normal distribution with mean 330 kg and a standard deviation of 30 kg. A non-informative distribution is used as prior for k_s. The prior information for the damping coefficient (c_s) is estimated based on a free vibration test of the structure. A damping ratio of $\zeta = 0.2\,\%$ is estimated. Therefore the prior PDF for c is $P(c) = N(31, 3.1)$. The prior PDFs assume that the parameters are not dependent. However, as shown in the results, Bayes inference allows us to find dependencies between parameters.

Experimental data is taken in two steps. First, data of the empty structure is obtained and the experimental transfer functions of the empty structure (D_e) are estimated. Then, the process is repeated for the structure with a person standing, which obtains the occupied experimental transfer function D_o. Experimental transfer functions are estimated using impact hammer tests. An accelerometer is placed in the middle of the span close to the location where the person stands. More information about the experimental setup is discussed in the following section. The estimation of the transfer function is performed using (Eq. 7.10)

$$\widehat{TF} = \frac{P_{xy}(f)}{P_{xx}(f)} \tag{7.10}$$

Where P_{xy} is the cross power spectral density between the acceleration of the structure and the force of the hammer, and P_{xx} is the auto power spectral density of the force of the hammer.

The likelihood is defined as a Gaussian distribution to maximize entropy. For example, for the empty structure, the likelihood is expressed by the equation

$$P(D_e|\Theta_e) = \prod_{i=1}^{n} \frac{1}{\sqrt{2\pi}\sigma_{TF_e}} e^{\left(-\frac{1}{2}\frac{TF_{e,i}-\widehat{TF}_{e,i}}{\sigma_{TF_e}}\right)} \tag{7.11}$$

where n is the total number of points of the Transfer Function (TF_e). TF and $\widehat{TF}$ represent the Transfer function using the Analytical and Experimental approach respectively.

7.3 Experimental Setup

The structure was specifically designed to represent flexible conditions similar to slabs with vibration problems and inspired on an existing structure built at Bucknell University [15]. Experimental tests for empty and occupied conditions were performed using impact hammer testing. The ratio between live and dead load was close to 0.2, similar to those used in service structures. The tests for occupied conditions consist of a single human standing with straight knees. Similar tests could be found in Matsumoto and Griffin [2], Salyards and Noss [15] and Brownjohn [20]. The person involved in the tests is a man, 29 years old, who has a mass of 72 kg. Five tests with the empty structure and five tests with the person over a slab were used to get experimental data.

Fig. 7.3 Analytical (*Gray-scale*) and experimental (*black*) transfer functions after Gibbs sampling
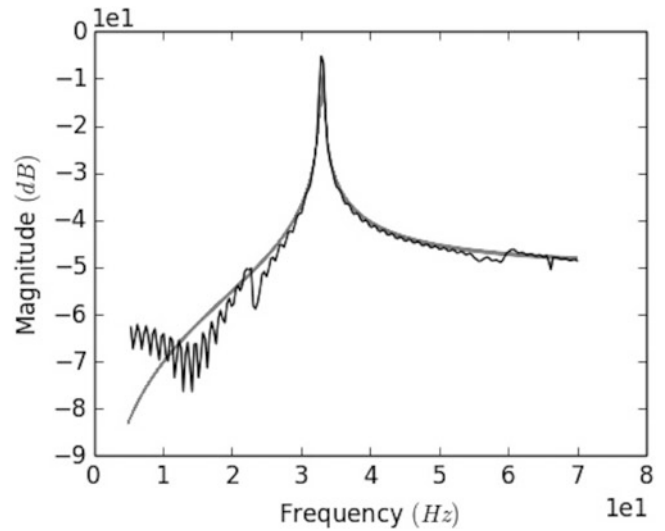
7.3.1 Instrumentation and Tests

The structure was instrumented with one PCB 333B50 accelerometer with a sensitivity of 100 mV/g. Impacts were performed using a PCB 096D50 Hammer with a sensitivity 0.2305 mV/N. The Hammer has a measurement range of $\pm$ 22240N peak. The sensor was placed in the vertical direction in the middle of the span, below the person. The hit was induced in the middle of the span, in a distance of less than 10 cm from the border of the concrete slab and in the middle of the person's legs. The acquisition system consists of a modular NI CompactDAQ with a NI9234 module. Data was acquired using a sampling frequency of 1,652 Hz, then resampled to 150 Hz. The records had a duration of 20 s, included 5 s before the hit.

7.3.2 Structural Parameters

The parameters of the empty structure $\Theta_e = k_s, m_s, c_s$ are estimated before the parameters of the HSI models (Θ_o). The likelihood was estimated using the $n = 25$ points closer to the peak on the transfer function. This corresponds to the values of the transfer function between $28\, rad/s$ and $38\, rad/s$. Figure 7.3 shows the experimental transfer function for the empty condition.

Figure 7.3 also compares the analytical and experimental transfer functions. The analytical Transfer Functions were obtained using Gibbs sampling [21] with 200,000 samples for the posterior PDF ($P(\Theta_e|D_e)$. Figure 7.4 shows the marginal histograms for each variable. The figure shows a high correlation between the stiffness k_s and mass m_s. This correlation is expected because the location of the peak in the Transfer Function corresponds to the main natural frequency of the structure. This natural frequency is dependent on the mass and stiffness of the structure. The figure also shows that both mass m_s and stiffness k_s are independent of the damping constant c_s.

7.4 Results

The posterior PDF of the parameters of all models were sampled using Gibbs sampling. The marginal distributions as well as the correlation between parameters can be observed from the samples. Figures 7.5 and 7.6 show the samples of $P(\Theta_o|D_e, D_o)$ for the SDOF human model. Figure 7.6 shows no correlation between the variables of the human model and the variables for the structure. The values of the mass are close to the expected value (72 kg). This indicates that given the experimental data collected for this paper, the parameters of the human are independent to the dynamic characteristics of the structure. Further research should be performed to explore the validity of this conclusion based on more experimental data (e.g. structures with higher and lower damping, etc). The results for the 2DOF, PD and PID models show a similar behavior and are omitted from the paper.

Fig. 7.4 Histograms of k_s, m_s, c_s for SDOF model of the structure
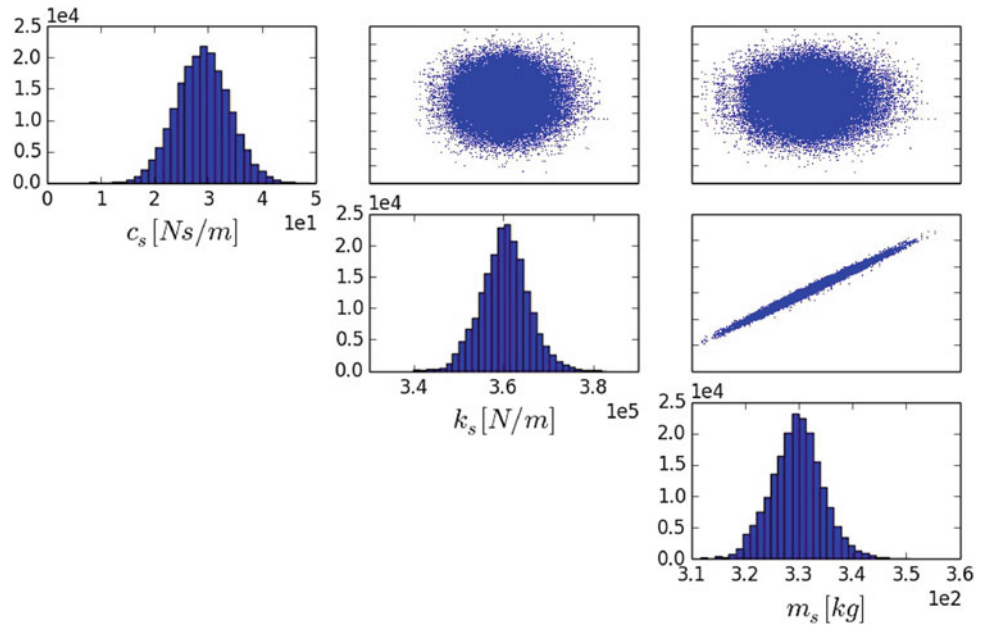
Fig. 7.5 Histograms of k_h, m_h, c_h for SDOF model of the human body
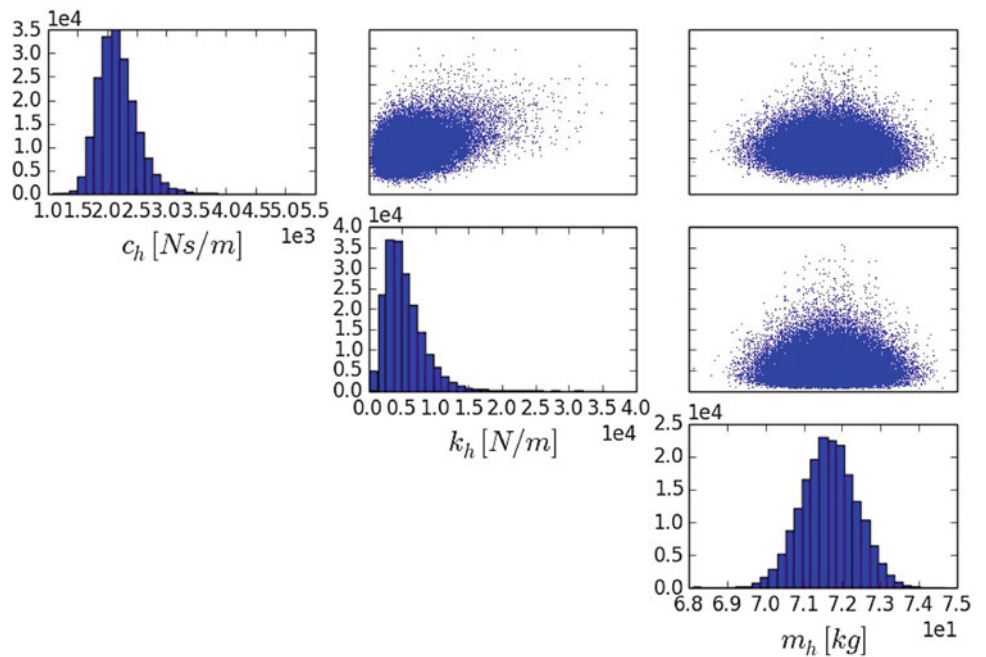
The performance of the different models is evaluated by comparing the transfer functions of each model with the experimental transfer function (similar to Fig. 7.3). Figure 7.7 shows the results for all models. The models based on closed loop control theory show better agreement with the experimental data (black line) than the models based on MDS systems. The analytical transfer function is shown in gray-scale. Darker color indicate a higher probability than lighter color.

7.5 Conclusions

This paper studies the performance of four different models for HSI. Two models are based on closed loop control theory and two models are based on traditional MDS models. Models are used to simulate a human with straight knees in a structure that can be modeled as a SDOF. Overall all models did a good job representing the transfer function between the force

Fig. 7.6 Samples for structure parameters $\Theta_e = k_s, m_s, c_s$ and human model $\Theta_o = k_h, m_h, c_h$ (SDOF human model)
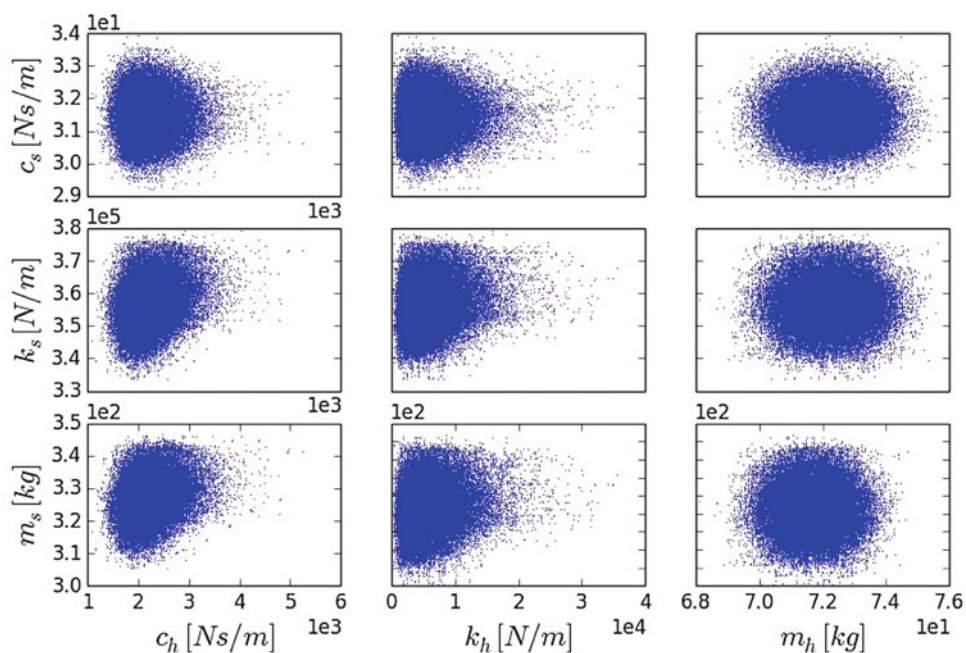
Fig. 7.7 Transfer function comparison. (**a**) SDOF model. (**b**) 2DOF model. (**c**) PD model. (**d**) PID model
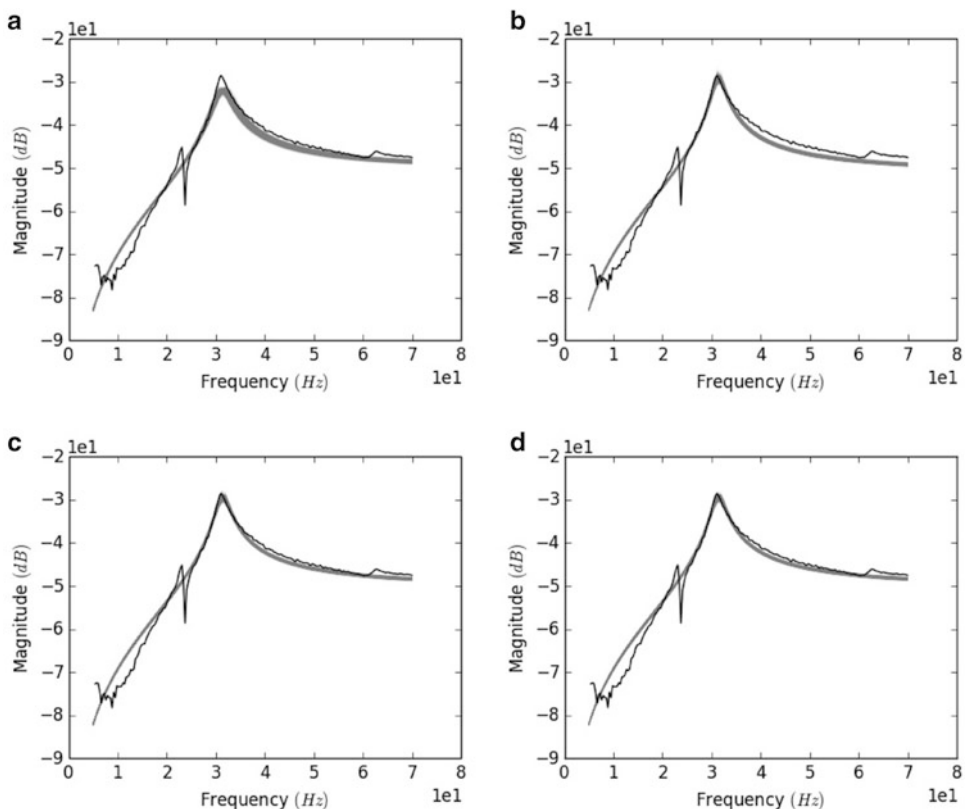
applied to the structure and the acceleration of the structure. However, the closed loop controller models did over performed the traditional MDS models. The performance of the models can be seeing in Fig. 7.7. The human model based on a SDOF system does not effectively represent the shape of the peak of the transfer function. This implies that this model is not being able to represent the damping of the overall HSI model. The line representing the model's transfer function is also wider than other models, indicating higher uncertainty.

The 2DOF human model shows a better agreement than the SDOF, however, it has six variables. Models based on closed loop control theory present the best agreement with the experimental transfer function. These models also have the less number of variables. The PD model only has a total of two variables. Small differences were found between the PD and PID models. This suggests that the T_i has little influence on the model and it could be omitted.

References

1. Agu E, Kaspersky M (2011) Influence of the random dynamic parameters of the human body on the dynamic characteristics of the coupled system of structure-crowd. J Sound Vib 330:431–444
2. Matsumoto Y, Griffin M (2003) Mathematical models for the apparent masses of standings subjects exposed to vertical whole-body vibration. J Sound Vib 260:431–451
3. Wei L, Griffin M (1998) Mathematical models for the apparent mass of the seated human body exposed to vertical vibration. J Sound Vib 212:855–874
4. Mansfield N, Griffin M (2000) Non-linearities in apparent mass and transmissibility during exposure to whole-body vertical vibration. J Biomech 33:933–941
5. Sim L, Blackeborough A, Williams M (2007) Modelling of joint crowd structure system using equivalent reduced-dof system. Shock Vib 14:261–270
6. Sachse R, Pavic A, Reynolds P (2002) The influence of a group of humans on modal properties of a structure. In: Proceedings of the fourth international conference on structural dynamics, vol 2. Pitman, Munich
7. Ortiz-Lasprilla AR, Caicedo JM, Ospina GA (2014) Modeling human-structure interaction using a closed loop control system. In: Proceedings of the XXXII international modal analysis conference, Orlando, FL
8. Ogata K (2002) Modern control engineering. Prentice-Hall, Upper Saddle River
9. Zivanovic S, Pavic A, Reynolds P (2005) Vibration serviceability of footbridges under human-induced excitation: a literature review. J Sound Vib 279:1–74
10. Jone C, Reynolds P, Pavic A (2011) Vibration serviceability of stadia structures subjected to dynamic crowd loads: a literature review. J Sound Vib 330:1531–1566
11. Venuti F, Bruno L (2009) Crowd-structure interaction in lively footbridges under synchronous lateral excitation: a literature review. Phys Life Rev 6:176–206
12. Ingólfsson E, Georgakis C, Jönsson J (2012) Pedestrian-induced lateral vibrations of footbridges: a literature review. Eng Struct 45:21–52
13. World Medical Association (2013) Declaration of Helsinki: ethical principles for medical research involving human subjects. World Medical Association Inc., Helsinki
14. Falati S (1999) The contribution of non-structural components to the overall dynamic behaviour of concrete floor slabs. University of Oxford, Oxford
15. Salyards K, Noss N (2013) Experimental results from a laboratory test program to examine human-structure interaction. In: Proceedings of the XXXII international modal analysis conference, Garden Grove, CA
16. Brownjohn J (1999) Energy dissipation in one-way slabs with human participation. In: Proceedings of the Asia-Pacific vibration conference 99, Singapore
17. ISO (1981) Vibration and shock: mechanical driving point impedance of the human body. International Organization for Standardization (ISO)
18. Beck J, Katafygiotis LS (2009) Updating models and their uncertainties i: Bayesian statistical framework. J Eng Mech 124:455–461
19. Cheung SH, Beck J (2009) Bayesian model updating using hybrid monte carlo simulation with application to structural dynamic models with uncertain parameters. J Eng Mech 135:243–225
20. Brownjohn J (2005) Vibration serviceability of footbridges. In: Proceedings of the 23rd international modal analysis conference, Springer
21. Robert C, Casella G (2004) Monte Carlo statistical methods. Springer, New York

Chapter 8
Stochastic Load Models and Footbridge Response

Lars Pedersen and Christian Frier

Abstract Pedestrians may cause vibrations in footbridges and these vibrations may potentially be annoying. This calls for predictions of footbridge vibration levels and the paper considers a stochastic approach to modeling the action of pedestrians assuming walking parameters such as step frequency, pedestrian mass, dynamic load factor, etc. to be random variables. By this approach a probability distribution function of bridge response is calculated. The paper explores how sensitive estimates of probability distribution functions of bridge response are to some of the decisions to be made when modelling the footbridge and when describing the action of the pedestrians (such as for instance the number of load harmonics). Focus is on estimating vertical structural response to single person loading.

Keywords Vibration serviceability • Walking load models • Human-structure interaction • Footbridge vibrations • Probability-based response predictions

Nomenclature

a	Bridge acceleration
f_0	Bridge fundamental frequency
f_s	Step frequency
f	Walking load
l_s	Step length
L	Bridge length
m	Weight of pedestrian
M_0	Bridge modal mass
M	Number of modes
N	Number of harmonics
P	Distribution function
R	Ratio
α	Dynamic load factor
ζ	Bridge damping ratio
μ	Mean value
σ	Standard deviation
Θ	Phase
Φ	Mode shape

8.1 Introduction

Bridge vibrations generated by pedestrians are addressed in this paper. Although it is unlikely that such vibrations would cause safety problems, the serviceability limit state may be an issue for consideration. The London Millennium Bridge incident [1], where the bridge was closed due to excessive vibrations resulting from pedestrian traffic, drew much attention

L. Pedersen (✉) • C. Frier
Department of Civil Engineering, 9-11 Sofiendahlsvej, DK-9200 Aalborg, Denmark
e-mail: lp@civil.aau.dk

and in the slipstream of the incident more focus was placed on modelling of walking loads and ways of evaluating the serviceability limit state. However, still today, there are unresolved issues within this area.

Deterministic modelling of the loads has been used for many years in codes of practise (such as [2, 3]) even though by nature the walking loads are stochastic [4–6]. Parameters of the load model comprise static weight of the pedestrian, the dynamic load factor of the pedestrian (which is not the same for all pedestrians [7]), and the step frequency of walking (which neither is the same for all pedestrians [4, 5]). Same can be said about the step length which too is a parameter used when calculating loads from pedestrian traffic.

An alternative to the deterministic approach of modelling the action is a probabilistic approach quite recently developed [5]. In this approach, the parameters of the load model can be entered as random variables. This approach will be applied for the studies of this paper. The approach outputs a probability distribution function of bridge response to the studied conditions. The present paper focuses on how sensitive the probability distribution is to selected inputs and assumptions made for its calculation.

Prior to any calculation of bridge vibration response there are decisions to be made such as the number of vibration modes to consider and the number of harmonics of the walking load to account for. Had the load been modelled deterministically then the chosen step frequency would more or less dictate which vibration modes that can be excited. However, when the step frequency is modelled as a random variable it changes from one pedestrian to the next and a broader range of frequencies might be excited.

Hence, the paper defines a study focusing on how sensitive the probability distribution function of bridge response is to decisions made concerning the number of vibration modes and the number of harmonics of the walking load accounted for. The study cannot encompass all bridges but a few bridges will be selected so as to give some idea of implications.

Basically there are many other decisions to make when a probabilistic approach is applied for modelling walking loads, covering choices of mean values and standard deviations of the walking parameters (step length, step frequency etc.). Implications of many of these choices have already been thoroughly studied in for instance [6, 8]. However, a few considerations along this line is also made in this paper so as to allow comparison of implications.

To facilitate the investigations, a footbridge model is required, and the footbridges employed for the studies are defined in Sect. 8.2.

Walking load modelling is addressed in Sects. 8.3 and 8.4 describes how probability distribution functions of bridge response are obtained. The response characteristic given focus is the midspan peak acceleration. Section 8.5 presents the results, which are discussed.

8.2 Dynamic Characteristics of Bridges

The dynamic characteristics of the bridges considered for the studies of this paper are shown in Table 8.1 (focusing on the fundamental mode of vibration in bending), along with the assumed bridge length, L. M_0 is modal mass and ζ is the damping ratio, and f_0 is the bridge frequency.

It appears that different bridge frequencies (f_0) are considered. Bridge I is expected to encounter higher vibration levels to walking loads than bridge II as its fundamental frequency is relatively close to the mean value of step frequency of 1.99 Hz suggested by Matsumoto [4].

Bridge II is to be considered a reference case, where resonant action as a result of walking loads is not very likely to occur (as the bridge frequency is above 2.4 Hz and not likely to be excited by the second harmonic of walking load).

For any structure/bridge there might be higher modes possibly relevant to consider. The bridges considered above will be assumed to be single span pin-supported bridges, and on this assumption the second vibration mode would be at 8 Hz (for bridge I) and for bridge I it would be at 10 Hz.

As a reference case, a bridge which is not a single span pin-supported bridge will also be considered. This bridge has several well/separated vibration modes below 12 Hz.

Table 8.1 Bridge dynamic characteristics and length

Bridge	f_0 (Hz)	M_0 (kg)	ζ (%)	L (m)
I	2.00	$40.0 \cdot 10^3$	0.3	40
II	2.50	$40.0 \cdot 10^3$	0.3	40

8.3   Modelling of Walking Loads

8.3.1   The Load Model

For the studies of this paper, the load model described below is assumed.

A pedestrian is assumed to generate the time varying vertical load, $f(t)$, described in Eq. 8.1.

$$f(t) = mg \; + mg \sum_{i=1}^{N} \alpha_i \cos \left(2\pi \, i \, f_s t - \theta_i\right) \tag{8.1}$$

This is in accordance with [9–11] and a number of other references.

The harmonic excitation has a base frequency, f_s, representing the step frequency of walking but multipliers of this frequency also provide loads. The paper assumes that the value of f_s will change from one pedestrian to the next, hence f_s is treated as a random variable. When a pedestrian traverses the bridge, his step frequency will be assumed to be constant. How the dynamic load factors, α_i, and the pedestrian weight, m (in kg), are modelled will be presented later. The parameter g represents acceleration of gravity.

Modeshape functions for vertical bending of the bridge are defined in Eq. 8.2 representing their values at the position of the pedestrian.

$$\Phi^{(n)}(t) = \sin \left(n\pi \, f_s l_s t / L\right) \tag{8.2}$$

In the equation, l_s represents the step length. It is assumed that the pedestrian starts his locomotion at one end of the bridge and traverses the bridge using a constant step length but that the step length may vary from one pedestrian to the next.

Combining the walking load defined in Eq. 8.1 with the modeshape functions allow calculation of bridge response.

For the studies, the walking parameters m, f_s, l_s and α_i are treaded as random variables in ways outlined in the next sections.

8.3.2   Models for Dynamic Load Factors

The following assumptions are made for the dynamic load factors.

The first dynamic load factor is modelled to depend on the step frequency, f_s, in the way defined in Eq. 8.3:

$$\alpha_1 = c_1 \, f_s^3 + c_2 \, f_s^2 + c_3 \, f_s + c_4 \tag{8.3}$$

where

$$c_1 = -0.2649 \quad c_2 = 1.306 \quad c_3 = -1.7597 \quad c_4 = 0.7613 \tag{8.4}$$

This equation is a result of work by Kerr [7] and defines the relationship between the mean value of the dynamic load factor (also denoted μ_α) for a given step frequency, f_s. and the equation is valid in the step frequency range of 1 Hz $< f_s <$ 2.7 Hz. Kerr also identified a standard deviation of the dynamic load factor (denoted σ_α), and suggested it to be calculated as shown in Eq. 8.5.

$$\sigma_\alpha = 0.16 \; \mu_\alpha \tag{8.5}$$

Modelling the dynamic load factor as a random variable is beyond the level of detail for modelling walking loads applied in many codes on the subject still today. For instance the codes [2, 3] employs deterministic load models.

For the present studies also the load factors for higher harmonics are modelled as random variables. Table 8.2 defines the assumptions.

The values in the table are found in [12]. For all dynamic load factors a normal distribution is assumed.

Table 8.2 Mean values and standard deviations for α_i

Dynamic load factor	μ_α	σ_α
α_2	0.07	0.03
α_3	0.05	0.02
α_4	0.05	0.02
α_5	0.03	0.015

Table 8.3 Mean values and standard deviations

Variable	Unit	μ	σ
f_s	Hz	1.99	0.173
l_s	m	0.71	0.071
m	kg	75	15

Table 8.4 Mean values and standard deviations

Phase	Θ_1	Θ_2	Θ_3	Θ_4	Θ_5
Value	0	$\pi/2$	$\pi/2$	0	0

8.3.3 Models for Other Parameters in the Load Model

The mean values (μ) and standard deviations (σ) assumed for other walking parameters are shown in Table 8.3 along with the assumptions made for pedestrian weight.

For all variables a normal distribution is assumed. The values for the step frequency are the result of works by Matsumoto [4] and for the step length it is a result of works by Živanovic [5]. The values for the pedestrian weight are a result of measurements made at Aalborg University on a selected number of students. At least the values are not far from the measured distribution.

The phases in the load model (Θ_i) are modelled deterministically and with the values defined in Table 8.4.

The first three phases are those suggested in [10].

8.4 Calculation of Bridge Responses and Probability Distribution Functions

Newmark time integration is employed to calculate bridge accelerations on various study assumptions. Specifically it is the midspan peak accelerations of the bridge that are determined in these calculations.

To explore the stochastic nature of walking loads, a pedestrian crossing is simulated many times by conducting MonteCarlo simulations. This allows for determining probability distribution functions of bridge accelerations. Instead of presenting the actual probability distribution, the paper focuses on selected quantiles of the distributions, namely the 95 %, the 75 %, and the 50 % quantile, denoted a_{95}, a_{75}, and a_{50}, respectively. The acceleration level a_{95} is expected to be exceeded in 1 of 20 bridge crossings. High quantiles of the probability distribution function, such as a_{95}, are believed to be of primary interest but for completeness, the two other quantiles are also determined.

In the range of 100,000 simulations runs are made for establishing a probability distribution function of bridge response.

8.5 Results

8.5.1 Implications of Choices Made About Number of Degrees of Freedom and Number of Harmonics in Load Model

Focus is on the relative difference between quantiles determined on different load and structural assumptions.

The reference case is where a SDOF model for the structure (first vertical bending mode) is assumed and where only the first harmonic (α_1) is considered when computing the probability distribution function for bridge response. Quantiles determined on other assumptions are normalised by the result obtained for the reference case.

Table 8.5 Study assumptions and results (ratios), bridge I

Degrees of freedom (M)	Harmonics (N)	r_{95}	r_{75}	r_{50}
1	1	1	1	1
1	3	0.999	1.010	1.022

Table 8.6 Study assumptions and results (ratios), bridge II

Degrees of freedom (M)	Harmonics (N)	r_{95}	r_{75}	r_{50}
1	1	1	1	1
1	3	1.04	1.12	1.20

Table 8.7 Study assumptions and results (ratios), bridge III

Degrees of freedom (M)	Harmonics (N)	r_{95}	r_{75}	r_{50}
1	1	1	1	1
1	3	1.03	1.10	1.17
5	3	1.76	2.39	2.28
5	5	1.84	2.66	2.64

Hence, it is useful to define the ratio r in the way shown in Eq. 8.6.

$$r\,(M, N) = \frac{a\,(M, N)}{a\,(M = 1, N = 1)} \tag{8.6}$$

where M is the number of degrees of freedom considered for the bridge and N is the number of harmonics considered in the load model. In the following an index will be applied to the ratio r signifying which quantile is considered. The ratio r_{95} thus represent the result of a calculation entering values for a_{95} in Eq. 8.6.

The results for bridge I are presented in Table 8.5.

It is recalled that the bridge has a fundamental frequency (at 2 Hz) in close vicinity of the mean step frequency assumed for the walking load model (1.99 Hz).

It can be seen that generally the ratios are only marginally influenced by the study assumption (the choice of M and N) and thus that modelling the bridge as a SDOF system and considering only the first load harmonic provides good estimates of the probability distribution function of bridge response.

This has to do with the fact that the resonant action of the first mode predominates the vibrations due to (i) the high value of the dynamic load factor exciting the first mode ($\alpha_1 > \alpha_2 > \alpha_3$) (ii) the high likelihood of exciting the first mode of vibration as the mean value of step frequency is in close proximity of the fundamental frequency of the bridge.

On this note focus is shifted to a bridge were excitation of the fundamental mode of vibration is less likely than for bridge I.

The results for Bridge II are presented in Table 8.6.

It is recalled that the bridge has a fundamental frequency (at 2.5 Hz) which is somewhat distant from the mean step frequency assumed for the walking load model (1.99 Hz).

For this bridge an increase is seen in response ratios when accounting for more than the first load harmonic. Probably this has to do with the fact that the excitation is not driven by resonant action. In the case where only the first load harmonic is taken into account, excitation at a frequency of 2.5 Hz will not occur often. Consequently, the addition of load harmonics 2 and 3 (although small) is seen to be able to influence the probability distribution function to a notable degree.

Although the influence is as high as 4–20 % (depending on the quantile) it must be recalled that bridge II is a bridge which generally is not very likely to come into high levels of vibration as a result of pedestrian traffic, because of the low probability of exciting its fundamental frequency. This is also reflected in the values of, for instance, a_{95}, which is about 10 times higher for bridge I than for bridge II, suggesting that the importance of the change in the ratios is not very significant.

Basically it is believed that it is quite useful to employ a simple SDOF bridge model and a load model employing only a single harmonic for most situations where the probability distribution function is to be determined for a single span pin-supported bridge. At least the results presented here do not indicate otherwise.

Up until know the studies have only considered single-span pin-supported bridges, but other bridges can be erected.

Hence, yet another bridge (bridge III) is considered, which is a bridge having five natural frequencies in the frequency range below 12 Hz (allowing several modes to be excited by walking loads). Details about this bridge are not reported here as would take up too much space and generally it is more interesting to look at the results.

The results for Bridge III are presented in Table 8.7.

Table 8.8 Ratios for the two bridges

Bridge	r_{95}	r_{75}	r_{50}
I	0.91	0.64	0.62
II	0.62	0.65	0.64

Clearly, the results suggest that a reasonable estimate of the probability distribution function for bridge response is not obtained if the bridge is modelled as a SDOF system considering only the fundamental mode ($M = 1$) and considering only the first load harmonic ($N = 1$). Both the number of vibration modes and the number of load harmonics considered is seen to have a relatively high influence on the estimate of the probability distribution function. The calculated value of a_{95} is almost doubled by accounting for all the five vibration modes and by accounting for all the first five harmonics in the load model.

8.5.2 Implications of Other Choices: Perspectivation

When deciding on employing a stochastic approach for analysing the bridge responses to walking loads, there are other decisions to make than those studied in the previous section.

One such decision relates to the choice of mean value and standard deviation for the step frequency of the pedestrian. In the studies above, a stochastic model was employed with a mean value and standard deviation as observed in investigations by Matsumoto [4]. However, investigations by Živanovic [5] suggested a mean value of 1.87 Hz and a standard deviation of 0.186 Hz somewhat different from the values suggested by Matsumoto (1.99 and 0.173 Hz), especially for the mean value.

Below the implications of the choice between the two step frequency models are investigated for bridge I and II.

For bridge I and II the ratio defined in Eq. 8.7 is computed.

$$r\ (M,N,f_s) = \frac{a\ (M=1, N=1,\ f_s\ (1.87\,Hz, 0.186\,Hz))}{a\ (M=1, N=1,\ f_s\ (1.99\,Hz, 0.173\,Hz))} \tag{8.7}$$

Basically, the ratio relates calculated quantiles determined assuming the step frequency model by Matsumoto to those determined assuming the step frequency model by Živanovic, using the results obtained assuming the step frequency model by Matsumoto for normalisation. Values of r below unity will be indicative of a reduction in responses when shifting the step frequency model from that by Matsumoto to that by Živanovic.

Table 8.8 presents the results obtained for the two bridges.

It can be seen that shifting parameters of the step frequency model has a quite substantial effect on most of the ratios.

For bridge I and II, the implications of changing the step frequency model is seen to be higher than any shift in study assumptions considered in Sect. 8.5.1 The reason why the r values are below unity is that the likelihood of encountering resonance reduces when the mean value of step frequency moves further away from the fundamental frequency of the bridge being at 2 Hz.

For bridge II, the implications of changing the step frequency model are also seen to be significant.

8.6 Conclusion and Discussion

The present paper has focused on how sensitive the calculated probability distribution function of bridge response is to selected inputs and assumptions made for its calculation, hereunder the choice of number of bridge vibration modes and the choice of number of harmonics of the walking load.

For the two single-span bridges considered for the study there is a noticeable difference in how sensitive the probability distribution function is to these assumptions. For the bridge having a fundamental frequency in close vicinity of the mean value of step frequency assumed for the study, the probability density function is fairly insensitive to whether the bridge is excited by only the first harmonic of walking loads or whether excited by more load harmonics. For the bridge having a fundamental frequency 0.5 Hz from the mean value of step frequency assumed for the study, the probability density function is quite sensitive to which of the two assumptions are made. It can be argued though that for this bridge the importance of actually doing a calculation of the probability distribution function is not that high as vibration levels for this bridge are quite small.

For reference, a calculation of a probability distribution function of bridge response is made for a bridge which cannot be characterised as a "single-span pin-supported bridge", and here the choices made concerning the number of vibration modes and the number of harmonics accounted for in the load model had a relatively high impact on the calculated distribution.

Hence, the results suggest that there are limitations to the degree of simplification of matters that is sensible. Probably the best advice is to be aware of main bridge modal characteristic and the general load mechanisms as well as their stochastic nature when making decisions about assumptions studied here.

A reference study was made changing the values of statistical parameters assumed for modelling the stochastic nature of step frequency to another proposal found in literature. From the results it is seen that definitely this choice/change has a high impact on the probability distribution function calculated of bridge response.

References

1. Dallard P, Fitzpatrick AJ, Flint A, Le Bourva S, Low A, Ridsdill-Smith RM, Wilford M (2001) The London Millennium Bridge. Struct Eng 79:17–33
2. Ontario Highway Bridge Design Code (1983) Highway engineering division. Ministry of Transportation and Communication, Ontario
3. British Standard Institution (1978) Steel, concrete and composite bridges. Specification for loads. BS 5400: Part 2. British Standard Institution, London
4. Matsumoto Y, Nishioka T, Shiojiri H, Matsuzaki K (1978) Dynamic design of footbridges. In: IABSE proceedings, No. P-17/78, pp 1–15
5. Živanovic S (2006) Probability-based estimation of vibration for pedestrian structures due to walking. Ph.D. thesis, Department of Civil and Structural Engineering, University of Sheffield, Sheffield
6. Pedersen L, Frier C (2009) Sensitivity of footbridge vibrations to stochastic walking parameters. J Sound Vib. doi:10.1016/j.jsv.2009.12.022
7. Kerr SC, Bishop NWM (2001) Human induced loading on flexible staircases. Eng Struct 23:37–45
8. Pedersen L, Frier C (2009) Sensitivity study of stochastic walking load models. In: International modal analysis conference (IMAC XXVIII), Jacksonville
9. Ellis BR (2000) On the response of long-span floors to walking loads generated by individuals and crowds. Struct Eng 78:1–25
10. Bachmann H, Ammann W (1987) Vibrations in structures – induced by man and machines. In: IABSE structural engineering documents 3e, Zürich
11. Rainer JH, Pernica G, Allen DE (1998) Dynamic loading and response of footbridges. Can J Civ Eng 15:66–78
12. Živanovic S, Pavic A, Reynolds P (2007) Probability-based prediction of multi-mode vibration response to walking excitation. Eng Struct 29:942–954. doi:10.1016/j.engstruct.2006.07.004

Chapter 9
Pedestrian Induced Lateral Vibrations with Emphasis on Modal Energy Transfer

Anders Rønnquist

Abstract Already on the opening day of the Lardal Bridge in 2001 were large lateral vibrations observed. These excessive vibrations were seen as relatively dense and continuous flow of people was crossing the bridge. This type of observation has later been made for several other bridges, old as well as new. These observations have initiated an extensive investigation program quantifying structural properties such as natural frequencies, mode shapes and damping and their influence on the pedestrian induced vibration. Thus, the pedestrian lateral load phenomenon has equally been thoroughly investigated. As part of the pedestrian load investigation at the Lardal Bridge were a large number of time series with different sized groups of people recoded. This paper aims to re-analyze these data with the emphasis on the energy transfer between modes. It is clear from these response recordings that the lateral displacement is often not initially initiated, rather vertical or torsion motions. This is also true for several crossings of larger groups of pedestrians. This raises some interesting questions of how and when the pedestrian induced energy transfers between modes. From short time Fourier transforms (STFT) it can be seen that energy transfers after certain levels of response are reached. Interestingly, the horizontal mode, a reversed pendulum motion, includes a small vertical component with twice the frequency of the horizontal mode. The investigation explores the system sensitivities to group size, initially triggered response modes and the pacing frequencies of the pedestrian motion.

Keywords Pedestrian induced vibration • Bridge dynamics • Modal analysis • Short time Fourier analysis • Energy transfer

9.1   Introduction

In Norway the Lardal Bridge has exhibited excessive lateral vibrations during the crossing of large groups of pedestrians, see [1]. The bridge, shown in Fig. 9.1, crosses the river Lågen in the area of Lardal. On the opening day in 2001 a good number of people attended the event. This created a relatively dense and continuous flow of people crossing the bridge. At this time the excessive lateral vibration was for the first time observed. People grabbed the handrails and expressed concern about the behavior. Locals who often attend different arrangements within the area have later become used to the vibrations, and some have even expressed their amusement over the situation. When there are no major events on either side of the bridge there will only be a few occasional pedestrians or groups of pedestrians crossing the bridge. This has never created any major problems concerning excessive vibration in any direction.

The problems experienced at the Lardal Bridge are equivalent to those that occurred at the Millennium Bridge in London, an event which has been the source of many publications; see e.g. [2]. This bridge is often seen together with the Solférino Bridge, crossing the river Seine in Paris [3], as major contributors to the beginning of new and much sought after research of the pedestrian structure interaction. Both bridges had to be temporarily closed for the installation of mitigation devices, i.e. various types of dampers.

The Lardal Bridge is included in a project to create a recreation area around their famous rapids with old traditional salmon fishing and two outdoor amphitheaters used for concerts. Its main purpose is to connect the parking place located on the west side of the river with the amphitheaters located on the east side, which implies that there is a considerable risk of high concentrations of pedestrians on the bridge. To investigate how the suggested load model works for groups of pedestrians there have also been performed full-scale observations [1]. These consist of response acceleration recordings from the Lardal Bridge. The recordings have also been used to obtain the necessary structural dynamic parameter. The Lardal Bridge is a rather complex structure. It contains components of laminated wood beams, steel wind truss and steel cables, and

A. Rønnquist (✉)
Department of Structural Engineering, Norwegian University of Science and Technology, Richard Birkelandsv. 1a, Trondheim 7491, Norway
e-mail: anders.ronnquist@ntnu.no

Fig. 9.1 The Lardal Bridge, built in 2001, with a total length of 130 m as it crosses the river Lågen in Norway

there are sliding joints also playing an important part in the complete structural behavior. These effects are further explored by the FEM-analyses presented in [4] which show that small alteration of structural properties can give large changes of the resulting natural frequency as well as the corresponding mode shape.

9.2 Operational Modal Analysis for Dynamic Assessment of the Pedestrian Induced Response

In this paper, the dynamic assessment is performed using two types of modal analyses. The first is the estimation of the power spectral density (PSD) of the dynamic response, in which the frequency content of the sampled time series is estimated. The choice of the spectral estimation method is dependent on the duration of the signal and the frequency distribution within the time signal. The second analysis uses the short-time Fourier transform (STFT) to estimate the changes in the frequency content during the crossing of the bridge. This information is essential in the investigation of the energy input and transfer between frequencies due to the pedestrians. The resulting spectrograms are useful for understanding and visualizing the differences between the initial vibrations, the dominating vibrations to final decaying vibrations on the vertical and horizontal directions. This is used to determine in which modes energy is introduced and which modes the dynamic response energy is transferred to as the pedestrians' passes by.

9.3 Power Spectral Density (PSD) Estimation

The choice of the method used to estimate the PSD of the response will depend on the duration. Additionally, if the frequency distribution and energy transfer in the frequency domain are to be investigated in detail, the current time series will quickly become very short. Therefore, it is important to choose the method accordingly. For the estimation of the PSD, there are two common types of PSD estimators that are frequently used: parametric and non-parametric methods [5]. In the parametric methods, the signal is assumed to be the output of a linear system driven by white noise, i.e., parametric methods estimate the PSD by first estimating the parameters of the linear system that is assumed to generate the signal. These methods generally produce smoother estimates of the PSD than do non-parametric methods. In the investigation of the pedestrian induced vibrations, the Burg method is used for PSD estimation [6]. The method does not apply a window function to the dataset, as is common in non-parametric methods. Although the Burg method may be considered to be better than non-parametric methods for a given application, it is important to be aware of some of its disadvantages. For example, the Burg method exhibits spectral line splitting, especially at high signal-to-noise ratios. In high-order systems, the method can also introduce spurious spectral peaks, and when estimating sinusoids in noise, it shows a bias that is initial-phase dependent [7].

9.4 Short-Time Fourier Transform (STFT) and Spectrogram Analysis

Using the STFT to analyze time series provides more complete and precise information about the energy distribution along a pedestrian crossing of the bridge. Calculated spectrograms will give a visual representation of the motion, providing a useful time-frequency representation. In the STFT, time series are segmented into time intervals that are sufficiently narrow to be

considered stationary [8]. However, it is important to recognize that the time resolution, i.e., how well two peaks in time can be separated from each other, and the frequency resolution, i.e., how well two spectral components can be separated from each other, cannot be arbitrarily determined because they are both directly related to the time window size. The shorter the window is the better the time resolution will be; however, this will result in a lower frequency resolution. It is equally important to consider the amount of overlap between the chosen windows. Avoiding overlap will result in more distinct differences between windows, whereas in overlapping windows, the results will be averaged for a better overall result. Therefore, the STFT can also be used as a sliding discrete Fourier transform, which is analyzed for each incremental shift using overlapping windows [9]. The time-dependent Fourier transform is defined by

$$X(\tau, \omega) = \int_{-\infty}^{\infty} x(t) w(t - \tau) e^{-i\omega t} dt \tag{9.1}$$

where τ and ω are the time and frequency parameters. Similarly, the discrete STFT for sampling in frequency and in time is given by

$$X(n, k) = X(n, \omega)|_{\omega = \frac{2\pi}{N} k} = \sum_{m=-\infty}^{\infty} x(m) w(n - m) e^{-i\frac{2\pi}{N} km} \tag{9.2}$$

where $x(m)w(n-m)$ is a segment of the given time series $x(n)$ using the applied window function $w(n)$ for the STFT at time n and at frequency k. The N frequencies are equally spaced over the interval $2\pi/N$ (see also [9, 10]). Finally, the spectrogram of the function is found by squaring the magnitude. It is commonly given in log units as

$$S_{xx}(n, k) = \log |X(n, k)|^2 \tag{9.3}$$

In the following investigations, the STFT is used as a sliding discrete Fourier transform in which the STFT is evaluated for each shift of the window function. To evaluate the frequencies in the short-windowed time series, the Burg spectrum method is used.

9.5 Full Scale Measurements at the Lardal Bridge

At three different occasions full-scale measurements were carried out on the Lardal Bridge, all done during the summer months of 2002 and 2003. The weather varied from rather cold and rainy to hot and sunny. The first part of the test program was intended to study the structural properties of the bridge, while the second part focused on pedestrian induced response recordings with the main interest in the horizontal response accelerations. The Lardal Bridge possesses an unfortunate vibration property. In an arch-like type of structure the first mode shape is in fact three dimensional and can be seen to act as a reversed pendulum motion where the horizontal displacement component has an natural frequency of 0.83 Hz while at the same time the vertical component exhibit a frequency of 1.66 Hz. This is illustrated by the lissajous diagram between the horizontal and the vertical components at mid-span in Fig. 9.2. Traces of response at the first horizontal natural frequency as well as two times the first horizontal frequency have is observed in the recordings of the vertical direction, representing contributions from torsion and vertical motion of a spacial mode shape.
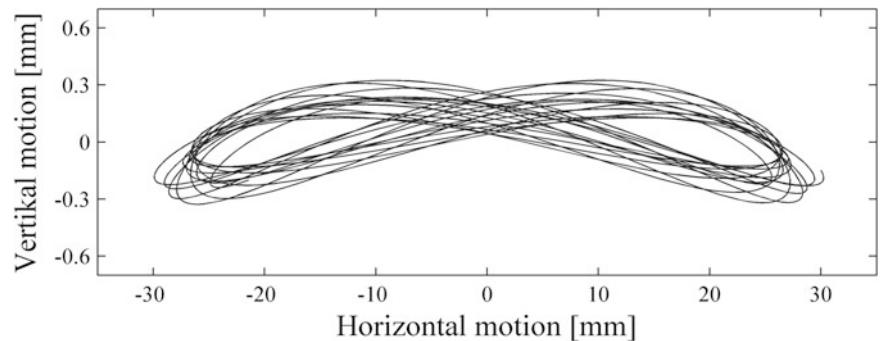
Fig. 9.2 Pendulum traces of filtered time series, vertical 1.67 Hz and horizontal 0.83 Hz

Table 9.1 Recorded natural
frequencies given in Hz

Natural frequency	1st	2nd	3rd
Horizontal	0.83	2.10	3.30
Torsion	1.12	2.45	4.10
Vertical	1.45	2.85	4.85
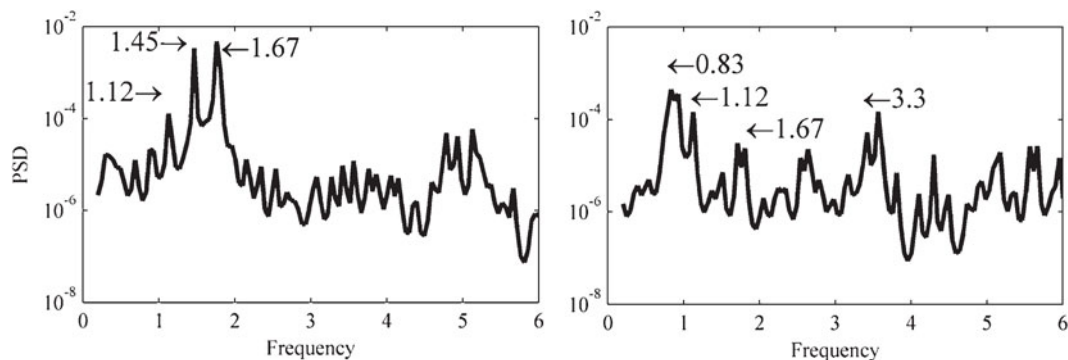
Fig. 9.3 PSD plots of acceleration response in the horizontal direction, *left*, and vertical direction, *right*

This means that even though the horizontal load might be too small to create the response needed to trigger any significant pedestrian horizontal load the vertical part might be more onerous. Small motions in the vertical direction will due to the pendulum coupling create larger displacements in the horizontal direction and thereby create motions that might trigger the pedestrian load effect. This is often associated with the synchronization phenomenon of pedestrian induced load impulses.

9.6 Instrumentation and Data Acquisition

The recording of response time series on the Lardal Bridge involved the use of eight accelerometers, four ceramic shear piezoelectric model 393B12 (PCB Piezotronics), with a frequency range of 0.15–1,000 Hz (depending on acceptable deviation levels), and four of the inductive type HBM B12/500 with a frequency range of 0–250 Hz. The sampling frequency and length of time series were set at $f_s = 50$ Hz and $T = 60$, 120 s or occasionally longer if deemed necessary. After amplification the accelerometer signals were converted to a digital format using a Spider 8 type of recorder. Prior to storage the time series were digitally filtered, high as well as low pass filtered below 0.3 Hz and above 20 Hz. Resulting natural frequencies identified from the full scale measurements are given in Table 9.1, see also [4]. Spectral density plot of the horizontal motion as one pedestrian passes across the bridge is included in Fig. 9.3. The PSD plot of the horizontal motion shows the 1st horizontal (0.83 Hz), 1st torsion (1.12 Hz), coupling frequency at 1.67 Hz and the 3rd horizontal frequency (3.3 Hz). The vertical PSD plot also shows the 1st torsion frequency, the 1st vertical frequency and the coupling motion at 1.67 Hz.

9.7 Pedestrian Induced Vibrations

There is a special issue for the Lardal Bridge that should be mentioned. When a group of pedestrians enter the bridge they will due to the uphill sloping bridge deck have a lower vertical pacing frequency than the usual 2 Hz. For most cases the crucial lateral natural frequency for structures with pedestrian loads will be half the natural walking frequency as listed in Table 3 (the ranges is suggested in [11]). However, for the Lardal Bridge the 1st purely vertical natural frequency at 1.45 Hz and the vertical component of the 1st horizontal (0.83 Hz), which is obviously excited from a vertical pacing frequency of $2 \cdot 0.83 = 1.66$ Hz. Due to the inclination both of these values are well within the range of expected pedestrian group pacing frequencies.

It is below shown that if the pedestrians first excited a purely vertical resonance response during the first phase of walking on to the bridge, then the event of excessive horizontal vibrations is delayed or for some cases with small groups non-existing.

On the other hand if a horizontal resonance is firstly excited then this will dominate the response over the entire crossing. Furthermore, the investigation shows how response which clearly initially is vertical dominated may transfer to the horizontal direction where the horizontal response then dominates the remainder of the crossing. It is also interesting to note that the recording of the vertical response clear shows signs of frequency shift within the same direction where the load frequency goes towards the natural frequency rendering response recording showing rapid increase.

To fully understand the frequency content of the response and its variation in time and for different number of pedestrians' time series and STFT are given for different scenarios. This includes time series from just a few walking pedestrians to groups over 40 pedestrians. The investigation also includes a crossing of jogging pedestrians to give a picture of the response at higher pacing frequencies. The system response for a few pedestrians is mostly dominated by random response where each pedestrian acts individually and independent of each other as well as of the bridge response. As the response becomes dominated by a very large dynamic kinetic input from the pedestrians, interacting with the bridge, the response is clearly of a harmonic nature given by one or two main components.

The first crossing, shown in Fig. 9.4, is the response from four pedestrian jogging across the bridge. The figure shows the horizontal motion and includes several contributing frequencies as expected from the higher load frequency, see also Table 9.2. It shows contributions from the 1st and 3rd horizontal natural frequencies as well as the 1st and 3rd torsion natural frequencies. It is interesting to see that the response is relatively low and dominated by higher frequency components, quite different from the pedestrian structure-interaction phenomena also observed at the bridge.

The vertical response of the same event is given in Fig. 9.5. Here the vertical components to be strongly influenced by the load frequency ($\sim$2.5 Hz) in the range of the 2nd torsion vertical as well as the load multiple frequency reaching the 3rd torsion and vertical natural frequencies. After approximately 40 s the response decays and the vertical frequency component separates in to the 1st vertical and torsional frequencies respectively. As expected the 1st horizontal component from the coupling motion is also clearly present in the response.

Fig. 9.4 STFT of four pedestrians jogging across the bridge

	Slow	Normal	Fast	Total	
Walking	1.4–1.7	1.7–2.2	2.2–2.4	1.4–2.4	Continuous ground contact
Running	1.9–2.2	2.2–2.7	2.7–3.3	1.9–3.3	Discontinuous ground contact
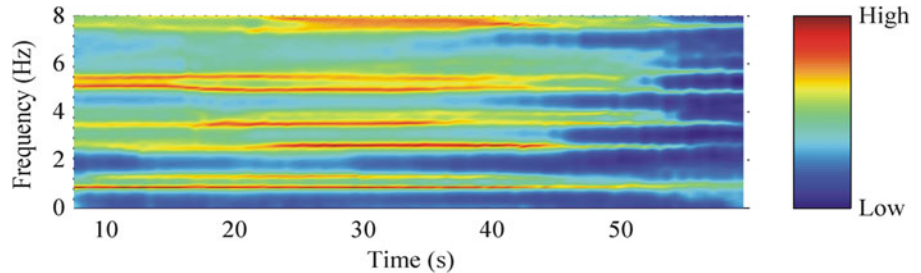
Table 9.2 Characteristic pedestrian pacing frequencies [Hz] given by Bachmann and Ammann [11]

Fig. 9.5 Vertical response of four pedestrians jogging across, *upper*: the STFT and *lower*: the corresponding time series
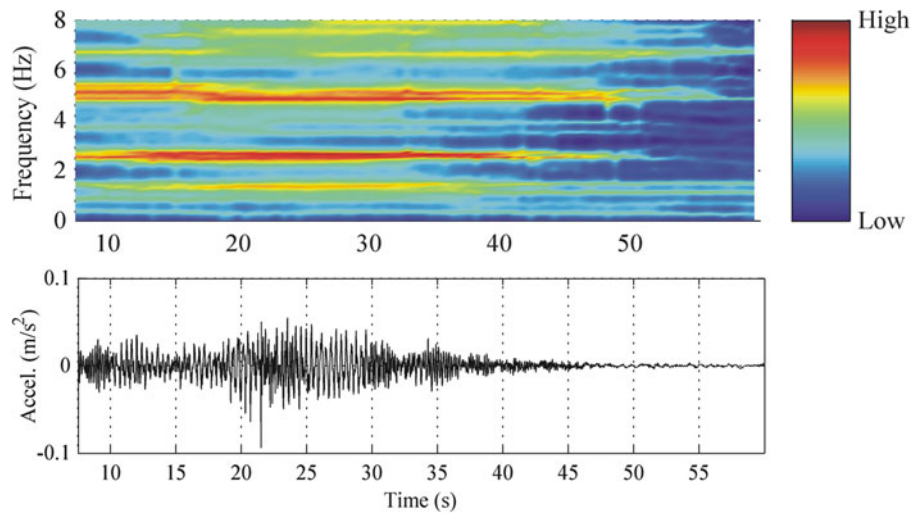
Fig. 9.6 Vertical response of four pedestrian walking across, given by the STFT
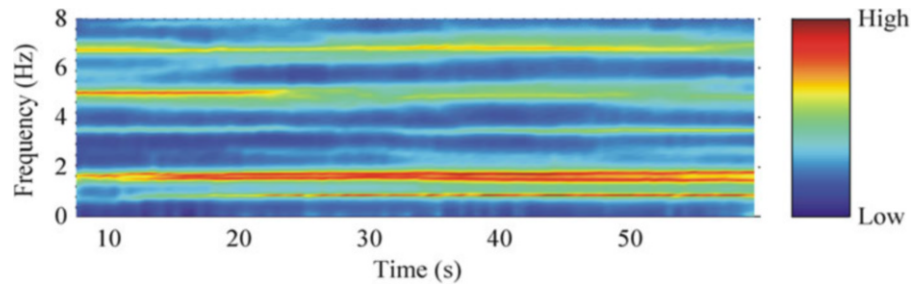
Fig. 9.7 Vertical response of four pedestrian walking across, *upper*: vertical response and *lower*: horizontal response time series
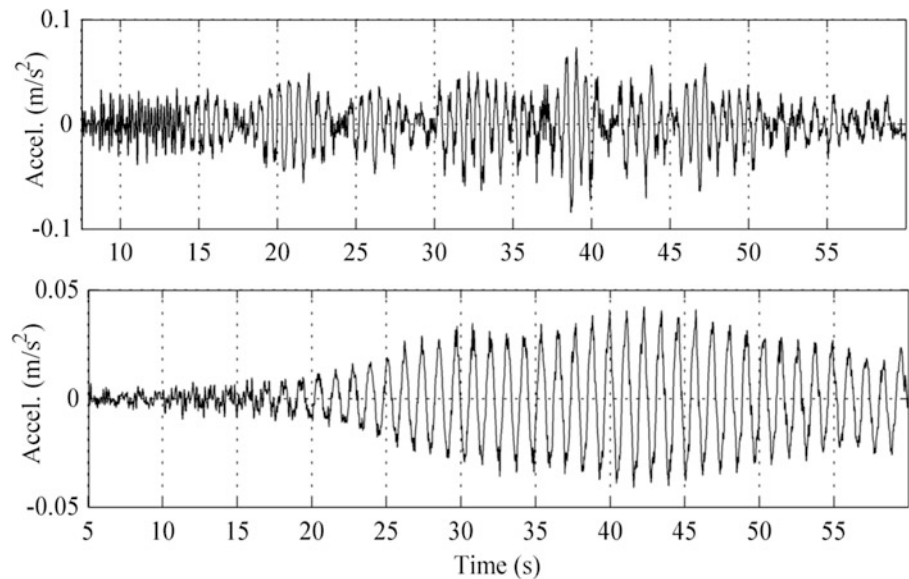
The next event is from four pedestrians walking across the bridge, shown in Figs. 9.6 and 9.7. The load is here, as previously explained, closer to the 1st horizontal natural frequency, but never the less, clearly the vibration is induced in the vertical motion which directly excites the coupling frequency at 1.66 Hz. The latter is shown as two frequency components towards the end of the time series. The horizontal motion enters approximately at 15 s and clearly dominates the response already after 20 s. The two diagrams in Fig. 9.7 show the vertical and horizontal time series respectively where the effects also are clearly visible.

Time series in Fig. 9.8 shows a vertical induced motion at the middle of the bridge. Here the load comes at the 1st vertical frequency of 1.45 Hz which then also excites the coupling frequency of 1.67 Hz. The upper spectrogram also shows that the 3rd vertical frequency contributes. The motion starts close to the 1st vertical frequency and quickly stabilizes. It is interesting to see the decay and energy transfer which starts close to 30s and onwards. The lower STFT diagram shows the same event but in the horizontal direction. Here the motion initial shows the same load frequencies and a short period of the 1st horizontal frequency which almost disappears as the vertical load stabilize. As soon as the input stops right before 30s the energy is transferred to the 1st horizontal motion. This occurs via the coupling motion of the two directions. After just 5 s the motion is completely horizontal and has actually increased in intensity as the motion becomes one harmonic motion.

As the number of pedestrian increases the motion will move easier towards the 1st horizontal motion. In Fig. 9.9 is the response of a group including 45 pedestrians crossing the bridge shown. The vertical motion STFT also shows traces of the 3rd vertical natural frequency and strongly the coupling frequency of 1.67 Hz. As the group arrives at the mid-point the spacial motion is clearly dominating the horizontal direction with load frequency at the vertical frequencies between 1.5 and 2 Hz.

The last event shown in Figs. 9.10 and 9.11 represents time series of 13 pedestrians crossing the bridge. These time series clearly show how initially the motion starts vertically. First the 1st vertical frequency is excited with only minor response horizontally. Then, clearly the energy is transferred through the coupled motion, now also exciting the horizontal motion at 0.83 Hz. The vertical transfer starts at around 45 s and the new frequency component dominates after 50 s, to change again at roughly 65 s, see especially the time series in Fig. 9.11.

Fig. 9.8 Vertical induced response at the bridge mid-point. *Upper*: STFT of the vertical motion, *middle*: vertical acceleration time series and *lower*: STFT of the corresponding horizontal motion
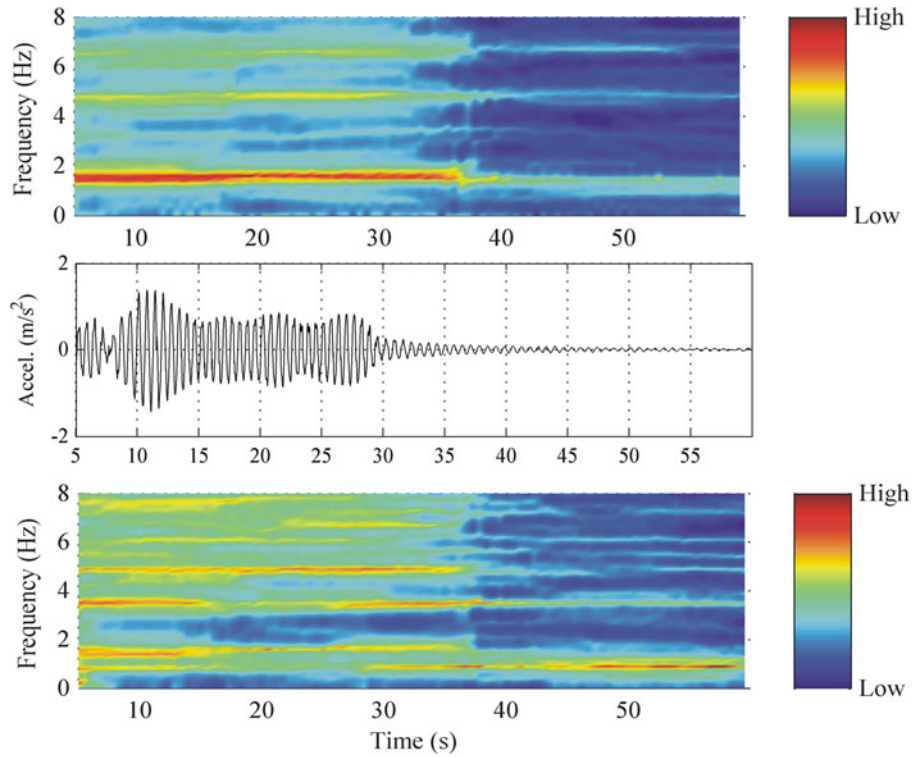
Fig. 9.9 Vertical response of 45 pedestrians walking across. *Upper*: the STFT and *lower*: the acceleration time series
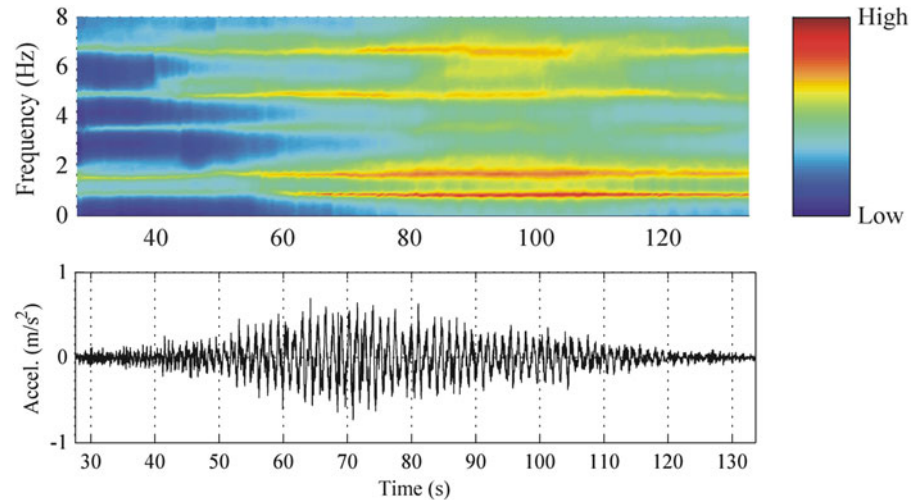
9.8 Conclusions

The assessment of the dynamic behavior of the Lardal Bridge has been investigated to determine the dynamic response through sampling and modal analyses. It has been shown that different information can be extracted from the different parts of a passage time series. The full scale data includes information about the load frequencies as well as structural parameters such as the fundamental frequencies and mode shapes. The sensitivity to time variation shows that introduction of the STFT is very useful in determining the frequency content and to interpret the pedestrian structure interaction. Additionally, the analysis facilitates a good understanding of the energy input and transfer between frequencies originating from the pedestrian crossing the bridge. The STFT shows when and how the changes occur, whereas the PSD provides distinct predictions that can be related to the expected frequency components. The investigation shows how the lateral pacing of the pedestrians

Fig. 9.10 Vertical motion of 13 pedestrians crossing the bridge, represented by STFT. *Upper* vertically and *lower* horizontally
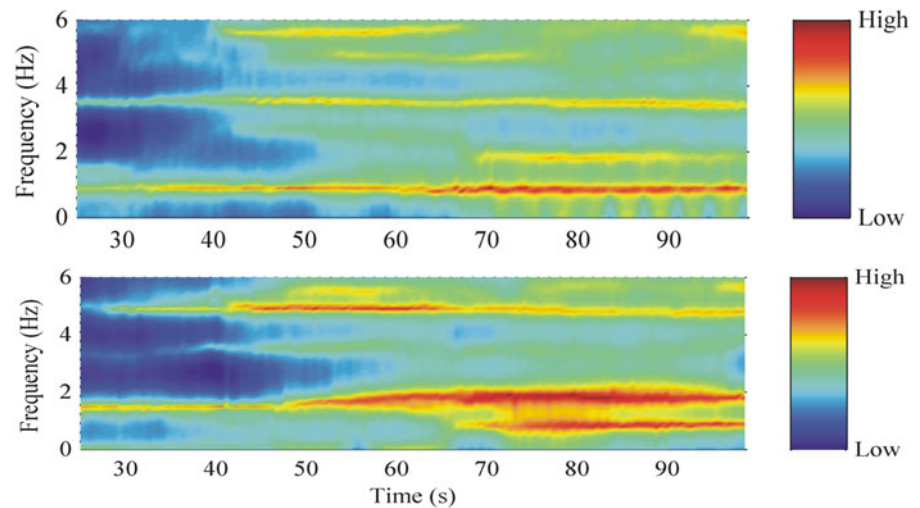
Fig. 9.11 Vertical motion of 13 pedestrians crossing the bridge, shown as acceleration. *Upper* vertically and *lower* horizontally
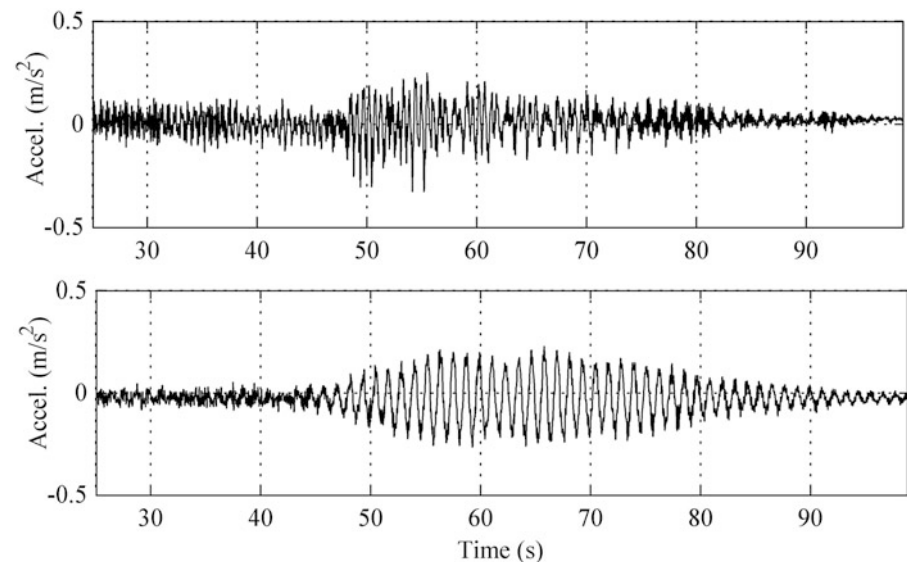
setts the initial vibrations as a group enters. For this bridge there is a spacial mode coupling which simplifies the energy transfer between vertical and horizontal, rendering a bridge prune to experience excessive lateral vibrations from rather small number of pedestrians. As the forced vibration reduces by pedestrian leaving the bridge summit will remaining energy transfer towards the 1st horizontal natural frequency, rendering an increase in the response which is documented by the recorded time series.

References

1. Rönnquist A (2005) Pedestrian induced lateral vibrations of slender footbridges. Doctoral theses at NTNU (2005:102). ISBN 82-471-7082-5, 176 pp
2. Fitzpatrick T, Dallard P, Le Bourva S, Low A, Ridsdill Smith R, Willford M (2002) Linking London: the Millennium Bridge. The Royal Academy of Engineering, London
3. Blume M (2000) Pont Solferino: water under a Troubled Bridge. International Herald Tribune. www.iht.com, 29 July 2000, Paris, 3 pp
4. Rönnquist A, Strømmen E, Wollebæk L (2008) Dynamic properties from full scale recordings and FE-modeling of slender footbridge with flexible connections – SEI 4/2008 structural engineering international. IABSE
5. Bendat JS, Piersol AG (1986) Random data, analysis and measurement procedures, 2nd edn. Wiley, New York
6. Burg JP (1975) Maximum entropy spectral analysis. PhD thesis, Stanford University, Stanford
7. Jung L (2009) System identification, theory for the user, 2nd edn. Prentice Hall, Upper Saddle River

8. Rabiner L, Allen JB (1980) On the implementation of a short-time spectral analysis method for system identification. IEEE Trans Acoust Speech Signal Process 28:69–78
9. Jacobsen E, Lyons R (2003) The sliding DFT. IEEE Signal Process Mag 20:74–80
10. Allen JB (1977) Short term spectral analysis, synthesis, and modification by discrete Fourier transform. IEEE Trans Acoust Speech Signal Process 25:235–238
11. Bachmann H, Ammann W (1987) Chap 2: Man-induced vibrations and Appendix A: case reports. In: Vibrations in structures induced by man and machine. Structural Engineering Document 3e. 3e, pp 13-44 + 87-110. IABSE, Zürich

Chapter 10
Implications of Interaction Between Humans and Structures

Lars Pedersen

Abstract Many civil engineering structures are occupied by humans, and often humans are considered as a static load in calculations. However, active humans on structures can cause structural vibrations. Passive humans might also be present on that structure and they do change the structural system (such as structural damping and therefore also structural vibration levels). The paper addresses this subject and explores implications of having passive humans present on the structure. In experimental tests with a laboratory floor it is examined to which degree the posture of humans passively sitting on the floor influences the damping added to the floor. A numerical case study explores how passive humans may influence vibration levels of a floor.

Keywords Human-structure interaction • Floor vibrations • Experimental testing • Numerical prediction • Human postures

Nomenclature

a	Acceleration
f_F	Floor natural frequency
f_H	Human natural frequency
f_s	Jumping frequency
m	Mass of jumping person
M_F	Floor modal mass
M_H	Crowd mass
n	Number of persons
r	Ratio
q	Jumping load
α	Dynamic load factor
ζ	Damping ratio
ζ_F	Floor damping ratio
ζ_H	Human damping ratio
Θ	Phase

10.1   Introduction

Floors in buildings often carry humans. If the floor is relatively stiff it is common to consider the human occupancy as a static weight. However, if the floor is flexible it can become relevant to divide the occupancy into an active part (humans walking, jumping or bouncing) and a passive part (humans sitting or standing on the floor). The dynamic forces generated by the active persons may cause structural vibrations and potentially serviceability problems.

L. Pedersen (✉)
Department of Civil Engineering, 9-11 Sofiendahlsvej, DK-9200 Aalborg, Denmark
e-mail: lp@civil.aau.dk

This paper mainly focuses on the passive humans and how they influence damping characteristics of the floor on which the humans are placed. Field measurements made on structures carrying passive crowds of humans have revealed that the passive crowd influences the dynamic characteristics of the structure such as its damping [1–3]. Similar observations are found when testing laboratory floors carrying passive humans [4, 5].

It must be recognised that not all humans will assume similar postures when sitting on a floor and that a sitting human might well alter his/her posture over time or some persons may alter their posture while others may not. Hence, the nature of the dynamic interaction between humans and floor might change over time even in a short time perspective.

In laboratory tests reported in literature mostly humans have assumed a specific posture when the structure was put into vibration. Little effort has been made to study how and to which degree the posture of the humans (sitting on the structure) influences the damping which the sitting humans add to the structure.

For the study of this paper an experimental test programme is devised exploring how sensitive floor damping (added by sitting humans) is to different human postures.

Some implications of modelling dynamic interaction between a sitting crowd and the supporting structure are presented by showing results of a numerical calculation of acceleration responses of a floor to jumping loads with and without the presence of a passive crowd of humans on the floor.

The experiments are addressed and discussed in Sects. 10.2 and 10.3 presents a numerical study considering a model describing dynamic human-structure interaction.

10.2 Experiments

10.2.1 The Tests

This section describes the tests covering a description of the test floor and details about the tests.

The floor used in tests is a one-way spanning hollow-core prestressed concrete element pin-supported at both ends. The length of the floor is about 11 m and it weighs more than 5 t.

10.2.1.1 Tests and Determination of Floor Damping

First the empty floor is tested impacting it at floor mispan causing it to vibrate freely in vertical bending while vibrations damp out. A displacement sensor records the vertical motion of the floor at midspan during the decaying vibrations.

The logarithmic decrement method is employed to determine the damping ratio of the floor. For the empty floor this is denoted $\zeta(n = 0)$, where n is the number of passive persons on the floor.

Following this test, a similar test sequence is carried out now with humans atop the floor ($n = 1, 2, 3, 4$). In these tests the humans are passively sitting on chairs placed close to floor midspan. At this position an impact is made bringing the floor into vibrations. From the recorded free decay, the damping of the human-occupied floor is determined and it is denoted $\zeta(n)$.

The weight of each test person is recorded prior to the tests, and the difference in weight was within 10 kg. Due to the small deviation it is considered useful to present results in terms of ζ as a function of the number of passive persons on the floor (n) rather than as a function of the exact weight of the group of persons on the floor. This eases overview of measured relationships.

A small series of impacts are made allowing dynamic characteristics to be determined as mean values.

The chair used in tests is a chair with backrest. A 4-legged metallic frame carries the seat (made of wood but provided with a thin softening layer on top) and a metallic frame carries the backrest (also made of wood and with a thin softening layer). This a chair type often used at ventures where several persons assemble at meetings (at Aalborg University).

The postures that the test persons assume while seated:

A. Sitting relaxed with hands resting on knees. No use of backrest
B. Sitting relaxed with hands resting in the lap. Use of backrest

The variety of postures that a sitting person can assume is not restricted to the postures A and B but they are believed to represent quite common postures.

Following the tests with posture A and B, a test with mixed postures in the sitting crowd is made. In this test half of the sitting persons assumed posture A and the other half assumed posture B.

Table 10.1 Ratio r_ζ for different test conditions

Ratio	Posture	n, number of persons present on floor				
		0	1	2	3	4
r_ζ	A	1	10	18	28	34
r_ζ	B	1	8	19	28	36
r_ζ	A + B	1	–	17	–	33
r_ζ	S	1	1	1	1	1

Table 10.2 Ratio r_ζ for different test conditions. Supplementary tests

Ratio	Posture	n, number of persons present on floor				
		0	1	2	3	4
r_ζ	A	1	9	16	29	30
r_ζ	B	1	8	18	26	36
r_ζ	A + B	1	–	19	–	35

10.2.2 Results

For the presentation of results it is useful to introduce the ratio defined in Eq. 10.1.

$$r_\zeta(n) = \frac{\zeta(n)}{\zeta(n = 0)} \tag{10.1}$$

The ratio relates the damping ratio of the human-occupied floor (with n persons present) to the damping ratio of the empty floor.

The response ratio, r_ζ, calculated for each test condition is listed in Table 10.1.

It can be seen that (employing posture A), the damping increases when the number of persons present on the floor increases. The increase is quite considerable. Even a single person present on the floor increased damping by a factor of about 10.

Posture B also resulted in considerable increases in floor damping, and interestingly the two postures (A and B) resulted in almost similar increases with the number of persons on the floor. This would suggest that the posture (at least whether posture A or posture B is assumed) does not have much bearing on the damping added to the floor.

The results obtained for the mixed posture (denoted A + B) are fairly close to those obtained for the postures A and B.

A posture denoted S is also included in Table 10.1. Basically, this does not represent a posture but instead the results of tests made with a sandbag of 80 kg placed in the seat of the chair instead of a test person. In these tests basically no damping is found to be added to the floor irrespectively of the number of chairs provided with sandbags.

Supplementary tests were made in order to investigate whether the tendencies seen above are also valid for a different group of four persons. Hence another group of four persons were chosen for participation in tests.

The test procedures were similar and results in terms of the ratio r_ζ are listed in Table 10.2.

It can be seen that yet again, the number of persons present on the floor quite significantly influences the ratio r_ζ. The monitored variation with the number of persons present on the floor is not identical with that observed for the first group but similarities are evident (comparing Tables 10.1 and 10.2). This goes for both postures as well as the test with mixed postures.

Hence, the overall tendencies found in the first tests are also valid in the second test.

10.2.3 Discussion

The results quite clearly suggest that a human mass in sitting posture cannot with reasoning be modelled as a simple added mass attached to the vibrating structure, as a sandbag mass placed in the seat of the chair did not add damping to the floor. Oppositely, when a human was placed in the seat, a quite considerable amount of damping was added to the floor.

One reason to the large amount of damping added is that the empty test floor is quite lowly damped ($\zeta(n = 0)$ was found to lower than 0.25 %). Had the empty floor damping been higher, the influence would probably be less significant.

Is it also found that the damping added by the sitting persons did not to a large degree depend on which of the two postures the sitting persons assumed. Neither when mixing the postures no significant difference in the variation of floor damping with crowd size was noticed. Similar tendencies in results were found when another group of persons were tested.

These are useful observations as it might suggest that it would be meaningful to apply a model describing the dynamic interaction between a sitting human and the floor that does not require considering the specific posture of the sitting person. At least the amount of damping added to the structure is almost equal for the studied postures.

The findings suggest that it may be useful to model humans as a mass dynamically interacting with the floor mass. The approach of considering the human body as a dynamic system is in agreement with the modelling approach applied in biomechanics [6].

Such approach will be considered in the subsequent section (Sect. 10.3) attempting to highlight to which extend passive humans on a floor can influence floor vibration levels when the floor is exposed to actions of a person in motion.

10.3 Numerical Case Study

10.3.1 The Interaction Model

For the case study, a 2DOF human-structure interaction model will be assumed with the structure (floor) representing the grounded system and with the crowd mass attached to the structural mass by a linear spring and a linear dashpot. A similar type of connecting is assumed between ground and floor mass.

The structure will be a SDOF floor and the dynamic characteristics of the floor are listed in Table 10.3.

The values represent the natural frequency of the first bending mode (f_F), the modal mass of this mode of vibration (M_F) and the damping ratio (ζ_F). The values are realistic as equal to those measured on the real floor.

The dynamic characteristics of the crowd of persons are given in Table 10.4.

These are the natural frequency and damping ratio, respectively. The mass of the crowd (m_H) is not assigned a specific value as different values for this parameter will be assumed for calculations. The frequency and damping characteristics are considered to be fairly representative.

10.3.2 The Load Model

A jumping person is assumed to excite the floor. Perhaps it would have been more realistic if it was a pedestrian that excited the floor but it is not that important as the idea is to study the relative difference in floor response as found with and without a stationary crowd atop the floor.

For the studies of this paper, the jumping force ($q(t)$) is described by Eq. 10.2.

$$q(t) = mg \sum_{i=1}^{5} \alpha_i \sin\left(2\pi i \, f_j t + \theta_i\right) \tag{10.2}$$

The general load model is in accordance with [7, 8]. In Eq. 10.2, f_j is the motion frequency (jumping frequency) and the equation reflects that excitation is modelled to occur at the jumping frequency and at multipliers of this frequency. The load amplitude is $mg\alpha_i$ where mg is the weight of the jumper and where α_i is the dynamic load factor for harmonic i.

It is established that there is the overall tendency that the value of the dynamic load factor reduces with increases in the jumping frequency. This tendency is modelled using Eq. 10.3.

$$\alpha_i = \begin{cases} 2 & if \;\; if_j < 3 \;\; \text{Hz} \\ -0.19if_j + 2.57 \; if & 3 \;\; \text{Hz} \le if_j < 13 \;\; \text{Hz} \\ 0.1 & if \;\; if_j \ge 13 \;\; \text{Hz}. \end{cases} \tag{10.3}$$

This relationship is employed for the present studies but has also been employed for numerical studies for instance in [9].

Table 10.3 Dynamic characteristics of floor

f_F	M_F	ζ_F
8.5 Hz	$6.8 \cdot 10^3$ kg	1.6 %

Table 10.4 Dynamic characteristics of crowd

f_H	ζ_H
6.5 Hz	0.38

Table 10.5 Response ratio r_{rms} and its variation with m_H

m_H	0 kg	90 kg	180 kg
r_{rms}	1	0.7	0.5

10.3.3 Calculated Floor Response

For the jumping frequency various values are considered (2.00 Hz, 2.01 Hz, 2.03 Hz up to 3.00 Hz) and on each assumption, the load and the accompanying acceleration level of the floor is computed. For the present study, the steady state rms-value of floor response at midspan is extracted.

A maximum rms-value is calculated for the empty floor (denoted $a_{rms}(m_H = 0)$) as well as for situations where a passive crowd is assumed present at the center of the floor (denoted $a_{rms}(m_H)$).

From these properties the following ratio is computed:

$$r_{rms}(m_H) = \frac{a_{rms}(m_H)}{a_{rms}(m_H = 0)} \qquad (10.4)$$

which basically is a normalisation of rms-values obtained for the floor carrying passive persons (of total mass m_H) with the rms-value calculated for the empty floor. For values of r smaller than 1, the presence of the sitting person has attenuated the structural vibrations.

The ratio r was computed on different assumptions for the mass of the stationary crowd of people m_H and results are shown in Table 10.5.

It is seen that by having available a model for human-structure interaction, it is possible to predict floor vibrations levels on various assumptions concerning the mass of the humans atop the floor.

In the studied case, even a small passive human mass atop the floor is found to be capable of reducing the vibration response of the floor quite significantly. The vibration attenuating effect is not as high as in the experimental tests reported in this paper, but it is still considerable and maybe worth taking into account when predicting floor vibrations.

10.4 Conclusion and Discussion

The paper has investigated whether and to which degree the posture of sitting humans influences floor damping behaviour.

Experimental investigations with a laboratory floor with test persons sitting in different and mixed postures on fairly rigid chairs suggested that the floor damping behaviour to a limited degree was sensitive to the posture assumed by the sitting persons.

This might be a useful observation as it might suggest that it would be meaningful to apply a model describing the dynamic interaction between a sitting human and the floor that does not require considering the specific posture of the sitting person – and still obtain results that are meaningful when attempting to predict dynamic behaviour of the coupled dynamic system.

It is however to be noted the experimental results presented in this paper only rely on a few tests, studying only a few postures of a sitting person and considering only a single chair-type in tests, etc. (as time allowed).

But the findings are believed to be useful as displaying tendencies and relationships not previously studied or considered when focus is on dynamic interaction between sitting humans and the floor which they occupy, thus providing information useful for understanding and modelling the quite complex interaction taking place and for designing additional tests.

References

1. Ellis BR, Ji T (1997) Human-structure interaction in vertical vibrations. In: Proceedings of the ICE: structures and buildings, London, UK, vol 122, pp 1–9
2. Brownjohn JMW (2001) Energy dissipation from vibrating floor slabs due to human-structure interaction. Shock Vib 8(6):315–323
3. Reynolds P, Pavic A, Ibrahim Z (2004) Changes of modal properties of a stadium structure occupied by a crowd. In: Proceedings of the 22nd international modal analysis conference, Dearborn, Michigan
4. Pedersen L (2005) Updating of the dynamic model of floors carrying stationary humans. In: Proceedings of the 1st international operational modal analysis conference, Copenhagen, Denmark, pp 421–428

5. Sachse R, Pavic A, Prichard S (2002) The influence of a group of humans on modal properties of a structure. In: Proceedings of the fifth international conference on structural dynamics, Munich, Germany, pp 1241–1246
6. Griffin MJ (1990) Handbook of human vibration. Academic, London
7. Ji T (1994) Floor vibrations induced by dance-type loads: theory. Struct Eng 73(2):37–44
8. Bachmann H, Ammann W (1987) Vibrations in structures – induced by man and machines. IABSE structural engineering documents 3e, Zürich
9. Pedersen L (2014) Interaction between humans and structures. In: Proceedings of the 33th international modal analysis conference, Jacksonville

Chapter 11
A Correlation Analysis Regarding the Temperature Effect for a Suspension Bridge

Jin-Woo Jung, Dae-Joong Moon, Ji-Won Jung, Sang-Kon Ro, and Ji-Hyun Park

Abstract The monitoring for measuring structural behavior has been advanced. Recently, many researchers have studied on the structural health monitoring using the GNSS (Global Navigation Satellite System). This paper presents temperature behavior for a Gwang-An bridge which is three span suspension bridge in Korea. The behavior of a middle span have analyzed on ambient temperature change. As the time passed from January to June in 2013, the vertical displacement was decreased and the temperature was increased more and more at the middle span. And the correlation analysis was performed between the temperature and the vertical displacement using the thermometer and GNSS. Also monthly changes of the temperature and natural frequency had been measured. And then the correlation analysis was performed between the temperature and natural frequency. As a result of the evaluation regarding thermal effect at the middle span, relationship between the temperature and natural frequency seemed to have trend of inverse proportion.

Keywords Suspension bridge • GNSS • Dynamic characteristics • Temperature effect • Correlation analysis

11.1 Introduction

Computerized maintenance and management system have installed for systematic control and safety assessment in cable stayed bridges and suspension bridges that have been completed recently. Previous studies assumed that the temperature effect was meager or nothing and not reflected to structural analysis due to difficulty of mathematical formularization in the dynamic characteristics estimation of structures. However, changes of dynamic characteristics according to the temperature was occurred in bridges which have exposed in the severe temperature environments. And some study described that these characteristics changes might be stronger than changes due to structural damage [1]. For the purpose of quantitative evaluation of uncertainty factors and reliable analysis of dynamic behavior for the bridge, the Gwang-An bridge has been accumulating data about dynamic characteristics by measuring ambient vibration for a long time. There are many previous studies focusing on the dynamic behavior characteristics of bridges using ambient vibration. However there have been performed these studies at the initial safety inspection or precision safety diagnosis after bridge completion. Therefore it was rare that long-term dynamic behavior change of the structure was monitored and analyzed through the real-time measurement. In this paper, possibility of the dynamic characteristics change was evaluated based on accumulated measurement data from January to June in 2013.

11.2 Bridge-Measurement

11.2.1 The Gwang-An Bridge

Gwang-An bridge was constructed in 2002 and Busan Infrastructure Corporation has been maintaining in Korea. This bridge is three-span, two-hinge stiffened, earth-anchored suspension bridge with a total length of 900 m (200 m + 500 m + 200 m) (Figs. 11.1 and 11.2).

J.-W. Jung (✉) • D.-J. Moon • J.-W. Jung

EJ tech Co., Ltd., Seokjeong B/D, 204-5 Gumi-dong, Bundang-gu, Seongnam-si, Gyeonggi-do 463-871, Republic of Korea
e-mail: jinu8505@hanmail.net

S.-K. Ro • J.-H. Park

Busan Infrastructure Corporation, 1 Suyeong Gangbyeondaero, Haeundae-gu, Busan-si 618-828, Republic of Korea

11.2.2 Bridge Measurement System

The Gwang-An bridge measurement system monitors and analyzes the status of the bridge by receiving signals from sensors that were installed at some parts of the bridge in real-time. Nine types of sensors such as accelerometer, seismometer, thermometer, laser displacement meter and GNSS were installed in the suspension bridge. Static signals such as temperature are accumulated 1 time per 10 min and dynamic signals such as vibration are accumulated 100 times per second. Accelerometers that can measure vertical vibration signals were installed at up and down line of the girder. Accelerometers are force-balance type for low-frequency range with the dynamic range of 140 dB and bandwidth of accelerometers is from DC to 200 Hz. Two GNSS were installed for measuring displacement at up and down line of the middle span, and GNSS perform monitoring by receiving data in real-time (Fig. 11.3).

Fig. 11.1 An overview of the Gwang-An bridge
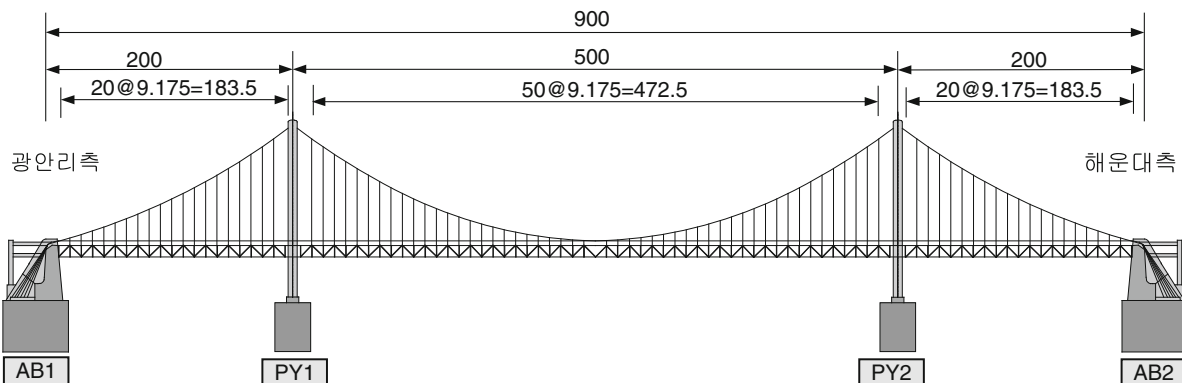
Fig. 11.2 A front view

Fig. 11.3 A cross section of the pylon
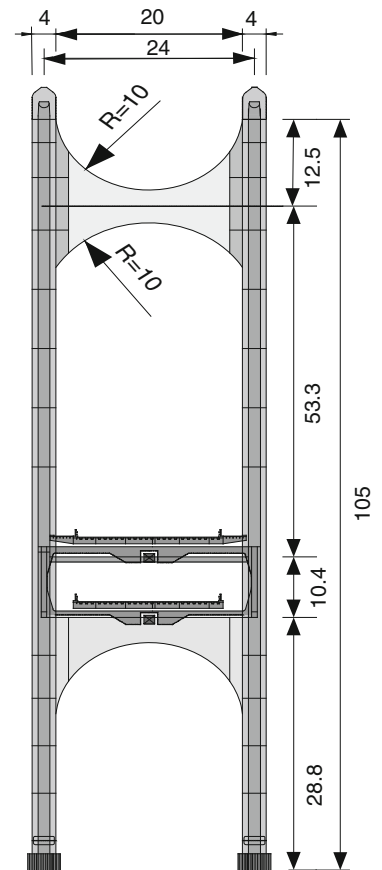
Fig. 11.4 Changes of temperature at the middle span
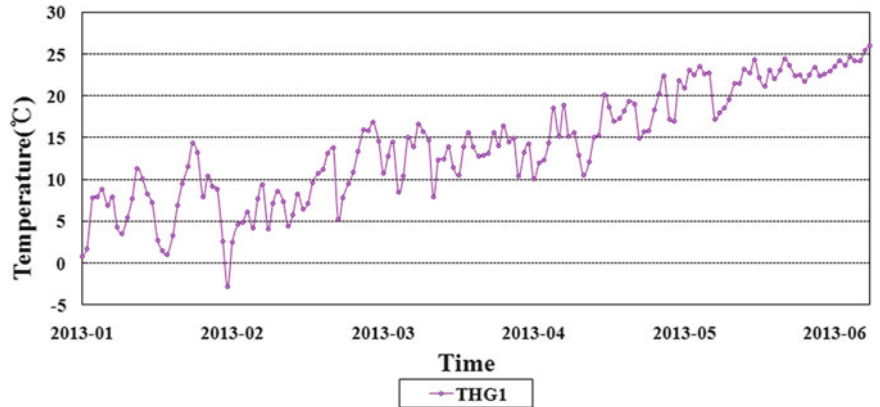
11.3 Analysis Results

11.3.1 Results of Long-Term Measurements

Figure 11.4 is changes of temperature and Fig. 11.5 is changes of vertical displacement at the middle span. Where GNSS_MSL indicates the landward GNSS in the middle span, GNSS_MSS indicates the seaward GNSS in the middle span and THG1 is the thermometer in the middle span. As a result of analysis for measurement data from January to June in 2013, maximum temperature was 26.0 °C, minimum temperature was −2.8 °C, maximum vertical displacement at the middle span was 46.1 mm and minimum was −353.7 mm, when reference point was measurement data in January 1st, 2013. Measurement data from GNSS are 10 Hz, and data in Fig. 11.5 is average value during an one-day. As the time passed from January to June, temperature was increased and vertical displacement was decreased more and more at the middle span. That was why stiffness of the middle span became small according as the temperature increased.

Fig. 11.5 Changes of vertical displacement at the middle span
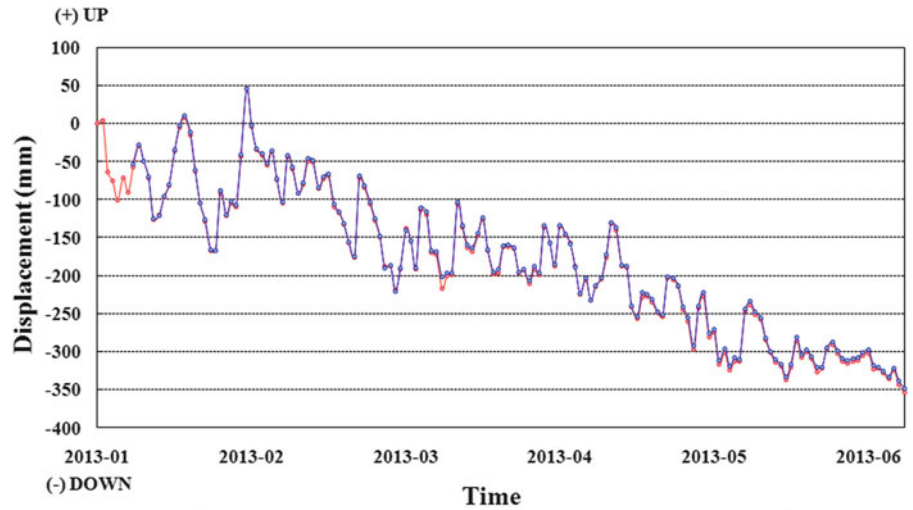
Fig. 11.6 Correlation analysis results between the temperature and displacement
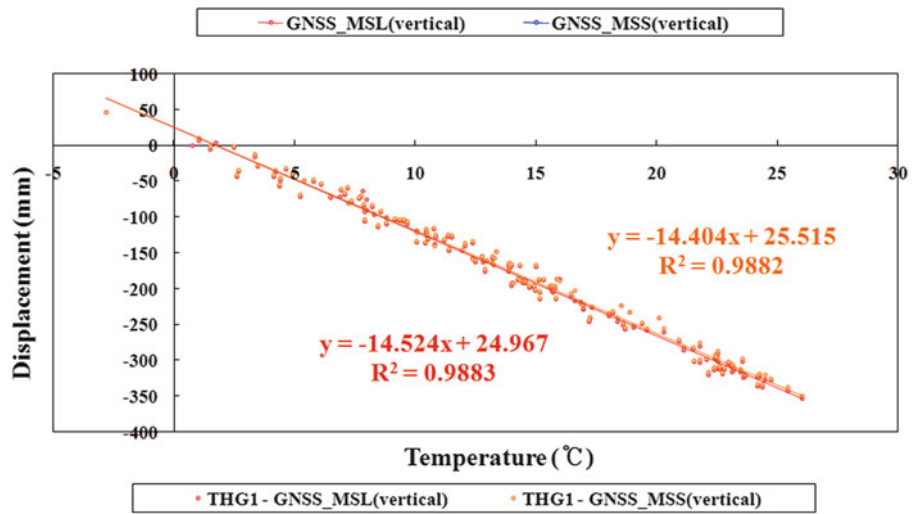
Correlation analysis was performed for the purpose of grasping correlation between the temperature and vertical displacement at the middle span. As a result, large negative correlation coefficient(R) of 0.9941 and 0.9940 were shown in the Fig. 11.6.

11.3.2 FFT Analysis

Dynamic characteristics of the Gwang-An bridge was analyzed using GNSS and accelerometers that were installed in the girder. GNSS data have been measured at the frequency 10 Hz. Also a modal frequency response was analyzed using FFT (Fast Fourier Transform) analysis. The GNSS data was transformed into the acceleration data by double-differentiating with respect to time. In case of bending vibration, FFT analysis was performed by extracting signals with respect to bending vibration after signals with respect to torsional vibration was eliminated by adding acceleration of point a and b as shown in the Fig. 11.7.

Figure 11.8 is the acceleration data stream which collected from accelerometer and Fig. 11.9 is the result of the FFT analysis using acceleration data. Figure 11.10 is the displacement data of the GNSS. And the acceleration data of the time-domain is deduced by double-differentiating GNSS displacement data as shown in the Fig. 11.11. When the FFT analysis is performed using the acceleration data of the time-domain, the acceleration data of the frequency-domain can be deduced as shown in the Fig. 11.12.

Fig. 11.7 An example girder for the acceleration analysis
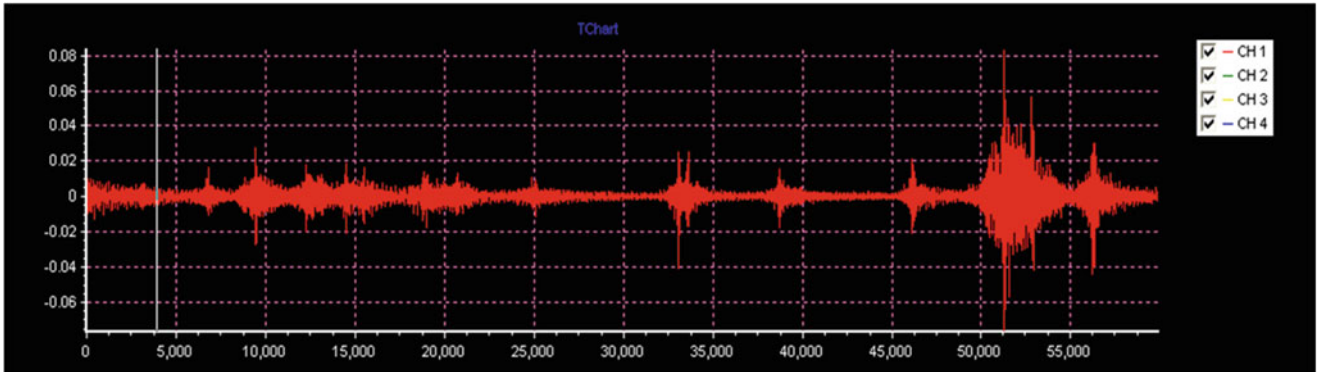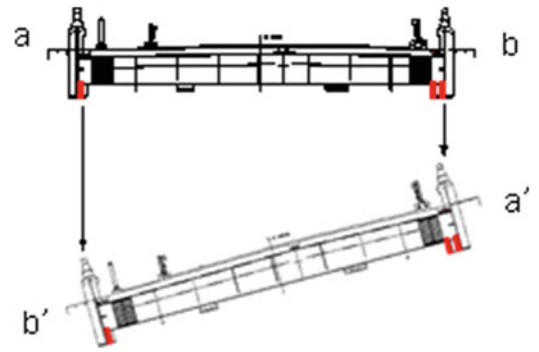
Fig. 11.8 The acceleration data stream collected from accelerometer
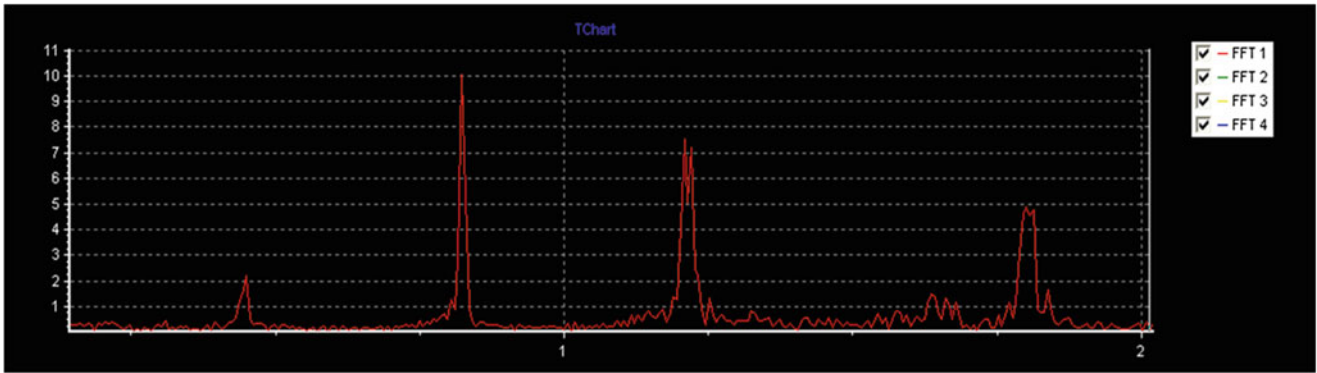
Fig. 11.9 The result of the FFT analysis using acceleration data
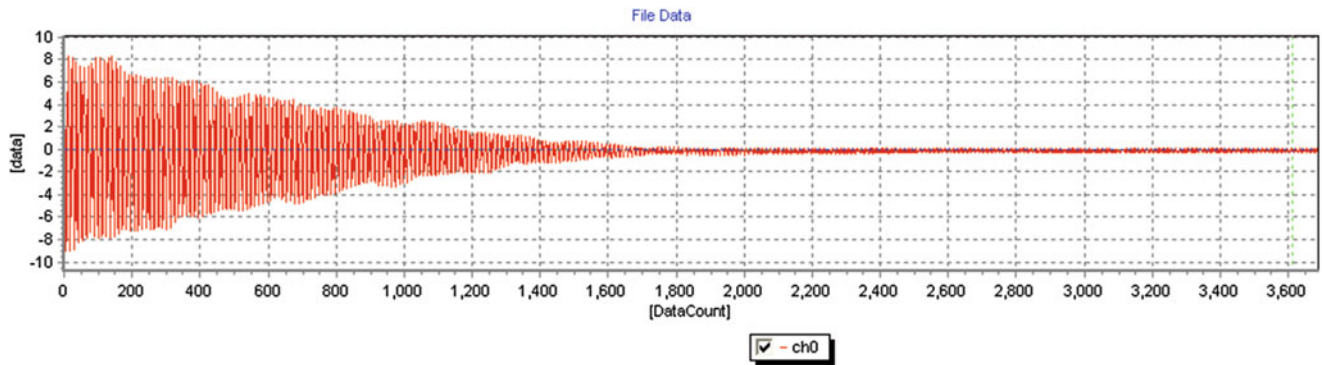
Fig. 11.10 The displacement data of the GNSS
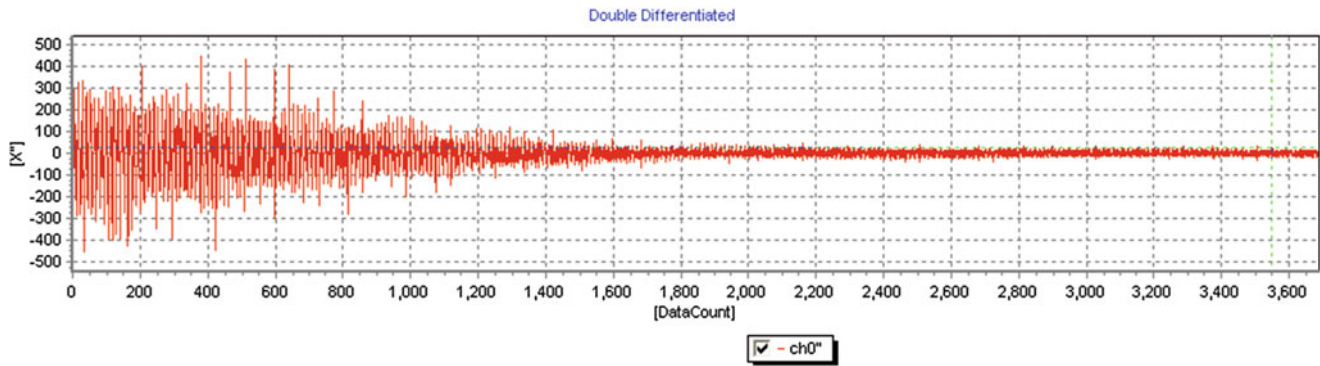
Fig. 11.11 The acceleration data deduced by double-differentiating GNSS displacement data
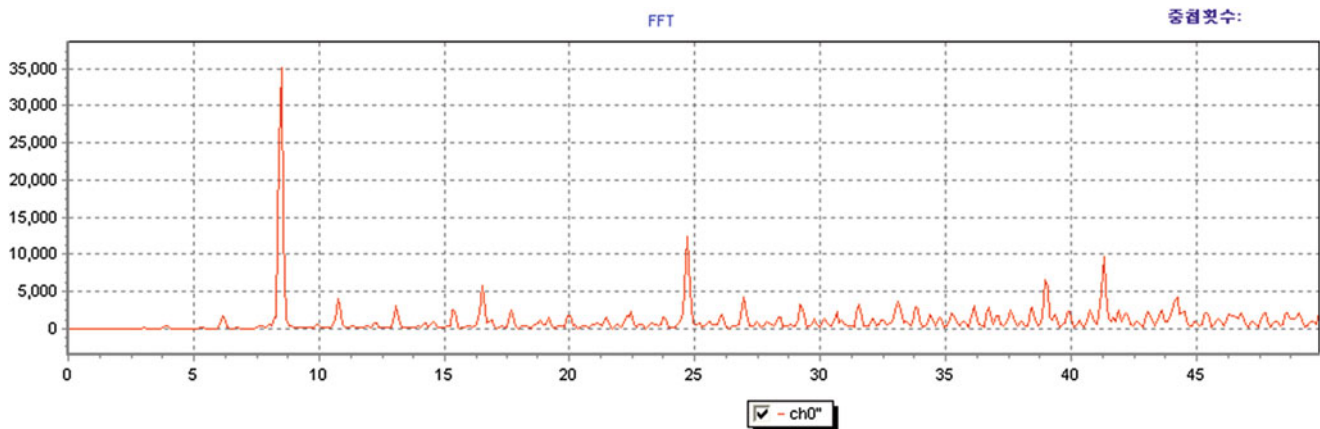
Fig. 11.12 The result of the FFT analysis using GNSS data

11.3.3 The Results of Dynamic Characteristics Analysis Using the GNSS and Accelerometer

Vertical displacement factor by the ambient vehicle loading is dominant in GNSS signals that was measured from the suspension bridge because GNSS signals is displacement value of the corresponding measuring point with respect to time. Besides various error and noise factor is contained in GNSS signals. For reducing these effects in GNSS signals of the Gwang-An bridge, signals of the only interested range between from 0.1 to 1.0 Hz were separated by using band pass filter.

Also GNSS displacement data was transformed by double-differentiating the acceleration data so dynamic characteristics extraction was performed effectively. Table 11.1 is the FFT results that are monthly analysis results of the bending vibration based on data which was deduced from GNSS and accelerometer.

Natural frequency measurement results of GNSS and accelerometer signals were compared in the same time. Natural frequency extraction was performed correctly in that these data were very similar. Therefore, if proper filtering and double-differentiating technique are applied to measured GNSS signals, it is possible to extract numerous natural frequency. And it means that GNSS can replace accelerometer of corresponding points.

11.3.4 Correlation Analysis Between Temperature and Natural Frequency

As the time passed from January to June in 2013, natural frequency was decreased as seen in the Table 11.1. In other words, relationship between the temperature and natural frequency seemed to have trend of inverse proportion. And then the correlation analysis was performed between the temperature and natural frequency. As a result of the evaluation regarding thermal effect at the middle span, the temperature and natural frequency had a large negative correlation coefficient(R) (Fig. 11.13).

Table 11.1 Monthly analysis results of the bending vibration

Bending vibration		Middle span	
		GNSS	Accelerometer
2013.01.	1st	0.2610	0.2598
	2nd	0.2840	0.2837
	3rd	0.4634	0.4642
2013.02.	1st	0.2605	0.2605
	2nd	0.2831	0.2830
	3rd	0.4612	0.4633
2013.03.	1st	0.2591	0.2601
	2nd	0.2825	0.2822
	3rd	0.4610	0.4621
2013.04.	1st	0.2561	0.2592
	2nd	0.2821	0.2815
	3rd	0.4605	0.4610
2013.05.	1st	0.2552	0.2582
	2nd	0.2818	0.2810
	3rd	0.4597	0.4603
2013.06.	1st	0.2547	0.2573
	2nd	0.2811	0.2806
	3rd	0.4601	0.4598

Fig. 11.13 The result of correlation analysis between temperature and natural frequency
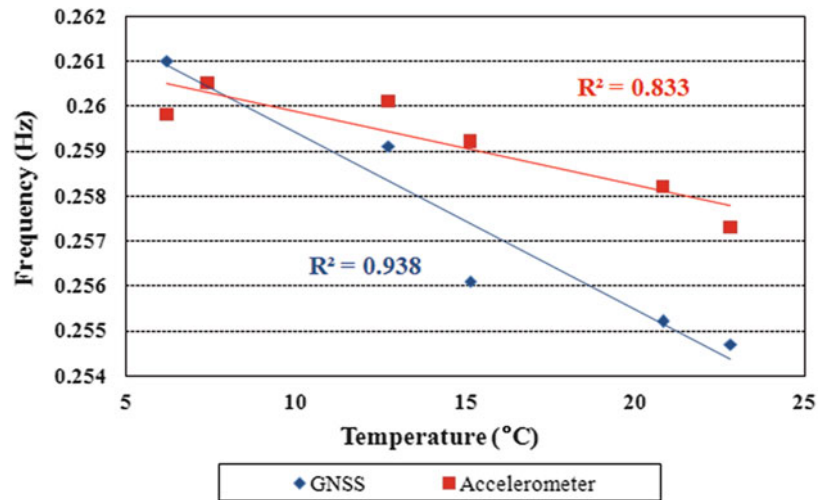
11.4 Conclusions

This paper presents that vertical displacement behavior of the girder and dynamic characteristics analysis was performed for the Gwang-An bridge in Korea. As the time passed from January to June in 2013, temperature had been increased from −2.8 °C to 26 °C and vertical displacement had been decreased from 46.1 to −353.7 mm at the middle span. Also the natural frequency at the middle span seemed to have decreasing trend. That was why stiffness of the middle span became small according as the temperature increased. Therefore temperature effect should be considered in case of reflecting dynamic characteristics such as vibration test, analysis model design and state valuation of the suspension bridge.

References

1. Wenzel H, Pichler D (2005) Ambient vibration monitoring. Wiley, Chichester
2. Roberts GW, Brown C, Atkins C, Meng X (2008) The use of GNSS to monitor the deflections of suspension bridges. In: 13th FIG symposium
3. Meng X, Dodson AH, Roberts GW (2007) Detecting bridge dynamics with GPS and triaxial accelerometers. Eng Struct 29:3178–3184
4. Figurski M, Galuszkiewicz M, Wrona M (2007) A bridge deflection monitoring with GPS. Artif Satell 42:229–238
5. Gil HB, Park JC, Cho JS, Jung GJ (2010) Renovation of structural health monitoring system for Seohae bridge, Seoul, South Korea. J Transp Res Board 2201:131–138

Chapter 12
Total Load Effects of Portal Frame Bridges in High-Speed Railway Lines

Daniel Cantero and Raid Karoumi

Abstract This paper studies the maximum total load effects of short span portal frame railway bridges when traversed by high-speed trains. It is generally assumed that in single span bridges the maximum stresses, displacements and accelerations occur at the mid-span section. However, this in not necessarily correct and the maximum might be located in a wide area around the mid-span. This study aims to quantify the underestimation of the mid-span assumption when calculating maximum load effects. A numerically validated 2D Vehicle-Bridge Interaction model is used to analyze the stresses, displacements and accelerations that develop during the passage of high-speed trains. These load effects are studied along the full length of the structure and compared to the maximum obtained at the mid-span section. Particular attention is given to the resonant speeds near the operational speeds of high-speed railways. The results show that significantly higher load effects can be expected. The presented study is the preliminary work for deciding on the optimum configuration of empirical field tests.

Keywords Maximum • Railway • Bridge • Dynamics • High-speed

12.1 Introduction

Traffic loading of bridges is a crucial aspect either at the design stage before construction or for the assessment of existing bridges. The maximum total Load Effect (LE), which consists of the combined contribution of static and dynamic effects, needs to be correctly evaluated. In single span bridges it is generally assumed that the mid-span section features the maximum displacements, bending moments and accelerations. This assumption is not necessarily correct. In a vibrating structure the location where the actual maximum occurs might be far apart from the mid-span region due to the contribution of higher modes of vibration. Also the true maximum LE experienced by the bridge might be significantly larger than its mid-span counterpart. This has been investigated for road bridges in [1] indicating that big differences might exist. However, [2] showed that the mid-span assumption leads to characteristic design values that are very similar to the values obtained if the whole structure is considered. It can be concluded that for the particular case of road bridges the small load underestimation due to the mid-span assumption is covered by the inherent safety coefficients in the design process.

The dynamic effects of railway bridges are generally larger than in road bridges due to higher speeds of the traversing vehicle. Additionally, the repetitive configuration (long trains composed of wagons with identical axle distances) combined with its traversing speed introduces loading frequencies that lead to resonant behavior of the bridge. The LE at resonance can be several times greater than in a non-resonant situation. For one particular train configuration the LE displays resonant peaks at certain critical speeds. These critical speeds and the magnitude of the LE at resonance define the design (or assessment) values of the bridge under consideration. This is a fundamental difference with road bridges, which are loaded by traffic with a mixture of axle configurations and separated by arbitrary gaps between vehicles. Even multiple vehicle events do not produce resonant behavior to the same extent as in railway bridges. Thus, the effect of the mid-span assumption has not been sufficiently investigated for railway bridges in general, and at resonance in particular.

It is an obvious consideration, that the structures should be designed to withstand the maximum LE that it will be subjected to, regardless its location. For instance, the Eurocode [3] limits the maximum deck acceleration for ballasted tracks to 3.5 m/s^2 to avoid ballast instability. By definition this considers any location on the bridge deck. For the remaining LEs codes usually define some sort of dynamic allowance or Dynamic Amplification Factor (DAF). These factors are generally derived from extensive measurement campaigns. Due to budget constraints, limited number of sensors and other technical questions,

D. Cantero (✉) • R. Karoumi
Civil and Architectural Engineering, KTH Royal Institute of Technology, 23 Brinellvägen, Stockholm, Sweden
e-mail: dacl@kth.se

measurements are performed only at the locations where the extreme LEs are expected. It is not feasible to monitor every section of the bridge. However, the relation between the maximum LE at the expected location compared to the rest of the structure has not been sufficiently studied.

It is well known that short span bridges have the highest dynamic effects and constitute the majority of the bridge stock in any network. In particular the portal frame bridges are predominant in railway lines, especially in Sweden. Therefore, this paper studies the underestimation of the bridge response because of the mid-span assumption in portal frame bridges. Three LEs are investigated, namely accelerations, bending moments (BM) and vertical displacements. Special attention is given to resonant situations and the bridge sections where the maxima are located. A numerical analysis of the phenomenon is presented in this document using a validated 2D numerical model that includes the vehicle, track, ballast and bridge.

For the deck acceleration, the difference between the maximum at mid-span to the maximum in the rest of the bridge is done in absolute terms and given in m/s^2, since the same acceleration limit exists regardless the span. However, for the BM and vertical displacements, the comparison is done in relative terms, which allows contrasting results of different lengths and properties. The definition of DAF (Eq. (12.1)) can be extended to account for the maximum LE on the bridge, as in Eq. (12.2) where FDAF stands for Full bridge length DAF. Also the Location Of the Maximum, which will be termed LOM, is analyzed and expressed in terms of percentage of span length. LOM offers some insights of the problem and gives an idea of where sensors should be located to record the actual maximum LEs.

$$DAF = \frac{Max.\ LE_{mid-span}}{Max.\ Static\ LE_{mid-span}} \tag{12.1}$$

$$FDAF = \frac{Max.\ LE_{full-length}}{Max.\ Static\ LE_{mid-span}} \tag{12.2}$$

The document starts with the description of the model used in the numerical study. Then it continues with the analysis of one particular bridge. After briefly describing the bridge, the maximum acceleration is compared to its mid-span counterpart. Next, the study of the influence of the traversing speed shows the resonant behavior and the consequences of the mid-span assumption. The last section of this document presents the analysis of a collection of bridges that are part of a 190 km long railway line in Sweden. The local authorities are considering upgrading the line to higher speeds. The mid-span assumption is evaluated for this group of bridges. The document ends providing some conclusions of the results presented here.

12.2 Numerical Model

This section introduces the numerical model used in this study, which is a planar model that incorporates the behavior of train, ballasted track and bridge. It correctly accounts for the interaction between the vehicle and the infrastructure. Compared to the simple moving load models (commonly used in relevant literature) the one presented here gives more accurate results because it includes the Vehicle-Bridge Interaction (VBI). Furthermore, this model by considering the rail-sleeper-ballast system distributes the load along the bridge. It has been shown [4] that considering the load distribution is particularly important for short span bridges. On the other hand, a planar model is certainly less accurate than more complex 3D models. However, the solutions that more complex models provide are particular to the selected bridge and vehicle configuration and it is difficult to draw general conclusions from them. In addition, the 3D models need many additional parameters, their exact numerical values are difficult to determine and are computationally very expensive. The presented model is a trade-off between result's accuracy and model complexity, which has been validated in [5].

The train has been modelled as a succession of individual vehicles. Providing the correct dimensions and properties for each vehicle, it is possible to model locomotives and passenger wagons. Each vehicle consists of a combination of lumped masses, rigid bars, springs and dashpots as presented in Fig. 12.1a. This vehicle model with 6-DOF is extensively used in related literature. The wheels, represented as masses on the rail, are connected to the bogies by the primary suspension. The secondary suspension links the bogies and the main body mass. Each suspension system is made of a combination of linear springs and viscous dampers. The main body and bogies are represented as rigid bars with mass and moments of inertia properties.
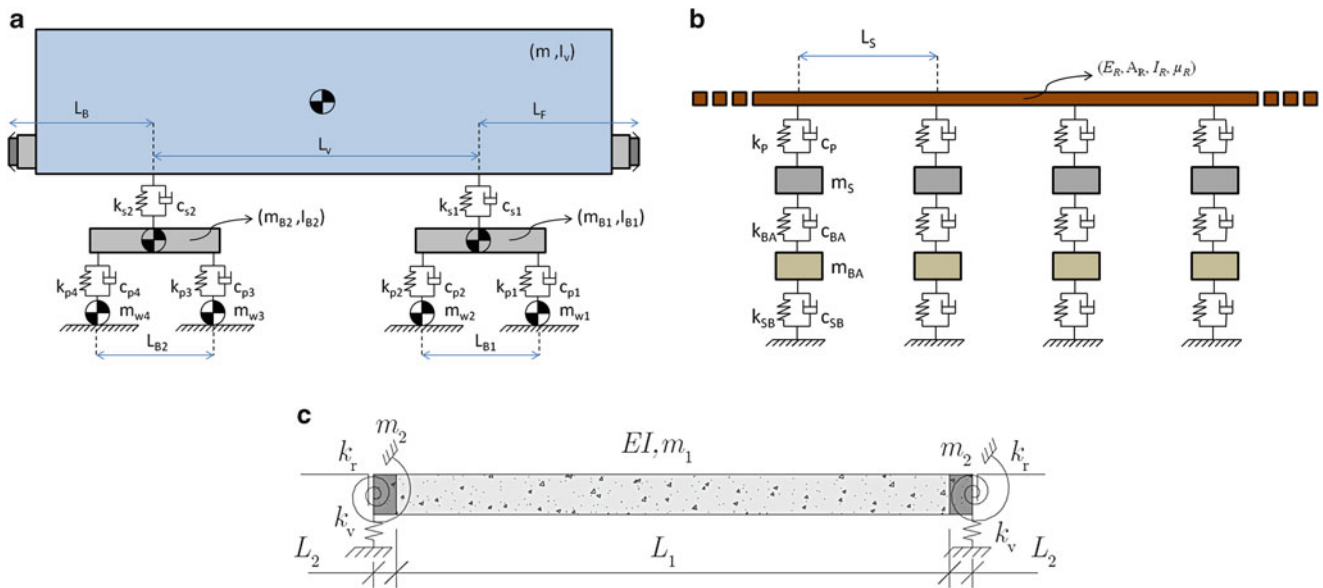
Fig. 12.1 Sketches of models; (**a**) 6-DOF vehicle; (**b**) ballasted track; (**c**) portal frame bridge [7]

Fig. 12.2 Simplified model for frame bridges
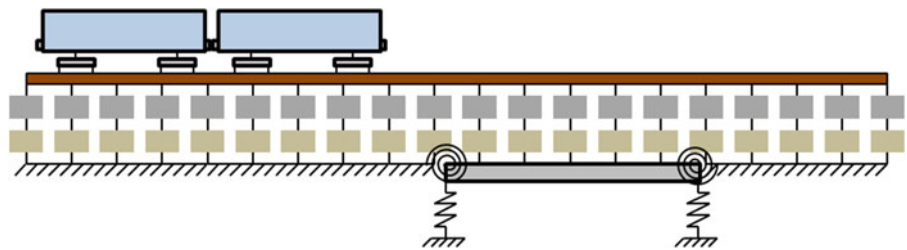
The track is modelled as a beam resting on periodically spaced sprung mass systems (see Fig. 12.1b). This is a generally accepted model that correctly predicts the dynamic vertical displacements of the track system. The rail is modelled by beam elements in a FEM framework, whereas the masses represent the sleepers and ballast. Beam and masses are connected by spring/dashpot systems that represent the pad, ballast and sub-ballast.

The bridge is modelled as an Euler-Bernoulli beam using a Finite Element Model (FEM) discretization (Fig. 12.1c). The beam is restrained by vertical and rotational sprung supports and has lumped masses near the ends. This model has been introduced in [6] in order to obtain a simplified model of a portal frame bridge and has been validated against more complex 2D and 3D models [4]. The use of elastic springs is to take into account the soil-bridge interaction. Additionally, the wing walls comprise a significant volume of concrete that has to be considered in order not to overestimate the frequencies of the bridge, and are included as lumped masses. It is acknowledged that the described model is not suited for very short bridges (>5 m), which do not behave like beams, and a 3D plate model should be used instead.

Vehicle, track and beam are linked together to give the full model as shown in Fig. 12.2. The vehicle configuration adopted here is the ICE 2 train, which is composed of 1 locomotive at each end of the convoy and 8 passenger wagons. The dimensions and mechanical properties for the train have been taken from [8]. The track has been modelled with an approach distance for the travelling vehicle and is long enough after the bridge in order to allow for the whole vehicle to exit the bridge. The particular mechanical properties of the track can be found in [9] and no track irregularities have been considered. The properties of the bridge under consideration are provided in following sections.

The model gives the solution of the three systems (vehicle, track and bridge) coupled together, which is achieved by updating the coupling terms of the equations of motion at every time step. The numerical integration is achieved with the Newmark-β method and a sufficiently small time step. The reader can refer to [5] for additional details about the numerical model.

12.3 Analysis of Norra Kungsvägen Bridge

This section studies the maximum load effects and their location for one particular structure, namely the Norra Kungsvägen Bridge. This particular bridge has been chosen because of its ease of access and accessibility of the soffit. Additionally, there are plans to install a permanent monitoring system and the following analysis is part of a preliminary study of its structural behavior.

12.3.1 Bridge and Model Description

The Norra Kungsvägen Bridge is located in Sweden in the railway line that links the cities of Umeå and Sundsvall. It was finished in 2007 and a general view of the structure can be seen in Fig. 12.3. The bridge can be represented using the simplified beam model (Fig. 12.1c) presented in Sect. 12.2. The model properties that correctly represent this bridge have been calculated in [7] and reproduced in Table 12.1 for the reader's convenience.

A modal analysis of the bridge was performed and its first four modes and frequencies are presented in Fig. 12.4. The dynamic response of the structure can be represented as a linear combination of these modes where each mode has a different weight on the final response. Some modes do not have their maximum value at the mid-span section, for instance modes 2 and 4. It is easy to see that a combination of these modes might result in maximum LE located in sections other than the mid-span one.

12.3.2 Maximum Acceleration

Figure 12.5a shows the acceleration signal at mid-span during the passage of an ICE 2 train travelling at 350 km/h. It is known that the maximum is not necessarily at this location. Thus, Fig. 12.5b presents the last second of the mid-span acceleration signal together with the true acceleration maxima (and minima) anywhere along the bridge length. It can clearly be seen that significant differences exist. The peak acceleration at mid-span is 0.70 m/s^2 and reached approximately at 2.7 s while the true maximum acceleration is 0.94 m/s^2. This corresponds to a 34.29 % increase in acceleration, which is a significant difference and indicates that a closer analysis of the mid-span assumption is necessary.

Note that in the rest of the document maximum acceleration refers to the maximum of the acceleration in absolute value, regardless of its sign. This avoids the need of defining maximum and minimum acceleration separately.

Fig. 12.3 General view of Norra Kungsvägen Bridge

Table 12.1 Numerical values for the Norra Kungsvägen Bridge model

Variable (unit)	Numerical value
L_1 (m)	15.7
E (GPa)	20.4
I_x (m^4)	1.59
m_1 (kg/m)	21,712
m_2 (kg)	547,456
k_v (MN/m)	2,294
k_r (MNm/rad)	6,581
ζ (%)	1.8
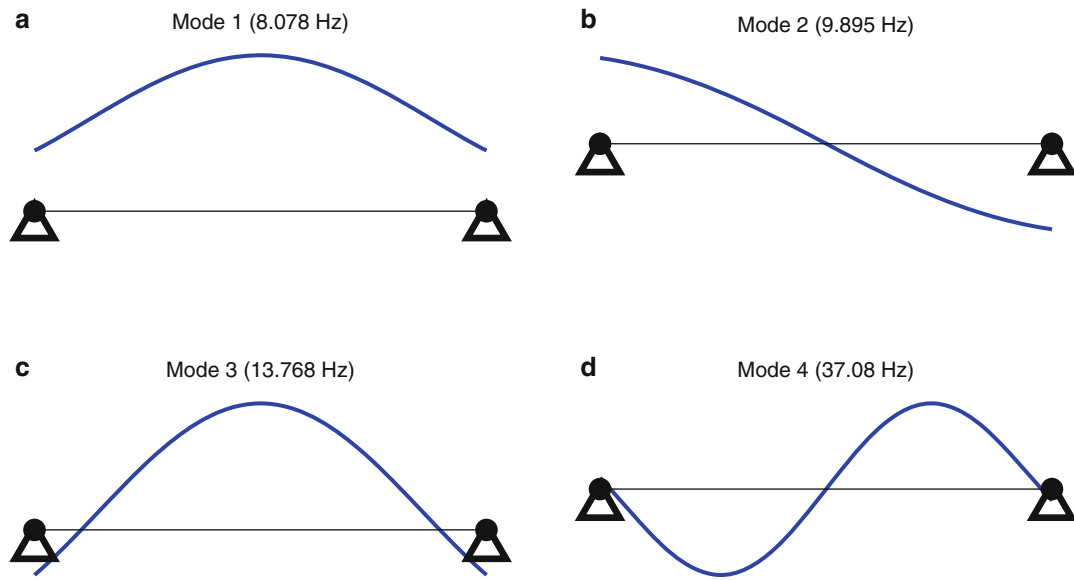
Fig. 12.4 First four modes of vibration of simplified model of the Norra Kungsvägen Bridge

Fig. 12.5 Acceleration of Norra Kungsvägen Bridge for ICE 2 train at 350 km/h, (**a**) mid-span acceleration for the whole crossing event, (**b**) detail of last second of signal at mid-span (*solid*) and maxima/minima in any section (*dashed*)
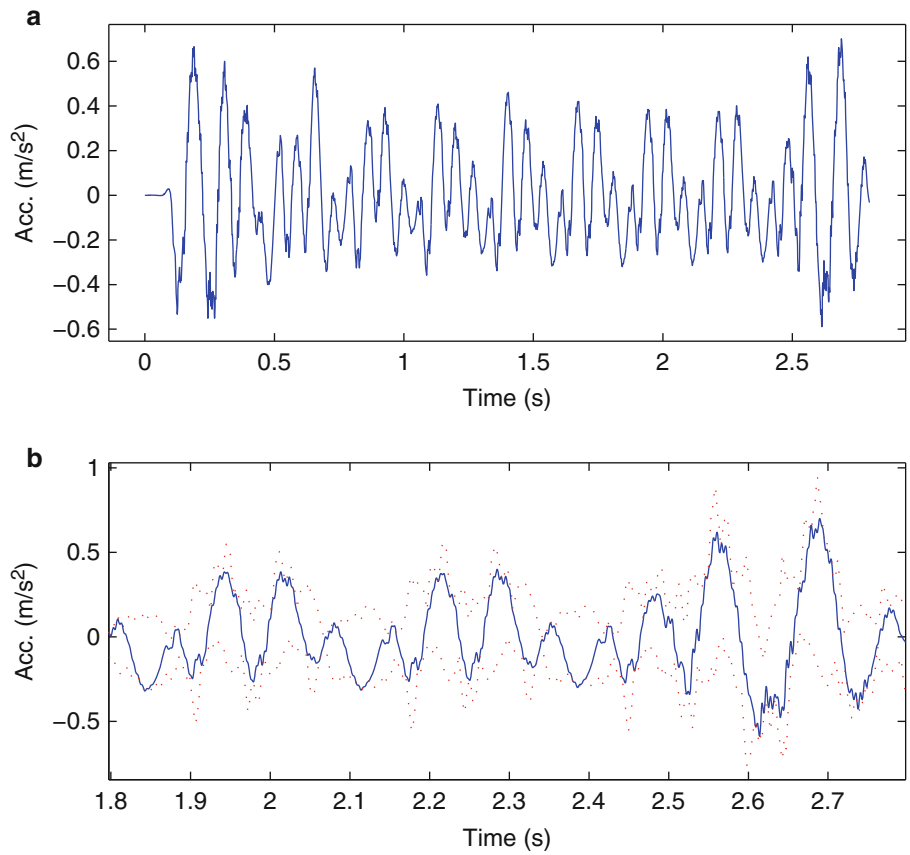
Fig. 12.6 Comparison of
maximum load effect at mid-span
(*dashed*) and full length of beam
(*solid*); (**a**) acceleration;
(**b**) bending moment DAF;
(**c**) vertical displacements DAF
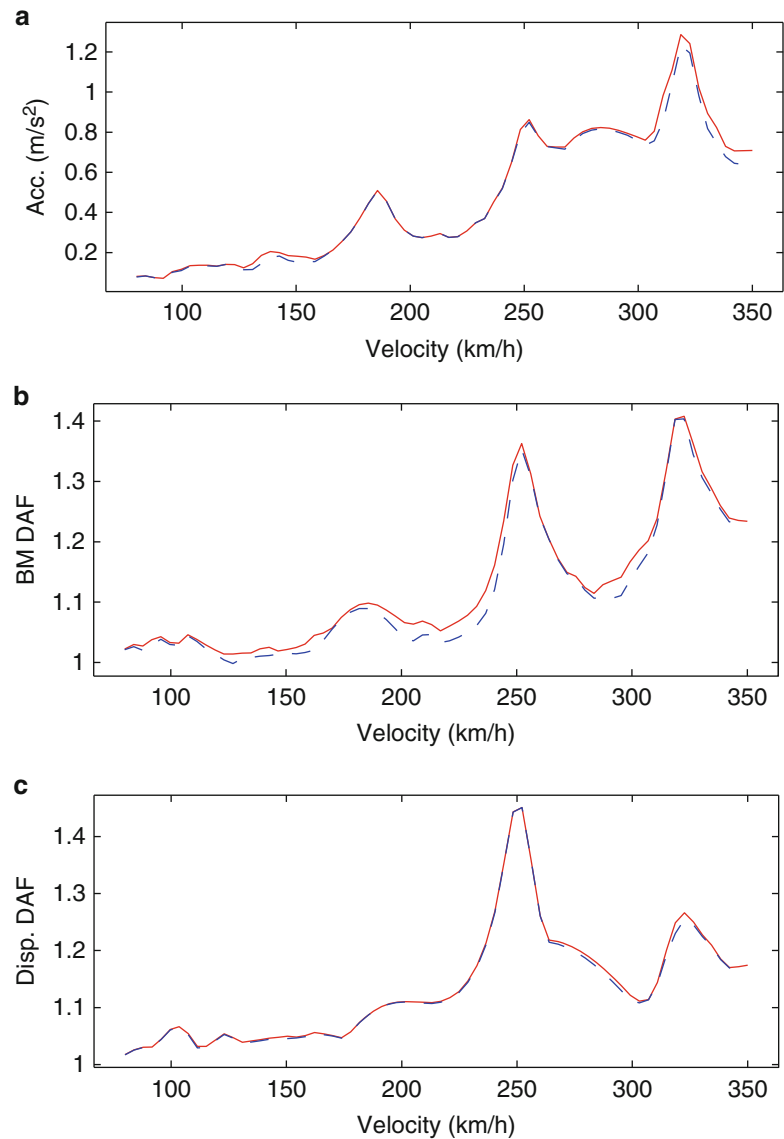
12.3.3 Influence of Speed

Of particular interest is to see what are the differences between mid-span and full length maxima at resonance. Thus the numerical model of the ICE 2 train traversing the Norra Kungsvägen Bridge was studied for a variety of speeds ranging from 80 to 350 km/h. The results (Fig. 12.6) clearly show two main resonant speeds, namely at 251 and 320 km/h, which will be termed first and second resonant speeds respectively.

Figure 12.6 shows that the LE for mid-span compared to the true maximum considering the full length of the beam. The maximum acceleration (Fig. 12.6a) is only slightly different to the mid-span maximum near the second resonant speed. At resonance the maximum acceleration is 1.29 m/s^2 while at mid-span is 1.23 m/s^2, a difference of only 4.88 %. On the other hand, bending moment BM (Fig. 12.6b) shows distinct differences for a wider range of speeds, but these differences are small and almost zero at the resonant speeds. The difference between FDAF and DAF at the second resonant speed is only 0.28 %. The vertical displacements (Fig. 12.6c) show virtually no difference.

The Location of Maximum (LOM) is different depending on what Load Effect (LE) is under investigation and changes significantly with the speed of the vehicle. The biggest variability in the location of the maximum load effect is obtained for the accelerations (Fig. 12.7a) and the critical section can be located anywhere on the bridge. On the other hand, for BM (Fig. 12.7b) and displacements (Fig. 12.7b) the critical section varies only within a small range near the mid-span location. Note that because calculations have been performed at discrete speed increments the results in Fig. 12.7 are presented using one dot for each calculation.

Fig. 12.7 Location of maximum
(LOM) for various load effects
(*big dots*) and mid-span reference
(*dotted line*); (**a**) acceleration;
(**b**) bending moment DAF;
(**c**) vertical displacements DAF
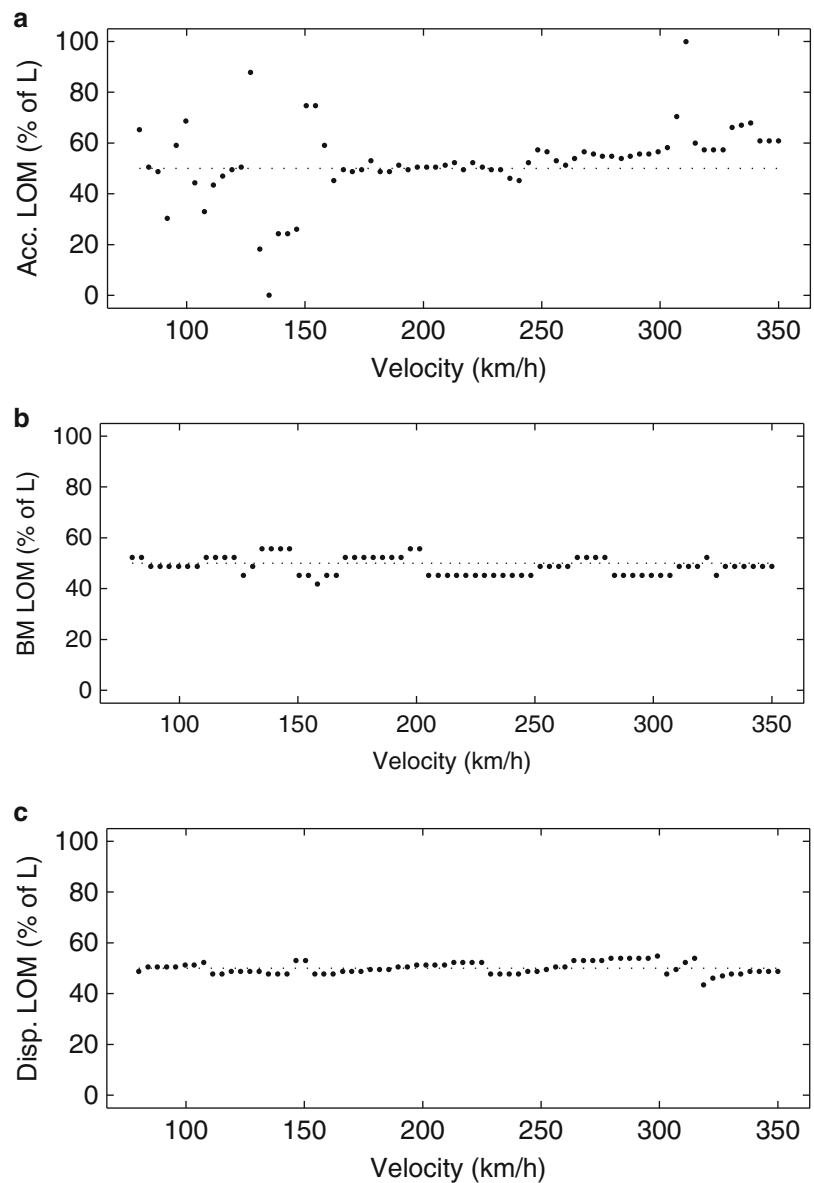
12.4 Bridge Stock Analysis

The results of the Norra Kungsvägen Bridge show that the mid-span assumption introduces only small mistakes, especially at the resonant speeds. In order to be able to give a general conclusion of the phenomenon the analysis should be performed for multiple bridges. For this purpose, a group of 28 portal frame bridges are considered in this section. They are part of the so called Bothnia Line, which is a recently finished 190 km railway line that connects the cities of Umeå and Sundsvall in Sweden. The current maximum operational speed of this line is 200 km/h, but local authorities are considering upgrading the line to higher speeds.

Each bridge has been modelled using the simplified beam model presented in Sect. 12.2. The equivalent bridge properties have been obtained and validated in [7] and used in this study. The span lengths of these bridges range from 5 to 19 m. The same analyses as in Sect. 12.3 were performed for each of the 28 bridges, i.e., the LEs have been calculated for an ICE 2 train traversing the bridge with speeds ranging from 80 to 350 km/h. However, now only the results at the resonant speed will be presented since these maxima determine the design values.

Figure 12.8 shows the relative difference between true maximum to mid-span maximum at resonance for various LE, indicating that there is a big scatter in results. Nevertheless, a quadratic curve was interpolated to the data in order to be able to appreciate the existence of any underlying trend. The equation of the interpolated curve is provided also in each figure for

Fig. 12.8 Relative difference
between true maximum to
mid-span maximum at resonance
for various LE: (**a**) acceleration;
(**b**) bending moment; (**c**) vertical
displacements
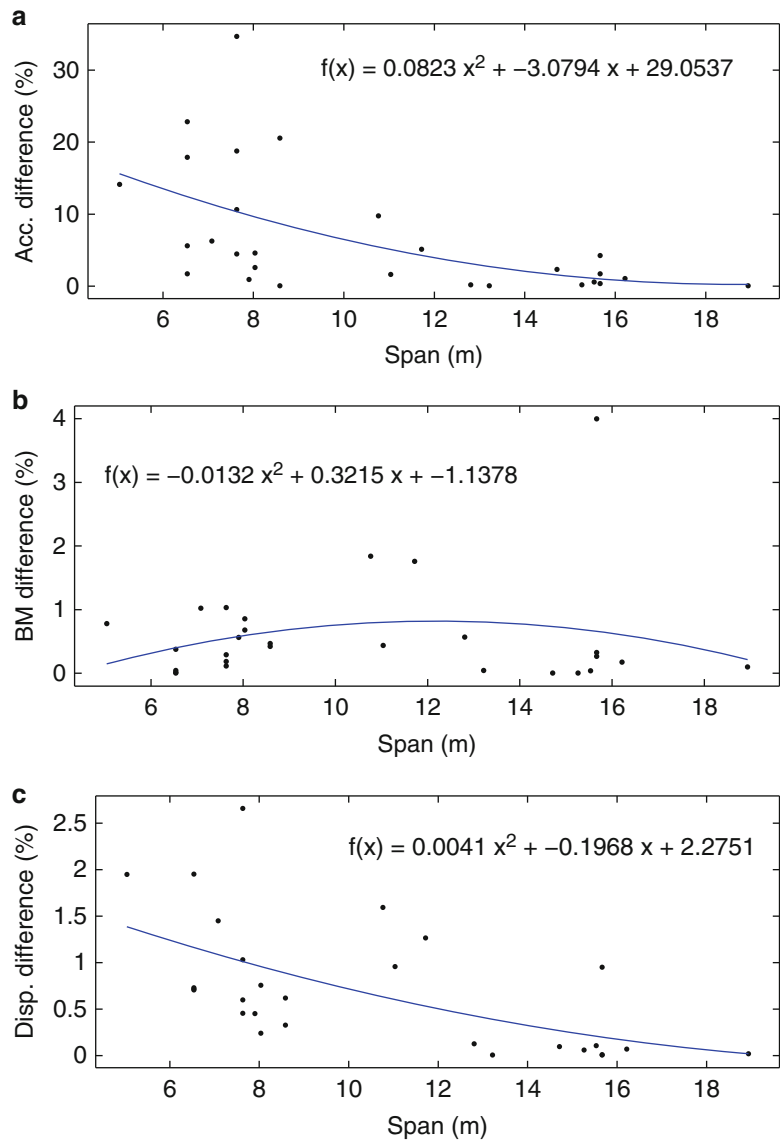
completeness. The results for the acceleration (Fig. 12.8a) clearly indicate that the differences are greater for shorter spans
and that differences as high as 30 % can be reached at the resonant speed. In that case, the true maximum acceleration is 30 %
larger than the one at mid-span section. In comparison, the differences for Bending Moment BM (Fig. 12.8b) and vertical
displacements (Fig. 12.8b) are rather small, in general below 2 %.

It is interesting to study the location where these true maxima really occur on the bridge. As in Sect. 12.3, it can be seen
in Fig. 12.9b, c that the LOM for BM and vertical displacements are generally near the mid-span section. However, for the
acceleration (Fig. 12.9a) the critical sections might be far away from the expected mid-span location.

12.5   Conclusions

This paper has investigated the consequences of assuming that the maximum load effect in portal frame structures is at mid-
span, focusing on accelerations, bending moments and vertical displacements. The numerical study was performed using a
model that accounted for the vehicle, ballasted track and the bridge and was deemed appropriate to draw general conclusions
for the dynamic effects of portal frame bridges. First, one particular bridge has been studied as an example, and then a group
of 28 bridges were analyzed. The results indicate that in general the mid-span assumption introduces only small differences.

Fig. 12.9 Location of maximum (LOM) at resonance (*big dots*) and mid-span reference (*dotted line*), for various LE; (**a**) acceleration; (**b**) bending moment; (**c**) vertical displacements
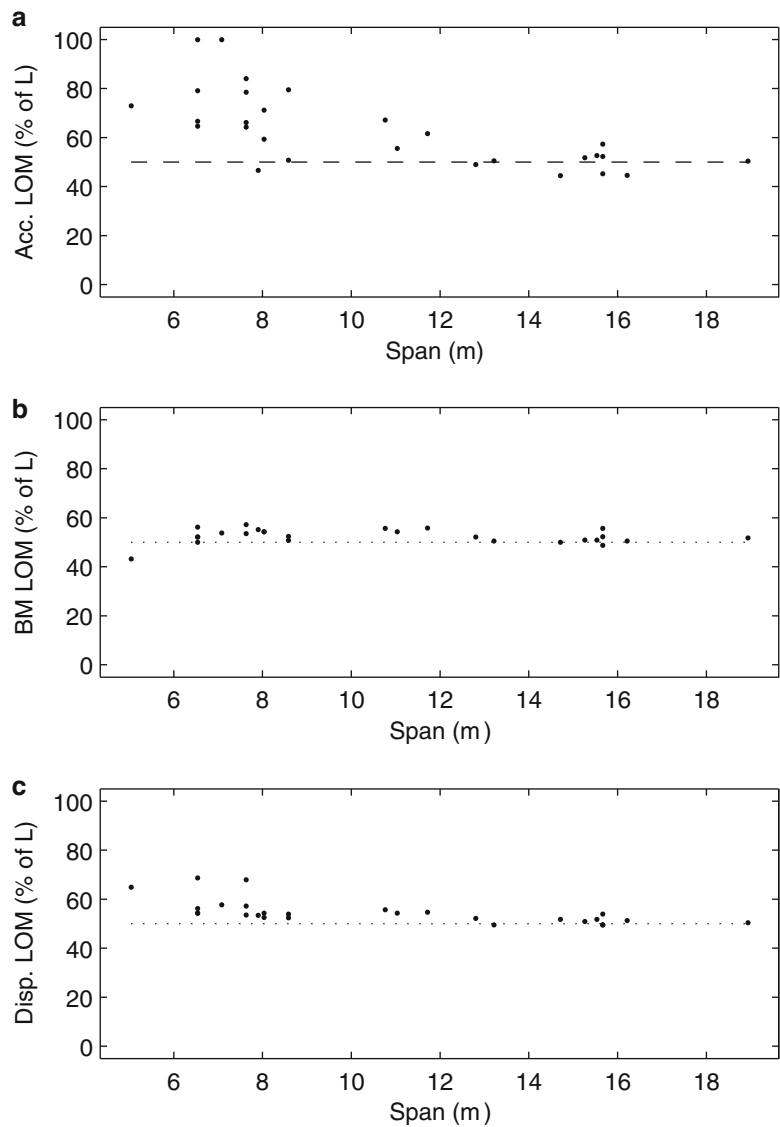
In particular, for bending moments and displacements, the differences are almost negligible. Greater differences are found for the accelerations, even up to 30 %, but this discrepancy is likely to be covered by the inherent safety coefficients in the design process. The results show that no additional differences are encountered during resonant behavior. The results are reassuring, indicating that the mid-span assumption is appropriate, even if not exactly correct. However, the results are not conclusive. Additional investigations are necessary for different vehicle configuration, bridge properties, and modelling complexities. Furthermore, this phenomenon needs to be investigated experimentally by measuring the load effects of a bridge in multiple locations along its length.

References

1. Cantero D, González A, OBrien E (2009) Maximum dynamic stress on bridges traversed by moving loads. ICE Bridg Eng 162(BE2):75–85
2. OBrien E, Cantero C, Enright B, González A (2010) Characteristic dynamic increment for extreme traffic loading events on short and medium span highway bridges. Eng Struct 32:3827–3835
3. European Committee for Standardization (2003) Eurocode 1: actions on structures – part 2: traffic loads on bridges. EN 1991-2

4. Johansson C, Arvidsson T, Martino D, Solat M, Andersson A, Pacoste C, Karoumi R (2011) Höghastighetsprojekt – Bro: Inventering av jämvägsbroar för ökad hastighet på befintliga banor (In Swedish). TRITA-BKN, Rapport 141
5. Cantero D, Ardvidsson T, Karoumi R, OBrien E Train-track-bridge dynamic simulation toolbox – validation and results (Submitted for publication)
6. Johansson C, Ní Nualláin NA, Pacoste C, Andersson A (2014) A methodology for the preliminary assessment of existing railway bridges for high-speed traffic. Eng Struct 58:25–35
7. Johansson C, Andersson A, Pacoste C, Karoumi R (2013) Järnvägsbroar på Botniabanan. Dynamiska kontroller for framtida höghastighetståg – Steg 1 (In Swedish). TRITA-BKN, Rapport 145
8. Doménech A, Museros P, Martínez-Rodrigo MD (2014) Influence of the vehicle-structure interaction in the design of high-speed railway bridges. In: Pombo J (ed) Proceedings of the second international conference on railway technology: research, development and maintenance, paper 76
9. Zhai WM, Wang KY, Lin JH (2014) Modelling and experiment of railway ballast vibrations. J Sound Vib 270:673–683

Chapter 13
Monitoring Wind Velocities and Dynamic Response of the Hardanger Bridge

Ole Øiseth, Anders Rönnquist, Knut Andreas Kvåle, and Ragnar Sigbjörnsson

Abstract The Hardanger Bridge is the longest suspension Bridge in Norway and among the top 10 longest suspension bridges in the world. A comprehensive monitoring system was installed after it was completed in August 2013. The monitoring system is designed to provide data that can be used to verify the numerical methods used to predict wind induced dynamic response of slender bridges located in complex terrain. The monitoring system is outlined in this paper together with preliminary analysis of the accuracy of the model used to describe the self-excited forces acting on the bridge deck. Extensive wind tunnel testing was performed in the design of the Hardanger Bridge to achieve an excellent aerodynamic behaviour of the cross-section of the bridge deck. The experimental results of the aerodynamic derivatives that describe the self-excited forces have been combined with a finite element model of the bridge to predict the in-wind natural frequencies and damping ratios of the combined structure and flow system. The numerical predictions have been compared to results obtained from measured data using data-driven and covariance-driven stochastic subspace identification. It is concluded that the model for the self-excited forces provides in-wind frequencies and damping ratios that corresponds well to the observations from measured data.

Keywords Suspension bridge • Wind loading • Modal analysis • Finite element method • Stochastic subspace identification

13.1 Introduction

The Norwegian Public Roads Administrations (NPRA) is currently investigating the possibility to establish a ferry free costal route E39 between Trondheim and Kristiansand. The project implies that several strait crossings need to be established. Since some of the straits are up to 5 km wide and 1.5 km deep, the project will call for significant extension of present bridge technology. Cable-supported bridges will be the most effective solution for many of the strait crossings implying that prediction of wind induced vibrations is a crucial issue in the design. The west coast of Norway is well known for its fjords and mountains. The terrain makes prediction of wind induced dynamic response challenging since the tall mountains will have a significant influence on the wind field and thus the wind induced dynamic response of the bridges.

The Hardanger Bridge, displayed in Fig. 13.1, is the longest suspension bridge in Norway and among the top 10 longest suspension bridges in the world. It has a main span of 1,310 m while the towers are 186 m high. A comprehensive monitoring system was installed on the bridge after it was completed in August 2013. The objective of the monitoring project is to supply data that can be used to verify the models used to predict wind induced dynamic response of slender bridges located in complex terrain. The self-excited forces generated by the motion of the structure are of particular interest in the design of suspension bridges. This is mainly because the self-excited forces might make the combined structure unstable like the infamous Tacoma Narrows Bridge that collapsed in 1940 and since it is the self-excited forces that generate aerodynamic damping which is crucial to minimize the wind induced dynamic response. The self-excited forces are most commonly modelled by experimentally determined aerodynamic derivatives introduced to bridge engineering by Scanlan and Tomko [1]. Extensive wind tunnel experiments was carried out in the design of the Hardanger Bridge to ensure a superior aerodynamic

O. Øiseth (✉) • A. Rönnquist • K.A. Kvåle • R. Sigbjörnsson
Department of Structural Engineering, Norwegian University of Science and Technology,
Richard Birkelands vei 1A, Trondheim 7491, Norway
e-mail: ole.oiseth@ntnu.no

Fig. 13.1 The Hardanger Bridge

performance [2]. A finite element model is combined with the aerodynamic derivatives of the bridge deck to predict the in-wind natural frequencies and damping ratios of the bridge in this paper. Similar analysis has been presented by the authors previously focusing on the flutter stability limit of the combined structure and flow system [3–5].

Even though the finite element method and increased computational resources is readily available, verification of the analysis procedures is still a crucial issue. This is particularly important when modelling structures subjected to environmental loading where a coupled analysis is necessary due to fluid structure interaction. Operational modal analysis has become a versatile tool for inverse modelling of structures when experimental modal analysis is hard or impossible. A comprehensive overview of relevant methods and how they can be implemented is given by Rainieri and Fabbrocino [6]. A comprehensive study of the performance of different operational modal analysis methods using the Humber Bridge as case study have been presented by Brownjohn et al. [7]. It is concluded that the stochastic subspace identification outperforms the other methods, in particular for the estimated damping ratios. The in-wind natural frequencies and damping ratios of the Hardanger Bridge have therefore been estimated using data-driven and covariance-driven stochastic subspace identification in this paper. The estimates are compared with results predicted using experimental data of aerodynamic derivatives and the finite element method.

13.2 Prediction of Frequencies and Damping Ratios

Due to the fluid structure interaction the natural frequencies and damping ratios of a suspension bridge is in general dependent on the aerodynamic properties of the structure and the mean wind direction and velocity. The wind loading can be divided into four parts. (i) Static loading originating from the mean wind velocity, (ii) dynamic wind loading caused by vortex shedding, (iii) buffeting loading caused by the turbulence in the wind field and (iv) self-excited loading generated by the motion of the structure. Since the self-excited forces are dependent on the motion of the structure these needs to be taken into account when calculating natural frequencies and damping ratios when the mean wind velocity is different from zero.

13.2.1 Self-Excited Forces

The self-excited forces acting on a bridge deck section are commonly represented by the aerodynamic derivatives introduced in bridge engineering by Scanlan and Tomoko [1]. For a two-dimensional bridge deck section (see Fig. 13.2), this can be expressed in matrix notation as follows:

Fig. 13.2 Aerodynamic forces
acting on the cross section of a
bridge deck
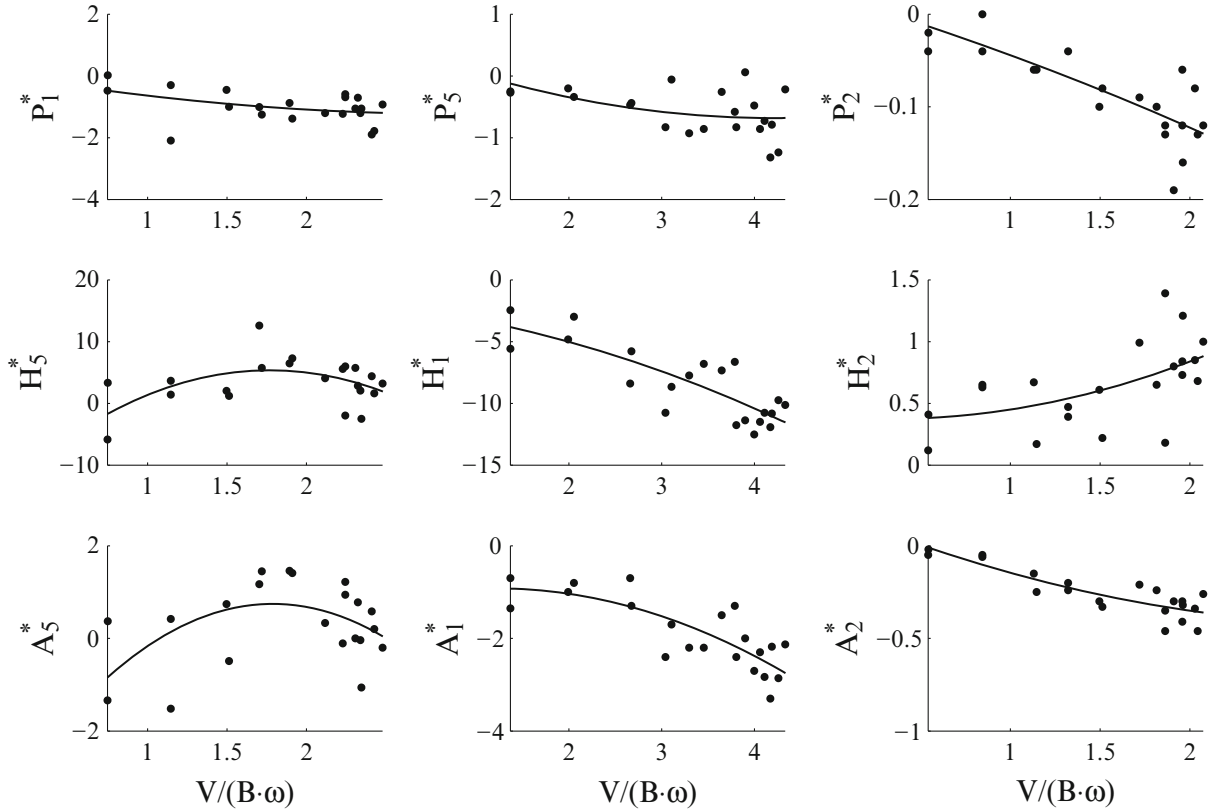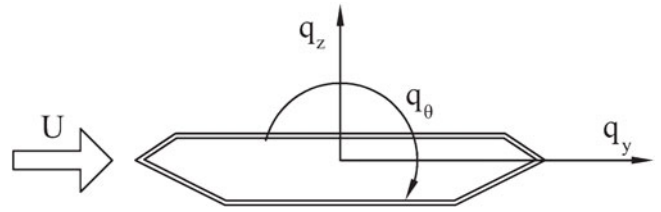
Fig. 13.3 Aerodynamic derivatives related to the velocity of the box girder

$$\mathbf{q} = \mathbf{C}_{ae}(K)\dot{\mathbf{u}} + \mathbf{K}_{ae}(K)\mathbf{ux}$$

$$\mathbf{C}_{ae}(K) = \frac{1}{2}\rho VKB \begin{bmatrix} 0 & 0 & 0 & 0 \\ 0 & P_1^* & P_5^* & BP_2^* \\ 0 & H_5^* & H_1^* & BH_2^* \\ 0 & BA_5^* & BA_1^* & B^2A_2^* \end{bmatrix}, \mathbf{K}_{ae}(K) = \frac{1}{2}\rho V^2 K^2 \begin{bmatrix} 0 & 0 & 0 & 0 \\ 0 & P_4^* & P_6^* & BP_3^* \\ 0 & H_6^* & H_4^* & BH_3^* \\ 0 & BA_6^* & BA_4^* & B^2A_3^* \end{bmatrix}$$

$$\mathbf{q} = \begin{bmatrix} q_x \ q_y \ q_z \ q_\theta \end{bmatrix}^T \qquad \mathbf{u} = \begin{bmatrix} u_x \ u_y \ u_z \ u_\theta \end{bmatrix}^T \tag{13.1}$$

Here, V is the mean wind velocity; ρ is the air density; B is the width of the cross section; $K = B\omega/V$ is the reduced circular frequency of motion; the vector $\mathbf{u}$ contains the displacements along the girder, where u_x symbolizes the longitudinal displacement, u_y the transverse horizontal displacement, u_z the transverse vertical displacement and u_θ The rotation of the girder. The displacements are positive in the same direction as the forces displayed in Fig. 13.2. P_n^*, H_n^*, A_n^* $n \in \{1, 2, \ldots 6\}$ are the dimensionless aerodynamic derivatives, which are characteristic cross-sectional properties given as functions of the reduced frequency of motion.

Extensive wind tunnel testing was carried out in the design of the Hardanger Bridge to ensure a superior performance in strong winds [2]. Experimental results of the aerodynamic derivatives of the bridge deck are shown in Figs. 13.3 and 13.4 together with a least squares fit to the data.
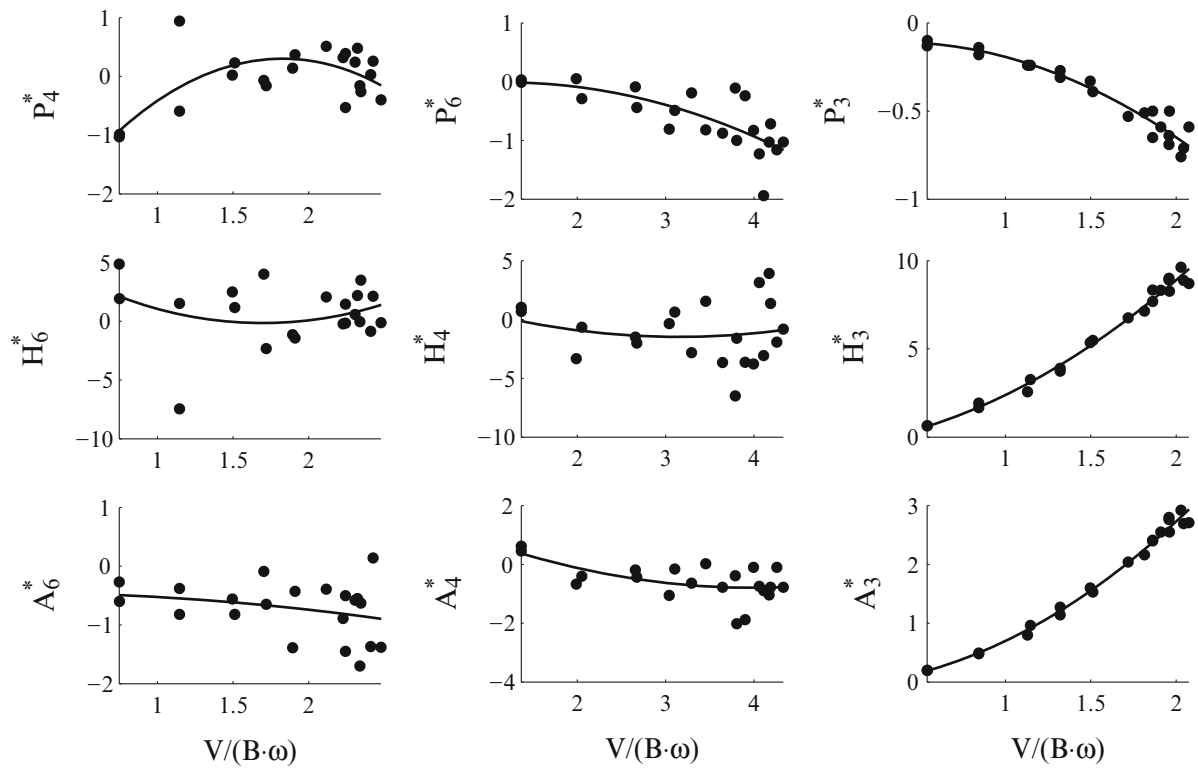
Fig. 13.4 Aerodynamic derivatives related to the displacements of the box girder

Fig. 13.5 First symmetric horizontal still-air vibration mode
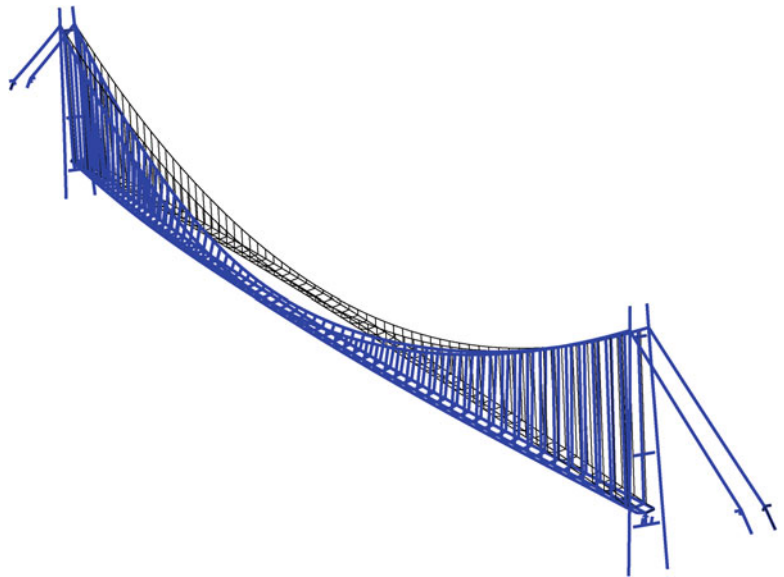
13.2.2 The Eigenvalue Problem

A detailed finite element model of the Hardanger Bridge is displayed in Figs. 13.5, 13.6, and 13.7. The entire bridge is modelled using a total of 1,358 beam elements. The FE model is used to obtain still air vibration modes and natural frequencies. The still-air vibration modes are then used as generalized coordinates to obtain the equation of motion of the combined structure and flow system. The natural frequencies and damping ratios of an aeroelastic second order system,

Fig. 13.6 First symmetric
vertical still-air vibration mode
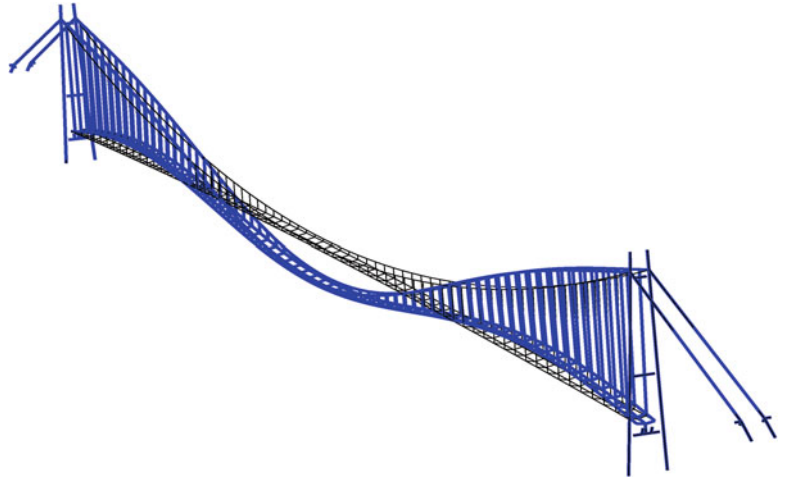
Fig. 13.7 First symmetric
torsional still-air vibration mode
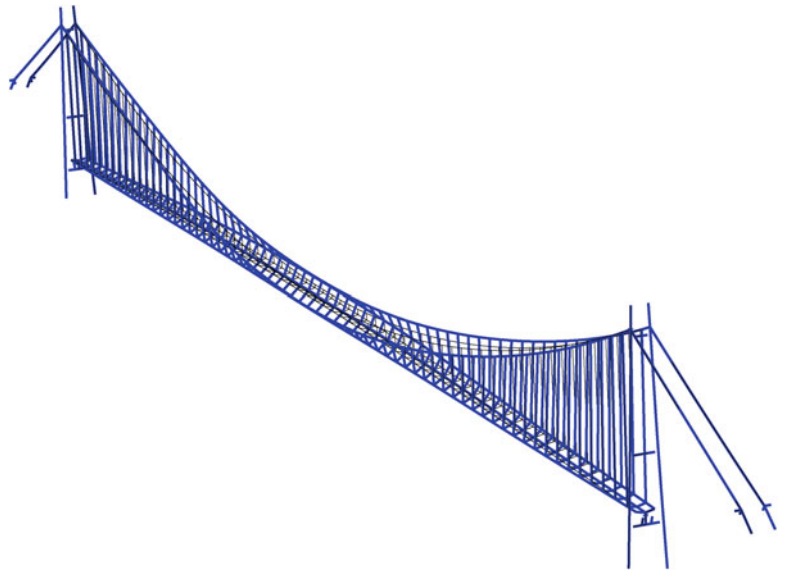
where N still-air vibration modes are used as generalised degrees-of-freedom can be predicted considering the following quadratic eigenvalue problem:

$$\left(S_n^2\tilde{\mathbf{M}}_0 + S_n\left(\tilde{\mathbf{C}}_0 - \tilde{\mathbf{C}}_{ae}\left(V, \omega\right)\right) + \left(\tilde{\mathbf{K}}_0 - \tilde{\mathbf{K}}_{ae}\left(V, \omega\right)\right)\right)\mathbf{Z}_n = 0 \qquad n = 1, 2 \ldots 2N. \tag{13.2}$$

Here, $\tilde{\mathbf{M}}_0$ represents the generalised structural mass matrix, $\tilde{\mathbf{C}}_0$ denotes the generalised damping matrix and $\tilde{\mathbf{K}}_0$ represents the generalised structural stiffness matrix, where the subscript 0 indicates that the matrices contain properties obtained in still air. The function $\tilde{\mathbf{C}}_{ae}\left(V, \omega\right)$ stands for aerodynamic forces proportional to the velocity of the system, commonly referred to as the aerodynamic damping matrix, while $\tilde{\mathbf{K}}_{ae}\left(V, \omega\right)$ symbolises aerodynamics forces proportional to the displacement of the system, sometimes referred to as the aerodynamic stiffness matrix. These two matrices are a function of the oscillation frequency, ω, and the wind velocity, V. Furthermore, they also depend on the aerodynamic derivatives as outlined in Eq. (13.1). The oscillation frequency, ω, and the wind velocity, V, are treated as continuous and independent variables in the following analysis.

The solution of Eq. (13.2) gives $2N$ eigenvalues, S_n, and corresponding eigenvectors $\mathbf{Z}_n$, where N is the number of degrees-of-freedom. Real roots imply that the system behaviour is non-periodic. When the root S_n is real and positive, the solution reveals exponential divergence; if it is real and negative, the solution exhibits exponential convergence. On the other hand, complex roots result in system behaviour of periodic or oscillatory nature. These roots appear in complex conjugated pairs of the form $S_n = \mu_n + i\omega_n$ and $S_{n+1} = S_n^* = \mu_n - i\omega_n$. The quantity ω_n is the damped natural frequency of

Fig. 13.8 Natural frequencies and damping ratios as function of mean wind velocity
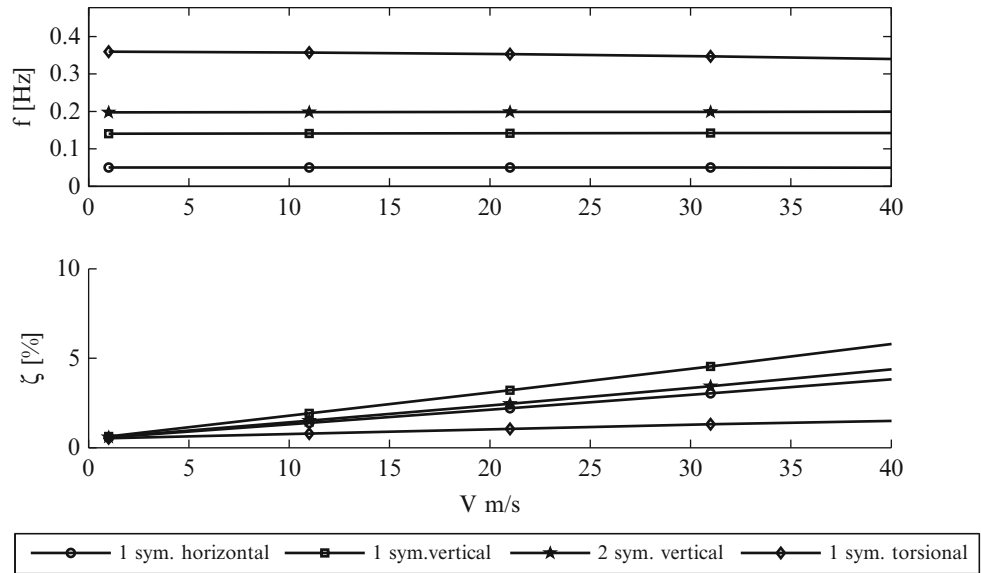
the aeroelastic system, while μ_n is a measure of the damping or diverging behaviour of free oscillations. The damping ratio and the natural frequency of the system can be obtained as

$$\omega_n = |S_n|, \qquad \xi_n = -\frac{\mu_n}{|S_n|} \tag{13.3}$$

The eigenvalue problem, Eq. (13.2), has to be solved by an iterative procedure since the flutter derivatives are functions of the frequency of motion as well as the wind velocity. Further details of the problem formulation and the solution procedure applied herein can be found in [5].

The natural frequencies and the critical damping ratio of the aeroelastic system when 5 still air vibration modes are used as generalized coordinates are displayed in Fig. 13.8. An initial damping ratio of 0.5 % has been assumed for all still-air vibration modes. The natural frequencies hardly change in the velocity interval considered while higher damping is achieved at higher wind velocities. It can also be noticed that the aerodynamic damping is highest for the vertical motion, a bit lower for the horizontal motion, while the increase in damping for the torsional motion seems to be small.

13.3 Field Testing

A front elevation of the Hardanger Bridge and the monitoring system is displayed in Fig. 13.9 and an overview of the monitoring system is presented in Fig. 13.10. There are eight anemometers distributed along the main span and one anemometer located at the top of the Vallavik tower. Two accelerometers were installed at the top of each tower while 16 accelerometers are distributed along the main girder. There are eight recorders distributed along the girder and one recorder at the top of each tower. The main recorder is located at the top of the Vallavik tower. This location was selected to provide best possible views for the wi-fi antennas. Digital sensors, a GPS antenna and a wifiantenna are connected to each recorder. The GPS antennas provide time stamps that are used to align data from all recorders while the wi-fi antennas provides an Ethernet connection between the recorders. During each recording, the data is transferred to the main recorder. The main recorder saves the data and transfers it to a server at NTNU by an internet connection. The RSYNC protocol is used to ensure a complete data transfer. The recorders are supplied with a 12 V battery to ensure that the monitoring system is working during a power failure. The monitoring system is recording data continuously, but user defined trigger criteria is used to decide which data that should be kept. In the Hardanger project we have primary used the 1 min mean wind velocity to trigger recordings. The trigger thresholds have been adjusted to ensure that data in all relevant velocity ranges are obtained.
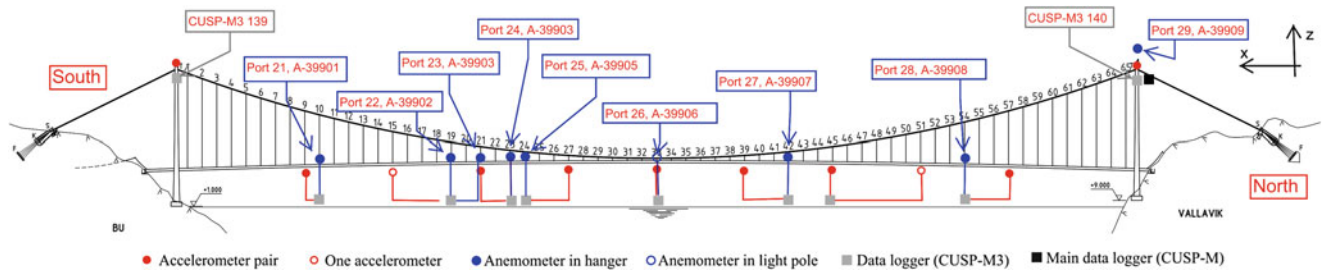
Fig. 13.9 Sensor outline

Fig. 13.10 Overview of the monitoring system installed at the Hardanger Bridge
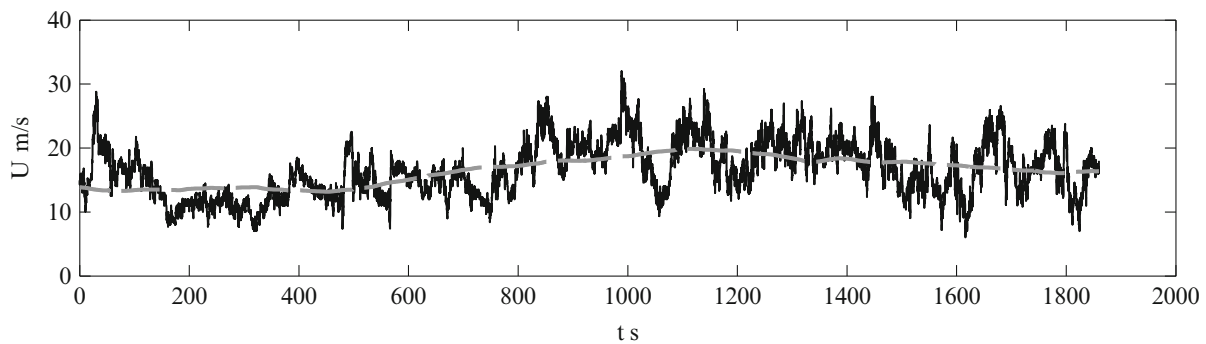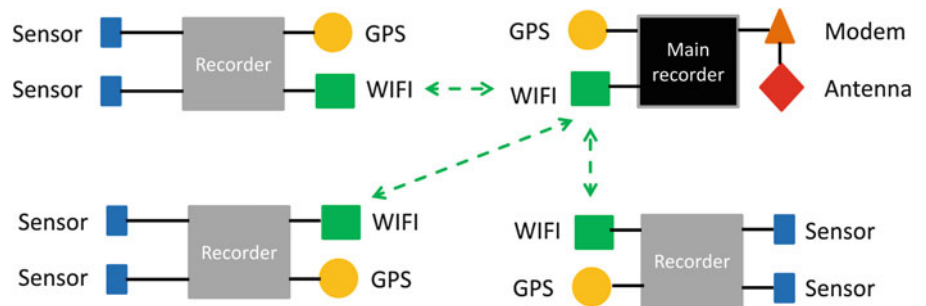
Fig. 13.11 Wind velocity at the mid-span of the bridge

13.4 Operational Modal Analysis

One recording of 30 min duration will be considered in this study. The wind velocity at the mid span of the bridge is displayed in Fig. 13.11. As can be seen the average wind velocity was about 17 m/s. The wind direction was perpendicular to the bridge. Acceleration data from all the accelerometers at a sampling rate of 200 Hz have been used in the analysis. The natural frequencies and damping ratios have been estimated using covariance-driven and data-driven stochastic subspace identification [6] applying the MACEC software developed at the University of Leuven [8]. The data was first de-trended, filtered using a low pass fourth order Butterworth filter with a cut off frequency of 10 Hz, and resampled to 10 Hz before the identification was performed. The number of block rows used for the data-driven (SSI-data) and covariance-driven (SSI-cov) identification was 50 and 100 respectively. It was necessary to use a higher number of block rows for the covariance-driven approach to get stable results for the first horizontal vibration mode. Stabilization plots for both cases are shown in Figs. 13.12 and 13.13. The resulting natural frequencies and damping ratios are displayed in Table 13.1 together with the numerical predictions from Sect. 13.2. As expected the SSI-data and SSI-cov identification provides almost the same natural frequencies, while there are some discrepancies in the identified damping ratios. The identified frequencies corresponds very well to the results predicted combining the finite element model and the experimental results of the aerodynamic derivatives. It also seems like the model for the self-excited forces applied in the eigenvalue solution in Sect. 13.2 is able to capture the aerodynamic damping with a fair accuracy, since the damping ratios predicted using all three approaches are similar and that the vertical motion provides the highest, while the torsional motion provides the lowest damping.
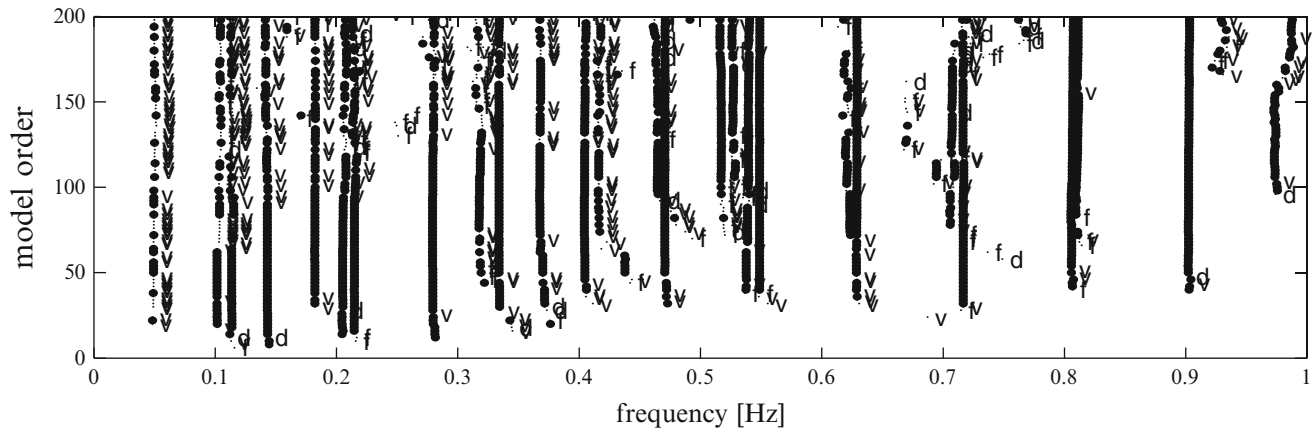
Fig. 13.12 Stabilization plot for data-driven stochastic subspace identification
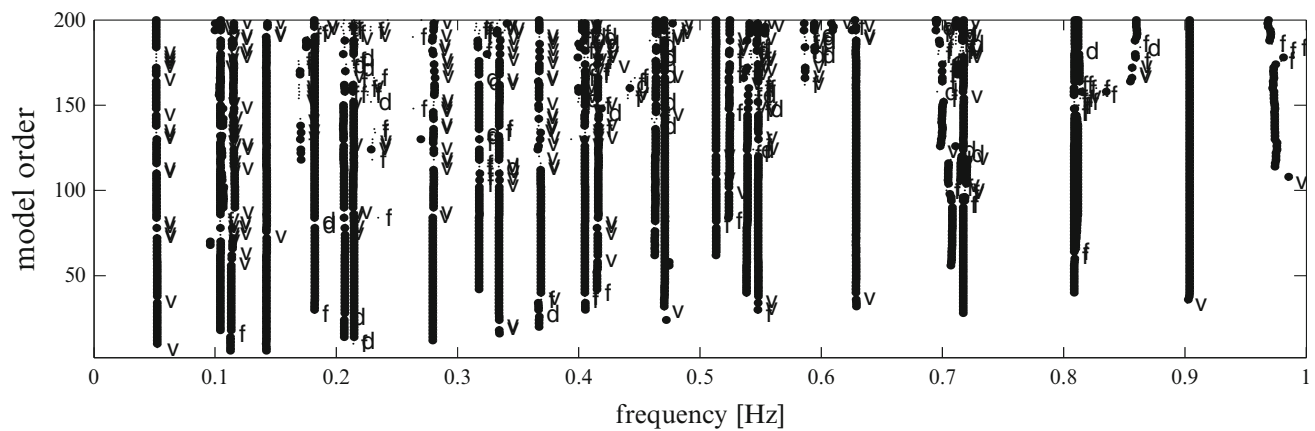
Fig. 13.13 Stabilization plot for covariance-driven stochastic subspace identification

Table 13.1 Identified frequencies and damping ratios at a mean wind velocity of 16 m/s

Method	SSI-data		SSI-cov		Prediction	
Mode	f [Hz]	ξ [%]	f [Hz]	ξ [%]	f [Hz]	ξ [%]
1. Symmetric horizontal	0.05	0.69	0.05	1.07	0.05	1.6
1. Symmetric vertical	0.14	2.56	0.14	2.27	0.14	3.0
2. Symmetric vertical	0.21	2.4	0.21	2.75	0.20	2.3
1. Symmetric torsional	0.37	0.79	0.37	0.9	0.35	1.0

13.5   Concluding Remarks

A wireless monitoring system consisting of 20 tri-axial accelerometers, 9 tri-axial anemometers, and 11 recorders have been installed at the Hardanger Bridge to verify the models used to predict the wind induced dynamic response of slender bridges. Operational modal analysis using data-driven and covariance-driven stochastic subspace identification have been performed for a single recording of 30 min in this paper. Both methods provided almost equal natural frequencies and similar estimates for the critical damping ratio. A finite element model of the Hardanger Bridge has also been used to obtain still-air vibration modes and natural frequencies, which are used as generalized coordinates to obtain the system of equations for the coupled structure and flow system. The self-excited forces have been modelled using measured aerodynamic derivatives. The natural frequencies and damping ratios of the aeroelastic system have been calculated solving the quadratic eigenvalue problem. The resulting damping ratios and frequencies corresponds well to results obtained by operational modal analysis. This indicates that the model for the self-excited forces seems to be adequate. More data and further research is however necessary in order make a final conclusion.

References

1. Scanlan RH, Tomko JJ (1971) Airfoil and bridge deck flutter derivatives. J Eng Mech Div 97:1717–1737
2. Hansen SO et al (2006) The Hardanger Bridge: static and dynamic wind tunnel tests with a section model. Svend Ole Hansen ApS, Copenhagen
3. Øiseth O, Rönnquist A, Sigbjörnsson R (2010) Simplified prediction of wind-induced response and stability limit of slender long-span suspension bridges, based on modified quasi-steady theory: a case study. J Wind Eng Ind Aerodyn 98(12):730–741
4. Øiseth O, Rönnquist A, Sigbjörnsson R (2011) Time domain modeling of self-excited aerodynamic forces for cable-supported bridges: a comparative study. Comput Struct 89(13–14):1306–1322
5. Øiseth O, Sigbjörnsson R (2011) An alternative analytical approach to prediction of flutter stability limits of cable supported bridges. J Sound Vib 330(12):2784–2800
6. Rainieri C, Fabbrocino G (2014) Operational modal analysis of civil engineering structures: an introduction and guide for applications. Springer, New York, XX, 322s. 100 illus., 67 illus. in color. online resource
7. Brownjohn JMW et al (2010) Ambient vibration re-testing and operational modal analysis of the Humber Bridge. Eng Struct 32(8):2003–2018
8. Peeters B, De Roeck G (1999) Reference-based stochastic subspace identification for output-only modal analysis. Mech Syst Signal Process 13(6):855–878

Chapter 14
Modal Analysis of a Floating Bridge Without Side-Mooring

Knut Andreas Kvåle, Ole Øiseth, Anders Rønnquist, and Ragnar Sigbjörnsson

Abstract The Norwegian Public Roads Administration is currently planning a ferry-free Coastal Highway Route E39. Floating bridges represent feasible options in this project with already two long span floating bridges in function, i.e. the Bergsøysund and Nordhordaland Bridges. In connection with this project, one of the main objectives is to quantify the accuracy of the numerical methods used to predict dynamic behaviour of floating bridges. An extensive monitoring system is installed to measure structural response as well as environmental actions from wind and waves on an existing floating bridge: the Bergsøysund Bridge. These measurements are used to estimate the modal system properties of the structure. The system identification is performed using a parametric time-domain Stochastic Subspace Identification method as well as the Frequency Domain Decomposition method. Challenges of system identification for highly damped structural systems, such as a floating bridge, are especially emphasized. The results are also compared with numerical predictions from a two part combined linear frequency-domain model set-up. The first part consists of a hydrodynamic model, including wave excitation as well as fluid-structure interaction, and relies on linearized potential theory. The results from this are thereafter introduced into a finite element model, for a complete structural dynamic analysis.

Keywords Floating bridge • Highly damped systems • Modal analysis • Finite element method • Frequency domain decomposition • Stochastic subspace identification

14.1 Background

The Norwegian Public Roads Administration (NPRA) is currently building the new Coastal Highway, E39, along the Norwegian West-coast. According to NPRA, about 50 % of the traditional Norwegian export is generated by industry in the areas along this coastal route. Due to the deep and relatively wide fjord crossings along the route, floating bridges are feasible alternatives for many of the crossings. Some of the straits are up to 5 km wide and 1.5 km deep and will call for significant extension of present day bridge technology. The installations have to resist extreme environmental loads and accidental actions with acceptable safety levels.

Even though the history of floating bridges may be traced back as far as 2000 BC [1], it is only during the last three decades or so that floating bridges are being developed to the degree of sophistication so they can be applied as a critical part of modern infrastructure. In spite of this fact, compared with land-based bridges, including cable-stayed bridges, limited information is currently available on floating bridges. This concerns especially construction records, environmental conditions, durability, operations and performance. This is obvious from the fact that currently there are only about 20 long floating bridges in the world.

To be able to further develop present day floating bridge technology it is crucial to have detailed knowledge about the performance of existing floating bridges. As a means to achieve this, an extensive measurement program is planned for the Bergsøysund Bridge. The Bergsøysund Bridge is one of two end-supported floating bridges in the world, and is therefore a very interesting case study. This paper concerns operational modal analysis based on accelerometeric recordings of the Bergsøysund Bridge. The next step in this project will be to include wave height sensors and anemometers to supplement the setup with environmental data, but that is not considered in this paper.

K.A. Kvåle (✉) • O. Øiseth • A. Rønnquist • R. Sigbjörnsson
Norwegian University of Science and Technology, Richard Birkelands vei 1A, 7491 Trondheim, Norway
e-mail: knut.a.kvale@ntnu.no

Fig. 14.1 *Left*: the Bergsøysund Bridge. *Right*: one of the two steel rods taking all axial action at the abutments

Fig. 14.2 Overview of the Bergsøysund Bridge, showing the pontoon numbering used as well as the accelerometer positions
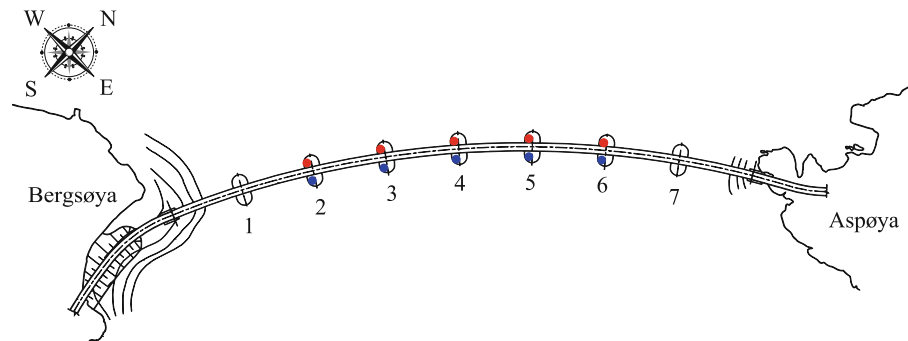
14.1.1 The Bergsøysund Bridge

The Bergsøysund Bridge is a 931 m long curved floating bridge, crossing the strait between Aspøya and Bergsøya, located on the north-west coast of Norway. It consists of a steel truss supported by seven evenly distributed light-weight concrete pontoons, as seen in Figs. 14.1 and 14.2. The bridge is resting on rubber bearings in the vertical and horizontal direction at the ends, while a steel rod supports it in the axial direction. The steel rod is shown to the right in Fig. 14.1. No mooring is present, making the bridge a very interesting case study; the Bergsøysund Bridge is the second longest end-supported floating bridge in the World.

14.1.2 Dynamic Testing

Traditionally, dynamic testing relies on the estimation of terms in the Frequency Response Function (FRF) matrix, which requires control of both excitation forces and selected response quantities. For operating structures, such as bridges exposed to both traffic loads and environmental action, this is not always practically viable. Therefore, modal analysis based on ambient vibrations, often referred to as operational modal analysis (OMA) or output-only modal analysis, provide the most cost-efficient and convenient basis for dynamic testing. The identified parameters presented in this paper are results of output-only modal analysis.

McLamore et al. [2] presented one of the first operational modal analysis studies, which concerns the dynamic properties of two suspension bridges. The techniques used in [2] have been established as standard procedures for the simplest operational modal analysis: peak-picking (PP) for natural frequency estimates; half-power bandwidth method (HPBM) for damping estimates; and relative spectral density amplitudes for mode shapes. Using measurements of ambient vibrations of the Golden Gate Bridge in San Fransisco, Abdel-Ghaffar and Scanlan [3] carried out similar analyses to successfully

establish estimates of the structure's modal parameters. This serves as a good example of the effectiveness of the simplest non-parametric methods, which often work well with structures that are lightly damped and where the natural frequencies of the different modes are sufficiently separated. Floating bridges are prone to much higher damping levels than suspension bridges, due to the damping contribution from the fluid-structure interaction, calling for more sophisticated methods.

An ever-growing toolbox of output-only system identification and modal analysis methods exists, and the acronyms FDD, SSI, ARMA and NExT have become everyday expressions for the modal analysis community. One method that sophisticates the well-established, yet crude, PP-method is the Frequency Domain Decomposition (FDD) technique, introduced in its current form by Brincker et al. [4]. This can help tackle the problem with closely spaced modes. It decomposes the spectral density function matrix into several single degree of freedom (SDOF) systems corresponding to the individual modes, by means of Singular Value Decomposition (SVD) (see e.g. [5]). Among the most renowned system identification methods are the time-domain parametric Stochastic Subspace Identification (SSI) methods. These are based on a state-space formulation of the problem, and are able of both deterministic (known forces) and stochastic (unknown forces) system identification. The different SSI methods were unified to the currently most common methodology by van Overschee and De Moor [6, 7], under the acronym N4SID (Numerical algorithms for Subspace State Space System Identification).

There exist a relatively large amount of papers comparing system identification techniques, for different practical uses. One such comparison is made by Brownjohn et al. [8] for the Humber Bridge, where it is concluded that SSI outperforms the alternative methods under consideration, especially regarding damping estimates. Andersen et al. [9] also compared the identification methods PP, LSCE, SSI, ERA and ARMA in a study of ambient response test data of the Swiss Z34 highway bridge. This survey concluded that all methods give reasonable estimates of natural frequencies and mode shapes, and that the three latter yield comparative values of critical damping ratios.

The system identification methods available are usually tested for structural dynamics on lightly damped structures. Therefore, when attempting to identify the modal parameters of a floating bridge, one important question emerges: how do these methods handle a floating structure? For the current paper, the covariance-driven variant of SSI (Cov-SSI) and FDD are chosen.

14.2   Numerical Model and Eigenvalue Solution

14.2.1   Linear Frequency Domain Model

Within the framework of a Finite Element Method (FEM) formulation, the equations of motion for a floating structure can be written (see e.g. Naess and Moan [10]):

$$[M_S]\{\ddot{u}(t)\} + [C_S]\{\dot{u}(t)\} + [K_S]\{u(t)\} = \{p_h(t)\},\tag{14.1}$$

where t is the time, $\{p_h(t)\}$ is the total hydrodynamic action, including the fluid-structure interaction as well as the wave action; $[M_S]$, $[C_S]$ and $[K_S]$ are the structural mass, damping and stiffness, respectively; and $\{u(t)\}$ is the displacement vector. The total hydrodynamic action can be written as the superposition of the wave excitation force and the fluid-structure interaction, with fluid-structure interaction contributions represented by frequency dependent mass, damping and stiffness contributions in the frequency domain:

$$\{P_h(\omega)\} = \{P(\omega)\} \underbrace{- [M_h(\omega)]\{\ddot{U}(\omega)\} - [C_h(\omega)]\{\dot{U}(\omega)\} - [K_h]\{U(\omega)\}}_{\text{fluid-structure interaction}}.\tag{14.2}$$

Here, ω is introduced as the angular frequency variable; $\{P(\omega)\}$ and $\{P_h(\omega)\}$ are the frequency domain representations of the wave excitation force and the total hydrodynamic action, respectively; and $\{U(\omega)\}$ is the frequency domain displacement vector. This leads to the following frequency domain representation of the equations of motion:

$$-\omega^2 [M(\omega)]\{U(\omega)\} + i\omega [C(\omega)]\{U(\omega)\} + [K]\{U(\omega)\} = P(\omega),\tag{14.3}$$

where $[M(\omega)]$, $[C(\omega)]$ and $[K]$ are the total mass, damping and stiffness matrices and i the imaginary unit number. Because the damping levels cannot be considered as low for the test subject, the damping has to be included in the eigenvalue solution, yielding complex eigenvalues and eigenvectors. The complex eigenvalue problem reads out:

$$\left(\lambda^2 [M(\omega)] + \lambda [C(\omega)] + [K]\right)\{u\} = \{0\},\tag{14.4}$$

where the eigenvalue λ is introduced. The complex eigenvalue problem is solved by introducing a state-space formulation. The eigenvalues for an under-critically damped frequency *in*dependent single degree of freedom (SDOF) system are:

$$\lambda_r = -\xi_r \omega_r \pm \sqrt{1 - \xi_r^2} \omega_r i. \tag{14.5}$$

Here, the damping and the undamped natural frequency corresponding to eigenvalue λ_r are introduced as ξ_r and ω_r, respectively. From the preceding equation, it is easy to show that $\omega_r = |\lambda_r|$ and $\xi_r = -\mathrm{Re}\,(\lambda_r)\,/\,|\lambda_r|$, where the absolute value operator $|\ |$ and real argument operator $\mathrm{Re}(\ )$ are used. The state-space variable $\{z\} = \lfloor\, \{u\}^T\ \{\dot{u}\}^T\, \rfloor^T$ is introduced:

$$\left\{ \begin{array}{c} \{\dot{u}\} \\ \{\ddot{u}\} \end{array} \right\} + \left[\begin{array}{cc} [0] & -[I] \\ [M]^{-1}[K] & [M]^{-1}[C] \end{array} \right] \left\{ \begin{array}{c} \{u\} \\ \{\dot{u}\} \end{array} \right\} = \{0\}. \tag{14.6}$$

On condensed form this is written $\{\dot{z}\} + [A]\{z\} = \{0\}$, yielding $\lambda \cdot \{z\} + [A]\{z\} = 0$. This has the following total solution:

$$\{z\} = \sum_{r=1}^{2N} \{q_r\}\ e^{\lambda_r t}, \tag{14.7}$$

where $\{q_r\}$ and λ_r are the r th eigenvector and eigenvalue corresponding to solution r of Eq. (14.6); and $2N$ the total number of modes. Note that the number of modes resulting from this is twice that of the original displacement eigenvalue problem, namely N. This comes from the fact that the state vector contains both the displacements and the velocities of the predefined DOFs. Half of the resulting eigenvalues and eigenvectors are complex conjugates to the remaining half. This can be further rewritten representing the displacements only, in this compact manner:

$$\{u\} = [\Phi]\{y\}, \tag{14.8}$$

where $[\Phi]$ is the modal transformation matrix containing the complex mode shapes and $\{y\}$ are the generalized DOFs. It is obvious that the eigenvalue problem represented in Eq. (14.4) is frequency dependent. This obstacle is overcome by the iterative algorithm presented in Table 14.1.

14.2.2 System Matrices

The model set-up is similar to that found in Kvåle et al. [11]. As indicated in the preceding section, both the fluid-structure interaction and the steel structure itself are needed to establish the total system matrices $[M(\omega)]$, $[C(\omega)]$ and $[K]$. The problem was therefore divided into two sub-domains; (i) the first consisting of the FE-model including the static contributions from the hydrodynamics, (ii) the second consisting of the contributions from hydrodynamics except for the static parts. The outline of the process used to establish the total system matrices this is illustrated in Fig. 14.3.

Table 14.1 Pseudo-code describing the iterative algorithm

INPUT $\omega_{n,dry}$, N, tolerance
FOR n = 1 to 2N
    $\omega = \omega_{n,dry}$
    diff = tolerance +1
    WHILE diff > tolerance
        solve eigenvalue problem for chosen $\omega \Rightarrow \lambda_r, \{q_r\}$
        sort the eigenvalues λ_r, and sort the eigenvectors $\{q_r\}$ correspondingly
        $\omega_0 = \omega$
        $\omega = \omega_{d,n} = \mathrm{Im}(\lambda_n)$ (r = n)
        diff $= |\omega_0 - \omega|$
    END
    store eigenvalue $\lambda_n = \lambda_r$ and eigenvector $\{q_n\} = \{q_r\}$
END

Sub-structure I   Sub-structure II
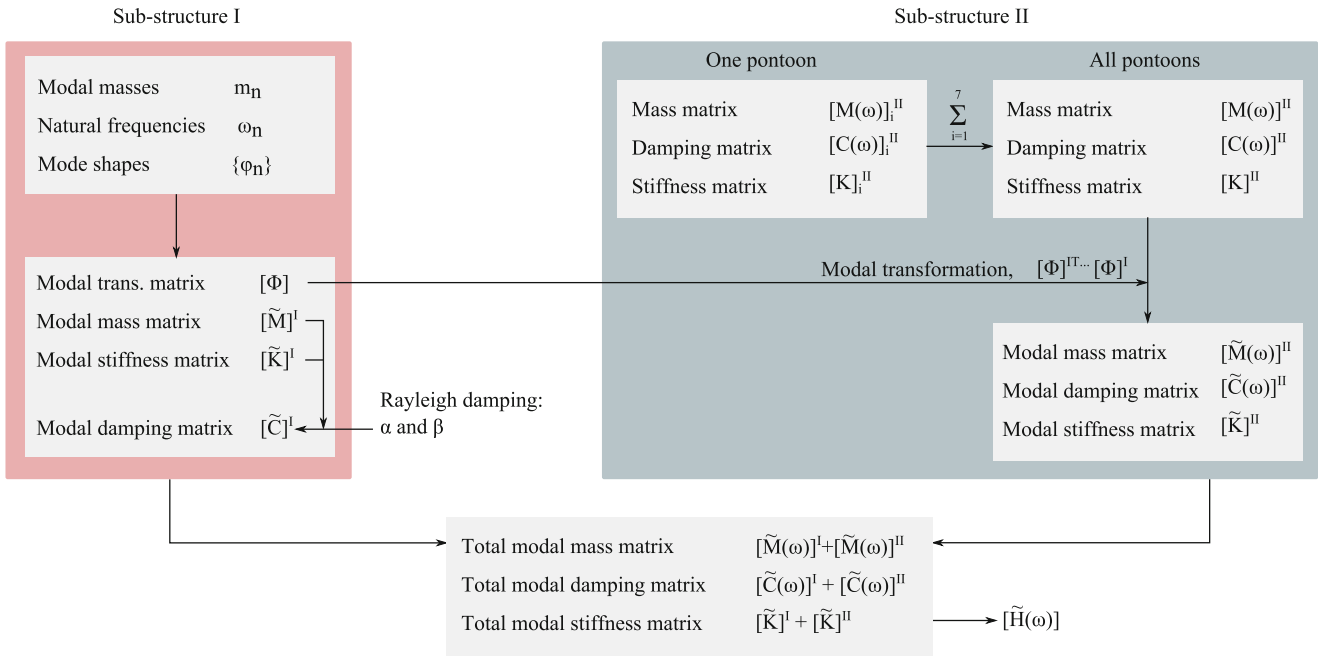
Fig. 14.3 Float scheme describing the connection of the sub-structures

First, the modal properties from the FE-model representing sub-structure I were extracted. This FE-model included the mode shapes, modal masses and natural frequencies, and resulted in modal system matrices $\left[\tilde{M}\right]^{I}$ and $\left[\tilde{K}\right]^{I}$. The modal damping matrix $\left[\tilde{C}\right]^{I}$ was further established by enforcing Rayleigh damping with $\alpha = \beta = 5\ \mathrm{e}-3$. Subsequently, the local frequency dependent mass, damping and stiffness matrices for a single pontoon were calculated by means of the hydrodynamics software DNV HydroD WADAM. The software simulates unit height waves acting on the pontoon, for a discretized frequency domain, which results in pressure distributions on the pontoon. By integrating the pressures acting on the wetted part of the pontoon, forces and moments are established, which are proportional to displacements (stiffness), velocities (damping) or accelerations (mass). The frequency dependent local system matrices resulting from WADAM, were thereafter stacked and transformed, so that it matched the global format of the FEM formulation. This was repeated for all seven pontoons, and summed, to give the total system matrices. Finally, the system matrices corresponding to sub-structure II were transformed to the modal space corresponding to sub-structure I, and the contributions added. The total eigenvalue problem for the modal frequency dependent system could then be solved, by following the procedure in the preceding section. The eigenvalues stemming from the solution of this *modal* eigenvalue problem are exactly the same as those from an equivalent *physical* eigenvalue problem. However, the mode shapes will be different; the coordinate values of the mode vectors represent the contributions from each of the modes for sub-structure I. The modal transformation corresponding to the first sub-structure only can be written like this:

$$\{u\} = [\Phi]\{y\}. \tag{14.9}$$

By solving the complex and frequency dependent eigenvalue resulting on modal form following the procedure in the preceding section, this second modal transformation is introduced:

$$\{y\} = [\Psi]\{q\}. \tag{14.10}$$

The total transformation then simply is:

$$\{u\} = [\Phi][\Psi][q]. \tag{14.11}$$

Thus, $[\Phi]$ is the modal transformation matrix from *first-level* modal coordinates $\{y\}$ to *physical* coordinates $\{u\}$ and $[\Psi]$ is the modal transformation matrix from *second-level* modal coordinates $\{q\}$ to the *first-level* modal coordinates $\{y\}$.

A selected subset of the mode shapes resulting from the eigenvalue solution is seen in Figs. 14.4 and 14.5.
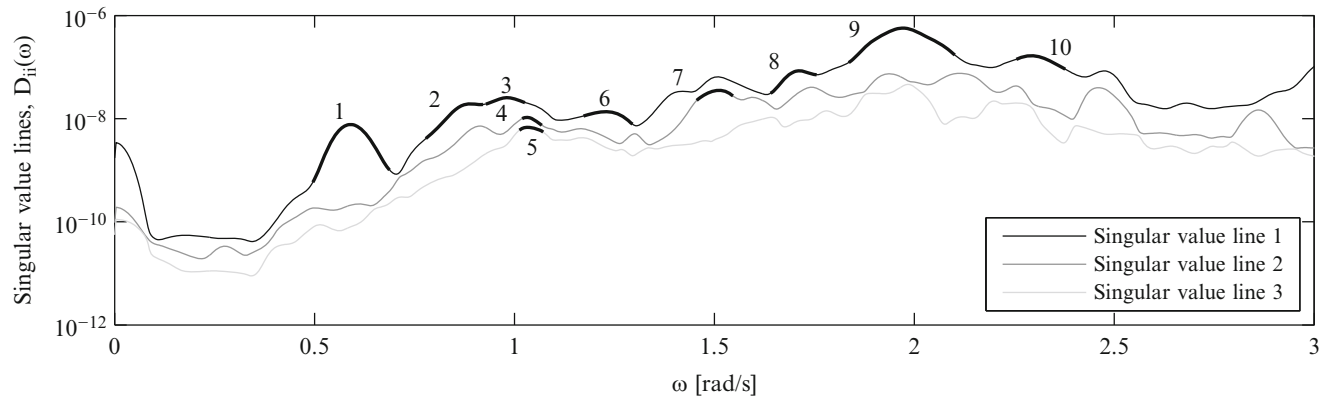
Fig. 14.4 Peaks corresponding to modes identified with FDD

Fig. 14.5 One dimensional spectral density of wave height, representing the energy in the wave loading process
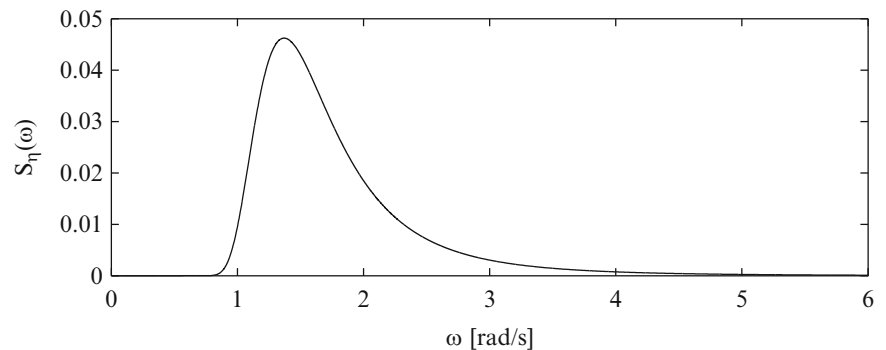
14.3 Modal Analysis

14.3.1 Test Set-up

In the testing period preceding this paper, the Bergsøysund Bridge was instrumented by a total of 10 tri-axial accelerometers placed on the five midmost pontoons, as indicated by the dots in Fig. 14.2, yielding a total of 30 channels. To obtain information about torsional movement, both sides of the bridge were monitored. The accelerometers were delivered by Canterbury Seismic Instruments, and were operating at a sample frequency of 200 Hz. Each pair of accelerometers was coupled with a GPS antenna to ensure accurate and common time stamps for all recordings. The time series were finally sent to a main logger unit by means of WiFi, where time series data from all sensors were stored into one file for each recording. The findings presented in this paper are based on recordings established between 03:30 and 04:00 local time on September 29, 2014.

14.3.2 Pre-processing of Recordings

The recordings were low-pass filtered with the built-in the MATLAB Butterworth filter (*butter*), with a low-pass frequency of 2 Hz and order 8, on all 30 channels. The mean was removed from each channel, to ensure zero-mean measurements. Furthermore, the time series were resampled with a decimation factor of 40, yielding a resample frequency of 5 Hz. The low-pass filtering and resampling had two purposes: (i) to focus the identification procedures on the lowest natural modes and (ii) to reduce computational straining. The lowest modes are found in the frequency range where the hydrodynamics contribute to the system, which makes this a frequency range of particular interest.
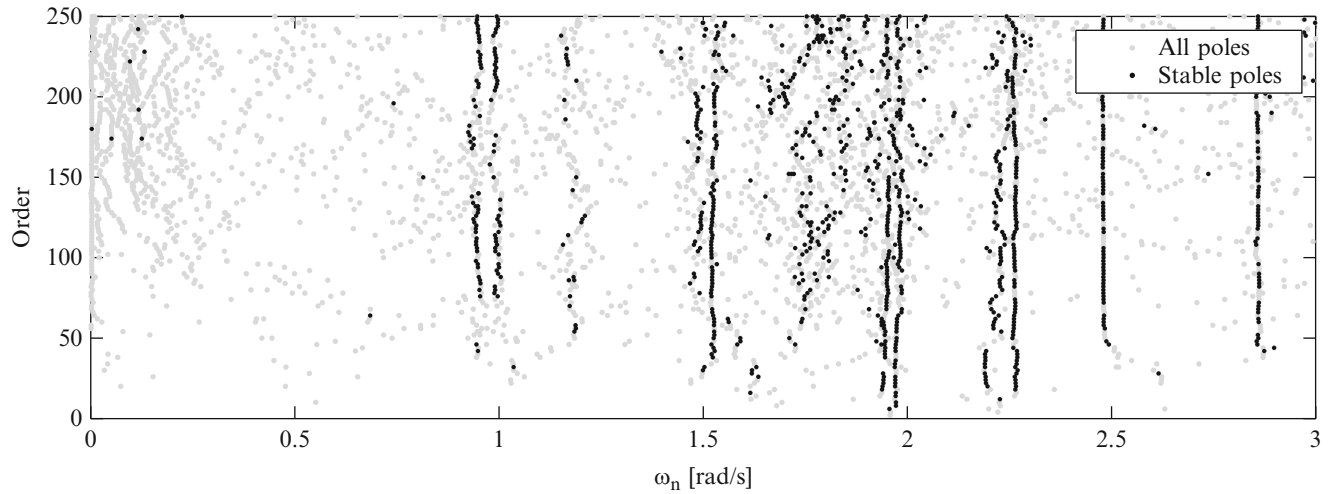
Fig. 14.6 Stabilization plot from covariance-driven SSI with number of block rows $i = 13$

14.3.3 Modal Analysis: Frequency Domain Decomposition

Initially, a FDD analysis was carried out. The FDD improves the peak-picking method on some of its weak spots, but keeps the hands-on feeling provided. FDD performs a singular value decomposition of the cross-spectral density matrix for each frequency value, as follows:

$$[S_{uu}(\omega_k)] = [U(\omega_k)] \ [\Sigma(\omega_k)] \ [U(\omega_k)]^H, \tag{14.12}$$

where $[S_{uu}(\omega_k)]$ is the cross-spectral density matrix for frequency ω_k; $[U(\omega_k)]$ is a unitary matrix with singular vectors; and $[\Sigma(\omega_k)]$ is a diagonal matrix with the corresponding singular values. The singular values represent SDOF spectral densities near the peaks, while the columns of $[U(\omega_k)]$ represent the corresponding mode shapes. The singular values in $[\Sigma(\omega_k)]$ are sorted by their significance at each discrete frequency value, as are the corresponding mode shapes in $[U(\omega_k)]$. In this case study, Welch's periodogram method [12] was used to estimate the cross-spectral density matrix, with the built-in MATLAB function *cpsd*. The time series were divided into 15 segments with a Hanning windowing function and 50 % overlap.

The resulting peaks found in the singular values from the FDD procedure are shown in Fig. 14.6. Damping estimates can also be established by means of the *Enhanced* FDD method [13], but this has not been considered in this case. The mode shapes resulting from FDD are not presented in this paper.

14.3.4 Modal Analysis: Covariance-Driven Stochastic Subspace Identification

The output-only Cov-SSI algorithm in Rainieri and Fabbrocino [14] was applied on the accelerometer recordings. This method relies on the Toeplitz matrix, which consists of block co-variance matrices for all channel readings between different instances defined by time shifts (related to the number of block rows). By performing singular value decomposition on the resulting Toeplitz matrix – to sort the co-variances according to their significance – a subset of the total matrix can be extracted. The size of the subset is defined by the input *order*, which in turn directly affects the resulting eigenvalues and eigenvectors. Because it is far from straight-forward to determine an optimal order a priori, the absolute values of the eigenvalues, corresponding to the undamped natural frequencies, are plotted in a *stabilization plot*. In the current case study, a pole is considered stable if it does not vary by more than 1 % in natural frequency or 5 % in damping ratio during the last two order levels. Stability with regard to the eigenvectors, e.g. by means of the MAC [15] number, was not considered.

An implementation of the mentioned Cov-SSI method was run with 13 block rows, yielding a maximum system order of $30 \times 13 = 390$. Orders between 2 and 350 were enforced, and the resulting stabilization plot is seen in Fig. 14.7. A lot of fuzziness is observed in this stabilization plot in the range between 1.5 and 2.5 rad/s, which complicates the system identification in this area. The reason for this behaviour is suspected to come from the wave loading. By comparison with
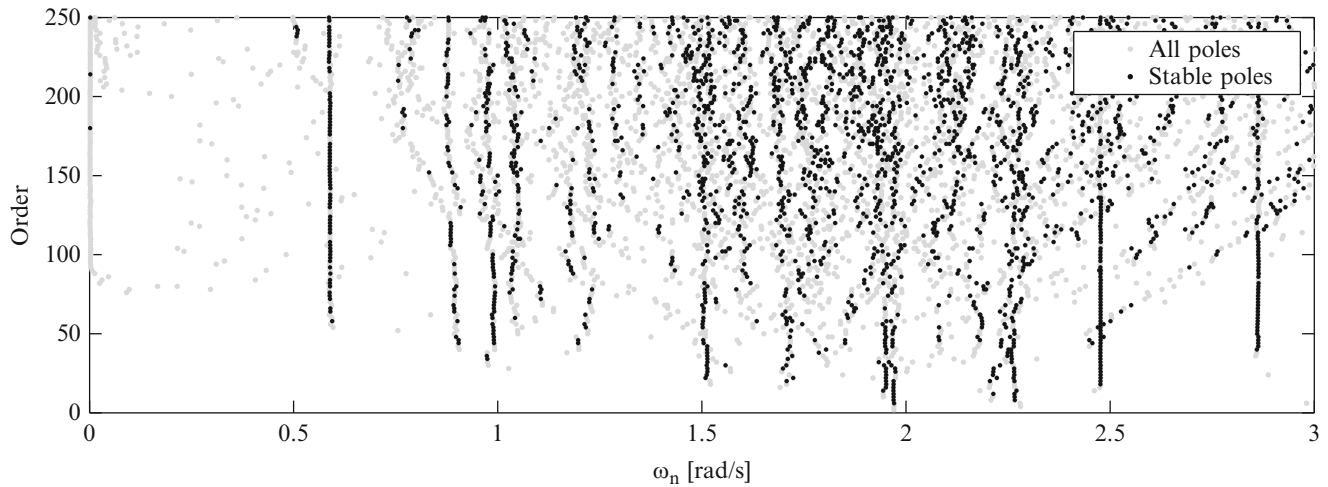
Fig. 14.7 Stabilization plot from covariance-driven SSI with number of block rows $i = 100$

Fig. 14.8 Horizontal modes from Cov-SSI (seen from above)

0.588 rad/s

1.9823 rad/s

Fig. 14.9 Horizontal modes from eigenvalue problem (seen from above)

0.651 rad/s

1.977 rad/s

Table 14.2 Identification results from Cov-SSI with 100 block rows ($i = 13$)

Mode type	SSI			Eigenvalue problem			
	Figure	ω_n[rad/s]	ξ_n[%]	Figure	ω_n[rad/s]	ξ_n[%]	MAC (%)
Horizontal	14.10a[a]	0.588	2.44	14.4a	0.651	1.14	63
Vertical	14.11a[b]	0.948	6.90	14.5a, b	1.016	15.5	57
					1.056	14.8	25
Vertical	14.11b[b]	0.997	12.9	14.5a, b	1.016	15.5	41
					1.056	14.8	42
Vertical	14.11c	1.165	10.3	14.5c	1.233	11.3	63
Vertical	14.11d	1.527	2.81	14.5d	1.550	6.03	92
Vertical	14.11e	1.950	1.64	14.5f	1.977	4.17	90
Ver./hor.	14.10b	1.982	2.90	14.4b	2.016	2.37	42

[a]$i = 100$
[b]Two modes blended together

the FDD peaks, it is also observed that the first mode is not revealed in the SSI identification. This is amended by increasing the number of block rows, enabling modes at even lower frequencies to be identified successfully. The trade-off, however, is a poorer representation of the modes in the difficult region in the assumed frequency range of the wave load. This affects in particular the highly damped modes located around 1 rad/s. The resulting stabilization plot, where the number of block rows was increased to 100, is seen in Fig. 14.8.

The output-only Cov-SSI method assumes white noise input, whilst the structure in reality is significantly loaded by waves, far from a white noise process. This is illustrated in Fig. 14.9, which shows the spectral density of the wave height corresponding to a realistic sea state on site. Poles (eigenvalues) were selected from the stabilization plot. The resulting natural frequencies, damping ratios and MAC-numbers, comparing identified mode shapes with the mode shapes from the eigenvalue problem, are presented in Table 14.2. The corresponding mode shapes are found in Figs. 14.10 and 14.11.
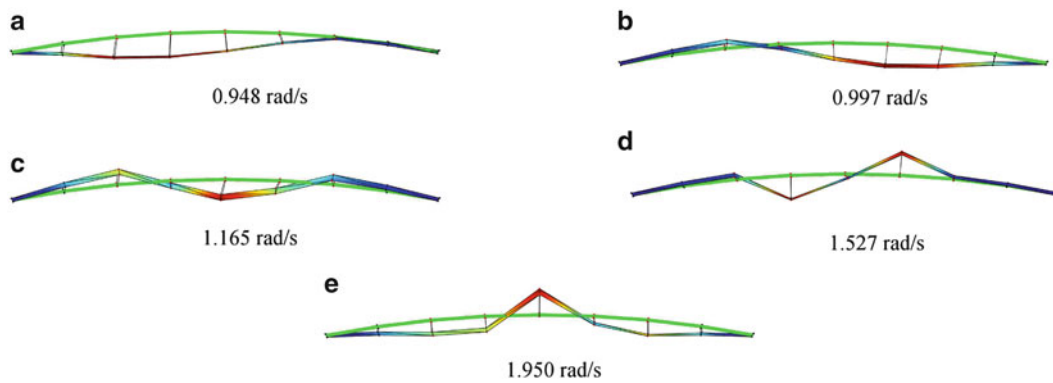
Fig. 14.10 Vertical modes from Cov-SSI (seen from side)

Fig. 14.11 Vertical modes from eigenvalue problem (seen from side)
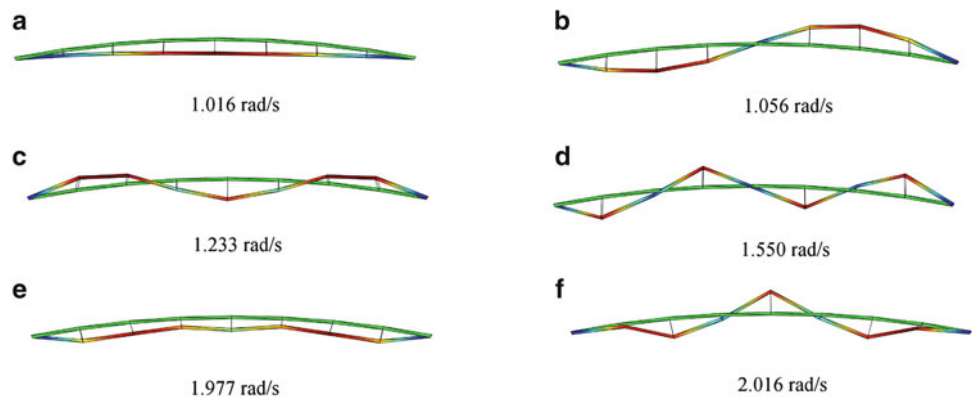
14.4   Concluding Remarks

Two different operational modal analysis procedures have been used to gain some insight of the behaviour of the floating bridge studied; the Bergsøysund Bridge, with emphasis on the covariance-driven stochastic subspace identification technique. Both natural frequencies and damping levels match quite well with the eigenvalue solution of the numerical model, especially given the fact that no measurement-based model updating has been performed. The estimated mode shapes are easily recognized amongst the mode shapes from the eigenvalue problem, but the MAC values are in general poor. A model updating procedure might be necessary to remedy this. Some of the modes established using the Cov-SSI technique also appear to consist of combinations of multiple closely spaced modes from the eigenvalue solution.

The modal parameters from Cov-SSI appear to be very sensitive with regard to the number of block rows defined for the algorithm; no good compromise was found, and no single number of block rows provided stable results for the identification of both the first, and the second and third natural mode. This lead to the need for an additional analysis designated to the first mode only. The bridge is exposed to wave action, which results in a loading that deviates drastically from the white noise approximation that output-only Cov-SSI relies on. This affects the stability of the poles in the stabilization plot and makes the modes with natural frequency in the range of the wave loading are harder to identify.

References

1. Watanabe E (2003) Floating bridges: past and present. Struct Eng Int 13(2):128–132
2. McLamore VR, Hart GC, Stubbs IR (1971) Ambient vibration of two suspension bridges. J Struct Div 97(10):2567–2582
3. Abdel-Ghaffar A, Scanlan R (1985) Ambient vibration studies of Golden Gate Bridge: I. Suspended structure. J Eng Mech 111(4):463–482
4. Brincker R, Zhang L, Andersen P (2001) Modal identification of output-only systems using frequency domain decomposition. Smart Mater Struct 10(3):441

5. Trefethen LN, Bau III D (1997) Numerical linear algebra, vol 50. SIAM
6. Van Overschee P, De Moor B, Van Overschee P, De Moor B (1993) Subspace algorithms for the stochastic identification problem. Automatica 29(3):649–660
7. Van Overschee P, De Moor B (1996) Subspace identification for linear systems: theory, implementation, applications. Kluwer Academic Publishers, Boston/London/Dordrecht
8. Brownjohn JMW, Magalhaes F, Caetano E, Cunha A (2010) Ambient vibration re-testing and operational modal analysis of the Humber Bridge. Eng Struct 32(8):2003–2018
9. Andersen P, Brincker R, Peeters B, De Roeck G, Hermans L, Krämer C (1999) Comparison of system identification methods using ambient bridge test data. In: Proceedings of the 17th international modal analysis conference, Kissimee, pp 7–10
10. Naess A, Moan T (2012) Stochastic dynamics of marine structures. Cambridge University Press, New York
11. Kvåle KA, Øiseth O, Sigbjörnsson R (2014) Modelling of the stochastic dynamic behaviour of the Bergsøysund Bridge: an application of the power spectral density method. In: Proceedings of the 9th international conference on structural dynamics, EURODYN 2014, Porto, pp 2921–2928
12. Welch PD (1967) The use of fast Fourier transform for the estimation of power spectra: a method based on time averaging over short, modified periodograms. IEEE Trans Audio Electroacoust 15(2):70–73
13. Brincker R, Ventura C, Andersen P (2001) Damping estimation by frequency domain decomposition. In: 19th international modal analysis conference, Kissimmee, pp 698–703
14. Rainieri C, Fabbrocino G (2014) Operational modal analysis of civil engineering structures. Springer, New York
15. Allemang RJ (2003) The modal assurance criterion–twenty years of use and abuse. Sound Vib 37(8):14–23

Chapter 15
Investigation of a Novel Pseudo Ambient Vibration Testing Approach

K.A. Grimmelsman and D. Samudio Castillo

Abstract The practical and inexpensive nature of ambient vibration testing has contributed to this approach being widely used by researchers and practitioners for identifying the dynamic characteristics of a wide range of laboratory and full-scale structures. The dynamic characteristics identified from such testing can be used for validating and calibrating analytical models, for quantifying and evaluating actual operating or performance characteristics, or for identifying damage and structural health monitoring. Although ambient vibration testing has been used extensively, it remains subject to a number of assumptions and limitations that are not always readily apparent in the results and that can reduce the reliability and utility of these results for many structures and applications. The authors believe that a pseudo ambient vibration testing approach using controlled excitation from a spatially distributed network of low-cost excitation devices could provide more consistent and reliable dynamic characterizations while maintaining many of the desirable attributes of ambient vibration testing. The writers conducted a study of the proposed testing approach using a large-scale laboratory model. The dynamic properties of the structure were identified by ambient vibration testing and by different implementations of the proposed pseudo ambient vibration testing approach. The results obtained from the testing are compared and discussed.

Keywords Ambient vibration testing • Hybrid testing • Stochastic • Tactile transducers • Bridges

15.1 Introduction

Ambient vibration testing is commonly used to obtain dynamic characterizations for a broad range of constructed systems. The resulting dynamic characterization may be used for assessing the in-service performance of a structure, to obtain the quantitative data needed for structural identification, or for structural health monitoring and damage detection applications. Ambient vibration testing is often the only practical method available for dynamic testing of very large structures; however the testing approach is also cost-effective and easy to implement and analyze and has been successfully used to dynamically characterize a wide range of different structures [1]. This test method has largely become the principal vibration testing approach used for nearly all in-service civil infrastructure systems. Despite the rather obvious cost and practical advantages associated with ambient vibration testing, this output-only testing method is unable to obtain mass normalized modal vectors that are possible from input-output vibration testing methods and is also subject to many possible sources of uncertainties. Much of the potential uncertainty is derived from the uncontrolled and unmeasured dynamic excitation used for ambient vibration testing [2–4]. The dynamic excitation is assumed to have very specific characteristics, namely that it is stationary and uncorrelated white noise that is spatially distributed over the entire structure. Evaluating and validating these assumptions related to the inputs is practically impossible, and the uncertainties in the dynamic characterization results arising from violations to these assumptions are often coupled with uncertainties arising from the structure and its interactions with environmental and service loads. The uncertainties that may be present in the identified modal parameters can significantly limit the reliability and utility of the results for many objectives related to assessing civil infrastructure systems.

Hybrid testing approaches have been previously explored as a means for enhancing the capabilities, reliability and effectiveness vibration testing results for civil infrastructure systems. Perhaps the most well-known example of a hybrid vibration testing approach is Operational Modal Analysis in the presence of eXogenous Inputs (OMAX) testing [5].

K.A. Grimmelsman (✉)
Intelligent Infrastructure Systems, 3001 Market Street, Suite 200, Philadelphia, PA 19104, USA
e-mail: kgrimmelsman@iisengineering.com

D.S. Castillo
Department of Civil Engineering, University of Arkansas, 4190 Bell Engineering Center, Fayetteville, AR 72701, USA
e-mail: dsamudio@email.uark.edu

In this approach, deterministic dynamic excitation is employed in conjunction with uncontrolled stochastic excitation from ambient environmental sources and operating loads to obtain the dynamic characterization. The OMAX test approach has implemented and evaluated for a two footbridge structures using a single drop hammer, impact hammer and pneumatic artificial muscle (PAM) actuator to provide the deterministic component of the dynamic excitation [6, 7]. Although the OMAX approach was found to be more capable and accurate than conventional ambient vibration testing, the devices used for the deterministic excitation component are still somewhat cumbersome to deploy on structures and the resulting dynamic excitation was single input, multiple output (SIMO) for the deterministic source and multiple input, multiple output (MIMO) for the stochastic excitation.

The writers propose a different hybrid dynamic testing approach for constructed systems that is different from the OMAX approaches implemented previously in that it employs controlled and uncontrolled stochastic excitation sources that permit the overall test to be described as a MIMO implementation. The novelty of the approach presented in this paper stems from the use of a network of low-cost, small-scale tactile transducers that are used to provide the controlled stochastic excitation. The novel dynamic testing approach using tactile transducers was devised and developed by the corresponding author, and the operating and performance characteristics of the system were systematically evaluated in a prior study [8, 9]. The novel dynamic excitation system has also been evaluated for conventional experimental modal analysis (EMA) testing [10], and has been used to characterize and evaluate the excitation related uncertainty in conventional ambient vibration testing of in-service bridges [11].

The proposed testing approach that is presented in this paper seeks to use this excitation system to provide controlled dynamic excitation that is consistent with the normally assumed, but uncontrollable characteristics of ambient dynamic excitation employed for conventional ambient vibration testing of structures (e.g. stationary and uncorrelated Gaussian white noise). As a result, the writers describe the proposed hybrid testing approach as pseudo ambient vibration testing. The obvious advantage of the proposed approach is the one to one correspondence with the assumptions and methods employed in conventional ambient vibration testing. The artificial dynamic excitation provided to the structure being tested by the tactile transducers is known and controlled, but the actual dynamic excitation forces supplied to the structure are not measured. This avoids the additional expense associated with the deploying force transducers to measure the actual input forces, and permits the test data to be processed and evaluated using the same output-only identification approaches that are already well-established for ambient vibration testing. The transition from ambient vibration testing to the proposed pseudo ambient vibration testing approach is therefore very transparent, and also avoids many of the logistical challenges associated with deploying and operating controlled input devices such as drop hammers, impact hammers, or large scale shakers on a structure. The added cost associated with the proposed test approach is also very minimal relative to conventional ambient vibration testing. The prototype excitation system using tactile transducers developed by the corresponding author is capable of providing 16 individually controlled and simultaneous excitation inputs and only cost about $6,000 to construct. It should be noted that the proposed pseudo ambient vibration testing approach will not permit scaled modal vectors to be identified; however, the writers believe that improving the consistency and reliability of the modal parameters identified from the vibration test is a more paramount consideration for advancing the utility of the dynamic characterization results for a broader spectrum civil infrastructure systems.

A laboratory evaluation of the proposed pseudo ambient vibration testing approach was performed for a large-scale steel grid structure. Both conventional ambient vibration testing and the pseudo ambient vibration testing approach with some different variations to the controlled component of the dynamic excitation were implemented for the structure. The modal parameters for the various test cases were all identified using the same output-only identification method. The results obtained for the modal parameters from each test case are compared, and the effectiveness of the proposed pseudo ambient vibration test is evaluated.

15.2   Description of the Investigation

An investigation program was developed and implemented with the objective of first assessing and evaluating the effectiveness of the pseudo ambient vibration testing approach on a structure in the laboratory where the sources of uncertainty related to the behavior of the structure and its interactions with its operating loads and the environment could be minimized. The testing approach evaluated in this research is expected to be applicable for dynamic testing of short to medium span length bridges and other constructed systems of a similar scale, but an experimental evaluation and validation of the approach in the relatively stable environs of a laboratory for a structure with only a limited degree of complexity was determined to be a logical first step before implementing this approach with full-scale structures in the field. In addition,

the writers believed that an experimental evaluation of the testing approach would incorporate many of the uncertainties and challenges associated with dynamic testing of full-scale structures more realistically than would be possible from a purely analytical study of this approach.

The experimental testing program devised for this study consisted of a comparative study of the modal parameters identified for a large-scale steel structure by conventional ambient vibration testing with no artificial dynamic excitation applied to the structure, and by the proposed pseudo ambient testing approach in which uncorrelated white noise excitation was applied to the structure in a spatially distributed manner by a network of low-cost and small scale shakers. The pseudo ambient excitation cases considered for this investigation included variations in the quantity and spatial locations of the dynamic inputs to the structure and to the characteristics of the dynamic excitation. Although the full testing program included a total of 10 different excitation cases, the focus of this paper is on the results obtained from a subset of four of these test cases. These test cases discussed in this paper include an uncontrolled ambient excitation case and three cases in which pseudo ambient excitation having different characteristics was applied to the grid by a network of 15 shakers. The vibration responses were measured and processed in the same way for all test cases. The dynamic excitation applied to the structure in each test case was also considered to be unmeasured and uncontrolled during the modal parameter identification stage. The details of the test structure and the experimental program are described in the following sections.

15.2.1   Test Structure

A large steel structure was used as the test specimen for this research. The model can be nominally described as a grid structure, although it was designed and constructed to notionally represent various behavior characteristics common to many different types of civil infrastructure systems. The grid structure is simply−supported with a single span length of 7,315.2 mm and a width of 2,743.2 mm. The grid framing system consists of three continuous longitudinal girder lines spaced on 1,371.3 mm centers and 7 transverse girder lines spaced on 1,219.2 mm centers. The ends of each longitudinal girder are supported by 1,066.8 mm tall steel pedestals and pin and roller bearings. The steel pedestals sit on the approximately 130 mm thick unreinforced concrete slab on grade floor in the laboratory. The 3 longitudinal girder sections and the 14 transverse girder sections are all W8 × 10 rolled steel beams that are joined together with bolted connections employing top and bottom cover plates and vertical clip angles which results in fairly rigid connections between the members. A photograph of the test structure and a schematic illustrating the grid numbering convention employed in this study are provided in Fig. 15.1.

15.2.2   Test Setup and Measurement Equipment

The grid structure was instrumented for the vibration testing using a total of 21 accelerometers (Model 393C from PCB Piezotronics, Inc.) placed at the intersections of the longitudinal gridlines 1–3 and the transverse gridlines B–F, H and J as defined in Fig. 15.1. The accelerometers were attached to the structure using magnets and were oriented to measure the vertical accelerations of the structure. A total of 15 shakers (tactile transducers) were attached to the grid model using c-clamps to provide the controlled pseudo ambient dynamic excitations in the vertical direction. The shakers were installed at the intersections of longitudinal gridlines 1–3 and transverse gridlines B, C, D, E and F. Since the weight of the 15 shakers could potentially alter the modal characteristics of the structure, they were left in place on the structure during all test cases. The vibration measurements were recorded using National Instruments Model 9234 dynamic signal acquisition modules. Uncorrelated white noise excitation signals specific characteristics were generated and sent to the shaker amplifiers through independent channels of a National Instruments Model 9264 analog output module. The time duration of the vibration measurements recorded in each test case was 60 min. The digitized measurements were subsampled to an effective sampling rate of 413.05 Hz in before being saved for subsequent data analysis.

15.3   Vibration Test Cases and Dynamic Excitation

The results obtained from a total of four different vibration test cases are presented and discussed in this paper. Case 1, represents the baseline ambient vibration test for the structure. The only dynamic excitation acting on the structure was from uncontrolled and unmeasured ambient sources present in the laboratory facility. This test case is representative of the ambient excitation that might act on a bridge that is closed to traffic. The ambient dynamic excitation of the grid structure in this case
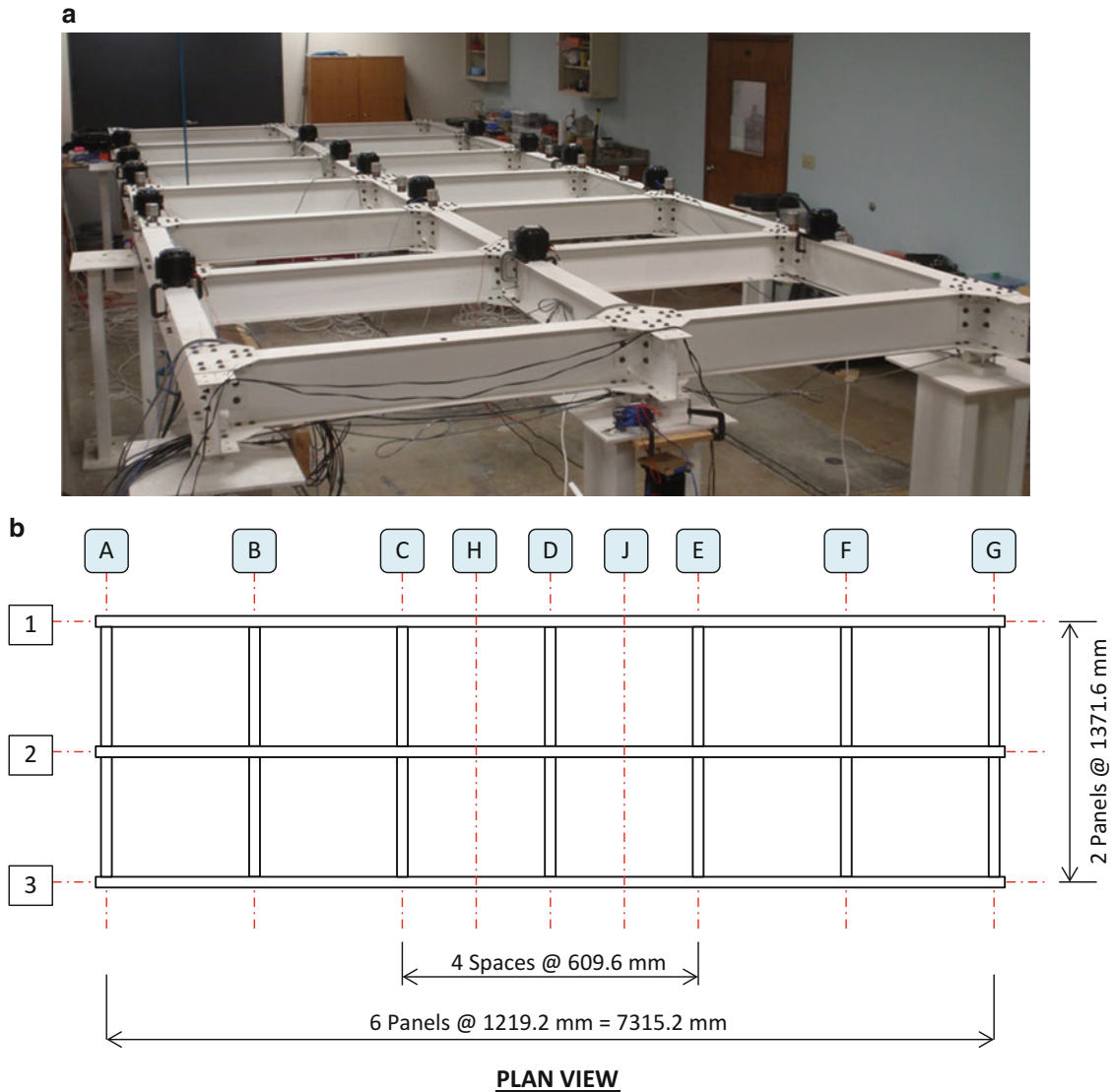
Fig. 15.1 (**a**) Photograph of the grid structure and (**b**) grid numbering convention

is assumed to be stationary Gaussian white noise that is spatially distributed over the entire structure. The actual sources of the ambient excitation in this test case were most likely from the operation of the HVAC system and from individuals walking around and working in other areas of the building.

The three remaining test cases all included controlled pseudo ambient dynamic excitation produced by the small-scale shakers in addition to the uncontrolled and unmeasured excitation from ambient sources. The pseudo ambient excitation used in these test cases was uncorrelated Gaussian white noise that was simultaneously applied to the grid structure at 15 different spatial locations. The 15 independently generated excitation signals used in these cases were bandpass filtered between 5 and 180 Hz to align the bandwidth of the excitation with the global vibration modes of the structure and the optimum operating characteristics of the shakers. In Case 2 and Case 4, the voltage ranges for the generated noise signals were half as large as the voltage ranges used for the generated noise signals used in Case 3. The voltage range used for the signals generated in Case 3 were determined by identifying the maximum output voltage that could be sent to the tactile transducers that were used as shakers without causing the internal mass to reach its stroke limit and produce an impact type excitation force. As a result, Case 2 and Case 4 were described as low input force level excitation cases while Case 3 was referred to as a high input force level excitation case. The white noise signals were continuously generated throughout the 60 min test duration in Case 2 and Case 3. The generated white noise signals used in Case 4 were only 4 min long and were replayed through the shakers a total of 15 times over the 60 min test duration. This was done to gain some insight as to how to best utilize the pseudo ambient vibration testing approach for characterizing the structure. In other words, to evaluate whether more unique realizations of

the white noise excitation signals would yield more consistent modal identification results than multiple applications of the same stochastic excitation signals, or vice-versa.

15.4 Data Analysis and Results

The data analysis for the vibration measurements recorded from each test case were first evaluated in the time domain to characterize the nature of the pseudo ambient excitation cases (Cases 2–4) relative to the baseline ambient vibration test (Case 1). This stage of the data analysis was implemented in two steps: (1) the root-mean-squared (RMS) acceleration amplitude was computed for each accelerometer location from the raw time domain acceleration records, and (2) the RMS acceleration amplitudes computed for each of the 21 accelerometer locations were added together to obtain a total RMS acceleration amplitude value for the response of the grid structure from each vibration test case. The total RMS acceleration amplitude is a convenient and effective global index for evaluating and comparing the nature of the unmeasured ambient dynamic excitation from the measured structural vibration responses [11]. The 60 min long measurement records were divided into 15 equal length segments of 4 min each and the total RMS acceleration was computed for each to evaluate the stationarity of the excitation. The total RMS acceleration amplitudes were also computed for the 60 min long records for comparison purposes with statistical values computed from the segment results. The mean value of the total RMS accelerations computed for the 15 segments of data from each test case was also normalized relative to the mean value computed from Case 1 to assess the effectiveness of the shakers in producing the pseudo ambient excitation. The total RMS acceleration results computed for each test case are tabulated in Table 15.1.

The second stage of the data analysis was to identify the modal parameters of the structure for each test case. The vibration measurements of the grid structure recorded for each test case were evaluated using the stochastic subspace identification (SSI) algorithm [12] to identify the natural frequencies, mode shapes and damping ratios of the grid structure. This data analysis was performed on each of the 15 segments of 4 min in length extracted from the overall 60 min long data sets for each test case. Modal analysis results obtained from an un-calibrated analytical model of the grid structure indicated that the first 12 global bending and torsion modes were located in the frequency band of 9.2–168.3 Hz. The modal parameters (natural frequencies, damping ratios, modal vectors) were identified for the 15 data segments using stability plots created from the SSI analysis with increasing model orders. Modal assurance criterion (MAC) values [13] were computed from the experimentally identified modal vectors and the modal vectors extracted from the analytical model of the grid. Individual modal parameters that could not be confidently identified for a given data segment were excluded from the results. The number of data segments (n) for which the modal parameters were confidently identified along with the mean value and standard deviation of the modal

Table 15.1 Total RMS acceleration amplitude (g's) for each test case

Data record	Test case			
	Case 1	Case 2	Case 3	Case 4
Segment 1	0.0010	1.1237	2.4149	1.0925
Segment 2	0.0008	1.1288	2.4101	1.0861
Segment 3	0.0008	1.1351	2.3931	1.0864
Segment 4	0.0008	1.1227	2.4261	1.0861
Segment 5	0.0008	1.1351	2.3956	1.0866
Segment 6	0.0008	1.1299	2.3946	1.0931
Segment 7	0.0009	1.1313	2.4145	1.0893
Segment 8	0.0008	1.1101	2.1021	1.0879
Segment 9	0.0008	1.1152	2.2418	1.0859
Segment 10	0.0008	1.1319	2.4181	1.0831
Segment 11	0.0012	1.1227	2.0901	1.0817
Segment 12	0.0012	1.1313	2.3404	1.0833
Segment 13	0.0020	1.1157	2.2761	1.0893
Segment 14	0.0010	1.1106	1.9711	1.0882
Segment 15	0.0015	1.1164	2.3913	1.0814
Overall (60 min)	0.0011	1.1241	2.3164	1.0867
Mean (segments)	0.0010	1.1240	2.3120	1.0867
Std. deviation (segments)	0.0004	0.0087	0.1459	0.0035
Normalized mean	1	1,115	2,293	1,078

Table 15.2 Natural frequency results (Hz) for each test case

Mode	n	Avg. Freq.	Std. Dev.	n	Avg. Freq.	Std. Dev.	n	Avg. Freq.	Std. Dev.	n	Avg. Freq.	Std. Dev.
	Case 1 – baseline ambient			Case 2 – low force pseudo ambient			Case 3 – high force pseudo ambient			Case 4 – low force pseudo ambient repeated[a]		
1	15	8.891	0.021	15	8.712	0.018	14	8.635	0.063	15	8.780	0.017
2	15	10.134	0.013	15	10.066	0.037	15	10.072	0.052	15	10.050	0.006
3	15	33.523	0.949	15	32.780	0.017	15	32.747	0.023	15	32.717	0.005
4	15	36.433	0.542	15	36.988	0.020	15	36.838	0.044	15	37.010	0.013
5	15	67.640	0.115	15	67.869	0.036	15	67.542	0.093	15	68.090	1.204
6	10	73.047	0.642	15	73.698	0.039	15	73.869	0.114	15	73.571	0.015
7	15	76.923	0.188	15	78.162	0.031	15	78.000	0.109	15	78.190	0.027
8	5	80.527	0.688	15	82.191	0.036	15	82.148	0.066	15	81.971	0.013
9	3	106.862	0.390	15	106.358	0.207	15	105.720	0.628	12	107.031	0.353
10	14	110.242	0.523	15	110.365	0.225	15	110.166	0.229	15	110.258	0.055
11	13	117.204	0.329	15	130.949	0.356	15	131.351	0.631	15	131.309	0.052
12	2	151.587	0.602	15	155.397	0.162	15	155.368	0.342	15	155.590	0.153

[a]Same 4 min long stochastic excitation signals repeated 15 times

Table 15.3 Damping ratios identified for each test case

Mode	n	Avg. Damp.	Std. Dev.	n	Avg. Damp.	Std. Dev.	n	Avg. Damp.	Std. Dev.	n	Avg. Damp.	Std. Dev.
	Case 1 – baseline ambient			Case 2 – low force pseudo ambient			Case 3 – high force pseudo ambient			Case 4 – low force pseudo ambient repeated[a]		
1	15	0.010	0.002	15	0.018	0.002	14	0.036	0.009	15	0.017	0.001
2	15	0.007	0.001	15	0.023	0.003	15	0.032	0.004	15	0.019	0.000
3	15	0.010	0.005	15	0.012	0.001	15	0.011	0.001	15	0.010	0.000
4	15	0.009	0.003	15	0.010	0.000	15	0.010	0.001	15	0.009	0.000
5	15	0.011	0.003	15	0.017	0.001	15	0.027	0.003	15	0.016	0.002
6	11	0.014	0.006	15	0.010	0.000	15	0.009	0.000	15	0.011	0.000
7	15	0.008	0.002	15	0.010	0.000	15	0.011	0.001	15	0.010	0.000
8	5	0.017	0.006	15	0.012	0.000	15	0.009	0.000	15	0.015	0.000
9	3	0.022	0.012	15	0.039	0.001	15	0.045	0.004	12	0.038	0.006
10	7	0.014	0.002	15	0.020	0.002	15	0.023	0.002	15	0.016	0.001
11	13	0.005	0.006	15	0.019	0.006	15	0.034	0.007	15	0.018	0.001
12	2	0.016	0.002	15	0.019	0.001	15	0.014	0.001	15	0.016	0.002

[a]Same 4 min long stochastic excitation signals repeated 15 times

parameters from the collection of data segment results were computed for the first 12 modes of the structure. These results are summarized in Table 15.2 (natural frequencies), Table 15.3 (damping ratios) and Table 15.4 (MAC values).

15.5 Discussion

The total RMS acceleration amplitudes summarized in Table 15.1 indicate that the dynamic excitation in each test case produced vibration responses that were generally consistent for each of the 4 min long segments of the measurements. Furthermore, the mean values of the total RMS acceleration computed from each data segment were also consistent with the total RMS acceleration amplitudes computed for the overall 60 min long data record for each test case. A comparison of the normalized mean total RMS accelerations indicates that the global vibration response of the grid structure was 1,115 times larger with the low force pseudo ambient excitation applied (Case 2) than the vibration response when only conventional uncontrolled ambient dynamic excitation (Case 1) was exciting the structure. The normalized mean total RMS acceleration of the grid in Case 3 was even larger at 2,293 times the global vibration response level observed from Case 1. In Case 3, the force amplitude of the pseudo ambient excitation was twice as large as the force amplitude used in Case 2 and Case 4, and accordingly the mean total RMS acceleration from this case is just about twice as large as the mean total RMS acceleration values from those cases. Case 4 employed 4 min long stochastic excitation signals that were repeated 15 times and the mean total RMS acceleration value for this case is just slightly smaller than the value produced in Case 2 where the excitation

Table 15.4 MAC values for each test case

Mode	Case 1 – baseline ambient			Case 2 – low force pseudo ambient			Case 3 – high force pseudo ambient			Case 4 – low force pseudo ambient repeated[a]		
	n	Avg. MAC	Std. Dev.	n	Avg. MAC	Std. Dev.	n	Avg. MAC	Std. Dev.	n	Avg. MAC	Std. Dev.
1	15	0.992	0.012	13	0.993	0.007	14	0.999	0.001	15	0.981	0.006
2	15	0.991	0.002	15	0.994	0.003	15	0.996	0.009	15	0.997	0.001
3	15	0.991	0.004	15	0.994	0.002	15	0.992	0.003	15	0.992	0.000
4	15	0.991	0.011	15	0.992	0.001	15	0.993	0.002	15	0.994	0.000
5	15	0.988	0.007	15	0.992	0.002	15	0.987	0.006	15	0.983	0.011
6	3	0.974	0.005	15	0.991	0.002	15	0.992	0.001	15	0.993	0.002
7	15	0.992	0.003	15	0.994	0.001	15	0.994	0.000	15	0.994	0.000
8	3	0.950	0.039	15	0.991	0.003	15	0.991	0.002	15	0.985	0.006
9	3	0.921	0.022	15	0.970	0.016	15	0.958	0.015	8	0.978	0.002
10	4	0.941	0.011	15	0.951	0.014	13	0.957	0.027	15	0.975	0.003
11	11	0.873	0.076	15	0.968	0.015	15	0.980	0.013	15	0.964	0.004
12	2	0.960	0.002	13	0.988	0.008	15	0.989	0.008	15	0.976	0.005

[a]Same 4 min long stochastic excitation signals repeated 15 times

signals were continuously generated for the entire 60 min test duration. Overall, the total RMS acceleration results indicate that the pseudo ambient vibration excitation approach caused the grid structure to have significantly larger vibration response than was produced by the conventional uncontrolled ambient dynamic excitation sources present in the laboratory.

The identified natural frequencies summarized in Table 15.2 indicate that the conventional ambient vibration test of the grid structure (Case 1) enabled the natural frequencies for 6 of the 12 modes considered to be confidently identified in all 15 of the 4 min long data sets that were considered. Furthermore, the natural frequencies identified from the Case 1 measurements were generally only as consistent with those identified from the pseudo ambient vibration test cases for only the first two modes of the structure, which were located in the frequency band from 0 to 11 Hz. Outside of this frequency band, the pseudo ambient vibration test cases generally enabled the natural frequencies of the structure to be identified with far greater consistency. Another noteworthy observation that can be made from the results shown in Table 15.2 is that the high force level pseudo excitation input (Case 3) did not lead to more consistent identification of the natural frequencies than did its lower input force level counterpart (Case 2). This could be the result of nonlinearities being excited in the grid structure with the higher level pseudo ambient excitation. On average, the 15 repetitions of the 4 min long low force level pseudo excitation inputs yielded the most consistent and reliable results for the identified natural frequencies across the full frequency band of interest for the structure. This observation would indicate that multiple averages of shorter length pseudo ambient excitation inputs yields more consistent results than does a larger number of realizations of the stochastic excitation signal, provided that the length of the stochastic excitation signals is sufficient to obtain enough realizations covering the frequency band of interest for the structure. For this structure, the 4 min duration pseudo ambient excitation signal appears to have satisfied this requirement.

Inspection of the damping ratio and MAC results summarized in Tables 15.3 and 15.4, respectively, lead to similar observations as those made for the identified natural frequencies. The damping ratios identified from the baseline ambient vibration test (Case 1) were generally smaller for each mode than the values obtained from the cases in which pseudo dynamic excitation was applied to the structure. In addition, the damping ratios identified from Case 1 quickly became more uncertain than those identified from the pseudo ambient vibration cases above the frequency associated with the second mode of the structure (10.1 Hz). The damping ratios identified from both of the low force level pseudo ambient excitation cases (Case 2 and Case 4) were generally consistent with each other, and also provided the most reliable damping estimates overall across the full bandwidth of the grid structure. The MAC value results obtained from the test cases employing pseudo ambient vibration excitation were generally superior in consistency and reliability to those obtained from the baseline ambient vibration test (Case 1). The higher level pseudo ambient excitation force (Case 3) did not provide substantially different MAC values from those that were obtained from the lower level pseudo ambient excitation force cases (Case 2 and Case 4). The repeated pseudo ambient excitation signals used in Case 4 were generally a little more consistent for each data segment evaluated across the full frequency band of the structure than from Case 2 in which there were more realizations of the frequencies in the band of interest.

15.6 Conclusions and Recommendations

A large-scale, steel grid structure was evaluated in the laboratory by conventional ambient vibration testing and the proposed pseudo ambient vibration testing approach. The pseudo ambient vibration testing approach combined the uncontrolled and unmeasured ambient dynamic excitation sources in the laboratory with controlled and broadband, stochastic dynamic excitation provided to the structure by a novel, low-cost dynamic excitation system. The dynamic excitation system consisted of a spatially distributed array of off-the-shelf tactile transducers that could provide uncorrelated Gaussian white noise excitation to the structure that had characteristics consistent with those normally assumed in a conventional ambient vibration test. Both low force level and high force level controlled stochastic excitations were evaluated against the baseline uncontrolled ambient vibration test. A pseudo ambient vibration test using multiple averages of a shorter duration of low input force level stochastic excitations was also evaluated in the test program.

The output accelerations recorded from the grid structure from each test case indicated that the pseudo ambient vibration testing approach produced significantly larger global vibration responses for the grid structure ($>1,000$ times larger) than did the uncontrolled sources of ambient dynamic excitation present in the laboratory. This presumably produced greater signal-to-noise ratios in the resulting vibration measurements. The unmeasured outputs from the tactile transducers used as excitation devices for the pseudo ambient vibration test cases produced dynamic excitation of the grid structure that was consistent with the stochastic signals sent to these devices.

The modal parameters (natural frequencies, damping ratios and modal vectors) identified from each of the pseudo ambient vibration test cases were generally found to be superior in terms of consistency and reliability to those identified from the baseline ambient vibration test case. The baseline ambient vibration test case only provided modal parameters that were of a similar level of quality to those obtained from the pseudo ambient vibration test cases in only a very limited band of the overall frequency range of interest of the structure. The frequency band for which the conventional ambient vibration test provided results of a comparable quality to the pseudo ambient vibration test cases was from DC to 11 Hz. The pseudo ambient vibration test case enabled consistent and reliable identification of the grid structure's modal parameters over a much larger frequency band (DC to 156 Hz). The modal parameter identification results also indicated that using multiple averages of limited duration stochastic excitation signals provided results that were consistent with those obtained from a much longer input signal and that the modal parameters identified from the averages of the limited duration input signals were generally more consistent across for the 15 min segments extracted from the 60 min duration vibration measurements. This observation is especially important for the design of similar pseudo ambient vibration tests for full-scale structures.

The pseudo ambient vibration testing approach explored in this paper permitted more consistent and reliable modal parameter results to be identified for the grid structure than did the conventional ambient vibration test. The novel dynamic excitation system provided excellent capabilities for this laboratory application. The structure evaluated in this study is a relatively light and simple structure compared to full-scale constructed systems; but the results of this study provide excellent justification for further exploring the proposed pseudo ambient vibration testing approach on such structures to obtain more consistent and reliable dynamic characterization results without requiring significant experimental and numerical investment above and beyond what is typically required for conventional ambient vibration testing of smaller-scale constructed systems such as short and medium span length bridges. The proposed pseudo ambient vibration testing approach, if implemented on such structures, may lead to more extensive and reliable dynamic characterizations, and more robust damage detection capabilities for these structures than are possible from conventional ambient vibration testing.

References

1. Brincker R, Ventura CE, Andersen P (2003) Why output-only modal testing is a desirable tool for a wide range of practical applications. In: Proceedings of the 21st IMAC, a conference on structural dynamics, society for experimental mechanics, Kissimmee, FL
2. Ciloglu K, Zhou Y, Moon F, Aktan AE (2012) Impacts of uncertainty in operational modal analysis. J Eng Mech 138(9):1059–1070
3. Alwash M, Sparling BF, Wegner LD (2009) Influence of excitation on dynamic system identification for a multi-span reinforced concrete bridge. Adv Civil Eng 2009:1–19
4. Dorvash S, Pakzad S (2013) Uncertainties in identification of a steel bridge dynamic characteristic. In: Proceedings of the 2013 structures congress, ASCE, Pittsburgh, PA, pp 328–339
5. Guillaume P, De Troyer T, Devriendt C, De Sitter G (2007) OMAX – operational modal analysis in presence of eXogenous inputs. In: Proceedings of the 25th IMAC, a conference on structural dynamics, society for experimental mechanics, Orlando, FL
6. Reynders E, Degrauwe D, De Roeck G, Magalhaes F, Caetano E (2010) Combined experimental-operational modal testing of footbridges. J Eng Mech 136(6):687–696
7. Reynders E, Degrauwe D, De Roeck G, Van den Broeck P, Deckers K, Guillaume P (2011) OMAX testing of a steel bowstring footbridge. In: Proceedings of the 29th IMAC, a conference on structural dynamics, society for experimental mechanics, Jacksonville, FL

8. Fernstrom EV, Carreiro JL, Grimmelsman KA (2013) Evaluation of economical dynamic exciters for vibration testing of bridges. In: Proceedings of the 31st IMAC, a conference on structural dynamics, society for experimental mechanics, Garden Grove, CA, pp 423–434

9. Carreiro JL, Fernstrom EV, Grimmelsman KA (2013) Evaluation of low-cost dynamic exciters for controlled dynamic testing of bridges. In: Proceedings of the 2013 structures congress, ASCE, Pittsburgh, PA

10. Fernstrom EV, Grimmelsman KA (2014) Comparative evaluation of excitation schemes for multi-shaker testing of bridges. In: Proceedings of the 32nd IMAC, a conference on structural dynamics, society for experimental mechanics, Orlando, FL

11. Grimmelsman KA, Lindsey J, Norris JT, Dufour RT (2014) A study on the effects of excitation characteristics in operational modal analysis of bridges. In: Compendium of papers, transportation research board 93rd annual meeting, Washington, DC

12. Van Overschee P, De Moor B (1996) Subspace identification for linear systems: theory, implementation, applications. Kluwer Academic Publishers, Boston

13. Allemang R (2002) The modal assurance criterion – twenty years of use and abuse. In: Proceedings of the 20th IMAC, a conference on structural dynamics, society for experimental mechanics, Los Angeles, CA

Chapter 16
Ambient Vibration Testing of Historic Steel-Composite Bridge, the E. Torroja Bridge, for Structural Identification and Finite Element Model Updating

E. García-Macías, R. Castro-Triguero, R. Gallego, and J. Carretero

Abstract The E. Torroja Bridge is a steel-composite bridge which combines inverted steel arch trusses with a concrete deck. This bridge crosses the Guadalquivir River in the small town of Posadas, 30 km far from Córdoba, Spain. It was E. Torroja, the renowned civil engineer who designed and built it until its inauguration in 1951 with an original deck 7 m width. Nevertheless, in 1995 it was remodeled by the author's grandson, José Antonio Torroja, who raised the width of the deck to 11 m and added two new inverted steel arches beside the original ones. In order to assess the structural health condition of the bridge, ambient vibration tests were carried out in June 2014.

The assessment procedures include full-scale ambient vibration testing, modal identification from ambient vibration responses, finite element modelling and dynamic-based identification of the uncertain structural parameters. All the changes experienced by the structure suppose a high level of uncertainty, which affects material's properties and structural schemes in relation to deterioration processes and the structural modifications. Hence, a rigorous updating process in the finite element model was necessary to approach the experimental data with the numeric calculations.

Keywords Ambient vibration • Dynamic characteristics • Finite element model updating • Historic bridge • Operational modal analysis

16.1 Introduction. Description of the Structure

Eduardo Torroja y Miret (1899–1961) is considered one of the most famous engineers in Spain, pioneer in the design of light concrete shell structures. His oeuvre can be understood through his book "Razón y Ser de tipos estructurales" (Philosophy of structures). Most of his structures are now considered as Historic Patrimony.

In 1940, Eduardo-Torroja was commissioned to construct the Bridge over the Guadalquivir River in Posadas, a village located at the south-west of Córdoba, Spain. Because of the civil war, the materials of the bridge, still under construction then, had been seriously damaged. Eduardo-Torroja redesigned the deck, with five spans of 43 m, as well as the structural typology, a steel-concrete composite solution consisting on a compressive reinforced concrete deck bonded to two steel arches, both defined by an upper horizontal beam and a parabolic arch with maximum rise of 6 m. In Fig. 16.1, shots (a) and (b) reflect this original bridge in construction and service phases respectively.

The bridge was repaired in 1983, with some treatments in the deck, making dilatation joints, injections, repairs on the piles' and abutments' walls, as well as replacing some steel components, and finally painting the metallic structure and handrails. Nevertheless, the structural typology was not altered.

In 1991, D. José Antonio Torroja, original author's grandson, was commissioned to carry out an extension of the bridge, changing the deck's width from 6.5 to 11 m. Due to its historic and artistic value, the proposed solution tried to maintain,

E. García-Macías (✉) • R. Castro-Triguero
University of Cordoba, Cordoba, Spain
e-mail: me2gamae@uco.es; me1catrr@uco.es

R. Gallego
University of Granada, Granada, Spain
e-mail: gallego@ugr.es

J. Carretero
INECO
e-mail: jcarreterop@ineco.com
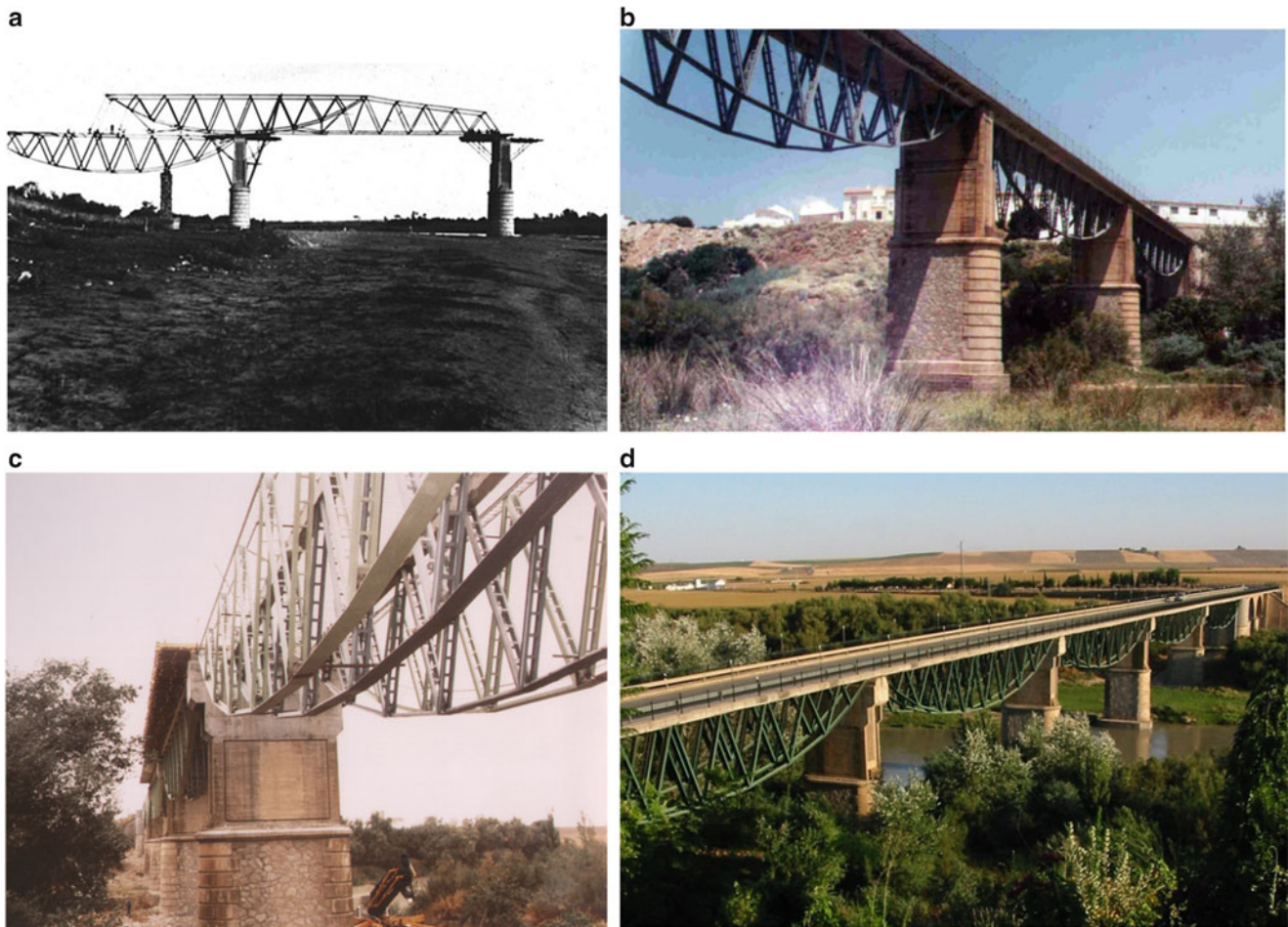
Fig. 16.1 (**a**) Original Bridge under construction, 1940; (**b**) original Bridge in-service; (**c**) operations of deck's width increment; (**d**) current bridge in service

as much as possible, the structural typology. In order to support the new increased deck, two new arches were added and attached to the original ones by a tubular truss structure. They are exact to the original ones which were conserved thanks to their good state of conservation. The original deck was completely removed because the new configuration required the definition of upper reinforcements so that they could resist negative transversal bending efforts.

Since then, the structure has not suffered any modification else. At the current state, the bridge is composed on five simply supported spans of 43 m, as well as two lateral spans of 20.8 and 48.60 m, supported by a rigid system of arches made of concrete and masonry. The deck is defined by a concrete slab with 11 m width. This deck has two different variants. On one hand, the five simply-supported spans are defined with a concrete slab of 22 cm thick. It is also defined four concrete longitudinal beams at the heads of the steel arches, with a section of 47×43 cm. In the case of the two lateral spans, the original deck was completely removed and new prefabricated concrete slabs of $3 \times 5.075 \times 0.424$ m^3 were set up instead.

Historic Bridges are those which have a special interest: social, cultural or artistic. Hence, inhabitants are especially concerned about the importance of the conservation of these structures, part of their historic heritage. Because of this, the need of Structural Health Monitoring (SHM), which employs non-destructive monitoring techniques, as well as damage detection algorithms are acquiring an increasing interest in the definition of the actual state of the structure and the planning of preventative actions or repairs. However, these techniques require well-defined theoretical models of these structures. Normally, these models are developed with finite element models, which usually require some simplifying assumptions. These assumptions refer to topology, material's behavior, stiffness of supports, non-structural elements, differences between designed and as-built structure . . . etc. These models may or may not truly represent the actual behavior of the structure, concretely their dynamic properties (natural frequencies and mode shapes). This aspect is even more dramatic in the case of Historic Bridges because of the uncertainty associated with time, deterioration and lack of reliable information in some cases.

Identification techniques provide a real value of the dynamic characteristics of the bridge. Thus, the analytical models can be updated in some way so that they will be able to predict natural frequencies and mode shapes with an appropriate level of accuracy. Updating can be carried out by modifying some uncertain parameters as boundary conditions, links between certain elements, material's properties ... etc., in order to minimize the differences between analytical and experimental results [1].

The State of the Art contains many studies of finite element analysis and experimental investigation of historic bridges. Ercan and Nuhoglu [2] carried out a 3D solid finite element model of a historical aqueduct called Vezigasi in Turkey. Furthermore, based on an ambient vibration monitoring, discrepancies between analytical and experimental dynamic properties were minimized by varying boundary conditions and material's properties. Despite the old age of the structure, which dates from 1678, and the great uncertainty associated to masonry, excellent fittings were reached between analytical and experimental results. An excellent work carried out by Marques et al. [3] shows the results of an ambient vibration of the Trezói Bridge, a metallic riveted bridge opened to service in 1956. A 3D very complex finite element model was developed what led to a very good agreement between numerical and experimental frequencies. Gentile and Saisi [4] showed the results of the dynamic tests of two historic structures: a masonry bell tower, dated back to the sixteenth century, and an iron arch bridge built in 1889. Altunisik et al. [5] developed a 3D solid finite element model for a mid-nineteenth century solid arch in Turkey, the Mikron arch. Moreover, they carried out an updating process based on ambient vibration testing, with good fittings between analytical and experimental natural frequencies, below 2.5 %. Brencich and Sabia [6] studied the Tanaro Bridge, 18-span masonry structure built in 1866. Investigation of the bridge's natural frequencies, mode shapes, and damping ratios, identified by dynamic testing, were carried put both during service and at different stages of its demolition.

This current research investigates the details of finite element modeling, OMA, and finite element model updating of E. Torroja's Bridge. The first part of the study shows the 3D finite element modeling of the historic bridge and the numerical modal analysis using the SAP2000 software. Subsequently, the modal testing and the enhanced frequency domain decomposition (EFDD) method in the frequency domain and the SSI method in the time domain extracted the bridge's experimental dynamic characteristics. A comparison of analytically and experimentally identified dynamic characteristics revealed some differences among results. Last, changing of boundary conditions reflected the current behavior updated in the finite element model of the bridge.

16.2 Finite Element Modeling

16.2.1 Effects of the Change in Original Design

The structure experienced a remarkable process of transformation in its typology. Some original elements were kept in the re-design so some uncertainties due to this fact are expected. In order to better understand the actual change in the structural behavior of the bridge, there were generated two FEM models: Original stage and current stage of the bridge, so that they could be compared in terms of their analytical dynamic properties.

In both models, lateral spans were not considered because of their much stiffer behavior in comparison with steel-concrete composite ones. Due to the large size of the E. Torroja's bridge including five simply supported spans, the FE models of the overall bridge would result in a large computational cost. Therefore, a simplified model of a single span was applied. The structures were modeled after the design drawings as shown in Figs. 16.2 and 16.3, by using the general FE software SAP2000. All elements were modeled with beam elements except for the deck for which thick shell elements were used. Where there were considerable distances between beam's gravity centers as well as the simulation of the exact bearing

Fig. 16.2 Elevation view of E. Torroja Bridge
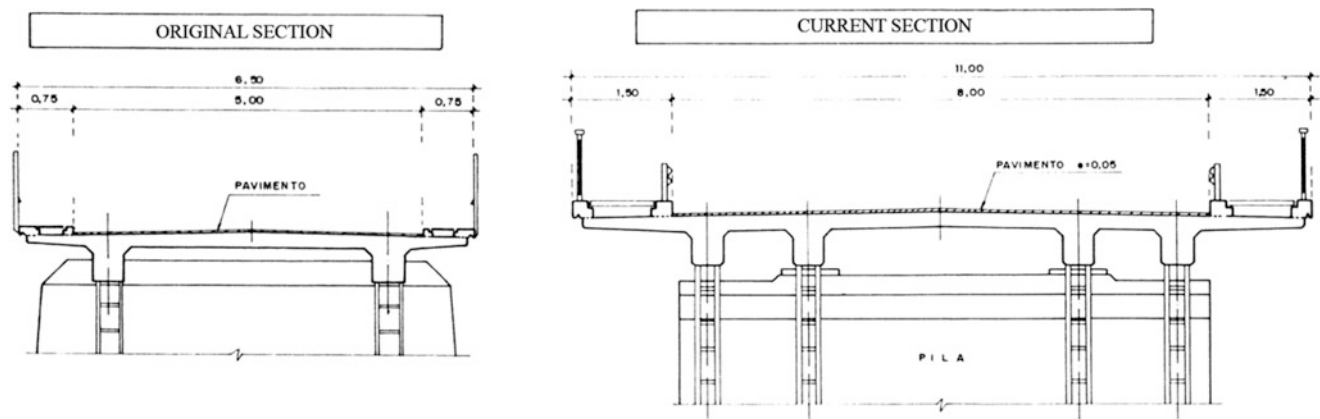
Fig. 16.3 Original and re-designed cross sections
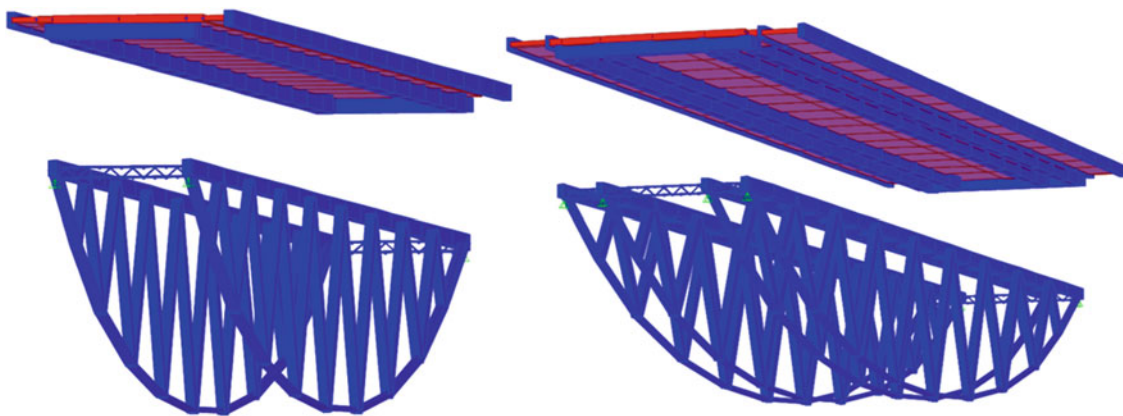
Fig. 16.4 (*Left*) FEM original state; (*Right*) FEM current state

Table 16.1 Comparison in terms of natural frequencies between old and new design

–	Old design	Current design
Mode of vibration	Freq (Hz)	Freq (Hz)
First torsional mode	3.12	3.44
First bending mode	4.11	4.35
First transversal bending mode	5.12	4.12
Second torsional mode	6.32	6.44
Second bending mode	8.56	8.94

points, infinitely rigid beams were employed (only several higher orders to avoid instability of the modal analysis). It was also considered the deck to be orthotropic with an increment of 20 % (according to normal experience) in transversal bending stiffness in the concrete slab in order to take into account the increment of steel reinforcement in that direction. The two FE models are shown separately for deck and steel arches in Fig. 16.4.

The properties of the employed materials are summarized in Table 16.1. Notice the density of steel is increased to 8 t/m^3 in order to include secondary elements not considered in the model as welds, bolts, ancillaries . . . etc.

A good way to understand the changes introduced by its re-design in 1991, is to compare the steelwork tonnage (weight of steel per area of deck), as well as its dynamic properties in terms of natural frequencies. The weight ranges are 66.22 and 79.33 kg/m^2 for old and new design respectively. The comparison in terms of natural frequency is indicated in Table 16.1.

As it can be seen in Table 16.1, the differences are minimal in terms of natural frequencies. This fact indicates that the actual behavior of the structure did not deeply changed because of adding the two new arches. It can be thought that the addition of new mass as much to bending as to torsional modes is counteracted by an increment of stiffness: bending stiffness with just the addition of the new arches and deck's extension, and torsional stiffness by distance between original and new arches.

16.2.2 Current Design's FEM Model

Once both the original and current bridges were compared, the FEM model of the current one was fully developed in order to count on a model as much accurate as possible. The elements of the steel arches are defined as built-up sections, composed by standard steel sections bonded by plates acting as battens. The horizontal brace of the arches are defined by two UPN120 and the arches by two IPN200, joined in both flanges by steel plates of dimensions $400 \times 50 \times 8$ mm and $210 \times 50 \times 8$ mm every 50 cm, respectively. The complete modelling of all the elements was unfeasible, thus beam elements were implemented with effective mechanic properties (area, moments of inertia and torsional constant taken from the equivalent hollow section according to Spanish code EAE). The weight of the battens were taken into consideration as a uniform load acting on arches' beams. The rest of masses and material's properties are summarized in Table 16.2.

Once the model were defined, a modal analysis were carried out in SAP2000. This software only permits the definition of concentrated masses, therefore a sensitivity analysis of the natural frequencies were studied by varying the mesh-size of the elements. The five main mode shapes are illustrated in Fig. 16.5.

Table 16.2 Masses and materials of the E. Torroja Bridge's FEM model

Item	Unit	Value
Per-unit-length mass of security barriers	kg/m	14.66
Per-unit-area mass of asphalt	kg/m^2	110
Young's modulus of concrete slab	MPa	30,000
Poisson's ratio of concrete slab	–	0.3
Density of concrete slab	kg/m^3	2,500
Young's modulus of steel	MPa	210,000
Poisson's ratio of steel	–	0.3
Density of steel	kg/m^3	8,000
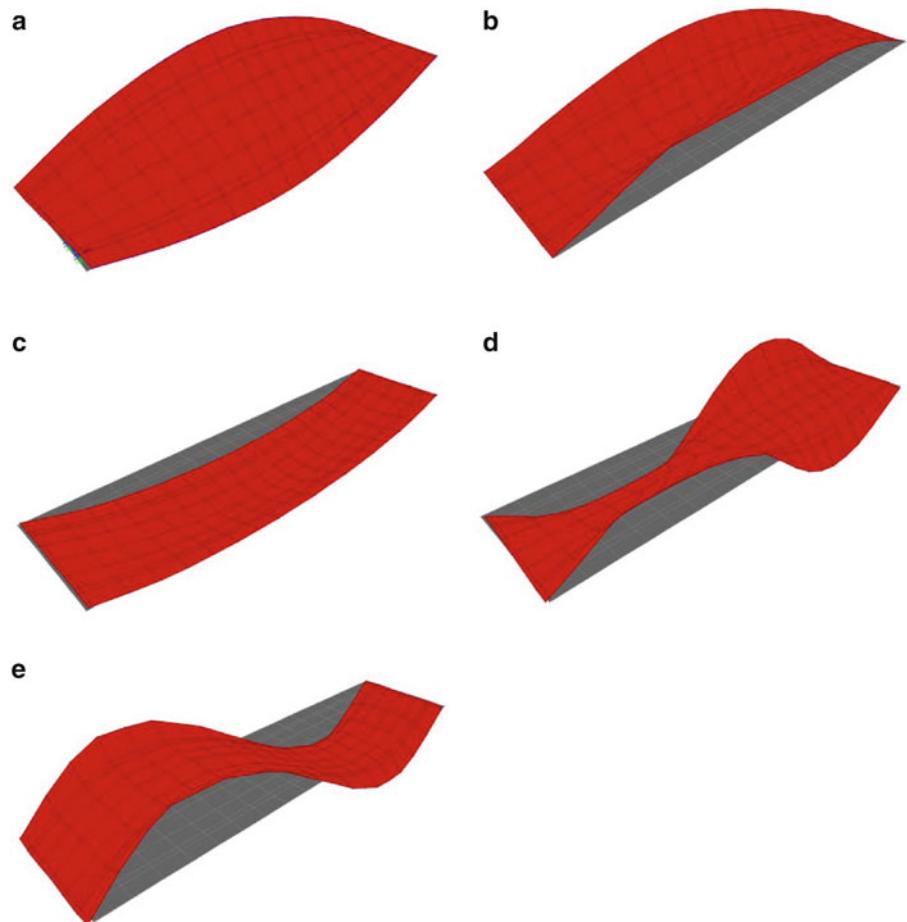
Fig. 16.5 (**a**) First torsional mode f = 3.44 Hz; (**b**) second torsional mode f = 4.11 Hz; (**c**) first bending mode f = 4.35 Hz

16.3 Operational Modal Analysis

Structural Health Monitoring (SHM) is the technology which led the maintenance politics into a more effective stage, through a more reliable knowledge of the actual behavior of the structure what provides more realistic computational models. It is possible to include some parameters so that to simulate the existence of structural failures, hence, structural damage identification can be also carried out.

Identification of dynamic characteristics of the system (mode shapes, natural frequencies and damping ratios) from the accelerations records, the classical techniques of Experimental Modal Analysis (EMA) [7] obtains the dynamic properties under well-known forces. However, this technique is toughly scaled to civil structures because of their huge dimensions. On the contrary, in last years the appearance of Operational Modal Analysis (OMA) permits the monitoring of a structure with no need to know the exterior excitements. This technique permits the monitoring of the structure in service, with no need to install excitation devices on the structure. This technique was proposed by Farrar et al. [8], from the James et al.'s works [9].

The equipment used for the ambient vibration tests includes 12 uniaxial accelerometers, a 17-channel data acquisition system, and approximately 300 m of uniaxial accelerometer cables (Fig. 16.6). The minimum frequency range and sensitivity of the accelerometers are 0.1 Hz and 10 V/g, respectively. Ambient vibration tests selected the frequency span of each measurement to be 0–50 Hz. Total duration of each measurement test setup was 30 min. The accelerometers were placed as shown in Fig. 16.7. The span was divided in four lines, 2 and 3.8 m from the center, in where the accelerometers were placed in four set-ups. Two references were kept steady along the whole process so that the set-ups could be related later to define the mode shapes. According to the numerical simulations, Fig. 16.5, it was only seen to be necessary to monitor the vertical responses. The collected signals were transferred into the own software.

The six modes represented in Fig. 16.5 were taken from the numerical simulation to be compared to the ones obtained experimentally. Figure 16.8 depicts these same modes obtained from experimental measurements. A summary of the comparison of modal parameters obtained analytical and experimentally appears in Table 16.3.

16.4 Finite Element Model Updating

As it can be seen in Figs. 16.5 and 16.8, there exists a reasonable correlation between analytical and experimental mode shapes. Despite the similarities, some differences between natural frequencies arise from uncertainties included in the theoretical simulation. In order to approximate the simulated behavior to reality, an updating process of the initial finite element model of the bridge was carried out to minimize the discrepancies as much as possible. It was not possible to test the materials' properties (Young's modulus, Poisson's ratios and densities), thus they remained constant during the process. This research studied the sensitivity of the dynamic parameters to boundary conditions and rigidity of the joints between steel elements by manual tuning.
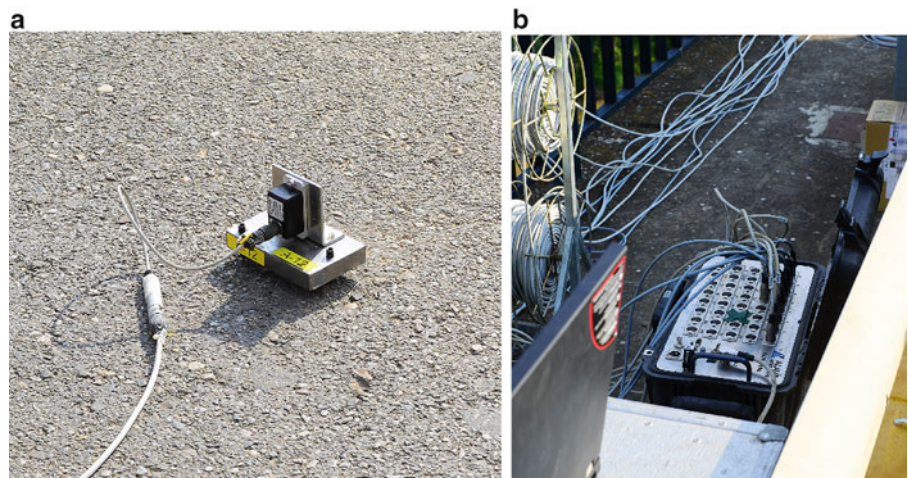
Fig. 16.6 Ambient vibration testing equipment. (**a**) Data logger and (**b**) accelerometer
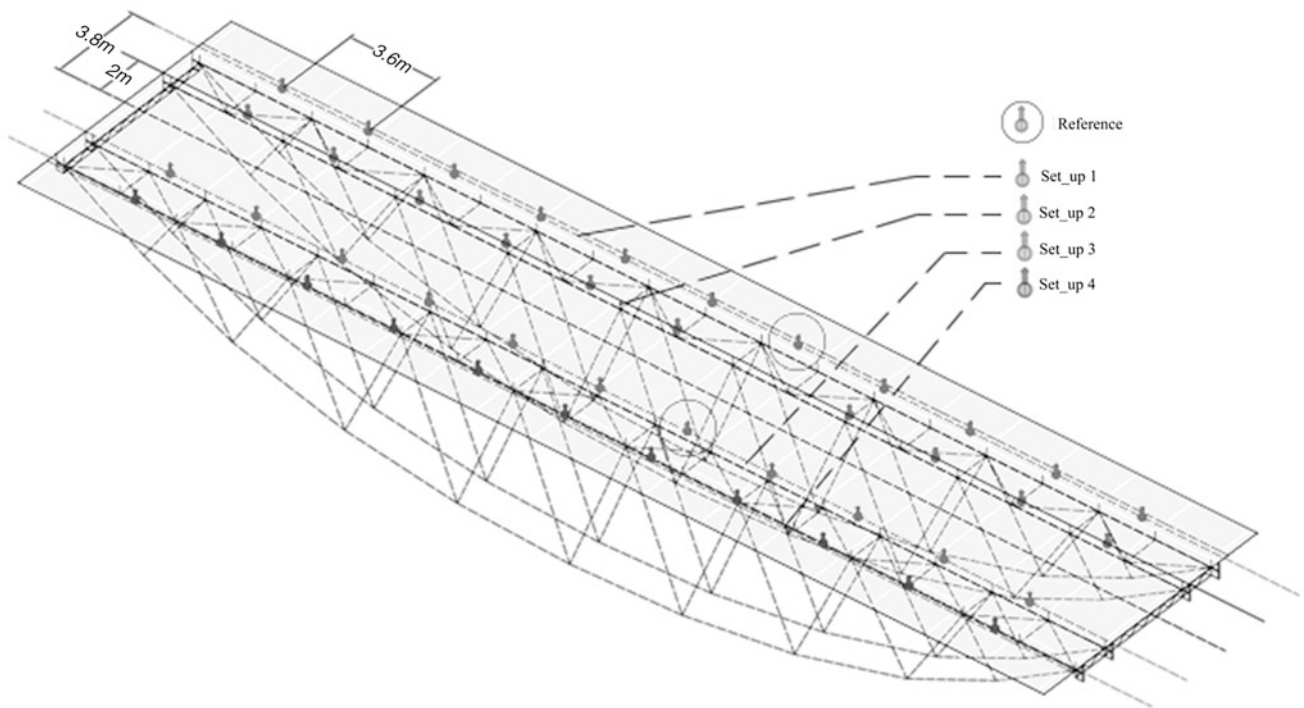
Fig. 16.7 Accelerometer locations on the E. Torroja's Bridge

Fig. 16.8 Experimentally identified modal shapes
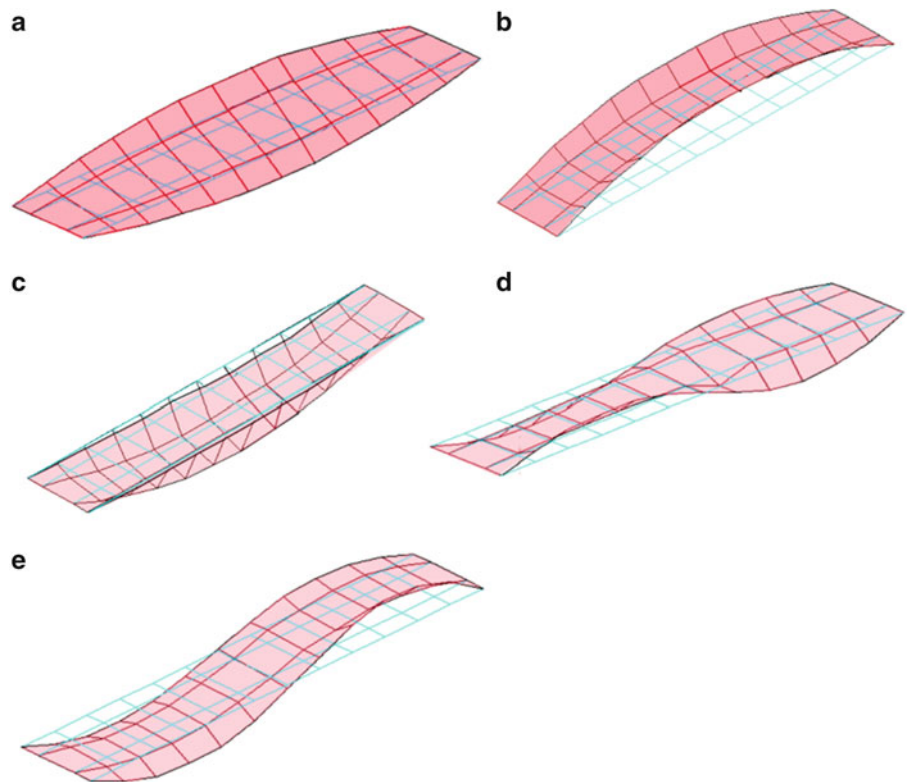
Finally, the best fitting was obtained by considering free longitudinal translation in one support as well as free rotation on arches' and horizontal braces' trusses. A comparison of the modal parameters of the updated model with the experimental modal parameters appears in Table 16.4. Apparently, the updated model exhibits good correspondence between the natural frequencies and the measured ones.

Table 16.3 Comparison of analytically and experimentally identified dynamic characteristics

–	FEM	Experimental
Mode number	Frequencies (Hz)	(Hz)
a	3.440	3.273
b	4.110	3.677
c	4.353	3.876
d	5.883	5.753
e	8.951	7.700

Table 16.4 FEM and experimental frequencies after finite element model updating

–	FEM frequencies (Hz)		Maximum differences n%)	
Mode shape	Before update	After update	Before update	After update
a	3.440	3.358	5.10	2.60
b	4.110	3.83	11.78	4.16
c	4.353	4.26	12.31	9.91
d	5.883	5.65	11.77	1.79
e	8.951	8.23	16.25	6.88

Nevertheless, there are still some differences up to 10 %. It could be due to material's uncertainties, such as the elastic properties of the original arches, as well as semi-rigid joints of elements and some connectivity between adjacent spans (through non-structural members).

16.5   Conclusion

This study summarizes the dynamic-based assessment of E. Torroja's bridge, a historic bridge which dates from 1940. The outlined research includes 3D finite element modeling, OMA, and finite element model updating. The conclusions and suggestions for further studies arising from this research are the following:

- Two 3D FEM models of the E. Torroja's bridge were developed and compared: original and current state. The variations only changed the dynamic properties slightly, because of a compensated adding of mass and stiffness. Moreover, it was carried out a modal analysis and the main bending and torsional shape modes were collected.
- The experimental measures provided information from the frequency range of 0–50 Hz. Also, modal damping ratios were calculated. Within this frequency range, by using EFDD and SSI methods, the mode shapes corresponding to the theoretically observed were identified. A good correlation appeared between the dynamic characteristics obtained from analytical and experimental results.
- Despite good correlation between mode shapes, when comparing the analytical and experimental model parameters some differences arose among natural frequencies. An updating process of the finite element model of the bridge was carried out by changing the boundary conditions and rigidity of joints to minimize the differences.
- The difference between analytical and experimental natural frequencies before finite element model updating reached a maximum value of 12.31 %; however, this difference became less than 10 % after finite element updating.
- Better fitting between analytical and experimental dynamic properties could be reached by updating of some other parameters as rigidity of joints, connectivity of adjacent spans and elastic material's properties.
- All these results show that OMA is applicable to check the state of historic bridges in which destructive methodologies results unfeasible.

References

1. Chang CC, Chang TYP, Zhang QW (2001) Ambient vibration of long-span cable-stayed bridge. J Bridg Eng 6(1):46–53
2. Ercan E, Nuhoglu A (2014) Identification of historical Veziragasi aqueduct using the operational modal analysis. Sci World J 2014:1–8
3. Marques F, Moutinho C, Magalhães F, Caetano E, Cunha Á (2014) Analysis of dynamic and fatigue effects in an old metallic riveted bridge. J Constr Steel Res 99:85–101
4. Gentile C, Saisi A (2013) Operational modal testing of historic structures at different levels of excitation. Construct Build Mater 48:1273–1285
5. Altunisik AC, Bayraktar A, Sevim B, Birinci F (2011) Vibration-based operational modal analysis of the Mikron historic arch bridge after restoration. Civ Eng Environ Syst 28(3):247–259
6. Brencich A, Sabia D (2008) Experimental identification of a multi-span masonry bridge: the <i> Tanaro Bridge. Constr Build Mater 22(10):2087–2099
7. Maia NMM, e Silva JMM (1997) Theoretical and experimental modal analysis. Research Studies Press, Taunton
8. Farrar CR, James GH III (1997) System identification from ambient vibration measurements on a bridge. J Sound Vib 205(1):1–18
9. James III GH, Carne TG, Lauffer JP (1993) The natural excitation technique (NExT) for modal parameter extraction from operating wind turbines. NASA STI/Recon technical report No, 93, 28603

Chapter 17
Tuning of Finite Element Models of Multi-girder Composite Structures

Elena Mola, Murathan Ahmet Paksoy, Giovanni Rebecchi, Giorgio Busca, Matteo Scaccabarozzi, and Marta Berardengo

Abstract Dynamic load testing is an important part of the acceptance process for new bridges in Italy. This paper is an overview of a part of a field-testing program carried out to investigate the dynamic properties of the five main new viaducts along the Brescia-Milano highway (BreBeMi) before their operation. Among them, the focus of the paper is on the Muzza Bridge and the VX1 Bridge: they are examples of continuous multi-girder composite structures. VX01 Bridge has a total length of 112 m with three continuous spans while Muzza spans approximately 80 m with a significant skew angle. Structural analysis was performed with the commercial FE software named Midas Gen. Modal parameters were obtained from experimental testing and were then employed in the calibration of the numerical models. The experimental evaluation of the performances of bridges proves very advantageous since it provides a benchmark for the validation of the numerical simulations, which often exhibit an inherent uncertainty. The presence of simplifications and assumptions in the numerical analysis may lead to results that don't accurately predict the service life conditions of the bridge. In this case study, a comparative discussion of experimental results and numerical predictions is carried out with reference to the two different, seismic isolated, highway bridges mentioned above, both of which were tested using both environmental excitation and forcing: a large set of data was thus collected and an extensive model tuning activity could be carried out, allowing a thorough sensitivity analysis of a number of modelling parameters. The effects of different assumptions used when modelling some peculiar features of composite bridges, such as diaphragms, stiffeners, skew angle, expansion joints, rubber bearings etc., on the prediction of the dynamic properties of the composite viaducts, were investigated. At the same time, a comparison between the experimental results provided by ambient and forced vibration test results was carried out, based on their effectiveness in providing a reliable and useful benchmark for model tuning. Some conclusive suggestions based on the case study are finally addressed to structural engineers needing to set up an efficient procedure to perform similar tests and computer analyses.

Keywords Operational modal analysis • Experimental modal analysis • Finite element model • Model tuning

17.1 Introduction

The new highway called BreBeMi, connecting the Northern Italian cities of Bergamo, Brescia and Milano, was opened to traffic in July 2014. The highway is 65 km long and includes five large bridges: three of them are r.c. hollow core girder bridges, two of them are composite steel-concrete girder bridges. In Italy, the latest version of the Italian Building Code, i.e. '[1]', requires that, before bridges considered 'strategically relevant' can be opened to the public, some dynamic tests be carried out, in addition to the traditional static load tests. In the case of the BreBeMi highway, the five above mentioned bridges were considered 'strategically relevant' by the Owner and by the design validator, so that a full experimental campaign was designed and carried out on all of them.

E. Mola (✉) • M.A. Paksoy • G. Rebecchi
ECSD Srl, Via Goldoni, 22, Milan 20129, Italy
e-mail: elena.mola@ecsd.it

G. Busca • M. Scaccabarozzi • M. Berardengo
Dipartimento di Meccanica, Politecnico di Milano, via La Masa 1, Milan, Italy

In particular, for design and construction validation purposes, [1] requires for the first experimentally identified modal frequency to be 'comparable' to the first modal frequency derived from 'the analysis'. Such a generic sentence does not offer proper guidance to the project validator, to the structural designer and to the designer of the experimental tests. In this regard, the current Italian code is lacking, which calls for the designers, analysts and validators to merge their respective skills in order to draft testing protocols able to provide a larger set of data than the one strictly required by the normative documents.

In fact, in order to properly carry out a meaningful comparison between the dynamic properties of a flyover as derived by an eigenvalue analysis of a FE model of the bridge and the dynamic properties as experimentally identified by means of Operational or Experimental Modal Analysis, it is necessary to extend the comparison not only to the 'first natural frequency', but to a significant number of natural frequencies and, most of all, to the related mode shapes.

In fact, when a good match, not only between the natural frequencies, but also between the mode shapes is attained, a much better validation for the model is provided and a deeper insight into the correspondence between the design assumptions and the as-built structure is guaranteed.

In this framework, it is easy to understand that a number of different, specialized skills are necessary when carrying out dynamic tests for design and construction validation purposes: on one hand, the measured data and the data treatment procedures adopted to experimentally estimate the dynamic properties must be accurate and efficient, on the other hand, the numerical counterpart, i.e. the parameters and assumptions used when implementing the finite element model and the structural analysis techniques used to derive the dynamic properties, must be refined and accurate enough to provide a reliable numerical benchmark for the experimental data.

Since every numerical model is affected by a degree of uncertainty, though, due to the inherent statistical nature of the material properties, boundary conditions, loads, mass distribution, computational errors, etc., there are a number of modelling parameters that affect the results. It is usually necessary to carry out a parameter sensitivity test on most numerical models in order to determine how strongly the variation of some of the basic or most critical modelling assumptions affect the results. Such sensitivity tests gauge the reliability and robustness of the model, which is very useful for the designer to determine, but most of the time they remain a purely numerical simulation exercise that has no experimental benchmark. Having an external database to use as a benchmark for model validation is thus a very rare but very useful opportunity.

When dynamic tests are carried out, they do provide this set of data: when comparing the results of a numerical analysis to the results of OMA or EMA tests, a very useful model validation tool thus becomes available to the analyst.

The comparison between the experimental and numerical results, in fact, provides an invaluable wealth of information about the behaviour of the as-built structure vs the prediction of the model: when the initial match between the numerical and experimental results is carried out, a model tuning or updating process can be started, which in the end will allow a refinement of the numerical analysis model and the reduction of the inherent uncertainty in the definition of some of its parameters.

It must be clarified that a correct and useful model tuning procedure cannot be carried out by simply varying all the possible parameters without engineering judgment in order to try and match the experimental data set in the best possible way: this kind of approach is totally useless and even counterproductive.

On the other hand, the correct approach to model tuning takes into account that the error between the measured data and the numerical prediction can be due to a vast number of reasons, not last inadequacies and/or mistakes in the construction process, which must be properly highlighted by the testing activity, whose main purpose is in fact to provide insight on the quality of the constructed structure. If, even after a refinement of the numerical model, a significant mismatch between the predictions and the results remains, then a red flag must be raised and some other reasons for said mismatch must be found, not in the numerical model but in the construction process or in the tests themselves, because even the data measurement and treatment process is affected by uncertainties or mistakes.

In the following, the model tuning activity carried out on the numerical models of two of the five main bridges of the BreBeMi highway will be presented. The testing and modelling activities carried out on the other bridges is thoroughly reported in (Cigada et al. [2]). The two chosen bridges, named Muzza and VX01, have composite steel concrete decks and were analysed by means of the commercial structural analysis software Midas Gen v.13.

Both bridges were then tested: both Operational and Experimental Modal Analysis were carried out and the results of the two sets of tests were used as a benchmark to tune the models. In the following paragraphs, at first, a description of the bridges will be provided, followed by a detailed description of the numerical models. The experimental results will then be presented and compared to the numerical ones. In the final section, the model tuning activity will be discussed and the results from the tuned model will be compared to the experimental ones, highlighting the improvement in the match between the two data sets.

17.2 Description of the Structures

17.2.1 VX01 Bridge

The new VX bridge was constructed between 2011 and 2013 as an essential link for the motorway between Brescia and Milano and is now in operational phase. The bridge consists of three spans for a total length of 112 m, with the longest span, 44 m long, in the middle, and two 33 m long side spans, as represented in Fig. 17.1. The deck is 17.05 m wide including the 0.7 m wide curbs to support the safety barriers. The three-span composite multi-girder bridge consists of four continuous 180 cm thick IPE girders and a 30 cm thick concrete deck. The girders and deck are connected by shear studs to achieve composite section behaviour. Each girder is spaced 3.7 m (center to center), as shown in Fig. 17.2. Lateral and torsional restraints to the girders are achieved at the supports and by means of intermediate transverse diaphragm beams along the bridge length.

The bridge is supported at the midspan by two wall-type piers and at the ends by abutments. High damping rubber bearing pads are used as supports, between the deck and the piers. On each pier, four elastomeric pads are placed under each longitudinal beam. The technical properties of the rubber pads are summarized in Table 17.1. The bridge is equipped with expansion joints at two abutments. The expansion joint is designed to allow relative displacements up to 20 cm only in the longitudinal direction of the bridge.

Fig. 17.1 VX bridge: view
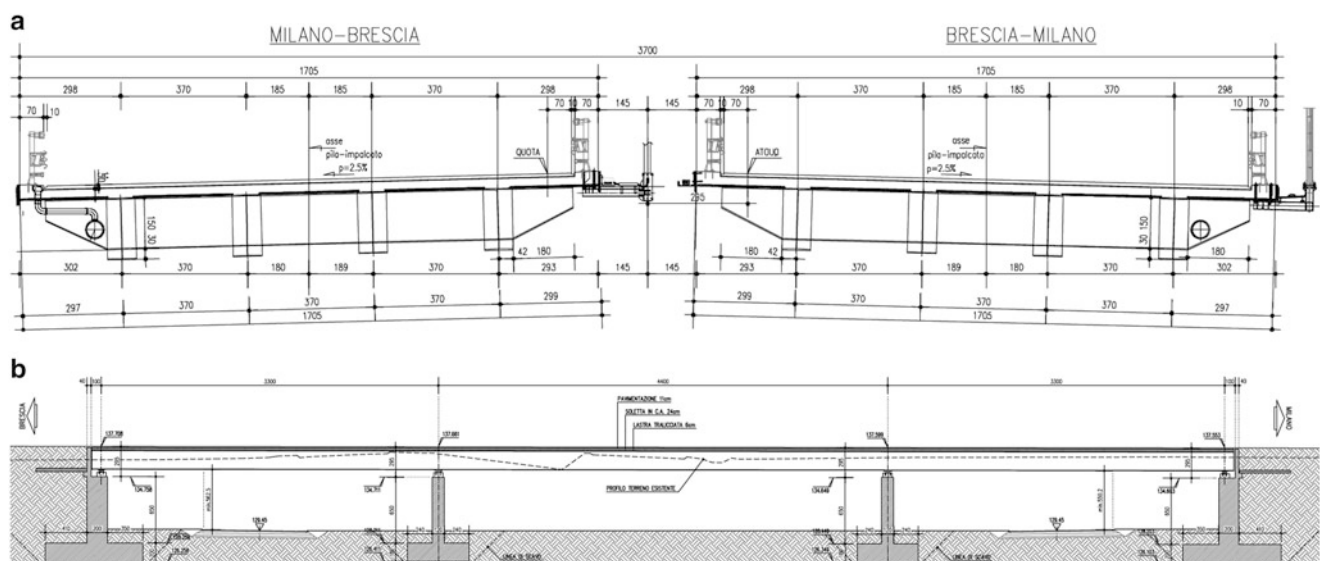
Fig. 17.2 VX bridge, (**a**) cross section (**b**) longitudinal section

Table 17.1 Technical details of the elastomeric isolators

	Diameter (mm)	G_{rubber} (MPa)	Δ (mm)	K_h (kN/mm)	K_v (kN/mm)
Abutment(Milano)	400	0.8	200	1.01	912
Abutment(Brescia)	400	0.8	200	1.01	912
Pile	550	0.8	200	1.81	1,683
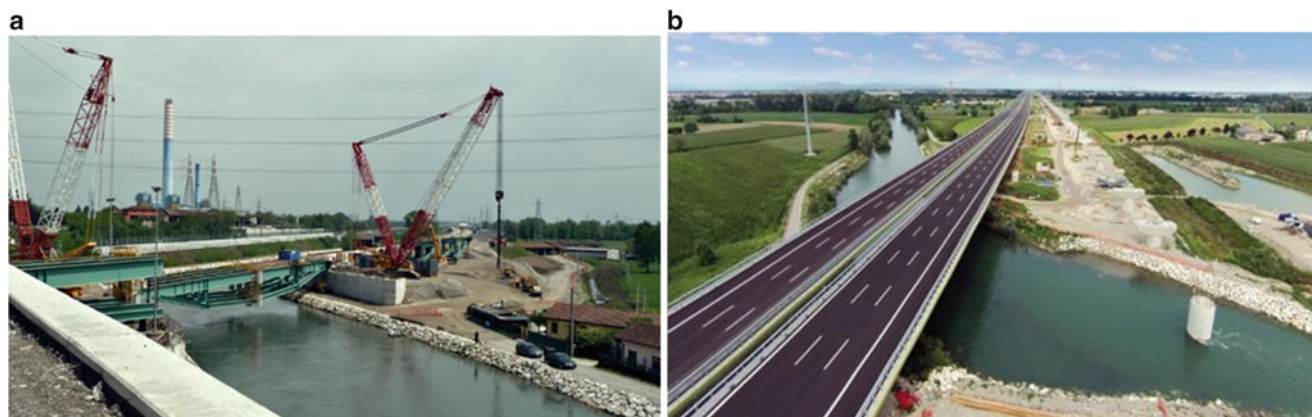
Fig. 17.3 Muzza bridge, (**a**) view during construction, (**b**) view in final configuration
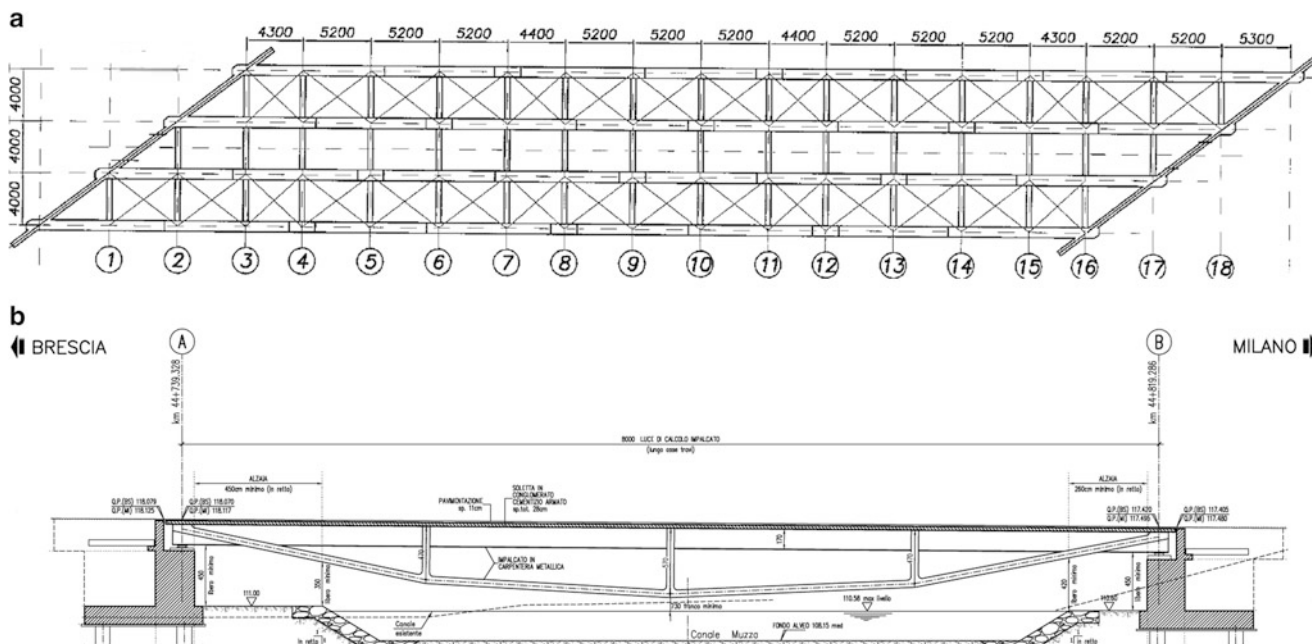
Fig. 17.4 Muzza bridge, (**a**) plan view (**b**) longitudinal section

17.2.2 MUZZA Bridge

The new Muzza bridge consists of two skewed, parallel sections, one for the northern and one for the southern way. The construction of the bridge was completed in 2013 and the flyover now serves as an important part of the BreBeMi motorway between Brescia and Milano (Fig. 17.3). The bridge consists of a single span with a total length of 80 m, as represented in Fig. 17.4. The deck is 17.05 m wide including the 0.7 m wide curbs to support the safety barriers. The deck consists of four continuous 170 cm thick IPE girders and of top a concrete slab, approximately 28 cm thick. The girders and deck are connected by shear studs to achieve composite section behaviour. Each girder is spaced 4.0 m (center to center). Three struts for each girder provide the load transfer to the steel elements located below. Lateral and torsional restraints to the girders are achieved at the supports and by means of intermediate transverse bracings along the bridge length.

Table 17.2 Technical details of the elastomeric isolators

	Diameter (mm)	G_{rubber} (MPa)	Δ (mm)	K_h (kN/mm)	K_v (kN/mm)
Abutment(Milano)	500	1.4	150	3.52	2,406
Abutment(Brescia)	500	1.4	150	3.52	2,406

The bridge is supported at two ends by reinforced concrete abutments. The bridge superstructure is supported on the abutments by using high damping rubber bearing pads. The technical properties of the rubber pads are summarized in Table 17.2. The bridge is equipped with expansion joints at two abutments. The joint is designed to allow relative displacements up to 20 cm only in the longitudinal direction of the bridge.

17.3 Numerical Analysis: Structural Model and Engineering Assumptions

The models of the two bridges were developed in order to provide the estimate of the modal properties to be compared to the experimentally derived results. In principle, the main dynamics of interest is that of the deck, in ordinary service life condition, i.e. in the low vibration field. The presence of the elastomeric isolators almost completely disconnects the dynamic behaviour of the deck from that of the substructure, i.e. piers and foundations: the much lower lateral stiffness of the rubber bearing supports can be assumed as a low stiffness spring working in series with a spring with a much higher stiffness, representing the piers. In order to gauge the contribution of the piers to the global dynamic, though, it was decided to include them in the modelling, to increase the accuracy of the model, even if, for practical purposes, the rubber bearings could be considered as directly restrained to the ground.

As for the deck, it is crucial to make wise modelling choices in order to replicate in the most accurate possible way the stiffness and the mass distribution, because these parameters strongly affect the estimate of the dynamic properties.

A finite element model of composite decks can be developed in several ways. Simple models with large elements are quick to implement and solve but they may provide overly approximated results. Complex models with a fine mesh can yield more realistic results, at the cost of increased computational time. An ideal model yields accurate results with minimal computational time.

In the present case, the most common element types, i.e. beams, trusses and shells, were used for modelling the global behaviour of the bridges. Special structural elements like springs and rigid connections were also employed in the models to provide the most accurate internal constraints and boundary conditions. In order to achieve the most efficient balance between computational time and accuracy, the analyst should decide on a good meshing size for the elements. In the present study, the mesh size is not governed by a variation in the geometry of the bridge along the longitudinal axis, as both of the bridges do not contain a curvature: the geometry remains constant along the length of the bridge. Of course the main factor to decide on the mesh size of the elements depends very much on the types of element used in modelling, and on their shape functions. For this reason, there is no general hand rule to fit the needs of an engineer. The meshing is a specific property of each individual model. In this specific case, it was also important to correctly locate the joints of the mesh where the accelerometers would be installed during the tests, or close enough. In this way, the local values of the mode shapes vectors derived by the model could be easily compared to those derived from the tests at the exact location of the sensors.

The difficulty presented by these bridges is the composite steel concrete structure of the deck: it is difficult to choose the best modelling technique to replicate the interaction between the two substructures, which in turns affects the dynamic properties. Different finite element modelling options used are shown in Figs. 17.5 and 17.6 for VX and Muzza bridges. Model N.1 is an equivalent beam representation of the composite structure with an equivalent Poisson's ratio, mass density, and Young's modulus. In Model N. 2 of the bridge, two different layers of structural nodes were arranged to model the superstructure. The first layer of nodes were defined to create the plate elements representing the reinforced concrete deck and the second layer, below the first, was defined to represent the girders with beam elements. The plate elements used in the model have 5 degrees of freedom per node, whereas the steel girder elements have 6 degrees of freedom per node. A final model named Model 3 represents the entire superstructure by using only plate elements. Except for Model N.1, all the models are capable of capturing the effect of the offset between the center of gravity of the steel girder and the center of gravity of the deck slab. In Model N.3, the error induced by the incompatibility between the in-plane rotational degree of freedom and the drilling degree of freedom of plate elements was overcome by decreasing the mesh size.

In general, all of the three above-mentioned modelling options give reasonable results for the first mode of vibration but differ significantly in their ability to predict subsequent modes. The representation of composite action presented the first challenge in the construction of the finite element models. After the results of the experimental tests, though, a direct comparison between the modal parameters given by the different modelling options and those derived from the tests was carried out, as will be detailed in the following, in order to confirm the final choice of the most effective model.
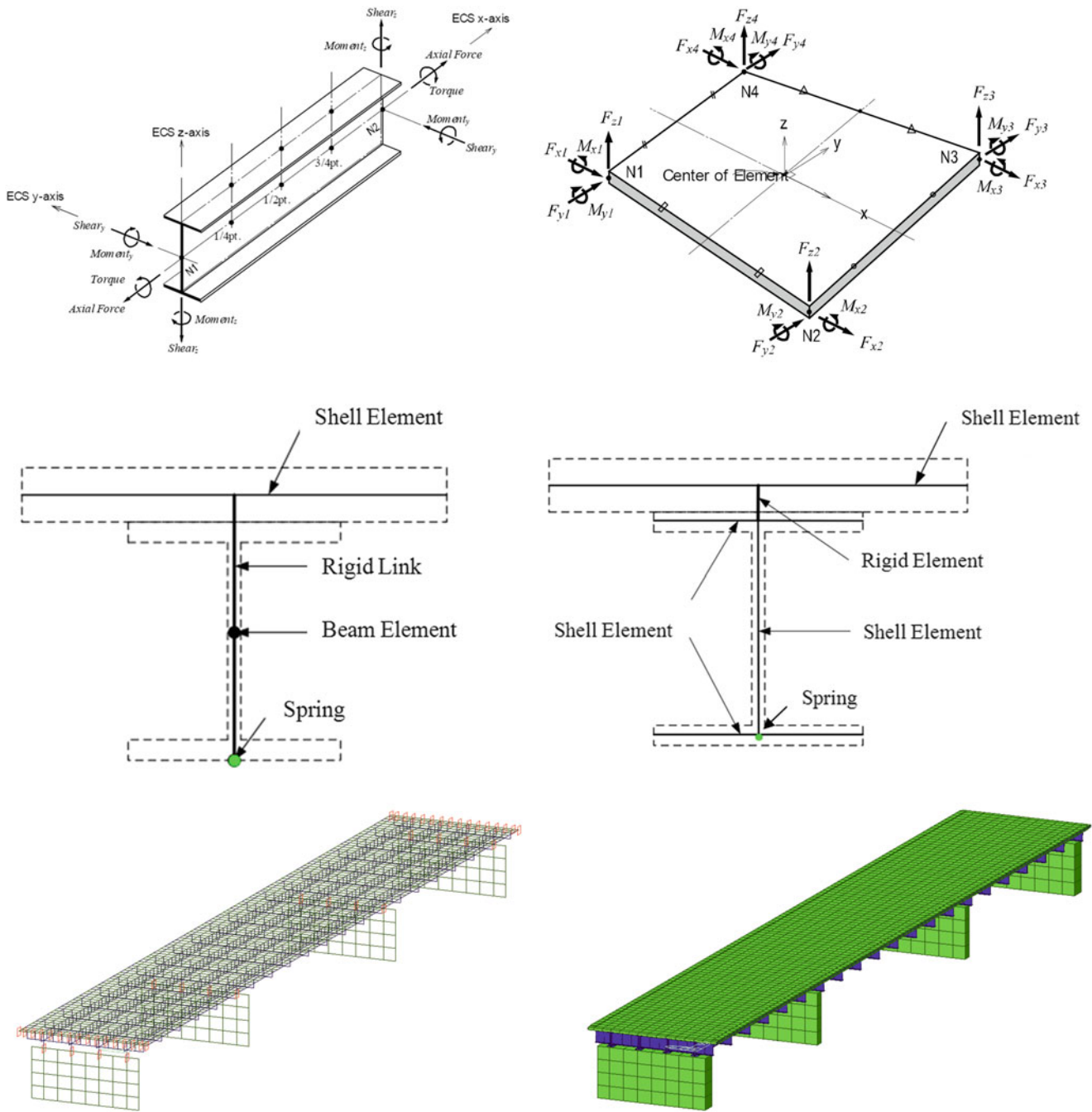
Fig. 17.5 Superstructure idealization of VX bridge for Model 2 and Model 3

In order to correctly replicate the boundary conditions, the rubber bearing supports in both bridges were modelled by means of elastic links: the bearings exhibit a practically linear lateral displacement vs force behavior. The stiffness values provided by the producer and reported in Tables 17.1 and 17.2 (for VX01 and for Muzza respectively) were assigned to the rigid links in the model, Fig. 17.7.

Both the VX01 Bridge and the Muzza Bridge were designed to be equipped with expansion joints at the sides: these joints allow thermal deformations and also allow the larger, earthquake-induced relative displacements between the deck and the rest of the road to take place without inducing damage in the structural elements. The two bridges were equipped with peculiar side joints that allow longitudinal displacements to take place but restrain the transverse displacements. The correct boundary condition to represent the effects of this kind of joint in the low displacement field must thus be enforced by assigning the side elements of the bridge free ends longitudinally and restrained ends transversally, otherwise the predicted mode shapes will not be accurate.
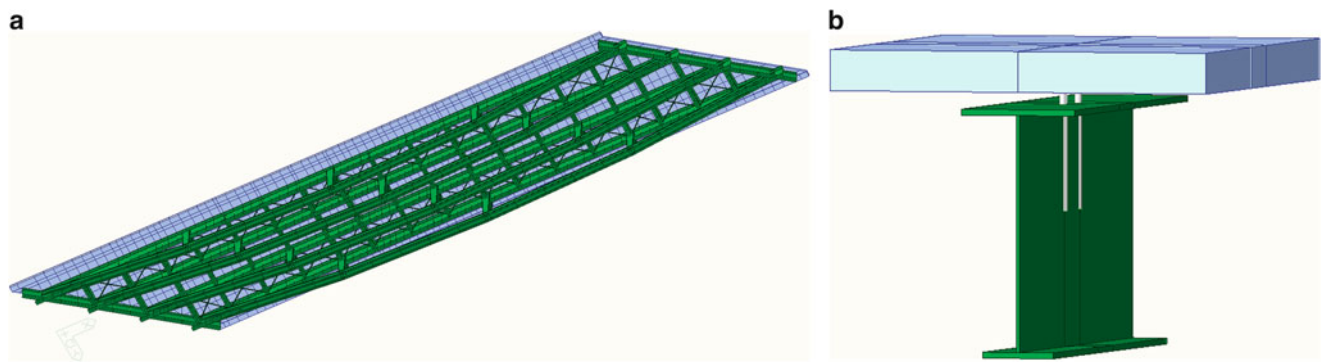
Fig. 17.6 FE model of Muzza bridge, (**a**) final model, (**b**) detail of the beam-slab connection

Fig. 17.7 FE model of Muzza bridge, detail of the elastic link used to model the elastomeric supports

Elastic link representing the elastomeric supports
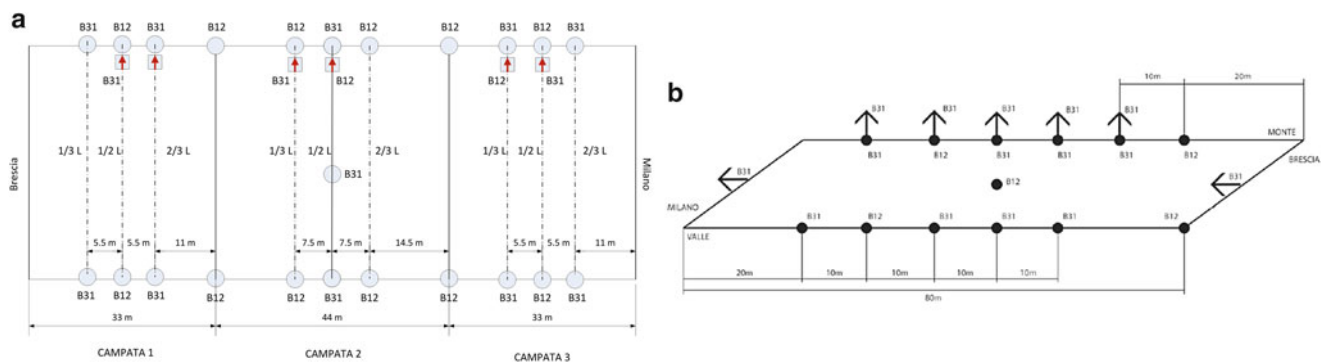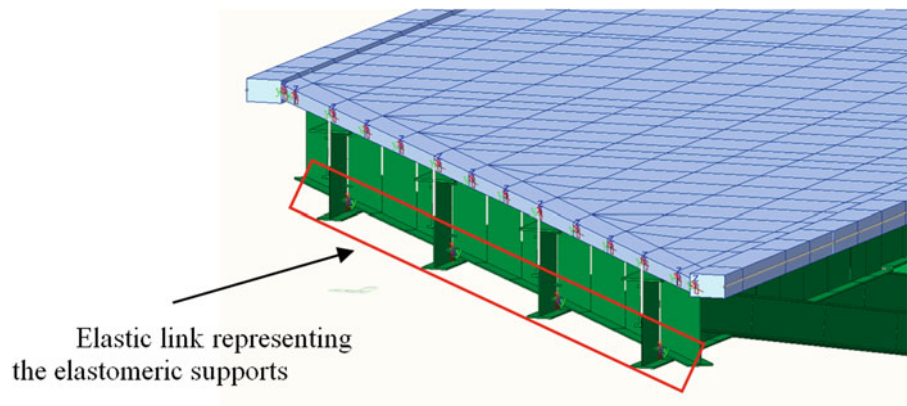
Fig. 17.8 Location of the sensors, (**a**) VX01 bridge, (**b**) Muzza bridge

The four main aspects mentioned above, i.e. composite section behaviour, isolating supports behaviour, presence of the sound barriers and of the lateral expansion joints, can be assumed as the main parameters affecting the estimate of the modal properties. In the following, their influence will be shown when comparing the numerical and experimental results.

17.4 Experimental Campaign

The experimental campaign on the VX01 bridge consisted of OMA tests only. The one on the Muzza Bridge consisted of both OMA and EMA tests, with vertical and horizontal forcing, transverse to the longitudinal axis of the bridge.

For each test, the measurement set up consisted in measurement points in the vertical direction, transversal direction and longitudinal direction. The transducers are seismic low noise piezoelectric accelerometers conditioned and recorded using a 24 bit A/D converter with built in anti-aliasing filters. The location of the sensors is reported in Fig. 17.8.

Table 17.3 Modal frequencies
identified from OMA test on
VX01 and from OMA and EMA
tests on Muzza

VX01 OMA		MUZZA OMA		MUZZA EMA	
F [Hz]	ξ [%]	F [Hz]	ξ [%]	F [Hz]	ξ [%]
2.20	0.48	1.72	0.38	1.72	0.42
2.37	0.38	1.83	0.76	1.82	1.28
3.10	0.71	2.34	2.5	2.28	2.28

In order to obtain robust spectral quantities estimates in the OMA tests, the system was left recording on the bridges for 8 h. For the EMA tests on the Muzza Bridge, both a vertical forcing and a horizontal one were provided. The vertical and horizontal forcing point was located in the center of the bridge, both longitudinally and in the transverse direction.

The accelerations were analyzed using the Polyreference Least Square Frequency Domain algorithm [3, 4]. The identified modal frequencies and dampings are reported in Table 17.3, for the OMA tests on VX01 Bridge and for the OMA and EMA tests on the Muzza Bridge.

In Fig. 17.9, the Power Spectral Densities for the measured signals, during the OMA tests for VX01 and for Muzza Bridge, are represented. The peaks highlighting the first natural frequencies are clearly visible in both cases.

The results from the tests show consistency between the OMA and EMA identification methods. The experimental damping values are low for both bridges, which is compatible with the structural configuration and the low levels of vibration. The mode shapes corresponding to the identified modes will be presented in the following paragraph and directly compared to those provided by the numerical eigenvalue analysis.

17.5 Numerical and Experimental Result Comparison

As mentioned in the previous paragraph, the comparison between the experimentally derived frequencies and corresponding mode shapes and those yielded by the different models for each bridge allowed the initial phase of model tuning to be carried out. In Tables 17.4, 17.5 and 17.6, the measured flexural and torsional frequencies and mode shapes obtained from the experimental tests are compared with the numerical model results. As both bridges are completely isolated above the substructure, the comparison for the different modelling options was based on the obtained flexural and torsional responses. The translational response of these bridges is not strongly affected by how accurately the composite behaviour is captured. According to the results, both Model N.1 and Model N.3 appear to respond more flexibly than Model N.2. The comparison between the mode shapes of Model N.2 and Model N.3 also reveals that there is a switch between the flexural and torsional modes of the deck response. Instead, the line model fails to accurately estimate the response frequency of the bridges due to its inability of simulating the composite behaviour. In addition to these outcomes, Model N.1 also performs weakly in estimating the torsional response of the system because of the inaccurate representation of the torsional stiffness of the system. From what was observed in the present case studies, the best choice among the preliminary modelling options was thus confirmed to be Model N.2 based on the best match between experimental and numerical frequencies and mode shapes as discussed above.

17.6 Model Tuning Activity

After choosing the best modelling option for the deck, model tuning activity was carried out: the effect of the previously mentioned critical parameters was investigated, i.e. rubber bearing, expansion joints, sound barriers, bracing connections.

For example, it was learnt that the effects of the presence of the joint device on the service life, low vibration level behaviour of the flyover is, in fact, non-negligible: the joints provide a lateral restraint that is usually neglected in the design phase as it would get damaged under seismic excitation, but cannot be disregarded when determining the modal properties to be compared to the test result.

Also, the effects of the sound barriers were found out to be important in terms of additional dynamic mass to the global mass matrix of the system due to the light weight of the steel structure. In the present case studies their stiffness contribution was not found to be important but it needs further investigation for longer bridges.

The correct modelling of the lateral stiffness of the rubber bearings, as provided by the producers, turned out to be important to correctly catch the transverse and longitudinal components of the mode shapes. The elastomeric isolators are characterized by an effective shear modulus and this modulus is dependent on the shear strain experienced by the bearings.
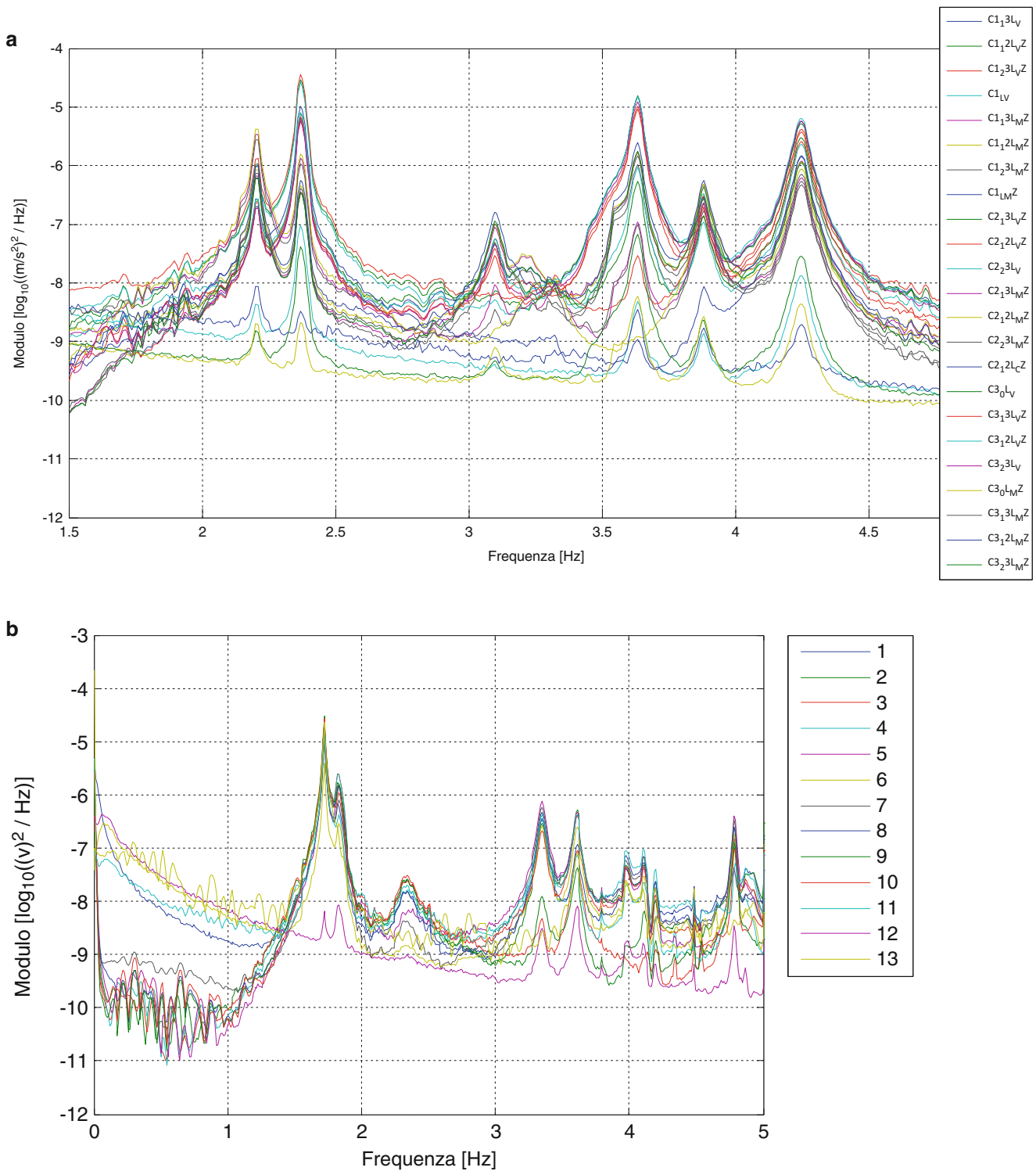
Fig. 17.9 PSD plots of (**a**) vertical channels during the OMA test on VX01, (**b**) vertical channels during the OMA test on Muzza bridge

As the experimental eigenmode 3 of Muzza is sensitive to the characteristics of the bearing stiffness, the stable stiffness value assumed in modelling was verified through the eigenfrequency obtained from the experiment. On the other hand, by analysing the experimental mode shapes, the assumption that the dynamics of the piers and that of the deck are completely disconnected was confirmed: in this case, the substructure could have been excluded from the model with no significant error on the prediction of the mode shapes involving the decks and the supports.

Table 17.4 Comparison between numerical and experimental frequencies for VX01 and Muzza bridges

VX				MUZZA			
Experimental modes	Model 1	Model 2	Model 3	Experimental modes	Model 1	Model 2	Model 3
2.42	f3: 1.62	f4: 2.40	f4: 2.21	1.72	Not applicable	f4: 1.77	f4: 1.67
2.45	f4: 1.63	f5: 2.45	f5: 2.31	1.82	Not applicable	f5: 1.78	f5: 1.69
3.60	f5: 2.72	f6: 3.59	f6: 3.27	2.29	Not applicable	f6: 2.95	f6: 2.68
3.74	f6: 3.01	f7: 3.74	f7: 3.59		Not applicable	f7: 3.26	f7: 3.01

Close examination of Tables 17.7 and 17.8 reveals the importance of updating the sensitive parameters that affect the dynamic characteristics of the bridge. As the experimental test configuration and accelerometer locations corresponded to the initial model results, horizontal response of Muzza together with bending response was expected at frequency levels lower than 2 Hz. However, the translational mode coupled with a vertical bending was obtained at 2.3 Hz, Fig. 17.10. While the initial model for Muzza predicts another bending mode just after the second torsional response, the tuned model predicts a translational mode with 2.3 Hz accurately. One must care when comparing eigenmodes for a system with different boundary conditions and concentrated mass distribution. According to Table 17.7, with the addition of expansion joints and sound barriers to VX model, the effect is more important than other parameters investigated. This change does not only create nearly identical mode shapes with different eigenfrequencies, but the Eigen mode shapes are completely different than the previously obtained ones (Table 17.9).

17.7 Concluding Remarks

From the dynamic testing activity carried out on the main bridges of the new BreBeMi highway, a wealth of information regarding the dynamic behaviour of composite girder flyovers was gathered; moreover, a thorough model tuning activity was carried out, and a sensitivity test on many parameters affecting the results of numerical analyses was performed, so that the FE models of the bridges implemented in MidasGen were validated against a reliable experimental benchmark and can now be used in predictive mode.

Summarizing the lessons learnt from the activity, first of all it must be remarked that the basic requirement of [1], i.e. that the comparison between experimental and numerical first natural frequency is not enough to provide reliable information for model validation. For example, in both of the bridges discussed in the present paper, both for the first and for the subsequent modes, the frequencies alone could not provide a thorough identification because some of the experimentally identified frequencies were in-between two subsequent, closely spaced, numerical frequencies, so it was impossible to match either of the two adjacent numerical frequencies to the experimental data. Only by comparing the corresponding mode shapes, the identification could be completed.

Moreover, in the first part of the present paper, the effect of different analytical modelling techniques on the response of a straight and skewed composite bridge was studied, by comparing the results of three different FE models to the experimental data. It was found out that two simplified modelling approaches, named Model N.2 and Model N.3, give very similar and equally reliable results, if the elements are provided an adequate mesh discretization, whereas Model N.1 can thus be deemed accurate enough to be used in setting up an experimental test configuration but it is not adequate for validating the final response of composite bridges.

In the second part of the present paper, a manual model updating was performed by means of a sensibility study for uncertain parameters like expansion joint stiffness, inclusion of noise barriers, dynamic stiffness of rubber bearings, and connection stiffness of truss elements. The flexural and torsional mode responses of both bridges were not found to be very sensitive to the bracing connections and the rubber bearing stiffness. The resulting FE model included more realistic structural parameters and provided dynamic properties that are better matching with the experimental test response of the bridge.

In this model tuning phase, it was found out that the contribution of the expansion joints on the experimental test response is crucial: when implementing the model, it must be clarified if the expansion joints are functional in the transverse direction or not, in order to assign the correct restraints to the side elements of the bridge. In low to moderate seismic sites, many structural designers are used to designing the expansion joints only along the axis of the bridge, neglecting the transverse restraint they provide, which affects the dynamic properties under low vibrations.

Table 17.5 Comparison between numerical and experimental mode shapes for VX01
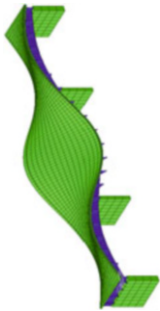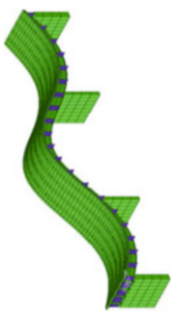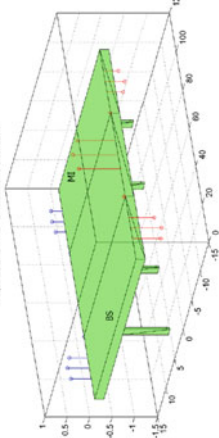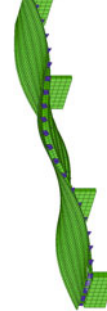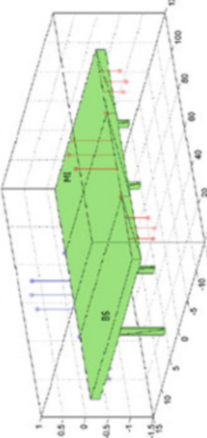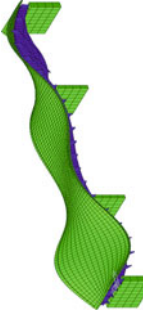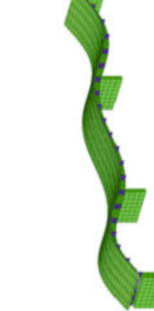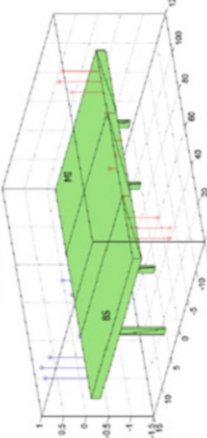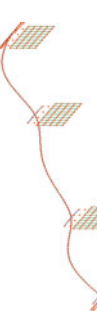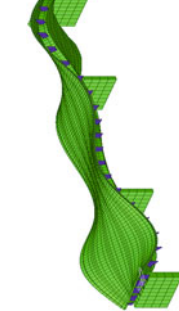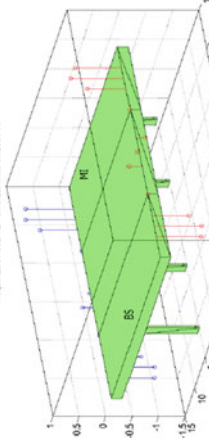
Model 1	Model 2	Model 3	Experimental

Table 17.6 Comparison between numerical and experimental mode shapes for Muzza
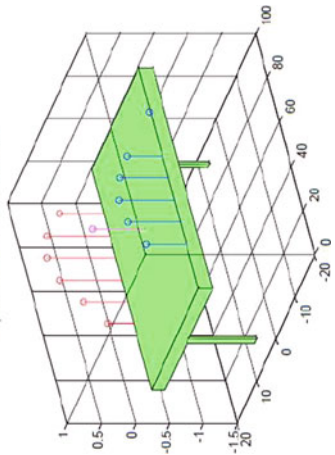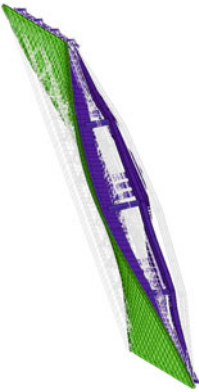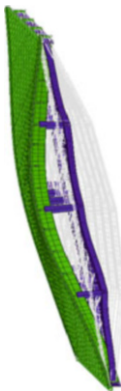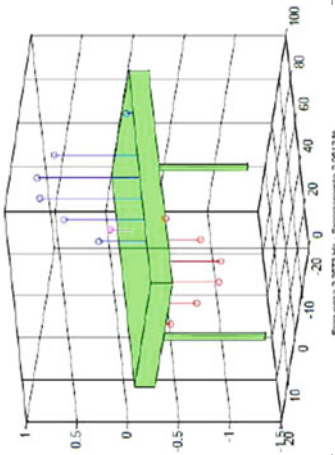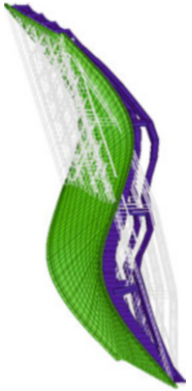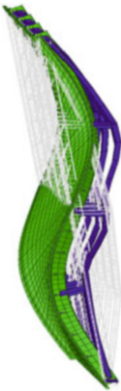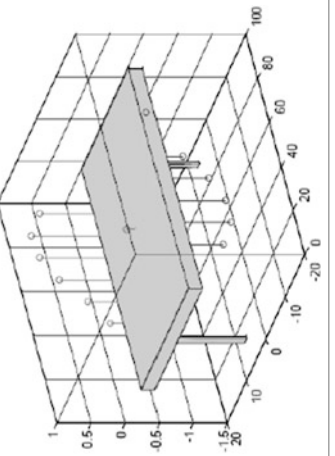
Model 2	Model 3	Experimental

Table 17.7 Frequency comparison between the experimentally measured values and FE model before and after model updating for VX

Mode nos. named after experiment	Measured frequencies (Hz)	Mode shapes	Initial model (Hz)	Mode shapes	Updated model (Hz)
1	2.20	Sliding perpendicular to bridge axis	0.55	Sliding perpendicular to bridge axis	2.20
2	2.20	Torsional response of deck	2.40	Torsional response of deck	2.34
3	2.37	Vertical bending of deck	2.45	Vertical bending of deck	2.43
4	3.10	Torsional response of deck	3.60	Torsional response of deck	3.51

Table 17.8 Frequency comparison between the experimentally measured values and FE model before and after model updating for Muzza

Mode nos. named after experiment	Measured frequencies (Hz)	Mode shapes	Initial model (Hz)	Mode shapes	Updated model (Hz)
		Sliding along the bridge axis	0.58		
		Sliding perpendicular to bridge axis	0.58		
1	1.72	Vertical bending of deck	1.77	Vertical bending of deck	1.75
2	1.83	Torsional response of deck	1.78	Torsional response of deck	1.76
3	2.34			Sliding response	2.30
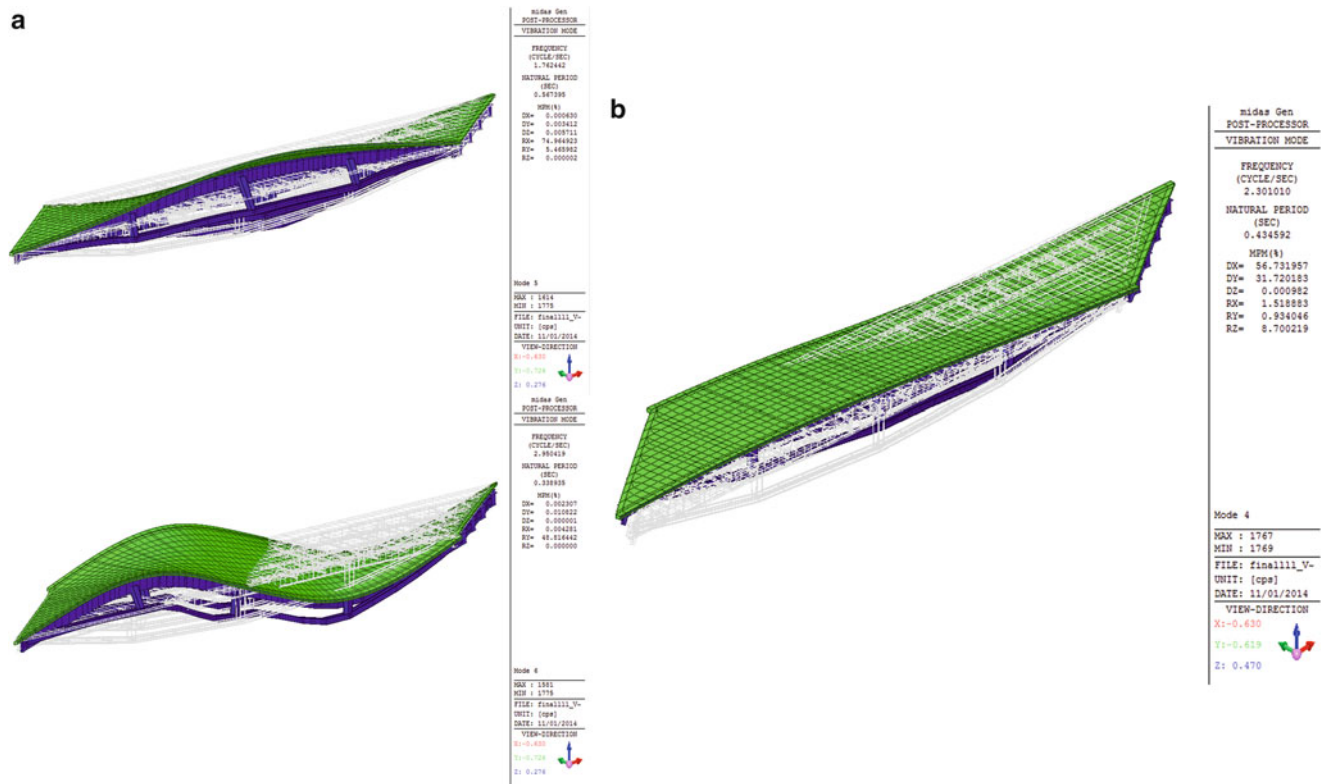
Fig. 17.10 The dynamic response in the frequency range of 1.5–2.7 (**a**) before model update, (**b**) after model update

Finally, the presence of sound barriers was also found out to be important in terms of additional dynamic mass to the global mass matrix of the system due to the light weight of the composite steel-concrete structure, even if their stiffness contribution was not found to be important. For slender, light bridges, the presence of additional sources of mass during the dynamic tests must thus be carefully considered in the models in order to provide good estimates for the dynamic properties.

Table 17.9 Eigenmode shape comparison for VX

Mode nos. named after experiment	Initial model	Updated model
2		
3		
4		

References

1. NTC (2008) Nuove Norme Tecniche per le Costruzioni, D.M., 14 Jan 2008, Italian
2. Cigada A, Mola E, Moschini S, Paksoy M, Pozzuoli C, Vanali M (2014) Numerical modelling and dynamic testing on the Oglio Flyover of the new BreBeMi highway in Italy. In: Conference proceedings of the society for experimental mechanics series 2014, Dynamics of Civil Structures, vol 4, pp 381–394
3. Peeters B, Van der Auweraer H, Guillaume P, Leuridan J (2004) The PolyMAX frequency-domain method: a new standard for modal parameter estimation? Shock Vib 11(3–4):395–409. IOS Press
4. Peeters F, Vanhollebeke H, Van der Auweraer H (2005) Operational PolyMAX for estimating the dynamic properties of a stadium structure during a football game. In: Proceedings of international conference IMAC XXIII, Orlando

Chapter 18
A Bayesian State-Space Approach for Damage Detection and Classification

Zoran Dzunic, Justin G. Chen, Hossein Mobahi, Oral Buyukozturk, and John W. Fisher III

Abstract The problem of automatic damage detection in civil structures is complex and requires a system that can interpret sensor data into meaningful information. We apply our recently developed switching Bayesian model for dependency analysis to the problems of damage detection, localization, and classification. The model relies on a state-space approach that accounts for noisy measurement processes and missing data. In addition, the model can infer statistical temporal dependency among measurement locations signifying the potential flow of information within the structure. A Gibbs sampling algorithm is used to simultaneously infer the latent states, the parameters of state dynamics, the dependence graph, as well as the changes in behavior. By employing a fully Bayesian approach, we are able to characterize uncertainty in these variables via their posterior distribution and answer questions probabilistically, such as "What is the probability that damage has occurred?" and "Given that damage has occurred, what is the most likely damage scenario?". We use experimental test data from two laboratory structures: a simple cantilever beam and a more complex 3-story, 2-bay structure to demonstrate the methodology.

Keywords Graphical models • Bayesian inference • Structural health monitoring • State-space model • Damage classification

18.1 Introduction

Structural inspection has been necessary to ensure the integrity of infrastructure for almost as long as structures have existed, ranging from informal subjective methods such as visual or hammer testing, to quantitative modern methods including ultrasound, x-ray, and radar non-destructive testing techniques. These testing methods are relatively intensive as they depend on the experience of the inspector and the time to inspect suspected damaged locations in the structure. Inspections are typically carried out periodically, however if additional sensors could be added to the structure such that some indication of where potential locations of damage might be such that they can be closely inspected, it would be useful for reducing the time and effort necessary for structural inspection.

Structural health monitoring (SHM) involves instrumenting a structure with sensors and deriving some information from the data they collect in order to determine if the structure has changed [1]. This change in the structure could then be attributed to some sort of damage that would be more closely investigated. In general, data is processed into features that may indicate these changes in the structure and in some cases statistical or probabilistic discrimination of these features are used to separate data collected from intact and changed structures [2]. Statistical methods are essential for being able to discriminate feature changes as a result of structural changes from measurement or environmental variability.

Bayesian inference is a probabilistic method of inference that allows one to form probabilistic estimates of certain parameters given a series of observations. The method can be used in a couple of different ways in SHM including model updating of structural parameters [3], monitoring by inferring structural parameters over time [4], and determining the

Z. Dzunic • H. Mobahi • J.W. Fisher III (✉)
Computer Science and Artificial Intelligence Laboratory, Massachusetts Institute of Technology, 77 Massachusetts Avenue, Cambridge, MA 02139, USA
e-mail: fisher@csail.mit.edu

J.G. Chen • O. Buyukozturk
Department of Civil and Environmental Engineering, Massachusetts Institute of Technology, 77 Massachusetts Avenue, Cambridge, MA 02139, USA

optimal placement of sensors [5]. Bayesian inference can be used in either a model-based situation where a structural model is either formulated or updated as a basis for damage detection, a data-based situation where there is no prior information on the structural model and only the sensor data is used, or a mixture of the two situations.

We apply a recently developed framework for Bayesian switching dependence analysis under uncertainty [6] to time-series data obtained from accelerometers located at multiple positions on a building. This model is effectively a computational representation of not only the physical structural system, but also the act of collecting information on that system through the use of sensors. By accounting for interactions between sensor signals collected from the system in different locations, the hope is to infer a representation of the structural connections between locations in the structure or the underlying physics without have any knowledge of the actual structural configuration or dynamics. Assuming that the model learned from a set of data is exclusive to the corresponding physical structural configuration and condition, a change in the model parameters could be indicative of a change in the measured physical structure which might be caused by damage. In order to see if these assumptions might hold true, we test the methodology on data from a model structure in various intact and damaged conditions.

We present the experimental setup in Sect. 18.2, the Bayesian framework and its modification for a classification problem in Sect. 18.3, and experimental results in Sect. 18.4. We summarize conclusions in Sect. 18.5.

18.2 Experimental Setup

Two experimental test structures were used to generate data to test the approach for application on a structure. Both structures are made of modular elements that are based on steel columns that are $60 \times 5.08 \times 0.64$ cm, and bolted together by four bolts at each connection as shown in Fig. 18.1a as an example of a typical connection. The structures are bolted to a heavy concrete foundation as a reaction mass. They are instrumented with piezoelectric triaxial accelerometers that have a sampling rate of 6,000 Hz, and the number used differs for each structure.

The first, simpler structure is a vertical cantilever beam that consists of three steel column elements shown in Fig. 18.1b. Damage is introduced on one of the two middle bolted connections in either a minor damage case where two of four bolts in the flexible direction are removed, or a major damage case where the four bolts are loosened to only be hand tight. This
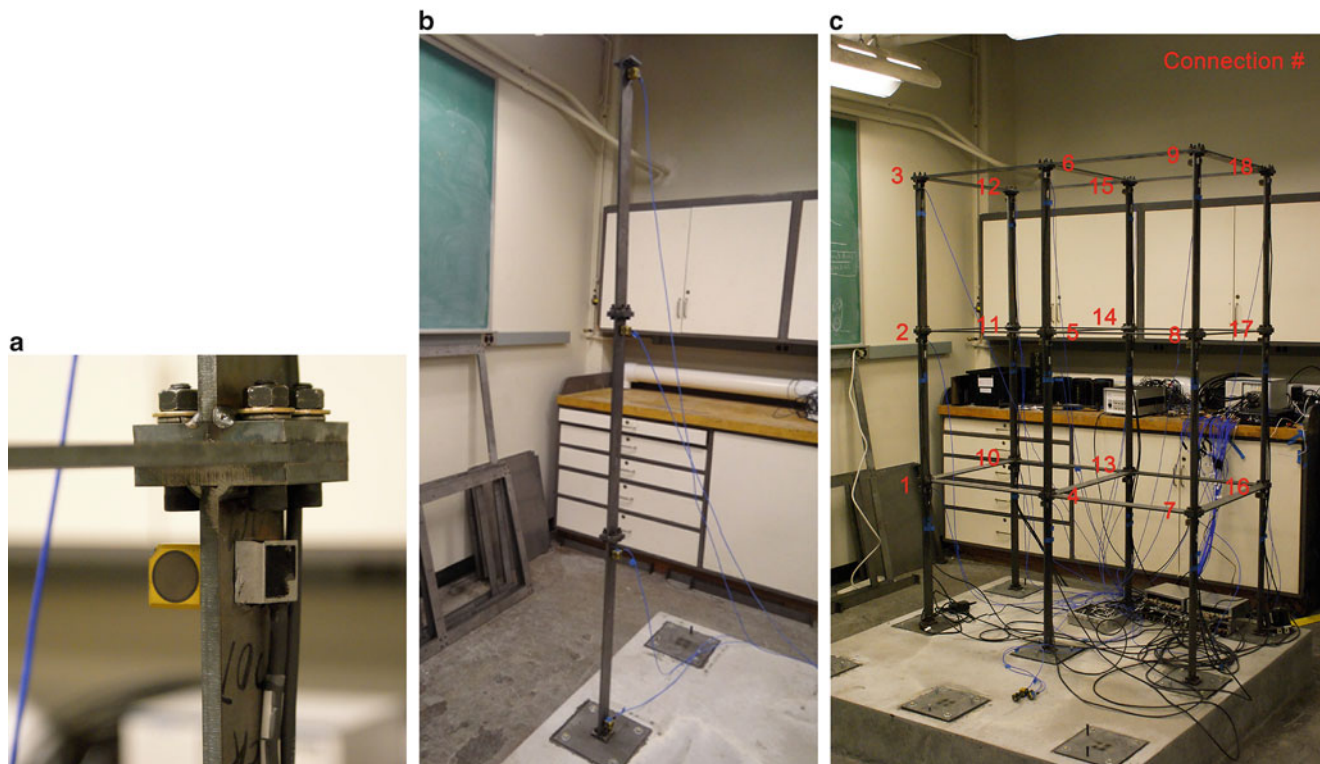
Fig. 18.1 Details of the experimental setup. (**a**) Bolted connection. (**b**) Simple column structure. (**c**) 3 story 2 bay structure

Table 18.1 Test cases and damage scenarios for structural models

(a) Column structure		(b) 3 story 2 bay structure	
Test case	Damage scenario	Test case	Damage scenario
1	Intact column	1	Intact column
2	Minor damage, lower joint	2	Minor damage at 17
3	Major damage, lower joint	3	Major damage at 17
4	Minor damage, upper joint	4	Minor damage at 1
5	Major damage, upper joint	5	Major damage at 1
		6	Major damage at 1 and 17

structure is instrumented with four accelerometers, one at each connection, including the connection with the foundation, and at the top of the structure. In order to excite the cantilever beam, it is displaced by approximately 5 cm and then released and allowed to freely vibrate for 10 s, during which data was collected. There are ten test sequences for each damage scenario, and they are summarized in Table 18.1a.

The second structure is a 3 story 2 bay configuration with a footprint of 120×60 cm as shown in Fig. 18.1c. The structure consists of steel columns and beam frames of similar dimensions for each story that are bolted together to form each story. Damage is similarly introduced on the bolted connections with the minor and major damage cases by removing two bolts or loosening all four at connections 1 and 17, which are on opposite corners of the structure, with 1 being on the first story, and 17 being on the second. This structure is instrumented with 18 triaxial accelerometers at each of the connections between elements. For this structure the excitation is a small shaker with a weight of 0.91 kg and a piston weight of 0.17 kg that was attached to the top corner of the structure at connection 18, which provided a random white Gaussian noise excitation in the frequency range of 5–350 Hz in the flexible direction. Test measurements lasted for 30 s, during which the shaker is always exciting the structure, thus there is no ramp up or unforced section of the data. The damage scenarios are summarized in Table 18.1b. For each damage scenario, ten sequences were acquired.

18.3   Theory

We describe the state-space switching interaction model (SSIM) of [6] in Sect. 18.3.1 and its modification for the application to classification of time-series in Sect. 18.3.2.

The relevant background for this paper are probabilistic graphical models (Bayesian networks and dynamic Bayesian network in particular) and principles of Bayesian inference. Graphical models are a language that uses graphs to compactly represent families of joint probability distributions among multiple variables that respect certain constraints dictated by a graph. In particular, a Bayesian network (BN) consists of a directed acyclic graph $G = (V, E)$, whose nodes $X_1, X_2, \ldots, X_N$ represent random variables, and a set of conditional distributions $p(X_i \mid pa(X_i))$, $i = 1, \ldots, N$, where $pa(X_i)$ is a set of variables that correspond to the parent nodes (parents) of node X_i. Dynamic Bayesian networks (DBNs) are Bayesian networks that model sequential data, such as time-series. Each signal in a model is represented with a sequence of random variables that correspond to its value at different indices, or discrete time points. Edges are allowed only from a variable with a lower index to a variable with a higher index (i.e., they must "point" forward in time). An introduction to the Bayesian approach and Bayesian networks can be found in [7]. An introduction to dynamic Bayesian networks can be found in [8].

18.3.1   State-Space Switching Interaction Model (SSIM)

We assume that N multivariate signals evolve according to a Markov process over discrete time points $t = 0, 1, \ldots, T$. The value of signal i at time point $t > 0$ depends on the value of a subset of signals $pa(i, t)$ at time point $t - 1$. We refer to $pa(i, t)$ as a parent set of signal i at time point t. While the preceding implies a first-order Markov process, the approach extends to higher-ordered Markov processes. A collection of directed edges $E_t = \{(v, i); i = 1, \ldots, N, v \in pa(i, t)\}$ forms a dependence structure (or so-called interaction graph) at time point t, $G_t = (V, E_t)$, where $V = \{1, \ldots, N\}$ is the set of all signals. That is, there is an edge from j to i in G_t if and only if signal i at time point t depends on signal j at time point $t - 1$.

Let X_t^i denote a (multivariate) random variable that describes the latent state associated to signal i at time point t. Then, signal i depends on its parents at time t according to a probabilistic model $p(X_t^i \mid X_{t-1}^{pa(i,t)}, \theta_t^i)$ parametrized by θ_t^i, where

Fig. 18.2 Dynamic Bayesian network (*DBN*) representation of switching interaction among four signals. They initially evolve according to interaction graph E_1. At time point 4, the interaction pattern changes, and they evolve according to interaction graph E_2. Self-edges are assumed
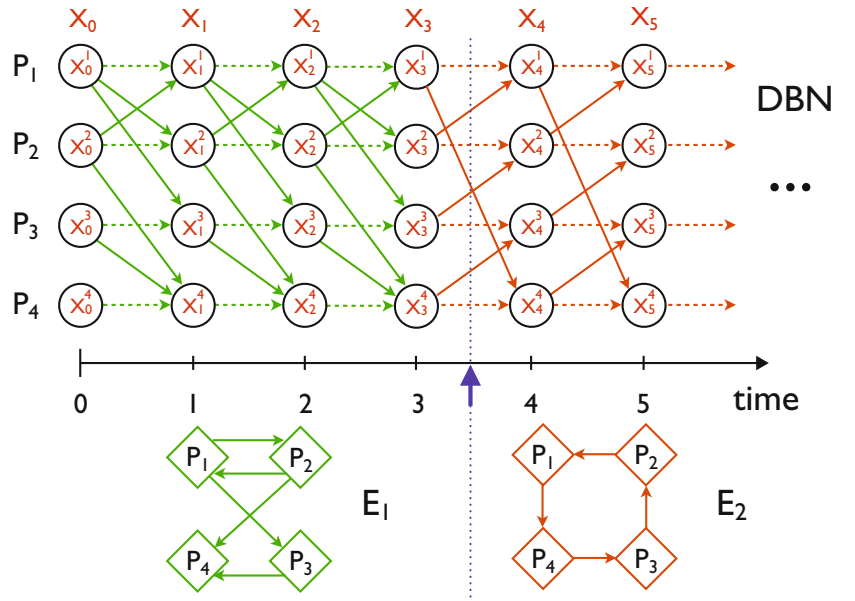
$X_{t-1}^{pa(i,t)}$ denotes a collection of variables $\{X_{t-1}^v; v \in pa(i,t)\}$. Furthermore, we assume that conditioned on their parents at the previous time point, signals are independent of each other:

$$p(X_t|X_{t-1}, E_t, \theta_t) = \prod_{i=1}^{N} p(X_t^i|X_{t-1}^{pa(i,t)}, \theta_t^i) , \qquad (18.1)$$

where $X_t = \{X_t^i\}_{i=1}^N$ (i.e., X_t is a collection of variables of all signals at time point t) and $\theta_t = \{\theta_t^i\}_{i=1}^N$. Structure E_t and parameters θ_t determine a dependence model at time t, $\mathcal{M}_t = (E_t, \theta_t)$. Finally, we express a joint probability of all variables at all time points, X, as

$$p(X) = p(X_0|\theta_0) \prod_{t=1}^{T} p(X_t|X_{t-1}, E_t, \theta_t) = \prod_{i=1}^{N} p(X_0^i|\theta_0^i) \prod_{t=1}^{T} \prod_{i=1}^{N} p(X_t^i|X_{t-1}^{pa(i,t)}, \theta_t^i) . \qquad (18.2)$$

The stochastic process of Eq. 18.2 can be represented using a dynamic Bayesian network (DBN), such that there is a one-to-one correspondence between the network and the collection of interaction graphs over time, as shown in Fig. 18.2.

In order to learn time-varying interaction from time-series data, we assume that the dependence model switches over time between K distinct models, $\tilde{\mathcal{M}}_k = (\tilde{E}_k, \tilde{\theta}_k), k = 1, \ldots, K$. More formally, for each time point t, $\mathcal{M}_t = \tilde{\mathcal{M}}_k$ for some $k, 1 \le k \le K$. One interaction may be active for some period of time, followed by a different interaction over another period of time, and so on, switching between a pool of possible interactions. This is illustrated in Fig. 18.2. Let $Z_t, 1 \le t \le T$, be a discrete random variable that represents an index of a dependence model active at time point t; i.e., $\mathcal{M}_t = \tilde{\mathcal{M}}_{Z_t}$, $Z_t \in \{1, \ldots, K\}$. We can now rewrite the transition model (Eq. 18.1) as

$$p(X_t|X_{t-1}, Z_t, \tilde{E}, \tilde{\theta}) = p(X_t|X_{t-1}, \tilde{E}_{Z_t}, \tilde{\theta}_{Z_t}) = \prod_{i=1}^{N} p(X_t^i|X_{t-1}^{\tilde{pa}(i,Z_t)}, \tilde{\theta}_{Z_t}^i) , \qquad (18.3)$$

where $(\tilde{E}, \tilde{\theta}) = \{(\tilde{E}_k, \tilde{\theta}_k)\}_{k=1}^K$ is a collection of all K models and $\tilde{pa}(i,k)$ is a parent set of signal i in $\tilde{E}_k$. We can also rewrite Eq. 18.2 as $p(X|Z, \tilde{E}, \tilde{\theta}) = p(X_0|\theta_0) \prod_{t=1}^T p(X_t|X_{t-1}, Z_t, \tilde{E}, \tilde{\theta})$, where $Z = \{Z_t\}_{t=1}^T$. To distinguish from signal state, we call Z_t a switching state (at time t) and Z a switching sequence. Furthermore, we assume that Z forms a first order Markov chain:

$$p(Z) = p(Z_1) \prod_{t=2}^{T} p(Z_t|Z_{t-1}) = \pi_{Z_1} \prod_{t=2}^{T} \pi_{Z_{t-1}, Z_t} , \qquad (18.4)$$

where $\pi_{i,j}$ is a transition probability from state i to state j and π_i is the initial probability of state i.

Multinomials π are sampled from Dirichlet priors parametrized by α as
$(\pi_1, \ldots, \pi_K) \sim \mathcal{D}ir(\alpha_1, \ldots, \alpha_K)$,
$(\pi_{i,1}, \ldots, \pi_{i,K}) \sim \mathcal{D}ir(\alpha_{i,1}, \ldots, \alpha_{i,K}) \; \forall i$.

K structures $\tilde{E}_k$ and parameters $\tilde{\theta}_k$ are sampled from the corresponding priors as
$\tilde{E}_k \sim p(E; \beta)$, $\tilde{\theta}_k \sim p(\theta | \tilde{E}_k; \gamma)$, $\forall k$.

Parameters of the observation model are sampled as $\xi^i \sim p(\xi^i; \delta)$, $\forall i$.

Initial values X_0 and Y_0 are generated as $X_0 \sim p(X_0 | \theta_0)$ and $Y_0 \sim p(Y_0 | X_0, \xi)$.

For each $t = 1, 2, \ldots, T$ (in that order), values of Z_t, X_t and Y_t are sampled as
$Z_t \sim \mathcal{M}ult(\pi_{Z_{t-1},1}, \ldots, \pi_{Z_{t-1},K})$ or
$Z_t \sim \mathcal{M}ult(\pi_1, \ldots, \pi_K)$ if $t = 1$,
$X_t \sim p(X_t | X_{t-1}, \tilde{E}_{Z_t}, \tilde{\theta}_{Z_t})$ and $Y_t \sim p(Y_t | X_t, \xi)$.

Fig. 18.3 State-space switching interaction model (*SSIM*) and its conditional distributions (generative procedure)

Finally, we model that the observed value Y_t^i of signal i at time t is generated from its state X_t^i via a probabilistic observation model $p(Y_t^i | X_t^i, \xi_t^i)$ parametrized by ξ_t^i. For simplicity, we assume that the observation model is independent of the state ($\xi_t^i = \xi^i$, $\forall t, i$),

$$p(Y | X, \xi) = \prod_{t=0}^{T} \prod_{i=1}^{N} p(Y_t^i | X_t^i, \xi^i), \tag{18.5}$$

where $Y = \{Y_t\}_{t=1}^{T}$ is the observation sequence and ξ is the collection of parameters $\{\xi^i\}_{i=1}^{N}$.

The choice of dependence and observations models is application specific and will impact the complexity of some of the inference steps, as discussed in Sect. 18.3.1.1.

The full SSIM generative model, shown in Fig. 18.3, incorporates probabilistic models described above along with priors on structures and parameters.

Here, β are the hyperparameters of the prior on dependence structure, $p(E; \beta)$, and γ are the hyperparameters of the prior on dependence model parameters given structure, $p(\theta | E; \gamma)$. We assume that these priors are the same for all K models. Since the distribution on structure is discrete, in the most general form, β is a collection of parameters $\{\beta_E\}$ (one parameter for each structure), such that β_E is proportional to the prior probability of E:

$$p(E; \beta) = \frac{1}{B} \beta_E \propto \beta_E, \tag{18.6}$$

where $B = \sum_E \beta_E$ is a normalization constant. Note that the prior on parameters, $p(\theta | E; \gamma)$, may depend on the structure and γ is, in general, a collection $\{\gamma_E\}$ of sets of hyperparameters, such that $p(\theta | E; \gamma) = p(\theta; \gamma_E)$.

Learning Bayesian network structures (under reasonable assumptions) is NP hard [9]. The number of possible structures is superexponential in the number of nodes, and, in the worst case, it may be necessary to calculate the posterior of each one separately. The same holds in the case of inference of a dependence structure described above (i.e., a dependence structure of a homogenous DBN). The number of possible such structures is 2^{N^2}.

We employ two fairly general assumptions in order to reduce the complexity of inference over structures. First, we assume a modular prior on structure and parameters [10–13], which decomposes as a product of priors on parent sets of individual signals and associated parameters:

$$p(E, \theta | \beta, \gamma) = \prod_{i=1}^{N} p(pa(i) | \beta) \, p(\theta^i | pa(i); \gamma) . \tag{18.7}$$

As a result, parent sets can be chosen independently for each signal [14], and the total number of parent sets to consider is $N2^N$, which is exponential in the number of signals. Also, β is no longer a collection of parameters per structure, but rather a collection of parameters $\{\beta_{i,pa(i)}\}$ (one parameter for each possible parent set of each signal), such that

$$p(pa(i); \beta) = \frac{1}{B_i} \beta_{i,pa(i)} \propto \beta_{i,pa(i)} , \qquad (18.8)$$

where $B_i = \sum_s \beta_{i,s}$ are normalization constants. Modularity is also reflected in the posterior:

$$p(E, \theta \,|X; \beta, \gamma) = \prod_{i=1}^{N} p(pa(i) \,|\, X; \beta) \; p(\theta^i \,|X, pa(i); \gamma) . \qquad (18.9)$$

If, in addition, the number of parents of each signal is bounded by some constant M (a structure with bounded in-degree [11–13]), the number of parent sets to evaluate is further reduced to $O(N^{M+1})$, which is polynomial in N.

Linear Gaussian SSIM Linear Gaussian state-space switching interaction models (LG-SSIM) are an instance of SSIM in which the dependence and observation models of each signal i at each time point t are linear and Gaussian:

$$\begin{aligned}
X_t^i &= \tilde{A}_{Z_t}^i \, X_{t-1}^{\tilde{pa}(i, Z_t)} + w_t^i , & w_t^i &\sim \mathcal{N}(0, \tilde{Q}_{Z_t}^i) \\
Y_t^i &= C^i \, X_t^i + v^i , & v^i &\sim \mathcal{N}(0, R^i) .
\end{aligned} \qquad (18.10)$$

$\tilde{A}_k^i$ and $\tilde{Q}_k^i$ are the dependence matrix and the noise covariance matrix of signal i in the kth dependence model (i.e., $\tilde{\theta}_k^i = (\tilde{A}_k^i, \tilde{Q}_k^i)$), while C^i and R^i are the observation matrix and the noise covariance matrix of the observation model of signal i (i.e., $\xi^i = (C^i, R^i)$). We adopt a commonly used matrix normal inverse Wishart distribution as a conjugate prior on the parameters of a linear Gaussian model (more details are given in Appendix).

Latent autoregressive LG-SSIM The model above implies a first order Markov process. However, it extends to a higher, rth order process by defining a new state at time t as $X_t' = [X_t \, X_{t-1} \, \ldots \, X_{t-r+1}]$, i.e., by incorporating a history of length r as a basis for predicting a state at time $t + 1$. We will refer to this model as a latent autoregressive (AR) LG-SSIM of AR order r, since the autoregressive modeling is done in the latent space.

18.3.1.1   Inference in SSIM and LG-SSIM

Exact inference for the SSIM is generally intractable, and one need to resort to approximate methods. An efficient Gibbs sampling procedure is developed in [6] and shown in Algorithm 18.1. The procedure alternates between sampling of (1) latent state sequence X, (2) latent switching sequence Z, (3) parameters of switching sequence dependence models π, (4) parameters of K state sequence transition models $(\tilde{E}, \tilde{\theta})$, and (5) parameters of the observation model ξ. In each step, a corresponding variable is sampled from the conditional distribution of that variable given other variables (i.e., the rest of the variables are assumed fixed at that step).

This procedure is particularly efficient when the dependence model and the observation model distributions have conjugate priors, such as in LG-SSIM, as steps 4 and 5 are reduced to performing conjugate updates. In addition, an efficient message-passing algorithm for batch sampling of the state sequence X (step 1) is developed in [6]. On the other hand, steps 2 and 3 are independent of these choice, and thus inherent to SSIM in general. Step 3 is simply a conjugate update of a Dirichlet distribution, while an efficient message passing algorithm for batch sampling of the switching sequence Z is shown in [14].

Algorithm 18.1 SSIM Gibbs sampler	Algorithm in LG-SSIM
1. $X \sim p(X|Z, Y, \tilde{E}, \tilde{\theta}, \xi)$	Gaussian-MP block sampling
2. $Z \sim p(Z|X, \tilde{E}, \tilde{\theta}, \pi)$	discrete-MP block sampling
3. $\pi \sim p(\pi|Z; \alpha)$	conjugate update
4. $\tilde{E}, \tilde{\theta} \sim p(\tilde{E}, \tilde{\theta}|Z, X; \beta, \gamma)$	conjugate update
5. $\xi \sim p(\xi|X, Y; \delta)$	conjugate update

Fig. 18.4 Part of the SSIM model modified for the application to multiple homogenous sequences
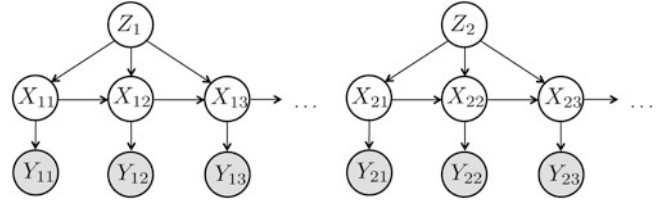
18.3.2   Classification with SSIM

The data collected from the two structures consists of multiple sequences taken under intact and different damage scenarios. Since there is no change in conditions during recording of a single sequence, the SSIM model is modified to produce a single switching label on the entire sequence. The modified part of the model is shown in Fig. 18.4. Each observation sequence $\mathcal{Y}_i = (Y_{i0}, Y_{i1}, \ldots, Y_{iT_i})$ has an associated state sequence $\mathcal{X}_i = (X_{i0}, X_{i1}, \ldots, X_{iT_i})$ and a switching label Z_i, where i is a sequence index and T_i denotes the length of sequence i. We consider the problem of classification of sequences according to the structure condition. Intact structure and each of the damage scenarios are associated with different class labels. The switching label of sequence i, Z_i, indicates its class membership.

Each classification problem has the following form. There are K classes, and a training sequences $\mathcal{Y}_k^{tr}$ is given for each class $k \in \{1, 2, \ldots, K\}$, thus implicitly assuming $Z_k^{tr} = k$. Note that in case there are multiple training sequences from a single class, one can simply assume that $\mathcal{Y}_k^{tr}$ denotes a collection of such sequences. Given a test sequence $\mathcal{Y}^{test}$ and the training data, the goal is to find the probability distribution of the test sequence label, i.e., $P(Z^{test} = k \mid \mathcal{Y}^{test}, \mathcal{Y}_1^{tr}, \mathcal{Y}_2^{tr}, \ldots, \mathcal{Y}_K^{tr})$, for each k. This probability can be computed in the following way:[1]

$$P(Z^{test} = k \mid \mathcal{Y}^{test}, \mathcal{Y}_1^{tr}, \mathcal{Y}_2^{tr}, \ldots, \mathcal{Y}_K^{tr}) \tag{18.11}$$
$$\propto P(Z^{test} = k, \mathcal{Y}^{test} \mid \mathcal{Y}_1^{tr}, \mathcal{Y}_2^{tr}, \ldots, \mathcal{Y}_K^{tr})$$
$$= P(Z^{test} = k \mid \mathcal{Y}_1^{tr}, \mathcal{Y}_2^{tr}, \ldots, \mathcal{Y}_K^{tr}) \, P(\mathcal{Y}^{test} \mid Z^{test} = k, \mathcal{Y}_1^{tr}, \mathcal{Y}_2^{tr}, \ldots, \mathcal{Y}_K^{tr})$$
$$\propto P(\mathcal{Y}^{test} \mid Z^{test} = k, \mathcal{Y}_k^{tr})$$

assuming that, given the training data, the prior probability of a test sequence belonging to class k (prior to seeing the actual test sequence) is uniform, i.e., $P(Z^{test} = k \mid \mathcal{Y}_1^{tr}, \mathcal{Y}_2^{tr}, \ldots, \mathcal{Y}_K^{tr}) \propto const$. Therefore, the probability of the test sequence belonging to class k is proportional to its likelihood under the class k model, given the training sequence $\mathcal{Y}_k^{tr}$ from that class. We will commonly write $P(\mathcal{Y}^{test} \mid \mathcal{Y}_k^{tr})$ for this likelihood, thus implicitly assuming conditioning on $Z^{test} = k$. It is computed by marginalizing out model structure and parameters (model averaging):

$$P(\mathcal{Y}^{test} \mid \mathcal{Y}_k^{tr}) = \sum_{\tilde{E}_k} \int_{\tilde{\theta}_k} P(\mathcal{Y}^{test} \mid \tilde{E}_k, \tilde{\theta}_k) \, P(\tilde{E}_k, \tilde{\theta}_k \mid \mathcal{Y}_k^{tr}) \, d\tilde{\theta}_k. \tag{18.12}$$

The term $P(\tilde{E}_k, \tilde{\theta}_k \mid \mathcal{Y}_k^{tr})$ is the posterior distribution of model structure and parameters given the training sequence $\mathcal{Y}_k^{tr}$, which then serves as a prior for evaluating the test sequence likelihood. The posterior distribution of the test sequence label, Z^{test}, is then obtained by normalizing the likelihoods of the test sequence against training sequences:

$$P(Z^{test} = k \mid \mathcal{Y}^{test}, \mathcal{Y}_1^{tr}, \mathcal{Y}_2^{tr}, \ldots, \mathcal{Y}_K^{tr}) = \frac{P(\mathcal{Y}^{test} \mid \mathcal{Y}_k^{tr})}{\sum_{k'} P(\mathcal{Y}^{test} \mid \mathcal{Y}_{k'}^{tr})}, \tag{18.13}$$

and the test sequence is classified according to the label that maximizes this distribution:

$$\hat{Z}^{test} = \arg\max_k P(Z^{test} = k \mid \mathcal{Y}^{test}, \mathcal{Y}_1^{tr}, \mathcal{Y}_2^{tr}, \ldots, \mathcal{Y}_K^{tr}) = \arg\max_k P(\mathcal{Y}^{test} \mid \mathcal{Y}_k^{tr}). \tag{18.14}$$

---

[1] In this section, hyperparameters are omitted from equations for brevity.

Computing the likelihood in Eq. 18.12 in closed form is intractable in general. The latent training and test state sequences, $\mathcal{X}_k^{tr}$ and $\mathcal{X}^{test}$, need to be marginalized out to compute $P(\tilde{E}_k, \tilde{\theta}_k \mid \mathcal{Y}_k^{tr})$ and $P(\mathcal{Y}^{test} \mid \tilde{E}_k, \tilde{\theta}_k)$, respectively, and simultaneous marginalization of a state sequence and model structure and parameters is analytically intractable. Instead, this likelihood can be computed via simulation:

$$P(\mathcal{Y}^{test} \mid \mathcal{Y}_k^{tr}) \approx \frac{1}{N_s} \sum_{j=1}^{N_s} P(\mathcal{Y}^{test} \mid \hat{E}_j, \hat{\theta}_j), \quad (\hat{E}_j, \hat{\theta}_j) \sim P(\tilde{E}_k, \tilde{\theta}_k \mid \mathcal{Y}_k^{tr}). \tag{18.15}$$

N_s instances of dependence models, $(\hat{E}_j, \hat{\theta}_j)$, are sampled from the posterior distribution of the model given training sequence. The test sequence likelihood is evaluated against each of the sampled models, and then averaged out. On the other hand, in an approximate model which assumes no observation noise (i.e., $\mathcal{X}_i \equiv \mathcal{Y}_i$), the likelihood in Eq. 18.12 can be computed in closed form by updating the conjugate prior on dependence structure and parameters with the training data and then evaluating the likelihood of the test data against thus obtained posterior.

18.4 Results

The basic goals here are to detect changes in a structure due to damage, provide some probabilistic description of the occurrence of damage, and try to infer the physical structure without any knowledge of the actual structure.

We consider the problem of classification of sequences according to the structure condition, as described in Sect. 18.3.2. In each dataset, there are ten sequences of each class. We perform ten rounds of classification. In round j, sequence j from each class is included in the training set, while the other nine sequences of each class are used for testing. Classification results are then averaged over all ten rounds.

We employ a latent-AR LG-SSIM model for classification. We find that AR order 5 is sufficient to produce good classification result, although there is a slight advantage by further increasing this order. Hyperparameter values are either estimated from data or set in a general fashion (e.g., implying a broad prior distribution). In all experiments, we assume presence of a self edge for each node in the dependence structure. The bound on the number of additional allowed parents is set to 3 (maximum) in the single column case. In the 3 story 2 bay structure data, however, we found that the best classification results are obtained when no additional parents (other than self) are allowed. Explaining this result requires further investigation.

We compared the classification results obtained by the full SSIM model and an approximate model which assumes no observation noise (Sect. 18.3.2) and found that on the datasets presented here the full model performs only slightly better, but at the significant additional computational cost (mainly due to step 1 in the inference algorithm). Therefore, we present here detailed results obtained using the approximate model.

18.4.1 Single Column Results

First, for each pair of classes i and j, we compute the average log-likelihood of a test sequence from class i given a training sequence from class j (the average is over all pairs of sequences from classes i and j). Note that the average log-likelihoods do not account for the variability within a class and thus can only partially predict classification results. However, they can be considered as a measure of (asymmetric) similarity between classes. In particular, the comparison of log-likelihoods of a test class given different training classes is useful to indicate its possible "confusion" with other classes. The log domain is chosen to bring likelihoods closer to each other for the purpose of illusrtation, since the differences in likelihoods are huge in their original domain.

The resulting class-class log-likelihood matrix is shown in Fig. 18.5a. For the purpose of visualization, each column is normalized to contain values between 0 and 1, which does not change the relative comparison of values within a column. A different visualization of the same log-likelihood matrix is shown in Fig. 18.5b, in which each group of bars corresponds to a single test class, while bars within a group correspond to different training classes. Clearly, the average log-likelihood of each class is the highest when conditioned on sequences from the same class (diagonal entries). This suggests that the model indeed captures important features pertained to each class via posterior distribution of parameters. However, for some classes, the log-likelihood is also relatively high when conditioned on some of the classes other than itself. For example, the intact class (1) and the two minor damage classes (2 and 4) are the closest to each other in that sense. Also, the two major
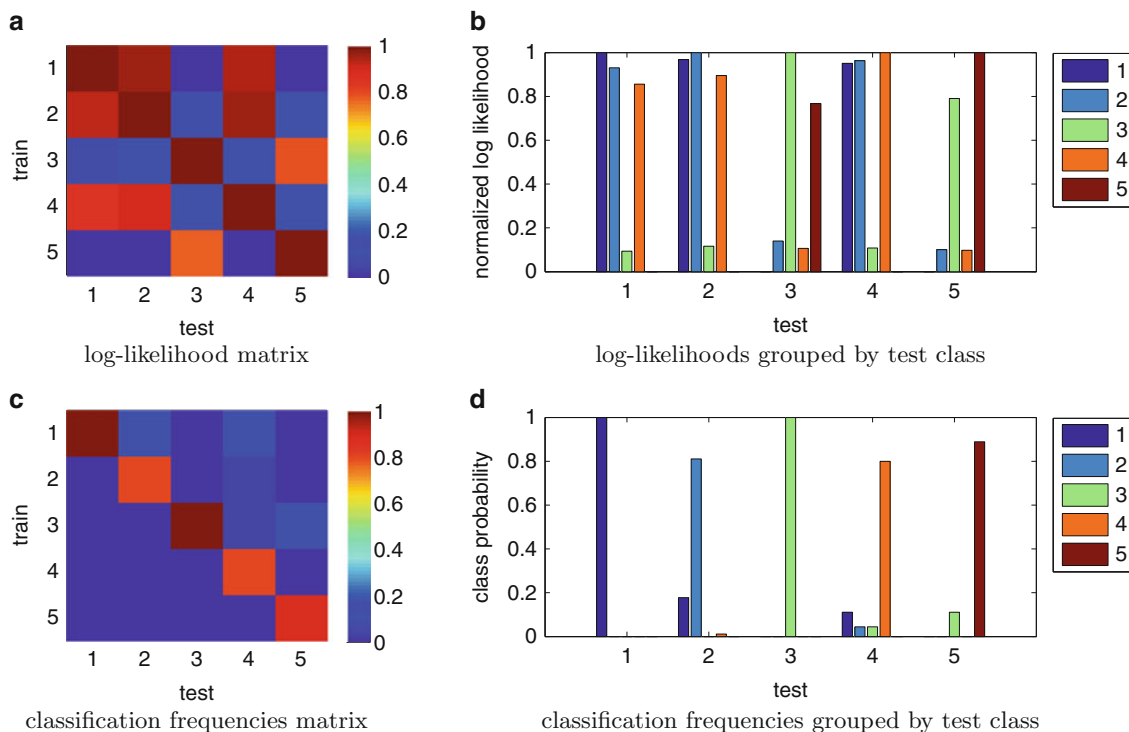
Fig. 18.5 Column structure data class-class log-likelihoods are shown as (**a**) matrix and (**b**) bar groups. Similarly, classification frequencies are shown as (**c**) matrix and (**d**) bar groups
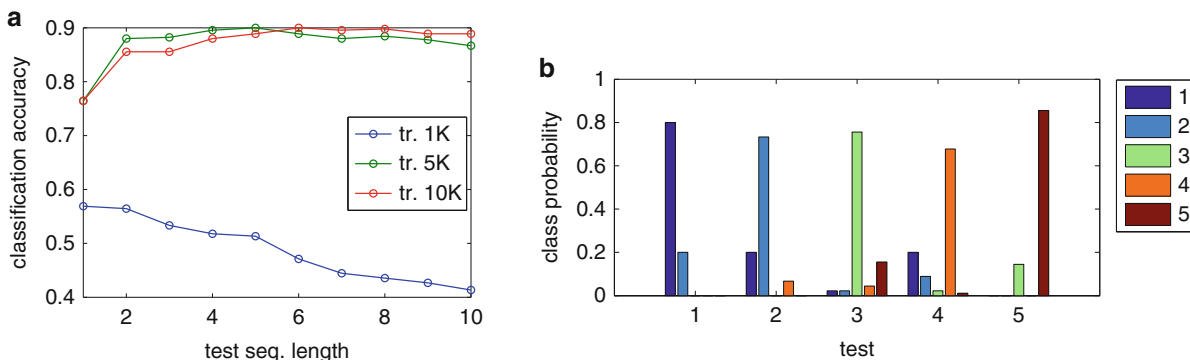
Fig. 18.6 (**a**) Overall classification accuracy on column structure data as a function of training and test sequence lengths. (**b**) Classification frequencies (by test class) when training and test sequence lengths are $5K$ and $1K$, respectively

damage classes (3 and 5) are close to each other, although less than the previous three classes. On the other hand, there is a significantly higher separation between the low- and high-damage classes, and, as we will see next, a sequence from one of these groups is rarely misclassified as belonging to a class from the other group.

Classification results are shown in Figs. 18.5c, d. Again, these are two different visualizations of the same results. For each pair of classes, test class i and training class j, the frequency of classifying a test sequence from class i as belonging to class j is shown. Therefore, each column in the matrix in Fig. 18.5c, as well as each group of bars in Fig. 18.5d, must sum to one. Overall, sequences are classified correctly most of the times (high diagonal values). Sequences from the two minor damage classes (2 and 4) are occasionally misclassified as belonging to the intact class (1), while sequences from the two major damage classes (3 and 5) are never misclassified as belonging to one of the low-damage classes and occasionally misclassified as belonging to the other major damage class.

Finally, we analyze classification accuracy as a function of training and test sequence lengths. Figure 18.6a shows the overall classification accuracy (averaged over all classes) for three different training sequence lengths, 1,000, 5,000 and 10,000, and ten test sequence lengths ranging from 1,000 to 10,000. Interestingly, for a fixed training sequence length,

classification accuracy increases as the test sequence length increases only until it becomes equal to the training sequence length, after which it start decreasing. This result suggests that the properties of these time-series data change over time. Namely, subsequence for training and testing are always extracted starting at the same time in all sequences. Therefore, when training and test sequences are of the same length, they are aligned with respect to where they are in the measurement process (assuming that different sequences are measured under the same or very similar conditions). However, when the test sequence length increases beyond the training sequence length, test sequences start to increasingly incorporate parts of the process that was not included in training. Similarly, when test sequences are shorter than training sequences, training sequences include characteristics of a broader window of the process than is tested. This also can explain why the classification results are overall not better when the training sequence length is 10,000 than when it is 5,000. Likely, a window of 10,000 is too broad and the additional amount of data, the second 5,000 samples, does not help, since it differs in behavior than the first 5,000 time samples. Naturally, there is a tradeoff between this behavior and the sequence length. For example, 1,000 is too short, and the results with that length are clearly much worse. The phenomenon explained here could be attributed to the nature of excitation used in this setup, which is free vibration. The results with the shaker excitation, shown below, do not follow this pattern and behave as with one's expectations—more test or training data consistently yields higher accuracy. Lastly, Fig. 18.6b shows classification results for training and test sequence lengths equal to 5,000 and 1,000, respectively, which could be compared to the results in Fig. 18.5d, in which both lengths are 5,000.

18.4.2 3-Story 2-Bay Structure Results

We present the same set of results on the 3-story 2-bay structure data. Average log-likelihoods between all pairs of classes are shown as a matrix in Fig. 18.7a and as bars grouped by test class in Fig. 18.7b. Again, these log-likelihoods are normalized such that each column in the matrix are between 0 and 1. As with the single column structure, the average log-likelihood of a sequence of one class is the highest when conditioned on a sequence from that same class (diagonal elements), and the highest confusion is between the low-damage classes, namely, the intact class, 1, and the two minor damage classes, 2 and 4. The lesser major damage classes, 3 and 5, seem to be occasionally confused as classes with either smaller or higher damage relative to them. Finally, the greater major damage class, 6, is most similar to the lesser major damage classes.

Classification results in terms of frequencies (fraction of times a sequence from one class is classified as belonging to another class) are shown as a matrix in Fig. 18.7c and as bars grouped by test class in Fig. 18.7d. Sequences from major damage classes (3, 5 and 6) are classified almost perfectly. On the other hand, some confusion between the three low-damage classes (1, 2 and 4) is present. In particular, sequences from the class that corresponds to a minor damage at node 17 are often misclassified as belonging to the intact class. This could possibly be attributed to the closeness of this node to the shaker.

The overall classification accuracy as a function of training and test sequence lengths is shown in Fig. 18.8a. Three different training sequence lengths were used, 1,000, 5,000 and 10,000, while the test sequence length is varied from 1,000 to 10,000. Unlike with the single column structure results, classification accuracy on the 3 story 2 bay structure data consistently improves with the increased length of either training or a test sequence. This trend suggests that there is likely no significant variability in the dynamics of a sequence over time, and, consequently, longer sequences represent effectively more data. This is an expected behavior, since excitation provided by the shaker is uniform over time. Finally, for comparison with the results in Fig. 18.7d, in which both lengths are 5,000, Fig. 18.8b shows classification results when training and test sequence lengths are 5,000 and 1,000.

We also analyze the the results of inference over dependence structures. The most likely parent set of each node obtained by structure inference on a single sequence (from intact class) is shown in Table 18.2. Three different results are shown, in which the number of additional parents (other than self, which is assumed) is bounded to 1, 2 and 3. As can be seen, these data favor larger parent sets and the most likely parent set for each node in each scenario exhausts the constraint. Clearly, each node is most often best explained by nearby nodes. The exact meaning of these results and they correspond to the physics of the problem requires further investigation. Besides explaining data and properties of a physical structure, one possible application of dependence structure analysis is in recovering the topology of a physical structure when it is unknown. Another interesting observation is that, while by increasing the number of allowed parents, the new "best" parent set of a node is most commonly a superset of the previous one, this is not always the case. For example, the best parent of size 1 of node 5 is 14. However, node 14 is not included in its best parent sets of sizes 2 and 3. This reiterates the need for dependence inference at the structure level rather than at the pairwise level—simply adding nodes from k most likely pairwise relationships does not result in the mostly likely parent set of size k.
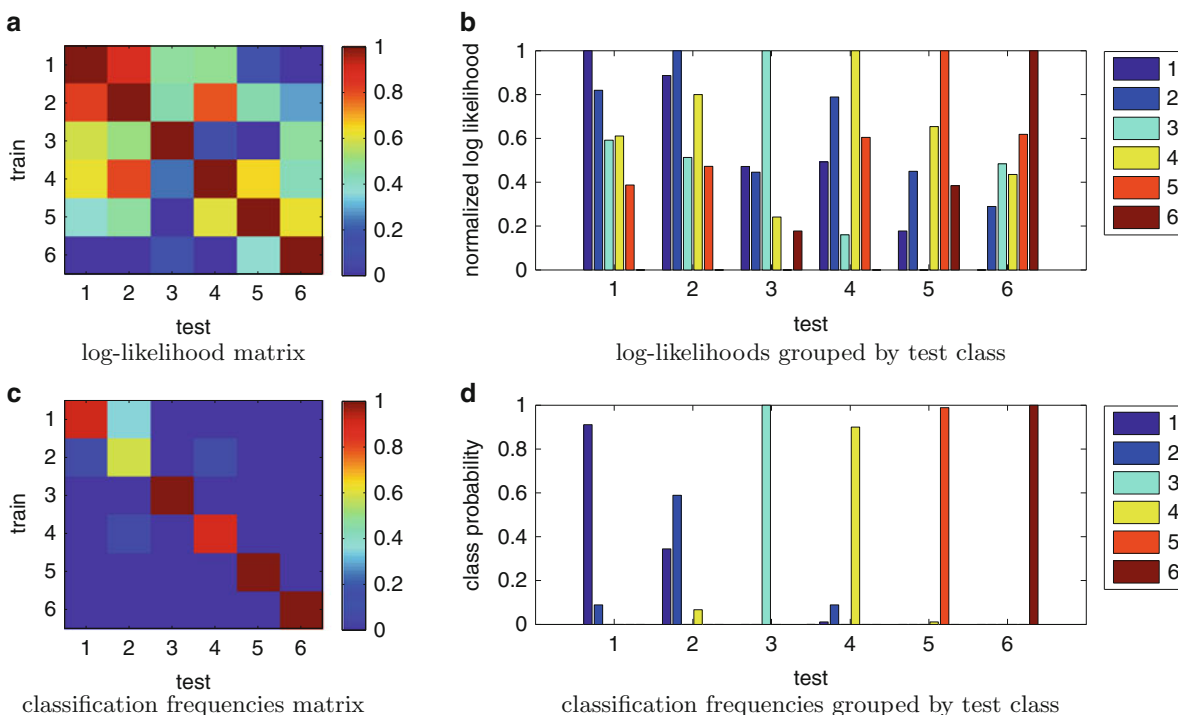
Fig. 18.7 3 story 2 bay structure data class-class log-likelihoods are shown as (**a**) matrix and (**b**) bar groups. Similarly, classification frequencies are shown as (**c**) matrix and (**d**) bar groups
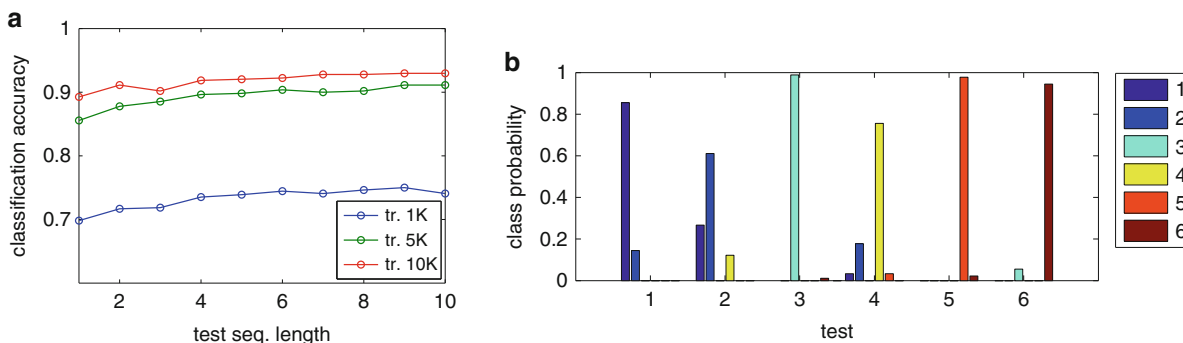
Fig. 18.8 (**a**) Overall classification accuracy on 3 story 2 bay structure data as a function of training and test sequence lengths. (**b**) Classification frequencies when training and test sequence lengths are $5K$ and $1K$, respectively

Table 18.2 Most likely parent sets of each node when the number of additional parents is bounded to 1, 2, and 3

Node	1	2	3	4	5	6	7	8	9	10	11	12	13	14	15	16	17	18
1-bound	10	11	6	7	14	3	8	2	3	1	2	15	14	5	12	13	18	12
2-bound	7	5	6	1	2	3	1	2	3	1	2	15	7	5	12	13	11	12
	10	11	9	7	8	9	8	9	6	2	17	18	14	11	18	17	18	16
3-bound	4	1	2	1	2	3	1	2	3	1	2	9	14	5	3	10	11	12
	7	5	6	7	8	9	4	5	6	2	10	15	15	11	12	13	15	15
	10	11	9	16	17	15	8	9	15	7	17	18	16	18	18	17	18	16

Each node is assumed to be its own parent. Only additional parents are shown

18.5   Conclusion

In this paper we have presented an approach using Bayesian inference on a state-space switching interaction model to detect and classify changes indicative of damage in a model structure. Data was collected with accelerometers from two laboratory models, a steel cantilever column and a larger 3 story 2 bay steel structure, and analyzed using the damage detection approach by obtaining the log-likelihoods of test sequences given a different training sequence. For both structures, test data were classified correctly to their respective damage scenarios or the intact structure case with relatively high accuracy. It was also found that generally longer test and training sequences provide better classification accuracy. Inference was done over the dependence structures in the model, and it was determined that the parents of a node were most likely physically connected to that node, possibly providing information about the physical structure. Future work involves testing the approach on more structural configurations and damage scenarios, classification using the edges in the dependency graph, and use as a single-class classifier, but with these preliminary results this approach joins the growing arsenal of effective damage detection methods for statistical based structural health monitoring.

Appendix: Matrix Normal Inverse Wishart Prior

Here, we consider a linear Gaussian model of a multivariate signal X_t,

$$X_t = A\,X_{t-1} + w_t\,, \qquad w_t \sim \mathcal{N}(0, Q)\,, \tag{18.16}$$

with parameters A (transition matrix) and Q (noise covariance matrix).

We assume that $\Theta = (A, Q)$ follows a matrix-normal inverse-Wishart distribution, which is a conjugate prior to the dependence model $\mathcal{N}(X_t; AX_{t-1}, Q)$:

$$p(A, Q; M, \Omega, \Psi, \kappa) = \mathcal{MN}\text{-}\mathcal{IW}(A, Q; M, \Omega, \Psi, \kappa) = \mathcal{MN}(A; M, Q, \Omega)\,\mathcal{IW}(Q; \Psi, \kappa)\,. \tag{18.17}$$

It is a product of (1) the matrix-normal distribution

$$\mathcal{MN}(A; M, Q, \Omega) = \frac{\exp\left(-\frac{1}{2}\operatorname{tr}\left[\Omega^{-1}(A-M)^T Q^{-1}(A-M)\right]\right)}{(2\pi)^{dl/2}|\Omega|^{d/2}|Q|^{l/2}}\,, \tag{18.18}$$

where d and l are the dimensions of matrix A ($A_{d\times l}$), while $M_{d\times l}$, $Q_{d\times d}$ and $\Omega_{l\times l}$ are the mean, the column covariance and the row covariance parameters; and (2) the inverse-Wishart distribution

$$\mathcal{IW}(Q; \Psi, \kappa) = \frac{|\Psi|^{\kappa/2}}{2^{\kappa d/2}\Gamma_d(\kappa/2)}\,|Q|^{-(\kappa+d+1)/2}\exp(-\frac{1}{2}\operatorname{tr}(\Psi Q^{-1}))\,, \tag{18.19}$$

where d is the dimension of matrix Q ($Q_{d\times d}$) and $\Gamma_d()$ is a multivariate gamma function while κ and $\Psi_{d\times d}$ are the degree of freedom and the inverse scale matrix parameters. Note how the two distributions are coupled. The matrix normal distribution of the dependence matrix A depends on the covariance matrix Q, which is sampled from the inverse Wishart distribution.

Due to conjugacy, the posterior distribution of parameters A and Q given data sequence $X_0, X_1, \ldots, X_T$ is also a matrix-normal inverse-Wishart distribution:

$$p(A, Q | X_{0:T}; M, \Omega, \Psi, \kappa) = \mathcal{MN}\text{-}\mathcal{IW}(A, Q; M', \Omega', \Psi', \kappa') = \mathcal{MN}(A; M', Q, \Omega')\,\mathcal{IW}(Q; \Psi', \kappa')\,, \tag{18.20}$$

where

$$\Omega' = \left(\Omega^{-1} + \sum_{t=0}^{T-1} X_t X_t^T\right)^{-1}$$

$$M' = \left(M\Omega^{-1} + \sum_{t=1}^{T} X_t X_{t-1}^T\right)\Omega' \tag{18.21}$$

$$\kappa' = \kappa + T$$

$$\Psi' = \Psi + \sum_{t=1}^{T} X_t X_t^T + M\Omega^{-1}M^T - M'\Omega'^{-1}M'^T.$$

References

1. Brownjohn JM (2007) Structural health monitoring of civil infrastructure. Philos Trans Roy Soc A Math Phys Eng Sci 365(1851):589–622
2. Sohn H, Farrar CR, Hemez FM, Shunk DD, Stinemates DW, Nadler BR, Czarnecki JJ (2004) A review of structural health monitoring literature: 1996–2001. Los Alamos National Laboratory, Los Alamos
3. Beck JL, Katafygiotis LS (1998) Updating models and their uncertainties. I: Bayesian statistical framework. J Eng Mech 124(4):455–461
4. Vanik MW, Beck J, Au S (2000) Bayesian probabilistic approach to structural health monitoring. J Eng Mech 126(7):738–745
5. Flynn EB, Todd MD (2010) A Bayesian approach to optimal sensor placement for structural health monitoring with application to active sensing. Mech Syst Signal Process 24(4):891–903
6. Dzunic Z, Fisher III J (2014) Bayesian Switching interaction analysis under uncertainty. Proceedings of the 17th international conference on artificial intelligence and statistics, pp 220–228
7. Heckerman D (1995) A tutorial on learning with Bayesian networks. Technical reports, MSR-TR-95-06, Microsoft Research, Mar 1995
8. Ghahramani Z (1998) Learning dynamic Bayesian networks. In: Giles, CL, Gori M (eds) Adaptive processing of sequences and data structures. Springer, London, pp 168–197
9. Chickering DM (1996) Learning Bayesian networks is NP-complete. In: Fisher D, Lenz H (eds) Learning from data: artificial intelligence and statistics V. Springer, New York, pp 121–130
10. Buntine W (1991) Theory refinement on bayesian networks. In: Proceedings of the 7th conference annual conference on uncertainty in artificial intelligence (UAI-91). Morgan Kaufmann, San Mateo, pp 52–60
11. Cooper GF, Dietterich T (1992) A Bayesian method for the induction of probabilistic networks from data. Mach Learn 9:309–347
12. Heckerman D, Geiger D, Chickering DM (1995) Learning Bayesian networks: the combination of knowledge and statistical data. Mach Learn 20:197–243
13. Friedman N, Koller D (2003) Being Bayesian about Bayesian network structure: a Bayesian approach to structure discovery in Bayesian networks. Mach Learn 50(1–2):95–125 (full version of UAI 2000 paper)
14. Siracusa MR, Fisher III JW (2009) Tractable Bayesian Inference of time-series dependence structure. In: Proceedings of the 12th international conference on artificial intelligence and statistics

Chapter 19
Iterative Spatial Compressive Sensing Strategy for Structural Damage Diagnosis as a BIG DATA Problem

Ruigen Yao, Shamim N. Pakzad, Parvathinathan Venkitasubramaniam, and Jamie M. Hudson

Abstract Accurate structural damage identification calls for dense sensor networks, which are becoming more feasible as the price of electronic sensing systems reduces. To transmit and process data from all nodes of a dense network would be an onerous task which creates a BIG DATA problem; therefore scalable algorithms are needed so that decision on the current state of the structure can be made based on efficient data processing. In this paper, an iterative spatial compressive sensing scheme for damage existence identification and localization will be introduced. At each iteration, a subset of sensors is selected for data transmission and relevant information will be extracted at central station for damage existence identification/localization. This information will also provide useful guidance in future selection of sensing locations. The devised algorithm is applied to identify damage in a simulated gusset plate.

Keywords BIG DATA • Structural health monitoring • Dense sensor network • Damage detection • Hypothesis testing • Ant colony optimization

19.1 Introduction

As the technology of structural health monitoring (SHM) matures, sensor networks comprising of large numbers individual sensing units are becoming more implementally and financially feasible [1–4]. In order to transmit and process the large amount of data (BIG DATA) acquired from continuous and/or long-term monitoring, efficient compression/information extraction algorithms are needed.

In this paper a compact sensing framework on subset selection within dense sensor network for damage detection is introduced. It complements the existing chronological compressive sensing methods, where time histories are compressed at individual sensor nodes [5, 6]. In this scheme, damage existence is first identified via hypothesis testing on the determinant of sample correlation matrix, as a damage feature, among several random locations. Then damage is localized as the location where the maximum Damage Location Indicator (DLI) from iterative random sampling occurs. At each iteration damage indices are computed from the newly drawn random samples, damage location is recognized as that of maximum DLI, and the random sampling distribution is updated according to the accumulated damage indices using an Ant Colony Optimization (ACO) [7, 8] inspired algorithm. The iteration continues until convergence criteria for the damage location is met. Lastly, the presented methodology is applied to identify single-point and multi-point damage in a gusset plate simulated in ABAQUS using the strain measurements under uniaxial tension.

R. Yao (✉) • S.N. Pakzad • J.M. Hudson

Department of Civil and Environmental Engineering, Lehigh University, ATLSS Engineering Research Center, 117 ATLSS Drive, Imbt Labs, 18015 Bethlehem, PA, USA
e-mail: yaoruigen@gmail.com

P. Venkitasubramaniam

Department of Electrical and Computer Engineering, Lehigh University, Packard Laboratory, 19 Memorial Drive West, 18015 Bethlehem, PA, USA

19.2   Damage Detection Using Hypothesis Testing on Spatial Correlation of Random Samples

Damage features/indices are certain functions of structural responses that can reflect the condition of monitored structure (or part of a structure) [9–17]. For damage existence detection applications in this paper, structural measurements will be collected continuously from n random locations. Denoting the collected sample vectors as $X_1, X_2, \ldots, X_n$, its covariance matrix can be estimated as below:

$$\widehat{Cov}(X) = 1/N \left(\left[X_1 - \overline{X}_{1b}, \ X_2 - \overline{X}_{2b}, \ldots X_n - \overline{X}_{nb} \right]^T \left[X_1 - \overline{X}_{1b}, \ X_2 - \overline{X}_{2b}, \ldots X_n - \overline{X}_{nb} \right] \right) \tag{19.1}$$

where N is the number of samples taken at each location (thus also the length of each vector). The macron accent $\overline{\{\cdot\}}$ represents the mean of the vector group, and subscript b denotes points from baseline condition. If measurements at these locations are jointly Gaussian random variables, then the covariance estimator follows a Wishart distribution [18]. Statistics based on this assumption can be devised to test whether the mean/variance of the signal vectors has changed simultaneously. Note that in order to examine mean shift, means of baseline signals should be used for computing the covariance matrix as in Eq. (19.1).

One shortcoming of covariance-based hypothesis testing is that it is affected by changes in excitation/input level. As such, estimated correlation matrix, which is the covariance estimator normalized by the measurement variance at separate locations, is examined instead:

$$\widehat{Corr}(X) = \mathrm{diag}([Var\,(X_1),\ Var\,(X_2),\ldots, Var\,(X_n)])^{-1/2}\,\widehat{Cov}(X)\,diag([Var\,(X_1),\ Var\,(X_2),\ldots, Var\,(X_n)])^{-1/2} \tag{19.2}$$

Correlation is robust to input magnitude variation, but its distribution under Gaussian sample assumption is harder to express analytically. Gupta and Nagar [19] provided a formula for computing the probability density function (PDF) of the determinant of the correlation matrix given that the samples are spatially uncorrelated:

$$f(w) = c\,(p, N)\, w^{-1} G_{p-1,p-1}^{p-1,0} \left[w \left| \begin{matrix} \frac{N-1}{2}, \frac{N-1}{2}, \ldots, \frac{N-1}{2} \\ \frac{N-2}{2}, \frac{N-3}{2}, \ldots, \frac{N-p}{2} \end{matrix} \right| \right], \quad 0 < w < 1.$$

$$c\,(p, N) = \Gamma^{p-1}\left(\frac{N-1}{2}\right) \bigg/ \prod_{j=2}^{p} \Gamma\left(\frac{N-j}{2}\right).$$

$$G_{p,q}^{m,n} \left[z \left| \begin{matrix} a_1, \ldots, a_p \\ b_1, \ldots, b_q \end{matrix} \right| \right] = (2\pi i)^{-1} \int_L \left\{ \frac{\prod_{j=1}^{m} \Gamma\,(b_j + h) \prod_{j=1}^{n} \Gamma\,(1 - a_j - h)}{\prod_{j=m+1}^{q} \Gamma\,(1 - b_j - h) \prod_{j=n+1}^{p} \Gamma\,(a_j + h)} \right\} z^{-h} dh \tag{19.3}$$

In Eq. (19.3), p is number of Gaussian random variables, N is the sample size, Γ is the gamma function and $G_{::}^{::}$ is the Meijer's G-function, which is a general expression encompassing many elementary functions such as exponential and logarithmic functions. As measurements happen at individual sensor nodes, it can be assumed that the measurement noise is spatially independent and this PDF is a fit for joint testing the statistical properties of measurements at the selected locations. Left-sided hypothesis testing will be used here, as when there is a mean drift in the random samples, vectors in Eq. (19.1) will have stronger correlation, leading to a reduction in correlation determinant value.

19.3 Ant Colony Optimization Based Aggregation Algorithm for Damage Localization

As part of a larger effort to introduce biological swarm intelligence to optimization procedures, researchers have attempted to simulate the ant foraging mechanism for a near-optimal solution [7, 8]. Ants, when go searching for food, leave chemicals (phermone) along their trails. The more frequent a trail is travelled, the more amount of pheromone is deposited on it, which will in turn attract more ants. By simulating this process, optimization algorithms identify those subpaths that are shared by more explored solutions as more probable components of optimal solutions.

For our iterative-compressive-sensing based damage localization, each ant/agent is a sample made (or to be made) at a location. So basically, a batch of 'worker ants' is released every iteration and their destinations are determined from the current spatial sampling distribution. Initially the distribution is uniform and routinely updated based on two considerations: (1) the DLI value of the nearest neighbor (from available samples) of each sample location, and (2) whether the location's nearest neighbor is current and has a higher DLI value than its former nearest neighbor. The first criterion is denoted 'desirability' or 'sweetness' of a location, while the second criterion is defined its 'pheromone' or 'potential'. The explicit formulas for desirability, pheromone, and sampling probability computation are shown as below:

$$Dsrb(x, y)_i = \begin{cases} 1, & i = 1 \\ DLI\left(NN\left\{[x\ y], [x_{kn}\ y_{kn}]_i\right\}\right), & i > 1 \end{cases}$$

$$Pher(x, y)_i = \begin{cases} 1, & i \leq 2 \\ \text{logical}\left(Dsrb(x, y)_i > DLI\left(NN\left\{NN\left\{[x\ y], [x_{kn}\ y_{kn}]_i\right\}, [x_{kn}\ y_{kn}]_{i-1}\right\}\right)\right), & i > 2 \end{cases}$$

$$p(x, y)_i = \begin{cases} 0, & [x\ y] \in [x_{kn}\ y_{kn}]_i \\ \dfrac{Pher(x,y)_i \cdot Dsrb(x,y)_i}{\displaystyle\sum_{[x\ y] \notin [x_{kn}\ y_{kn}]_i} Pher(x,y)_i \cdot Dsrb(x,y)_i}, & [x\ y] \notin [x_{kn}\ y_{kn}]_i \end{cases} \tag{19.4}$$

Here subscript i denotes the iteration number, subscript 'kn' stands for 'known', and $NN\{set1, set2\}$ is the operation of finding the nearest neighbors of $set1$ in $set2$. Note here $[x_{kn}\ y_{kn}]_i$ refers to the collection of known samples prior to ith round of sampling starts. The search stops either after a preset number of iteration (N_{iter}) or after the variation of the 'phermone'/'potential' map becomes negligible and stable:

$$CC = i \geq N_{iter}\ ||\ \left(\left|1 - \frac{|Pher_i|}{|Pher_{i-1}|}\right| < 5\%\ \&\&\ \left|1 - \frac{|Pher_{i-1}|}{|Pher_{i-2}|}\right|\right.$$

$$\left. < 5\%\ \&\&\ (Pher_i - Pher_{i-1})(Pher_{i-1} - Pher_{i-2}) < 0\right) \tag{19.5}$$

The 'negligibility' requirement here is expressed as that the incremental normalized difference of pheromone is within 5 % for two consecutive times, while the 'stability' requirement is evinced as a sign change in the difference in meantime. The detailed flow chart of this CS scheme is presented in Fig. 19.1.

The framework of these two metaheuristic methods are advantageous in that they do not rely on assumptions on DLI surface forms and thus adapt to different possible damage scenarios. In the subsequent section, they will be validated through a simulation example.

19.4 Numerical Validation

To evaluate the effectiveness of the proposed damage existence detection/localization algorithms, they are applied to detect damage in a two-way gusset plate connection (Fig. 19.2a) simulated in ABAQUS [20] using shell elements. The connection is set under uniform tension from both sides.
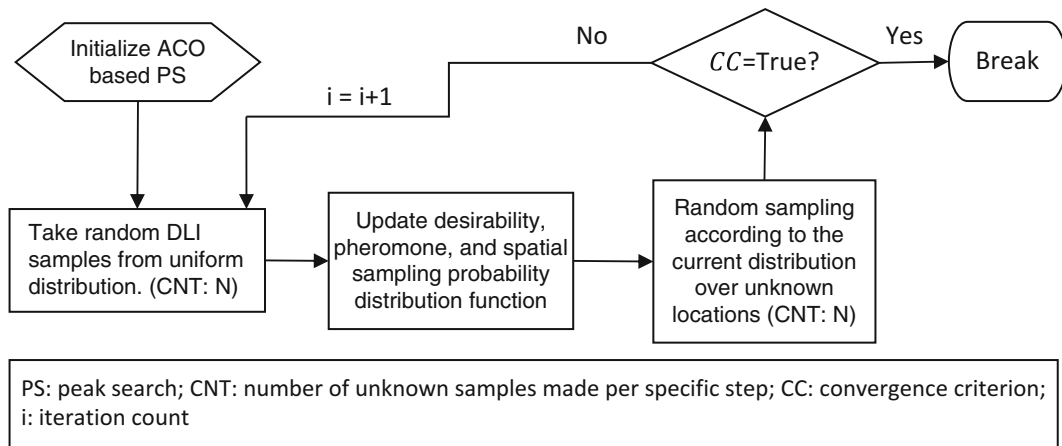
Fig. 19.1 Flow-chart illustration of the ACO inspired damage localization algorithm
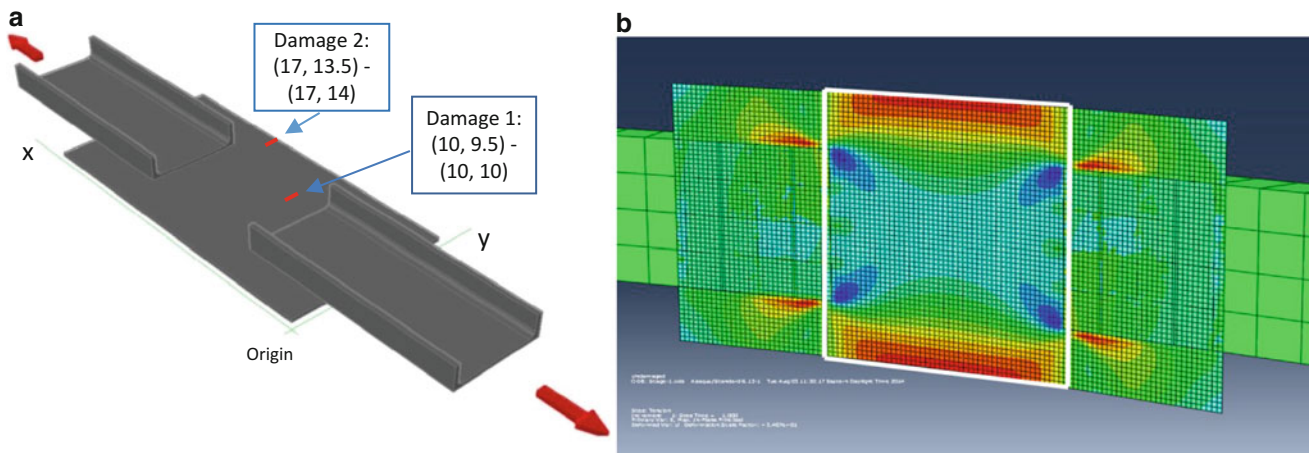
Fig. 19.2 (**a**) Simulation/test setup; (**b**) close-up of the undamaged gusset-plate in ABAQUS

Table 19.1 Damage existence identification result via hypothesis testing for the simulated gusset plate

	Stage 1	Stage 2	Stage 3
$\mathrm{Det}\left(\widehat{Corr}\right)$	0.4236	0.2469	0.2498
$Prob\left(\mathrm{Det}(Corr) < \mathrm{Det}\left(\widehat{Corr}\right)\right)$	0.7484	0.0154	0.0198

The specimen was composed of two $C8 \times 11.5$ channel members welded (simulated by tie constraints) to a 14×28 in. plate that had a thickness of ¼ in.. Each of the connecting members was 20 in. long and has 8 in. overlap with the main plate. The locations of damage on the plate occur in the middle portion of the plate that is left free of connections to allow ease of data analysis. The assembled connection, shown in Fig. 19.2 was 52 in. in length and was designed to withstand up to 100 kips of axial tensile force.

The simulation consisted of three stages: (1) the plate was undamaged, providing control readings of strain with which to compare the results of the subsequent stages, (2) a crack was made with a cutting grinder plate from (10, 10) to (10, 9.5), (3) another crack was added on the edge of the plate from (17, 13.5) to (17, 14). Cracks on the plate were simulated using the 'SEAM' option. The (x, y) coordinate system and damage locations are illustrated in Fig. 19.2a.

Nodal train data from the plate was acquired for use as input for the calculation of the damage indices and for the iterative sampling scheme. Figure 19.2b shows the strain on the plate at Stage 1. The adopted element size is 0.25 in., and the area outlined in white defines the 12×14 in. range of data used later for the sampling scheme.

Table 19.1 shows the hypothesis testing results out of three datasets obtained respectively from three structural conditions. The metric presented here is the exceeding probability corresponding to the correlation determinant calculated from measurements at six randomly selected locations. It can be seen that as the system becomes damaged, the exceeding probability reduces drastically (<5 %), signaling a statistically significant change.

Fig. 19.3 Damage location identification result via ACO algorithm for the simulated gusset plate
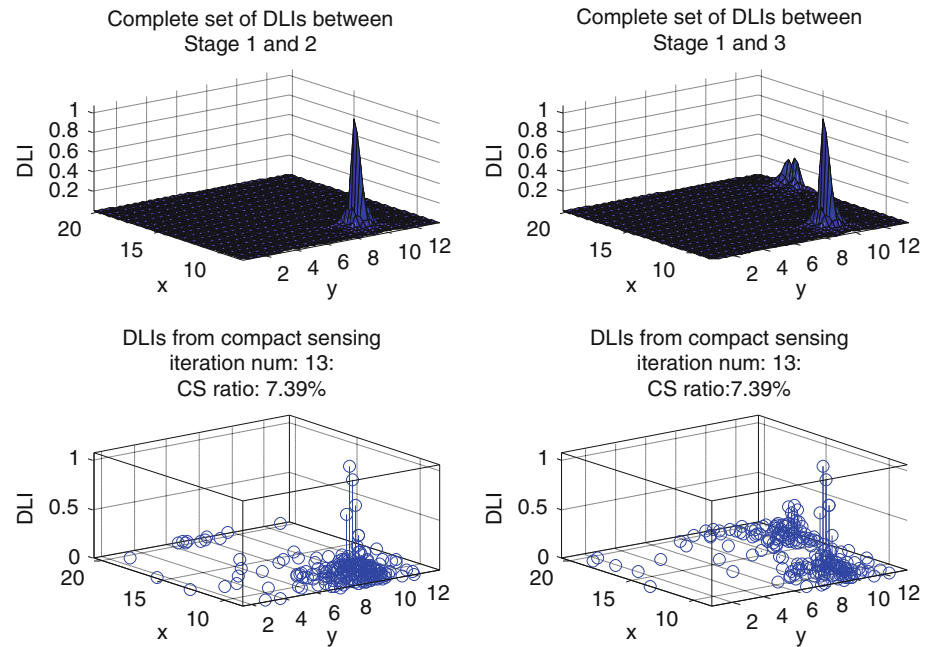
The damage localization result is shown in Fig. 19.3. Assuming decentralized DLI computation, here the spatial sampling is performed directly on the damage location indicators, which is defined as the average of the correlation coefficients between strain measured at current location and each of the nearest neighbor locations in this case. It can be seen that though compressive sensing picks up only a fraction of the DLIs over the total sensing region, most of its 'catches' are around the actual damage, and thus carry relatively significant information for damage characterization. It is therefore concluded that the ACO based iterative compressive sensing scheme has much reduced the amount of information needed to be collected from the individual nodes to the central station, thus achieving greater energy efficiency.

19.5   Conclusion

In this paper, a damage existence identification and localization strategy for BIG DATA based on compact sensing of dense sensor network(s) is outlined. Existence identification of damage is accomplished via theoretical hypothesis testing on the spatial correlation matrix of randomly collected samples, and if a change is thus detected, localization is performed using selective sensor 'sampling'. The sampling distribution is routinely updated on incoming sensor measurements through ant colony inspired optimization algorithm, which helps the selection to converge to the true damage location after a few rounds of measurement retrieval at random sensor locations.

In another perspective, the idea of iterative subspace sampling based damage detection is to decrease the amount of data need to be remotely transmitted from sensors at the expense of increased computation activity in the base station. This exchange could lead to total energy savings and improvement of the flow of sensing/control for structural health monitoring, especially when wireless sensors are involved.

References

1. Lynch J, Loh K (2006) A summary review of wireless sensors and sensor networks for structural health monitoring. Shock Vib Dig 38(91): 91–128
2. Farrar CR, Park G, Allen DW, Todd MD (2006) Sensor network paradigms for structural health monitoring. Struct Control Health Monit 13(1):210–225

3. Pakzad S (2010) Development and deployment of large scale wireless sensor network on a long-span bridge. Smart Struct Syst 6(5–6):525–543
4. Cheng L, Pakzad SN (2009) Agility of wireless sensor networks for earthquake monitoring of bridges. In: 2009 sixth international conference on networked sensing systems (INSS), IEEE, pp 1–4
5. O'Connor SM, Lynch JP, Gilbert AC (2014) Compressed sensing embedded in an operational wireless sensor network to achieve energy efficiency in long-term monitoring applications. Smart Mater Struct 23(8):085014
6. Mascarenas D, Cattaneo A, Theiler J, Farrar C (2013) Compressed sensing techniques for detecting damage in structures. Struct Health Monit 12(4):325–338
7. Dorigo M, Birattari M (2010) Ant colony optimization. Encyclopedia of machine learning
8. Putha R, Quadrifoglio L, Zechman E (2012) Comparing ant colony optimization and genetic algorithm approaches for solving traffic signal coordination under oversaturation conditions. Comput-Aided Civ Infrastruct Eng 27(1):14–28
9. Yao R, Pakzad SN (2012) Autoregressive statistical pattern recognition algorithms for damage detection in civil structures. Mech Syst Signal Process 31:355–368
10. Yao R, Pakzad SN (2014) Time and frequency domain regression-based stiffness estimation and damage identification. Struct Control Health Monit 21(3):356–380
11. Dorvash S, Pakzad S, Labuz E (2014) Statistics based localized damage detection using vibration response. Smart Struct Syst (in press)
12. Shahidi SG, Pakzad SN (2014) Generalized response surface model updating using time domain data. J Struct Eng 140(8):A4014001
13. Dorvash S, Pakzad SN, Labuz E, Ricles J, Hodgson IC (2014) Localized damage detection algorithm and implementation on a large-scale steel beam-to-column moment connection. Earthq Spectra (in press)
14. Nigro MB, Pakzad SN, Dorvash S (2014) Localized structural damage detection: a change point analysis. Comput-Aided Civ Infrastruct Eng 29(6):416–432
15. Shahidi SG, Nigro MB, Pakzad SN, Pan Y (2014) Structural damage detection and localisation using multivariate regression models and two-sample control statistics. Struct Infrastruct Eng:1–17
16. Yao R, Pakzad SN (2014) Damage and noise sensitivity evaluation of autoregressive features extracted from structure vibration. Smart Mater Struct 23(2):025007
17. Yao R, Pakzad SN (2014) Multi-sensor aggregation algorithms for structural damage diagnosis based on substructure concept. J Eng Mech (in Press)
18. Conradsen K, Nielsen AA, Schou J, Skriver H (2003) A test statistic in the complex Wishart distribution and its application to change detection in polarimetric SAR data. IEEE Trans Geosci Remote Sens 41(1):4–19
19. Gupta A, Nagar D (2004) Distribution of the determinant of the sample correlation matrix from a mixture normal model. Random Oper Stochastic Equ 12(2):193–199
20. ABAQUS V (2013) "6.13," Dassault systemes. Pawtucket

Chapter 20
Numerical Enhancement of Nonlinear Model Tracking for Health Monitoring

Timothy A. Doughty and Michael J. Hector

Abstract Crack formation in a vibrating cantilever beam has been identified with the in situ nondestructive health monitoring Nonlinear Model Tracking (NMT) technique. The nonlinear cubic stiffness parameter has been chosen as the system's dominant nonlinearity and has been tracked until catastrophic failure using a Continuous Time based system identification. The use of a nonlinear model allows for a range of healthy but complex system dynamics, such as changing natural frequency, which indicates a change in system health in traditional linear system health monitoring. Previous research has shown that significant change in the nonlinear parameter indicates a transition from a healthy to unhealthy system. The purpose of this study is to improve the robustness of the NMT method by investigating new data processing techniques. Numerical integration, regression fit with linear FRF, and strain gage sensors were introduced. The results of these new techniques were then compared with results from previous techniques to highlight effectiveness in determining change in a system's health.

Keywords Health monitoring • Nonlinear • Fatigue • System identification • Non-destructive

20.1 Introduction

Fatigue contributes to roughly 90 % of all mechanical service failures. Oscillating systems tend to form cracks at stress concentrations, which then grow and propagate through the material to cause failure. Nondestructive Evaluation (NDE) Techniques have been developed in the past few decades to produce failure indicators without causing damage to the system; see Doebling et al. for a comprehensive view [1]. Traditional NDE often relies on shifts in natural frequencies to detect a crack forming. The change in natural frequency is assumed to be caused by changing stiffness which is assumed to be caused changes in cross-sectional area associated with crack formation.

Although traditional NDE techniques have been used with success, they generally assume that the monitored systems are linear. For systems that are not weakly nonlinear, this assumption can lead to poor results [2]. In nonlinear vibrations, natural frequency is dependent on the excitation amplitude, thus a change in the healthy system's natural frequency may be caused by an increased forcing on the system rather than a changing stiffness due to crack initiation [3]. Thus, traditional NDE techniques may trigger false premonition of failure. By adapting NDE techniques to account for system nonlinearities, the robustness of the technique can be improved. Progress in NDE has been made using nonlinear crack dynamics as indicators for premonition of failure [4–6].

This paper focuses on the dynamics of an estimated nonlinear parameter for an oscillating slender cantilever beam to detect crack initiation and propagation. These changes in the nonlinear parameter can be interpreted as early warnings of system failure. A cantilever beam is used as a building block for more complicated systems, and the slenderness of the beam will pronounce the system's nonlinearity [7]. The second mode of vibration has been chosen in accordance with the performance of the shaker used in testing. Stimulus and two sets of response data are measured and are used to populate Continuous Time system identification which produces estimates for the nonlinear parameter over time [7]. This method has been shown to be sensitive to subtle changes in health while not flagging changes in behavior associated with healthy but nonlinear systems.

T.A. Doughty (✉) • M.J. Hector
University of Portland, 5000 N Willamette Blvd, Portland, OR 97203, USA
e-mail: doughty@up.edu; hector15@up.edu

20.2 Methodology

The NMT method presented here is the result of several iterations in an ongoing study. It successfully detects the initiation of crack prior to catastrophic failure. Past studies have indicated the technique does not require correctly identified linear system parameters and benefits from a single simple nonlinear model term, even when multiple nonlinear terms better model the system being studied. Previous study has also shown that few data points are necessary to accurately identify the linear system parameters. Thus, minimal effort is needed to use this technique for each individual test beam.

Determining the nonlinearity to study has also been an iterative process. Models studied have included cubic nonlinearities associated with both bending stiffness and inertia, and quadratic nonlinearities due to drag. Consequently, as the complexity of the system grew, the robustness of results was diminished to the effect of giving no premonition of failure. It has been found that the cubic stiffness has the greatest effect on the dynamics of the beam while still being sensitive to small changes in system dynamics.

The method of data processing consists of two steps. First the linear parameters are treated as unknowns. Data is then collected and processed to determine the linear parameters. Three variations of this linear parameter estimation are done in this study. One is traditional, using measurements of mass, geometry, and free response. Another allows the Continuous Time system identification technique to estimate these parameters, and a third performs a curve fit to the steady state frequency response data. These linear parameters are then fixed for the rest of the analysis. For The second step the model is rearrange with the linear parameters now treated as known and the Continuous Time identification is used with active testing data and the initial records of healthy system data to produce estimations of just the nonlinear parameter for each time step [Doughty].

To collect the data for populating the identification algorithm, a typical beam is given an impulse and sweep stimuli to determine rough estimates of resonance and the potential for a multi-modal response. Then healthy data is taken as a series of steady state excitation and response records near resonance. The beam is then excited at a near-resonant frequency at high excitation levels and allowed to oscillate until failure.

20.3 Theoretical Model

In this study, a slender cantilever beam is subjected to vertical excitation. An excitation frequency near the beam's second natural frequency is chosen because of low frequency limitations on the excitation device. The theoretical model is shown in Fig. 20.1.

For this model v is the beam's spatially dependent displacement, m is mass per unit length, c is damping per unit length, D_ξ is the bending stiffness, A is the amplitude of base displacement, Ω is the frequency of excitation, t is time, s is length down the beam, and L is beam length.

The governing equation for this model with a nonlinear stiffness, is given by the following partial differential equation and boundary conditions:

$$m\ddot{v} + c\dot{v} + D_\xi \left\{ v^{iv} + \left[v' \left(v'v'' \right)' \right]' \right\} = -mA\Omega^2 \cos\left(\Omega t\right), \tag{20.1}$$

$$v\left(0, t\right) = v'\left(0, t\right) = v''\left(L, t\right) = v'''\left(L, t\right) = 0. \tag{20.2}$$
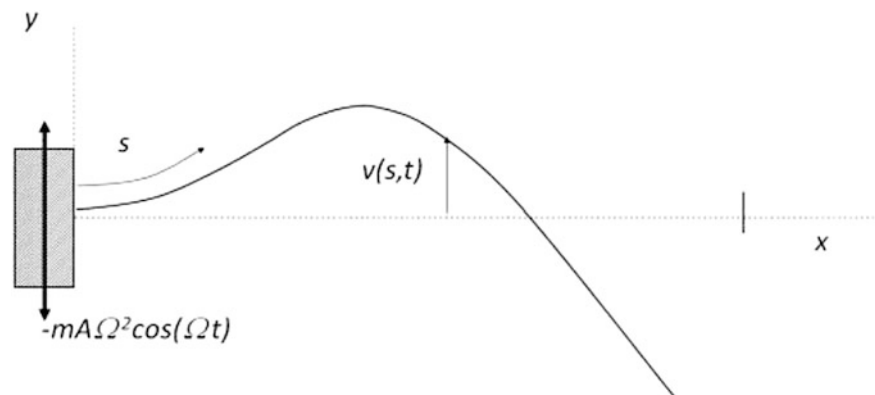
Fig. 20.1 Cantilever beam attachment and excitation with second mode shape shown

When the excitation is modal, the displacement is known to be spatially dependent. Let $\phi(s)$ be the orthonormalized mode shape given by

$$\phi(s) = C \left[\sin(\beta s) - \sinh(\beta s) - \Psi(\cos(\beta s) - \cosh(\beta s))\right] \tag{20.3}$$

Where:

$$\Psi = \frac{\sin(\beta L) + \sinh(\beta s)}{\cos(\beta L) + \cosh(\beta L)} \tag{20.4}$$

And for the second mode,

$$\beta L = 4.694 \tag{20.5}$$

Then, letting $v(s,t) = a(t) \cdot \phi(s)$, the nonlinear differential equation of one variable:

$$m\ddot{a} + c\dot{a} + ka + \dot{\alpha}a^3 = F(t) \tag{20.6}$$

Is derived where:

$$K = \left\{ D_\xi \int_0^L \phi\phi^{iv} ds \right\}, \tag{20.7}$$

$$\alpha = \left\{ D_\xi \int_0^L \phi\phi''^3 + 4\phi\phi'\phi''\phi''' + \phi\phi'^2\phi^{iv} ds \right\}, \tag{20.8}$$

$$F(t) = -mA\Omega^2 \cos(\Omega t) \cdot \int_0^L \phi ds \tag{20.9}$$

This model is very similar to the classic mass-spring-damper model, but with a single nonlinear term. Thus, in systems which have very weak nonlinearity, the model is reduced to the linear mass-spring-damp system. Now, if forcing and response can be obtained, the system parameters can be estimated. Previous studies have concluded that the cubic nonlinearity is dominant over quadratic and combination nonlinearities.

20.4 Experimental Setup

The experimental setup used to study the fatigue life of a slender cantilever beam is shown in Fig. 20.2. As in previous studies, readily available 6061 aluminum bar stock with dimensions $12.7 \times 1.57 \times 500$ mm was fixed to the platform of shaker. This was excited with a 45 N shaker over a range of frequencies to find each beam's second natural frequency. National instruments and LabVIEW were used as the function generator to produced sinusoidal excitation, as well as to acquire and process accelerometer and strain data. Accelerometers were attached at the shaker platform and at 4.5 cm down the beam. A strain gage was attached 4.5 cm down the beam. The two accelerometer data sets were subtracted to find the response of the beam which was plotted over a range of frequencies to find the second natural frequency.

Once the natural frequency was found, steady state points are measured at ± 1.5 and ± 3 Hz from the natural frequency. This is later used to determine the linear system parameters using frequency response fit. Previous studies have found this spread of frequencies to be effective in calculating the linear system parameters. Figure 20.3 shows these steady state points among data collected from the sweep.

After obtaining steady state points, the beam is then excited at its natural frequency and allowed to shake until failure. During this time, acceleration of the two accelerometers and strain from the strain gage are recorded.

Fig. 20.2 Experimental setup
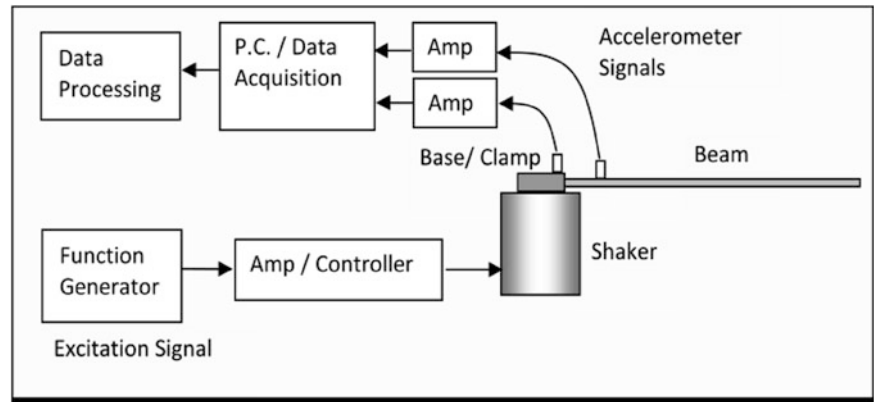
Fig. 20.3 Steady state points
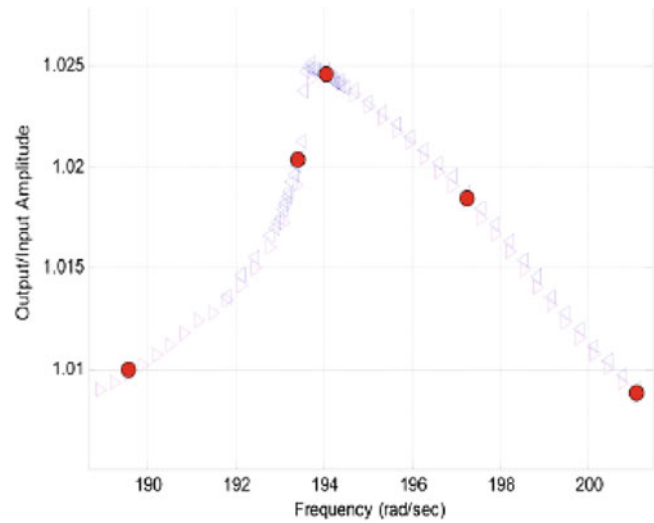
20.5 Continuous Time Identification

The Continuous Time system identification (CT) is used to estimate the nonlinear coefficient, alpha. After estimating the linear parameters, the model is rewritten in matrix notation as

$$\begin{bmatrix} \ddot{a} & \dot{a} & a & a^3 \end{bmatrix} [m \ c \ k \ \alpha]^T = F(t) \tag{20.10}$$

Where $\ddot{a}$, $\dot{a}$, a, and F are vectors of acceleration, velocity, displacement, and forcing respectively. Solving for α the equation becomes,

$$\alpha = \left\{ F(t) - ma\!\left(\ddot{t}\right) - ca\!\left(\dot{t}\right) - ka(t) \right\} \cdot \{a^3\}^T \tag{20.11}$$

Thus, with any length of vector, a least squares approximation will give estimation for the value of the nonlinear parameter, α.

In previous studies the nonlinear parameter has been estimated by the use of the Healthy-Unhealthy method (HUH) in which the five healthy two-second steady state data vectors that generated the linear parameters are concatenated with two seconds of active data to estimate the nonlinear parameter. Because this method is weighted by healthy data, it is assumed that severely unhealthy data would result in very different values of alpha. This method has been very successful in predicting the premonition of failure, but it also often includes regions of random spikes, typically near the end of life, which are difficult to interpret.

In this study another method has been tested to estimate alpha. The Concatenate method simply concatenates all accrued data before using CT. As the CT data is weighted by all previous data, large changes of alpha have less overall effect on parameter estimates as more data is collected.

20.6 Linear Parameter Estimation

A regression of the linear frequency response function was used to estimate linear parameters: mass, stiffness, and damping. While in no obvious way impairing the NMT method's effectiveness, estimations of linear parameters by the CT method were known to be inaccurate. This lack of accuracy has been seen as a positive: recall that the inaccuracy of the model is also an indication of the robustness of the model. As a debugging tool, and to explore any limitations in the method, a new way to accurately identify the linear models has been developed. A curve fit of the linear frequency response function was used to estimate the linear parameters.

The traditional frequency response function given by:

$$T = \frac{1}{\sqrt{(k - m\omega^2)^2 + (c\omega)^2}} \tag{20.12}$$

was manipulated to produce a polynomial whose coefficients are related to the linear parameters of the system, as:

$$\frac{1}{T^2} = \omega^4 \left(m^2\right) + \omega^2 \left(c^2 - 2km\right) + k^2 \tag{20.13}$$

Traditional polynomial regression was then used to determine the coefficients which were then related back to the linear parameters.

Five data points were recorded near the natural frequency to curve fit. The curves were individually checked to ensure close fit. In most cases, the natural frequency was weighted to raise the peak of the curve to ensure an accurate natural frequency.

Nonlinearity in the frequency responses was attenuated by using low amplitude excitation during frequency sweeps.

20.7 Numerical Integration

Numerical integration was investigated as an alternative to Fourier fitting and analytical integration of acceleration data to obtain velocity and displacement. However, noise in accelerometer data, such as DC drift, led to accumulating error in estimations of velocity and displacement. Higher sample rates were used to reduce this error, to date these have not led to sufficiently accurate values of displacement.

20.8 Strain Gage Application

As an attempt to improve precision and accuracy of displacement measurements, a strain gage was applied to the beam. Using Euler-Bernoulli beam theory, it was shown that strain is proportional to displacement. Thus, a quasi-static calibration was used to calibrate the strain gage to displacement. This strain gage data could then be numerically differentiated to produce velocity and acceleration. By implementing the strain gage and accelerometer, the NMT method can now use a variety of processing routes to obtain the system states.

20.9 Results

The FRF fit to determine linear parameters for system identification returned different values for each of two beams of similar composition and geometry. These values are given in Table 20.1 below compared with the parameters measured by traditional methods.

Figure 20.4 shows a weighted FRF curve fit with steady state responses near the natural frequency.

Using the linear parameters from the FRF fits plots of the nonlinear parameter were made. The new method of producing nonlinear parameters using Concatenation is compared to the previous methods (HUH) of alpha estimation. Several beams were tested under similar conditions to determine if either gave an enhanced premonition of failure.

Plots were made comparing the two methods and varying the use of the strain gage: SG0 uses no strain data, SG1 uses strain to determine displacement, SG2 uses strain to determine displacement and velocity, SG3 uses strain to determine displacement, velocity, and acceleration, everything not strain is accelerometer data which has been Fourier fit and analytically integrated. Figures 20.5 and 20.6 show the estimated value of the nonlinear parameter, alpha.

The Beam 1 test failed around minute 605. With each processing method the value of the nonlinear parameter, α, changes very gradually at the beginning of the test and then changes slightly at minute 180. Around minute 200, alpha changes dramatically, in some instances increasing and in the case of SG0 decreasing. The Concatenated CT plots then level out. In the HUH CT plots, alpha then gradually decreased until minute 550 when large spikes in the value occur. The beam fails shortly after.

The figure below shows the SG1 alpha plots.

In Fig. 20.7, the SG1 plots of another beam are compared. It is noted that a pronounced change in alpha is not clear in either plot. The most significant change begins near minute 3000 where the concatenated alpha starts to climb and the HUH increases significantly.

Table 20.1 FRF fit linear parameter estimates

Beam	Mass per length (kg/m)	Stiffness per length (N/m^2)	Damping per length (Ns/m^2)
Beam 2	0.054	2.16e + 03	0.47
Beam 1	0.069	2.52e + 03	0.14
Traditional	0.050	2.35e + 03	0.1827
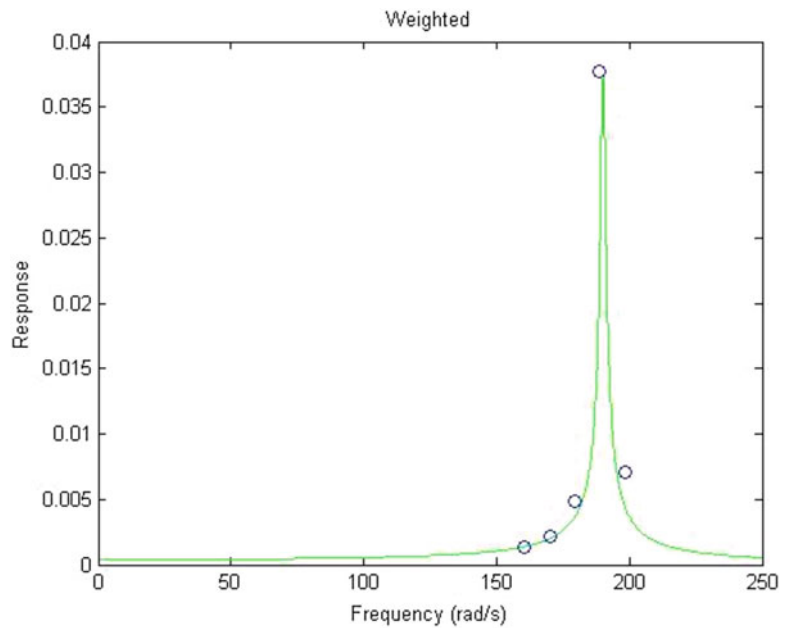
Fig. 20.4 Weighted FRF fit from Beam 1

Fig. 20.5 Concatenated data for Beam 1
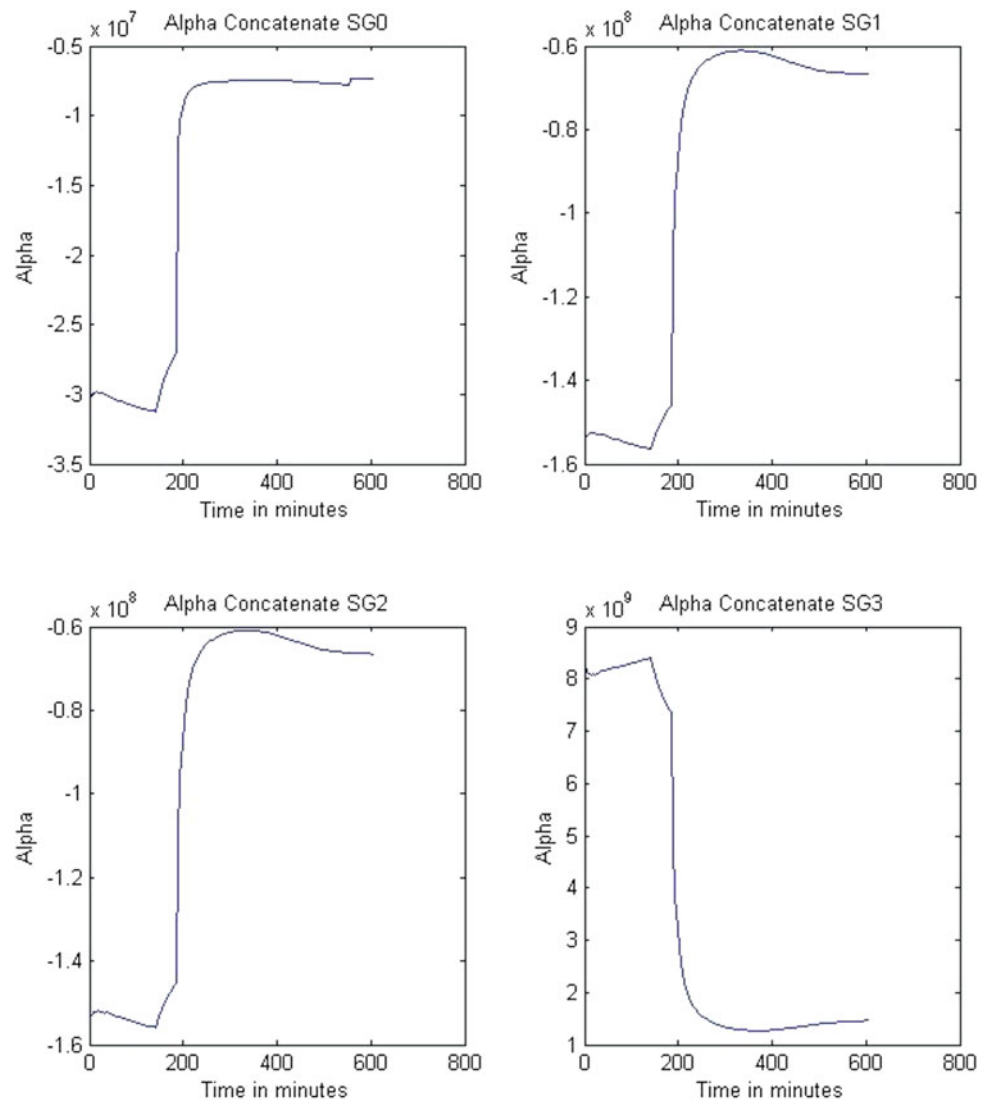
20.10 Conclusions

This study has continued to show the robustness of the NMT Method to successfully indicate crack initiation and propagation. Although previous research has been successful with inaccurate linear system parameters, by determining the parameters, confidence in results has been increased and there is now a mechanism for identifying when the assumed NMT model may be unusable.

Additionally, the application of the strain gage produced another avenue for determining system states, and the possibility to eliminate Fourier fitting. This is particularly attractive as the NMT method addresses systems not under harmonic excitation. Using the strain gage data for the displacement and velocity (SG2) does not noticeably change the value of the nonlinear parameter when compared to using the strain gage for displacement (SG1). The plots are so similar for these two cases that a single integration or differentiation has virtually no effect on the estimates of alpha. While the double integration (SG0) and double differentiation (SG3) do produce different estimates, all four methods still accurately predict failure, and all at the same times. Because of the similarity of the SG1 and SG2 graphs in Fig. 20.6, the use of Fourier fitting acceleration data and analytically integrating to obtain velocity data is unnecessary. Thus, further research may find better results by using an accelerometer to determine acceleration and a strain gage to determine displacement and velocity.

The use of the Concatenation method has been shown to smooth the estimation of the nonlinear parameter. Figures 20.5 and 20.6 show that the smoothing can take place without affecting the premonition of failure. This is contrasted with results in Fig. 20.7 for which the smoothing has smoothed out indication of failure. Therefore, this smoothing should be reserved for highly dynamic changes of alpha in which premonition is difficult to distinguish from noise. By using both CT methods and using some discretion, the method can be better informed and predict failure with more certainty.

Fig. 20.6 HUH data for Beam 1
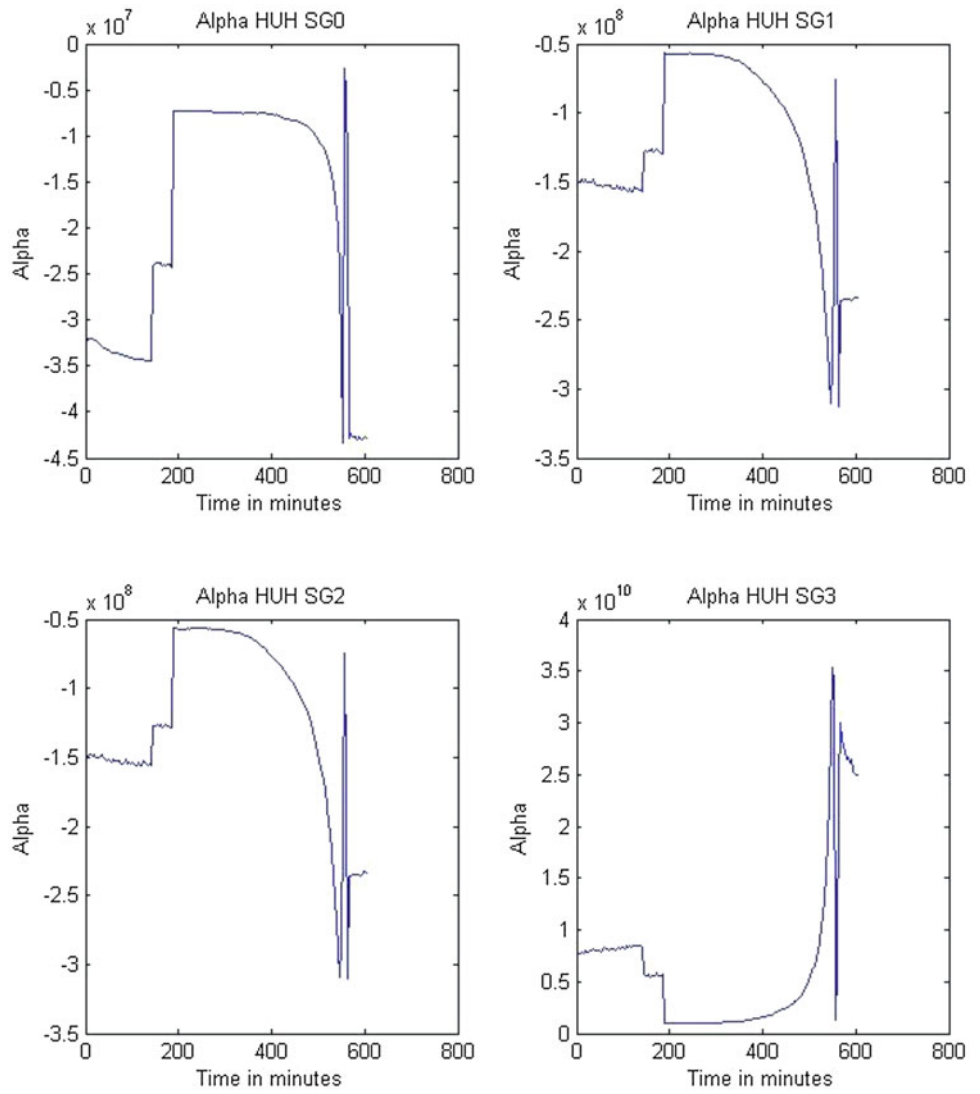
Fig. 20.7 Comparison of continuous time for Beam 2
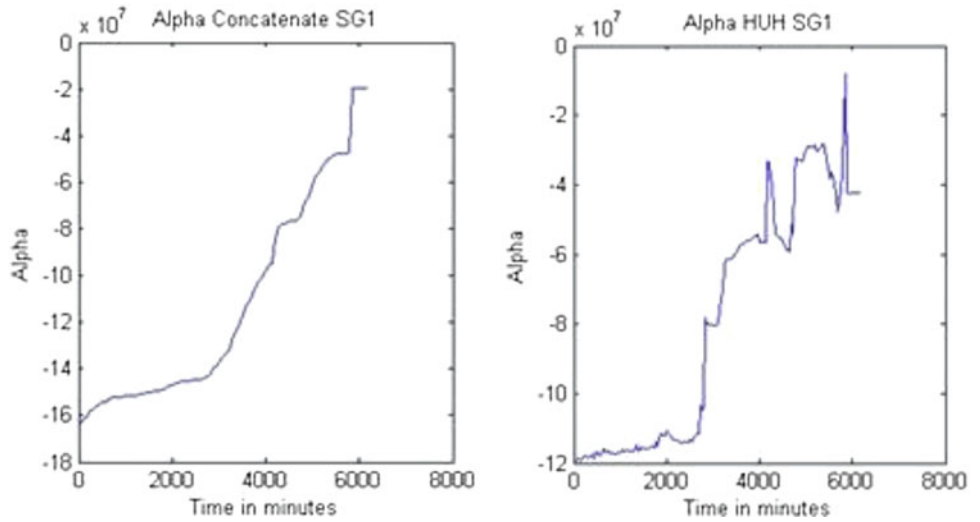
Though still in iteration, the NMT method has repeatedly shown to be a promising method for health monitoring. Further research will focus on adapting the data processing code to run in real time. By doing this, previous research can be validated, and a relationship between large changes in nonlinear parameter and crack propagation can be made.

References

1. Doebling SW, Farrar CR, Prime MB (1998) A summary of vibration-based damage identification methods. Shock Vib Dig 30:91–105
2. Andreaus U, Casini P, Vestroni F (2007) Non-linear dynamics of a cracked cantilever beam under harmonic excitation. Proc Int J Non Linear Mech 42:566–575
3. Andreaus U, Casini P, Vestroni F (2005) Nonlinear features in the dynamic response of a cracked beam under harmonic forcing. In: Proceedings of the ASME international design engineering technical conferences and computers and information in engineering conference – DETC2005, v 6 C, 5th international conference on multibody systems, nonlinear dynamics, and control, Long Beach, CA, pp 2083–2089
4. Ding JL, Pazhouh J, Lin SB, Burton TD (1994) Damage characterization by vibration test. Scripta Metallurgica et Materialia 30:839–834
5. Bovsunovsky A, Bovsunovsky O (2007) Crack detection in beams by means of the driving force parameters variation at non-linear resonance vibrations. Key Eng Mater 34:413–420. Damage assessment of structures VII
6. Vanlanduit S, Parloo E, Guillaume P (2004) An on-line combined linear-nonlinear fatigue crack detection technique. NDT & E Int 37:41–45
7. Doughty T, Higgins N, Etzel N (2011) Nonlinear model tracking in application to failed nondestructive evaluations. In: Proceedings of the ASME 2011 international mechanical engineering congress & exposition – IMECE2011-63896, Denver, CO

Chapter 21
A Material Basis Frame Approach for Global Deflection Reconstruction of Rod-Like Structures from Strain Measurements

Michael Todd

Abstract This paper presents an approach for determining three-dimensional global displacement (for arbitrarily-sized deformations) of thin rod- or tether-like structures from a limited set of scalar strain measurements. The approach is rooted in exploiting a reference frame that is materially adapted, i.e., it moves with the cross section. Local linearization of the frame evolution equations is shown to yield local solutions that may be assimilated into a global solution via continuity relationships. The solution is shown to be robust to potential singularities from vanishing bending and twisting angle derivatives and from vanishing measured strain, and the approach includes strain resulting from pure neutral axis extension (such as due to thermal loads). Validation of the approach is performed through comparison with finite element simulations. The average root mean square reconstruction error of 0.01–1 % of the total length, for reasonable sensor counts. Analysis of error due to extraneous noise sources and boundary condition uncertainty shows how error scales with those effects.

Keywords Shape reconstruction • Material basis frame • Distributed strain • Directors • Cosserat rod

21.1 Introduction

Many applications require monitoring the deflection of long, slender, highly flexible structures such as cables, long rods, tethers, or any structure whose geometry is dominated by a single length scale. Such structures all tend to share a kinematic state characterized by arbitrarily large multi-mode deflection (bending, twisting, torsion, extension) under relatively linear, elastic stress/strain material behavior. Euler is credited with initiating studies in the *Elastica*, followed by more modern theories [1–5]. In most structural monitoring applications of interest, a common objective is to obtain the displacement of the these structures from distributed measurements of some kind, whether the measurements are direct non-contact measures of displacement (such as with laser vibrometry), acceleration (requiring integration), or indirectly through distributed local measurements of a kinematically-related quantity, such as strain. This last approach comprises the scope of the present paper, since strain gages are a highly ubiquitous and a useful sensor modality for structural load and response. The main challenge in this class of monitoring problems lies in obtaining a reasonable inverse model that converts a finite number of local strain measurements into global displacement estimations. For small displacements of certain geometrically simple structural models for which analytical solutions exist (beams, plates), classical theories may be directly inverted or forward models may be fit to data directly, but no such viable method currently exists for long, highly-deformable structures. This paper presents a kinematic model rooted in Cosserat theory and introduces a material basis reference frame to describe the deformation more precisely in a way that measurable strain metrics are estimable from the theory. Then, under local linearization assumptions, the resulting displacement/material frame evolution equations are integrated in terms of the strain metrics to obtain global displacement. The approach is validated against several full finite element displacement simulations of a rod-like structure loaded to arbitrarily large deflections in this paper.

M. Todd (✉)

Department of Structural Engineering, University of California San Diego, La Jolla, San Diego, CA 92093-0085, USA

e-mail: mdtodd@ucsd.edu
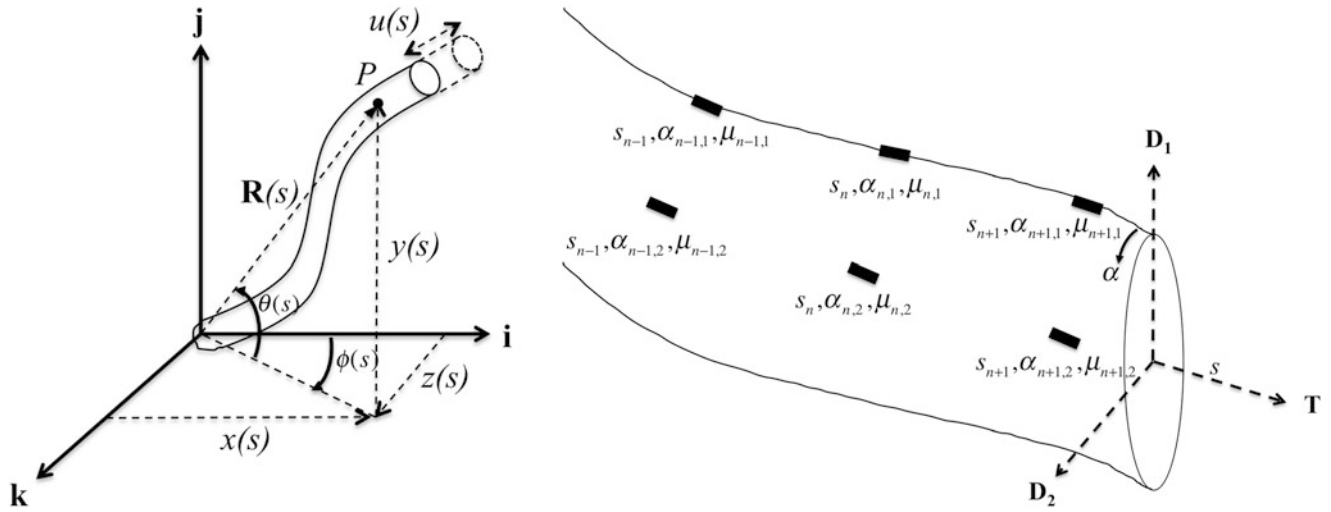
Fig. 21.1 (*Left*) Fundamental geometric description of the deformed structure and (*right*) the geometry of the cross section

21.2 Kinematic Modeling and Solution Approach

Todd et al. [6] presented an earlier version of this approach that was limited to bending and twisting. The present approach has relaxed the previous assumptions and including extension of the centerline. Figure 21.1 (left) shows the geometry of an arbitrarily deformed structure with relevant length scales; the circular cross section shown is arbitrary, although the negligible warping assumptions made shortly will strictly only hold true for circular cross sections.

The fundamental independent variable is the arc-length coordinate s, which moves along a line tangent to the dominant length direction. An arbitrary point P on the centroid of the deformed structure may be described in the inertial **i**-**j**-**k** reference frame by parameterization of three functions, a pitch function $\theta(s)$, an azimuth function $\phi(s)$, and a stretch function $u(s)$. The vector locator $\mathbf{R}(s)$ for P may be thus expressed as

$$
\mathbf{R}(s) = \left(\int_0^s \cos\theta(p) \cos\phi(p) \left(1 + u'(p) \right) dp \right) \mathbf{i} + \left(\int_0^s \sin\theta(p) \left(1 + u'(p) \right) dp \right) \mathbf{j}
$$
$$
+ \left(\int_0^s \cos\theta(p) \sin\phi(p) \left(1 + u'(p) \right) dp \right) \mathbf{k}, \tag{21.1}
$$

where a prime mark denotes differentiation with respect to s. When there is no centerline stretching, i.e. $u' = 0$, all deformation is due to bending and twisting, and the distal end of the structure resides on a sphere for all deformation possibilities (hence the spherical angular parameterization). When there is no bending or twisting, i.e. $\theta = \phi = 0$, the vector $\mathbf{R}$ reduces to $\mathbf{R}(s) = (s + u(s))\mathbf{i}$, which is just the location along the initially straight (undeformed) structure, plus any additional pure stretch. In the present formulation, it is assumed that the initial configuration is straight (for convenience) and unstrained (a more strict assumption). Furthermore, warping of the cross section of the structure and transverse shearing are neglected in the present approach.

While the vector $\mathbf{R}$, written in the inertial basis, is sufficient to locate the loci of centroids, it does not successfully describe the material deformation about P, other than the case of pure stretch (as just shown in the previous paragraph). Thus, recourse is made to connecting $\mathbf{R}$ to a reference frame that is better adapted to the structure, i.e., it evolves with the

deformation. The Frenet basis, consisting of a tangent vector $\mathbf{T}$, a normal vector $\mathbf{N}$, and a binormal vector $\mathbf{B}$, is such an adapted frame, and its evolution is described by the well-known Frenet-Serrat equations, where all explicit dependences upon s are dropped for brevity:

$$
\begin{bmatrix} \mathbf{R}' \\ \mathbf{N}' \\ \mathbf{B}' \\ \mathbf{T}' \end{bmatrix} = \begin{bmatrix} 0 & 0 & 0 & 1+u' \\ 0 & 0 & \tau & -\kappa \\ 0 & -\tau & 0 & 0 \\ 0 & \kappa & 0 & 0 \end{bmatrix} \begin{bmatrix} \mathbf{R} \\ \mathbf{N} \\ \mathbf{B} \\ \mathbf{T} \end{bmatrix},
\tag{21.2}
$$

where κ and τ are the local curvature and torsion of the deformed centroid, both of which may be related back to complicated expressions involving the pitch, azimuth, and stretch functions by substituting Eq. (21.1) into Eq. (21.2). The Frenet basis, while useful, is nonetheless not material-adapted; rather, it is adapted to the curvature and torsion of the centroid and not to the actual physical bending and rotation of the material, which is what directly encodes the strain. As a consequence, the Frenet frame suffers discontinuities at inflection points, where $\mathbf{N}$ will vanish. This singularity in $\mathbf{N}$ prohibits its use in estimating local strain, which is not discontinuous. Thus, a material twist function $\sigma(s)$ is used to relate the $\mathbf{N}$-$\mathbf{B}$ orientation at a particular cross section to a new vector basis $\mathbf{D}_1$-$\mathbf{D}_2$ that evolves with the cross section, as shown in Fig. 21.1 (right). The definitions of $\mathbf{D}_1$ and $\mathbf{D}_2$ define the cosines of the two angle functions, $\mathbf{D}_1 \cdot \mathbf{j} = \cos\theta$ and $\mathbf{D}_2 \cdot \mathbf{k} = \cos\phi$, such that the material twist and its derivative are defined by

$$
\begin{aligned}
\kappa \cos\sigma &= -\phi' \cos\theta \\
\kappa \sin\sigma &= \theta' \\
\sigma' &= -\tau - \phi' \sin\theta,
\end{aligned}
\tag{21.3}
$$

and Eq. (21.2) may be rewritten in this new material-adapted reference frame as

$$
\begin{bmatrix} \mathbf{R}' \\ \mathbf{D}_1' \\ \mathbf{D}_2' \\ \mathbf{T}' \end{bmatrix} = \begin{bmatrix} 0 & 0 & 0 & 1+u' \\ 0 & 0 & -\phi' \sin\theta & -\theta' \\ 0 & \phi' \sin\theta & 0 & -\phi' \cos\theta \\ 0 & \theta' & \phi' \cos\theta & 0 \end{bmatrix} \begin{bmatrix} \mathbf{R} \\ \mathbf{D}_1 \\ \mathbf{D}_2 \\ \mathbf{T} \end{bmatrix}.
\tag{21.4}
$$

Equation (21.4) clearly shows how the material-adapted frame encodes the pitch, azimuth, and stretch functions in its evolution description. In fact, these matrix components are the material-adapted frame's strain measures, which are obtained by

$$
\begin{array}{cc}
\text{direct shear and axial :} & \text{bending and torsional :} \\[6pt]
\begin{aligned} \mathbf{R}' \cdot \mathbf{D}_1 \\ = 0 \end{aligned} & \begin{aligned} \tfrac{1}{2}\left(\mathbf{D}_1 \times \mathbf{D}_1' + \mathbf{D}_2 \times \mathbf{D}_2' + \mathbf{T} \times \mathbf{T}'\right) \cdot \mathbf{D}_1 \\ = -\phi' \cos\theta \end{aligned} \\[12pt]
\begin{aligned} \mathbf{R}' \cdot \mathbf{D}_2 \\ = 0 \end{aligned} & \begin{aligned} \tfrac{1}{2}\left(\mathbf{D}_1 \times \mathbf{D}_1' + \mathbf{D}_2 \times \mathbf{D}_2' + \mathbf{T} \times \mathbf{T}'\right) \cdot \mathbf{D}_2 \\ = \theta' \end{aligned} \\[12pt]
\begin{aligned} \mathbf{R}' \cdot \mathbf{T} \\ = 1 + u' \end{aligned} & \begin{aligned} \tfrac{1}{2}\left(\mathbf{D}_1 \times \mathbf{D}_1' + \mathbf{D}_2 \times \mathbf{D}_2' + \mathbf{T} \times \mathbf{T}'\right) \cdot \mathbf{T} \\ = -\phi' \sin\theta. \end{aligned}
\end{array}
\tag{21.5}
$$

The direct shearing strain measures are both zero, in accordance with the kinematic assumptions made earlier.

The total strain at the surface of the structure (where a strain gage could be arbitrarily located), say point Q in Fig. 21.1 (right), is comprised of the orientation change in the coordinate system (which gives rise to bending and torsional strain) and any length change in the $\mathbf{T}$ direction (which gives rise to the axial strain). Thus, vector of non-zero strains in the material-adapted frame is given by

$$
\begin{aligned}
\boldsymbol{\varepsilon} &= \mathbf{r}'_{Q/P} + u'\mathbf{T} \\
&= r\cos\alpha \mathbf{D}_1' + r\sin\alpha \mathbf{D}_2' + u'\mathbf{T} \\
&= r\phi' \sin\theta \left(\mathbf{D}_1 \sin\alpha - \mathbf{D}_2 \cos\alpha\right) \\
&\quad + \left(u' - r\theta' \cos\alpha - r\phi' \sin\alpha \cos\theta\right)\mathbf{T},
\end{aligned}
\tag{21.6}
$$

where $\mathbf{r}_{Q/P}$ is the vector locating Q relative to P. This strain vector is then dotted with the orientation vector of an arbitrary strain gage, given by $-\sin\mu\sin\alpha\mathbf{D}_1 + \sin\mu\cos\alpha\mathbf{D}_2 + \cos\mu\mathbf{T}$ where μ is an angle relative to the $\mathbf{T}$ direction (i.e., a gage aligned in the tangential direction corresponds to $\mu = 0$). The final scalar strain at the point Q is then obtained by dotting Eq. (21.6) with this gage orientation vector to obtain

$$
\begin{aligned}
\varepsilon &= \boldsymbol{\varepsilon} \cdot (-\sin\mu\sin\alpha\mathbf{D}_1 + \sin\mu\cos\alpha\mathbf{D}_2 + \cos\mu\mathbf{T}) \\
&= \cos\mu\,(u' - r\theta'\cos\alpha - r\phi'\cos\theta\sin\alpha) - r\sin\mu\phi'\sin\theta \\
&= \cos\mu\,(e_1 - \cos\alpha e_2 - \sin\alpha e_3) - \sin\mu e_4,
\end{aligned}
\tag{21.7}
$$

where the definitions of the strain metrics e_m, $m = 1\ldots 4$,

$$
\begin{aligned}
e_1 &= u' \\
e_2 &= r\theta' \\
e_3 &= r\phi'\cos\theta \\
e_4 &= r\phi'\sin\theta
\end{aligned}
\tag{21.8}
$$

were made.

It is then assumed that arrays of strain gages are placed on the surface of the structure, with each array having a gage at a discrete location $s = s_n$, circumferential position $\alpha = \alpha_{n,m}$, and orientation $\mu = \mu_{n,m}$, as shown in Fig. 21.2.

Thus, in the n-th cross-sectional neighborhood of each gage, Eq. (21.4) may be written

$$
\begin{bmatrix} \mathbf{R}'_n \\ \mathbf{D}'_{1,n} \\ \mathbf{D}'_{2,n} \\ \mathbf{T}'_n \end{bmatrix}
=
\begin{bmatrix}
0 & 0 & 0 & 1 + e_{n,1} \\
0 & 0 & -e_{n,4}/r & -e_{n,2}/r \\
0 & e_{n,4}/r & 0 & -e_{n,3}/r \\
0 & e_{n,2}/r & e_{n,3}/r & 0
\end{bmatrix}
\begin{bmatrix} \mathbf{R}_n \\ \mathbf{D}_{1,n} \\ \mathbf{D}_{2,n} \\ \mathbf{T}_n \end{bmatrix}.
\tag{21.9}
$$

The predicted strain in Eq. (21.7) for the n-th neighborhood may subsequently be written as

$$
\varepsilon_{n,m} = \cos\mu_{n,m}\,(e_{n,1} - e_{n,2}\cos\alpha_{n,m} - e_{n,3}\sin\alpha_{n,m}) - \sin\mu_{n,m}e_{n,4}.
\tag{21.10}
$$
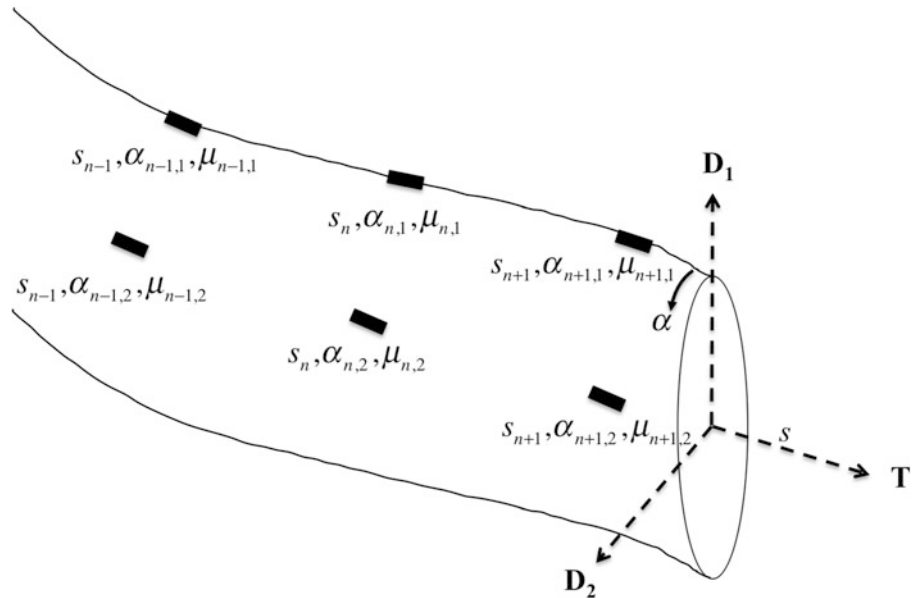
Fig. 21.2 Strain gage location nomenclature

As it stands, Eq. (21.9) is still nonlinear through the definitions made in Eq. (21.8), but given a sufficient sensor density, it is assumed that the strain metrics $e_{n,j}$ are constant in their n-th neighborhood. Then, Eq. (21.9) comprises a linear system with constant coefficients that may be solved. Defining $\gamma_n = \sqrt{e_{n,2}^2 + e_{n,3}^2 + e_{n,4}^2}$, the solution for the local position vector is

$$
\begin{aligned}
\mathbf{R}_n(s) = \mathbf{a}_{n,1} &+ \frac{(1 + e_{n,1})\, e_{n,4}\, (-\mathbf{a}_{n,3} e_{n,2} + \mathbf{a}_{n,2} e_{n,3} + \mathbf{a}_{n,4} e_{n,4})}{\gamma_n^2}\, s + \frac{r}{\gamma_n^2}\, (1 + e_{n,1})\, (\mathbf{a}_{n,2} e_{n,2} + \mathbf{a}_{n,3} e_{n,3}) \left(1 - \cos\left(\frac{\gamma_n s}{r}\right)\right) \\
&+ \frac{r}{\gamma_n^3}\, (1 + e_{n,1})\, \big(\mathbf{a}_{n,4} \left(e_{n,2}^2 + e_{n,3}^2\right) + e_{n,4}\, (\mathbf{a}_{n,3} e_{n,2} - \mathbf{a}_{n,2} e_{n,3})\big) \sin\left(\frac{\gamma_n s}{r}\right),
\end{aligned}
\tag{21.11}
$$

where the $\mathbf{a}_{n,m}$ are vector constants of integration, and the strain metrics $e_{n,m}$ are linearly related to the actual measured strains $\varepsilon_{n,m}$ through Eq. (21.10). Equation (21.11) represents the basis set solution, assuming locally constant strains, for the global displacement of the structure as a function of the measured strains. Similar-looking solutions with the same functional form but different integration constants describe the other vector components of Eq. (21.9). The solution contains no obvious singularities other than potentially in the case of vanishing bending/torsional strain measures, i.e., $e_{n,m} = 0$ for $m = 2 \ldots 4$ (implying that $\gamma_n = 0$ also). However, a careful limiting process of Eq. (21.11) shows that

$$
\lim_{e_{n,2}, e_{n,3}, e_{n,4}, \gamma_n \to 0} \mathbf{R}_n(s) = \mathbf{a}_{n,1} + \mathbf{a}_{n,4}\, (1 + e_{n,1})\, s,
\tag{21.12}
$$

which is a local linear stretch in the s direction only. Clearly, if there is also no stretching, i.e. $e_{n,1} = 0$, then $\mathbf{R}_n$ remains linear in the n-th neighborhood, but with a different slope. The situation of vanishing bending/torsional strain would only occur in situations where the derivatives of both θ_n and ϕ_n vanish simultaneously, implying a vanishing local curvature.

Thus, the algorithm proceeds by determining if all the measured strains at a given cross section are zero (or nearly zero by some tolerance) and then selects either the solution Eqs. (21.11) or (21.12) appropriately. Then, conditions of continuity between neighborhoods are imposed, along with boundary conditions, to fully determine the integration constants and arrive at a unique solution for the global displacement. The final displacement vector is then just assimilated by summing up over each n-th local contribution to get

$$
\mathbf{R}(s) = \sum_{n=1}^{N} \mathbf{R}_n(s) \left[u\left(s - s_{n-1}^*\right) - u\left(s - s_n^*\right) \right],
\tag{21.13}
$$

where the s_n^* are the locations chosen to impose continuity between regions (a typical choice may be the midpoint between strain sensors), and $u(*)$ is the Heaviside function.

Although not absolutely required if global displacement is all that is needed, the local pitch, azimuth, and stretch functions may be computed from Eq. (21.8) to be

$$
\begin{aligned}
u_n &= a_n + e_{n,1} s \\
\theta_n &= b_n + e_{n,2} s / r \\
\phi_n &= c_n + \frac{e_{n,3}}{e_{n,2}} \sin \theta_n - \frac{e_{n,4}}{e_{n,2}} \cos \theta_n,
\end{aligned}
\tag{21.14}
$$

where the a_n, b_n, and c_n are integration constants whose values are also determined by imposing continuity and boundary-related conditions on these functions (consistent with whatever other conditions were imposed).

21.3 Validation of the Approach

The proposed described was tested on finite-element based simulation of large deformations of a hollow plastic pipe of length 50 m, inner diameter 20 cm, and outer diameter 30 cm. The material constants chosen were an elastic modulus $E = 2.3$ GPa and Poisson's ratio $\nu = 0.39$. Abaqus S4R general-purpose shell elements were employed to model this structure, given their superior capability and computational efficiency in modeling large-scale bending and torsional behavior. Four strain gages at each cross section were simulated at 90° separation circumferentially (α direction) and alternating orientations (μ) of $\pm 45^O$. There is nothing optimal about this arrangement, but the use of four fibers with orientation diversity adds robustness; if $\mu = 0$ is chosen to orient all gages, then in principle only three strain gages at each cross section would be required. In all cases, the gage clusters were spread at $50/N$ m apart, i.e., uniformly spaced.

Fig. 21.3 Simulation #1
reconstruction results for various
sensor counts
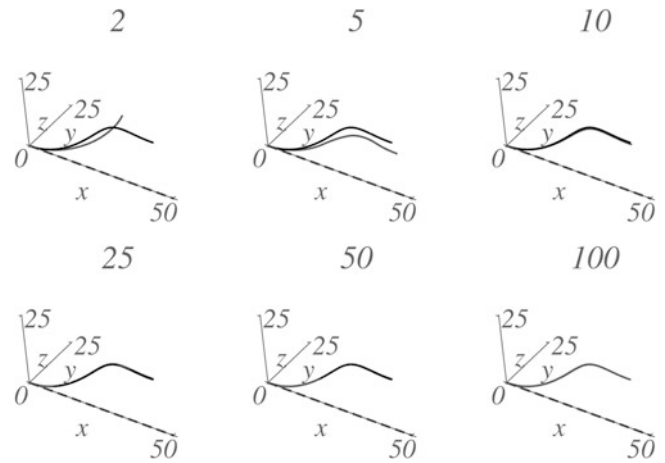
Fig. 21.4 Simulation #2
reconstruction results for various
sensor counts
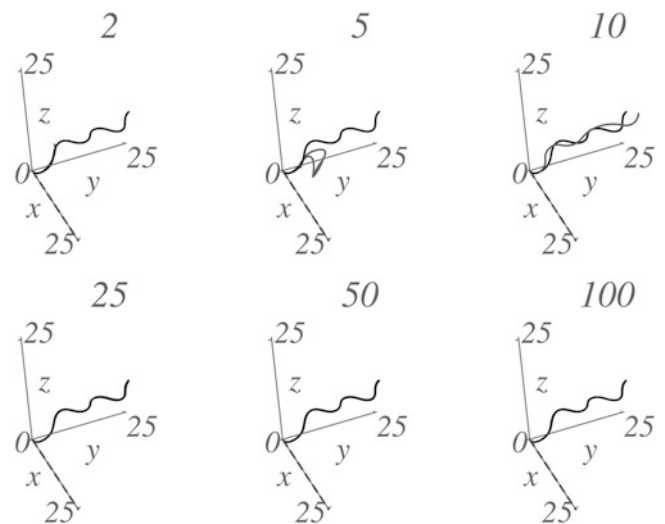
Figure 21.3 shows the results of the reconstruction approach for one simulation that contained only two major changes in curvature/torsion (and negligible stretch). The finite element simulation of the cylinder centerline is shown as the solid black line (the dashed black line is the initially straight, undeformed cylinder), and the gray line is the continuous reconstruction from the algorithm of Sect. 21.2. For this first shape, even for just $N = 5$, fairly good reconstruction is observed, with an average (over the total length) rms error of about 2 m (4 % of the length); this error decreases quite rapidly, and for $N = 25$, the average rms error is only 1 mm.

Figures 21.4 and 21.5 show the same kind of results for two increasingly complex deformations with added stretch components and multiple curvature and torsion changes. The complexity increases naturally demand higher sensor counts before equivalent levels of accuracy are obtained, essentially 50 sensor locations for simulation #2 and 100 sensor locations for simulation #3. In all cases, however, the algorithm smoothly converges. The largest errors are typically at locations farthest from whatever location a boundary condition was imposed. In this work, it was assumed that the proximal end of the cylinder was at a known location (the origin); consequently, the error is maximal at the distal end. This propagation of error would be different if a known condition were imposed at a different location.

In practical applications, the measurements of strain from a real sensor array contain noise, and additionally other sources of external uncertainty can corrupt the algorithm's performance. To address robustness, Monte Carlo simulations on all three shapes were performed with uniform noise added at both the $[-5, 5]$ microstrain and $[-50, 50]$ microstrain levels to each gage. The average root mean square error over the length of the cylinder between prediction and finite element simulation was computed for the first simulation only (for illustrative purposes) for a number of cross section sensor counts. Figure 21.6 shows these results. The error is dominated by algorithm performance at very low sensor counts, but above about $N = 25$, the error becomes more noise-dominated. For noise-free data, the algorithm approaches 0.001 % of length in rms error for $N = 100$.

Fig. 21.5 Simulation #3
reconstruction results for various
sensor counts
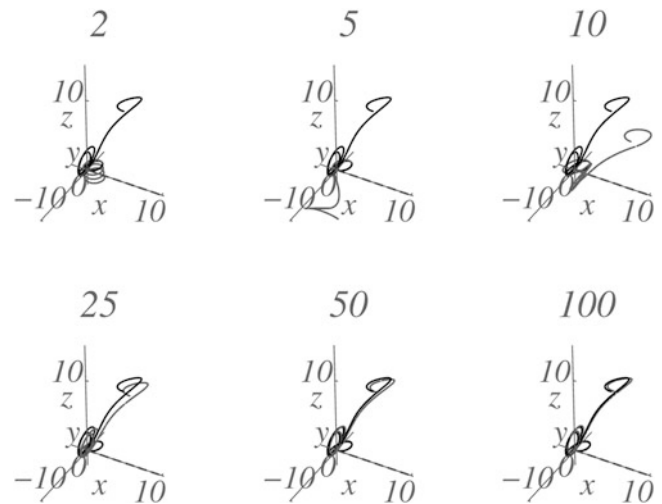
Fig. 21.6 RMS reconstruction
error for different sensor counts
for simulation case #1
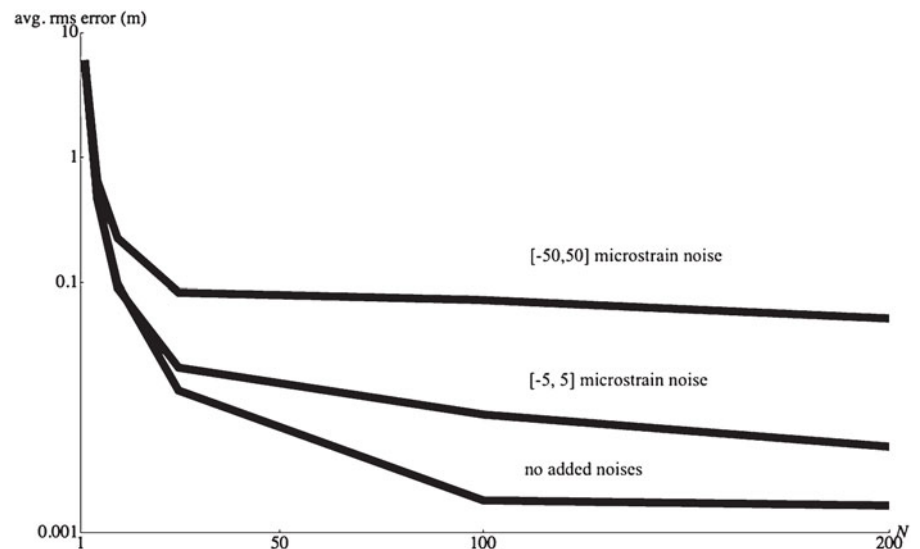
21.4   Summary

This paper proposed a model-based method for obtaining the global three-dimensional displacement of rod-like structures from discrete strain measurements. The method utilizes a material-adapted reference and finds an analytical solution for local strain neighborhoods. The solution is robust to singularities and was validated with three finite element models of a 50 m hollow plastic cylinder undergoing significant three-dimensional deformations. Average rms errors of a few mm (hundredths of a percent of length) were obtained which were either noise- or sensor count-limited, depending on shape complexity. The approach has good applicability for embedded platforms, since the only computation involves a matrix inversion.

References

1. Bishop RL (1975) There is more than one way to frame a curve. Am Math Mon 82(3):246–251
2. Cosserat E, Cosserat F (2001) Theorie des Corps Deformables. Herman, Paris
3. Love AEH (1909) A treatise on mathematical theory of elasticity. Dover, New York
4. Langer J, Singer D (1996) Lagrangian aspects of the Kirchoff elastic rod. SIAM Rev 38(4):605–618
5. Reisner E (1981) On finite deformations of space-cured beams. J Appl Math Phys 32:723–744
6. Todd MD, Stull CJ, Dickerson M (2013) A local material basis solution approach to reconstructing the three-dimensional displacement of rod-like structures from strain measurements. ASME J Appl Mech 80(4):041028(1–10)

Chapter 22
Influence of Prestressing Strand Damage on Modal Parameters of a Hybrid Composite Bridge Beam

Timothy P. Kernicky, Matthew J. Whelan, and Cristopher D. Moen

Abstract In-service condition assessment of large civil infrastructure systems has remained a particularly challenging area of research in the fields of nondestructive evaluation and structural health monitoring (SHM). Extensions of theoretically-based and laboratory verified vibration-based methods for assessing damage have been investigated experimentally on full-scale structures within several studies offering mixed conclusions. This paper introduces a recent experimental test program conducted on a full-scale bridge beam subjected to prescribed damage to the tension reinforcement. Details of the experimental testing program and vibration testing of the full-scale bridge beam both prior to and after damage to tension reinforcement are presented. System identification is applied to compare estimates of the natural frequencies, relative damping factors, and mode shapes obtained in the as-built state against those obtained after cutting over half of the tension reinforcement strands in the beam. A data-driven damage detection algorithm previously applied to detect damage in a full-scale bridge is also explored for application to the current dataset.

Keywords Structural health monitoring • Hybrid composite beams (HCB) • Full-scale testing of structures • Damage detection • Bridge dynamics

22.1 Introduction

Vibration-based damage detection has received considerable attention over the past several decades as technologies for wireless monitoring of civil infrastructure with low-cost MEMS sensors have facilitated the economics of applied structural health monitoring. Data-driven methods for structural health monitoring have been shown to be particularly effective for identifying the presence and, in many cases, isolating the spatial location of structural damage [1]. One of the predominant approaches to feature extraction for structural health monitoring has been to develop a linear model from baseline measurements and use such a model to predict the measured response following the introduction of damage. Statistical properties of the probability density function of residual errors between the actual measurements and predictions are typically analyzed against the properties of the model to classify damage from the deviation from the distribution. Although there is not yet any reported instances of damage detection on a real-world structure with naturally occurring and previously unknown damage identified to validate any single approach, prior studies have demonstrated the potential of data-driven approaches on full-scale bridge measurements following prescribed damage [2].

While numerous strategies, both data-driven and physics-based, have been proposed and evaluated on numerical and laboratory testbeds, full-scale experiments that faithfully capture the effects of structural damage as well as incorporate measurement uncertainties and errors representative of current technology remain an important contribution toward the development and validation of vibration-based structural health monitoring approaches. In contrast to many numerical and scale model experiments, these full-scale tests often emphasize the practical challenges in applied structural health monitoring stemming from the relative insensitivity of measured modal parameters to often even significant damage in full scale structures [3, 4]. This paper aims to add to the growing literature of practical experimental case studies by presenting measurements from a full-scale bridge beam subjected to significant damage to the tension reinforcement.

T.P. Kernicky • M.J. Whelan (✉)

Department of Civil and Environmental Engineering, University of North Carolina at Charlotte,
9201 University City Boulevard, Charlotte, NC 28223-0001, USA
e-mail: mwhelan3@uncc.edu

C.D. Moen
The Charles E. Via, Jr. Department of Civil and Environmental Engineering, Virginia Polytechnic Institute
and State University, 200 Patton Hall, Blacksburg, VA 24061, USA

22.2 Details of Experimental Test Program

This paper presents results from experimental modal analysis of a full-scale bridge beam both in the as-built condition as well as following cutting of a significant number of prestressing strands at the midspan of the beam. This experimental test data is unique from past research on the influence of prestressing strand damage on modal parameters since the tension reinforcement in the beam tested, while being designed with prestressing strand, is not actually prestressed.

22.2.1 Structural Details

The experimental test program encompassed experimental modal analysis of a Hybrid Composite Beam (HCB), a unique prestressed bridge beam design conceptualized and developed by John Hillman, P.E., S.E. of HCB, Inc. [5] (Fig. 22.1). The HCB design is lightweight and modular in design, which are features that have led the design to be adopted for use in both highway and railway Accelerated Bridge Construction (ABC) projects across numerous states. The HCB design is a composite structure that consists of three primary components. The first is a fiber reinforced polymer (FRP) shell that provides a protective, corrosion resistant exterior that encapsulates a rigid polyisocyanurate foam formwork used to develop the reinforced concrete structure within. A concrete arch is formed within the beam by pumping self-consolidating concrete into void space in the foam. As seen in the cross-sectional view (Fig. 22.2a), this concrete arch also has a concrete "shear fin" that includes shear connectors to facilitate transfer of forces from the reinforced concrete deck to the arch of the beam. Lastly, the ends of the beam are developed with concrete blocks extending the full depth to provide anchorage for tension reinforcement running along the bottom flange of the beam. The tension reinforcement in the particular beam tested consisted of 22 unstressed prestressing strands with nominal diameter of 0.5 in. and tensile strength of 270 ksi. It is important for this study to emphasize that although prestressing strands are used in this design to increase the stiffness and strength of the beam, they are not subject to prestressing. The number of prestressing strands included in the beam design is typically governed not by strength limit states but rather by the associated AASHTO deflection limit. Additional information on the HCB design and performance, including results from full-scale performance tests of beams of the same design as investigated in this paper, can be found in [6–8]. Field performance evaluations of HCB bridges are reported in [9, 10].
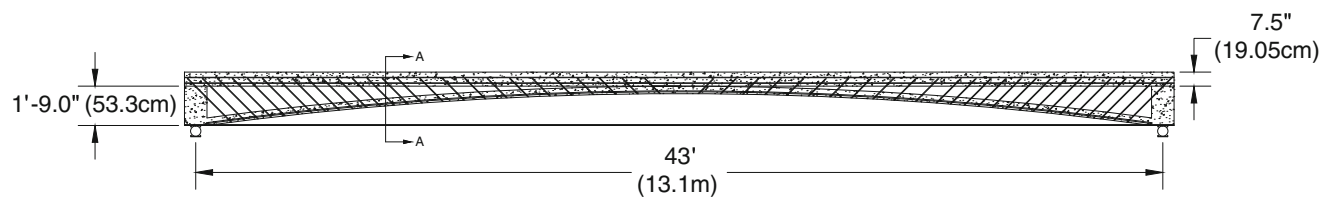
Fig. 22.1 Elevation view of hybrid composite bridge (*HCB*) beam featured in experimental tests
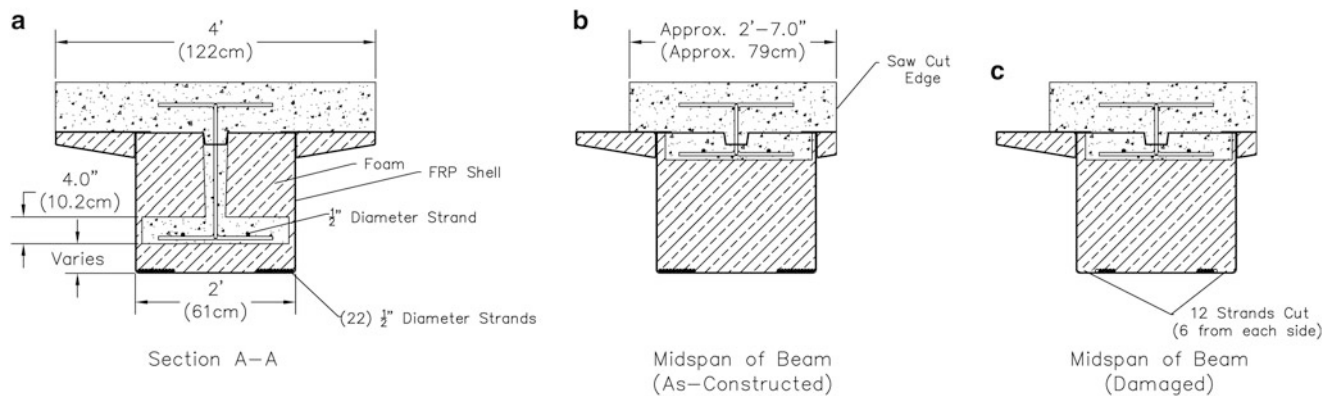
Fig. 22.2 Cross section of HCB beam: (**a**) typical cross sectional design; (**b**) typical cross section of tested beam indicating saw cut edge; (**c**) midspan cross section of tested beam after introduced damage

Fig. 22.3 Photographs of damage introduced to beam through cutting of prestressing strands (symmetric cuts on both sides of beam)

The beam specimen instrumented in this study was originally cast as a member of a test bridge consisting of three adjacent HCB's with a 45° angle skew. During cutting of this beam from the full bridge test structure, an asymmetric cross-section was developed as one of the wing flanges of the FRP shell was removed during the cutting (Fig. 22.2b). To simulate damage to the tension reinforcement in this study (a condition that is plausible under the influence of vehicular impact to the beam) a number of strands in the tension reinforcement were mechanically cut at the midspan of the beam. In total, six strands per side of the beam were cut, resulting in damage to 60 % of the prestressing strand at the bottom of the beam (Fig. 22.2c). Photographs of the damage introduced to the beams at the midspan are presented in Fig. 22.3. Note that the large opening in the webs of the FRP shell and removal of polyiso foam were performed prior to the initial vibration testing of the beam so the only difference between pre- and post-damage experiments was the v-shaped notches cut into the bottom flange of the beam and through the outermost six strands on each side of the beam.

22.2.2 Experimental Modal Analysis

The current study utilized a Single-Input-Multiple-Output (SIMO) vibration test setup featuring a reaction mass shaker and a network of 30 distributed accelerometers. The accelerometers used were Measurements Specialties model 4,000 A piezoresistive accelerometers with a range of ± 2 g, 0–200 Hz bandwidth, and spectral noise of $3 \mu g/\sqrt{Hz}$. These accelerometers were distributed in a regular pattern across the deck surface of the HCB beam by bonding with a thin layer of wax (Fig. 22.4). These uniaxial sensors were oriented to measure the response in the vertical direction. Excitation was provided by an APS Electro-Seis long-stroke electromagnetic shaker equipped with 17 kg reaction masses (Fig. 22.5). The bandwidth of the shakers is also 0–200 Hz and the long-stroke motion offered by the shaker design is well suited for testing of buildings and other civil structures with low natural frequencies. This shaker was driven by an APS power amplifier and controlled by analog output signals generated by a National Instruments PXI-5412 14-bit arbitrary waveform generator. Several excitation waveforms were used during the experimental test program; the data analysis presented in this paper stemmed from swept sine testing conducted from 0–200 Hz over a test duration of 60 s. Synchronously clocked National Instruments PXIe-4497 24-bit simultaneous sampling dynamic signal analyzers were used for signal conditioning and data acquisition of the accelerometer signals and voltage and current monitors from the power amplifier at a 5 kHz sampling rate.

Experimental modal analysis of the HCB was performed for the as-constructed beam and then again after introduction of damage. The beam was simply supported on cylindrical steel pin and roller supports that were in-turn supported by steel beams anchored to a strong floor. The damage introduced to the beam was developed by mechanically cutting the six external strands from each side of the beam at the midspan, as previously described and referenced in Fig. 22.3. In both experimental tests, a W14 × 311 steel beam used in a later quasi-static load test was positioned along the centerline of the beam on simple supports. However, this beam was not moved or repositioned between the baseline and damaged vibration tests. Furthermore, since the experiments were conducted within a laboratory environment, nominal changes in ambient temperature or humidity are not expected to significantly affect the dynamic properties of the beam between the pre- and post-damage experimental modal analyses.

Fig. 22.4 Photographs of instrumented HCB bridge beam with reaction mass shaker and array of uniaxial accelerometers
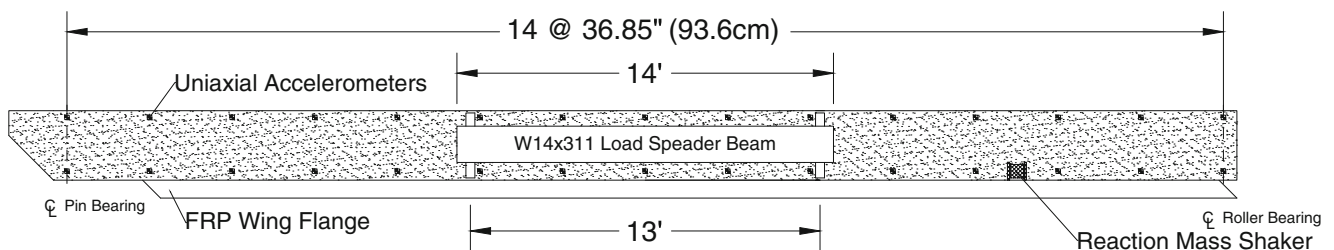
Fig. 22.5 Plan view of instrumentation layout on surface of deck

22.3 System Identification

For each of the acquired experimental data sets, the modal parameters (undamped natural frequencies, f_n, relative damping factors, ξ, modal shapes, ψ, and modal participation factors, Γ) were estimated as described in this section. The entire processing routine was written and performed within the MATLAB computing environment. Preprocessing of the signals including detrending and decimation of the acquired time series. The original data was sampled at approximately 25 times the bandwidth of interest to reconstruct the signal well in the time domain and ensure that the digital filters in the dynamic signal analyzers were not saturated by out of bandwidth response. An additional advantage of sampling at a high rate with subsequent decimation is the improved effective resolution of the conversion achieved by averaging in the down sampling process. The decimation process utilized a multirate finite impulse response (FIR) filter, which simultaneously provides excellent anti-alias rejection and resampling of the data to the lower effective rate.

The average accelerance function corresponding to the shaker force at the excitation location was computed using the classical H1 frequency response function estimator. A comparison between the accelerance estimates obtained before and after cutting the tension reinforcement is presented in Fig. 22.6 and illustrates that the frequency spectrum is relatively free of significant differences that might readily indicate the presence of major damage in the beam using this simple measure alone. However, the most significant difference revealed in the average frequency response function is associated with the fundamental mode of the beam, where it can be seen that the influence of damage to the strands produced both a reduction in the resonance frequency and an increase in the amplitude of the average accelerance. This change is consistent with the significant reduction in flexural stiffness in the beam as a result of mechanically cutting the prestressing strands along the bottom flange.

The system identification algorithm chosen for extraction of modal properties was the combined deterministic-stochastic subspace state-space identification algorithm, as developed by Van Overschee and De Moor [11]. This system identification algorithm allows for direct use of the time-domain data from the input excitation channels and response measurements. The eigenproperties were calculated by eigenvector decomposition of the state matrix produced by the subspace identification algorithm. The undamped natural frequencies and relative damping factors were then computed from the poles and modes
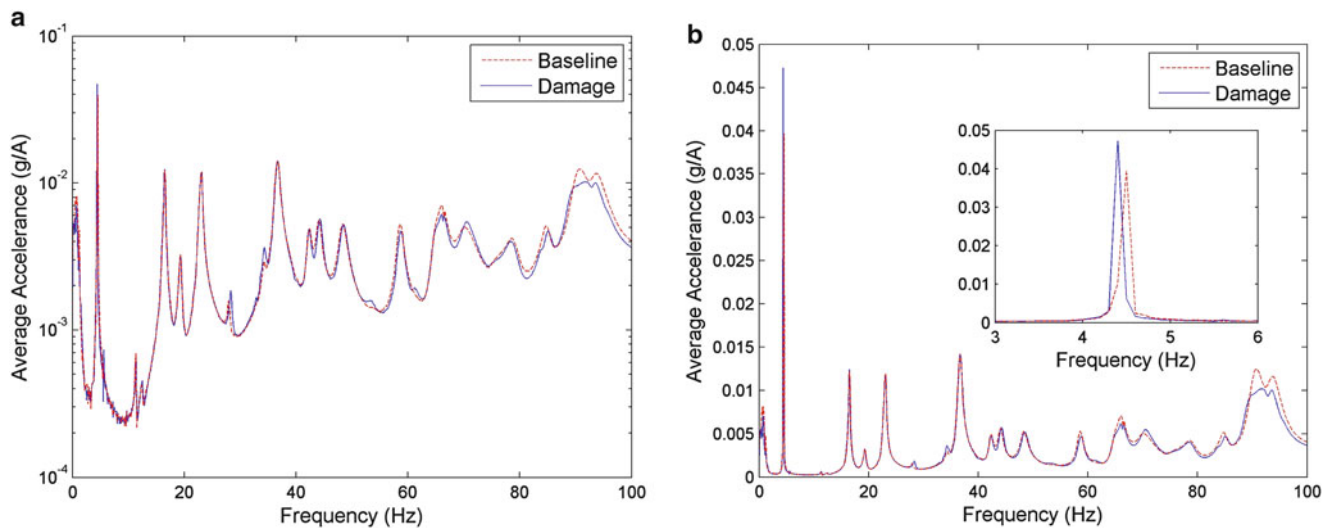
Fig. 22.6 Comparison of average accelerance functions: (**a**) Logarithmic scale; (**b**) Linear scale with close-up view of change at the first resonance peak

shape estimates and were transformed to the physical coordinates using the output matrix. System identification at sequential model orders was used to develop stabilization plots to evaluate the modal property estimates and aid in selection of stable poles. These plots facilitate the selection of consistent system poles and the rejection of spurious computational poles that do not reflect physical behavior. Poles were plotted based on percent variations in frequency, mode shape, and damping. The percent variations chosen were 1 %, 1 %, and 5 % for frequency, mode shape, and relative damping factor, respectively. To overcome noise and uncertainty for a better estimation of the modal properties, fifteen stable poles were averaged for each experimental mode identified across three independent datasets.

22.3.1   Modal Parameter Estimates and Changes in Modal Parameters Following Damage

Experimentally derived estimates of undamped natural frequencies, relative damping factors, and mode shapes for the beam are presented in Fig. 22.7. Note that the asymmetry in the mode shapes is a product of the original skew design and asymmetric cutting of the cross-section. Each of the mode shapes are presented on an biharmonic spline interpolated surface of the 30 measurement locations to improve the clarity of the figures for the higher-order modes. In general, there are no visually apparent differences in the experimentally reconstructed mode shapes obtained prior to and after the cutting of the strand reinforcement. While only the first ten mode shapes with significant vertical component of response are included in this figure, no significant differences were visually apparent in any of the roughly 25 modes extracted from the experimental data. As expected from the spectral information in Fig. 22.6, the relative damping factors for the beam are relatively low (consistently around 1 %) and did not experience any significant changes after the introduction of the damage.

To quantitatively compare the differences in dynamic properties observed after the introduction of strand damage, the percent change in undamped natural frequencies and differences in relative damping factors were computed for each modal parameter estimate (Fig. 22.8). The most significant change was recorded for the fundamental natural frequency, which was reduced by just over 1 %. Since the mass of the system was essentially unchanged by the introduction of the strand damage, this reduction in the fundamental natural frequency is consistent with the expected loss of flexural stiffness introduced by the damage at the midspan of the beam. The remaining undamped natural frequencies all changed by less than 0.4 %, with many of the higher-order modes exhibiting an increase in natural frequency. Relative damping factor estimates exhibited negligible changes with the introduction of the strand damage, although the majority of modes underwent a reduction in damping. To compare the consistency of the mode shapes, the Modal Assurance Criteria (MAC) was computed for corresponding modes in the pre- and post-damage states. In general, the eigenvector estimates are very consistent despite the introduction of strand damage, with nearly all mode comparisons generating MAC values greater than 99 %. The most significant change was observed for the 5th mode, but it should be noted that this mode is closely spaced to the 6th mode and was weakly excited relative to most of the other modes.

From an applied structural health monitoring perspective, modal parameter estimates would generally be limited to this set of undamped natural frequencies, relative damping factors, and mode shape estimates since ambient vibration monitoring
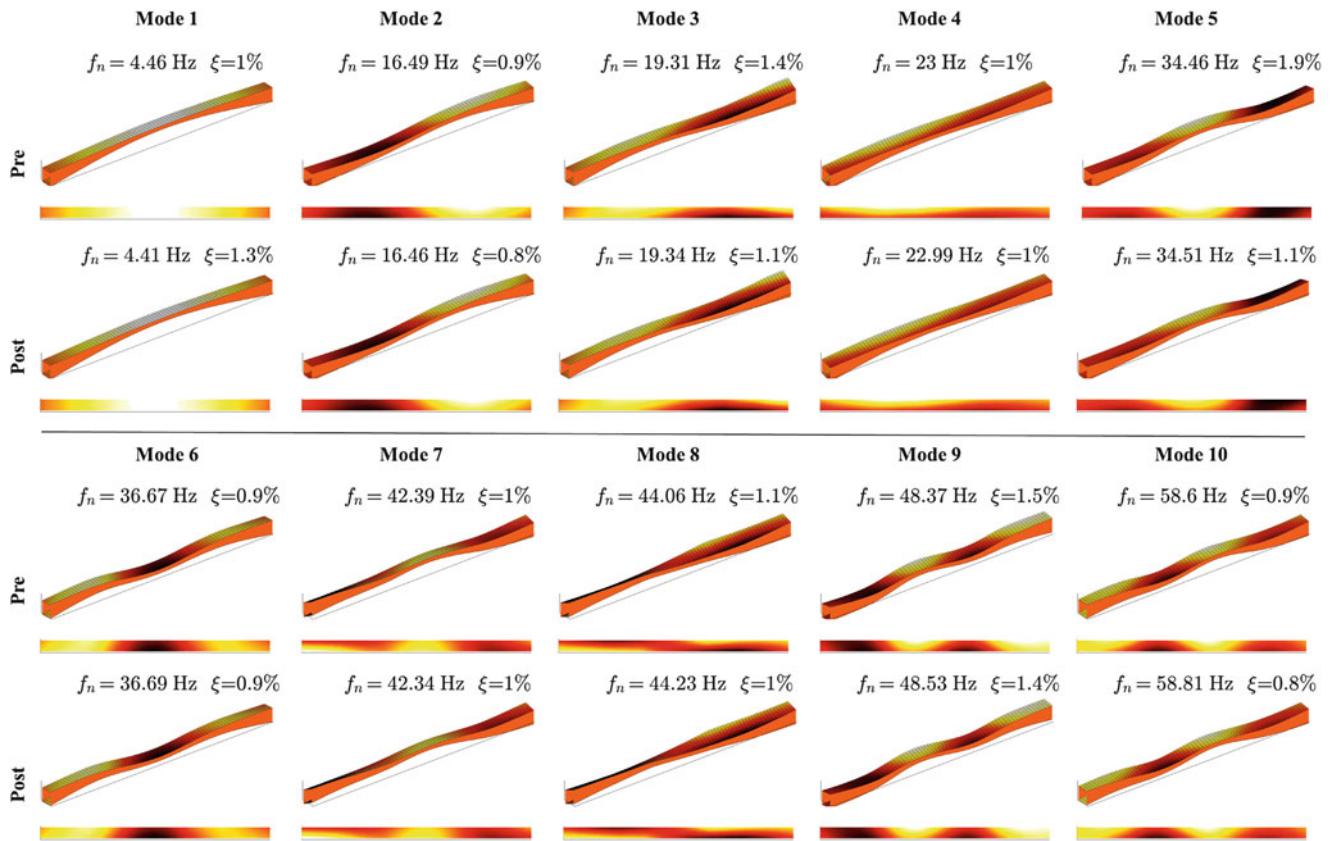
Fig. 22.7 Comparison of experimental estimates of mode shapes, natural frequencies, and relative damping factors for beam prior to and after cutting of tension reinforcement
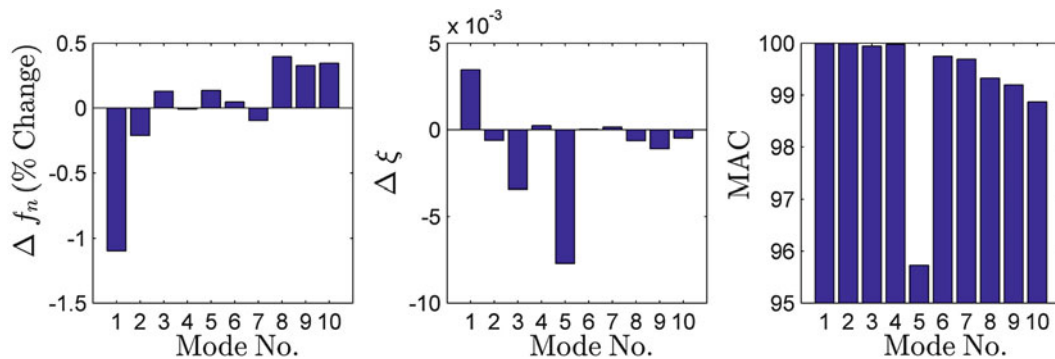
Fig. 22.8 Relative changes in natural frequencies, relative damping factors, and mode shapes developed after cutting strands in tension reinforcement

restricts applications to output-only system identification approaches. Under these conditions, the nominal observed changes in dynamic properties of the beam following very significant damage to the tension reinforcement emphasize the challenges associated with vibration-based damage detection. In real-world applications outside the laboratory, such changes could be very well be attributed to environmental influences rendering these modal parameter estimates unreliable indicators of damage in the beam. However, the applied excitation force imparted from the reaction mass shaker can be indirectly monitored from the electrical current required to drive the shaker in this experiment. Consequently, the modal participation factors for each mode could be computed to develop mass normalized mode shape estimates. Unfortunately, since a drive-point measurement was not established in the experimental setup, pseudo-modal participation factors were alternatively estimated by averaging the complex eigenvector components from two sensors positioned equidistant and in close proximity to the shaker.
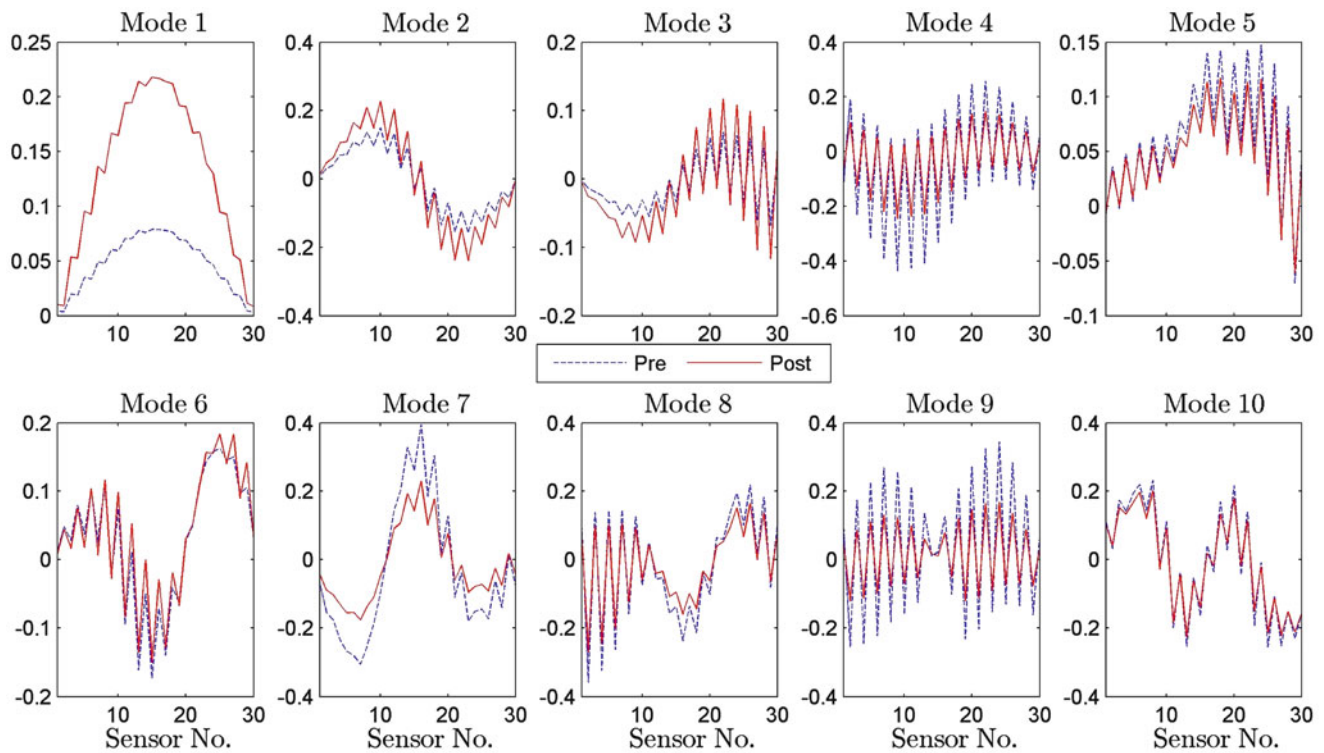
Fig. 22.9 Pseudo-mass normalized mode shape comparisons for the beam before and after strand damage

The resulting mass normalized mode shapes are presented in Fig. 22.9 and indicate a significant increase in flexibility of the beam as a result of mechanical cutting of the strands in the tension reinforcement. Specifically, there is a significant change in the amplitude of the fundamental mode. While damage at the midspan is expected to affect the fundamental mode, localized damage is generally most noticeable in the higher-order bending modes since the sensitivity of the mode shape to the damage increases as the wavelength of bending approaches the length scale of the damage. Since the fundamental mode appears to be disproportionately affected by the strand damage, the measurement data seems to indicate that the effect was not localized but affected the stiffness along the entire span length of the beam. Given the unique design of this beam where the tension reinforcement is external to the concrete over the length of the span, it is plausible that the effect of the strand damage to the beam is not a localized effect. While the strands are infused with the resin in the bottom FRP flange of the beam, there has been conflicting data reported on whether these strands are perfectly bonded or whether there is separation and slip at the interface [12]. Furthermore, experimental research has demonstrated that the FRP shell does not act compositely with the internal arch and deck of the HCB [6, 7], so it is plausible that, even with sufficient bonding between the strands and the bottom flange of the beam, the strand damage may not produce a highly localized effect on the dynamic response.

22.3.2 Application of a Data-Driven SHM Index

To explore the application of data-driven methods for SHM on the full-scale measurement database, the general approach developed by Yan et al. [13] and applied by Whelan and Janoyan to a full-scale highway bridge case study [2] has been examined. In the current paper, the prior implementations of the state-space model as a prediction tool have been modified from the output-only case to the full input-output model since excitation was applied using a reaction mass shaker. Otherwise, the implementation and formulation of the damage index remain unchanged from those presented in [2]. However, since it is expected that significant ambient vibrations were introduced to beam during the testing, damage indexes were computed by averaging over those generated by a matrix of nine pairs of baseline-damage time history pairs. This averaging is performed in order to attenuate uncorrelated residual errors in the prediction models due to these unmeasured external excitation in the laboratory. In total, three baseline and three damage time history sets were used in the post-processing and each were
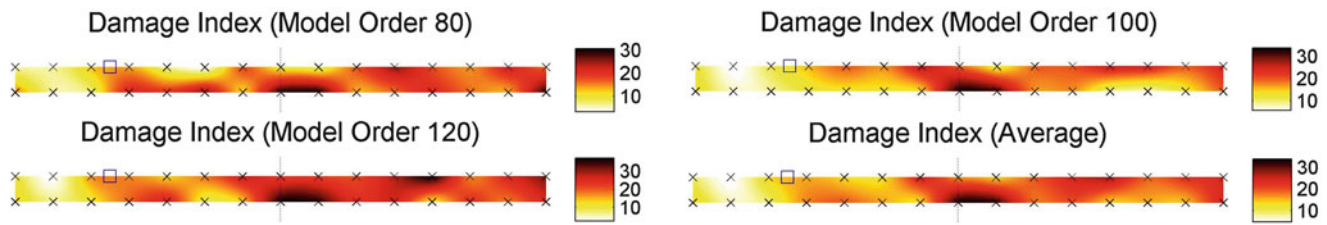
Fig. 22.10 Damage localization results from application of data-driven algorithm for damage detection

decimated from the original 5 kHz sampling rate to 500 Hz. Additionally, these swept-sine time histories were reduced to just the first 30 s of the sweep to limit the bandwidth of excited frequencies in the datasets to those below approximately 100 Hz.

A series of models constructed at different model orders were used to explore the consistency of the damage index estimates for the experimental case. In general, while there is some variation in the indexes across the preliminary damage detection models developed from the data, the highest index consistently occurs toward the midspan of the beam where the strands were cut (Fig. 22.10). However, while the highest index is localized around the midspan of the beam, the algorithm fails to properly identify that the damaged introduced was symmetric about the centerline of the beam. Furthermore, it should be emphasized that the damage indexes produced for this case study are far less consistent than those generated in the prior study [2] and appear to be significantly more sensitive to the frequency bandwidth included in the linear prediction model. Since the damage artificially created in the current study was formed by relatively wide notched cuts through the bottom flange of the beam, the degree of nonlinearity introduced through crack opening and closing may be significantly small enough that the damage is not as readily identified by this approach as in the previously published cases involving bolt removal and settlement in the full-scale bridge. Further, given that the fundamental mode exhibited the most significant change in both natural frequency and modal participation, it is not surprising that the damage localization technique struggles to faithfully isolated the damage along the span length. If damage to strands in the HCB design can be confirmed to yield more of a global than localized impact on the dynamic properties of the arch and deck, then alternative instrumentation strategies should be pursued for structural health monitoring systems suitable for this beam design. In particular, placement of accelerometers on the bottom flange of the beam might significantly improve the sensitivity of the measurements to damage in the strands, whereas the placement of accelerometers on the deck might be more suitable for monitoring the condition of the concrete arch and deck.

22.4 Summary

A unique experimental dataset for structural health monitoring of an innovative bridge beam has been developed through experimental modal analysis of the beam both prior to and after prescribed damage to the tension reinforcement. Comparisons of changes in the modal parameter estimates indicates that damage to the tension reinforcement in the beam may yield more of a global reduction in structural stiffness than one highly localized to the region where the strands are cut. Application of a data-driven structural health monitoring technique for damage detection shows some early promise, but an expanded study of the damage detection methodology and its application to this particular damage scenario is needed before the plausibility of these results can be confirmed. Future work will include finite element modeling of the beam to examine whether the measured changes in dynamic properties can be replicated through simulation. Further understanding of the behavior of this unique beam system is necessary to design an effective performance and health monitoring system, which may require unique approaches not yet investigated for conventional bridge designs.

References

1. Farrar CR, Worden K (2012) Structural health monitoring: a machine learning perspective. Wiley, Chichester
2. Whelan MJ, Janoyan KD (2009) In-service diagnostics of a highway bridge from a progressive damage case study. J Bridge Eng 15(5):597–607
3. Farrar CR, Baker W, Bell T, Cone K, Darling T, Duffey T, Eklund A, Migliori A (1994) Dynamic characterization and damage detection in the i-40 bridge over the rio grande. Technical report. Los Alamos National Laboratory, Los Alamos
4. Peeters B, De Roeck G (2001) One-year monitoring of the z 24-bridge: environmental effects versus damage events. Earthquake Eng Struct Dyn 30(2):149–171
5. Hillman J (2008) Product application of a hybrid-composite beam system. Final report, NCHRP IDEA program
6. Ahsan S (2012) Evaluation of hybrid-composite beam for use in Tide mill bridge. Master's thesis, Virginia Polytechnic Institute and State University
7. Mascaro M, Moen C (2012) Out-of-plane deformation and relative arch movement of hybrid-composite beams based on photogrammetry. MS report CE/VPI-ST-12/08. Virginia Polytechnic Institute and State University, Blacksburg
8. Van Nosdall S, Moen CD, Cousins TE, Roberts-Wollmann CL (2013) Experiments on a hybrid-composite beam for bridge applications. Transp Res Rec J Transp Res Board 2332(1):43–52
9. Myers J, Aboelseoud M, Earley C, Washer G, Schmidt J (2014) Field evaluation of hybrid-composite girder bridges in Missouri. Technical report, NUTC R281. Center for Transportation Infrastructure and Safety, Missouri S&T, Rolla
10. Civitillo J, Harris D, Gheitasi A, Saliba M, Kassner B (2014) In-service performance and behavior characterization of the hybrid composite bridge system - a case study. In: 9th international conference on short and medium span bridges (SMSB), Calgary
11. Van Overschee P, DeMoor B (1996) Subspace identification for linear systems. Kluwer Academic Press, Boston/London/Dordrecht
12. Aboelseoud M, Myers J (2015) Finite-element modeling of hybrid composite beam bridges in Missouri. J Bridge Eng 20(1):04014054. doi:10.1061/(ASCE)BE.1943-5592.0000635
13. Yan A-M, De Boe P, Golinval J-C (2004) Structural damage diagnosis by kalman model based on stochastic subspace identification. Struct Health Monit 3(2):103–119

Chapter 23
Data-Driven Structural Damage Identification Using DIT

S. Golnaz Shahidi, Ruigen Yao, Michael B.W. Chamberlain, Mallory B. Nigro, Andrew Thorsen, and Shamim N. Pakzad

Abstract Vibration-based damage detection research aims to develop efficient algorithms to identify structural damage from monitoring data. One of the main categories of such algorithms is data-driven techniques which extract features from measured signals, and identify the damage by evaluating the significance of potential changes in these features. This paper presents application of several data-driven damage identification methodologies on a multivariate simulated data set. First, general regression models are applied to data collected through clusters of sensors and damage sensitive features are extracted. For systems with linear topology, it is shown that substructural regression modeling can also be performed on time- and frequency-domain transforms of the measured signals to estimate local stiffness of the structure as damage features. Subsequently, change detection techniques are utilized to statistically determine the significance of changes in the extracted features in order to distinguish between assignable changes as a result of damage and common changes due to environmental factors. Finally, a toolsuite is developed to facilitate application of the developed algorithms and improve the damage identification performance through incorporation of various combinations of regression models, damage features and statistical tests.

Keywords Health monitoring • Damage detection • Change point analysis • Regression models • Damage threshold

23.1 Introduction

The ultimate goal of vibration-based structural health monitoring (SHM) research is to develop efficient algorithms capable of detecting the time, location, and severity of any damage induced changes in structural components of monitored systems. Toward this goal, multitudes of methods have been proposed over recent decades that commonly establish a baseline for selected damage features and monitor their change from the baseline in the following unknown health conditions. Various features have been used for the purpose of damage identification; uncertain parameters of a finite element (FE) simulation of the structure that is calibrated with reference to modal quantities extracted using system identification (SID) algorithms [1, 2], or features that are directly extracted from measured signals without using FE or SID procedures to train the data [3–6]. Each group of these damage identification methods has their own advantages and drawbacks. The first group is usually more laborious to implement and require certain a priori knowledge of structural properties, and location of damage; however, the calibrated model could be beneficial in design of repair scenarios or estimating the remaining life of the structure. The main advantage of the second group is their efficiency, and that they can be readily applied to measured signals without any prior information. Therefore, their application for a general automated damage detection platform is more promising. However, these data-driven methods are ineffective without statistical analyses to determine the change threshold for the extracted features. This paper presents application of multiple data-driven damage detection procedures through a simulated example and introduces a damage identification toolsuite developed in order to facilitate comparison of various data-driven damage detection methods.

S.G. Shahidi (✉) • R. Yao • M.B. Nigro • S.N. Pakzad
Department of Civil and Environmental Engineering, ATLSS Engineering Research Center, Lehigh University, 117 ATLSS Drive, Bethlehem, PA 18015, USA
e-mail: sgs310@lehigh.edu

M.B.W. Chamberlain
Department of Earth and Planetary Science, University of California Berkeley, 307 McCone Hall, Berkeley, CA 94720, USA

A. Thorsen
Department of Civil and Environmental Engineering, Carnegie Mellon University, 5000 Forbes Avenue, Pittsburgh, PA 15213, USA

23.2   Time Series Analysis for Damage Detection

Direct use of vibration data for feature extraction is believed to be one of the efficient methods for structural damage detection [7]. One of the common approaches for data-driven damage detection is to use a regressive model to train the data and extract damage sensitive features. Previous research has shown that these regression models are successful in identifying the time and location of structural damage when they are applied to measured structural responses in the form of acceleration or strain signals [8–11]. Autoregressive (AR) models are one form of these regression models. They are beneficial mainly because they can be used on univariate measurements possibly to find the timing of a change in structure's behavior. With the use of multivariate measurement networks, performance of these models can be extended to localizing the damage as well. Several studies have investigated performance of AR models regressed on measured signals [12, 13]. These models can be written as:

$$y_i(n) = \sum_{p=1}^{P} \alpha_p y_i (n-p) + \varepsilon(n) \tag{23.1}$$

where y is the measured response of structure at location i, and α_p's are AR coefficients, n, $\varepsilon(n)$, and P represent the time index, residuals, and order of the AR model, respectively. This model can be extended to relate structure's response in two locations. The general from of this extended mapping relation is a p-order autoregressive with exogenous (ARX) input model:

$$y_j(n) + \sum_{p=1}^{P} \alpha_{jp} y_j (n-p) = \sum_{q=0}^{Q} \alpha_{iq} y_i (n-q) + \varepsilon(n) \tag{23.2}$$

In this equation, y_i and y_j represent the outputs at locations i and j, α_{jp}'s and α_{iq}'s are ARX coefficients, n, $\varepsilon(n)$, and P represent the time index, residuals, and order of the ARX model, respectively. Several features can be extracted from these models that are functions of model coefficients or residuals.

23.3   Stiffness Estimation Based on Substructural Modeling

For the case of shear structures, both mass matrix **m** and stiffness matrix **k** are 'banded matrices' that have zero entries outside a certain 'band' centered on the main diagonal. Under the assumption of classical Rayleigh damping ($\mathbf{c} = \mu \mathbf{m} + \lambda \mathbf{k}$, where μ and λ are constants), matrix **c** has bandwidth 3 as in this case **m** has bandwidth 1 and **k** has bandwidth 3. Therefore, the following equation holds for the response measurements of a shear frame model at floor i-1, i, and i + 1:

$$m_i \ddot{u}_i = k_{i,i-1} (u_{i-1} - u_i) + k_{i,i+1} (u_{i+1} - u_i) - c_i \dot{u}_i - c_{i-1} \dot{u}_{i-1} - c_{i+1} \dot{u}_{i+1} + p_i. \tag{23.3}$$

Here damping (c_{i-1}, c_i, c_{i+1}) is not assumed to be related to relative displacements/velocities because part of the effect also comes from the system's interaction with the surrounding environment, which depends on the absolute displacements/velocities. Thus given the mass of the middle node m_i, its acceleration $\ddot{u}_i$, the displacement and velocity response at the three nodes, $u_{i-1}, u_i, u_{i+1}, \dot{u}_{i-1}, \dot{u}_i, \dot{u}_{i+1}$, and the excitation acting on the middle node, p_i, the local stiffness and damping parameters can be obtained through a linear least squares regression.

The excitation, velocity, and displacement data are often not available in SHM applications, where accelerometers are primarily used. Also, through simulation it is found that regression using Eq. (23.3) is quite sensitive to noise, making it necessary to search for other alternative formulations. Assuming that the excitation is chronologically uncorrelated, correlations of the middle node acceleration response and the two sides of the equation can be taken to eliminate p_i.

$$m_i E \left[\ddot{u}_i(t) \ddot{u}_i (t-\tau) \right] = k_{i,i-1} E \left[(u_{i-1}(t) - u_i(t)) \ddot{u}_i (t-\tau) \right] + k_{i,i+1} E \left[(u_{i+1}(t) - u_i(t)) \ddot{u}_i (t-\tau) \right]$$
$$- c_i E \left[\dot{u}_i(t) \ddot{u}_i (t-\tau) \right] - c_{i-1} E \left[\dot{u}_{i-1}(t) \ddot{u}_i (t-\tau) \right] - c_{i+1} E \left[\dot{u}_{i+1}(t) \ddot{u}_i (t-\tau) \right]. \tag{23.4}$$

Where τ is a positive time lag. Therefore, an acceleration-based time domain regression formula can be obtained via ignoring damping and using reconstructed displacement from acceleration, and a frequency domain regression formula constructed from taking the Fourier Transform of Eq. (23.4). For further details on the theoretical development and various applications, please see [14, 19].

Regardless of the type of extracted features from these regression models, proper statistical tests are required to distinguish the damage induced changes from their common changes due to random variation of measurements. Control statistic can make this distinction with the use of a threshold value; once this threshold is crossed, occurrence of damage is inferred. Since damage features have different sensitivities [15], it is expected that combination and comparison of several regression models, features, and test statistics would improve the reliability of detection and localization results. In order to facilitate this comparison, a damage identification toolsuite is developed. The following sections describe the functionalities of this damage detection package through a simulated bridge model.

23.4 Damage Identification Toolsuite (DIT)

Damage Identification Toolsuite (DIT) offers several (time- and frequency-domain) regression models to train the monitoring data, extract damage sensitive features, establish a baseline, and test significance of possible deviation of the features from the baseline [16]. Figure 23.1 summarizes all the algorithms implemented in DIT. General regression models include AR and ARX models, as well as Single Variate Regression (SVR) and Collinear Regression (CR); special cases of the ARX model discussed in [17]. Several damage features are available using these models: (1) coefficient-based features [12, 17, 18]: regression coefficients themselves, angle coefficients, Mahalanobis distance, and spectral distance of regression coefficients. (2) residual-based damage features [12]: (normalized) variance, (normalized) standard deviation, and Ljung-Box statistics of the residual vectors. Time Domain Regression Method (TDRM), and Frequency Domain Regression Method (FDRM) are stiffness estimation methods for structures with linear topology [14]. As stated previously, in these methods, (mass) normalized stiffness of each component of the system is estimated using time and frequency transforms of acceleration signals measured on a substructure.

Once regression analysis is performed and damage features are generated, significance of any potential changes in the features should be evaluated through proper statistical tests. For this purpose, DIT offers several change point statistics to be created from damage features for which control threshold is constructed using resampling methods (bootstrapping and permutation) as well as test of significance (where applicable).
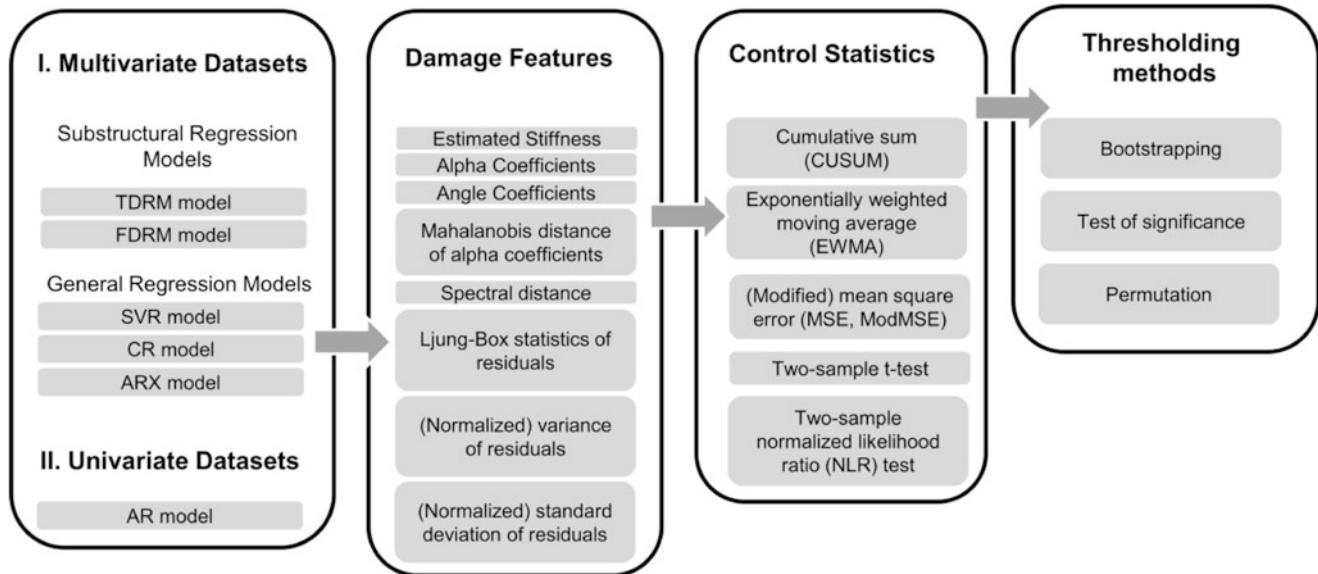
Fig. 23.1 Flowchart illustrating algorithms implemented in DIT (DIT can be downloaded from dit.atlss.lehigh.edu)

23.5 Damage Detection Using DIT

This section illustrates various applications of DIT through a simulated 8 degree-of-freedom (dof) bridge model. Figure 23.2 shows the model in its undamaged ("healthy") state. Damage in the model is introduced as 15 % reduction in k_6. At each state, the bridge model is excited 40 times with random vibrations and acceleration at all dofs ($a_1(t)$ to $a_8(t)$) are generated with 200Hz sampling frequency for 20 s (4,000 samples per each dof). Maximum standard deviation of the acceleration signals is about 0.05 g to resemble the ambient vibration.

23.5.1 Comparison of Several Damage Features

First, every acceleration signal is processed using (eighth order) AR models and performance of three different features is compared. Here first 10 tests are assumed to come from a "healthy" and "known" state of system. Figure 23.3 presents NLR test statistics of damage features extracted form AR models, along with a 95 % confidence change threshold. x axes in these plots show the test number of the unknown state of the system. The figure shows that all statistics are successful in identifying the occurrence of damage. However, their performance in detecting the time and location of damage is different; Mahalanobis distance has the best performance by pinpointing to fifth and sixth dofs at the 30th test from unknown state of structure (i.e. 40th undamaged test overall).
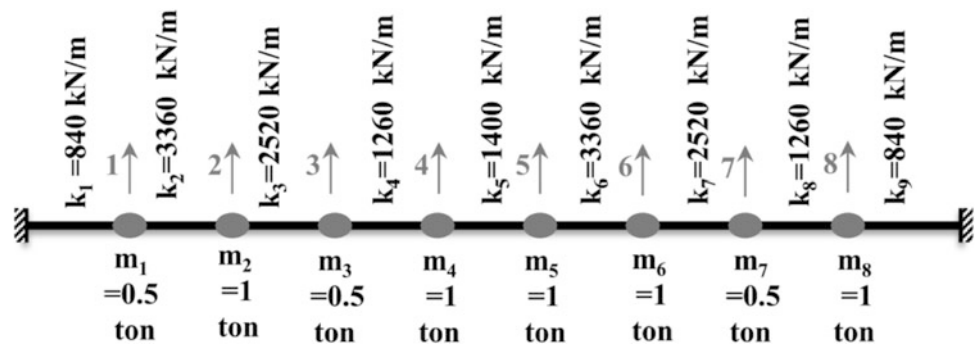
Fig. 23.2 Bridge model used to simulate the acceleration signals
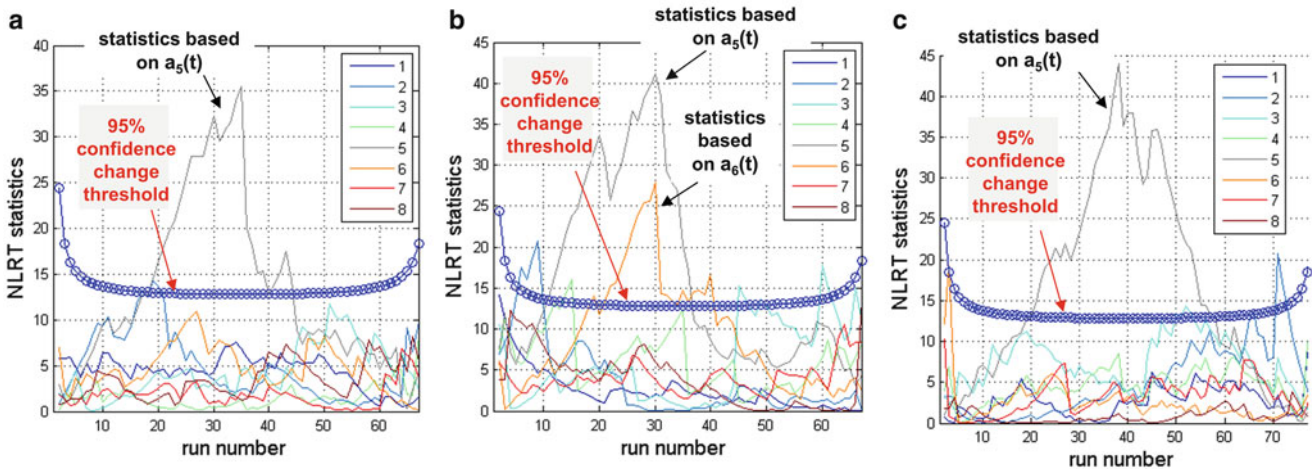
Fig. 23.3 Comparison of features extracted from AR models: (**a**) angle coefficients, (**b**) Mahalanobis distances of AR coefficients, and (**c**) variance of residuals
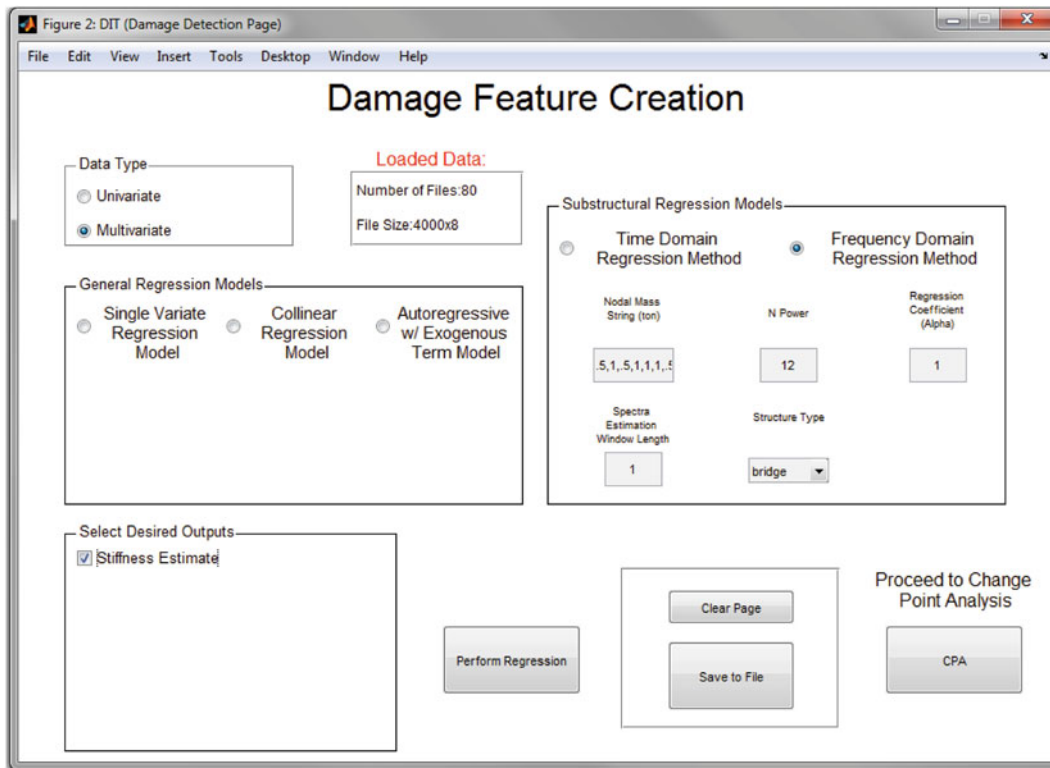
Fig. 23.4 DIT feature creation interface
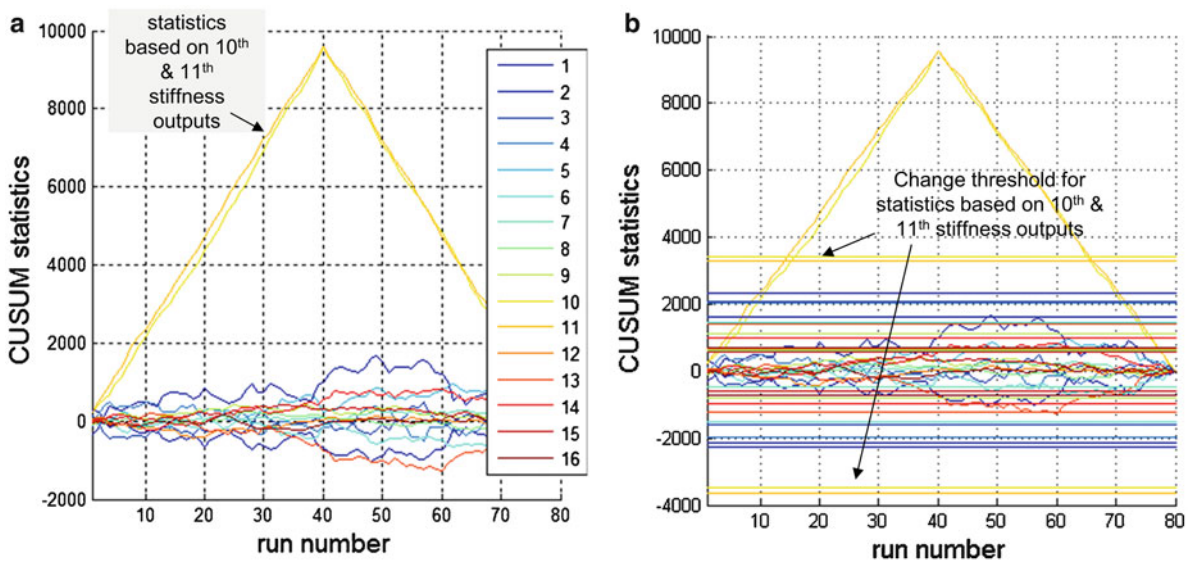
Fig. 23.5 Results of FDRM algorithm tested using CUSUM statistics: (**a**) & (**b**) before and after threshold construction

23.5.2 Stiffness Estimation Using FDRM

The second algorithm used is FDRM along with Cumulative sum (CUSUM) control chart to test the change in the stiffness of each component. Figure 23.4 shows DIT damage detection page when FDRM is selected [16]. Figure 23.5 displays the test statistics before and after threshold construction using 200 bootstrapped samples. Since FDRM algorithm estimates the stiffness of components based on acceleration response form two subsets of their neighboring nodes, stiffness output of this

method include one estimate for elements that are attached to the ground, and two estimates for stiffness locating between two dofs (i.e. 2 N output quantities for an N-dof bridge model). Figure 23.5b shows that the test statistics from 10th and 11th stiffness outputs (corresponding to k_6) are the only test statistics crossing their thresholds.

23.5.3 Threshold Construction Methods

Finally, ARX models are used to regress acceleration responses of every adjacent node pairs onto one another. This can be accomplished by providing DIT with a text file containing the desired sensor numbers for each senor pair. Figure 23.6 shows DIT's change point analysis page when two-sample t-test statistics are used to test the Mahalanobis distance of ARX coefficients [16]. In this example, the first 20 simulations on undamaged model are considered as reference. This figure shows distinct peaks at 20th unknown test (40th overall) corresponding to sensor parings 5–6, 6–5, and 6–7. It is also observed that statistics related to sensor paring 1–2 cross the 95 % confidence threshold (although with much smaller test statistics). Figure 23.7a, b show change thresholds constructed for two sets of features based on paring 1–2 and pairing 6–7. These plots show that for sensor pair 1–2 the statistics does not cross the threshold constructed using 200 permutated samples, while the statistics based on sensor pair 6–7 does cross the threshold constructed based on 200 bootstrapped samples.
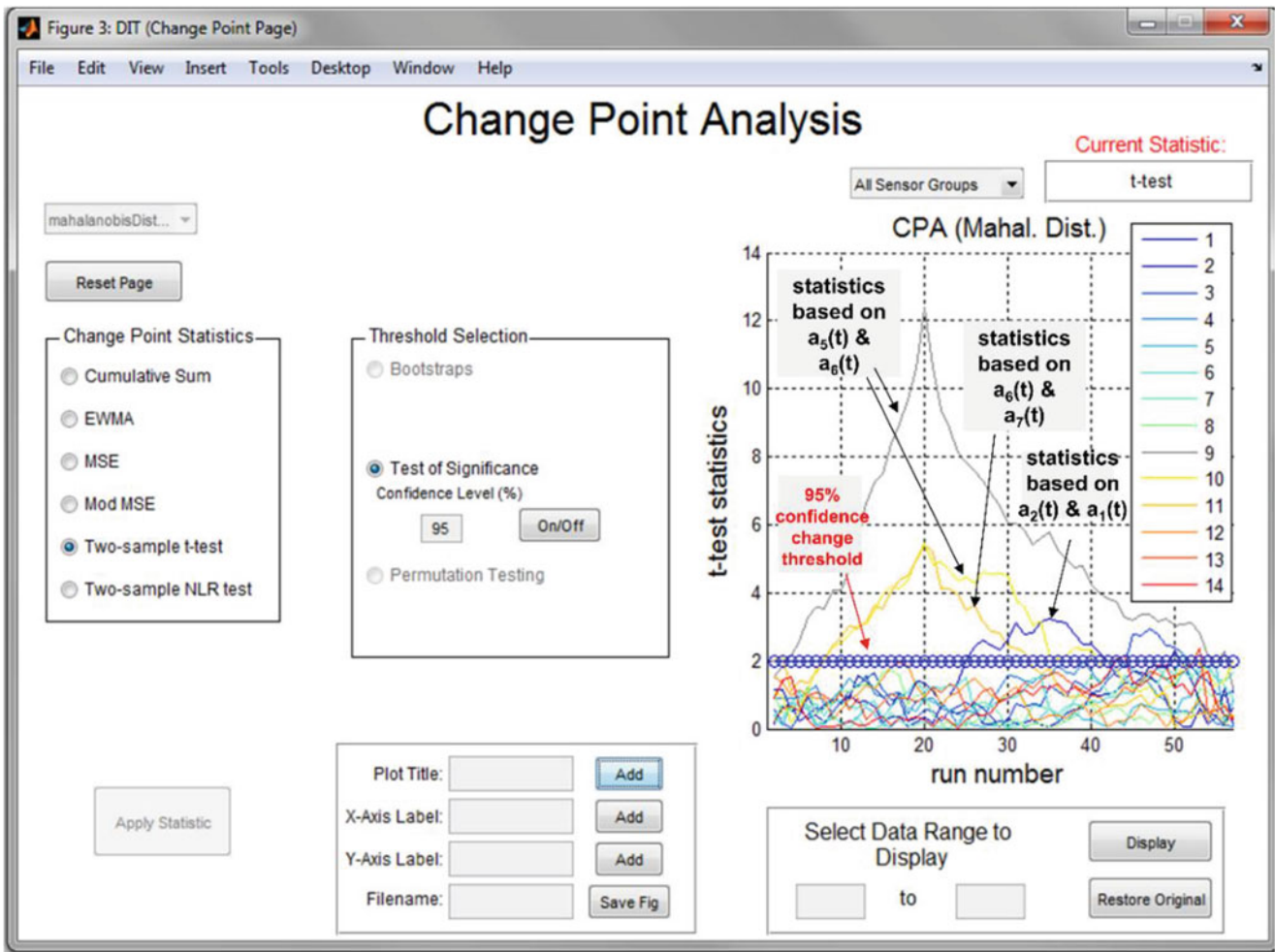
Fig. 23.6 DIT change point analysis interface
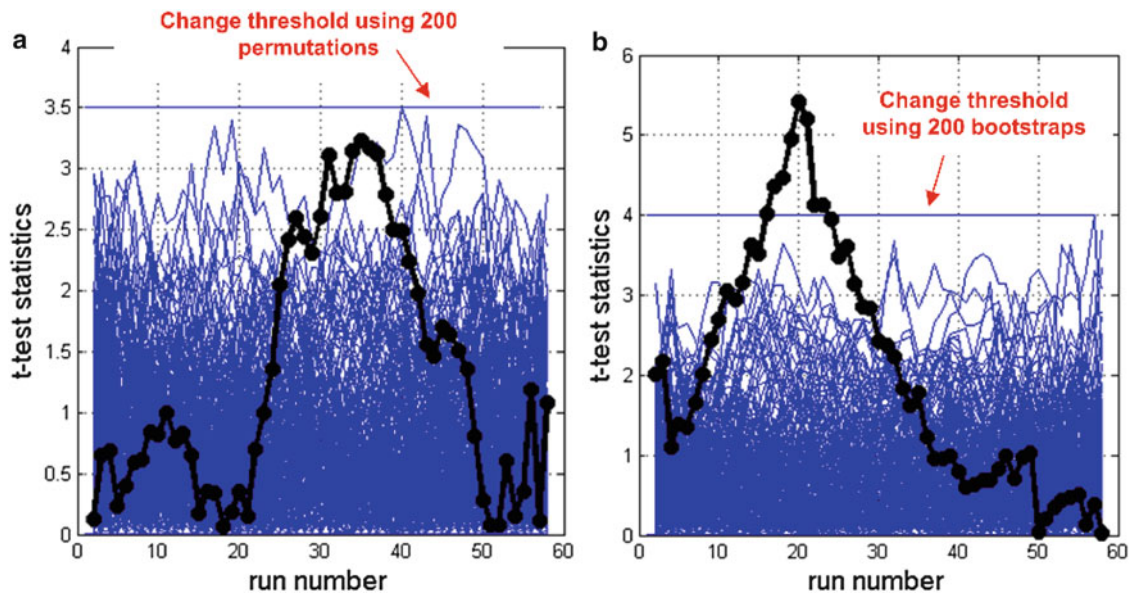
Fig. 23.7 Damage detection results using ARX models, statistics based on (**a**) $a_1(t)$ and $a_2(t)$, (**b**) $a_6(t)$ and $a_7(t)$

23.6 Conclusions

This paper presents a comparison in performance of several data-driven damage detection methods. An 8-dof bridge model is simulated in healthy and damaged conditions. The model is excited at ambient level vibration and acceleration responses at its dofs are used for identifying the timing and location of the simulated damage. It is shown that incorporating multiple mathematical models, damage sensitive features and change detection tests improves the overall performance of these data-driven structural damage detection techniques. This comparison study is conducted using a damage identification software package: DIT. This package offers several regression models to train the monitoring data and create damage sensitive features. Multiple change point statistics are also available to test the significance of the potential changes in the generated features. The change thresholds for these statistics can be established based on test of significance or resampling techniques. This damage identification toolsuite is developed to facilitate combination and comparison of various data-driven methods in other damage detection problems.

References

1. Huth O, Feltrin G, Maeck J, Kilic N, Motavalli M (2005) Damage identification using modal data: experiences on a prestressed concrete bridge. J Struct Eng 131(12):1898–1910
2. Jafarkhani R, Masri SF (2011) Finite element model updating using evolutionary strategy for damage detection. Comput-Aided Civ Infrastruct Eng 26(3):207–224
3. Posenato D, Kripakaran P, Inaudi D, Smith IFC (2010) Methodologies for model-free data interpretation of civil engineering structures. Comput Struct 88(7–8):467–482
4. Torres-Arredondo MA, Tibaduiza DA, Mujica LE, Rodellar J, Fritzen C-P (2014) Data-driven multivariate algorithms for damage detection and identification: evaluation and comparison. Struct Health Monit 13(1):19–32
5. Kumar RP, Oshima T, Mikami S, Miyamori Y, Yamazaki T (2012) Damage identification in a lightly reinforced concrete beam based on changes in the power spectral density. Struct Infrastruct Eng 8:715–727
6. Labuz EL, Chang M, Pakzad SN (2010) Local damage detection in beam-column connections using a dense sensor network. In: Proceedings of the ASCE's 42nd structures congress, Orlando, pp 3143–3154. doi:10.1061/41130(369)282
7. Cavadas F, Smith IFC, Figueiras J (2013) Damage detection using data-driven methods applied to moving-load responses. J Mech Syst Signal Process 39(1–2):409–425

8. Dorvash S, Pakzad SN, Labuz EL, Chang M, Li X, Cheng L (2010) Validation of a wireless sensor network using local damage detection algorithm for beam-column connections. In: Proceedings of the SPIE sensors and smart structures technologies, vol 7647, San Diego, pp 76719–1. doi:10.1117/12.847581

9. Dorvash S, Pakzad SN, LaCrosse EL (2014a) Statistics based localized damage detection using vibration response. Smart Struct Syst Int J 14(2):85–104

10. Dorvash S, Pakzad SN, Labuz EL, Ricles JM, Hodgson IC (2014b) Localized damage detection algorithm and implementation on a large-scale steel beam-to-column moment connection. Earthq Spectra (in press). doi:http://dx.doi.org/10.1193/031613EQS069M

11. Yao R, Pakzad SN (2010) Data-driven methods for threshold determination in time-series based damage detection. In: Proceedings of the ASCE's 43rd structures congress, Las Vegas, pp 77–88. doi:10.1061/41171(401)8

12. Yao R, Pakzad SN (2012) Autoregressive statistical pattern recognition algorithms for damage detection in civil structures. J Mech Syst Signal Process 31:355–368

13. Figueiredo E, Figueiras J, Park G, Farrar CR, Worden K (2011) Influence of the autoregressive model order on damage detection. Comput-Aided Civ Infrastruct Eng 26(3):225–238

14. Yao R, Pakzad SN (2014) Time and frequency domain regression based stiffness estimation and damage identification. Struct Control Health Monit 21(3):356–380

15. Yao R, Pakzad SN (2014) Damage and noise sensitivity evaluation of autoregressive features extracted from structure vibration. Smart Mater Struct 23(2):025007. doi:10.1088/0964-1726/23/2/025007

16. Pakzad SN, Shahidi SG, Yao R, Chamberlain MBW (2014) Damage identification toolsuite (DIT) user's guide. ATLSS 14-05 (dit.atlss.lehigh.edu)

17. Shahidi SG, Nigro MB, Pakzad SN, Pan Y (2014) Structural damage detection and localisation using multivariate regression models and two-sample control statistics. Struct Infrastruct Eng. doi:10.1080/15732479.2014.949277

18. Nigro MB, Pakzad SN, Dorvash S (2014) Localized structural damage detection: a change point analysis. Comput Aided Civ Infrastruct Eng 29(6):416–432

19. Yao R, Pakzad SN (2014) Multisensor aggregation algorithms for structural damage diagnosis based on a substructure concept. J Eng Mech 04014164. doi:10.1061/(ASCE)EM.1943-7889.0000879

Chapter 24
Modal Identification of Superconducting Magnetic Levitating Bogie

R. Alaggio, F. Benedettini, F. D'Innocenzo, G. D'Ovidio, D. Sebastiani, and D. Zulli

Abstract A novel superconducting magnetic levitation transportation systems has been proposed at University of L'Aquila, Italy. The bogie floats due to a passive, self-balancing interaction between high temperature superconducting skaters on board and permanent magnets on the track, in all phases of motion, zero speed included. A scaled superconducting skater has been statically tested measuring the repulsive-attractive magnetic forces varying, in a controlled way, the distance between the skater and the track. A non linear hysteretic characteristic curve has been identified averaging a set of suitable measures. In a first step, considering the thinness of the hysteretic cycles, the characteristic curve has been simplified in a non linearly elastic one. On the same time the equivalent tangent stiffness of such a curve has been identified, knowing the geometry and the mass characteristics of the bogie, by an experimental modal analysis conducted in operational conditions. A companion numerical model of the system has been introduced to forecast the working conditions with particular attention to dynamic behavior.

Keywords Magnetic levitation • Maglev train • Dynamics • Identification

24.1 Introduction

The levitation technologies, usually identified as MagLev, due to lack wheel-rail contact, represent a new frontier of mass transportation systems. Until now many MagLev technical solutions have been proposed in various parts of the world and a large number of applications have been realized.

The main MagLev technological approaches can be divided in the following three methods:

- Electro-Magnetic Suspension (EMS), based on the attractive force between actively controlled electromagnets on the vehicle undercarriage and the steel yoke of track;
- Electro-Dynamic Suspension (EDS), based on the repulsive force between low temperature superconductive electromagnets on board and short-circuited conductive coils on the track;
- Superconducting Magnetic Levitation (SML), with high temperature superconducting (HTS) materials on board levitating in the static magnetic field of the track, is based on superconductor's diamagnetic property. The pinning of the quantized flux of HTS generates both repulsive and attractive forces whose combination determines stable suspension without the need for any active control.

The research activities of the first two technologies started in the 70's, and have reached a high level of technological and operational reliability with deployments in China (Transrapid) and in Japan (JR-MagLev).

The development of the third MagLev method started thanks to the discovery, in the late 80's, of new sintered magnetic materials, such as $Nd_2Fe_{14}B$ (NdFeB) permanent magnets (PM) and $YBa_2Cu_3O_X$ (YBCO) bulk high temperature superconductors. Superconductors are the only type of material known today which has a perfect diamagnetic response and zero electrical resistance. The interaction between superconductor and PM gives rise to a conservative force field.

This technology, while still at an experimental stage, potentially allows to overcome operating limitations of the current maglev systems (egmagnetic resistance to motion, power consumption, etc.).

R. Alaggio • F. Benedettini (✉) • G. D'Ovidio • D. Sebastiani • D. Zulli
DICEAA-University of L'Aquila, Via G. Gronchi 18, L'Aquila 67100, Italy
e-mail: francesco.benedettini@univaq.it

F. D'Innocenzo
DIIIE-University of L'Aquila, Via G. Gronchi 18, L'Aquila 67100, Italy

In this contest, the UAQ4 superconducting magnetic levitation system has been developed at Transportation Laboratory of the University of L'Aquila. The dynamic behaviour of the suspended vehicle is a key and complex phenomenon since it is influenced by several variables depending on the system technology, load, motion condition (running speed), etc. Several numerical approaches [1–5] have been proposed for studying the SML vehicle dynamics. This paper is focused on the experimental evaluation of the magnetically levitated forces of the UAQ4 system as well as the identification of its modal characteristics, through the application of Enhanced Frequency Domain Decomposition (EFDD) and Sub-Space Identification (SSI) techniques in operational modal conditions [8–11], in order to calibrate a companion numerical model.

24.2 UAQ4 System

The core of the UAQ4 (University of L'Aquila, model 4) project is the demonstrator which was built as the experimental module for the system components, namely the guideway and vehicle. Laboratory system feasibility of all the suspension and propulsion components has been successfully proved by constructing the demonstrator that consists of two main contactless parts:

(a) A track (3.72 m long and 0.81 m wide) with three parallel permanent magnet guideways, where the outer two are "V" shaped and the central one is "U" shaped. All guideways consist of iron beams with NdFeB permanent magnets arranged in the inner beams surfaces, according to a proper polarity configuration.
(b) A bogie (0.72 m long, 0.81 m wide, 75 kg mass) with four "V" shaped superconducting "skaters" aboard, fixed to both sides of the body, and with the primary of a linear motor in the middle of the frame. The "skaters" consist of "V" assembled close arrays of melt textured YBCO bulks immersed in liquid nitrogen (77 K) kept in a suitable cryogenic vessel.

Stable lift and guidance of vehicle are generated, under both static and dynamic conditions, by the interaction between lateral guide-ways topside magnetic flux and the super-conductive skaters [6, 7]. The vehicle floats with a large constant air-gap in all phases of motion, zero speed included. Contrary to EDS and EMS technologies, no magnetic drag to motion are generated. Propulsion and braking are provided by an innovative direct current linear stepper motor, safely operating along the whole speed range.

24.3 Identification of Constitutive Magnetic Mechanism

The constitutive identification of levitation mechanism related to MagLev module of the UAQ4 system has been investigated by constructing and testing a scaled set up. A proper one-degree-of-freedom (DOF) measurement system has been realized and used for testing magnetic forces. This test equipment includes:

1. a "V" shaped guideway section (380 mm long, 147 mm large, 60 mm high) includes iron beam within a NeFeB PM, the polarity of which are arranged in such a way to obtain a gradient field along the vertical Z and the transverse Y directions and homogeneous field behavior along the X direction;
2. a simplified "V" shaped superconducting skater (200 mm long) uses melt textured YBCO bulks that are fixed in a non-magnetic cryogenic vessel filled with liquid nitrogen.

The vessel is mounted above the fixed magnetic guideway section by means of a servomotor, joined to a precision mechanical device, permitting variation in one direction of the operational gap between the two components (vessel and guideway).

The levitation forces were tested on the vessel using a load cell. All the devices have been linked to an electronic processor in order to control and pick up data about force, displacement and speed of vessel.

Levitation performance in terms of vertical force (F_Z) and lateral force (F_Y) have been separately tested by diversifying the setup structure as allows, respectively: (i) vertical configuration (Fig. 24.1) in which the Z displacements (gap) of vessel are imposed and Y movements are blocked; (ii) horizontal configuration (Fig. 24.2) in which the Y displacements (offset) of vessel are imposed and Z movements are blocked.

By forcing these movements, the consequent forces trends have been monitored.

The experiments were performed by filling the cryostat with liquid nitrogen (−196 °C) in order to achieve the critical temperature in correspondence of which the YBCO samples reach superconductive state.

Fig. 24.1 Detail of equipment to test vertical force
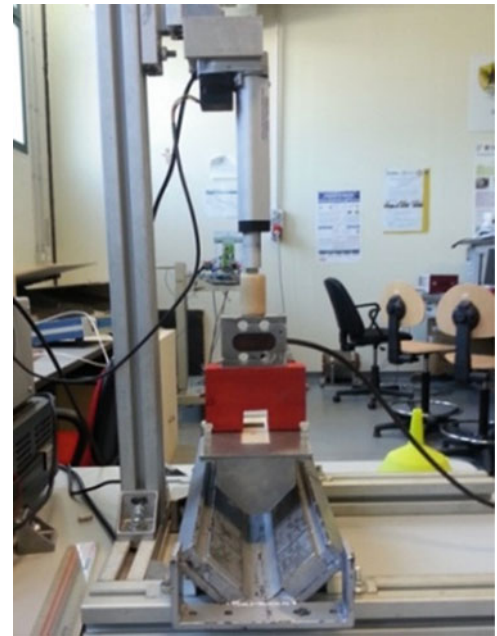
Fig. 24.2 Detail of equipment to test lateral force
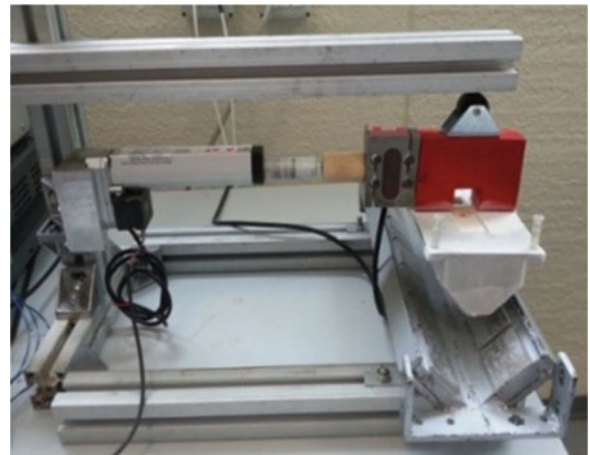
During the cooling process the magnetic field of the guideway is trapped in the superconductors, which are positioned and vertically centered at a set cooling distance ($H_0 = 25$ mm) from the magnetic way. This enables them to hold a certain position above the PM to the rail inherently.

Starting from H_0, a first movement of vessel was imposed until reaching the minimum gap/maximum offset in correspondence of which the movement direction was inverted with the aim to come back toward the starting point, to pass the same, to maximize the displacement and to came back at H_0 point.

Throughout the experiments the velocity of the vessel was set at 0.83 mm/s with the maximum displacements of ± 20 mm from H_0.

Fig. 24.3 shows the lift force (F_Z) between the vessel and guideway, where the origin coincides with H_0. The arrows in the graph shows the path made in the tests. One can see that the phenomenon has a non linear and hysteretic behavior; moreover in correspondence of gaps smaller than H_0, the forces are repulsive otherwise are attractive. In other words, starting from H_0, the vessel is repelled when it tends to move closer to the guideway while it is attracted when moving away.

Fig. 24.4 shows the lateral force (F_Y) Vs. offset (Y). Also in this case the curves show a clear non linear hysteretic trend. The lateral forces tend to center the vessel on the guideway because they increase with offset increasing. Both Figs. 24.3 and 24.4 show the experimental curves (continuous line) and mean value curves (dashed lines), with the corresponding analytical expressions, which are used for the model discussed in the next sections.

Fig. 24.3 Vertical force vs. gap at $H_0 = 25$ mm

$$F(z) = 0{,}0008z^3 + 0{,}118z^2 + 3{,}0079z - 0{,}0140$$
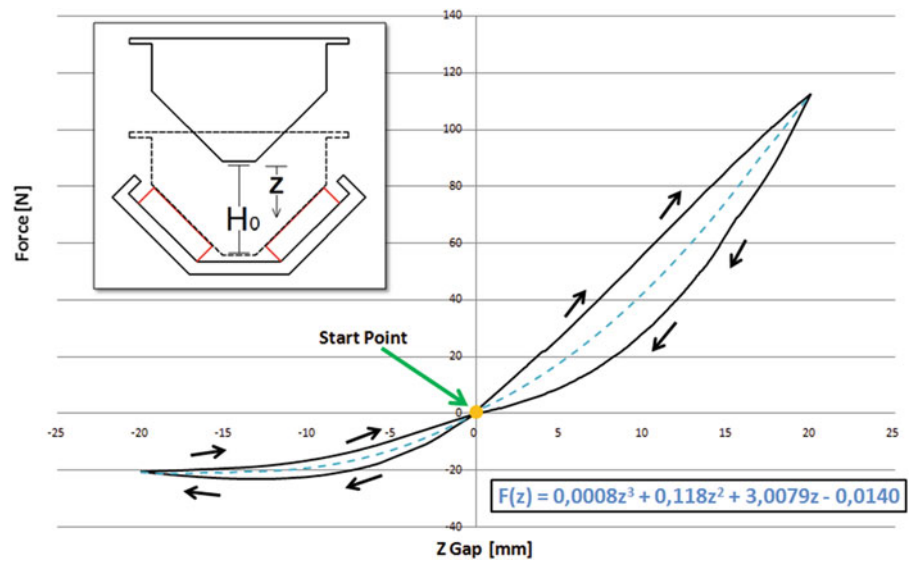
Fig. 24.4 Lateral force vs. offset at $H_0 = 25$ mm

$$F(y) = 0{,}001y^3 + 0{,}409y + 0{,}392$$
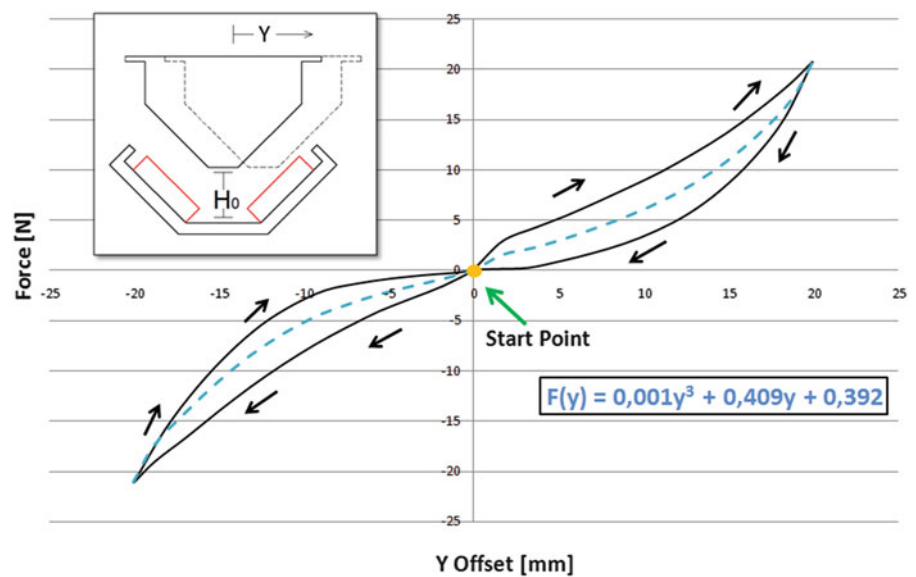
24.4 Modal Identification of the Bogie

The aim of the test is to estimate modal shapes, the frequencies and the damping coefficients of the bogie, that is lifted and guided by magnetic forces due to the interaction between four superconducting skaters guideway magnetic field (Fig. 24.5). Once the setup has been built, the magnetic skates are cooled at $H_0 = 25$, i.e., the operational condition is reached, and the levitated bogie is forced by means random pulses of low intensity, generated by rubber hammers.

Each of the acquired time series has a duration of 15 min and a sampling frequency of 200 Hz.

The measure chain consists of four triaxial velocimeters (SARA SR04DA) and each sensor has its own 24 bit AD converter onboard, with synchronized data flow towards a pc.

24.5 Modal Identification Results

The modal identification of the UAQ4 demonstrator system has been performed both in the time and in the frequency domains [8–11].

Fig. 24.5 The experimental
setup: the bogie and the four
sensors

Mode	Frequency [Hz]	Std. Frequency [Hz]	Damping Ratio [%]	Std. Damping Ratio [%]	Comment	Creation Date & Time
EFDD Mode 1	4.57	0	3.544	0		11-06-2014 09:54:49
EFDD Mode 2	5.015	0	4.8	0		11-06-2014 09:55:22
EFDD Mode 3	6.653	0	4.196	0		22-05-2014 22:27:58
EFDD Mode 4	8.024	0	3.677	0		11-06-2014 09:54:52
EFDD Mode 5	9.746	0	3.726	0		11-06-2014 09:54:56
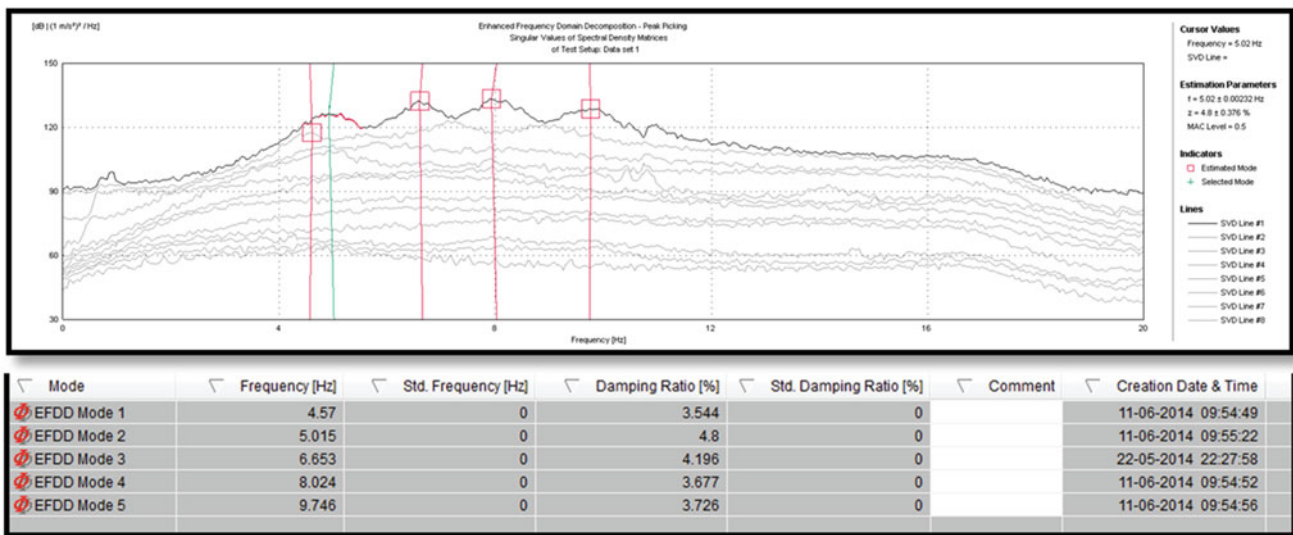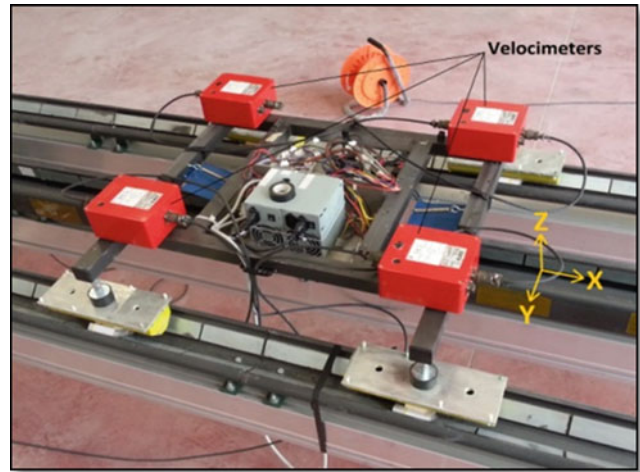
Fig. 24.6 Results from EFDD analysis

Results relevant to Enhanced Frequency Domain Decomposition (EFDD) are shown in Fig. 24.6, where singular values of spectral density matrices are reported, together with damping coefficients and frequencies for the first five identified modes.

On the other hand, results relevant to the Sub-Space Identification (SSI) are illustrated in Fig. 24.7, where stabilization diagram of estimated state space models and identified modal parameters are reported.

In the following Fig. 24.8 the modal shapes are shown together with identified frequencies and damping coefficients.

The Modal Assurance Criterion (MAC), evaluated among shapes obtained in the frequency domain and in the time domain, respectively, furnishes a validation criterion of the quality of results (see Figs. 24.9 and 24.10).

24.6   Model

The model describes a rigid body in the shape of a parallelepiped, with edges $2a$, $2b$, and $2c$ long in X, Y, and Z directions, respectively. The parallelepiped has uniformly distributed mass, therefore its center of mass coincides with the geometric center of the body, where the origin of the orthogonal reference is applied (see Fig. 24.11). The mass is indicated as m and the three principal moments of inertia are I_x, I_y and I_z. Eight spring-dashpot devices are applied at the four lower vertices of the body (two devices for any vertex, indicated as 1,2,3,4), in Y and Z directions, while in the direction of motion, X, is body is free to move.
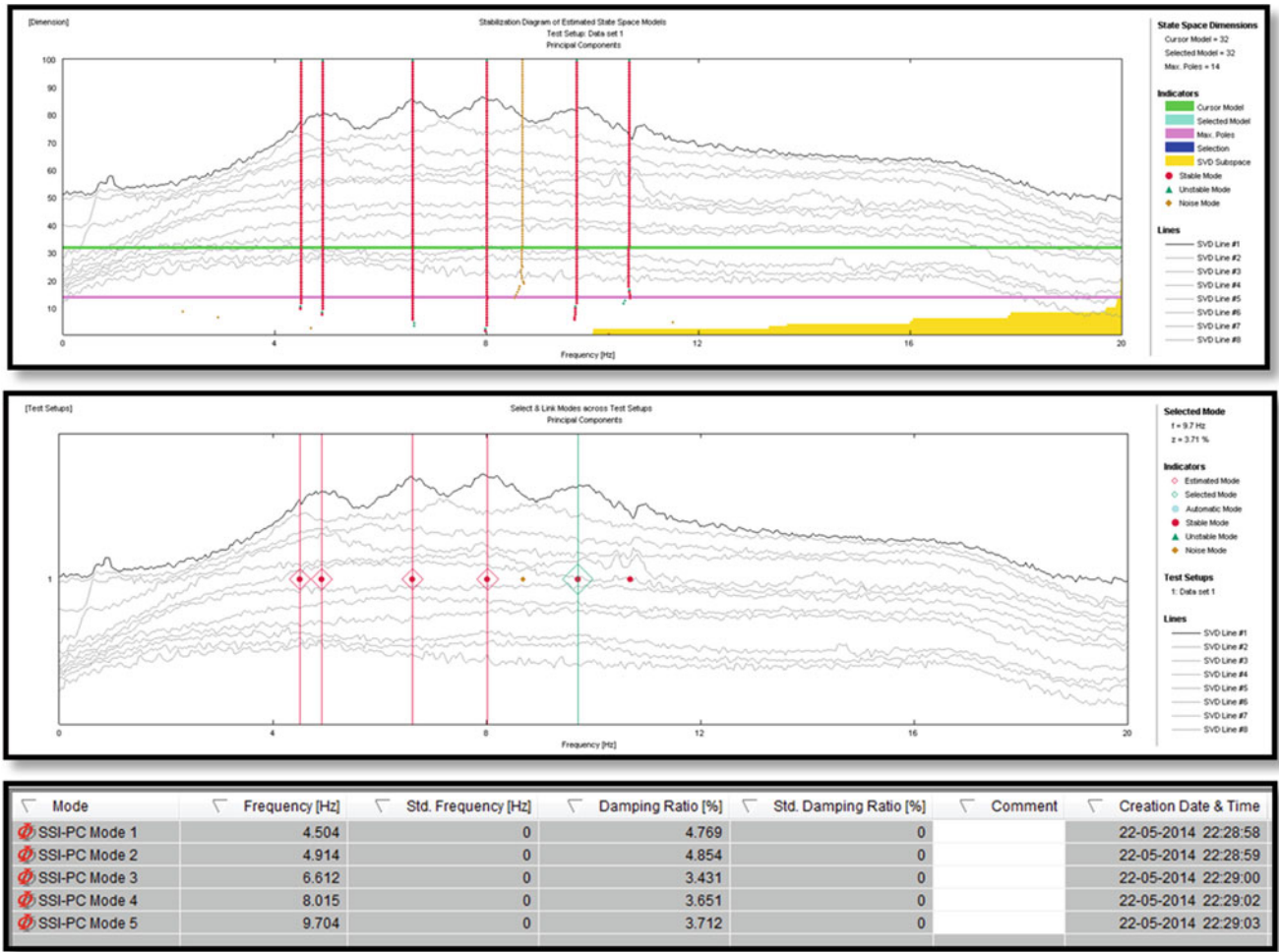
Fig. 24.7 Results from SSI analysis

The body has six d.o.f. and the kinematics is evaluated in the hypothesis of small displacements and rotations. The six time-dependent Lagrangian parameters are assumed as the three components of the displacement of the center of mass $\{u_0, v_0, w_0\}$ along X, Y, and Z directions, respectively, and the three angles of rotation $\{\theta_x, \theta_y, \theta_z\}$ around the coordinate axes. Moreover, imperfections of the magnetic guide are assumed as known time-depending terms, which appear as imposed strain contribution of the devices in the Y and Z directions, and are indicated as $\{v_d, w_d\}$. In particular, the imperfections of the magnetic guide are assumed having a sinusoidal time-dependence:

$$\begin{cases} v_d = Y_0 cos\left(\Omega t\right) \\ w_d = Y_0 cos\left(\Omega t\right) \end{cases}$$

where Ω is a function of the velocity V of the body (assumed as a constant) and of the wave length of the imperfection λ, as $\Omega = \frac{2\pi V}{\lambda}$, while Y_0 is its amplitude.

Therefore the stretch of the devices assumes the following expressions in terms of the Lagrangian parameters:

$$\begin{aligned} \varepsilon_{y1} = v_0 + a\theta_z + d\theta_x - v_d \quad \varepsilon_{y2} = -v_0 - a\theta_z - d\theta_x + v_d \quad \varepsilon_{y3} = -v_0 + a\theta_z - d\theta_x + v_d \quad \varepsilon_{y4} = v_0 - a\theta_z + d\theta_x - v_d \\ \varepsilon_{z1} = w_0 - a\theta_y - b\theta_x - w_d \quad \varepsilon_{z2} = w_0 - a\theta_y + b\theta_x - w_d \quad \varepsilon_{z3} = w_0 + a\theta_y + b\theta_x - w_d \quad \varepsilon_{z4} = w_0 + a\theta_y - b\theta_x - w_d \end{aligned}$$

$$(24.1)$$

The response law for each spring-dashpot device is assumed as nonlinear function of the stretch and of its rate of change:

$$\begin{aligned} \sigma_{yi} = f_{yi}\left(\varepsilon_{yi}\right) + g_{yi}\left(\dot{\varepsilon}_{yi}\right) \\ \sigma_{zi} = f_{zi}\left(\varepsilon_{zi}\right) + g_{zi}\left(\dot{\varepsilon}_{zi}\right) \end{aligned}$$

$$(24.2)$$

MODE 1: YAW	MODE 2: LEEWAY
MODE 3: UPLIFT	**MODE 4: PITCH**

MODE 5: ROLL	

Mode	Frequency V [Hz]	Damping Coefficient
Yaw (I)	4.504	4.769%
Leeway (II)	4.914	4.854%
Uplift (III)	6.612	3.431%
Pitch (IV)	8.015	3.651%
Roll (V)	9.704	3.712%
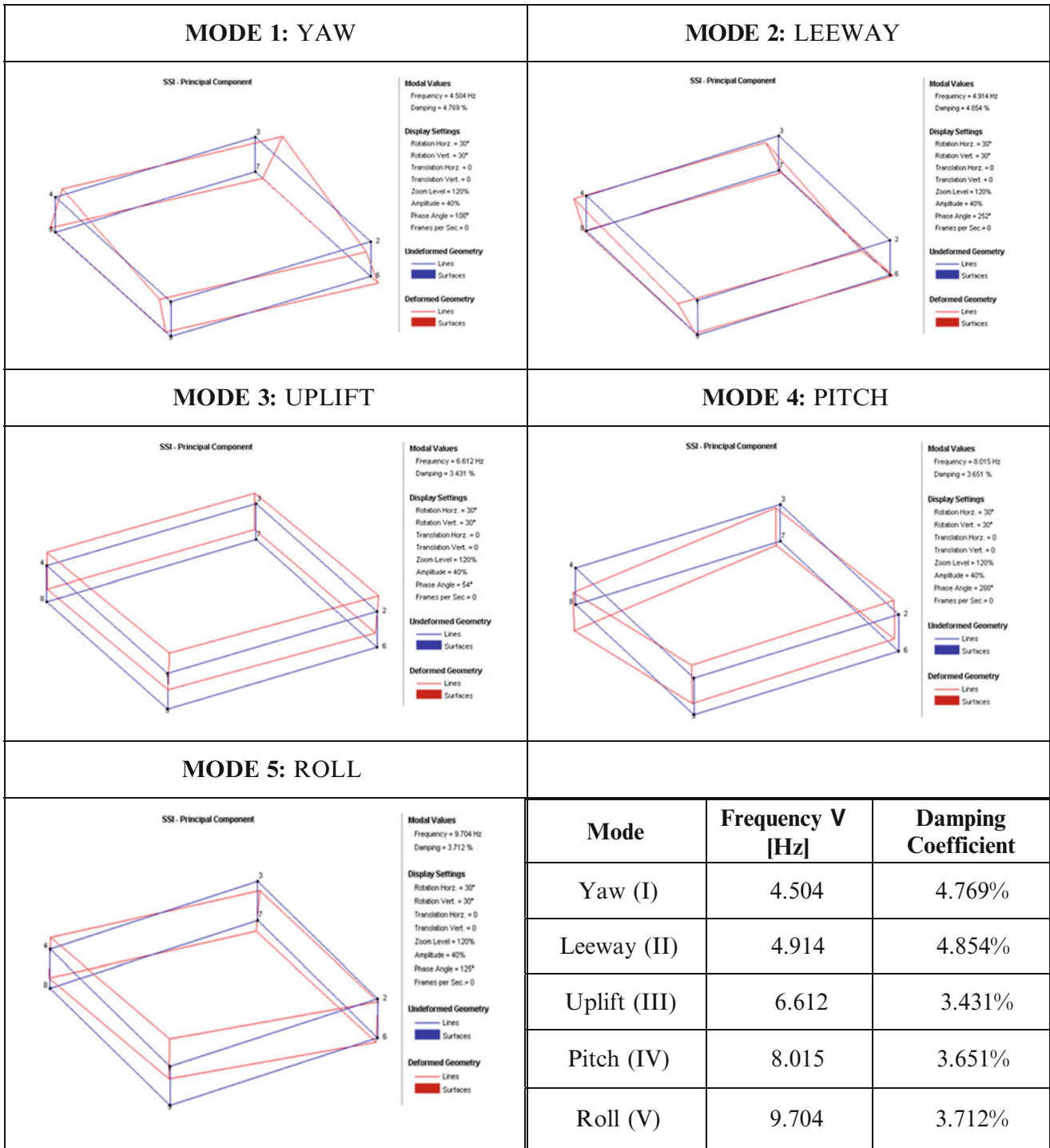
Fig. 24.8 Modal shapes, frequencies and damping factors

for $i = 1, \ldots, 4$, where σ is the force exerted by the device, f and g will be identified after experimental measures on the prototype, and the dot stands for derivative with respect to the time. Here and in Eq. (24.1), the first index indicates the direction (Y or Z) and the second one indicates the vertex number.

The use of the Virtual Work Theorem allows one to get the dynamic equilibrium equations, by imposing that the following Virtual Work Equation holds for any independent variation of the Lagrangian parameters $\{\delta u_0, \delta v_0, \delta w_0, \delta\theta_x, \delta\theta_y, \delta\theta_z\}$, where δ is the (linear) variation operator, i.e.,:

Fig. 24.9 MAC criterion
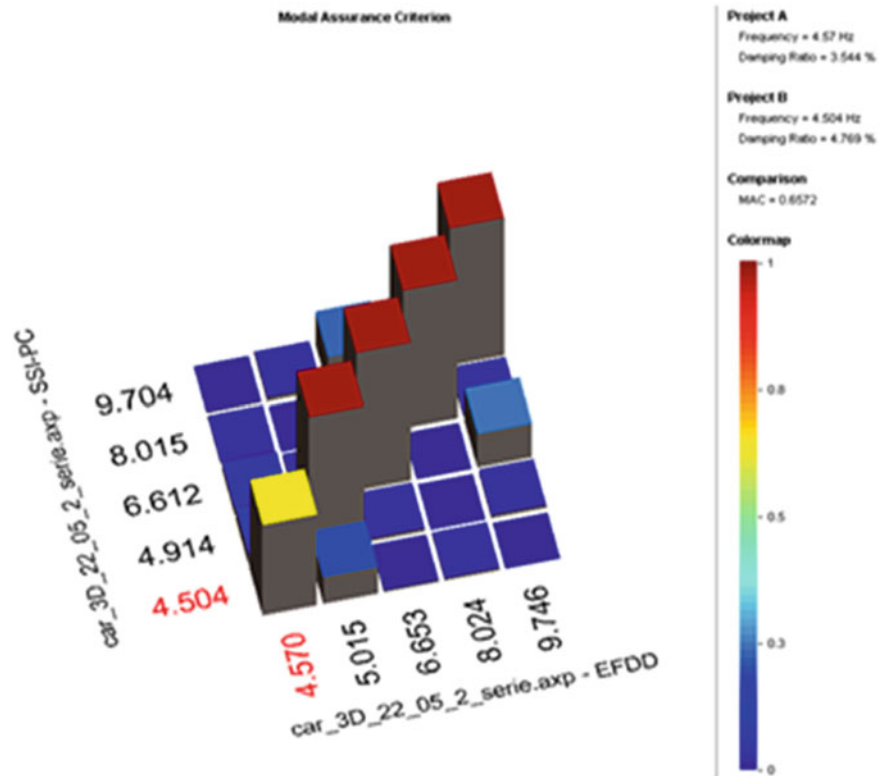
Fig. 24.10 MAC matrix

	4.504 Hz	**4.914 Hz**	**6.612 Hz**	**8.015 Hz**	**9.704 Hz**
4.57 Hz	0.6572	0.08321	0.04973	0.01823	0.007329
5.015 Hz	0.1957	0.9868	0.02309	0.001518	0.02841
6.653 Hz	0.01374	0.02294	0.9983	0.002567	0.2359
8.024 Hz	0.01806	0.001301	0.004119	0.9989	0.02383
9.746 Hz	0.002764	0.02305	0.2465	0.02641	0.9996
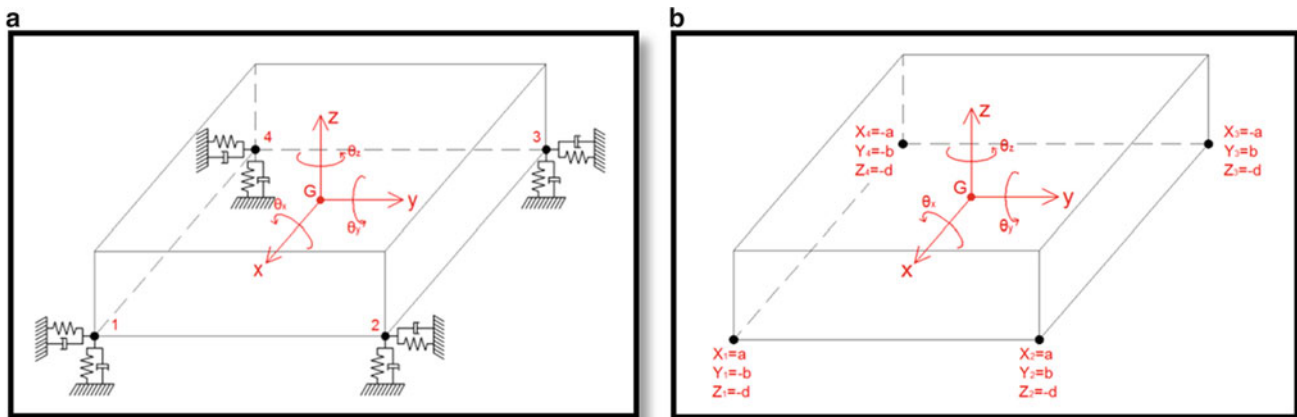
Fig. 24.11 The rigid body with the spring-dashpot devices in Y and Z directions (**a**); coordinates of the vertices (**b**)

$$\sum_{i=1}^{4} \left(\sigma_{yi} \delta \varepsilon_{yi} + \sigma_{zi} \delta \varepsilon_{zi} \right) = -m \left(\ddot{u}_0 \delta u_0 + \ddot{v}_0 \delta v_0 + \ddot{w}_0 \delta w_0 \right) - I_x \ddot{\theta}_x \delta \theta_x - I_y \ddot{\theta}_y \delta \theta_y - I_z \ddot{\theta}_z \delta \theta_y \tag{24.3}$$

where the right hand side of Eq. (24.3) describes the work of the linear and angular inertia forces. Substituting Eq. (24.1) in Eq. (24.3) and separately vanishing the coefficients of $\{\delta u_0, \delta v_0, \delta w_0, \delta \theta_x, \delta \theta_y, \delta \theta_z\}$, the equations of motions are obtained:

$$\begin{aligned}
& m\ddot{u}_0 = 0 \\
& m\ddot{v}_0 + \sigma_{y1} - \sigma_{y2} - \sigma_{y3} + \sigma_{y4} = 0 \\
& m\ddot{w}_0 + \sigma_{z1} + \sigma_{z2} + \sigma_{z3} + \sigma_{z4} = 0 \\
& I_x \ddot{\theta}_x + d \left(\sigma_{y1} - \sigma_{y2} - \sigma_{y3} + \sigma_{y4} \right) + b \left(-\sigma_{z1} + \sigma_{z2} + \sigma_{z3} - \sigma_{z4} \right) = 0 \\
& I_y \ddot{\theta}_y + a \left(-\sigma_{z1} - \sigma_{z2} + \sigma_{z3} + \sigma_{z4} \right) = 0 \\
& I_z \ddot{\theta}_z + a \left(\sigma_{y1} - \sigma_{y2} + \sigma_{y3} - \sigma_{y4} \right) = 0
\end{aligned} \tag{24.4}$$

Substitution of Eqs. (24.2) and (24.1) in Eq. (24.4) gives the system of ordinary differential equations in the Lagrangian parameters, describing the forced dynamics of the bogie under magnetic imperfections. It is worth noticing that, in direction X, the motion of the body is uniform, of initial velocity assumed as *V*.

Experimental identification allows one to express the response laws f and g in Eq. (24.2) as nonhomogeneous cubic polynomials:

$$\begin{aligned}
f_{yi} &= h_{0i} + h_{1i} \varepsilon_{yi} + h_{2i} \varepsilon_{yi}^2 + h_{3i} \varepsilon_{yi}^3 \\
f_{zi} &= k_{0i} + k_{1i} \varepsilon_{zi} + k_{2i} \varepsilon_{zi}^2 + k_{3i} \varepsilon_{zi}^3 \\
g_{yi} &= p_{0i} + p_{1i} \dot{\varepsilon}_{yi} + p_{2i} \dot{\varepsilon}_{yi}^2 + p_{3i} \dot{\varepsilon}_{yi}^3 \\
g_{zi} &= q_{0i} + q_{1i} \dot{\varepsilon}_{yi} + q_{2i} \dot{\varepsilon}_{yi}^2 + q_{3i} \dot{\varepsilon}_{yi}^3
\end{aligned} \tag{24.5}$$

where $h_{ji}, k_{ji}, p_{ji}, q_{ji}$ ($j = y, z, i = 1, \ldots, 4$) assume values provided by the experiment.

The presence of nonhomogeneous terms in Eq. (24.5) indicates that a nontrivial equilibrium position exists, indicated as $\{u_{0e}, v_{0e}, w_{0e}, \theta_{xe}, \theta_{ye}, \theta_{ze}\}$. Linearization of Eq. (24.4) around the equilibrium point and vanishing of the known terms $\{v_d, w_d\}$ gives the free linear vibration problem in terms of the sliding parameters ζ_j ($j = 1, \ldots, 6$), defined so that $\{u_0, v_0, w_0, \theta_x, \theta_y, \theta_z\} = \{u_{0e} + \zeta_1, v_{0e} + \zeta_2, w_{0e} + \zeta_3, \theta_{xe} + \zeta_4, \theta_{ye} + \zeta_5, \theta_{ze} + \zeta_6\}$, which reads:

$$\begin{aligned}
& m\ddot{\zeta}_1 = 0 \\
& M\ddot{z} + C\dot{z} + Kz = 0
\end{aligned} \tag{24.6}$$

where $z = \{\zeta_2, \zeta_3, \zeta_4, \zeta_5, \zeta_6\}$ and M, C, K are the mass, damping and stiffness matrices, respectively (their expression is not reported here for the sake of brevity).
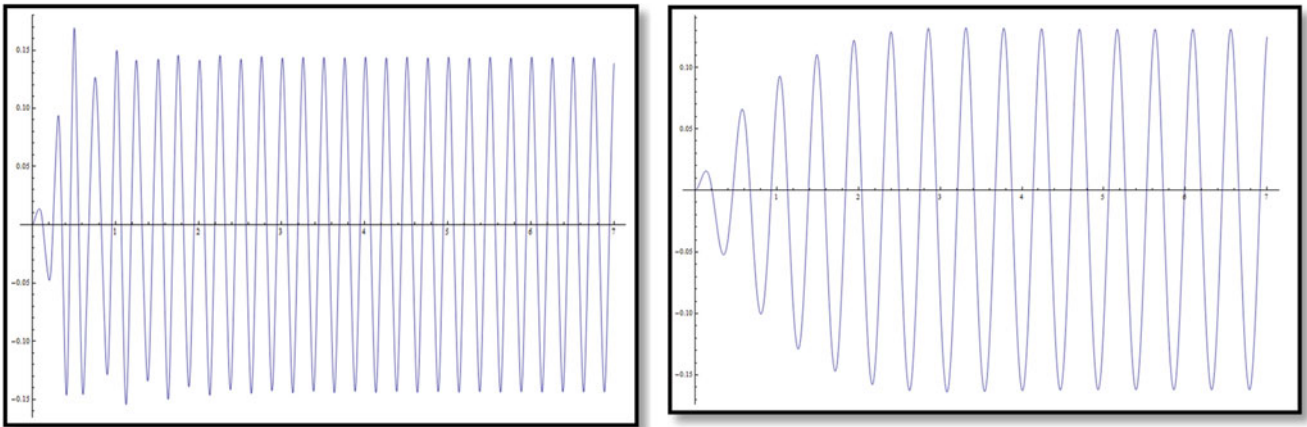
Fig. 24.12 Time evolution of the Y displacement (**a**) and Z displacement of the bogie

24.7 Numerical Results

Preliminary numerical results are obtained after integration of Eq. (24.4) and are shown in Fig. 24.12. They show steady periodic oscillations of moderate amplitude in Y and Z directions, respectively.

24.8 Conclusions

A prototype of novel superconducting magnetic levitation transportation systems, proposed at University of L'Aquila, Italy, has been experimentally tested in order to describe the attractive and repulsive magnetic forces exerted between the bogie and the guideway. A non linear hysteretic characteristic curves for lifting and centering have been tested and, for preliminary studies, they have been simplified in a non linearly elastic ones. Moreover, modal characteristics of the system have been identified in operational conditions, using both Enhanced Frequency Domain Decomposition and Sub-Space Identification. A corresponding numerical model has been drawn, and preliminary results in terms of vertical and transverse oscillations of the body under imperfections of the magnetic field are shown.

References

1. Zhang Y, Xu SG (2000) Analysis of dynamic response for HTS MagLev vehicle model. Phys C Superconduct Appl 341–348:2603–2604
2. Wang J, Wang S, Zheng J (2009) IEEE Trans Appl Superconduct 19(3):2142–2147
3. W. Wang, J. Wang et Alii: "Characteristic study of high-TC superconducting maglev under side-loading" Physica C 469 pp. 188–191 (2009)
4. D'Ovidio G, Carpenito A (2013) Two-degrees of freedom model for dynamic analysis of experimental maglev bogie. In:Proceedings of the 17th transport means 2013 international conference, Lituania, pp 5–8
5. D'Ovidio G, Crisi F (2014) Suspension dynamic behaviour of HTS magnetically levitated bogie applied electromagnetic engineering for magnetic, superconducting, multifunctional and nano materials (MSF), vol 792. Switzerland, pp 198–203
6. D'Ovidio F, Crisi, Lanzara G (2008) A "V" shaped superconducting levitation module for lift and guidance of a magnetic transportation system. Physica C Supercond, vol 468, July 2008, pp 1036–1040
7. D'Ovidio G, Crisi F, Lanzara G (2011) Design and optimization of UAQ4 experimental maglev module. Mater Sci Forum Appl Electromag Eng 1058:42–47
8. Brincker R, Zhang L, Andersen P (2000) Modal identification from ambient responses using frequency domain decomposition. In: Proceedings of XIIX IMAC conference
9. Peeters B, De Roeck G (1999) Reference-based stochastic subspace identification for output-only modal analysis. MSSP 13(6):855–878
10. ARTeMIS Extractor software ver.3.2 (2002) issued by Structural Vibration Solution ApS, NOVI Science Park, NielsJernesVej 10, DK 9220, Aalgorg East, Denmark
11. Benedettini F, Gentile C (2011) Operational modal testing and FE model tuning of a cable-stayed bridge. Eng Struct 33:2063–2073

Chapter 25
Uplift-Monitoring for Dynamic Assessment of Electrical Railway Contact Lines

Petter Nåvik and Anders Rønnquist

Abstract Although international railways have seen a massive increase in high speed rail there are still large amounts of older existing infrastructure designed for completely different criteria. The current supply systems of old electric railway lines, called soft catenary systems, are characterized by their design towards an optimal quasi-static behaviour. To increase the speed it is important to explore possible limiting factors, i.e. to identify the dynamic consequences and limitations. This paper explores a newly developed sensor system. Several sensors are placed over approximately 150 m to capture the dynamic behaviour. This is then used to create a base line for future monitoring as well as for assessing the possibilities of increased speed. For soft contact lines it is important to control maximum uplift at the pole support and the dynamic behaviour. The stiffness of the system changes between poles as well as along the section depending especially on track geometry; this makes it equally important to assess several other points between pole supports. Excessive vibrations can produce loss of contact rendering arching, increased wear and disrupted power supply. In the present paper acceleration time series were used to predict maximum vertical displacement, train speed, to assess the dynamic behaviour and to quantify modal parameters.

Keywords Railway catenary systems • Monitoring • Dynamic assessment • Modal analysis • Pantograph-catenary interaction

25.1 Introduction

The quest to make railways the preferred way to travel is amongst others correlated with the time the train uses on a distance of travel. Several countries around the world are either building high-speed railways or have plans to build them [1]. This initiative will in addition to reducing the travel time be climate friendly if they are built to shift the demand of transportation to rails from cars and aeroplanes [2]. The same effects can also be achieved by increasing the speed on existing railway sections with catenary systems designed for relatively low velocities. Increased speed will be more carbon intensive due to energy consumption, but makes the rail more attractive [2]. The design of these old existing railway catenary systems was aimed for an optimal quasi-static response. Thus an increase of train speed on these catenary systems requires an investigation of limiting factors such as the dynamic behaviour. For a certain increase of speed changes of the properties of the catenary and pantographs running along the rail line is required [1].

The dynamic system investigated consists of the interaction between two non-linear dynamic systems, the pantograph and the catenary system. An uninterrupted contact between the pantograph and the contact wire is essential for the supply of electrical power to the train. This contact interaction will render static and dynamic loading of the system and it varies with the train speed. The complexity of this interaction and the dynamic response of the system progressively increase with increasing train speed [3]. As the speed of the train is increased above design speed the dynamic response of the catenary system becomes an important problem to address [4]. Railway catenary systems are in general considered to have low damping. This is especially a problem when trains are running with multiple pantographs because the later pantographs will run into oscillations made by the first [5]. It is still recognized that it is a challenge to estimate the amount of structural damping in the catenaries [1]. The assessment of the dynamic behaviour of railway catenary systems is generally done be evaluating the contact force between the catenary and the pantograph. The force is measured close to the contact interface, and describes the dynamic behaviour at the contact point. This has then been used to validate numerical models which in turn have been used to evaluate the dynamic response of different catenary systems. Other measurements are needed to evaluate

———————————

P. Nåvik (✉) • A. Rønnquist

Department of Structural Engineering, Norwegian University of Science and Technology, Rich. Birkelandsvei 1A, Trondheim 7491, Norway

e-mail: petter.r.navik@ntnu.no; anders.ronnquist@ntnu.no

the behaviour of the catenary continuously from before the train passes, as the train passes and after it passes. By placing three additional poles within a span for mounting of measuring equipment Drugge [6] sampled displacement time series at five points within a pole span as a validation of the displacements in the numerical model. Measurements of the accelerations in the catenary as the train pass the section can also be used to assess the behaviour of the catenary. Several different properties can be assessed if the sensors used for sampling are well positioned. The speed of the train can be estimated by the use of the cross-correlation function if a sufficiently long distance between sampling points is used. This has been shown from analyses on numerical models that maximum displacement can be estimated by integration of sampled acceleration time series [7]. A range of different operational modal analysis (OMA) methods can be used on output-only data, such as the acceleration time series, for modal parameter estimation [8].

The aim for this study is to use monitoring of vertical accelerations for the assessment of the dynamic behaviour of electrical railway contact lines. A newly developed sensor system is used to obtain the sample records of acceleration time series as train passes. The system developed is easy to mount and demount to be able to easily change the sampling positions. A wireless system where the sensors can be clipped on and off the wires in the system has thus been developed. Sensors have been mounted in different positions along the railway line to be able to predict different parameters. The proposed methods have been used to estimate the speed of the train and the maximum vertical displacement of the contact wire. Power spectral densities (PSD) estimated by the Welch procedure [9] and the Covariance-driven Stochastic Subspace Identification (Cov-SSI) method with stabilization diagrams [8] have been used for estimation of modal parameters. Brownjohn et al. [10] tested several OMA techniques on accelerations from a bridge and stated that Cov-SSI performed the best.

25.2 Railway Catenary Systems

The railway catenary system consists of a contact wire, a messenger wire, droppers, registration arms and brackets as seen in Figs. 25.1 and 25.2. The contact wire is the conductive part which transfers the electricity to the train through a pantograph. The messenger wire carries the contact wire via droppers, and makes it possible to obtain a desired geometry, stiffness and elasticity. The brackets carry the messenger wire and are fastened to the poles along the line. The main function of the registration arms, which are fastened to the contact wire at the supports, is to obtain the desired horizontal geometry of the contact wire.

A pantograph is a device mounted on top of the train. Its only purpose is to ensure an uninterrupted and reliable energy transfer to the train. Two bow strips of coal at the top of the pantograph are the actual components which transfers the electricity. Simeon and Arnold [11] describe this contact as the most critical part in the transmission of the electricity to the trains of today. The contact is mainly ensured by introducing an upwards pressure in the pantograph. To obtain the desirable geometry of the catenary system a tension force is introduced in both the contact wire and the messenger wire. The tension forces are obtained by the use of a tensioning device like the one illustrated in Fig. 25.3. The device can also be seen on the left in Fig. 25.2.

25.3 Case Study: Alna Railway Station, Oslo

The test location was close to Alna railway station outside of Oslo, Norway. This location was chosen due to a desired amount of traffic and accessibility. The Norwegian rail network uses distance in kilometre along the track as their method to identify positions. The sensors were mounted between 7.188 and 7.471 km on a rail line named Hovedbanen. The catenary system at the investigated section is named System 35 MS. This is a system with 7.06 kN tension in both the contact and messenger wire, and without a stitch wire. This part of the rail line includes a change of catenary section. The geometry of the railway catenary part investigated is shown in Fig. 25.4. A complete railway catenary section is much longer than the few spans shown here. The section called Section 1 is 14 spans long and the length of each span varies between 52 and 60 m. Section 2 is 21 spans long.
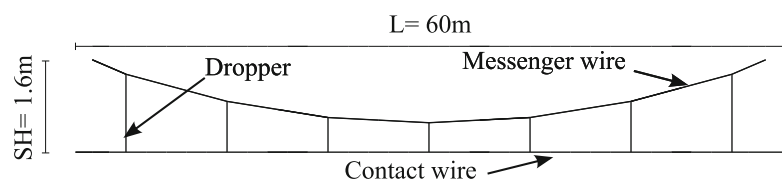
Fig. 25.1 A discretization of the catenary system. SH is the system height, and L is the length of one span

Fig. 25.2 The bracket, the registration arm and the pole at an existing railway section in Norway
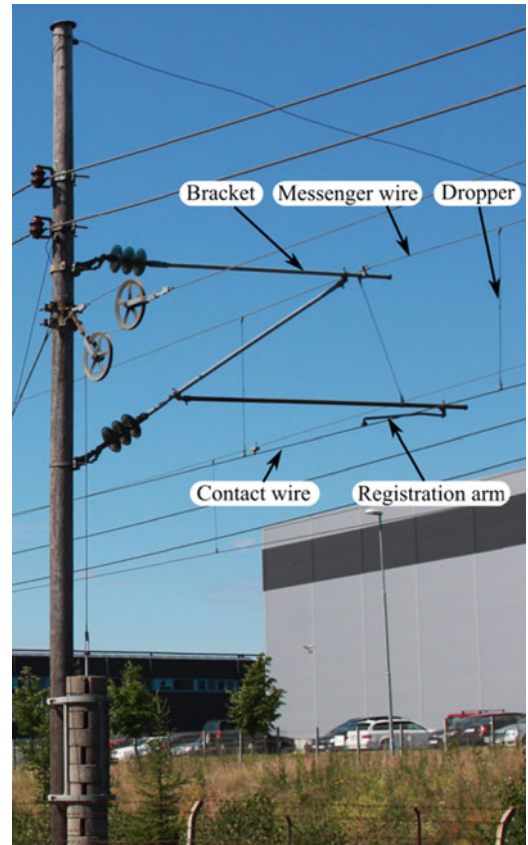
Fig. 25.3 The tensioning equipment in use at an existing railway section
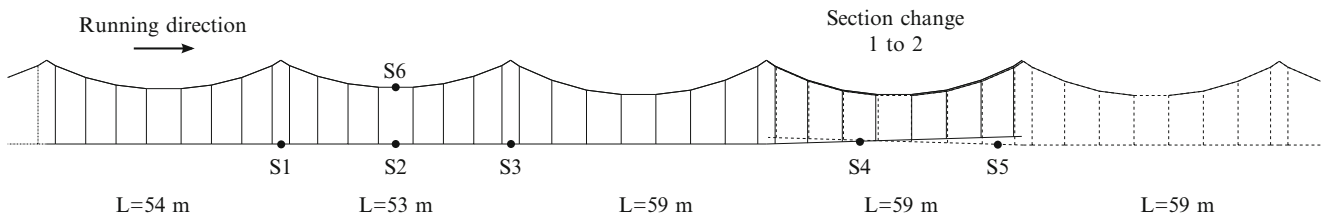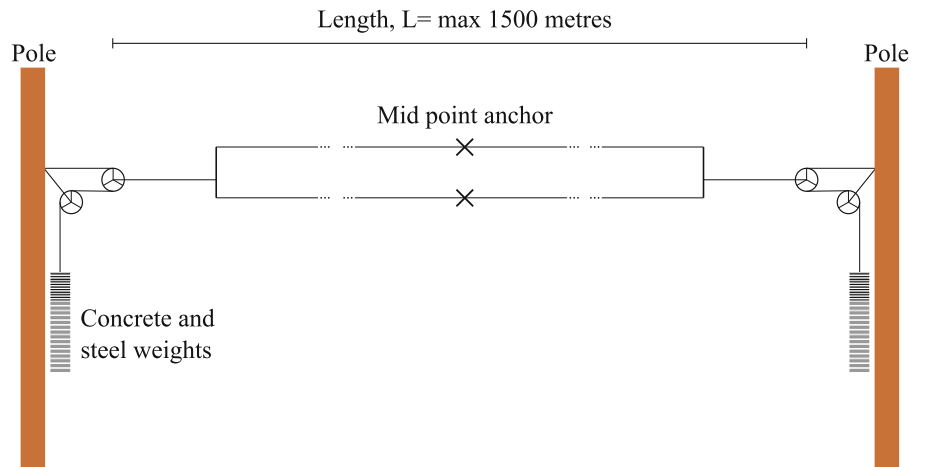
Fig. 25.4 The geometry of the railway catenary part investigated

Table 25.1 Position of the sensors used for sampling

Sensor	S1	S2	S3	S4	S5	S6
Wire	CW	CW	CW	CW	CW	MW
Position [m]	0	27	52	137	155.4	27
Section	1	1	1	1	2	1

The newly developed sensor system contains of 10 sensors and 1 master. The sensors measures acceleration in three axes and rotational velocity about three axes. The sensors are mounted on the catenary system in different location and transmit the sampled data to the master via radio transmission. The system can handle 16 sensors if desirable. Six sensors were used in this investigation. They were placed in different location along the section to be able to describe different phenomena of the pantograph-catenary interaction. They are in the rest of the paper referred to as S1–S6. Their position can be seen in Fig. 25.4, and the distance between them is shown in Table 25.1.

Sampling from several train passages were done during the testing period, and these have been used to investigate which methods should be used to identify different properties of the single train passage, and the catenary system in general.

25.3.1 Maximum Displacement

The maximum displacement is an important property to be able to identify for evaluation of the pantograph-catenary interaction. The sample records of the acceleration in the vertical direction have been used to identify the maximum displacement in the different sample positions. This has been done by numerical integration with the constant average acceleration assumption. The procedure used is:

1. Resampling from 100 to 1,000 Hz with 'spline'-function
2. Introducing an exponential window function for a smoother start reducing frequency leakage due to finite time series
3. High-pass filtered to remove DC effects close to 0 Hz, with a cut-off frequency of 0.3 Hz, second order Butterworth filter
4. Integrating to velocities
5. High-pass filtered
6. Integrated to displacement
7. Identify the peak value as the maximum displacement

The use of this procedure estimates the maximum of the displacement series well for some points. The maximum displacement in mid-span of the contact wire, S2, is between 40 and 60 mm, while it is around 20 mm in the mid-span of the messenger wire, S6. This has been compared to a video of the response. The result from this is that the displacement in the contact wire is slightly overestimated and has a bit too high variation which is a known issue for these types of acceleration time series with relatively high frequency content [12]. However, overestimation of displacement is a conservative solution. The displacement in the messenger wire is slightly underestimated. Improvement of the methods is thus sought to describe all points better and to get a better description of the whole displacement time series.

25.3.2 The Speed of the Train

The speed of the train has been estimated by the use of cross-correlation between acceleration time series in two different points along the investigated catenary section. Estimation of the train velocity has been done for several train passages. These have shown that the best estimations of the velocity are from cross-correlation between acceleration in S1 and S4, S1 and S5, and S2 and S5. Cross-correlation between S2 and S4 has also given likely results. Results from cross-correlation between other sensors has not been as satisfactory which indicates that a sufficiently long distance between the points used in the study is essential. It also shows that the chosen sampling frequency has to be taken into account for shorter distances. Some of the estimated train velocities are shown in Table 25.2.

Table 25.2 Estimated train velocities from cross-correlation of acceleration time series

Estimated velocity [km/h]	Point 1	Point 2	Length between points [m]
67.2	S1	S5	155.4
69.1	S2	S5	128.4
67.4	S1	S4	137.0
79.8	S2	S4	110.0
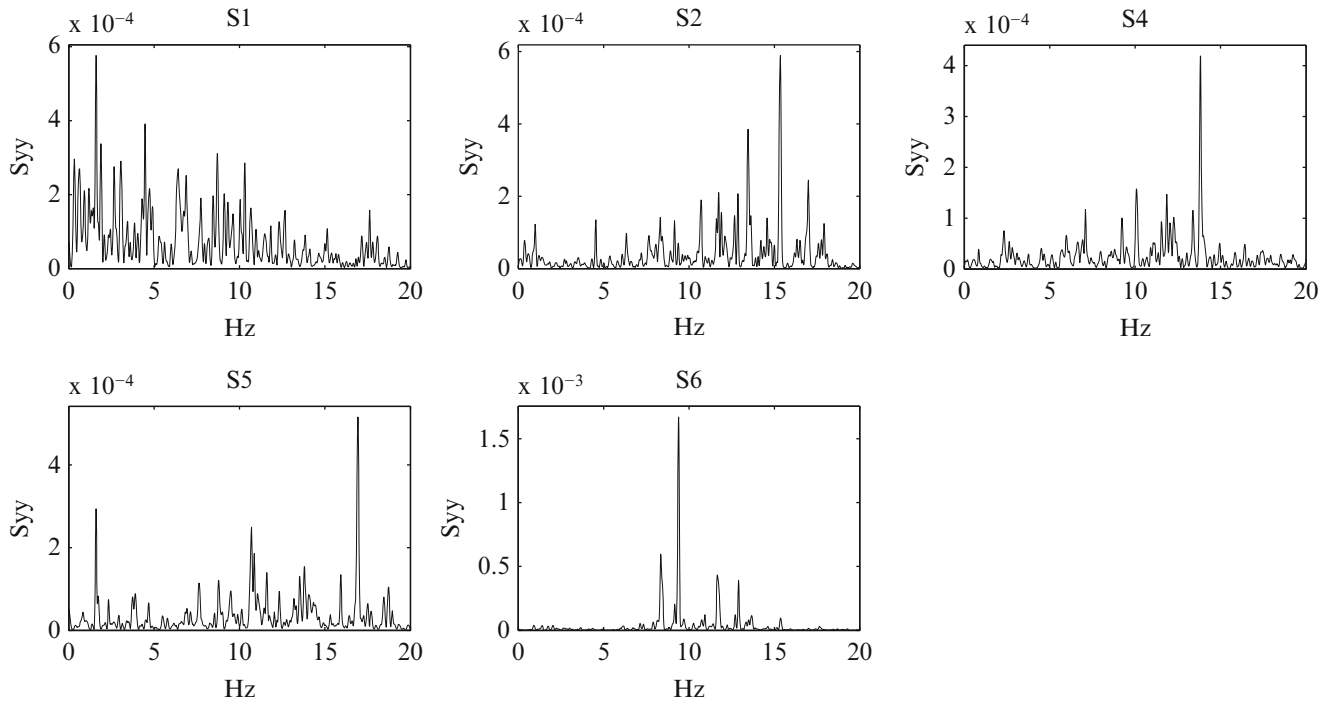
Fig. 25.5 The power spectral densities estimated by Welch's method for five sensors

25.3.3 Dynamic Behaviour

The dynamic behaviour of the system has been evaluated using both time and frequency domain methods. The Welch procedure with peak picking and the covariance driven stochastic subspace identification (Cov-SSI) method have been used for modal identification. All analyses in this part of the paper are done on the sampling records from the same train passage. The sampled records have been low-pass filtered to 20 Hz because this is in research on railway catenary systems used as the normal maximum frequency of interest to be used. Since all records have originally been sampled at 100 Hz this means that the maximum frequency used is well below the Nyquist frequency and that aliasing will not be a problem.

The different location of the sensors along the section, as shown in Fig. 25.4, will highly affect the sampling records and the frequency content of these. The geometry of the catenary sections changes for almost every new span. Different span lengths give changed dropper lengths which in turn will change the elasticity along the span. In addition, the elasticity of a span is affected by the properties of the nearby spans. These effects result in different stiffness and mass properties in almost every span along a section.

The first step towards identifying modal parameters of the system has been to evaluate the frequency content from the different sensors using power spectral densities estimated by the Welch method. This has been done on the acceleration time series from five sensors, and the results from these analyses can be seen in Fig. 25.5. It is evident from this that the frequency content in the sampled acceleration time series varies much with the placement of the sensor. Sensor S2 and S4 shows quite similar result because both are measuring from the middle of a span. S1 is by the registration arm which is the least elastic point in a span. Sensor S5 is placed in the section change between Section 1 and 2 may be different from S2 and S4 because the pantograph head runs into a small downward gradient of the contact wire height. The placement of S6 in the mid-span of the messenger wire rather than the contact wire shows that the messenger wire is most influenced by different frequencies than the contact wire. From these analyses some of the frequencies which might be natural frequencies, but a more sophisticate method is needed to confirm these and to identify others.

The second step in the investigation has been to use Cov-SSI method to estimate natural frequencies and corresponding damping ratio. Nonphysical modes may be present in the result from this type of analyses depending on if the correct order of the system is chosen. A stabilization diagram has been used to separate the physical modes from the nonphysical modes. This method has been used on different combination of sensor measurements. The combinations investigated are a lone sensor; S2, the sensors in one span; S1, S2, S3 and S6, and all sensors in Section 1; S1, S2, S3, S4 and S6. The stabilization diagrams from these analyses can be seen in Figs. 25.6, 25.7, and 25.8, respectively. From these figures the frequencies of interest have been extracted and plotted in Fig. 25.9. The first three natural frequencies of the system are approximately 0.71, 1.23 and 1.86 Hz. The biggest difference between the three analyses is that the lone sensor lack frequencies the two other have in some frequency ranges. This is because the sensor was mounted in the middle of a span and will not be able to
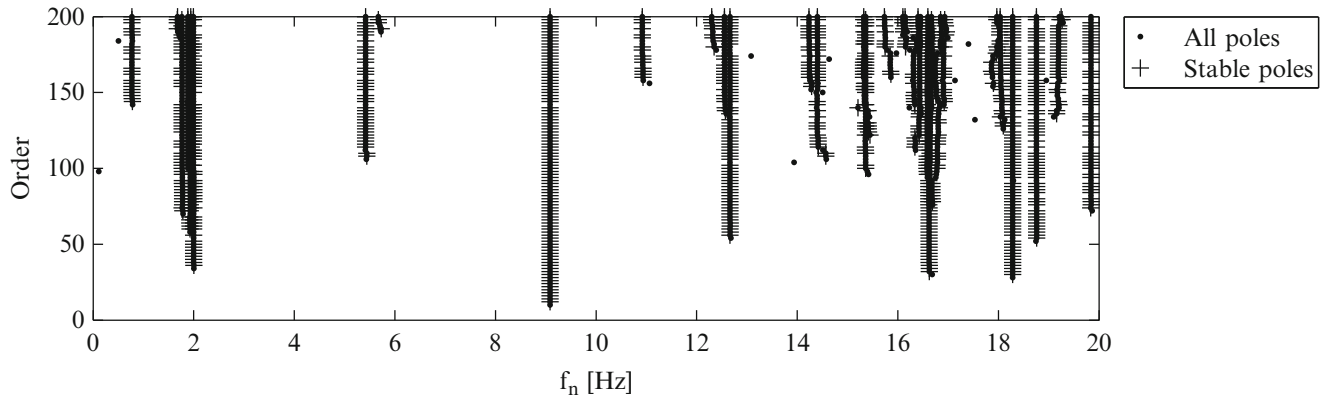
Fig. 25.6 Stabilization diagram of Cov-SSI analysis of the acceleration time series from sensor S2
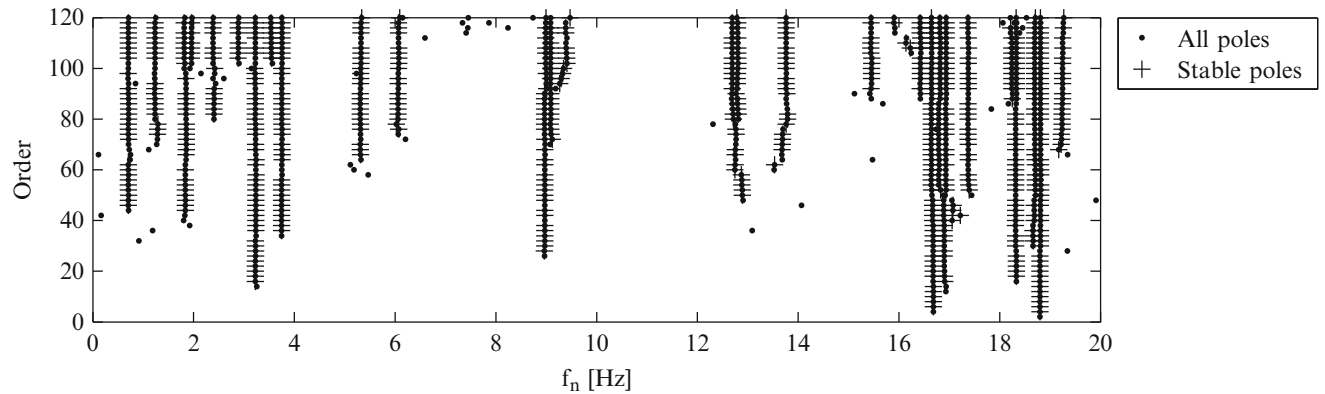
Fig. 25.7 Stabilization diagram of Cov-SSI analysis of the acceleration time series from one span, including sensors S1, S2, S3 and S6
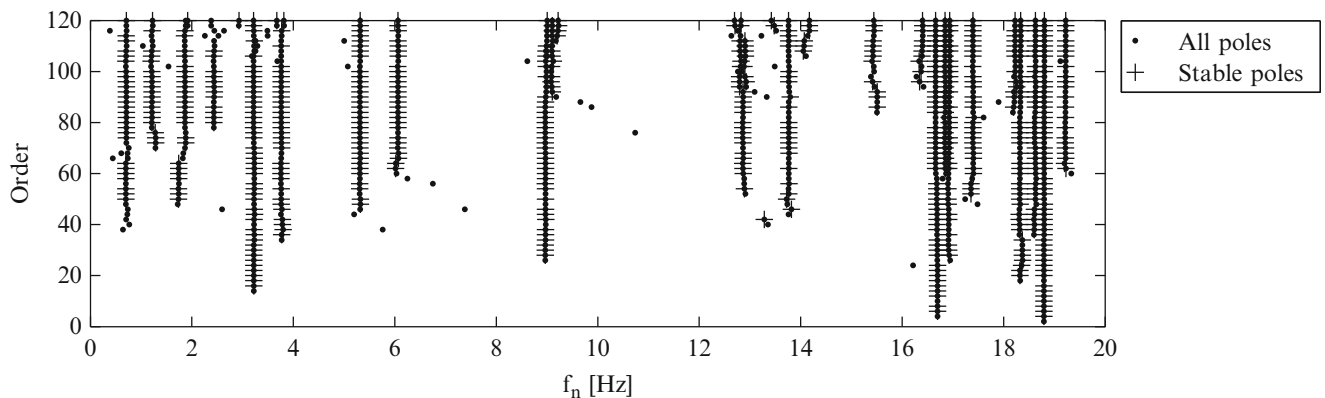
Fig. 25.8 Stabilization diagram of Cov-SSI analysis of the acceleration time series from Section 1, including sensors S1, S2, S3, S4 and S6
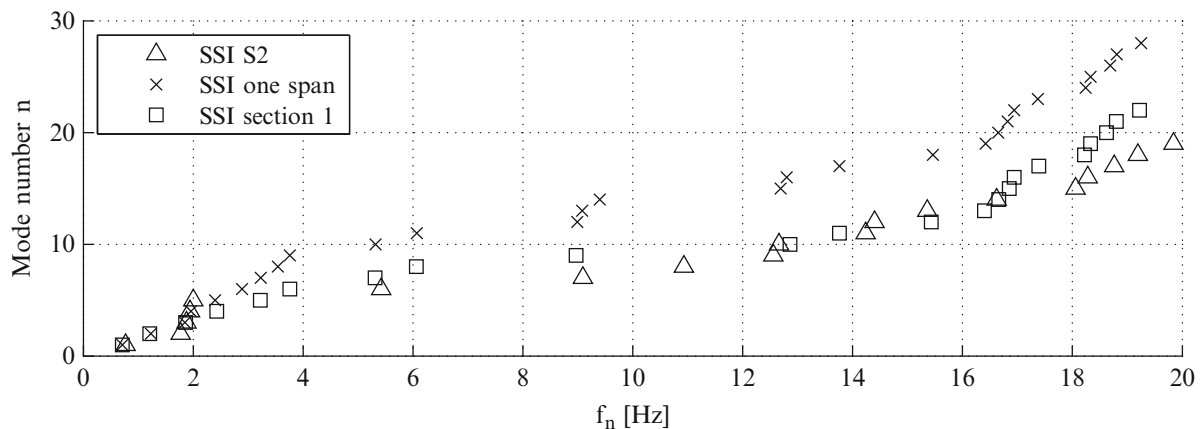
Fig. 25.9 The natural frequencies found from the three Cov-SSI analyses

Fig. 25.10 The estimated damping ratios found from analysis of Section 1
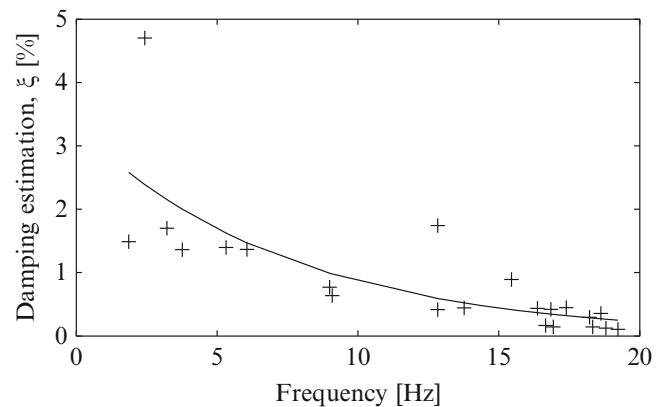
describe modes with reversal point there. This will include the motion of a full sine wave in one span, and multiples of this. One can for instance see that the second natural frequency of the system, 1.23 Hz, lacks from Fig. 25.6. Another difference is that the results from the whole section describe the frequencies of the whole dynamic system in a better way, and these frequencies are the ones most likely to cause problems when more energy is put into the system. This can either be effects due to an increase of the train speed, wrong set-up of the running pantograph or errors in both the pantograph and the catenary system. The second stabilization diagram, Fig. 25.7, will clearest show the properties of one span, and for optimization of the geometry this might be the most desirable set-up.

The damping in the system has been estimated from the Cov-SSI analysis on the sample records from whole of Section 1, Fig. 25.8. The estimation looks in general very good, but damping in some of the lowest frequencies of interest can be improved. The estimated damping ratios are shown in Fig. 25.10. The figure shows that damping in the system is mostly mass-proportional since the damping ratio decreases for increasing frequency. An exponential fit of the data is included in the figure to show this trend. A different set-up of sensors and different kind of excitation can in the future be used for a more thorough investigation of the damping in the system, especially for estimation at the lowest frequencies.

25.4 Conclusion

Dynamic assessment of railway catenary systems using monitoring of the vertical acceleration in the catenary has been suggested. This has been tested by sampling acceleration from different positions along a railway catenary section close to Oslo, Norway. Several sensors from a newly developed sensor system have been used for the sampling. The data collected has been used to estimate the speed of the train while it passes the section, the maximum vertical displacement at sampling points and modal parameters of the system. The constant average acceleration method has been employed to integrate the acceleration time series to displacement time series. A quite accurate estimation of the maximum value of the displacement

has been successful for some points, but by the registration arm, which is the stiffest part of a pole span, it has proved to be more difficult. An improved procedure of the integration has to be developed in the future to improve this. The speed of the train has been successfully predicted by using the cross-correlation function on sample records from two different positions along the rail line. Estimation of modal parameters has been employed by the use of two different methods; peak-picking from power spectral densities estimated by the Welch procedure and stabilization diagrams constructed from several Covariance-driven Stochastic Subspace Identification analyses. The first method was used as an initial face to locate natural frequencies, and the second used as a more thorough study for identifying both natural frequencies and corresponding damping ratios. This has in general resulted in a good estimation of both the frequency and the damping. The damping estimation at low frequencies needs improvement. A different set-up of the sensors and a different type of excitation is planned to improve this in the future. Changing the set-up of sensors will also make it possible to identify mode shapes of parts of a railway catenary section which in turn will help the validation of the estimated natural frequencies as physical solutions of the problem.

References

1. Ambrósio J, Pombo J, Pereira M, Antunes P, Mósca A (2012) Recent developments in pantograph-catenary interaction modelling and analysis. Int J Railw Technol 1(1):249–278
2. Givoni M, Brand C, Watkiss P (2009) Are railways climate friendly? Build Environ 35(1):70–86
3. Kiessling F (2009) Contact lines for electric railways: planning, design, implementation, maintenance. Publicis, Munich, p 994 s.: ill., fig
4. Scott GA, Cook M (1996) Extending the limits of pantograph/overhead performance. In: Better journey time – better business, IMechE conference transactions 1996–8, vol 8, pp 207–218
5. Poetsch G, Evans J, Meisinger R, Kortüm W, Baldauf W, Veitl A, Wallaschek J (1997) Pantograph/catenary dynamics and control. Veh Syst Dyn 28(2–3):159–195
6. Drugge L (2000) Modelling and simulation of pantograph-catenary dynamics. Luleå tekniska universitet
7. Rønnquist A, Nåvik P (2014) Dynamic assessment of a Norwegian contact line: exploring higher speed in sharp curves. In: Proceedings of the second international conference on railway technology: research, development and maintenance. Civil-Comp Press, Stirlingshire, UK
8. Rainieri C, Fabbrocino G (2014) Operational modal analysis of civil engineering structures. Springer, New York
9. Welch P (1967) The use of fast Fourier transform for the estimation of power spectra: a method based on time averaging over short, modified periodograms. IEEE Trans Audio Electroacoust 15(2):70–73
10. Brownjohn JMW, Magalhaes F, Caetano E, Cunha A (2010) Ambient vibration re-testing and operational modal analysis of the Humber Bridge. Eng Struct 32(8):2003–2018
11. Simeon B, Arnold M (2000) Coupling DAEs and PDEs for simulating the interaction of pantograph and catenary. Math Comput Model Dyn Syst 6(2):129–144
12. Lincoln A (2007) Calculating velocity or displacement from acceleration time histories [Online]. http://signalprocessing.prosig.com/VelFromAccel.pdf. Accessed 24 Oct 2014

Chapter 26
Finite Element Model Updating Using an Evolutionary Markov Chain Monte Carlo Algorithm

I. Boulkaibet, L. Mthembu, T. Marwala, M.I. Friswell, and S. Adhikari

Abstract One challenge in the finite element model (FEM) updating of a physical system is to estimate the values of the uncertain model variables. For large systems with multiple parameters this requires simultaneous and efficient sampling from multiple a prior unknown distributions. A further complication is that the sampling method is constrained to search within physically realistic parameter bounds. To this end, Markov Chain Monte Carlo (MCMC) techniques are popular methods for sampling from such complex distributions. MCMC family algorithms have previously been proposed for FEM updating. Another approach to FEM updating is to generate multiple random models of a system and let these models evolve over time. Using concepts from evolution theory this evolution process can be designed to converge to a globally optimal model for the system at hand. A number of evolution-based methods for FEM updating have previously been proposed. In this paper, an Evolutionary based Markov chain Monte Carlo (EMCMC) algorithm is proposed to update finite element models. This algorithm combines the ideas of Genetic Algorithms, Simulated Annealing, and Markov Chain Monte Carlo techniques. The EMCMC is global optimisation algorithm where genetic operators such as mutation and crossover are used to design the Markov chain to obtain samples. In this paper, the feasibility, efficiency and accuracy of the EMCMC method is tested on the updating of a real structure.

Keywords Bayesian • Finite element model updating • Markov chain Monte Carlo • Evolutionary Markov chain Monte Carlo • Simulated annealing • Genetic algorithms

26.1 Introduction

A Finite Element Model (FEM) [1, 2] is by definition a particular mathematical approximation of some real system. This approximation can be reasonably accurate for simple systems. For sufficiently complex systems the accuracy of this approximation degrades. Complex systems are those where a number of uncertain variables have to be defined, modelled and valued, and in dynamics systems this can be very difficult to do.

If it is clear which variables are uncertain, one approach is to understand and/or define their probability distributions. This is possible for FE models of real systems because the uncertain variable values have to be of realistic magnitudes. The sampling techniques can be employed to quantify these uncertain parameters. However, the challenge is that sometimes the distribution of these uncertain variables is not known a prior, and sometimes the updated models have multiple optimal (or near optimal) solutions.

The most popular sampling algorithms are of the Markov chain Monte Carlo type [1, 3, 4]. They have the advantage that the sampling procedures draw samples with an element of randomness while being guided by their performance on the problem objective function (also known as the Posterior function). Thus some samples will be rejected while others will be accepted and this effectively forms a chain of samples. The learning part of the sampling procedure proposed in this paper uses the paradigm of evolution-based algorithms [5–7].

These algorithms are based on the notion that in evolution, new individuals are an improvement based on their parents' performance in a particular problem. As such, new individuals can be developed if we can understand/model the characteristics/variables that made their parents good. The analogy of individuals in evolution algorithms to FEM context is

I. Boulkaibet (✉) • L. Mthembu • T. Marwala
The Centre for Intelligent System Modelling (CISM), Electrical and Electronic Engineering Department, University of Johannesburg,
PO Box 524, Auckland Park 2006, South Africa
e-mail: iboulkaibet@student.uj.ac.za

M.I. Friswell • S. Adhikari
College of Engineering, Swansea University, Singleton Park, Swansea SA2 8PP, UK

the particular combination of uncertain variable values that form a potentially correct solution to the FEM problem. Thus individuals in evolution algorithms are all the potential solutions to the FE model. The individual's performance on the problem is evaluated by the fitness function. In this paper, the fitness function is defined by the logarithm of the posterior Density Distribution Function (PDF), see next section.

There are two fundamental mechanisms of developing new individuals in evolution algorithms; mutation and crossover. Mutation is when a variable, randomly selected, changes its value. The crossover is the process where two individuals exchange their variable values at certain positions, also known as crossover points, in the uncertain variable vector. The selection of the positions can either be done via a roulette wheel selection or a random selection [8, 9]. The algorithm proposed in this work has an extra operator called the exchange [8, 10]. This operator allows for the mixing of individuals within a population to eliminate premature convergence. In order to characterise the uncertainties of the update variables, we formulate the problem in the Bayesian context. The next section introduces the Bayesian formulation. Section 26.3 describes the Evolutionary MCMC algorithm while Sect. 26.4 presents the results when an Unsymmetrical H-shaped Structure is updated using the Evolutionary MCMC algorithm. The paper is concluded in Sect. 26.5.

26.2 The Bayesian Formulation

The Bayesian method is used to solve the FEM updating problem in the modal domain. Bayesian approaches are governed by Bayes rule [3, 4, 11–13]:

$$P\left(\boldsymbol{\theta}\middle|\mathcal{D}, \mathcal{M}\right) \propto P\left(\mathcal{D}\middle|\boldsymbol{\theta}, \mathcal{M}\right) P\left(\boldsymbol{\theta}\middle|\mathcal{M}\right) \tag{26.1}$$

$\mathcal{M}$ represents the model class for the target system which is defined by the model updated variables $\boldsymbol{\theta} \in \boldsymbol{\Theta} \subset \mathcal{R}^d$. $\mathcal{D}$ is the measured modal data (typically the natural frequencies f_i^m and mode shapes ϕ_i^m) in the FE model field. The quantity $P\left(\boldsymbol{\theta}\middle|\mathcal{M}\right)$ is the prior probability distribution function (PDF). It represents our knowledge of the uncertain variables given a particular model $\mathcal{M}$ in the absence of any measured data $\mathcal{D}$. The quantity $P\left(\boldsymbol{\theta}\middle|\mathcal{D}, \mathcal{M}\right)$ is the posterior PDF of the variables once we have observed the data and the assumed model class $\mathcal{M}$. $P\left(\mathcal{D}\middle|\boldsymbol{\theta}, \mathcal{M}\right)$ is the likelihood function [3, 12–15] which calculates the difference between the measured data and the FE model results for given variables and assumed model. The dependence on the model class $\mathcal{M}$ is only relevant in cases where more than one model class is investigated and in this paper only one model class is considered. For simplicity we ignore the class notation in subsequent notations.

In the FEM context the likelihood PDF form is given by:

$$P\left(\mathcal{D}\middle|\boldsymbol{\theta}\right) = \frac{1}{\left(\frac{2\pi}{\beta_c}\right)^{N_m/2} \prod_{i=1}^{N_m} f_i^m} \exp\left(-\frac{\beta_c}{2} \sum_i^{N_m} \left(\frac{f_i^m - f_i}{f_i^m}\right)^2\right) \tag{26.2}$$

where β_c is a constant, N_m is the number of measured modes, f_i^m and f_i are the ith analytical natural frequency and the ith measured natural frequency.

The prior PDF represents our prior knowledge of the updating variables $\boldsymbol{\theta}$ and it is chosen as a Gaussian distribution

$$P\left(\boldsymbol{\theta}\right) = \frac{1}{(2\pi)^{Q/2} \prod_{i=1}^{Q} \frac{1}{\sqrt{\alpha_i}}} \exp\left(-\sum_i^{Q} \frac{\alpha_i}{2} \left\|\boldsymbol{\theta}^i - \boldsymbol{\theta}_0^i\right\|^2\right) = \frac{1}{(2\pi)^{Q/2} \prod_{i=1}^{Q} \frac{1}{\sqrt{\alpha_i}}} \exp\left(-\frac{1}{2}(\boldsymbol{\theta} - \boldsymbol{\theta}_0)^T \Sigma^{-1} (\boldsymbol{\theta} - \boldsymbol{\theta}_0)\right) \tag{26.3}$$

where Q is the number of variables to be updated, $\boldsymbol{\theta}_0$ represents the mean value of the updated vector and α_i is the coefficient of the prior PDF for the ith updating variables. The notation * denotes the Euclidean norm of *.

The posterior PDF of the variables $\boldsymbol{\theta}$ given the observed data $\mathcal{D}$ is denoted as $P\left(\boldsymbol{\theta}\middle|\mathcal{D}\right)$ and is obtained by applying Bayes' theorem in Eq. (26.1). The distribution $P\left(\boldsymbol{\theta}\middle|\mathcal{D}\right)$ is calculated by substituting Eqs. (26.2) and (26.3) into Eq. (26.1) to give:

$$P\left(\boldsymbol{\theta}\middle|\mathcal{D}\right) \propto \frac{1}{Z_s\left(\alpha, \beta_c\right)} \exp\left(-\frac{\beta_c}{2}\sum_i^{N_m}\left(\frac{f_i^m - f_i}{f_i^m}\right)^2 - \sum_i^Q \frac{\alpha_i}{2}\left\|\boldsymbol{\theta}^i - \boldsymbol{\theta}_0^i\right\|^2\right) \tag{26.4}$$

where

$$Z_s\left(\alpha, \beta_c\right) = \left(\frac{2\pi}{\beta_c}\right)^{N_m/2}\prod_{i=1}^{N_m}f_i^m(2\pi)^{Q/2}\prod_{i=1}^Q\frac{1}{\sqrt{\alpha_i}} \tag{26.5}$$

In complex systems (e.g. those that have a large number of uncertain variables and model intricate systems) obtaining a posterior PDF analytical form is not possible. Sampling techniques, such as Markov chain Monte Carlo (MCMC) methods, can provide a numerical approximation to this function [1, 12, 13, 15–17].

If Y is an observation of certain variables at different discrete time instants, then the prediction of the future responses of this parameter Y at different time instants can be achieved by the total probability theorem:

$$P\left(Y\middle|D\right) = \int_\theta P\left(Y\middle|\boldsymbol{\theta}\right) P\left(\boldsymbol{\theta}\middle|D\right) d\boldsymbol{\theta} \tag{26.6}$$

Equation (26.6) depends on the posterior PDF. Therefore, given a set of N_s random variable vectors drawn from a probability distribution function ($P\left(\boldsymbol{\theta}\middle|D\right)$, the expectation value of any observed function Y can be easily estimated.

The integral in Eq. (26.6) can be solved using sampling algorithms [1, 3, 4, 12, 13]. These algorithms are used to generate a sequence of vectors $\{\boldsymbol{\theta}_1, \boldsymbol{\theta}_2, \ldots, \boldsymbol{\theta}_{N_s}\}$, where N_s is the number of samples of these vectors, that can be used to form a Markov chain. This generated vector is then used to predict the form of the posterior distribution function $P\left(\boldsymbol{\theta}\middle|D\right)$. The integral in Eq. (26.6) can be approximated as

$$\widetilde{Y} \cong \frac{1}{N_s}\sum_{i=1}^{N_S} G\left(\boldsymbol{\theta}_i\right) \tag{26.7}$$

where G is a function that depends on the updated variables $\boldsymbol{\theta}_i$. As an example, if $\mathbf{G} = \boldsymbol{\theta}$ then $\widetilde{Y}$ becomes the expected value of $\boldsymbol{\theta}$. Generally, $\widetilde{Y}$ is the vector that contains the modal properties and N_s is the number of retained states. In this paper, the evolutionary Markov chain Monte Carlo (EMCMC) method is used to sample from the posterior PDF.

26.3   The Evolutionary MCMC Algorithm

Genetic algorithms (GA) make use of the two operators; crossover and mutation to succeed in many hard optimization problems [8, 18]. The EMCMC [9, 19] algorithm combines these GA operators with the dynamics of MCMC algorithms to better sample and learns from the sampling procedure. In this section, the basics of the EMCMC technique are described.

Let $\boldsymbol{\theta} = \{\boldsymbol{\theta}^1, \boldsymbol{\theta}^2, \cdots, \boldsymbol{\theta}^i, \cdots, \boldsymbol{\theta}^N\}$ denote a population of samples, where $\boldsymbol{\theta}^i = \{\theta_1^i, \theta_2^i, \cdots, \theta_d^i\}$ is a d-dimensional vector called an individual or a chromosome in GA and N is the population size. In Bayesian statistics, $\boldsymbol{\theta}^i$ is often a vector of variables while the fitness function $F(\boldsymbol{\theta}^i)$ is the negative of the log-posterior of $\boldsymbol{\theta}^i$. In EMCMC, a different temperature T_i is attached to each individual $\boldsymbol{\theta}^i$, and the temperatures form a ladder with the ordering $T_1 > T_1 > T_2 > \cdots > T_N = 1$.

A Boltzmann distribution for each individual $\boldsymbol{\theta}^i$ can be defined as:

$$g\left(\boldsymbol{\theta}^i\right) = \frac{1}{Z_i\left(T_i\right)}exp\left(-\frac{F\left(\boldsymbol{\theta}^i\right)}{T_i}\right) \tag{26.8}$$

where $Z_i(T_i)$ is the normalizing constant, $Z_i\left(T_i\right) = \sum_{\{\boldsymbol{\theta}^i\}}exp\left(-\frac{F\left(\boldsymbol{\theta}^i\right)}{T_i}\right)$

26.3.1 Mutation

In the mutation operator [9], an individual, say θ^k is randomly selected from the current population $\theta = \{\theta^1, \theta^2, \cdots, \theta^k, \cdots, \theta^N\}$, it is then mutated to a new individual $\widetilde{\theta}^k$ by changing the values of some bits which are also chosen randomly. A new population is thus created as $\widetilde{\theta} = \{\theta^1, \theta^2, \cdots, \widetilde{\theta}^k, \cdots, \theta^N\}$, and it is accepted with probability $min(1, r_m)$ according to the Metropolis rule, where r_m is the Metropolis-Hastings [20, 21] ratio which is given by [9]:

$$r_m = \frac{g\left(\widetilde{\theta}^k\right)}{g\left(\theta^k\right)} \cdot \frac{Tr\left(\theta^k \middle| \widetilde{\theta}^k\right)}{Tr\left(\widetilde{\theta}^k \middle| \theta^k\right)} = \exp\left(-\frac{\left(F\left(\widetilde{\theta}^k\right) - F\left(\theta^k\right)\right)}{T_k}\right) \cdot \frac{Tr\left(\theta^k \middle| \widetilde{\theta}^k\right)}{Tr\left(\widetilde{\theta}^k \middle| \theta^k\right)} \tag{26.9}$$

and $Tr\left(. \middle| .\right)$ denotes the transition probability between populations. If the proposal is accepted, the current population θ is replaced by $\widetilde{\theta}$, otherwise the population θ is unchanged. In this paper, the 2-point mutation operator is performed which means that $Tr\left(\theta^k \middle| \widetilde{\theta}^k\right) = Tr\left(\widetilde{\theta}^k \middle| \theta^k\right)$.

26.3.2 Crossover

In the crossover operator [9]; two individuals, say θ^a and θ^b $(a \neq b)$, are selected from the current population θ according to some selection procedure. In the analysis we assume $F\left(\theta^a\right) \geq F\left(\theta^b\right)$. From these two individuals, now known as parents, two new individuals are generated according to the crossover operator. This can be done by randomly selecting a crossover position in the uncertain variable vector. That is if we let position p in the size d element variable vector be the crossover position then the elements from position $p + 1$ in θ^a will be moved to individual θ^b and vice versa. The offspring with a smaller fitness value is denoted $\widetilde{\theta}^b$ and the other $\widetilde{\theta}^a$. A new population of individuals is proposed as $\widetilde{\theta} = \{\theta^1, \cdots, \widetilde{\theta}^a, \cdots, \widetilde{\theta}^b, \cdots, \theta^N\}$. According to the Metropolis rule, the new population is accepted with probability $in(1, r_c)$ [9],

$$r_c = \frac{g\left(\widetilde{\theta}^a\right) \cdot g\left(\widetilde{\theta}^b\right)}{g\left(\theta^a\right) \cdot g\left(\widetilde{\theta}^b\right)} \cdot \frac{Tr\left(\theta \middle| \widetilde{\theta}\right)}{Tr\left(\widetilde{\theta} \middle| \theta\right)} = \exp\left(-\frac{\left(F\left(\widetilde{\theta}^a\right) - F\left(\theta^a\right)\right)}{T_a} - \frac{\left(F\left(\widetilde{\theta}^b\right) - F\left(\theta^b\right)\right)}{T_b}\right) \cdot \frac{Tr\left(\theta \middle| \widetilde{\theta}\right)}{Tr\left(\widetilde{\theta} \middle| \theta\right)} \tag{26.10}$$

where $Tr\left(\theta \middle| \widetilde{\theta}\right) = P\left(\left(\theta^a, \theta^b\right) \middle| \theta\right) \cdot P\left(\left(\widetilde{\theta}^a, \widetilde{\theta}^b\right) \middle| \left(\theta^a, \theta^b\right)\right)$. The $P\left(\left(\theta^a, \theta^b\right) \middle| \theta\right)$ denotes the selection probability of individuals (θ^a, θ^b) from the population θ, and $P\left(\left(\widetilde{\theta}^a, \widetilde{\theta}^b\right) \middle| \left(\theta^a, \theta^b\right)\right)$ denotes the generating probability of individuals $\left(\widetilde{\theta}^a, \widetilde{\theta}^b\right)$ from the parents (θ^a, θ^b).

In this paper, the parental individuals are chosen as follows; the first individual θ^a is chosen according to a roulette wheel procedure with Boltzmann weights, i.e. θ^a is chosen with probability defined in Eq. (26.8). The second individual θ^b is chosen randomly from the rest of the population. The selection probability of θ^b is then [9]:

$$P\left(\left(\theta^a, \theta^b\right) \middle| \theta\right) = \frac{1}{(N-1) \cdot Z\left(\theta\right)} \cdot \left(exp\left(-\frac{H\left(\theta^a\right)}{T_a}\right) + exp\left(-\frac{H\left(\theta^b\right)}{T_b}\right)\right) \tag{26.11}$$

where $Z\left(\theta\right) = \sum_{\{\theta^a\}} exp\left(-\frac{H\left(\theta^a\right)}{T_a}\right) \cdot P\left(\left(\widetilde{\theta}^a, \widetilde{\theta}^b\right) \middle| \widetilde{\theta}\right)$. The crossover operator used is a 2-point crossover.

26.3.3   Exchange

This operation was first introduced in the parallel tempering sampling method in [22] and exchange Monte Carlo sampling method [10]. Given the current population $\boldsymbol{\theta}$ and the temperature ladder $\mathbf{T}$, $(\boldsymbol{\theta}, \mathbf{T}) = \{\boldsymbol{\theta}^1, T_1, \boldsymbol{\theta}^2, T_2, \cdots, \boldsymbol{\theta}^N, T_N\}$, we make an exchange between individuals $\boldsymbol{\theta}^a$ and $\boldsymbol{\theta}^b$ without changing their temperatures, i.e., we try to change $(\boldsymbol{\theta}, \mathbf{T}) = \{\boldsymbol{\theta}^1, T_1, \boldsymbol{\theta}^a, T_a, \cdots, \boldsymbol{\theta}^b, T_b, \cdots, \boldsymbol{\theta}^N, T_N\}$ to $(\overline{\boldsymbol{\theta}}, \mathbf{T}) = \{\boldsymbol{\theta}^1, T_1, \boldsymbol{\theta}^b, T_a, \cdots, \boldsymbol{\theta}^a, T_b, \cdots, \boldsymbol{\theta}^N, T_N\}$. The new population is accepted with probability $min(1, r_e)$ according to the Metropolis rule, where [9]:

$$r_e = \frac{g\left(\overline{\boldsymbol{\theta}}\right)}{g\left(\boldsymbol{\theta}\right)} \cdot \frac{Tr\left(\boldsymbol{\theta}\middle|\overline{\boldsymbol{\theta}}\right)}{Tr\left(\overline{\boldsymbol{\theta}}\middle|\boldsymbol{\theta}\right)} = \exp\left(-\left(H(\boldsymbol{\theta}^a) - H(\boldsymbol{\theta}^b)\right) \cdot \left(\frac{1}{T_a} - \frac{1}{T_b}\right)\right) \cdot \frac{Tr\left(\boldsymbol{\theta}\middle|\overline{\boldsymbol{\theta}}\right)}{Tr\left(\overline{\boldsymbol{\theta}}\middle|\boldsymbol{\theta}\right)} \qquad (26.12)$$

and $Tr\left(.\middle|.\right)$ denotes the transition probability between populations. Typically, the exchange is only performed on states with neighbouring temperature values, i.e., $|a - b| = 1$ where $Tr\left(\boldsymbol{\theta}\middle|\overline{\boldsymbol{\theta}}\right) = Tr\left(\overline{\boldsymbol{\theta}}\middle|\boldsymbol{\theta}\right)$ [9].

The EMCMC algorithm is summarized as follows:

1. Initialization: generate N individuals and evaluate the posterior (fitness) of each individual.
2. Selection: Certain individuals are selected from the current population.
3. Crossover: Offspring are produced by a recombination of the vector elements in the mating individuals where this operation is accepted by $min(1, r_c)$.
4. Mutation: Offspring are produced by random changes in individuals in the population, these offspring are accepted by $min(1, r_m)$.
5. Exchange: The exchange is performed for each set of neighboring individuals in the population, and these are accepted by $min(1, r_e)$.
6. Repeat 2–4 steps until a N_s samples are obtained.

In next sections we present the application and results of this algorithm. The real system modelled is an unsymmetrical H-shaped beam structure. The objective is to predict the uncertain variable values along with their errors. The performance of the proposed algorithm, EMCMC, is compared with the performance of the classic MCMC algorithm Metropolis-Hasting on the same beam.

26.4   Application: Unsymmetrical H-Shaped Structure

In this paper, an unsymmetrical H-shaped aluminium structure (see Fig. 26.1) is updated using the EMCMC algorithm. The structure was divided into 12 elements and each was modelled as an Euler-Bernoulli beam. The Structural Dynamics Toolbox SDT®, which is a Matlab package, is used to model the beams. The position indicated by the double arrow is the location where the structure was excited. The acceleration was measured at 15 different positions. The structure was excited using an electromagnetic shaker and a roving accelerometer was used to measure the response. A set of 15 frequency-response functions were calculated. See [14] for more details about the structure.

26.4.1   H-Beam Simulation

The measured frequencies are: 53.9, 117.3, 208.4, 254.0 and 445.0 Hz. the moments of inertia and the cross section areas of the left, middle and right subsections of the beam are selected to be updated. The updating parameter vector is then given by: $\boldsymbol{\theta} = \{I_{x1}, I_{x2}, I_{x3}, A_{x1}, A_{x2}, A_{x3}\}$. The Young's modulus for the structure is set to $7.2 \times 10^{10} \mathrm{N/m}^2$, the density is set to 2,785 kg/m^3 and the structure dimensions are presented in Fig. 26.1. The updating parameters θ_i are bounded by maximum values equal to $\left[3.73 \times 10^{-8}, 3.73 \times 10^{-8}, 3.73 \times 10^{-8}, 4.16 \times 10^{-4}, 4.16 \times 10^{-4}, 4.16 \times 10^{-4}\right]$ and minimum values are equal to $\left[1.73 \times 10^{-8}, 1.73 \times 10^{-8}, 1.73 \times 10^{-8}, 2 \times 10^{-4}, 2.16 \times 10^{-4}, 2.16 \times 10^{-4}\right]$. These boundaries help to keep the updated vector physically realistic.

Fig. 26.1 The H-shaped aluminium structure
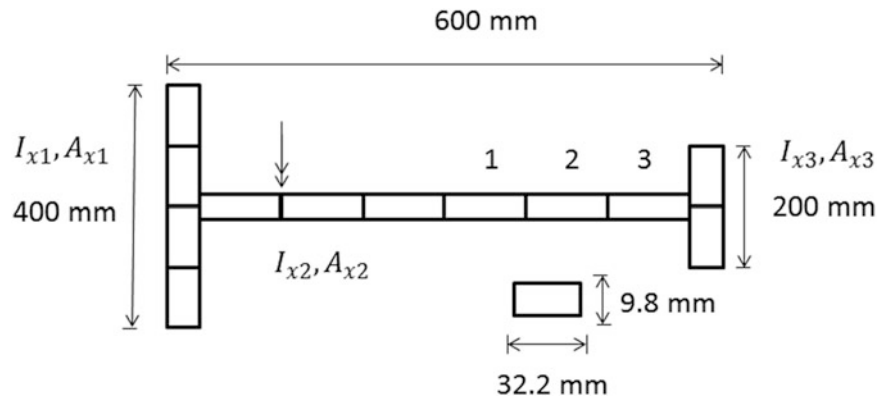
Table 26.1 Initial and updated parameters using EMCMC and M-H algorithms

	Initial θ_0	θ vector EMCMC method	$\frac{\sigma_i}{\mu_i}$ (%)	θ vector M-H method	$\frac{\sigma_i}{\mu_i}$ (%)
I_{x1}	2.73×10^{-8}	2.578×10^{-8}	0.75	2.31×10^{-8}	22.59
I_{x2}	2.73×10^{-8}	2.576×10^{-8}	0.78	2.68×10^{-8}	15.25
I_{x3}	2.73×10^{-8}	2.533×10^{-8}	3.84	2.17×10^{-8}	13.96
A_{x1}	3.16×10^{-4}	3.693×10^{-4}	0.04	2.85×10^{-4}	14.36
A_{x2}	3.16×10^{-4}	2.157×10^{-4}	0.001	2.83×10^{-4}	14.36
A_{x3}	3.16×10^{-4}	3.006×10^{-4}	0.003	2.77×10^{-4}	13.08

Table 26.2 Natural frequencies and errors when using EMCMC and M-H algorithms

Mode	Measured frequency (Hz)	Initial frequency (Hz)	Error (%)	Frequencies EMCMC method (Hz)	Error (%)	Frequencies M-H method (Hz)	Error (%)
1	53.9	51.40	4.63	53.1	1.49	53.92	0.04
				(0.013 %)		(3.96 %)	
2	117.3	116.61	0.59	119.99	2.29	122.05	4.05
				(0.041 %)		(4.28 %)	
3	208.4	201.27	3.42	210.23	0.88	210.93	1.22
				(0.172 %)		(4.95 %)	
4	254.0	247.42	2.59	249.01	1.97	258.94	1.94
				(0.091 %)		(4.81 %)	
5	445	390.33	12.28	431.84	2.96	410.33	7.79
				(0.044 %)		(4.74 %)	
Total average error			4.70		1.92		3.01

The constant β_c of the posterior distribution (see Eq. (26.4)) is set equal 1 for the EMCMC algorithm while the β_c is set to 10 for the M-H algorithm. In this paper, the EMCMC results will be compared with those obtained by M-H algorithm (see [23] for more details about the M-H algorithm results). The coefficients α_i are set equal to $\frac{1}{\sigma_i^2}$, where σ_i^2 is the variance of the i th parameter and the variance vector is defined as $\sigma = [5 \times 10^{-8}, 5 \times 10^{-8}, 5 \times 10^{-8}, 5 \times 10^{-4}, 5 \times 10^{-4}, 5 \times 10^{-4}]$. The number of samples N_s is set to 1,000. The population size for the EMCMC algorithm is set to 12; the mutation rate is 0.2 while the selection rate is set to 0.5. The temperatures used in this implementation are given as follows: T = [1,557.8, 1,277.4, 1,054.8, 915.4, 880.7, 815.8, 651, 308.2, 212.2, 189.4, 138.5, 1].

The Bayesian simulation results are presented and evaluated in terms of the mean values of the obtained samples for each method (see Table 26.1). The updated natural frequencies and the prediction error percentage are stored in Table 26.2. The acceptance rate for the EMCMC algorithm is 61.9 % while the acceptance rate of M-H algorithm is 46.9 %. The reason that the M-H algorithm gave a poor acceptance rate is that the move step used for this algorithm was chosen relatively large to have acceptable results with fast convergence (the variance of the proposal distribution is relatively large). The EMCMC algorithm has an acceptable acceptance rate where the reason could be the exchange probabilities used in this implementation (accept with a probability equal to 0.8 when the selected chromosome (or individual) is the first and the last. Otherwise, the probability is equal to 0.5).

Fig. 26.2 The correlation
between the updated parameters
(EMCMC algorithm)
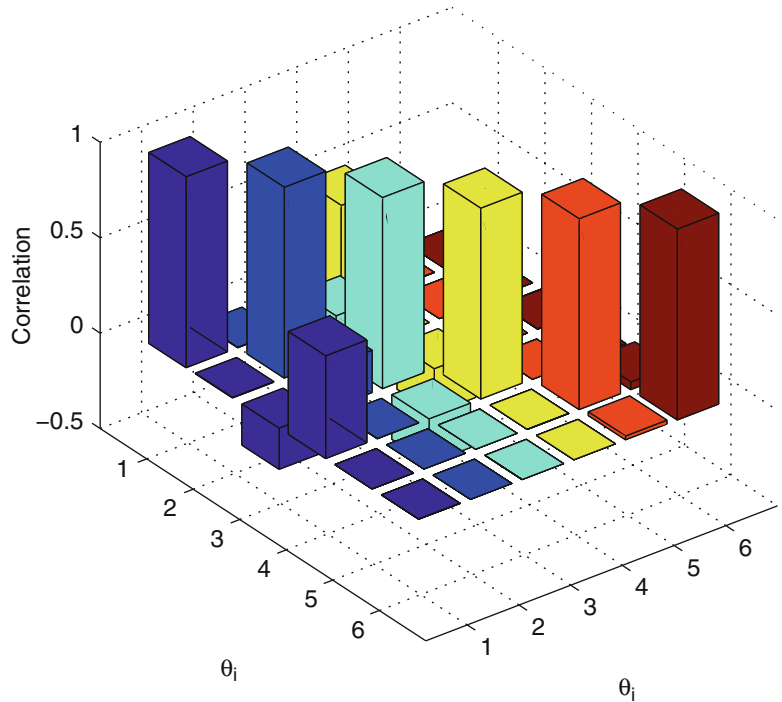
Fig. 26.3 The correlation
between the updated parameters
(M-H algorithm)
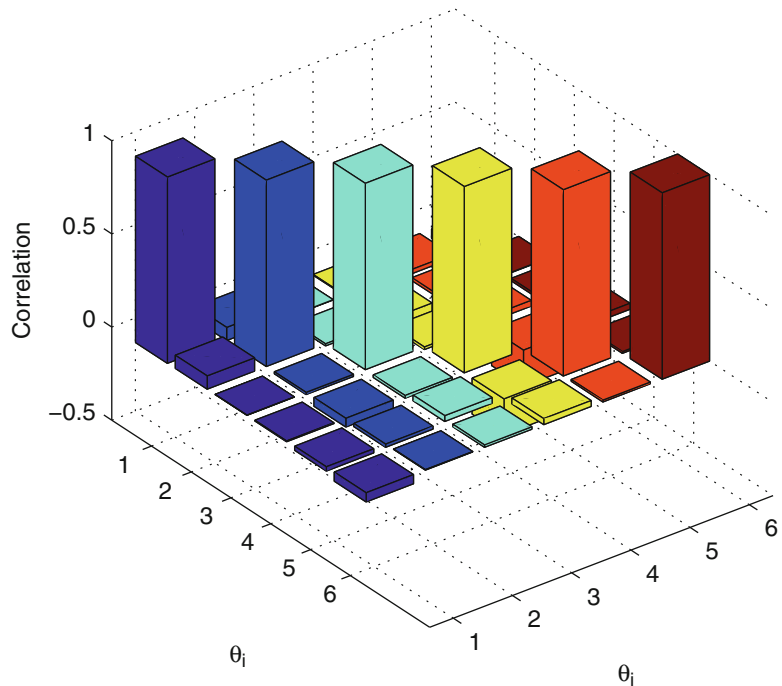
Table 26.1 shows the initial values of the parameters, the updated values and the coefficient of variation (c.o.v) of both EMCMC and M-H algorithms. All algorithms updated the $\boldsymbol{\theta}$ vector where the updated values are different than the initial $\boldsymbol{\theta}_0$. The updated vectors obtained by both algorithms are physically realistic. The coefficients of variance obtained by M-H algorithm are large compared with those obtained by EMCMC algorithm. The reason for this is that large move steps were used for both M-H algorithm to ensure a fast convergence and to improve the total average errors, while the EMCMC algorithm uses the mutation and the crossover operators to move from one sample to the next.

Figures 26.2 and 26.3 show the correlation between all updated parameters for both algorithms. The figures indicate that all parameters are correlated for all algorithms (all values are not 0), where most of the parameters are weakly correlated except the pair (A_{x1}, A_{x3}) which is found to be correlated (the correlation is 0.51) by the EMCMC algorithm.
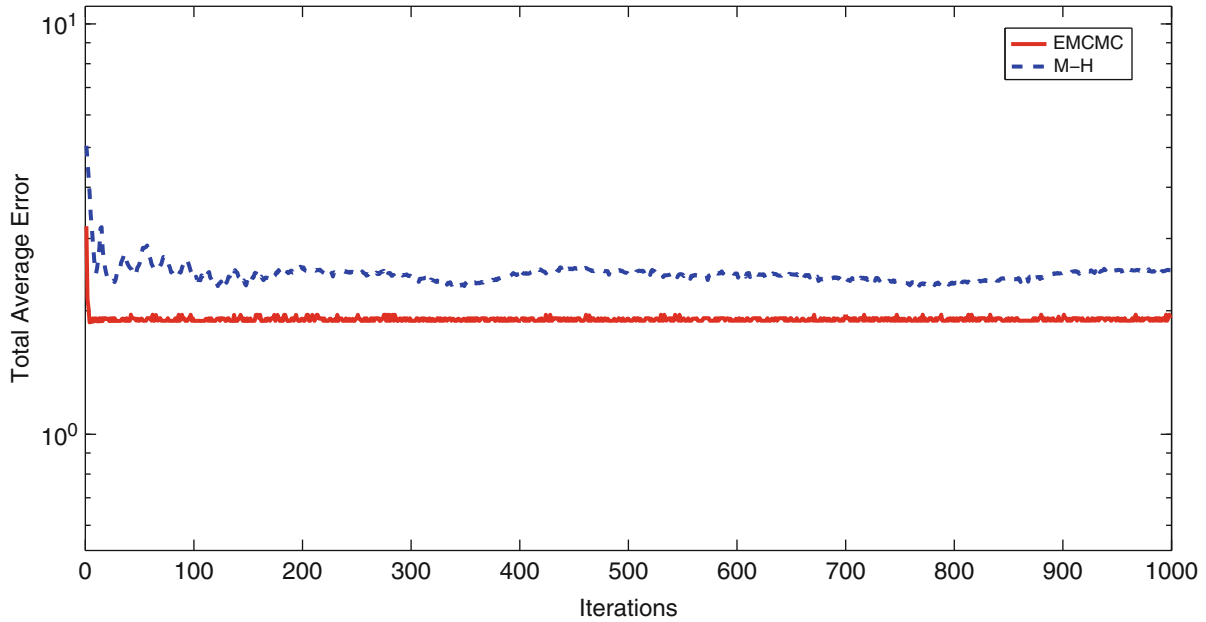
Fig. 26.4 The total average error using HMC, SS and M-H methods

Table 26.2 shows the absolute mode errors, the total average errors, the FEM updated frequencies and the coefficient of variations in brackets when both EMCMC and M-H algorithms are implemented to update the structure. The absolute mode error is given by $\frac{|f_i^m - f_i|}{f_i^m}$, while the Total Average Error (TAE) is given by: $\text{TAE} = \frac{1}{N_m} \sum_{i=1}^{N_m} \frac{|f_i^m - f_i|}{f_i^m}$. The error between the first measured natural frequency and that of the initial model was 4.63 %. When applying EMCMC algorithm this error was reduced to 1.49 %; however the M-H algorithm reduced the error to 0.04 %. The overall updated FEM natural frequencies for both algorithms are better than the initial FEM. However, The EMCMC algorithms produced better total average error results than the M-H algorithm. The updating procedure using the EMCMC method improved the error from 4.7 % to 1.92 %. The c.o.v values obtained by the EMCMC algorithm are very small compared to those obtained by the M-H algorithm which indicates that the EMCMC algorithms produces more accurate results than the M-H algorithm.

Figure 26.4 shows the absolute total average error for the three algorithms for 1,000 iterations. The *y*-axis (Total Average Error) is plotted by using the base 10 logarithmic scale. To obtain Fig. 26.4, the samples previously accepted are used to compute the mean value of samples which is given by: $\hat{\boldsymbol{\theta}} = E(\boldsymbol{\theta}) \cong \frac{1}{N_s} \sum_{j=1}^{i} \boldsymbol{\theta}^i$ where *i* represents the current iteration.

Then, the absolute total average error is computed according to $\text{TAE}(i) = \frac{1}{N_m} \sum_{j=1}^{N_m} \frac{|f_j^m - f_j|}{f_j^m}$. The results obtained show that both algorithms converge fast (within the first 100 iterations for the M-H algorithm while the EMCMC algorithm uses less than 50 iteration to start converging). The reason that the M-H algorithm has a high convergence rate is that large move steps are used in these algorithms. However, the mutation and the crossover procedures helped the EMCMC algorithm to converge faster. The figure also shows that the error obtained by the EMCMC algorithm is smaller than that obtained by the M-H algorithm.

26.5 Conclusion

This paper presented the applicability and performance of the Evolutionary MCMC algorithm on the finite element model updating problem. We briefly stated the limitation of the initial finite element model and the need to update it. We then explained the origins of the EMCMC algorithm; it is a combination of the characteristics found in evolution – type algorithms (e.g. Genetic algorithm) and the dynamics of Markov chain Monte Carlo sampling methods. The resulting EMCMC is then posed in the Bayesian context where the objective function is a probability distribution. This is advantageous as this allows for the different variable distributions and samples to be calculated in a formal way.

The EMCMC algorithm was tested on a real beam structure with a number of uncertain variables. This method was compared with a classic MCMC algorithm; the Metropolis-Hasting. The structural example shows the efficiency of the EMCMC approach to sampling over the M-H algorithm methods. The M-H algorithm performance decreases with the complexity of the system and the size of the uncertain vector. As results, the total average error of the M-H algorithm was relatively large compared to that obtained by the EMCMC algorithm. Moreover the acceptance rate of the M-H algorithm was small. Future work will introduce further operators to this algorithm and the results obtained will be compared with those of other sampling techniques. To get further incite into the performance characteristics (e.g. stability and consistency) of these algorithms and their combinations; they will be tested on significantly more complex structures.

References

 1. Marwala T (2010) Finite element model updating using computational intelligence techniques. Springer Verlag, London
 2. Friswell MI, Mottershead JE (1995) Finite element model updating in structural dynamics. Kluwer, Dordrecht
 3. Bishop CM (2006) Pattern recognition and machine learning. Springer, New York
 4. Boulkaibet I, Marwala T, Mthembu L, Friswell MI, Adhikari S (2012) Sampling techniques in Bayesian finite element model updating. Proc Soc Exp Mech 29:75–83
 5. Goldberg DE (1989) Genetic algorithms in search, optimization and machine learning. Addison-Wesley, Boston
 6. Holland JH (1975) Adaptation in natural and artificial systems. The University of Michigan Press, MIT Press, Cambridge, MA
 7. Mitchell M (1996) An introduction to genetic algorithms. MIT Press, Cambridge, MA
 8. Davis L (1991) Handbook of genetic algorithms. Van Nostrand Reinhold, New York
 9. Liang F, Wong WH (2000) Evolutionary Monte Carlo: application to Cp model sampling and change point problem. Stat Sin 10:317–342
10. Hukushima K, Nemoto K (1996) Exchange Monte Carlo method and application to spin glass simulations. J Physical Soc Japan 65:1604–1608
11. Yuen KV (2010) Bayesian methods for structural dynamics and civil engineering. Wiley, New York
12. Boulkaibet I, Mthembu L, Marwala T, Friswell MI, Adhikari S (2014) Finite element model updating using the shadow hybrid Monte Carlo technique, Mech Syst Signal Process, 52:115–132
13. Boulkaibet I, Mthembu L, Marwala T, Friswell MI, Adhikari S (2014) Finite element model updating using Hamiltonian Monte Carlo techniques. J Sound Vib (submitted for publication)
14. Marwala T (2010) Finite element model updating using computational intelligence techniques. Springer, London
15. Marwala T, Sibisi S (2005) Finite element model updating using Bayesian approach. In: Proceedings of the international modal analysis conference, Orlando. ISBN: 0-912053-89-5
16. Bishop CM (1995) Neural networks for pattern recognition. Oxford University Press, Oxford
17. Ching J, Leu SS (2009) Bayesian updating of reliability of civil infrastructure facilities based on condition-state data and fault-tree model. Reliab Eng Syst Saf 94(12):1962–1974
18. Chatterjee S, Carrera C, Lynch LA (1996) Genetic algorithms and traveling salesman problems. Eur J Oper Res 93:490–510
19. Liang F, Wong WH (2001) Real parameter evolutionary Monte Carlo with applications in Bayesian mixture models. J Am Stat Assoc 96:653–666
20. Metropolis N, Rosenbluth AW, Rosenbluth MN, Teller AH, Teller E (1953) Equations of state calculations by fast computing machines. J Chem Phys 21:1087–1092
21. Hastings WK (1970) Monte Carlo sampling methods using Markov chains and their applications. Biometrika 57(1):97–109
22. Geyer CJ (1991) Markov chain Monte Carlo maximum likelihood. In: Keramigas EM (ed) Computing science and statistics: proceedings of the 23rd symposium on the interface. Interface Foundations, Fairfax, pp 156–163
23. Cheung SH, Beck JL (2009) Bayesian model updating using hybrid Monte Carlo simulation with application to structural dynamic models with many uncertain parameters. J Eng Mech 135(4):243–255

Chapter 27
Formal Analysis of Critical Infrastructures by Structural Identification Using Constraint Programming Paradigm

Usman Rauf, Timothy Kernicky, Matthew J. Whelan, and Ehab Al-Shaer

Abstract Structural identification of civil infrastructures, using measured modal properties, remains a promising research field with many applications in performance-based civil engineering and structural health monitoring. In particular, either computationally swift or direct methods for identifying structural models from partially described and incomplete modal parameter estimates are of foremost interest to facilitate near real-time and reliable structural performance assessment and diagnostics. This paper proposes modeling structural systems as Constraint Satisfaction Problems (CSPs) for structural identification to solve for uncertain parameters in structural models. Consistent with measurement data, modal parameter estimates are treated as truncated both in terms of the number of modes measured and the number of measured degrees of freedom relative to the analytical model, which yields a challenging nonlinear inverse eigenvalue problem. Using nonlinear constraints and parameter bounds, the Constraint Programming approach is demonstrated to be capable of properly reconstructing estimates of both uncertain structural parameters and unmeasured modal parameters for a truss model with only a limited number of measured degrees of freedom.

Keywords Structural identification • Finite element model updating • Constraint programming • Constraint satisfaction problem • Structural health monitoring

27.1 Introduction

Vibration-based structural health monitoring has to-date been pursued largely through two primary approaches: data-driven methods and physics-based methods. The first approach relies on signal processing, machine learning, pattern recognition, or other data-based methods and models to statistically classify anomalous responses in direct measurements relative to an established baseline response [1, 2]. While these approaches have shown success across several real-world applications, they are often better at identifying the onset of anomalous response and localizing the likely region of the structure where the behavior originates than determining the severity of the damage in actionable, engineering quantities related to load capacity or service life [3, 4]. Alternatively, physics-based approaches rely on correlation and updating of an analytical model (often a high-fidelity finite element model) of the monitored structure to reconstruct estimates of structural parameter assignments that would lead to actionable quantification of damage severity. However, this approach toward structural identification by model updating of an inverse eigenvalue problem is particularly challenging due to the often limited number of sensors relative to degrees of freedom in the model, existence of non-unique solutions, and uncertain influence of measurement errors on the identified solution [5].

Specifically, the structural identification problem, or finite element model updating problem (FEMUP), has most commonly focused on application of the governing eigenvalue equation for undamped models of dynamic systems:

$$K_{n \times n} \Phi_{n \times n} = M_{n \times n} \Phi_{n \times n} \Omega^2_{n \times n} \tag{27.1}$$

U. Rauf • E. Al-Shaer
Department of Software and Information Systems, University of North Carolina at Charlotte,
9201 University City Boulevard, Charlotte, NC 28223-0001, USA

T. Kernicky • M.J. Whelan (✉)
Department of Civil and Environmental Engineering, University of North Carolina at Charlotte,
9201 University City Boulevard, Charlotte, NC 28223-0001, USA
e-mail: mwhelan3@uncc.edu

where K and M are the stiffness and mass matrices of the model, respectively, Φ are the eigenvectors or mode shapes associated with the matrices, and Ω^2 is the eigenvalue matrix, which contains the undamped natural frequencies. The FEMUP aims to leverage experimentally derived estimates of Φ and Ω to update the structural matrices, K and M, under constraints that ensure that the results are physically meaningful. As shown in the equation, the analytical eigenvector and eigenvalue matrices are square matrices, where n is the number of degrees of freedom in the model. However, it is often logistically unfeasible or impossible to experimentally identify more than a small subset of the total number of mode shapes and corresponding natural frequencies. Furthermore, it is also not practical to install a large enough array of sensors to measure all corresponding degrees of freedom in the analytical model. These limitations have significant practical consequences in the application of FEMUP, as the governing eigenvalue equation is reduced to:

$$K_{n\times n} \begin{bmatrix} \Phi_{s\times m} \\ \Phi^*_{(n-s)\times m} \end{bmatrix} = M_{n\times n} \begin{bmatrix} \Phi_{s\times m} \\ \Phi^*_{(n-s)\times m} \end{bmatrix} \Omega^2_{m\times m} \tag{27.2}$$

where s is the number of measured degrees of freedom or sensors and m is the number of experimentally reconstructed mode shapes. In this statement of the eigenvalue problem, the Φ^* terms indicate the unmeasured components of the eigenvectors, which can represent a significant number of additional unknowns, particularly if the number of degrees of freedom in the analytical model is much larger than the number of sensors used in the experimental test. To ensure physically meaningful results, FEMUP approaches generally prescribe the connectivity structure of the mass and stiffness matrices by assembling them by parameterization of a finite element model. In this way, the matrices are formed by elemental contributions that satisfy meaningful structural constraints:

$$\left[\sum_{j=1}^{p} \alpha_j K^j_{n\times n} \right] \begin{bmatrix} \Phi_{s\times m} \\ \Phi^*_{(n-s)\times m} \end{bmatrix} = \left[\sum_{j=1}^{p} \beta_j M^j_{n\times n} \right] \begin{bmatrix} \Phi_{s\times m} \\ \Phi^*_{(n-s)\times m} \end{bmatrix} \Omega^2_{m\times m} \tag{27.3}$$

where α and β are unknown scalars that are used to identify structural stiffness or mass of elements or groups of elements in the model that are uncertain or likely to be affected by structural damage. In this parameterized formulation, K^j is the stiffness contribution of the jth element normalized to α_j and M^j is the mass contribution of the jth element normalized to β_j.

The resulting form of the inverse eigenvalue problem presents a challenging nonlinear equation that cannot be directly solved. Numerous optimization schemes, including gradient-based methods [6], simulated annealing [7], genetic algorithms [8], and many other computational intelligence techniques [9], have been explored for producing solutions to the FEMUP problem. However, significant challenges remain before structural identification can serve as a reliable and attractive alternative to data-driven approaches to structural health monitoring. Predominantly, the challenges are associated with computational speed and the generation and evaluation of multiple or alternative solutions in the presence of measurement noise. Additional issues related to effective parameterization of the model for damage detection and uncorrected discretization and idealization errors inherent to the finite element model are also persistent challenges.

In this paper, we first explore a novel approach for structural identification based upon formalizing a set of nonlinear constraint equations from the governing eigenvalue problem and using the paradigm of Constraint Logic Programming (CLP) to solve for uncertain parameters in the structural model. By casting the FEMUP as a constraint satisfaction problem rather than an optimization problem, we seek to explore a potential paradigm shift in the structural identification method that may lead to an effective means of generating multiple or alternative solutions in the presence of measurement noise. An overview of the basic ideas essential to our approach to structural identification by nonlinear constraint satisfaction programming is provided followed by a preliminary application of the proposed methodology on a numerical model of a truss.

27.2 Methodology

In the domain of engineering sciences, many applications require finding all possible and isolated solutions satisfiable to a set of constraints over real numbers. The system may be non polynomial and the computational complexity to inherently solve such systems is NP-hard. These set of problems are called *Constraint Satisfaction Problems (CSPs)* [10–12]. Our aim is to model the FEMUP problem as a CSP and later to intersect mechanics-based constraints with advanced computer science

techniques to improve the performance and scalability of the approach. The following discussion provides some details about the basics of CSPs essential for the understanding of rest of the paper. A CSP can be defined as a *4-tuple <V,D,C,L>* where;

- $V = \{v_1, v_2, \ldots, v_n\}$ *is a set of variables*
- $D = \{d_1, d_2, \ldots, d_n\}$ *is a set of domains for prospective variables*
- $C = \{c_1, c_2, \ldots, c_n\}$ *is a set of constraints over the variables*
- *L is a set of labels that maps constraints to the pair of variables and corresponding domains, formally;* $L : C_i \rightarrow (v_i, d_i)$

Each variable v_i can assume any value in the corresponding non empty domain d_i. The constraint $c_i \in C$ is defined over a pair (v_i, d_i) through a label function $l_i \subset L$. In the process of finding a satisfiable solution, different values are assigned to the variable (in set V) from domain set (D) through constraint propagation algorithms (also called filtering/contraction algorithms). The evaluation of the label (true/false) determines whether the corresponding assignments to variables for a given constraint lead to a satisfiable solution or not. While assigning values to different variable (through "systematic search process") consistency algorithms [13] take into account whether any violation of constraints has occurred during any assignment. If it is determined that there is constraint violation, backtracking is performed to find a new satisfiable assignment. This whole process is called constraint propagation [13]. The paradigm for solving CSPs through integration of Systemic Search and Arc Consistency techniques is called Constraint Programming (CP) [10–12]. Therefore, constraint programming is a domain in which the relationships among variables are defined in the form of constraints. It differs from conventional imperative programming since, rather than defining the flow of the program in sequential steps, it describes the criteria which all solutions must adhere.

A sub-domain of constraint programming that deals with variables over the set of reals and integrates interval arithmetic with conventional constraint programming is called Interval Constraint Programming (ICP). Interval arithmetic, or interval based computation, is a method that has been an area of interest for mathematicians since early 1930s as a means of placing bounds on round off errors in mathematical computations and measurement errors in experimentation [14–16]. The notion of interval arithmetic combined with constraint programming can be very useful. In interval arithmetic, variable functions, and relations among them (constraints) are defined over intervals rather than exact values. Therefore, rather than defining the exact value of a variable/constant it is defined over an interval, assuming that it may take any value within that interval. The Cartesian product of intervals (Interval Vectors) generates boxes (cf. Eq. 27.5), which can be contracted according to given set of constraints using the concepts from contractor programming [17]. Formally, a variable *"X"* defined over an interval and the realization of boxes (cf. Fig. 27.1) can be explained as follows:

$$X : [a, b] \rightarrow \{X \in \mathbb{R} | a \leq X \leq b\} \tag{27.4}$$

$$[X] = [x_1] \times [x_2] \times [x_3] \ldots \times [x_n] \tag{27.5}$$
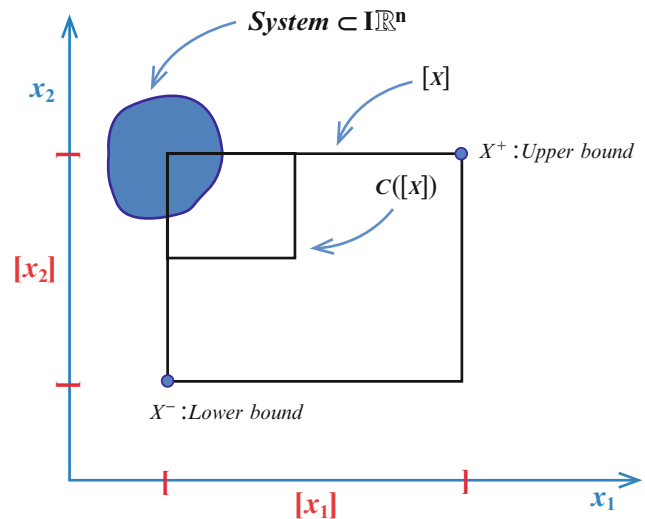
Fig. 27.1 Realization of box $[X] = [x_1] \times [x_2]$ and its contraction

---

Algorithm 27.1 Branch and Prune Algorithm

$List \leftarrow \{[X_0]\}$ where $[X_0]$ is an initial box and $List$ is a construct which contains all boxes;
while $List \neq \emptyset$ **do**

    Select *box* $[X]$ from *List*;

    if *box* $[X] \neq \emptyset$ *and diameter* $([X]) < \epsilon;$ **then**

        $[X]$ may contain a solution*;

    end

    if *box* $[X] \neq \emptyset$ *and diameter* $([X]) > \epsilon;$ **then**

        Bisect$([X])$ into $[X_1]$ and $[X_2]$ on one dimensional variable

    end

    $List \leftarrow List \bigcup [X_1] \bigcup [X_2];$

end

---

*Note that Epsilon (ϵ) is a threshold value which is being provided by interval analysis methods (Interval Newtonian), which certifies the existence of a solution in a box [14, 15, 21]. Figure 27.1 gives a realization of this algorithm, demonstrates how branch and prune algorithms shave an interval, and illustrates how bisection is performed without losing potential solutions.

The main challenges in CSPs are to guarantee correctness and completeness along with the assurance of termination of the solving procedure. In the past, CSPs have been approached by several different methods, e.g., Continuation methods [18], Constraint satisfaction methods [12], and interval methods [19–22]. In the most state-of-the-art approaches, the most critical aspect of the framework is generally the branch and prune algorithms, which only require initial ranges of the variables and constraints over them as an input. Typically branch and prune algorithm are a recursion over two steps:

- Pruning the search space
- Making a choice to generate two or more sub-problems

Pruning ensures that some local consistency holds. In simpler terms, pruning reduces/contracts/filters an interval/box (search space) only when it can prove that the upper bound and lower bound of a box does not satisfy some given constraints. Formally: $X = [X_{lower}, X_{upper}]$ and $c = \{x_1, x_2, \ldots, x_n\}$; where $c \in C$ (set of constraints over variables). Whenever $c = \{x_1, x_2, \ldots, x_n\}$ does not hold for any value $V \in X = [X_{lower}, X_{upper}]$ then X may be reduced or shrink-ed to $X' = [X'_{lower}, X'_{upper}] \subset X$. Formally, the algorithm can be defined in following steps:

One recent effort towards this integration is Contractor Programming [17]. The contractors can be viewed as a mathematical function that takes a system (box) as an input and shrinks/contracts it according to given set of constraints. Contractor yields a reliable set of satisfiable solutions since they must satisfy properties of soundness and completeness. Formal definition of a contractor and the properties can be defined as follows: A contractor (**C**) is a function from $\mathbf{C} : \mathbb{IR}^n \rightarrow \mathbb{IR}^n$, where $\mathbb{IR}$ is interval over reals, with the following properties:

- $\forall [X] \in \mathbb{IR}^n : \mathbf{C}([X]) \subset [X]$; *where* $\mathbf{C}([X])$ *represents box* $[X]$ *after contraction*
- $\mathbf{C}([X]) \bigcap System = [X] \bigcap System$

The first property ensures that the contraction algorithm or procedure is sound and the result achieved after the contraction contains the subset of original box (which means it remains within that box) (cf. Fig. 27.2). The second property elaborates the completeness of the contraction algorithm/procedure, which states that no potential solution is lost after contraction is performed. Adhering to these two properties, contractor programming yields reliable results with a guarantee that feasible solutions are not lost within the search space (cf. Fig. 27.1). In application, the contraction algorithm is performed repeatedly until a desired time limit or interval precision on the solutions is reached.

For the detailed understanding of the reader, we present a small example of a ring function solved using the IBEX C++ library [17] to implement the concept of Contractor Programming. Figure 27.2 illustrates how satisfiable solution space is explored for a given function $f(x, y) = x^2 + y^2$ and a set of constraints $\{x^2 + y^2 \leq 60, x^2 + y^2 \geq 20\}$. Contraction starts in an initial box $([-10, 10] \times [-10, 10])$, then by recursively applying (branch and prune) algorithms the unsatisfiable regions are shaved/pruned around the external and internal edges of the ring.

27.3 Numerical Example

To illustrate the application and performance of the nonlinear constraint satisfaction approach, the partially described inverse eigenvalue problem is solved using numerically generated data from an analytical model of a first-order statically indeterminate truss (Fig. 27.3). The analytical model is developed using properties for steel members (E = 200 GPa,

Fig. 27.2 An enclosure of function, $f(x, y) = x^2 + y^2 \in$ ($[-10, 10] \times [-10, 10]$), and its contraction according to set of constraints $\{x^2 + y^2 \leq 60,$ $x^2 + y^2 \geq 20\}$

$$A_{AB} = 40 \, cm^2 \qquad A_{DE} = 40 \, cm^2$$
$$A_{BC} = 50 \, cm^2 \qquad A_{CD} = 50 \, cm^2$$
$$A_{AH} = 20 \, cm^2 \qquad A_{EF} = 20 \, cm^2$$
$$A_{BH} = 10 \, cm^2 \qquad A_{DF} = 10 \, cm^2$$
$$A_{CH} = 60 \, cm^2 \qquad A_{CF} = 60 \, cm^2$$
$$A_{HG} = 30 \, cm^2 \qquad A_{FG} = 30 \, cm^2$$
$$A_{CG} = 20 \, cm^2$$
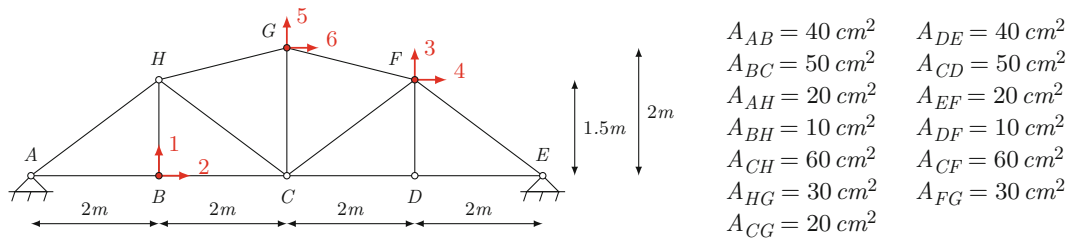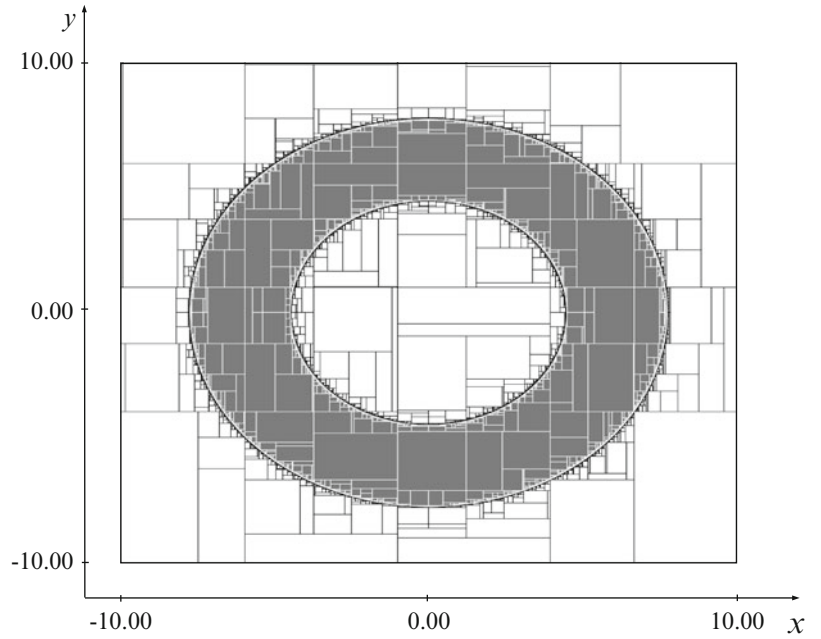
Fig. 27.3 Numerical example of a gambrel truss with 12 unrestrained degrees of freedom. Locations of synthetically measured degrees of freedom are indicated with *red arrows* (Color figure online)

$\rho = 7,850 \, \text{kg/m}^3$) and symmetric, arbitrary assignments of cross-sectional areas (although the structural symmetry is not applied as a constraint in the implementation of the CSP). The IBEX C++ library was used to implement a contractor programming approach to generate feasible solutions to nonlinear constraint satisfaction problems with interval arithmetic [23]. Solution times are reported from application on a Dell Latitude E6410 notebook computer with a 2.67 GHz Intel M560 i5 processor with 4GB of RAM. It should be noted that the default solver in the IBEX library utilizes only one processor core. However, strategies can be developed to implement multi-threading of this constraint solver for improved performance and this is a current area of development being pursued by the research team to improve the scalability of the methodology.

For this inverse eigenvalue problem, the truss was parameterized into the 13 member contributions where the stiffness of each element was taken to be an uncertain parameter through scaling of the cross-sectional area. The mass of each element was assumed to be known *a priori*, since it is often the case that a reasonably accurate estimate of the mass matrix can be assembled from the geometry and unit weights of the as-built design. From this assumption and the modified governing eigenvalue problem adapted for experimental application (Eq. 27.3), the following matrix of constraint equations is developed:

$$\left| \left[\sum_{j=1}^{p} \alpha_j K_{n \times n}^j \right] \begin{bmatrix} \Phi_{s \times m} \\ \Phi_{(n-s) \times m}^* \end{bmatrix} - M_{n \times n} \begin{bmatrix} \Phi_{s \times m} \\ \Phi_{(n-s) \times m}^* \end{bmatrix} \Omega_{m \times m}^2 \right| \leq \epsilon_{n \times m} \tag{27.6}$$

where α_j is the cross-sectional area of the jth member if the elemental contribution to the stiffness matrix, K^j, is formulated from the unit cross-sectional area. Notice that the constraint equation is formulated as an inequality constraint using a relaxation parameter, ϵ. This relaxation allows the constraint equation to accommodate numerical precision errors as well

as experimental noise and uncertainty in the eigen information estimates. In addition to the governing eigenvalue problem equation, the mass orthogonality of the eigenvectors was also introduced as an additional set of constraints. As with the statement of the governing eigenvalue problem, the mass orthogonality constraint was stated in the form of an inequality:

$$\left| \begin{bmatrix} \Phi_{s\times m} \\ \Phi^*_{(n-s)\times m} \end{bmatrix}^T M_{n\times n} \begin{bmatrix} \Phi_{s\times m} \\ \Phi^*_{(n-s)\times m} \end{bmatrix} \right| \leq \begin{bmatrix} \infty & & \gamma \\ & \ddots & \\ \gamma & & \infty \end{bmatrix} \tag{27.7}$$

where γ is a user-defined relaxation. Note that the constraint equations on the diagonal are not implemented as the modal masses of the structure are unknown and therefore cannot serve as either an equality or inequality constraint. In the practical application of this constraint to measurement data, the relaxation should accommodate the experimental reality that measured mode shapes are rarely exactly orthogonal. The inclusion of the mass orthogonality constraint does not actually represent the introduction of unique constraint equations since the orthogonality is implicit in Eq. 27.6. However it has empirically been found to improve the computational speed of the nonlinear constraint satisfaction processor.

27.3.1 Application to Partially Described Eigenvalue Problem with Incompletely Measured Mode Shapes

To demonstrate the performance of the proposed approach for structural identification, a numerical case is explored using placement of three biaxial accelerometers on the nodes B, F, and G of the truss, as illustrated in Fig. 27.3. This results in incompletely measured mode shapes, where only half of the analytical degrees of freedom in the model have associated eigenvector measurements. Furthermore, the inverse eigenvalue problem is treated as partially described in the example with only the first five natural frequencies and partially complete modes being taken as known. This particular example results in a matrix of 60 constraint equations from application of Eq. 27.6 and a total of 43 unknowns (13 member cross-sectional areas and 30 missing eigenvector values across the five modes). Parameter bounds for the cross-sectional areas were assigned using $0\,\text{cm}^2$ as the lower bound for every element and $80\,\text{cm}^2$ as the upper bound. Since the mode shapes were unit normalized prior to assignment in the constraint equations, the unknown entries in the incomplete eigenvectors were assigned bounds of $[-1, 1]$. Under these conditions with a requested interval precision of 0.01, the inverse eigenvalue solution was returned in just over 88 s and successfully identified the actual cross-sectional areas of the members (Table 27.1). Furthermore, the missing entries in the first five eigenvectors were reconstructed exactly (Fig. 27.4).

Table 27.1 Identified feasible intervals for cross-sectional areas of members from case with five incompletely measured modes

A_{AB}	40	[39.9908, 40.0069]	A_{DE}	40	[39.9627, 40.0232]
A_{BC}	50	[49.9824, 50.0142]	A_{CD}	50	[49.9553, 50.0218]
A_{AH}	20	[19.9922, 20.0075]	A_{EF}	20	[19.9979, 20.0014]
A_{BH}	10	[9.9999, 10]	A_{DF}	10	[10, 10]
A_{CH}	60	[59.9889, 60.0091]	A_{CF}	60	[59.9970, 60.0014]
A_{HG}	30	[29.9965, 30.0044]	A_{FG}	30	[29.9985, 30.0022]
A_{CG}	20	[19.9884, 20.0175]			
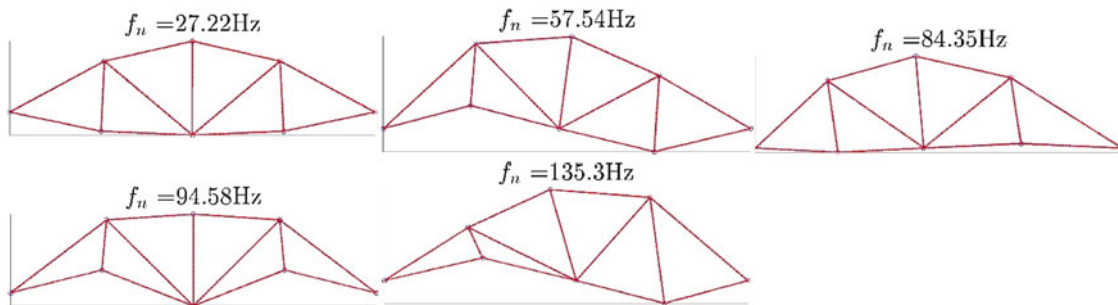
Fig. 27.4 Updated mode shapes plotted over the actual mode shapes of the original model (exact reconstruction of missing components of eigenvectors)
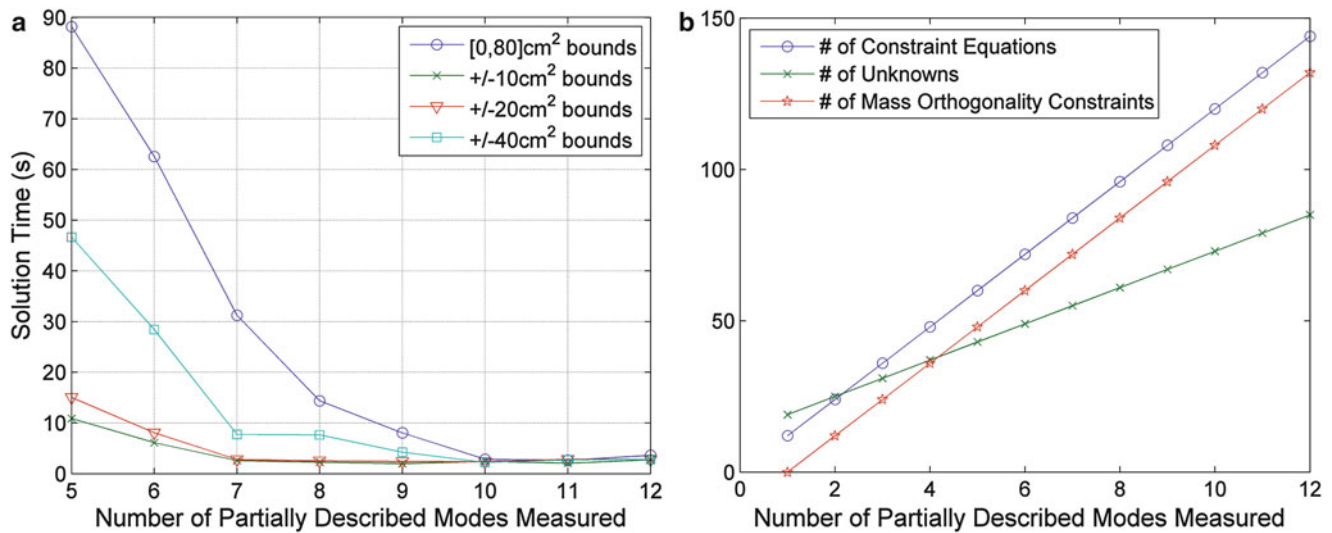
Fig. 27.5 (**a**) Performance of nonlinear constraint satisfaction processor with different parameter bounds and number of partially described modes included in the constraint equation; (**b**) Relationship between number of constraint equations and number of unknowns generated for the number of partially described modes measured

The prior example represents a case more similar to a generalized inverse eigenvalue problem rather than FEMUP since the stiffness of elements can generally be predicted within much tighter relative bounds than the wide $[0, 80]\,\text{cm}^2$ range provided for all elements. To explore the influence of the parameter bounds on the required solution time, a series of analyses were performed using tighter intervals around the actual member cross-sectional areas. The application of these bounds was implemented using $[max\{0, A_{element} - \theta\,\text{cm}^2\}, A_{element} + \theta\,\text{cm}^2]$, where the lower bound formula ensures that no element is allowed to be assigned negative cross-sectional area. Analyses were performed for $\theta = \{10, 20, 40\}$ for all partially described inverse problems generated from the case of all 12 modes down to only 5. The solution times are reported in Fig. 27.5a, which illustrates the significant improvement in performance of the constraint satisfaction processor when the bounds are more tightly assigned around the expected values. With less than 5 modes included in the formulation of the constraint equations, the performance of the nonlinear constraint processor suffers a significant increase in required solution time. Under these conditions, the number of mass orthogonality constraints that aid in the contraction of the solution by operating on the intervals for the missing eigenvector data are less than the number of unknowns in the system of equations (Fig. 27.5b).

27.3.2 Generation of Multiple Solutions

In addition to being able to generate feasible solutions to the partially described inverse eigenvalue problem with incompletely measured modes, the constraint satisfaction approach has also been found to be very effective at identifying non-unique or multiple solutions to the inverse eigenvalue problem. To illustrate this capability, a second analysis was performed using only the first two modes of the structure as measurements. In this analysis, only the first two mode shapes were applied in the constraint equation, but they were applied as fully described modes. In other words, this particular analysis considers there to be a sensor measuring all twelve of the unrestrained degrees of freedom in both modes. The nonlinear constraint satisfaction processor was run using a required interval precision of $0.1\,\text{cm}^2$ on the uncertain area assignments for all 13 members of the truss and a total of 285 solutions were generated in 2.25 s. The interval boxes for all solutions are presented in Fig. 27.6. Note that the solutions for all cross-sectional areas other than $A_{AB}, A_{BC}, A_{CD}, A_{DE}$ were returned as exact solutions. Furthermore, the variable cross-sectional areas that yield non-unique solutions correspond to those of the four bottom chords of the truss and the feasible parameter assignments are symmetric, which is expected.
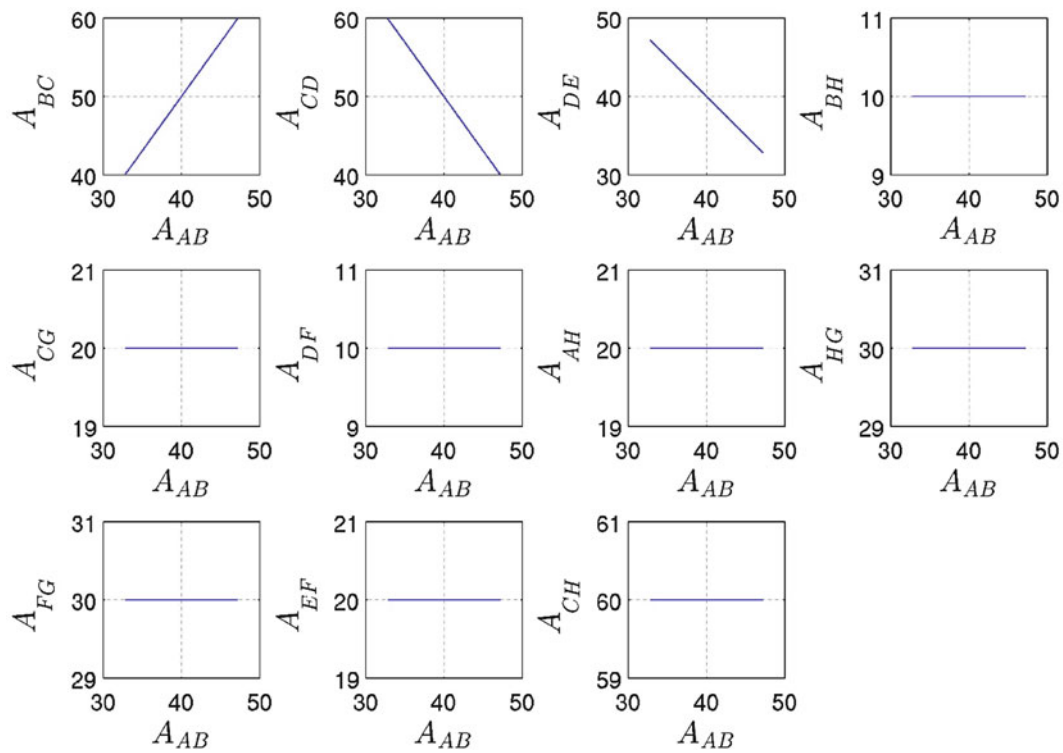
Fig. 27.6 Generation of multiple solutions from a non-unique inverse eigenvalue problem (all degrees of freedom measured, but only the first two eigen information pairs provided as measurement). A total of 285 interval solutions are presented in these plots

The capability to identify multiple solutions is particularly powerful for several reasons:

1. It can be used to readily identify whether or not the solution to the inverse eigenvalue problem is unique or non-unique;
2. In non-unique problems, the set of feasible solutions can be examined to determine individual parameter assignments that may still be unique (such as the case for all cross-sectional areas for members other than the bottom chords in the numerical example) and to determine the relative sensitivity of the non-unique parameter assignments; and
3. In unique problems, alternative solutions can be generated by adjusting the relaxation parameter in Eq. 27.6 to explore whether using partitioner input and heuristics can provide a means for evaluating whether alternative solutions with more physical likelihood than the global minimum exist. This is particularly important within practical applications due to the presence of measurement noise and uncertainty and the propagation of these errors in the constraint equations.

Delivering these capabilities has been identified as a key challenge in applied structural identification [8], but has been a serious limitation in the application of global optimization approaches to structural identification. By proposing a paradigm shift from optimization-based techniques for model updating to a constraint satisfaction problem, the new approach appears to offer unique advantages that may overcome critical challenges in the applied use of structural identification for performance-based civil engineering and structural health monitoring.

27.4   Summary

Nonlinear Constraint Programming with interval arithmetic and contractors has been explored for application in finite element model updating, or structural identification, of civil infrastructure systems. Since this approach is different than the global optimization techniques that are most pervasive in structural identification, an overview of Constraint Satisfaction Problems has been presented alongside an example application to a numerical problem of an indeterminate truss. The methodology has been shown to yield solutions to the challenging nonlinear partially described inverse eigenvalue problem with incomplete mode shape measurement. Furthermore, it has been shown that the approach can also identify non-unique and multiple solutions to the inverse eigenvalue problem without any additional computational burden. While this approach is still in the early stages of development, validation, and refinement, the capabilities demonstrated in this numerical example suggest that this approach offers significant promise as a potential breakthrough toward facilitating FEMUP of structures and, ultimately, physics-based structural health monitoring.

References

1. Worden K, Manson G (2007) The application of machine learning to structural health monitoring. Philos Trans Roy Soc A Math Phys Eng Sci 365(1851):515–537
2. Farrar CR, Worden K (2012) Structural health monitoring: a machine learning perspective. Wiley, Chichester
3. Whelan MJ, Janoyan KD (2009) In-service diagnostics of a highway bridge from a progressive damage case study. J Bridge Eng 15(5):597–607
4. Gul M, Catbas FN (2010) Damage assessment with ambient vibration data using a novel time series analysis methodology. J Struct Eng 137(12):1518–1526
5. Catbas FN, Ciloglu SK, Hasancebi O, Grimmelsman K, Aktan, AE (2007) Limitations in structural identification of large constructed structures. J Struct Eng 133(8):1051–1066
6. Mottershead JE, Link M, Friswell MI (2011) The sensitivity method in finite element model updating: a tutorial. Mech Syst Signal Process 25(7):2275–2296
7. Levin R, Lieven N (1998) Dynamic finite element model updating using simulated annealing and genetic algorithms. Mech Syst Signal Process 12(1):91–120
8. Caicedo JM, Yun G (2011) A novel evolutionary algorithm for identifying multiple alternative solutions in model updating. Struct Health Monit 10(5):491–501
9. Marwala T (2010) Finite-element-model updating using computional intelligence techniques. Springer, New York
10. Dechter R (2003) Constraint processing, 1st edn. Morgan Kaufmann, San Mateo
11. Rossi F, van Beek P, Walsh T (2006) Handbook of Constraint programming (Foundations of artificial intelligence). Elsevier Science, New York
12. Hentenryck PV (1999) The OPL optimization programming language. MIT Press, Cambridge
13. Hyvnen E (1992) Constraint reasoning based on interval arithmetic: the tolerance propagation approach. Artif Intell 58:71–112
14. Hansen E (2003) Global optimization using interval analysis, 2nd edn. CRC Press, Boca Raton
15. Jaulin L, Kieffer M, Didrit O, Walter E (2001) Applied interval analysis. Springer, New York
16. Kearfott R (1996) Rigorous global search: continuous problems. Springer, Berlin
17. Chabert G, Jaulin L (2009) Contractor programming. Artif Intell 173:1079–1100
18. Verschelde J (2003) The database of polynomial systems
19. Hensen ER (1992) Global optimization using interval analysis, 1st edn. CRC Press, Boca Raton
20. Krawczyk R (1969) Newton-algorithmen zur bestimmung von nullstellen mit fehlerschranken. Computing 4:187–201
21. Moore R (1966) Interval analysis. Prentice Hall, Englewood Cliffs
22. Neumaire A (1991) Interval methods for system of equations, 1st edn. Cambridge University Press, Cambridge
23. Chambert G (1999) IBEX C++ library for constraint processing over real numbers

Chapter 28
Model Updating of a Nine-Story Concrete Core Wall Building

Steve McDonald, Lisa Tobber, Adam Gerber, and Carlos E. Ventura

Abstract This paper describes the model updating techniques utilized for a nine-story concrete core wall building located on the University of British Columbia campus in Vancouver, Canada. Constructed in 1963, in a region of high seismic risk, the tower is slated for retrofit in the near future. The first five floors of the tower are connected to an adjacent, recently retrofitted five-story building. A structural model was created in finite element software using the original design documents. The dynamic properties of the structure were then determined experimentally through an ambient vibration test. Model updating was implemented to better match the model predictions to experimental results. The model updating targeted many parameters for specific structural elements to arrive at a strong correlation with the experimental results. A total of seven natural frequencies were matched.

Keywords Model updating • Sensitivity analysis • Structural parameters • Ambient vibration • Modal analysis

28.1 Introduction

Located in Vancouver, at the University of British Columbia, there exists a nine-story concrete core wall building that was built in 1963. Because Vancouver is an area of high seismic risk, and the tower was completed before modern seismic design considerations, the building will be undergoing a seismic retrofit. This study seeks to develop a calibrated analytical model of the tower to be used for future research purposes.

This paper presents the results of an updating study performed on a finite element model of the office tower. Model updating incorporates experimental data with analytical data together to arrive at a more representative finite element model. Ambient vibration testing was conducted by researchers from the University of British Columbia, and the analysis was completed using ARTeMIS Modal V3.5 [1]. The finite element model was created using SAP2000 [3] and converted into FEMTools [4] for its robust model updating features.

28.2 Description of Structure

The tower is a reinforced concrete structure that rises nine stories above grade and one below. It is utilized for office space on floors 1–8, with conference rooms occupying the ninth floor. The tower was originally eight stories after construction in 1963; however, a renovation was conducted in 2010 in order to add a steel-framed penthouse that makes up the current ninth floor. Figure 28.1 shows the tower as it stands today.

With the exception of the penthouse floor, the structure consists of reinforced concrete two-way slabs supported on stairwell and elevator walls and evenly spaced columns along the length. The concrete stair and elevator core walls are continuous throughout the height of the tower. In the north–south direction, there are four discontinuous concrete perimeter walls that are supported by concrete columns between the ground and second level and continue to the eighth floor. The exterior beams on the north and south faces of the tower extend the length of the tower. Above the first story, the beams are connected to each other with architectural precast concrete mullions.

The eastern side of the tower is attached at every floor level to a five story adjacent building (classroom block) that is used primarily as classroom space. The classroom block recently underwent an extensive seismic retrofit. The low aspect ratio,

S. McDonald • L. Tobber • A. Gerber (✉) • C.E. Ventura
Civil Engineering Department, University of British Columbia, 6250 Applied Science Lane, Vancouver, BC V6T 1Z4, Canada
e-mail: adam@gerber.ca

Fig. 28.1 Office tower and
added penthouse

Table 28.1 Summary of mode
shapes using FDD method

Mode	Period (s)	Freq. (Hz)	Description
1	1.14	0.88	Site period[a]
2	0.39	2.56	1st lateral
3	0.36	2.81	1st longitudinal
4	0.31	3.25	1st torsional
5	0.22	4.50	Torsional
6	0.17	5.75	Torsional
7	0.14	7.38	2nd longitudinal
8	0.11	9.00	2nd torsional
9	0.09	11.00	2nd lateral
10	0.07	14.13	3rd longitudinal

[a]Rigid body structural mode

coupled with the retrofitted steel braced frames as the lateral load resisting system, causes the classroom block to be very stiff in the north–south direction. In the southeast corner of the classroom block there are nine-inch thick concrete walls that extend the height of the tower. The tower connects to these walls at each of the first five floor levels through concrete beams. Since no seismic releases or seismic isolation gaps were observed, it was expected that the connection to this building could influence the dynamic behaviour of the tower.

28.3 Summary of Ambient Vibration Test Results

Vibration measurements were performed on March 15, 2014 by researchers from the University of British Columbia. For a detailed testing procedure, refer to [5]. A total of ten mode shapes were identified using the FDD method. Table 28.1 displays the resulting modes with their associated periods and frequencies.

28.4   Finite Element Model

A 3D finite element model was created using SAP2000 V15 [3]. The model consists of concrete beams, columns, walls, and slabs with some steel sections at the penthouse level. This section discusses the assumptions made for modelling the office tower. A typical floor plan of the tower itself is shown in Fig. 28.2, and an isometric view of the model can be seen in Fig. 28.3. The main tower is about 30.5 m by 16 m and the story height is approximately 2.7 m.

28.4.1   Material Properties

All of the materials were assumed to be in the elastic range and uncracked. The modulus of elasticity for structural steel was assumed to be approximately 200,000 MPa. The modulus of elasticity for the concrete was estimated based on the 28-day compressive strength; however, the compressive strength had to be estimated because it was not specified in the design drawings. ASCE 41-06 [2] provides lower-bound compressive strengths for concrete, so a value of 34.5 MPa was used, resulting in a modulus of elasticity of 28 GPa.
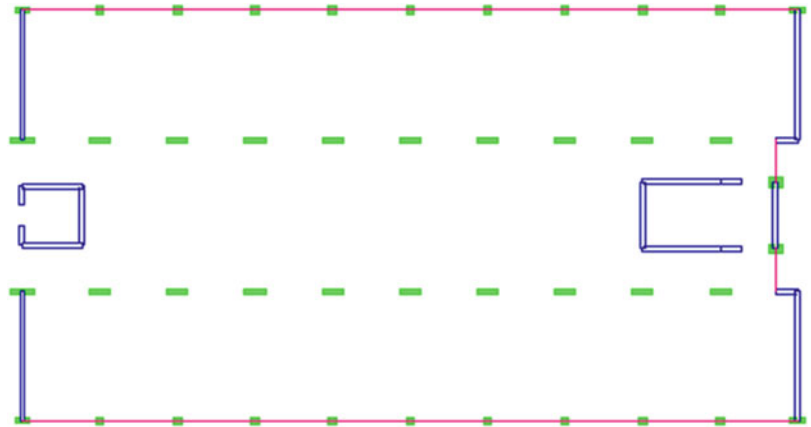
Fig. 28.2 Typical floor plan of the tower structure [3]
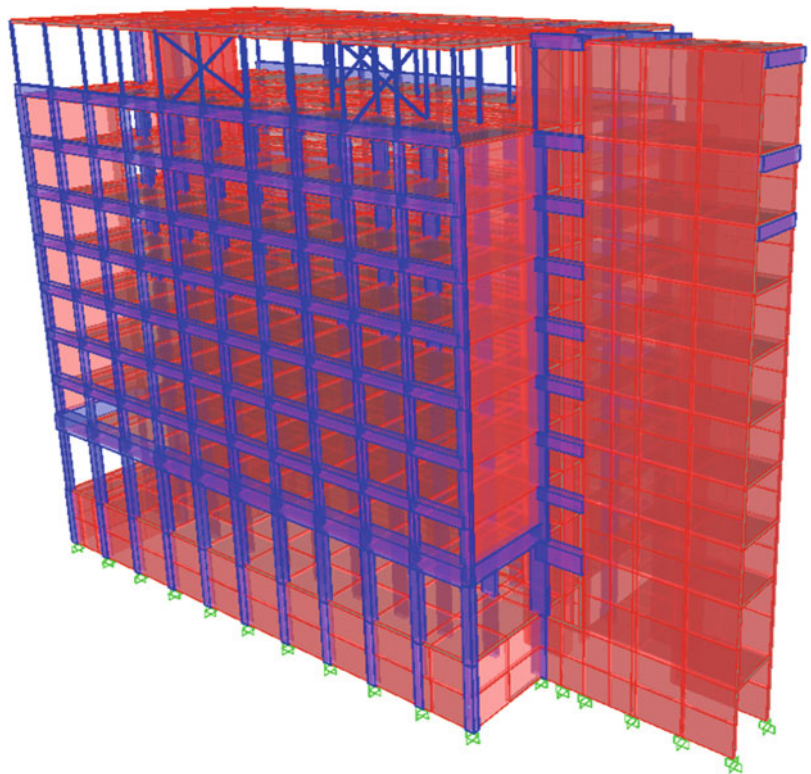
Fig. 28.3 SAP2000 model of structure [3]

Fig. 28.4 Finite element model depicting embedded walls and classroom block [3]
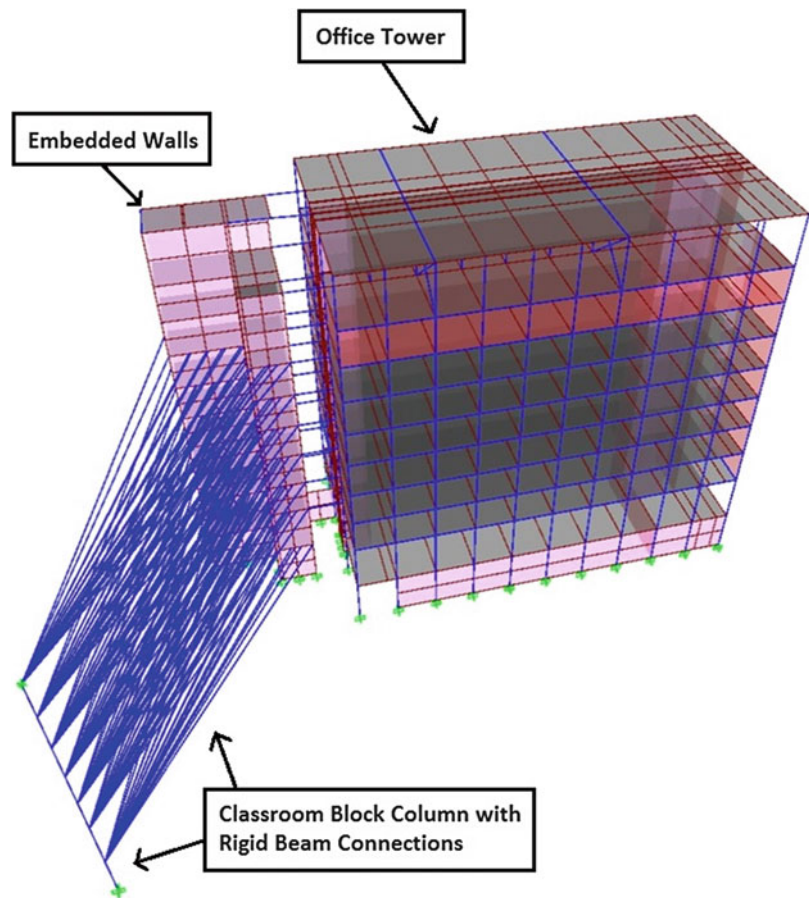
28.4.2 Elements

All of the columns and beams were modelled as elastic frame elements with expected elastic modulus values. The wall and slab elements were modelled as elastic quad shell elements. Mullions were assumed to provide some stiffness, so they were modelled as elastic truss elements. For simplicity, a rigid diaphragm was used for the roof despite it being constructed out of steel decking.

In order to model the interaction between the connected classroom block and the tower, various assumptions were made. The concrete walls embedded in the southwest end of the classroom block were modelled because these walls are of considerable stiffness and they were assumed to have a significant structural influence. The remainder of the connecting classroom block was modelled as a singular column located at its centre of geometry. This column represented the braced-framed retrofitted structure, which was assumed to have similar behaviour as a shear beam element. To connect the single classroom block element to the embedded walls, rigid beams were used at each joint. The classroom block column, rigid beams, and embedded walls can be seen in Fig. 28.4.

28.4.3 Modal Analysis Results

The modal analysis results from SAP2000 are displayed in Table 28.2, which compares with the experimental testing results.

Table 28.2 SAP2000 model results vs. AVT results

Mode	Description	SAP2000 results freq. (Hz)	AVT results freq. (Hz)	Difference (%)
1	Site period*	–	0.88	–
2	1st lateral	2.05	2.63	−22.05
3	1st longitudinal	3.16	2.78	13.67
4	1st torsional	Not found	3.23	–
5	Coupled torsional-translational	5.63	4.55	23.74
6	Coupled torsional-translational	6.08	5.88	3.40
7	2nd longitudinal	7.14	7.14	0.00
8	2nd torsional	7.38	9.09	−18.81
9	2nd lateral	8.93	11.11	−19.62
10	3rd longitudinal	8.47	14.29	−40.73

* Site period not included in SAP2000 model

Fig. 28.5 Finite element model paired with the test model [4]
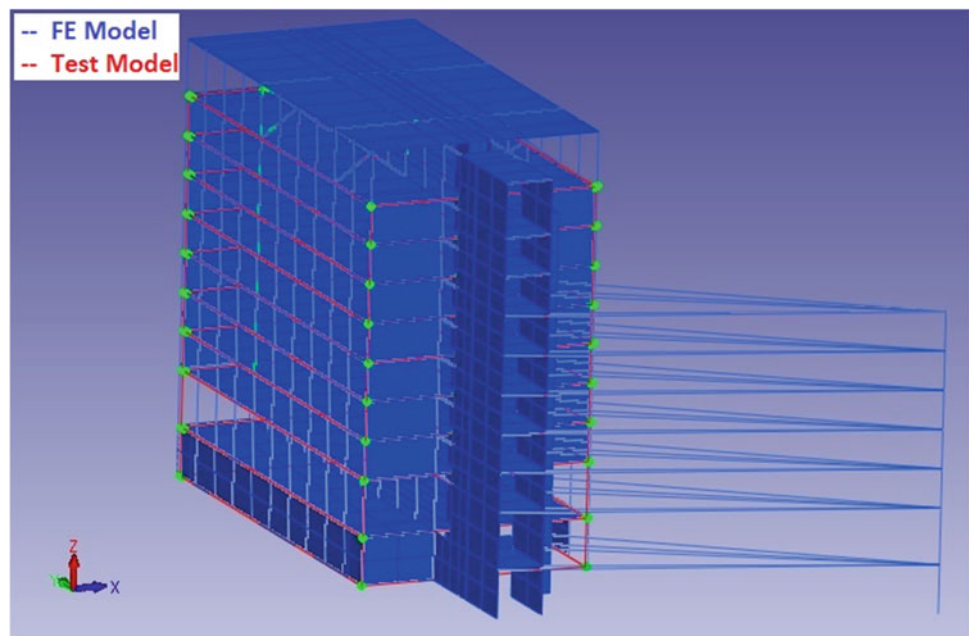
28.5 Finite Element Model Updating

The SAP2000 model was transferred into FEMTools for the updating procedure. There was a noticeable difference in the SAP2000 frequency results when compared with the FEMTools results. This may be due to the algorithms for modal analysis for each program and the modeling assumptions incorporated into each program. Future work may involve exploring the source of this variation and accounting for it. For the purposes of this study, the FEMTools model was used for calibrating.

The model updating of the finite element model involved defining parameters to update and response quantities as the target result. The finite element model and the test model were superimposed as shown in Fig. 28.5, and mode shapes from both were paired together based on MAC values.

28.5.1 Response Quantities

This study focused mainly on refining the frequencies of the mode shapes obtained from AVT results. The mode shapes were paired between the finite element model and the AVT results based on their MAC values; however, some modes observed from the experimental results were not identified in the finite element model. The modal frequencies targeted for each step of updating varied depending on the results of the update step. At the beginning, only the first two mode shapes were targeted and calibrated, and then more mode shapes were added after each update step in order to reach convergence. In total, seven modes were targeted for the updating procedure.

28.5.2　Parameters to Update

It was decided to separate the structure into six sets, where each set included similar structural components. The sets were separated by the following:

- Beams and columns
- Elevator core walls
- Shear walls
- Classroom block "column"
- Rigid beams from classroom block
- Connecting beams between embedded walls and the tower

Of particular importance are the classroom block column and the rigid beams connected to that column, because these were large assumptions made to try to account for the coupling of the two buildings. For each set, a sensitivity analysis was conducted to determine which properties would affect the dynamic behaviour the most. In total, eight different parameters were chosen to use for applicable set groups. These parameters are as follows:

- Modulus of elasticity
- Mass density
- Cross sectional area
- Shear stiffness area
- Moment of inertia about x, y, and z
- Shell thickness
- Poisson's ratio
- Shear modulus

This resulted in 45 different parameters. The sensitivity analysis plot is shown in Fig. 28.6. An attempt was made to reduce the amount of parameters to only the most sensitive ones, but unfortunately convergence could not be reached. Therefore, further investigation would be needed.
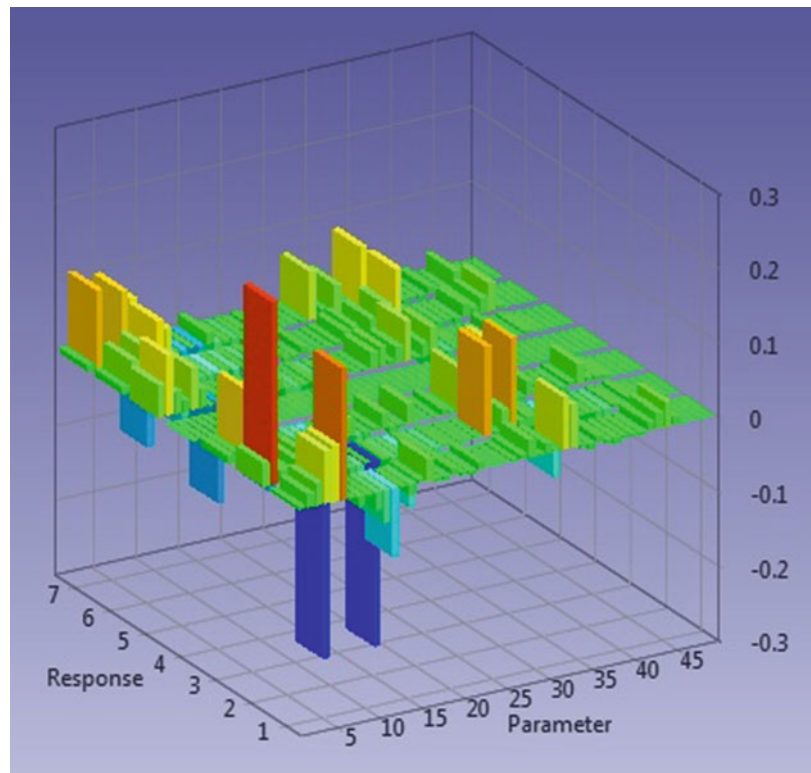
Fig. 28.6 Sensitivity plot for all parameters chosen [4]

Table 28.3 Initial FEMTools model compared to the updated FEMTools model

Mode	Description	FT results (initial) freq. (Hz)	AVT results freq. (Hz)	Difference (%)	FT results (updated) freq. (Hz)	Difference (%)
1	Site period	–	0.88	–	–	–
2	1st lateral	3.05	2.56	18.99	2.56	−0.13
3	1st longitudinal	4.42	2.81	57.11	2.84	0.95
4	1st torsional	–	3.25	–	–	–
5	Torsional	8.16	4.50	81.28	4.49	−0.25
6	Torsional	–	5.75	–	–	–
7	2nd longitudinal	8.87	7.38	20.23	7.35	−0.37
8	2nd torsional	12.42	9.00	37.96	8.93	−0.81
9	2nd lateral	13.56	11.00	23.23	11.72	6.51
10	3rd longitudinal	10.08	14.13	−28.66	14.25	0.85

28.5.3   Results

After the automatic updating was completed, a good correlation was reached in terms of frequency for the seven paired mode shapes. The MAC value ranged from 46.5 to 85.7 %, with an average of 67.9 % (Table 28.3).

There were some significant parameter changes to the system during this update, specifically with the classroom block column. The elastic modulus of the classroom block column was decreased by 57 %, its moment of inertia about the y-axis decreased by 51 %, and its shear modulus decreased by 47 %, and this is understandable because the representation of the classroom block was one of the larger uncertainties of the finite element model. Most of the remaining parameters were increased or decreased in the range of 1–17 %. For example, the elevator core walls had its modulus of elasticity increase by 13 %, thickness increase by 17 %, and shear modulus increase by 10 %.

28.6   Summary

This paper presented the results of a model updating study on a reinforced concrete core wall office tower. The office tower is connected to a five-story classroom block that was recently retrofitted, so it was very important to account for the dynamic coupling effects that the classroom block has on the tower. A finite element model was created with assumptions made in an effort to model the interaction with the adjacent classroom block, and this was known to be a large source of uncertainty in the model. Utilizing past experimental testing results, the finite element model was calibrated by modifying many parameters. The largest parameter changes were related to the classroom block "column" assumption, with significant changes to its stiffness.

As a result, close correlation was made with seven mode shapes, leaving an average error of 1 %. Future research with the new calibrated model will include linear and nonlinear dynamic analyses using a large set of ground motions. With the results of the dynamic analyses, researchers will be able to see if any members are being overstressed.

References

1. Artemis Modal Software (1999–2014). Structural Vibration Solutions, Inc. Retrieved from http://www.svibs.com/
2. ASCE/SEI 41 (2007) Seismic rehabilitation of existing buildings. American Society of Civil Engineers, Reston
3. Computers and Structures Inc. (2014) SAP2000 V15. Retrieved from http://www.csiamerica.com/products/sap2000
4. Dynamic Design Solutions NV (2014) Retrieved from FEMTools software: www.femtools.com
5. McDonald S, Gerber A, Tobber L, Ventura CE (2015) Operational modal analysis of a nine-story concrete core wall building. In: International modal analysis conference XXXIII, Orlando

Chapter 29
Numerical Study and Experimental Validation of a Method for Model Updating of Boundary Conditions in Beams

Christian E. Silva and Shirley J. Dyke

Abstract The study of vibrations in beams has been largely addressed by authors and researchers. However, relatively few researchers have considered the case of unknown boundary conditions, as usually it is reasonable to assume the classical cases such as simply supported, clamped or free. Indeed, there are a wide variety of boundary-condition configurations, each one representing a whole different problem with its own modal characteristics. A method for updating experimental beam models to specifically address the issue of unknown boundary conditions is proposed; this methodology takes advantage of vector comparison techniques such as the modal assurance criterion based on the Cauchy-Schwartz inequality to determine the degree of linear relationship between two mode shapes systematically and iteratively until an acceptable parametric match is found.

This paper includes the phases of numerical study and experimental validation. A brief introduction with some relevant previous publications is presented, before explaining the methodology derivations and considerations in the numerical study section. A section devoted to demonstrate the methodology with an experimental example is presented in the Experimental validation section, and finally some conclusions and future work.

Keywords Modal analysis • Mode shape correlation • Model updating • Boundary conditions • Beam vibrations

29.1 Introduction

Boundary conditions in structures are important and should never be overlooked. Nevertheless, most of the ongoing structural design of beam elements is performed assuming simple classic boundary conditions such as simply-supported or fixed. However, most structures have 'unknown' or different boundary conditions as those assumed. To properly predict the behavior of a structure, a suitable model must be selected. This step requires experience and some understanding of the structure's behavior. Even though many models have already been developed by engineers and researchers, no model can be picked off-the-shelf for a determined problem. Every structure, no matter how similar it is to a previous one, has a different behavior due to uncertainties that are present from many sources: material non-homogeneities, environmental surroundings, usage, assembly discrepancies and of course, boundary conditions. Therefore, the selected model must be corrected so it can properly predict the system's behavior. But to determine how much a model has to be modified or which parameter should be updated, after having some knowledge of the behavior of the structure, some sort of identification process has to be performed.

The proposed methodology has been conceived from the idea of emergent bridges and structures that are installed on a temporary basis and whose structural parameters are not constant from one case to another. Two good examples of such structures are a military-type rapidly emplaced bridge structure/ditch; and a physical substructure of a hybrid simulation experiment consisting of a beam subjected to cyclic excitations whose distance between supports can be changed constantly. These two examples show how an apparently small change in distance between supports could produce a significant change in the model and therefore in its modal parameters.

Modal testing has provided researchers the means of obtaining modal parameters from experimental information collected from a wide range of setups. However, all the collected information needs to be compared with the chosen mathematical model to define, with a fair amount of certainty, the desired behavior of the system. This comparison between observed results and expected ones is called correlation; in this particular case, modal correlation is the link that connects analytical and experimental structural dynamics and mechanical vibrations. The most popular modal parameter correlation is called

---
C.E. Silva (✉) • S.J. Dyke
Department of Mechanical Engineering, Purdue University, 585 Purdue Mall, West Lafayette, IN 47907-2088, USA
e-mail: silva15@purdue.edu

modal assurance criteria (MAC), which is basically a squared linear regression coefficient based on the Cauchy-Schwartz inequality and was first proposed by Allemang [1]. As Allemang wrote: "The historical development of the modal assurance criteria originated from the need for a quality assurance indicator for experimental modal vectors that are estimated from measured response functions" [1], and whose intended purpose was orthogonality checks. Since then, many modal assurance criterion variations have been developed depending on the specific correlation analysis that needed to be performed. These include the coordinate modal assurance criterion (COMAC), frequency response assurance criterion (FRAC), frequency-scaled modal assurance criterion (FMAC), partial modal assurance criterion (PMAC), scaled modal assurance criterion (SMAC) and reciprocal modal vector assurance criterion (RVMAC.) Some of these methods will be briefly described herein. Validation of experimentally-obtained modal parameters such as mode shape vectors or natural frequencies can be performed both in vector or scalar fashion; the former, through calculating the complex modal scale factor; and the latter, through a scalar measure of vector consistency. The vectorial correlation technique is called modal scale factor (MSF), whereas the scalar is called modal assurance criterion. The COMAC utilizes both the mode shape vector and the natural frequency, called together mode pairs, to verify linear relationship between modes either experimental or analytical. However, its direction is more towards identifying which DOF of the measurements contribute negatively to a low value of MAC. It was developed by Lieven [2].

Various authors extended this methodology to the frequency-domain. Heylen and Lammens proposed a similar technique to compare, not modal vectors but frequency response function vectors using also a squared linear regression coefficient [3]; such method took the name of frequency response assurance criterion (FRAC), and later Fotsch and Ewins introduced a frequency scaling upgrade to the MAC method "such that the mode shape correlation, the degree of spatial aliasing and the frequency comparison can be displayed in a single plot" [4]. Specialized extensions of the MAC are used commonly when only a desired part of the information is needed. For such cases, Heylen and Janter proposed the partial modal assurance criterion (PMAC), and the spatial modal assurance criterion (SMAC) [5]. The former is used to correlate parts of modal vectors, and it is specially useful when computational efficiency needs to be achieved by disregarding non-relevant information; the latter compares vector spaces. When rotational degrees of freedom are used, a special scaled MAC was proposed by Brechlin et al., where the weighting matrix is such that it balances the scaling of translational and rotational DOF's in the modal vectors [6].

The method proposed herein has a close relation to those cited above but with a different scope than to determine damage in structures. However, the conception of the proposed method in this paper is quite similar inasmuch as both approaches propose an iterative comparison of vectors.

In the present study, the use of a model-correlation-based method will be used only for comparison of experimental and analytical mode shape vectors; therefore, to construct a mapping matrix between analytical and experimental mode shapes. As many of the MAC formulations use Hermitian matrices instead of transposed ones, this proposed formulation will deal only with real mode shape vectors. Should a case where complex modal vectors arise, the formulation must be corrected accordingly.

29.2 Problem Formulation

Having a wrongfully assumed model could lead to an incorrect estimation of natural frequencies and mode shapes that could also lead to a catastrophic response of the structure due to vibrations. The related mathematical principle used for this development is the Cauchy-Schwartz inequality, which states that for all vectors x and y of an inner-product space it is true that:

$$|\langle x, y \rangle|^2 \leq \langle x, x \rangle \cdot \langle y, y \rangle. \tag{29.1}$$

Therefore, the relationship between the left side and the right side of the inequality is always less than or equal to unity.

$$\frac{|\langle x, y \rangle|^2}{\langle x, x \rangle \cdot \langle y, y \rangle} \leq 1 \tag{29.2}$$

which can be used as a suitable correlation index between vectors x and y.

29.2.1 Methodology

The correlation method proposed herein is the application of Cauchy-Schwartz inequality which is a squared linear regression correlation coefficient used originally for orthogonality checks. This coefficient is very sensitive to large differences between the comparing vectors (squared error minimization) and consequently, not very sensitive to small changes. This indicator provides a means for comparing vectors originated in different sources: e.g., a FEM-originated modal vector versus an experimentally-originated one; or any other source. Therefore, no analytical model is needed for this methodology to work.

The **modal assurance criterion** is defined as the relationship between the degree of linearity between two vectors, in this case two modal vectors: one reference and one experimentally-obtained. The equation for this relationship is:

$$MAC = \frac{|\langle \psi_a \psi_e \rangle|^2}{\langle \psi_a \psi_a^T \rangle \langle \psi_e \psi_e^T \rangle} \tag{29.3}$$

where ψ_a and ψ_e are the vectors which relation is to be studied, and the T superscript refers to 'transposed'. The modal assurance criterion is a scalar value from zero to one. Zero represents no correlation whatsoever and a MAC value of unity represents a consistent correspondence. The modal assurance criterion is an indicator of consistency only, that is to say that it will indicate whether two vectors are similar or not; but it will not indicate if a given vector is correct or valid. Therefore, the use of an analytical or finite element generated reference vector is always recommended to provide a valid analysis.

The comparison procedure is made not with the mode shape vectors themselves, but with stacked mode shape vectors as shown in Eq. 29.4. Consider vectors ψ_1, ψ_2 and ψ_3 to be the first three mode shapes of an arbitrary structure, using r sensors as the experiment's resolution:

A correlation array is formed by combining the selected number of mode shapes along with these same mode shapes successively arranged in a stacked fashion: the first stacked vector will include the first two mode shape vectors; the second stacked vector will include the first three mode shape vectors, and so forth.

$$\psi_1 = \begin{Bmatrix} a_1 \\ a_2 \\ \vdots \\ a_r \end{Bmatrix}, \quad \psi_2 = \begin{Bmatrix} b_1 \\ b_2 \\ \vdots \\ b_r \end{Bmatrix} \cdots \psi_3 = \begin{Bmatrix} n_1 \\ n_2 \\ \vdots \\ n_r \end{Bmatrix}, \hat{\psi}_1 = \begin{Bmatrix} a_1 \\ a_2 \\ \vdots \\ a_r \\ b_1 \\ b_2 \\ \vdots \\ b_r \end{Bmatrix} \cdots \hat{\psi}_n = \begin{Bmatrix} a_1 \\ \vdots \\ a_r \\ b_1 \\ \vdots \\ b_r \\ \vdots \\ n_1 \\ \vdots \\ n_r \end{Bmatrix}. \tag{29.4}$$

In Eq. 29.4, ψ_i represents mode shape vectors; and $(\hat{\psi}_i)$, represent stacked mode shape vectors. The reference array must have the same structure so a MAC calculation can be performed between the two to obtain a correlation matrix of the following structure:

$$CM = \begin{bmatrix} \hat{\psi}_1 \hat{r}_1 & 0 & \dots & 0 \\ 0 & \hat{\psi}_2 \hat{r}_2 & \dots & 0 \\ \vdots & \ddots & \dots & \vdots \\ 0 & 0 & \dots & \hat{\psi}_n \hat{r}_n \end{bmatrix} \tag{29.5}$$

where $\hat{\psi}_i$ and $\hat{r}_i$ are the experimental or case study and the reference correlation mode shape vectors, respectively. The diagonal terms correspond to correlation between stacked mode shape vectors of identical dimension, which means that each diagonal value is obtained by calculating the MAC value between ψ_i and r_i, using Eq. 29.3. A high correlation result will have values close to 1 in the entire CM matrix diagonal. The reason for correlating only stacked vectors instead of individual mode shapes is to increase the model coincidence. When analyzed individually, poor results are usually obtained due to individual mode shape similarity. On the other hand, when comparing stacked-modes vectors only, the correlation matrix turns into a powerful tool for modal correlation from the analyst standpoint.

The results of the correlation matrix or vector can be presented by either the matrices themselves or bar plots, whether presented in 3D for the case of correlation matrices and in 2D for the case of vectors, which are much more easy to

Fig. 29.1 An example of a 5 × 5 correlation bar plot
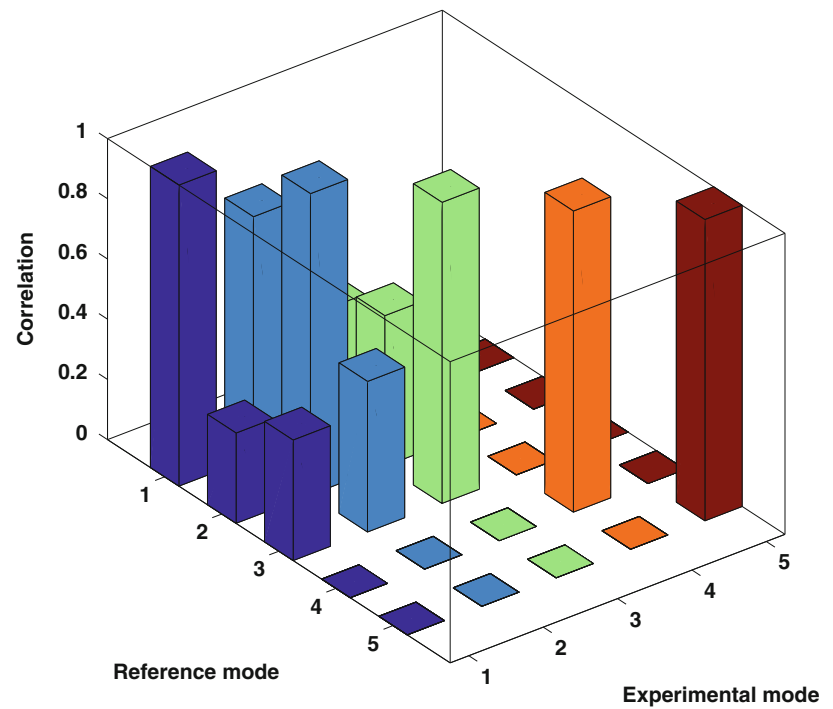
understand. An example of this plot for a 5 × 5 successful correlation matrix is presented in Fig. 29.1. Model correlation matrices are very common when a mode needs to be checked for validity in cases of computational or torsional modes. For this particular project, the benefits of the modal assurance techniques are used with a distinct objective: to implement a methodology for verifying the closeness of a model boundary condition parameters to those of an experimental result. This is why the method will be further referred to as "MAC-based" instead of modal assurance criteria.

29.3 Numerical Validation

As stated previously, the development of the mathematical models used in this study is the first part of a much broader procedure which is the numerical verification of the proposed technique. A model correlation method has been proposed but before it can be implemented with experimental data, it has to be tested with unpolluted data so that it can prove its reliability. In the present chapter, this verification will be performed in an iterative way so that it can be further implemented with real data. Two sources of data can be used instinctively from the mathematical models already discussed: the analytical and the finite element models. It is expected that for the analytical case, a perfect correlation occurs; whereas for the finite element case, which is an approximation, a close-to-perfect-correlation occurs.

29.3.1 Numerical Example

A correlation procedure against the three developed mathematical models, each one with different parameter values will be made. This constitutes the 'model space', a group of distinct parametrized models to which the experimental case is going to be compared until the best match is determined. The mathematical models to be used are:

1. Simply supported beam with both ends free for rotation.
2. Simply supported with:

   - Rotational springs on both ends with three different $k_{\theta i}$ values on one end, and five proportional values going from 20 % to 100 % of $k_{\theta i}$ on the other end. This gives a total of twenty five cases.

- Rotational inertial mass on both ends, with five different I_{ri} values on one end, and five proportional values going from 20 % to 100 % of I_{ri} on the other end. This gives a total of twenty five cases.

3. Clamped boundary on both ends (clamped-clamped beam).

The described list contains roughly 80 different analytic models to compare from. It is clear that the solution space can be as wide as needed to determine the closest parameter correlation. The procedure to simulate the unknown boundary condition case is detailed below:

1. Define the number of modes n to be simulated.
2. Obtain the eigenvalues, ω_n and mode shape vectors ϕ_n from the analytical equations or FEM.
3. Approximate each mode to a state-space model corresponding to the associated degree of freedom.
4. Obtain the response of the system to a simulated input signal for each degree of freedom by solving the equations of motion. This constitutes the simulated data.
5. Apply an identification technique (FFT or ERA) to generated data to obtain the modal parameters. This step is to replicate a similar procedure of experimental modes. Noise or any other disturbance can be added in this step.
6. Compare the obtained mode shapes to those of the analytical models using the correlation method.
7. Plot the correlation matrix in a bar plot to determine the highest value and, therefore, the best model match.

29.3.2   Model Selection

Figure 29.2b presents five subplots, three for individual and two for combined (stacked) mode shapes. In each subplot, four curves are overlaid which correspond to the simulation, the simply-supported, the clamped-clamped and the rotational mass models. By inspection of this figure, it is evident that there are some lines not matching in all five subplots. In the figure, the red dotted lines with squared markers represent the mode shape of the case study; i.e., the simulation obtained from an analytical equation which is considered the "experiment". The continuous blue lines represent the analytical model of the same case but obtained through the FFT process to recreate the method as close as possible to the real experiment. The dashed black and dashed green lines correspond to the simply-supported and clamped-clamped cases, respectively.

In the first subplot, all four lines are almost coincident and a no conclusions can be made to determine which model is closer to the simulated case. The second subplot shows an almost collinear behavior between the simulation and the rotational mass models, whereas a slight deviation of the simply-supported and clamped-clamped models from that of the simulation. Although a deviation is observed, no conclusions can be made at this point either. The third subplot shows a significant deviation of the simply-supported and clamped-clamped models from that of the simulation and, at the same time, it shows how a consistent convergence between the simulation and the rotational mass analytical model. The last two subplots show a comparison between models but using stacked vectors instead of individual vectors; for these two cases, a consistent collinearity is observed between the rotational mass model and the simulation. Three modes have been used for explaining this step. Depending on the necessity, more mode shapes can be used to have a better convergence, depending on the complexity of the model and the availability of good experimental high mode shapes.

Although the previous step produces a fair amount of information about which model to select, it does not provide a parametric result regarding the boundary conditions of such a model. The goal of this technique is to determine with a great deal of certainty the parameters involved in the chosen model. For example, if a spring-supported model is selected, the method would provide an interval of spring-stiffness values as parameters of the system.

29.3.3   Correlation Analysis

Once the visual inspection has been conducted, the ultimate mathematical verification is done through the correlation methods described in Sect. 29.2.1 consider again the simulated experiment just detailed in the previous section. Suppose that some given mode shape vectors have been obtained after performing impact testing to a structure. Such vectors obtained from a simulation are shown in Fig. 29.2a. This is going to be the experimental "case study". Suppose also that the only assumption made for this mode shape is that it corresponds to the vibration of a beam of known dimensions and material constants but unknown boundary conditions (which is usually the case); i.e., parameters $\mathbf{M}$, $\mathbf{C}$ and $\mathbf{K}$ have been experimentally obtained. The proposed technique's aim is to compare this case study vector with several analytical model cases to determine which resembles the closest to it.
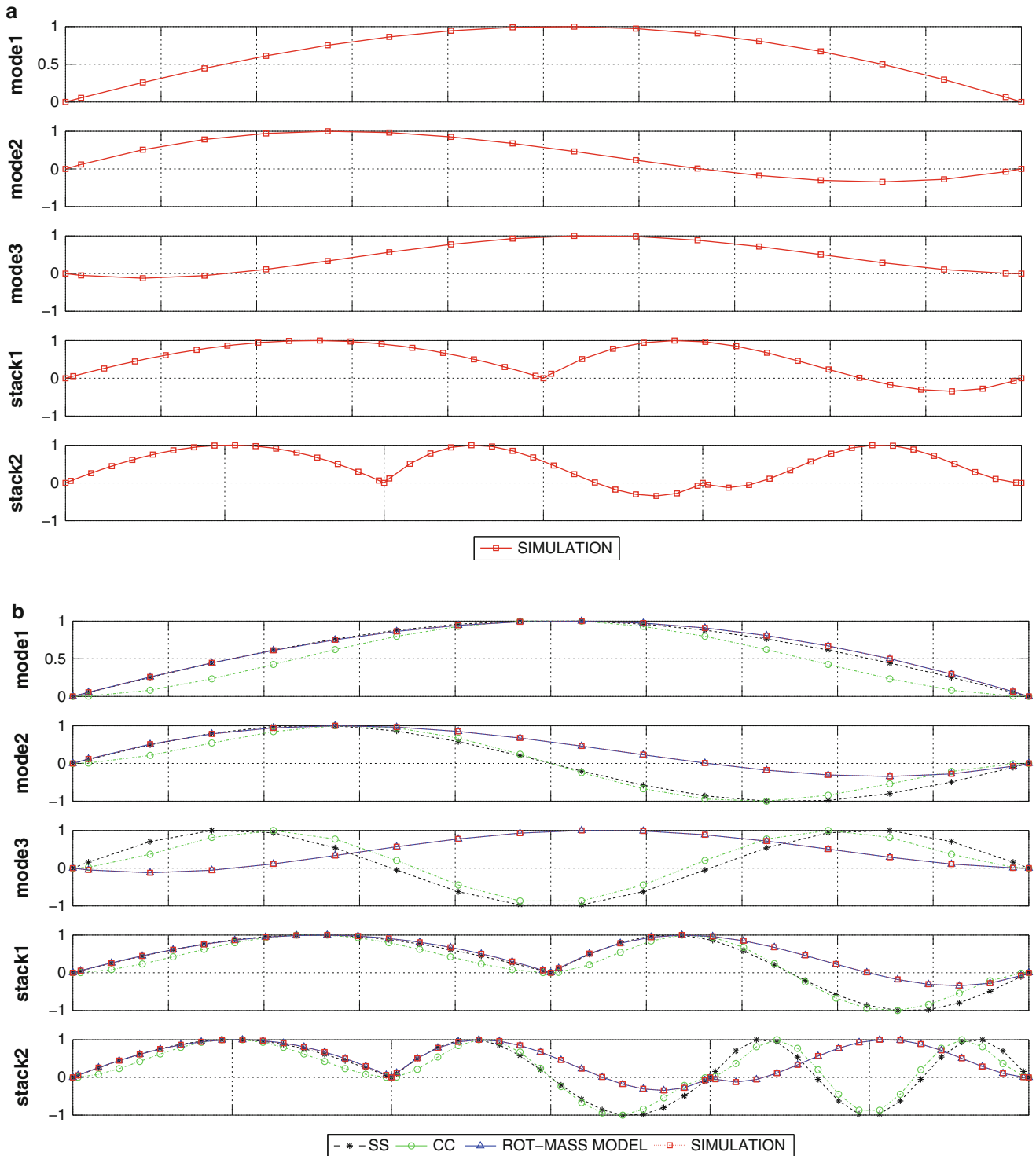
Fig. 29.2 MAC-based correlation results. (**a**) Simulation mode shapes. (**b**) Modal vector comparison

29.4 Results

After comparing this mode shape with the classical boundary-condition models similar to the step described in Sect. 29.3.2 one can conclude preliminarily that the obtained mode shape corresponds to a beam with rotational masses on both ends. However, this is still a vague conclusion because such a beam could have infinite number of combinations of rotational
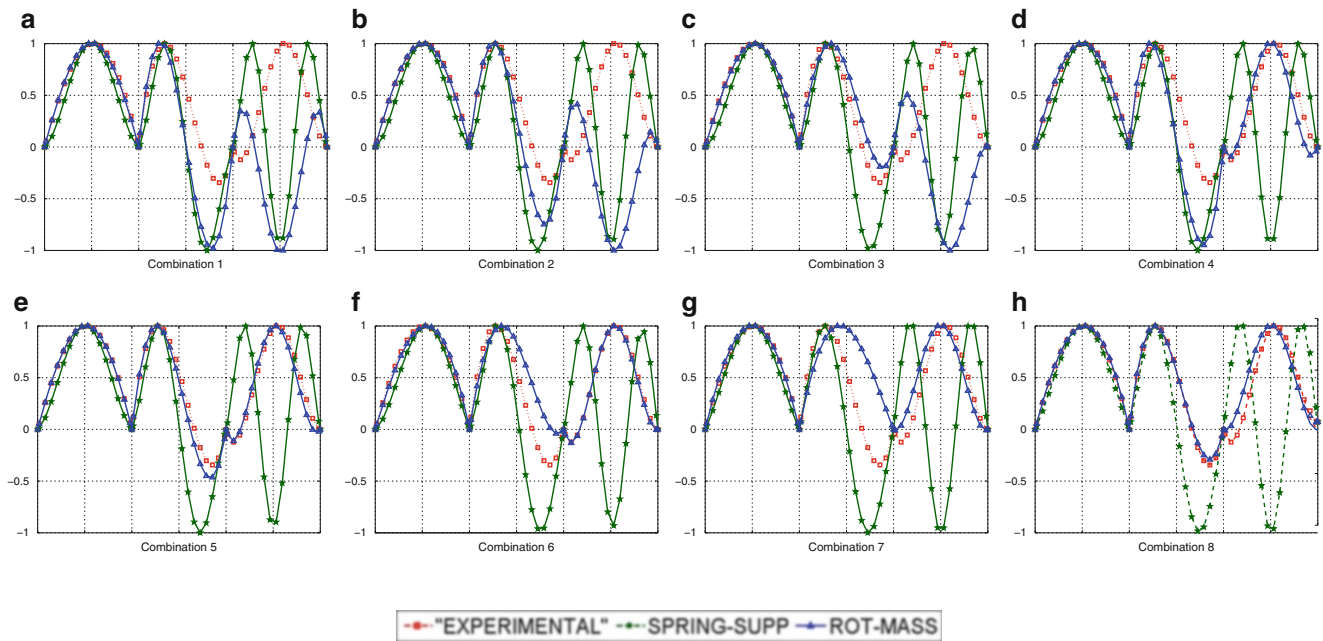
Fig. 29.3 Correlation comparison of spring-supported and rotational-mass parameter combinations

inertias at its ends; therefore, a refined model updating step is to be performed to determine with an acceptable tolerance, the values of such parameters. As an example, nine rotational-inertia and nine spring-stiffness combinations are going to be used leaving aside the simply-supported and clamped-clamped cases, since these are special cases of the spring-supported beam. The model space is then composed of eighteen candidates just for this example. These possible models are going to be correlated with the simulated "experimental" case whose model is supposedly unknown. The graphical results are shown in Fig. 29.3, where it is clear that the unknown case (red w/square marker) is significantly off from any spring-supported model case (dark-green w/star marker). This will be evident in the bar plot of the correlation values. On the other hand, when comparing the rotational mass model cases (blue w/triangle marker), a much closer relationship is observed. In fact, one of the cases gets really close to the experimental case. For a refined result, the analyst could just add more case combinations to the model space to get rather close match.

A good preliminary conclusion can be obtained from observation. Indeed, from a quick look to these, it is clear that for cases (e) and (h), very close correlations between the experimental (red /w square marker) and rotational mass (blue w/triangle marker) models are occurring. However, our aim is to determine which parameters are causing this correlation; therefore, further study shall be performed to obtain such values. The algorithm carries out comparisons between the experimental model and all the models included in the model space, giving one correlation index for each comparison. Each mode shape vector of the model space has two additional cells containing the two boundary condition parameters which can be easily extracted after determining the highest correlation index. These results are shown in Fig. 29.4a, b; the first, corresponding to the spring-supported beam cases; and the second one, to the rotational-inertia cases.

Figure 29.4b confirms the preliminary visual conclusion made from Fig. 29.3: that is to say that combinations 5 and 8 are the closest-related models to the experimental one because the lines corresponding to the model and the simulation are mostly coincident in these two plots.

The obtained parameters are $I_1 = 52.712$ and $I_2 = 31.627 \, \text{Nm}^2/\text{rad}$. The exact values used to simulate the experimental case were $I_1 = 58.213$ and $I_2 = 34.982 \, \text{Nm}^2/\text{rad}$, which yield errors of 9.44 % for I_1, and 6.1 % for I_2 and an overall correlation parameter of 0.9987 which is acceptable to adopt this model combination as the correct boundary conditions for this experimental setup.
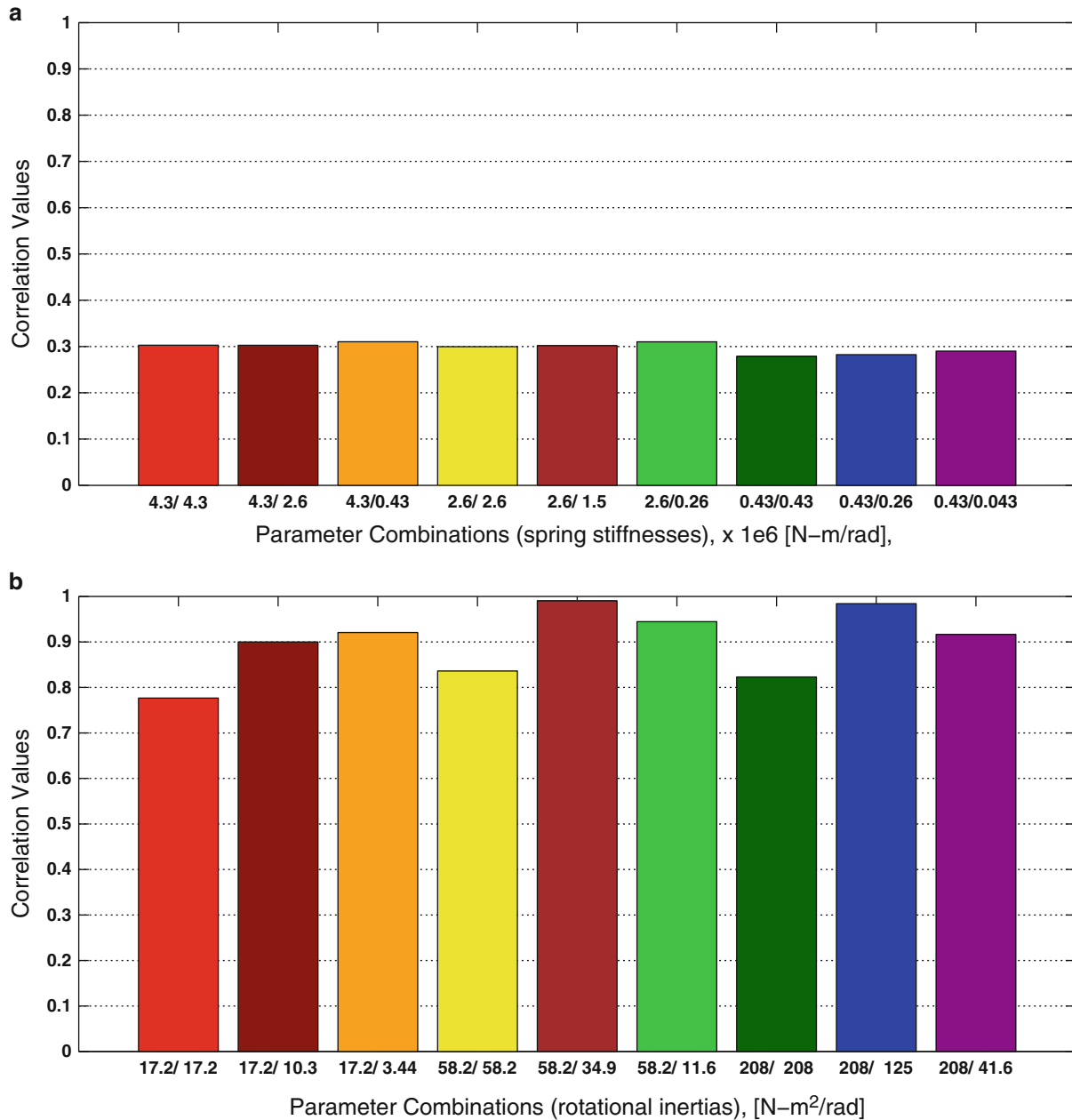
Fig. 29.4 MAC-based correlation results. (**a**) Spring-supported. (**b**) SS w/rotational masses

29.5   Conclusions

A novel methodology for establishing an accurate model for predicting the behavior of the vibrations in a beam has been developed, in which a linear correlation equation is applied to compare the degree of linearity between an experimentally obtained mode shape vector and a group of suitable analytical mode shape vectors extracted from selected model candidates (model space). The procedure is performed iteratively comparing one by one until the highest correlation index is achieved.

After performing the proposed methodology, if deviations are still present in the model, classical model updating techniques can be further applied to tweak the response to a most accurate state. However, the correlation technique should be enough.

Table 29.1 Final frequency comparison (in Hertz)

Analytical	FEM	Exp.
5.7071	5.8918	3.6328
13.3434	14.4385	13.8516
22.1749	25.8347	27.8750
49.8844	50.6847	47.8203
93.2855	93.6796	94.2180

Finding natural-frequency correlations may not yield the most accurate model as mode shape correlations. However, a good extra check for the analyst is to compare mode shapes in a first step; and natural frequencies in a second step to approximate the model as much as possible to the real structure.

Almost all the classical models along with the non-classical combination cases studied give a high correlation for the first mode shape and fairly high values for the second mode shape. When analyzing from the third mode shape onwards, is when correlation study can be clearly distinguished. Therefore, a good result is obtained when constructing a vector of at least the three first mode shapes stacked together. Correlation cannot be studied when comparing individual mode shapes as many of these are similar from one model to another.

An updated model in which the manipulable parameters are those corresponding to the boundary conditions instead of structural or material parameters, is a much more realistic model to work with. The main source of model discrepancies should be looked for in the most unknown aspect of a structural system which precisely are its boundary conditions. This also holds for model variations over lifespan, as boundary conditions are the most likely aspect of a system to change due to use and wear.

The proposed methodology can be used as a supplementary or complementary technique. The former, for cases where computational costs and time requirements are not a big issue; and the latter, where high accuracy of the updated model is required. Nevertheless, once a model has been narrowed enough with the correlation method, computational costs can drop significantly if compared to applying the traditional model updating techniques for the whole process.

Model spaces can be constructed either from analytical equations, or finite element models; the method does not require a closed-form solution of any model equation, but only a mode shape vector, which makes the methodology much more user-friendly and straightforward.

Deviations of the observed natural frequencies from those of the predicted by the updated model are expected for higher modes. Indeed, Table 29.1 shows good concordance for the first three modes and an increasing deviation for higher modes due to noise implications and system uncertainties.

References

1. Allemang RJ (2003) The modal assurance criterion–20 years of use and abuse. Sound Vib 37(8):14–23
2. Lieven N, Ewins D (1988) Spatial correlation of mode shapes, the coordinate modal assurance criterion (COMAC). In: Proceedings of the 4th international modal analysis conference, vol 1, pp 690–695
3. Heylen W, Lammens S (1996) FRAC: a consistent way of comparing frequency response functions. In: Proceedings of conference on identification in engineering systems, pp 48–57
4. Fotsch D, Ewins D (2000) Application of MAC in the frequency domain. Rolls Royce PLC-Report-PNR
5. Heylen W, Janter T (1990) Extensions of the modal assurance criterion. J Vib Acoust 112(4):468–472
6. Brechlin E, Bendel K, Keiper W (1999) A new scaled modal assurance criterion for eigenmodes containing rotational degrees of freedom. In: Proceedings of the International Seminar on Modal Analysis, vol 3, pp 1175–1182

Chapter 30
Coordination of Groups Jumping to Popular Music Beats

Lefteris Georgiou, Vitomir Racic, James M.W. Brownjohn, and Mark T. Elliot

Abstract Prediction of coordinated dynamic loads induced by groups and crowds of people remains one of the most significant problems faced by designers of grandstands in entertaining venues, such as stadia and concert halls. Available guidance portrays humans as deterministic robot-like force generators moving at a single frequency with either perfect synchronisation or with random phases. Humans are not robots, and natural variability and imperfect synchronisation of individuals point to a random approach for crowd loading.

This research aims to tackle this challenging topic by studying, measuring and quantifying coordination between force signals measured from 15 individuals jumping to a selection of popular pop and rock songs with different dominant beats. The results show a lack of strong synchronisation pattern between individuals in a group at all given songs and rhythms. However, there is a moderate level of synchronisation at songs with predominant beats in the range 2–3 Hz.

Keywords Vibration serviceability • Crowd loading • Synchronisation

30.1 Introduction

Modern entertaining venues often include long-span open plan floors with low natural frequencies, making them prone to vertical vibration under group and crowd loading. Concert events are becoming a particularly sensitive issue as music beats help individuals to adopt a "regular" motion pattern and also serve as a common stimulus that could improve coordination (also called "synchronisation") of the body motion of individuals in the group/crowd [1]. High levels of synchronisation at bouncing rates that resonate or nearly resonate with natural frequencies of the supporting floor may cause vibration response so large that vibration serviceability and even public safety can be jeopardised. For example, in 2003 Leeds Town Hall had to be evacuated after only 30 min of a rock concert as a 1,000-strong crowd of fans induced vibrations so large that the floor occupied visibly cracked [2].

Prediction of the nature of coordinated dynamic loads induced by groups and crowds of people remains one of the most challenging topics in vibration engineering. In case of concert events, the popular belief is that bouncing is a good representative of dancing in a spot (i.e. within a limited space) and activity that people can effortlessly perform for a long period of time [3, 4]. For this reason, bouncing loads feature the majority of relevant design guideline [5]. However, when people get visibly excited, bouncing spontaneously turns to jumping leading to far higher dynamic load amplitudes acting on the supporting structure.

This paper is designed to study synchronisation between 15 individuals while bouncing to a range of popular pop songs and metronome beats. The aim of the study is to identify rhythms at which people coordinate their movement best, yielding the most critical group dynamic forces relevant for vibration serviceability assessment.

Section 30.2 describes experimental data collection while processing the measured data is elaborated in Sect. 30.3. Finally, key findings from the study are summarised in Sect. 30.4.

L. Georgiou • V. Racic (✉)
Department of Civil and Structural Engineering, The University of Sheffield, Sir Frederick Mappin Building, Mappin Street, Sheffield S1 3JD, UK
e-mail: v.racic@sheffield.ac.uk

J.M.W. Brownjohn
College of Engineering, Mathematics and Physical Sciences, University of Exeter, North Park Road, Exeter EX4 4QF, UK

M.T. Elliot
Department of Psychology, The University of Birmingham, Edgbaston, Birmingham B15 2TT, UK

30.2   Data Collection and Analysis

Individual jumping forces generated by a group of 15 students were recorded using a full-scale instrumented grandstand available in the Department of Civil and Structural Engineering in the University of Sheffield (Fig. 30.1). The grandstand has three rows with five seats each, as shown in Fig. 30.2. Each seating place is instrumented by a force plate designed to measure the vertical contact forces between the feet and the structure.

The test protocol comprising 24 tests is summarised in Table 30.1. The tests were designed to cover a wide frequency range 1.5–4 Hz of possible dominant frequencies observed in the contemporary popular (mainly pop and rock) music. At each frequency the participants were given two types of auditory cues: a steady metronome beat and three songs with a dominant beat at the selected frequency. The dominant frequencies were randomised in successive tests to avoid 'habituation' and adjusting their performance to increasing or decreasing beats. To minimise tiredness, a 5 min break was given between the tests when refreshments were provided. Each test lasted about 40 s as suggested in a similar study by Comer et al. [6]. The individual force time histories were sampled at 1,000 Hz. An example of measured force signals is given in Fig. 30.3.

30.3   Data Analysis and Results

This section presents two approaches to quantify the level of synchronisation within the group. The first approach features the coefficient of linear correlation between the measured signals (Sect. 30.3.1), while the second approach is based on the analysis of their Fourier amplitudes (Sect. 30.3.2).

Fig. 30.1 Experimental setup – instrumented grandstand in The University of Sheffield

11	12	13	14	15
6	7	8	9	10
1	2	3	4	5

Fig. 30.2 Arrangement of test subjects

Table 30.1 Test protocol

Test no	Frequency [Hz]	Song no/metronome
1	2	metronome
2	3	10
3	1.5	1
4	2.5	7
5	3.5	13
6	2	4
7	4	16
8	2.5	8
9	3	11
10	1.5	Metronome
11	4	17
12	3.5	14
13	3	Metronome
14	2.5	9
15	1.5	2
16	3.5	15
17	2.5	Metronome
18	2	5
19	4	18
20	3	12
21	2	6
22	3.5	Metronome
23	1.5	3
24	4	Metronome

30.3.1 Correlation Coefficients

For each of the 24 tests, the correlation coefficient ρ was calculated between the individual force-time histories. An example is illustrated in Table 30.2.

The root-mean-square (RMS) of all correlation coefficients of kind shown in Table 30.2 was then taken as a representative of the group correlation in each test. The results are summarised in Fig. 30.4.

The correlation is not significant in any test (i.e. RMS < 0.75). This can be interpreted as the human inability to strongly coordinate their body motion during jumping at any rate. However, the highest correlation observed for songs and metronome beats with dominant frequencies 2 and 2.5 Hz indicates mild correlation and suggests that the participants were synchronised best in this frequency range. This is in line with observations previously reported by Comer et al. [6]. Interestingly, there is no strong evidence to support the hypothesis that people follow music beats better than metronome beats. It seems that the correlation is stronger or weaker depending on how much people enjoy a particular song.

30.3.2 Synchronisation Analysis in Frequency Domain

Each force record was first detrended (i.e. the mean removed) and scaled by the corresponding body weight of the individual, then their Fourier amplitude spectra were calculated. Examples of the spectra are shown in Figure. The key information extracted from each spectrum is the peak Fourier amplitude A_i, which corresponds to the dominant frequency of the force signal. They were further used to roughly estimate synchronisation factor alpha using the following equation:

$$\alpha = \frac{A}{\sum_{i=1}^{15} A_i} \tag{30.1}$$
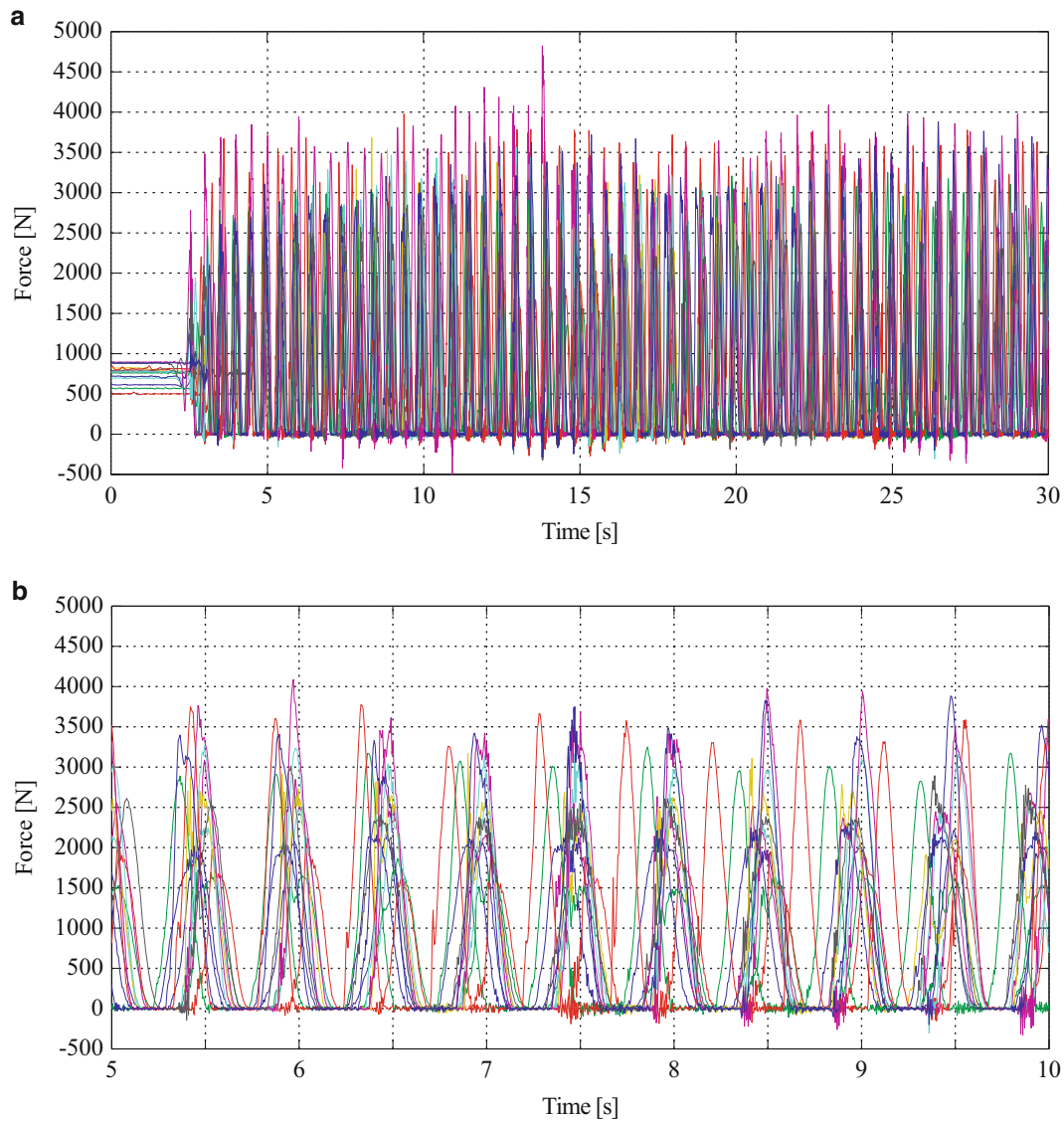
Fig. 30.3 (**a**) An example of recorded force-time history, (**b**) a portion of the force record shown in (**a**)

Here, A is the peak amplitude in the spectrum of the group force, i.e. the sum force of individual 15 force-time histories. Values of α close to 1 indicate a good synchronisation of the group. On the other hand, values close to zero are a sign of poor synchronisation. The results across all the tests are summarised in Fig. 30.5.

As in the previous section, the results presented in Figure show mainly low levels of synchronisation at very fast bouncing rates. Moreover, the peak value indicates that the best synchronisation was achieved when the participants were bouncing at metronome beats and songs with dominant frequency of 2 Hz. On the other hand, the mean value corresponding to 2.5 Hz is on the lower side and is very similar to the value corresponding to the low rate of 1.5 Hz.

30.4 Summary and Conclusions

Based on experimentally measured force-time histories generated by a group of 15 individuals bouncing to a range of pop songs and metronome beats, this study quantifies the level of synchronisation of individuals in the group using two methods. The first method features the linear correlation between the measured signals in time domain, while the second method compares contribution of the dominant Fourier amplitudes of individual force signals to the amplitude of the group force.

Table 30.2 An example of the correlation matrix for Song No. 04 (2.5 Hz)

ρ	1	2	3	4	5	6	7	8	9	10	11	12	13	14	15
1	1	0.89	0.97	0.69	0.73	0.85	0.83	0.86	0.91	0.21	0.74	−0.21	0.68	0.80	0.83
2	0.89	1	0.88	0.48	0.60	0.88	0.64	0.88	0.83	0.13	0.86	−0.40	0.77	0.92	0.92
3	0.97	0.88	1	0.68	0.72	0.83	0.82	0.82	0.95	0.23	0.71	−0.24	0.64	0.79	0.81
4	0.69	0.48	0.68	1	0.85	0.51	0.89	0.52	0.72	0.34	0.31	0.24	0.33	0.49	0.35
5	0.73	0.60	0.72	0.85	1	0.63	0.85	0.59	0.73	0.08	0.45	0.03	0.42	0.58	0.49
6	0.85	0.88	0.83	0.51	0.63	1	0.67	0.83	0.76	0.05	0.82	−0.36	0.81	0.83	0.86
7	0.83	0.64	0.82	0.89	0.85	0.67	1	0.68	0.80	0.25	0.45	0.09	0.43	0.62	0.51
8	0.86	0.88	0.82	0.52	0.59	0.83	0.68	1	0.75	0.22	0.75	−0.19	0.68	0.87	0.86
9	0.91	0.83	0.95	0.72	0.73	0.76	0.80	0.75	1	0.29	0.59	−0.22	0.52	0.76	0.71
10	0.21	0.13	0.23	0.34	0.08	0.05	0.25	0.22	0.29	1	−0.05	0.46	0.01	0.15	0.05
11	0.74	0.86	0.71	0.31	0.45	0.82	0.45	0.75	0.59	−0.05	1	−0.43	0.88	0.78	0.92
12	−0.21	−0.40	−0.24	0.24	0.03	−0.36	0.09	−0.19	−0.22	0.46	−0.43	1	−0.35	−0.34	−0.43
13	0.68	0.77	0.64	0.33	0.42	0.81	0.43	0.68	0.52	0.01	0.88	−0.35	1	0.69	0.82
14	0.80	0.92	0.79	0.49	0.58	0.83	0.62	0.87	0.76	0.15	0.78	−0.34	0.69	1	0.85
15	0.83	0.92	0.81	0.35	0.49	0.86	0.51	0.86	0.71	0.05	0.92	−0.43	0.82	0.85	1

Fig. 30.4 Summary of the group correlation coefficients extracted from the 24 tests. The black lines connect the mean values across the tests with common dominant frequency, while the whiskers represent 95 % confidence intervals
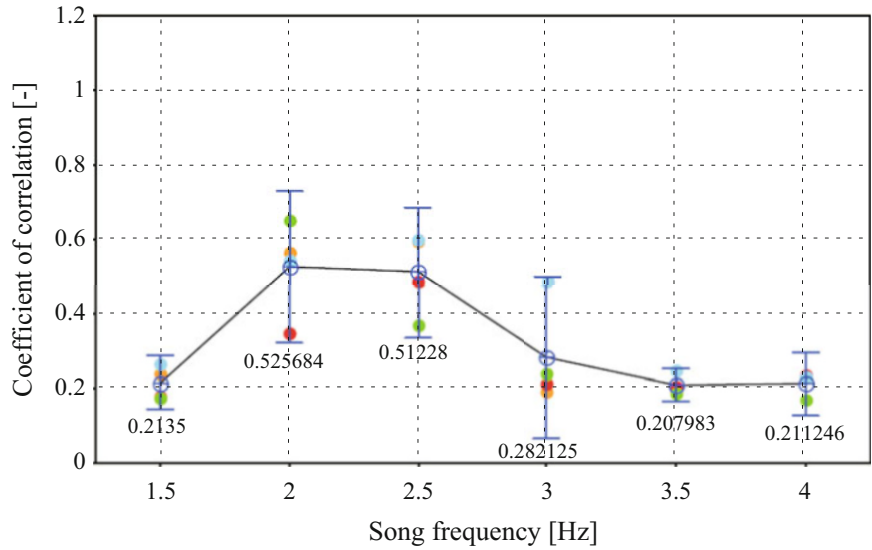
Fig. 30.5 Summary of α-coefficients extracted from the 24 tests. The black lines connect the mean values across the tests with common dominant frequency, while the whiskers represent 95 % confidence intervals
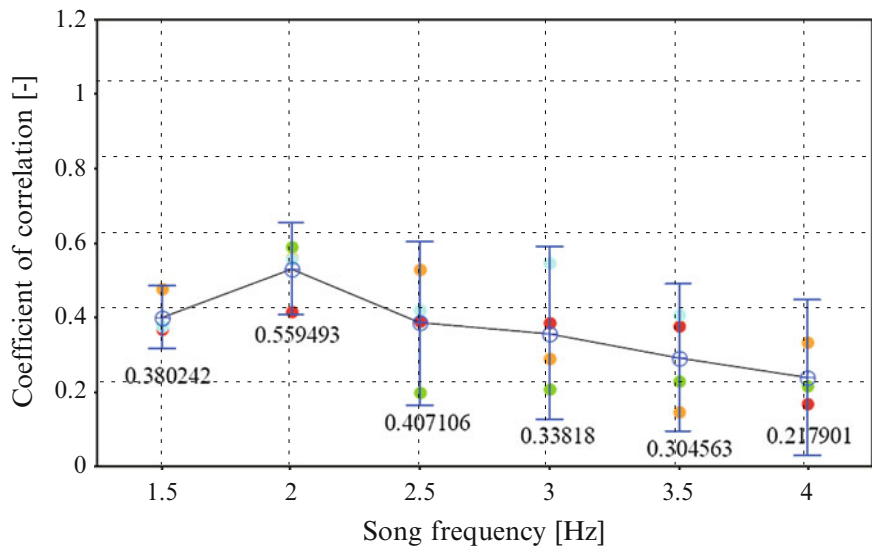
Both methods showed best synchronisation at moderate bouncing rates in the range 2–2.5 Hz and significantly lower levels of synchronisation at slower and faster rates. This is totally in line with results reported in similar studies in the past. A possible interpretation of the findings is that the moderate rates were the most comfortable to the majority of test subjects, thus making their bouncing motion more consistent long term. Interestingly, the results derived from the tests where songs were played were not significantly different to those derived from the tests where the metronome beats were provided. However, in feedback after the experiments the majority of test subjects agreed that the metronome beats were less stimulating that music, although the beats gave them impression that they could control their repetitive motion better.

The results presented are derived from the forces generated by a single group of students following a single set of selected pop songs and metronome beats. Testing groups of different sizes, age, professions and ethnical background while bouncing to a wider range of music genres would provide a much closer insight into synchronisation patters among groups and ultimately crowds.

References

1. Jones CA, Reynolds P, Pavic A (2011) Vibration serviceability of stadia structures subjected to crowd loads: a literature review. J Sound Vib 330(8):1531–1566
2. Parker D (2003) Rock fans uncover town hall floor faults. New Civil Engineer, 20 November
3. Yao S, Wright JR, Pavic A, Reynolds P (2006) Experimental study of human-induced dynamic forces due to jumping on a perceptibly moving structure. J Sound Vib 296(1–2):150–165
4. Sim JHH, Blakeborough A, Williams M (2008) Statistical model of crowd jumping loads. ASCE J Struct Eng 134(12):1852–1861
5. IStructE/DCLG/DCMS Working Group (2008) Dynamic performance requirements for permanent grandstands subject to crowd action: recommendations for management, design and assessment. The Institution of Structural Engineers, The Department for Communities and Local Government and The Department for Culture Media and Sport, London
6. Comer A, Blakeborough A, Williams MS (2010) Grandstand simulator for dynamic human-structure interaction experiments. Exp Mech 50(6):825–834

Chapter 31
Effects of People Occupancy on the Modal Properties of a Stadium Grandstand

Anna Cappellini, Alessandro Cattaneo, Stefano Manzoni, Matteo Scaccabarozzi, and Marcello Vanali

Abstract It is well known that of people standing or sitting on a structure can change the dynamic behavior of the structure itself. Particularly, when a significant number of people are occupying a structure, high variations of non-dimensional damping ratios and natural frequencies are often experienced. The extent of these changes depends not only on the number of persons, but also on the properties of the empty structure and on people position and postures.

This work analyses the effects of the presence of people on a grandstand of the San Siro stadium during some football matches and concerts. These effects are analyzed in terms of changes in modal parameters and amplitudes of vibrations. The impact of the number of people present on the structure on its dynamic behavior is also analyzed. The first results of an analytical approach, based on a FE model of the stand and a lumped parameter model of the people, to foresee the effect of people presence on stadia grandstands, is proposed in the end of the paper. The obtained results show that if an accurate model of the structure and detailed description of the stand occupancy are available the predicted results are in good agreement with the experimental evidence.

Keywords Human structure interaction • Vibrations • Modal properties • Modal analysis • Damping

31.1   Introduction

In the last years a great attention has been paid to all problems related to vibration serviceability issues of civil structures, particularly to human induced vibrations and Human-Structure Interaction (HSI). The first key aspect of HSI is the influence of structural movement on the active forces exerted by humans to the structure itself; the second is the influence of humans on the dynamic properties of the structure they occupy. This influence has been widely studied for the last decades for structural engineering purposes. Pedestrian walking bridges and staircases are deeply investigated and most of the research focuses on Stadia serviceability issues [1–5]. International standards and codes [6–9] exist to the purpose of both designing and evaluating the structure dynamics under the crowd action and they are the natural reference when vibration serviceability is assessed. Unlike other standards, the recent guidance [9] (Joint Working Group 2008) regarding dynamic performance requirements for permanent grandstands subjected to crowd action recommends to considered human structure interaction.

This work fits within the context of Human-Structure (H-S) phenomena, in particular dealing with the analysis of the vibrations of a grandstand of the San Siro Stadium. Four football matches and three concerts are analyzed in this work. The analysis is performed both in the time and frequency domain. The modal parameters of the structure occupied by people during the matches were extracted by means of Operational Modal Analysis (OMA) [10–13] techniques and compared. The recorded time histories were analyzed in terms of Root Mean Square (RMS) of the measured accelerations. In the last part of the work, the use of a model [14] to predict changes in modal parameters of a structure occupied by passive people is also investigated.

A. Cappellini • S. Manzoni • M. Scaccabarozzi
Department of Mechanical Engineering, Politecnico di Milano, Via G. La Masa 34, 20156 Milan, Italy

A. Cattaneo
Los Alamos National Laboratories, Los Alamos, NM, USA

M. Vanali (✉)
Industrial Engineering Department, Università degli Studi di Parma, Parco Area delle Scienze 181/A, Parma 43124, Italy
e-mail: marcello.vanali@unipr.it

Below is the work layout:

- Section 31.2 reports a short description of the structure under analysis
- Section 31.3 describes the experimental set-up used to measure the accelerations in selected points of the grandstand
- Sections 31.4 and 31.5 summarize the results of the analysis performed on the experimental data of football matches and concerts respectively
- Section 31.6 reports the prediction of changes in modal parameters of the joint Human-Structure (H-S) system obtained with the model proposed in [14].

31.2 The Structure

The construction of the Giuseppe Meazza Stadium, commonly known as San Siro, started in 1925. The structure was initially made up of four back straight bleachers (first level) that could contain up to 35,000 spectators. A first expansion, consisting in the construction of connection curves between the bleachers and in increasing the capacity of the two front ones, was performed in 1935. A supporting structure for a second level of grandstands, which stood over, and partly covered, the old grandstands was built in 1955. More recently, in 1990, on the occasion of the World Cup played in Italy, the Milan City Council began a profound change and renewal of the stadium. The project consisted in placing independent backings for the new level (third level) all around the existing stadium. Eleven cylindrical towers of reinforced concrete were built for this purpose. Seven towers are 30 m tall, while the four corner towers are 51 m tall as they also provide support for the roof of the stadium. The third level, object of this paper, is then composed of 10 grandstands supported by 11 concrete towers. Every grandstand, about 50 m long, consists of a pre-compressed box beam sustained by four bearings and every grandstand is structurally separated from the contiguous ones. Moreover, the 3rd ring is totally independent from the other stadium structures and no physical link exists between the 3rd and the 2nd ring. This work focuses on the analysis of vibrations of the portion of grandstand located between the tower 5 and the tower 6 (Figs. 31.1 and 31.2).

The next sections report the measurement set-up and the results of data collected during some football matches and concerts.
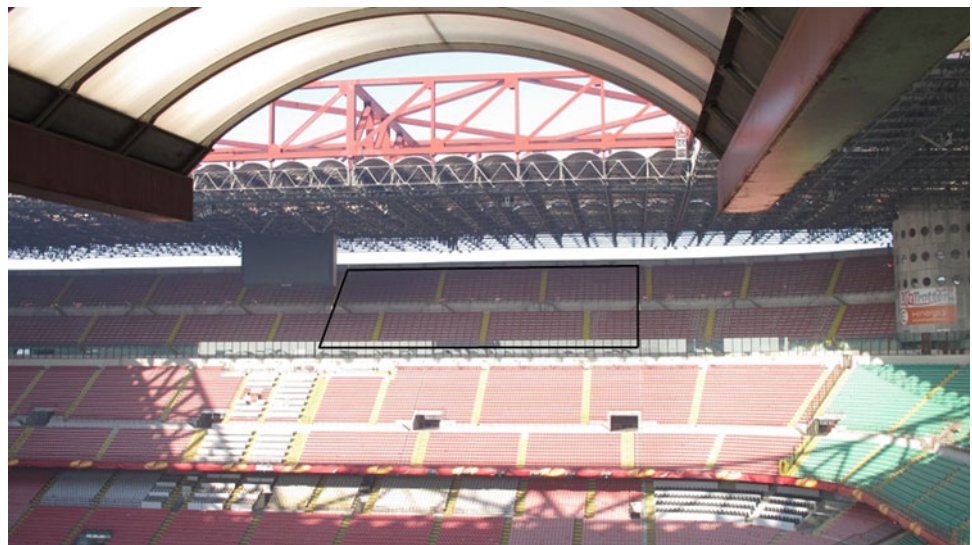
Fig. 31.1 Grandstand section

Fig. 31.2 Grandstand section – plan
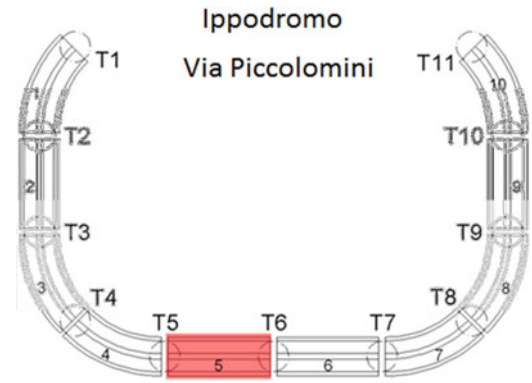
Table 31.1 Sensors main features

Sensor	Measurement range [g]	Frequency range [Hz]	Sensitivity [V/g]
PCB 393B12	0.5	0.15–5,000	10
PCB 393B31	0.5	0.1–200	10

Fig. 31.3 Setup of the accelerometers – football matches
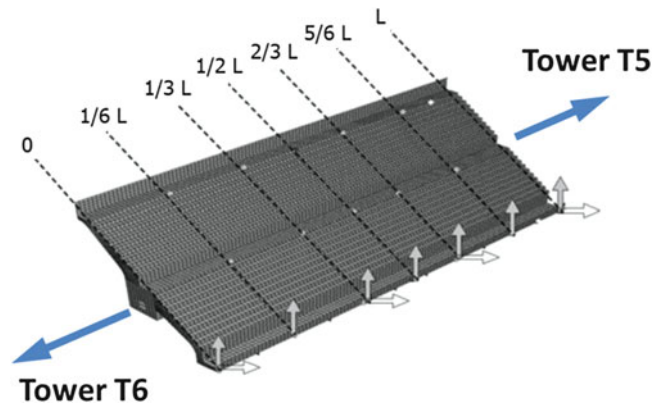
31.3 Experimental Setup

In order to derive the dynamic response of the grandstand, sensors were positioned in such a way not to disturb the normal operating conditions. Particularly, accelerometers were placed at the lower edge of the grandstand in a non-accessible position. Such a choice allowed to measure the accelerations in operating conditions. High sensitivity seismic piezo-accelerometers have been used to measure the accelerations in selected points of the grandstand. Their features are reported in Table 31.1.

The selected sensors have proven to be adequate for ambient vibration testing having a very low noise floor and an adequate full scale value. Eleven and four accelerometers were used during the football matches and the concert respectively. The configurations are reported in the next subparagraphs.

31.3.1 Football Matches

During the football matches 11 accelerometers were available on the grandstand. Seven accelerometers measured the vibrations in the vertical direction and the remaining four accelerometers measured the vibrations in the horizontal direction. Figure 31.3 shows the experimental configuration.

Fig. 31.4 Setup of the
accelerometers – concerts
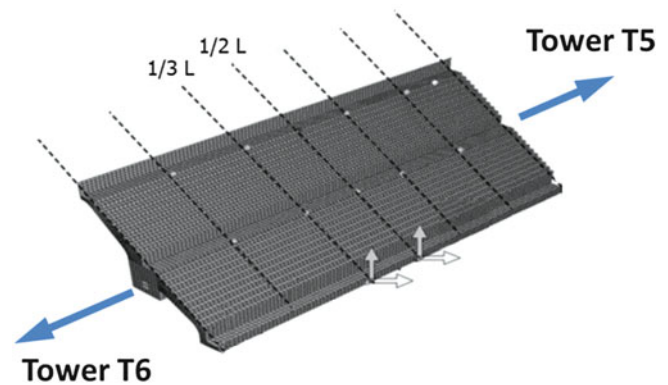
Fig. 31.5 Inter – Milan – PSD
(accelerometer 1/3 L V)
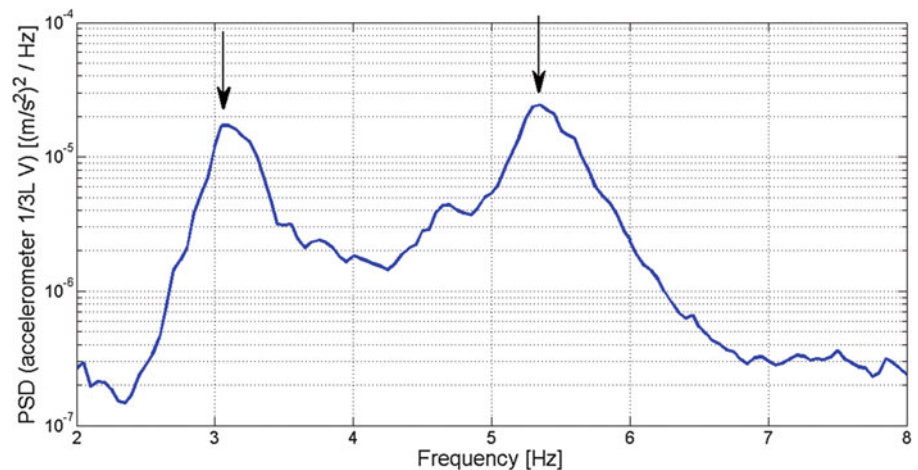
31.3.2 Concerts

During the concerts only four accelerometers were available on the grandstand. Two accelerometers measured the vibrations
in the vertical direction and the other two in the horizontal direction. Figure 31.4 shows the experimental configuration.

31.4 Football Matches Analysis

Four football matches are analyzed in this paper. The considered football matches are:

1. Milan – Parma (February 15, 2013)
2. Milan – Barcelona (February 20, 2013)
3. Inter – Milan (February 24, 2013)
4. Milan – Lazio (March 2, 2013)

During the first match (Milan – Parma) the grandstand occupancy was scarce, approximately 14 % of the total capacity.
During the last match (Milan – Lazio) the occupancy was about 31 %. Conversely, during the second and third considered
matches the grandstand was almost full.

31.4.1 Frequency Domain Analysis

Figure 31.5 shows an example of Power Spectral Density of the grandstand.

Table 31.2 Football matches – modal parameters – mode 1

Match	f_n [Hz]	ξ [%]
Milan – Parma	3.29	2.18
Milan – Barcelona	3.18	3.83
Inter – Milan	3.10	4.45
Milan – Lazio	3.21	2.90
Empty structure (ambient vibration testing)	3.29	1.42

Table 31.3 Football matches – modal parameters – mode 2

Match	f_n [Hz]	ξ [%]
Milan – Parma	5.46	1.84
Milan – Barcelona	5.33	3.20
Inter – Milan	5.37	2.78
Milan – Lazio	5.41	2.13
Empty structure (ambient vibration testing)	5.44	1.35

The structure shows two dominant modes around 3.30 and 5.40 Hz. These are not the only modes of the structure in the frequency range 0–8 Hz. However, accelerometers were placed at the lower end of the structure, where the other modes of the structure have small amplitudes. Therefore, the identification was considered reliable only for the two dominant modes.

As for the frequency domain analysis, the first half of all the considered matches was then analyzed. Indeed, the first half is the part of the match were people are seen to sit on the grandstand for most of the time. During the other parts of the event, such as the entrance or the interval and the last part of the second half, people move on the structure. This causes at least two problems: (a) the dynamic behavior of the structure changes in time; (b) people introduce a force that may contain dominant harmonic components. These two aspects make the analysis of such data not reliable. The firsts half of the matches were analyzed by means of OMA techniques. Tables 31.2 and 31.3 reports the obtained natural frequencies and damping ratios. A comparison with the values obtained from the analysis of the vibrations of the empty structure is also proposed.

The results show that people generally cause a decrease of the natural frequencies and an increase of the damping ratios. The obtained changes are mostly proportional to the number of people on the grandstand. In addition, experimental results show that the influence of people is higher for the first mode.

31.4.2 Time Domain Analysis

The recoded data were also analyzed in the time domain. At first the accelerations have been filtered with a low pass filter with cutoff frequency 25 Hz in order to avoid high-frequency phenomena (shocks) that do not affect the comfort. This value, discussed and used internationally [15], is certainly restrictive in terms of comfort, providing a conservative assessment. Then, the RMS of the recorded accelerations was analyzed. The RMS depends on the time basis used for the calculation. As reported in [9], a value of 10 s is frequently used. Therefore, the RMS was calculated using a time base of 10 s and 90 % overlap.

The analysis was performed to compare the effect of different occupancies of the grandstand and different events.

The maximum acceleration is recorded at 1/3 L in the vertical direction. Figures 31.6 and 31.7 show examples of time histories and RMSs for the football matches Milan – Barcelona and Inter – Milan.

The maximum of the RMSs of all the football matches are reported in Table 31.4.

The results show that the RMS values generally increase with the number of people. Furthermore, as for football matches the maximum of the RMS is linked to particular events of short duration (e.g. a goal).

Fig. 31.6 Milan – Barcelona –
1/3 L V – time history and RMS
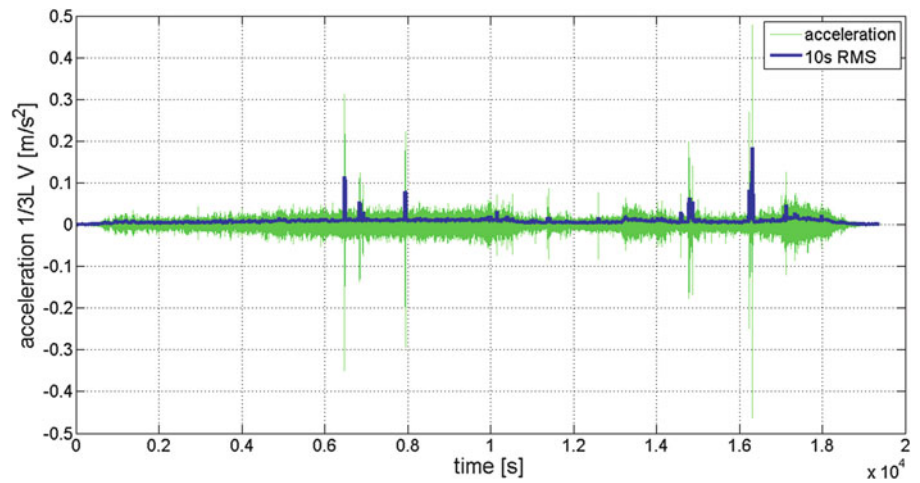
Fig. 31.7 Inter – Milan –
1/3 L V – time history and RMS
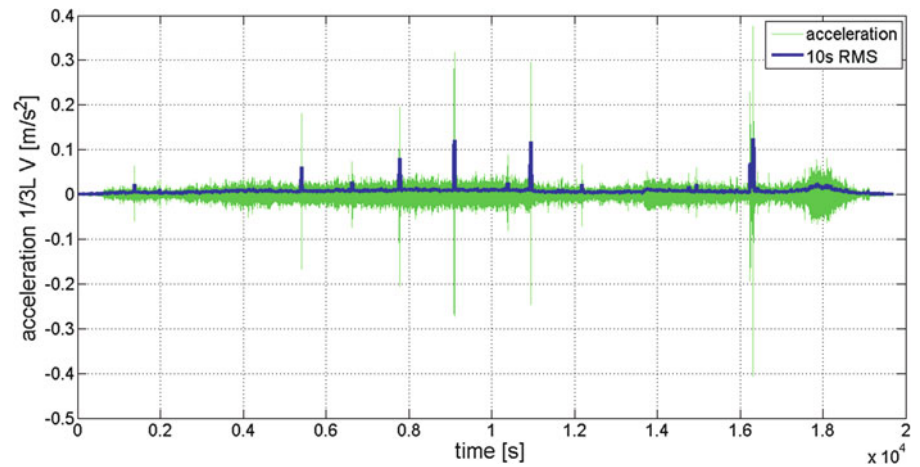
Table 31.4 Football matches –
maximum RMS

Match	RMS (1/3 L V) [m/s^2]
Milan – Parma	0.0247
Milan – Barcelona	0.1848
Inter – Milan	0.1255
Milan – Lazio	0.0400

31.5 Concerts Analysis

Three concerts are analyzed in this paper. The considered concerts are:

1. Jovanotti (Lorenzo Cherubini Italian Singer) (June 19, 2013)
2. Depeche Mode (July 18, 2013)
3. Robbie Williams (July 31, 2013)

The first two concerts sold out. Conversely, Robbie William's concert didn't sell out though also in this case the stadium was almost full.

31.5.1 Frequency Domain Analysis

The identification of modal parameters of data acquired during concerts is generally a difficult or even impossible task. Indeed, during concerts people generally move on the structure according to the audio stimulus of the music. Therefore, the

force exerted by people on the structure is often much closer to a pure harmonic than to white noise. This makes the use of OMA techniques to identify modal parameters a tough task. Therefore, for the considered concerts only a time domain analysis was performed.

31.5.2 Time Domain Analysis

The recorded accelerations of the concerts were processed in the time domain. Also in this case the RMS was used to analyze people's effect.

Figures 31.8, 31.9, and 31.10. show the time histories and RMSs of the considered concerts. The maximum of the RMSs are reported in Table 31.5.

With respect to the football matches, looking at the obtained results it is possible to notice that during the concerts the RMS of the accelerations keeps high values for longer times. Nevertheless the maximum values are comparable for the two kinds of event.
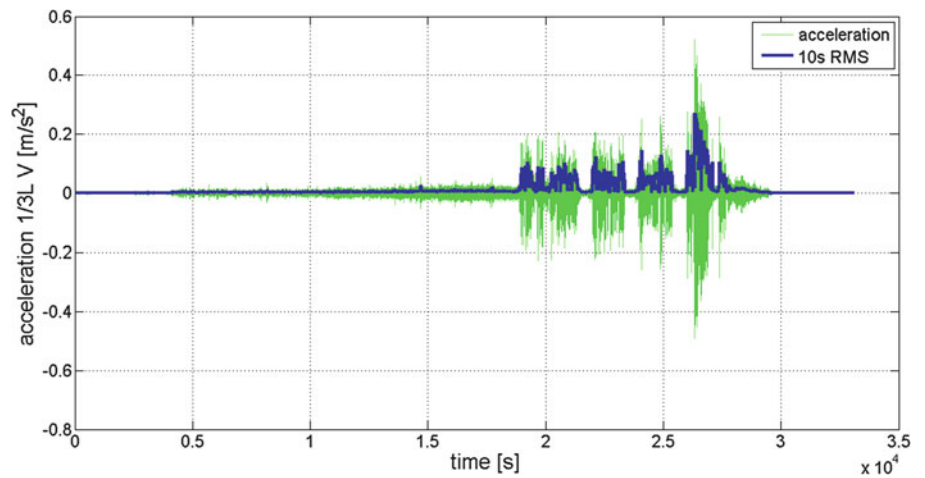
Fig. 31.8 Jovanotti – 1/3 L V – time history and RMS (0.2726 m/s^2)
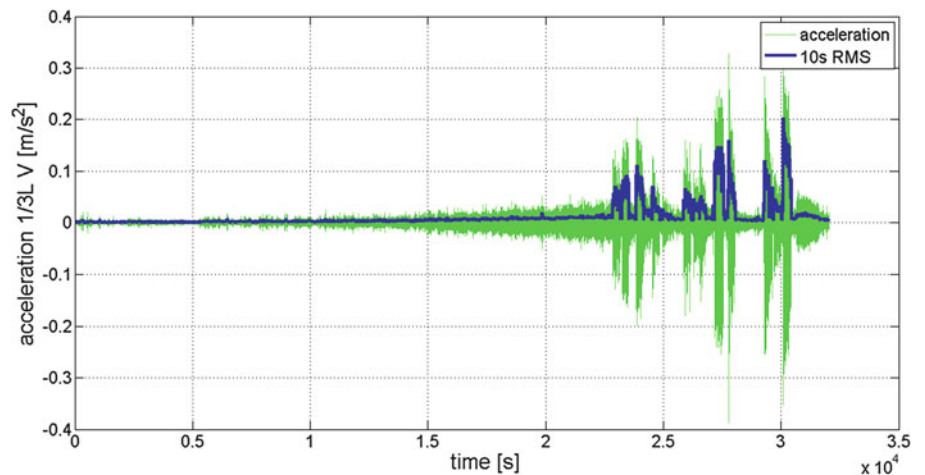
Fig. 31.9 Depeche mode – 1/3 L V – time history and RMS

Fig. 31.10 Robbie Williams –
1/3 L V – time history and RMS
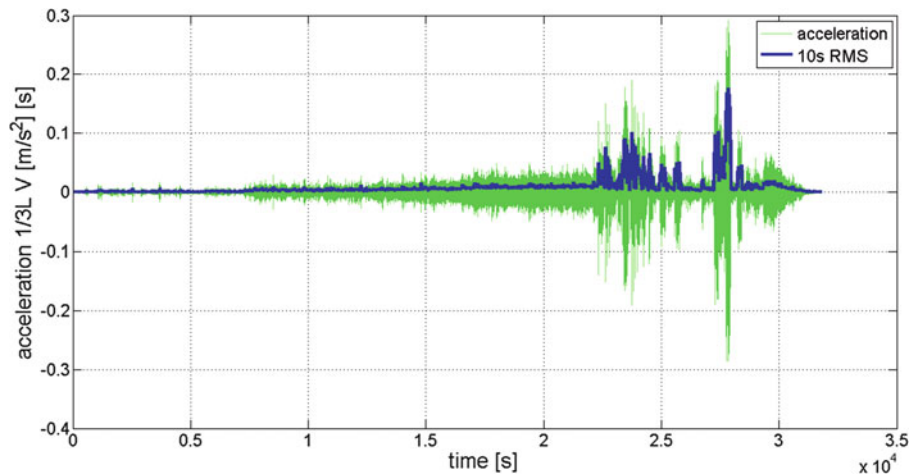
Table 31.5 Concerts –
maximum RMS

Match	RMS (1/3 L V) [m/s^2]
Jovanotti	0.2726
Depeche mode	0.2040
Robbie Williams	0.1762

Table 31.6 Modal parameters –
empty structure

	f_n [Hz]	ξ [%]
Empty structure (FEM)	5.40	1.94

31.6 Model of Human-Structure Interaction

In order to obtain a prevision of the changes in modal parameters due to people's presence the method proposed in [14] was used. The approach proposed in [14] was validated considering the simple case of a slender staircase. In that case people were asked to stand still on the structure while the staircase was forced with an electro-mechanical shaker. In such a case the experimental Frequency Response Functions (FRFs) of the staircase plus passive subjects could be estimated and modal parameters of the joint human-structure system were estimated by means of Experimental Modal Analysis Techniques. In [14] it was proved that a reliable estimate of the modal parameters of the joint human-structure system can be achieved. As regards real-life structures, such as the stadia grandstand considered in this work, the actual force exerted on the structure in unknown. Thus, the experimental data were analyzed by means of Operational Modal Analysis (OMA) techniques to extract the modal parameters. Therefore, the results obtained from the OMA of the football matches were compared with those predicted with this method.

The method requires the knowledge of:

- *the modal model of the empty structure.* To this purpose a FE model of the grandstand was employed. However, the available FE model of the grandstand was not able to provide an accurate description of the mode around 3.30 Hz. Therefore, only the mode around 5.40 Hz was analyzed when modelling the dynamic behavior of the joint Human-Structure system.

  As for the FE model of the structure, the modal parameters of the mode around 5.40 Hz are reported in Table 31.6. It is possible to notice that these parameters slightly differ from those obtained from the analysis of the ambient vibration data (Table 31.3).
- *the driving point FRF (apparent mass) of each subject on the structure*. As for a stadium grandstand, during football matches people are expected to sit for most of the time. Many works regarding the dynamic behavior of the seated human body are proposed in literature. Some of these works [16–18] were employed to model the behavior of sitting humans.

The FRFs of the joint H-S system are obtained combining the model of the empty structure and the apparent mass of seated subject. The modal parameters extracted from the analysis of these FRFs were compared with those obtained experimentally. The next subsections report the obtained results.

Table 31.7 H-S predicted modal parameters – full grandstand

	f_n [Hz]	ξ [%]
Full – with backrest	5.30	3.23
Full – without backrest	5.32	3.45

Table 31.8 H-S predicted modal parameters – Milan – Parma

	f_n [Hz]	ξ [%]
Milan – Parma	5.39	2.11

Table 31.9 H-S predicted modal parameters – Milan – Lazio

	f_n [Hz]	ξ [%]
Milan – Lazio	5.36	2.54

31.6.1   Milan-Barcelona and Inter-Milan

As for the matches Milan – Barcelona and Inter – Milan, the grandstand was almost full. Hence, the grandstand was supposed to be full when modeling the joint H-S system. Therefore, the results are identical for the two matches. For these two matches, two kinds of model available in literature for the apparent mass of seated human body were used and compared. Particularly, apparent masses with [16, 17] and without seat backrest [18] were used. Table 31.7 shows the obtained results.

It is possible to notice that the choice of the model to represent the dynamic behavior of the seated human body (with or without backrest) lowly influences the result.

The results obtained with model of H-S interaction (Table 31.7) have to be compared with those obtained experimentally (Table 31.3). The results show that the predicted damping ratios are slightly higher than those obtained from the analysis of the experimental data. However, the damping ratio used in the FE model is slightly higher than the damping ratio obtained from the analysis of the ambient vibration data. Indeed, the FE model was based and tuned on experimental modal testing performed in a different time of the year. Therefore, the experimental and predicted results are compatible in terms of increase in damping ratio. The same considerations apply to the decrease of the natural frequency.

31.6.2   Milan-Parma

During the football match Milan – Parma the grandstand occupancy was scarce, approximately 14 %. Pictures of the grandstand were taken before and during the match. Therefore, from the analysis of the pictures it was possible to know the approximate location of the spectators during the match. One of the main advantages of the approach proposed in [14] is the possibility of introducing the subjects locally on the structure. This allowed to simulate accurately people's distribution on the structure. The obtained results are reported in Table 31.8**.**

Also in this case the obtained damping ratio is consistent with the value obtained from the analysis of the experimental data. As for the natural frequency, results confirmed a small variation of its value.

31.6.3   Milan-Lazio

Like the football match Milan – Parma, the analysis of the football match Milan – Lazio was performed introducing people locally on the structure to simulate the FRFs of the joint H-S system on the basis of pictures of the grandstand during the match. Table 31.9 reports the obtained results.

Also in this case the results of the H-S model are consistent with the experimental values, both in terms of increase in damping ratio and decrease in natural frequency.

31.7 Conclusions

This paper dealt with the analysis of the vibrations of a grandstand of the San Siro Stadium. Particularly, some data related to football matches and concerts were analyzed.

The analysis of the football matches by means of OMA techniques showed the influence of people on the modal parameters of the structure. Particularly, increase in damping ratios and decrease in natural frequencies were found. The experimental results were compared with those obtained with a model to predict changes of modal parameters due to people's presence. The results of the model were consistent with the experimental evidence.

The time histories of football matches and concerts were analyzed through the RMSs of the recorded accelerations. The analysis of the RMSs showed that comparable maxima accelerations are reached during matches and concerts. However, as for the concerts the highest levels of accelerations are kept for much shorter times.

References

1. Reynolds P, Pavic A (2005) The dynamic performance of sports stadia under crowd dynamic loading at concert events. Structural Dynamics EURODYN 2005, Mill Press, Rotterdam, pp 473–479
2. Reynolds P, Pavic A, Ibrahim Z (2004) Changes of modal properties of a stadium structure occupied by a crowd. In: Proceedings of XXII international modal analysis conference, Orlando
3. Ellis BR, Ji T, Littler JD (1994) The response of grandstands to dynamic forces induced by crowds. Australasian Structural Engineering Conference, Sydney
4. Caprioli A, Vanali M (2009) Comparison of different serviceability assessment measures for different events held in the G. Meazza stadium in Milano. IMAC-XXVII, Orlando, 9–12 Feb 2009
5. Caprioli A, Reynolds P, Vanali M (2007) Evaluation of serviceability assessment measures for different stadia structures and different live concert events. IMAC XXV, Orlando, 19–22 Feb 2007
6. BS EN 1990:2002 Eurocode Basis of structural design BSI, 389 Chiswick High Road, London, W4 4AL
7. ISO 10137 (2007) Bases for design of structures – serviceability of buildings and walkways against vibration, International Organization for Standardization
8. Sètra Technical Guide (2006) Assessment of vibrational behaviour of footbridges under pedestrian loading, Sétra, 46 avenue Aristide Briand BP 100 92225 Bagneux Cedex, France. www.setra.equipement.gouv.fr
9. Institution of Structural Engineers (2008) Dynamic performance requirements for permanent grandstands subject to crowd action: recommendations for management, design and assessment, London
10. Peeters B, Van der Auweraer H, Guillaume P, Leuridan J (2004) The PolyMAX frequency-domain method: a new standard for modal parameter estimation? Shock Vib 11(3–4):395–409
11. Peeters B, Vecchio A, Van Der Auweraer H (2004) PolyMAX modal parameter estimation from operational data. In: Proceedings of the 2004 international conference on noise and vibration engineering, ISMA, Ku Leuven, pp 1049–1063
12. Peeters B, Vanhollebeke F, Van Der Auweraer H (2005) Operational PolyMAX for estimating the dynamic properties of a stadium structure during a football game. In: Proceedings of the XXIII IMAC, no.1, SEM publishing
13. Ewins DJ (2001) Modal testing: theory, practice and application, 2nd edn. Taylor and Francis Group, London
14. Cappellini A, Manzoni S, Vanali M (2013) Quantification of damping effect of humans on lightly damped staircases. In: Proceedings of XXXI international modal analysis conference, Garden Grove, 11–14 Feb 2013
15. Rebelo C et al (2010) Cable tensioning and modal identification of a circular cable-stayed footbridge. Exp Tech 34(4):62–68
16. Toward MGR, Griffin MJ (2009) Apparent mass of the human body in the vertical direction: effect of seat backrest. J Sound Vib 327(3–5): 657–669
17. Qiu Y, Griffin MJ (2011) Modelling the fore-and-aft apparent mass of the human body and the transmissibility of seat backrests. Veh Syst Dyn 49(5):703–772
18. Kim K-S, Kim J, Kim K-j (2011) Dynamic modeling of seated human body based on measurements of apparent inertia matrix for fore-and-aft/vertical/pitch motion. J Sound Vib 330(23):5716–5735

Chapter 32
Serviceability Assessment of Two Different Stadium Grandstand During Different Events

Anna Cappellini, Ramona Fagiani, and Marcello Vanali

Abstract This work presents an analysis of the measured vibration levels during different events on two different grandstands of the Milano stadium (Giuseppe Meazza). The stands vibration is nowadays measured 24 h a day all year long, providing a huge quantity of data coming from ambient vibration, football matches and live rock concerts. A part of these data, the one gathered during different events, is here analyzed according to international standards and recognized national guidance in order to assess the stadium serviceability against people induced vibrations during different events and to critically face the limits imposed by the standards.

The analysis also puts into evidence how the different dynamic properties of the selected stands affect the measured vibration levels and how concerts and football matches provide a totally different excitation source.

Keywords Operational modal analysis • Strategic infrastructures • Finite element model

32.1 Introduction

Vibration serviceability of stadium grandstands and other crowd occupied structures has become one of the important design facts in new structures and an important concern in the already built ones. There is a wide number of works in literature assessing the problem, starting from Kasperski papers [1, 2] up to recent reviews, Reynolds [3] and wide doctoral thesis works [4, 5]. A number of national guidance and standards deals with this issue, among them it is worth to cite ISO 2631, ISO 10137, BS 6841, the National Building code of Canada 2005 and the "Dynamic performance requirements for permanent grandstands subject to crowd action" from the Joint Working Group of IStructE [6–11].

In all the existing guidances limits are given in term of the frequency response of new structures to be built in order to avoid possible serviceability issues and if these limits are not respected dynamic investigations are requested, providing load models for the synchronous crowd action and acceleration limits. The standards on the other side provide, or not, reference magnitudes, measurement and analysis techniques, and reference levels to compare the vibrations to in order to asses structures serviceability.

Going through the published literature it is a well-accepted fact that few real measurements results have been published concerning live crowd events held in stadia or other structures [12, 13], while cases are reported in which vibration levels caused problems, BRASIL MARACANA stadium, Old Trafford in Manchester (1996), Liverpool's Anfield Road (2000), Millenium stadium in Cardiff, Ullevi stadium in Sweden. On the other hand all literature papers agree on the fact that live rock concerts are the most lively events in terms of vibrations, due to crowd synchronization effects that are not happening, or seldom happen, during sports events.

Since from the summer of 2003 a lot of measurements have been taken in the Giuseppe Meazza stadium in Milano [14–16] it has been decided to analyze some of the events that took place in the stadium according to the existing standards, guidance and literature reviews. Moreover in the stadium a permanent vibration monitoring system is nowadays active providing a huge amount of data collected both during football matches and music concerts. The aim of this paper is to provide a number of real life numbers and to critically face the most common serviceability analysis criteria that are applied to grandstands vibrations. At first a brief description of the considered grandstand is proposed, then the standard and guidance considered are described and the results are presented.

A. Cappellini
Dipartimento di Meccanica, Politecnico di Milano, via La Masa 1, Milan, Italy

R. Fagiani • M. Vanali (✉)
Dipartimento di Ingegneria Industriale, Università degli studi di Parma, Parco Area delle Scienze, 181/A, Parma, Italy
e-mail: marcello.vanali@unipr.it

32.2 Structure Description

The G. Meazza stadium is a famous and huge concrete structure, capable of around 80,000 seated places during football matches, and a similar number in other occasions, such as live rock concerts. The stadium is composed of three different sub-structures built at different times, from the late 1920s up to the early 1990s; each sub-structure (ring) is independent from the others and behaves differently when excited by the moving crowd. The stands are cantilevered, a feature which may give rise to concern of susceptibility to excitation by the jumping action of people.

In Fig. 32.1 a cross-section of the structure and a plan view are shown highlighting the three main rings composing the structure and the considered stands.

At the moment each of the stadium stands is monitored in one point [16], vertical and horizontal accelerations are measured 24 h a day. In this paper two stands, one 2nd ring and on 3rd ring are considered. These stands have been chosen as they have two different dynamic response and they face the stage during rock concerts making them some the most attractive places for the crowd.

The different dynamic response of the considered stands is highlighted in Fig. 32.2, where the frequency response functions measured during forced modal testing [15] is shown in the vertical direction for both stands, and in the horizontal directions for the 2nd ring stand only.

As can be seen in Fig. 32.2 the second ring stand has a main vertical resonance around 4.5 Hz and a Horizontal mode which is located around 2.2 Hz, on the other hand the 3rd ring one has two main vertical resonances, one around 3.2 Hz and the other in the 5.6 Hz area (actually both have more modes interacting in the same time [14]). Both stands have resonances that can be forced during synchronous crowd motion as stated in the different guidance and standards [8, 10, 11, 17, 18]. These two stands have been chosen as due to their position they will be the most excited during all kind of events held in the Giuseppe Meazza Stadium.

In the next paragraph the considered standards and guidance will be briefly described.
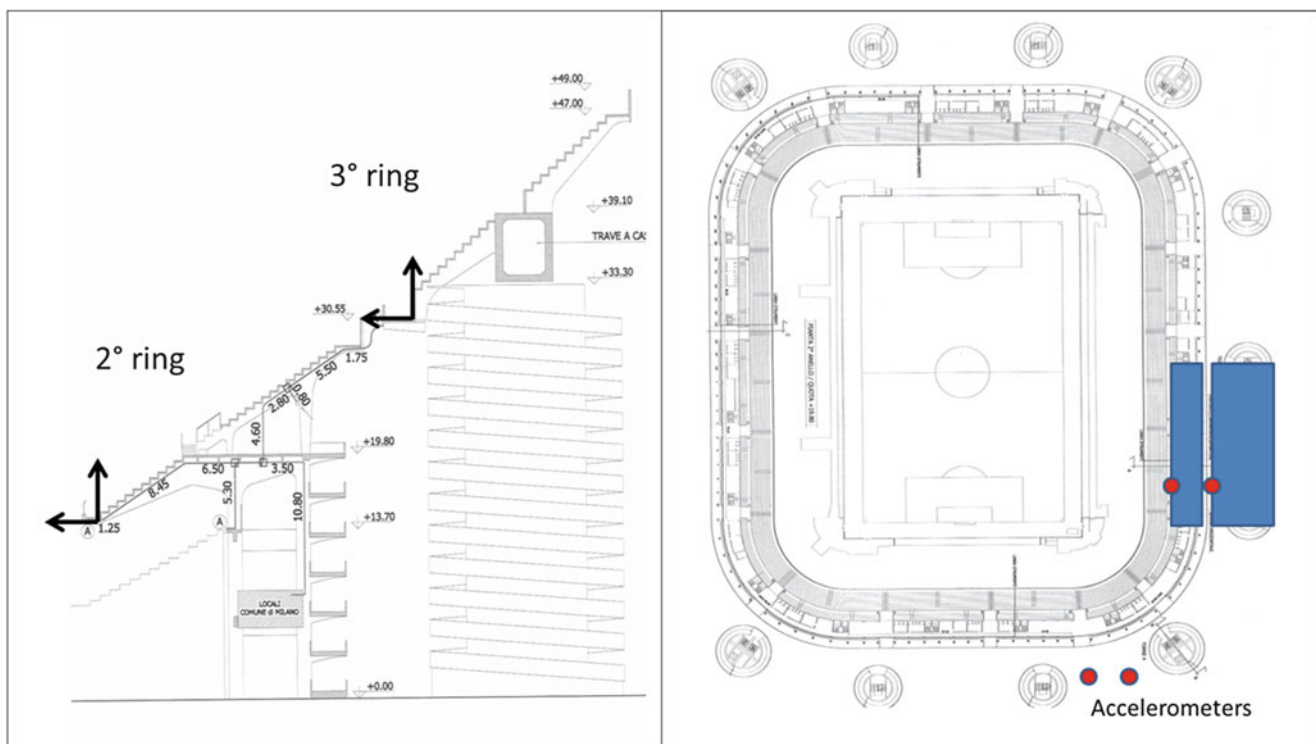
Fig. 32.1 Cross section and plain view of the Giuseppe Meazza Stadium, the *rectangles* highlights the considered grandstands, *dots* show the installed accelerometers position and the *arrows* the measurement directions
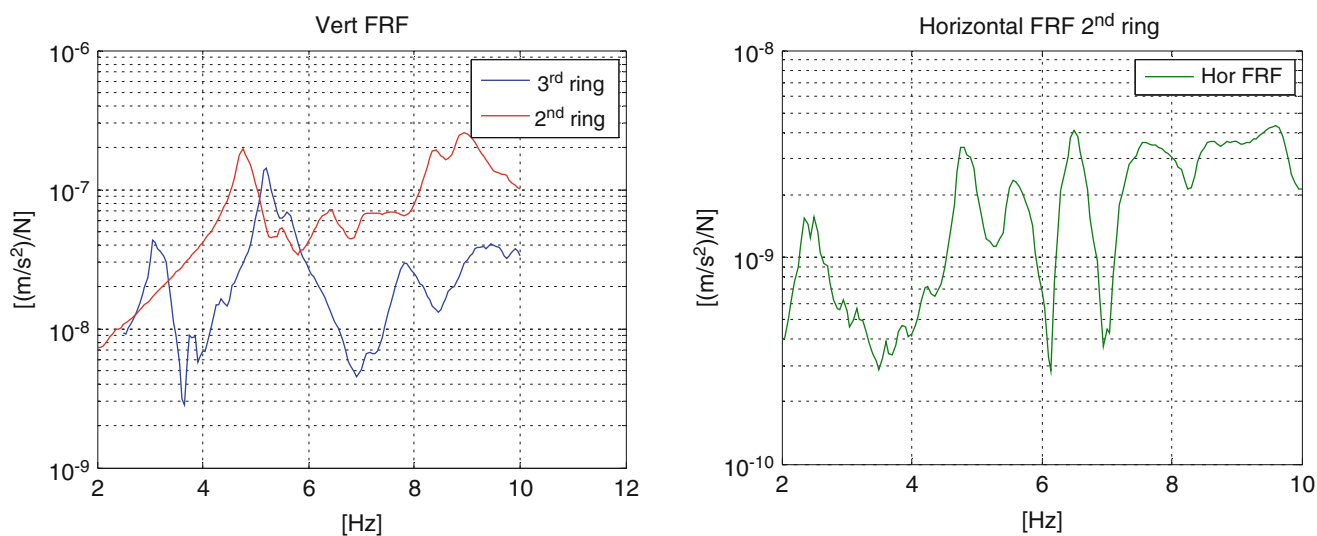
Fig. 32.2 Frequency response functions (*FRF*) of the considered stands

Table 32.1 Limit values for RMS (BS6841 and ISO2631) [6, 7, 9]

Frequency weighted RMS (ms^{-2})	Human reaction
<0.135	Not uncomfortable
0.135–0.63	A little uncomfortable
0.5–1.0	Fairly uncomfortable
0.8–1.6	Uncomfortable
1.25–2.5	Very uncomfortable
>2.5	Extremely uncomfortable

32.3 Considered Standards and Guidance

Since stadia host very large numbers of people attending both sporting events and rock/pop concerts some concerns arise on the loading that these civil structures have to support. Dynamic loads generated by people can be short random excitations like happens for goals during football matches and/or repeated periodic loading caused by motion synchronized with song rhythm. The achieved vibration level has to be analyzed from two different points of view. The first regards the structure damages while the second concerns the evaluation of people perception from a disturbing to a panic sensation.

Since publication of BS6399 Part 1 (1984) and of SCOSS 6th report (1986) great attention was given to structure safety and structure design to avoid risk of crowds accidents [19, 20]. The idea is to avoid structure resonance in the frequency range excited by jumping people. The fundamental natural frequency of the empty structure has to be above a value given for each direction (8.4 Hz vertically and 4 Hz horizontally). Actual limits on design of permanent grandstands subjected to dynamic crowd actions are given in IStructE 2008: vertical limit is 3.5 Hz for sport events and classical concerts and 6 Hz for pop concerts, horizontal limit is 1.5 Hz [21].

Despite all the British Standards and Design Guides realized in the recent years, the human acceptance criteria are based on limited published researches. The first step in this direction was made by the BS6841:1987 Guide to Measurement and Evaluation of Human Exposure to Whole-Body Mechanical Vibration and Repeated Shock [9]. This British Standard guide allows to quantify vibration in relation to human health, interference with activities, discomfort, perception and motion sickness. It deals with vibrations due to transport, machinery and industrial activities. Vibration limits are not presented but appendices provide current information on the possible effects of vibration. The guide suggests to evaluate vibration magnitude by the weighted root-mean-square acceleration (RMS). Different frequency weightings are required for the different axes of vibration to account for the different effects on human. People reaction is considered dependent on vibration frequency and posture. This method based on the RMS evaluation may be used when the crest factor does not exceed 6.0. The weighted root-mean-square acceleration value ranges related to human comfort given in the standard concerning vehicle comfort are shown in Table 32.1.

Table 32.2 Limit values
for VDV

VDV(m/s$^{1.75}$)	Human reaction
<0.66	Reasonable for passive person
0.66–2.38	Disturbing
2.38–4.64	Unacceptable
>4.64	Probably causing panic

No limits are given in specific for building vibrations. No information is given on the RMS time window length. If the Crest Factor exceed 6.0 an alternative method of evaluation is provided by the vibration dose values (VDVs):

$$VDV = \left(\int_0^T a^4(t)dt \right)^{1/4}$$

where a(t) is the frequency weighted acceleration and T the total measurement period. The guide specifies that no consensus of opinion exists on the relation between VDVs and risk of injury.

Very similar, in terms of frequency weighting and guideline values, to the British Standard 6841:1987 is the ISO 2631-1:1997 Mechanical Vibration and Shock-Evaluation of Human Exposure to Whole-body Vibration-Part 1: General Requirements. This standard evaluates vibration magnitude by the weighted root-mean-square acceleration in relation to human health and comfort, perception and sickness. Like for the BS, there is no explicit vibration limit. The frequency range considered is from 0.5 to 80 Hz for health, comfort and perception, and form 0.l to 0.5 Hz for motion sickness. In this standard the crest factor limit is 9.0. If the limit is exceeded a VDV evaluation is suggested or a 1 s sliding RMS evaluation but no clues are given in order to have some limits.

In the recent literature, exists some VDV value range especially related to serviceability of stadia [17] (Table 32.2).

The ISO 2631-2:2004 Mechanical Vibration and Shock-Evaluation of Human Exposure to Whole-body Vibration-Part 2: Vibration in Buildings (1–80 Hz) analyzes the weighted acceleration RMS with respect to the comfort and annoyance of the occupants but again no real limits are given in the standard.

More details on vibration serviceability are given in the ISO 10137:2007 [8]. The ISO 10137:2007 Bases for Design of Structures-Serviceability of Buildings Against Vibration analyzes different sources of vibrations in relation to the effects on structures and on human. Specifically for the stadia, two vibration criteria should be considered. The first criterion is the comfort of the passive part of the audience. The second is the safety of the audience. Large vibration amplitudes may alarm both passive and active persons and in extreme cases can result in panic. The two maximum vibration limits may be obtained as a base curve given by the standard with a multiplying factor of 200 and of 400 respectively. The parameter compared with the reference curves is the acceleration r.m.s calculated on an averaging time of 10 s for the comfort criterion, and of 1 s for the panic criterion and filtered in 1/3rd octaves in order to be compared with the given limits.

As for the other guides and standards, the different vibration directions x, y and z (vertically and horizontally) are treated in a different manner. The given curve shape (amplitude vs frequency) reflects the frequency weighting given in the ISO 2631.

With the respect to the last codes, the Dynamic performance requirements for permanent grandstands subject to crowd action (2008) gives two possible approaches for design and assessment of grandstand [11]. The first is based on limiting values of natural frequency of the empty grandstand. The second estimates performance in specific events. The suggested design event scenario are four: events with less than maximum attendance, classical concerts and sporting events, high profile sporting events and pop concerts with cross generation appeal, high energy concerts. Each scenario is related with crowd behaviour, expected crowd make up, crowd expectation and acceptance criteria. The crowd expectation is focused on comfort except for the last scenario that involves safety. For each scenario the two possible design approaches are suggested (natural frequency or acceleration limit). In the present analysis, the interest falls on the second and the third scenario characterized by a design RMS acceleration limit of 3 and a 71/2 %g max. No clues are given in terms of frequency weighting of the measured acceleration and only a 10 s time window for the evaluation of the RMS is suggested, but not imposed.

Considering human perception of vibrations BRE Digest 426 (2004) still suggests the use of Kasperski peak acceleration limits (EuroDYN 1996) [1, 2]. Kasperski's peak acceleration limits for a frequency range <10 Hz are shown in Table 32.3

In this paper analysis has been carried out according to all the mentioned standards and limits in order to provide a numerical data base to assess their validity.

Table 32.3 Kasperski limits [1]

Peak acceleration (%g)	Perception
5	Reasonable for passive people
5–18	Disturbing
18–35	Unacceptable
>35	Panic

32.4 Events and Numerical Analysis

A number of different events held in the Giuseppe Meazza Stadium between summer 2013 and summer 2014 have been considered. These are:

- Vasco Rossi, Italian Rock Singer 4 concerts
- Luciano Ligabue, Italian Rock Singer, 2 concerts
- Pearl Jam
- Jovanotti, Italian Pop Singer 2 concerts
- Moda, Italian Pop
- Bruce Springsteen
- Robbie Williams
- Depeche Mode
- Negramaro, Italian Rock Melodic
- Milan-Parma, stadium not full
- Milan-Lazio, stadium full
- Milan-Barcellona, stadium full
- Inter-Milan Stadium full
- Inter-Cluj, stadium empty
- Inter-Chievo, stadium empty
- Inter-Bologna, stadium empty

All data were originally sampled at 256 Hz and the anti-aliasing filter is set at 85 Hz. It has to be said that this is quite a large amount of numbers and presenting them it is not an easy task. So we consider for each analysis the maximum recorded magnitude of each event on each measurement channel. Channels ending with 1 (351, 271) are vertical, and channels ending with 2 (352, 272) are horizontal.

At first we consider the absolute maximum recorded acceleration, both in the horizontal and vertical directions, for all the considered events. Results are shown in Fig. 32.3 together with the limits given by Kaspersky. Different curves are shown one for each filtering option. Unfiltered data, Band Pass filtered 0.5–15 Hz, BS6841 and ISO 2613 filtered are shown.

Maximum levels are experienced during the Ligabue and Pearl Jam concerts on the 3rd ring stand in the vertical direction (channel 351). Different filtering options are influencing the obtained results, even if this is more evident on the data coming from football matches. During many events the disturbing limit is overcame but no data are over the Unacceptable value. This kind of analysis gives no clues on how the highest levels are held in time. It is a common opinion that a slight acceleration burst will not worry the spectators while a long lasting high acceleration will be perceived as disturbing.

In order to understand if a situation will be perceived as disturbing or not it is far more useful to look at the averaged RMS values. Averaging on the whole events is not representative of the real disturbances and this can be seen by looking at CF values calculated for the RMS of the whole events, Fig. 32.4.

Looking at the CF values in Fig. 32.4 it can be seen that they are always above 10, no matter which filtering option is considered and that the highest CF are experienced during football matches where high bursts are experienced during goals or penalties etc. and a relative calm is present during the match. These CF values are indicated in all standards (BS 6841 and ISO 2631) as too high to consider the RMS as representative of the vibrations. In the ISO a sliding RMS on 1 s windows is suggested. This has been calculated and the maximum value for each event is shown in Fig. 32.5.

As a general comment it can be seen that the values calculated for the band pass filtered signals and the unfiltered ones are practically the same, while a difference is evidenced for the ISO and BS filtering in the vertical direction (horizontal filters are the same in both standards).
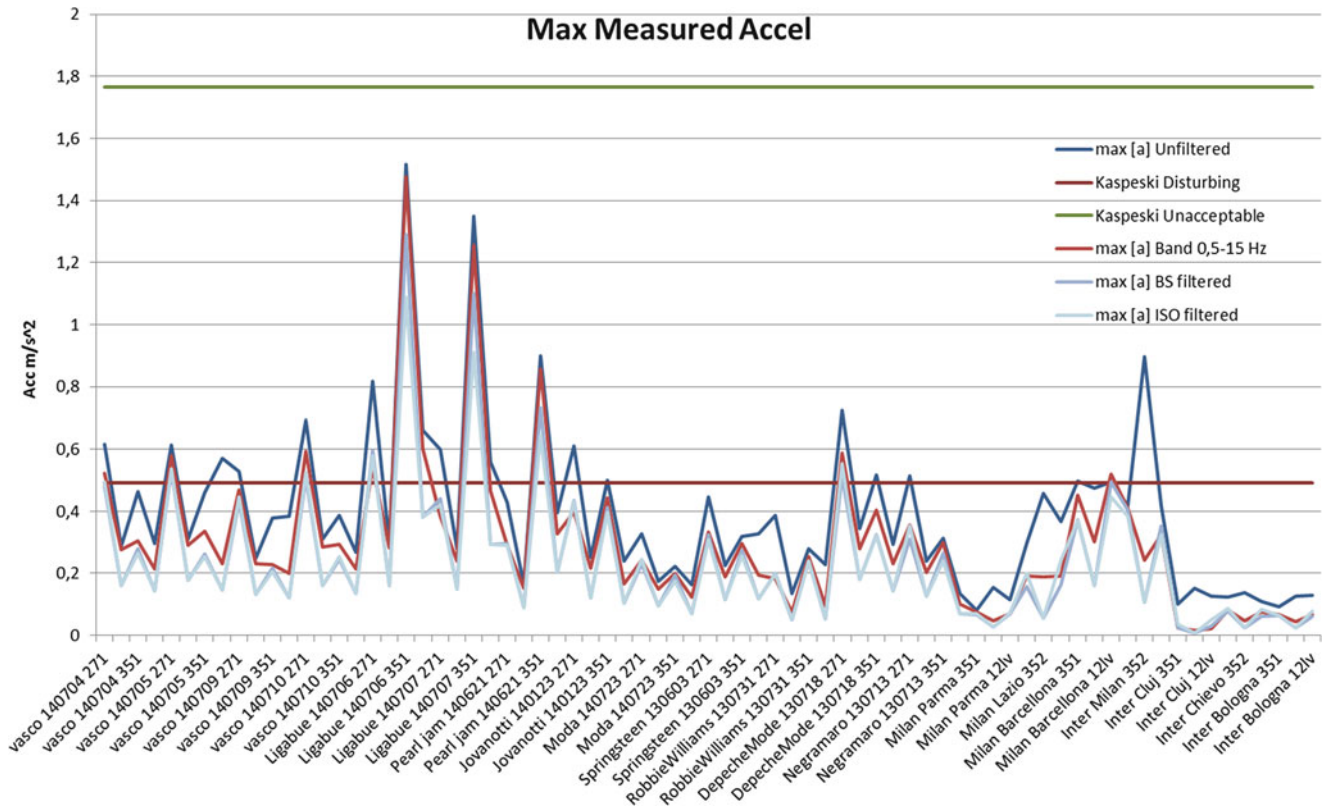
Fig. 32.3 Maximun peak acceleration all events different filtering + Kaspersky limits
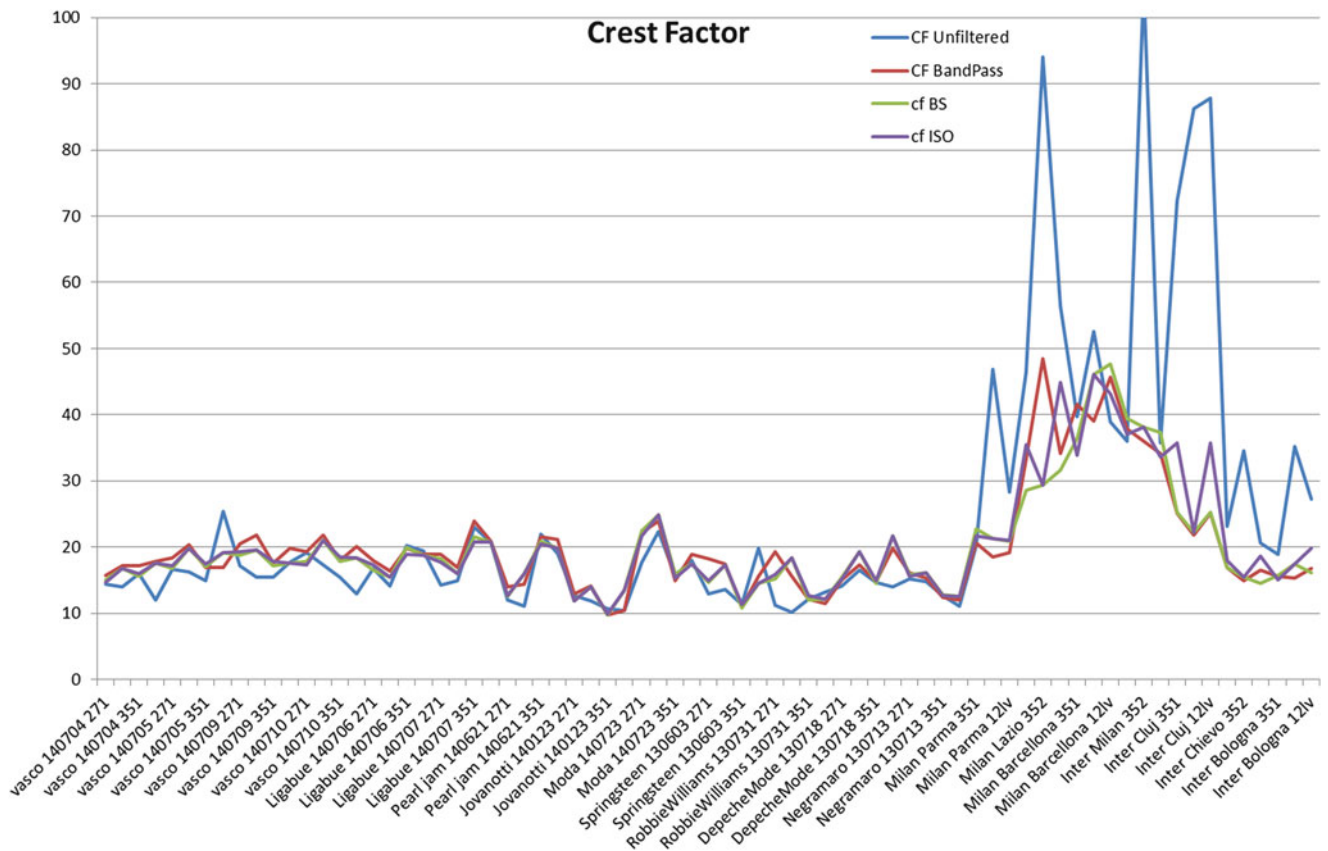
Fig. 32.4 Calculated crest factor on the whole event
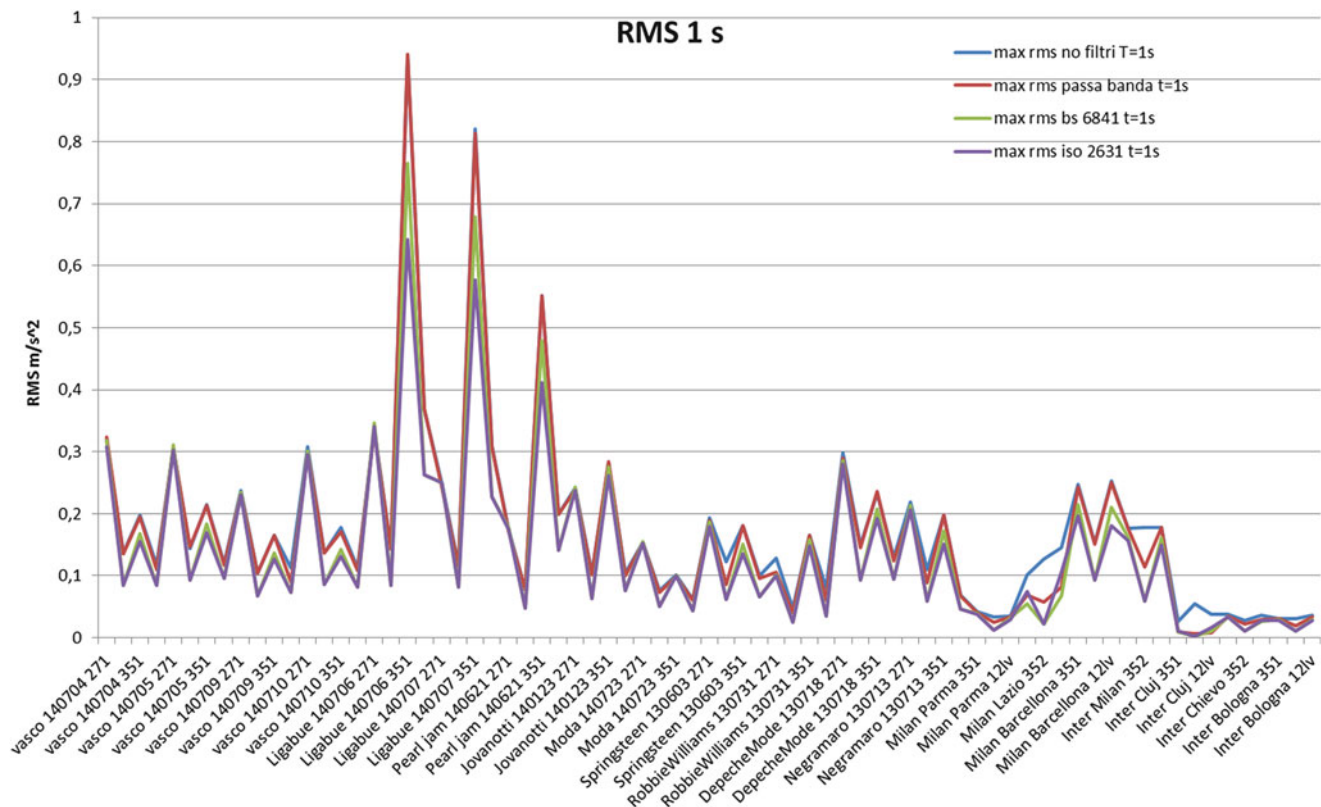
Fig. 32.5 1 s window sliding RMS, different filtering

Again maximum values are recorded during the Ligabue and Peral Jam concerts in the vertical direction on the 3rd ring, values calculated with the ISO filtering are lower as this filter penalize the frequencies at which 3rd ring resonances are located (3.2, 5.1 Hz).

The CF factors calculated for the 1 s sliding RMS are always in the limit to be accepted, anyway no limits are given in the standards and guidance for this evaluation and no idea of how long the maximum level is maintained is evident in the analysis. If the limits given in Table 32.1 are considered, it is remembered that these values are given for a longer RMS average and intended to represent comfort riding vehicles, the achieved maximum fall into the fairly uncomfortable range for the BS weighting and nearly in the same range for the ISO.

In the authors opinion a high level vibration perceived for just 1 s is not enough to cause a real worry in spectators attending a rock concert which are naturally involved in the action and music.

In the British Guidance [11] a 10 s sliding RMS is suggested and some comparison limits are given (mainly an RMS transposition of Kaspersky limits).

The 10 s sliding window RMS has been calculated and results are shown in Fig. 32.6.

Looking at Fig. 32.6 it can again be noticed that band pass filtering and unfiltered data achieve the same maximum values while ISO and BS filtering affects the calculated RMS. Maximum levels are always found for the above cited events, and horizontal values are always lower. Comparing the results with the British guidance given limits (3 %g for comfort and 7.5 %g for lack of comfort) it can be noticed that only the highest peaks are above comfort level. It has to be said that during rock concerts a strong horizontal motion of the 2nd and 3rd ring stand is clearly perceptible and this is not evidenced by any of the up to now considered analysis.

The next considered index is the VDV, this index is a continuous integral of the measured acceleration, and is continuously growing as the considered time lapse increases. The index has been calculated taking into account the whole concerts duration and the whole matches, including the mid time break. Calculated VDV's for the considered events are shown in Fig. 32.7.
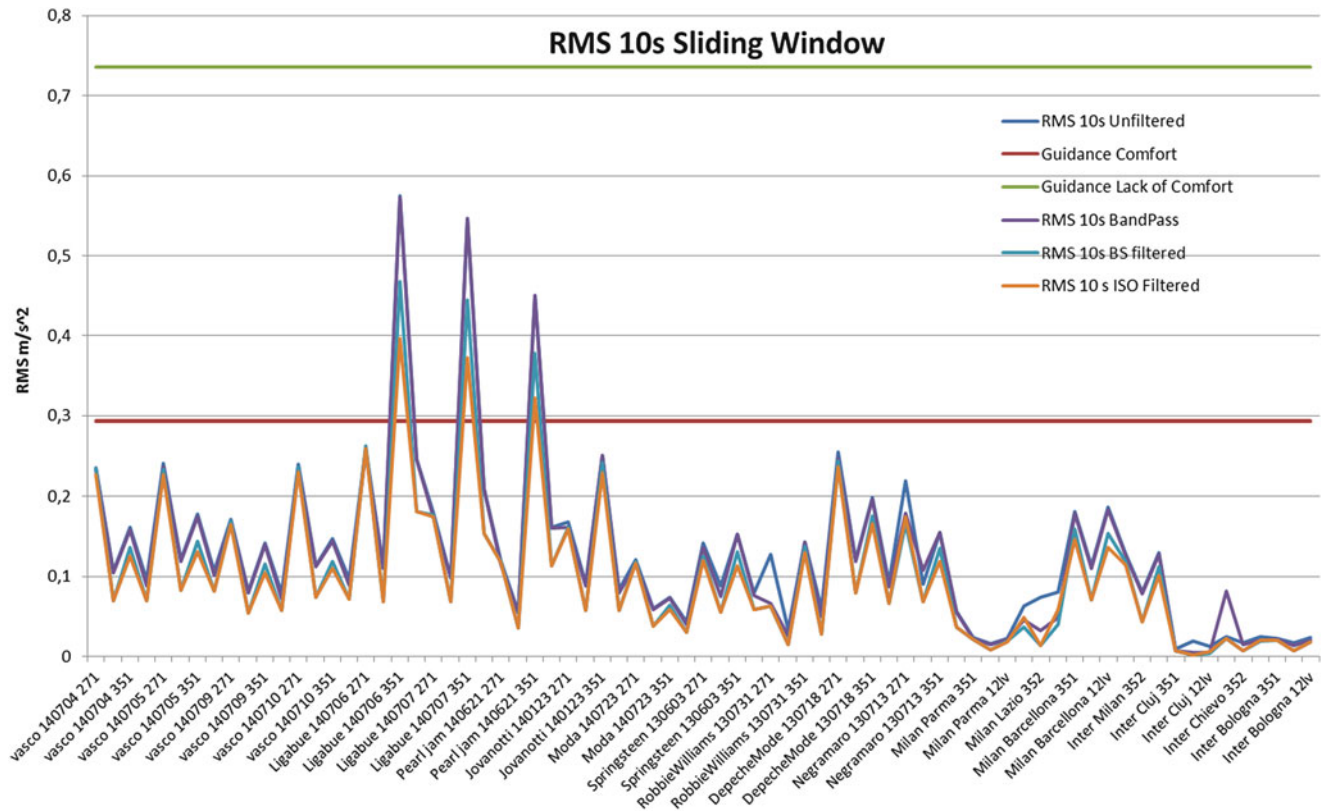
Fig. 32.6 10 s window sliding RMS, different filtering
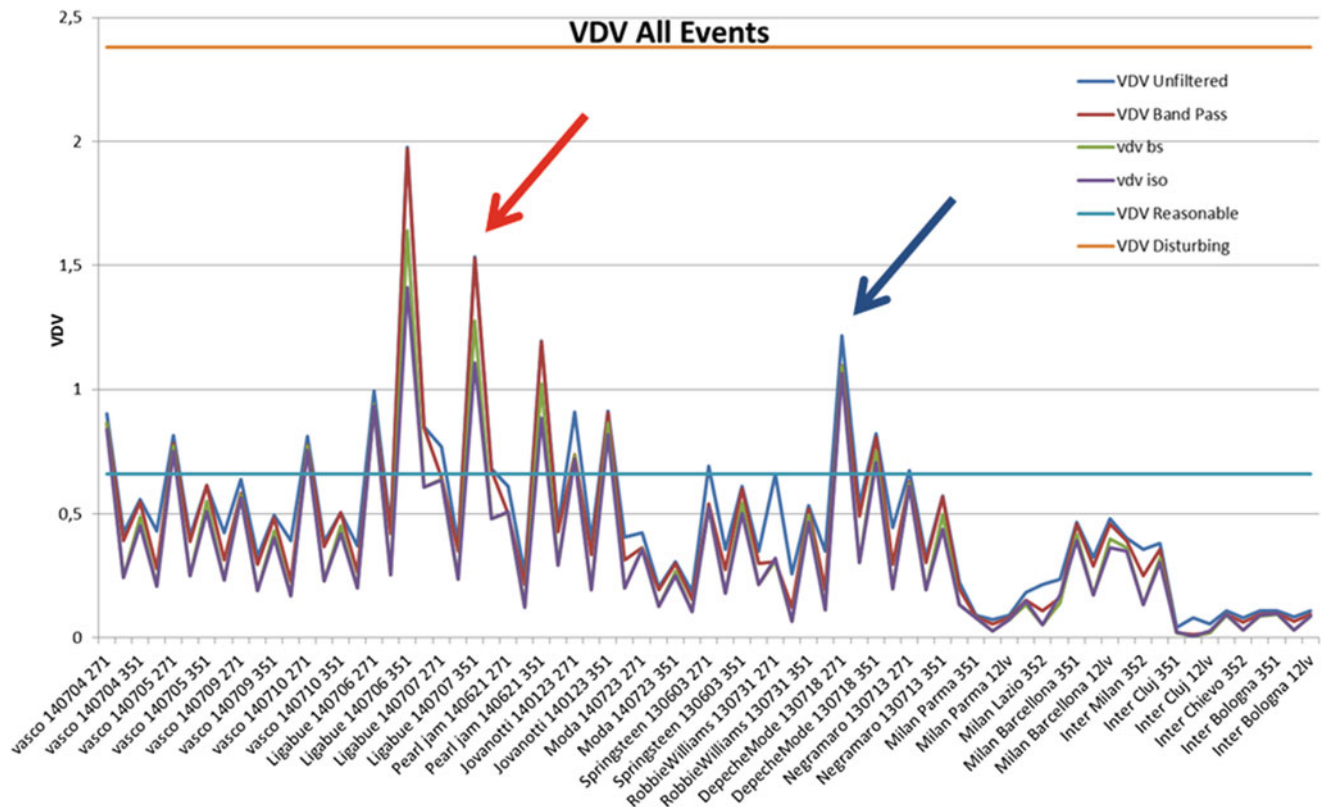
Fig. 32.7 VDV on the whole event, different filtering
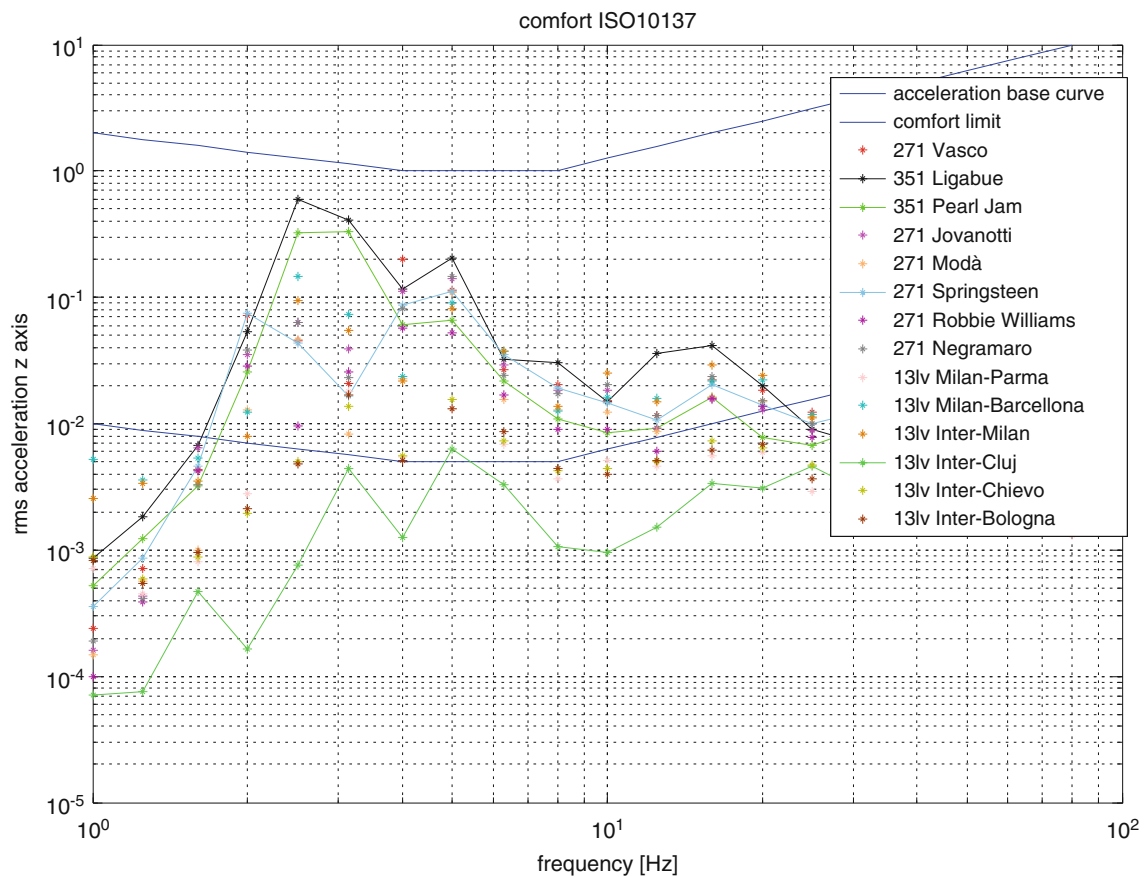
Fig. 32.8 ISO 1037 evaluation, comfort vertical direction

Same consideration can be applied to Fig. 32.7 results. Dashed and continuous arrows highlight the maximum disturbing events. In the dashed arrow peaks the 3rd ring stand are involved and filtering according to the ISO or BS standards affects the maximum achieved levels; the continuous arrow indicated peak is involving motion on the 2nd ring stand and here the filter effect is not so evident.

The last considered serviceability evaluation approach is the one described in the ISO 10137. The standard prescribes to evaluate the RMS in 1/3rd octave bands on two different sliding time windows (1 s for panic and 10 s for comfort). The maximum calculated value has to be compared with a limit curve given as a base curve multiplied per 400 (panic) or 200 (comfort).

In the standards section dedicated to grandstands only the vertical acceleration are considered, while the base curve is given for both the vertical and horizontal directions. In this work we examined both directions considering the same multiplier to obtain the limit curve in the horizontal direction.

Results for the vertical direction are shown in Figs. 32.8 and 32.9 for comfort and panic respectively.

Vertical vibrations are always below the given comfort and panic limits. In this case too, the highest values are reached for the Ligabue and Pearl Jam concerts on the 3rd ring and the lowest in the Inter-Cluj football match.

Figures 32.10 and 32.11 show the same results for the horizontal measured accelerations.

All values are under comfort and panic levels, even if the horizontal motion is clearly perceptible during rock concert and in some cases it raised worries in passive people.
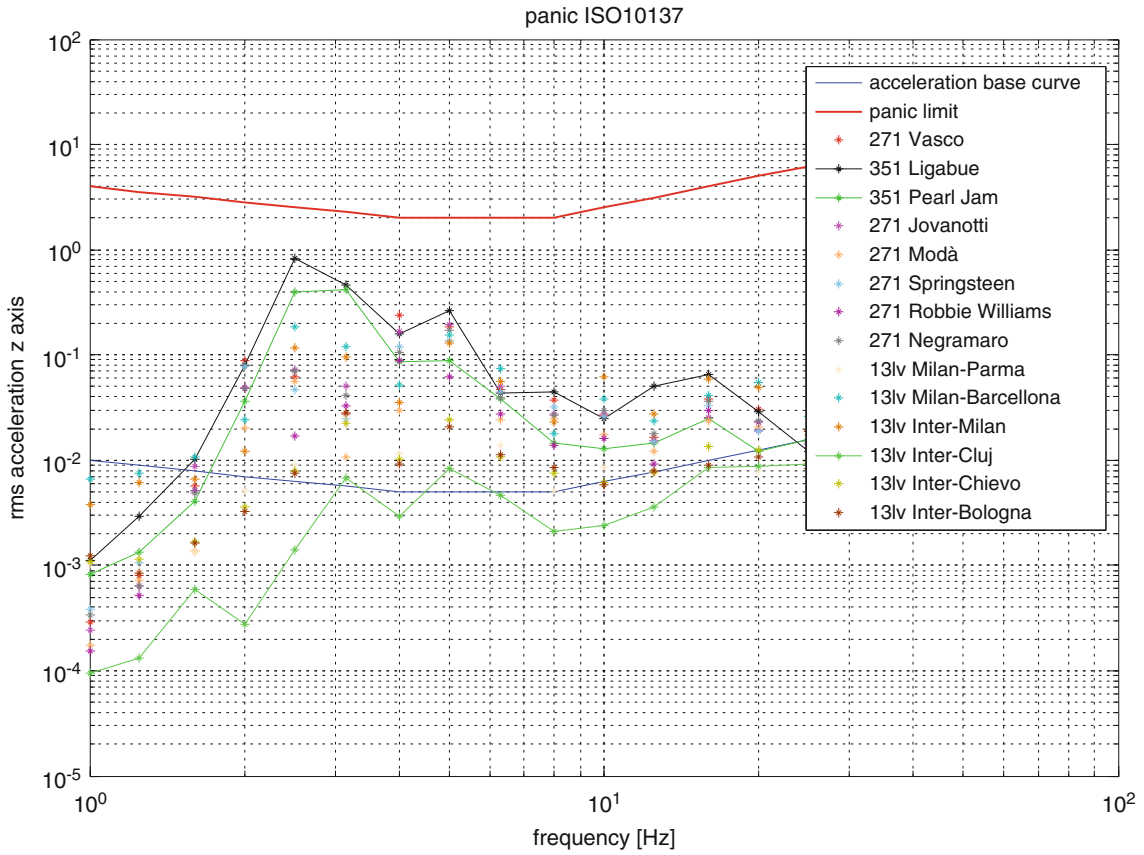
Fig. 32.9 ISO 1037 evaluation, panic vertical direction
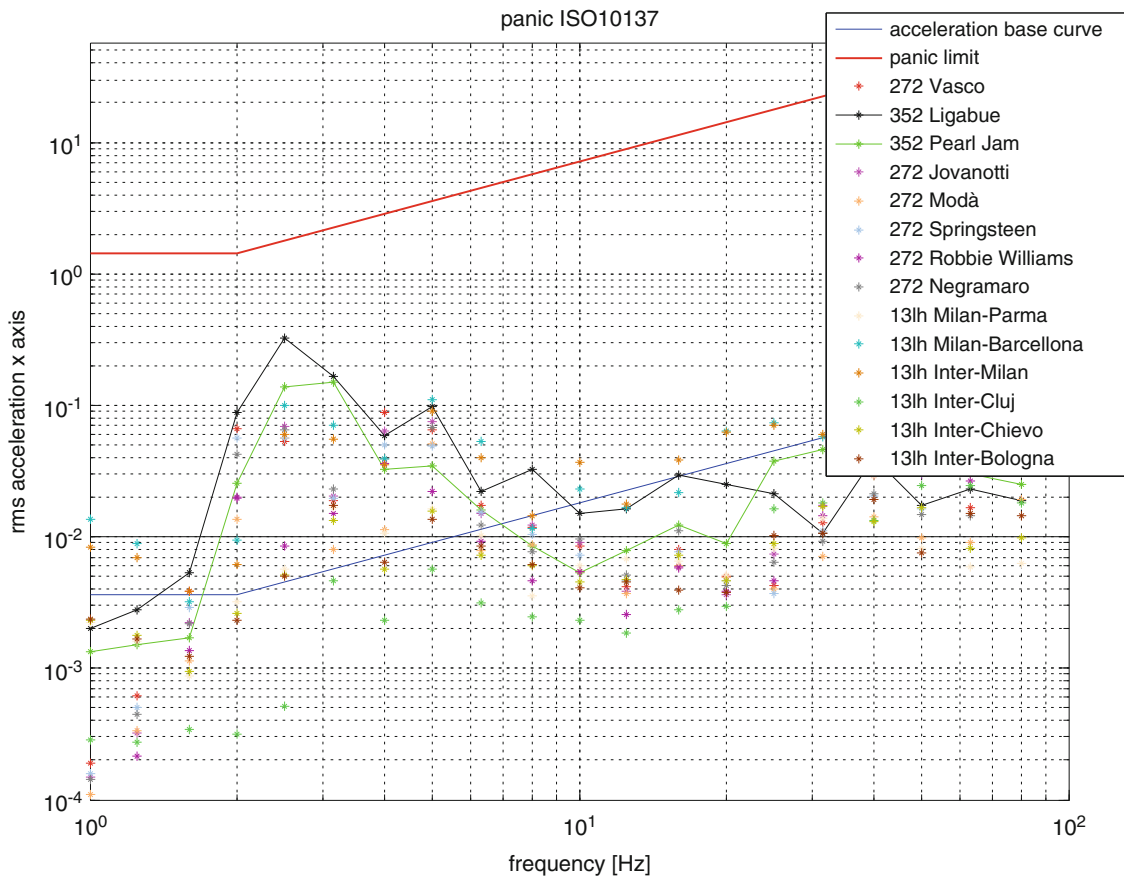
Fig. 32.10 ISO 1037 evaluation, panic horizontal direction
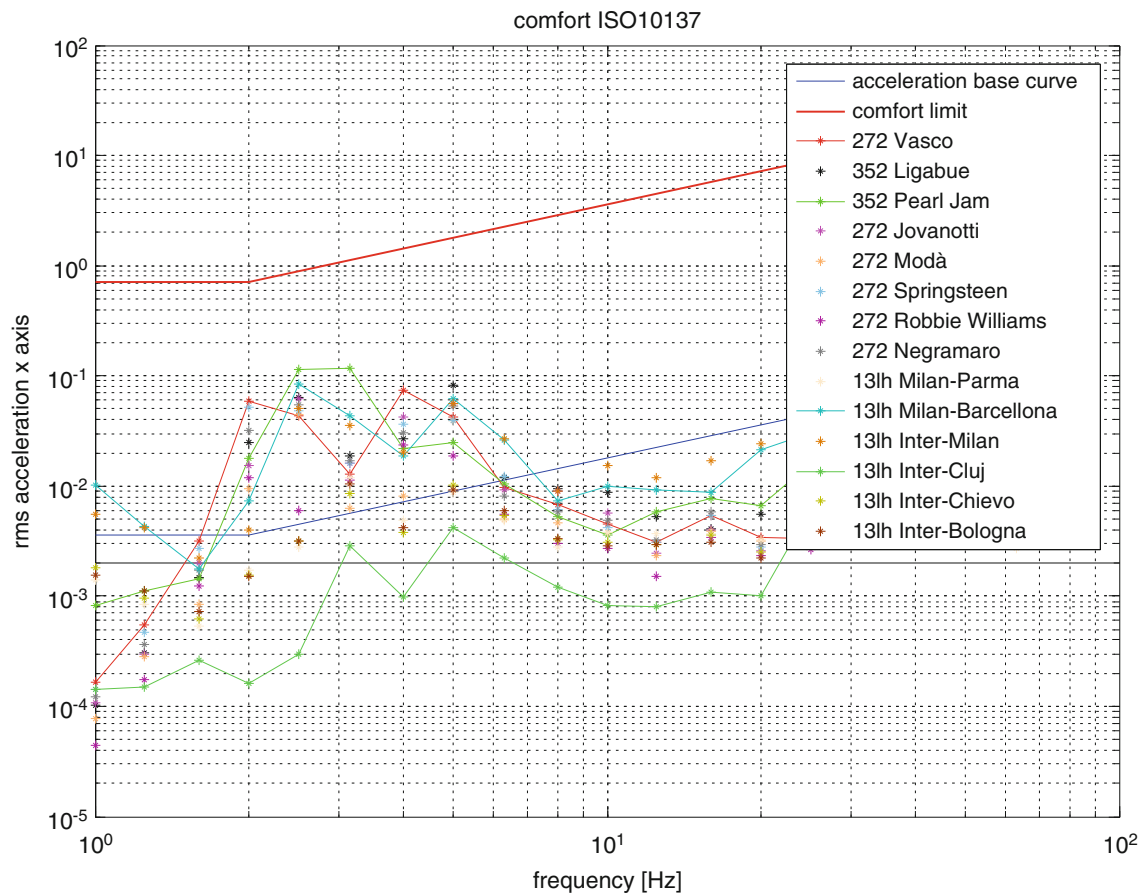
Fig. 32.11 ISO 1037 evaluation, comfort horizontal direction

32.5 Concluding Remarks

A number of events held in the Giuseppe Meazza Stadium has been analyzed under the vibration serviceability point of view. Two stands having different dynamic response have been considered in the paper. Measured vibrations have been compared to existing standards and guidance highlighting that rock concerts are the most worrying situations in terms of vibrations due to crowd synchronization phenomena.

The analysis show that according to some standards the comfort limits are sometimes exceeded while panic related limits are never reached. Frequency weighting has an effect on the computed value and the chosen weighting has to be correctly specified in order to provide valid data for further comparison.

In the ISO10137 case it seems that the proposed comfort limits are somehow high and discomfort could possibly be reached before overtaking the proposed limits. All standards and guidance are more focused on vertical vibrations discarding the effects of horizontal ones, and according to the authors opinion this should be further investigated.

References

1. Kasperski M (1996) Actual problems with stand structures due to spectator induced vibrations. In: Proceedings of the 3rd European conference on structural dynamics: EURODYN '96, Florence, 5–8 June 1996. Balkema, Rotterdam, vol 1, pp 455–461
2. Kasperski M, Niemann HJ (1993) Man induced vibrations of a stand structure. In: Proceedings of the 2nd European conference on structural dynamics: EURODYN '93, Trondheim, 21–23 June 1993. Balkema, Rotterdam, pp 977–983
3. Reynolds P, Pavic WM (2005) Prediction and measurement of stadia dynamics properties. IMAC XXIII

4. Browning GG (2011) Human perception of vibrations due to synchronised crowd loading in grandstands. PhD thesis, University of Bath, Department of architecture and civil engineering

5. Nhlenko S (2011) Human-induced lateral excitation of public assembly structure. PhD thesis University of Oxford Trinity term

6. ISO 2631-1 (1997) Mechanical vibration and shock-evaluation of human exposure to whole body vibration part 1: general requirements

7. ISO 2631-2 (2004) Mechanical vibration and shock-evaluation of human exposure to whole body vibration part 2: vibration in buildings (1 Hz to 80 Hz)

8. ISO 10137 (2007) Bases for design of structures-serviceability of buildings and walkways against vibrations

9. BS6841 (1987) Measurement and evaluation of human exposure of whole-body mechanical vibration and repeated shock

10. National Building Code of Canada (NBCC) (2005) User's guide – NBC 2005, structural commentaries (Part 4 of Division B) Commentary D. IRC

11. Institution of Structural Engineers (2001) Dynamic performance requirements for permanent grandstands subject to crowd action- interim guidance on assessment and design

12. Caprioli A, Vanali M (2009) Comparison of different serviceability assessment measures for different events held in the G. Meazza Stadium in Milano. IMAC-XXVII, Orlando, 9–12 Feb 2009

13. Caprioli A, Reynolds P, Vanali M (2007) Evaluation of serviceability assessment measures for different stadia structures and different live concert events. IMAC XXV, Orlando, 19–22 Feb 2007

14. Cigada A, Caprioli A, Redaelli M, Vanali M (2008) Numerical modeling and experimental modal analysis of a concrete grand-stand structure to structural health monitoring purposes. In: Proceedings of international conference IMAC XXVI, Orlando

15. Cigada A, Caprioli A, Redaelli M, Vanali M (2008) Vibration testing at Meazza Stadium: reliability of operational modal analysis to health monitoring purposes. J Perform Constr Facil 22(4):228–237

16. Cigada A, Moschioni G, Vanali M, Caprioli A (2010) The measurement network of the San Siro Meazza Stadium in Milan: origin and implementation of a new data acquisition strategy for structural health monitoring. Exp Tech 34(1):70–81

17. Ellis BR, Ji T, Littler JD (2000) The response of grandstands to dynamic crowd loads. Proc Inst Civ Eng Struct Build 140(4):355–365

18. Ellis BR, Ji T (2004) BRE Digest 426: the response of structures to dynamic crowd loads. Proc Inst Civ Eng Struct Build 140(4):355–365

19. British Standards for BS6399 Part 1 1984 with details of 1985,1988 and 1989 Amendments. Loading for buildings part 1: code of practice for dead and imposed loads. BSI, London

20. SCOSS 6th Report (1986) Structural safety 1983–85: review and recommendations – incl safety of demountable grandstands. Sixth report of SCOSS (The Standing Committee on Structural Safety) published in the Structural Engineer, Jan 1986, vol 64A (1), pp 28–32

21. Institution of Structural Engineers (2008) Dynamic performance requirements for permanent grandstands subject to crowd action: recommendations for management, design and assessment. IStructE, London

Chapter 33
SMD Model Parameters of Pedestrians for Vertical Human-Structure Interaction

Mengshi Zhang, Christos T. Georgakis, Wenjun Qu, and Jun Chen

Abstract Predictions of footbridge or long-span floor vibrations induced by pedestrian crowds can often prove inaccurate. One of the main deficiencies of the methods used for predicting these vibrations is the lack of consideration or erroneous representation of human-structure interaction (HSI). In this paper, the results from a series of footbridge tests designed to observe and then model HSI are presented. A laboratory footbridge was excited to three predetermined vibration amplitudes by an actuator, with and without the presence of pedestrians. In the tests with pedestrians, 4, 7 and 10 pedestrians were asked to walk repeatedly across the footbridge. Frequency response functions (FRF) of the footbridge with and without pedestrians were extracted from test data. To account for the HSI, pedestrians on the bridge were modeled as a spring-mass-damper (SMD) system attached to the footbridge. The mass, damping and stiffness of a single pedestrian were calculated by fitting the FRF obtained from the tests. It was found that the SMD models of pedestrians could adequately model HSI between a structure and its walking occupants. Furthermore, the stiffness and damping of the SMD model of a single pedestrian were found to be close to half of a standing person with two bent legs.

Keywords Human-structure interaction • Human-induced vibration • SMD model • Model parameters

33.1 Introduction

Noticeable vibrations can be induced by pedestrians for structures such as footbridges and long-span floors, particularly when they have natural frequencies close to pacing frequencies. These vibrations may be considered excessive for users when they become uncomfortable or if they affect the user's balance or gait, thus limiting the usefulness of the structure. The Millennium Bridge in London experienced excessive lateral vibrations on its opening day and was subsequently closed to the public while this vibration problem was addressed [1].

Although significant amounts of research in this field have been undertaken in the years after the opening of the Millennium Bridge, the accurate prediction of the vibrations induced by a large walking crowd or a stream of pedestrians is still not readily obtainable. Randomness from the inter- and intra-subject variability of human loading, human-human interaction, and HSI account for the difficulties in predicting the vibrations induced by a walking crowd or a stream of pedestrians.

HSI should be understood as a coupling of human and structural characteristics, such that changes in a structure's properties leads to changes in the way humans walk and vise-versa. Structural vibrations affect pedestrians' gait through the pedestrians' nervous systems: they sense the vibration and make changes to their gait. Conversely, the mechanical characteristics of the pedestrians are coupled with the structure as they walk, run, jump or stand still. This interaction inevitably takes place because human beings have variable mechanical properties wherever they are and whatever they are doing.

M. Zhang (✉) • W. Qu • J. Chen
College of Civil Engineering, Tongji University, Siping Road 1239, Shanghai 200092, People's Republic of China
e-mail: 061324zms@tongji.edu.cn

C.T. Georgakis
Department of Civil Engineering, Technical University of Denmark, Building 118, Brovej, 2800 Kgs, Lyngby, Denmark

Two main perspectives are considered when examining how the mechanical characteristics of human beings interact with a structure. The first perspective is to consider how pedestrians change the mass and damping properties of the structure they occupy. Most published research to date has focused on the interaction between static/passive people and structures, although there are a few notable works that examine the effects of moving persons [2–6]. There is no consensus on how people effectively change the mass of the structure they are occupying. Structural natural frequencies have been found to both increase and decrease [2–6], corresponding to an effective decrease or increase of mass, respectively. There is general agreement though that people add damping to the structure [2–6].

Conclusions on how people in motion influence the dynamic properties of structures are limited. Ellis and Ji [3] concluded that people in motion simply load the structure rather than changing its modal properties, but Johns, Reynold and Pavic [7] argued that for activities when people are in contact with the structure, people have the potential to influence a structure's modal properties and this argument would explain why human structure interaction could not be found by Ellis and Ji [3]. Zivanovic et al. [4] found by experiment that people effectively extracted mass but added damping to the footbridge on which they were walking. Georgakis and Jørgensen found that people added both mass and damping to the footbridge they occupied [5, 6].

The fact that there is no consensus on how people change the effective mass of the structures they occupy reveals that people are more likely to act not only as mass and damper, but as a self-contained dynamic system attached to the structure they are occupying [3, 8]. This is the second perspective for HSI and seems more intuitive, as it is difficult to justify the analogy e.g., of a human acting as a fixed damper. Dougill et al. [9] investigated the dynamic properties of a bobbing person using a single-degree-of-freedom (SDOF) spring-mass-damper system and coupled it with a SDOF structure. A pair of forces representing the biomechanical force within the bobbing human excited the coupled 2DOF system. Alexander [10] also proposed a similar mass-spring-damper-actuator system to model an active crowd at arbitrary locations on the structure and coupled it to a structure. The theoretical dynamics of the crowd-structure interaction system indicated that an increase in any predominant frequency would be observed. To date, no experimental investigation of pedestrian-structure interaction, using a coupled dynamic system consisting of both the pedestrians and the structure, appears to have been published.

A footbridge with its fundamental frequency close to 2.2 Hz was designed and built at Technical University of Denmark to investigate HSI. The footbridge was excited to vibration amplitudes 1, 2.5 and 5 mm at mid-span by an hydraulic actuator within the frequency range 2.0–2.25 Hz and 0.2–4.3, with and without various numbers (4, 7 and 10) of pedestrians walking repeatedly across the bridge. The pedestrians walked with a slower pacing frequency than the natural frequency of the bridge and thus the excitation of the dynamic system caused by the pedestrians could be regarded as negligible compared to the excitation from the actuator. The Frequency Response Functions (FRFs) of the footbridge with and without pedestrians were extracted from test data. Note that the FRF used in this paper is not the strict definition of FRF, but it describes the amplitudes the footbridge response to sinusoidal excitation and therefore. It is similar to the function of FRF and therefore the terminology FRF is used here and hereafter. The spring-mass-damper system of the pedestrians was employed to model HSI and the dynamic properties of a single pedestrian were found by fitting the FRF from tests.

33.2 Experiment and Methodology

33.2.1 Description of the Structure

The footbridge was a simply supported 16 m-long steel double U-beam construction, located in the Structures Laboratory of the Department of Civil Engineering at Technical University of Denmark. Masses were added to the footbridge crossbeams and also to the center of the footbridge to increase the modal mass, decreasing the footbridge's fundamental frequency to a level close to the average human pacing frequency. Medium density fiberboard plates with a width of 1,840 mm were attached to the steel bridge with screws to form the walking surface. Wooden platforms accessed by stairways were constructed on either side of the footbridge for the pedestrians to begin their walking and to be able to turn around. The footbridge with pedestrians walking on it can be seen in Fig. 33.1.
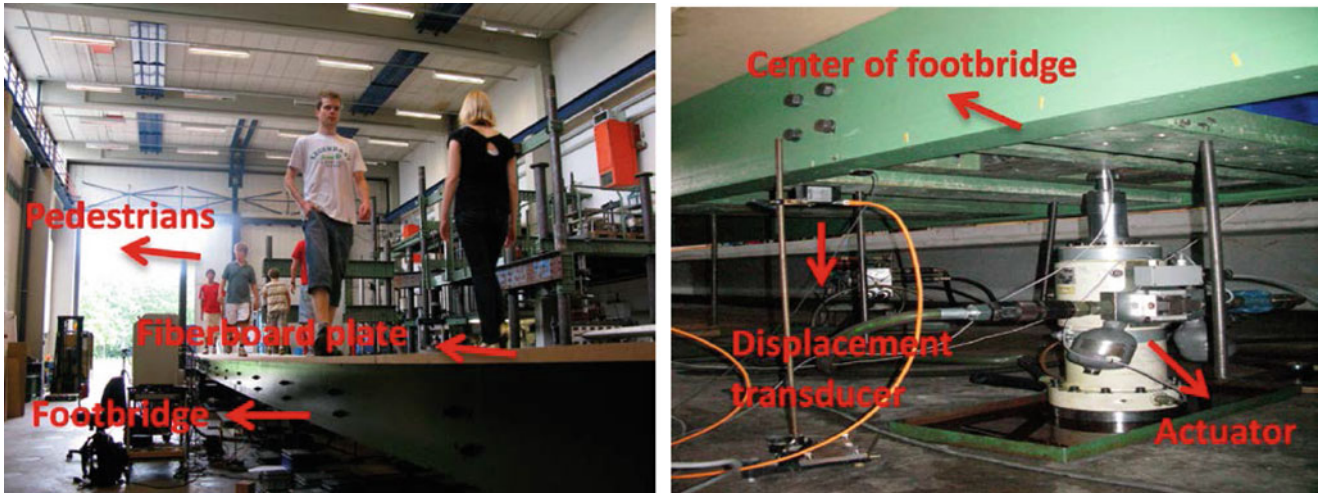
Fig. 33.1 Pedestrians walking on the fiberboard plates attached to the footbridge (*left*) and the actuator and laser displacement transducer at mid-span of the footbridge (*right*)

Table 33.1 Excitation frequencies of the empty footbridge

Frequency [Hz]												
f_1	f_2	f_3	f_4	f_5	f_6	f_7	f_8	f_9	f_{10}	f_{11}	f_{12}	f_{13}
0.2	0.4	0.6	0.8	1.0	1.2	1.4	1.6	1.8	2.0	2.1	2.2	2.25
f_{14}	f_{15}	f_{16}	f_{17}	f_{18}	f_{19}	f_{20}	f_{21}	f_{22}	f_{23}	f_{24}	f_{25}	
2.3	2.4	2.5	2.7	2.9	3.1	3.3	3.5	3.7	3.9	4.1	4.3	

33.2.2 Footbridge Modal Analysis

A modal analysis of the empty footbridge was undertaken to determine the modal mass, stiffness, damping and mode shapes for the first several modes of the footbridge. The modal analysis was performed through a serious of free-decay tests. The modal frequency and damping were both found to be amplitude dependent through Hilbert transformation of the free-decay signals. The first natural frequency of the footbridge f_n and the damping ratio ξ of the first mode were found to be 2.213 Hz and 0.0048, when the footbridge's mid-span vibrates at the amplitude of 5 mm respectively. First modal mass M_1 of the footbridge was calculated as:

$$M_1 = \frac{K_1}{\omega_{n1}^2} \tag{33.1}$$

in which $K_1 = 666,969$ N/m and is the stiffness of the footbridge measured from concentrated loading at mid-span; ω_{n1} is the first circular frequency equal to $2\pi f_n$. The first mode shape of the bridge is a half sine wave. This is why the first modal stiffness of the footbridge can be approximated as the stiffness of the footbridge's mid-span under concentrated loading at mid-span. Detailed results for the footbridge modal testing have been reported in [5]. In the following analysis, the footbridge is treated as SDOF system with properties of its first mode.

33.2.3 Tests

A 100 kN Instron hydraulic actuator, placed vertically beneath the central mid-span, was used to excite the footbridge. Tests on the bridge were performed under two different conditions: with and without pedestrians. Three vibration amplitudes were imposed (1, 2.5 and 5 mm) at the footbridge's mid-span with the vibration frequencies listed in Table 33.1 without the pedestrians.

Table 33.2 Excitation frequencies of the actuator for the occupied footbridge

Pedestrians	Amplitude [mm]	Frequency [Hz]							
		f_1	f_2	f_3	f_4	f_5	f_6	f_7	f_8
4	1.0	2.086	2.136	2.155	2.174	2.195	2.211	2.230	2.280
	2.5	2.073	2.123	2.142	2.162	2.182	2.201	2.220	2.270
	5.0	2.029	2.072	2.097	2.115	2.134	2.152	2.170	2.220
7	1.0	2.022	2.072	2.104	2.135	2.167	2.198	2.230	2.280
	2.5	2.009	2.059	2.091	2.123	2.156	2.188	2.220	2.270
	5.0	1.965	2.015	2.046	2.077	2.108	2.139	2.170	2.220
10	1.0	1.980	2.030	2.074	2.118	2.162	2.206	2.250	2.300
	2.5	1.970	2.020	2.064	2.108	2.152	2.196	2.240	2.290
	5.0	1.950	2.000	2.044	2.088	2.132	2.176	2.220	2.270

4, 7 and 10 pedestrians were asked to walk repeatedly across the footbridge, whilst the footbridge was actuated (Fig. 33.1). The actuation frequencies for the footbridge with pedestrians are listed in Table 33.2. Each test with pedestrians lasted 180 s. This duration was calculated to be sufficient so that steady-state conditions could been achieved and so that the excitation of the pedestrians evolved into a stationary process. Further details of the tests can been found in [6].

33.2.4 Measurements

A calibrated Instron (8.516) load cell was used to measure the force between the actuator and the footbridge throughout all the tests, as shown in Fig. 33.1. Displacement of the mid-span of the bridge was recorded with a laser displacement transducer fixed at the mid-span of the footbridge as shown in Fig. 33.1 (right). The sampling frequencies of the displacement transducer and the force from the load cell were 2,048 Hz.

The observed pacing frequencies of the pedestrians in the tests were approximately calculated by counting the steps and measuring the time it took to traverse the bridge. The pacing frequencies observed during the tests were lower than the frequencies of actuation. As the actuation frequencies were closer to the natural frequency of the footbridge, the excitation from the pedestrians was considered negligible, as their mean pacing frequencies (at around 1.7 Hz) were significantly lower than that of the actuator (at around 2.25 Hz). In that way, the influence of excitation from pedestrians was omitted in the later analysis. This is an important assumption, as the pedestrian excitation could not be measured.

33.2.5 HSI Using an SMD Model for Pedestrians

In biomechanics, humans are often modeled as a SDOF system [11]. In the specific domain, passive/static human beings are usually of interest. The SDOF parameters have been shown to be dependent on body configuration. People standing with legs bent on a platform have been found to have a natural frequency of 2.9 Hz and damping ratio of 0.34. For normal standing, the natural frequency and damping were found to be 5.74 Hz and 0.695 respectively [12]. Seated people had a 5 Hz natural frequency and a damping ratio of 0.45 [13]. Alexander [10] reported the natural frequency of a human being in various postures, ranged from 1 to 16 Hz and the damping ratio of a human being as ranging from 0.3 to 0.5. The parameters of active people have seldom been reported. Dougill et al. [9] found for a SDOF model of a bouncing person, that the natural frequency and damping ratio were 2.3 Hz and 0.25, respectively. No parameters of this kind have been reported for a walking person. Even though a walking person may in some sense be considered as similar to standing, it has not ever been shown that the parameters for standing persons are equivalent to those of walking persons. Walking is different from standing in two ways. Firstly, walking people are active and some active mechanism such as a pair of biomechanical forces should be added to the SMD model to account for human muscle's activeness [9, 10]. Secondly, during walking, two legs are swinging alternately and thus the leg configuration is constantly changing and different from that of standing person.
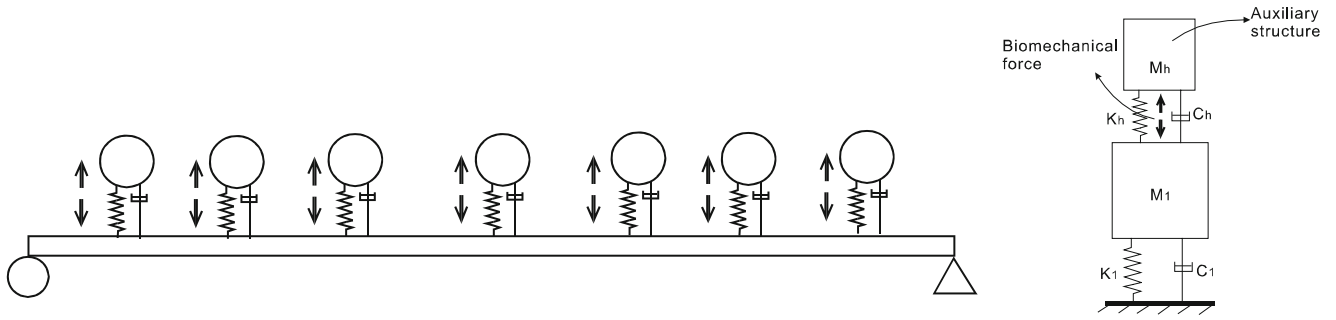
Fig. 33.2 HSI modelled equating pedestrians with added SMD system

To assess HSI, a spring-mass-damper model with a pair of biomechanical forces was employed to model the pedestrians on the footbridge. All pedestrians were assumed here to have a uniform mass, damping and stiffness and with this assumption, all SMD models of each pedestrian can be combined into a single SMD representing all pedestrians. When only the first mode of the footbridge is considered, the pedestrians and the footbridge form a 2DOF system as shown in Fig. 33.2.

The parameters of the upper secondary SMD (Fig. 33.2 right) correspond to the dynamic parameters of the walking pedestrians, including mass, damping coefficient and stiffness. For the 2DOF system, the FRF of the main mass when it is loaded with a sinusoidal force of unit amplitude can be derived theoretically from the parameters of the coupled 2DOF system. The damping ratio of the primary system (footbridge) is 0.0048, which is much smaller than the generally reported damping ratio of human beings. Therefore, for convenience, the following equation was used to calculate the FRF of the primary system when the main mass is loaded with a harmonic force with unit amplitude [14]:

$$\frac{x_1^2}{P_0^2} = \frac{\left(K_h - M_h\omega^2\right)^2 + \omega^2 C_h^2}{\left[\left(-M_1\omega^2 + K_1\right)\left(-M_h\omega^2 + K_h\right) - M_h\omega^2 K_h\right]^2 + \omega^2 C_h^2\left(-M_1\omega^2 + K_1 - M_h\omega^2\right)^2} \tag{33.2}$$

in which, x_1 is the amplitude of the motion of the primary system; P_o is the amplitude of the harmonic force acting on the primary mass; M_1 and K_1 are the mass and stiffness of the primary system; M_h, C_h and K_h are the mass, damping and stiffness of the upper mass; ω is the circular frequency of the harmonic excitation.

The parameters of the secondary SMD system were found by means of a trial and error method leading to an FRF of the footbridge that best fit the experimentally obtained FRF. The M_h, C_h and K_h of the SMD of all the pedestrians were further divided by the effective number in each test to obtain the mass, damping and stiffness for a single pedestrian m_h, c_h and k_h. The natural frequency f_h and damping ratio ξ_h of a walking human could be obtained from these three parameters.

33.3 Results

Model parameters for the SMD system representing the pedestrians were extracted from tests of 5 mm vibration amplitude using a trial and error method and are shown in Table 33.3, in which m_h, c_h and k_h are the mass, damping and stiffness of the SMD model of a single pedestrian and f_h and ξ_h are the natural frequency and damping of a single pedestrian.

The fitting of a theoretical FRF from the HSI model to the experimentally obtained FRF for the case 5 mm with 10 pedestrians is shown in Fig. 33.3 and the effects of the pedestrians on the FRF of the footbridge are also shown in Fig. 33.3. The fitting figures for the other two cases with pedestrian number 4 and 7 are not presented here as they were similar to this case.

Table 33.3 Mass, stiffness and damping of a single pedestrian from fitted FRF

Test case	m_h [kg]	c_h [kg/s]	k_h [N/s]	f_h [Hz]	ξ_h [−]
5 mm-4ped	73	410	10,600	1.9178	0.2330
5 mm-7ped	73	520	10,000	1.8628	0.3043
5 mm-10ped	73	635	9,150	1.7816	0.3886
Average	73	521	10,600	1.8541	0.3087
M & G :M1[a]	75.19	3766.8	97,820	5.74	0.695
M & G :M2[b]	60.81	759.2	20,367	2.9	0.34
M & G: M3[c]	65.554	1277.5	37,084	3.78	0.4103
Search range	0–73	0–10,000	0–100,000	/	
Search step	1	5	100		

[a] M & G: M1 refers to parameters from [12] for human being of a normal standing posture

[b] M & G: M2 refers to parameters from [12] for a standing human being of a legs bent standing posture

[c] M & G: M3 refers to parameters from [12] for a standing human being in one leg posture
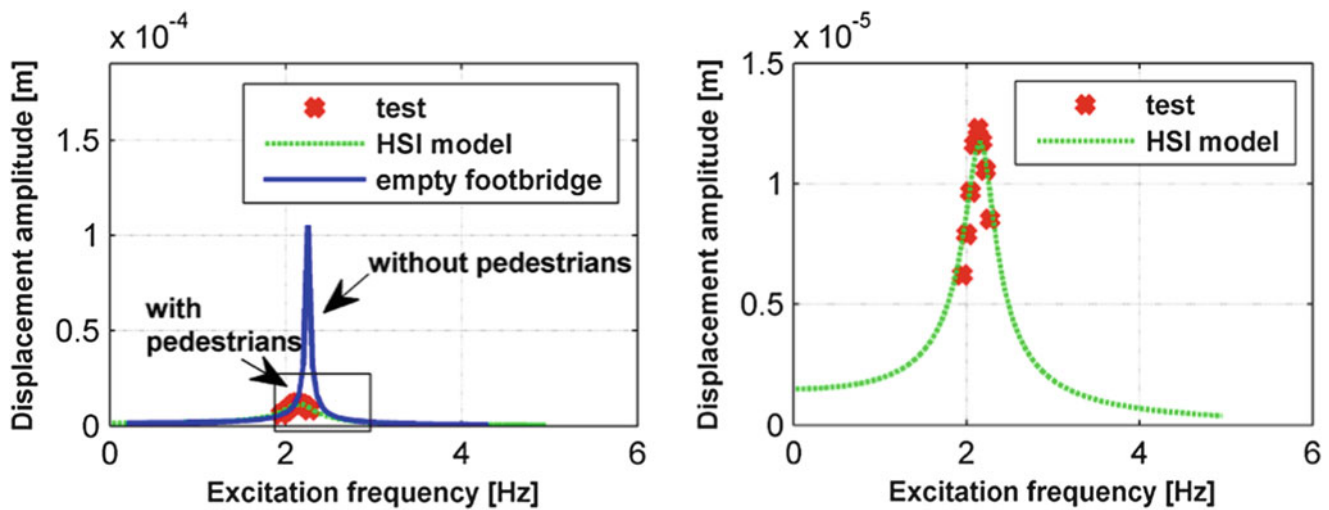
Fig. 33.3 FRF curves of the empty footbridge and the occupied footbridge (from test and from HSI model) for case 5 mm with 10 pedestrians (*left*) and magnified plot of the rectangular area on the left (*right*)

33.4 Discussion and Conclusions

Modeling pedestrians as equivalent SMDs was found suitable for modeling HSI between pedestrians and a footbridge, as theoretically derived FRFs based on an SMD model were found to fit experimentally obtained FRFs of a footbridge with traversing pedestrians. The natural frequency of the SMD model of a single pedestrian was estimated to be 1.85 Hz and the damping ratio was found to be 0.30. These values are in reasonable agreement with Matsumoto and Griffin's results [12]. The dynamic properties of a pedestrian obtained from the SMD model were an average mass equal to their actual static mass, a stiffness of 10,600 N/s and a damping constant of 521 kg/s. The estimated stiffness and damping were close to half the values that were measured for a standing person with both legs bent. The values seem intuitively correct, as during walking only a single leg is in contact with the ground most of the time. The present results suggest that during the stance phase of walking, the stance leg is bent rather than straight. The FRF of the heavily damped two degrees of freedom structure consisting of the pedestrians and the footbridge was shown to have only one resonant frequency. This is contrary to the common belief that there should be two resonant frequencies for a 2DOF system, as was first observed for the HSI in [3]. However, Wang et al. [8] provided an explanation for this phenomenon by showing that there are strict conditions under which two resonance frequencies can appear for a heavily damped 2DOF system. In the present case, with a mass ratio of 0.107 between pedestrians and the footbridge, a frequency ratio of 0.84 between the pedestrians and the footbridge and a pedestrian damping ratio of 0.30, only one resonance frequency would be expected in the FRF of the footbridge [8].

References

1. Dallard P et al (2001) The London millennium footbridge. Struct Eng 79(22):17–33
2. Salyards KA, Noss NC (2014) Experimental evaluation of the influence of human-structure interaction for vibration serviceability. J Perform Constr Facil 28(3):458–465
3. Ellis B, Ji T (1997) Human-structure interaction in vertical vibrations. Proceed ICE Struct Build 122(1):1–9
4. Zivanovic S, Diaz IM, Pavić A (2009) Influence of walking and standing crowds on structural dynamic properties. In: Conference proceedings of the society for experimental mechanics series
5. Georgakis CT, Jørgensen NG (2013) Change in mass and damping on vertically vibrating footbridges due to pedestrians. In: Topics in dynamics of bridges, vol 3. Conference proceedings of the society for experimental mechanics series. Springer, New York, pp 37–45
6. Jørgensen NG (2009) Human structure interaction: influence of walking pedestrians on the dynamic properties of footbridge structures they occupy. Master thesis, Technical University of Denmark
7. Jones CA, Reynolds P, Pavic A (2011) Vibration serviceability of stadia structures subjected to dynamic crowd loads: a literature review. J Sound Vib 330(8):1531–1566
8. Wang D et al (2014) Presence of resonance frequencies in a heavily damped two-degree-of-freedom system. J Eng Mech 140(2):406–417
9. Dougill JW et al (2006) Human structure interaction during rhythmic bobbing. Struct Eng 84(22):32–39
10. Alexander NA (2006) Theoretical treatment of crowd – structure interaction dynamics. Proc Inst Civil Eng Struct Build 159(SB6):329–338
11. Griffin MJ (1996) Handbook of human vibration. Elsevier, Amsterdam
12. Matsumoto Y, Griffin MJ (2003) Mathematical models for the apparent masses of standing subjects exposed to vertical whole-body vibration. J Sound Vib 260(3):431–451
13. Wei L, Griffin J (1998) The prediction of seat transmissibility from measures of seat impedance. J Sound Vib 214(1):121–137
14. Hartog JPD (1985) Mechanical vibrations. Courier Dover Publications, New York

Chapter 34
Identification and Modelling of Vertical Human-Structure Interaction

Katrien Van Nimmen, Kristof Maes, Stana Živanović, Geert Lombaert, Guido De Roeck, and Peter Van den Broeck

Abstract Slender footbridges are often highly susceptible to human-induced vibrations, due to their low stiffness, damping and modal mass. Predicting the dynamic response of these civil engineering structures under crowd-induced loading has therefore become an important aspect of the structural design. The excitation of groups of pedestrians and crowds is generally modelled using moving loads but also the changes in dynamic characteristics due to human-structure interaction are found to significantly affect the footbridge response. The present contribution investigates the influence of the presence of the pedestrians onto the dynamic characteristics of the occupied structure by means of an extensive experimental study on a footbridge in laboratory conditions. The analysis shows that the natural frequencies slightly reduce due to the additional mass but more significant is the observed increase in structural damping. Similar observations are made on a in situ footbridge. This interaction is simulated using a coupled human-structure model in which the human occupants are represented by simple biomechanical models.

Keywords Human-induced vibrations • Footbridge • Human-structure interaction • Full-scale testing • Vibration serviceability

34.1 Introduction

Pedestrian excitation is generally represented by simplified (moving) loads. In fact, pedestrians are mechanical systems on their own, interacting with the supporting structure. Their presence is found to result in changes of both natural frequencies and modal damping ratios with respect to the characteristics of the empty footbridge [1, 2]. It is expected that the modification of the dynamic behaviour is proportional to the ratio of the occupants' mass to the structural mass and hence expected non-negligible for slender footbridges [3, 4].

On a footbridge, both *active* (e.g. walking, jogging, . . .) and *passive* (e.g. standing still, sitting on benches, . . .) human occupants are expected to be present. Passive persons most likely assume a standing posture with two straight or slightly bent legs, e.g. while gently resting against the parapet. The posture of the active human occupants on the other hand is changing continuously during the gait cycle.

The objective of this contribution is to identify the dynamic characteristics of the human body and to investigate the effect of the presence of human subjects onto the dynamic behaviour of the coupled system, i.e. the human subjects and the footbridge. In view of the vibration serviceability assessment of slender footbridges, focus is put on the low frequency behaviour (0–10 Hz). Section 34.2 first discusses the dynamic characteristics of the human body as reported in literature. The equations of motion of the coupled human-bridge system are derived in Sect. 34.3. Based on an experimental study in laboratory conditions, the dynamic properties of the human body in the vertical direction are identified for four relevant body postures in Sect. 34.4. In Sect. 34.5, the predicted dynamic behaviour of the coupled human-bridge system is verified with observations on a real footbridge.

K. Van Nimmen (✉) • P. Van den Broeck
Department of Civil Engineering, Structural Mechanics, KU Leuven, 3001 Leuven, Belgium

Department of Civil Engineering, Technology Cluster Construction, Structural Mechanics, KU Leuven, 9000 Ghent, Belgium
e-mail: katrien.vannimmen@kuleuven.be

K. Maes • G. Lombaert • G. De Roeck
Department of Civil Engineering, Structural Mechanics, KU Leuven, 3001 Leuven, Belgium

S. Živanović
School of Engineering, University of Warwick, Coventry CV47AL, UK

34.2 Dynamic Characteristics of the Human Body

The extensive experimental studies of Griffin and Matsumoto et al. [5–8] show that the behaviour of standing subjects exposed to vertical whole-body vibrations (WBV) over the frequency range between 0.5 and 30 Hz, is similar to that of a SDOF system or a 2 degree of freedom (2-DOF) system subjected to base excitation. In the normal standing posture one peak is identified at about 5 Hz and, for most subjects, a second broad peak in the frequency range between 10 and 15 Hz. Table 34.1 shows that in literature there is a general consensus that the main resonance frequency of the human body in the normal standing posture is found between 5 and 6 Hz. It is therefore assumed that a SDOF representation of the human body will most likely be sufficient to describe its vertical motion up to 10 Hz, i.e. the frequency range of interest. Sometimes, an additional rigid mass is considered at the support, e.g. such that the total mass of the system equals the nominal mass of the subject ($m_H = m_{H,1} + m_{H,0}$). These SDOF models are presented in Fig. 34.1a, b. For the case where a rigid mass is considered at the support, this mass usually remains limited to 5 % of the nominal mass of the human body.

The lateral dynamic behaviour of the human body has been given much less attention. The fundamental natural frequency is found to be much lower (between 0.5 and 1.0 Hz) but up to now, no mathematical models have been fitted [7].

34.2.1 Effect of Posture

Nearly all research concerned with whole-body vibrations, consider the human body in seated or normal standing posture, i.e. with two straight legs. However, a crowd on a footbridge is most likely composed of subjects adopting different postures. When people are moving, their posture changes continuously along the gait cycle. The corresponding postures are roughly characterised by the angle between the upper and lower leg [12].

Figure 34.1 shows that the apparent mass (M_H), i.e. defined as the ratio between the input force and input acceleration at the supporting surface [13], for a person with the legs bent and the one leg posture is similar to the one of the normal standing posture. The main resonance frequency has however decreased from 5.5 Hz to 2.75 Hz and 3.75 Hz respectively. The effect of these postural changes can be represented by adequate modifications in stiffness and damping [5].

Table 34.1 Mean values and corresponding standard deviation σ (when available) of the dynamic characteristics of the human body in a normal standing posture exposed to whole body vibrations (WBV) after different authors

Type	Author	Model	Frequency (Hz)	Damping (%)
Vertical	Zheng and Brownjohn [9, 10]	SDOF	$f_{H,1} = 5.24, \sigma(f_{H,1}) = 0.40$	$\xi_{H,1} = 39, \sigma(\xi_{H,1}) = 5$
Vertical	Matsumoto and Griffin [5]	SDOF	$f_{H,1} = 5.7, \sigma(f_{H,1}) = 0.57$	$\xi_{H,1} = 69, \sigma(\xi_{H,1}) = 7$
		2DOF	$f_{H,1} = 5.5$	$\xi_{H,1} = 40$
			$f_{H,2} = 13.9$	$\xi_{H,2} = 37$
Vertical	ISO 5982 [11]	2DOF	$f_{H,1} = 5.0$	$\xi_{H,1} = 36$
			$f_{H,2} = 12.5$	$\xi_{H,2} = 46$
Lateral	Matsumoto and Griffin [7]	–	$f_{H,1} = 0.4 - 0.8$	–

Fig. 34.1 Mathematical models to represent the standing human body with (**a**) *model-1a* and (**b**) *model-1b* and (**c**) the effect of posture on the normalised apparent mass of the human body (M_H/m_H) exposed to vertical WBV after Matsumoto et al. [5]: with normal standing (*solid*), bent legs (*dashed*), 1 leg (*dotted*)
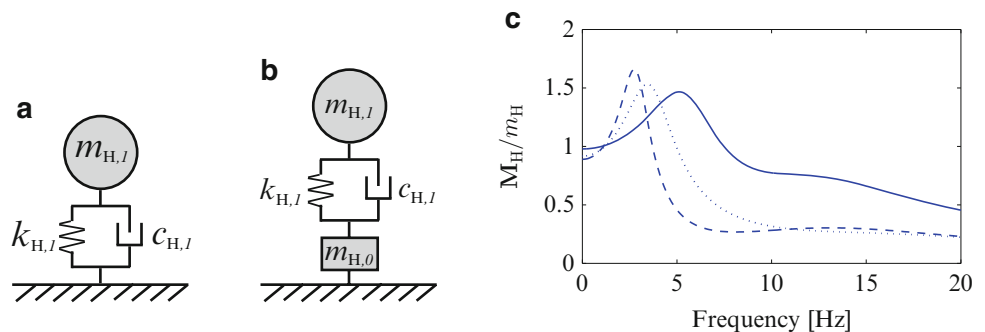
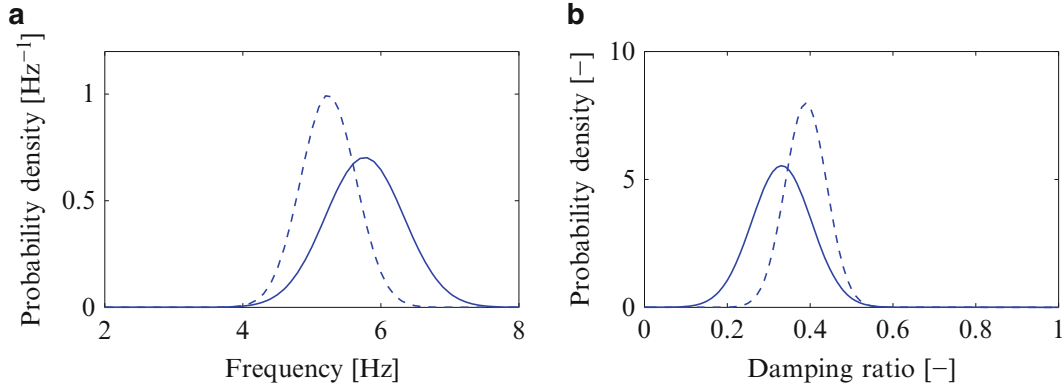**Fig. 34.2** The variability of (**a**) the fundamental natural frequency of the human body in normal standing posture and (**b**) corresponding damping ratio as identified by Matsumoto et al. [5] (*solid*) and Zheng et al. [9] (*dashed*)

34.2.2 Inter-Subject Variability

To the author's knowledge, the experimental studies involving standing subjects to date include a total of only 42 subjects. In the extensive experimental study performed by Matsumoto et al. [5], the mechanical response of the human body of 12 male subjects was measured under controlled conditions and in observance of postural effects. Zheng and Brownjohn [9] investigated the effect of a normal standing person at midspan of a 4 m long simply-supported reinforced concrete slab with a fundamental natural frequency of 12.8 Hz. In total, 30 individuals were involved. The variability as identified by Matsumoto et al. [5] and Zheng and Brownjohn [9], as listed in Table 34.1, is compared in Fig. 34.2a, b, assuming a Gassuian distribution of the identified natural frequencies and damping ratios respectively. These results show that the dynamic characteristics of the human body show a significant degree of inter-subject variability. When in addition the variety of postures is included, the fundamental natural frequencies of the human body in vertical motion are expected between 2 and 7 Hz. The corresponding SDOF models are characterised by a high modal damping ratio varying between 20 and 60 %.

34.3 Coupled Human-Bridge Model

When a person is present on a footbridge, either active or passive, interaction occurs between the human body of the occupant and the footbridge. In the following, it is assumed that the all the persons on the footbridge are stationary, i.e. the fact that an active pedestrian is moving along the bridge deck is ignored. The two subsystems, i.e. the footbridge and the occupant, interact with each other through contact forces. These forces are induced at the contact points between the feet of the occupant and the bridge deck. The governing equations of motion can be written for the linear dynamic systems representing the human body and the bridge separately. In order to ensure coupling, compatibility and equilibrium conditions at the contact points need to be satisfied. In the following, the occupant is represented by a SDOF system. The derivation can easily be generalised for other types of linear lumped parameter models. As the human occupants are assumed stationary, the coupled human-bridge system is time-invariant. The decoupled governing equations of motion in modal coordinates for a linear finite element model with n_{dof} degrees of freedom and proportional damping read:

$$\ddot{\mathbf{z}}(t) + \Gamma\dot{\mathbf{z}}(t) + \Omega^2\mathbf{z}(t) = \Phi^{\mathsf{T}}\mathbf{P}(t) = \mathbf{S}_{\text{p}}\mathbf{p}(t) \tag{34.1}$$

where $\mathbf{z}(t) \in \mathbb{R}^{n_m}$ is the modal coordinate vector, n_m the number of modes retained in the modally reduced system, $\Phi \in \mathbb{R}^{n_{\text{dof}} \times n_m}$ collecting the mass-normalised eigenvectors as columns, $\Omega^2 \in \mathbb{R}^{n_{\text{dof}} \times n_{\text{dof}}}$ is a diagonal matrix containing the square of the natural frequencies ω_j, $\Gamma \in \mathbb{R}^{n_{\text{dof}} \times n_{\text{dof}}}$ is a diagonal matrix containing the terms $2\xi_j\omega_j$ with ξ_j representing the modal damping ratio, $\mathbf{P}(t) \in \mathbb{R}^{n_{\text{dof}}}$ is the vector of the forces representing the load time histories in the corresponding DOFs of the structure and $\mathbf{S}_{\text{p}} \in \mathbb{R}^{n_{\text{dof}} \times n_p}$ is a selection matrix such that the vector with n_p externally applied forces, $\mathbf{p}(t) \in \mathbb{R}^{n_p}$, only has non-zero entries.

When a number of n_H occupants is considered, each occupant is represented by a SDOF system and the model of the structure is extended accordingly. The equations of motion for the combined system (footbridge + occupants) are obtained by eliminating the contact forces:

$$\mathbf{I}_H \ddot{\boldsymbol{\zeta}}_H(t) + \boldsymbol{\Gamma}_H \dot{\boldsymbol{\zeta}}_H(t) + \boldsymbol{\Omega}_H^2 \boldsymbol{\zeta}_H(t) = \begin{bmatrix} \boldsymbol{\Phi}^\top \mathbf{S}_p \\ \mathbf{0} \end{bmatrix} \mathbf{p}(t), \quad \text{with :} \tag{34.2}$$

$$\boldsymbol{\zeta}_H = \begin{bmatrix} \mathbf{z}(t) \\ \mathbf{u}_H(t) \end{bmatrix}, \quad \boldsymbol{\Omega}_H^2 = \begin{bmatrix} \boldsymbol{\Omega}^2 & -\boldsymbol{\Phi}^\top \mathbf{S}_H \mathbf{k}_H \\ -\mathbf{k}_H \mathbf{S}_H^\top \boldsymbol{\Phi} & \mathbf{k}_H \end{bmatrix} \tag{34.3}$$

$$\mathbf{I}_H = \begin{bmatrix} \mathbf{I} & \mathbf{0} \\ \mathbf{0} & \mathbf{m}_H \end{bmatrix}, \quad \boldsymbol{\Gamma}_H = \begin{bmatrix} \boldsymbol{\Gamma} & -\boldsymbol{\Phi}^\top \mathbf{S}_H \mathbf{c}_H \\ -\mathbf{c}_H \mathbf{S}_H^\top \boldsymbol{\Phi} & \mathbf{c}_H \end{bmatrix} \tag{34.4}$$

in which $\mathbf{u}_H \in \mathbb{R}^{n_H}$ collects the total displacements of the n_H occupants, $\mathbf{S}_H \in \mathbb{R}^{n_{\text{dof}} \times n_H}$ is a selection matrix that indicates the corresponding DOF and $\mathbf{m}_H \in \mathbb{R}^{n_H \times n_H}$, $\mathbf{k}_H \in \mathbb{R}^{n_H \times n_H}$ and $\mathbf{c}_H \in \mathbb{R}^{n_H \times n_H}$ are diagonal matrices containing the mass m_H, damping c_H and stiffness k_H parameters of the different SDOF models representing the human occupants.

34.4 Experimental Identification of the Human Body Model Parameters

In this section, the dynamic characteristics of the human body are identified indirectly, through the effect that its presence has on the dynamic characteristics of the occupied structure [14]. The experiments are performed on the footbridge of the Structures Laboratory at the University of Warwick for which the experimentally identified modal characteristics are discussed in [15]. As the footbridge is excited, either artificially using a shaker or through ambient excitation, the occupants are exposed to whole-body vibrations predominantly at the natural frequencies of the coupled structure. Section 34.2 showed that the dominant natural frequency of the standing human body is expected in the range between 2 and 7 Hz. The level of interaction between the human body and the Warwick footbridge is expected to be significant as the structure has four modes with considerable vertical modal displacements in frequency range of 0–12 Hz.

34.4.1 Method

Random shaker excitation (0–12.8 Hz) is applied vertically to the bridge deck (see Fig. 34.3). Each measurement setup had a duration of 2 min and was repeated three times. The bridge deck was occupied by 4 or 6 subjects all assuming one of the following four postures: (1) two straight legs, (2) two slightly bent legs, (3) one slightly bent leg and (4) the double-stance posture (Fig. 34.4). The input force and output accelerations are recorded with a Quattro acquisition system with a sampling frequency of 25.6 Hz (Fig. 34.3). The input-output data have been processed using the following OMAX algorithm: reference-based data-driven combined deterministic-stochastic subspace Identification (CSI-data/ref [16–18]) algorithm. In the following, the FRF is considered with input force and output acceleration at the location of the shaker (Fig. 34.3).
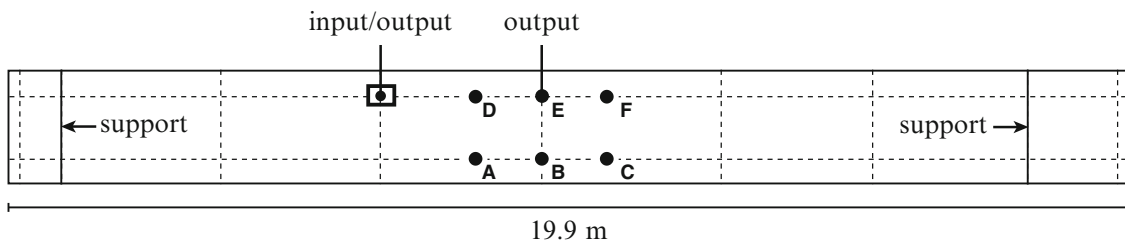

Fig. 34.3 The experimental setup on the Warwick footbridge with the location of the shaker (input), the accelerometers (output) and the subjects (A–F)
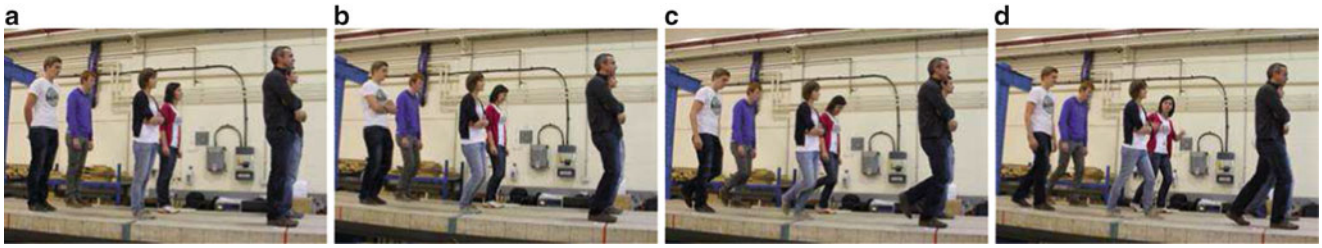
Fig. 34.4 The six subjects all assuming one of the four postures: (**a**) two straight legs; (**b**) two slightly bent legs; (**c**) one slightly bent leg; (**d**) the double-stance posture
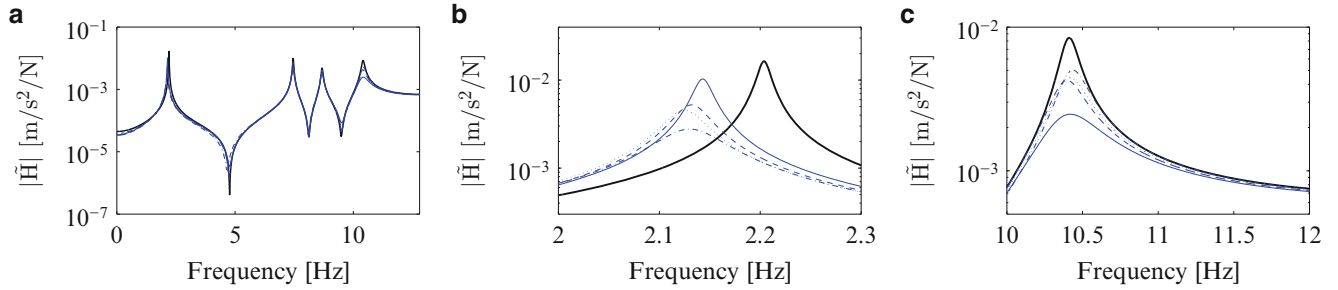

Fig. 34.5 FRF of the identified discrete-time deterministic state-space model of (*black-bold*) the unoccupied structure and the structure occupied with six subjects with respectively (*solid*) straight legs, (*dashed*) slightly bent legs, (*dash-dot*) one leg slightly bent and (*dotted*) the double-stance posture for a random shaker input force: for the relevant frequency range (**a**) and a detailed view around the first (**b**) and the fourth peak (**c**)

Figure 34.5 presents the experimental FRF of the empty structure and the structure occupied by six subjects, all assuming one of the considered postures. The four modes of the Warwick footbridge with a natural frequency within the frequency range of interest can clearly be identified. Figure 34.5a suggests that when the structure is occupied, the identified dynamic behaviour is unchanged. However, when closely observing the individual peaks of the FRF it is clear that the presence of the subjects on the footbridge—in each of the postures—has a significant effect on the identified model. This effect is most pronounced for the fundamental mode (Fig. 34.5b) and the fourth mode with a natural frequency of 10.4 Hz (Fig. 34.5c).

34.4.2 Parameter Estimation

In view of the frequency range of interest (0–10 Hz), the human body is represented by a SDOF system with a rigid mass at the support (model 1-b, see Fig. 34.1b). To estimate the corresponding model parameters, an optimisation problem is formulated where the objective function contains the differences between the identified ($\tilde{H}$) and the simulated (H) FRF of the occupied structure within a frequency range defined by a lower (Ω_1) and upper bound (Ω_2) respectively, i.e. $\omega_k = \Omega_1, \ldots, \Omega_2$ [rad/s]. Additionally, the residuals are weighted by the factors α_k ($0 \leq \alpha_k \leq 1$).

The decision variables in this optimisation problem are the natural frequency f_H, the damping ratio ξ_H and the mass ratios $\mu_{H,1} = m_{H,1}/m_H$ and $\mu_{H,0} = m_{H,0}/m_H$ of the assumed lumped parameter model. These parameters are assumed identical for the different subjects on the footbridge. Apart from the physical constraints ($f_H > 0$, $\xi_H > 0$, $\mu_{H,1} > 0$, $\mu_{H,0} > 0$), an additional constraint is formulated enforcing the sum of the lumped masses to be equal to the total mass of the corresponding subject ($m_H = m_{H,1} + m_{H,0} \Leftrightarrow \mu_{H,1} + \mu_{H,0} - 1 = 0$). In this way, the total number of decision variables is reduced to three. The problem, subject to four inequality constraints, formulated in standard form:

$$\underset{\mathbf{x} \in \mathbb{R}^3}{\text{minimise}} \quad \sum_{\omega_k} \alpha_k \left\| \tilde{H}(\omega_k) - H(\omega_k, \mathbf{x}) \right\| \quad \text{for } \omega_k = \Omega_1, \ldots, \Omega_2 \tag{34.5}$$

$$\text{subject to} \quad \mu_{H,1} > 0 \tag{34.6}$$

$$1 - \mu_{H,1} > 0 \tag{34.7}$$

$$f_H > 0 \tag{34.8}$$

$$\xi_H > 0 \tag{34.9}$$

and can be categorised as a nonlinear programming problem due to the nature of the objective function. The inequality constrained optimisation problem is solved using the fmincon-solver (Matlab) using the Interior Point algorithm [19, 20]. In the present application, the selected frequency range is 1–12 Hz and all weighting factors are set to one.

34.4.3 Results

For all six trials involving the same posture, regardless of the fact that 4 or 6 subjects are considered on the bridge, highly similar model parameters are identified. Table 34.2 lists the corresponding mean values of the identified dynamic characteristics of the human body for each of the four postures. Figure 34.6 illustrates that an excellent fit is found between the experimentally identified and the simulated FRF of the occupied structure. The natural frequencies and damping ratios of the two straight and two bent legs postures are in close agreement with the results reported by Matsumoto and Griffin [5]. For postures 3 (1 leg slightly bent) and 4 (double stance phase) it can be observed that the natural frequencies decrease from 5.5 Hz to 3.1 Hz and 3.3 Hz respectively. The identified SDOF models are characterised by a high modal damping ratio varying between 25 and 50 %.

Table 34.2 The identified natural frequency (f_H), damping ratio (ξ_H) and mass ratios (μ) of the human body in four standing postures represented by the lumped parameter model 1b

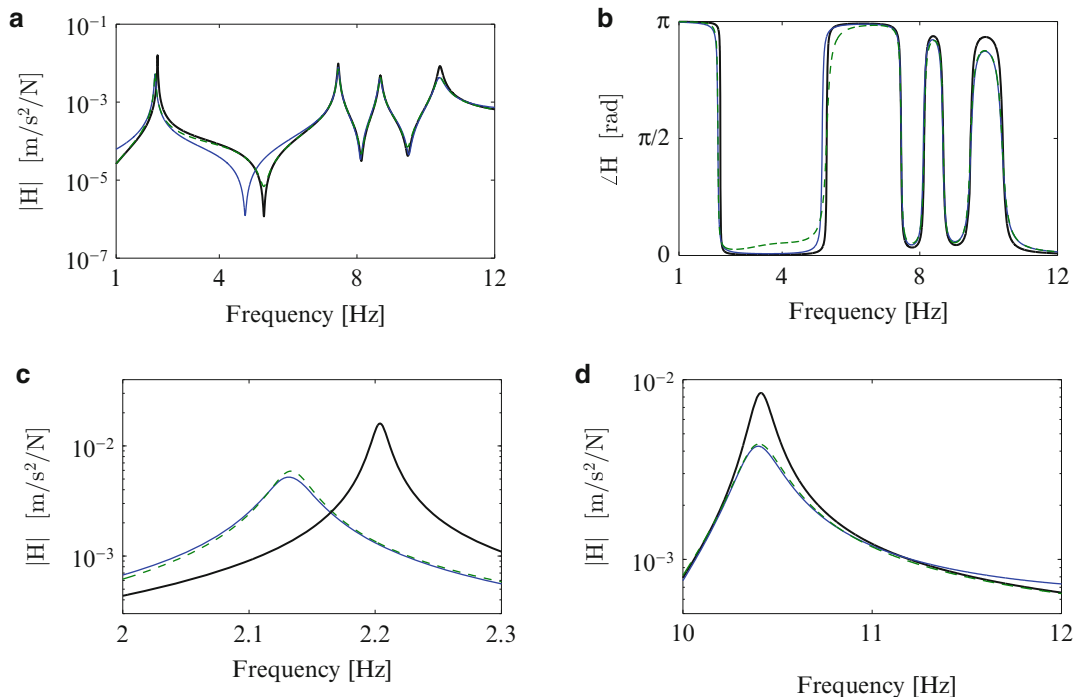| Posture	f_H (Hz)	ξ_H [-]	μ_1 [-]	μ_0 [-]
Straight legs	5.67	0.44	0.94	0.06
Slightly bent legs	3.55	0.34	0.88	0.12
One leg slightly bent	3.06	0.35	0.99	0.01
Double stance phase	3.34	0.26	0.95	0.05

Fig. 34.6 (a) The amplitude ($|H|$) and (b) angle ($\angle H$) of the FRF of the empty structure (*bold*) and the structure occupied with six subjects in normal standing posture (*solid*) and the corresponding FRF simulated with the identified human body characteristics (*dashed*), and a zoom around the (c) first and (d) fourth peak

34.5 Full-Scale Experimental Verification

The SDOF representation of the human body as derived from the laboratory experiment, is verified with observations on a lightweight steel footbridge. The Eeklo footbridge is subject of a comprehensive experimental study involving both passive and active occupants (Fig. 34.7). The experimental identification of the modal characteristics and the calibration of the numerical model of this footbridge, is previously discussed in [21]. The two modes of interest are the fundamental lateral-torsional mode (f_1 = 1.71 Hz, ξ_1 = 2 %, m_1 = 34 ton) and the first vertical bending mode (f_2 = 2.99 Hz, ξ_2 = 0.2 %, m_2 = 22 ton) where m_j represents the corresponding modal mass, i.e. indicating the proportion of the physical mass of the structure that is engaged in that particular mode [22].

This section aims to verify if the coupled human-bridge model is able to predict the experimentally identified dynamic behaviour of the occupied structure. To this end, each occupant is represented by a lumped parameter model (model 1-b) for which the parameters are set based on the results from the previous sections. The structural response is registered during free vibration tests, induced by rhythmical activities of the occupants, as well as trials involving ambient and random walking excitation. The free vibrations, aimed to be dominated by the contribution of a single mode, are induced by the bobbing of the different subjects on the structure. Their activities are synchronised using a metronome signal chosen to match the selected natural frequency. Once the desired level of vibration is reached, the subjects cease bobbing and get into the selected body posture, thereby initiating the free decay. The natural frequency and modal damping ratio of the considered mode of the occupied structure are subsequently identified based on free decay analysis. For the trials involving ambient and random walking excitation, the natural frequency and modal damping ratio of the first and the second mode of the occupied structure are identified based on the operational modal analysis.

34.5.1 Free Decay Analysis

The experiments include trials with a different number of subjects on the bridge deck. Each of the subjects is positioned at a point where a stringer crosses a cross girder. In the first setup, just three persons are positioned at midspan (Fig. 34.7). For each of the following setups, the number of subjects is increased by six, three on the left and three on the right adjacent cross girder respectively. For the setups where the free vibration is aimed to be dominated by the fundamental torsional mode, the subjects on the stringer are omitted. In addition, the influence of the body posture of the subjects onto the dynamic behaviour of the coupled system is examined. The experiments therefore consider the human body in the normal standing posture with (1) straight legs and (2) slightly bent legs (Fig. 34.7b, c).
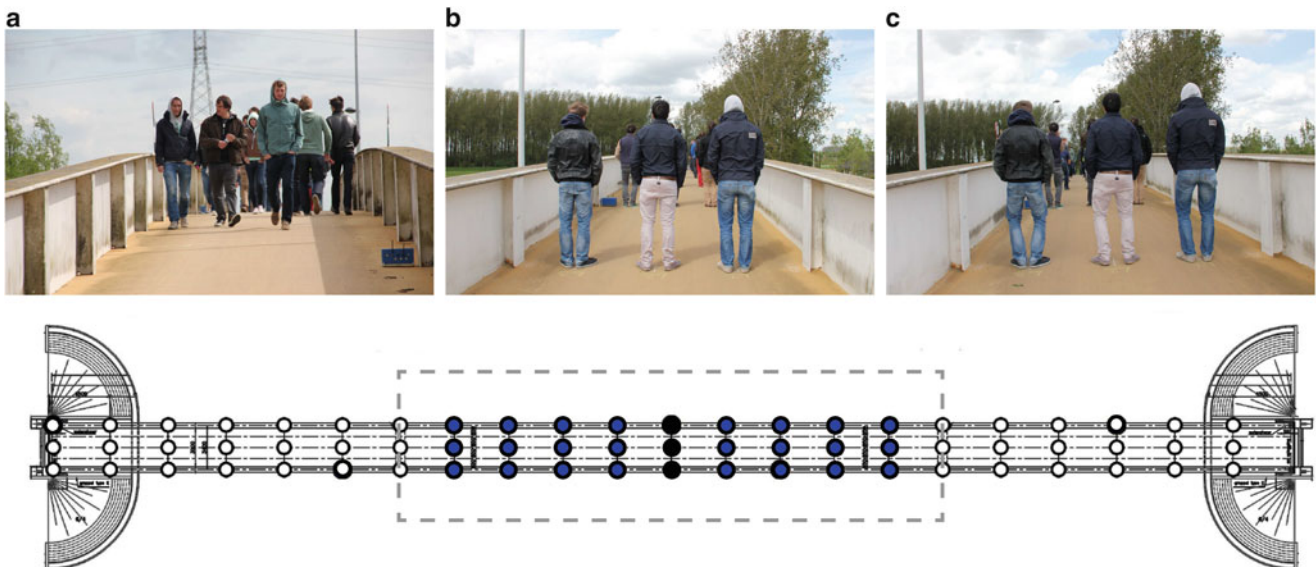

Fig. 34.7 The Eeklo footbridge occupied with (**a**) pedestrians and subjects in (**b**) the normal standing and (**c**) legs slightly bent posture, and (*bottom*) top view of the bridge with indicated walking area (*dashed*) and stationary subject locations (*solid*)
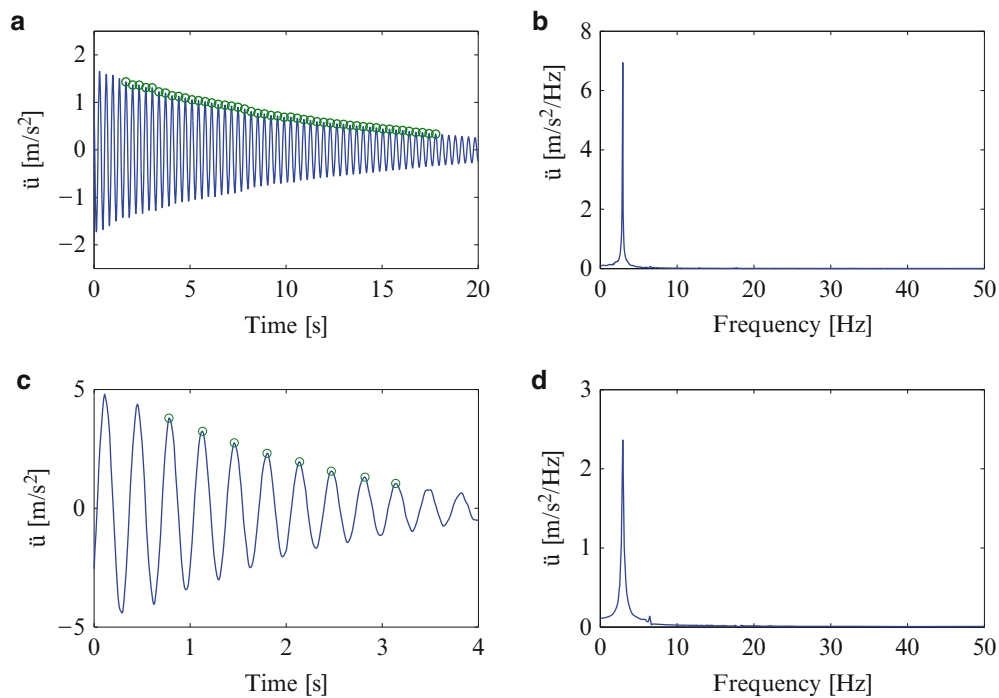
Fig. 34.8 Measured vertical free vibration response of the footbridge at midspan including the presence of 15 test-subjects (**a**, **b**) with straight legs and (**c**, **d**) slightly bent legs: (**a**, **c**) time series with selected extremes, (**b**, **d**) corresponding amplitude spectrum

In order to estimate the effective modal damping ratio, an exponential function is fitted to the relative maxima of the recorded decay with amplitudes between 90 % and 20 % of the maximum acceleration [23]. From Fig. 34.8b, d, it can be observed that the applied excitation indeed leads to a free vibration dominated by a single mode as assumed for the derivation of the effective modal damping ratio and natural frequency.

34.5.2 Operational Modal Analysis

For the setups considering ambient excitation, 9 or 21 subjects were requested to stand still during 3 min, all adopting one of the two investigated postures. In addition, the subjects were asked to walk slow, normal (self-selected) or fast along the main span of the bridge during 3 min (Fig. 34.7). The output-only data have been processed using the reference-based data-driven stochastic subspace identification (SSI-data/ref) [16, 24] algorithm.

34.5.3 Characteristics of the Coupled Human-Bridge Model

The dynamic behaviour of the footbridge is simulated with experimentally identified natural frequencies and modal damping ratios and the corresponding mode shapes of the calibrated FE model of the structure. For all the subjects involved, the static weight was identified in the laboratory. For each trial involving stationary persons, the exact location of each of the subjects involved is known. Apart from the total mass which is set to match the mass of the corresponding subject, the different human body models are assumed to have the same natural frequency, damping ratio and mass ratios. To account for the expected inter-subject variability, the natural frequency f_H and damping ratio ξ_H of the human body model are considered to be random variables characterised by a Gaussian distribution defined by μ and σ, i.e. the mean and standard deviation of the selected parameter. The mean values and corresponding standard deviation are chosen in accordance with the results from Sect. 34.4 and the variability as identified by Matsumoto et al. [5] and Zheng and Brownjohn [9] (see Sect. 34.2.2):
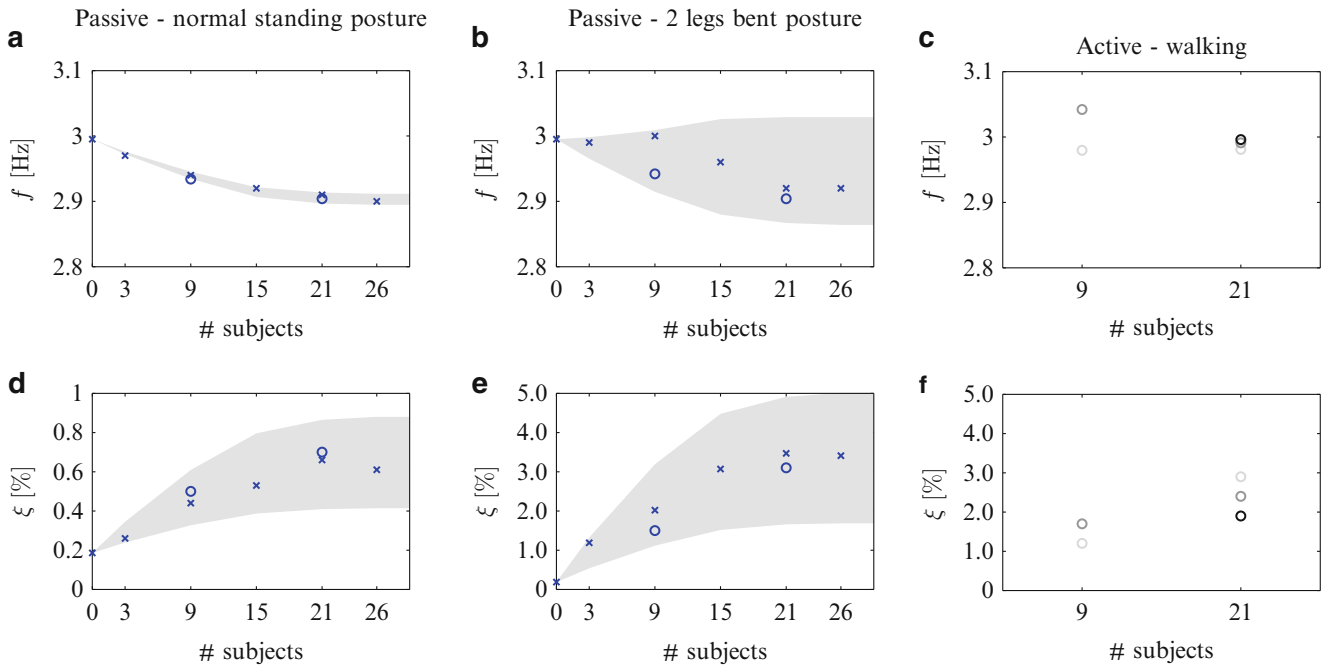
Fig. 34.9 The effective natural frequency (**a–c**) and damping ratio (**d–f**) of the vertical bending mode: simulated with the coupled human-bridge model (*gray*), identified from the free decay analysis (*crosses*) and identified from the OMA (*opencircles*), for the human body in normal standing posture (**a, d**), the two legs bent posture (**b, e**) and for persons walking (**c, f**) at a low (*light*), normal (*dark*) and fast (*black*) speed

Normalstandingposture : $\mu(f_H) = 5.5,\ \sigma(f_H) = 0.33;\ \mu(\xi_H) = 45\,\%,\ \sigma(\xi_H) = 6\,\%$ (34.10)

Twolegsslightlybentposture : $\mu(f_H) = 3.25,\ \sigma(f_H) = 0.25;\ \mu(\xi_H) = 30\,\%,\ \sigma(\xi_H) = 6\,\%$ (34.11)

For each Gaussian distribution, 100 samples are evaluated. For each scenario, the maximum and minimum effective natural frequency and damping ratio are retained.

34.5.4   Results

Figure 34.9 summarises the results for the effective natural frequency and modal damping ratio of the vertical bending mode, involving the subjects in the normal standing posture, the two legs bent posture and active subjects, i.e. walking at midspan.

For the normal standing posture (Fig. 34.9a, d), a reduction of the natural frequency of the footbridge is observed that is proportional to the amount of added (modal) mass. Despite the low mass ratio, the effective damping increases substantially which is owed to the very low inherent damping of the empty structure. Both effects are accurately predicted by the relevant human body models.

For the two legs slightly bent posture (Fig. 34.9b, e), a slight modification of the natural frequency and a enormous increase of the effective damping ratio is observed. As in this case the ratio of the natural frequency of the vertical bending mode and the human body models is close to one, the level of interaction is significant which results in a considerable increase of the effective modal damping ratio. Although small variations of the natural frequencies of the human body models cause a large scatter in the predicted effective damping ratio, the trend is clear and corresponds well with the observations. The attained effective modal damping ratio is much higher (5 times!) than for the normal standing posture.

These results show that the effect on both the effective natural frequency and damping ratio highly depends on the level of interaction between the human body and the considered mode of the structure which, in turn, depends on the ratio of the natural frequencies of the two systems. This explains why the effect on the effective natural frequency and modal damping ratio also depends on the body posture.

Figure 34.9c, f show that the results from the OMA involving active, i.e. walking, subjects, are in good agreement with the predictions that take into account the human body models for the legs bent posture. This observation confirms that also the
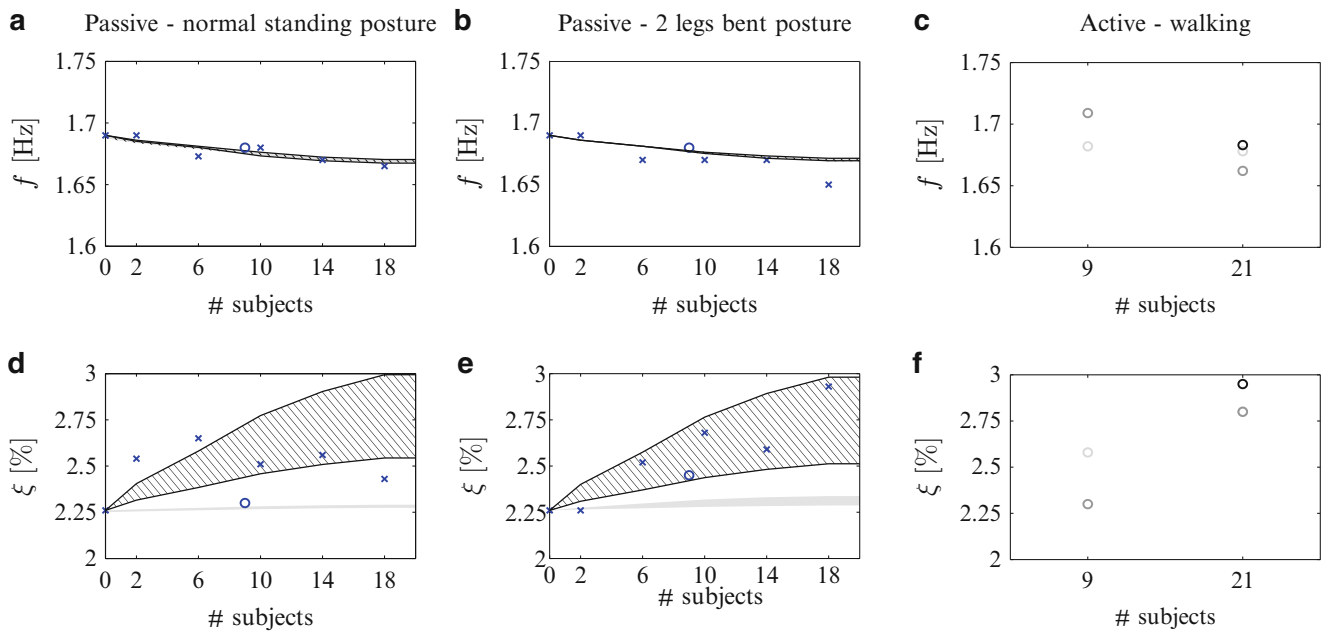
Fig. 34.10 The effective natural frequency (**a**–**c**) and damping ratio (**d**–**f**) of the lateral-torsional mode: simulated with the coupled human-bridge model (*gray*), including in addition the horizontal human body models (hatched), identified from the free decay analysis (*crosses*) and identified from the OMA (*opencircles*), for the human body in normal standing posture (**a**, **d**), the two legs bent posture (**b**, **e**) and for persons walking (**c**, **f**) at a low (*light*), normal (*dark*) and fast (*black*) speed

presence of pedestrians affects the dynamic characteristics of the coupled system in a way that appears to be similar to the effect of passive occupants with two legs bent. The amount of added damping appears to decrease with increasing walking speed.

Figure 34.10 summarises the results for the effective natural frequency and modal damping ratio of the fundamental lateral-torsional mode, involving the subjects in the normal standing posture, the two legs bent posture and active subjects. For both postures, the effect of the presence of the vertical human body models is similar to that of a mass, resulting in a small reduction in natural frequency. The latter can be explained by the fact that in both cases, the ratio of the human body models to the natural frequency of the considered mode and is relatively high (>1.5).

Figure 34.10d, e however show that experimentally, also an increase of the effective damping ratio is identified. It is believed that this mode, which has a dominant lateral modal component, is also affected by the lateral behaviour of the human body. This was confirmed by simulations where the human body model in addition is composed of a lateral SDOF system with a fundamental natural frequency between 0.5 and 1 Hz, i.e. in agreement with the preliminary results as reported by Matsumoto et al. [7] (see Fig. 34.10d, e).

Figure 34.10c, f show that the results from the OMA involving walking subjects, are in good agreement with the simulated coupled human-bridge model when the horizontal body motion is accounted for.

The results show that the way in which the two subsystems, crowd and structure, interact with each other is primarily determined by the natural frequencies of the two subsystems. As the fundamental natural frequency of the human body in the vertical direction is expected between 2.5 and 7 Hz, the level of interaction with low frequency footbridges is expected to be significant, especially for large groups and crowds.

34.6   Conclusions

The low-frequency (0–10 Hz) dynamic behaviour of the human body in the vertical direction, can be approximated by a highly damped SDOF system. The corresponding mechanical properties have been found to largely depend on the body posture.

The dynamical characteristics of six persons in the normal standing and two legs bent posture are identified experimentally and corroborate the findings of other researchers. In addition, the experimental study involved the postures corresponding to the single and double stance phase of the walking cycle. Based on the identified behaviour, the corresponding natural

frequencies for this *passive* pedestrian are expected to be between 2.5 and 4 Hz. The mass is approximately 95 % of the static mass with the remaining 5 % as rigid support, and the damping ratios are found to vary between 20 and 40 %. For the human body in normal standing posture, the natural frequencies and damping ratios increase to 5.5–6.5 Hz and to 35 %–55 % respectively.

Based on a comprehensive experimental study involving the Eeklo footbridge, it is shown that the coupled human-bridge model, where the persons are modelled as SDOF systems, is able to predict the experimentally identified dynamic behaviour of the occupied structure. For structural modes characterised by considerable lateral components, supplementary interaction with the horizontal dynamic behaviour of the human body is expected. Although the corresponding mechanical models are not yet available, the fundamental natural frequency is expected to be between 0.5 and 1 Hz. The results from the experimental tests involving walking subjects showed good agreement with the simulated coupled human-bridge model. This observation confirms that also the presence of pedestrians affects the dynamic characteristics of the coupled system in a way that appears to be similar to the effect of passive occupants with two legs bent.

It can be concluded that the presence of human subjects influences the dynamic behaviour, and particularly the effective damping, of the coupled structure considerably. It is therefore expected that simple force models lead to an overestimation of the response to pedestrian excitation as the interaction with the human body is disregarded.

References

1. Bocian M, Macdonald J, Burn J (2013) Biomechanically-inspired modelling of pedestrian-induced vertical self-excited forces. J Bridg Eng 18:1336–1346
2. Brownjohn J, Fok P, Roche M, Omenzetter P (2004) Long span steel pedestrian bridge at Singapore Changi airport - part 2: crowd loading tests and vibration mitigation measures. Struct Eng 82(16):28–34
3. Jones C, Reynods P, Pavić A (2011) Vibration serviceability of stadia structures subjected to dynamic crowd loads: a literature review. J Sound Vib 330:1531–1566
4. Dougil J, Wright J, Parkhouse J, Harrison R (2006) Human structure interaction during rhytmic bobbing. Struct Eng 84(22):32–39
5. Matsumoto Y, Griffin M (2003) Mathematical modesl for the apparent masses of standing subjects exposed to vertical whole-body vibration. J Sound Vib 260:431–451
6. Matsumoto Y, Griffin M (1998) Dynamic response of the standing human body exposed to vertical vibration: influence of posture and vibration magnitude. J Sound Vib 212(1):85–107
7. Matsumoto Y, Griffin MJ (2011) The horizontal apparent mass of the standing human body. J Sound Vib 330:3284–3297
8. Subashi G, Matsumoto Y, Griffin MJ (2008) Modelling resonances of the standing body exposed to vertical whole-body vibration: effects of posture. J Sound Vib 317:400–418
9. Zheng X, Brownjohn J (2001) Modelling and simulation of human-floor system under vertical vibration. In: Davis L (ed) Proceedings of SPIE: smart structures and material, vol 4327, pp 513–520
10. Brownjohn J (2001) Energy dissipation from vibration floor slabs due to human-structure interaction. J Shock Vib 8:315–323
11. International Organisation for Standardization (1981) ISO 5982:1981 vibration and shock - mechanical driving point impedance of the human body
12. Racić V, Pavić A, Reynolds P (2009) Experimental identification and analytical modelling of walking forces: a literature review. J Sound Vib 326:1–49
13. Mansfield N (2005) Impedance methods for assessment of the biomechanical response of the seated person to whole-body vibration. Ind Health 43:378–389
14. Sachse R, Pavić A, Reynolds P (2003) Human-structure dynamc interaction in civil engineering dynamics: a literature review. Shock Vib Dig 35(1):3–18
15. Zivanovic S, Johnson R, Dang H, Dobric J (2013) Design and construction of a very lively bridge. In: T. S. of Experimental Mechanics (ed) Proceedings of the 31st IMAC. A conference on structural dynamics. Topics in dynamics of civil structures, vol 4
16. Peeters B, De Roeck G (1999) Reference-based stochastic subspace identification for output-only modal analysis. Mech Syst Signal Process 13(6):855–878
17. Reynders E, De Roeck G (2008) Reference-based combined deterministic-stochastic subspace identification for experimental and operational modal analysis. Mech Syst Signal Process 22(3):617–637
18. Reynders E (2012) System identification methods for (operational) modal analysis: review and comparison. Archives of Computational Methods in Engineering 19(1):51–124
19. Nocedal J, Wright S (2006) Numerical optimization, 2nd edn. Springer, Springer Science + Business Media?
20. Boyd S, Vandenberghe L (2004) Convex optimization. Cambridge University Press, Cambridge

21. Van Nimmen K, Lombaert G, Jonkers I, De Roeck G, Van den Broeck P (2014) Characterisation of walking loads by 3d inertial motion tracking. J Sound Vib 333:5212–5226
22. Brownjohn J, Pavić A (2007) Experimental methods for estimating modal mass in footbridges using human-induced dynamic excitation. Eng Struct 29:2833–2843
23. Magalhães F, Cunha A, Caetano E, Brincker R (2010) Damping estimation using free decays and ambient vibration tests. Mech Syst Signal Process 24:1274–1290
24. Reynders E, Pintelon R, De Roeck G (2008) Uncertainty bounds on modal parameters obtained from stochastic subspace identification. Mech Syst Signal Process 22(4):948–969

Chapter 35
Identification of Stiffness, Damping and Biological Force of SMD Model for Human Walking

Jiayue Lou, Mengshi Zhang, and Jun Chen

Abstract This paper proposes an iterative identification approach to extract the stiffness, damping and coefficients of biological force of a spring-mass-damper (SMD) model for human beings in walking. Gait experiment records from 73 test subjects were used for the identification. The three-dimensional motion capture technology was adopted in the walking tests. Thirty-nine reflective markers were attached to each test subject during the test and the trajectories of each marker were monitored by motion capture system. The displacement, velocity and acceleration of center-of-mass of a subject in each test case were then obtained by the system. Assume that the biological force can be expressed by Fourier series, the parameters, including stiffness and damping of SMD model and coefficients of biological force, are identified by the following two steps. Step 1, initial guesses of damping ratio and natural frequency of SMD are introduced into the equation of motion to identify the coefficients of the first several orders of Fourier series and a new stiffness parameter. Step 2, acceleration resonance assumption is adopted to determine a new damping ratio parameter. Replace the conjectured/identified values in the previous step with the new values and repeat the above two steps until presumed convergence criteria is satisfied. The identified mean value of damping ratio and natural frequency of SMD slightly increase with the increase of walking frequency. The identified damping ratios are found larger than published values for people in standing posture.

Keywords Human-structure interaction • Spring-mass-damper model • Identification • Walking • Motion capture system

35.1 Introduction

The vibration serviceability problem induced by occupant activities such as walking, jumping and running is a major concern or even a dominant design issue for long-span floors. Modern structural floor systems are prone to human-induced vibration because structures have become lighter and more slender with the use of high-strength lightweight materials. When the frequency of crowd is at or close to harmonics of natural frequency of the structure, the resonance response may cause discomfort to occupants or even structural damage. Therefore, vibration serviceability problems can't be ignored at the floor's design stage. Among several issues regarding vibration serviceability assessment, the human-structure-interaction (HSI) is a new one that addresses the influence of occupants on the dynamic properties of the system and the structural responses. Researchers have proposed some models to consider the influence of human-structure-interaction on the prediction of structural responses to human activities. Griffin [1] suggested six models to represent standing person as either a single degree-of-freedom (DOF) system or two DOFs system. Kasperski [2] proposed a probabilistic model for standing person. The internal biological forces were not included in these models. As for the person in bobbing, a simple and classical structural dynamic model has been used by Dougill [3], which represents the human body as a spring-mass-damper (SMD) model with an internal pair of biological force. The biological force was expressed by Fourier series. The SMD model can be easily integrated with the floor structure system to form a new dynamic system for analysis. The dynamic parameters, i.e., damping ratio and natural frequency (or damping coefficient and stiffness), are thus critical for application of SMD model. In Dougill's paper, these parameters were determined from previous experiments by try-and-error procedure. In particular, the damping parameter was limited in a predetermined small range.

A series of experiments were conducted by the authors on human-induced walking, jumping and bobbing loads. Three-dimensional motion capture technology was adopted in the experiment. The trajectories of test subjects in the test were

J. Lou • M. Zhang • J. Chen (✉)
College of Civil Engineering, Tongji University, Siping Road 1239, Shanghai 200092, People's Republic of China
e-mail: cejchen@tongji.edu.cn

331

recorded. Based on the SMD model, the experimental results provided an opportunity to identify the dynamic properties of a person in different activities. This paper suggests an iterative identification approach to simultaneously extract parameters of SMD model and coefficients of biological force from experiment records.

35.2 Experiment

35.2.1 Test Procedures

The experiments were conducted on rigid floor using Vicon three-dimensional motion capture technology (Fig. 35.1). 73 subjects took part in the experiment. A summary of the statistics of all test subjects is given in Table 35.1. Each subject completed four test cases, which were: walking at fixed frequency of 1.50, 1.75, 2.00 and 2.25 Hz guided by a metronome. For each test case, the subject walked six or seven times. In each test, 39 reflective markers were attached to the test subject. When the subject performed the test, the spatial trajectories of all of the markers were monitored by a Vicon Motion Capture System with 10 T-40 cameras at a sampling frequency as 1,000 Hz. Readers are referred to Chen et al. [4] for more details of the experiment.

35.2.2 Data Processing

Time histories of markers' position were record by motion capture system. The velocity and acceleration of the center-of-mass of human body were obtained by differentiating the original displacement once and twice respectively. The results of one test subject are shown in Fig. 35.2. It can be seen that there are noises in the time histories. The noises result from two major sources: the change of experimental environment and the movement of the skin relative to the underlying bone. Many researches have indicated that the coordinates could be smoothed by running them twice (once forward, once backward) through a Butterworth low-pass filter and differentiating twice to gain the acceleration data of the markers [5]. We also found that the filtering process could significantly reduce the signal noise [6]. In this study, a fourth order Butterworth filter having cut-off frequency 15 Hz was applied to the original measurements to reduce the measurement noise. Figure 35.3 shows that the Butterworth filter has a good performance in de-noising the accelerations. Therefore, the Butterworth-filter procedure was used to obtain acceleration data of all the markers before the parameter identification.
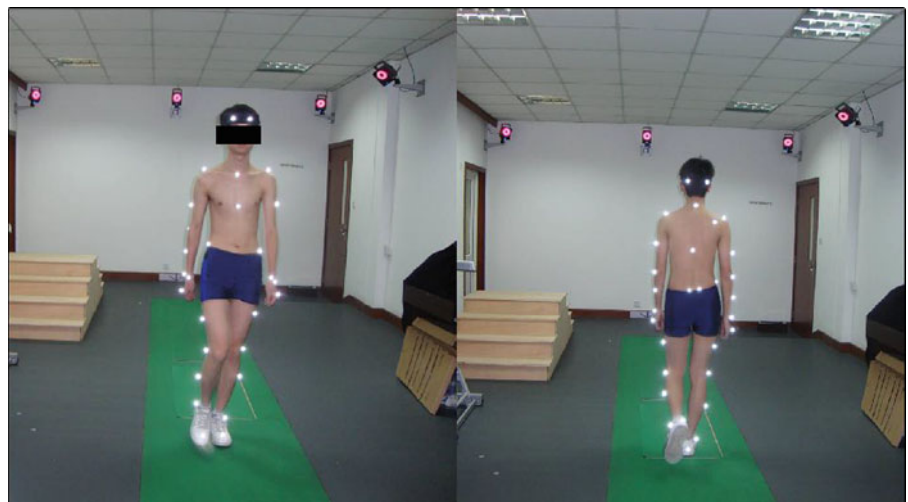
Fig. 35.1 Experimental setup and participant with markers

Table 35.1 Statistics of test subjects

Gender	Number	Weight(39–88 kg)		Height(1.55–1.85 m)	
		Mean	Std.	Mean	Std.
Male	57	65.4	9.85	1724.8	146.71
Female	16	51.6	6.87	1616.9	30.81
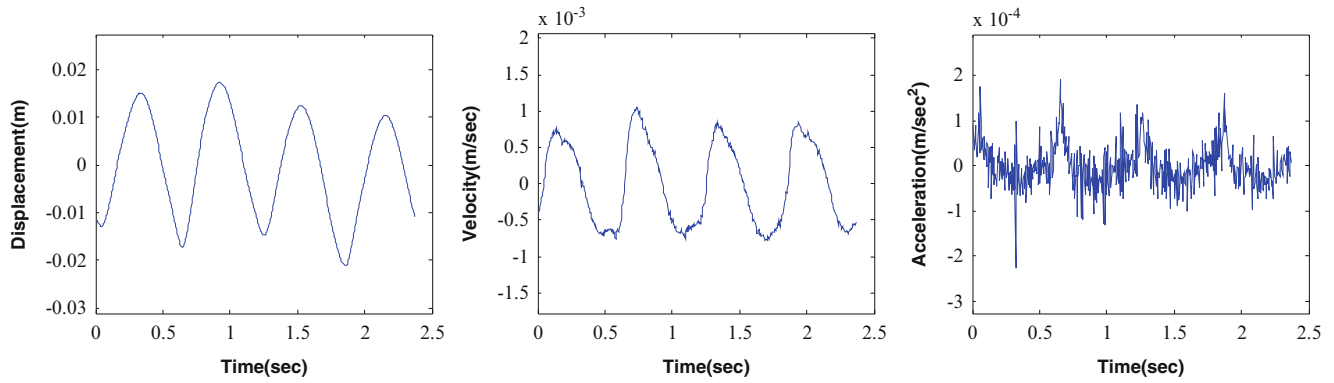
Fig. 35.2 Time histories of displacement, velocity and acceleration of center-of-mass of human body

Fig. 35.3 Raw and filtered acceleration time history
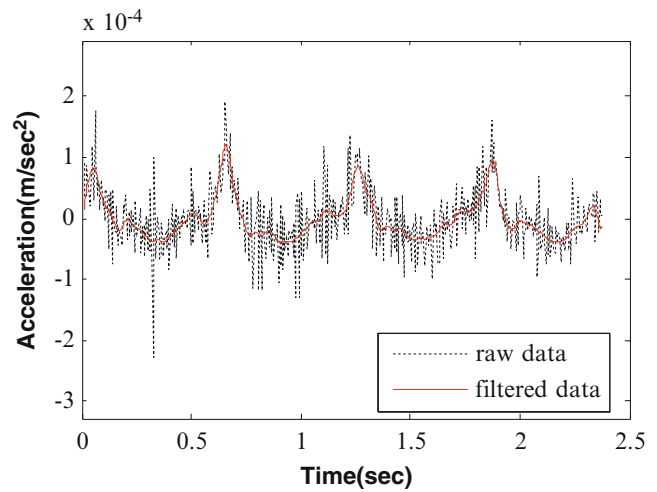
Fig. 35.4 SMD model
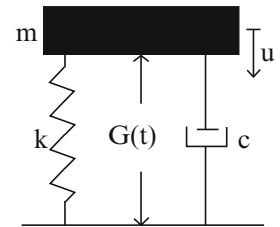
35.3   Parameter Identification for SMD Model

35.3.1   SMD Model

Figure 35.4 shows the SMD model for bobbing person proposed by Dougill [3]. In this model, the human body is represented as a single DOF system with a pair of biological forces $\tilde{G}(t)$. Assume the displacement is measured from the static equilibrium position of the body, the equation of motion of the SMD system will be:

$$m\ddot{u}(t) + c\dot{u}(t) + ku(t) = -\tilde{G}(t) \tag{35.1}$$

where m is the mass of human body, c is a damping coefficient and k is the body unit spring stiffness, $u(t)$, $\dot{u}(t)$, $\ddot{u}(t)$ are the displacement, velocity and acceleration of the center of the mass respectively. The biological force was modeled by Fourier series as given by Eq. 35.2.

$$\tilde{G}(t) = \sum_{i=1}^{4} [a_i \cdot \sin(\omega_d \cdot i \cdot t) + b_i \cdot \cos(\omega_d \cdot i \cdot t)] \tag{35.2}$$

where a_i, b_i represent the *ith* coefficients of biological force. Note that in the Eq. 35.2, the frequency of the biological forces is assumed to be the same as the walking frequency represented as ω_d.

35.3.2 Parameters Identification Procedure

Based on the equation of motion (35.1), the parameters of the SMD model and coefficients of biological force can be obtained by an iterative identification method containing the following two steps.

Step 1: To start the iterative procedure, initial guesses of damping ratio and natural frequency of SMD model are necessary. From previous researches, the initial values of the natural frequency f_n and damping ratio ξ of human body are randomly selected from 3 to 5 Hz and 0.2–0.5 respectively. Consequently, the damping coefficient can be calculated using the 'known' natural frequency f_n and damping ratio ξ by

$$c = 2m\omega_n \cdot \xi = 2m \cdot 2\pi f_n \cdot \xi \tag{35.3}$$

Substituting these initial values ($u(t)$, $\dot{u}(t)$, $\ddot{u}(t)$ and c) into Eq. 35.1 yields the equations at any time instant t_k,

$$\begin{cases} ku(t_1) + \sum_{i=1}^{4} [a_i \cdot \sin(\omega_d \cdot i \cdot t_1) + b_i \cdot \cos(\omega_d \cdot i \cdot t_1)] = -m\ddot{u}(t_1) - c\dot{u}(t_1) \\ ku(t_2) + \sum_{i=1}^{4} [a_i \cdot \sin(\omega_d \cdot i \cdot t_2) + b_i \cdot \cos(\omega_d \cdot i \cdot t_2)] = -m\ddot{u}(t_2) - c\dot{u}(t_2) \\ \qquad\qquad\qquad\qquad . \\ \qquad\qquad\qquad\qquad . \\ \qquad\qquad\qquad\qquad . \\ ku(t_N) + \sum_{i=1}^{4} [a_i \cdot \sin(\omega_d \cdot i \cdot t_N) + b_i \cdot \cos(\omega_d \cdot i \cdot t_N)] = -m\ddot{u}(t_N) - c\dot{u}(t_N) \end{cases} \tag{35.4}$$

To separate the unknown parameters, i.e., the stiffness parameter and coefficients of biological force, we can rewrite Eq. 35.4 into the following matrix form

$$\begin{bmatrix} u(t_1) & \sin(\omega t_1) & \cos(\omega t_1) & \cdots & \sin(4\omega t_1) & \cos(4\omega t_1) \\ u(t_2) & \sin(\omega t_2) & \cos(\omega t_2) & \cdots & \sin(4\omega t_2) & \cos(4\omega t_2) \\ \cdots & \cdots & \cdots & \cdots & \cdots & \cdots \\ u(t_N) & \sin(\omega t_N) & \cos(\omega t_N) & \cdots & \sin(4\omega t_N) & \cos(4\omega t_N) \end{bmatrix} \begin{bmatrix} k \\ a_1 \\ b_1 \\ \cdots \\ a_4 \\ b_4 \end{bmatrix} = \begin{bmatrix} -m\ddot{u}(t_1) - c\dot{u}(t_1) \\ -m\ddot{u}(t_2) - c\dot{u}(t_2) \\ \cdots \\ -m\ddot{u}(t_N) - c\dot{u}(t_N) \end{bmatrix} \tag{35.5}$$

Equation 35.5 can be expressed as the general form

$$H\widehat{\theta} = \widehat{F} \tag{35.6}$$

so that the unknown matrix can be calculated

$$\widehat{\theta} = H^+ \widehat{F} \tag{35.7}$$

Here the components in matrix H and matrix $\widehat{F}$ are known, and vector $\widehat{\theta}$ contains all the unknown parameters. Using the least square method (35.7), the unknown matrix $\widehat{\theta}$, which contains coefficients of the first four orders of Fourier series and body stiffness, can be obtained from Eq. 35.5.

Step 2: Using the identified stiffness value derived from Step 1, new natural frequency can be determined using Eq. 35.8

$$\omega_0 = \sqrt{k/m}$$
$$f_n = \omega_0/2\pi$$

(35.8)

As for the new damping ratio, an assumption had been proposed. The human body is an intelligent system with self-adjusting function. At different motion states, the body will adjust itself so as to keep itself in the most relaxed state and consume the minimum energy [7]. In a forced system, resonance is defined as the frequency at which the driving force required to maintain oscillations at a fixed amplitude is minimized. Thus, under the biological force, the walking human is expected at the state of acceleration resonance. The relationship between the natural frequency of the human body and the excitation frequency from the biological force can be written:

$$\omega_d = \omega_0/\sqrt{1 - 2\xi^2}$$

(35.9)

Here is ω_d the excitation frequency equal to the walking frequency, ω_0 is the human natural frequency, ξ is the damping ratio.

The equation provides the link between the body biological excitation and the body natural dynamic properties through frequency and damping ratio. Consequently, the new damping ratio ξ can be calculated by Eq. 35.9 with the known values of ω_d and ω_0.

The model parameters were optimized to satisfy the following convergence criteria (35.10). If the criteria is satisfied, optimized SMD parameters (f_n, ξ) were obtained. Otherwise, adopt the coefficients and the stiffness to provide new estimation of SMD parameters, which are in turn used to replace the conjectured values in the previous step 1. Then repeat the above two steps until the optimized SMD parameters are obtained.

$$err = \max\left(|\xi_{i+1} - \xi_i|/\xi_i, |f_{i+1} - f_i|/f_i\right) \le tol$$

(35.10)

35.3.3 Identification Results

The above identification approach was applied to all the gait experiment records. The identified results of natural frequency and damping ratios are shown in Fig. 35.5. The mean values of all the results are shown in Fig. 35.5 by triangles. Note that,
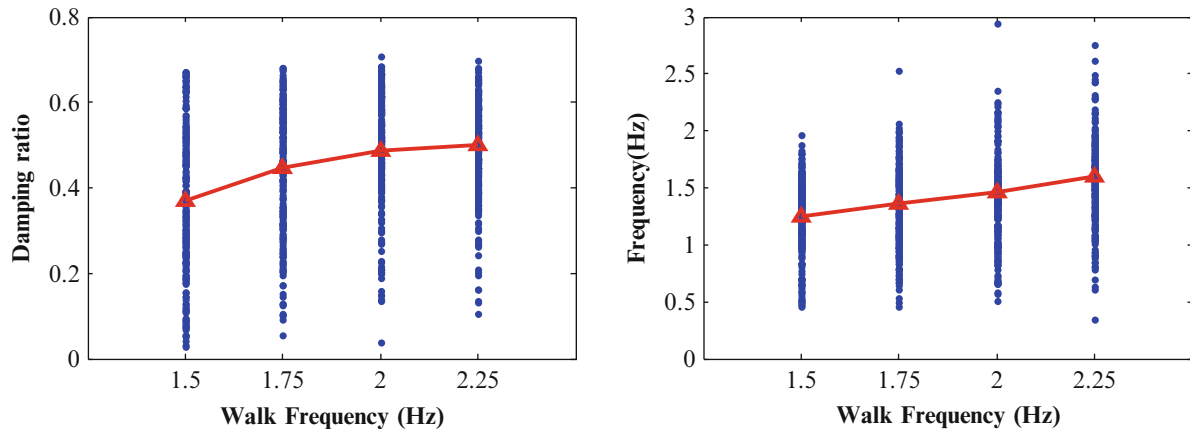

Fig. 35.5 Influence of the walk frequency on the damping ratio (*left*) and natural frequency (*right*) of the human body

Table 35.2 Identified SMD parameters for eight subjects among all members at four kinds of walking rates

| Parameters	Damping ratio average				Frequency average [Hz]			
Walking freq. in the test [Hz]	1.50	1.75	2.00	2.25	1.50	1.75	2.00	2.25
Test sub. 1	0.20	0.34	0.47	0.48	1.49	1.62	1.43	1.57
Test sub. 2	0.40	0.33	0.42	0.46	1.23	1.55	1.43	1.66
Test sub. 3	0.19	0.26	0.49	0.54	1.53	1.61	1.42	1.37
Test sub. 4	0.25	0.51	0.56	0.54	1.46	1.18	1.23	1.35
Test sub. 5	0.29	0.45	0.57	0.51	1.43	1.29	1.10	1.51
Test sub. 6	0.37	0.40	0.44	0.49	1.28	1.40	1.55	1.61
Test sub. 7	0.25	0.32	0.46	0.41	1.41	1.51	1.49	1.82
Test sub. 8	0.36	0.42	0.53	0.53	1.25	1.37	1.28	1.46
Mean value	0.37	0.44	0.49	0.50	1.25	1.36	1.46	1.60
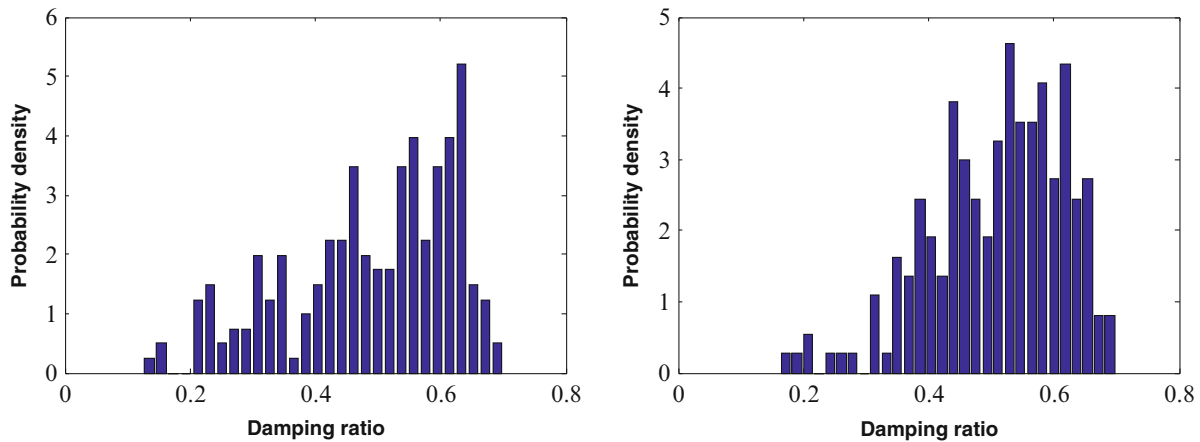
Fig. 35.6 Probability distribution of damping ratio in 1.75 Hz (left) and 2.25 Hz (right) walking frequency

though the identified results are very scattered, the mean damping ratio and natural frequency of SMD show a slight increasing trend with the increase of walking frequency. Table 35.2 shows the results for eight test subjects. For each test walking frequency, i.e., 1.75 Hz, each test subject conducted 6–7 times, thus the value shown in Table 35.2 is the mean value for each walking frequency. Figure 35.6 shows the distribution of identified damping ratios for walking frequencies 1.75 and 2.0 Hz. Further investigations are needed to model the probability property of the SMD parameters.

Table 35.3 gives the identified Fourier series coefficients for the biological force. The amplitude of each order is given

$$r_i = \sqrt{a_i^2 + b_i^2} \tag{35.11}$$

From Table 35.3, the fourth coefficient of all Fourier series coefficients is much smaller than the first three orders. Thus, order four is enough to present the biological force using Fourier series model.

35.4 Discussions

This paper adopts the spring-mass-damper model to represent walking people and suggests an iterative identification method to extract model parameters from gait experiment records. The assumption that the walking human is in acceleration resonance is derived from self-adjusting function of human body. The suggested identification method successfully extracts both parameters of SMD model and coefficients of biological force. It is also found that this method is not sensitive to the initial guess of damping ratio and natural frequency. For the gait experiment records used in this study, the identified results for test cases 1.5, 1.75, 2, 2.25 Hz are: the mean damping ratio 37 %, 44 %, 49 %, 50 % respectively and the natural frequency 1.25, 1.36, 1.46, 1.6 Hz.

The identified values of damping ratios are in the range of 37–50 % and natural frequencies in 1.25–1.6 Hz. The damping ratios are larger than 28 % damping ratio (with 2.9 Hz natural frequency) given by Matsumoto and Griffin [8] for passive

Table 35.3 Identified Fourier series coefficients for the biological force of four subjects among all members

Coefficients	Walking freq. [Hz]	r_1	r_2	r_3	r_4
Test sub. 1	1.50	0.1164	0.0329	0.0307	0.0157
	1.75	0.1621	0.0260	0.0553	0.0353
	2.00	0.1021	0.0184	0.0275	0.0143
	2.25	0.0536	0.0112	0.0179	0.0237
Test sub. 2	1.50	0.1398	0.0719	0.0227	0.0131
	1.75	0.1559	0.0451	0.0239	0.0284
	2.00	0.2264	0.0395	0.0234	0.0260
	2.25	0.1072	0.0349	0.0140	0.0189
Test sub. 3	1.50	0.1251	0.0491	0.0482	0.0174
	1.75	0.1942	0.0325	0.0687	0.0476
	2.00	0.2128	0.0301	0.0741	0.0703
	2.25	0.2002	0.0235	0.0810	0.0714
Test sub. 4	1.50	0.1205	0.0344	0.0295	0.0180
	1.75	0.1609	0.0232	0.0356	0.0183
	2.00	0.1666	0.0443	0.0311	0.0204
	2.25	0.2124	0.0709	0.0318	0.0361
Test sub. 5	1.50	0.1158	0.0180	0.0367	0.0122
	1.75	0.1918	0.0195	0.0426	0.0195
	2.00	0.2477	0.0373	0.0503	0.0293
	2.25	0.2696	0.0536	0.0571	0.0293

standing people with legs bent on a platform, which vibrated with known frequency and amplitude. Additionally, Wei and Griffin [1] found that seated passive people had a natural frequency of about 5 Hz with 45 % damping ratio; Dougill [3] suggested the bobbing body unit had a natural frequency of about 2.3 Hz with 25 % critical damping ratio. It is reported by Kasperski [2] recently that the induced damping of walking person exceeds that of a passive person and the damping value depends on the walking frequency. At this point of view, it is reasonable that the damping ratio of human body in walking is larger than the damping ratio of passive person in standing position. Comparing with the published values above, it might be supposed that the change of the level of activity i.e., walk frequency leads to an increase of the damping ratio and natural frequency. Further research is required to exploit these observations.

References

1. Wei L, Griffin MJ (1998) Mathematical models for the apparent mass of the seated human body exposed to vertical vibration. J Sound Vib 212(5):855–874
2. Agu E, Kasperski M (2011) Influence of the random dynamic parameters of the human body on the dynamic characteristics of the coupled system of structure–crowd. J Sound Vib 330(3):431–444
3. Dougill JW et al (2006) Human structure interaction during rhythmic bobbing. Struct Eng 84(22):32–39
4. Chen J, Peng YX, Ye T (2013) On methods for extending a single footfall trace into a continuous force curve for floor vibration serviceability analysis. Struct Eng Mech 46(2):179–196
5. Bobbert MF, Schamhardt HC, Nigg BM (1991) Calculation of vertical ground reaction force estimates during running from positional data. J Biomech 24(12):1095–1105
6. Chen J, Zhang MS, Zhao YF et al (2014) Kinematic data smoothing using ensemble empirical mode decomposition. J Med Imaging Health Inform 4(4):540–546
7. Holt KG, Obusek JP, Fonseca ST (1996) Constraints on disordered locomotion a dynamical systems perspective on spastic cerebral palsy. Hum Mov Sci 15(2):177–202
8. Matsumoto Y, Griffin MJ (2003) Mathematical models for the apparent masses of standing subjects exposed to vertical whole-body vibration. J Sound Vib 260(3):431–451

Chapter 36
Producing Simulated Time Data for Operational Modal Analysis

Esben Orlowitz and Anders Brandt

Abstract Producing simulated test data from models of mechanical structures is often important for validation of analysis methods, for example parameter identification methods. Whereas investigations of test procedures and identification methods for operational modal analysis (OMA) are widely reported based on simulations, little attention is often given to the actual procedures to produce simulated response signals. For example the influence of the excitation strategy in a simulation on the following identified properties. In the present work different excitation strategies are applied to simulate responses of a modal model of a Plexiglas plate. OMA parameter identification is performed on the simulated responses and the results are compared to see the influence of chosen excitation strategy. Furthermore OMA results from a lab measurement of the real physical Plexiglas plate are presented and compared to the simulation results.

Keywords Operational modal analysis • Simulation • Excitation strategy • Comparison • Experimental data

36.1   Introduction

Producing simulated time data from mathematical models of mechanical structures is often important for validation of analysis methods, for example parameter identification methods. Whereas investigations of test procedures and identification methods for operational modal analysis (OMA) are widely reported based on simulations, little attention seems to have been given to the actual procedures to produce simulated response signals. For example the influence of the excitation strategy in a simulation on the following identified properties and its similarity with experimental measurements.

There seems to be three common excitation strategies used in the literature for producing simulated OMA response data:

- Responses from simulation codes, especially for wind turbines, where the excitation is not explicitly stated, see e.g. references [1, 2]
- Responses due to random Gaussian excitation in a single degree of Freedom (DOF), see e.g. references [3–5]
- Responses due to independent (and identically distributed) Gaussian excitation of all DOFs, see e.g. references [6, 7]

As none of these strategies, to the authors' knowledge, haven been applied to the same system (model of a structure), the influences of the excitation seems not to have previously been considered. Responses from simulation codes often simulate complex physics, e.g. aerodynamics, and are in addition not easy to generalize for which reason such data are outside the scope of the present work. However, if such a simulation code is well designed it should deliver realistic excitations and thus also realistic responses.

Excitation of a single DOF obviously simplifies the simulation of responses. However, such a situation seems unlikely in many real-life situations were forces acting on more DOFs (if not all) should be expected.

From experimental experience only a few (2–4) independent sources are often observed to be dominant. In situations where there are more independent sources, it still seems unlikely that a force acting on one DOF is independent of a force acting in another DOF. For instance a wind load on a civil structure of two spatially well separated DOFs should be expected to be correlated and thus they are dependent. An example from a full scale measurement of a ship in operation, see the principal components in Fig. 36.1, show 2–3 dominant sources. In the present example, Fig. 36.1, the principal components are calculated between 45 responses and thus theoretically should enable to distinguish between 45 independent sources.

—————————
E. Orlowitz (✉) • A. Brandt

Department of Technology and Innovation, University of Southern Denmark, Odense, Denmark

e-mail: eo@iti.sdu.dk; abra@iti.sdu.dk

Fig. 36.1 Principal components of 45 DOF measurement on a ship, see [8] for further details
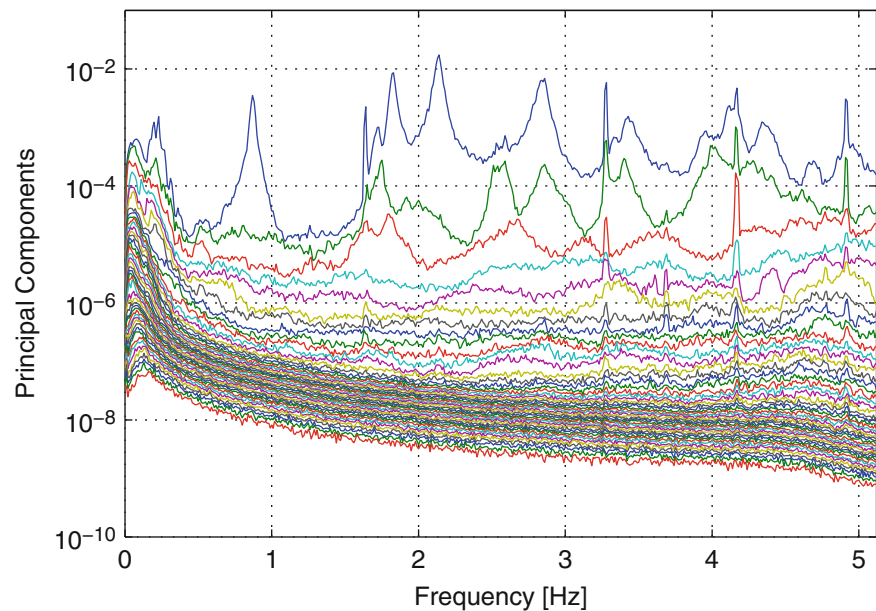
In the present work a 35-DOF modal model of a Plexiglas plate has been exposed to four different excitation strategies. These strategies are the following: a single source exciting a single DOF, independent excitation of all DOFs, excitation of all DOFs randomly mixed of 35 independent sources and finally excitation of all DOFs randomly mixed of four independent sources. All sources are generating identically distributed zero mean Gaussian distributed sequences. Modal parameters are estimated from the responses of the four excitation strategies for comparison.

The modal model used for the simulations is extracted from an experimental OMA of a Plexiglas plate that is also documented in the present work. A comparison between the experimental data and the simulated data is included together with a comparison of the four excitation strategies for producing simulated time data responses.

36.2 Methods

The variety of methods for OMA modal parameter estimation is large, many of them being modifications of some basic methods. In the present paper the Multiple-reference Ibrahim Time Domain (MITD) Method is used and shortly reviewed in the following section.

The next section describes the strategies used for generation of excitation forces for simulating response data. For estimation of the number of independent sources principal component (PC) analysis is applied in the present work, for details about PC analysis the reader is referred to e.g. chapter 15 in [9].

36.2.1 Modal Parameter Estimation Method

The original basis functions for the multi-reference Ibrahim time domain (MITD) method [10] are impulse responses, which in the OMA case are replaced by correlation functions (CFs). In the present work CFs have been estimated from time data by the (indirect) correlogram approach, see e.g. [11]. First, correlation functions between all sensors (or between reference sensors and all sensors, depending on measurement strategy) are collected in a Hankel matrix. Noise suppression is performed by singular value decomposition of the Hankel matrix and finally eigenvalues for different system order (by including more and more of the singular vectors) are solved for in a classical matrix polynomial (difference equation) formulation.

From the eigenvalues and eigenvectors the corresponding modal parameters are obtained straightforwardly. The challenge is to distinguish between physical modes of the measured structure and spurious modes occurring from model errors, measurement noise and numerical errors. Manual selection of physical modes is commonly done by use of stabilization diagrams (sometimes referred to as consistency diagrams) which is also the approach in the present work.

36.2.2   Generation of Excitation Forces

The forces exciting the N DOFs of the modal model are collected in a force matrix $\mathbf{F}$ constructed from a number N_S of independent sources. The time sequences of the sources are collected in a source matrix $\mathbf{S}$ with M samples each. The distribution of the sources on the DOFs is controlled by a distribution matrix $\mathbf{D}$ and the force matrix is then constructed as follows,

$$\mathbf{F}^{M \times N} = \mathbf{S}^{M \times N_S} \mathbf{D}^{N_S \times N}$$

$$\begin{bmatrix} | & | & & | \\ F_1 & F_2 & \dots & F_N \\ | & | & & | \end{bmatrix}^{M \times N} = \begin{bmatrix} | & | & & | \\ S_1 & S_2 & \dots & S_{N_S} \\ | & | & & | \end{bmatrix}^{M \times N_S} \begin{bmatrix} | & | & & | \\ D_1 & D_2 & \dots & D_N \\ | & | & & | \end{bmatrix}^{N_S \times N} \tag{36.1}$$

For the case of independent excitation of all DOFs the distribution matrix $\mathbf{D}$ equals the identity matrix and for the dependent cases were sources are randomly mixed for each DOF, $\mathbf{D}$ is created randomly from a uniform distribution within the interval $]0, 1[$. Equation (36.1) can be interpreted by considering a column D_n of the distribution matrix as weighting factors of sources in a single DOF. The influence of each source is thus different in all DOFs, but the influence is constant in time controlled by the columns of $\mathbf{D}$.

36.2.3   Note on Randomly Mixed and Identical Distribution

The method applied for creating the dependent excitations in the present work has some implicit idealizations that should not be expected for real life cases. For instance the dependency of the excitations at two close DOFs should be stronger than the dependency between two not so close DOFs, which is not the case in the present work. However, without a realistic physical model of the spatial distribution it is impossible to implement dependency between the excitation of the individual DOFs. For this reason, in the present work the independent sources are randomly mixed in the case of dependent excitation.

Another aspect of the idealization is that all sources in the present work are identical distributed, for which there seems no reason in practices. For example for a bridge the distribution of the wind load should not be expected to be the same as for the load from traffic. For a generic study as the present one, identical distributions seems like an obvious choice.

36.3   Experimental OMA Test

The physical Plexiglas (PMMA) plate has been experimentally tested, see Fig. 36.2a. The plate dimensions are 533×321 mm and thickness 20 mm. It is similar to the so-called IES-Plate proposed in [12], however, for practical reasons, the plate thickness was chosen slightly different from the IES-Plate, by choosing 20 mm thickness, which is a standard thickness in Europe. The measurement grid consist of 35 DOFs distributed uniformly out of plane on the plate as shown in Fig. 36.2b and all DOFs are measured simultaneously. Influences by the instrumentation are neglected; te structure of interest is thus the combined Plexiglas plate including its instrumentation.

For measurements the following data acquisition (DAQ) and sensor equipment were used:

- 3x National Instruments 4497, 16 channel, 24bit analog inputs cards
- 35x Dytran 3097A2 accelerometers, 100 mV/g, IEPE, 4.3 grams
- In-house software for DAQ control, based on MATLAB DAQ-toolbox

Fig. 36.2 (**a**) The Plexiglas plate freely suspended and equipped with 35 accelerometers. (**b**) The used measurement grid, consisting 35 measurement points with a separation of 75×85 mm and the full plate dimensions are 533×321 mm and thickness 20 mm
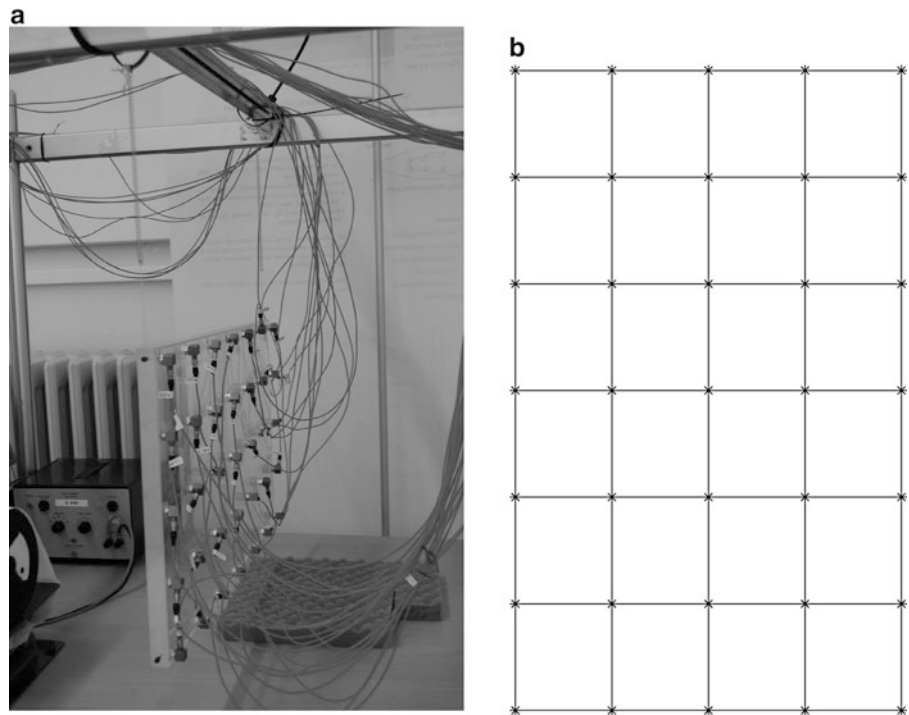
The plate was suspended in springs via thin fishing line, see Fig. 36.2a, giving it relative low rigid body modes (3 Hz). The plate was excited by a pencil, gently scratched around the plate, originally a technique suggested by Rune Brincker [13]. The sampling frequency was 5 kHz and the measurement time 360 s, corresponding to approx. 50,000 periods of the lowest natural frequency. This rather long measurement time is chosen to reduce possible effects of limited measurement time that is outside the scope of the present work.

36.4   Simulations Cases

The Plexiglas plate presented in the previous section was simulated in order to investigate different excitation strategies. The first ten modes obtained from the experimental OMA test was used directly in the simulation by the time domain method described in Section 6.5 in [9] for 360 s as for the experimental test. This method is based on modal superposition, using a simple IIR filter for each mode, and is equivalent to using state-space simulation with zero-order hold, commonly used in control applications.

Four different excitation strategies have been used for the simulations, these are the following:

- **Sim. 1** A single source exciting a single DOF
- **Sim. 2** independent excitation of all DOFs
- **Sim. 3** excitation of all DOFs randomly mixed from 35 independent sources and
- **Sim. 4** excitation of all DOFs randomly mixed from four independent sources.

All sources generated Gaussian distributed sequences and again a sampling frequency of 5 k was used. To increase the strength of the comparison of the two mixed cases a common distribution matrix, **D**, of 35×35 elements was generated (by the MATLAB *rand*) and in the case of four independent sources only the first four rows of this distribution matrix were used. For the same reasons also a common source matrix of 35 independent sources was generated for which the used number of columns depend on the excitation strategy, e.g. for the case of a single source exciting a single DOF only the first column was used. Recall that for the single source and independent excitation the distribution matrix equals the identity matrix.

It should be noted that the Plexiglas plate tested in the present work is designed to have two closely spaced modes (the first bending and torsion). Two sources will in general be needed in order to decouple the modes in an experimental modal analysis. This fact is not fulfilled in the case of a single source (Sim. 1) for which reason sufficient estimates are not expected for the first two modes. However, the remaining modes are well separated and therefore the case (Sim. 1) is included in this work.

36.5   Results

First the experimental results are presented. These experimental results are the basis for the simulations from which results are presented in the next section. For increased transparency of the OMA results the same analysis parameters haven been used for all five analyse, hence no individual optimization of the analysis parameters has been applied. For the MITD method 80 lags of the CFs have been used, corresponding to 15 ms (approx. half a period of the lowest natural frequency). Comparable results as presented in the following were also obtained by the correlation (co-variance) driven stochastic subspace identification method [6] but are not included. Cross-spectral densities for principal components analysis have been estimated by Welch method with a blocksize of 2,048 and 50 % overlap (approx. 1,800 averages).

Selections of estimated modes were conducted subjectively from 'the best stabilization' of the modes in the stabilization diagram. It has been observed that often a stable mode has a region of model order where it is more stable, see Fig. 36.3. This is often seen after the modes have obtained the typical stabilization criteria and before the often observed increasing scatter at higher model orders. The stabilization criteria used in the present work were a consecutive relative difference of less than 0.1 % and 5 % for frequency and damping respectively and a MAC value of at least 0.9, which is comparable to what is often used in the literature.

36.5.1   Experimental Results

Principal components of the experimental data, see Sect. 36.3, are shown in Fig. 36.4 indicating a few dominant independent sources. A clear distinction is not as obvious here as it is seen from the simulation cases in the next section. The estimated natural frequencies and damping ratios are presented in Table 36.1. The mode shapes are omitted, but the auto MAC matrix from the estimated mode shapes is shown in Fig. 36.5, from which a sufficient decoupling of modes can be seen. The stabilization diagram from the MITD method is presented in Fig. 36.6 for completeness.The extracted modes were used as basis for the simulations and their values are treated as 'true' when compared to the simulation results.

36.5.2   Simulation Results

Principal components of each simulation case are shown in Fig. 36.7. In Fig. 36.7b,c only ten principal components at an equal level are observed even though there should be 35. The reason for this is that the modal model of the plate only contain ten modes, hence the actual rank of the model is 10 and eigenvalues below rank 10 should be small [9].
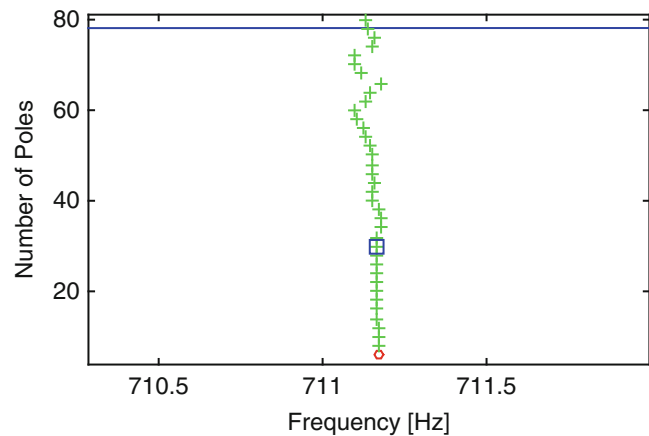
Fig. 36.3 Illustration of the evolution of a stable mode for increasing model order. Here for mode 8 in the simulation case with independent excitation of all DOFs (Sim. 2)

Fig. 36.4 Principal components of the experimental responses
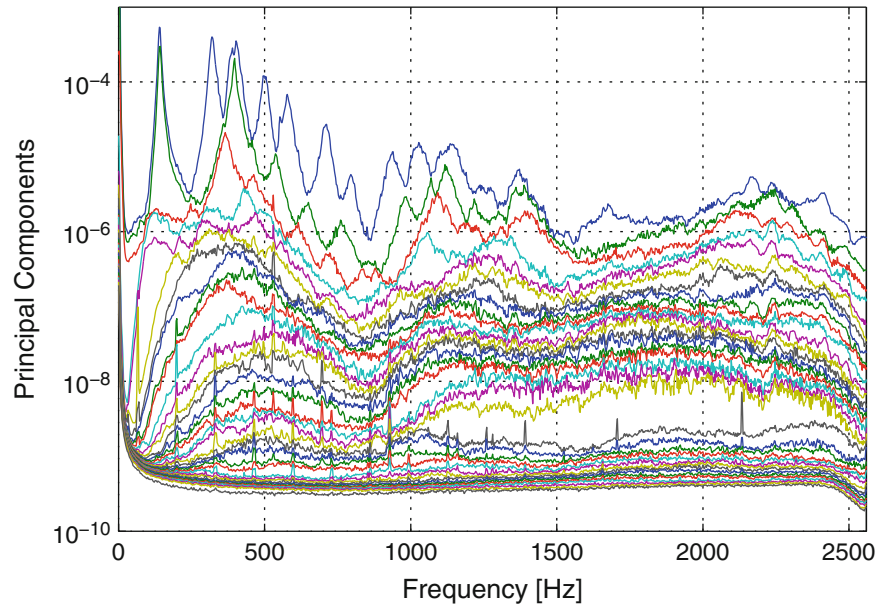
Table 36.1 Estimated natural frequencies and damping ratios from the experimental test

Mode #	f_n [Hz]	ζ_n [%]
1	140.533	3.479
2	141.588	3.335
3	319.717	3.013
4	388.531	3.034
5	405.072	2.708
6	500.982	2.551
7	580.990	3.286
8	711.052	2.298
9	793.589	2.813
10	935.535	2.871

Fig. 36.5 Auto MAC matrix for the experimentally estimated mode shapes

Auto MAC matrix
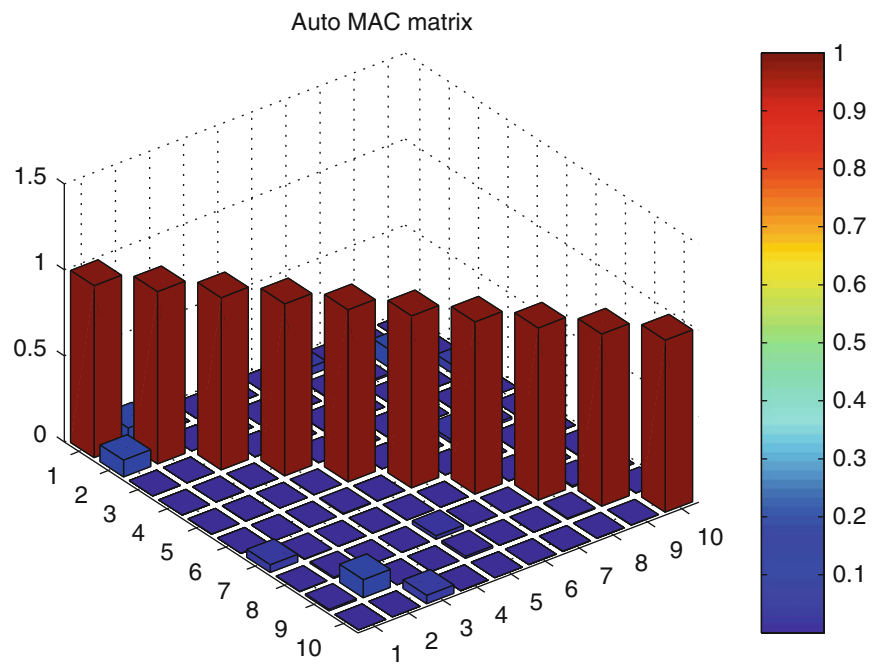
Fig. 36.6 Stabilization diagram
from the experimental test of the
Plexiglass plate. '+' mean stable
pole and mode shape, '○'
unstable and '◇' only stable
frequency. The *solid line* in the
background is the power
spectrum from DOF 1 (Color
figure online)
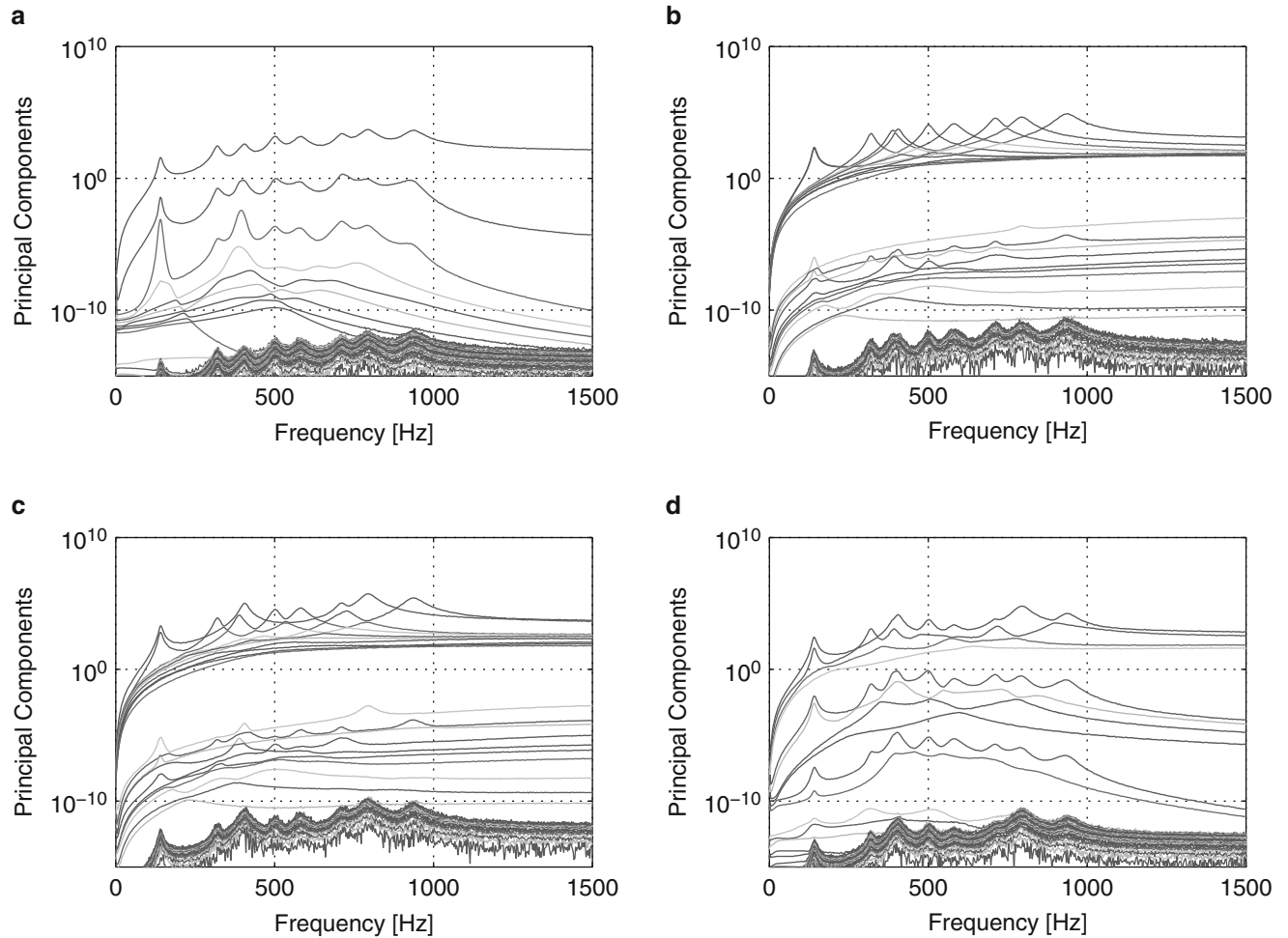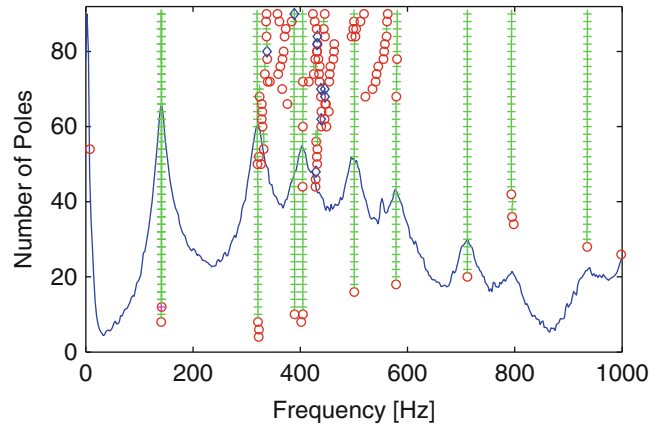
Fig. 36.7 Principal components of the responses (**a**) for (Sim. 1) the single DOF excitation case. The first principal component is approx. 60 dB higher than the next, indicating a single independent source as expected. (**b**) For (Sim. 2) the case of independent excitation of all DOFs. Ten principal components of similar level can be observed (approx. 100 dB higher than the rest), indicating ten independent sources. The reason why 35 independent sources are not observed is that model has only ten modes. (**c**) For (Sim. 3) the case of excitation of all DOFs randomly mixed of 35 independent sources. Ten principal components of equivalent level can be observed (approx. 90 dB higher than the rest), indicating ten independent sources. (**d**) Principal components for (Sim. 4) the case of excitation of all DOFs randomly mixed of four independent sources. Four principal components are observed to be at an equal level, with the next one approx. 30 dB below

The estimated natural frequencies and damping ratios for the four simulation cases are presented in Table 36.2 together with the 'true' values from the experimental test reprinted for completeness. In addition, the deviations of the simulation results from the 'true' values too are stated in Table 36.2 and so also cross-MAC values calculated with respect to the 'true' mode shapes. Stability diagrams for the simulations are shown in Fig. 36.8.

Table 36.2 Estimated natural frequency and damping for the four simulation cases and their deviation from the true values

	f_n [Hz]	Diff. f_n [%]	ζ_n [%]	Diff. ζ_n [%]	MAC
Mode1					
Experimental	140.533	–	3.479	–	–
Sim 1	140.147	−0.275	3.178	−8.631	0.877
Sim 2	140.929	0.282	3.613	3.871	0.993
Sim 3	140.848	0.224	3.654	5.041	0.973
Sim 4	140.623	0.064	3.456	−0.658	0.966
Mode2					
Experimental	141.588	–	3.335	–	–
Sim 1	142.055	0.330	3.555	6.610	0.884
Sim 2	141.928	0.241	3.548	6.391	0.976
Sim 3	141.678	0.063	3.508	5.202	0.992
Sim 4	141.680	0.065	3.418	2.484	0.963
Mode3					
Experimental	319.717	–	3.013	–	–
Sim 1	319.708	−0.003	3.042	0.963	1.000
Sim 2	319.779	0.019	2.985	−0.940	1.000
Sim 3	319.948	0.072	3.004	−0.294	1.000
Sim 4	319.754	0.012	2.991	−0.744	1.000
Mode4					
Experimental	388.531	–	3.034	–	–
Sim 1	388.502	−0.008	3.036	0.065	0.999
Sim 2	388.488	−0.011	3.013	−0.682	1.000
Sim 3	388.581	0.013	2.974	−1.972	1.000
Sim 4	388.574	0.011	2.981	−1.748	1.000
Mode5					
Experimental	405.072	–	2.708	–	–
Sim 1	405.118	0.011	2.668	−1.476	1.000
Sim 2	405.116	0.011	2.715	0.251	1.000
Sim 3	405.113	0.010	2.700	−0.282	1.000
Sim 4	405.175	0.025	2.673	−1.297	1.000
Mode6					
Experimental	500.982	–	2.551	–	–
Sim 1	501.090	0.022	2.552	0.070	1.000
Sim 2	501.052	0.014	2.534	−0.647	1.000
Sim 3	501.194	0.042	2.537	−0.552	1.000
Sim 4	501.087	0.021	2.528	−0.877	1.000
Mode7					
Experimental	580.990	–	3.286	–	–
Sim 1	581.209	0.038	3.262	−0.747	1.000
Sim 2	581.054	0.011	3.277	−0.290	1.000
Sim 3	580.848	−0.024	3.248	−1.174	1.000
Sim 4	580.841	−0.026	3.315	0.884	1.000
Mode8					
Experimental	711.052	–	2.298	–	–
Sim 1	711.129	0.011	2.305	0.304	1.000
Sim 2	711.168	0.016	2.308	0.470	1.000
Sim 3	711.037	−0.002	2.284	−0.595	1.000
Sim 4	710.972	−0.011	2.299	0.040	1.000

Table 36.2 Continued

Mode9					
Experimental	793.589	–	2.813	–	–
Sim 1	793.629	0.005	2.803	−0.375	1.000
Sim 2	793.420	−0.021	2.831	0.623	1.000
Sim 3	793.629	0.005	2.815	0.067	1.000
Sim 4	793.756	0.021	2.787	−0.922	1.000
Mode10					
Experimental	935.535	–	2.871	–	–
Sim 1	935.870	0.036	2.915	1.529	1.000
Sim 2	935.329	−0.022	2.907	1.270	1.000
Sim 3	935.560	0.003	2.871	−0.010	1.000
Sim 4	935.551	0.002	2.864	−0.234	1.000

The cross-MAC value are also calculated with respect to the true mode shape

36.5.3   Discussion

From Table 36.2 it is seen that the deviations from the true value of the natural frequencies are considerable smaller than the deviation for the damping ratio. (This fact is common accepted with in the community of experimental modal analysis and OMA.) In addition, a look at differences of the damping ratios with respect to the true values shows that the damping estimates are both over- and underestimated. This indicates that the deviations are due to random error and not bias error. With the single source and DOF excitation it was possible to estimate the poles of the two closely modes, however at a rather high system order. Nevertheless the estimates of these two modes are poor compared to the estimates when more sources and DOFs are used and especially the mode shapes where badly estimated as should be expected, see the cross-MAC values in Table 36.2.

Comparing the deviations from the true values of the other three excitation strategies, see Table 36.2, there does not seem to be a different influence of the excitation strategy on the identified properties. This also applies for the single source and DOF excitation for the higher modes, which are comparable to those of the other simulation cases.

Comparing the stabilization diagrams, Fig. 36.8, there seems to be a tendency of a less clear diagram when the excitation of the DOFs gets dependent, however it seems not significant. Note that for the case of a single source, Fig. 36.8a, increasing the number of poles in the model above 60 no further information is obtained from the chosen amount of data. The reason is a drastic decrease in the singular value from order 60 to 62 with following very values close to zero. However this effect is not expected (and have never been experienced by the authors) for real data.

Having observed that there does not seem to be an influence of the excitation strategies applied in the present work it is, however, observed that the two closely spaced modes are not well estimated when comparing the mode shapes, see the cross-MAC values between the estimated mode shapes and the experimental (true) mode shapes. For simulated cases such as the present, it should be expected to have cross-MAC values exceeding, say, 0.99.

To further investigate the separation of the two closely spaced modes, excitation equivalent to an EMA approach was applied. Two independent excitation sources were thus applied at two corners of one of the narrow ends of the plate, since this is well known to allow to separate the modes in EMA. The source signals were taken from the previously mentioned common source matrix, so they were identical to the source signals used for the previous simulations. The identification settings were identical to the others in this work and the resulting stabilization diagram is seen in Fig. 36.9 and the estimated natural frequencies and damping ratios are shown in Table 36.3 together with the deviations from the true values. Also in Table 36.3 the cross-MAC values are shown and it can be seen that the estimation of the mode shapes is better than for the previously simulation cases. In Fig. 36.9 it can be seen that the two closely spaced modes are stabilizing considerable better than for the other excitation strategies tested (Fig. 36.9). This somewhat surprising result seems to indicate that there could be some challenges with estimation of mode shapes of closely spaced modes using OMA techniques, compared to traditional EMA techniques. We have, however, no plausible explanation of the reason for this at the moment.
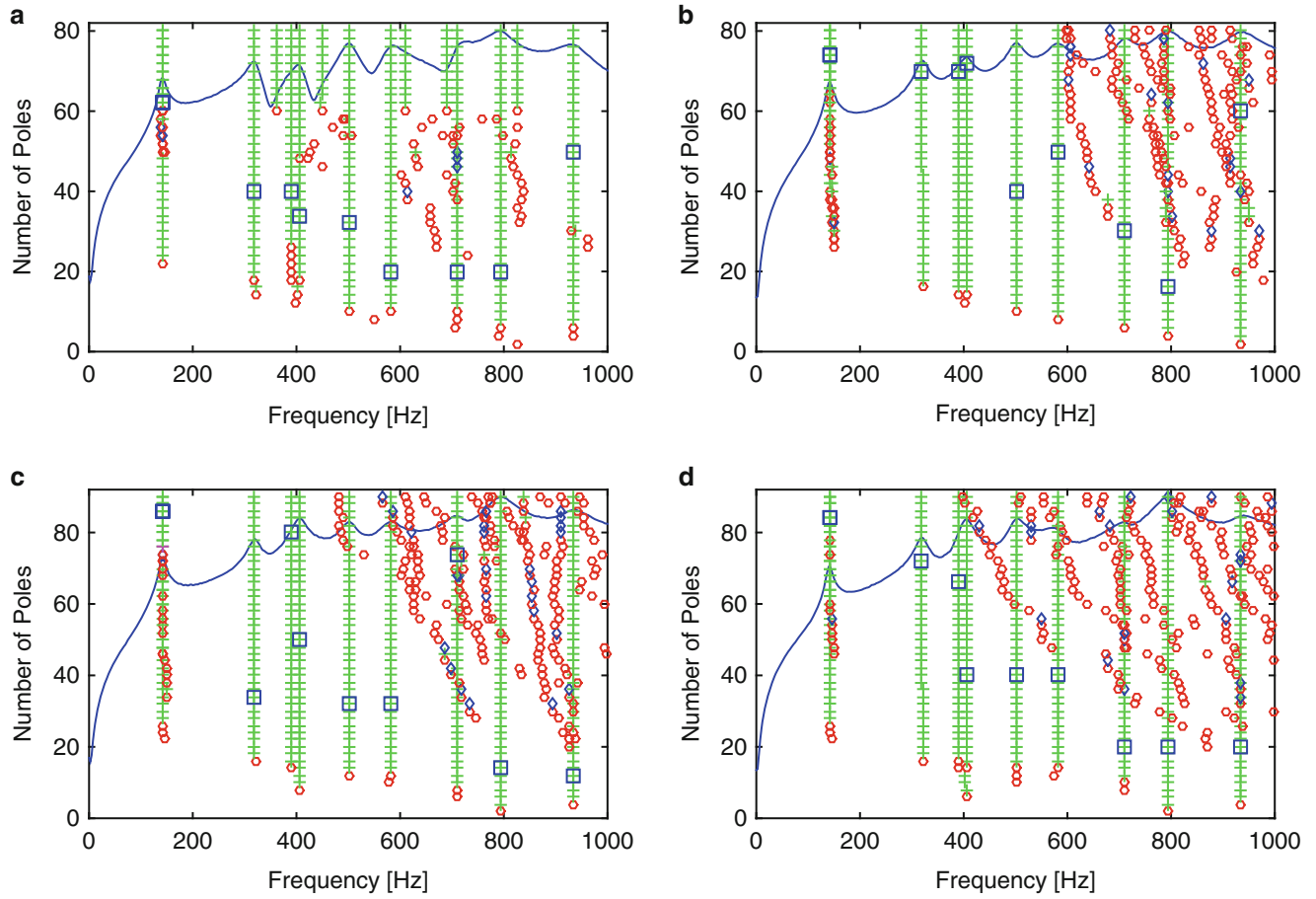
Fig. 36.8 (**a**) Stabilization diagram for (Sim. 1) the case of a single source exciting a single DOF. (**b**) For (Sim. 2) independent excitation of all DOFs. (**c**) For (Sim. 3) the case of excitation of all DOFs randomly mixed of 35 independent sources. (**d**) For (Sim. 4) the case of excitation of all DOFs randomly mixed of four independent sources

Fig. 36.9 Stabilization diagram for the case of two DOFs excited by independent sources
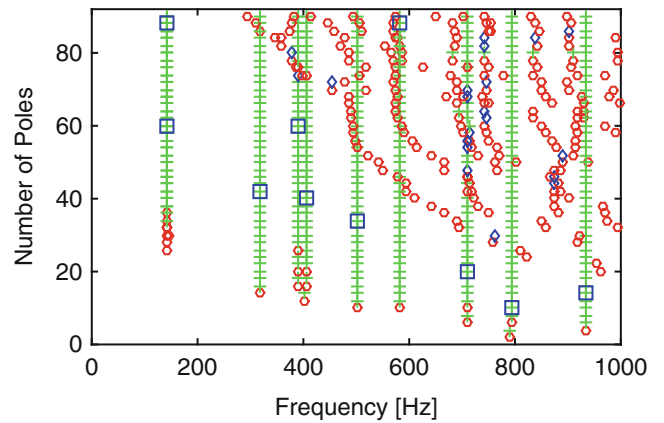
Table 36.3 Estimated natural frequency and damping for the extra simulation case with excitation by two independent sources at two DOFs

Mode # (n)	f_n [Hz]	Diff. f_n [%]	ζ_n [%]	Diff. ζ_n [%]	MAC
1	140.615	0.058	3.401	−2.221	0.999
2	141.507	−0.057	3.311	−0.725	0.993
3	319.753	0.011	3.043	0.988	1.000
4	388.405	−0.033	3.001	−1.086	0.999
5	405.142	0.017	2.657	−1.877	1.000
6	501.014	0.007	2.567	0.643	1.000
7	580.909	−0.014	3.253	−1.000	1.000
8	711.157	0.015	2.301	0.125	1.000
9	793.707	0.015	2.780	−1.200	1.000
10	935.407	−0.014	2.842	−1.003	1.000

Also their deviations and the cross-MAC value with respect to the true mode shape is shown

36.6   Conclusions

Four different ways of producing simulated time data for operational modal analysis (OMA) has been tested. The focus has been on how the analytical model is excited as it has been observed that the methods typically stated in the literature differ from what is observed in experimental OMA tests. In experimental OMA often one will only observe 2–4 dominant independent sources whereas it seems common to apply independent excitation in all DOFs in cases of simulating OMA data.

In the present work the four excitation strategies studied were: a single source exciting a single DOF, independent excitation of all DOFs, excitation of all DOFs by randomly mixing 35 independent sources, and finally excitation of all DOFs by randomly mixing four independent sources. All sources were generated using zero mean, Gaussian distributed sequences.

As is common knowledge, the case of a single source exciting a single DOF is an insufficient excitation to separate the mode shapes of closely spaced modes. This excitation strategy was, however, included since it seems to be quite commonly used, and we wanted to see how it performs for the uncoupled modes compared to the other more elaborate excitation strategies.

The four different excitation strategies do not seem to influence identified modal properties, although the clarity of the stabilization diagram was somewhat better for the more realistic case of four independent sources randomly mixed over all DOFs than for the other excitation strategies.

Another observation is that excitation evenly distributed over the structure showed some weakness in separating two closely spaced modes. This could indicate that OMA may not be as efficient as EMA to separate closely spaced modes. Applying only two sources, in two corners of the plate structure used for the simulations, resulted in better separation of the closely spaced modes. However, this exciting strategy is not particularly relevant in most real operating cases.

References

1. James GH, Carne TG, Lauffer JP (1995) The natural excitation technique (next) for modal parameter extraction from operating structures. Int J Anal Exp Modal Anal 10:260–277
2. Allen MS, Sracic MW, Chauhan S, Hansen MH (2011) Output-only modal analysis of linear time-periodic systems with application to wind turbine simulation data. Mech Syst Signal Process 25(4):1174–1191
3. Reynders E, Pintelon R, De Roeck G (2008) Uncertainty bounds on modal parameters obtained from stochastic subspace identification. Mech Syst Signal Process 22(4):948–969
4. Tondreau G, Deraemaeker A (2014) Numerical and experimental analysis of uncertainty on modal parameters estimated with the stochastic subspace method. J Sound Vib 333(18):4376–4401
5. Ceravolo R, Abbiati G (2013) Time domain identification of structures: comparative analysis of output-only methods. J Eng Mech 139:537–544
6. Peeters B, G De Roeck (1999) Reference-based stochastic subspace identification for output-only modal analysis. Mech Syst Signal Process 13:855–878

7. Chauhan S, Phillips AW, Allemang RJ (2008) Damping estimation using operational modal analysis. In: Proceedings of international modal analysis XXVI, Orlando, Florida
8. Orlowitz E, Brandt A (2014) Modal test results of a ship under operational conditions. In: Proceedings of international modal analysis XXXII, Orlando, Florida
9. Brandt A (2011) Noise and vibration analysis - signal analysis and experimental procedures. Wiley, Chichester
10. Allemang R, Brown D (1987) Experimental modal analysis and dynamic component synthesis – vol 3: Modal parameter estimation. Technical Report, USAF
11. Orlowitz E, Brandt A (2013) Influence of correlation estimation methods on damping estimates. In: Proceedings of 5th international operational modal analysis conference, Guimaraes, Portugal
12. Smallwood D, Gregory D (1986) A rectangular plate is proposed as an ies modal test structure. In: Proceedings of international modal analysis IV, Los Angeles, California
13. Brincker R (2013) Personal conversation

Chapter 37
Evaluation of Damping Using Frequency Domain Operational Modal Analysis Techniques

Anela Bajrić, Christos T. Georgakis, and Rune Brincker

Abstract Operational Modal Analysis (OMA) techniques provide in most cases reasonably accurate estimates of structural frequencies and mode shapes. In contrast though, they are known to often produce uncertain structural damping estimates, which is mainly due to inherent random and/or bias errors. In this paper a comparison is made of the effectiveness of two existing OMA techniques in providing accurate damping estimates for random stationary loading, varying levels of signal noise, number of added measurement channels and level of structural damping. The investigation is focusing on the two frequency domain techniques, the Frequency Domain Decomposition (FDD) and the Frequency Domain Polyreference (FDPR). The response of a two degree-of-freedom (2DOF) system is numerically established with specified modal parameters subjected to white noise loading. The system identification is evaluated with well separated and closely spaced modes. Finally, the results of the numerical study are presented, in which the error of the structural damping estimates obtained by each OMA technique is shown for a range of damping levels. From this, it is clear that there are notable differences in accuracy between the different techniques.

37.1 Introduction

In 2011, Georgakis et al. [1] reported negative aerodynamic damping in the presence of rain for the longest cable on the Øresund Bridge between Denmark and Sweden. The aerodynamic damping was identified from full scale measurements of the bridge using two time domain techniques, the Eigenvalue Realization Algorithm (ERA) [2] and Stochastic Subspace Identification (SSI) [3]. The OMA estimates of damping were identified to be inconsistent and coarse in all cases. The poor damping estimation is thought mainly to be due to inherent random and/or bias errors.

The reliability and accuracy of damping estimates using techniques in the time domain were reported by Bajric et al. [4]. The other approach is to preform identification in the frequency domain. The accuracy of the different frequency domain techniques in determining damping remains unknown. Thus the robustness and accuracy of the existing frequency domain OMA techniques for various levels of damping, was evaluated.

The loading on civil engineering structures is often random and the will be random. The basic idea of most OMA techniques in the frequency domain is to perform identification based on the spectral density function estimates. The input response spectral density function from a random response measurement is finite and suffers therefore from bias. The input for identification is further disturbed by high noise to signal ratios, and it becomes a challenge to determine the physical modes of the system. Moreover for structures with some degree of symmetry, closely spaced modes are often encountered. The proximity of natural frequencies reduces the quality of the estimates [5, 6], however it is unknown by how much.

Two existing techniques were chosen for the evaluation of damping estimation, namely the Frequency Domain Decomposition (FDD) [7] and Frequency Domain Polyreference (FDPR) [8]. The evaluation of the techniques in estimating damping is based on the performance for configurations of response to white noise loading, separated and closely spaced

A. Bajrić (✉) • C.T. Georgakis

Department of Civil Engineering, Technical University of Denmark, Building 118, Brovej, 2800 Kgs, Lyngby, Denmark
e-mail: abaj@byg.dtu.dk; bajric.anela@gmail.com

R. Brincker

Department of Engineering, Aarhus University, Dalgas Avenue 2, 800, Aarhus C, Denmark

modes, varying levels of signal noise, additional measurement channels and varying levels of damping. Numerical results are presented in support of the proposed configurations, giving an overview of the performance of each identification technique for the estimation of structural damping.

37.2   Identification Algorithms

In the classical frequency domain approach, any structural mode with light damping is only influencing the response of the structure in a narrow frequency band around the natural frequency of the considered mode [9]. Therefore a limited frequency band is considered in which each mode is dominating, rather than the full time span as in the time domain. The two time domain techniques were used as implemented in the OMA toolbox [10].

The Frequency Domain Decomposition is derived according to Brincker et al. in 2000. This version of a frequency domain approach is based on the decomposition of the spectral matrix into auto spectral density functions which correspond to a single degree of freedom system (SDOF). The decomposition is performed by taking the Singular Value Decomposition of the spectral matrix. The singular values are then directly related to the natural frequencies squared and the singular vectors are related to the mode shapes, however under the assumption of white noise loading, geometrically orthogonal modes and light damping.

Typically in the FDD identification, the modal parameters and damping are estimated by using the information around the peak of the spectral density for the SDOF system and transforming it back to time domain by inverse Fast Fourier Transformation to obtain the auto correlation function. In that case the natural frequencies and damping are estimated from the zero crossing times and the logarithmic decrement of the SDOF system's auto correlation function. The damping in this paper is estimated using the obtained auto correlation function as an input to the Single-Input-Multiple-Output (SIMO) version Ibrahim Time Domain (ITD) technique [11].

The Frequency Domain Polyreference technique is on the other hand based on ARMA models transformed to the frequency domain by the Z-transform. The present technique is the simplest possible version of this technique where only one single Moving Average (MA) matrix is being used. As a result, the technique only works well when the estimation is performed in smaller frequency bands.

37.3   Numerical Simulations and Results

The numerical simulations were performed for stationary random white noise loading, separated and closely spaced modes, varying noise levels and addition of measurement channels. These variations led to 18 tested configurations listed in Table 37.1. The input was the estimated spectral density function of the stimulated response to white noise loading.

Identification problems in OMA arise due to limited time series length, as it is generally assumed that the spectral density function estimate tends to the exact solution when the time series is infinite. Therefore the window size was set to ensure reasonable estimates of the spectral density function, such that the estimated damping includes minimal influence from leakage bias. The time step was set to 0.05 sec and was held constant. Increasing the time step, for this system, will limit the noise and vice versa. The number of data points in the segment was 2,048. For the FDD response, the spectral density matrix function was estimated using the Welch averaging technique with a Hanning window and 50 % overlap. The input for the FDPR was a half spectrum, an estimated spectral density function based on a computation of the correlation function matrix where all the negative parts of the correlation function are forced to zero and half of the outermost part of the correlation function are also forced to zero using a triangular window.

The total time window was adjusted according to the estimated correlation function. The first five data points were removed to avoid the influence of measurement noise and the amplitude of the correlation function determined the length of the time window. The correlation function was truncated at the point where the amplitude was below 20 % of the maximum amplitude thus excluding the noise tail. The time windows were of equal length for each DOF. For the identification, the frequency band was chosen based on the natural frequency of interest, and ensured to be included within the adjusted time window.

The two mode shapes of the system were random and geometrically orthogonal, and the closeness of the modes was adjusted by the natural frequencies of the modes, where both modes had equal damping. Signal noise was simulated as white noise with a level of either $1\%_0$ or $2\%_0$ of the maximum value of the response. For each level of signal noise the damping estimate was evaluated with the addition of five measurement channels.

Table 37.1 Tests denotes the variation of simulation configurations

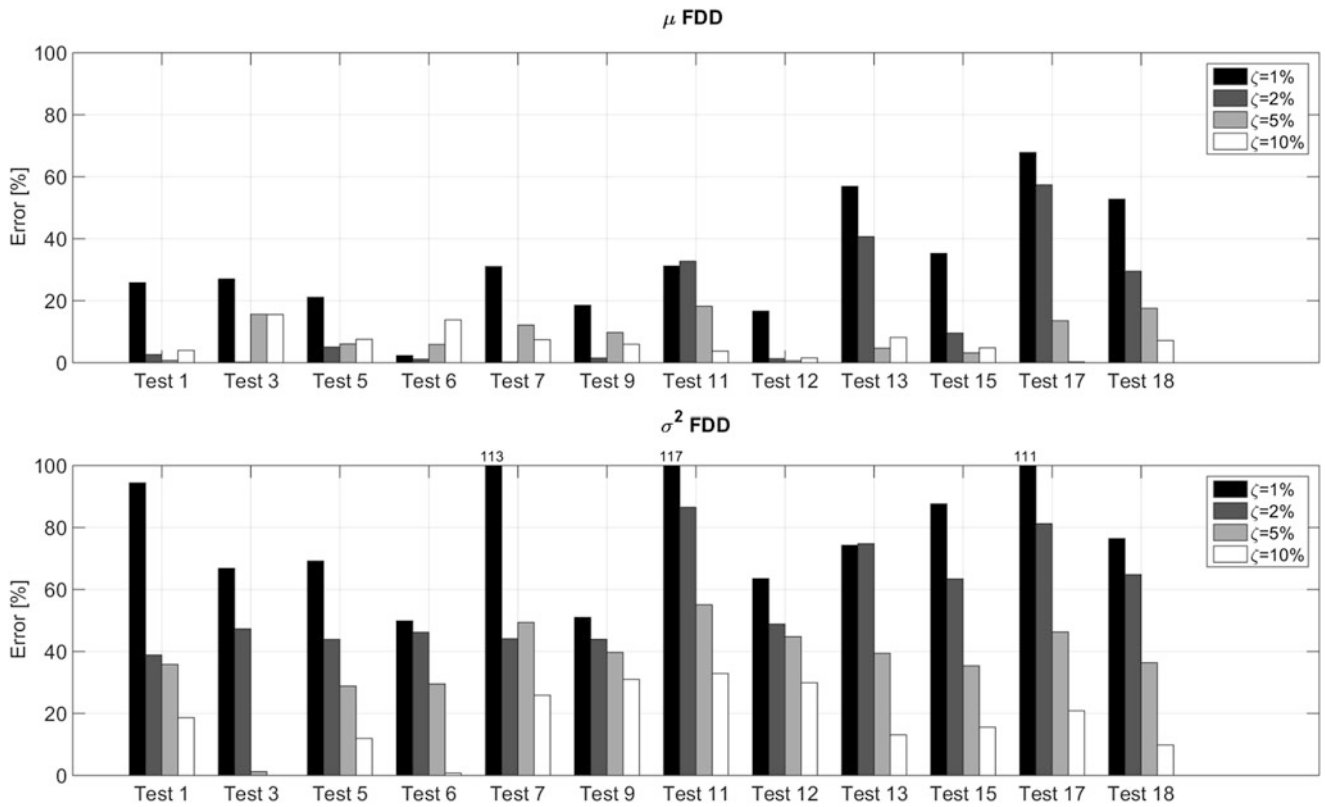| Spectral density	Frequency	Signal noise level	Additional channels	Test
G_{yy}	$f_1 = 1.00$ Hz	0 %	5	*1*
			10	*2*
	$f_2 = 3.00$ Hz	1‰	5	*3*
			10	*4*
		2‰	5	*5*
			10	*6*
	$f_1 = 1.00$ Hz	0‰	5	*7*
			10	*8*
	$f_2 = 1.20$ Hz	1‰	5	*9*
			10	*10*
		2‰	5	*11*
			10	*12*
	$f_1 = 1.00$ Hz	0‰	5	*13*
			10	*14*
	$f_2 = 1.02$ Hz	1‰	5	*15*
			10	*16*
		2‰	5	*17*
			10	*18*

Fig. 37.1 Bias error (*top*) and random error (*bottom*) presented as relative absolute percentage deviation of the mean of the estimated damping from the true value of the damping of identification using Frequency Domain Decomposition (FDD) for varying structural damping ratios and simulations denoted test 1, 3, 5, 6, 7, 9, 11, 12, 13, 15, 17 and 18

Using the two frequency domain techniques, each identification was repeated 100 times. The results presented are for 12 chosen configurations for the evaluation of the damping estimation. These are the test numbers in bold in Table 37.1. The results from the simulation are illustrated in Figs. 37.1 and 37.2 for each identification technique and structural damping ratios of 1 %, 2 %, 5 % and 10 %.
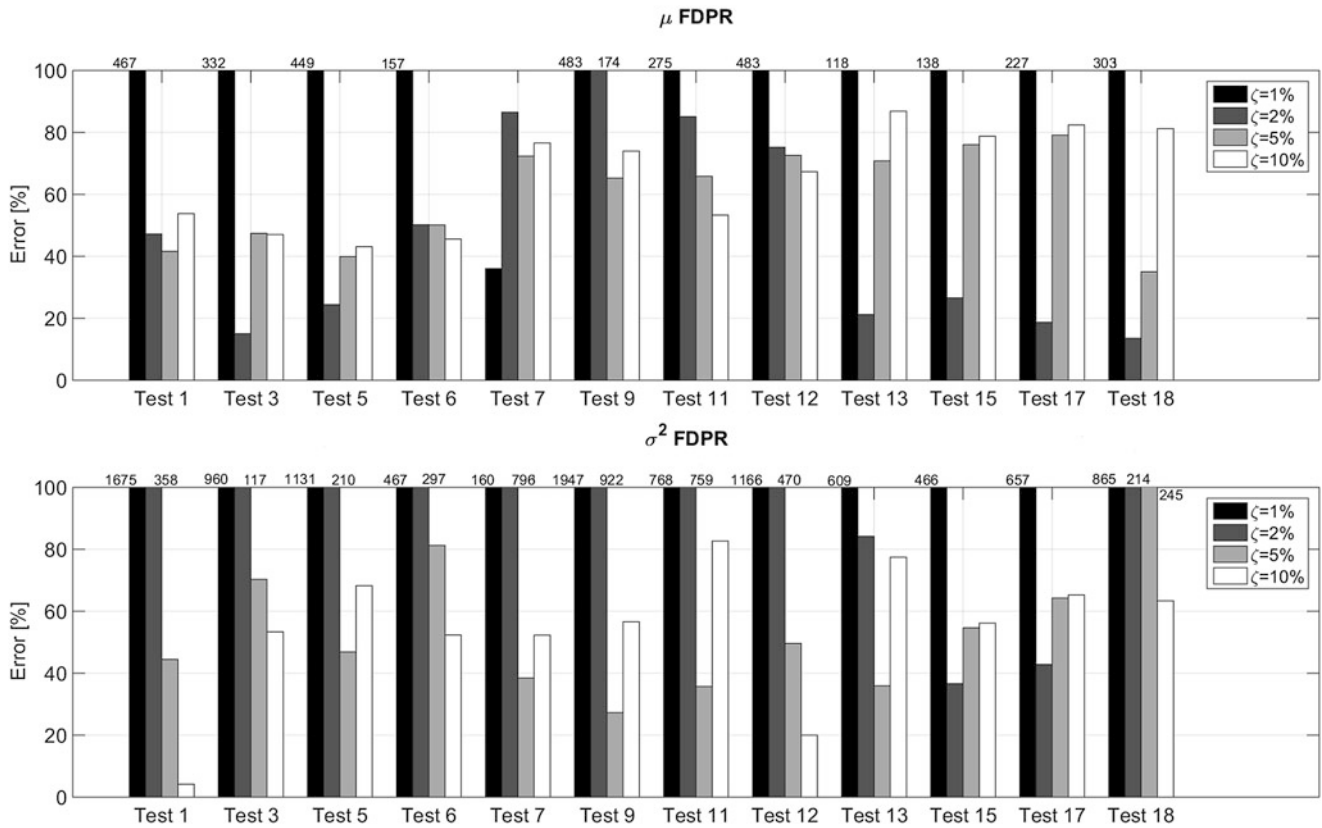
Fig. 37.2 Bias error (*top*) and random error (*bottom*) presented as relative absolute percentage deviation of the mean of the estimated damping from the true value of the damping of identification using Frequency Domain Polyreference (FDPR) for varying structural damping ratios and simulations denoted test 1, 3, 5, 6, 7, 9, 11, 12, 13, 15, 17 and 18

It should be noted that in the FDD the user decides where the natural frequency is placed. In these simulations the exact natural frequency of the system is known and therefore the users' decision is exact.

37.4 Discussion

The lower bound error of the frequency domain OMA techniques in estimating damping is identified from the input of the response spectral density function free from signal noise, a system with separated modes and a large number of measurement channels. It is especially significant for the frequency domain techniques that additional measurement channels reduce the mean and standard deviation of the error on the damping estimates. An increased number of measurement channels improves the fit of the spectral density function and makes space for the noise modes. Signal noise influences the identification of the physical system as the fit of the spectral density around the frequency of interest is disturbed. This reduces the accuracy of the damping estimate.

Several difficulties were encountered using the FDPR. This technique is dependent on an oversized model and identification is only suited for narrow frequency bands. Furthermore the identification for light damping is inaccurate with a percentage error above 100 % for a structural damping ratio of 1 % for the presented configurations 1, 3, 5, 6, 7, 9, 11, 12, 15, 17 and 18. These results are unexpected.

37.5 Summary

The damping estimates using the FDD and FDPR are sensitive to closeness of modes and signal noise. The sensitivity can be minimized by including additional measurement channels The FDD technique is more robust in estimating damping for the presented simulations, and more user friendly than the FDPR. The FDPR is dependent on an oversized model and identification is only suited for narrow frequency bands

It is important to note that in this paper the damping estimates of a 2DOF linear system with normal modes and proportional damping have been evaluated. Due to the non-proportional nature of damping and the possible presence of non-linearities, the modal damping ratio identification should be examined in future for complex modes.

References

1. Georgakis CT, Acampora A (2011) Determination of the aerodynamic damping of dry and wet bridge cables from full-scale monitoring. In: 9th international symposium on cable dynamics (ISCD) -October, 2011, Shanghai
2. Juang JN, Pappa RS (1985) An eigen system realization algorithm for modal parameter identification and modal reduction. J Guidance 8(5):620–627
3. Van Overschee P, and Bart De Moor (1996) Stochastic Identification. Subspace Identification for Linear Systems. Springer, US, pp. 57–93
4. Bajric A, Brincker R, Georgakis CT (2014) Evaluation of damping using time domain Operational Modal Analysis techniques. In: 2014 Society of experimental mechanics conference and international symposium on intensive loading and its effects (2014 SEM) –October, Beijing
5. Magalhães F, Brincker R, Cunha A Damping estimation using free decays and ambient vibration tests. J Mech Syst Signal Process 24:1274–1290
6. Malekjafarian A, Brincker R, Ashory MR, Khitibi MM (2010) Identification of closely spaced modes using Ibrahim time domain method. In: Proceedings of the fourth international operational modal analysis conference, Istanbul
7. Brincker R, Zhang L, Andersen P (2000) Modal identification from ambient responses using frequency domain decomposition. In: Proceedings of IMAC 18, the international modal analysis conference, San Antonio, pp. 625–630, February 2000
8. Peeters B, Van der Auweraer H, Guillaume P, Leuridan J (2004) The PolyMAX frequency-domain method: a new standard for modal parameter estimation. Shock Vib 11:395–409
9. Bendat JS, Piersol AG (1993) Engineering applications of correlation and spectral analysis, 2nd edn. Wiley, New York
10. Brincker R, Ventura CE (2014) Introduction to operational modal analysis. Wiley
11. Ibrahim SR, Milkulcik EC (1977) A method for direct identification of vibration parameters from the free response. Shock Vib Bulletin 47:183–196

Chapter 38
An Example of Correlation Matrix Based Mode Shape Expansion in OMA

Rune Brincker, Edilson Alexandre Camargo, and Anders Skafte

Abstract In cases of reducing the number of modes in an operating response – for instance when using band pass filtering – often time domain identification techniques suffer from a tendency to over fitting. As a consequence, it might be useful to decrease the number of measured DOF's to moderate the number of modes in the modal model. In these cases the dimension of the identified mode shapes is diminished accordingly and therefore it is preferable to have a way to expand back to the full set of DOF's so that the estimated mode shapes can be animated in detail. In the present paper it is considered to use the correlation matrix for the filtered response including all measured DOF's as a basis for the mode shape expansion. This matrix contains the normal modes that can easily be extracted from the column space of the correlation matrix. In this investigation the main focus has not been on the reduction problem, so engineering judgment has been used to secure a reasonable choice of reduced channels. The technique is illustrated on an OMA case where the modes of the tail part of a Panther helicopter is estimated during different flight conditions.

Keywords OMA • DOF reduction • Expansion • Helicopter • Time domain

38.1 Introduction

Nearly all classical modal analysis techniques in the time domain can be used for OMA using the correlation functions as input for the techniques instead of impulse response functions. This is true for instance for techniques like the Ibrahim time domain (ITD) technique [1–4], the poly reference (PR) technique [5, 6] and the Eigen realization algorithm (ERA) technique [7–9] that has been used in the present analysis.

These techniques typically have a lower limit to (or a fixed size like the classical ITD) to the number of modes included in the model. This lower limit is normally equal to the number of measured degrees of freedom (DOF's). For instance in the PR technique, normally the lowest model order to be considered corresponds to 2 auto regressive matrices, defining the lowest number of modes in the model to be equal to the number of measured DOF's. This is also the case for the classical ITD technique.

It is well known that it is normally an advantage to use an oversized model including a reasonable number of noise modes in order to obtain good modal estimates. However, it is also well known, that if too many noise modes are being used, problems with over fitting might arise, and the modal results can be affected in a negative way. The over fitting problem often becomes severe in cases with a high amount of noise in the signals. In such case it might be useful to consider a reduced number of measured DOF's in the identification, so that the number of noise modes can be reduced accordingly.

If the modes are identified in a reduced number of DOF's, then the estimated mode shapes are only known in these DOF's, and therefore, after the identification in the reduced set, it is useful to expand the mode shapes to the full set of DOF's.

In the following we will consider the case where the random response to be used for OMA is band pass filtered in order to reduce the number of modes present in the random response. This means that the number of modes is often quite small such as 2–4 modes. Further we will consider the possibility to perform the mode shape expansion based on the correlation matrix of the band pass filtered response.

First we will present the basic theory for why it makes sense to use the correlation matrix for expansion, the main reasons being that in case of band pass filtered signals containing only a limited number of modes and in case of OMA tests with a

R. Brincker (✉) • A. Skafte
Department of Engineering, Aarhus University, Aarhus, Denmark
e-mail: rub@eng.au.dk

E.A. Camargo
Institute of Aeronautics and Space – IAE, São José dos Campos, Brazil

reasonable channel count, the correlation matrix provides a very good way of checking the number of modes in the band pass filtered signal and for expansion. The resulting modes will be normal modes (real mode shapes) so that direct comparison can be made with a finite element model.

It is clear that going from a high number of measured DOF's to a small number of DOF's for identification might also be dangerous, because in such case there is a risk of excluding important modal information if the number of identification DOF's are not chosen reasonably. In this investigation however the main focus is not been on the reduction problem, so engineering judgment has been used to secure a reasonable choice of reduced channels.

In the following we will illustrate how the classical techniques mentioned above combined with the proposed reduction/expansion technique perform on a difficult OMA case with a relative high channel count and high amount of noise. The considered case is OMA of the tail part of a Panther helicopter estimated during different flight conditions.

38.2   Correlation Matrix Theory

Let us consider a zero mean random response $\mathbf{y}(t)$ with N_d number of measured DOF's, i.e. the response vector $\mathbf{y}(t)$ is a column vector with N_d number of components. In this case the response correlation matrix is $N_d \times N_d$ and is defined by

$$\mathbf{C}_y = \mathrm{E}\left[\mathbf{y}(t)\mathbf{y}^T(t)\right] \tag{38.1}$$

For a measured time series, the matrix will normally be calculated in terms of time averaging

$$\mathbf{C}_y = \frac{1}{T_0} \int_0^{T_0} \mathbf{y}(t)\mathbf{y}^T(t)dt \tag{38.2}$$

where T_0 is the length of the considered random response. However, if the response is given as a spectral density function, we can use that the correlation function matrix is defined as

$$\mathbf{R}_y(\tau) = \mathrm{E}\left[\mathbf{y}(t)\mathbf{y}^T(t+\tau)\right] \tag{38.3}$$

So that the correlation matrix can be found as

$$\mathbf{C}_y = \mathbf{R}_y(0) \tag{38.4}$$

Since the correlation function matrix is the inverse Fourier transform of the of spectral density matrix we can obtain the correlation matrix from

$$\mathbf{C}_y = \int_{-\infty}^{\infty} \mathbf{G}_y(\omega)\,d\omega \tag{38.5}$$

Thus, the correlation matrix can be found as the integral of the spectral density matrix. It should be noted that in case we are dealing with sampled data, the integration should be performed only over the Nyquist band. Further it should be noted that since the imaginary part of a spectral density function is an odd function of frequency, the integral will always be real as it is given by the definition in Eq. 38.1.

Assuming that the measured response is a linear combination of N normal modes we have

$$\begin{aligned} \mathbf{y}(t) &= \mathbf{a}_1 q_1(t) + \mathbf{a}_2 q_2(t) + \cdots \mathbf{a}_N q_N(t) \\ &= \mathbf{A}\mathbf{q}(t) \end{aligned} \tag{38.6}$$

where $\mathbf{A}$ is the mode shape matrix $\mathbf{A} = [\mathbf{a}_1, \mathbf{a}_2, \cdots, \mathbf{a}_N]$ and $\mathbf{q}(t)$ is the modal coordinate vector $\mathbf{q}(t) = \{q_1(t), q_2(t), \cdots, q_N(t)\}^T$. Using this is Eq. 38.1 we have

$$\mathbf{C}_y = \mathbf{A}E\left[\mathbf{q}(t)\mathbf{q}^T(t)\right]\mathbf{A}^T = \mathbf{A}\mathbf{C}_q\mathbf{A}^T \tag{38.7}$$

where $\mathbf{C}_q$ is the correlation matrix of the modal coordinates.

38.3   Expansion from a Smaller Set of DOF's

We shall assume that the external loading on the considered structure is not of a kind where $\mathbf{C}_q$ has a rank that is smaller than the number of modes, in fact we shall consider a situation where the modal coordinates are approximately stochastically independent. Further we shall assume that the number of modes N in the response is significantly smaller than the number N_d of measured DOF's. In this case, when taking a singular value decomposition of the response correlation matrix

$$\mathbf{C}_y = \mathbf{USU}^T \tag{38.8}$$

any mode shape **a** participating in the response given by Eq. 38.6 is in the subspace **U** and the rank of $\mathbf{C}_y$ is equal to the number of modes N in the response. We then have the linear relation between the modal matrix **A** and the subspace **U**

$$\mathbf{A} = \mathbf{UT} \tag{38.9}$$

where the transformation matrix **T** is $N \times N$. If we have reduced the response to consider only N_r number of measured DOF's, $N_r < N_d$, then we have the similar equation in the reduced set of DOF's

$$\mathbf{A}_r = \mathbf{U}_r \mathbf{T} \tag{38.10}$$

If we have obtained the experimental modes in the reduced set of DOF's, we can find the transformation matrix from Eq. 38.10. If the reduced number of DOF's N_r is larger than the number of modes, then the equation can be solved approximately

$$\widehat{\mathbf{T}} = \mathbf{U}_r^+ \mathbf{A}_r \tag{38.11}$$

where $\mathbf{U}_r^+$ is the pseudo inverse of the matrix $\mathbf{U}_r$. In this case we solve the equation in an over determined way and the estimate $\widehat{\mathbf{T}}$ is then less sensitive to the noise on the mode shape estimates. In cases where the reduced set of DOF's is equal to the number modes (usually a model without noise modes), Eq. 38.10 is a normal equation that can be solved taking the inverse of the matrix $\mathbf{U}_r$ that is now square (and full rank)

$$\widehat{\mathbf{T}} = \mathbf{U}_r^{-1} \mathbf{A}_r \tag{38.12}$$

In this case it should be considered if the noise on the mode shape estimate might significantly influence the transformation matrix estimate $\widehat{\mathbf{T}}$.

When we have an estimate of the transformation matrix we can expand the mode shapes to full size using Eq. 38.9 to get an estimate of the mode shapes in all the measured DOF's

$$\widehat{\mathbf{A}} = \mathbf{U}\widehat{\mathbf{T}} \tag{38.13}$$

38.4   Panther Helicopter Test Case

The test case is an investigation of the tail part of the Panther helicopter shown in Fig. 38.1a. The helicopter was tested in different flight conditions where some results for two of the flight conditions are reported here. A more comprehensive reporting of the results of all investigated flight conditions can be found in Camargo and Brincker [10].

The measurement of the flight condition analyzed in this article, were performed with the aircraft flying in a fixed altitude of 5,000 ft with cruising speed under constant weather conditions and payload (Fig. 38.1a). The altitude of the flying, at cruising speed, is taking place according to the simple principle that the pitch of the rotor determines the forward speed, and power determines the altitude of the aircraft. As a consequence, in the cruising speed condition considered here, the flight condition is characterized by constant rotor pitch angle and constant power consumption of the engine.

The experimental setup was configured with 40 measurement channels, divided into three measurement units with 17 channels each, using 16 unidirectional accelerometers 4515 type (8 in X axis and 8 in Y axis) and 10 tri-axial accelerometer 4520 type. Of the 10 tri-axial accelerometers four where using all three channels, and two where using only two of the three
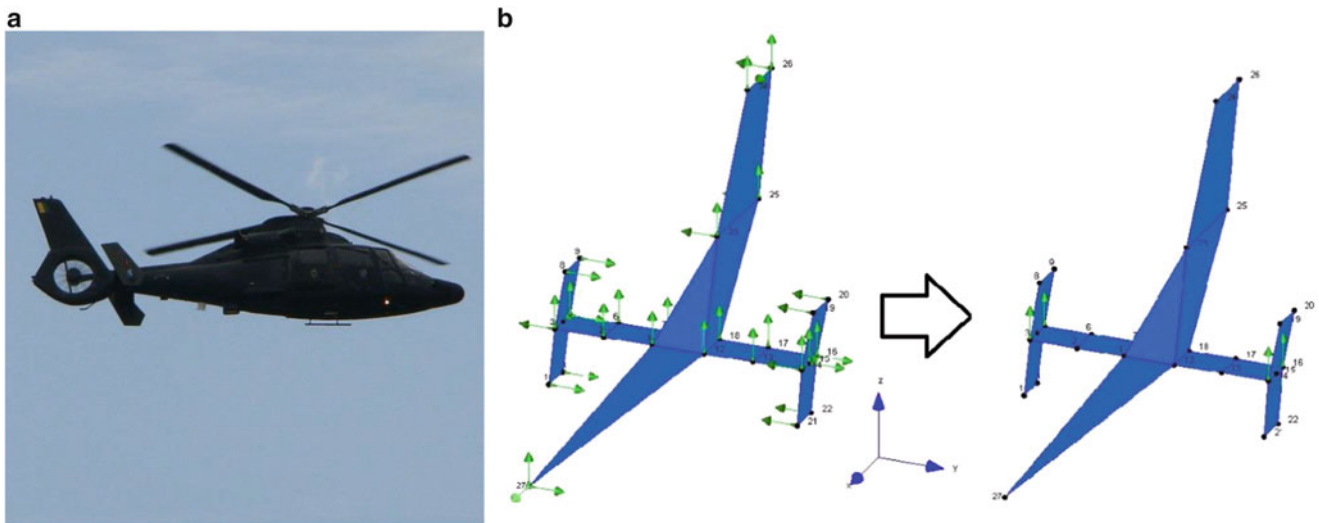
Fig. 38.1 (**a**) The Panther helicopter at cruiser speed, (**b**) The sensor locations, *left*: all 40 measured DOF's, *right*: The four DOF's used in the OMA (reduced set)
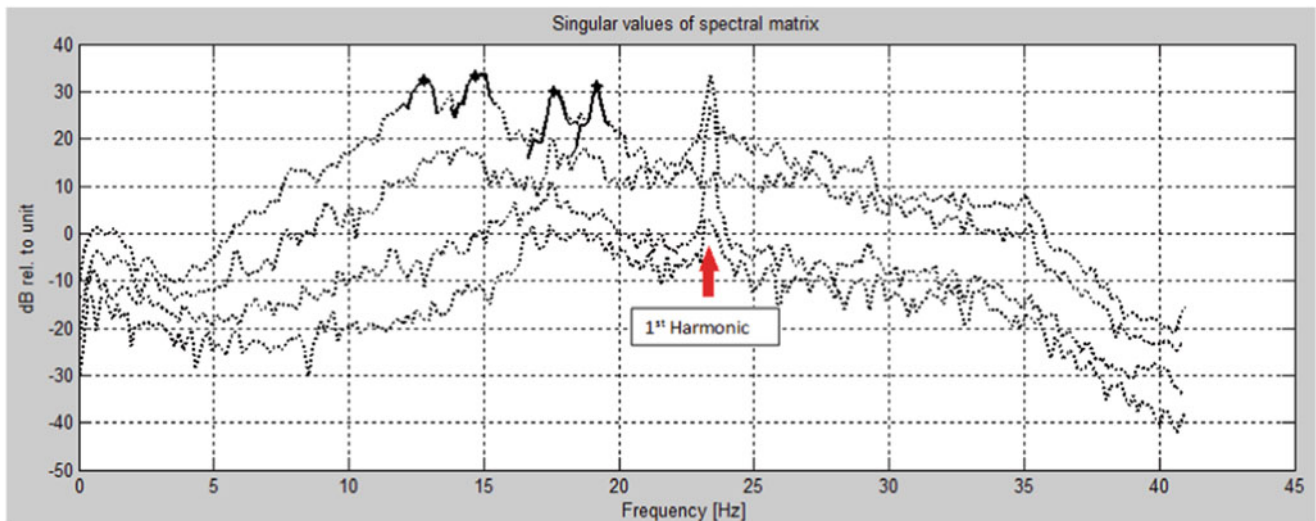

Fig. 38.2 FDD plot showing the singular values of the spectral density matrix of the cruiser speed measurements. The *highlighted* peaks indicate the first four modes of the tail part and the first harmonic of the rotor is also indicated in the plot

channels in the OMA. The placement of the sensors is shown in Fig. 38.1b. The data acquisition was performed using the software called LabShop® from Brüel & Kjaer (B&K) and the analysis were done, in time domain, using the OMA MatLab® toolbox related to the OMA book by Brincker and Ventura [11].

The measurements of the full set of 40 DOFs were performed for 60 s at an acquisition rate of 2,000 samples per second. Analysis were performed using just four DOFs, located at the edge of the horizontal stabilizers (HS), see Fig. 38.1b right, decimating the data to a Nyquist frequency of 80 Hz with sampling interval of 0.01221 s. This resulted in a spectral density estimate with a resolution of 1,024 lines giving a frequency step of 0.04 Hz as shown in Fig. 38.2.

A main goal of the test was to identify the first four modes of the tail part of the helicopter, that is the XX mode, that is the first tail torsion mode, the first HS bending mode, the first tail bending mode, and finally the first HS torsional mode. The natural frequencies of these modes were known to be around 12,8, 14,8, 17,7 and 19,5 Hz respectively.

In order to isolate these four modes, the data were band-pass filtered using the fftfilt.m function in the OMA toolbox for each mode with the center frequency of 12.8, 14.8, 17.7 and 19.5 Hz respectively for each mode, a flat band around the center frequency with a band width of 1 Hz and roll-off bands on each side with a width of 1 Hz. Figure 38.2 shows the highlighted peaks of the four modes with the small cross marking the central frequency. The first harmonic of the main rotor of the helicopter at 23.6 Hz is also indicated in Fig. 38.2.

Table 38.1 OMA of the first mode (12.8 Hz) using 40 DOF's

PR	Mode 1	Mode 2	Mode 3	Mode 4	Mode 11	Mode 13	Mode 15	Mode 27
Frequency, [Hz]	10.7200	11.6982	11.8332	11.9496	12.5278	**12.7650**	12.8577	13.8354
Damping, [%]	22.54	0.03	0.10	0.23	1.62	**0.91**	0.68	0.40
Contribution, [%]	0.33	0.136	0.410	1.052	21.3460	**22.8774**	20.9932	0.0818
ITD	**Mode 1**	**Mode 2**	**Mode 3**	**Mode 4**	**Mode 7**	**Mode 9**	**Mode 11**	**Mode 19**
Frequency, [Hz]	11.8457	11.9454	12.1648	12.2992	12.5669	**12.8363**	12.9889	13.8173
Damping, [%]	0.05	0.57	0.42	0.44	0.17	**0.83**	0.11	0.32
Contribution, [%]	0.3159	0.5550	0.1748	0.2814	11.6434	**24.4022**	22.2611	1.1580
ERA	**Mode 1**	**Mode 2**	**Mode 3**	**Mode 4**	**Mode 11**	**Mode 13**	**Mode 15**	**Mode 27**
Frequency, [Hz]	10.7200	11.6982	11.8332	11.9496	12.6038	**12.7650**	12.8577	13.8354
Damping, [%]	22.54	0.03	0.10	1.18	0.14	**0.91**	0.68	0.40
Contribution, [%]	0.33	0.0136	0.0410	0.1052	0.8026	**22.8774**	20.9932	0.0818

Table 38.2 OMA of the first mode (12.8 Hz) using 4 DOF's

PR	Mode 1	Mode 2	Mode 3	Mode 4
Frequency, [Hz]	12.2331	**12.8426**	13.0047	13.5416
Damping, [%]	2.77	**2.03**	1.42	2.06
Contribution, [%]	11.9135	**84.4596**	0.2860	3.3409
ITD	**Mode 1**	**Mode 2**	**Mode 3**	**Mode 4**
Frequency, [Hz]	12.2350	**12.8409**	13.0341	13.5510
Damping, [%]	2.66	**1.99**	1.13	2.02
Contribution, [%]	12.7687	**83.3878**	0.1713	3.6722
ERA	**Mode 1**	**Mode 2**	**Mode 3**	**Mode 4**
Frequency, [Hz]	12.2331	**12.8426**	13.0047	13.5416
Damping, [%]	2.77	**2.03**	1.42	2.06
Contribution, [%]	11.9135	**84.4596**	0.2860	3.3409

The numbers of block rows on the AR/PR and ITD were chosen to na = 2. For the ERA, the numbers of block rows of the Hankel matrices used was equal to s = 2, and the realization was not reduced so that the returned number of modes were the same for the three techniques. In all three techniques, the correlation matrix was used as multiple input, and 100 discrete time lags were used in the identification.

Using all 40 measurement channels the techniques return in principle 40 modes of which some might be non-physical due to non-positive damping, so typically 20–30 modes were returned. Since we have band pass filtered the signal to contain only one single mode, among the returned modes we need to identify only the single mode that we are looking for. In the following we will illustrate the identification principle on the first of the four modes indicated in Fig. 38.2, this mode has a natural frequency around 12.8 Hz.

The modal participation for each mode was estimated as described in Brincker and Ventura [11], and used to identify the physical mode following the principle that noise modes should have a small modal participation and a physical mode should have a strong modal participation. Some of the returned modes are shown in Table 38.1 for the case where we are using all 40 DOF's. From the results in Table 38.1 we see that the mode with the highest participation using the PR technique is mode 13 with a modal participation of 22.9 %.

It seems like a reasonable result since the corresponding natural frequency of 12.77 Hz is also close to the expected value. However, we see that the modal participation is also high for adjacent modes with frequencies quite close to the target frequency. A similar picture is seen to be present for identification using ITD and ERA identification. As a result in this case it is difficult to use the modal participation clearly to distinguish between noise modes and physical modes.

Reducing the number of DOFs to the four sensor signals shown in Fig. 38.1b, the identification techniques return only four modes. Table 38.2 shows the similar results for the first mode. We see that in this case mode 2 has a modal participation that is significantly larger than all other modal participation factors, and thus, using the reduced set of DOF's we can much easier make a decision of which mode to choose as the physical one.

The distribution of the modal participating factors of the modes is shown in Fig. 38.3 and as it appears, all three techniques have a high modal participation of 2–3 modes making it difficult to distinguish noise modes from the physical mode. The plot to the left shows the similar distribution of the modal participation factors in the case of using the reduced set of DOF's and as it appears, in this case only one mode has a modal participation factor that is significantly larger than the other ones.
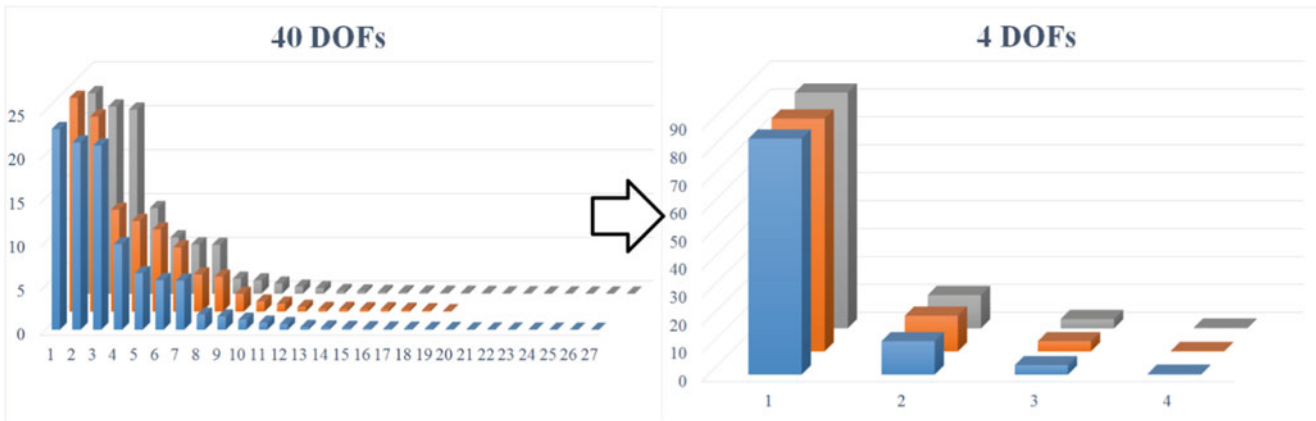
Fig. 38.3 The plots show the modal participation factors of the three different techniques PR (*blue*), ITD (*red*) and ERA (*gray*)

First tail torsion mode
(12.8 Hz)

First HS bending mode
(15Hz)

First tail bending mode
(17.8Hz)
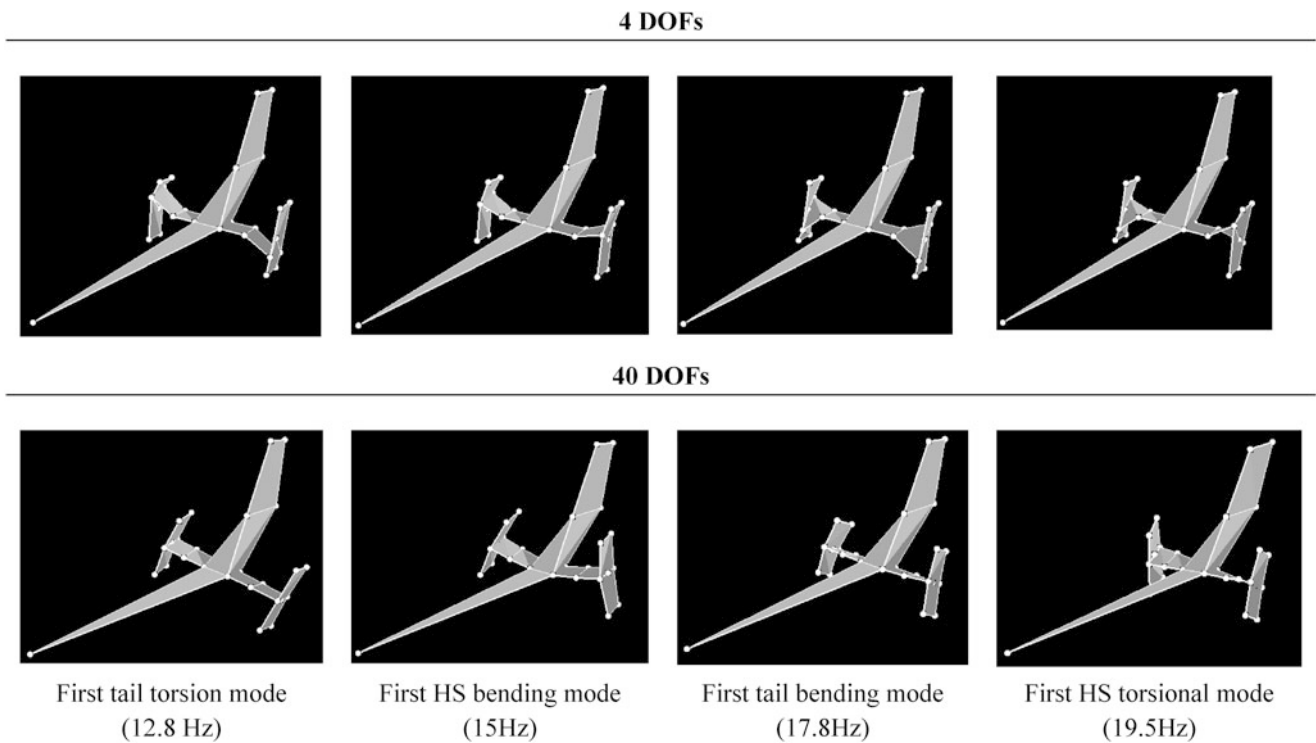
First HS torsional mode
(19.5Hz)

Fig. 38.4 Mode shapes of 4 DOFs and after expand the modes for 40 DOFs. *Top* plot: Mode shape plots using only 4 DOFs. *Middle* plot: Full mode shapes for flight condition cruising speed, *bottom* plot: Full mode shapes for the flight condition maximum speed

38.5 OMA Results Using Expansion

The top plots of Fig. 38.4 shows the results when only the four DOF's are being used, and as it appears from the plots, using only four DOFs the mode shapes are not well defined in a graphical representation. The mode shapes were then expanded using Equation (11/13) and the results shown the bottom plots of Fig. 38.4 clearly shows the advantage of using the mode shape in full resolution.

38.6   Conclusions

It is shown that the correlation matrix can be used of expansion of mode shapes and it has been illustrated how the expansion can be applied in cases with high channels counts and where over fitting might occur when performing identification using classical time domain techniques. The use of some classical time domain techniques has been illustrated using OMA on a Panther helicopter under different flight conditions.

References

1. Ibrahim SR, Milkulcik EC (1977) A method for direct identification of vibration parameters from the free response. Shock Vib Bull 47: 183–196
2. Ibrahim SR (1977) Random decrement technique for modal identification of structures. J Spacecraft Rock 14:696–700
3. Ibrahim SR (1978) Modal confidence factor in vibration testing. J Spacecraft Rock 15:313–316
4. Fukuzono K (1986) Investigation of multiple-reference Ibrahim time domain modal parameter estimation technique. M.Sc. thesis, Department of Mechanical and Industrial Engineering, University of Cincinnati
5. Vold H, Kundrat J, Rocklin GT, Russell R A multi-input modal estimation algorithm for mini-computers. SAE paper number 820194, 1082
6. Vold H, Rocklin GT (1982) The numerical implementation of a multi-input modal estimation method for mini-computers. In: Proceedings of the international modal analysis conference (IMAC), pp 542–548
7. Juang JN, Pappa RS (1985) An eigen system realization algorithm for modal parameter identification and modal reduction. J Guid 8(5): 620–627
8. Pappa RS, Elliott KB, Schenk A (1993) Consistent-mode indicator for the eigensystem realization algorithm. J Guid Control Dyn 16(5): 852–858
9. Pappa RS (1994) Eigensystem realization algorithm, user's guide for VAX/VMS computers. NASA technical memorandum 109066
10. Camargo EA, Brincker R Operational modal analysis of a Panther helicopter during different flight conditions. To be submitted to XX
11. Brincker R, Ventura CE (2014) Introduction to operational modal analysis. Wiley

Chapter 39
Experimental vs Operational Modal Analysis: A Flyover Test Case

Giorgio Busca, Alessio Datteo, Murathan Paksoy, Chiara Pozzuoli, Carlo Segato, and Marcello Vanali

Abstract Expo 2015 is about to begin and the theme will be *Feeding the Planet, Energy for Life*. This exhibition will be focused on the nutrition issue but it is also important because of its economic benefits for the country, mainly for the development of the infrastructures necessary to support the event. For instance, one of the most strategic construction site is the BreBeMi highway connecting the cities of Brescia, Bergamo and Milan, which will host the exhibition.

This paper will present a comparative discussion about a BreBeMi flyover, crossing the Oglio river, which was deeply studied by means of operational modal analysis, experimental modal analysis and finite element simulations. The bridge is made by hollow core prestressed elements with unbounded tendons, supported by hollow core circular piers. Friction pendulum isolators are used at the supports to disconnect the deck from the piers as for seismic actions. The FE model was tuned by the comparison of the eigenvalues and eigenvectors computed by a linear modal analysis and the data obtained by the experiments. The results show the good correlation between the model and the real structure in terms of frequencies and mode shapes. Moreover this bridge is a remarkable test case to compare benefits and drawbacks of using operational and/or experimental modal analysis.

Keywords Operational modal analysis • Experimental modal analysis • Flyover • Vibrations • Finite element model

39.1   Introduction

According to the prescriptions enforced by the Italian Code, i.e., NTC 2008 [1], when a new building is a significant infrastructure, which means that it needs to guarantee increased performance levels in case of an emergency, the construction validation protocol needs to include dynamic experimental analyses. This standard does not specify what kind of dynamic tests must be carried out, but the only requirement is the identification of the first vibration frequency at least, and its comparison to the one predicted by the numerical model. These recommendations show how much dynamic analysis is far to be a well-established procedure in the civil engineering industry and how much still has to be done to encourage the use of the dynamic parameters as auxiliary information necessary to reinforce the finite element model validation and the prediction of behaviour of the structure during uncommon situations such as earthquakes.

In Italy, the most common technique used to estimate the modal properties of civil structures is Operational Modal Analysis (OMA) [2, 3], but sometimes Experimental Modal Analysis is required too [4]. In some cases, when the government authorities think the infrastructure is critical or a continuous/periodic monitoring program is planned for the future, Operational Modal Analysis is considered not accurate enough for the dynamic parameters estimation. In order to comply with the authorities' concerns and prove the robustness of the data, a common procedure is the use of Operation Modal Analysis to get the first picture of the structure behaviour. The second step is then to use of these results to design the tests for Experimental Modal Analysis, which is considered more reliable, since the forcing source is controlled. At the end of the experimental campaign, both the analysis (OMA and EMA) should provide the same results and the dynamic analysis should be validated beyond doubt.

G. Busca (✉) • A. Datteo
Dipartimento di Meccanica, Politecnico di Milano, via La Masa 34, Milan, Italy
e-mail: giorgio.busca@polimi.it

M. Vanali
Dipartimento di Ingegneria Industriale, Università degli studi di Parma, Parco Area delle Scienze, 181/A, Parma, Italy

M. Paksoy • C. Pozzuoli • C. Segato
ECSD Srl, Via Goldoni 22, Milan, Italy

In the case at hand, Regione Lombardia, the County authorities of the region where the highway is located, required both an operational and an experimental modal analysis to be carried out. Besides the above-mentioned reasons, government of Regione Lombardia enforced a monitoring program of all the flyovers during their service life. In this case, the validation tests provided by EMA were the initial step of the monitoring activity because the testing protocols needed to guarantee full repeatability over the service life, so that any change in the modal properties can be used for damage detection [5–7].

The staff of Politecnico di Milano and University of Parma thus carried out the operational modal analysis of the Oglio flyover in the month of May 2013, whereas the experimental modal analysis was performed on March 2014; the staff of ECSD was in charge of the interpretation of the results and the comparison with the results from numerical analyses.

This paper is going to present a comparative study between numerical results and experiments, and a critical discussion about the controversial belief that experimental modal analysis is more reliable than operational modal analysis. The results of Operational Modal Analysis were deeply discussed in a paper presented in the previous IMAC XXII Conference in February 2014 [8]. This manuscript completes the analysis adding the Experimental Modal Analysis and the subsequent discussion about its results.

39.2 Oglio Flyover and FEM

BreBeMi highway is a strategic infrastructure built on the occasion of EXPO2015 which will be hosted in Milan. The highway connects the cities of Brescia, Bergamo and Milan and it is part of a wide plan for the improvement of transport routes in order to support the exhibition. The highway has a total amount of six flyovers and this paper will be focused on the one crossing the Oglio River.

The bridge is designed so that the two ways (i.e., North Way and South Way), consisting of two lanes each, are completely separated. Each way of the flyover consists of reinforced concrete piers supporting precast prestressed reinforced concrete decks built by the cantilever method. The precast deck elements are hollow core girders with ordinary reinforcement and unbounded tendons. Each way of the flyover, consisting of two lanes, is 17.05 m wide and eleven spans long; most of the spans are 45 and 60 m long, whereas the central span, crossing the Oglio river, is 90 m long. The deep foundations of the hollow core reinforced concrete piers consist of large piles, having a diameter of 1,200 mm.

In order to guarantee the necessary seismic performance of the bridge, the deck is seismically isolated, by means of friction pendulum damping devices inserted as supports between the piers and the deck elements. The friction pendulum elements were chosen because of their excellent isolating properties coupled with high self-centering capacity, thus ensuring low shear demands on the piers and foundations and very limited residual displacements at the supports even after a major earthquake.

Under low lateral loads (i.e., service life pseudo-dynamic loads, such as wind or traffic), the friction pendulum devices behave as fixed supports, whose vertical stiffnesses are slightly different from each other, depending on the actual vertical load insisting on each support. In order to provide the necessary lateral restraint under service life loads, a fixed support is created on pier N.6 by means of a shear connector. The shear connector is designed to break under earthquake induced lateral loads, being effective only under service life lateral loads. As a result, the friction pendulum devices become effective when an earthquake hits, allowing energy dissipation through their sliding surfaces.

In Fig. 39.1 a scheme of the longitudinal configuration of the South and North ways is represented: the eleven spans are shown, and their lengths are reported, together with the total length of the flyover. In Fig. 39.2, the bridge in the in the final configuration is represented.

The dynamic properties of the Oglio flyover were numerically analysed by means of a finite element (FE) model which was developed using the commercial software for structural analysis MidasGen 2012 V3. Since the main purpose of this model is to provide a numerical counterpart for the experimental results of the operational modal analysis, great attention
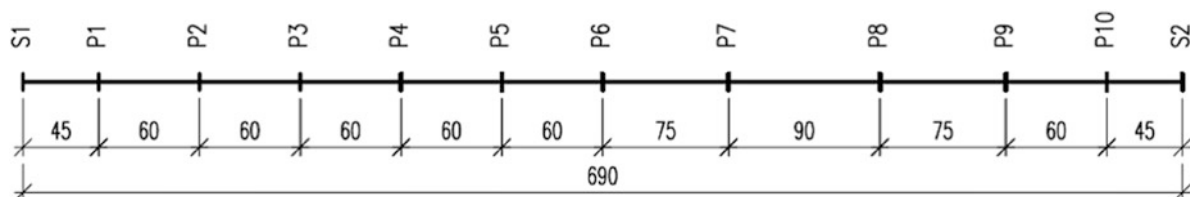

Fig. 39.1 Scheme of the longitudinal configuration of the Oglio Flyover, dimensions in meters
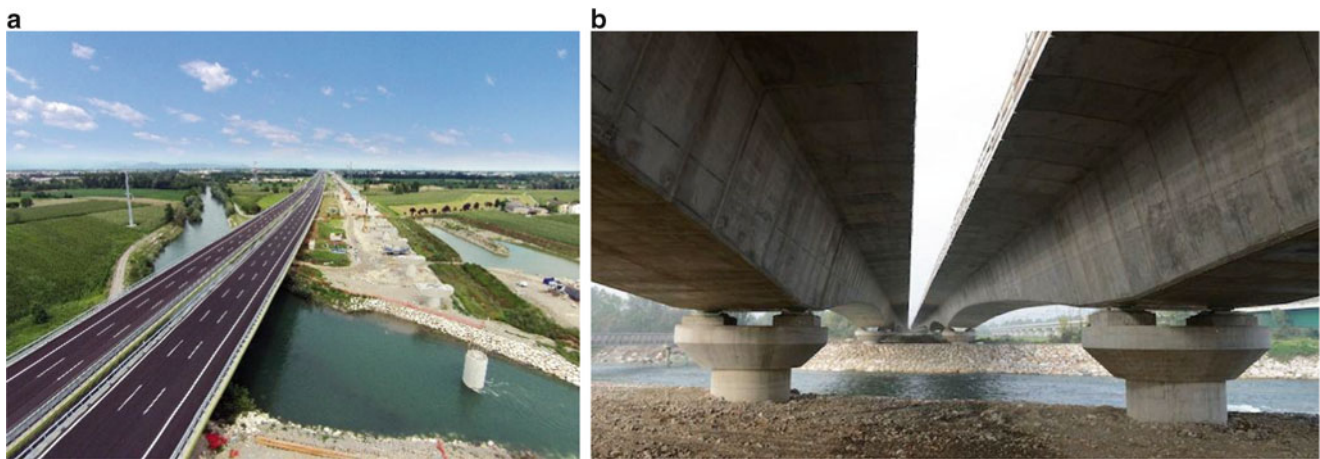
Fig. 39.2 Pictures of Oglio Flyover

was paid in accurately replicating the actual longitudinal and transverse geometry of the bridge and its loads and boundary conditions at the stage of the dynamic tests. The finite element model developed is three-dimensional and was implemented using a refined mesh of shell elements, considering only the deck, since the dynamic of the piers is totally disconnected from that of the deck because of the presence of friction pendulum isolators. The refined 3D models allows a realistic description of the bridge geometry and of the mass and loads distribution together with a more reliable definition of the mode shapes, especially those involving the torsional behaviour of the bridge deck. The friction pendulum damping devices were modelled considering their force-displacement curve provided by the producers. In order to correctly replicate the boundary conditions, proper four-joints shell elements were defined at the positions of the seismic bearings, replicating their physical dimensions. The isolators were then modeled by means of four springs connected to the four joints of the shell elements of the beam. The value of the horizontal stiffness of these springs was taken equal to $ki^* = ¼ ki$ as a function of the vertical load.

39.3 Numerical Analysis Results

The numerical eigenvalues and eigenvectors of the flyover, to be compared with the experimental values, derived from the operational modal analysis, were evaluated through a linear modal analysis.

Since the experimental tests were carried out in lack of any other loads except the self-weights of structural and non-structural elements, the source of mass was characterized using only these loads.

Table 39.1 illustrates the first 12 modal frequencies and mode shapes evaluated from linear modal analysis.

The modes characterized by relevant vertical displacement, for instance Mode 1 and Mode 7, will be characterized by higher deck vibrational levels with respect to the mode denoted mainly by deck and piles lateral deflection, for instance Mode 2 and Mode 3. As a result, the modes vibrating predominantly in the vertical direction will be easier to identify during the experimental tests due to the magnitude of the displacements proper of those modes.

These mode shapes and frequencies will be compared to the ones derived from a preliminary operational modal analysis that will be described in the next section.

39.4 Experimental Setup

This section will show the results of the two analysis carried out on the bridge. As stated previously, both OMA and EMA were used to estimate the dynamic parameters. The operational analysis was used to get the first picture of the flyover dynamic behaviour, then, based on these data, the experimental analysis was settled and then performed to get a new set of parameters. These two sets of results were compared in order to validate the analysis and overcome the ambiguities which both tests intrinsically have because of their nature.

Table 39.1 Linear modal analysis results: modal frequencies and mode shapes

# Mode	f (Hz)	Vibration mode	# Mode	f (Hz)	Vibration mode
1	1.31		2	1.62	
3	1.70		4	1.73	
5	1.76		6	1.80	
7	1.87		8	1.95	
9	2.05		10	2.12	
11	2.18		12	2.35	
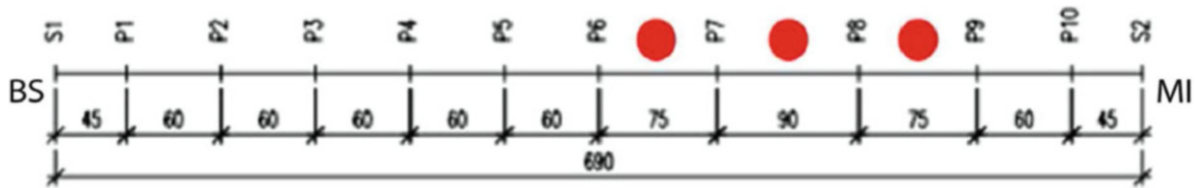
Fig. 39.3 Oglio Flyover, South way, spans under test
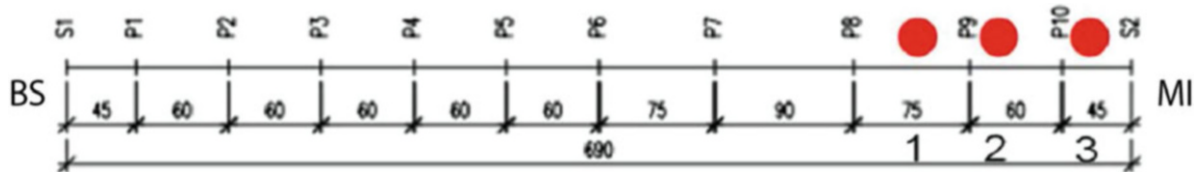
Fig. 39.4 Oglio Flyover, North way, spans under test

OMA allows to determine the structure dynamic characteristics (modal parameters) in operational conditions without measuring the excitation. Several techniques of operational modal analysis (OMA) have been developed over the years to allow the modal parameters extraction from output only data resulting from environmental excitation. This form of excitation can be regarded as a broad band white noise. Stochastic input implies stochastic structural response leading to a mandatory data averaging procedure. In this framework, the duration of the test is a key point to obtain good modal parameter estimation. The excitation level can be indeed very low producing low structural vibration levels. The availability of a large amount of data by the use of low noise transducers allows to obtain an output frequency spectrum characterized by an acceptable signal to noise ratio.

EMA generally guarantees a complete control on the test conditions: the excitation source is controlled by the tester and its level may be fixed for every analysis and the results, obtained with different forcing amplitudes, can be compared to each other. Moreover, it is possible to keep a detailed record of all the external influencing parameters, such as temperature and humidity. Nevertheless, EMA is expensive and time consuming, a proper actuator has to be placed on the structure, the tests may be repeated more than one time by forcing in different positions and measurements cannot be taken continuously.

The investigated spans are different for the two ways of the flyover, as shown in Figs. 39.3 and 39.4. The North way was tested on three spans near the abutment, whereas the South way from pier 6 to pier 9, where the longest span is present. The measurement setup was the same for both OMA and EMA.
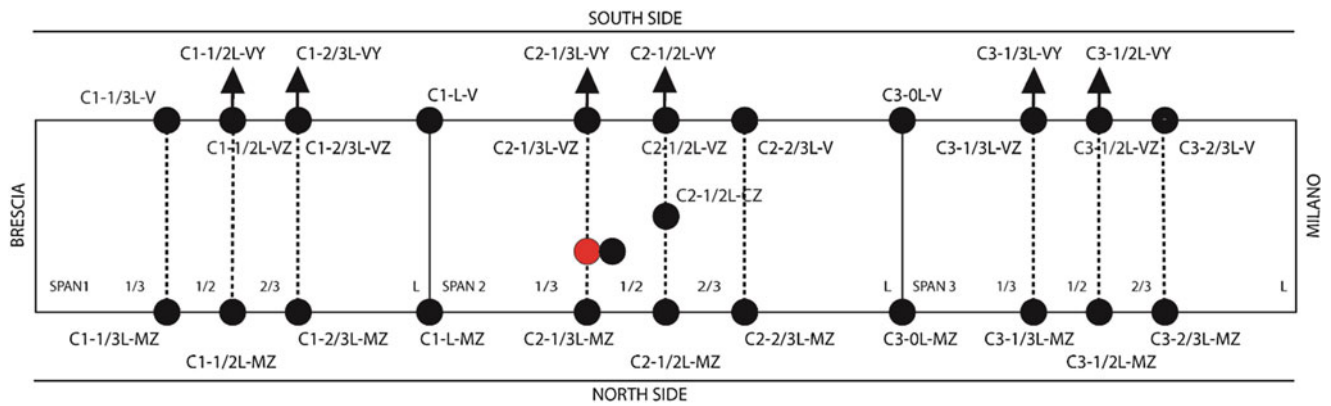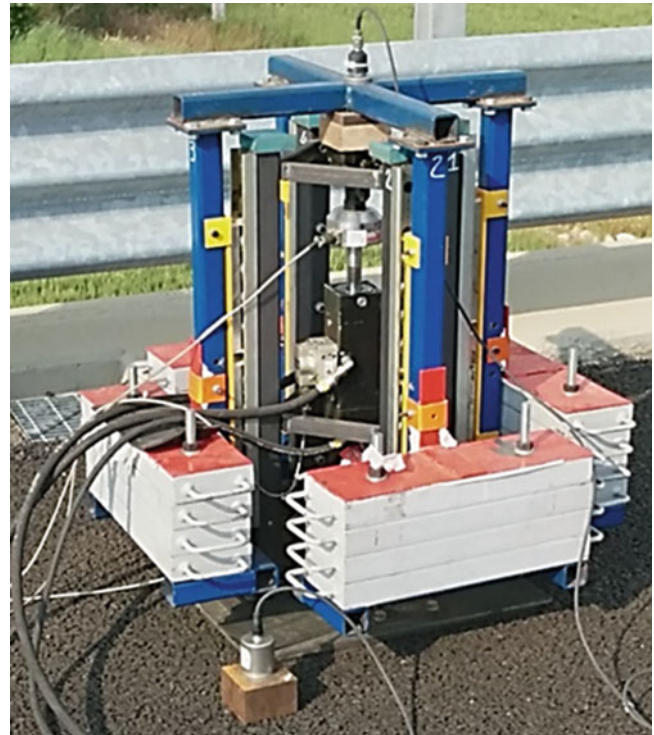
Fig. 39.5 OMA and EMA measurement setup

Fig. 39.6 Inertial hydraulic actuator

The measurement set up is made by 23 measurement points in the vertical direction, six in the transverse direction and one in the longitudinal direction (Fig. 39.5). The transducers are seismic low noise piezoelectric accelerometers conditioned and recorded using a 24 bit A/D converter with built in anti-aliasing filters. OMA tests were carried out by recording data for 24 h and then extracting a 6 h frame, taking care of avoiding transducers saturations and to provide stability in the surrounding boundary conditions. EMA tests were carried out by forcing the structure in the vertical direction by means of an inertial hydraulic actuator placed in correspondence of the grey dot of Fig. 39.5. A stepped sine harmonic excitation, covering the band between 1 and 3 Hz, was used, using a frequency resolution of 0.01 Hz in correspondence of the resonances. The actuator moved an inertial mass of 500 Kg with a maximum oscillation amplitude of 40 mm (Fig. 39.6).

39.5 Experimental Results

This section will present the results obtained by the two analysis carried out on the bridge. As already stated, both OMA and EMA were used to estimate the dynamic parameters. The operational analysis was used to get the first picture of the flyover dynamic behavior, then, using these data, the experimental analysis was carried out in order to get a new set of parameters.
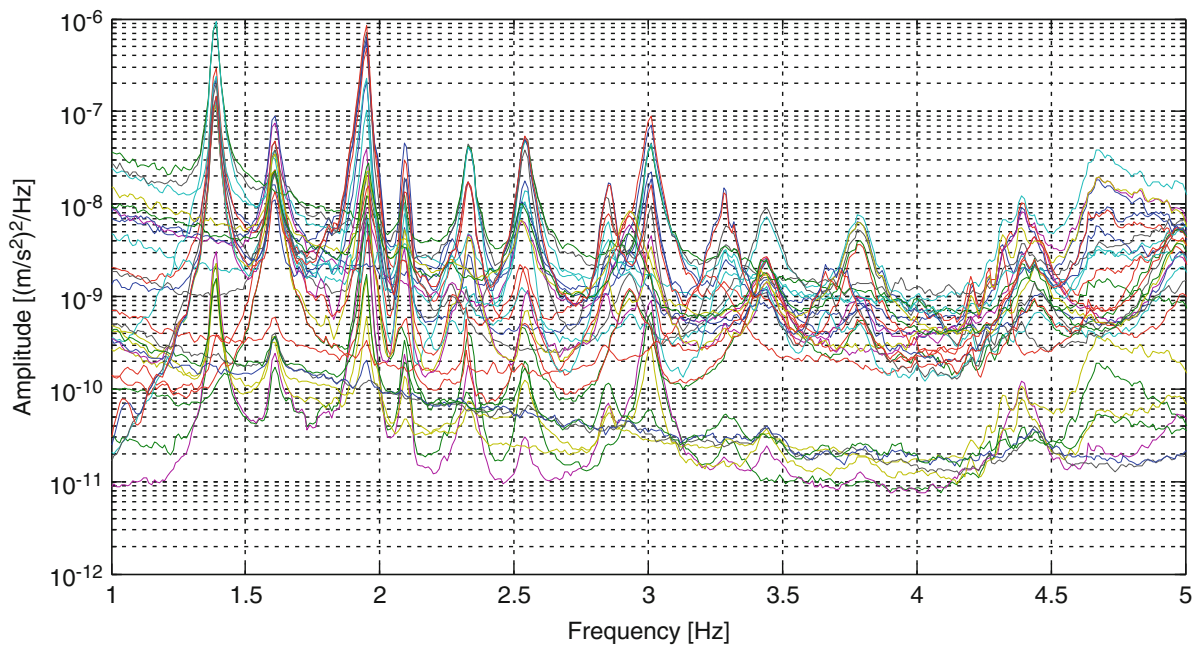
Fig. 39.7 PSD of all the channels for the South way

Table 39.2 South way: OMA
frequencies and damping factors

# Mode	Frequency [Hz]	Damping ratio %
1	1.38	0.63
2	1.61	1.00
3	1.95	0.67
4	2.09	0.42
5	2.33	0.65
6	2.53	0.66

The two sets of results were compared in order to validate the analysis and overcome the ambiguities, which both the tests inherently present.

39.5.1 South Way

This section reports the results of the tests on the South way from pier 6 to pier 9 (see Fig. 39.3). Beginning from the OMA data, the PSD functions of all the channels are shown in Fig. 39.7. The PSD have been averaged on 6 h to obtain a good signal to noise ratio [9]. The peaks corresponding to the first modes of vibration are clearly separated and identifiable in the frequency range from 1 to 3 Hz. It has to be pointed out that during the measurement day a very high temperature and sun radiation has been experienced, leading to overheating problems in the measurement system and to subsequent very high noise levels in the low frequency range were the thermal noise gives the most important contribution.

The Polyreference Least Squares Complex Frequency Domain method [10–12] has been adopted to analyse the experimental results and estimate the modal parameters of the first six modes. The damping ratios and natural frequencies identified for the modes of interest are reported in Table 39.2. As these results were already presented in a previous work [8], the mode shapes and the comments about the results will be focused on the EMA tests.

Figure 39.8 shows the FRF functions estimated for all the channels acquired during the EMA tests. The results confirm what the OMA tests has identified: both experimental campaigns identify the same peaks in the 1–3 hz frequency range.

Polyreference Least Squares Complex Frequency Domain method was used also to analyse these data and the results are shown in Table 39.3. The values are compatible with those provided by OMA analysis, since the estimations are given with a 1 % deviation on the stable frequencies and 10 % deviation on the stable damping values. Moreover, it should be noticed that the two analyses were carried out in two different weather conditions, because March is a late winter month in Italy,
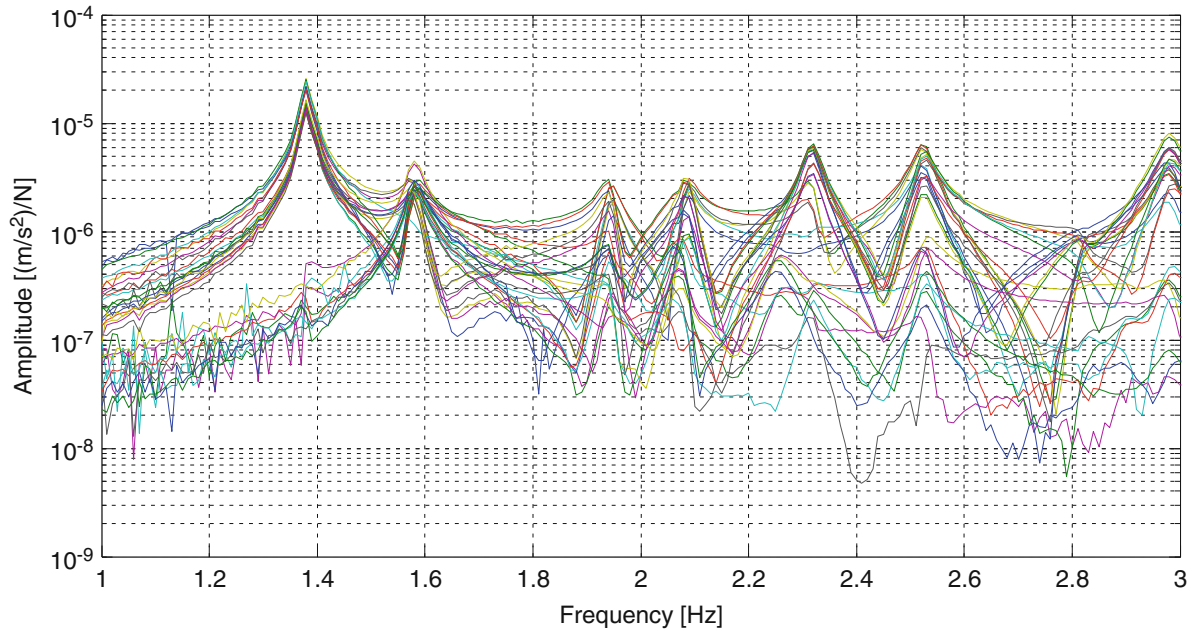
Fig. 39.8 FRF functions of all the channels for the South way

Table 39.3 South way: EMA frequencies and damping factors

# Mode	Frequency [Hz]	Damping ratio %
1	1.38	0.62
2	1.58	0.98
3	1.94	0.64
4	2.09	0.67
5	2.32	0.66
6	2.52	0.67

whereas May is a very warm early summer month. For this reason, the difference could also depend on different temperature and radiation conditions.

The mode shapes of each identified mode are displayed in the following figure, where the bridge is seen from the side and the modal residues are divided in South and North side (see Fig. 39.9). The data refer to the EMA tests.

Mode 1, Mode 3 and Mode 5 are typical bending modes with the higher displacement in the Z direction. Mode 2 and Mode 6, on the other hand, are a combination of bending of the way in the Z direction and of flexural mode of the deck in the Y direction, which is not graphically reported.

39.5.2 North Way

The same approach adopted for the South way has been considered to obtain robust spectral estimates for the channels installed on the North way. Figure 39.10 shows the PSD functions of all the acquired channels during the OMA tests. As for the South way (Fig. 39.7) the peaks corresponding to the first modes of vibration are sufficiently separated and clearly identifiable in the frequency range from 1 to 3 Hz.

The modal parameters identified for the North way are reported in Table 39.4 and they are coherent with those identified for the South way (Table 39.2) in terms of either natural frequencies or damping ratios.

Concerning the EMA tests, the FRF functions are shown in Fig. 39.11, where the same modes identified during the OMA tests (see Fig. 39.10) are clearly visible. By applying the Polyreference Least Squares Complex Frequency Domain method to the data, the frequencies and damping values were estimated (see Table 39.5).
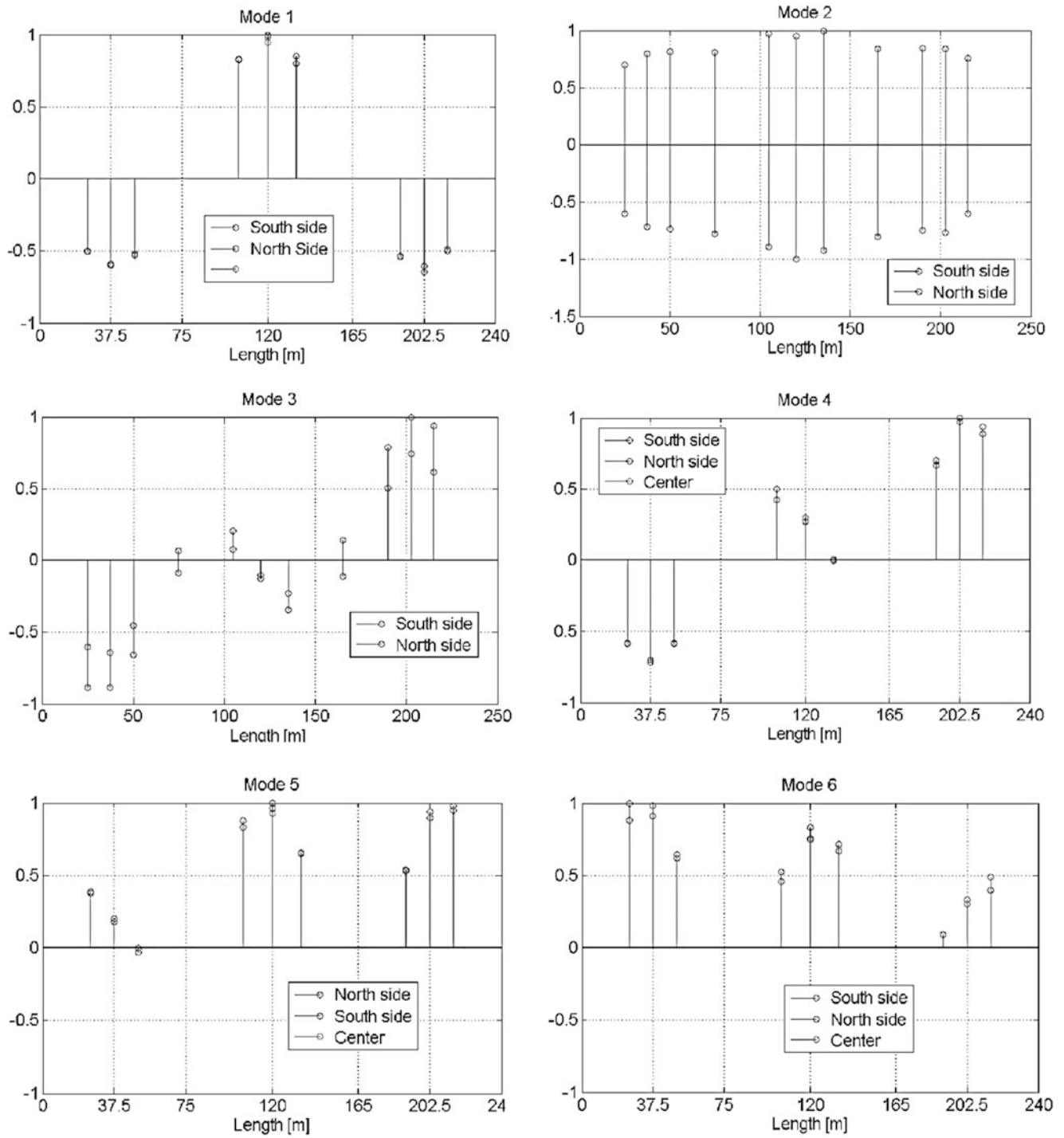
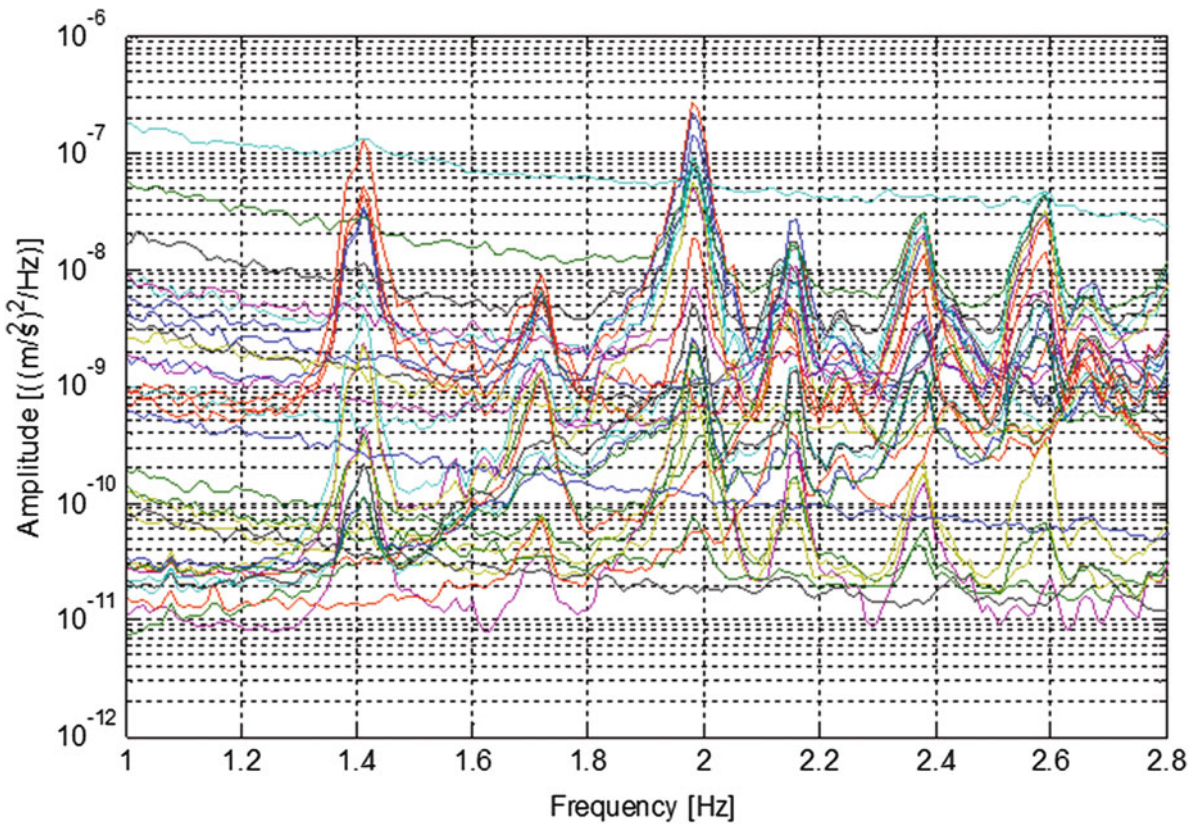**Fig. 39.9** South way mode shapes

Fig. 39.10 PSD of all the channels for the North way

Table 39.4 North way: EMA frequencies and damping factors

# Mode	Frequency [Hz]	Damping ratio %
1	1.4	0.63
2	1.72	0.98
3	1.98	0.7
4	2.16	0.44
5	2.37	0.57
6	2.57	0.52

The mode shapes of each identified mode are displayed in the following figures. Mode 1, Mode 3 and Mode 5 are typical bending modes with the higher displacement in the Z direction. Mode 2 and Mode 6, instead, are a combination of bending of the way in the Z direction and of flexural mode of the deck in the Y direction (Fig. 39.12).

39.5.3   Results Comparison

All of the results shown in the previous sections confirm the robustness of the analysis performed on the flyover. EMA and OMA tests identify the same mode shapes and the values of the frequencies and the damping ratio are compatible, since their values are given with a 1 % and 5 % uncertainty bandwidth on the estimation. Tables 39.6 and 39.7 show the frequencies and the damping values obtained by the two experimental tests. The only value where the difference between the two datasets is bigger than the estimation uncertainty is the damping ratio of the forth mode on the South way, which could depend on several sources, such as the estimation algorithm, the measurements or the environment conditions. This difference is shown both for the south and the north way. The two tables also report the correspondence of the experimental modes with the numerical model and the frequencies of the simulated vibrating modes. The frequencies match very well in all the cases.
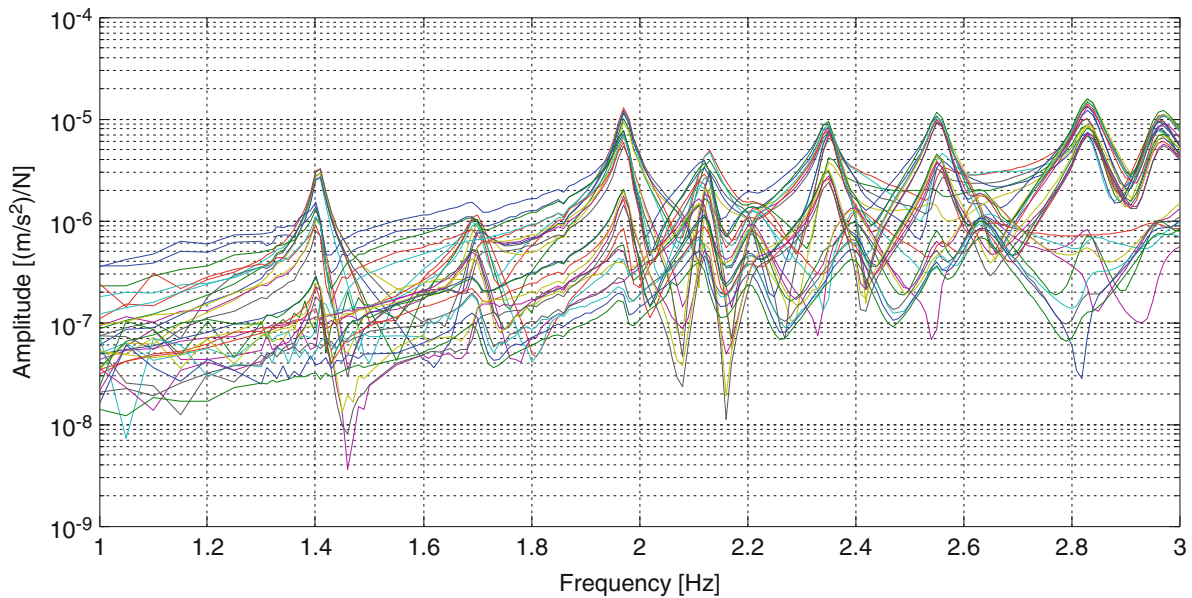
Fig. 39.11 Amplitudes of the FRF functions of all the channels for the South way

Table 39.5 North way: OMA frequencies and damping factors

# Mode	Frequency [Hz]	Damping ratio %
1	1.41	0.61
2	1.70	1.00
3	1.97	0.54
4	2.12	0.42
5	2.35	0.55
6	2.55	0.54

Finally, it can be seen that, being the two ways formally identical, the identified frequencies are practically the same; the North way values are just slightly higher (approx. 1.5 %).

The comparison among the three data sets (OMA, EMA and FEM) might be concluded with the mode shapes evaluation by means of the Modal assurance criterion (MAC). Since the two ways are practically identical, all the modal residues of homologous mode shapes havebeen considered in the MAC calculation.

Table 39.8 shows the MAC values between the Operational Modal Analysis and the Experimental Modal Analysis. All the modes find a good correspondence between the two datasets, except for the second mode where the MAC is around only 55 %. This second mode has torsional movement and it seems that the environment excitation did not properly force the structure at that frequency. This statement can be confirmed by Table 39.9, where the MAC is estimated between the EMA modal residues and the FEM simulation. In this case, the second mode finds a good correspondence and the MAC value is around 70 %.

It should also be noticed that some modes have good correspondence with the near modes in both the tables. For instance, mode 3 and mode 4 show a MAC around 65–70 %, but also mode 5 and mode 6 have a good agreement. Indeed, if the FEM simulation is considered, these modes are basically the same for the spans under test. Mode 5 and mode 6 have the same mode shape on the measured spans and the difference between them only remains in the amplitude. Mode 4 was not thoroughly identified by the OMA test, and for this reason it was initially omitted from the comparison with the FEM results [8]; after the EMA tests and some model tuning activity, it was possible to improve the identification, but still the MAC values are not as high as those of Modes 1-2-3. Besides these ambiguities, which are due to the nature of the structure, these results can be considered good.
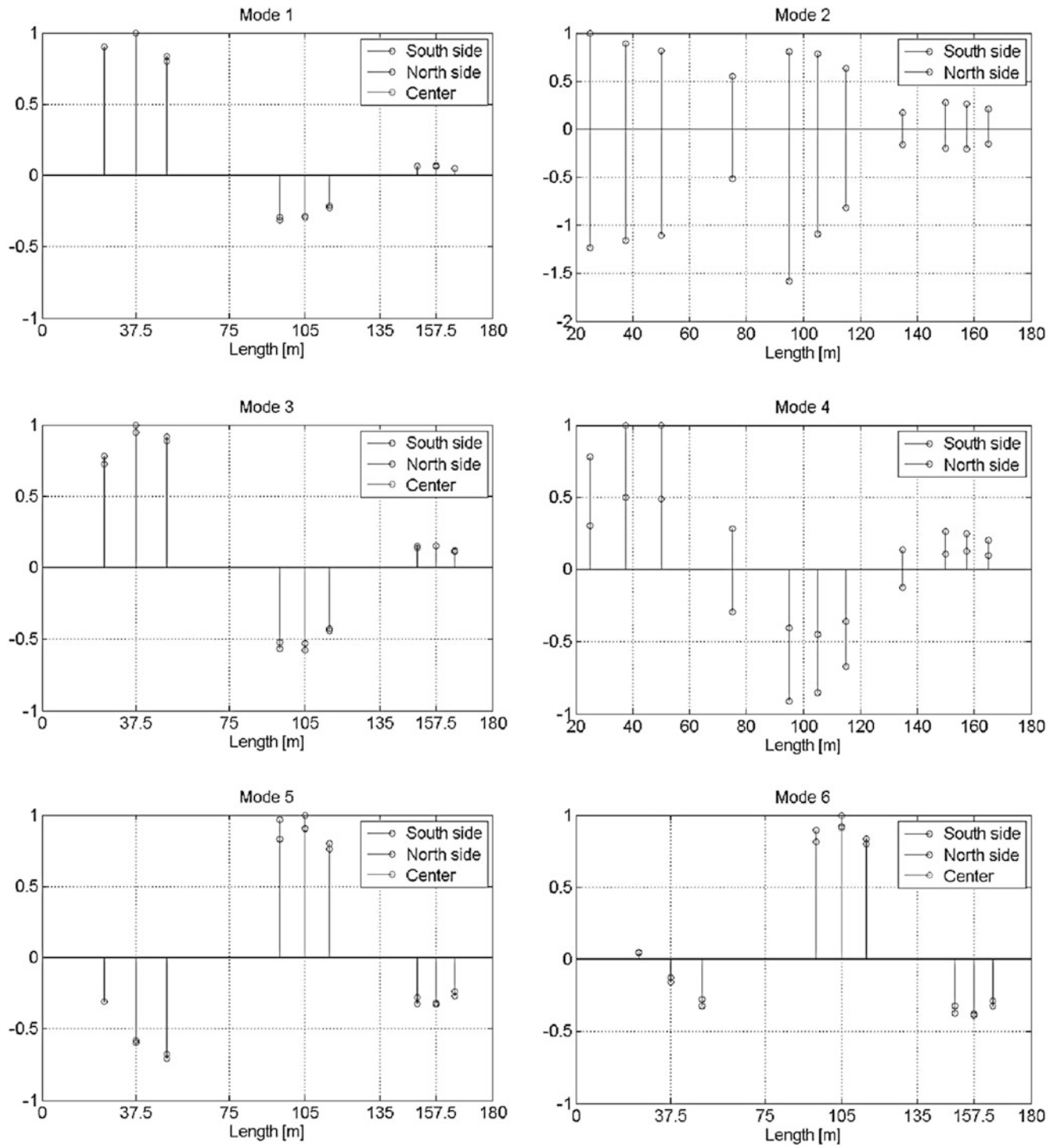
Fig. 39.12 North way mode shapes

Table 39.6 OMA vs EMA: South way frequencies and damping ratios

	South way					
	OMA		EMA		FEM	
# Mode	Freq.[Hz]	Damp. ratio %	Freq. [Hz]	Damp. ratio %	# Mode	Freq. [Hz]
1	1.38	0.63	1.38	0.62	1	1.31
2	1.61	1.00	1.58	0.98	2	1.62
3	1.95	0.67	1.94	0.64	7	1.87
4	2.09	0.42	2.09	0.67	9	2.05
5	2.33	0.65	2.32	0.66	11	2.18
6	2.53	0.66	2.52	0.67	12	2.35

Table 39.7 OMA vs EMA: North way frequencies and damping ratios

	North way					
	OMA		EMA		FEM	
# Mode	Freq.[Hz]	Damp. ratio %	Freq. [Hz]	Damp. ratio %	# Mode	Freq. [Hz]
1	1.4	0.63	1.41	0.61	1	1.31
2	1.72	0.98	1.70	1.00	2	1.62
3	1.98	0.7	1.97	0.54	7	1.87
4	2.16	0.44	2.12	0.58	9	2.05
5	2.37	0.57	2.35	0.55	11	2.18
6	2.57	0.52	2.55	0.54	12	2.35

Table 39.8 MAC matrix between EMA and OMA data

		EMA					
		1	2	3	4	5	6
OMA	1	89.86	2.26	27.96	6.07	1.42	2.03
	2	5.93	56.70	9.06	6.41	7.41	6.59
	3	17.16	5.29	90.08	65.93	26.67	1.62
	4	2.91	4.36	66.09	64.59	37.82	8.41
	5	1.13	8.63	27.21	41.01	72.75	45.57
	6	3.09	6.72	1.03	10.17	58.72	83.24

Table 39.9 MAC matrix between EMA and FEM data

		FEM					
		1	2	3	4	5	6
EMA	1	85.96	10.41	27.64	7.59	0.91	0.02
	2	0.02	71.85	0.01	2.15	0.02	0.03
	3	19.07	3.84	87.24	71.47	30.41	1.33
	4	6.95	3.41	66.45	68.24	81.50	34.31
	5	11.85	6.31	32.08	32.27	80.30	73.92
	6	8.86	9.51	42.83	44.89	84.77	64.93

39.6 Concluding Remarks

A comparison among numerical modeling, operational modal analysis and experimental modal analysis of the Oglio flyover in the northern part of Italy has been presented. The results show a good agreement between finite element prediction and test results for the flyover dynamic behavior. The comparison of the north and south measurements of the bridge show that the dynamic characteristics of the two ways are close as supposed. Considering the different environmental conditions at the measurement dates, the relative variety of material properties in the north and south bound, the results are within the limits of required accuracy.

The OMA tests carried out in 2013 were considered just a preliminary analysis in order to define the EMA tests layout, but the results prove that operational analysis was able to identify all the modal parameters with the same estimation uncertainty of those provided by the experimental analysis. Under this background, the experimental modal analysis just confirmed the results obtained in the previous measurement campaign. Mode 4 was barely identified by the OMA test, but also the EMA tests showed difficulties for a thoroughly identification. Indeed, the MAC value still stays low.

Concluding, this test case shows that a well-planned OMA test can provide all the information needed to validate the numerical model of a structure. The advantages are both practical and economical, because no forcing devices are needed, the human control on the data acquisition is limited, the forcing source is distributed over all the structure, so that it is possible to identify twin modes.

References

1. NTC 2008 (2008) D.M. 14-01-2008 Nuove Norme Tecniche per le Costruzioni (in Italian)
2. Caprioli A, Cigada A, Gentile C, Vanali M (2009) Comparison of two different OMA techniques applied to vibration data measured on a Stadium grandstand. In: Proceedings of international conference IOMAC'09–3rd international operational modal analysis conference, Ancona, pp 81–87
3. Cigada A, Caprioli A, Redaelli M, Vanali M (2008) Vibration testing at Meazza stadium: reliability of operational modal analysis to health monitoring purposes. J Perform Constr Facil 22(4):228–237
4. Cigada A, Caprioli A, Redaelli M, Vanali M (2008a) Numerical modeling and experimental modal analysis of a concrete grand-stand structure to structural health monitoring purposes. In: Proceedings of the international conference IMAC XXVI, Orlando
5. Ewins J (2001) Modal testing: theory, practice and application", 2nd edn. Taylor and Francis Group, London
6. Cigada A, Mola E, Mola F, Stella G, Vanali M, Zappa E (2011) L'importanza del collaudo dinamico delle strutture. TUTTO MISURE, (ISSN:2038–6974), 277–280
7. Cigada A, Moschioni G, Vanali M, Caprioli A (2010) The measurement network of the San Siro Meazza stadium in Milan: origin and implementation of a new data acquisition strategy for structural health monitoring. Exp Tech 34(1):70–81
8. Cigada A, Mola E, Moschini S, Paksoy M, Pozzuoli C, Vanali M (2014) Numerical modeling and dynamic testing on the Oglio flyover of the new BreBeMi highway in Italy. In: Conference proceedings of the society for experimental mechanics series 2014, dynamics of civil structures, vol 4, pp 381–394
9. Bendat JS, Piersol AG (2000) Random data: analysis and measurement procedures, 3rd edn. Wiley-Blackwell, Hoboken
10. Peeters F, Vanhollebeke H, Van der Auweraer H (2005) Operational PolyMAX for estimating the dynamic properties of a stadium structure during a football game. In: Proceedings of the international conference IMAC XXIII, Orlando
11. Peeters B, Van der Auweraer H, Guillaume P, Leuridan J (2004) The PolyMAX frequency-domain method: a new standard for modal parameter estimation? Shock Vib 11(3–4):395–409, IOS Press
12. Cornwell PJ, Farrar CR, Doebling SW, Sohn H (1999) Environmental variability of modal properties. Exp Tech 23(6):45–48

Chapter 40
Operational Modal Analysis in the Presence of Harmonic Excitations: A Review

Kenny Motte, Wout Weijtjens, Christof Devriendt, and Patrick Guillaume

Abstract Over the past years the use of Operational Modal Analysis (OMA) for Structural health monitoring has become more and more widespread. Such a methodology would also be relevant to wind farm owners that want to monitor the integrity of their turbines' foundations.

However, harmonic components, originating from the rotor and periodic aerodynamic forces, are present within the measured vibrations. The harmonics violate the set of assumptions of common OMA techniques and as a result, these techniques potentially fail. This paper explores the different techniques presented in the literature to handle these harmonics. The techniques are first presented and later applied on data of an offshore wind turbine in the Belgian North Sea.

Keywords Operational Modal Analysis • Parameter estimation • Output-only • Harmonics • Wind turbine

40.1 Introduction

To identify the modal parameters of a structure modal analysis can be used. If the considered structure is small enough experimental modal analysis (EMA) [1] is applicable. In this case the experiment is carried out on a laboratory scale and a known excitation is applied to the structure. Both the excitation and the response of the structure are measured. For larger structures applying a known excitation to the structure becomes more difficult and operational modal analysis (OMA) [2] can be a good alternative to EMA. In this case the excitation is ambient and cannot be measured. Therefore, in order to carry out the identification, a set of assumptions needs to be made [1]. Modal analysis requires that the whole frequency band of interest is excited; the system is linear and time invariant. OMA furthermore requires that the excitation is steady state random white noise. The main advantage of OMA is that the modal parameters are identified under operational conditions, e.g. the blade of a wind turbine becomes stiffer if the rotational velocity is larger [3]. Moreover, the system can be studied on a continuous basis, which is important if one wants to monitor the health of the structure. The boundary conditions can also be difficult to be reproduced if EMA is used. Therefore OMA can be used to continuously monitor the integrity of the offshore wind turbine [4] and several bridges in Portugal [2].

Due to the rotor harmonics and periodic aerodynamic effects the excitation is no longer white noise, but becomes colored. The harmonics are more excited than others frequencies. This can lead to failure of general OMA techniques [5].

The failure can occur in three different ways. First of all it possible that the harmonics are identified as structural modes. However, in this case it should be possible to distinguish between harmonics and structural modes using some prior knowledge about the harmonic frequencies. A second failure mechanism occurs when the actual structural modes are close to the harmonic frequencies and the estimation of the structural modes is affected by the harmonic. Typically this will result in a poor damping estimate. Lastly, it is possible that the harmonics inhibit the identification of the structural modes. Examples of the different types of failure are given in [6–8].

For the wind turbine it typically occurs that the harmonics are being identified as structural modes. If the harmonics are however close to the structural modes, the identification results become unreliable, as it is unclear whether the structural mode, the harmonic, or a combination of both is being identified [9]. Unlike most literature on harmonics in OMA, the harmonics of wind turbines do not behave as (small-banded) spikes at a near fixed frequency. This paper will therefore investigate to what extent techniques to deal with harmonics can be used for OMA on wind turbines.

————————————

K. Motte • W. Weijtjens (✉) • C. Devriendt • P. Guillaume
Vrije Universiteit Brussel, Pleinlaan 2, 1050 Brussels, Belgium
e-mail: wweijtje@vub.ac.be

Fig. 40.1 Spectrum of one measurement of the FA motion of the wind turbine rotating at nominal speed. The structural modes (S), the harmonics (3p, 6p, etc.) and the wave period (W) are indicated
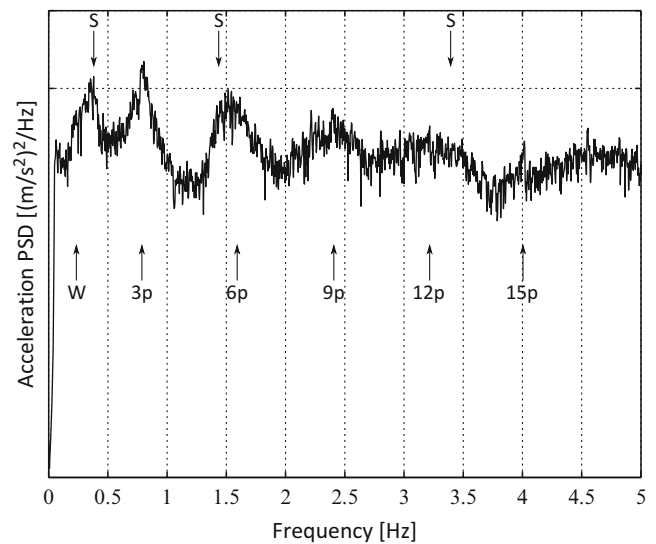
40.2 Available Techniques and Common Assumptions

In the literature several techniques have been proposed to resolve the issues of non-white excitation in OMA. These techniques can be divided into four different categories:

- **Statistics driven identification of the harmonics**: determine which resonance frequencies can be attributed to structural modes and which can be attributed to harmonics.
- **Preprocessing techniques**: remove the harmonics from the measured signals.
- **Modification to existing identification techniques**: modify existing identification techniques such that they incorporate the harmonic.
- **Input spectrum independent techniques**: these techniques deliver an identification of the modal parameters which is independent of the input spectrum and thus unaffected by the input coloration, for instance transmissibility based OMA (TOMA)[10] and poly-reference TOMA (pTOMA) [11].

The discussed techniques have been studied extensively in [12] on both simulations and actual measurements. An overview and an excerpt focussed on the application of a three-blade offshore wind turbine is provided here.

Generally it is assumed that harmonics will result in a sharp peak in the spectrum. If an identification of these peaks would be carried out, they would have a damping ratio of zero. In the case of the wind turbine this is no longer true [4, 5, 9]. The spectrum for the front-aft (FA) motion for one measurement of the wind turbine shows none of these sharp peaks, Fig. 40.1. The harmonics are in that case identified as if they were structural modes with a damping Fig. 40.2. In the continuation of this document we will refer to this type of harmonics as damped harmonics.

40.3 Statistics Driven Identification of the Harmonics

40.3.1 Probability Density Function

The use of the probability density function (PDF) [13] is based on the difference in statistic properties of a harmonic component and a narrow band stochastic response of a structural mode. The measured signal is band-pass filtered and the PDF is calculated. For a structural mode, typically the left shape in Fig. 40.3 is obtained. A harmonic results in the shape on the right.

A second important property is the symmetry of the PDF around a given frequency. In Figs. 40.4 and 40.5, a simulated system is considered with superposed harmonics at multiples of 1.5 Hz. In the legend the frequencies are shown around which the band-pass filtering is carried out. The shapes associated with the structural mode and the harmonic, both in red, correspond to the theoretical results. In both cases the amplitudes of the PDF reach a distinct minimum when the exact natural or harmonic frequency is reached. At equal frequency intervals of the exact natural frequency (or harmonic frequency), the

Fig. 40.2 Identification of the modal parameters of the wind turbine using PolyMAX (FA motion) for one measurement. The structural modes (S), the harmonics (3p, 6p, etc.) and the wave period (W) are indicated
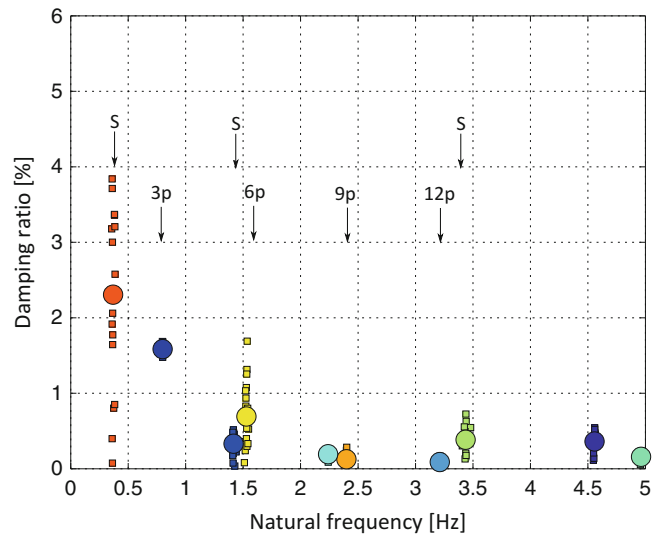
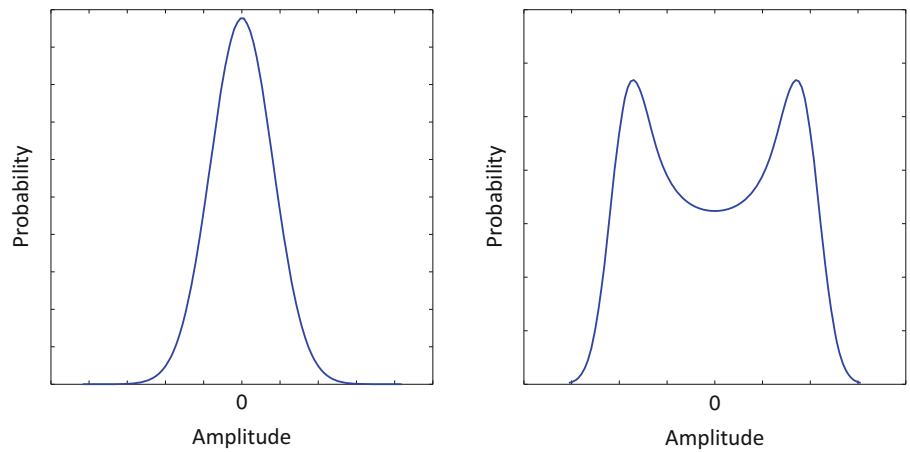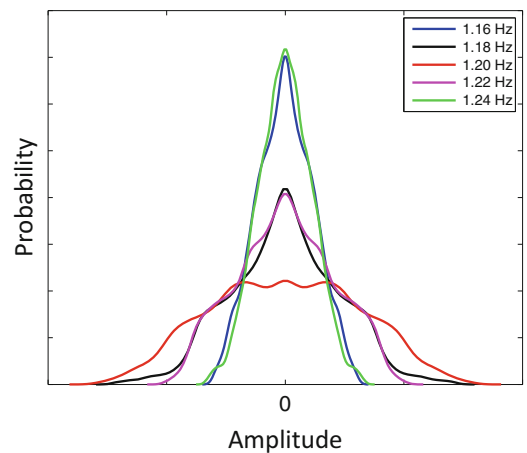**Fig. 40.3** Normalized PDF of pure structural mode (*left*) and pure harmonic component (*right*)

Fig. 40.4 PDF calculated for measurement filtered around the frequencies given in the legend. Structural mode at 1.2 Hz

shape of the PDF is also almost identical. For example, for the structural mode (Fig. 40.4) the shape when band-pass filtered around 1.18 Hz and 1.22 Hz is almost identical. This will be referred to as the symmetry of the PDF.

The PDF is an effective technique to distinguish between a structural mode and a harmonic. It can also distinguish between a structural mode and a mathematical mode, a mode identified by the estimators, e.g. LSCE, SSI-COV, LSCF, but without a physical meaning. The shape of a mathematical mode resembles the shape of a structural mode, but lacks this symmetry. Take for instance the previous example, around 1.34 Hz neither a structural mode nor a harmonic is located. The shape of the PDF around 1.32 Hz does not correspond to the shape around 1.36 Hz (Fig. 40.6). As long as the harmonic is not damped too

Fig. 40.5 PDF calculated for measurement filtered around the frequencies given in the legend. Harmonic at 1.5 Hz
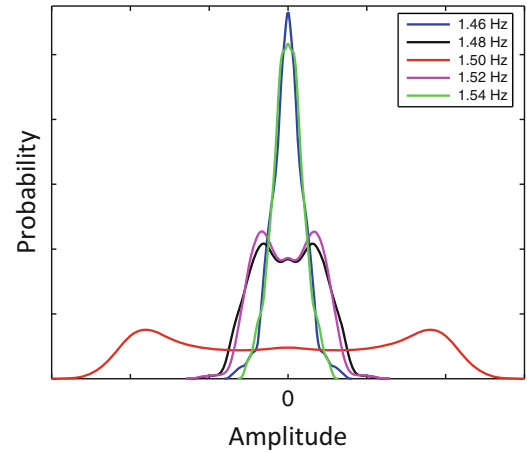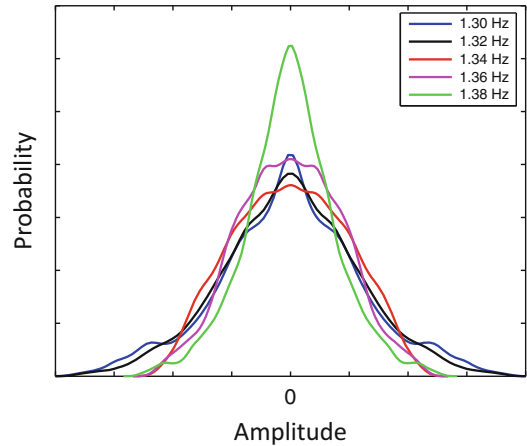

Fig. 40.6 PDF calculated for measurement filtered around the frequencies given in the legend

heavily the technique remains usable. The results however require to be interpreted and automation is therefore difficult. A possible method is to first use an identification technique, and later the PDF. The PDF will show which identified poles can be attributed to mathematical modes, harmonics or structural modes.

40.3.2 Kurtosis

The use of kurtosis has been proposed as a part of the new enhanced frequency domain decomposition technique (EFDD) [14]. The kurtosis describes how peaked or how flat the PDF of a stochastic variable is. The kurtosis γ is the fourth central moment of a stochastic variable x, normalised with respect to the standard deviation σ. The kurtosis γ is written as:

$$\gamma(x \mid \mu, \sigma) = \frac{E\left[(x - \mu)^4\right]}{\sigma^4} - 3 \tag{40.1}$$

In Eq. (40.1), μ represents the mean value of x and E denotes the expected value. The standard definition results in a value of 3 for the kurtosis if the PDF is normally distributed (structural mode). Therefore the modified definition is used [Eq. (40.1)], where 3 is subtracted, such that a structural mode results in a value of 0 and a harmonic in a value of -1.5 (value for a sinusoidal component).

The measured signal is band pass filtered in consecutive band over the whole frequency band of interest. The kurtosis is calculated and if a negative peak towards -1.5 is observed, a harmonic is indicated.

A laboratory set-up was used to demonstrate the use of kurtosis. A beam was excited with white noise and superposed sinusoidal harmonics, with the first harmonic located close to the first structural mode (Fig. 40.7). When the kurtosis is calculated, all the harmonics are clearly indicated by peaks to -1.5 (Fig. 40.8).

Fig. 40.7 Spectrum of the beam excited with white noise and sinusoidal harmonics superposed. The structural modes (S) and harmonics (H) are indicated
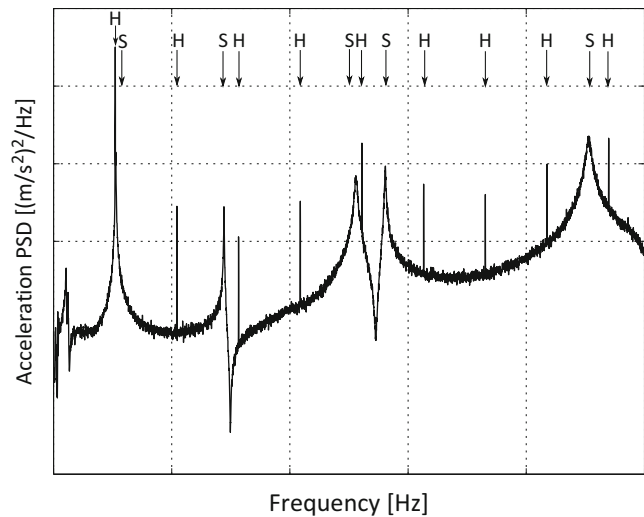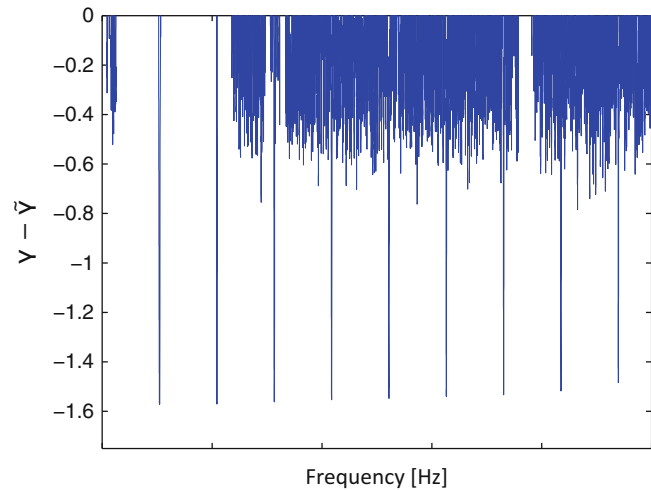

Fig. 40.8 Kurtosis calculated for the beam excited with white noise and sinusoidal harmonics superposed. The peaks towards −1.5 indicate the harmonics

The kurtosis is based on the same information as the PDF and will therefore also fail if the harmonics are damped too heavily. The kurtosis is however much easier to interpret than the PDF and can therefore be automated much more easily.

40.4   Pre-processing Techniques

40.4.1   *Non-parametric Removal of Disturbing Harmonics*

This technique is introduced in [15]. The harmonics are removed from the frequency spectrum via a non-parametric estimate of the harmonic frequency. To account for the non-perfectly constant harmonic frequency, the harmonic is modelled as a sum of H harmonically related sine waves with a non-linearly varying phase. The spectrum of a simulated system with superposed harmonics is shown in Fig. 40.9. The harmonics are modelled as damped poles to correspond to the wind turbine. Approximate knowledge of the harmonic frequency is necessary. The harmonic frequency is chosen to be the frequency where the frequency spectrum reaches its maximum value, in close proximity of the estimated harmonic frequency. The harmonic peak is separated from the spectrum by means of a rectangular window (Fig. 40.10). The obtained spectrum is taken back to the time domain by means of an Inverse Fast Fourier Transform (IFFT) and demodulated. This results in a non-parametric estimate of the phase harmonics. By means of a least-squares cost function the harmonic disturbance is reconstructed (Fig. 40.11) and subtracted from the original spectrum.

Fig. 40.9 The unmodified
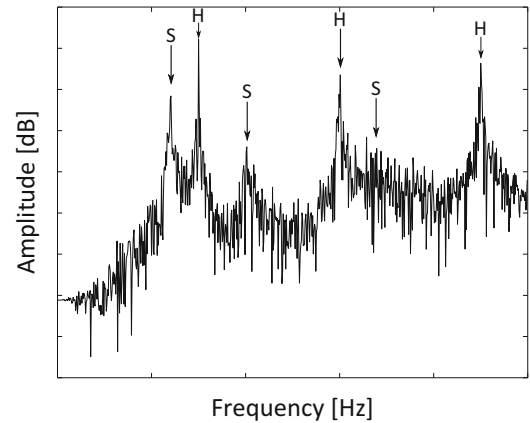spectrum including structural
modes and harmonics

Fig. 40.10 The harmonic is
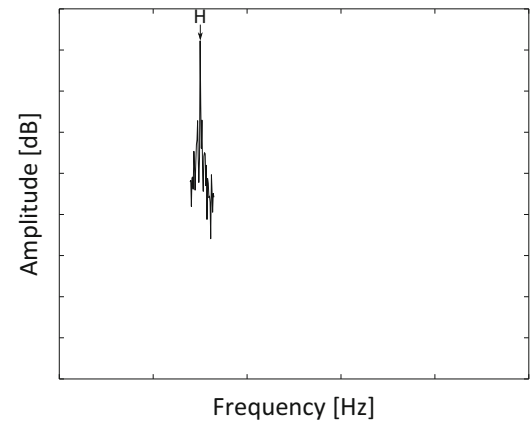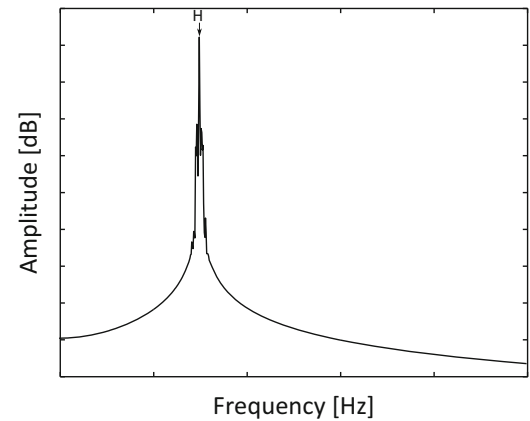selected by means a rectangular
window

Fig. 40.11 Estimate for the
harmonic

The advantages are that the harmonic can be damped and variable in frequency. This is for instance encountered in the wind turbine. Even when the wind turbine is rotating at nominal speed, the rotor speed is still varying slightly. The method also still works if the harmonic is located close to a structural mode.

40.4.2 Cepstrum Editing

Cepstrum editing can both be used as an identification and pre-processing technique. The cepstrum $C(t)$ is the spectrum of a logarithmic spectrum [16]. The general definition is given by Eq. (40.2).

$$C(t) = IFFT \left[\ln \left(X(f) \right) \right] \tag{40.2}$$

Fig. 40.12 Logarithmic amplitude derived from the example system with sinusoidal harmonics at multiples of 1.5 Hz
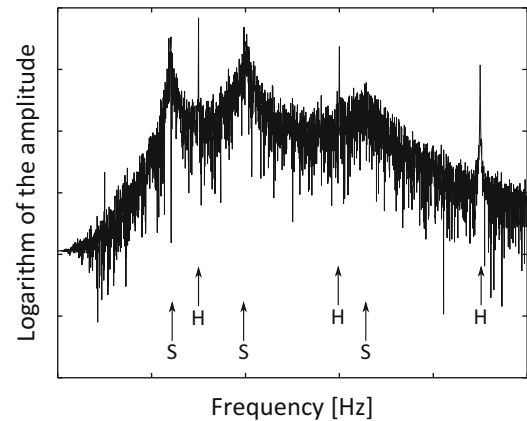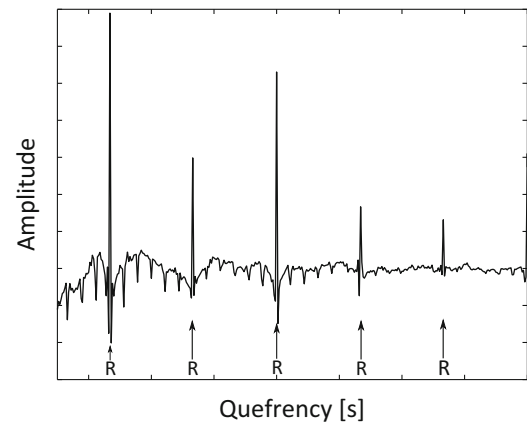

Fig. 40.13 Cepstrum calculated from the logarithmic amplitude. The rahmonics (R) are indicated

where $X(f)$ can be written as:

$$X(f) = FFT[x(t)] = A(f)e^{j\phi(f)} \tag{40.3}$$

with $x(t)$ it the measured signal, $A(f)$ the amplitude and $\phi(f)$ the phase.

Since harmonics show up at intervals in the spectrum, they also show up as distinct peaks in the cepstrum as long as there are enough multiples of the harmonic present. This occurs for the wind turbine, as the 3p, 6p and 9p multiples of the blade rotation are present in the spectrum. The equivalent of the harmonics are called rahmonics in the cepstrum domain. The equivalent of the frequency is likewise called the quefrency. Figures 40.12 and 40.13 respectively show the spectrum of a simulated system with superposed sinusoidal harmonics and the resulting cepstrum. Distinct peaks are indeed visible.

The algorithm for cepstrum editing was introduced in [17] (Fig. 40.14). By means of a Fast Fourier Transform (FFT) the spectrum of the measurement is calculated (Eq. (40.3), Fig. 40.12). The logarithm is calculated, such that the spectrum can be separated in the phase and the logarithmic amplitude. The IFFT of the logarithmic amplitude is calculated such that the real cepstrum is obtained (Fig. 40.13). The harmonics are removed by setting the amplitude of the rahmonics to zero (Fig. 40.15). Hence the edited cepstrum is obtained. Using a FFT the edited logarithmic amplitude spectrum is obtained which is combined with the original phase. The edited logarithmic spectrum is obtained (Fig. 40.16). The harmonics have been removed, while the structural resonances remain untouched. The complex spectrum is obtained by calculating the exponent. This edited spectrum can be used as an input for a frequency domain identification technique. The IFFT can be used to obtain an edited time signal, which can be used as input for a time domain identification technique. The usage of this technique on operational wind turbines was proposed in [3, 5].

The strength of cepstrum editing is that it is the cepstrum that is modified and not the spectrum. Hence, even if a harmonic frequency is located close to a resonance frequency of a structural mode, the structural mode remains unaffected as it is not located close to the harmonic in the cepstrum.

Aside from this, the harmonic frequencies are immediately identified by this technique, as long as enough multiples are present, and all harmonics are removed at once.

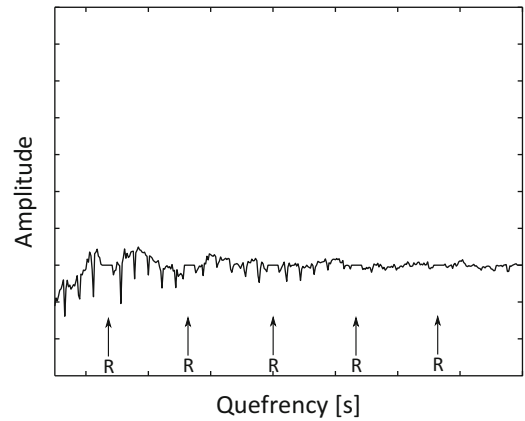**Fig. 40.14** Cepstrum after setting the amplitudes of the rahmonics to zero

Fig. 40.15 Logarithmic amplitude after removal of the rahmonics in the cepstrum. The harmonics have been removed
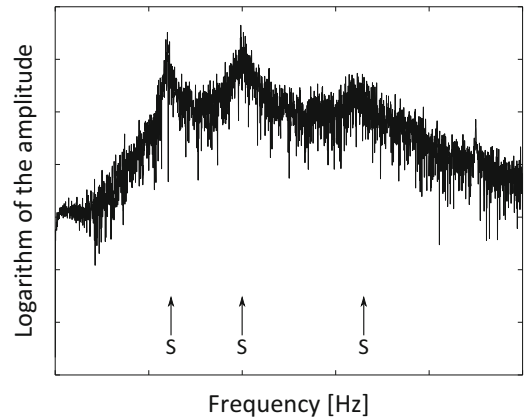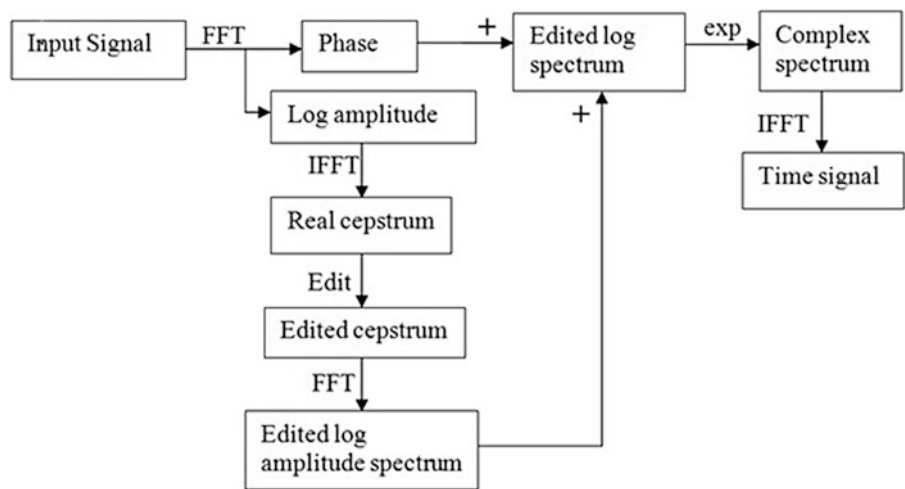

Fig. 40.16 Algorithm for cepstrum editing. Reprinted from [17]

It is possible to combine this technique with an exponential filter in the cepstrum domain (hence called a lifter) [17]. In [5] it is however shown that this lifter strongly affected the frequency content of the measured signals and resulted in poor automated identification results.

40.4.3 Other Techniques

Time synchronous averaging (TSA) [3, 6] is widely used in the dynamic analysis of rotating machineries. It requires however a rotational speed profile, either from direct measurement or estimation techniques, which is considered not to be available in this paper. In [3] it is shown that TSA is not able to remove periodic components from the original signals for operational

measurements on an onshore wind turbine. Also in [5] TSA is applied to operational measurement of an offshore wind turbine. In this last case a speed profile is not available. However, the variation on the rotational frequency is small enough that an average and fixed rotational speed can be chosen. In this case applying TSA lead to the structural modes being identified more often. The same data as used in [5] is used further on in this paper.

40.5   Identification Techniques

40.5.1   Reject Known Harmonics

General OMA techniques often identify the harmonics. If the harmonic frequencies are known, they can consequently be rejected. Increasing the model order can improve the initial results or even identify two closely spaced features, be it modes or harmonics. The model number should however not be exaggerated. If the model order is increased, also more mathematical poles are identified.

It is shown that the error on the estimate of the modal parameters is acceptable as long as both the structural mode and the harmonic are identified in [11]. Also the modal tracker explained in [9] is based on this. Within each dataset the average rpm is determined which can be directly related to the harmonic frequencies. Any resonance frequency within a 5 % range of a known harmonic is flagged. The analyst can than decide whether or not to reject these results.

40.5.2   Modified LSCE Method

The modified LSCE [18] method is an extension of the regular least-squares complex exponential method (LSCE). The LSCE method uses the Impulse Response Function (IRF) of the system to compute the modal parameters. In the Natural Excitation Technique (NExT) [19] it is shown that the correlation function $R_{ij}(T)$ between two response signals i and j of a linear system at a time interval T is similar to the response of the structure at i due to an input on j. Hence, the correlation between response signals of a linear system is a superposition of decaying oscillations. These oscillations are characterized by a natural frequencies and damping ratio equal to the natural frequencies and damping ratios of structural modes. As a consequence, the correlation functions can be used for OMA. In the case of the LSCE method, without going into too much detail, the correlation functions can be written in a Hankel matrix as is shown in Eq. (40.4). The β coefficients are to be identified and can be found in a least-squares sense using the pseudo-inverse.

$$
\underbrace{\begin{bmatrix} R_{ij}(0) & R_{ij}(\Delta t) & \dots & R_{ij}((2N-1)\Delta t) \\ R_{ij}(\Delta t) & R_{ij}(2\Delta t) & \dots & R_{ij}(2N\Delta t) \\ \vdots & & & \\ R_{ij}((L-1)\Delta t) & R_{ij}(L\Delta t) & \dots & R_{ij}((2N+L-2)\Delta t) \end{bmatrix}}_{[L \times 2N]} \underbrace{\begin{Bmatrix} \beta_0 \\ \beta_1 \\ \vdots \\ \beta_{2N-1} \end{Bmatrix}}_{[2N \times 1]} = - \underbrace{\begin{Bmatrix} R_{ij}(2N\Delta t) \\ R_{ij}((2N+1)\Delta t) \\ \vdots \\ R_{ij}((2N+L-1)\Delta t) \end{Bmatrix}}_{[L \times 1]}
\tag{40.4}
$$

In the modified LSCE method the harmonics are explicitly included in the algorithm. Exact prior knowledge of the harmonic frequency is thus assumed. The damping of the harmonics is considered to be zero in this algorithm. The correlation functions contain two extra terms per harmonic in order to include the harmonic [Eq. (40.5)]. The harmonics are taken into account by combining Eq. (40.4) with Eq. (40.5) (where ω_h indicates the harmonic pulsation) and solving exact for the harmonic components. This forces the algorithm to identify poles with zero damping at the harmonic frequencies. Consequently the harmonics are forced into the fitted model.

$$
\underbrace{\begin{bmatrix} 0 & \sin(\omega_h \Delta t) & \dots & \sin(\omega_h(2N-1)\Delta t) \\ 1 & \cos(\omega_h \Delta t) & \dots & \cos(\omega_h(2N-1)\Delta t) \end{bmatrix}}_{[2 \times 2N]} \underbrace{\begin{Bmatrix} \beta_0 \\ \beta_1 \\ \vdots \\ \beta_{2N-1} \end{Bmatrix}}_{[2N \times 1]} = - \underbrace{\begin{Bmatrix} \sin(2N\omega_h \Delta t) \\ \cos(2N\omega_h \Delta t) \end{Bmatrix}}_{[2 \times 1]}
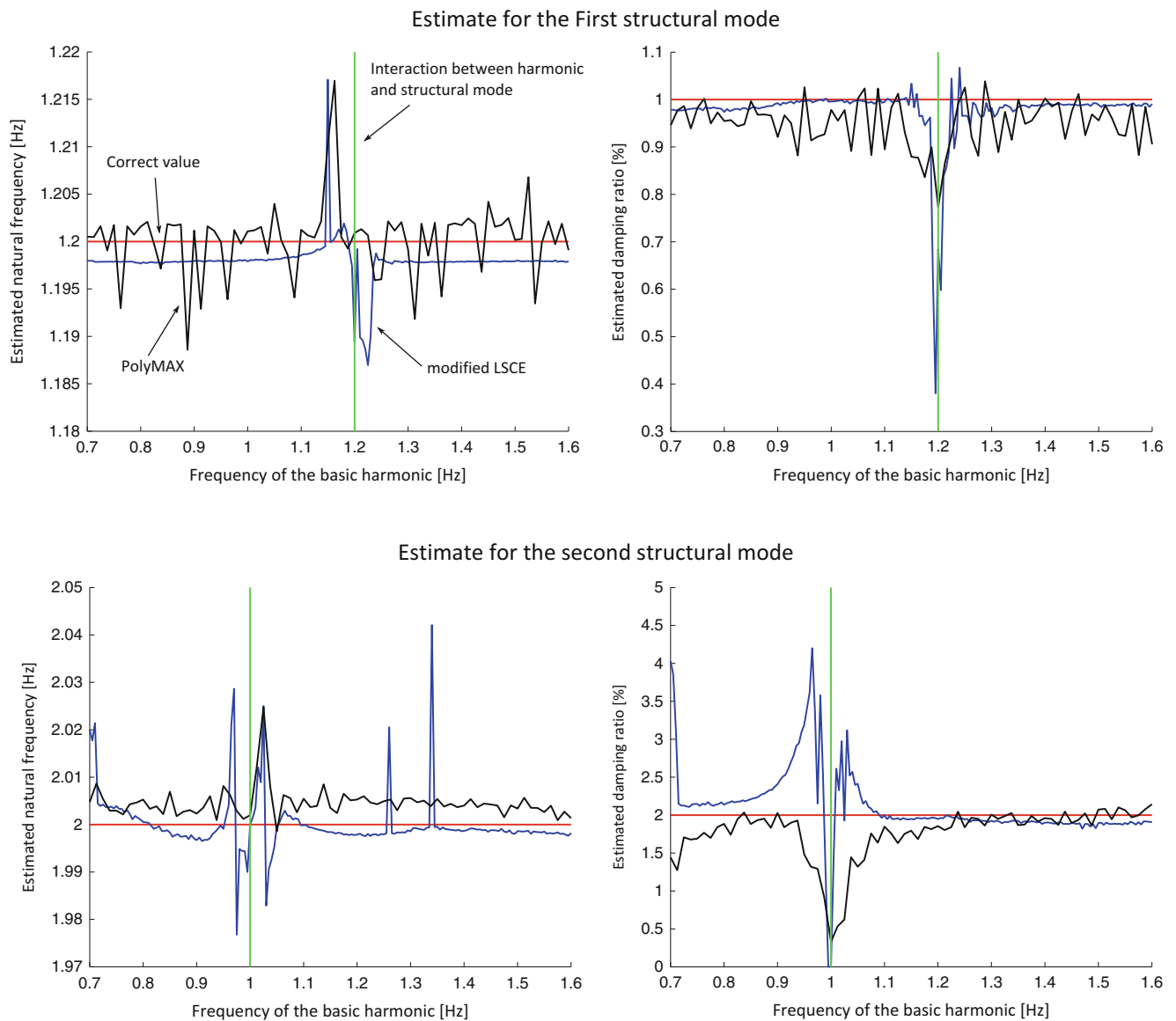\tag{40.5}
$$

Fig. 40.17 Application of the modified LSCE method and PolyMAX on a simulation with discretely varying sinusoidal harmonics, considering exact knowledge of the harmonic frequency. Both PolyMAX and the modified LSCE method are affected by the presence of the harmonic. The modified LSCE method however only tends to estimate the undamped harmonic when the harmonic approaches the structural mode closely

As a first example exact knowledge of the harmonic frequency is considered with sinusoidal harmonics superposed to a simulated system. The harmonic frequency is discretely varied. The estimated resonance frequencies and damping ratios for the first two structural modes of the simulated system are shown in Fig. 40.17. The figures show the estimates for the poly-reference Least Squares Complex Frequency method (pLSCF) [20], also known as PolyMAX, and modified LSCE method. Generally speaking the estimate of the modified LSCE method is comparable to the estimate of PolyMAX. However when the harmonic approaches the structural mode closely, the modified LSCE method tends to only estimate the (undamped) harmonic. PolyMAX also shows a drop in the estimated damping ratio, be it less pronounced. PolyMAX also delivers less mathematical poles compared to modified (and regular) LSCE method. This makes PolyMAX considerably easier to interpret. Figure 40.17 also shows that if the harmonic frequency is not too close to the natural frequency of the structural mode, the harmonic can simply be ignored, as it does not influence the model parameter estimate.

The results degrade strongly if the harmonic frequency is not exactly known. Figure 40.18 shows the estimate of the modified LSCE method for the simulated system with an harmonic superposed at 1.24 Hz, for which the estimate of the modified LSCE was comparable to the estimate of PolyMAX. In this case, the harmonic frequency used in the algorithm is varied and thus an error is introduced. It becomes visible that the estimate of the modified LSCE method tends to vary
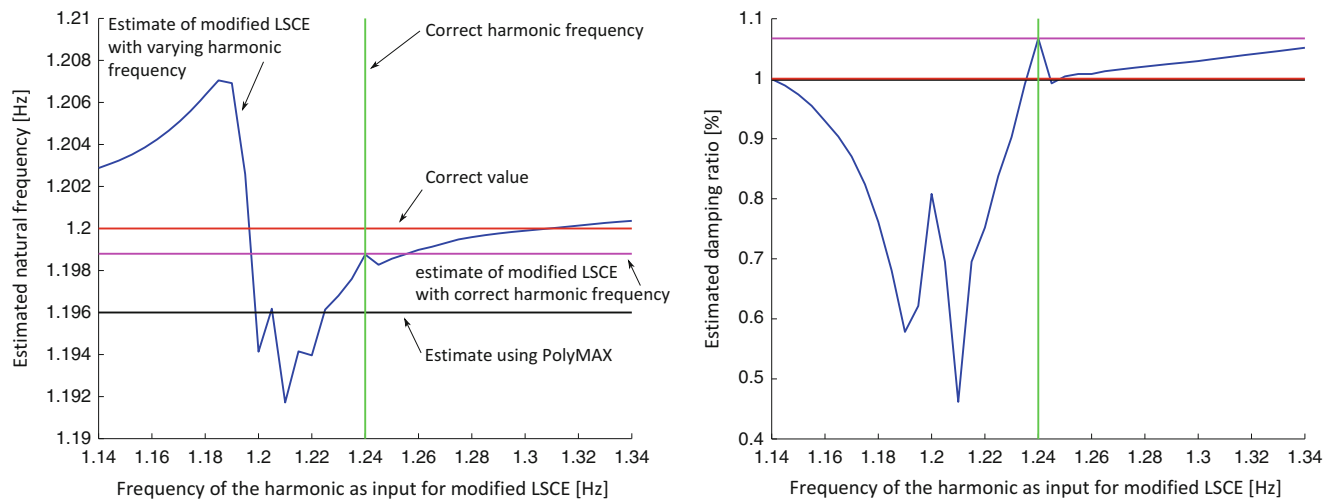
Fig. 40.18 Application of the modified LSCE with harmonic located at 1.24 Hz. The harmonic frequency presented to the algorithm is varied. The estimate of the modified LSCE method varies with the estimated harmonic frequency

strongly with the estimated harmonic frequency. The estimate is strongly disturbed when the estimated harmonic is placed between the structural mode and the actual harmonic. In this case a non-existent mode with zero damping is forced by the algorithm to be identified close to the structural mode. This strongly influences the estimate of the modal parameters of the structural mode. Dependent on the experiment, the estimates of the modified LSCE method vary from equally correct as to much worse than the estimate of PolyMAX. The modified LSCE method should be used with care and shows no direct advantage compared to PolyMAX.

A similar modification for the eigensystem realization algorithm (ERA) and the Ibrahim time domain algorithm is presented in respectively [21] and [22]. In [18, 21, 22] it is also proposed to extend these methods for damped harmonics. In order to apply this a foregoing estimate of these harmonics is necessary. However, if information based on an identification is used, there is no reason to suspect that the estimate of the model parameters will change in a second identification.

40.6 Input Spectrum Independent Techniques

Transmissibility based OMA (TOMA) [10] and poly-reference TOMA (pTOMA) [11] makes use of transmissibility functions. For this technique the unknown operational forces can be arbitrary. Hence this technique should not be disturbed by a harmonic input. This technique however does not lie in the scope of this work and will not be studied any further here.

40.7 Wind Turbine Rotating at Nominal Speed

The results presented in this paper are merely to illustrate the different methods of harmonic removal and should not be considered as actual values of damping and resonance frequencies. Only long term results as presented in [9] should be considered.

The considered three blade offshore wind turbine is located in the Belgian North Sea at the Belwind windfarm. Knowledge of the modal parameters is important for the lifetime prediction of the structure. However, the modal parameters are also influenced by a number of external factors (e.g. air temperature, tidal level and wave height). The excitation can not be considered to be white noise, as the structure is also excited by wind and wave forces and harmonic forces introduced by the rotor.

The structure and the measurement campaign are further explained in [9, 23]. In this paper the data is taken from the measurement described in [9] and is the same as is used in [5]. Here only the front-aft (FA) motion of the wind turbine rotating at nominal speed, be it 16 rpm, is considered. The spectrum is shown in Fig. 40.19. The structural modes (S), the harmonics (3p, 6p, etc.) and the wave period (W) have been indicated. The other datasets have been studied in [12].

Fig. 40.19 Spectrum of one measurement of the FA motion of the wind turbine rotating at nominal speed. The structural modes (S), the harmonics (3p, 6p, etc.) and the wave period (W) are indicated
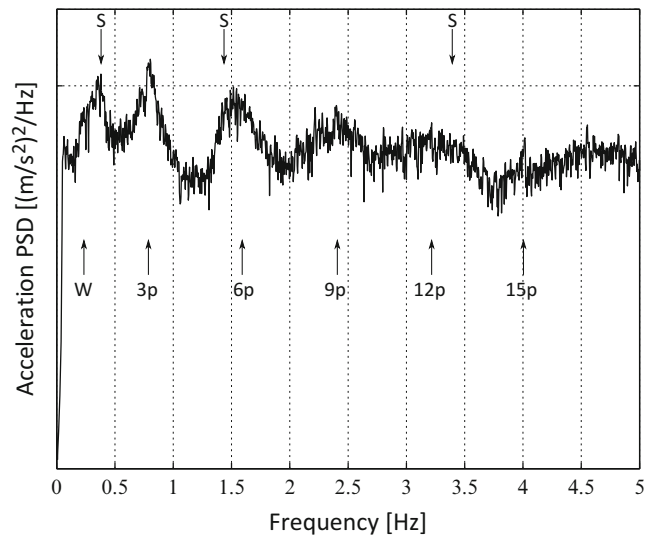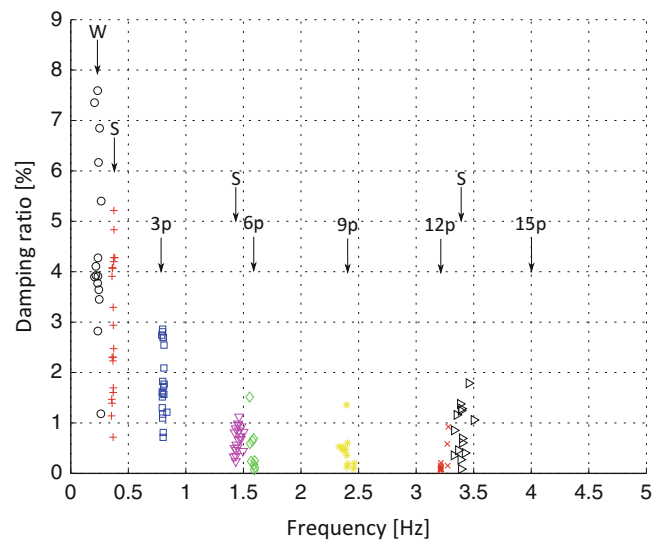

Fig. 40.20 Identification of the modal parameters of the wind turbine using PolyMAX (FA motion). The structural modes (S), the harmonics (3p, 6p, etc.) and the wave period (W) are indicated

Every measurement is 10 min long and the system is sampled at 12.5 Hz. The used dataset contains 20 measurements. PolyMAX is applied on each of the measurements to identify the harmonics and modal parameters (Fig. 40.20). The modes and harmonics which are recurring in the different measurements are shown. The 3p, 6p and 9p harmonics are clearly present. The 12p is only faintly present and the 15p is not identified. The structural modes have been indicated as they were identified in [9]. The estimates of the modal parameters show both for the harmonics and the structural modes a rather large spread. The damping ratio for the harmonics is also clearly different from zero.

40.7.1 Probability Density Function

The PDF is calculated for both the 3p harmonic and the second structural mode (Figs. 40.21 and 40.22). Both shapes are clearly different, but neither of them have a shape, nor a symmetry pronounced enough to be able to draw any conclusions from the PDF.

Fig. 40.21 PDF calculated for
the 3p harmonic. The shape nor
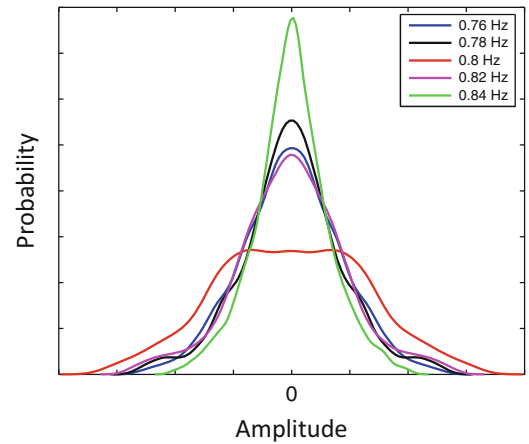the symmetry is strongly
pronounced

Fig. 40.22 PDF calculated for
the second structural mode. The
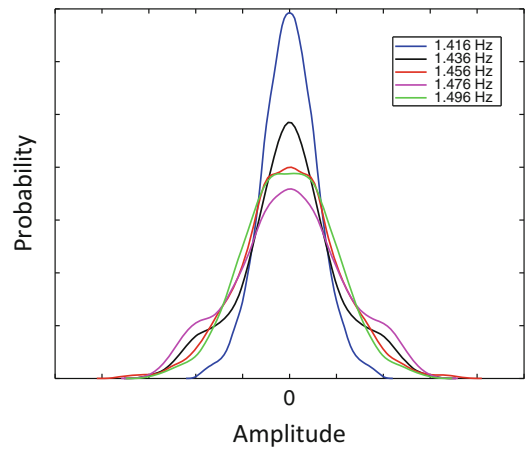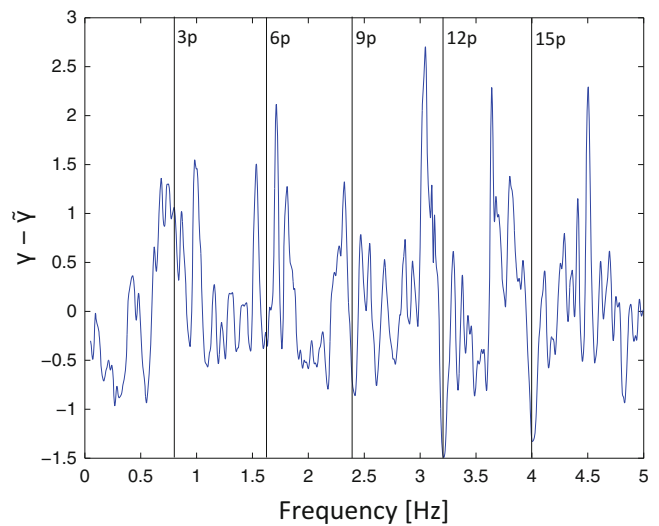shape nor the symmetry is
strongly pronounced

Fig. 40.23 Kurtosis calculated
for the third measurement. Only
the 12p and 15p harmonic are
detected

40.7.2   Kurtosis

The quality of the kurtosis varies with the measurements. Twenty measurements of each 10 min have been processed. As an example, the kurtosis for the third and fifteenth measurement are respectively shown in Figs. 40.23 and 40.24. The kurtosis for the third measurements detects the 12p and 15p harmonic, but none of the other multiples are indicated. Some of the measurements show similar behaviour. Unfortunately part of the measurements also show the behaviour of the fifteenth measurement, where no harmonics are indicated by the kurtosis.

Fig. 40.24 Kurtosis calculated for the 15th measurement. None of the harmonics are detected
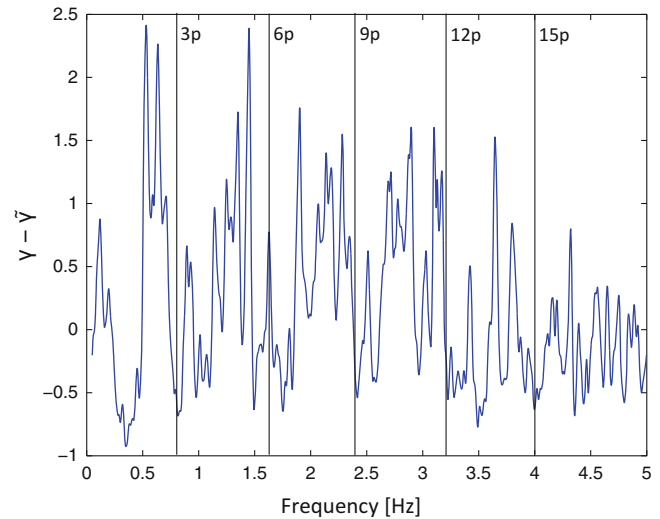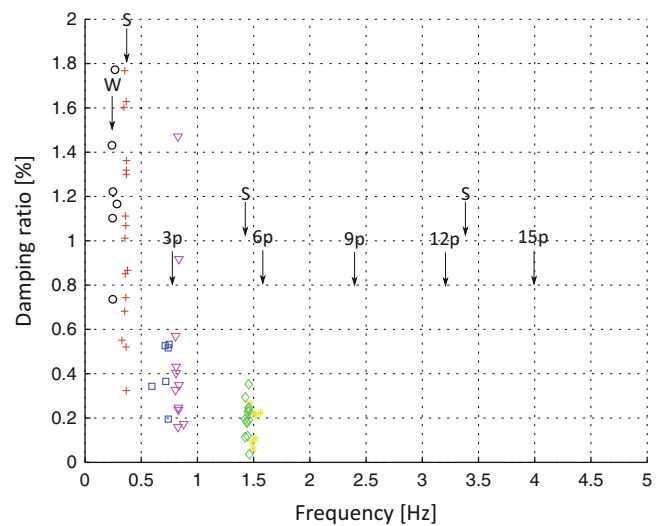

Fig. 40.25 Application of non-parametric removal. The 3p harmonic is removed and the spread of the damping ratios has been reduced. Also the third structural mode is removed

From these example it becomes visible that both the PDF and the kurtosis suffer if the harmonics become damped.

40.7.3 Non-parametric Removal

Non-parametric removal can be easily applied as the location of the harmonics is well known. Non-parametric removal was applied on every harmonic. The resulting estimates for the modal parameters is shown in Fig. 40.25. In some of the measurements the 3p harmonic is removed, in other cases it remains present. The spread of the damping ratios has however been reduced drastically and are generally estimated to be lower. The third structural mode is no longer being identified.

40.7.4 Cepstrum Editing

The cepstrum of one of the measurements is shown in Fig. 40.26. The rahmonic corresponding to the 3p harmonic (and higher multiples) is present. The modal parameter estimates for all measurements are shown in Fig. 40.27. The 6p, 9p and 12p harmonics have been removed, but the 3p harmonic is still present. The third structural mode is in this case present, but shows a larger spread on the frequency. The damping ratio for the second structural mode has been increased.

Fig. 40.26 Cepstrum calculated for the first measurement. One rahmonic (R) is clearly present
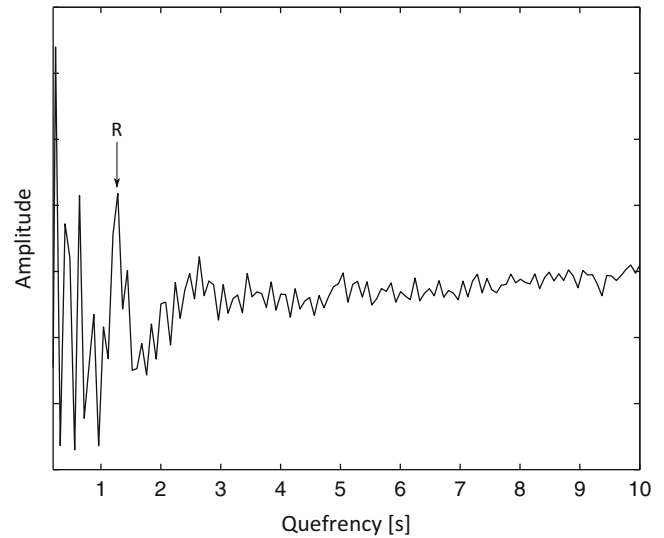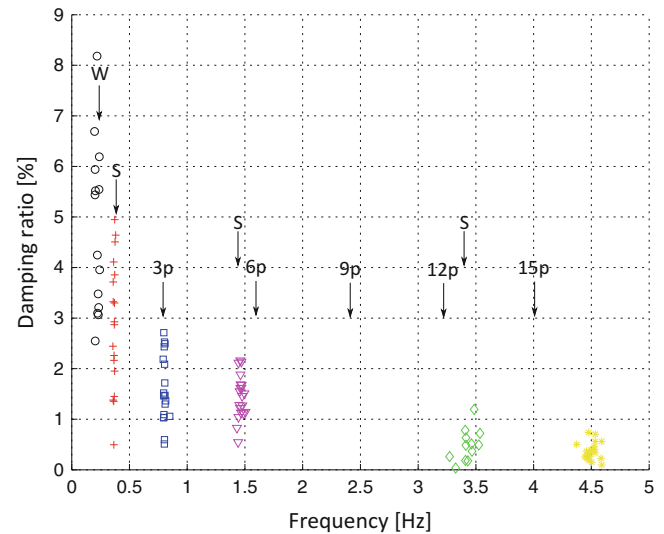

Fig. 40.27 Application of cepstrum editing. The 3p harmonic is still present, but all other are removed


40.7.5 Modified LSCE

When the modified LSCE method is applied the harmonics are forced to be identified. Consequently they should be present in the plots of the resonance frequencies and damping ratios as poles with zero damping. For clarity however, these poles are omitted in Fig. 40.28. However since the modified LSCE method also identifies more mathematical modes, therefore more modes are identified compared to PolyMAX (Fig. 40.20). The harmonics can still be observed even though there are also harmonic forced to be identified by the algorithm. It is likely that this behaviour originates in the non-exact rotational velocity of the wind turbine. Due to the larger amount of mathematical modes it is difficult to distinguish them from actual structural modes. The introduction of harmonics by the algorithm tends to disturb the estimates of the actual modes, rather than improve them.

40.8 Conclusions

All presented techniques have their own merits, but are limited to their respective boundaries. The PDF and kurtosis identify the harmonics very well as long as the harmonics are not damped too heavily. The PDF can distinguish structural modes, harmonics and mathematical modes. The kurtosis can only identify harmonics but can be interpreted and automated much

Fig. 40.28 Application of the modified LSCE method. The harmonics are still present after application and more mathematical poles are identified compared to PolyMAX
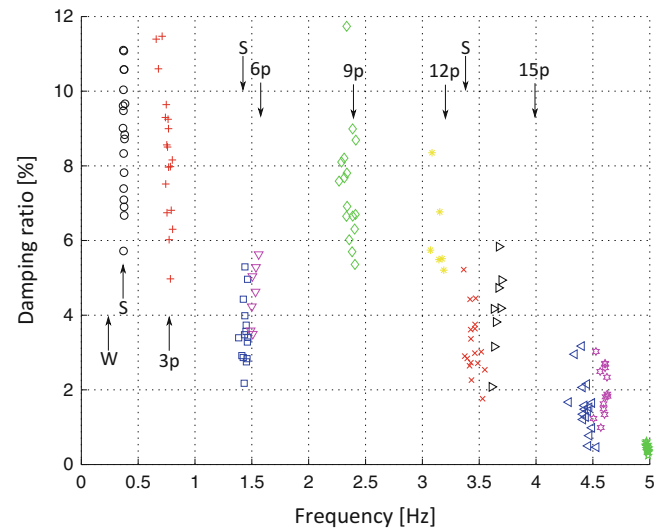
more easily. The non-parametric removal has as advantage that the harmonic can be damped and variable in frequency. An estimate of the harmonic frequency is however necessary. The cepstrum editing allows to identify the harmonics and does not modify the spectrum itself, but enough multiples of the harmonics need to be present. The modified LSCE method requires exact knowledge of the harmonic frequency and is therefore rather difficult to apply.

For the wind turbine it turns out that both non-parametric removal and cepstrum editing are promising techniques. From these two cepstrum editing seems to be the most effective and most easily applicable. If cepstrum editing is applied most harmonics have been removed.

Currently a tracking algorithm is applied to data in order to track the different modes in different circumstances [9]. This allows to retrieve the different structural modes when external factors (e.g. air temperature) and internal factors (e.g. rotational velocity) change. This technique is functional as long as no harmonic is interacting with a structural mode. In the future cepstrum editing could be applied additionally in order to improve performance. However if the rotational velocity of the wind turbine is changing (accelerating or decelerating rotor) the non-parametric removal might yield better results.

In this paper only the fixed 16 rpm case was studied. This case can still be considered one of the more easy operational conditions to study. Future work may extend this research to all operational cases.

References

1. Heylen W, Sas P (2006) Modal analysis theory and testing. Katholieke Universteit Leuven, Departement Werktuigkunde
2. Magalhães F, Cunha Á (2011) Explaining operational modal analysis with data from an arch bridge. Mech Syst Signal Process 25(5):1431–1450
3. Manzato S, White JR, LeBlanc B, Peeters B, Janssens K (2014) Advanced identification techniques for operational wind turbine data. In: Topics in modal analysis. Springer, New York
4. Weijtjens W, Verbelen T, De Sitter G, Devriendt C, et al. (2014) Data normalization for foundation shm of an offshore wind turbine: a real-life case study. In: EWSHM-7th European Workshop on Structural Health Monitoring
5. Manzato S, Devriendt C, Weijtjens W, Di Lorenzo E, Peeters B, Guillaume P (2014) Removing the influence of rotor harmonics for improved monitoring of offshore wind turbines. In: Dynamics of civil structures, vol 4. Springer, New York, pp 299–312
6. Peeters B, Cornelis B, Janssens K, Van der Auweraer H (2007) Removing disturbing harmonics in operational modal analysis. In: Proceedings of International Operational Modal Analysis Conference
7. Hermans L, Van der Auweraer H, Hatami A, Cooper E, Uhl T, Lisowski W, Wasilak A (1999) In-flight modal testing and analysis of a helicopter. In: Society for experimental mechanics, inc, 17 th international modal analysis conference, vol 1, pp 80–86
8. Qi K, He Z, Li Z, Zi Y, Chen X (2008) Vibration based operational modal analysis of rotor systems. Measurement 41(7):810–816
9. Weijtjens W, Shirzadeh R, De Sitter G, Devriendt C (2014) Classifying resonant frequencies and damping values of an offshore wind turbine on a monopile foundation for different operational conditions. In: Proceedings of EWEA
10. Devriendt C, De Sitter G, Vanlanduit S, Guillaume P (2009) Operational modal analysis in the presence of harmonic excitations by the use of transmissibility measurements. Mech Syst Signal Process 23(3):621–635

11. Weijtjens W, De Sitter G, Devriendt C, Guillaume P (2014) Operational modal parameter estimation of mimo systems using transmissibility functions. Automatica 50(2):559–564
12. Motte K (2014) Operational modal analysis in the presence of harmonic excitations: a review. Master's thesis, Vrije Universiteit Brussel
13. Jacobsen NJ (2006) Separating structural modes and harmonic components in operational modal analysis. In: Proceedings IMAC XXIV Conference
14. Brincker R, Zhang L, Andersen P (2000) Modal identification from ambient responses using frequency domain decomposition. In: Proceedings of 18th International Modal Analysis Conference, pp 625–630
15. Pintelon R, Peeters B, Guillaume P (2008) Continuous-time operational modal analysis in the presence of harmonic disturbances. Mech Syst Signal Process 22(5):1017–1035
16. Randall RB, Hee J (1982) Cepstrum analysis. Wirel World 88:77–80
17. Randall RB, Peeters B, Antoni J, Manzato S (2012) New cepstral methods of signal pre-processing for operational modal analysis. In: Proceedings of ISMA
18. Mohanty P, Rixen DJ (2004) Operational modal analysis in the presence of harmonic excitation. J Sound Vib 270(1):93–109
19. James GH, Carne TG, Lauffer JP (1995) The natural excitation technique (next) for modal parameter extraction from operating structures. Int J Anal Exp Modal Anal 10(4):260–277
20. Guillaume P, Verboven P, Vanlanduit S, Van Der Auweraer H, Peeters B (2003) A poly-reference implementation of the least-squares complex frequency-domain estimator. In: Proceedings of IMAC, vol 21, pp 183–192
21. Mohanty P, Rixen DJ (2006) Modified era method for operational modal analysis in the presence of harmonic excitations. Mech Syst Signal Process 20(1):114–130
22. Mohanty P, Rixen DJ (2004) A modified ibrahim time domain algorithm for operational modal analysis including harmonic excitation. J Sound Vib 275(1):375–390
23. Devriendt C, El-Kafafy M, De Sitter G, Guillaume P (2012) Estimating damping of an offshore wind turbine using an overspeed stop and ambient excitation. In: Proceedings of 15th International Conference on Experimental Mechanics

Chapter 41
Operational Modal Analysis of a Nine-Story Concrete Core Wall Building

Steve McDonald, Adam Gerber, Lisa Tobber, and Carlos E. Ventura

Abstract This paper describes the experimental modal identification techniques used to identify the dynamic properties of a nine-story concrete core wall building located on the University of British Columbia campus in Vancouver, Canada. Constructed in 1963, in a region of high seismic risk, the tower is slated for retrofit in the near future. In order to identify the dynamic properties of the structure, an ambient vibration test was performed using three instrument setups, synchronized via GPS, and positioned strategically throughout the building. Frequency domain decomposition and stochastic subspace identification methods were used to determine and validate the dynamic characteristics of the tower. The natural modes of vibration, frequencies, and damping ratios are presented. The results indicate that the structure exhibits rocking in the foundations as well as significant interaction with the adjacent structure.

Keywords Operational modal analysis • Ambient vibration test • Frequency domain decomposition • Dynamic interaction • Stochastic subspace identification

41.1 Introduction

Seismic assessment of existing structures requires a variety of assumptions regarding the demand and capacity of the structure. There is inherent uncertainty related to the estimations of dynamic characteristics (stiffness, mass), site soil conditions, and ground motion properties. Minimizing any one of these uncertainties leads to greater confidence in the analysis and assessment of the structure.

This study seeks to further understand the dynamic characteristics of a nine-story reinforced concrete tower by performing operational modal analysis using ambient vibration testing. The tower is located at the University of British Columbia (UBC), which is located in a region of high seismic risk. Being constructed in 1963, before modern seismic design considerations were incorporated into practice makes this tower potentially vulnerable to damage under strong ground motions. For this reason, the tower is slated for retrofit and must undergo seismic assessment.

This paper presents a summary of the experimental setup, instrumentation, operational modal analysis techniques used to determine the dynamic characteristics of the tower. The results from this paper are utilised in a model updating study, which are discussed in a companion paper "Model Updating of a Nine-Storey Concrete Core Wall Building."

41.2 Description of Structure

The tower is a reinforced concrete structure that rises nine stories above grade and one below. The tower was originally eight stories after construction in 1963; however, a renovation was conducted in 2010 in order to add a steel-framed penthouse that makes up the current ninth floor. Figures 41.1 and 41.2 below show the original tower and the current renovated structure as it stands today.

The building is occupied by offices on floors 1–8, and conference rooms on the 9th floor. The structural framing is consistent for all levels with the exception of the conference rooms on the 9th floor. A typical floor plan consists of two corridors running down the length of the structure with offices and meeting rooms on either side.

S. McDonald • A. Gerber (✉) • L. Tobber • C.E. Ventura
Civil Engineering Department, University of British Columbia, 6250 Applied Science Lane, Vancouver, BC V6T 1Z4, Canada
e-mail: adam@gerber.ca

Fig. 41.1 Tower in 1963

Fig. 41.2 Tower in 2014

With the exception of the penthouse floor, the structure consists of reinforced concrete two-way slabs supported on stairwell and elevator walls and evenly spaced columns along the length. The concrete stair and elevator core walls are continuous throughout the height of the tower. In the north-south direction, there are four discontinuous concrete perimeter walls that are supported by concrete columns between the ground and second level and continue to the eighth floor. The exterior beams on the north and south faces of the tower extend the length of the tower. Above the first story, the beams are connected to each other with architectural precast concrete mullions.

The eastern side of the tower is attached at every floor level to a five story adjacent building (classroom block) that is used primarily as classroom space. The classroom block recently underwent an extensive seismic retrofit which included the addition of steel brace frames. The low aspect ratio, coupled with the retrofitted steel braced frames as the lateral load resisting system, causes the classroom block to be very stiff in the north-south direction. In the southeast corner of the classroom block there are nine-inch thick concrete walls that extend the height of the tower. The tower connects to these walls at each of the first five floor levels through concrete beams. Since no seismic releases or seismic isolation gaps were observed, it was expected that the connection to this building could influence the dynamic behaviour of the tower.

41.3   Test Setup & Instrumentation

Ambient Vibration Testing (AVT) is a popular technique for the experimental determination of natural frequencies and mode shapes of civil engineering structures. AVT is advantageous as it does not require any knowledge of the inputs, instead relying solely on ambient excitation from wind, traffic or human activity. It should be noted that due to the low levels of excitation being measured during AVT, the mode shapes and frequencies correspond with the elastic properties of the structure. Structures expected to undergo strong shaking during an earthquake typically exhibit longer periods due to nonlinear behavior. Such considerations should be made by designers looking to use the results of the AVT for seismic assessment.

Ambient vibration testing took place on March 15, 2014 between the hours of 9:00 a.m. and 4:00 p.m. by graduate students Steve McDonald, Adam Gerber, Lisa Tobber, and Stevan Gavrilovic, supervised by Professor Carlos Ventura and Dr. Armin Bebamzadeh. The vibration measurement hardware and software used for the AVT are as follows:

1. Nine Tromino® 10 channel triaxial sensors [3] – capable of measuring high gain velocity, low gain velocity and acceleration in the horizontal and vertical directions. The Tromino® sensors can record synchronized data sets by synchronizing the internal clock with GPS at the beginning of each recording session. Sensors can sample at frequencies ranging from 128 Hz to 1,024 Hz. Each of the three triplets of channels have different sensitivity and saturation levels such that the same recording session can yield usable results even if one or more of the channels has saturated.
2. *Grilla* software [2] – proprietary software specific to Tromino® sensors for offline synchronization of data and data extraction.
3. ARTeMIS Modal Software [1] – experimental modal analysis software capable of time and frequency domain analysis of AVT data. Provides several modal identification and validation techniques for identification of mode shapes and frequencies.

The testing was composed of three test setups with one reference sensor on the top floor (level 9). The reference sensor recorded continuously for the duration of the testing while the remaining "roving" sensors were relocated between setups. The first setup recorded motions on floors 6–9, the second setup recorded motions on floors 2–5 and the final test setup recorded motions at all four corners of the ground floor and basement. All nine sensors were synchronized to GPS at the beginning of the first setup and the roving sensors were re-synchronized at the beginning of each subsequent setup. Ambient excitation was provided primarily by wind and human activity within the building. Figures 41.3 and 41.4 below shows the locations of the sensors for each setup

All sensors were oriented with their local north arrow in the east-west plan direction. See Fig. 41.5 for sensor orientation and placement.

A summary of the sensor locations, orientations and recording channels used in the analysis of the AVT data for each test setup are presented in Table 41.1 below.
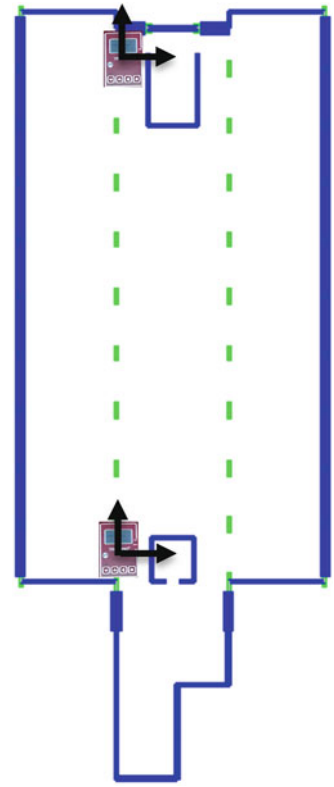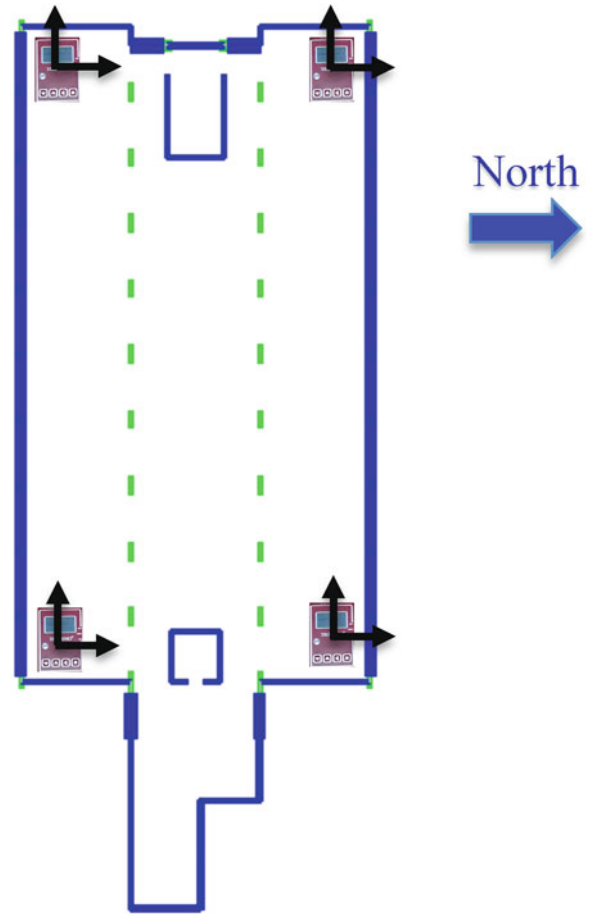
Fig. 41.3 Sensor layout for setup 1 and 2

Fig. 41.4 Sensor layout for setup 3

Fig. 41.5 Tromino sensor and placement locations

Table 41.1 Sensor locations and directions

Sensor	Setup 1		Setup 2		Setup 3	
	Level	*Location*	*Level*	*Location*	*Level*	*Location*
#1 (REF)	9	W Side	9	W Side	9	W Side
#2	9	E Side	5	E Side	Ground	SE Corner
#3	8	W Side	5	W Side	Ground	NE Corner
#4	8	E Side	2	E Side	n/a[a]	n/a[a]
#5	n/a*	n/a[a]	2	W Side	Ground	NW Corner
#6	7	E Side	4	E Side	Basement	SE Corner
#7	7	W Side	4	W Side	Basement	NE Corner
#8	6	E Side	3	E Side	Basement	SW Corner
#9	6	W Side	3	W Side	Basement	NW Corner

[a]Data not used due to sensor synchronization errors

41.4 Operational Modal Analysis

Operational modal analysis was performed using the software ARTeMIS Modal V3.5 (Artemis Modal Software 1999–2014). Within the program, two methods of modal identification were utilized: the "frequency domain decomposition" (FDD) method, and the "stochastic subspace identification" (SSI) method. The mode shapes generated from the two techniques were then validated using the modal assurance criteria (MAC) feature in ARTeMIS.

The FDD method decomposes the system response into a series of independent single degree of freedom systems for each mode. Casually referred to as the "peak-picking" method, resonance of natural vibration modes appear as peaks on a frequency-response plot. Thus selecting the peaks on the plot is a good starting place for identifying modal frequencies; after which, further verification techniques can be implemented.

The SSI techniques estimate the modal parameters directly from raw measured time histories. They have the added advantage that they are not reliant on frequency resolution since they are implemented in the time domain and are capable of working with closely spaced and repeated modes with variable levels of damping. The results obtained from both methods are presented in Figs. 41.6, 41.7 and 41.8 below.

A total of ten mode shapes were identified using the FDD method and nine using the SSI method; higher modes were possible to identify but are not expected to contribute significantly to the structural response under strong ground motions. Table 41.2 displays the resulting modes with their associated periods and equivalent viscous damping ratios. The damping values were obtained using the SSI procedure. Illustrations of six mode shapes are shown in Fig. 41.9. Note that torsional components were present in many of the observed shapes.
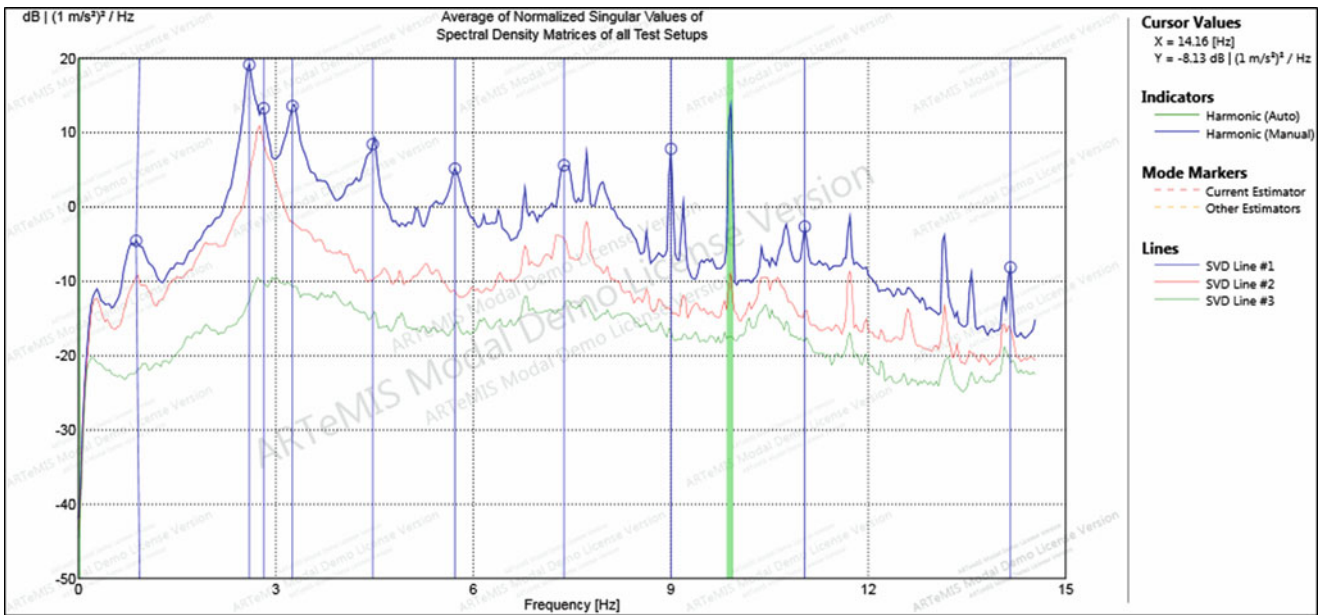
Fig. 41.6 Peak picking results for the FDD technique
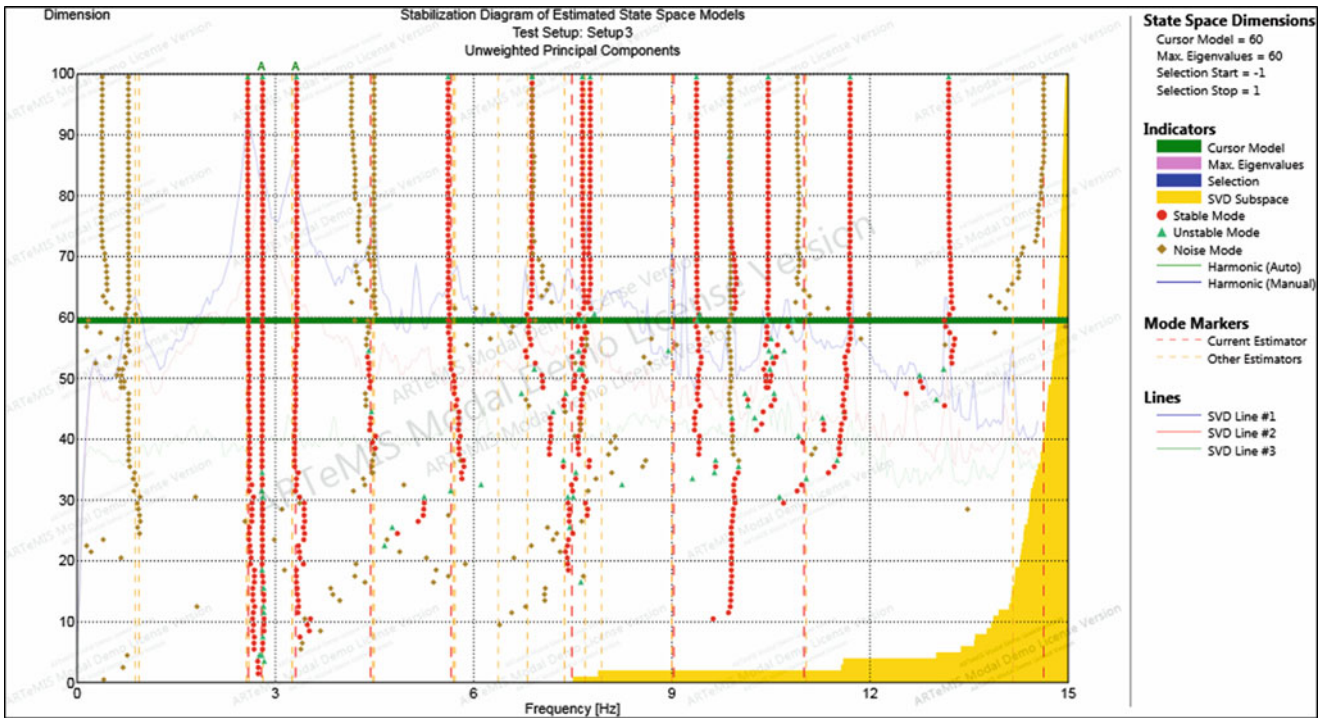
Fig. 41.7 Example stabilization diagram for the SSI technique

41.5   Discussion

The mode shapes captured through operational modal analysis appear in the expected order and general shape as would be expected for a typical shear wall building (ie. 1st lateral, 1st longitudinal, 1st torsional etc.). Also visible, however, are additional torsional components resulting from the connection to the adjacent building. This concentration of stiffness creates a large eccentricity between the center of mass and center of rigidity of the lateral load resisting system. The resulting deformations in the lateral modes thus tend to be amplified at the west end of the building.

Fig. 41.8 Modal assurance criteria

Table 41.2 Mode shapes found using FDD and SSI techniques

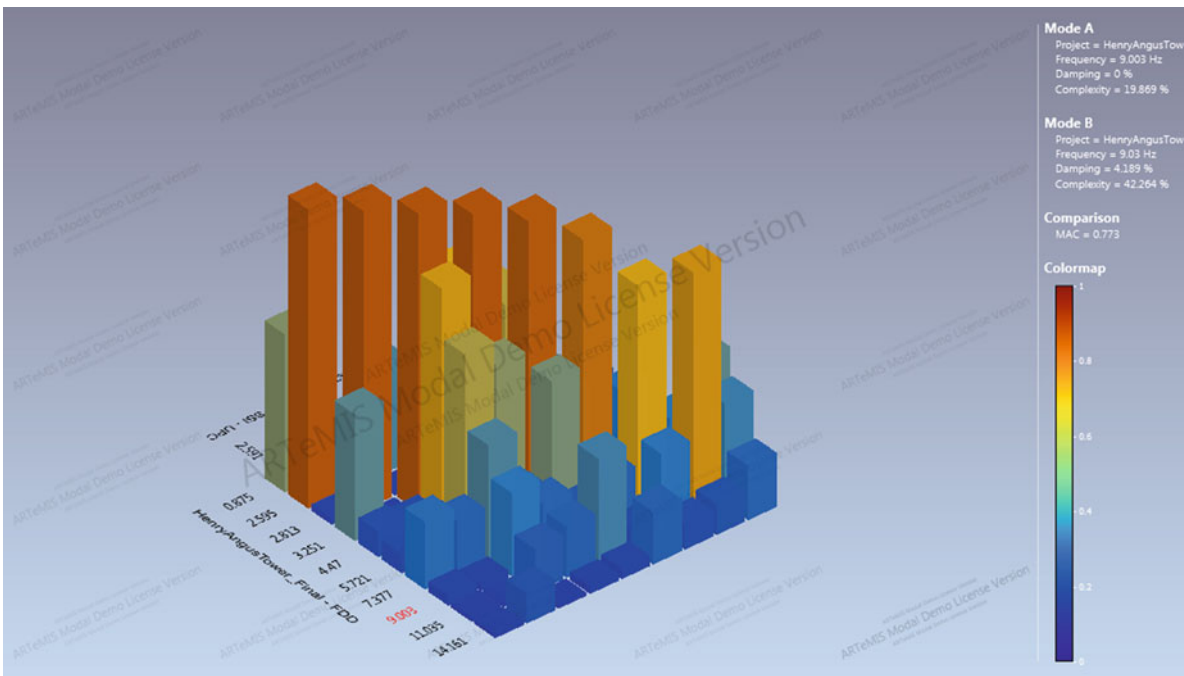| Mode	FDD Period (s)	SSI Period (s)	MAC	Damping Ratio (%)	Description
1	1.14	–	–	–	Site period[a]
2	0.38	0.39	1.00	2.43	1st lateral
3	0.36	0.36	1.00	1.60	1st longitudinal
4	0.31	0.30	0.99	3.67	1st torsional
5	0.22	0.23	1.00	2.48	torsional
6	0.17	0.18	0.98	0.62	torsional
7	0.14	0.13	0.92	1.33	2nd longitudinal
8	0.11	0.11	0.78	0.19	2nd torsional
9	0.09	0.09	0.82	0.16	2nd lateral
10	0.07	0.07	0.18	0.19	3rd longitudinal

[a]Rigid body structural mode

The fundamental mode is a lateral-dominated mode shape in the north-south direction; however, there is a slight torsional component due to the presence of the adjacent building. The connected building interacts with the tower by providing extra stiffness up to the fifth floor, and this is evident in the torsional components associated with predominantly lateral and longitudinal mode shapes.

The second mode shape for the tower is purely longitudinal. This mode is not significantly affected by the connected building because most of the building stiffness is in the north-south, or transverse, direction. Modes 4–6, the second lateral, longitudinal, and torsional modes respectively, have amplifications at the second floor indicative of a stiffness discontinuity. This is not surprising as the full height walls are discontinuous at the ground floor. In the second torsional mode there is also less amplitude on the east side due to the connected building.

The FDD method showed a dominant first mode with a period of 1.14 s, which was not detected using the SSI method. This mode shape showed a rigid body mode of the entire structure indicating that this mode is associated with the site characteristics.

The dynamic properties determined through this study are related only to the elastic properties of the structure at low vibration amplitudes. However, these properties hint at the building behavior under extreme shaking. In particular, the connection of the adjacent building as well as the wall discontinuities may lead to the building being damaged due to
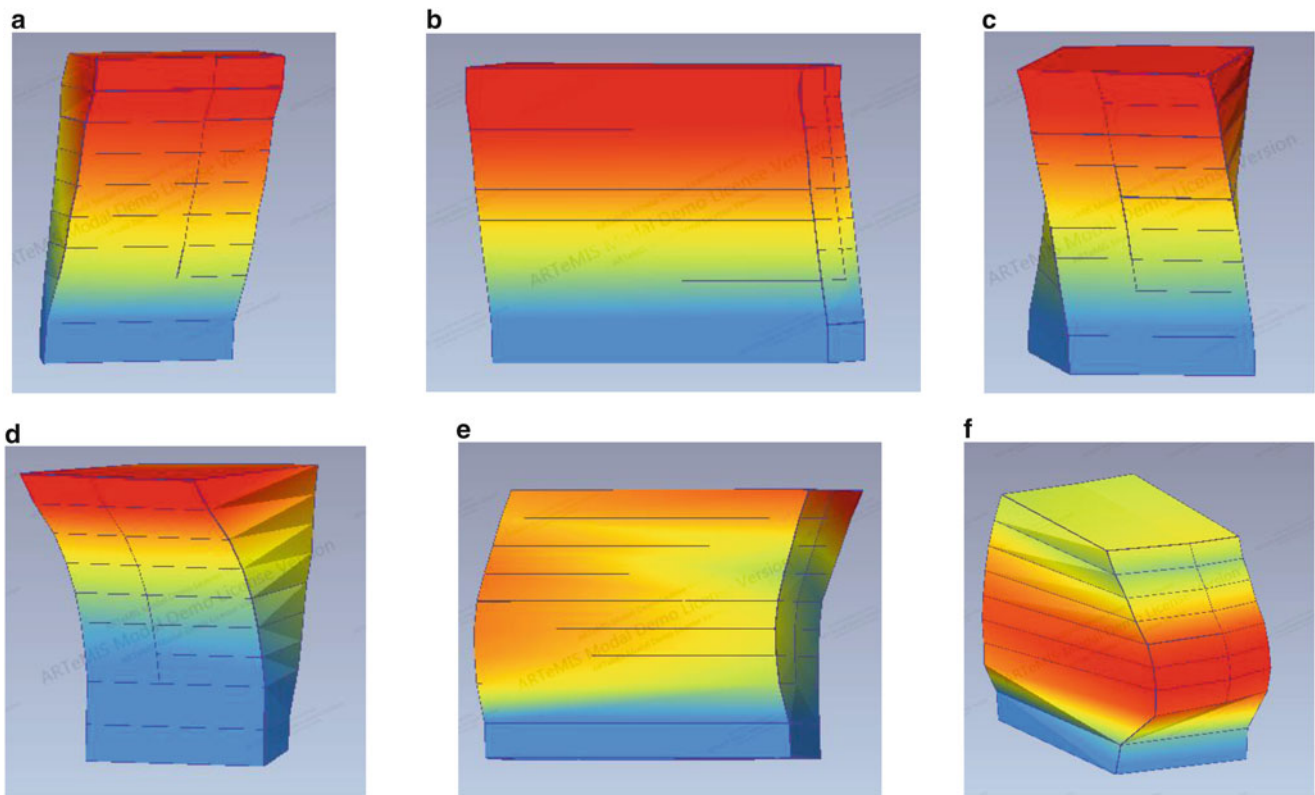
Fig. 41.9 Sample mode shapes. (**a**) First lateral (T = 0.39 s). (**b**) First longitudinal (T = 0.36 s). (**c**) First torsional (T = 0.30 s). (**d**) Second lateral (T = 0.09 s). (**e**) Second longitudinal (T = 0.13 s). (**f**) Second torsional (T = 0.11 s)

a torsional response to earthquake shaking. A companion paper "Model Updating of a Nine-Storey Concrete Core Wall Building," utilised the results of this study to update a structural analysis model, this paper will further examine the structural components and aspects that lead to the dynamic properties of the building.

41.6   Summary

Ambient vibration testing was carried out on a nine story reinforced concrete core wall building at the University of British Columbia. Results showed that the fundamental mode of vibration was a lateral mode with a period of 0.39 s (2.56 Hz) which contained significant torsional components due to interaction with an adjacent building. Using the FDD method, the first longitudinal and first torsional modes were found to be 0.36 s (2.78 Hz) and 0.22 s (4.55 Hz), respectively. The average modal damping ratio for the modes was 1.16 %, with the most significant being 2.43 %.

The FDD and SSI techniques showed good correlation with one another for most of the modes. The lowest MAC value was in the tenth mode shape with a value of 0.33.

The effect of the adjacent building was exhibited in the mode shapes and periods. It caused torsional components to be present in most of the higher longitudinal and lateral modes. Vertical discontinuities in shear walls showed amplification of the second story in higher modes.

References

1. Artemis Model Software (1999–2014) Structural vibration solutions, Inc. Retrieved from http://www.svibs.com/
2. Micromed S.p.A. (2011a) Grilla Software. Retrieved from http://www.tromino.eu/prodsel.asp?cat=3
3. Micromed S.p.A. (2011b) Tromino 10 channel triaxial sensors. Retrieved from http://www.tromino.eu/prodsel.asp?cat=1&prod=1

Chapter 42
Numerical Study of Reduction in Vibrations Induced by Water-Pipe System

Peter Persson, Kent Persson, and Göran Sandberg

Abstract In certain buildings such as synchrotrons and large ground telescopes, strict requirements are stated regarding the vibration levels. Both external and internal vibration sources, for example traffic and indoor water pumps, can have an appreciable effect on the vibration levels in the buildings. The synchrotron research facility MAX IV, which is currently under construction in Sweden, serves as an example case for the analyses. In MAX IV, several water-pipe systems used for cooling purposes will be placed near vibration sensitive equipment. These systems will transmit vibrations, into structural parts of the facility, which could exceed the vibration requirements. Structural modifications of pipe systems are investigated here by means of the finite element method in order to reduce vibration levels in the building. The finite element model employed includes a water-pipe system, adjacent building parts and the underlying soil. The use of fluid-structure interaction is investigated as well as the use of component mode synthesis. This paper focuses on the numerical procedure used as well as the effects on transmitted vibrations by different placements of the pipe supports.

Keywords Water-pipe system • Fluid-structure interaction • Component mode synthesis • Vibration reduction • Finite element method

42.1 Introduction

Occasionally, very strict vibrational requirements are specified for sensitive equipment used in high-tech facilities such as radar towers and synchrotron facilities. Various external and internal vibration sources such as traffic, indoor pumps and human activities can have appreciable effect on the vibration levels in a facility [1].

The new synchrotron facility MAX IV (cf. Fig. 42.1) is needed in order to improve research possibilities and to address new scientific challenges. Research fields of particular relevance include those of material science and medicine. In the large ring-shaped building at the MAX IV facility, a beam of electrons is to be controlled by a large number of magnets that are distributed along that building as well as along beam lines that lead electron beams to measurement stations. Since the quality of the measurements obtained is dependent upon the vibration levels of the magnets, very strict requirements are specified regarding the vibration levels in the facility. The vibration requirements regarding vertical displacements of the magnets are especially strict, its being required that these be less than 20–30 nm in RMS per second. At MAX IV, several pipe systems used for cooling purposes, supported by elastic foundations, will be placed near vibration sensitive parts at the facility and thus transmitting vibrations that could exceed the vibration requirements.

42.1.1 Literature Review

Vibrations originated from external vibration sources could efficiently be reduced by using wave obstacles such as trenches and shaped landscapes, see, for example [2, 3]. The present paper treats reduction in vibrations stemming from an internal vibrations source, namely water-pipe systems.

A literature review on liquid-filled pipe systems is presented in [4], treating waterhammer, cavitation, structural dynamics and fluid-structure interaction (FSI). The paper presents a survey of the history of research with focus on the development of mathematical models and validation to measurements. In order to very briefly summarise the extensive literature review;

P. Persson (✉) • K. Persson • G. Sandberg
Department of Construction Sciences, Lund University, John Ericssons väg 1, 223 63 Lund, Sweden
e-mail: peter.persson@construction.lth.se

Fig. 42.1 An architectural sketch of the MAX IV facility as planned

the basic equations of FSI analyses were derived already in the nineteenth century and in the 1950s, the corresponding analytical solutions were presented. In the 1970s, the basic FSI equations could be solved numerically and in the 1990s, commercial finite element (FE) codes for FSI analysis were released. Since the 1990s, several articles have been written in the field of FSI. In the following non-exhaustive literature review presented here, some of the important work within this field is presented. Several comprehensive studies have been conducted such as the review of several FE formulations used for solving FSI problems presented in [5]. Depending on the problem that is to be analysed, different formulations were concluded to be advantageous. In the paper, formulations for FE, boundary element and infinite element modelling of the fluid domain interacting with the FE structural domain are summarised. The formulations presented can be used for a variety of problems such as transient acoustics, acoustic cavity analyses and dynamics of fluid-filled pipes. In [6], an extensive bibliography containing references to papers, conference proceedings and theses treating FSI problems by employing the FE method as well as the BE method, that were published in 1995–1998 is presented. A review considering developments in the FSI research area, where essential mechanisms and phenomena are described, during primarily the 1990s is presented in [7].

Studies presenting numerical models in combination with measurement data test set-ups can be found for several numerical methods in the literature. The method of characteristics can, for example, be seen in [8, 9], considering dynamic FSI behaviour of liquid-filled pipes. The numerical models were validated by measurement data obtained from a test setup. The effect of considering interaction between the fluid and the structure is presented in, for example, [10] were an FE formulation for FSI analyses of a fluid-filled pipe system used in nuclear reactors is studied. The response from the numerical simulations was validated by a test set-up and it was concluded that FSI having a marked effect on the dynamical behaviour of the structure. In order to reduce the size of the often large finite element models needed to obtain results of adequate accuracy, the method of substructuring can be used. In [11], a multi-level substructuring technique for fluid-filled pipes considering FSI by employing the FE method is presented. The reduced model, using component mode synthesis, is compared to a full model as well as to measured data. Also in [12], a substructuring technique is used, where component mode synthesis (CMS) in combination to modal truncation are used in order to reduce the FE model of a fluid-filled pipe system considering FSI.

42.1.2 The Present Study

A preliminary study is presented in [13], where the influence of various parameters of the supports to a pipe system on the transmitted vibrations is studied. It was concluded that structural modifications of the supports can have a marked effect on the transmitted vibrations. Also, considering the example case MAX IV, it was observed that the bedrock can be excluded from the numerical analyses without affecting the results to any appreciable extent.

In the present paper, reduction of vibrations stemming from water-pipe systems is studied in order to ensure that the strict vibration requirements at the MAX IV facility are fulfilled. For extensive parametric studies, an efficient numerical procedure involving substructuring is needed in order to reduce the computational cost of the analyses. The study presented here is focusing on the development of an efficient numerical procedure using substructuring techniques. Structural modifications of the water-pipe systems were investigated in order to minimise the vibration levels in the facility by varying the position of the pipe supports. Coupled FSI and soil-structure interaction analyses, considering a water-pipe system, a concrete tunnel were the water-filled pipe system is located and the underlying soils, are performed by means of the FE method.

42.2 Governing Theory

42.2.1 Structural Dynamics

The governing finite element formulation of a dynamic problem can be written as

$$\mathbf{M\ddot{u}} + \mathbf{C\dot{u}} + \mathbf{Ku} = \mathbf{f} \tag{42.1}$$

where $\mathbf{M}$ is the mass matrix, $\mathbf{C}$ the damping matrix, $\mathbf{K}$ the stiffness matrix, $\mathbf{f}$ the load vector and $\mathbf{u}$ the nodal displacement vector [14, 15]. In harmonic loading, steady-state vibrations occur and the load and the resulting displacements can therefore be expressed as complex harmonic functions

$$\mathbf{f} = \mathbf{\hat{f}}e^{i\omega t} \; ; \quad \mathbf{u} = \mathbf{\hat{u}}e^{i\omega t} \tag{42.2}$$

where $\mathbf{\hat{f}}$ and $\mathbf{\hat{u}}$ denote the complex load amplitude and the complex displacement amplitude, respectively, i is the complex number involved and ω is the angular frequency. Inserting Eq. (42.2) into Eq. (42.1) results in the equation of motion in the frequency domain

$$\mathbf{D}(\omega)\mathbf{\hat{u}} = \mathbf{\hat{f}} \tag{42.3}$$

where $\mathbf{D}$ is the frequency-dependent dynamic stiffness matrix, which can be expressed as

$$\mathbf{D}(\omega) = -\omega^2\mathbf{M} + i\omega\mathbf{C} + K. \tag{42.4}$$

Since damping generally plays an important role in the dynamic response in soils, as well as in structures, it is introduced here. A rate-independent linear damping in the system was assumed. The loss factor, which represents the attenuation of the propagating waves, is defined as

$$\eta = \frac{1}{2\pi}\frac{E_D}{E_{So}} \tag{42.5}$$

where in a steady-state, the energy dissipated in the form of viscous damping during a cycle of steady-state vibration being denoted as E_D and the strain energy as E_{So} [16]. By considering the loss factor, the dynamic stiffness matrix becomes

$$\mathbf{D}(\omega) = -\omega^2\mathbf{M} + (1 + i\eta)\mathbf{K}. \tag{42.6}$$

42.2.2 Fluid-Structure Interaction

Two governing equations can be employed for describing an acoustic fluid, which is assumed to be inviscid, irrotational and compressible and to undergo small pressure changes. The equation of motion, the volumetric drag being neglected here, can be written as

$$\rho_0\frac{\partial^2\mathbf{u}_f}{\partial t^2} + \nabla p_d = 0 \tag{42.7}$$

where ρ_0 is the static density, $\mathbf{u}_f$ is the displacements of the fluid, t is the time, ∇ is the gradient operator and p_d is the dynamic pressure [14, 15, 17]. The constitutive equation can be written as

$$p_d = -c_0^2 \rho_0 \nabla \mathbf{u}_f \tag{42.8}$$

where c_0 is the speed of sound. With use of Eqs. (42.7) and (42.8), the wave equation for the acoustic fluid, the pressure serving as the field variable, can be written as

$$\frac{\partial^2 p_d}{\partial t^2} - c^2 \nabla^2 p_d = 0. \tag{42.9}$$

By expressing the pressure as a complex harmonic function, the wave equation in the frequency domain becomes

$$\nabla^2 \hat{p}_d + \frac{\omega^2}{c^2} \hat{p}_d = 0. \tag{42.10}$$

Continuity of $\mathbf{u}_f$ and the structural displacements ($\mathbf{u}_s$) is assumed in the direction normal to their common boundary S. By introducing a normal vector, $\mathbf{n}$, the coupling can be formulated as

$$\mathbf{u}_s \cdot \mathbf{n}|_S = \mathbf{u}_f \cdot \mathbf{n}|_S. \tag{42.11}$$

Due to the continuity in pressure at S, the coupling can be formulated as

$$\sigma_{s,n}|_S = -p_f \tag{42.12}$$

where $\sigma_{s,n}$ denote the stresses at S in the normal direction and p_f is the acoustic fluid pressure.

42.2.3 Component Mode Synthesis

In the substructuring process, a structure is divided into substructures, each of them described by the equation of motion, see Eq. (42.1) [18]. The size of a substructure is reduced by introducing a transformation, the equation of motion of the reduced system can then be written as

$$\mathbf{M}_R \ddot{\mathbf{u}}_R + \mathbf{C}_R \mathbf{u}_R + \mathbf{K}_R \mathbf{u}_R = \mathbf{f}_R \tag{42.13}$$

with

$$\mathbf{M}_R = \mathbf{T}^T \mathbf{M} \mathbf{T}, \quad \mathbf{K}_R = \mathbf{T}^T \mathbf{K} \mathbf{T}, \quad \mathbf{f}_R = \mathbf{T}^T \mathbf{f} \tag{42.14}$$

where $\mathbf{M}_R$, $\mathbf{C}_R$ and $\mathbf{K}_R$ are the reduced mass, damping and stiffness matrices, respectively, $\mathbf{f}_R$ is the reduced load vector, $\mathbf{u}_R$ is the reduced state vector and $\mathbf{T}$ is the transformation matrix. Introducing master and slave dofs, respectively, in the state vector allows the matrices in Eq. (42.13) to be partitioned as

$$\begin{bmatrix} \mathbf{M}_{mm} & \mathbf{M}_{ms} \\ \mathbf{M}_{sm} & \mathbf{M}_{ss} \end{bmatrix} \begin{bmatrix} \ddot{\mathbf{u}}_m \\ \ddot{\mathbf{u}}_s \end{bmatrix} + \begin{bmatrix} \mathbf{C}_{mm} & \mathbf{C}_{ms} \\ \mathbf{C}_{sm} & \mathbf{C}_{ss} \end{bmatrix} \begin{bmatrix} \dot{\mathbf{u}}_m \\ \dot{\mathbf{u}}_s \end{bmatrix} + \begin{bmatrix} \mathbf{K}_{mm} & \mathbf{K}_{ms} \\ \mathbf{K}_{sm} & \mathbf{K}_{ss} \end{bmatrix} \begin{bmatrix} \mathbf{u}_m \\ \mathbf{u}_s \end{bmatrix} = \begin{bmatrix} \mathbf{f}_m \\ \mathbf{f}_s \end{bmatrix}. \tag{42.15}$$

In the following derivations, the damping matrix is neglected.

Several substructuring methods have been developed, see for example [19]. The substructuring process used here, CMS by Craig-Bampton, is currently the most common method used for substructuring for structural dynamics problems [20]. In the Craig-Bampton method, the neglected inertia terms in condensation methods, for example Guyan reduction [21], are compensated by considering eigenmodes of the substructure that are obtained with fixed interface dofs, $\mathbf{u}_m = \mathbf{0}$ [18]. Therefore, a set of generalised coordinates $\boldsymbol{\xi}$ which represents the amplitudes of the eigenmodes is used. Assuming unloaded slave dofs, $\mathbf{f}_s = \mathbf{0}$, and a harmonic solution gives the following eigenvalue problem

$$\mathbf{K}_{ss} \Phi = \lambda \mathbf{M}_{ss} \Phi \tag{42.16}$$

from which the eigenmodes Φ can be calculated. Eigenmodes are selected as additional basis vectors to the approximation of the slave dofs, resulting in

$$\mathbf{u}_s = -\mathbf{K}_{ss}^{-1}\mathbf{K}_{sm}\mathbf{u}_m + \sum \Phi_i\xi_i = \mathbf{\Psi}\mathbf{u}_m + \mathbf{\Phi}\xi. \tag{42.17}$$

The transformation matrix, $\mathbf{T}_{\text{CMS}}$, can be defined by

$$\begin{bmatrix} \mathbf{u}_m \\ \mathbf{u}_s \end{bmatrix} = \begin{bmatrix} \mathbf{I} & \mathbf{0} \\ \mathbf{\Psi} & \mathbf{\Phi} \end{bmatrix} \begin{bmatrix} \mathbf{u}_m \\ \xi \end{bmatrix} = \mathbf{T}_{\text{CMS}} \begin{bmatrix} \mathbf{u}_m \\ \xi \end{bmatrix}. \tag{42.18}$$

The accuracy of the solution depends both on the selection of the master dofs, which affects the eigenmodes of the substructure (slave dofs), as well as on the selection of the retained eigenmodes.

42.2.4 Interface Reduction

Since the computational efficiency of CMS strongly depends on the number of retained dofs, reduction methods for reducing the number of retained dofs are called for. A condensation node (having three translation and three rotational dofs) is introduced with the intention to represent the motion of the interface in question, i.e. the dofs at the interface are coupled to the condensation node. The coupling can be realised in various ways, rigid coupling being used here. The coupling between the interface nodes and the condensation node is described, for rigid coupling, by

$$\mathbf{u}_i = \mathbf{u}_c + \mathbf{\Theta}_c \times \mathbf{r}_{ci} \tag{42.19}$$

where $\mathbf{u}_i$ is the displacement vector of the interface node, i, $\mathbf{u}_c$ is the displacement vector for the condensation node, $\mathbf{\Theta}_c$ is a vector containing the rotations of the condensation node and $\mathbf{r}_{ci}$ is a vector containing the distances from node i to the condensation node [22].

42.2.5 Evaluation

The modal assurance criteria (MAC), [23], is used here for comparing eigenmodes obtained from different FE models. The criteria provides a measure of the consistency of two eigenmode vectors. The MAC value for the jth eigenmode of model A, Φ_j^A, as compared with the ith eigenmode of model B, Φ_i^B, is defined as

$$\text{MAC} = \frac{\left|(\Phi_j^A)^T(\Phi_i^B)\right|^2}{(\Phi_j^A)^T(\Phi_j^A)(\Phi_i^B)^T(\Phi_i^B)}. \tag{42.20}$$

Root mean square (RMS) values were used as measures of the vibration magnitude. The RMS values of the complex magnitude of the vertical displacements from the steady-state analyses were determined here by two different equations. First, an RMS value was used in order to achieve one graph for evaluation points in an evaluation points pattern

$$u_{RMS}(f) = \frac{1}{n}\sqrt{\sum_{i=1}^{n} u_i^2} \tag{42.21}$$

where u_i is the magnitude of the displacement at node i and n is the number of considered nodes. The other RMS value was used in order to determine one value for the frequency dependent RMS value in Eq. (42.21) and is defined here by

$$u_{RMS} = \frac{1}{m}\sqrt{\sum_{j=1}^{m} u_{RMS}(f)_j^2} \tag{42.22}$$

where $u_{RMS}(f)_j$ is the magnitude of the displacement at frequency j and m is the number of frequencies considered.

Table 42.1 Properties of the solid materials

Property	Steel	Concrete	Low Baltic clay till	North-east clay till
Elastic modulus (MPa)	200,000	35,000	378	1,136
Loss factor	0.02	0.04	0.10	0.10
Mass density (kg/m^3)	7,900	2,400	2,125	2,125
Poisson's ratio	0.30	0.25	0.48	0.48

The normalised relative frequency difference (NRFD) was used to compare eigenfrequencies from different models to each other. It is defined, in percent, for the ith eigenmode as

$$\text{NRFD} = 100 \frac{\left| f_i^A - f_i^B \right|}{f_i^B} \tag{42.23}$$

where f_i^A is the ith eigenfrequency of model A and f_i^B is the ith eigenfrequency of model B.

42.3 Considered Materials

In the example case employed here, that of the synchrotron facility MAX IV, the soil consists of two different clay tills identified as Low Baltic clay till (12 m in depth) covering the stiffer North-east clay till (4 m in depth). The material parameters of the soils employed here were evaluated from both geotechnical and geophysical measurements, carried out at the MAX IV site by the companies *PEAB*, *TYRÉNS* and *NGI* in collaboration with the authors, as well as from comparison between FE simulations and those measurements in order for agreement to be achieved; see Table 42.1 [24]. The strength class of the concrete used in the analyses was assumed to be that of C40/50, i.e. having a cylinder strength of 40 MPa and a cubic strength of 50 MPa. The pipes and their supports were assumed to be made of the stainless steel type EN 1.4432 (ASTM 316L). Local variations in the involved materials, such as stratum and granularity, were assumed to be small as compared with the wavelengths in the frequency range of interest. Thus, they were modelled as isotropic homogeneous materials. The loss factors include material damping and geometrical attenuation effects such as the varying topography of the soils, as well as attenuation effects at joints. Strains corresponding to displacements at the nano-scale are usually at a level such that the assumption of linear elasticity is applicable for the involved materials. The water was modelled as an acoustic fluid, using acoustic pressure as field variable. The water was assumed to have a temperature of 10 °C, the static density of it, ρ_0, being set to 1,000 kg/m^3 and the speed of sound, c_0, to 1,450 m/s, resulting in a bulk modulus, K, of 2.10 GPa.

42.4 Finite Element Model

A three-dimensional FE model was developed with the use of the FE software package *Abaqus 6.12* [22]. The parts involved in the model were the pipes, including the water contained in them, the supports for the water-pipe system, attached to the ceiling in a concrete tunnel, and the ground involving two layers of soil, see Fig. 42.2. The pipe system was constituted by two different pipe cross-sections, DN150 and DN200, see Fig. 42.3. The outer dimensions of the cross-section of the concrete tunnel were 10 m by 4.1 m with a wall thickness of 0.3 m. Steel supports were used to attach the water-pipe system to the tunnel, each one of them having a length of 0.2 m and a squared cross-section with the side length 0.02 m.

Solid 20-node elements with quadratic approximation, using reduced integration, were employed for the supports, the concrete tunnel and the soil. In modelling the water, 20-node quadratic acoustic pressure elements were employed. Quadratic 8-node shell elements were used to model the steel pipes. In order to simulate the far-field conditions and avoid reflecting boundaries, 12-node quadratic one-way infinite elements, [25], were employed. To ensure that the analyses provided results of adequate accuracy, an element mesh with a minimum of seven element nodes representing the shortest wavelengths was employed. The model that in a latter section will be referred to as the full model, contained approximately 440,000 unknowns.

A harmonically varying acoustic unit pressure was applied to the free end of the DN150 pipe-section. At the other end of the water-pipe system, the gradient of the pressure of the acoustic medium was prescribed to zero representing a stiff boundary surface. In order to evaluate the frequency range of interest for the loading applied here, steady-state analyses of large frequency ranges were performed with various frequency steps. Displacements versus frequency for different sets
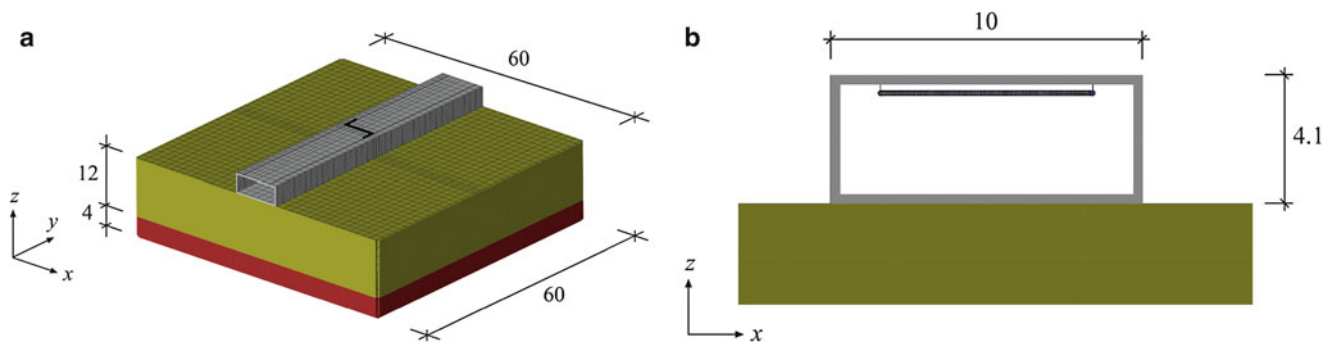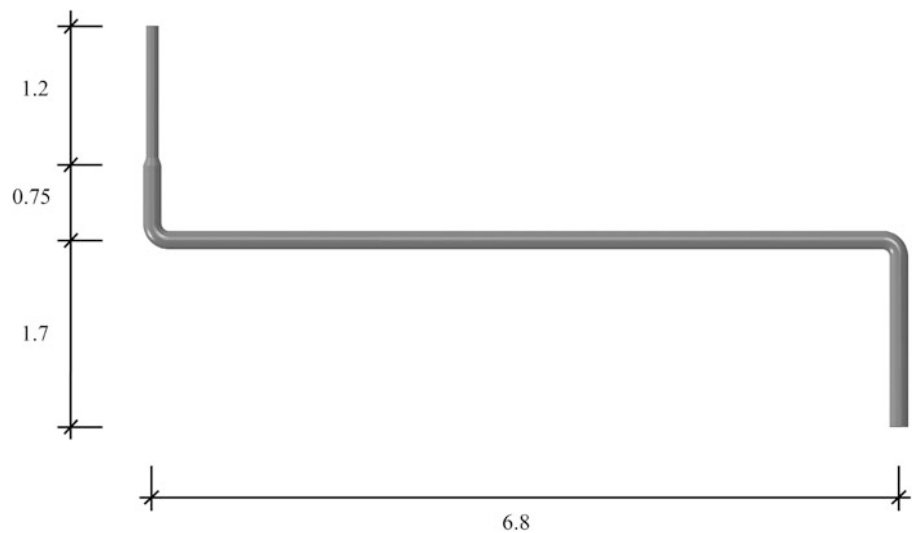
Fig. 42.2 (**a**) FE mesh of the complete model, the two soils being shown in *red* and *green colour*, respectively and the concrete tunnel in *grey*. (**b**) FE model zoomed in on the pipes, which are shown in *black*. The dimensions are in units of meters

Fig. 42.3 The modelled pipe system. The dimensions are in units of meters

of evaluation points were evaluated for different frequency ranges and frequency steps, respectively. As one example, the five highest displacement peaks occurs in the range of 5–30 Hz and the highest peak there is about 20 times higher than the highest peak in the range of 30–100 Hz. The analyses were, therefore, performed for frequencies from 5–30 Hz, in steps of 0.1 Hz.

42.4.1 FSI

In order to compare different ways of modelling the water in the pipes, eigenvalue analyses of solely the pipe system were performed, see Fig. 42.3. Two different models were used for the investigation; one model considering FSI of the pipes and their containing water, and one model considering the water as an additional mass modelled by increasing the mass density of the steel pipes, i.e. no interaction between the fluid and the structure was considered in the second model. The eigenvalue analyses were performed for frequencies up to 100 Hz, involving the first 12 eigenmodes (excluding the rigid body modes).

In Fig. 42.4a, the MAC values for the FSI model compared to itself are shown. As the eigenmodes are non-orthogonal in the dot-product, the off-diagonal terms are generally non-zero. In this particular case, the off-diagonal terms are less than 0.2 for the eigenmodes considered. In Fig. 42.4b, the eigenmodes of the FSI model are compared to the model where the water is treated as an additional mass. As can be seen, the two eigenmode vectors are not consistent. Especially, mode number 1 and 2 are shifted. Moreover, modes 6, 8–10 and 12 have very low MAC-values, i.e. bad resemblance. As can be seen in Fig. 42.5, those modes do not necessarily need to have a large NRFD value. The ninth mode, for example, has an NRFD value of approximately 1 %. Due to the low correlation between the model using FSI and the model where the water is treated as an extra mass, it is evident that there is need for considering FSI for dynamic analyses in these types of water-pipe systems.
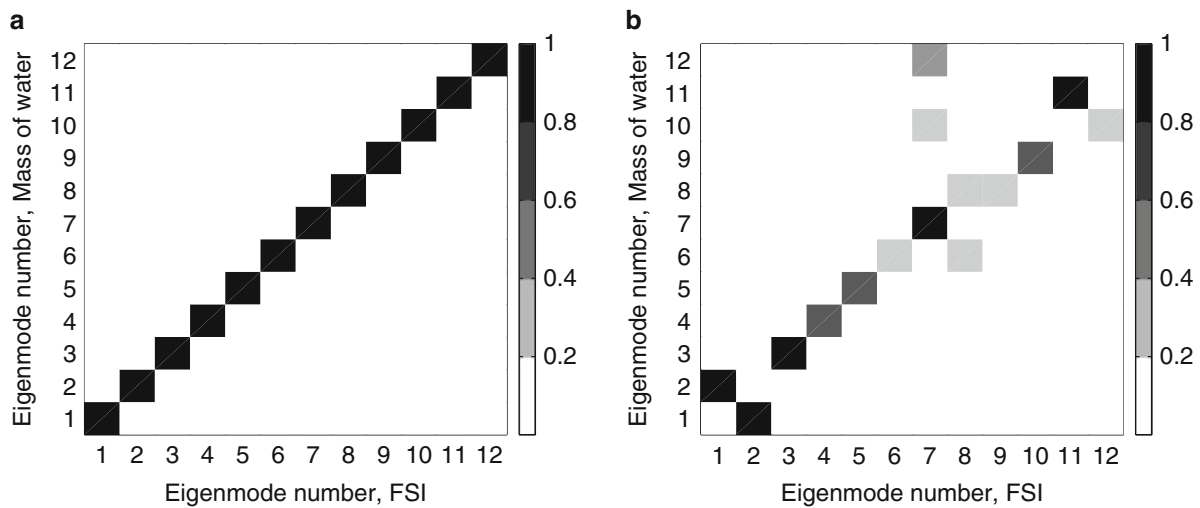
Fig. 42.4 The first 12 eigenmodes for the (**a**) model considering interaction between pipes and water, i.e. FSI, and the (**b**)model just taking the mass of the water into account
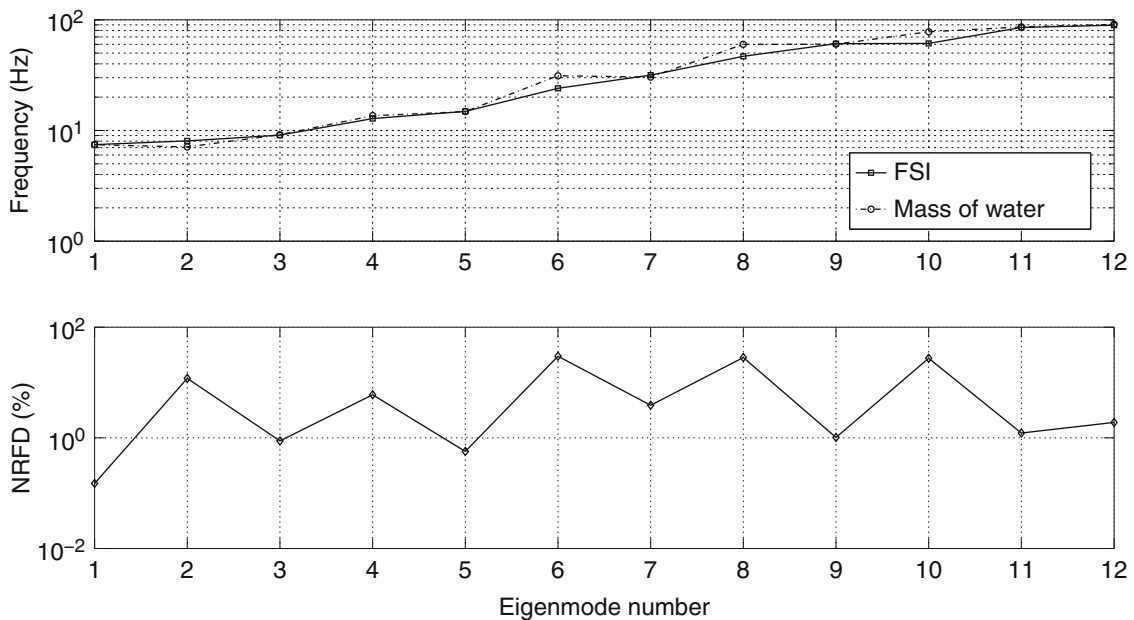

Fig. 42.5 Eigenfrequency and NRFD values, respectively, versus eigenmode number, considering FSI and mass of water, respectively

42.5 Model Order Reduction

In order to develop a numerically efficient model, substructuring in combination with interface reduction was used. Throughout this section, two supports are used for the pipe system in the FE model. In order to investigate the accuracy of the reduced order models, displacements were evaluated at the ground surface, see Fig. 42.6. Since the numerical efficiency of CMS is dependent on the number of retained interface dofs, interface reduction was applied. The supports are assumed to be rigidly attached to a part of the pipe, see red line in Fig. 42.7. In order to replace the interface nodes by one condensation node, rigid coupling was used.

Despite that 1,000 eigenmodes (eigenfrequency of 2,930 Hz) were retained in order to improve the substructural solution, large errors occurred at specific frequencies. The largest errors coincide in frequency to where the largest peaks in the displacement response was found. At the peaks, where the slope of the curve is large, the resolution of the sample points is of great importance, therefore a small shift in frequency can lead to a large difference in displacement magnitude at a specific frequency. This was, however, assumed not to affect the estimation of the vibration reduction that could be achieved

Fig. 42.6 *Top view* of the FE model, evaluation points shown as *black dots*. The dimensions are in units of meters
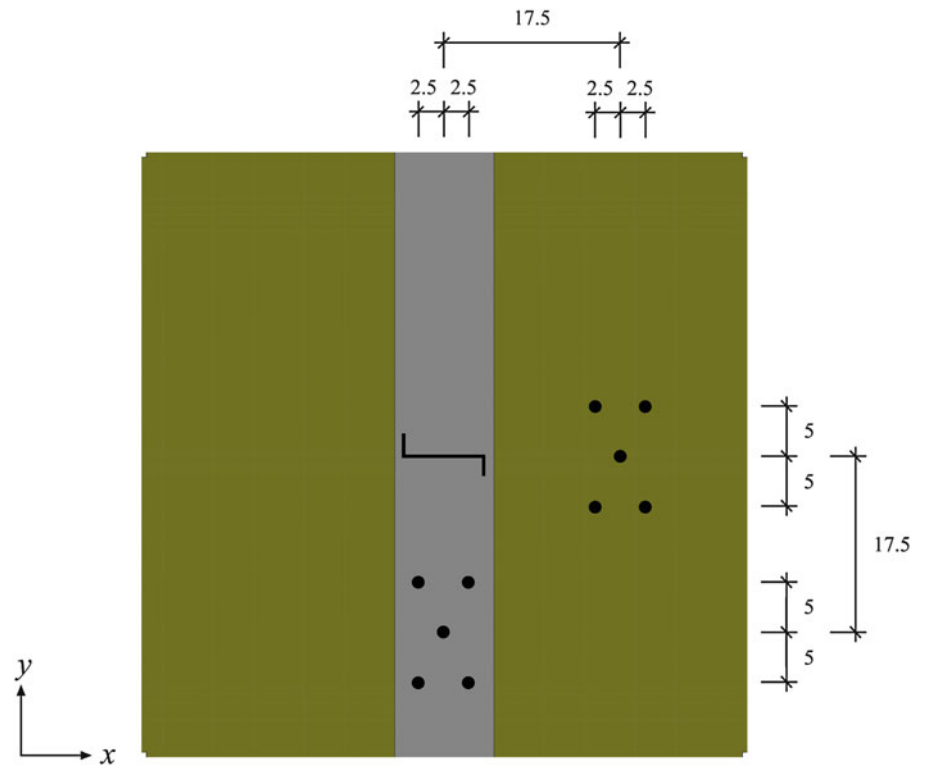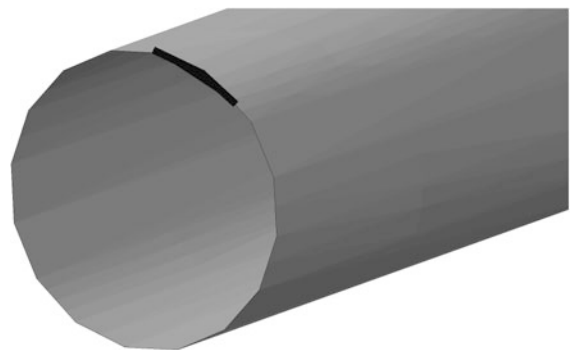

Fig. 42.7 *Thick black line* showing the coupling between the condensation node and the attachment nodes

by different placement of pipe supports. In order to evaluate the number of retained eigenmodes needed to obtain a reduced order model that will generate output of adequate accuracy, an average error as well as the difference of the RMS values of the full model compared to CMS models with various number of retained eigenmodes were obtained, see Table 42.2. It is seen in the table that convergence in both average error and difference in RMS, respectively, is found at 50 retained eigenmodes as it provides the same values as the model retaining 1,000 modes within reasonable accuracy. In Fig. 42.8, it is clearly seen that Guyan reduction (CMS model with no retained modes) provides a good approximation up to about 13 Hz. At higher frequencies, the inertia effects which are neglected in Guyan reduction start to affect the solution. By retaining one mode, a reasonably adequate approximation is obtained up to about 21 Hz. Adding more modes gives a better approximation, already at ten modes a good resemblance with the full model was found.

By using the reduced order model of the pipes and its contained water, the number of unknowns is reduced drastically from approximately 200,000 unknowns to 1,304 unknowns (50 retained modes +1254 retained dofs), which would drastically decrease the needed memory capacity of the computer. In order to evaluate the computational efficiency, due to the fact that the matrices will not be entirely banded in the reduced order model due to the full matrices that corresponds to the retained dofs, i.e. the total number of unknowns is not a sufficient measure of the computational efficiency of the reduced order model. Therefore, the steady-state analyses needs to be run on a computer in order to determine the simulation-time.

Table 42.2 Difference in RMS value and an average error, respectively, for CMS models retaining various number of eigenmodes, in comparison to the full model

Number of retained modes	Frequency of highest mode (Hz)	Average error (%)	Difference in RMS (%)
0	–	43.9	4.8
1	34.7	26.6	2.6
5	59.7	12.5	1.2
10	106	8.5	1.3
50	282	6.2	0.4
1,000	2,930	5.9	0.4

Displacements are evaluated on the ground surface, considering frequencies 5–30 Hz
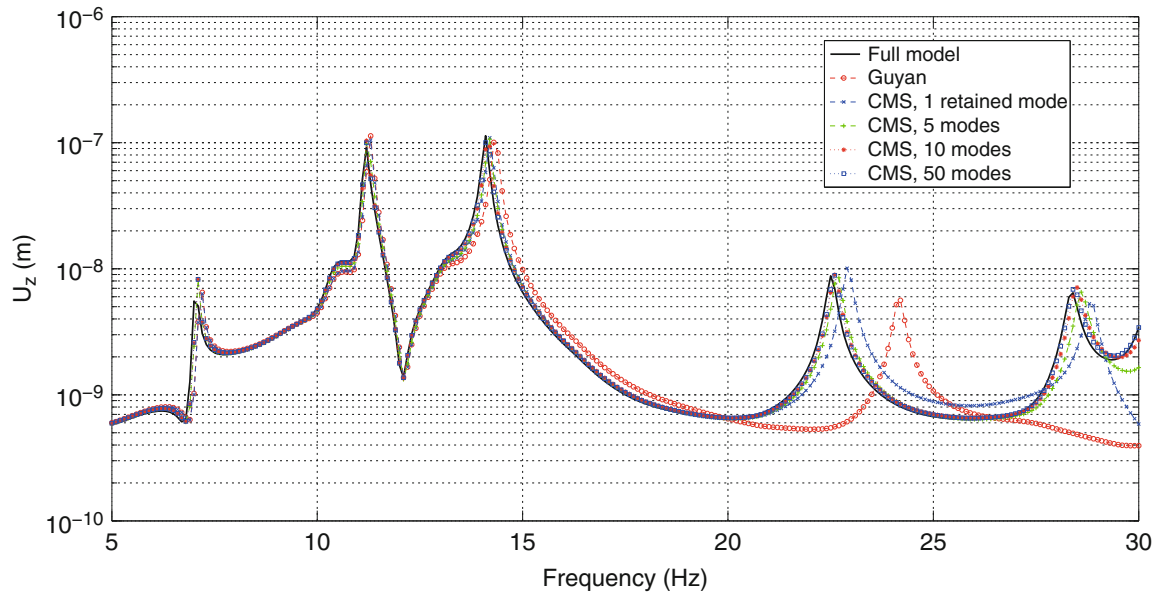

Fig. 42.8 Vertical displacements at the evaluation pattern on the ground surface versus excitation frequency of the load for the full model and for the substructure models using various number of retained modes

42.6 Mitigation Strategies

Once a computationally efficient reduced order model has been developed, mitigation strategies can be numerically investigated. In this paper, a passive isolation is used by investigating the influence on the transmitted vibrations from the water-pipe system by having different set-ups of the supports. Design due to static conditions being neglected here.

42.6.1 Location of the Supports

In the parametric study presented here, the same substructure model was used for all different possible locations of the supports that were analysed, i.e. retained dofs were selected at several locations. Considering the interface between the pipes and the supports, 36 retained dofs were used instead of 180 that would be the case if interface reduction was not used. The influence of different placements of the supports on the transmitted vibration levels was investigated by steady-state analyses, the frequency range being limited to 5–30 Hz, see Sect. 42.4. As concluded in Sect. 42.5, the number of retained modes needed for convergence in the reduced order model is 50, which is used throughout this parametric study. The displacements were obtained at the two evaluation point patterns; *ground surface* and *tunnel floor*, respectively, see Fig. 42.6. An RMS value of the displacements at each frequency of the five points, at each pattern was used to plot a single graph. Four different types of support set-ups were investigated, type A–D, see Fig. 42.9, as well as the reference case considering two supports

Fig. 42.9 The four different support locations (marked by *black squares*), type (**a**)–(**d**), all involving three supports whereof one in each end
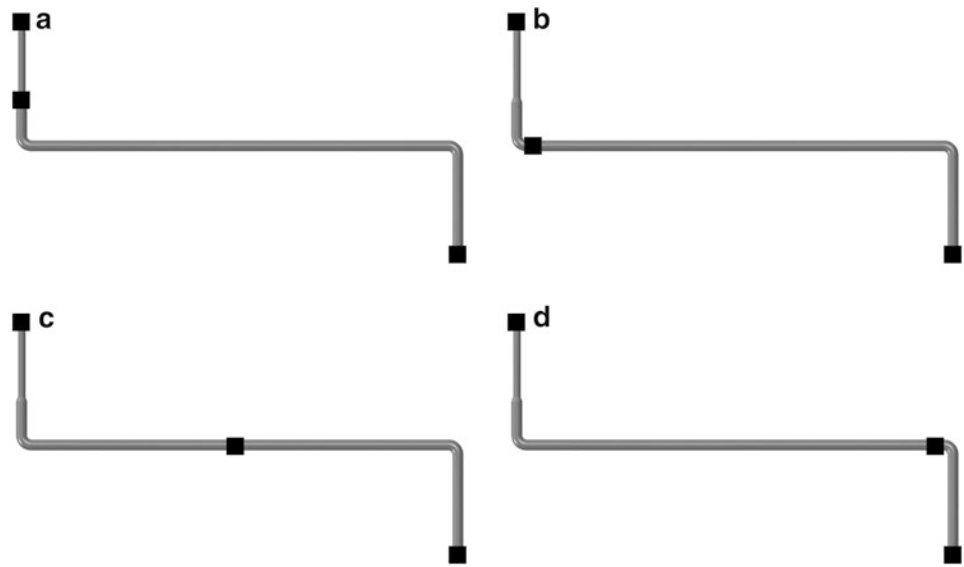
(one in each end of the pipe). Since six condensation nodes were retained, one at each possible location of a support, during the substructure generation process, the same substructure was used throughout this investigation.

In Fig. 42.10, the displacement magnitudes versus frequency for the different support configurations are shown for the two different evaluation point patterns. Displacements evaluated on the ground surface are shown in Fig. 42.10a and displacements evaluated on the tunnel floor are shown in Fig. 42.10b. In Tables 42.3 and 42.4, respectively, the amplification in RMS value of the vibration levels for the different set-ups, related to the set-up involving solely two supports are shown, see Table 42.3 for evaluation on the ground surface and Table 42.4 for evaluation on the tunnel floor.

By comparing the frequency response of the different types (A–D) in Fig. 42.10, it is clearly depicted that displacement peaks can be shifted in frequency by changing the location of the supports, which will result in appreciable difference in the transmitted vibrations. This gives the possibility to minimise the response at the important fundamental frequency of the soil, which can be an important design parameter for vibration-sensitive buildings. It is also seen that it is possible to affect the RMS value of the displacements. It is seen in Fig. 42.10, as well as in Tables 42.3 and 42.4, that it is possible to control and reduce vibrations stemming from a supported water-pipe system by changing the location of the supports, as well as adding or removing supports. In dynamic design of pipe supports it is most often advantageous to have few supports with low stiffness in order to minimise the vibration transmission. In Table 42.4 however, it can be observed that the displacements evaluated on the tunnel floor are reduced for set-up type *A* in relation to the reference set-up with two supports. This shows that, a detailed numerical study is needed in order to investigate the effects of supports and their location.

42.7 Discussion and Future Work

The investigation presented here deals with numerical methods for studying reduction of vibrations stemming from water-pipe systems. A parameter study was performed in terms of the location of the supports to the pipes. For this purpose, reduced order FE models were developed to address the problems in question in a computationally efficient manner. It was concluded that a marked change of vibration characteristics can be achieved by changing the position of the supports. Therefore, the issue of pipe supports should be thoroughly tackled during the design phase of such vibration-sensitive facilities, if the vibration levels in sensitive parts is to be minimised so as to fulfil the vibration requirements.

The study can advantageously be extended by involving more parameters in the investigations such as number of supports, the materials they are made of and their geometry. Likewise, various parameters of different building parts could also be studied such as thickness of the slab and the walls and the elastic modulus of the soil. The biggest contributing factor to the computational cost of the reduced order models are the number of dofs for the soils. A combination of the procedure presented here and an efficient method for reducing the soil, for example, the boundary element method [26, 27], can provide a very time-efficient analysis procedure to be used for vibration transmission problems of this sort.

a

b
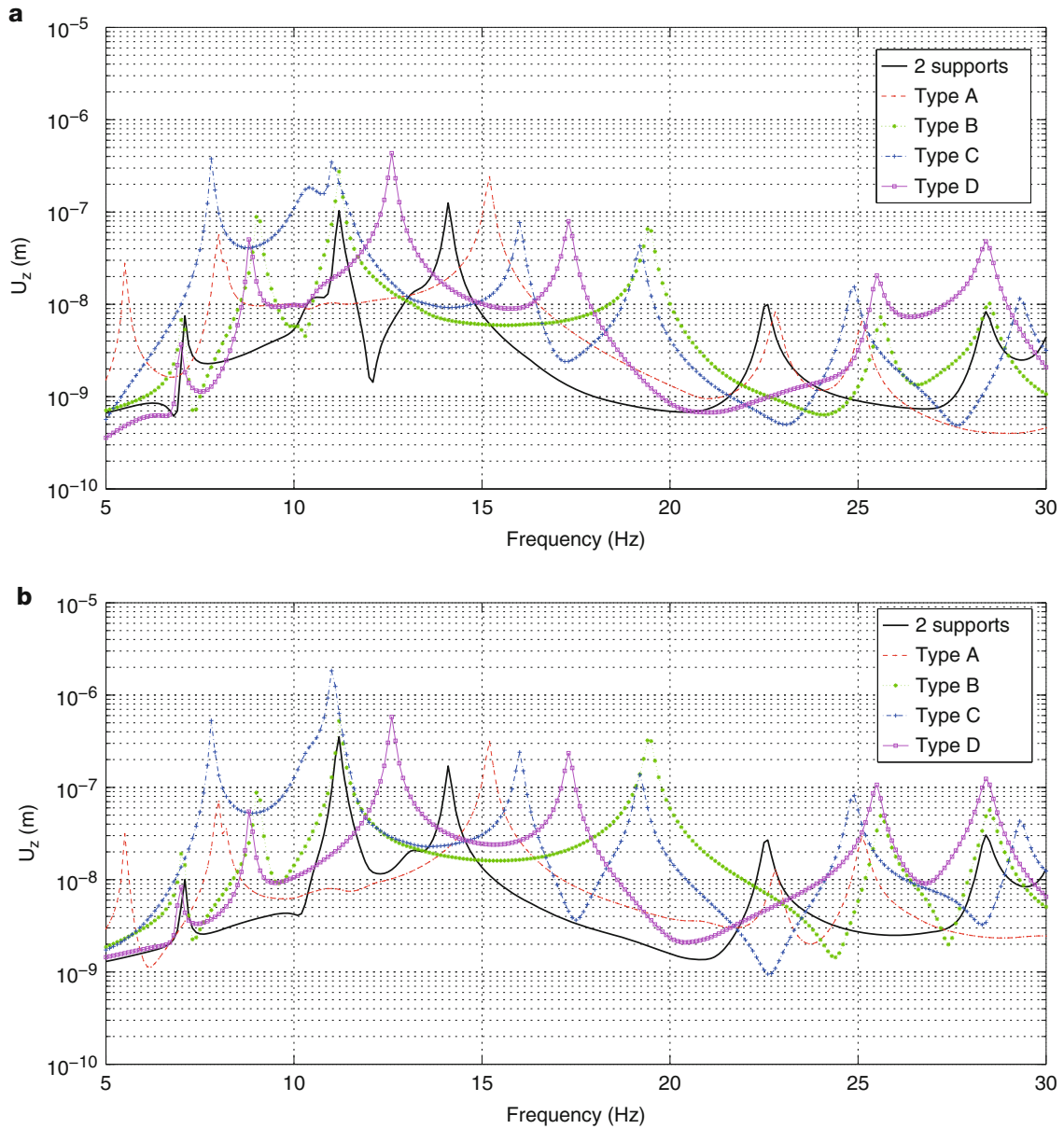
Fig. 42.10 Vertical displacement magnitudes versus frequency for different types of support set-ups, evaluated on (**a**) ground surface (**b**) tunnel floor, see Fig. 42.6

Table 42.3 RMS values for various support set-ups, evaluated on the ground surface, as well as amplification of RMS values as compared to the RMS value of the two support set-up

Set-up	Average RMS value (10^{-9} m)	Amplification (%)
Two supports	0.926	–
Three supports—Type A	1.52	64
Three supports—Type B	1.67	80
Three supports—Type C	3.71	300
Three supports—Type D	2.58	179

Table 42.4 RMS values for various support set-ups, evaluated on the tunnel floor, as well as amplification of RMS values as compared to the RMS value of the two support set-up

Set-up	Average RMS value (10^{-9} m)	Amplification (%)
Two supports	2.16	–
Three supports—Type A	1.97	−9
Three supports—Type B	3.92	81
Three supports—Type C	11.3	423
Three supports—Type D	3.91	81

References

1. Persson P (2010) Analysis of vibrations in high-tech facility. Lund University, Division of Structural Mechanics, TVSM-5164
2. Andersen L, Nielsen SRK (2005) Reduction of ground vibration by means of barriers or soil improvement along a railway track. Soil Dyn Earthq Eng 25(7–10):701–716
3. Persson P, Persson K, Sandberg G (2014) Reduction in ground vibrations by using shaped landscapes. Soil Dyn Earthq Eng 60:31–43
4. Tijsseling AS (1996) Fluid-structure interaction in liquid-filled pipe systems: a review. J Fluids Struct 10:109–146
5. Everstine GC (1997) Finite element formulations of structural acoustics problems. Comput Struct 65(3):307–321
6. Mackerle J (1999) Fluid-structure interaction problems, finite element and boundary element approaches, a bibliography. Finite Elem Anal Des 31:231–240
7. Wiggert DC, Tijsseling AS (2001) Fluid transients and fluid-structure interaction in flexible liquid-filled piping. ASME Appl Mech 54(5):455–481
8. Tijsseling AS, Vardy AE, Fan D (1996) Fluid-structure interaction and cavitation in a single-elbow pipe system. J Fluids Struct 10:395–420
9. Zhang L, Tijsseling AS, Vardy AE (1999) FSI analysis of liquid-filled pipes. J Sound Vib 224(1):69–99
10. Sreejith B, Jayaraj K, Ganesan N, Padmanabhan C, Chellapandi P, Selvaraj P (2004) Finite element analysis of fluid-structure interaction in pipeline systems. Nucl Eng Des 227:313–322
11. Maess MK, Gaul L (2006) Substructuring and model reduction of pipe components interacting with acoustic fluids. Mech Syst Signal Process 20:45–64
12. Maess MK, Gaul L (2007) Simulation of structural deformations of flexible piping systems by acoustic excitation. ASME J Press Vessel Technol 129:363–371
13. Persson P, Persson K, Sandberg G (2014) Fluid-structure interaction analysis of vibration reduction in pipe systems. In: Dynamics of civil structures. Proceedings of the 32nd IMAC, a conference and exposition on structural dynamics, vol 4, pp 459–468
14. Bathe KJ (2006) Finite element procedures. Prentice Hall, New York
15. Zienkiewicz OC, Taylor RL (1994) The finite element method, vols 1 and 2. MacGraw-Hill, London
16. Chopra AK (1995) Dynamics of structures. Prentice Hall, Upper Saddle River
17. Sandberg G (1986) Finite element modelling of fluid-structure interaction. Lund University, Division of Structural Mechanics, TVSM-1002
18. Craig Jr RR, Kurdila AJ (2006) Fundamentals of structural dynamics. Wiley, New Jersey
19. Flóden O, Persson K, Sandberg G (2014) Reduction methods for the dynamic analysis of substructure models of lightweight building structures. Comput Struct 138:49–61
20. de Klerk D, Rixen DJ, Voormeeren SN (2008) General framework for dynamic substructuring: history, review, and classification of techniques. AIAA J 46(5):1169–1181
21. Guyan RJ (1965) Reduction of stiffness and mass matrices. AIAA J 3:380
22. Dassault Systémes SIMULIA (2012), Abaqus documentation 6.12
23. Allemang RJ, Brown DL (1982) A correlation coefficient for modal vector analysis. In: Proceedings of International Modal Analysis Conference, pp. 110–116
24. TYRÉNS (2010) Geotechnical investigation report, Reference number 225686G, Helsingborg 2010-12-10
25. Lysmer J, Kuhlemeyer RL (1969) Finite dynamic model for infinite media. J Eng Mech Div ASCE, 95:859–877
26. Beskos DE (1987) Boundary element methods in dynamic analysis. Part I. Appl Mech Rev 40:1–23
27. Beskos DE (1997) Boundary element methods in dynamic analysis. Part II. Appl Mech Rev 50:149–197

Chapter 43
Seismic Performance Assessment of Steel Frames Upgraded with Self-Centering Viscous Dampers

Osman E. Ozbulut, Robert J. Michael, and Baikuntha Silwal

Abstract This study aims to evaluate the seismic performance of steel frames upgraded with shape memory alloy (SMA)-based self-centering viscous dampers. The proposed Superelastic Viscous Damper (SVD) relies on SMA elements for re-centering capability and employs viscoelastic (VE) damper that consists of two layers of a high damped (HD) blended butyl elastomer compound to augment its energy dissipation capacity. First, experimental tests are conducted to characterize behavior of SMA elements and VE damper and to assess the influence of various parameters such as displacement amplitude and loading frequency on their mechanical response. A prototype of the SVD is designed and fabricated. Then, an analytical model of a four-story steel special moment frame building with the installed SVDs is developed to determine the dynamic response of the structure. The incremental dynamic analysis is used to evaluate the behavior of controlled and uncontrolled buildings under 18 different ground motion records. The analytical results indicate that the buildings upgraded with the proposed passive control device effectively mitigate the peak interstory drifts and residual story drifts.

Keywords Shape memory alloys • Passive control • Viscoelastic damper • Earthquakes • Steel structures

43.1 Introduction

Passive energy dissipation systems can favorably affect the dynamic response of civil structures in both extant construction (in retrofit scenarios) as well as new design. These devices, which require no additional energy to operate, provide improved energy dissipation in structural systems. A number of passive energy dissipation systems have been proposed and developed to mitigate damaging effects of natural hazards on structures [1]. Passive energy dissipation devices can be grouped into two main categories: hysteretic devices and rate-dependent devices. Examples of hysteretic devices include metallic yielding devices and friction devices. Energy dissipation in hysteretic devices depends primarily on relative displacements within the device. These devices add initial stiffness until yielding or slip occurs and dissipate energy especially at large deformations. Metallic devices usually have a limited number of working cycles and may require replacement after a strong event. Friction devices may lead to permanent deformations if no restoring force mechanism is provided. Examples of rate-dependent devices include fluid viscous dampers and viscoelastic dampers. These devices can dissipate energy at all levels of vibration and may provide some stiffness [2]. The energy dissipation capacity of rate-dependent devices depends on the velocity across the device.

In addition to the immediate structural response to a dynamic event, the amount of residual deformation—once motion has stopped—is an important metric. McCormick et al. [3] studied the importance of residual drifts for building structures considering both structural safety and human elements. They concluded that the residual drift in buildings greater than 0.5 % might cause a complete loss of structures from an economic perspective. Another recent study [4] reported that the residual inter-story drift in traditional moment resisting frames greater than 0.5 % may cause human discomfort when structure subjected to long-duration earthquake motions. Erochko et al. [5] investigated the residual drift response of special moment-resisting frames (SMRFs) and buckling-restrained braced frames (BRBFs) and reported that both types of building systems reveal extensive residual drifts; 0.5–1.2 % for SMRFs and 0.8–1.8 % for BRBFs.

A number of studies have been carried out to develop new structural systems that can provide stable energy dissipation with full re-centering capabilities. Often referred to as self-centering or re-centering, these systems provide a restoring

O.E. Ozbulut (✉) • B. Silwal
Department of Civil and Environmental Engineering, University of Virginia, Charlottesville, VA, USA
e-mail: ozbulut@virginia.edu

R.J. Michael
Department of Mechanical Engineering, Gannon University, Erie, PA, USA

force which is either independent from or acts in addition to energy dissipation capabilities. Garlock and Li [6] evaluate the inherent energy-absorbing and re-centering characteristics of a self-centering moment-resisting frame subjected to earthquake loading. Through experimental and numerical simulation, the authors find that the system exhibits both energy dissipation and self-centering capacity. However, a trade-off exists between improving self-centering behavior and energy dissipation in overall structural performance. Eatherton and Hajjar [7] conducted a parametric study to evaluate the necessary maximum re-centering force relative to the yield strength of supplemental energy-absorbing devices as well as the ambient capacity of the structure.

Shape memory alloys (SMAs) are metallic alloys that can fully regain their original shape upon being deformed [8]. These materials are of particular interest primarily due to their unique re-centering ability and energy dissipating capacity, excellent corrosion resistance, and high fatigue resistance. Qian et al. [9] tested a device that relied solely on SMA wire for energy absorption while explicitly considering its re-centering behavior. In particular, they concluded that the response is not sensitive to loading frequencies greater than 0.5 Hz, and that by varying the level of pretension in the device, its behavior can be adapted to suit the parameters of a given application. Li et al. [10] also tested SMA based devices, but in two separate configurations: a tension-type—similar to Qian et al. —with deformations parallel to the direction of excitation, and scissor-type. The authors compared experimental results to non-linear simulations—concluding that the two agreed; both device configurations were effective in reducing seismic response. However, the scissor-type was more successful due to displacement magnification characteristics of the configuration.

However, previous studies on SMAs indicate that the quantity of equivalent viscous damping provided by superelastic SMA wires or bars is not sufficient to render the use of SMAs as the sole damping device implemented in a tall structure subjected to severe dynamic loadings [11]. Therefore, several researchers have explored the development of SMA-based control devices with supplemental energy dissipation capabilities. Yang et al. [12] and Zhu et al. [13] adopted a hybrid strategy by combining SMA wire with traditional hysteretic strategies; the former used energy absorbing struts while the later utilized a sliding friction-based configuration. Both devices were successful in improving structural response to dynamic loading while providing excellent re-centering capabilities. Ozbulut and Hurlebaus [14] proposed an SMA-based semi-active device that combines a variable friction damper and SMA wires and evaluated the performance of the hybrid device through numerical simulations. Ponzo et al. [15] completed numerical analysis and experimental testing in order to characterize a hybrid SMA and viscous damper device. They concluded that both methods demonstrated that the device was successful in limiting maximum interstory drift and acceleration. They also proposed an iterative design procedure in order to optimize device design relative to desired performance parameters.

This paper proposes a conceptual design for an innovative, SMA-based damper. The Superelastic Viscous Damper (SVD), combines the excellent energy-dissipating capacity of a conventional viscoelastic damper with the re-centering properties of SMA bars in a single device which demonstrates an improved, hybrid response. Compared with conventional structural control devices, the proposed SVD is an attractive alternative in both performance and design efficiency.

43.2 Shape Memory Alloy Cables

Shape memory alloy cables have been recently developed as an alternative and new structural element [16]. They leverage the superior mechanical characteristics of small diameter SMAs into large-size structural tension elements and possess several advantages over SMA bars. In this study, SMA cables are considered for the development of a hybrid seismic device. The material used in this research is SMA cable made of Nickel Titanium (NiTi) and obtained from Fort Wayne Metals, Research Products Corp. The SMA cable, which was produced in a helix configuration, composed of seven strands and each strand had seven wires. Each wire had a diameter of 0.885 mm providing outer cable diameter of 8 mm and total cross sectional area of 30.14 mm^2. Figure 43.1 presents schematic drawing of the cable cross section, and longitudinal section of the cable.

The uniaxial tensile tests are conducted at various loading rates and strain amplitudes to characterize the superelastic properties of the SMA cable and study the rate-dependent mechanical response of the SMA cable under dynamic loads. The test samples are obtained by cutting the cable into pieces with a length of 150 mm. Before formal tests, a training test procedure that consists of 10 load cycles at a stress amplitude of 450 MPa at 0.01 Hz was applied. Then, the specimen was cycled in a displacement-controlled test for three cycles at a loading frequency of 0.05 Hz and at about 5 % strain to calibrate the strain measurements of MTS system. The displacement data were recorded using both the MTS data acquisition and Digital Image Correlation (DIC) system provided by Correlated Solution, Inc. with a rate of 10 Hz. The strain data calculated from the DIC system were then used as a basis to calibrate the strain measurements of the MTS system. Afterwards, a thorough experimental testing program is followed.

Fig. 43.1 Shape memory cable: cross-sectional and longitudinal views
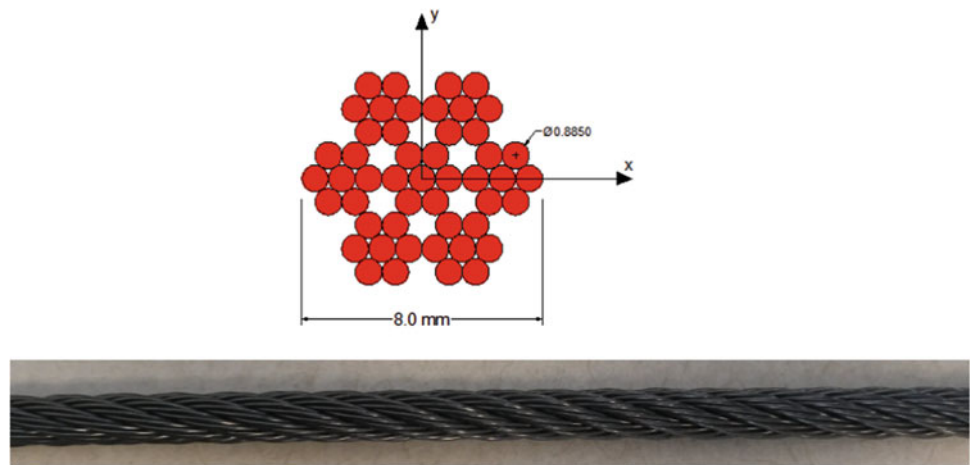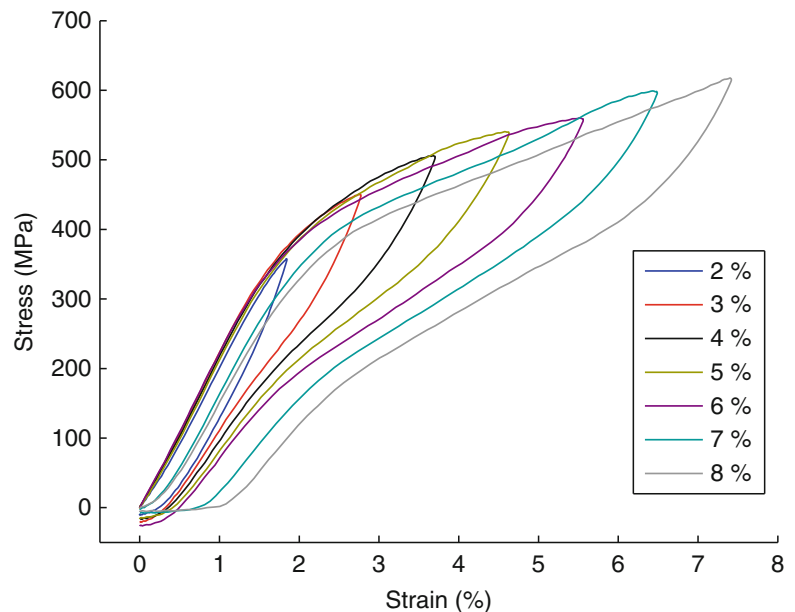

Fig. 43.2 Stress-strain curves of SMA cable tested under varying values of maximum applied strain

In order to investigate the cable behavior under different strain amplitudes, the cable was cycled, with a frequency of 0.05 Hz, to obtain strains of 2 %, 3 %, 4 %, 5 %, 6 %, 7 %, and 8 %. All the tests lasted for three cycles except the 6 % test, which lasted for six cycles to investigate the effect of cyclic loads on cable behavior. Figure 43.2 represents stress-strain curves for experimental tests at strain amplitudes varying from 2 % to 8 %. It can be observed that the material exhibits well-known flag-shaped cycles, which is a common behavior of SMAs, at 2–6 % strains. The SMA cable recovers almost all of its deformations upon unloading when it is loaded up to strain amplitude of 6 %. On the other hand, recorded residual strains at strain amplitudes of 7 % and 8 % are approximately 0.9 % and 1.1 %, respectively. It can be also seen that the strength of the cable decreased at those strain amplitudes possibly due to the failure of individual wires.

Tests matrix was then extended to include the behavior of the cable under higher frequency cyclic loads. The tensile loads were applied to the cable in a displacement controlled test to obtain 6 % strain using test frequencies of 0.1, 0.5, 1.0, and 2.0 Hz. Due to the limited capability of the DIC system at higher test frequencies, tests data was recorded using the MTS data acquisition system only. Figure 43.3 shows the evolution of stress-strain curves for six cycles to a maximum strain of 6 %. As shown in the figure, the stress level for the forward transformation decreases, while for the reverse transformation the stress increases slightly at higher number of cycles. It can also be observed that the increment of the residual strain progressively reduces during cyclical loading. This can be explained as the permanent localized deformations accumulate in the early cycles and start to disappear in later cycles.

Fig. 43.3 Stress-strain curves at 6 % strain level under different loading frequencies
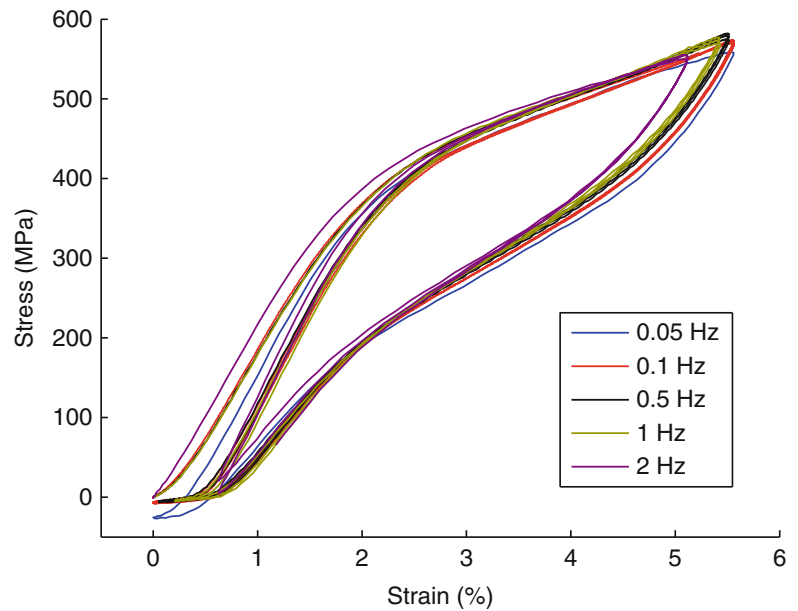
43.3 High Damped Butyl Elastomer

The HD butyl series is compounded specifically to produce high damping at moderate to low stiffness. These elastomers are currently in use in various VE dampers and a new base isolation system used to isolate storage racks from seismic events [17–19]. For these devices, the HD butyl has resulted in an increase in damping by more than a factor of two over traditional elastomers. In this study, the HD butyl compounds are considered for use in an SMA-based hybrid damper.

Butyl rubber is a synthetic rubber produced by polymerization of about 98 % isobutylene with about 2 % of isoprene. Butyl rubber is also known as polyisobutylene or PIB. It has excellent impermeability, inherently high damping and its long polymer chains give it excellent flex properties. The first major application of butyl was tire inner tubes because of its excellent impermeability to air. Butyl is also used extensively in vibration isolators due to its high damping. Other favorable properties include a low glass transition temperature, low modulus, low compression set and excellent resistance to aging and to weathering from atmospheric exposure.

The HD butyl compounds are highly loaded which means that the % rubber hydrocarbon (rhc) is lower than traditional industrial butyls. Since there is less elastomer in it, the damping tends to go up because carbon black and oil, the typical materials used to lower the rhc, generally have higher damping than the rubber alone. In addition, these compounds utilize a grade of carbon black that builds hardness slowly so in order to get an equivalent hardness to traditional butyls, more black is needed which tends to drive up damping. Also these compounds use a higher viscosity plasticizer, which tends to drive up damping even more.

Natural Rubber (NR) is a multi-purpose elastomer and the elastomer of choice for most conventional seismic base isolators (where supplemental damping such as a lead core is added). NR rubber offers high tensile strength, high elongation and resilience, good fatigue, low damping, as well as low cost. It should be noted that the NR polymer is intrinsically resilient and its formula does not contain ingredients that contribute heavily to damping.

In order to illustrate the differences of a typical NR compound, typical industrial butyl and HD butyl, static and dynamic shear tests were conducted. The NR and butyl compounds were 50 durometer Shore A, and HD butyl was 45 durometer Shore A. All testing performed is to ASTM D5992, which utilizes the Fast Fourier Transform (FFT) method to determine important elastomer properties such as static shear modulus (G), dynamic shear modulus (G'), loss factor (η) and other properties. The specimen geometry is a double shear with two identical rubber elements symmetrically disposed on opposite sides of a central rigid member. This specimen geometry is specified in ASTM D5992 and carefully designed to yield a length/wall thickness ratio of 8 ($=1.6''/.2''$) to achieve a state of pure shear. Also, the shear area and thickness allows modulus and stiffness to be easily converted (i.e., $G = K/10$ or $K = 10G$). A brief property summary for three compounds is provided in Table 43.1.

The static shear load deflection curves shown in Fig. 43.4 illustrate the difference in stiffness between the three compounds. The curve for NR and butyl shows an increase in stiffness at larger strains due to strain crystallization. For HD butyl, static modulus changes most at lower strains and softens by a factor of 2 as the strain increases from 10 % to

Table 43.1 Properties of different compounds

Polymer type	Static shear modulus G at 100% strain (MPa)	Dynamic shear modulus, $G\%$ (MPa) and loss factor, η at 10% strain, 1 Hz	Dynamic shear modulus, $G\%$ (MPa) and loss factor, η at 100% strain, 1 Hz
50 Duro natural Rubber	0.52	$G' = 0.75,\ \eta = 0.09$	$G' = 0.50,\ \eta = 0.08Z$
50 Duro industrial (generic) buty	0.40	$G' = 0.75,\ \eta = 0.30$	$G' = 0.41,\ \eta = 0.29$
45 Duro high damped butyl	0.23	$G' = 0.58,\ \eta = 0.40Z$	$G' = 0.24,\ \eta = 0.35$

Fig. 43.4 Static shear stress versus shear strain for three compounds
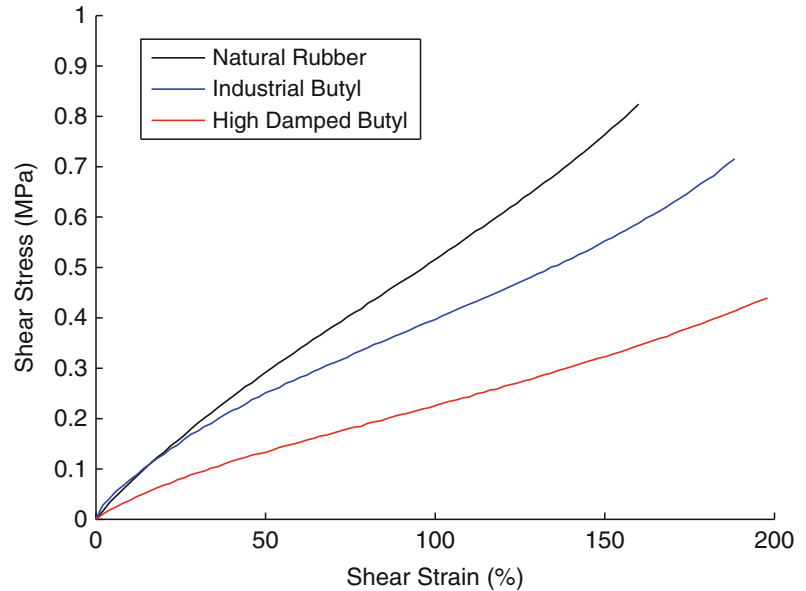
200 %. However, for strain values between 100 % and 200 %, the modulus is nearly constant (curve is nearly linear). Since the actual application strain will be in this range for a seismic application, it can be assumed that the modulus and therefore stiffness will be somewhat constant for the actual operating strain range.

The stress-strain hysteresis loops under shear for the three materials are shown in Fig. 43.5. The loops, recorded for +/−100 % strain and 1 Hz, show the difference between the three materials. The HD butyl loop has more area (higher damping) while the NR loop has a higher stiffness. Similarly, the HD butyl is significantly softer than the industrial butyl yet has slightly more damping. For the hybrid damper proposed in this study, the viscoelastic component is expected to provide high damping at low stiffness, i.e. the HD butyl is an ideal elastomer for this application. The combination of low stiffness and heavily damped is atypical for an elastomer and a direct result of compounding described above.

Figure 43.6 shows loops at a constant frequency of 1 Hz and cyclic strains of +/−10 %, +/−50 %, +/− 100 % and +/−200 %. This figure shows that properties are significantly impacted by strains. Modulus varies from 0.55 MPa at 10 % to 0.19 MPa at 200 % cyclic strain (more than a factor of 2 difference). Loss factor is impacted less but still varies from 0.39 at 10 % to 0.28 at 200 % cyclic strain.

In order to investigate the effects of loading rate on the performance of the HD butyl, shear tests were conducted at up to four specific and common frequencies (0.1, 0.5, 1.0, and 2.0 Hz) and at up to three specific and common strain (displacement) amplitudes (50 %, 100 %, and 200 %). In actual seismic application, the elastomer strain is expected to see between 100 % and 200 % strain and a frequency of .5–2 Hz. So the test range is adequate to determine mount behavior in actual use. All tests were conducted at room temperature. All samples were pre-flexed (conditioned) twice to eliminate Mullin's effect. Mullin's effect is a softening that occurs during the first several cycles of deformation due to breaking of weak bonds. After the first few cycles, the material stabilizes with little change in subsequent cycles. Figure 43.7 shows shear strain-stress curves under various loading frequencies for the HD butyl at various strain amplitudes. The results reveal that the dynamic shear modulus increases with increasing loading frequency. However, from Figs. 43.6 and 43.7, it can be seen that properties are more sensitive to strain (displacement) than frequency. For increasing frequencies, the lower branch of the hysteresis curve shifts downward. Also note the nonlinearity associated with the 200 % strain curves. In addition, properties seem to be more frequency sensitive at smaller dynamic strains. In other words, properties vary less at +/−200 % than they do at +/− 50 % dynamic strain across the frequency range of 0.1–2 Hz.

Fig. 43.5 Hysteresis loops for three compounds at a frequency of 1 Hz and 100 % strain
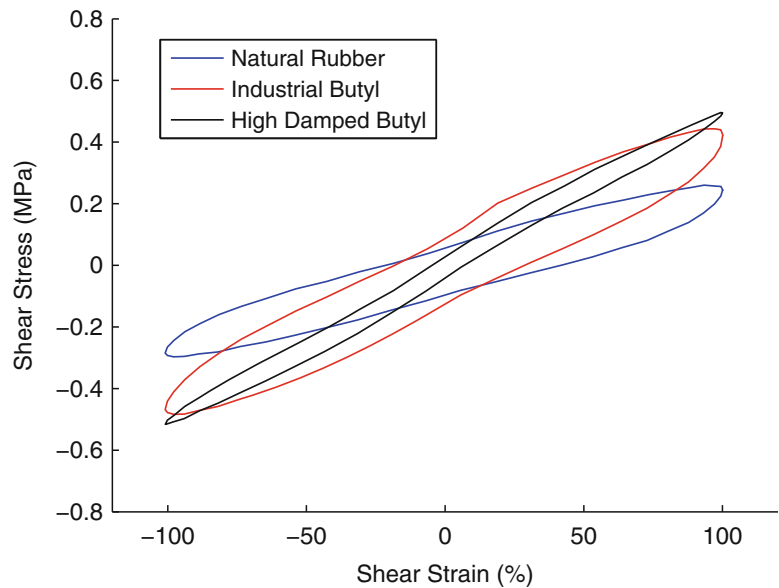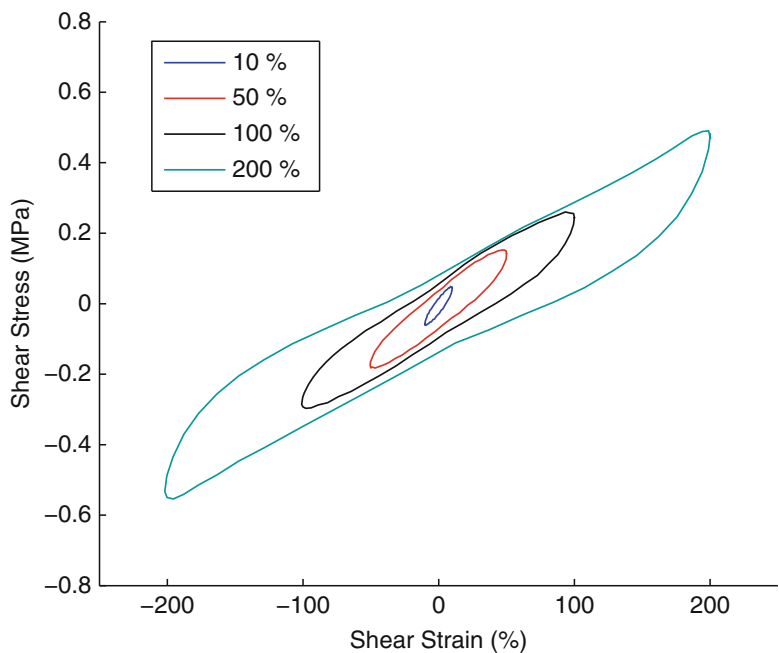

Fig. 43.6 Hysteresis loops for HD butyl at a frequency of 1 Hz and various strains

43.4 Superelastic Viscous Damper

The proposed Superelastic Viscous Damper combines re-centering capabilities of shape memory alloys with the energy dissipation ability of viscoelastic devices. The 3D renderings of the SVD and schematic diagrams of the device in the undeformed and deformed positions are given in Fig. 43.8. The module comprises two high damped elastomer compounds, sandwiched between and bonded to three identical steel plates and installed SMA cables. Each SMA cable forms a continuous loop; wrapping the loops around the outer two plates improves compactness and efficiency. Whether the device itself undergoes a compressive or tensile loading, the configuration ensures that the SMA elements will remain under tension.

Along the top and bottom of the device, the wires are threaded through guides, which ensure that the wires remain parallel to the direction of shear deformation in the elastomer layers. As the device moves through its design displacements, the SMA cables apply a re-centering force to the center plate through a second set of wire guides. Composed of three C-channels, two
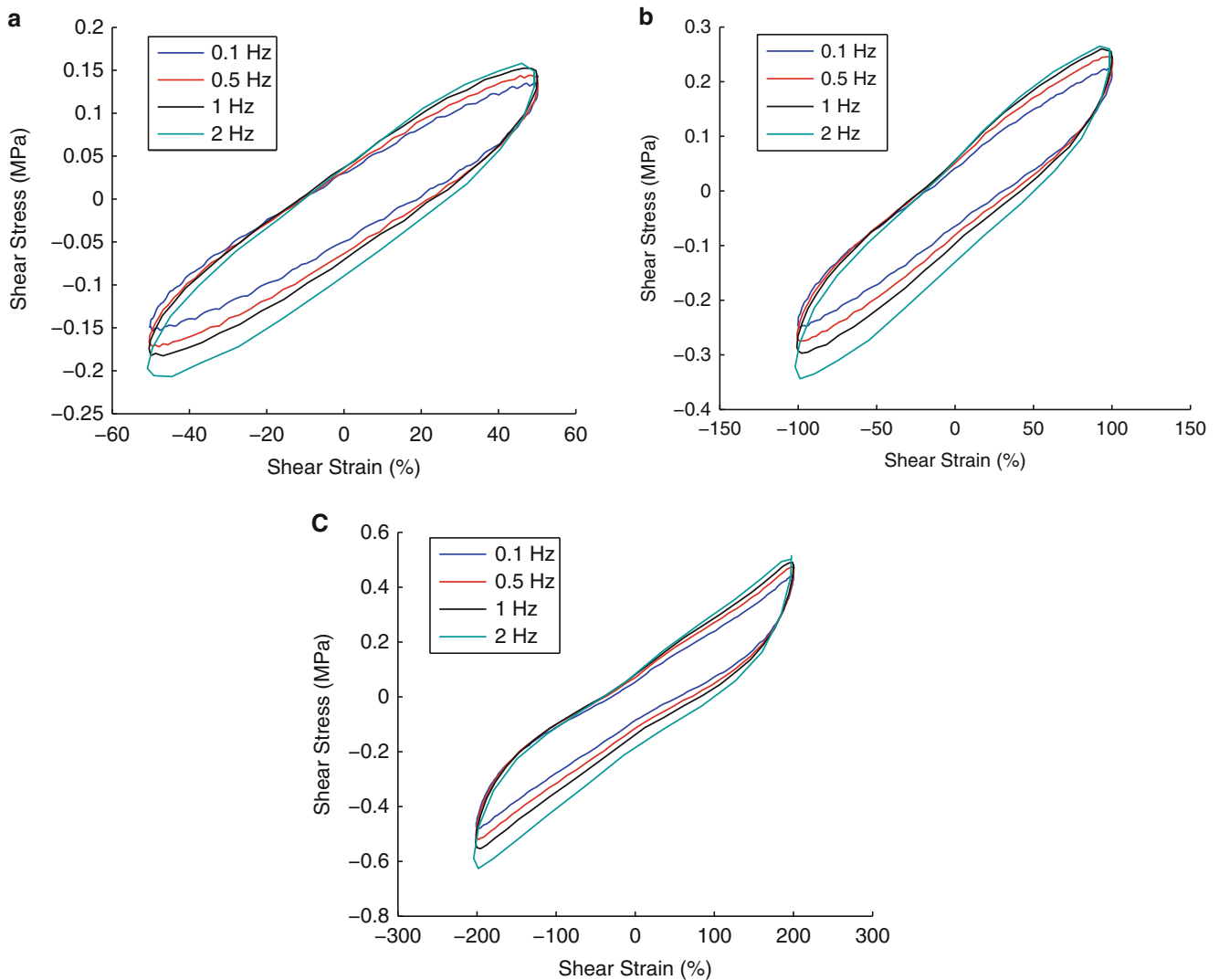
Fig. 43.7 Hysteresis loops for HD butyl at various frequencies and at (**a**) 50 % strain, (**b**) 100 % strain, and (**c**) 200 % strain

angle brackets, and four crescent-shaped steel sections (one for each strand), each guide distributes the design loads over a longer length of wire (the arc-length of each crescent, compared to the thickness of the center plate) in order to eliminate problematic stress concentrations.

Figure 43.9 shows the typical force-deformation curves of the SVD and its subcomponents. In the SVD, SMA bars are mainly used for its re-centering capability and the viscoelastic device is mainly employed to dissipate seismic energy. By a judicious specification of design parameters of each individual component, a re-centering device with enhanced energy dissipation can be realized.

43.5 Numerical Models

43.5.1 Building Description

In order to assess the performance of the proposed damper in mitigating seismic response of structures, a four-story steel building developed for the FEMA P-695 [20] is selected for numerical analyses. One of the perimeter steel special moment frames (SMF) that serves as the seismic-force-resisting system of the structure is analyzed and illustrated in Fig. 43.10. The building is designed with Reduced Beam Section (RBS) connection details in accordance with design standards, ASCE/SEI
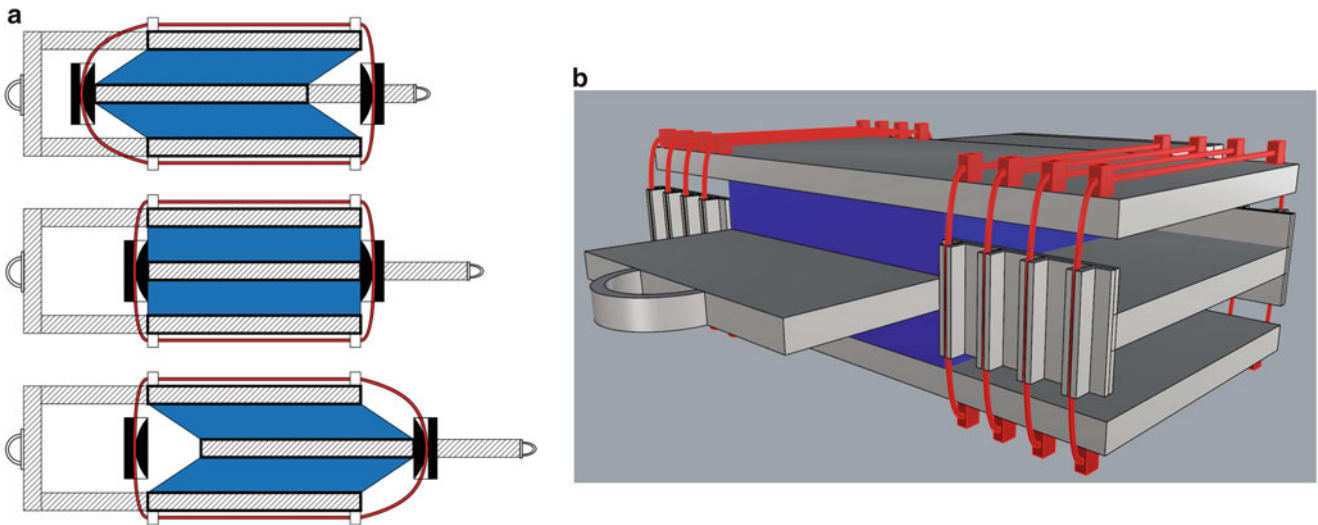
Fig. 43.8 (**a**) A schematic diagram of SVD at its undeformed and deformed positions, and (**b**) 3D Rendering of SVD
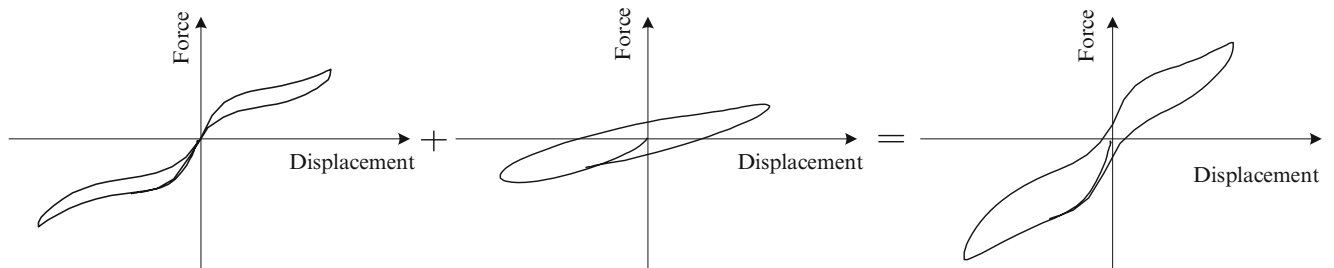
Fig. 43.9 Force-deformation curves of the SVD and its sub-components
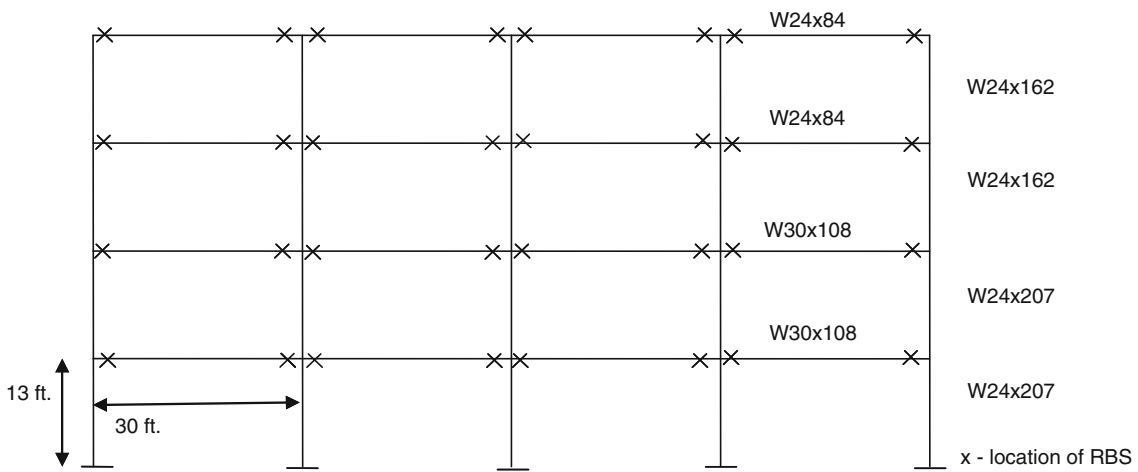
Fig. 43.10 Index archetype model of four-story steel special moment frame [20]

7–05 [21] and ANSI/AISC 341–05 [22]. The building is designed for a site located in Seismic Design Category (SDC) D and based Maximum Considered Earthquake (MCE) spectral demand. The seismic masses of the first, second, and third levels are 4.26×10^5 kg, and the mass of the roof level is 4.74×10^5 kg. Based on the eigenvalue analysis, the fundamental period of the building is found to be 1.05 s.

Fig. 43.11 Experimental stress-strain curve and model prediction
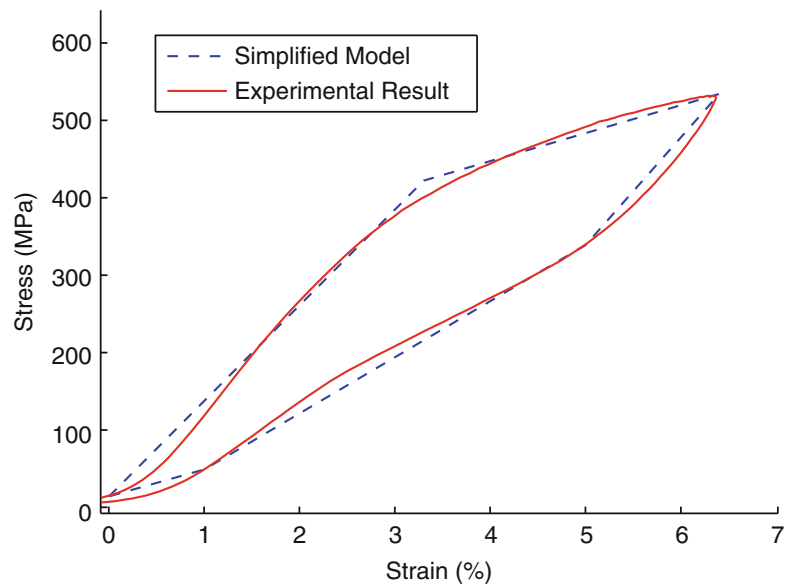
43.5.2   Analytical Models

The analytical models for four-story steel frame building and superelastic viscous device are developed in OpenSees, a finite element framework for nonlinear and dynamic analysis of structural systems. The plane frame elements of the structure are modeled as elastic beam-column elements with concentrated inelastic springs using the Ibarra-Krawinkler hysteretic model [23] with the bilinear hysteretic rules. The model considers cyclic stiffness and strength deterioration of the plastic hinges. Moment-rotation and cyclic deterioration parameters are adopted from Lignos [24]. The yield stress of structural steel is assumed to be equal to 375 MPa. Panel zones of beam-column joints are modeled using Joint 2D elements, which is also known as Altoontash-Lowes beam-column joint element [25]. To consider the P-Δ effects, leaning columns are connected to the plane frame with axially rigid truss elements at each story level. The model assumes Rayleigh damping with a 2 % damping ratio for the first and third modes.

To simulate the response of NiTi SMA cables of SVD, an element with uniaxial self-centering material property and finite-length is employed in OpenSees. The parameters of the self-centering material are assigned in accordance with the experimental tests results discussed above. In particular, since the SMAs will be subjected to dynamic loading rates during a seismic event, the material parameters for the SMA element are selected to match experimental response of the SMA cables at high loading frequencies. The stress-strain curves obtained from experiment and from simplified model implemented in OpenSees are shown in Fig. 43.11. It can be seen that the model predicts the response of NiTi SMA cables reasonably well. Hysteretic response of viscoelastic component of SVD is modeled using the Maxwell material property, which combines a linear spring and nonlinear dashpot in series. Based on the experimental test results discussed above, the parameters for the Maxwell model is selected as follows: elastic spring coefficient $K = 0.80$ kN/mm, viscous damping coefficient $C = 0.96$ kN (s/mm), nonlinear exponent coefficient $\alpha = 0.8$.

43.5.3   Ground Motions

In this study, 18 Far-Field ground motion records selected from PEER NGA database using the criteria described in the FEMA P695 [20] methodology are employed for nonlinear time history analyses. The set includes strong-motion records, i.e., records with PGA > 0.2 g and PGV > 15 cm/s, from event magnitudes range from M6.5 to M.7.6 and from stiff soil sites (site Class D) and very stiff soil sites (site Class C). The ground motions are normalized as described in FEMA P695 to eliminate unwarranted variability between records due to inherent differences in site conditions, source distance, source type, and event magnitude. Figure 43.12a shows acceleration spectra for individual records and the median response spectrum.

Ground motions are collectively scaled to maximum considered earthquake (MCE) level, as defined in ASCE/SEI 7–05, such that the median spectral acceleration of the record set matches the design spectral acceleration at the fundamental period of the benchmark structure. Figure 43.12b illustrates MCE response spectrum for Seismic Design Category (SDC) D_{max} and the median spectrum of the selected ground motions anchored to MCE response spectrum of SDC D_{max} at a period of 1.05 s.
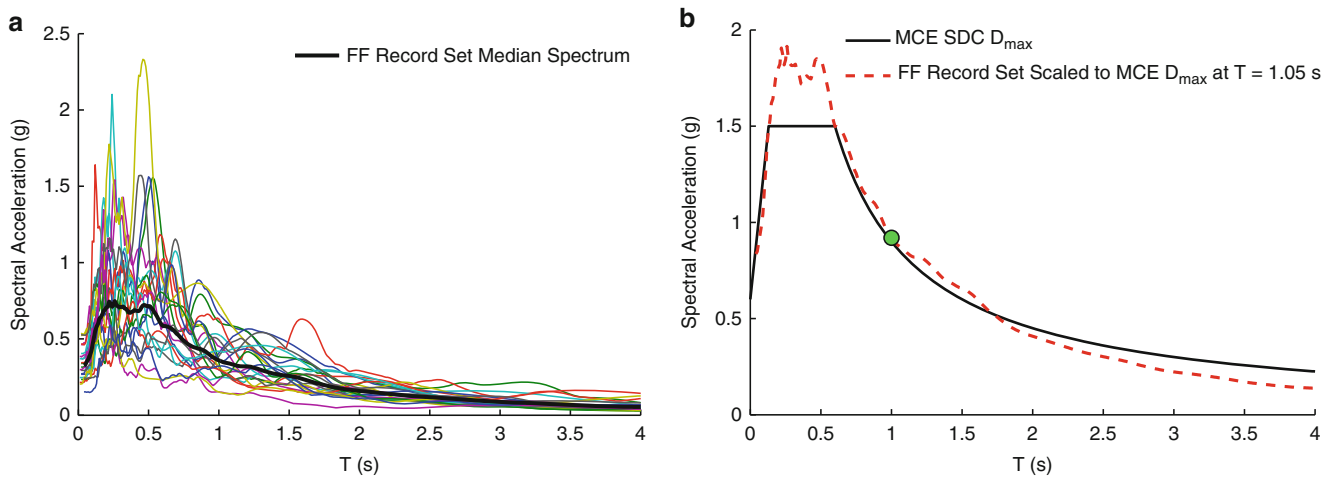
Fig. 43.12 (**a**) Acceleration spectra for individual ground motions and median spectrum, (**b**) Median spectra of the ground motion record set anchored to MCE response spectra of SDC Dmax at fundamental period of the structure
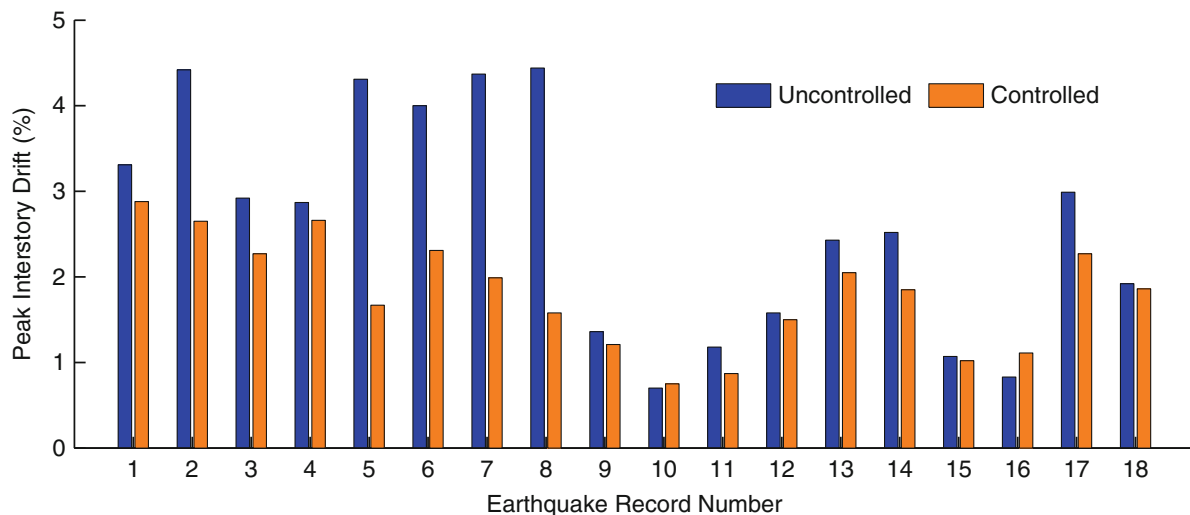

Fig. 43.13 Peak interstory drift for individual MCE level ground motions

43.6 Nonlinear Response History Analyses

Nonlinear response time history analyses of the four-story building with the set of 18-scaled ground motion records are conducted to evaluate efficacy of the SVD in mitigating the seismic response of structures. The SVDs are installed at the middle two bays at each story level using a chevron brace configuration. The number of control devices connected to the first and second stories, and the third and fourth stories are 16 and 11, respectively for the entire structure. The cross-sectional area and the length of the SMA elements in each SVD are set to be 402 mm^2 and 2 m, respectively. The selected cross-sectional area corresponds to 8 SMA cables with a diameter of 8 mm for each device. The length of the SMA elements is selected such that the strains experienced by the SMA elements are below 6 % strain for the maximum design interstory drifts.

Structural responses of the uncontrolled building and the building with installed hybrid dampers are computed under each ground motion record for MCE level earthquakes. Figures 43.13 and 43.14 illustrate the maximum interstory drift ratio and maximum residual interstory drift ratio, respectively under MCE level ground motion records for the uncontrolled and controlled buildings. It can be seen that the installed SVDs reduces the drift demand of the three-story building under almost all MCE level earthquakes. In particular, the median peak interstory drift is 2.2 % for the uncontrolled frame and 1.6 % in case SMA dampers are installed. It should be also noted that significant value of residual drifts (up to 4.4 %) occurred in the uncontrolled building under several ground motion records while the building equipped with SVDs considerably reduce
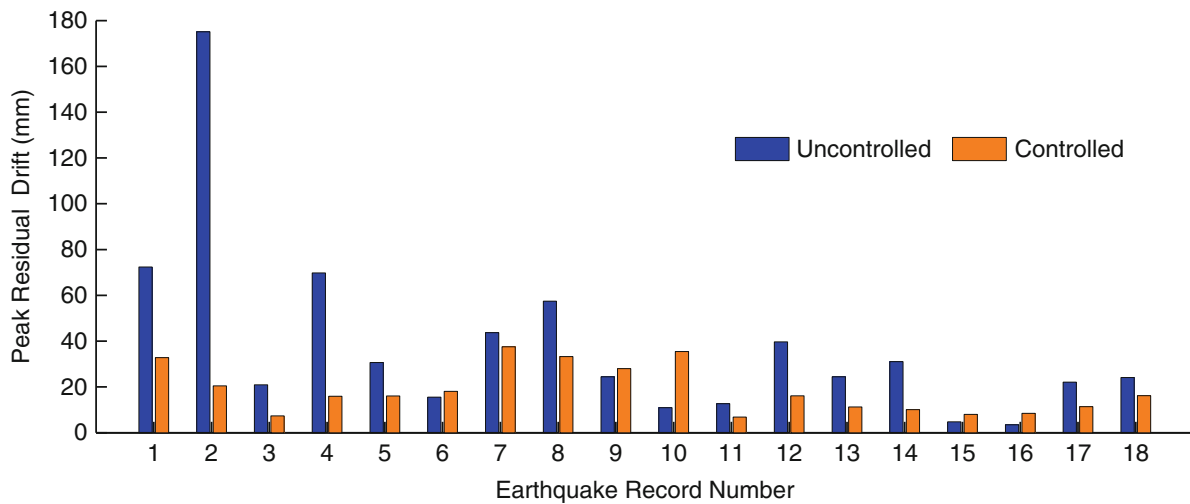
Fig. 43.14 Peak residual story drift for individual MCE level ground motions
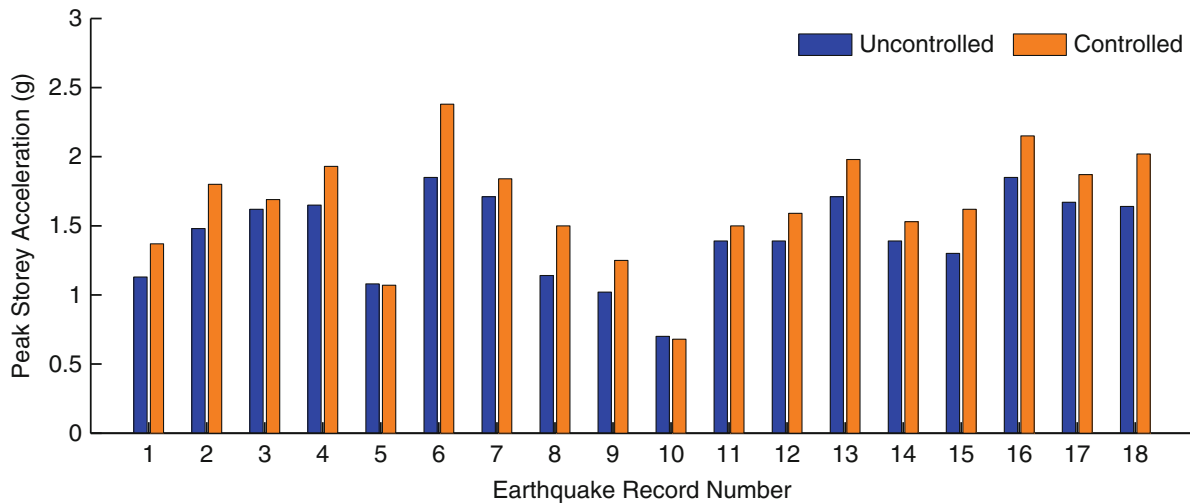
Fig. 43.15 Peak storey acceleration for individual MCE level ground motions

the residual drifts for most of the cases. Figure 43.15 illustrates the peak floor acceleration under MCE level ground motion records for the uncontrolled building and the building controlled with SVDs. It can be seen that the peak acceleration response slightly increase for the steel frame with installed dampers. However, this increase is only an average of 15 % for 18 ground motions.

43.7   Conclusions

The seismic performance of steel frame structures upgraded with a hybrid damper is investigated in this study. The damper, named as superelastic viscous damper, leverage the inherent recentering capability of SMA cables and energy dissipation ability of an elastomer compound for superior seismic performance. A heavily damped butyl compound, which provides high damping at low stiffness, is considered for the viscoelastic component of the hybrid damper. Experimental tests on the subcomponents of the hybrid damper, i.e., HD butyl compound and SMA cables, are conducted to characterize their mechanical response. Performance and effectiveness of the proposed damper in mitigating response of steel frame buildings under MCE level seismic loads are assessed through numerical studies. A four-story special steel moment frame structure is modeled as conventional moment-resisting frame and the frame with installed superelastic viscous dampers. A suite of 18 strong ground motion records are normalized and scaled as described in FEMA P695. Nonlinear response history analyses are

conducted and the peak response quantities are evaluated. Results show that the interstory drift demands and residual drifts of the buildings subjected to MCE level earthquakes can significantly be reduced with installed SVDs without a considerable increase in peak acceleration demand.

References

1. Symans MD, Charney FA, Whittaker AS, Constantinou MC, Kircher CA, Johnson MW, McNamara RJ (2008) Energy dissipation systems for seismic applications: current practice and recent developments. J Struct Eng 134(1):3–21
2. Soong TT, Dargush GF (1997) Passive energy dissipation system structural engineering. Wiley, Chichester
3. McCormick J, Aburano H, Ikenaga M, Nakashima M (2008) Permissible residual deformation levels for building structures considering both safety and human elements. In: Proceedings of the 14th world conference earthquake engineering, Seismological Press of China, Beijing, Paper ID 05-06-0071
4. Bojórquez E, Ruiz-García J (2013) Residual drift demands in moment-resisting steel frames subjected to narrow-band earthquake ground motions. Earthq Eng Struct Dyn 42(11):1583–1598
5. Erochko J, Christopoulos C, Tremblay R, Choi H (2010) Residual drift response of SMRFs and BRB frames in steel buildings designed according to ASCE 7–05. J Struct Eng 137(5):589–599
6. Garlock ME, Li J (2008) Steel self-centering moment frames with collector beam floor diaphragms. J Constr Steel Res 64(5):526–538
7. Eatherton MR, Hajjar JF (2011) Residual drifts of self-centering systems including effects of ambient building resistance. Earthq Spectra 27(3):719–744
8. Ozbulut OE, Hurlebaus S, Desroches R (2011) Seismic response control using shape memory alloys: a review. J Intel Mater Struct 22:1531–1549
9. Qian H, Ren W, Li H, Song G, Chen H (2009) Experimental investigation of steel structure with recentering shape memory alloy damper. In: Second international conference on smart materials and nanotechnology in engineering, Weihai, China, pp 74936Q–74936Q
10. Li H, Mao C, Ou J (2008) Experimental and theoretical study on two types of shape memory alloy devices. Earthq Eng Struct Dyn 37:407–426
11. Ozbulut OE, Hurlebaus S (2011) Re-centering variable friction device for vibration control of structures subjected to near-field earthquakes. Mech Syst Signal Process 25:2849–2862
12. Yang CSW, DesRoches R, Leon RT (2010) Design and analysis of braced frames with shape memory alloy and energy-absorbing hybrid devices. Eng Struct 32:498–507
13. Zhu S, Zhang Y (2008) Seismic analysis of concentrically braced frame systems with self-centering friction damping braces. J Struct Eng 134:121–131
14. Ozbulut OE, Hurlebaus S (2012) Application of an SMA-based hybrid control device to 20-story nonlinear benchmark building. Earthq Eng Struct Dyn 41:1831–1843
15. Ponzo FC, Dicesare A, Nigro D (2008) Visco-re-centring energy dissipating system for seismic protection of framed buildings. Recent Res Inform Sci Appl 7(4):268–273
16. Daghash S, Ozbulut OE, Sherif M (2014) Shape memory alloy cables for civil infrastructure systems. In: Proceedings of the ASME 2014 smart materials, adaptive structures and intelligent systems, SMASIS2014-7562, Newport, September
17. Sause R, Ricles J, Mahvashmohammadi A, Michael R, Sweeney S, Ferro E (2012) Advanced compressed elastomer dampers for earthquake hazard reduction to steel frames. In: Behaviour of steel structures in seismic areas (STESSA), Santiago
18. Michael RJ, Johnson DH, Pollino M, Redovan J, Moser E, MacDonald B (2012) Development of a seismic isolation system for commercial storage racks. In: International mechanical engineering conference and exposition, Houston
19. Sweeney SK, Michael RJ (2006) Collaborative product realization of an innovative structural damper and application. In: Proceedings of ASME international mechanical engineering congress, IMECE2006-13421, Chicago, November, pp 1–9
20. FEMA (2009) Quantification of building seismic performance factors. Report no. P695. Federal Emergency Management Agency, Washington, DC
21. ASCE (2005) Minimum design loads for buildings and other structures. ASCE 7–05. American Society of Civil Engineers, Reston
22. AISC (2005) Seismic provisions for structural steel buildings. ANSI/AISC 341–05. American Institute for Steel Construction, Chicago
23. Ibarra LF, Medina RA, Krawinkler H (2005) Hysteretic models that incorporate strength and stiffness deterioration. Int J Earthq Eng Struct Dyn 34(12):1489–1511
24. Lignos DG, Krawinkler H (2007) A database in support of modeling of component deterioration for collapse prediction of steel frame structures. In: Proceedings, ASCE structures congress, Long Beach, 18–20 May 2007
25. Lowes LN, Altoontash A (2003) Modeling of reinforced-concrete beam-column joints subjected to cyclic loading. J Struct Eng, ASCE 129(12):1686–1697

Chapter 44
Performance Analysis of Cables with Attached Tuned-Inerter-Dampers

Irina F. Lazar, Simon A. Neild, and David J. Wagg

Abstract Cables are structural elements designed to bear tensile forces and experience vibration problems due to their slenderness and low mass. In the field of civil engineering, they are mostly used in bridges where the vibrations are mainly induced by wind, rain, traffic and earthquakes. This paper proposes the use of a tuned-inerter-damper (TID) system, mounted on cables to suppress unwanted vibrations. These are to be attached transversally to the cable, in the vicinity of the support, connected between the deck and the cable. The potential advantage of using a TID system consists in the high apparent mass that can be produced by the inerter. Our analysis showed that the modal damping ratio obtained is much higher than in the case of traditional dampers or tuned mass dampers, leading to an improved overall response. An optimal tuning methodology is also discussed. Numerical results are shown with a cable subjected to both free and forced vibrations and the TID performance is improved when compared with equivalent dampers.

Keywords Cable • Tuned inerter damper • Vibration suppression • Support excitation • Viscous damper

44.1 Introduction

Bridge cables are prone to large amplitude vibrations due to a series of factors. The most common factors causing these vibrations are wind and rain action, deck vibration induced by traffic or earthquakes.

Several solutions aimed at reducing cable vibrations have been proposed. One of the most widely used solutions consists of the installation of dampers. These are generally located in the vicinity of the anchorage point, connected between each cable and the deck. The efficacy of this approach has been studied both theoretically and experimentally.

An important concept in understanding the behaviour of the combined cable and damper systems refers to the maximum attainable modal damping [1]. This means that the there exists an optimum damper that can be attached at a certain location along the cable length, in order to achieve maximum damping of the vibration mode that the device is tuned for. The optimum damper size can be determined using the universal curve for estimating the modal damping of stay cables, introduced by Pacheco et al. [2]. Later, the universal curve formulation was extended by Cremona [3] to inclined cables. The work of Main and Jones [4] extended these studies to the case when dampers trigger large shifts of the uncontrolled cable natural frequency. On the experimental side, the behaviour of cables with attached dampers was presented in several case studies [5].

One of the disadvantages of using dampers refers to the fact that their installation is restricted to the end of the cable, generally at a distance lower than 5 % of the cable length from the support [6]. A solution to this problem can be the use of tuned mass dampers (TMD) [7]. These can be located anywhere along the cable length and do not need to be connected to the ground or bridge deck. Wu and Cai [8] conducted a parametric study looking into the influence of the TMD and cable parameters (mass, damping, stiffness, location, cable inclination) on the behaviour of the combined cable and TMD system performance. Anderson et al. [9] compared the behaviour of cables with attached viscous dampers and TMDs and concluded that TMDs potentially become more effective than dampers when located at 40 % distance from the cable anchorage point. Their performance can be improved through adequate tuning of parameters or by using magneto-rheological dampers instead of viscous dampers.

I.F. Lazar (✉) • S.A. Neild
Department of Mechanical Engineering, University of Bristol, Bristol, BS8 1TR, UK
e-mail: Irina.Lazar@bristol.ac.uk

D.J. Wagg
Department of Mechanical Engineering, University of Sheffield, Sheffield, S1 3JD, UK

However, the fact that TMDs are most efficient when located close to the cable midspan represents a disadvantage from installation point of view, as cables are usually very long. Also, the size of the TMD mass is limited to ratios of under 10 % of the cable mass.

As an alternative, this paper proposes the use of a tuned inerter damper (TID) vibration suppression systems for cable vibration mitigation. The TID, a system comprising of a spring-inerter-damper system, was introduced by the authors in [10]. Its layout is similar to that of a passive TMD, where the mass element was replaced by an inerter.

The inerter was introduced by Smith [11] and used in modern suspension systems for Formula 1 racing cars [12]. The inerter is the mechanical equivalent of the capacitor, thus completing the force-current analogy between mechanical and electrical networks. The force produced by an inerter is

$$\mathbf{F} = b(\ddot{\mathbf{x}}_{i+1} - \ddot{\mathbf{x}}_i) \tag{44.1}$$

where b is the constant of proportionality of the device, named inertance and $\ddot{\mathbf{x}}_i - \ddot{\mathbf{x}}_j$ represents the relative acceleration between its nodes. The inertance is measured in kilograms.

The most important characteristic of the inerters consists of their capacity of generating high apparent masses, mainly through gearing. This leads to the generation of a high inertial force, that cannot be obtained using a traditional TMD, where the mass is restricted to low values. Gearing ratios of 200:1 have been achieved [13].

The application of inerters spans across many engineering fields from vehicle [14–16] and train suspension systems [17] to building suspension systems [18, 19]. Ikago et al. [13, 20] studied the performance of tuned viscous mass dampers, where the inerter is mounted in parallel to a damper, both elements being connected in series with a spring. Marian and Giaralis [21] propose the use of a tuned mass-damper-inerter systems (TMDI), where the inerter is mounted in series with a TMD, thus connecting it between two adjacent storeys. They study the performance of TMDIs when installed in support-excited structures.

The TID system provides a very good vibration suppression level of the host structure. Considering a simple multi-storey building model, it has been shown that it is most efficient when located at bottom storey level, this constituting an important advantage from installation point of view. Its performance was studied for a wide range of loading scenarios, including sinusoidal support and lateral excitation [22], earthquake excitation and wind loads [23]. The TID showed comparable or improved performance when compared to equivalent TMDs or damper systems.

As shown in [10], in case of multi-storey structures, the TID must be connected between the first floor and the ground. Similarly, when installed on cables, the TID is connected between the cable and the bridge deck. Therefore, its installation is restricted to locations situated in the vicinity of the cable anchorage point, as in the case of dampers. Given this, the TID is located within easy access, should maintenance or retrofitting become necessary. While in the case of dampers their location represents a disadvantage in terms of performance, in the case of TIDs the limitation can be overcome by adjusting the inerter's apparent mass. This represents an important advantage of the proposed system.

Based on the analysis of horizontal cables with attached viscous dampers [4] presented in the literature, we study the performance of cables with attached TIDs. Starting from the uncontrolled cable model, differential equations can be derived for calculating the modal damping ratio obtained using a TID. For simplicity, a finite element model has also been created. This reduces the computational effort without significant loss of accuracy.

An important aspect is represented by the device optimisation. This is more involved due to the fact that TIDs introduce a greater number of parameters (inertance, damping and stiffness), while in the case of dampers only one parameter needs to be set, namely the damping capacity. The optimisation is aimed at minimising the displacement at the cable's midspan when the cable is subjected to sinusoidal deck excitation.

Our analysis showed that better performance can be achieved by using TIDs, when connected at the same location as viscous dampers. Moreover, the optimal damping required in a TID is much lower than that of dampers. Considering the results shown, it was concluded that the TID represents a viable alternative to viscous dampers when used to limit unwanted cable vibration.

44.2 Structural System

The structural system considered is represented by a horizontal cable fixed at both ends, as shown in Fig. 44.1. The TID is connected at length l_1 from the left support of the cable. In case of a bridge this would correspond to the point of anchorage to the deck. l_2 represents the distance to the right support which could be associated to the cable connection to the bridge tower.

Fig. 44.1 Cable with an attached TID
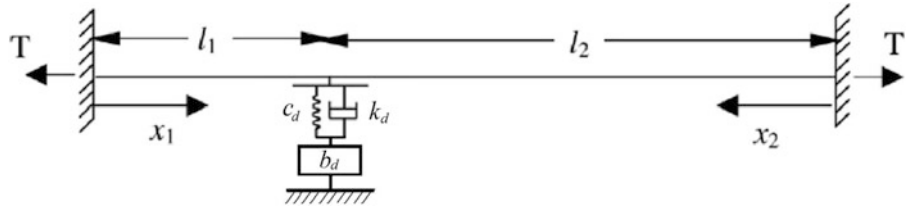
The elements of the TID, as described in [10] are the inerter (characterised by its inertance, b_d), a spring (with stiffness k_d) and a damper (with damping c_d). The TID is also connected to the bridge deck.

The cable used in the numerical examples has a total length $L = 100$ m and is subject to a tensile force $T = 5{,}000$ kN. Its mass per unit length is $m = 100$ kg/m and the resulting frequency of the first mode of vibration is $\omega_c = 7.02$ rad/s.

The system will be subject to sinusoidal deck excitation, which translates into a sinusoidal displacement of the left support of the cable and of the point of anchorage of the viscous damper or TID to the bridge deck.

The tuning of both devices is done such that we obtain minimum displacement at the cable's midspan, when the overall structure is subject to deck excitation.

44.2.1 Cable Differential Equations

In order to write the differential equations describing the cable, a series of simplifying assumptions are made. Namely, the tension in the cable is large compared to its weight, the bending stiffness and damping of the cable are small, and that the cable deflection is small, such that the tension force caused by deflection is negligible in comparison to the static tension. The following partial differential equation is satisfied over each segment of the cable:

$$T\frac{\partial^2 v_k(x_k,t)}{\partial x_k^2} = m\frac{\partial^2 v_k(x_k,t)}{\partial t^2} \tag{44.2}$$

where T is the tension force in the cable, x_k is the coordinate of the kth cable segment along the cable axis, v_k represents the transversal deflection and m is the cable mass per unit length. A non-dimensional time parameter $\tau = \omega_c t$ is introduced. Using the new notation, the cable displacement becomes

$$v_k(x_k,t) = \gamma(\tau)\frac{\sinh(\pi\lambda x_k/L)}{\sinh(\pi\lambda l_k/L)} \tag{44.3}$$

where λ is the dimensionless eigenvalue and γ is the displacement at the location where the device is connected [4].

The equilibrium equation at the TID connection point is

$$T\left(\left.\frac{\partial v_1}{\partial x_1}\right|_{x_1=l_1} - \left.\frac{\partial v_2}{\partial x_2}\right|_{x_2=l_2}\right) = k_d(v_1|_{x_1=l_1} - v_d) + c_d\left(\left.\frac{dv_1}{dt}\right|_{x_1=l_1} - \frac{dv_d}{dt}\right) \tag{44.4}$$

where v_d is the vertical displacement of the TID system. The equilibrium equation of the TID is

$$b_d\frac{d^2 v_d}{dt^2} + k_d(v_d - v_1|_{x_1=l_1}) + c_d\left(\frac{dv_d}{dt} - \left.\frac{dv_1}{dt}\right|_{x_1=l_1}\right) = 0 \tag{44.5}$$

where b_d is the inertance of the TID system.

As presented in [7], the TID system displacement can be expressed as $v_d = \beta\gamma(\tau)$, where β is the complex amplitude ratio between the TID and the corresponding cable point.

$$\beta = \frac{1 + 2\xi\rho\lambda}{1 + 2\xi\rho\lambda + \rho^2\lambda^2} \tag{44.6}$$

where $\xi = \frac{c_d}{2b_d\omega_d}$ is the TID damping ratio and $\rho = \frac{\omega_c}{\omega_d}$ is the ratio between the cable and the TID fundamental frequency ($\omega_d = \sqrt{\frac{k_d}{b_d}}$).

Substituting Eqs. 44.3 and 44.6 into 44.4, we obtain

$$\coth(\pi\lambda l_1/L) + \coth(\pi\lambda l_2/L) + \frac{\pi\lambda b_d}{Lm}\frac{1 + 2\xi\rho\lambda}{1 + 2\xi\rho\lambda + \rho^2\lambda^2} = 0 \qquad (44.7)$$

The solutions, λ, of Eq. 44.7 represent the eigenvalues of the combined cable plus TID system. Considering $\lambda = \sigma + \varphi i$ where $i = \sqrt{-1}$, and separating the real and imaginary terms, we obtain a system of equations that can be soled numerically and the modal damping ratio can be calculated as

$$\zeta_i = \left(\frac{\varphi_i^2}{\sigma_i^2} + 1\right)^{-\frac{1}{2}}. \qquad (44.8)$$

44.2.2 Finite Element Model

Although the analytical solution provides accurate results, it is difficult to use in practice, when we want to evaluate the structural response. To overcome this limitation, a finite element model using axial elements was created. We opted for a model formed of 20 elements. The resulting frequency of the first mode of vibration is $\omega = 7.03$ rad/s, very close to the frequency determined analytically, $\omega_c = 7.02$ rad/s. The resulting modal damping ratios have been validated using the analytical model. This simplified model has been employed in the following examples.

44.3 Analysis of Damper Systems Performance

This section is aimed at analysing the response of cables with attached viscous dampers. The approach is similar to the one presented in [4]. As explained by the authors, there is an optimal damping capacity that ensures a maximum level of modal damping in each vibration mode. This is illustrated in Fig. 44.2a, where we can see the variation of the modal damping ratio attained in the first, second and third mode of vibration of a cable plus damper system with damper capacity.
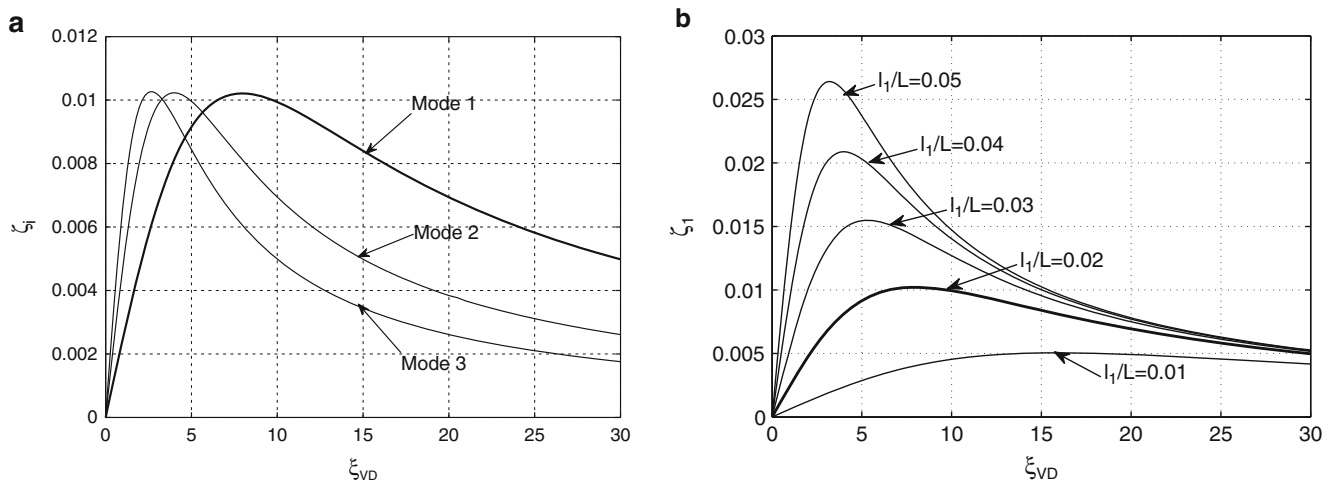

Fig. 44.2 (a) Modal damping ratio obtained in the first, second and third mode of vibration of a cable with an attached viscous damper, located at $0.02L$ distance from the left support; (b) Variation of the first modal damping ratio, ζ_1, with the damper location
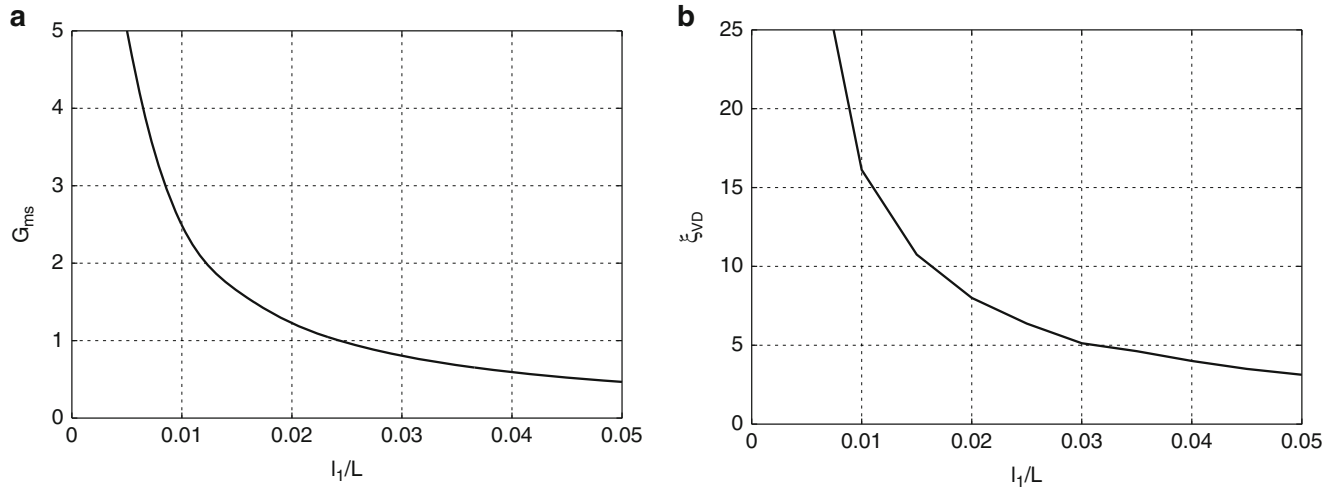
Fig. 44.3 (**a**) Variation of the midspan gain G_{ms} with length ratio; (**b**) Variation of the optimal damper capacity with length ratio

The damper capacity is expressed in terms of its damping ratio. This is defined as

$$\xi_{VD} = \frac{c}{2\sqrt{Tm}} \tag{44.9}$$

where c represents the damping coefficient of the viscous damper.

When the viscous damper is located at $l_1 = 0.02L$ distance from the left support, the maximum modal damping attached in the first three vibration modes is approximately $\zeta_i = 1\%$. However, these maxima cannot be attained concomitantly. A different damper capacity is needed in each case. For example, if the damper capacity is set to $\xi_{VD} = 7.9$, the corresponding modal damping ratios will be $\zeta_1 = 1\%$, $\zeta_2 = 0.8\%$ and $\zeta_3 = 0.6\%$. Similar results have been reported in [4] for a different scaling of the damping parameter.

In the present case, we are interested in tuning the damper such that we suppress the vibration of the first mode of vibration, therefore we will extend the system analysis in this direction. To do so, we are looking at the variation of the modal damping ratio achieved in the first mode of vibration when the damper is moved along the cable length. This is shown in Fig. 44.2b. The device becomes more effective when located at a larger distance with respect to the left support. The thick line representing the first modal damping ratio of the system in Fig. 44.2b is shown using the same legend in Fig. 44.2a. When the length ratio is increased to $l_1/L = 0.05$, the first modal damping ratio increases to $\zeta_1 = 2.6\%$.

Figure 44.3a shows the variation of the midspan gain with length ratio, for optimally tuned dampers. As the length ratio increases, the gain value drops, indicating the increased efficiency of the device. A value $G_{ms} = 0.5$ is attained when the device is located at 5 % distance from the left support. Also, the damping ratio necessary to obtain the minimum gain decreases as the length ratio is increased. This trend can be seen in Fig. 44.3b.

44.4 Analysis of TID Systems Performance

A similar analysis is now done in case of cables with attached TIDs. The device tuning is more complex in this case due to the increased number of parameters that need to be taken into account.

As explained in [10], the TID introduces a new degree of freedom in the system. This induces a TMD-like behaviour in the vicinity of the first fundamental frequency of the uncontrolled system. The aim of our optimisation was to tune the TID such that the amplitude of response at the newly created peaks is the same. In the same time, the response must be minimised. Therefore, after setting the desired mass ratio, μ, we will determine the optimum frequency ratio, ρ, and the corresponding damping ratio, ξ_{TID}. The TID damping ratio is calculated as $\xi_{TID} = \xi \frac{\pi\mu}{\rho}$, where $\xi = \frac{c_d}{2\omega_d b_d}$. This scaling is done in order to allow direct comparison with the damping coefficient definition for viscous dampers given in Eq. 44.9.

Figure 44.4a shows the variation of the modal damping ratio attained in the first, second and third mode of vibration of a cable plus TID system with the TID damping ratio. The maximum modal damping ratio in the first mode of vibration
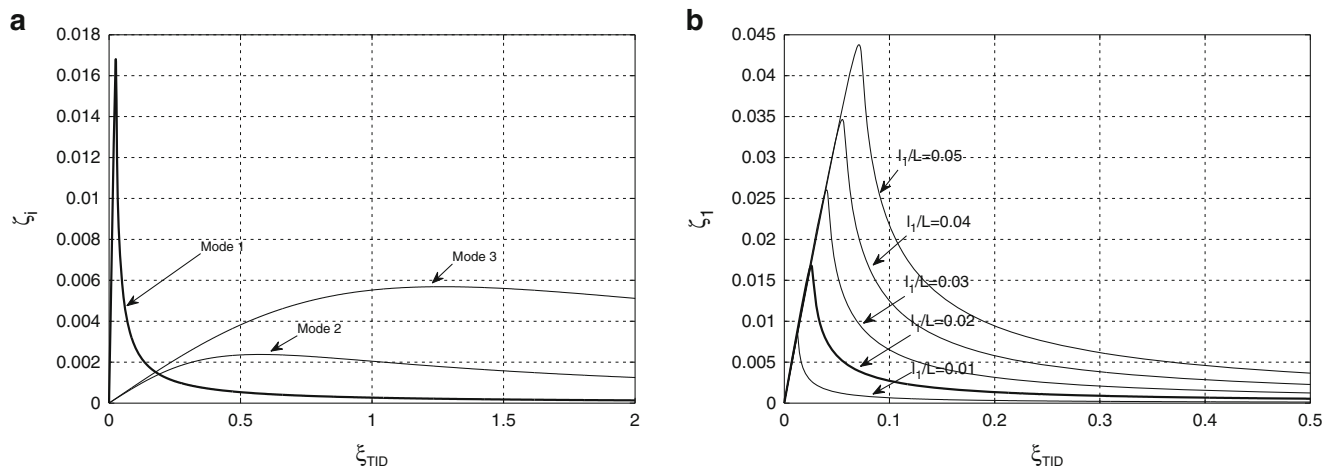
Fig. 44.4 (**a**) Modal damping ratio obtained in the first, second and third mode of vibration of a cable with an attached TID with mass ratio $\mu = 0.2$, located at $0.02L$ distance from the left support; (**b**)Variation of the first modal damping ratio, ζ_1, with the TID location, for a mass ratio $\mu = 0.2$
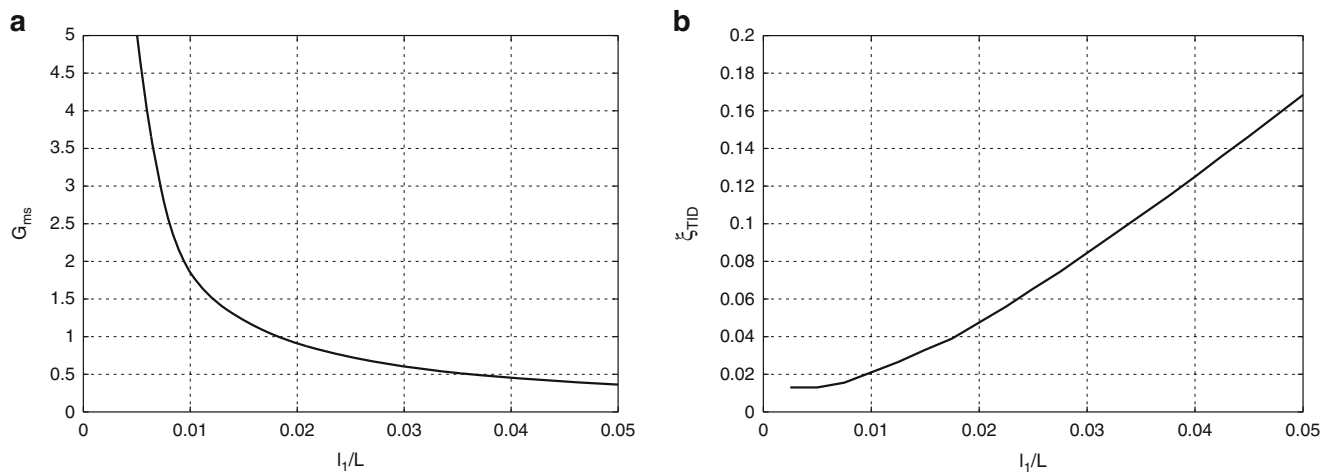

Fig. 44.5 (**a**) Variation of the midspan gain G_{ms} with length ratio for a TID with mass ratio $\mu = 0.2$; (**b**) Variation of the optimal damper capacity with length ratio for a TID with mass ratio $\mu = 0.2$

is approximately $\zeta_1 = 1.7\%$. As in the case of dampers, when tuning the device to suppress the vibration of the first mode, the corresponding second and third mode damping ratios are much smaller. If the optimisation criterion is changed, higher modal damping ratios can be obtained. However, this would not lead to an optimal response in terms of midspan gain, G_{ms}, as in the case of dampers.

Figure 44.4b gives the variation of the first modal damping ratio with the length ratio giving the TID position. As seen, the maxima obtained are considerably higher than in the case of dampers. When the TID is placed at $l_1/L = 5\%$, a modal damping ratio of $\zeta_1 = 4.5\%$ can be achieved.

The midspan gain variation with the length ratio is shown in Fig. 44.5a. As in the case of dampers, the gain decreases as the device is moved further from the support. The minimum value obtained using a TID with mass ratio $\mu = 0.2$, located at $l_1/L = 5\%$ from the support is $G_{ms} = 0.35$, smaller than in the case when dampers are used. This proves that the TID system is more effective.

Figure 44.5b shows the variation of the optimal damper capacity with length ratio for a TID with mass ratio $\mu = 0.2$. In this case, as the length ratio is increased, the optimal TID damping ratio increases as well. However, the necessary damper capacity is much smaller than in the case of dampers.

The results obtained indicate the fact that a TID with mass ratio $\mu = 0.2$ of the total cable mass is more efficient than viscous dampers, when connected at the same location along the cable's length.

44.5 Response to Vibrations Induced by Bridge Deck Motion: Performance Comparison

One of the most attractive aspects associated with the use of TIDs instead of viscous dampers is the fact that the performance of the TID can be adjusted by increasing its mass ratio. We are looking at the performance of different mass ratio TIDs, each optimised to minimise the midspan gain.

Figure 44.6 shows a comparison between the performance of TIDs and dampers in terms of midspan gain, G_{ms}. The dashed line representing the optimal damper performance lies between the curves corresponding to TIDs with mass ratios of $\mu = 0.05$ and $\mu = 0.2$. In case of TIDs, an improved performance can be obtained if the mass ratio is further increased to $\mu = 0.5$. These values are feasible due to the capacity of the inerter to generate high apparent mass.

For a better understanding of the TID and damper behaviour, Fig. 44.7 shows the frequency response to sinusoidal deck excitation for the case when the devices are located at $l_1/L = 2\%$ from the left support. It is considered that the uncontrolled
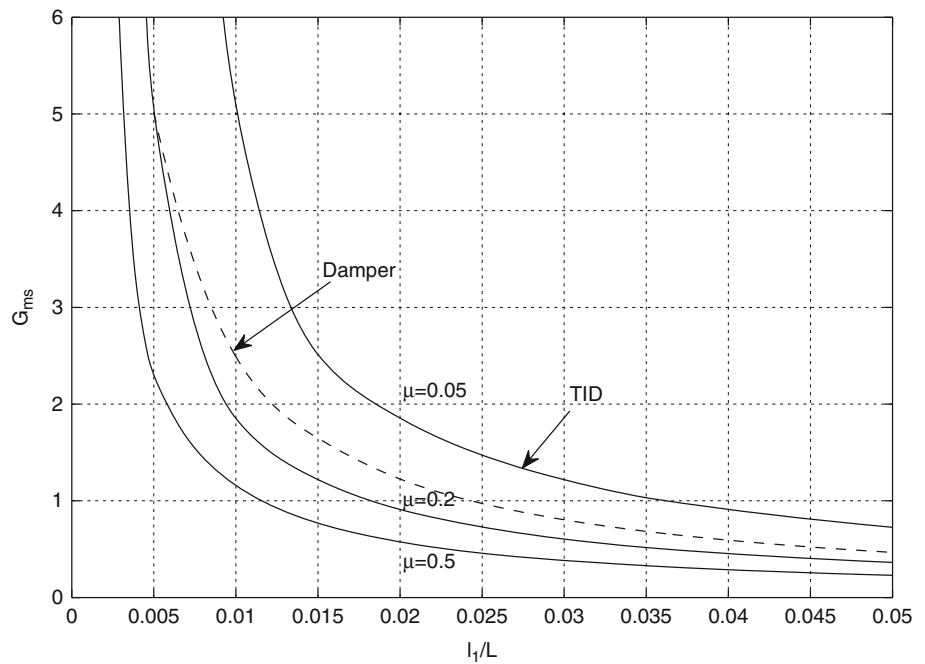

Fig. 44.6 Variation of midspan gain with length ratio optimal dampers and TIDs with mass ratios $\mu = 0.05$, $\mu = 0.2$ and $\mu = 0.5$
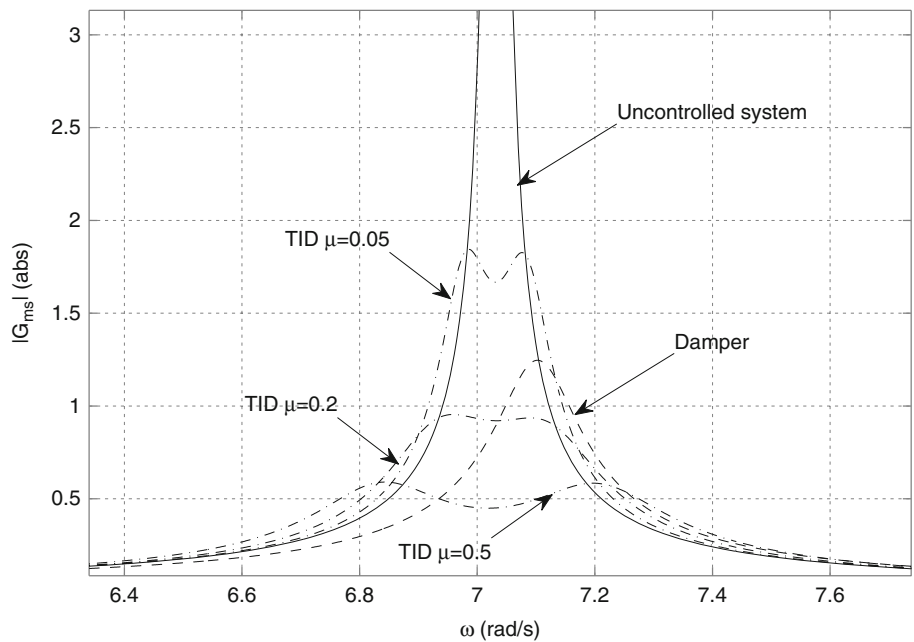

Fig. 44.7 Frequency response of the uncontrolled system, cable with an optimised damper and cable with an attached TID, at $l_1/L = 2\%$

cable has no inherent damping, thus the amplitude of its response near the first fundamental frequency is infinite. It can be seen that the high damper capacity induces a frequency shift in the overall system response. The TIDs display the equal-amplitude split-peak response characteristic for TMD-like systems. As shown in Fig. 44.6, the dampers performance lies in between that of a TID with $\mu = 0.05$ and $\mu = 0.2$, and an improved performance is obtained for $\mu = 0.5$.

44.6 Conclusion

In this paper we have assessed the possibility of using TIDs for cable vibration suppression, as an alternative to viscous dampers.

The inerter is an attractive device for vibration suppression application, given its ability of generating a high apparent mass compared to its physical mass. This leads to high inertial forces, proportional to the relative acceleration between the device terminals.

The performance of TIDs installed on cables is compared to that of optimised viscous dampers attached at the same location. Since the TID system introduces a higher number of design parameters and obtaining the highest modal damping ratio does not lead to an optimal response of the overall system, we introduced a new optimisation algorithm, based on the minimisation of the response gain at the cable's midspan.

As presented in previous literature, there is a maximum level of modal damping that can be achieved when a viscous damper is connected to a cable at a given location. In the case of TIDs, this is no longer valid as the device can be improved varying its mass ratio. This leads to very good vibration suppression levels.

It is shown that for the case when the system is subject to sinusoidal excitation of the left support, a better vibration suppression level can be achieved by using a TID than a viscous damper, when both devices are located at $l_1/L = 2\%$ from the support. Considering the results shown, it was concluded that the TID represents a promising alternative to viscous dampers when used to limit cable vibration.

References

1. Kovacs I (1982) Zur Frage der Seilschwingungen und der Seildampfung. Bautechnik 10:325–332
2. Pacheco BM, Fujino Y, Sulek A (1993) Estimation curve for modal damping in stay cables with viscous damping. J Struct Eng 119(6):1961–1979
3. Cremona C (1997) Courbe universelle pour le dimensinnement d'amortisseurs en pied de haubans. Revue Francaise du Genie Civil 1:137–159
4. Main JA, Jones NP (2002) Free vibrations of a taut cable with attached damper. I: linear viscous damper. J Eng Mech 128:1062–1071
5. Main JA, Jones NP (2001) Evaluation of viscous dampers for stay-cables vibration mitigation. J Bridge Eng 6:385–397
6. Cai CS, Wu WJ, Shi XM (2006) Cable vibration reduction with a hung-on TMD system. Part I: theoretical study. J Vib Control 12(7):801–814
7. Wu WJ, Cai CS (2006) Theoretical exploration of a taut cable and a TMD system. J Eng Struct 29:962–972
8. Wu WJ, Cai CS (2006) Cable vibration reduction with a hung-on TMD system. Part II: parametric study. J Vib Control 12(8):881–899
9. Main JA, Jones NP (2013) External damping of stay cables using adaptive and semi-active vibration control, ICSBOC. In: The 8th international cable supported bridge operators' conferene, Edinburgh, UK, 3–5 June 2013
10. Lazar IF, Neild SA, Wagg DJ (2014) Using an inerter-based device for structural vibration suppression. J Earthq Eng Struct Dyn 43(8): 1129–1147
11. Smith MC (2002) Synthesis of mechanical networks: the inerter. IEEE Trans Autom Control 47:1648–1662
12. Chen MZQ, Papageorgiou C, Scheibe F, Wang F-C, Smith MC (2009) The missing mechanical circuit. IEEE Circuits Syst Mag 1531-636X: 10–26
13. Ikago K, Saito K, Inoue N (2012) Seismic control of single-degree-of-freedom structure using tuned viscous mass damper. Earthq Eng Struct Dyn 41:453–474
14. Papageorgiou C, Smith MC (2005) Laboratory experimental testing of inerters. In: 44th IEEE conference on decision and control and the european control conference, pp 3351–3356. Seville, Spain
15. Papageorgiou C, Houghton NE, Smith MC (2009) Experimental testing and analysis of inerter devices. J Dyn Syst Meas Control 131(1):011001
16. Wang F-C, Chan H-A (2011) Vehicle suspensions with a mechatronic network strut. Int J Veh Mech Mobil 49(5):811–830
17. Wang F-C, Liao M-K, Liao B-H, Su W-J, Chan H-A (2009) The performance improvements of train suspension systems with mechanical networks employing inerters. Int J Veh Mech Mobil 47:805–830
18. Wang F-C, Chen C-W, Liao M-K, Hong M-F (2007) Performance analyses of building suspension control with inerters. In: Proceedings of the 46th IEEE conference on decision and control, pp 3786–3791. New Orleans, LA, USA
19. Wang F-C, Hong M-F, Chen C-W (2009) Building suspensions with inerters. Proc IMechE, J Mech Eng Sci 224:1605–1616

20. Ikago K, Sugimura Y, Saito K, Inoue K (2012) Modal response characteristics of a multiple-degree-of-freedom structure incorporated with tuned viscous mass damper. J Asian Architecture Building Eng 11(2):375–382
21. Marian L, Giaralis A (2014) Optimal design of a novel tuned mass-damper-inerter (TMDI) passive vibration control configuration for stochastically support-excited structural systems. J Probab Eng Mech http://dx.doi.org/10.1016/j.probengmech.2014.03.007
22. Lazar IF, Neild SA, Wagg DJ (2014) Design and performance analysis of inerter-based vibration control systems. In: IMAC XXXII conference and exposition on structural dynamics, Orlando, FL, USA
23. Lazar IF, Neild SA, Wagg DJ (2014) Inerter-based vibration suppression systems for laterally and base-excited structures. In: International conference on structural dynamics, Porto, Portugal

Chapter 45
Numerical Investigation of Vibration Reduction in Multi-storey Lightweight Buildings

Ola Flodén, Kent Persson, and Göran Sandberg

Abstract In order to reduce the vibration transmission in multi-storey wood buildings, it is common to insert viscoelastic elastomer materials between parts of the buildings. The studies presented here investigate to which extent different design choices for the elastomer layers affect the isolation of low-frequency vibrations (0–100 Hz). A finite element model of two storeys of a multi-storey wood building, involving blocks of elastomer material in between the storeys, was used to perform numerical investigations. Parametric studies were carried out, considering different properties of the elastomer material and different placements of the elastomer blocks. Considering the transmission from the floor of the upper storey to the underlying ceiling, the material properties of the elastomer material were found to affect the vibration levels appreciably. A too stiff elastomer material can result in an amplification of the vibration levels in the ceiling for certain frequencies, whilst a less stiff material, in general, reduces the vibration transmission. The placement of the elastomer blocks was varied by shifting the position of the blocks while maintaining their centre-to-centre distance, resulting in a small effect on the vibration levels.

Keywords Wooden buildings • Impact sound • Vibration reduction • Elastomer materials • Finite element method

45.1 Introduction

In 1994, a century-old ban on the construction of wooden buildings more than two storeys in height in Sweden was lifted, leading to the reintroduction of such buildings. The use of wood as a construction material has many advantages. The lightweight properties of wood, for example, lower the transportation costs involved and reduce the size of the foundations needed [1]. In addition, the energy consumption during the construction and the lifecycle of wooden buildings is lower than that of concrete buildings of comparable size [2]. At the same time, however, it is more difficult to build lightweight structures of wood such that noise and disturbing vibrations in the different storeys and rooms are avoided, especially at low frequencies [3]. The vibrations can be caused by, for example, footsteps, airborne sound, vibrating machines and external sources such as railway and road traffic.

Despite newly constructed multi-storey wood buildings fulfilling the requirements for sound insulation, many of the occupants perceive the impact sound as annoying [4]. In [5], an investigation is reported where vibrational and acoustical parameters were measured and the subjective ratings of occupants were evaluated, including a total of ten lightweight buildings of different construction types. The correlation between the impact sound insulation, evaluated according to ISO 717-2:2013 [6], and the perceived annoyance of the occupants was found to be weak. The ISO standard only considers frequencies above 50 Hz; the correlation was improved considerably by extending the range to include frequencies down to 20 Hz. This emphasises the need for updated regulations as well as improved low-frequency impact sound insulation in lightweight buildings.

45.1.1 Vibration Reduction Measures

In order to reduce the vibrations transmitted throughout the buildings, different measures can be taken. In [7], different types of vibration reduction measures are discussed, for example the tuned mass damper (TMD), consisting of a mass mounted to

O. Flodén (✉) • K. Persson • G. Sandberg
Faculty of Engineering, Department of Construction Sciences, Lund University, John Ericssons väg 1, 223 63 Lund, Sweden
e-mail: ola.floden@construction.lth.se

the vibrating structure by some elastic material acting as a spring. The TMD is tuned to have a certain natural frequency and provides an effective way of cancelling the vibrations caused by a single vibration mode. Another example is the semi-active absorber, which can change its damping properties rapidly to adjust for changes in the excitation. An even more sophisticated measure is the active control system, which drives the system through feedback loops, an effective but costly procedure due to the energy required to drive the system. Moreover, an experimental investigation is presented in [7], studying the use of viscoelastic materials as vibration isolators in the junctions of a floor-ceiling structure in steel. It was found to be an effective method for reducing the vibrations caused by modes in which the floor and the ceiling move out of phase, and it was concluded that viscoelastic materials function well for wider frequency ranges, as compared to TMDs.

Many of the newly constructed multi-storey wood buildings in Sweden are composed of timber volume elements (TVEs), such buildings being described in more detail in Sect. 45.1.2. TVE buildings are constructed by stacking volume modules which are separated by layers of viscoelastic elastomer materials. In the studies presented here, the TVE buildings will serve as example case for studying the effect of different design choices for the elastomer layers. The use of elastomer materials in junctions is common in different types of lightweight buildings.

In [8], measurements on full-scale structures were carried out in order to investigate the effect of a number of measures for reducing the impact sound in TVE buildings. Measures that were found to be effective in reducing the vibrations were, for example, an extra layer of plaster board on the floor structure and the use of a floating floor, in which mineral wool is placed between the beams and the boards of a floor structure. The use of a heavier mineral wool as insulation, or a larger cavity between floors and ceilings, were found to be less effective measures for reducing the vibrations. Elastomer layers in the junctions were also tested, leading to ambiguous results from two different measurement setups; one resulting in reduced sound pressure levels, compared to having no elastomer material in the junctions, the other in increased sound pressure levels. The majority of the tested measures were found to change the impact sound less than 2 dB when evaluated according to the ISO standards. This should be compared with the measured variance of 1.1 dB between theoretically identical constructions due to the varying quality of the workmanship.

An experimental investigation of the effect of using elastomer layers in junctions of wooden constructions is reported in [9]. A mock-up consisting of a floor structure, supported by three walls, was used to study the vibration transmission from the floor to the walls of the storey below. Marked differences in the behaviour was found for certain vibration modes when inserting elastomer materials in the junctions, as compared to a setup with the floor mounted directly on the walls. For example, the damping is larger for mode shapes where large deformations occur in the elastomer layers. It was also concluded that the step sound insulation can decrease for low frequencies (20–70 Hz), possibly due to shear resonances in the elastomer layers. This points out the need for a careful design of the elastomer layers with respect to the structure, the vibration sources and the requirements in question.

45.1.2 Timber Volume Element Buildings

The lightweight properties of wood simplify the use of prefabrication in the construction process compared to conventional concrete buildings. The TVE buildings are prefabricated multi-storey buildings, increasing in popularity in Sweden. A TVE is a module consisting of floor-, roof- and wall elements completed with, for example, electrical installations, flooring, cabinets and wardrobes. Each TVE typically constitutes a small apartment, one room or part of a larger room. Prefabricated TVEs are transported to a construction site where they are stacked to form the complete building. In Fig. 45.1, the conceptual layout of a TVE building is illustrated, and in Fig. 45.2, drawings of junctions between a floor-ceiling structure and an apartment separating wall (to the left) and a facade wall (to the right) are shown. An advantage regarding vibrations and acoustic performance is that a floor is structurally separated from the ceiling of the storey below; the upper volume contains the floor whereas the lower volume comprises the ceiling. Elastomer blocks are placed on the flanks in between the TVEs in order to reduce the vibration transmission through the junctions. The major structural connection between adjacent volumes is by means of the elastomers, the only additional connection being through a few studs and tie plates, used to position and fixate the TVEs.

45.1.3 Objective

In this paper, a numerical investigation is presented, aiming at an increased understanding of how the design of elastomer layers in junctions of multi-storey wood buildings affects the vibration transmission between storeys and rooms.
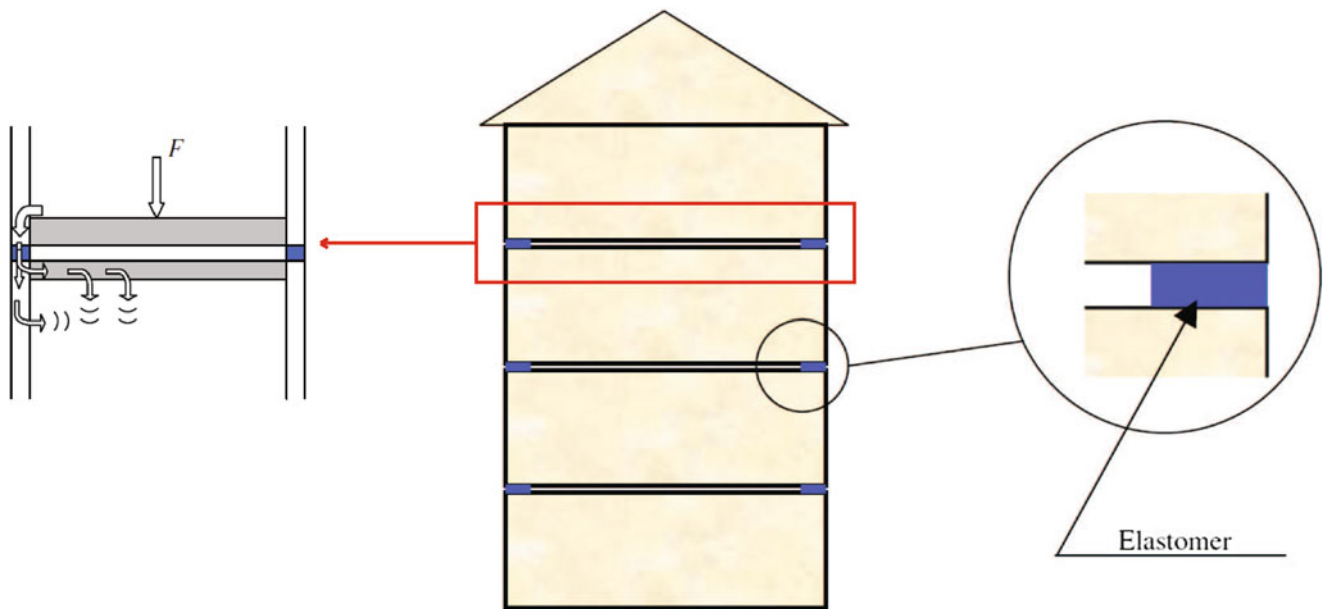
Fig. 45.1 Sketch of a TVE building [8]. The path of structural vibrations between storeys is illustrated in the figure to the *left* and an elastomer block is illustrated in the figure to the *right*
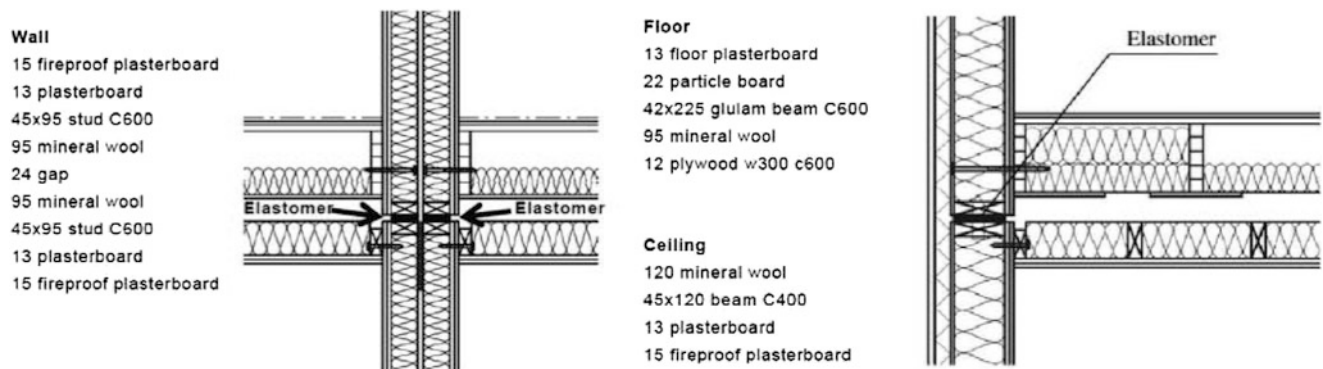

Fig. 45.2 Drawings of the TVE building system, showing sections of a floor-ceiling structure and junctions with an apartment separating wall (*left*) and a facade wall (*right*)

More specifically, parametric studies were carried out, considering different properties of the elastomer material and different placements of the elastomer blocks. The aim is to gain an understanding of the extent to which this type of design choices affect the vibration isolation. The result of the numerical investigation may then serve as input for designing experimental studies. A precise prediction of the sound insulation levels is outside the scope of the paper. The studies are limited to the low-frequency range, defined here as frequencies below 100 Hz.

In Sect. 45.2, the dynamic properties of the elastomer materials are discussed and investigated in order to provide input for the parametric studies. The numerical model employed is discussed in Sect. 45.3 and the parametric studies are presented in Sect. 45.4.

45.2 Properties of Elastomer Materials

In order to determine a realistic range for the properties of the elastomer materials, a type of elastomer often used in TVE buildings, *Sylodyn*, was studied. Sylodyn is a mixed cellular polyurethane dampening material developed by Getzner Werkstoffe GmbH, manufactured in five different types: NB, NC, ND, NE and NF. The stiffness of the materials are increasing from NB to NF, stiffer materials being used when the static loads are of higher magnitude. The elastomers are

normally exposed to static loads of such magnitude that the materials behave nonlinearly from a static point of view. The dynamic loads the buildings are exposed to are in most situations, however, of such magnitude that the nonlinear behaviour can be neglected. The dynamic response may then be regarded as a small perturbation of the static equilibrium. Linear and frequency-dependent viscoelastic material properties were determined for Sylodyn NE in [10]. The properties were calculated by finite element (FE) simulations, matching the results to experimental data found in data sheets provided by the manufacturer. The same procedure was employed here for Sylodyn NB and NF, respectively, in order to obtain the extreme values of the material parameters for the manufactured materials.

A linear viscoelastic material can be described by its bulk modulus K and shear modulus G, both being complex and frequency-dependent properties. The material is then described by four frequency-dependent parameters; $K_R(f)$, $K_I(f)$, $G_R(f)$ and $G_I(f)$, the subscripts R and I denoting the real and imaginary parts, respectively. Varying four different parameters in a parametric study is a time consuming procedure. Therefore, the possibility of using a single parameter to describe the variance in properties between the different materials was investigated. The idea was to scale the properties of Sylodyn NB to match the properties of both Sylodyn NE and NF. The following expressions were assumed for the scaling:

$$G_R(x, f) = (1 + x) \, G_R^{NB}(f),$$

$$G_I(x, f) = \left(1 + \alpha_1 x + \alpha_2 x^2\right) G_I^{NB}(f),$$

$$(45.1)$$

$$K_R(x, f) = \left(1 + \alpha_3 x + \alpha_4 x^2\right) K_R^{NB}(f),$$

$$K_I(x, f) = \left(1 + \alpha_5 x + \alpha_6 x^2\right) K_I^{NB}(f),$$

where x is the scaling parameter and α_i are coefficients. The coefficients were determined by comparing the four parameters of Sylodyn NE and NF, respectively, to parameters obtained through Eq. (45.1), while adjusting the coefficients until the average difference between the spectra for each material parameter was minimised. During the minimisation process, the scaling parameters, x^{NE} and x^{NF} for Sylodyn NE and NF, respectively, were set to values obtained through normalisations of $G_R(x, f)$ to $G_R^{NB}(f)$ at $f = 50$ Hz (the mid-point of the studied frequency range) for both materials, such that

$$x^{NE} = \frac{G_R^{NE}(50 \text{ Hz})}{G_R^{NB}(50 \text{ Hz})} - 1 = 4.53,$$

$$(45.2)$$

$$x^{NF} = \frac{G_R^{NF}(50 \text{ Hz})}{G_R^{NB}(50 \text{ Hz})} - 1 = 9.63.$$

The coefficients resulting from the minimisation process are given in Table 45.1. The frequency spectra for the shear modulus of Sylodyn NB, NE and NF and the scaled spectra of Sylodyn NB are shown in Fig. 45.3, and the corresponding plots for the bulk modulus are shown in Fig. 45.4. When comparing the scaled spectra to the original spectra for the material parameters of Sylodyn NE and NF, it was found that the error is below 6 % for the real parts of the bulk and shear moduli, and below 30 % for the imaginary parts. This shows that it is a relatively accurate approximation to use x as a single parameter for describing the variance in material properties between the different elastomer materials.

Moreover, the long-term bulk and shear moduli, $K_\infty = K_R(0 \text{ Hz})$ and $G_\infty = G_R(0 \text{ Hz})$, are required as input to the analyses. It was, for the scaled properties, assumed that $K_\infty = K_R(x, 1 \text{ Hz})$ and $G_\infty = G_R(x, 1 \text{ Hz})$ in the investigation of the material properties presented in Sect. 45.4.1.

Table 45.1 The values obtained for the coefficients of the scaling in Eq. (45.1)

α_1	α_2	α_3	α_4	α_5	α_6
1.57	0.005	1.14	0.011	1.80	0.019

Fig. 45.3 The real and imaginary parts of the shear modulus for Sylodyn NB, NE and NF, together with the scaled spectra of Sylodyn NB. The legend is valid for both plots
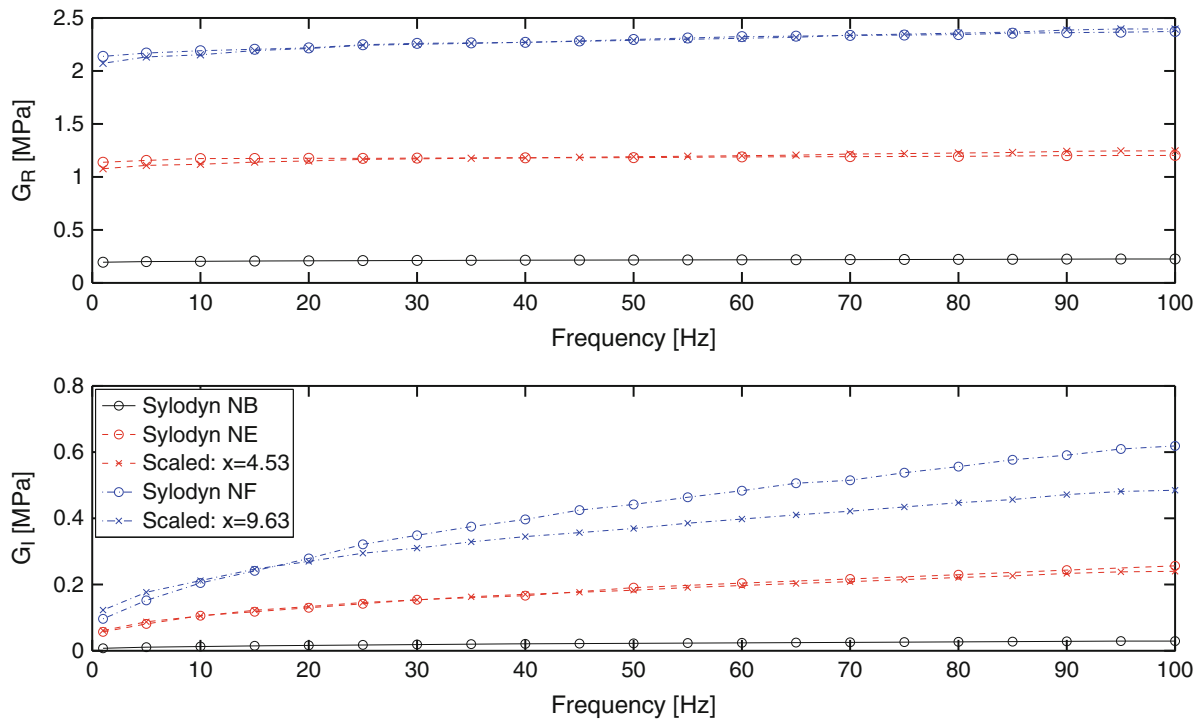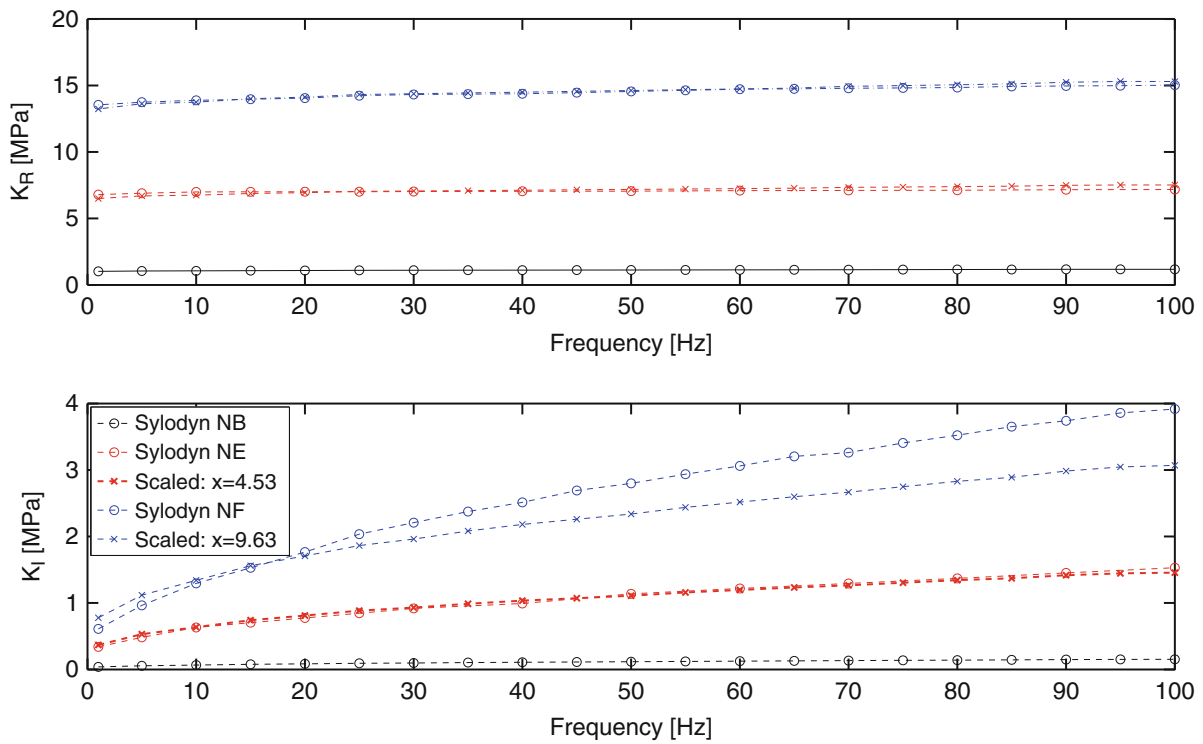

Fig. 45.4 The real and imaginary parts of the bulk modulus for Sylodyn NB, NE and NF, together with the scaled spectra of Sylodyn NB. The legend is valid for both plots

45.3 Numerical Modelling

The FE model, a quarter of it being shown in Fig. 45.5, was modelled in the commercial software Abaqus [11]. It includes two stacked TVEs, modelled according to the drawings in Fig. 45.2, separated by a number of elastomer blocks.

Each TVE is $9.0 \times 3.9 \times 3.4 \, \mathrm{m}^3$ in size, the long side walls being apartment separating and the short side walls being facades. The facade walls are constructed in the same manner as the apartment separating walls, shown in Fig. 45.2, but with $95 \times 220 \, \mathrm{mm}^3$ studs and a weatherboard covering the outside. The centre-to-centre distance for the beams in the floors and in the walls is 600 mm, whilst the distance is 400 mm for the beams in the ceiling. All the structural components listed in Fig. 45.2, except the mineral wools, were included in the model. All the interfaces between floors, walls and ceilings were modelled as fully fixed to each other, connecting the degrees of freedom at the interface surfaces by Lagrange multipliers. The exception is the connections between the walls and the floors, and between the walls and the ceilings, where only the beams in the floors and the ceilings were coupled to the walls; the particle and plaster boards being free at their ends.

The effect of modelling the air and the insulation in the cavity between the floor and the ceiling, in terms of acoustic media, was investigated in [12]. It was found to affect the vibration transmission appreciably, especially at low frequencies. The acoustic media is, however, neglected in the studies presented here as the objective is to investigate to which extent the structural transmission of vibrations can be affected by modifying the elastomer layers, assuming the acoustic media to have a negligible effect on the relative difference in structural transmission.

The particle board, the plaster board and the plywood were modelled as isotropic materials with properties according to Table 45.2, whereas the wood beams were modelled as orthotropic with properties according to Table 45.3. The weatherboard was assigned the same properties as the plaster board. The elastomer blocks modelled in this study were of dimensions $100 \times 95 \times 25 \, \mathrm{mm}^3$ and placed along the walls between the two stacked TVEs with a centre-to-centre distance from one another of 600 mm.

The structure was meshed with 20-node solid hexahedral elements, employing quadratic interpolation and reduced integration, except for the elastomer blocks which were meshed with elements using a hybrid formulation in order to avoid volumetric locking. The mesh sizes were decided based on the wavelengths expected to occur at the highest frequency of interest, namely 100 Hz.

Due to the complexity when assessing damping in building structures, a global damping ratio of 6 % was assigned to all materials, as opposed to considering damping for each material and for the different connections, the exception being the viscoelastic properties of the elastomers. The damping ratio was determined in [13], with use of experimental data obtained from measurements in a TVE building [14], by fitting an exponential function to the transient response of a floor structure. The damping ratio was used to establish a damping matrix by means of Rayleigh damping, see e.g. [15]. The damping matrix was, hence, constructed as a linear combination of the mass and the stiffness matrices, selecting the proportionality constants to be 17.37 and $9.77 \cdot 10^{-5}$, respectively.
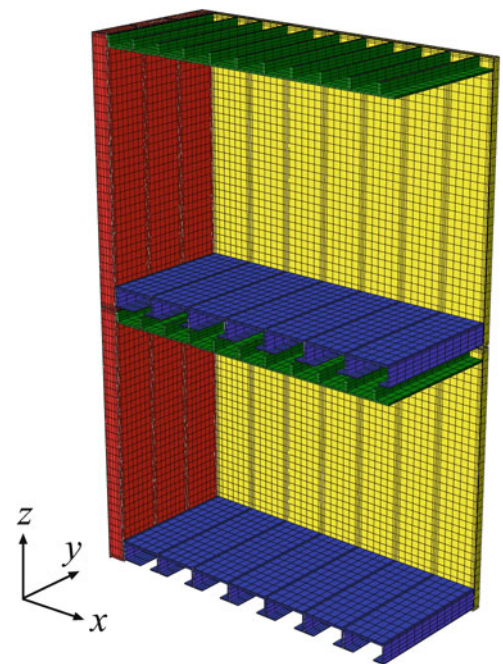

Fig. 45.5 A quarter of the FE model of two stacked TVEs. The apartment separating walls are shown in *yellow*, the facade walls in *red*, the ceiling in *green*, the floor in *blue* and the elastomer blocks in *grey*

Table 45.2 Material parameters used for the isotropic materials

Material	E (MPa)	ν (−)	ρ (kgm^{-3})
Particle board	3,000	0.3	767
Plaster board	2,000	0.2	692.3
Plywood	12,400	0.3	710

E is the Young's modulus, ν is the Poisson's ratio and ρ is the density

Table 45.3 Material parameters used for the wood beams

E_1 (MPa)	E_2	E_3	G_{12} (MPa)	G_{13}	G_{23}	ν_{12} (−)	ν_{13}	ν_{23}	ρ (kgm^{-3})
8,500	350	350	700	700	50	0.2	0.2	0.3	432

G is the shear modulus

The model was analysed in terms of steady-state frequency sweeps in order to study the vibration transmission from the floor in the upper TVE to the ceiling in the lower TVE at various frequencies. The surfaces at the four corners on the bottom of the lower TVE and on the top of the upper TVE, where elastomer blocks would be placed if further storeys were included, were modelled as clamped. A harmonic unit point load was applied in the vertical direction at the floor structure of the upper TVE, located in a point 300 mm in the x-direction (see Fig. 45.5) from the mid-point of the floor in order to be placed in the span between two beams.

The steady-state response was calculated for frequencies up to 100 Hz, the resulting acceleration amplitudes being evaluated at the surfaces of the floor in the upper TVE and the ceiling in the lower TVE. The magnitude of the complex acceleration amplitudes were calculated for the nodes at the surfaces. The accelerations were evaluated in a quarter of each surface due to conditions close to symmetry, the exception being the 300 mm shift of the position of the load. An RMS value was calculated for each frequency step in the analyses, and for each of the two surfaces, as

$$a_{\text{RMS}}(f) = \sqrt{\frac{1}{n} \sum_{i=1}^{n} a_i^2(f)}, \tag{45.3}$$

where f is the frequency, a_i is the magnitude of the complex accelerations in each node and n is the number of nodes at a quarter of the floor surface or a quarter of the ceiling surface. All the RMS values presented in the paper are given in decibel with 1 μm/s^2 as reference value.

45.3.1 Model Reduction

In order to improve the computational efficiency of the FE model, substructuring [16] was applied by considering each TVE as a substructure. Both interface reduction and model order reduction were employed to establish an efficient reduced order system. The number of degrees of freedom at the interfaces between the TVEs and the elastomer blocks were reduced by employing the concept of using a condensation node [17] for each interface surface. The coupling between a condensation node and its interface surface can be realised in different ways, a number of alternatives being compared in [18] for a model of a wooden floor-ceiling structure involving an elastomer layer. It was concluded that a rigid coupling should be employed for the interface surfaces of the elastomer parts and that a uniformly distributed coupling should be employed for the interface surfaces of the wooden parts. The latter type of coupling distributes the forces acting on the condensation node uniformly to the nodes of its interface surface. The findings in [18] were employed for the interface surfaces in the model investigated here.

A number of methods for model order reduction, applied to wooden building structures, were compared in [19]. It was found that the Craig-Bampton method [20] provides reduced order models with adequate accuracy compared to other available methods, and this method was, hence, used in the present study to create reduce order models of the TVEs. The Craig-Bampton method generates reduced models containing the interface degrees of freedom of the full model together with generalised coordinates representing some of the fixed-interface eigenmodes of the model. Reduced models of the two stacked TVEs, involving different numbers of retained eigenmodes in the Craig-Bampton reduction, were investigated in order to find a reduced model with acceptable accuracy and reasonable computation time. In the comparison of the reduced models, the elastomer blocks were modelled with the viscoelastic properties determined in [10], i.e the material properties of Sylodyn NE. When employing a reduced model with 400 retained eigenmodes in each of the two TVEs, the error in RMS

values at the ceiling surface, compared to the full model, was found to be below 50 % up to 100 Hz. At the floor surface, the error in RMS values was found to be less than 20 % up to 100 Hz. These levels of error were considered acceptable, bearing in mind that the parametric studies carried out in this investigation aim at establishing the relative differences in vibrations for the different models under study, and not at a quantification of the vibration levels.

45.4 Parametric Studies

The numerical model described in Sect. 45.3 was used as a reference model for investigating the effects of varying the properties of the elastomer material and the positioning of the elastomer blocks.

45.4.1 Material Properties

The properties of the elastomer material were varied by using different values of the scaling parameter x, described in Sect. 45.2. Setting $x = 0$ and $x = 9.63$ results in the parameters for the softest and the stiffest of the investigated elastomer materials, Sylodyn NB and NF, respectively. In the parametric study, x was varied from -0.5 to 20, these values resulting in a span of G_R from half the value for Sylodyn NB to twice the value for Sylodyn NF. The material properties obtained when x is set to -0.5, 0.0, 10 and 20 are shown in Fig. 45.6. The RMS values of the acceleration amplitudes in the floor and in the ceiling, obtained for different values of x, are shown in Fig. 45.7 and Fig. 45.8, respectively. In the figures, the frequency spectra of the RMS values obtained for different values of x are plotted, as well as the mean value of the frequency spectra as function of x. Moreover, the RMS values obtained from a model with the two TVEs stacked directly on top of each other, without any elastomer layer in between, are also presented in the results.

It can be observed in Fig. 45.7 that the effect of the properties of the elastomer material, on the acceleration amplitudes in the floor, is weak. Varying the parameters of the elastomer material results in a negligible difference in RMS values; 0.01 dB when studying the mean value of the frequency spectra. Compared to having no elastomer layer in between the TVEs, the RMS values in the floor are reduced by about 1 dB for frequencies above 30 Hz.
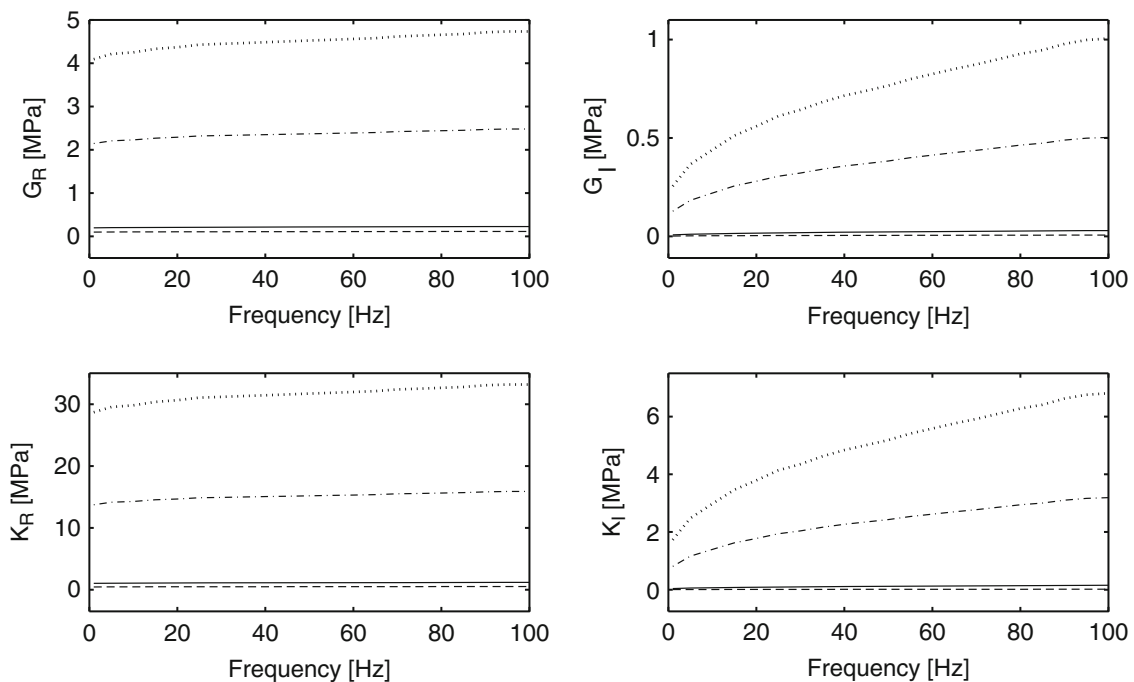

Fig. 45.6 The shear and bulk moduli obtained for $x = -0.5$ (*dashed line*), $x = 0.0$ (*solid line*), $x = 10$ (*dash-dot line*) and $x = 20$ (*dotted line*)
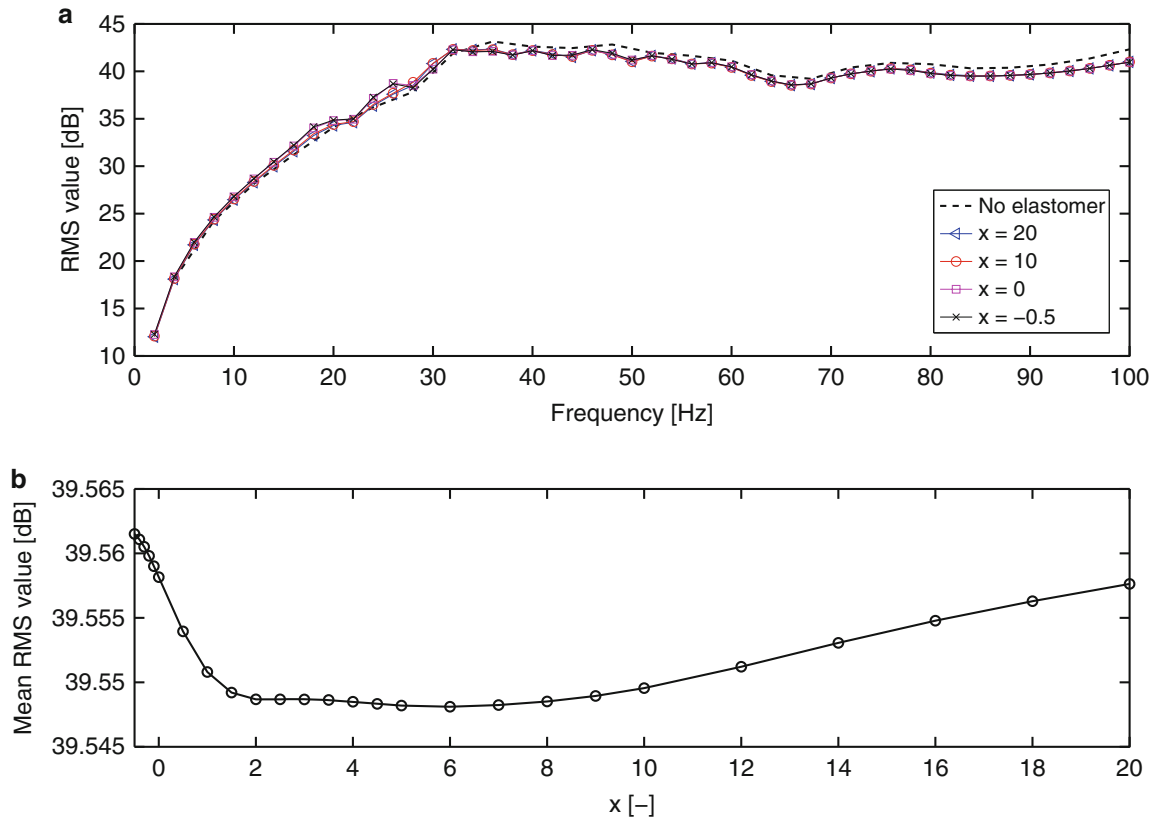
Fig. 45.7 The RMS values of the acceleration amplitudes at the floor surface presented as (**a**) function of frequency and (**b**) in terms of the mean value of each frequency spectrum, plotted versus the scaling parameter

The properties of the elastomer material have a larger effect on the RMS values in the ceiling, as can be observed in Fig. 45.7. The difference in mean value of the RMS values, when comparing the softest and the stiffest of the investigated material properties ($x = -0.5$ and $x = 20$, respectively), is about 9 dB. For frequencies below 50 Hz, there is a marked reduction in vibration levels compared to having no elastomer material in between the TVEs. Above 50 Hz, however, the use of elastomers in the junctions can lead to increasing acceleration amplitudes in the ceiling for certain frequencies. This observation is in agreement with the experimental results presented in [9]. Moreover, decreasing the stiffness of the elastomer material can lead to an amplification of the vibrations for certain, higher, frequencies and for certain degrees of stiffness of the material.

45.4.2 Placement

The placement of the elastomer blocks was varied by shifting all the blocks, except the blocks at the four corners, a certain distance along the gap between the walls of the two stacked TVEs, retaining the centre-to-centre distance of 600 mm. Three models were studied, in which the blocks were shifted 100, 200 and 300 mm, respectively. No model reduction was performed for the models compared in this study.

The RMS values of the acceleration amplitudes in the ceiling surface, obtained from the analyses of the different models, are shown in Fig. 45.9. It can be observed that the shifted placement of the elastomer blocks has a small effect on the vibration levels in the ceiling, resulting in acceleration amplitudes differing less than 0.5 dB from the reference model for all the investigated models and in the whole frequency range. This could be explained by the deformation pattern along the walls connecting to the elastomer blocks; the dominating wavelengths were larger than the centre-to-centre distance of the blocks. The effect of the placement is, therefore, low as long as the centre-to-centre distance of the blocks is retained.
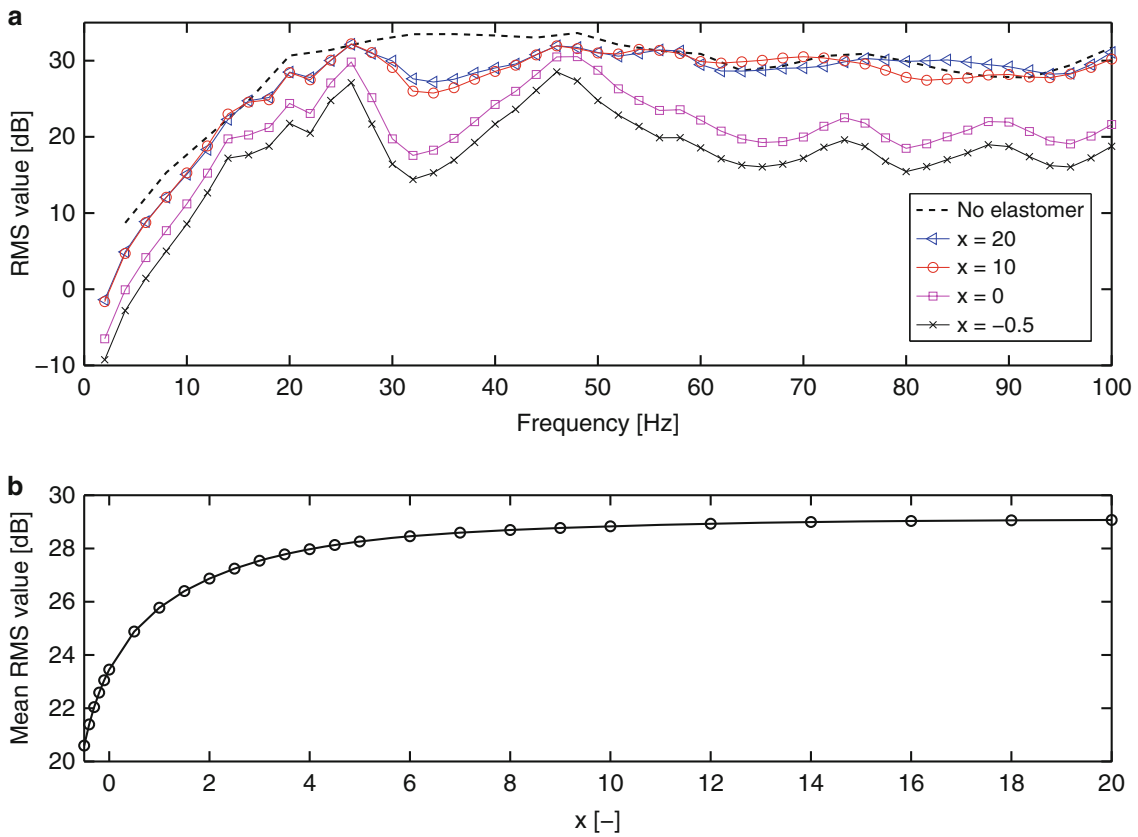
Fig. 45.8 The RMS values of the acceleration amplitudes at the ceiling surface presented as (**a**) function of frequency and (**b**) in terms of the mean value of each frequency spectrum, plotted versus the scaling parameter
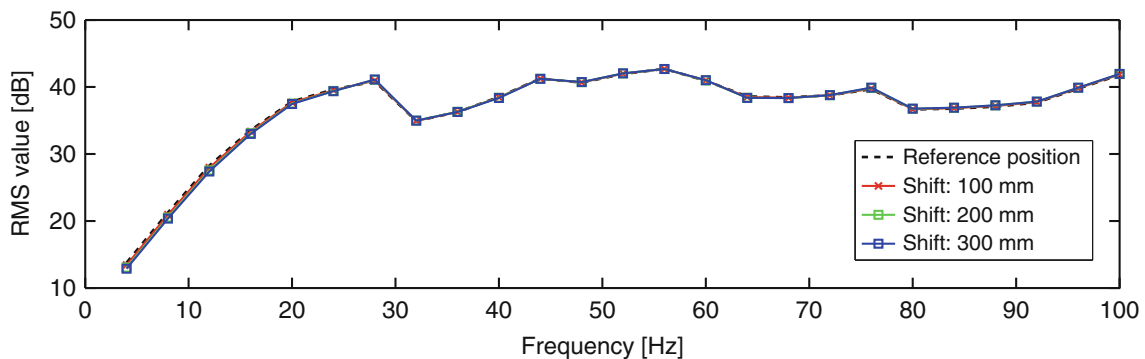
Fig. 45.9 The RMS values of the acceleration amplitudes in the ceiling for different placements of the elastomer blocks

45.5 Conclusions

The objective of the studies presented here was to investigate the extent to which the design of the elastomer layers involved in multi-storey wood buildings affects the vibration transmission between different storeys. This was carried out by performing parametric studies on numerical models of two storeys of a building, varying the material properties of the elastomer material within realistic ranges and modifying the placement of elastomer blocks, while studying the vibrations caused by a load acting on the floor of the upper storey.

The properties of the elastomer material were found to have a negligible effect on the acceleration amplitudes of the floor where the load is acting. For the transmission to the underlying ceiling, however, the properties of the elastomer material were found to affect the acceleration amplitudes appreciably. In general, softer elastomer materials result in decreased vibration

transmission to the ceiling, exceptions being found for certain frequencies. This indicates the importance of using elastomer materials which are no stiffer than what is required to withstand the static loads, in order to achieve the best possible vibration isolation in the buildings. In case a very stiff material is required, the elastomer layer can lead to an amplification of the vibration levels for some frequencies. For such situations, it could be preferable to develop other types of joints with better vibration isolation performance.

The placement of the elastomer blocks was found to have a small effect on the acceleration amplitudes both in the floor and in the ceiling, when assuming constant centre-to-centre distance between the blocks. This could be explained by the fact that the dominating wavelengths at the walls connecting to the blocks were larger than the centre-to-centre distance of the blocks. In order to affect the vibration transmission to a larger extent, through changes in the placement of the blocks, it is, hence, necessary to abandon the regular centre-to-centre distance between the blocks. The effect of adding or removing blocks at certain positions could be investigated for this purpose.

References

1. Stehn L, Rask LO, Nygren I, Östman B (2008) Byggandet av flervåningshus i trä – Erfarenheter efter tre års observation av träbyggandets utveckling. Technical Report, Luleå University of Technology, Sweden
2. Gustavsson L, Pingoud K, Sathre R (2006) Carbon dioxide balance of wood substitution: comparing concrete- and wood-framed buildings. Mitig Adapt Strateg Glob Change 11:667–691
3. Forssén J, Kropp W, Brunskog J, Ljunggren S, Bard D, Sandberg G, Ljunggren F, Ågren A, Hallström O, Dybro H, Larsson K, Tillberg K, Sjökvist LG, Östman B, Hagberg K, Bolmsvik Å, Olsson A, Ekstrand CG, Johansson M (2008) Acoustics in wooden buildings – State of the art 2008: Vinnova project 2007-01653. SP Technical Research Institute of Sweden, Report 2008:16
4. Simmons C, Hagberg K, Backman E (2011) Acoustical performance of apartment buildings – resident's survey and field measurements, AkuLite Report 2. SP Technical Research Institute of Sweden, Report 2011:58
5. Ljunggren F, Simmons S, Hagberg K (2014) Correlation between sound insulation and occupants' perception – Proposal of alternative single number rating of impact sound. Appl Acoust 85:57–68
6. ISO 717-2 (2013) Rating of sound insulation in buildings and of building elements – Part 2: impact sound insulation
7. Ljunggren F, Ågren A (2002) Development of a new damper to reduce resonant vibrations in lightweight steel joist floors. Appl Acoust 63:1267–1280
8. Ljunggren F, Ågren A (2011) Potential solutions to improved sound performance of volume based lightweight multi-storey timber buildings. Appl Acoust 72:231–240
9. Bolmsvik Å, Brandt A (2013) Damping assessment of light wooden assembly with and without damping material. Eng Struct 49:434–447
10. Negreira J (2013) Vibrations in lightweight buildings – Perception and prediction. Licentiate dissertation, Division of Engineering Acoustics, Lund University, Sweden
11. Dassault Systèmes (2012) Abaqus 6.12 documentation
12. Flodén O (2014) Vibrations in lighweight structures – Efficiency and reduction of numerical models. Licentiate dissertation, Division of Structural Mechanics, Lund University, Sweden
13. Negreira J, Bard D (2013) Finite element modelling of a Timber Volume Element based building with elastic layer insulators. SP Technical Research Institute of Sweden, Report 2013:27
14. AkuLite (2012) Mätrapport 10052. Brunnby Park, Upplands Väsby, Sweden
15. Chopra AK (2007) Dynamics of Structures. Prentice Hall, New Jersey
16. de Klerk D, Rixen DJ, Voormeeren SN (2008) General framework for dynamic substructuring: history, review and classification of techniques. AIAA J 46(5):1169–1181
17. Heirman GHK, Desmet W (2010) Interface reduction of flexible bodies for efficient modeling of body flexibility in multibody dynamics. Multibody Syst Dyn 24(2):219–234
18. Flodén O, Persson K, Sandberg G (2014) Coupling elements for substructure modelling of lightweight multi-storey buildings. In: Dynamics of Coupled Structures, vol 1, pp 113–124. Springer, New York
19. Flodén O, Persson K, Sandberg G (2014) Reduction methods for the dynamic analysis of substructure models of lightweight building structures. Comput Struct 138:49–61
20. Craig RR, Bampton M (1968) Coupling of substructures in dynamic analysis. AIAA J 6:1313–1319

Chapter 46
Dynamic Compensators for Floor Vibration Control

Donald Nyawako, Paul Reynolds, and Emma Hudson

Abstract In recent years, active control of flexible structures has been studied extensively. The motivation for continual studies with this approach is that the vibration performance of flexible structures can be improved significantly via control. For example, the performance of civil engineering floor structures, which the present research work is based on, is increasingly being governed by meeting permissible vibration serviceability limits depending upon their respective usages, and this can usually be enhanced via active control. This then offers designers increased flexibility to realise more lightweight, longer span and open-plan floor layouts that are in tune with the advancements in material and design technologies as well as meeting the challenges for reduced carbon footprint of new constructions.

The work presented here focuses on active control of human-induced vibrations in floor structures using dynamic compensators. These are formulated from reduced order plant models and vary in complexity depending on the number of plant modes of vibration used for their respective designs. It is demonstrated that there are increased options offered by higher dynamic compensator orders with respect to realising various vibration mitigation performance objectives: for example, the isolation and targeting of specific vibration modes. These compensators are found to possess desirable stability margins and are much less sensitive to disturbances at lower frequencies in comparison with direct velocity feedback (DVF). A study of the robustness of the dynamic compensators designed here to changes in structural properties, for example, that would arise under human-structure interaction is also presented. It is found that the performance of dynamic compensator performance can be sensitive to changes in structural dynamic properties as compared with a direct velocity feedback scheme, as seen in the closed-loop stability properties, which is not so obvious from a study of the disturbance rejection properties.

Keywords Vibration • Control • Stability • Compensators • Mitigation

46.1 Introduction

The advances in control theory that have been seen over the years have significantly enhanced the ability to control flexibility in structures more precisely and efficiently. They have comprised of the development and application of both linear and nonlinear controllers for a wide range of applications [1–8]. The motivation for continual studies with this approach is that the vibration performance of flexible structures can be improved significantly via control. For example, the performance of civil engineering floor structures which is increasingly being governed by meeting permissible vibration serviceability limits depending on respective usages can be enhanced via active control [4, 8, 9]. This would offer designers increased flexibilities to realise more lightweight, longer span and open plan floor layouts that are in tune with the advancements in material and design technologies as well as meeting the challenges for reduced carbon footprint of new constructions.

In past floor vibration control field trials with active vibration control (AVC) technology, predominantly direct output feedback approaches like the direct velocity feedback (DVF) has been investigated [4, 8–11].

Model-based control approaches have been extensively investigated and implemented in other sectors, for example, in the mechanical engineering and aerospace industries [5, 12, 13]. A family of model-based controllers of interest to this research work is observer-based compensators. With these schemes, all system states are generally not measurable and therefore state observers are included and incorporated in the pole placement design process. The complete controller is then given as an observer in cascade with the state variable feedback. Such controllers have been implemented for some specific applications such as improving air/fuel characteristics of spark ignition engines [14], control of permanent magnet synchronous motor without mechanical sensors [15] and torsion control of flexible shaft systems [16]. There have also been

---

D. Nyawako (✉) • P. Reynolds • E. Hudson

Vibration Engineering Section, College of Engineering, Mathematics and Physical Sciences, University of Exeter, Exeter EX4 4QF, UK

e-mail: d.s.nyawako@sheffield.ac.uk; p.reynolds@exeter.ac.uk; e.j.hudson@exeter.ac.uk

successful implementations of modal control schemes in other case studies, for example, in multi-modal control of beam and model frame structures [17, 18]. Some trials have been carried out in large-scale civil engineering structures [19, 20], but they have hardly been implemented in floor vibration control trials. Some challenges concerning design freedoms that guarantee both overall closed-loop stability and controller stabilities with these approaches have been addressed in some research works [21, 22].

The primary aim of the studies presented here is to investigate the potential benefits and design freedoms that may be derived from using higher order observer-based compensators and make comparisons with a typical Direct Velocity Feedback scheme. A further study investigates the performances and stability properties of the derived compensators for changes or perturbations in the structural dynamic properties, for example, under human-structure interactions. All the controllers are implemented in a single-input single-output (SISO) controller structure, with the collocated sensor and actuator pair sited at a chosen location on the structure. The structure whose dynamic properties are used in these studies is a walkway bridge structure in the Forum Building, University of Exeter.

46.2   Actuator and Walkway Bridge Dynamics

The actuators used in this research work are APS dynamics, model 400 electro-seis shakers. They have an inertial mass of 30.4 kg and a maximum stroke of 15 cm. The peak drive voltage to the amplifier is 2.0 V. Their drive power is obtained from a power amplifier, the APS Dynamics Model 124-EP. Figure 46.1a, b show the experimental force-voltage characteristics for the current drive mode in which the actuators are used here. Also within these plots are the traces of the derived analytical model in Eq. 46.1a, whose parameters are determined as: $K_{act} = 300$ N/V, $\zeta_{act} = 0.10$ and $\omega_{act} = 8.17$ rad/s. Equation 46.1b shows the displacement-voltage characteristic.

$$G_{act}(s) = \frac{F(s)}{V(s)} = \frac{K_{act}s^2}{s^2 + 2\zeta_{act}\omega_{act}s + \omega_{act}^2} \qquad (46.1a)$$

$$G_{actd}(s) = \frac{D(s)}{V(s)} = \frac{K_{actd}}{s^2 + 2\zeta_{act}\omega_{act}s + \omega_{act}^2} \qquad (46.1b)$$

Figure 46.2a, b are photos of the walkway bridge structure, and Fig. 46.2c shows the test grid for the EMA tests. For the EMA tests, two excitation shakers located at TP4 and TP7 were driven by statistically uncorrelated random signals. Their forces were measured using two Endevco 7754A-1000 accelerometers attached to their inertial masses, and walkway bridge responses were measured with 13 QA-750 force balance accelerometers that were roved along grid lines 1–13, 14–26 and 27–39. A Data Physics Mobilyzer II digital spectrum analyser was used for data acquisition. Force and vibration response data were sampled using a baseband setting of 80 Hz on the spectrum analyser, corresponding with a sampling rate of 204.8 Hz.
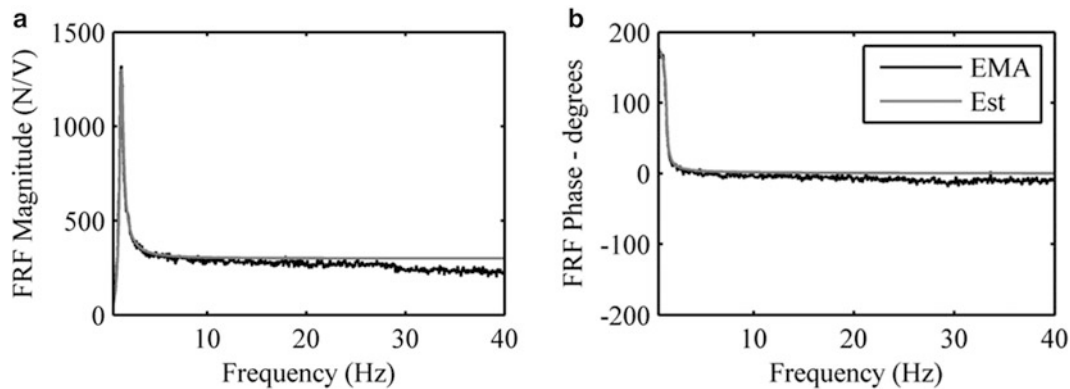

Fig. 46.1 Actuator dynamics – FRF magnitude and phase (EMA – experimentally measured trace, Est – analytical derived model trace). (**a**) FRF Magnitude, (**b**) FRF Phase
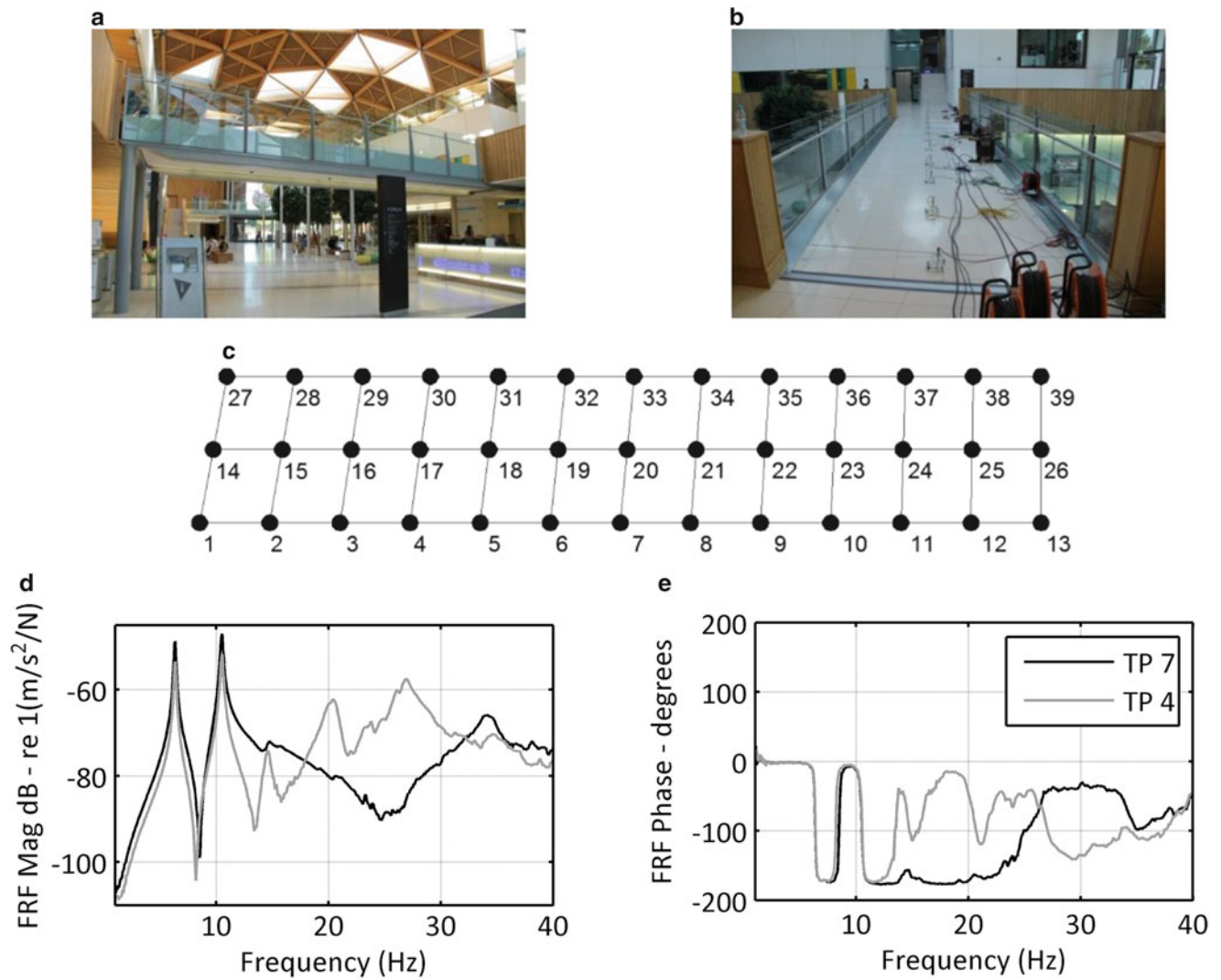
Fig. 46.2 Walkway bridge photos, test grid, and point acceleration FRFs (0–40 Hz). (**a**) Sectional photo. (**b**)Aerial photo. (**c**) Test grid for EMA. (**d**) Point acceleration FRF magnitudes. (**e**) Point acceleration FRF phases

Table 46.1 Summary of estimated modal properties from EMA

Mode	Natural frequency [Hz]	Damping ratio [%]
1	6.34	1.0
2	10.5	0.9
3	14.6	2.2
4	20.5	2.6
5	26.1	0.7
6	26.9	1.1
7	34.3	2.3

Each data acquisition window was 32 s in length, and the acquisitions were made using a Hanning window and 75 % overlap, which were averaged to calculate the uncontrolled FRFs. Figure 46.2d, e show point acceleration FRF magnitudes and phases at TPs 4 and 7.

The FRF data from the EMA test was analysed using ME'scopeVES parameter estimation software to determine the modal properties i.e. the natural frequencies, modal damping ratios and mode shapes of the structure. Some of the key results from this estimation process are summarised in Table 46.1, and mode shapes corresponding with the first two vibration modes are shown in Fig. 46.3a, b.

A lumped parameter model with n = 7 modal co-ordinates in Eq. 46.2a is formulated, and the state space representations derived in Eqs. 46.2b and 46.2c can be tailored to provide outputs in both modal or spatial velocities and accelerations.

Fig. 46.3 Typical mode shapes for modes 1 and 2. (**a**) Mode shape for mode 1–6.34 Hz. (**b**) Mode shape for mode 2–10.50 Hz
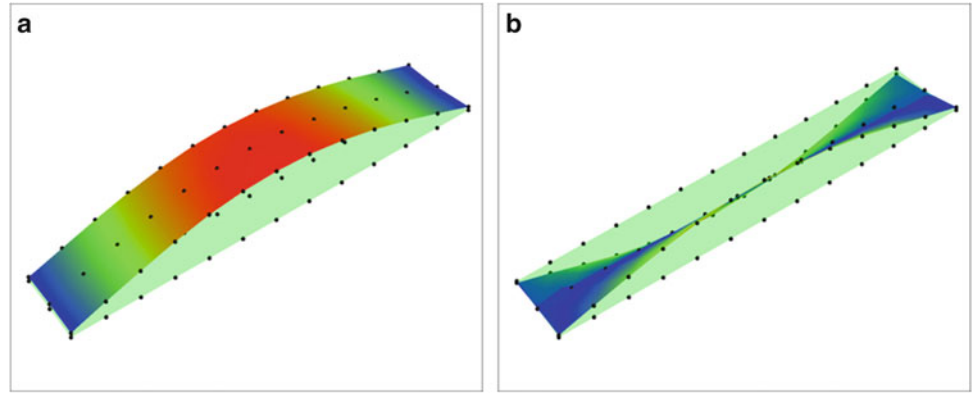
Appropriate reduced-order models (ROMs) can thus be extracted for controller designs. M^*, C^* and K^* are the n × n modal mass, modal damping and modal stiffness matrices, whilst $\varnothing$ is the m × n mass normalised modal transformation matrix. D is the m × m actuator location matrix and E is the m × m excitation force location matrix. ζ_i and ω_i are the modal damping and natural circular frequency coefficients of the i th vibration mode.

$$M^*\ddot{z} + C^*\dot{z} + K^*z = \varnothing^T Du + \varnothing^T Ef \qquad (46.2a)$$

$$\begin{Bmatrix} \dot{x}_1 \\ \dot{x}_2 \end{Bmatrix} = \begin{bmatrix} 0 & I \\ -\frac{K^*}{M^*} & -\frac{C^*}{M^*} \end{bmatrix} \begin{Bmatrix} x_1 \\ x_2 \end{Bmatrix} + \begin{bmatrix} 0 & 0 \\ \varnothing^T D & \varnothing^T E \end{bmatrix} \begin{Bmatrix} u \\ f \end{Bmatrix} \qquad (46.2b)$$

$$\begin{Bmatrix} y_1 \\ y_2 \end{Bmatrix} = \begin{bmatrix} 0 & I \\ -\frac{K^*}{M^*} & -\frac{C^*}{M^*} \end{bmatrix} \begin{Bmatrix} x_1 \\ x_2 \end{Bmatrix} + \begin{bmatrix} 0 & 0 \\ \varnothing^T D & \varnothing^T E \end{bmatrix} \begin{Bmatrix} u \\ f \end{Bmatrix} \qquad (46.2c)$$

$$K^* = \begin{bmatrix} \omega_1^2 & 0 & \cdots & 0 \\ 0 & \omega_2^2 & \cdots & 0 \\ \vdots & \vdots & \ddots & \vdots \\ 0 & 0 & \cdots & \omega_7^2 \end{bmatrix} \quad C^* = \begin{bmatrix} 2\zeta_1\omega_1 & 0 & \cdots & 0 \\ 0 & 2\zeta_2\omega_2 & \cdots & 0 \\ \vdots & \vdots & \ddots & \vdots \\ 0 & 0 & \cdots & 2\zeta_7\omega_7 \end{bmatrix}$$

where

$$M^* = \begin{bmatrix} 1 & 0 & \cdots & 0 \\ 0 & 1 & \cdots & 0 \\ \vdots & \vdots & \ddots & \vdots \\ 0 & 0 & \cdots & 1 \end{bmatrix} \quad \varnothing = \begin{bmatrix} \varnothing_{1,1} & \varnothing_{1,2} & \cdots & \varnothing_{1,7} \\ \varnothing_{2,1} & \varnothing_{2,2} & \cdots & \varnothing_{2,7} \\ \vdots & \vdots & \ddots & \vdots \\ \varnothing_{39,1} & \varnothing_{39,2} & \cdots & \varnothing_{39,7} \end{bmatrix}$$

For these SISO studies, TP7 is selected for siting the collocated sensor and actuator pair as it is closest to the antinodes of the two lowest modes of vibration in Table 46.1. Figure 46.4a, b show the magnitude and phase plots of both the EMA measurement and ROM that is derived based on the three dominant modes of vibration observable at TP7.

46.3 Controller Designs

A typical control scheme used in this work is shown in Fig. 46.5. $G_p(s)$, $G_{act}(s)$, $G_{bp}(s)$, $G_{not}(s)$ and $G_c(s)$ are the walkway bridge, actuator, band pass filter, notch filter and controller dynamics. For mitigation of human induced vibrations, the disturbance rejection property derived in Eq. 46.3 is the key objective as human walking forces cannot directly be measured.
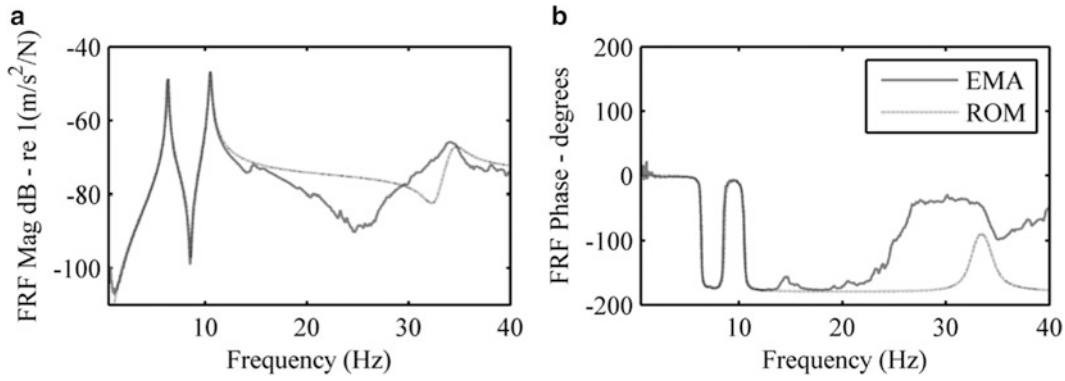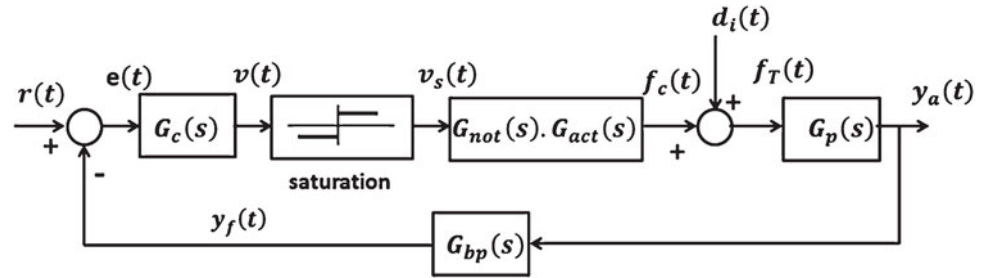
Fig. 46.4 EMA and ROM point accelerance FRF magnitudes and phases at TP7. (**a**) FRF magnitude, (**b**) FRF phase

Fig. 46.5 Controller scheme for both PI controller and observer based controller

The transfer function between the actuator displacement and the disturbance input is shown in Eq. 46.4. This is used to study the sensitivity of the actuator reactive mass displacement to the disturbance input mainly around the actuator resonant frequency which, coincidentally, falls within the range of human walking frequencies. Notch filters, $G_{not}(s)$, in Eq. 46.5 ($k_{not} > 1$) are designed to compensate for the low damping of actuator dynamics in the current drive mode.\vspace*{4pt}

$$Y_a(s) = \frac{G_p(s)}{1 + G_p(s)G_{not}(s)G_{act}(s)G_c(s)G_{bp}(s)} D_i(s) \tag{46.3}$$

$$Y_{actd}(s) = -\frac{G_{not}(s)G_{actd}(s)G_c(s)G_{bp}(s)G_p(s)}{1 + G_{not}(s)G_{actd}(s)G_c(s)G_{bp}(s)G_p(s)} D_i(s) \tag{46.4}$$

$$G_{not}(s) = \frac{s^2 + 2\zeta_{not}\omega_{not}s + \omega_{not}^2}{s^2 + 2k_{not}\zeta_{not}\omega_{not}s + \omega_{not}^2} \tag{46.5}$$

The governing requirements to be met by all controllers are set out as:

1. To meet minimum stability margins, i.e. Gain Margin (GM) of 3 dB and Phase Margin (PM) of 30 degrees.
2. The peak of Eq. 46.1b around the actuator resonance, i.e. $s = j\omega_{act}$, should not exceed the threshold of 0.05 mm/N. This is a dynamic quantity that reduces the potential for stroke saturation from the harmonics of walking around the actuator resonant frequency.

The two controller schemes studied in this work, and which are implemented at TP7 include:

(a) A direct velocity feedback (DVF) scheme

The optimum DVF controller here is defined as the maximum gain realizable that provides maximum enhancement in damping to the observable vibration modes at TP7, whilst meeting requirements (1) and (2) above. A second order Butterworth band pass filter with cut-off frequency, $G_{bp}(s) = 1.0$–30.0 Hz, is implemented with this controller together with the notch filter in Eq. 46.5, for $k_{not} = 6.4$, $\zeta_{not} = 0.12$, $\omega_{not} = 8.16$. This yields $K_g = 800$ in Eq. 46.6. The magnitude

Table 46.2 Minimum stability margins from all controllers

Controller	GM – dB	PM – degrees
$G_{DVF}(s)$	14.0	65.7
$G_{c1}(s)$	10.6	60.1
$G_{c2}(s)$	10.8	53.3
$G_{c3}(s)$	11.2	52.0

Fig. 46.6 Shortened form of dynamic regulator [23]
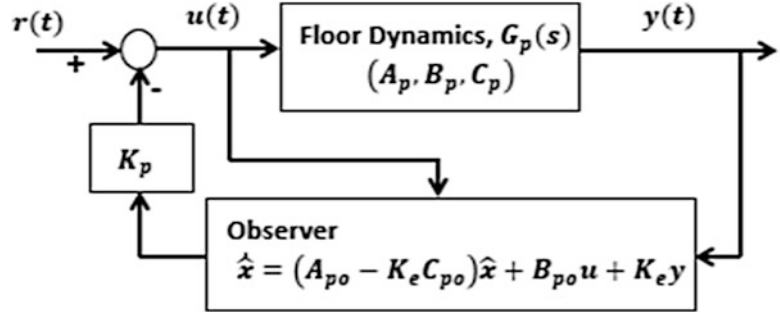
and phase characteristics of Eq. 46.6 are shown in Fig. 46.7. The minimum stability margins are outlined in Table 46.2, and Fig. 46.8a, b show the Nyquist contour plot of $G_{DVF}(s)G_{act}(s)G_{not}(s)G_{bp}(s)G_p(s)$ and the peaks of Eq. 46.4 within the critical frequency span 0.5–5.0 Hz.

$$G_c(s) = G_{DVF}(s) = \frac{K_g}{s} \tag{46.6}$$

(b) Dynamic controllers – a series of observer-based controllers are designed to meet some specified design objectives: $G_{c1}(s)$ is designed to isolate and control mainly the first vibration mode, $G_{c2}(s)$ is designed to isolate and control mainly the second vibration mode, whilst $G_{c3}(s)$ is designed to control both the first and second vibration modes.

The observer-based controllers are obtained from Fig. 46.6, in which (A_p, B_p, C_p) and (A_{po}, B_{po}, C_{po}) are the existing walkway bridge dynamics and its reduced-order model (ROM). The ROM considers the three dominant vibration modes observable at TP7. $\widehat{x}$ are estimated modal states of the observer, K_p are the modal feedback gains required to achieve desired closed-loop eigenvalues of the walkway bridge, and K_e are observer gains. Some literature on formulation of observer based controllers can be found in the works of [22, 23].

There are infinite choices of desired walkway bridge eigenvalues as well as observer eigenvalues. For this work, the desired closed-loop eigenvalues to be realised by each of the controllers are specified in Table 46.3, and the controllers that are designed to achieve these objectives are shown in Eqs. 46.7a, 46.7b and 46.7c. These are of sixth order by virtue of the number of plant modes used for their design. Their respective magnitude and phase characteristics are highlighted in Fig. 46.7, which show desirable low frequency characteristics compared to pure DVF controller as well as suitable roll-off characteristics at higher frequencies. Second order Butterworth band pass filters: $G_{bp1}(s)$, $G_{bp2}(s)$, $G_{bp3}(s)$ with cut-off frequencies of 0.5– 5.0 Hz, 0.5–30.0 Hz, and 0.5–40.0 Hz are implemented with $G_{c1}(s)$, $G_{c2}(s)$ and $G_{c3}(s)$, together with the notch filter in Eq. 46.5, with parameters: $k_{not} = 2.1$, $\zeta_{not} = 0.12$, $\omega_{not} = 8.16$. The notch filters are implemented to reduce potential of spillover instability from higher resonances. The minimum stability margins for all controllers are outlined in Table 46.2, and Fig. 46.8a, b show the Nyquist contour plots of $G_c(s)G_{act}(s)G_{not}(s)G_{bp}(s)G_p(s)$, in which $G_c(s)$ takes the form of either $G_{c1}(s)$, $G_{c2}(s)$ or $G_{c3}(s)$ and the peaks of Eq. 46.4 within the frequency span 0.5–5.0 Hz. Also within Table 46.3 are the resultant closed-loop eigenvalues from implementation of these controllers.

$$G_{c1}(s) = \frac{153.5 \, (s + 596.5) \, (s^2 + 2.9s + 4339) \, (s^2 + 89.2s + 2.6e4)}{(s^2 + 71s + 2161) \, (s^2 + 10.2s + 4266) \, (s^2 + 39.6s + 4.6e4)} \tag{46.7a}$$

$$G_{c2}(s) = \frac{349.2 \, (s + 969.2) \, (s^2 + 0.8s + 1582) \, (s^2 + 24.7s + 4.5e4)}{(s^2 + 189.5s + 8771) \, (s^2 + 9.6s + 1665) \, (s^2 + 31.2s + 4.6e4)} \tag{46.7b}$$

Table 46.3 Desired and achieved eigenvalues of modes 1 and 2 of the walkway bridge structure

		Desired closed-loop eigenvalues	Achieved closed-loop eigenvalues
$G_{c1}(s)$	Mode 1	$-8.1 \pm 39.6i$	$-7.9 \pm 41.1i$
	Mode 2	$-1.2 \pm 66.0i$	$-1.2 \pm 66.0i$
	Mode 3	$-8.4 \pm 215.4i$	$-8.4 \pm 215.4i$
$G_{c2}(s)$	Mode 1	$-0.4 \pm 39.8i$	$-0.4 \pm 39.8i$
	Mode 2	$-10.5 \pm 61.8i$	$-10.2 \pm 59.8i$
	Mode 3	$-7.0 \pm 215.4i$	$-7.0 \pm 215.4i$
$G_{c3}(s)$	Mode 1	$-8.3 \pm 41.5i$	$-8.1 \pm 40.5i$
	Mode 2	$-9.6 \pm 63.8i$	$-9.2 \pm 64.6i$
	Mode 3	$-5.6 \pm 215.4i$	$-5.6 \pm 215.4i$
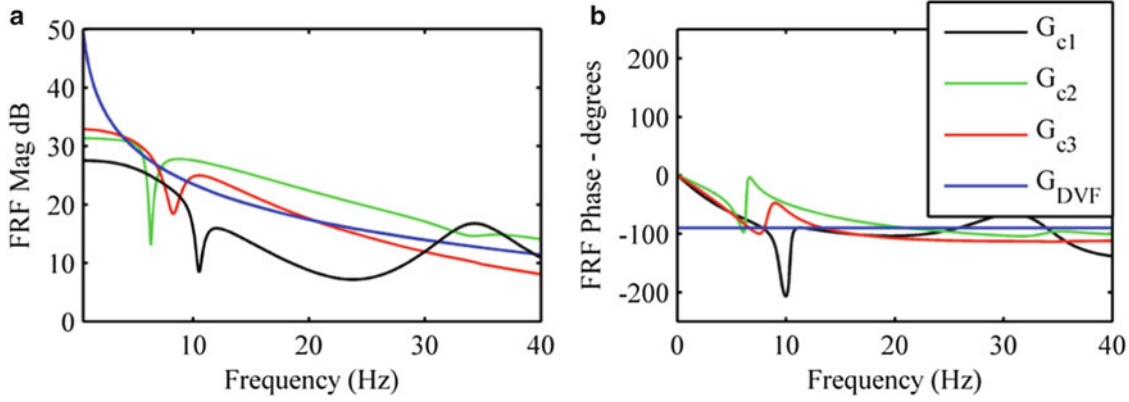
Fig. 46.7 FRF magnitude and phase plots of dynamic compensators and DVF controller. (**a**) FRF magnitudes. (**b**) FRF phases
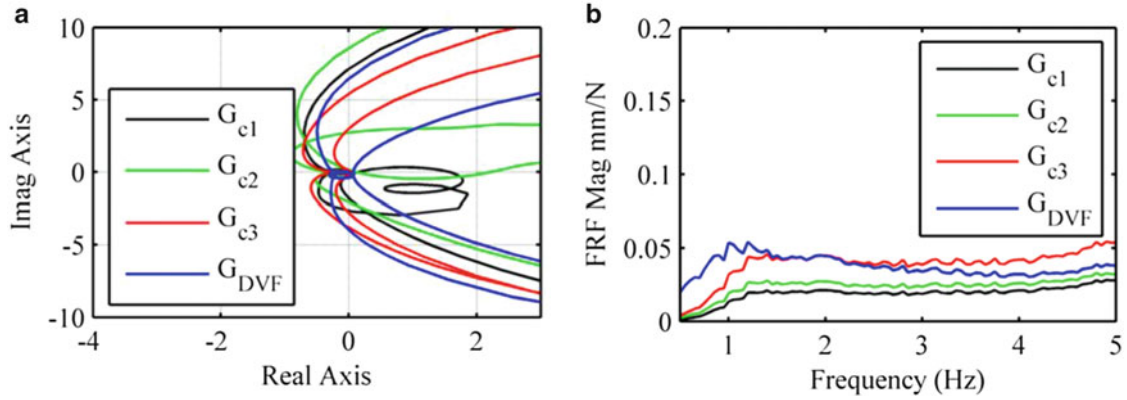
Fig. 46.8 Nyquist contour plots of $G_c(s)G_{act}(s)G_{not}(s)G_{bp}(s)G_p(s)$ and displacement-force characteristic in Eq. 46.4 for observer-based and DVF controller. (**a**) Nyquist contours, (**b**) Displacement-force characteristic

$$G_{c3}(s) = \frac{463.7\,(s + 244.1)\left(s^2 + 6.3s + 2706\right)\left(s^2 + 11.3s + 4.7e4\right)}{\left(s^2 + 80.9s + 2392\right)\left(s^2 + 20.3s + 2893\right)\left(s^2 + 11.2s + 4.6e4\right)} \tag{46.7c}$$

46.4 Analytical Studies

The analytical simulation studies presented here comprise of:

(a) Uncontrolled and controlled frequency response function (FRF) predictions with estimated ROM of walkway bridge in Eqs. 46.2a to 46.2c and implementation of compensators $G_{c1}(s)$, $G_{c2}(s)$, $G_{c3}(s)$, and $G_{DVF}(s)$.

Fig. 46.9 Uncontrolled and controlled frequency response functions with observer-based controllers and DVF scheme. (**a**) FRF magnitudes. (**b**) FRF phases

Table 46.4 Summary of modified walkway bridge modal properties from Table 46.1

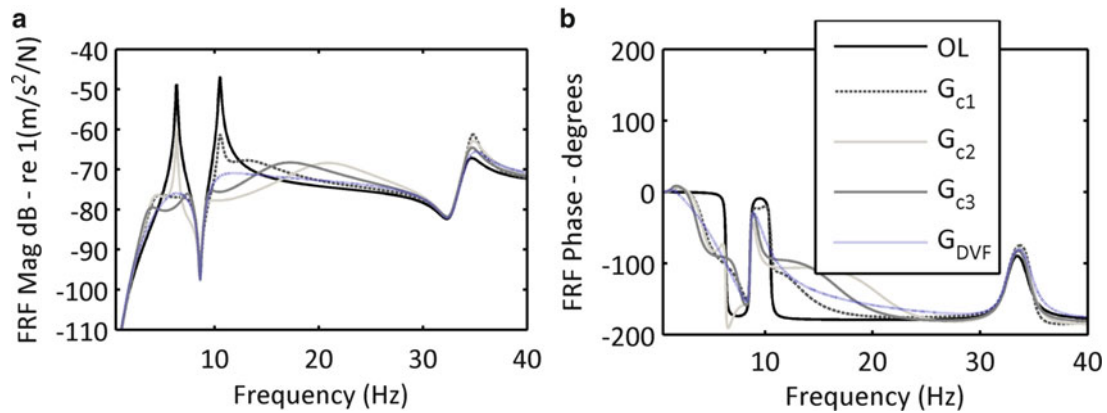| Mode	Natural frequency – M1 [Hz]	Damping ratio – M1 [%]	Natural frequency – M2 [Hz]	Damping ratio – M2 [%]
1	6.34	4.2	6.02	5.2
2	10.5	2.8	10.0	2.4
3	14.6	2.2	14.6	2.2
4	20.5	2.6	20.5	2.6
5	26.1	0.7	26.1	0.7
6	26.9	1.1	26.9	1.1
7	34.3	2.3	34.3	2.3

(b) Uncontrolled and controlled frequency response function (FRF) predictions with modified ROM of walkway bridge dynamics that reflect potential changes in the walkway bridge dynamics, for example, due to human-structure interactions, and again with implementation of the static controllers $G_{c1}(s)$, $G_{c2}(s)$, $G_{c3}(s)$, $G_{DVF}(s)$.

46.4.1 Uncontrolled and Controlled FRFS for Case (a)

For the estimated ROM from Eqs. 46.2a to 46.2c, the disturbance rejection estimates from Eq. 46.3, with all the controller sets: $G_{c1}(s)$, $G_{c2}(s)$, $G_{c3}(s)$, $G_{DVF}(s)$ in these analytical studies are presented in Fig. 46.9a, b.

46.4.2 Uncontrolled and Controlled FRFs for Case (b)

The presence of human subjects on structures, either in a passive or active form, as well as their numbers usually has the potential to change its dynamics in several ways, for example, through increased damping, or even increased damping and shifts in the resonant frequencies as seen in studies by [24]. In this research work, to simulate such scenarios and study the disturbance rejection properties of the controllers (static in a sense) designed: $G_{c1}(s)$, $G_{c2}(s)$, $G_{c3}(s)$, $G_{DVF}(s)$ to such perturbations, some realistic modifications were made to the estimated dynamics from the EMA test in Table 46.1 as shown in Table 46.4. Figure 46.10 shows the frequency response functions (FRFs) of the original ROM, as well as those with the modified dynamics (M1 and M2) in Table 46.5.

Figures 46.11a, b, c, d show typical simulated uncontrolled and controlled frequency response function magnitudes and phases for original ROM and modified ROM (in Table 46.4) for all controllers. OL and CL refer to open and closed-loop FRFs with original ROM, whilst M_{1U}, M_{2U} and M_{1C}, M_{2C} refer to open and closed loop FRFs with modified ROM in Table 46.4. Figure 46.12a, b show Nyquist contour plots of $G_c(s)G_{act}(s)G_{not}(s)G_{bp}(s)G_p(s)$, in which $G_c(s)$ takes the form of either $G_{c1}(s)$, $G_{c2}(s)$, $G_{c2}(s)$ or $G_{DVF}(s)$, and Table 46.5 shows the minimum stability margins with modifications M1 and M2.
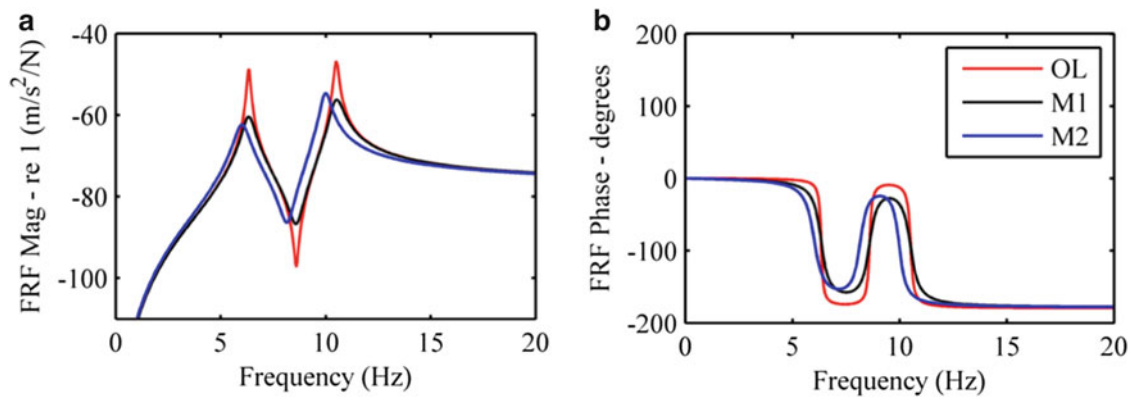
Fig. 46.10 Uncontrolled FRFs – estimated from EMA tests (OL) and altered (M1 and M2) to cater for potential changes due to presence of human subjects. (**a**) FRF magnitudes. (**b**) FRF phases

Table 46.5 Stability margins and displacement-force characteristics for all controllers

Controller	GM – dB (M1)	PM – degrees (M1)	GM – dB (M2)	PM – degrees (M2)
$G_{DVF}(s)$	13.1	61.1	12.2	62.3
$G_{c1}(s)$	6.6	54.1	6.6	49.9
$G_{c2}(s)$	8.7	48.9	6.8	43.3
$G_{c3}(s)$	9.4	52.1	7.9	45.8

46.5 Conclusions

This paper has been focused on active vibration suppression of human-induced vibrations in a walkway bridge structure. It has compared the vibration mitigation performances of two sets of controller schemes implemented in a SISO set-up: (1) a DVF controller based on measured walkway bridge acceleration response, and (2) a series of observer-based or dynamic controllers formulated from three structural vibration modes, respectively, also based on measured walkway bridge acceleration response. The studies also aimed at investigating potential implications on the performance and stability properties of these controllers under perturbations in the walkway dynamics, for example, caused by the presence of humans.

DVF controllers are attractive in the sense that they are quicker to formulate and they do offer appropriate enhancement to the damping properties of the walkway bridge structure. For purely SISO schemes, they attenuate resonant frequencies observable at a particular controller location.

With the observer-based (dynamic) compensators, the controller design requires both the selection of desired closed-loop eigenvalues of selected modes of vibration of the walkway bridge structure as well as appropriate observer eigenvalues. This can be quite a rigorous procedure and they do require appropriate plant models for their design. It is seen that higher order dynamic compensators, there is increased flexibilities for setting a range of objectives, ranging from isolation and control of specific resonances to the control of all resonant frequencies observable at a given location, even for a purely SISO scheme. The compensators are seen to be attractive in the sense that they possess low gains at low frequencies as compared with a pure DVF controller, which is reflected in Fig. 46.8b that studies the sensitivity of the actuator mass displacement to a disturbance input force.

It is seen, for example, from comparisons of Tables 46.2 and 46.5 that changes in structural properties can affect the stability properties of dynamic controllers whilst DVF is much less sensitive to such changes as seen in the Nyquist contour plots in Fig. 46.12. This is not obvious from an overview of Fig. 46.11 only.

Fig. 46.11 Uncontrolled and controlled FRFs – altered (M1 and M2) to cater for potential changes due to presence of human subjects. (**a**) FRF magnitudes (DVF). (**b**) FRF magnitudes ($G_{c1}(s)$). (**c**) FRF magnitudes ($G_{c2}(s)$). (**d**) FRF magnitudes ($G_{c3}(s)$)
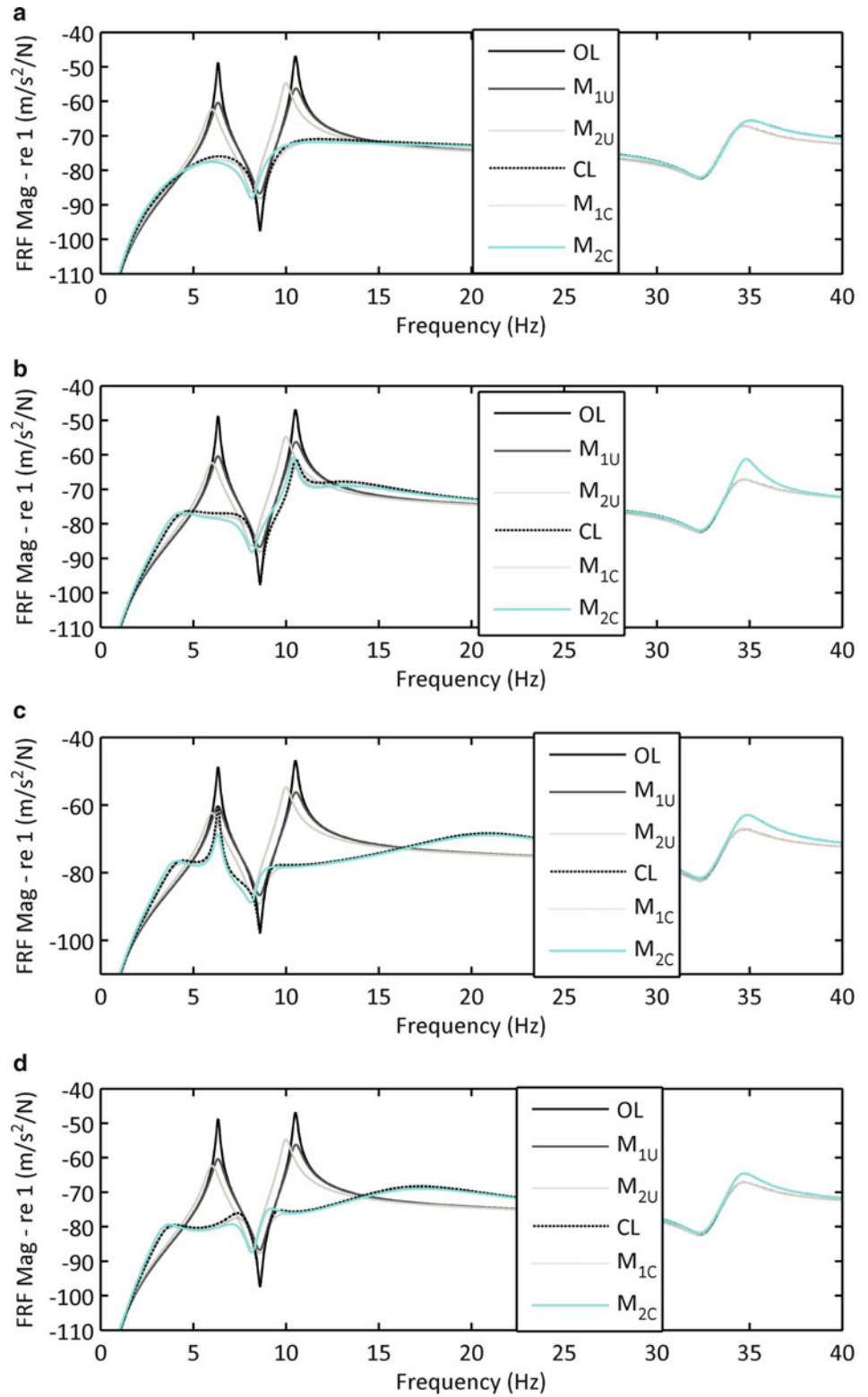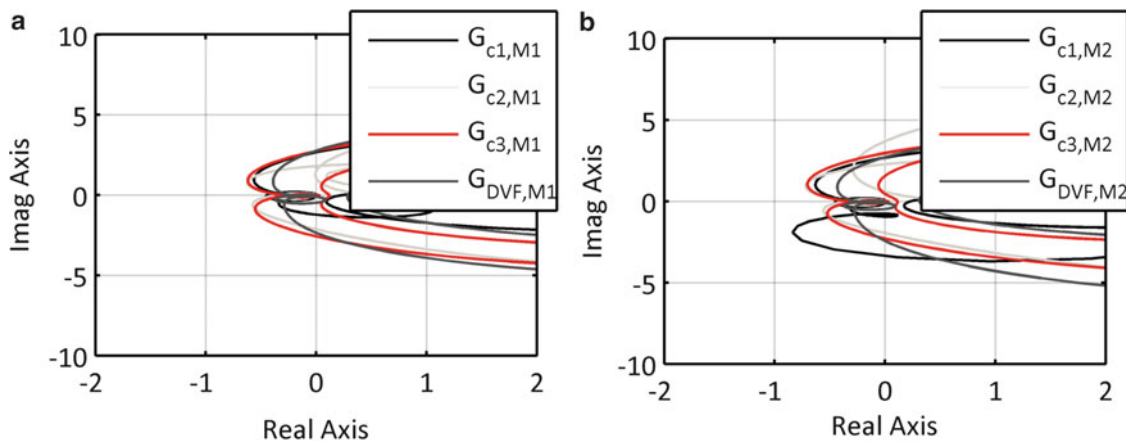
Fig. 46.12 Nyquist contour plots of $G_c(s)G_{act}(s)G_{not}(s)G_{bp}(s)G_p(s)$ for alterations in structural dynamic properties: M1 and M2 for observer-based and DVF controller. (**a**) Nyquist contours for M1. (**b**) Nyquist contours for M2

References

1. Chang CC, Yang HTY (1995) Control of buildings using active tuned mass dampers. J Eng Mech 121(3):355–366
2. Daley S, Johnson FA, Pearson JB, Dixon R (2004) Active vibration control for marine applications. Control Eng Pract 12(4):465–474. doi:10.1016/S0967-0661(03)00135-7
3. Gawronski W (2007) Servo-performance parameters of the NASA deep space network antennas. IEEE Antennas and Propagation Magazine 49(6), 40–46
4. Hanagan LM, Murray TM (1997) Active control approach for reducing floor vibrations. J Struct Eng 123(11):1497–1505. doi:10.1061/(ASCE)0733-9445(1997)123:11(1497)
5. Resta F, Ripamonti F, Cazzulani G, Ferrari M (2010) Independent modal control for nonlinear flexible structures: an experimental test rig. J Sound Vib 329(8):961–972
6. Bosse A, Lim TW, Shelley S (2000) Modal filters and neural networks for adaptive vibration control. J Vib Control 6(4):631–648. doi:10.1177/107754630000600408
7. Daley S, Wang J (2008) A geometric approach to the design of remotely located vibration control systems. J Sound Vib 318(4–5):702–714. doi:10.1016/j.jsv.2008.04.050
8. Diaz IM, Reynolds P (2010) Acceleration feedback control of human-induced floor vibrations. Eng Struct 32:163–173
9. Nyawako DS, Reynolds P, Hudson M (2013) Findings with AVC design for mitigation of human induced vibrations in office floors. In: 31st international modal analysis conference (IMAC XXVIII), Orange County, February 2013
10. Pereira E, Díaz IM, Hudson EJ, Reynolds P (2014) Optimal control-based methodology for active vibration control of pedestrian structures. Eng Struct 80:153–162
11. Hanagan LM, Murray TM (1998) Experimental implementation of active control to reduce annoying floor vibrations. Eng J 35(4):123–127
12. Houlston PR, Garvey SD, Popov AA (2007) Modal control of vibration in rotating machines and other generally damped systems. J Sound Vib 302:104–116
13. Fang JQ, Li QS, Jeary AP (2003) Modified independent modal space control of m.d.o.f systems. J Sound Vib 261:421–441
14. Choi SB, Hedrick JK (1998) An observer-based controller design method for improving air/fuel characteristics of spark ignition engines. IEEE Trans Autom Control 6(3):325–334
15. Sepe RB, Lang JH (1992) Real-time observer-based (adaptive) control of a permanent magnet sychronous motor without mechanical sensors. IEEE Trans on Ind Appl 28(6), 1345–1352
16. Korondi P, Hashimoto H, Utkin V (1998) Direct torsion control of flexible shaft in an observer-based discrete-time sliding mode. IEEE Trans Ind Electron 45(2):291–296
17. Sethi V, Song G (2005) Optimal vibration control of a model frame structure using piezoceramic sensors and actuators. J Vib Control 11(5):671–684. doi:10.1177/1077546305053396
18. Sethi V, Song G (2007) Multimodal vibration control of a flexible structure using piezoceramic sensor and actuator. J Intel Mater Syst Struct 19(5):573–582
19. Chung LL, Wu LY, Jin TG (1998) Acceleration feedback control of seismic structures. Eng Struct 20:62–74
20. Wu JC, Yang JN, Schmitendorf WE (1998) Acceleration feedback control of seismic structures. Eng Struct 20(3):222–236
21. Liu GP, Daley S (1998) Stable dynamical controller design for robust polynomial pole assignment. IEE Proc Control Theory Appl 145(3):259–264
22. Liu GP, Duan GR, Daley S (2000) Stable observer-based controller design for robust state-feedback pole assignment. Proc Inst Mech Eng 214(1):313–318
23. Xue D, Chen Y, Atherton DP (2007) Linear feedback control: analysis and design with Matlab. ISBN-13: 978–0898716382
24. Zivanovic S, Diaz IM, Pavic A (2009) Influence of walking and standing crowds on structural dynamic properties. In: Proceedings of the 27th international modal analysis conference, Orlando

Chapter 47
Active Tuned Liquid Column Gas Damper in Structural Control

Markus J. Hochrainer

Abstract Tuned liquid column gas damper (TLCGD) show excellent vibration absorbing capabilities appropriate for applications in wind- and earthquake engineering. However, in the early regime of strong motion seismic excitation or to counteract strong wind gusts the performance of the passive device can be increased substantially by active elements obtained from adding a pressurized gas supply with input–output valves to the sealed ends of the TLCGD. To prove the working principle of active TLCGD several small scale laboratory experiments have been performed with single and multiple degree of freedom host structures. To obtain a desired dynamic behavior, a conventional feedback control law is used to compute small active pressure inputs to the TLCGD. The experiments have proven that the active device is able to substantially reduce the dynamic system response in a broad frequency range. In fact, dangerous structural resonances of lightly damped structures can be avoided even if the passive absorber is not tuned perfectly. For multiple degree of freedom host structures a suitable control enables a single active TLCGD to counteract several modes of vibrations thereby avoiding the need to install numerous passive devices.

Keywords Active vibration damping • Active structural control • Tuned liquid column gas damper • Dynamic absorber • Small scale model

47.1 Introduction

Most vibration reducing devices are based on the absorption of vibrational energy to prevent a host structure from serious structural damage. A well known absorber principle is the energy-transfer from critical building vibration modes to dynamic damping devices used, e.g. for tuned mass damper (TMD), tuned liquid damper (TLD also called sloshing motion damper) or tuned liquid column gas damper (TLCGD). TMD have been applied successfully in high raised buildings, but it is difficult to guarantee a smooth, frictionless motion for huge masses, therefore the mass is often suspended vertically on cables, forming a pendulum type mass damper installed, e.g. in the Taipei 101 tower. Tuned liquid column damper (TLCD), originally developed to reduce the rolling motion of ships, use a controlled and guided liquid motion in a rigid piping system to overcome the suspension drawbacks of TMD. In the original design the restoring forces are due to gravity only, resulting in extremely low natural frequencies in the range of about 0.1–0.5 Hz for real size applications. The field of practical applications has been extended to frequencies up to 5 Hz by the invention of the passive gas spring effect, see Hochrainer [1], and a full TMD-TLCGD analogy is available to compare the performance of TLCGD to other dynamic absorber, Hochrainer [2, 3]. TLCGD have shown to be effective in reducing structural vibrations and simple guidelines for optimal placement and tuning of the TLCGD have been published by Hochrainer and Ziegler [4]. Distinguished properties of TLCGD comprise comparably low installation costs, easy retrofitting of existing structures, simple tuning mechanisms, virtually no maintenance requirements because there a no moving mechanical parts and little additional weight if a water reservoir is required, e.g. for the sake of fire fighting. TLCGD have caused an increased research interest, resulting in both, analytical and experimental analyses. So far, all research results indicate that the TLCGD is competitive when compared to TMD and could replace it in many structural applications, including applications to lightly damped asymmetric buildings, vibration prone structures like bridges (even under traffic loads), large arch-dams and offshore drilling platforms. Real size applications have been reported in a 26 storey, 106 m high hotel in Japan, Teramura and Yoshida [5], and the 48 storey One Wall Center in Vancouver, Canada, Samali et al. [6].

M.J. Hochrainer (✉)
University of Applied Sciences, 2700 Wiener Neustadt, Austria
e-mail: markus.hochrainer@fhwn.ac.at

In analogy to other passive dynamic absorber, the TLCGD is perfectly suited to counteract steady-state vibrations. For vibration reduction in the transient vibration regime, however, the active tuned liquid column gas damper (ATLCGD) is favorable. It is obtained from the passive device if the gas pressure at the sealed ends of the TLCGD is actively changed by controlled pressure input from a stand by high pressure reservoir. Again, a full analogy to active TMD is available for comparison of system dynamics, Hochrainer [7].

47.2 Absorber Dynamics

The TLCGD equation of motion can be derived directly by applying the nonstationary Bernoulli's equation in a moving reference frame, Ziegler [8, p. 497]. For a symmetric V-shaped TLCGD geometry and a plane horizontal motion described by the acceleration a_A the liquid column displacement u is given by [7]

$$
\begin{aligned}
&\ddot{u} + 2\zeta_A \omega_A \dot{u} + \omega_A^2 u = -\kappa a_A - \Delta \overline{p}_a, \quad \Delta \overline{p}_a = \frac{\Delta p_a}{\rho L_{eff}}, \quad f_A = \frac{\omega_A}{2\pi} = \sqrt{\frac{g/\pi^2}{4L_0}} \\
&L_{eff} = 2H + B \frac{A_H}{A_B}, \quad L_0 = L_{eff}/2 \left(\sin \beta + h_0/H_a \right), \quad h_0 = n p_0 / \rho g, \quad \kappa = \frac{B + 2H \cos \beta}{L_{eff}}, \quad H_a = \frac{V_0}{A_H},
\end{aligned}
\tag{47.1}
$$

with B and H denoting the length of the liquid filled pipe sections with piecewise constant cross sectional areas, A_H and A_B. The angle of inclination is denoted β, see Fig. 47.1, and L_{eff} defines the effective length of the liquid column. V_0, p_0, n, ρ, g denote the gas volume and the equilibrium gas pressure, the polytropic index, the liquid density (preferably water) as well as the constant of gravity, respectively. Since it depends on each TLCGD design, the polytropic index $1 \leq n \leq 1.4$ is determined experimentally in practical applications. To include energy losses by viscous and turbulent fluid flow the generally nonlinear fluid damping can be linearized for steady state conditions rendering the equivalent viscous damping coefficient ζ_A [3].

κ denotes a geometry dependent excitation factor and the ratio h_0/H_a of static pressure head h_0 to the virtual height H_a of the gas volume serves as frequency tuning parameter for the TLCGD natural frequency f_A. Contrary to the passive system the pressure difference $\Delta p_a = p_2 - p_1$ between the gas filled sealed ends of the TLCGD is used in the active configuration to prescribe a desired liquid motion. For the sake of simplicity it is assumed that the pressure difference Δp_a is independent of the liquid stroke u, thus $H_a = \infty$ and, in absence of active pressure input, $\Delta p_a = 0$, the device is still working as passive absorber. The coupling to real structures must be based on a substructure synthesis which additionally requires the determination of the horizontal interaction force F_A obtained from the conservation of momentum of the fluid mass m_f in horizontal direction,

$$
F_A = m_f \left(a_A + \overline{\kappa} \ddot{u} \right), \quad m_f = \rho A_H L_1, \quad L_1 = 2H + \frac{A_B}{A_H} B, \quad \overline{\kappa} = \kappa \frac{L_{eff}}{L_1},
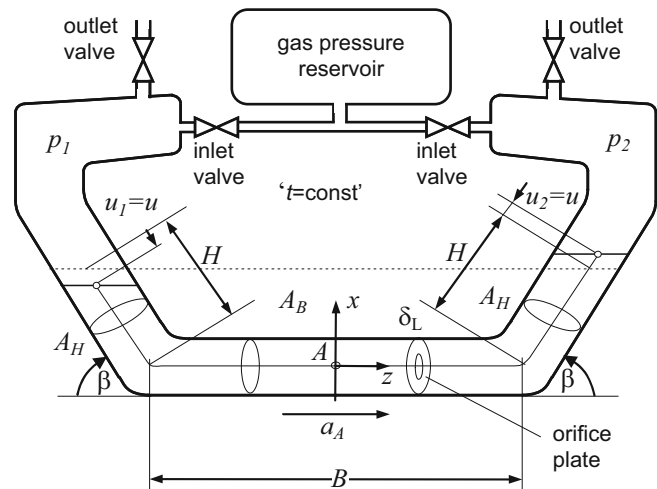\tag{47.2}
$$

Fig. 47.1 TLCGD of general shape with a relative streamline from 1 to 2 at a time instant t, symmetric arrangement with rigid pipe

where $\bar{\kappa}$ is a geometry dependent force factor. The horizontal interaction force is dependent on the relative liquid acceleration $\ddot{u}$ and the absolute housing acceleration a_A. With respect to F_A it is irrelevant whether the TLCGD is used in active or passive configuration, but the overall absorber performance is, nevertheless, strongly dependent on the active pressure input control strategy.

47.3 ATLCD Control

The dynamics of a linearized and properly discretized structural model with several ATLCGD installed can be given in matrix form

$$\mathbf{M}\ddot{\mathbf{x}} + \mathbf{C}\dot{\mathbf{x}} + \mathbf{K}\mathbf{x} = -\mathbf{M}\mathbf{E}_N\ddot{\mathbf{x}}_g + \mathbf{F} + \mathbf{F}_A, \tag{47.3}$$

where $\mathbf{x}$ denotes the vector of rigid floor displacements, $\mathbf{M}$, $\mathbf{C}$ and $\mathbf{K}$ are the mass, damping and stiffness matrix, respectively. $\mathbf{F}$ denotes the vector of external wind loading whereas $\ddot{\mathbf{x}}_g$ and $\mathbf{E}_N$ are the vector of horizontal ground acceleration and the ground excitation influence matrix, respectively. The wind and TLCGD-structure interaction (control) force vector is given by $\mathbf{F}_A$. Combining the structure's equation of motion (47.3), with the dynamic absorber Eq. (47.1) and the linearized interaction forces, Eq. (47.2), for all installed ATLCGD renders the system dynamics in state space formulation. With the state hyper vector $\mathbf{z}^T = \begin{bmatrix} \mathbf{x}^T & \mathbf{u}^T & \dot{\mathbf{x}}^T & \dot{\mathbf{u}}^T \end{bmatrix}$ consisting of the building displacements collected in $\mathbf{x}$ and the liquid strokes, collected in $\mathbf{u}$, the entire system dynamics can be given by first order differential equation [1]

$$\dot{\mathbf{z}} = \mathbf{A}_r\mathbf{z} + \mathbf{E}_g\ddot{\mathbf{x}}_g + \mathbf{E}_f\mathbf{F} + \mathbf{E}_a\Delta\bar{\mathbf{p}}_a, \tag{47.4}$$

where $\mathbf{A}_r$ represents the system matrix, $\mathbf{E}_g$, $\mathbf{E}_f$, $\mathbf{E}_a$ denote the base excitation, force and active pressure influence matrices, respectively, whereas $\Delta\bar{\mathbf{p}}_a$ denotes the vector of active pressure input which will be used to obtain a desired system dynamics. From linear quadratic optimal control it is known that the linear state feedback regulator

$$\Delta\bar{\mathbf{p}}_a = -\mathbf{S}^{-1}\mathbf{E}_a\mathbf{P}\mathbf{z}, \tag{47.5}$$

with constant and symmetric $\mathbf{P}$ defined by the algebraic Riccati equation

$$\mathbf{A}_r^T\mathbf{P} + \mathbf{P}\mathbf{A}_r - \mathbf{P}\mathbf{E}_a\mathbf{S}^{-1}\mathbf{E}_a^T\mathbf{P} + \mathbf{Q} = \mathbf{0} \tag{47.6}$$

will minimize the quadratic performance measure

$$J = \int_0^\infty \mathbf{z}^T\mathbf{Q}\mathbf{z} + \Delta\bar{\mathbf{p}}_a^T\mathbf{S}\Delta\bar{\mathbf{p}}_a dt \rightarrow \min \tag{47.7}$$

for a dynamic system described by Eq. (47.4) with unknown ground and force excitation. J accounts the for generalised structural vibration energy $\mathbf{z}^T\mathbf{Q}\mathbf{z}$ as well as the active pressure input $\Delta\bar{\mathbf{p}}_a^T\mathbf{S}\Delta\bar{\mathbf{p}}_a$. For given system dynamics the feedback gain matrix $\mathbf{K}_a = \mathbf{S}^{-1}\mathbf{E}_a\mathbf{P}$ will depend only on the positive definite weighing matrices $\mathbf{Q}$ and $\mathbf{S}$. Apparently, the structure of the state feedback control law, Eq. (47.5) does not change, if the equations of motion (47.3) are processed using modal coordinates, $\mathbf{x} = \mathbf{\Phi}\mathbf{q}$, for which the influence of specific modes on the performance index J can be determined directly. In linear optimal quadratic control the system performance is solely determined by the performance index, which can be extended to account for system robustness or input-state cross coupling terms, see e.g. Lubin and Athans [9]. During the iterative optimization process the weighing matrices $\mathbf{Q}$ and $\mathbf{S}$ are modified until a desired behavior is obtained. Form a theoretical point of view a full state feedback controller can be used to place the system poles arbitrarily, and thus any system characteristics (frequency, damping) can be assigned. Nevertheless, from a physical point of view this is hardly possible and it is strongly advised to tune an active TLCGD to a preselected mode, similar to the passive design. In this case the active input is only used for improving the performance of the passive device when necessary, but most of the energy dissipation is achieved without active control.

47.4 Experimental Results

As already discussed, it is, theoretically, possible to obtain any desired dynamic structural behavior using the active configuration. However, there are physical limitations especially in the medium to high frequency range and thus it is indispensable to prove the vibration reducing capacity of the proposed ATLCGD experimentally under laboratory conditions. For a single and double degree of freedom host structure Eidler [10] has performed steady state base excitation experiments, which have convincingly proven that an active TLCGD will absorb vibrations more efficient than passive devices. The experimental setup represents a plane shear frame structure with rigid floors connected by linear elastic, light weight steel columns with a single ATLCGD prototype attached to the top floor. Uniaxial base excitation is provided by an electrodynamic shaker, see Fig. 47.2a. The active pressure input Δp_a was controlled using proportional valves connected to a small pressure reservoir allowing a pressure difference of $\Delta p_{\max} = \pm 0.1$ bar. The gas release was controlled using magnetic switching valves which have turned out to be more effective than proportional valves. Experimental testing was performed with a SDOF structure of mass $m = 1.2$kg, natural frequency $\omega = 4.49$rad/s and light viscous damping $\zeta < 1\%$, determined from free decay experiments. In passive mode operation no pressure input was allowed, $\Delta p_a = 0$, while keeping both ATLCGD outlet valves open. In this configuration the frequency ratio of the passive device was chosen optimal according to Den Hartog's optimization criteria [11] for a given mass ratio of $\mu = m_f/m = 0.05$. However, the overall air flow resistance together with the inherent liquid damping yielded an effective absorber damping just above the optimal value, $\zeta_A > \zeta_{A,opt}$, see Fig. 47.2b. Since all states of the host structure were available from measurements, the linear output feedback control law

$$\Delta p_a = \alpha x + \beta \dot{x} \qquad (47.8)$$

was used to determine the required pressure input. Since the ATLCGD states u, $\dot{u}$ were not available from measurements their contribution to the state feedback was neglected. During the experiments the air flow dynamics was not considered, but instead it was assumed, that the actual ATLCGD pressure difference Δp_a is proportional to the opening of the input valve. Because the ATLCGD can be operated in passive or active mode a threshold level x_t of acceptable displacement amplitudes has been introduced, to ensure that for small vibrations amplitudes $|x| < x_t$ the TLCGD is operating in passive configuration only. Because of the low natural frequencies, there are no critical demands concerning the control hardware. The control algorithm, Eq. (47.8), including numerical differentiation to estimate x, was implemented in Standard LabVIEW. The software loop, running with a sampling time of 30 ms, interfaced the multifunction data acquisition hardware USB-6215 for input/output operations. In a comparative study, the steady state dynamic response amplification x/w_g has been measured
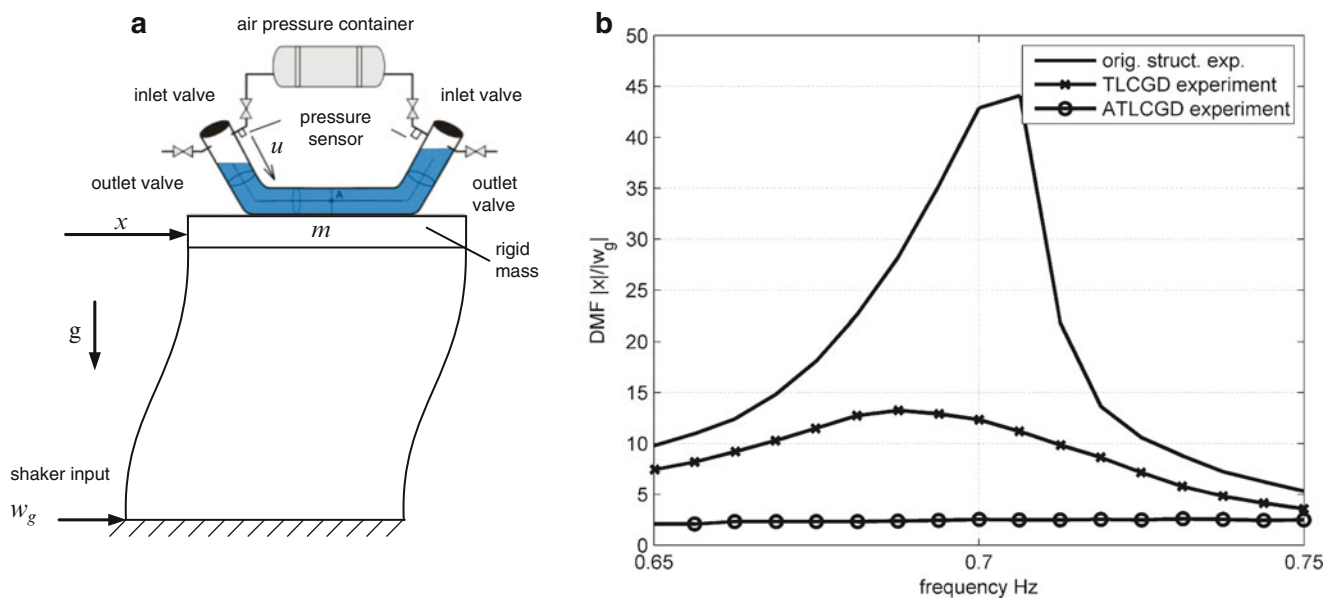

Fig. 47.2 Active TLCGD (**a**) Experimental setup with ground excitation w_g (**b**) Comparison of measured frequency response functions for original system with TLCGD in passive and active mode attached

using sine stepping excitation for the lightly damped host structure as well as the structure with TLCGD in passive and active configuration, see Fig. 47.2b. Due to little damping and thus large vibration amplitudes the dynamic magnification factor of the original structure shows first effects of nonlinear stiffening similar to a Duffing oscillator where the resonant frequency is dependent on the vibration amplitudes. The passive TLCGD reduces the resonance peaks by a factor of about four in the critical resonant frequency range and, in accordance with theory, the resonance frequency is reduced by the additional TLCGD dead weight loading. When inspecting the response amplification of the active system it is hard to decide if there is any significant response amplification at all. The displacement reduction is almost ideal with optimal vibration damping over the entire critical frequency range. Apparently, the choice of the control parameter α and β will significantly change the system dynamics, and excellent vibration reduction requires larger TLCGD vibration amplitudes together with higher input pressures. For this reason, the controller fine tuning was performed experimentally starting from a pure velocity based control with $\alpha = 0$. Furthermore, it turned out that that the assumption of Δp_a being proportional to the magnetic valve opening does not hold due to unmodelled dynamic effects in the pressurization process.

When compared to passive control, major advantages of an active system are its abilities to counteract several modes of vibration and to reduce multiple resonant peaks. To confirm these theoretical results in the laboratory, the ATLCGD was fixed at the top floor of a lightly damped two DOF shear frame structure with following dynamic parameters: mass of rigid floors $m_1 = m_2 = 2.15$, natural frequencies of $f_1 = 1.0 Hz$ and $f_2 = 2.8 Hz$, as well as small light modal damping of $\zeta_1 < 1\%$ and $\zeta_2 < 5\%$. The passive TLCGD parameters were chosen to reduce first mode vibrations. Because the modal matrix Φ was known from modal testing and the floor displacements $\mathbf{x} = (x_1, x_2)^T$ were available by measurements, the modal coordinates $\mathbf{q} = (q_1, q_2)^T = \Phi^{-1}\mathbf{x}$ were known. From a dynamic point of view it is desirable to influence the modal behavior individually, and thus active pressure input was chosen according to a modal state feedback

$$\Delta p_a = \alpha_1 q_1 + \beta_1 \dot{q}_1 + \alpha_2 q_2 + \beta_2 \dot{q}_2, \tag{47.9}$$

where the time derivatives were evaluated numerically. The frequency response curves were recorded using sine stepping excitation and fine tuning of the coefficients was performed experimentally to compensate for unmodelled pressure input and air flow dynamics. The measured dynamic response magnification is given in Fig. 47.3a for the original 2 DOF structure, and in Fig. 47.3b for the structure with a passive and active TLGCD installed on top floor. As expected, the purely passive system is capable of mitigating first mode vibrations, while the response amplification of the second mode remains almost unaffected. The active system, on the other side, is able to reduce both modes of vibration. With modal control, the feedback gain parameter α_i and β_i can be used to influence the i-th mode dynamics, e.g. setting $\alpha_i = \beta_i = 0$, the active pressure input will, besides minor spillover effects, not influence the original i-th mode dynamics.

From a practical point of view it is important to note that the system has proven to be fairly robust against pressure fluctuations in the pressure reservoir.
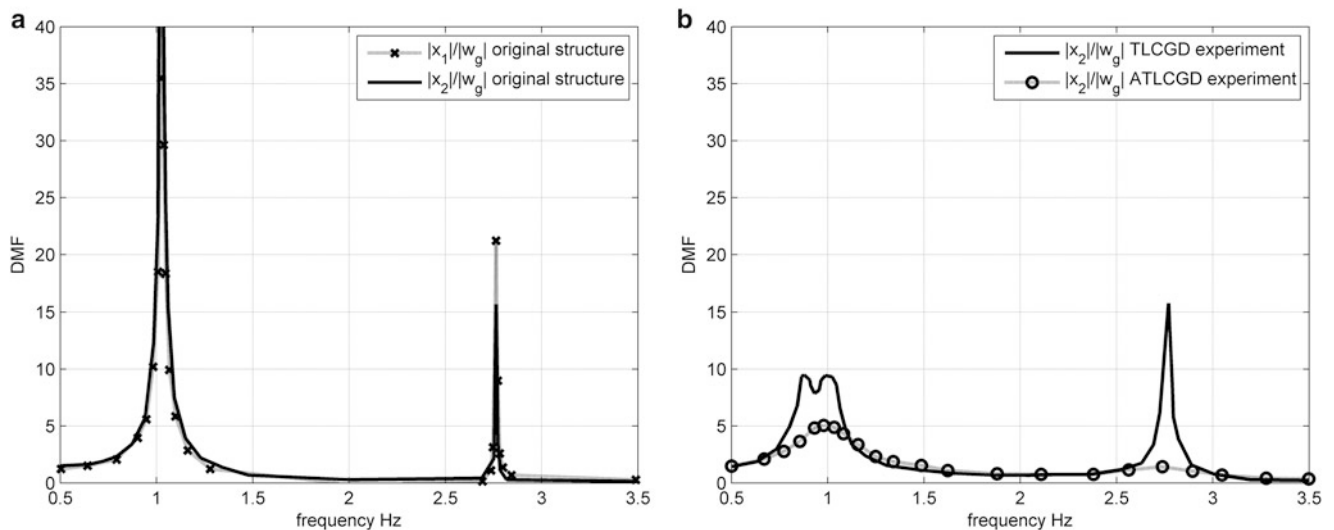

Fig. 47.3 Active TLCGD measurements (**a**) dynamic magnification factor (DMF) of the floor displacements $|x_1/w|$ and $|x_2/w|$ of the original structure (**b**) DMF of structure with TLCGD in active and passive configuration
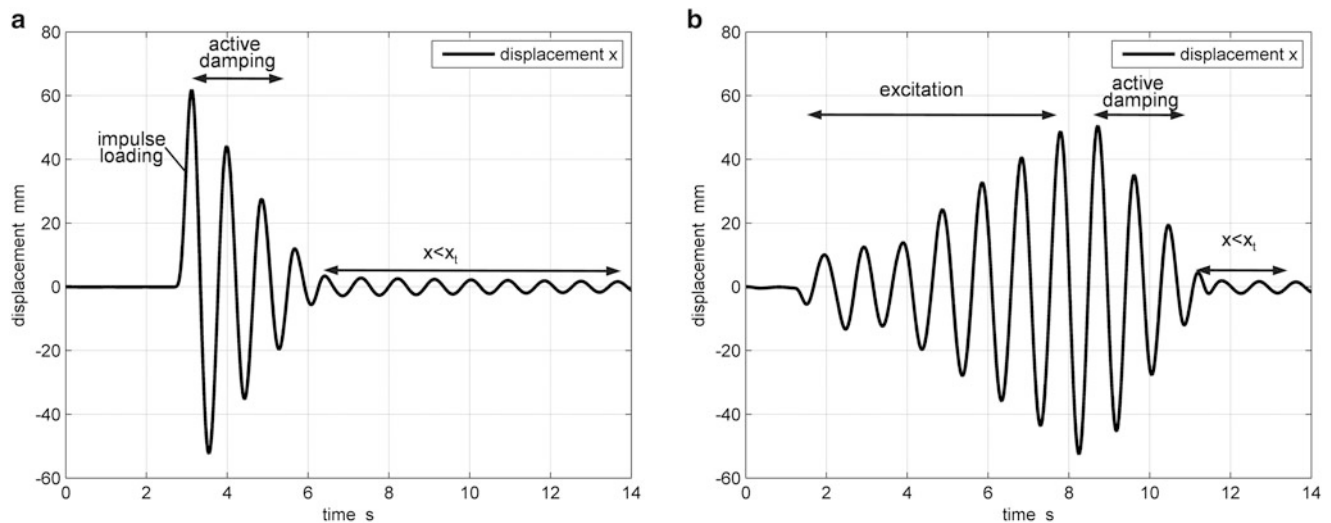
Fig. 47.4 Transient ATLCGD measurements (**a**) Transient response reduction after impulsive force loading (**b**) Autoresonant excitation of a SDOF shear frame structure for structural in-situ testing with subsequent active damping

The above experiments demonstrate that TLCGD are perfectly suited to mitigate steady state vibrations, but is equally important to counteract transient vibrations. The passive TLCGD dissipates energy only if the liquid column is in motion, which requires the host structure to vibrate (and induce liquid column vibrations) before passive vibration damping occurs. Because of the active energy input this drawback is resolved using ATLCD, see Fig. 47.4a, where the displacement response of a SDOF host structure with ATLCD attached is given for impulsive force loading. The ATLCD immediately starts to reduce the vibration amplitudes until it is switched off when it falls below x_t, the predefined level of acceptable vibrations.

Another remarkable property of the ATLCGD is its ability to determine the host structure dynamics by injecting vibration energy at predefined frequencies. Since it can be performed automatically, this is a simple and effective method of system identification and particularly useful if the building dynamics has changed due to addition loading or aging effects. To demonstrate this effect the ATLCGD was used to autoresonantly excite a SDOF plane shear frame, see Fig. 47.4b. Apparently vibration energy constantly accumulates to a high level of resonant excitation within several vibration periods. Subsequently the control is switched to active damping mode and the resonant vibration is compensated immediately.

47.5 Conclusions

The experimental work presented demonstrates convincingly, that is possible to improve the performance of the well-established TLCGD by a simple active air spring setup. A small scale prototype of the active TLCGD has been developed and installed on plane ground excited shear frame structures. The laboratory results indicate that the application of an active air spring is a very effective way to improve the absorber performance far beyond the possibilities of purely passive control. ATLCGD are effective in vibration reduction during the transient excitation regime but especially their steady state response performance is remarkable. If desired, the effect of critical structural resonances can be eliminated completely and ATLCGD can be used counteract several modes of vibration. If the control is adapted properly, the ATLCGD can also be used to excite the structure for modal testing, and, if the active control is switched off, the device will operate as passive absorber without any further modification. So far, all experimental results indicate that ATLCGD are appropriate and suitable for a wide range of structural control applications.

References

1. Hochrainer MJ (2001) Control of vibrations of civil engineering structures with special emphasis on tall buildings. Doctoral dissertation, Vienna University of Technology, full text available: http://www.ub.tuwien.ac.at/diss/AC03322409.pdf
2. Hochrainer MJ (2005) Tuned liquid column damper for structural control. Acta Mech 175(1–4):57–76

3. Hochrainer MJ, Ziegler F (2006) Control of tall building vibrations by sealed tuned liquid column dampers. Struct Control Health Monit 13(6):980–1002

4. Hochrainer MJ, Ziegler F (2013) Tuned liquid column gas damper in structural control: the salient features of a general purpose damping device and its application in buildings, bridges, and dams. In: Lagaros ND, Plevris V, Mitropoulou CC (eds) Design optimization of active and passive structural control systems. IGI Global

5. Teramura A, Yoshida O (1996) Development of vibration control system using U-shaped water tank. In: Proceedings of the 11th world conference on earthquake engineering (Sociedad Mexicana de Ingenieria Sismica, A.C.), paper no. 1343, Elsevier Science Ltd.

6. Samali B, Mayol E, Kwok KCS, Mack A, Hitchcock P (2004) Vibration control of the wind-excited 76-story benchmark building by liquid column vibration absorbers. J Eng Mech 130(4):478–485

7. Hochrainer MJ (2013) Experimental investigations of active tuned liquid column gas damper. In: Vienna congress of recent advances in earthquake engineering and structural dynamics, paper no. 142, 28–30 Aug 2013, Vienna

8. Ziegler F (1998) Mechanics of solids and fluids, 2nd reprint of second edition. Springer, New York/Vienna

9. Lubin L, Athans M (1996) Linear quadratic regulator control. In: Levine WS (ed) The control handbook. IEEE Press

10. Eidler M (2010) Development of active tuned liquid column damper. Bachelor thesis, University of Applied Sciences, Wiener Neustadt

11. Den Hartog JP (1956) Mechanical vibrations, reprint of 4th edn. McGraw-Hill, New York

Chapter 48
Semiactive Vibration Control in a Three-Story Building-Like Structure Using a Magnetorheological Damper

J. Enríquez-Zárate, G. Silva-Navarro, and A. Cabrera-Amado

Abstract This article considers the dynamic analysis and semiactive vibration control on a building-like structure, excited on its base through an external force generated by an electromechanical shaker providing harmonic and seismic motion at the base of the overall structure. The mathematical model of the overall system is obtained using Euler-Lagrange methods, which is validated by means of experimental modal analysis techniques. In fact, the external force excites the first three (lateral) vibration modes of the building-like structure. Therefore, to suppress and/or attenuate the undesirable vibrations on the structure, it is proposed a semiactive vibration control scheme considering a Magneto-Rheological damper directly coupled between the base and the first floor. The hysteretic behavior of the Magneto-Rheological damper is modeled by means of the polynomial approach proposed by Choi-Lee-Park. Finally, a Multi Positive Position Feedback controller combined with Sliding-Mode Control techniques is synthesized, using as output the position provided by an accelerometer collocated on the first floor. Some experimental results are presented to show the dynamic performance of the overall building-like structure.

Keywords Building-like structures • MR damper • Positive Position Feedback • Semiactive control • Sliding-mode control

48.1 Introduction

Many engineering systems and civil structures are commonly affected by exogenous and endogenous vibrations due to ground motion, seismic waves, etc. Structural control in buildings is now necessary to enhance and protect the structural performance from damages during seismic events [3, 4, 15]. The most effective solutions are the Tuned Mass Dampers (TMD), Hybrid Mass Dampers (HMD), Active Mass Dampers (AMD) and, more recently, the application of smart materials to get low cost actuators compensating high loads [7, 9, 11].

The Electro-Rheological (ER) and Magneto-Rheological (MR) fluids have been successfully applied to synthesize semiactive vibration control strategies in building and civil structures [1, 5, 14]. The main difficulty to use ER and MR dampers is their highly nonlinear and hysteretic behavior. However, different hysteresis models for ER and MR dampers have been proposed and experimentally validated in the literature [2, 5, 14].

This paper considers the application of a MR damper to synthesize a semiactive vibration control scheme for a three-story building-like structure by using the so-called Choi-Lee-Park polynomial model of a MR damper [2], Multi Positive Position Feedback (MPPF) control [8, 10, 12] and Sliding-Mode Control [16] to attenuate the overall system response under the effect of harmonic and seismic-type ground motion. A three degrees-of-freedom Euler-Lagrange model is validated by means of experimental modal analysis techniques. The semiactive vibration control scheme via the MR damper is synthesized by using the Choi-Lee-Park polynomial model and its inverse dynamics model to simplify the controller design. Some experimental results are performed on an experimental setup to illustrate the robust performance of the semiactive vibration controller.

J. Enríquez-Zárate (✉)
IMP-CONACYT, Centro de Tecnologías para Aguas Profundas CTAP, Boca del Río, Veracruz, Mexico
e-mail: jenriquezza@conacyt.mx

G. Silva-Navarro
Depto. de Ing. Eléctrica, Sección de Mecatrónica, Centro de Investigación y de Estudios Avanzados del I.P.N,
Av. IPN No. 2508, Col. S.P. Zacatenco, C.P, México, D.F. 07360, Mexico

A. Cabrera-Amado
Departamento de Ingeniería Mecatrónica, Universidad del Papaloapan, Loma Bonita, Oaxaca, Mexico

Fig. 48.1 Building-like structure with PZT actuator. (**a**) Schematic diagram, (**b**) experimental platform
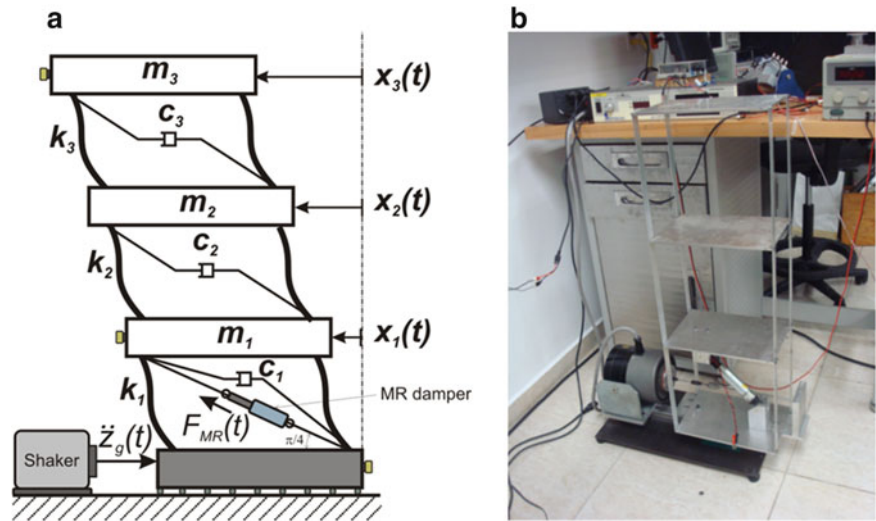
48.2 Description of the Building-Like Structure

The schematic diagram and experimental setup of the building-like structure are shown in Fig. 48.1. This structure consists of three floors made of aluminum alloy and supported by aluminum columns. The maximum height of the structure is 900 mm with rectangular floors of 200×300 mm. The structure is mounted on a rail with a ball bearing frictionless mobile base, connected directly to an electromagnetic shaker to excite the structure with sine sweeps and seismic-type motion. The overall system is connected to a PC using an acquisition system *Sensoray*® model 626 running under a *Matlab/Simulink*® platform.

The building-like structure consists of three masses (m_1, m_2, m_3) interconnected each one by four flexible columns at each end, denoted by equivalent stiffnesses (k_1, k_2, k_3), and each mass is associated with small viscous dampings (c_1, c_2, c_3) as shown in Fig. 48.1a. The semiactive damping control force $F_{MR}(t)$ is provided by a rectilinear MR damper, model RD-1097-01 manufactured by *Lord Corporation*®, connecting the base and first floor. This MR damper is attached in order to attenuate the forced vibrations due to ground motion $z_g(t) = Z_g sin(\omega t)$ at the base of the structure, generated by an electromechanical shaker coupled to the structure. Acceleration measurements are obtained on the base, first and third floors, using accelerometers connected to a data acquisition system. Displacements and velocities are filtered and numerically approximated by software. The experimental setup is depicted in Fig. 48.1b.

The harmonic or seismic-type ground vibrations acting on the structure can cause lateral displacements. In fact, the low-frequency components affect the first three lateral modes of the building-like structure, which are particularly concentrated on the lateral motion in the third floor. Therefore, a semiactive vibration control scheme will be implemented via the MR damper, using displacement information on the first floor (i.e., a collocated control problem), in order to reduce as possible the overall system response.

48.3 Building-Like Structure with MR Damper

The mathematical model for a three-story building, excited by ground motion and its associated inertial effects, including a MR damper located between base and first floor, is obtained as follows

$$M\ddot{x} + C\dot{x} + Kx + B_f F_{MR}(t) = -Me\ddot{z}_g(t), \ x = [x_1, \ x_2, \ x_3]^T \in R^3, \ \ddot{z}_g \in R, \ F_{MR} \in R \quad (48.1)$$

where x denotes the vector of generalized coordinates of relative displacement with respect to a main frame reference, $\ddot{z}_g \in R$ is the acceleration of the ground motion at the base of the structure and M, C, K are the associated mass, damping and stiffness real and symmetric 3×3 matrices, respectively. The vector $e = [1, \ 1, 1]^T \in R^3$ is used to describe the displacement of each mass due to the ground acceleration at the base. The fourth left-hand term includes the input matrix B_f and the MR damper

Table 48.1 System parameters for the 3-story building-like structure

$m_1 = 1.883\,kg$	$m_2 = 1.031\,kg$	$m_3 = 1.027\,kg$
$k_1 = 897.03\,N/m$	$k_2 = 933.39\,N/m$	$k_3 = 888.23\,N/m$
$c_1 = 0.1233\,Ns/m$	$c_2 = 0.3345\,Ns/m$	$c_3 = 1.8977\,Ns/m$

Table 48.2 Polynomial coefficients for the MR damper

i	Positive acceleration		Negative acceleration $\ddot{y}_{MR} < 0$	
	b_i^+	c_i^+	b_i^-	c_i^-
0	0.403	2.928	0.5426	-3.105
1	-18.3	1,156	-18.549	1,161
2	19.01	-561.3	8.6212	-372.5

control force F_{MR} applied to the structure, which is due to the passive restriction of the semiactive damping control force. The mass, damping, stiffness and input matrices are described by

$$M = \begin{bmatrix} m_1 & 0 & 0 \\ 0 & m_2 & 0 \\ 0 & 0 & m_3 \end{bmatrix}, \ C = \begin{bmatrix} c_1 + c_2 & -c_2 & 0 \\ -c_2 & c_2 + c_3 & -c_3 \\ 0 & -c_3 & c_3 \end{bmatrix}, \ K = \begin{bmatrix} k_1 + k_2 & -k_2 & 0 \\ -k_2 & k_2 + k_3 & -k_3 \\ 0 & -k_3 & k_3 \end{bmatrix}, \ B_f = \begin{bmatrix} cos\left(\frac{\pi}{4}\right) \\ 0 \\ 0 \end{bmatrix} \quad (48.2)$$

For modal analysis validation we consider proportional (Rayleigh) damping as $C = aM + bK$, where a, b are suitable real constants [6]. The system parameters of the building-like structure are given in Table 48.1.

48.4 Polynomial Model of the MR Damper

The MR fluids are smart materials that respond well to an applied magnetic field, leading to an important change in their rheological behavior (viscosity and stiffness). The viscosity and stiffness changes are continuous and reversible, which makes possible the application of MR dampers for vibration control [1, 2, 5, 14]. The passive nature of the MR dampers limits their practical use to semiactive vibration control, although this is sufficient to improve the dynamic response of a building-like structure. Specifically, via the application of feedback control to manipulate the electrical currents of the MR damper one can control a proper damping force to attenuate the overall system response.

In this work we employ the Choi-Lee-Park polynomial model for the MR dampers [2]. In a previous work we have used the polynomial model for a MR damper RD-1097-01, manufactured by *Lord Corporation*®, whose damping force is characterized by [13]

$$F_{MR}\left(\dot{y}_{MR}, \ddot{y}_{MR}, I\right) = \sum_{i=0}^{n=2} \left(\widehat{b}_i + \widehat{c}_i I\right) \dot{y}_{MR}^i \quad (48.3)$$

where $\dot{y}_{MR} \cong cos\left(\frac{\pi}{4}\right)\left(\dot{x}_1 - \dot{z}_g\right)$ is the piston velocity of the MR damper coupled between first floor and base, including the geometrical location of the MR damper, and I is the current control input applied to the MR damper, which is provided by a small power amplifier. The general coefficients $\widehat{b}_i$ and $\hat{c}_i$, with respect to the positive and negative acceleration, are expressed by

$$\widehat{b}_i = \frac{1}{2}\left[\left(b_i^+ + b_i^-\right) + \left|b_i^+ - b_i^-\right| sign\left(\ddot{y}_{MR}\right)\right], \ i = 0, 1, 2$$

$$\hat{c}_i = \frac{1}{2}\left[\left(c_i^+ + c_i^-\right) + \left|c_i^+ - c_i^-\right| sign\left(\ddot{y}_{MR}\right)\right] \quad (48.4)$$

Here $\ddot{y}_{MR} \cong cos\left(\frac{\pi}{4}\right)\left(\ddot{x}_1 - \ddot{z}_g\right)$ is the piston acceleration in the MR damper, which is computed from the relative acceleration between the first floor and base. The polynomials with best fitting to the experimental results are of order $n = 2$, whose coefficients are given in Table 48.2 [13].

This MR damper can provide forces up to 100 N using current inputs up to 1 A, with a response time about 25 ms, and, therefore, we can apply semiactive damping forces to control harmonic vibrations up to 40 Hz, employing a small total power of 2.5 W. However, to avoid possible damage the maximum current input is physically limited to 0.5 A.

In order to implement a semiactive vibration control scheme, using the damping control force F_{MR} in the building-like structure, it is assumed the so-called inverse model for the MR damper (3) to compute the current control inputs as [2, 13]

$$I(t) = \frac{F_{MRd}(t) - \sum_{i=0}^{n=2} \widehat{b}_i \, \dot{y}_{MR}^i}{\sum_{i=0}^{n=2} \widehat{c}_i \, \dot{y}_{MR}^i} \tag{48.5}$$

where $F_{MRd}(t)$ represents the *desired* damping control force, resulted from the semiactive vibration controller to be applied. There is no singularity in (48.5) because into the denominator the coefficient $\widehat{c}_0 \neq 0$ and the velocity and acceleration values at the piston do not lead to singularities.

48.5　Experimental Modal Analysis of the Building-Like Structure with MR Damper

The three-story building-like structure is harmonically excited with an electromagnetic shaker from 0 to 60 Hz and the MR damper without current control input (i.e., $I \approx 0$ A). The experimental Frequency Response Functions (FRF) are analyzed using modal analysis techniques like *Peak Picking* and *Curve Fitting* methods [6]. The experimental FRF for the acceleration and displacement at the first floor are described in Fig. 48.2, where one can observe the three dominant (lateral) modes.

The damping parameters were obtained indirectly from the FRF and the modal dampings were approximated by using *Peak Picking* and *Curve Fitting* methods. Considering damping ratios ξ_i, the modal frequencies of the structure ω_i are also experimentally obtained. A comparison of the numerical and experimental resonant frequencies and modal dampings is given in Table 48.3, where the results are sufficiently close to validate the simplified model of the three-story building structure up to the first three lateral vibration modes (Fig. 48.3).
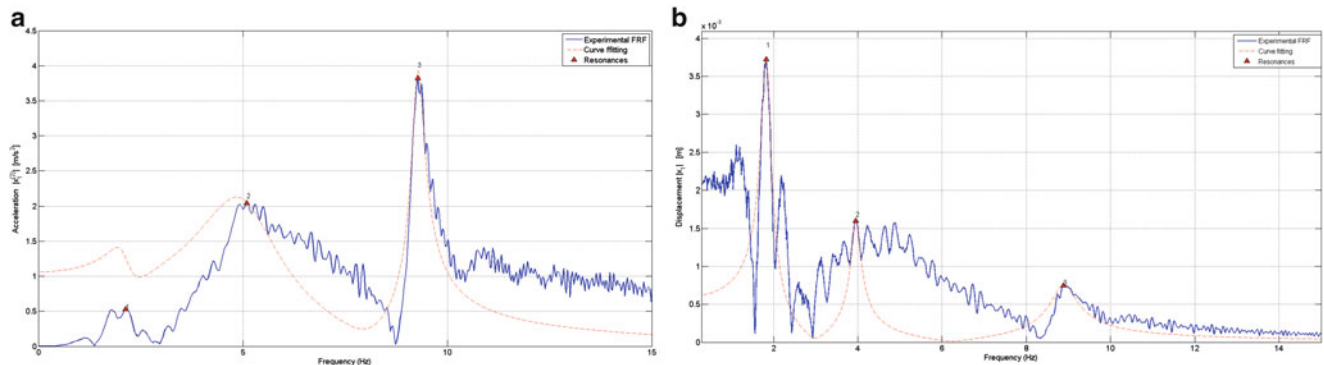

Fig. 48.2 Experimental FRF of the building structure and modal analysis using *Peak Picking* and *Curve Fitting* methods. (**a**) Acceleration $\ddot{x}_1$, (**b**) displacement x_1

Table 48.3 Modal parameters for the first three lateral dominant modes of the three-story building-like structure

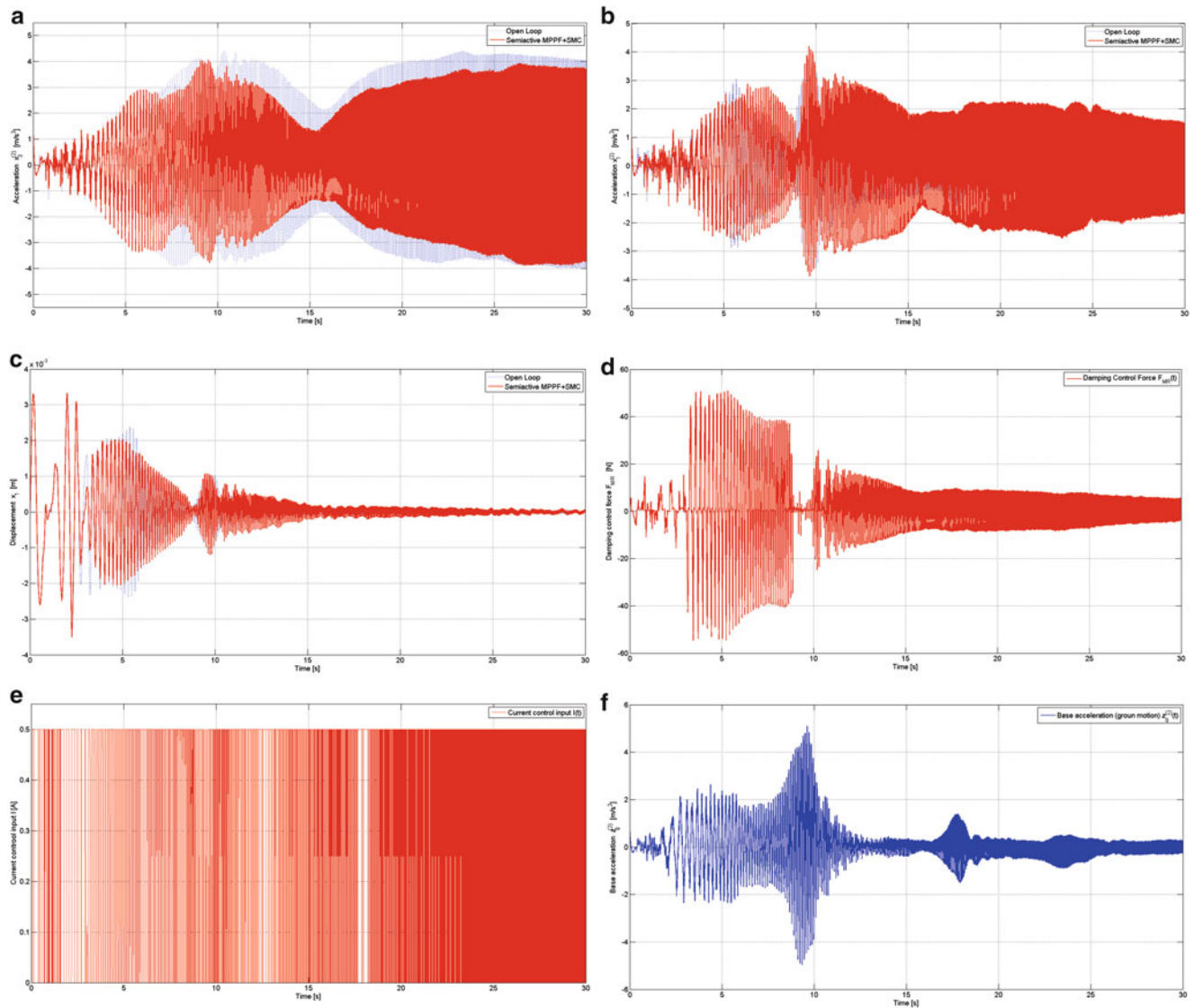| Mode	Resonant frequencies ω_i [Hz] Numerical	Resonant frequencies ω_i [Hz] Experimental	Modal dampings ξ_i Experimental
1	2.01	2.0	0.1428
2	4.86	5.1	0.1894
3	7.98	9.1	0.0174

Fig. 48.3 Experimental results in open-loop and closed-loop using semiactive MPPF + SMC for *harmonic* ground motion. (**a**) Acceleration $\ddot{x}_3$, (**b**) acceleration $\ddot{x}_1$, (**c**) displacement x_1, (**d**) damping force F_{MR}, (**e**) current I, (**f**) base acceleration $\ddot{z}_g$

48.6   Semiactive Vibration Control Using MPPF Control

Positive Position Feedback (PPF) control schemes are well-known in the literature as modal control methods for vibration attenuation [8, 10]. The parameters of this controller can be selected using experimental data, which in fact makes the PPF control technique quite popular for structural and motion control applications.

Here, we will apply a Multiple Positive Position Feedback (MPPF) control to attenuate the overall system response under harmonic or seismic ground motion acting on the base of the structure [12]. The positive position terminology comes from the fact that the position (displacement) coordinate of the system is positively fed to a virtual passive absorber or filter, and the damping force of the MR damper is positively feedback to the main system (building-like structure). The MPPF control scheme is an extension of the PPF controller for simultaneous attenuation of multiple vibration modes [8, 10, 12].

The overall three-story building-like structure is completely controllable and observable from the damping control force F_{MR} and displacement x_1, respectively. Note that, because the MR damper is placed between the base and first level of the structure then, this directly actuates the first floor dynamics. The output variable to be used for active vibration control of the overall structure is the displacement of the first floor x_1 and, therefore, the vibration control problem corresponds to a

collocated sensor and actuator. However, one could also use the displacement of the third floor x_3 but in this case the synthesis of the control problem will be non-collocated and, as a consequence, more difficult to be implemented [8, 9].

The proposed MPPF control scheme for the three-story building-like structure consists of three *virtual passive absorbers* (second order low pass filters) connected in parallel and the MPPF control law is the superposition of three single PPF controllers. Thus, we consider the three-story building structure with MR damper, affected by ground motion $\ddot{z}_g$. In this case, the synthesis of a MPPF control for the building-like structure (48.1, and 48.2) results in a closed-loop system given by

$$M\ddot{x}(t) + C\dot{x}(t) + Kx(t) + B_f F_{MR}(t) = -Me\ddot{z}_g(t), \qquad x \in R^3, \ \ddot{z}_g \in R, \ F_{MR} \in R \tag{48.6}$$

$$\ddot{N}(t) + 2ZW\dot{N}(t) + W^2 N(t) = W^2 G^T B^T x(t), \qquad N \in R^3 \tag{48.7}$$

$$F_{MR}(t) = GW^2 N(t) \tag{48.8}$$

where the mass, damping and stiffness matrices are given in (48.2) with $x \in R^3$ and ground motion $\ddot{z}_g \in R$. The three virtual passive absorbers $N \in R^3$ described in (48.7), with relative 3×3 (diagonal) damping matrix Z and virtual absorber natural frequency 3×3 (diagonal) matrix W, are coupled to the primary system (48.6) by the general positive position injection term $W^2 G^T B^T x(t)$, with $B^T = \begin{bmatrix} 1 & 0 & 0 \end{bmatrix}$. The MPPF control law (48.7 and 48.8) is described by the control force F_{MR}, where $G = \begin{bmatrix} g_1 & g_2 & g_3 \end{bmatrix}$ is a 1×3 control gain matrix to be selected in order to get reasonable multi-mode attenuation properties. The main difficulty of this control scheme relies with the tuning problem and the structural properties depending on the collocated or non-collocated array of sensors and actuators.

The overall closed-loop system (48.6, 48.7, and 48.8) can be also described as follows

$$\begin{bmatrix} M & 0 \\ 0 & I \end{bmatrix} \begin{bmatrix} \ddot{x} \\ \ddot{N} \end{bmatrix} + \begin{bmatrix} C & 0 \\ 0 & 2ZW \end{bmatrix} \begin{bmatrix} \dot{x} \\ \dot{N} \end{bmatrix} + \begin{bmatrix} K & +B_f GW^2 \\ -W^2 G^T B^T & W^2 \end{bmatrix} \begin{bmatrix} x \\ N \end{bmatrix} = \begin{bmatrix} -Me \\ 0 \end{bmatrix} \ddot{z}_g(t) \tag{48.9}$$

Because M is symmetric and positive definite the extended mass matrix is also symmetric and positive definite. The damping matrix C is symmetric and positive definite and leads to a similar extended damping matrix. The stiffness matrix K is symmetric and positive definite with collocated sensor and actuator (i.e., $B_f = \cos\left(\frac{\pi}{4}\right) B$ when x_1 is the output to be used for feedback) and, hence, to guarantee closed-loop asymptotic stability one have to select appropriate matrices G and W such that the closed-loop stiffness matrix

$$\widehat{K}_{MPPF} = \begin{bmatrix} K & +B_f GW^2 \\ -W^2 G^T B^T & W^2 \end{bmatrix}$$

be positive definite.

48.7 Semiactive Vibration Control Using MPPF and Sliding Mode Control

In order to improve the overall robustness of the MPPF control scheme, this is combined with a Sliding-Mode Control (SMC) part [16], for the first three vibration modes of the building-like structure, as follows

$$M\ddot{x}(t) + C\dot{x}(t) + Kx(t) + B_f F_{MR}(t) = -Me\ddot{z}_g(t), \qquad x \in R^3, \ \ddot{z}_g \in R, \ F_{MR} \in R \tag{48.10}$$

$$\ddot{N}(t) + 2ZW\dot{N}(t) + W^2 N(t) = W^2 G^T B^T x(t), \qquad N \in R^3 \tag{48.11}$$

$$F_{MR}(t) = GW^2 N(t) + \sum_{j=1}^{3} \mu_j \mathrm{sign}\sigma_j \left(_j - B^T x \right) \tag{48.12}$$
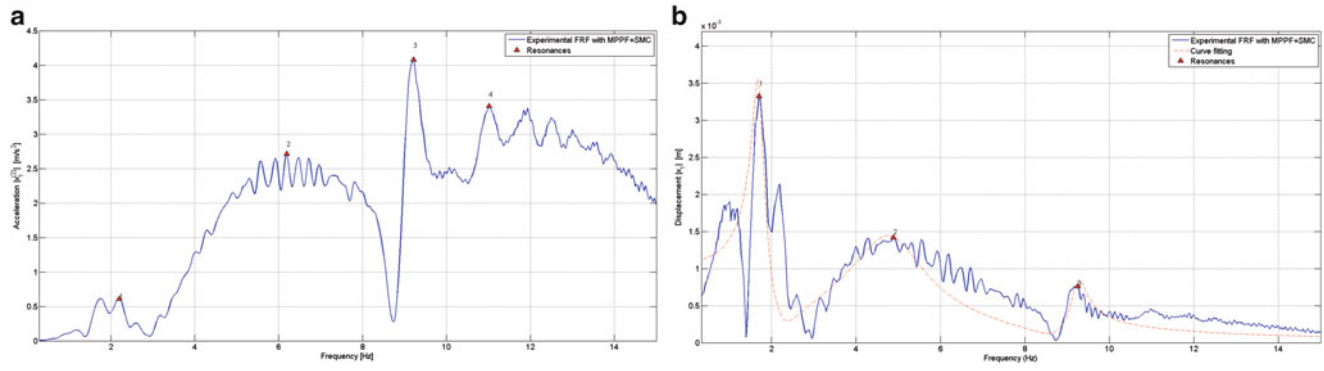
Fig. 48.4 Experimental FRF of the building-like structure with MPPF + SMC control. (**a**) Acceleration $\ddot{x}_1$, (**b**) displacement x_1

where sign (•) stands for the *signum* function and the PD-like switching surfaces are defined by

$$\sigma_j\left(_j - B^T x\right) = \alpha_{1j}\left[_j(t) - B^T x(t)\right] + \alpha_{2j}\left[`_j(t) - B^T \dot{x}(t)\right], \ j = 1, 2, 3 \tag{48.13}$$

with appropriate design constants μ_j and $\alpha_{1j}, \alpha_{2j}, \ j = 1, 2, 3$, which are selected to guarantee the closed-loop stability and robustness of the closed-loop system.

48.8 Experimental Results Under Harmonic and Seismic-Type Ground Motion

Some experiments were performed to evaluate the effectiveness of the semiactive MPPF with SMC control scheme using the MR damper. The design parameters selected for the semiactive MPPF + SMC controller with MR damper are the following:

$$W = \text{Diag}\begin{bmatrix} 2 & 5.1 & 9.1 \end{bmatrix} Hz, \ Z = \text{Diag}\begin{bmatrix} 0.7 & 0.7 & 0.7 \end{bmatrix}, \ G = \begin{bmatrix} 2 & 2 & 2 \end{bmatrix},$$

$$\mu_1 = \mu_2 = 10, \ \mu_3 = 5, \ \alpha_{1j} = 80, \ \alpha_{2j} = 40, \ j = 1, 2, 3$$

The building-like structure without (open-loop) and with semiactive MPPF + SMC (closed-loop) was firstly tested using harmonic excitation at the base provided by an electromagnetic shaker, with variable amplitude. The overall open-loop system response and closed-loop system response using the semiactive MPPF + SMC control are described in Fig. 48.4. The corresponding FRFs for the acceleration and displacement at the first floor are depicted in Fig. 48.5. Note the small attenuation in the first and third floors, particularly during the first and second mode (12 % and 14 %, respectively), employing small control efforts. The closed-loop system performance is not significant because of the small piston velocities and displacement in the MR damper for harmonic excitations. For more extreme situations (e.g., seismic motion), the effectiveness of the semiactive control scheme is more evident. Therefore, the building-like structure with semiactive MPPF + SMC control was evaluated for seismic-type ground motion corresponding to that case occurred at Mexico City in September 19, 1985. The results are shown in Fig. 48.5, where the system response can yield to attenuations up to 56 % with respect to the open-loop performance.

In general, the overall system response using the semiactive vibration control scheme using a MR damper and MPPF + SMC control results effective to attenuate large ground vibrations, as that occurring during seismic and/or shock forces. The damping control forces are relatively high but the control effort employs small power consumption. Moreover, the use of sliding-mode control techniques leads to a compromise between robustness and switching energy.
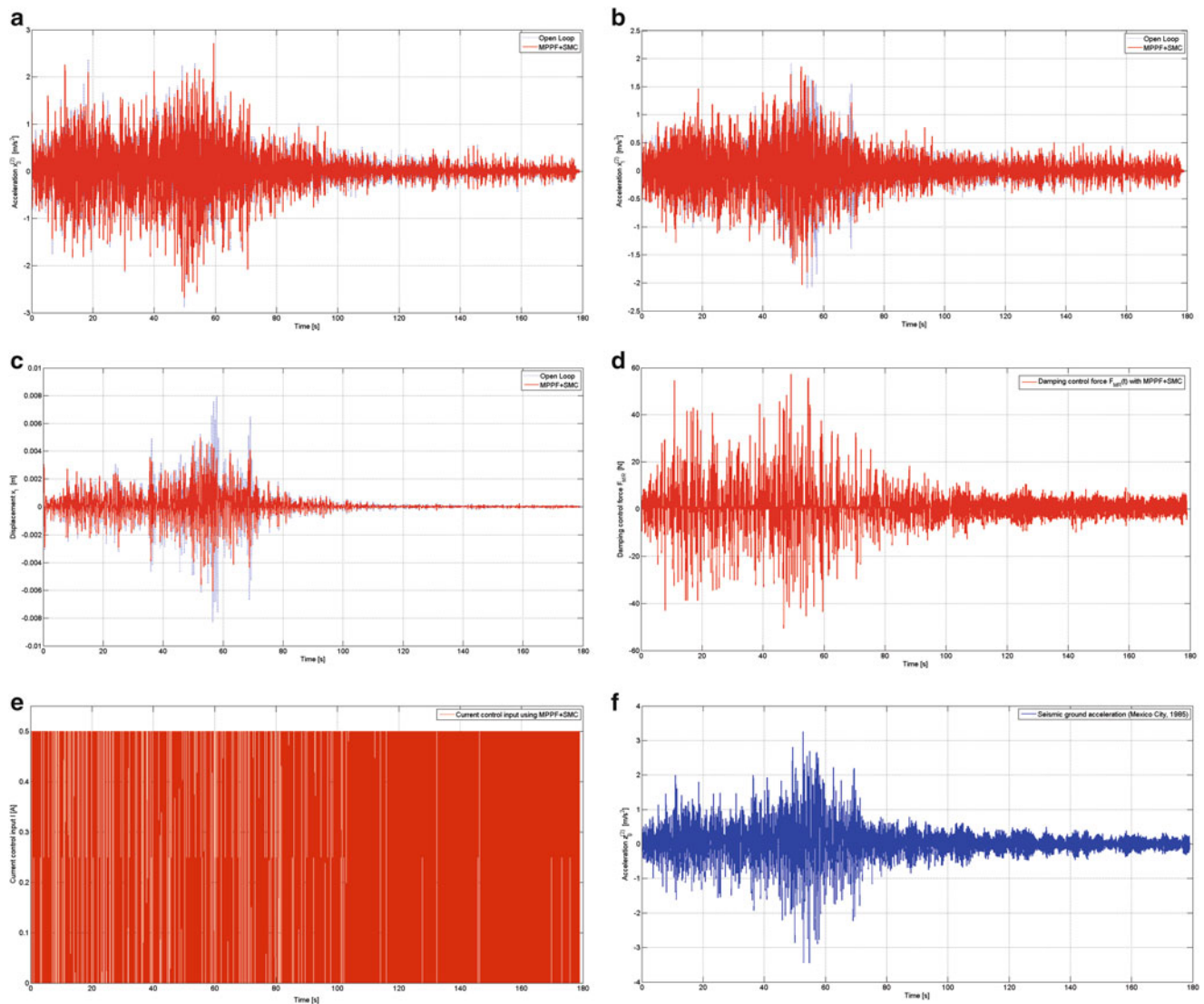
Fig. 48.5 Experimental results in open-loop and closed-loop using semiactive MPPF + SMC for *seismic-type* ground motion. (**a**) Acceleration $\ddot{x}_3$, (**b**) Acceleration $\ddot{x}_1$, (**c**) displacement x_1, (**d**) damping force F_{MR}, (**e**) current I, (**f**) base acceleration $\ddot{z}_g$

48.9 Conclusions

This paper describes the application of a semiactive vibration control scheme to a three-story building-like structure, employing a MR damper and a combination of a Multi Positive Position Feedback synthesized to attenuate the first three lateral vibration modes and Sliding-Mode Control to add robustness against unknown system parameters and ground motion. The experimental results are effective in case of seismic-type ground excitations in the structure. Further work is being is being conducted to improve the overall system performance.

References

1. Carlson JD, Catanzarite DM, St Clair KA (1996) Commercial magneto-rheological fluid devices. Int J Mod Phys B 10(23–24):2857–2865
2. Choi SB, Lee SK, Park YP (2001) A hysteresis model for the field-dependent damping force of a magnetorheological damper. J Sound Vib 245–2:375–383
3. Chopra AK (1995) Dynamics of structures theory and applications to earthquake engineering. Prentice-Hall, Englewood Cliffs

4. Craig RR Jr, Kurdila AJ (2006) Fundamentals of structural dynamics. Wiley, Hoboken
5. Dyke SJ, Spencer BF, Sain MK, Carlson JD (1996) Modeling and control of magnetorheological dampers for seismic response reduction. Smart Mater Struct 5(5):565–575
6. Ewins DJ (2000) Modal testing: theory, practice and applications. Research Studies Press, Baldock
7. Flatau AB, Chong KP (2002) Dynamic smart material and structural systems. Eng Struct 24:261–270
8. Friswell MI, Inman DJ (1999) The relationship between positive position feedback and output feedback controllers. Smart Mater Struct 8:285–291
9. Gawronski WK (2002) Advanced structural dynamics and active control of structures. Springer, New York
10. Inman DJ (2006) Vibration with control. Wiley, Hoboken
11. Korenev BG, Reznikov LM (1993) Dynamic vibration absorbers: theory and technical applications. Wiley, Chichester
12. Rios-Gutierrez M, Silva-Navarro G (2013) Active vibration control in building-like structures using piezoelectric actuators and positive acceleration feedback, *Dyna*, Year 80, Edition 179, pp 116–125, Medellin
13. Silva-Navarro G, Cabrera-Amado A (2007) Semiactive sliding-mode control of the unbalance response in a rotor-bearing system supported on MR dampers. In: Proceedings of the 46th IEEE conference on decision and control, New Orleans, pp 4513–4518
14. Spencer BF Jr, Dyke S, Sain M, Carlson JD (1997) Phenomenological model of a magnetoreological damper. ASCE J Eng Mech 123:230–238
15. Srbulov M (2010) Ground vibration engineering: simplified analyses with case studies and examples. Springer, New York
16. Utkin VI (1992) Sliding modes in control and optimization. Springer, Berlin

Chapter 49
Balancing Testing and Simulation for Design of a Research Facility

Brad Pridham, Stephen Price, and Brian Roeder

Abstract Vibration-sensitive equipment such as high-resolution imaging devices requires stable environments for optimal performance. It is often desirable to locate this equipment on ground, either at grade level or in basement areas, away from any significant sources of vibration. During planning, the site is surveyed to evaluate existing vibration conditions and to assess proposed equipment locations. This assessment informs the development of the structural scheme. If no significant changes to the site vibration environment are anticipated, the data from the site survey form the basis of design. However, in situations where significant changes to the ground vibration environment are anticipated, additional, more complex studies are often required.

This paper presents a case study involving the design of a vibration-sensitive research facility. Late in the development of the design the team was made aware of plans for a future light rail line directly adjacent to the building. A detailed evaluation of future rail vibration impacts was conducted using a combination of testing and simulation techniques to predict future site vibration levels and establish feasibility of colocation of sensitive equipment. The results from the assessment were used to finalize equipment selections, and to establish the final details of the structural design of the facility.

Keywords Ground-borne vibration • Floor vibration • Rail vibration • Imaging • Building design

49.1 Introduction

Research facilities located in dense urban settings are susceptible to ground-borne site vibrations that can impact facility performance. Ground-borne environmental vibration from sources such as roadway/railway traffic, mechanical equipment from adjacent buildings etc., can transmit to the building structure supporting vibration sensitive equipment and procedure rooms. If the vibration levels are sufficiently high, one or more of the following can occur:

- Failure to meet manufacturer's vibration specifications for the equipment/instrumentation;
- Substantial "noise" in measurement data is created that interferes with the accuracy of the research or experiments;
- Equipment performance or reliability is adversely affected;
- Laboratory animals can be adversely affected; and, in extreme cases,
- Vibration could damage or invalidate equipment calibration.

Early in the design of the facility a site vibration survey is conducted to characterize conditions at the site. The results from the survey are compared with vibration criteria, either generic or vendor-specific, to establish suitability for siting of sensitive instrumentation and procedures, and for development of control measures. Numerical modelling may be used to extrapolate measurement data to other areas at the site and to estimate vibration levels in spaces above/below grade, accounting for foundation attenuation effects, structural resonances etc.

The vibration survey provides a snapshot of the vibration environment at the time it is conducted. Some general allowance may be made in the design for moderate growth in the site vibration environment ('vibration creep'), that occurs over time such as the effects of future building developments and degradation of adjacent roadways. These allotments are generally

---

B. Pridham (✉)
Novus Environmental Inc, 150 Research Lane, Guelph, ON N1G4T2, Canada
e-mail: bradp@novusenv.com

S. Price
Datum Engineers, 6516 Forest Park Road, Dallas, TX 75235, USA

B. Roeder
Page Southerland Page, Inc, 400 W. Cesar Chavez Street Suite 500, Austin, TX 78701, USA

experience-based rather than being derived from detailed predictions or simulations. For example, an allowance may be made for a doubling of measured vibration levels due to further degradation of roadways having some knowledge of maintenance schedules and observations at other sites in the area. This approach can be used to verify the robustness of the proposed design, allowing for some conservatism.

For cases when significant increases in site vibration levels are anticipated in the future, further detailed studies may be required for development of the design. Particularly if/when the building owner has limited ability to mitigate or control these future sources, and the performance of critical research activities may be affected by this 'noisy neighbor'. In this paper we present a case study involving an assessment of future light rail vibration impacts on the design of a state-of-the-art medical research facility. Late in the development of the design the team was made aware of plans for a future light rail line installation adjacent to the facility. Given the highly-sensitive equipment to be located at ground level, it was necessary to evaluate potential vibration impacts and introduce necessary control measures to protect critical assets. By balancing vibration testing with modelling techniques, expected vibration impacts were established and the team was able to finalize equipment selections, finalize the structural design, and better plan for active control measures.

49.2 Facility Description and Design Criteria

The investigation involves a proposed multistory medical research facility, which will house several vibration-sensitive areas including high-resolution microscopy and medical imaging. Figure 49.1 is an aerial image of the existing site showing the footprint of the facility, location of sensitive imaging equipment and proposed light rail alignment. The site is bounded by roadways with steady traffic consisting of cars, commercial transport trucks and city busses throughout the day. When constructed, the closest vibration-sensitive space is anticipated to be approximately 80 ft from the rail alignment.

The geology at the site consists of alluvial deposits of approximately 10–15 ft depth overlaying limestone/chalk bedrock. The baseline survey of the site indicated a relatively efficient transfer of vibration from the roadway, across the building footprint. Further details are discussed below.
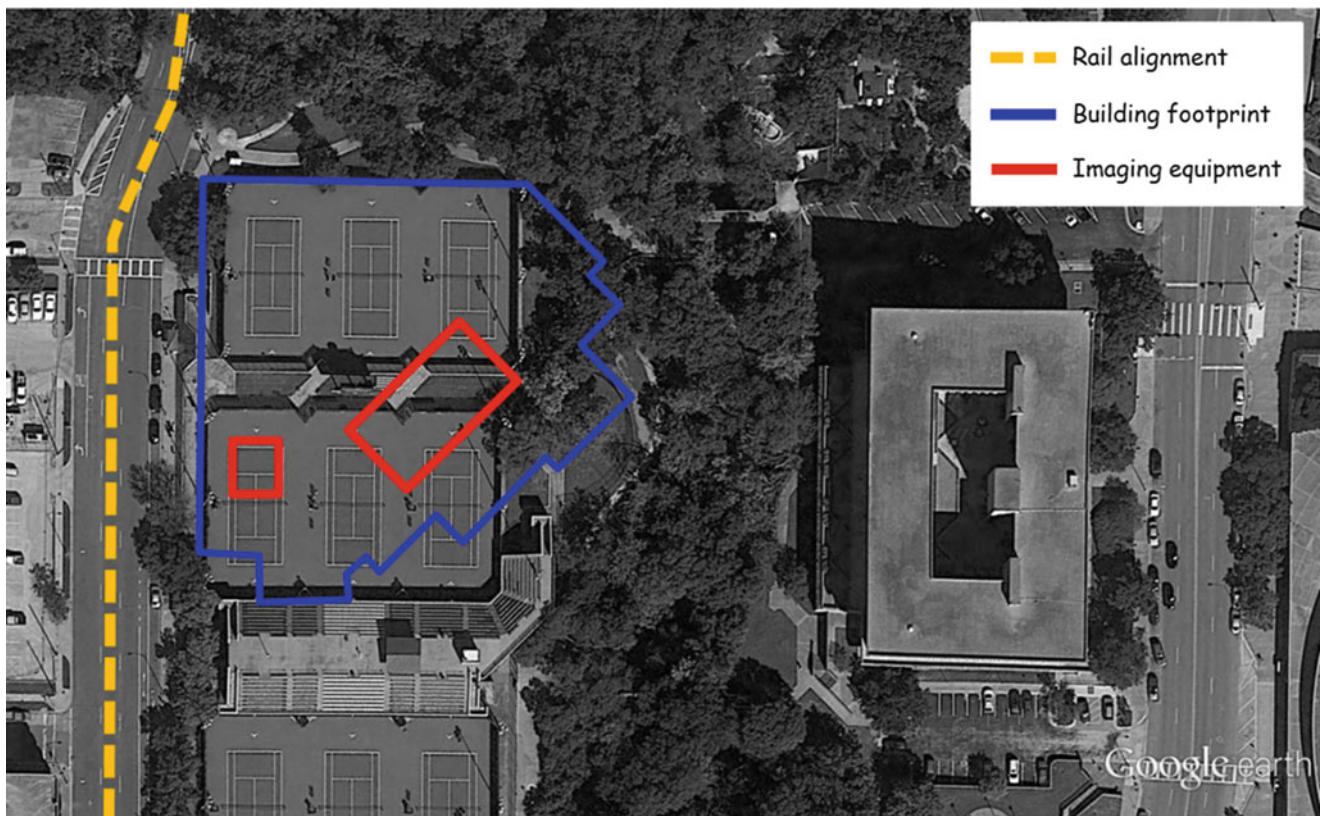

Fig. 49.1 Aerial photo of development site showing building footprint, location of equipment and rail alignment
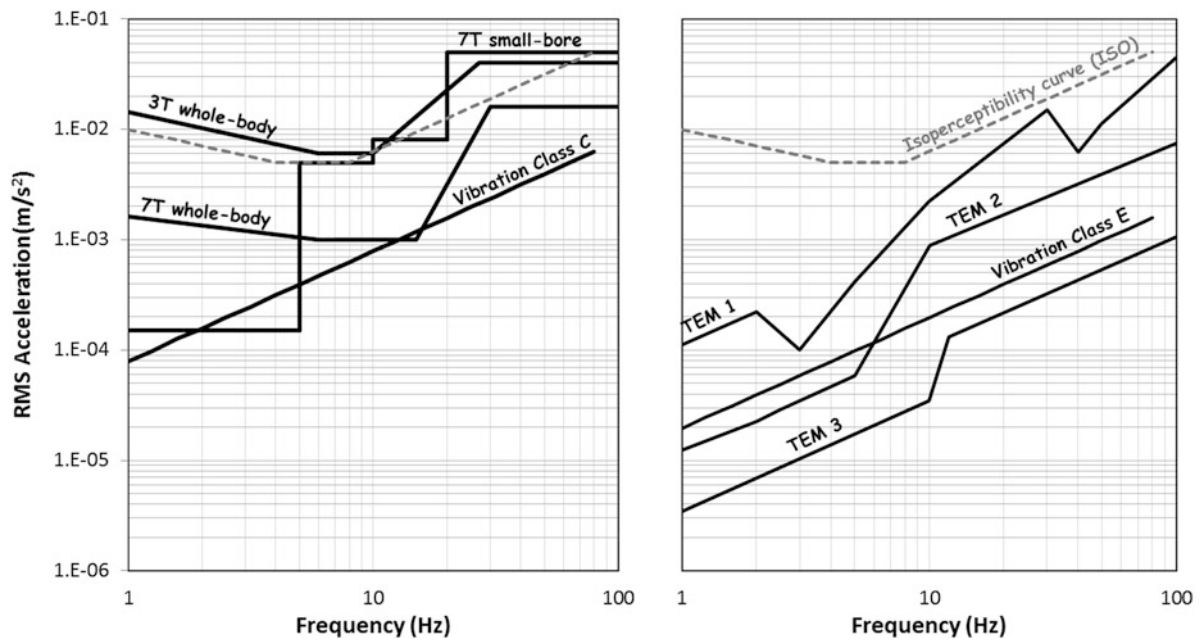
Fig. 49.2 Vibration thresholds for MRI (*left*) and transmission electron microscopes (*right*)

The types of research equipment contemplated for the facility included:

- 7 T investigational whole-body MRI;
- 3 T whole-body MRI;
- PET/CT scanners;
- 7 T small-bore animal MRI; and,
- High-resolution transmission electron microscope (TEM).

The assessment was completed using both vendor-specific and generic vibration criteria. As the design was in flux, final vendors had yet to be selected and so it was necessary to utilize multiple sets of criteria. The generic vibration criteria are widely accepted as a basis for designing and evaluating the performance of vibration sensitive equipment and the structures that support them, and are used in the absence of criteria from a vendor (typically early in design) [1, 2]. The criteria evolved from the isoperceptibility or 'base curve' published by the ISO, which represents the threshold of human perception to whole body vibration along the axis of the spine [3]. The ISO base curve is also referred to as the ISO Operating Room criteria, and is the basis for design of general surgical suites in healthcare facilities. This curve is also used in some jurisdictions to assess rail vibration impacts on residential dwellings [4].

Figure 49.2 shows the vibration criteria utilized in the assessment, together with the ISO base curve for reference. The criteria have been modified from their published forms for graphical display using similar units. Note the differences in threshold limits for the TEMs, particularly at frequencies less than 10 Hz. These are among the most vibration-sensitive instruments currently used in research environments, and often require active or passive control systems for optimal performance.

All devices, with the exception of the small-bore MRI were planned for locations at grade level, the same elevation as the new rail system.

49.3 Methodology

Assessment of rail vibration impacts was conducted based on a combination of numerical modeling and vibration testing. This included application of published rail vibration models, and an empirical model developed using information obtained from the project site and existing commuter and light rail installations. Details on the models and vibration testing aspects are outlined in the following sections.

49.3.1 Numerical Models

Predictions of rail vibration were developed using two models, the first (Model 1) is based on published techniques for rail vibration assessment using experimental techniques similar to modal testing; the second is a model derived using empirical data from measurements at the project site and at two existing rail installations.

49.3.1.1 Model 1: Force-Based Predictions

The first evaluation model was developed using the method published by the Federal Transit Administration, which is applied to the detailed design of rail transit systems throughout North America. The FTA model is summarized by the following equation [4]:

$$V = FDL + LSTM + SAF \tag{49.1}$$

Where:

V = the predicted vibration velocity;
FDL = the force density level for an LRT vehicle of a specified length, travelling at a specified speed;
LSTM = the line-source transfer mobility function representing the vibration level per unit force as a function of distance from the source. Units are decibels; and,
SAF = a safety factor accounting for track conditions, wheel flats and prediction uncertainties.

Evaluation of Eq. 49.1 requires knowledge of the force density level for a given rail vehicle, and measurement/computation of the line-source transfer mobility functions for the project site. The force density levels were constructed using published measurement data from light rail vibration assessments in other jurisdictions, as well as the upper bound design curve published in the FTA manual [5]. These data are shown in Fig. 49.3, together with the envelope curve used for the predictions. The selected curves are for LRT systems in urban settings having similar track conditions to that expected at the project site. The data in Fig. 49.3 were converted to narrow-band format for use in Eq. 49.1.

Safety factors were included in the model to account for increased vibration levels that result from special track conditions (cross-overs, frogs etc.), degradation in the wheels (flats), stiff vehicle suspensions, and uncertainties that result from the LSTM measurement procedure. A total adjustment of 25 dB was applied at all frequencies based on the guidance published
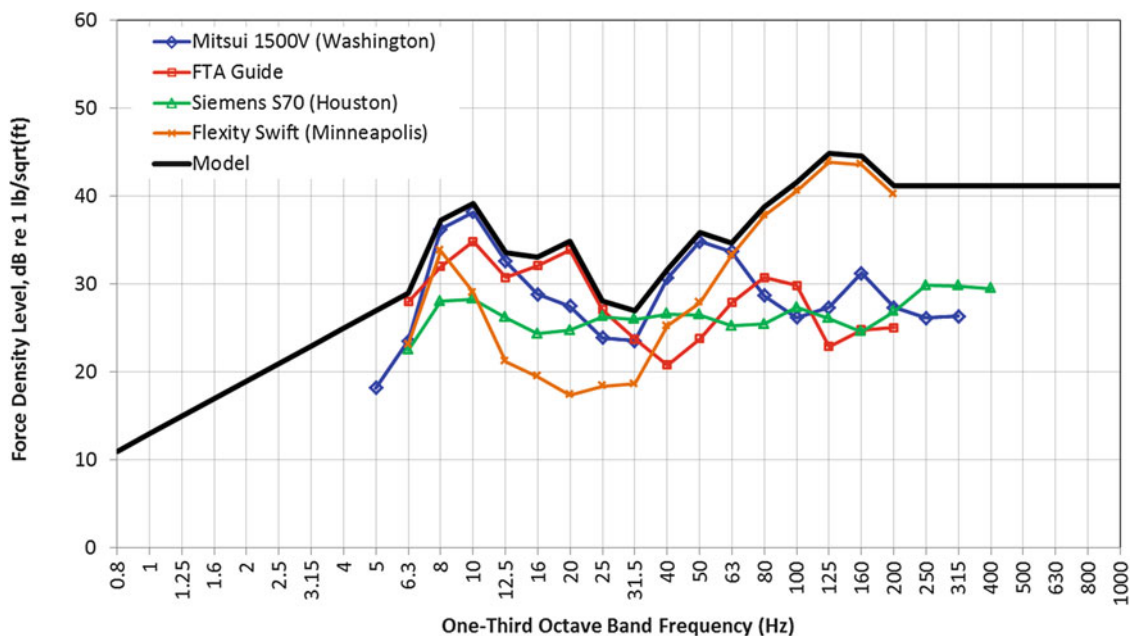

Fig. 49.3 Light rail force density envelope applied in the assessment

by the FTA. The model described by Eq. 49.1 produces estimates of the root-mean-square (RMS) vibration level at the receiver. Conversion to peak vibration levels was calculated by adding 12 dB to the estimates, or a peak factor (ratio of peak-to-RMS) of 4, which is typical for train vibrations.

49.3.1.2 Model 2: Measurement-Based Predictions

The measurement-based prediction model was constructed using a combination of measurements from the project site, a nearby commuter rail line founded on similar geology to the site and supported tie-on-ballast, and a light rail line located in another city founded on differing geology (deep clay deposit) and embedded rail. The model was developed using the following equation:

$$V = V_s + SDF + SAF \tag{49.2}$$

Where:

V = predicted vibration velocity at the location of the receiver;
V_s = the source train vibration level at a distance of 10 ft from the track;
SDF = the site vibration decay factor;
SAF = safety factor accounting for prediction uncertainties.

The source train vibration level V_s was constructed based on the rail measurements and the site vibration decay factors were computed based on measurements, as discussed in the next section. A safety factor of 5 dB was applied at all frequencies in Model 2 to account for some of the uncertainty associated with the process. This adjustment is less than that used in Model 1 since the measurements of the existing rail installations, which form the basis of the procedure, inherently include the effects of expected track conditions and typical wheel conditions for an in-service vehicle. No adjustments were made to the commuter rail data to account for the expected lighter weight of the light rail system, for conservatism.

Model 2 also produces estimates of the root-mean-square (RMS) vibration level at the receiver, and conversion to peak levels was based on a peak factor 4, similar to Model 1.

49.3.2 Vibration Testing

Vibration testing was necessary to compute the line source transfer mobility functions, site vibration decay factors and train source vibration levels for the commuter and light rail systems. Some key results from the testing are presented in this section.

49.3.2.1 Point Source Transfer Mobilities

Calculation of the line source transfer mobilities (LSTMs) for use in Model 1 was based on measurement of point source transfer mobilities (PSTMs) at the project site. Similar to impact testing in the context of experimental modal analysis, measurement of the force input and corresponding acceleration response of the ground is used to construct the point source frequency response functions at various measurement offsets from the hammer. These functions are then integrated numerically to compute the LSTM for a line source such as a train. The relationship between the applied force and ground response at a point is expressed as follows:

$$V(f) = PSTM(f) * F_{point}(f) \tag{49.3}$$

The LSTM at a distance y_0 is given by the line integral:

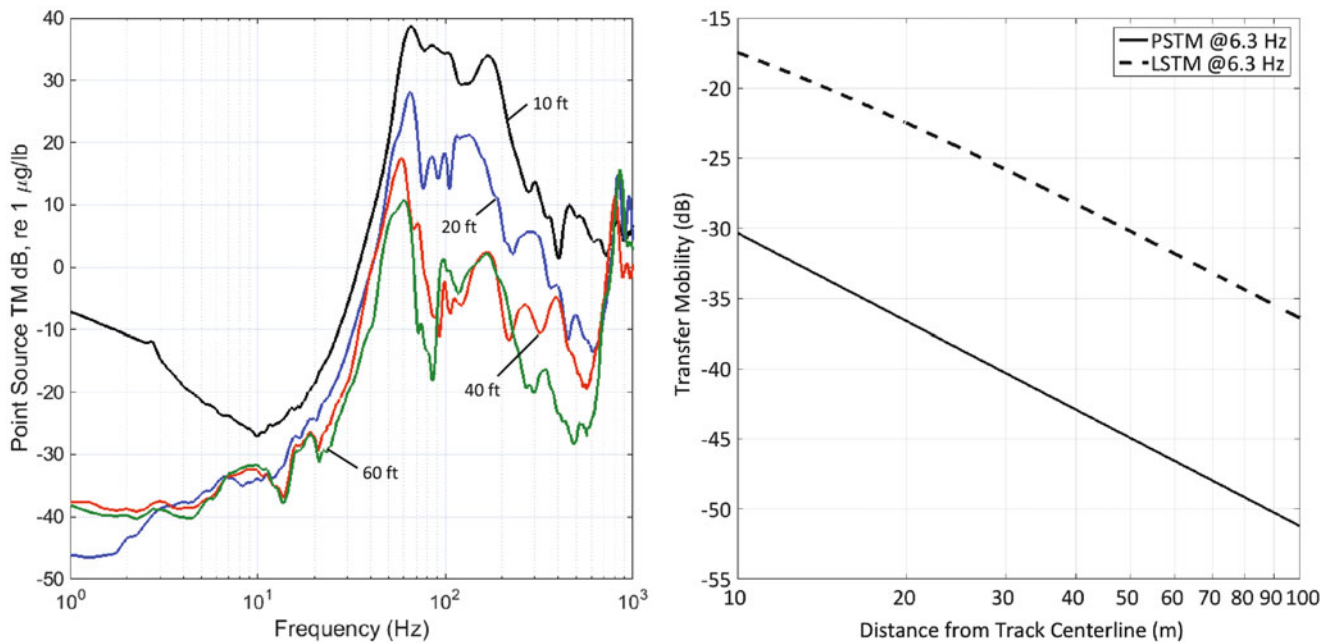$$LSTM^2(y_0) = \int_{-L/2}^{L/2} PSTM^2(y_0, x)\, dx \tag{49.4}$$

Fig. 49.4 Examples of measured PSTMs (*left*) and computed LSTM at 6.3 Hz (*right*)

The line integral is integrated numerically using a suitable assumption of the PSTM's relationship with distance. Figure 49.4 is an example of the measured PSTMs and computed LSTM at a frequency of 6.3 Hz.

Reliable estimation of the LSTM requires a high signal-to-noise ratio and sufficiently large force input throughout the frequency range of interest. A challenge with applying this method to the assessment of vibration environments sensitive to low frequencies is that impractical amounts of force can be required to excite energy below 5 Hz for measurement of the PSTM and reliable estimation of the LSTM. In fact, all of the published studies reviewed for this assessment excluded information in this frequency range. During our collection of data we were unable to achieve high signal-to-noise ratios below 5 Hz (a common problem using this approach). As such, predictions from Model 1 at frequencies below 5 Hz were excluded from the assessment.

49.3.2.2 Site Vibration Decay Factors

During the baseline survey of the site recordings of ground vibrations were obtained concurrently a several setbacks from the roadway. Using these measurements, as well as the impact test data obtained from the PSTM measurements, distance attenuation factors were calculated using a logarithmic fit to the data at each frequency. The results from this procedure are shown in Fig. 49.5.

As expected, the decay of vibration increases with frequency up to approximately 120 Hz. Data at higher frequencies were noisy, and generally not correlated to any sources at the site (traffic vibrations generally fall in the range of 10– 30 Hz). In light of this, an average attenuation of 15 dB was applied to frequencies above 120 Hz in the modeling.

49.3.2.3 Source Rail Measurements

Ground vibration levels for two rail installations were measured for use in Model 1. One installation, a commuter rail line, was located close to the site and on similar geology, whereas the second installation was located in a different jurisdiction on site geology generally consisting of clay with a large depth to bedrock. Several trains at both locations were measured during the surveys at varying setbacks from the track. A radar gun was used to measure train speed so that the results could be adjusted to a common speed using the methods suggested by the FTA. Photos of the two rail systems measured are shown in Fig. 49.6.

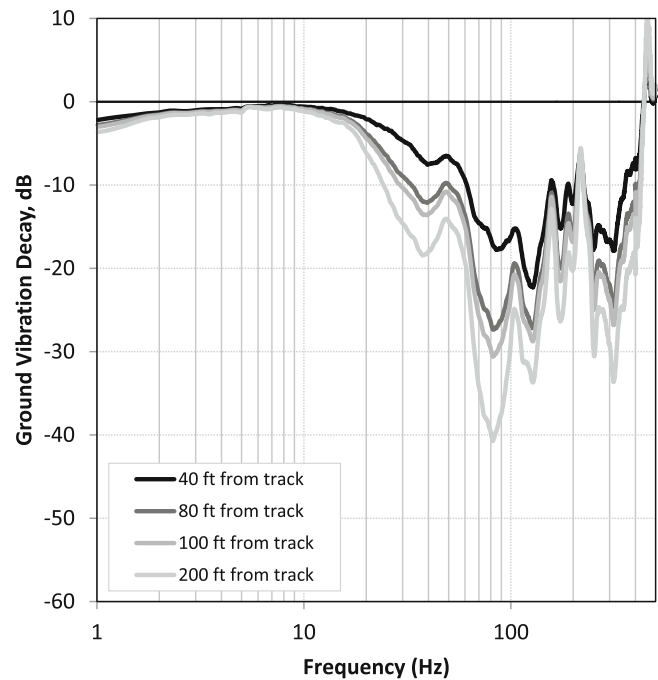**Fig. 49.5** Measured site spectral attenuation

Fig. 49.6 Commuter rail (*left*) and light rail (*right*) systems measured for use in the study

Figure 49.7 is the computed source vibration levels for the two rail systems at an offset of 10 ft from the track, together with the measured spectral decay for the two installation sites during rail vehicle passage. There is a distinct difference in the vibration energy from the two rail vehicles as a result of their different mass, suspensions and track conditions. Vibrations from the commuter rail are centered on a peak around 30 Hz, versus the peak at approximately 105 Hz for the light rail system. Data from the light rail system indicates higher vibrations at very low frequencies, although these are approximately 45 dB less than the peak level, where most of the vibration energy is concentrated.

The vibration decay characteristics are also different at the two installation sites with higher attenuation at frequencies less than 4 Hz for the site located in deep clay. At frequencies above 4 Hz the attenuation is of similar magnitude, with maximum attenuation occurring at the locations of peak input energy from the trains. The attenuation curves for the commuter rail line in Fig. 49.5 and site in Fig. 49.4 are similar in shape, with similar levels between 10 Hz and 100 Hz. The differences at low frequencies are likely a result of better signal-to-noise in the train measurements, i.e., greater energy in the ground at these frequencies from the train passage versus the measurements of vehicles and impact hammer strikes at the project site.
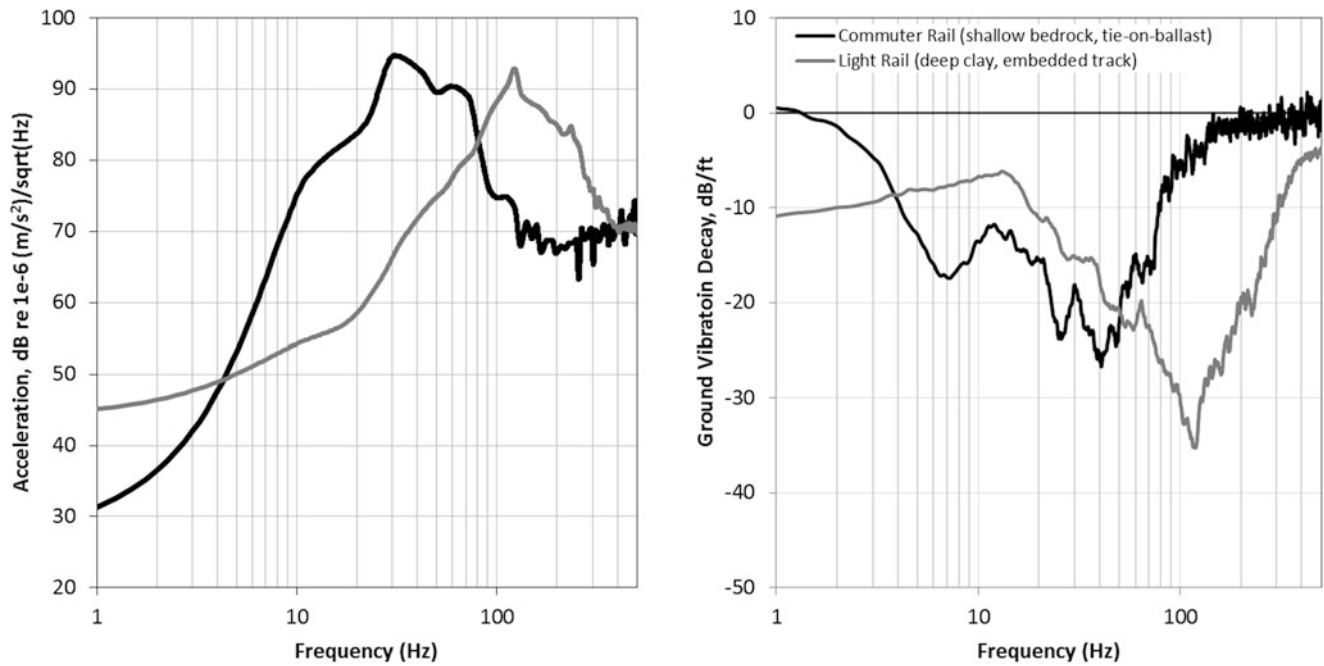
Fig. 49.7 Source acceleration PSDs (*left*) and measured rail vibration decay at the two installation sites (*right*)

49.3.3 Additional Modeling Assumptions

Limited information was available on the proposed rail system at the time of the assessment, and as such, it was necessary to apply assumptions regarding the vehicle type, speed of the train, the length of the train and the setback of the building from the rail line. The following assumptions were introduced in the modeling process:

- Vehicles having weight and suspension characteristics that are similar to the vehicles measured;
- A speed limit of 30 mph, which is the roadway speed limit for urban roads in the area;
- A train length of 100 ft, which is the typical length of a two-vehicle LRT in North America; and,
- A track setback of 30 ft from the building foundation.

49.4 Assessment Results

Predictions of rail vibrations were plotted together with equipment criteria to assess suitability of siting the instruments at the planned offsets from the rail. Some typical results are shown in Fig. 49.8. Note that the results are plotted in the units specified by the various vendors for the equipment, whereas these criteria were shown earlier in Fig. 49.2 in common units of RMS acceleration.

The results from the assessment indicate potential failure to comply with the vendor specifications for the TEM, 7 T whole-body MRI and marginal non-compliance of the 7 T small bore located on the second level of the building. All three models indicate non-compliance for the TEM, whereas only the Model 2 results based on the commuter rail line indicated non-compliance with vendor criteria.

49.5 Vibration Controls

Based on the findings from the assessment, options for vibration control were investigated for the equipment showing non-compliance (TEM and 7 T whole-body MRI). The solutions investigated included layout revisions to increase setback of equipment from the roadway/rail line; passive control using floating slabs; and, active control systems.
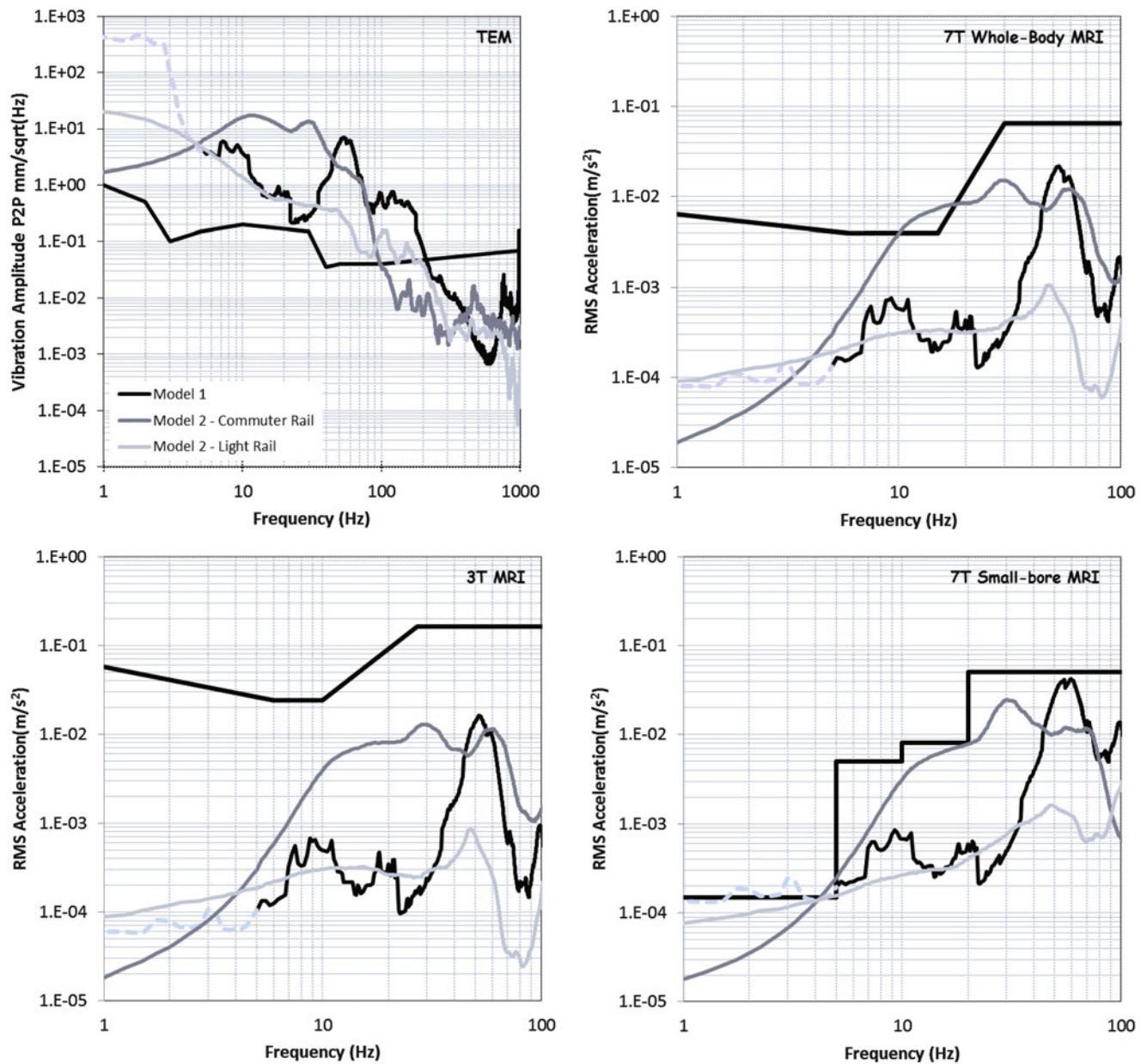
Fig. 49.8 Rail vibration predictions with vendor criteria

49.5.1 Layout Revisions

Increased setback results in additional attenuation of ground vibrations due to wave scatter and screening effects of the building foundation. This option is often possible during the early schematic/planning phases of the facility when layouts are in flux, and is perhaps the most common approach to ground vibration control. As the assessment was conducted late the design development phase of the project, it was impossible to revise the locations of sensitive instrumentation. This would require significant changes to the plan of the ground floor as it features controlled areas critical to the flow of procedures and materials at the facility. Design revisions would require significant re-work, impacting cost and schedule.

49.5.2 Passive Control

Passive control systems for vibration-sensitive equipment typically consist of a large blocking mass (inertia slab) beneath the equipment, and isolator elements between the blocking mass and supporting structure. When designed correctly, the system should behave as single-degree-of-freedom dynamic system having a resonant frequency that is determined based on the total mass and stiffness of the support isolators. Commercial isolators used in these systems are usually neoprene or rubber pads/mounts or steel or pneumatic springs.

A passive system is only effective when its resonant frequency is lower than the excitation frequencies from ground-borne vibrations, and the mass sufficiently large to limit dynamic displacements of the system when subject to ground motions. The practical lower limit of design for a steel spring system is approximately 1.4 Hz using commercially available springs, 1–2 Hz for pneumatic systems, and approximately 5.5 Hz for high quality rubber mounts. Systems featuring neoprene/rubber mounts or steel springs have little-to-no maintenance, making them favorable for tight spaces where access is limited – such as beneath and MRI. Pneumatic springs typically require replacement after some period of time, and can suffer from leakage, blow-outs etc. (although less common for some modern products). Pneumatic springs and rubber mounts generally have higher damping levels compared to steel springs so that there is negligible settlement time once excited by a disturbance. In order of cost, neoprene/rubber mounts are the cheapest followed by steel springs and pneumatic springs. For a typical MRI space in the proposed building, isolator costs ranged from \$5,000 for neoprene/rubber mounts, up to approximately \$45,000 for pneumatic springs.

49.5.3 Active Control

Active control systems are devices that monitor and respond to incoming ground vibrations allowing them to actively 'cancel' problematic motions, providing stable environments for the equipment they support. They are referred to as 'stiff systems' because they do not have resiliency like the passive systems described above. They are very much intended to behave as a stiff, highly stable support for the payload (equipment), providing a cancellation interface between ground/parent structure and isolated equipment. Because of its stiffness, the equipment and sensitive elements within may also be supported on active or passive isolation elements (e.g., pneumatic springs supplied by the manufacturer with the device) for effective isolation of ground motions. This stacking of isolation elements is typically challenging for passive systems due to the potential for dynamic interactions resulting in coupled motions of the blocking mass and internally isolated elements.

An active system is only effective when the parent structure supporting the active control device is very stable. Displacement thresholds on the order of 470 μin (12 μm) are required by one manufacturer. Achieving this requirement can often require very stiff equipment foundations. The devices do have some maintenance requirements, but these are generally less demanding than passive systems. Cost of these systems varies according to the size of the device/floor being isolated, and for a typical electron microscope contemplated for the facility in this study a quotation of \$40,000 was provided by one vendor.

Figure 49.9 is a plot of the acceleration transmissibility curves for the various control strategies considered in the assessment. Peaks on the curves correspond to the isolation system resonances and the height/width of the curves at the peaks is a function of the damping in the systems. The superior performance of the active control system is evident by transmissibilities less than one across the 1–100 Hz frequency range.

Using the transmissibility shown in Fig. 49.9, the models were updated to determine the most effective control strategies for the TEM and 7 T whole-body MRI. A suitable ground vibration environment for the TEM would require relocation to a setback of 200 ft from the rail line, installation of an active control device and inclusion of the vendor's internal pneumatic isolators. The 7 T whole-body MRI required support on a floating slab supported on rubber pucks for effective isolation. Both approaches were verified with the vendors to ensure there were no incompatibilities between equipment and isolation systems resulting in void of the installation warranty.

Fig. 49.9 Transmissibility functions for passive and active control systems
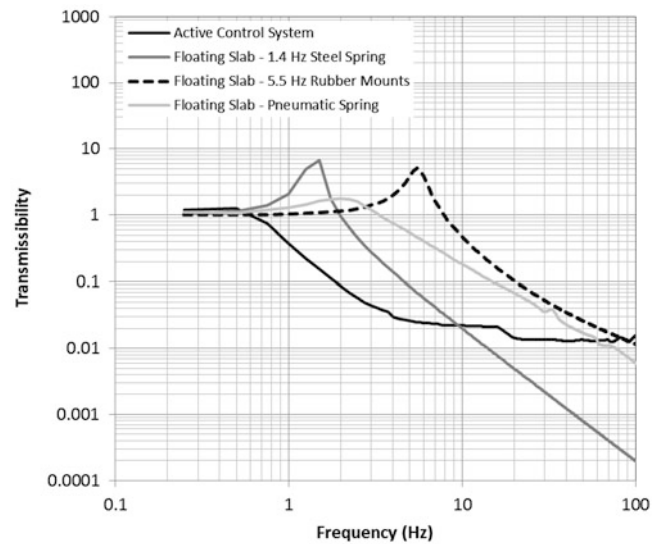
49.6 Concluding Remarks

Following completion of the assessment the design team and owner were able to select equipment that satisfies the research goals of the new facility and is expected to be compatible with the environmental site vibrations. The 7 T whole-body MRI was removed from programming due to the uncertainties associated with environmental conditions and research programming. The TEM space could not be relocated, and remains a part of the design with several years of use anticipated prior to activation or construction of the light rail line. Structural supports for the equipment will include isolated concrete slabs on piles, anchored to the bedrock. Engineered sand fill will be included beneath the slabs to increase the damping of the supports. Performance measurements will be conducted at a later date, following completion of the facility, for validation of the design.

References

1. Amick H, Gendreau M, Busch T (2005) Evolving criteria for research facilities: i vibration. In: Proceedings of SPIE conference 5933, San Diego
2. Watch DD (2008) Building type basics for research laboratories, 2nd edn. Wiley, New Jersey
3. ISO 2631–2 (2003) Evaluation of human exposure to whole-body vibration Part 2: continuous and shock-induced vibration in buildings (1 to 80 Hz), International Organization for Standardization
4. Transit Noise and Vibration Impact Assessment, Federal Transit Administration (FTA), Technical report no. FTA-VA-90-1003-06, May 2006
5. Rajaram S, Saurenman H (2010) Variation in measured force density levels of rail transit vehicles, NOISE-CON 2010, Baltimore

Chapter 50
Certain Uncertainties: Modelling Unusual Structures to Control Vibrations in Sensitive Areas

Michael J. Wesolowsky, Mihkel Toome, Buddy Ledger, Ramin Behboudi, and John C. Swallow

Abstract Mechanical equipment and occupant footfalls are often the most critical sources of floor vibration on the elevated floors of buildings. Achieving stringent vibration criteria on these floors requires sufficiently stiff and massive floor structures to effectively resist the forces exerted by mechanical equipment and user traffic. The difficulty for engineers in modelling these buildings can be exacerbated in structures that are very old and/or of unusual construction. In this paper, two case studies are presented of modelling such structures in order to predict vibrations in sensitive areas. The first structure dates to 1925, and is of massive concrete construction. A new 1 megawatt emergency generator is being installed directly above a floor containing vibration sensitive computer equipment. The challenges associated with the uncertainty of computer modelling of the dynamic properties of the historic structure are explored. The second structure is a large private residence, which has long span floors constructed of concrete, engineered wood joists and steel beams. Excessive vibrations due to footfall activity resulted in cracking of the concrete topping. The challenges associated with modelling this unique structure are explored. Field testing of both structures to examine and verify the accuracies of the assumed model parameters is presented.

Keywords Footfall vibration • Vibration measurements • Model validation • Sensitive floors • Dynamic loading

50.1 Introduction

The primary sources of vibration in most buildings are mechanical equipment and human activity, especially footfalls. For mechanical equipment, it is critical to provide sufficient vibration isolation to limit the transmission of vibration from the source to sensitive nearby areas. In the case of footfalls, as people walk, the impact from each footfall induces floor motions that may also easily transmit to nearby spaces. Quantifying vibration from either mechanical sources or walking, whether through measurement of existing spaces or numerical predictions for guiding the design of a new building, is a complex task. This task is complicated in cases where little or no information is available about the structural details of the building, which is often the case in older structures, or if the building is constructed of a hybrid structural system which is not commonly encountered.

This paper presents the two case studies to compare measurements to modelling assumptions in unusual structures. The first is a 90-year old concrete building, and the second is newly built wood/steel/concrete hybrid structure. In both cases the floors were bare and had minimal dead loads from services mounted below the floors, which provided an opportunity to focus on the effects of the dynamic property assumptions in the models.

50.2 Vibration Criteria

For human comfort, vibration criteria are normally expressed as the root mean square (RMS) response of each one-third octave band from 1 to 80 Hz [1]. For sensitive equipment, the criteria may be expressed in one-third octave bands, or other formats, including power spectral densities, peak-to-peak levels, etc. Over the past 25 years, generic vibration limits have been developed which provide frequency-dependent sensitivities for wide classes of equipment, and are used extensively in design of healthcare and research facilities [2]. These vibration criterion (VC) curves are internationally accepted as a basis

M.J. Wesolowsky, Ph.D., P.Eng. (✉) • M. Toome, M.Sc., P.Eng. • B. Ledger, P.Eng. • R. Behboudi, M.Eng., P.Eng.
• J.C. Swallow, M.A.Sc., P.Eng.
Swallow Acoustic Consultants Ltd, 23-366 Revus Ave, Mississauga, ON L5G 4S5, Canada
e-mail: mwesolowsky@swallowacoustic.ca

for designing and evaluating the performance of vibration sensitive equipment and the structures that support them. The VC curves range between Workshop (least stringent) through VC-G (most stringent). Most laboratories target at least VC-A as a maximum baseline for the majority of the facility, with certain areas requiring more stringent criteria, depending on the expected use of the space.

These curves were originally based on the ISO 2631–2 (1989) [3] base curve for human response to whole body vibration, which is considered the threshold of human perception, but have since evolved. The ISO base curve is often referred to as the ISO-Operating Room criteria. The above noted criteria are also specified as RMS velocities in one-third octave bands. The VC curves should not be used to replace manufacturers' specifications for vibration requirements, but are beneficial where manufacturers' specifications are non-existent, incomplete, or where specific equipment has not yet been selected.

The VC curves will be used as a basis of evaluating the performance of Structure #2 in this paper.

50.3 Case Study #1 – Historic Concrete Building

The building used for Case Study #1 was constructed in 1925 of concrete, and appears to have been designed as a two-way slab system (L/B ≅ 2). The original hand drawn structural drawings of the building were available (see Fig. 50.1), however portions of the notations were faded or illegible. The column and beam schedules were particularly difficult to decipher. The main slab was 114 mm deep, while the typical beams were either 570 mm or 700 mm deep. The columns were circular, having a diameter of 560 mm. The building has been used by a telecommunications company for its entire life, housing heavy equipment and was staffed by many employees.

A proposed 1 megawatt emergency diesel generator set (genset) was to be installed on the third floor of the building on a 4-in. high concrete housekeeping pad. The concern was that vibrations transmitted from the genset to the concrete slab it was to be mounted on could interfere with the computer equipment installed on the second floor of the building by the
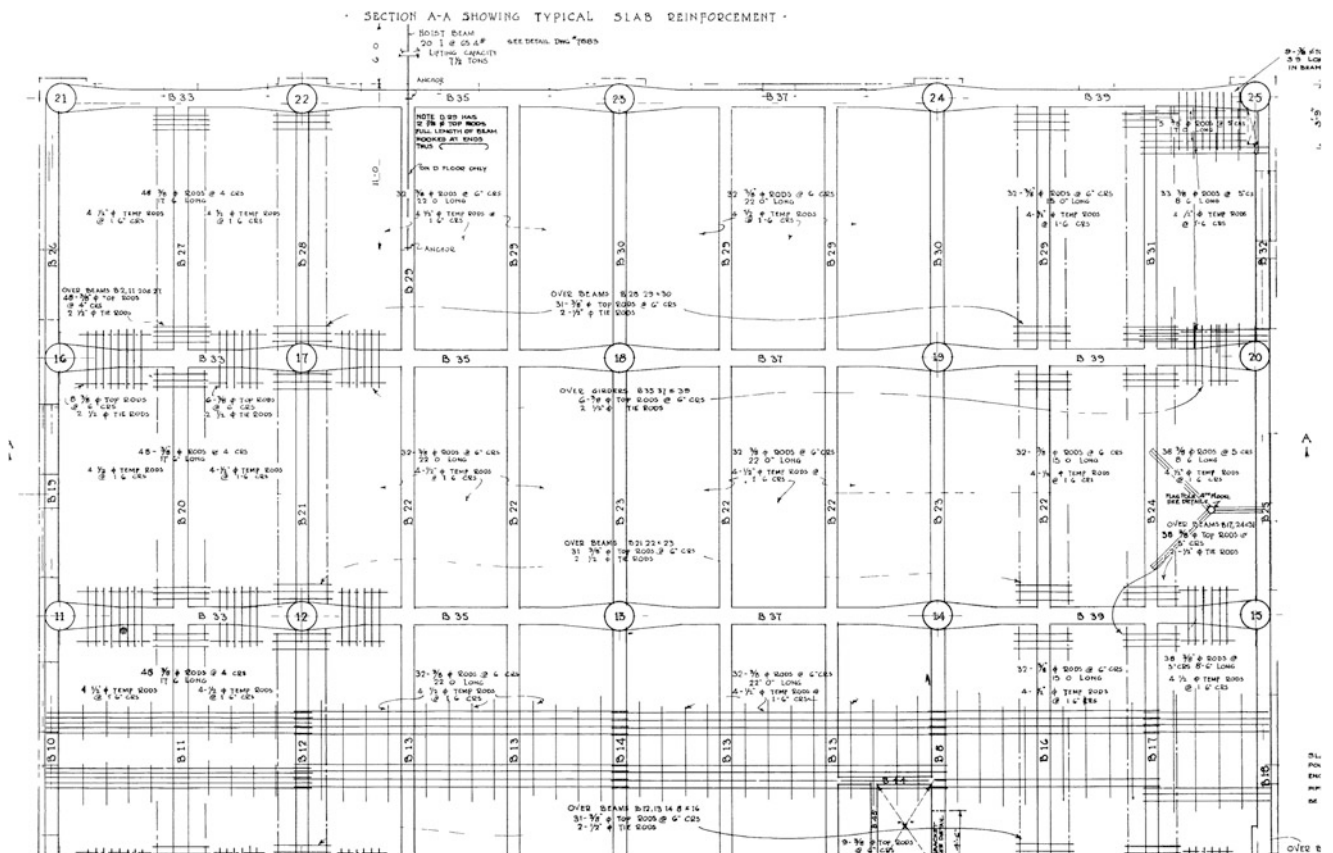

Fig. 50.1 Portion of original 1925 structural drawings of Structure #1

Fig. 50.2 Modal testing of Structure #1

Table 50.1 Modal frequencies

Mode	Measured natural frequency (Hz)	Modelled natural frequency (Hz)
1	20	32.0
2	24	36.4
3	27	32.5

transmission of these vibrations through the columns. This necessitated the modelling of both the second and third floors of the building using the SAP2000 Advanced v15 Finite Element Modeling (FEM) software package in order to input the dynamic loading of the genset.

A great deal of uncertainty was expected from this FEM model as a result of being based on old and partially illegible drawings, coupled with the assumptions of material properties which had likely evolved over the 90 years of service of the building. Finally, the addition of an 8,200 kg genset in a relatively compact area on an old floor was likely to further compound the difficulties associated with the modelling.

Impact frequency response function (FRF) measurements were conducted to determine the in-situ floor vibration characteristics before installation of the genset, and to verify the FEM modelling (see Fig. 50.2). The measurements were conducted by placing one uni-axial accelerometer (PCB type 393A03, 1 volt/g) at the centre of each of the four bays considered in the central area of the floor. Input excitation to the floor consisted of heel drops and impacts using a 5.5 kg instrumented sledge-hammer (PCB type 086B50). Data acquisition was via a LMS SCADAS Mobile real-time analyzer.

The analysis was based on measurement data using an impact at one location and measuring the response at four locations (e.g., roving accelerometer method). The plots of the mode shapes in this article are based on the deflection at the centre of each bay (i.e., the response measurement locations), with the remaining points being extrapolated. It should be noted that the floor was completely bare during testing, and that the underside of the slab did not have any appreciable dead load from building services. For the purposes of comparison to the FEM model, this allowed us to remove an assumed superimposed dead load from our model to directly compare modelled to measured bare floors.

Table 50.1 summarizesthe first three modes obtained from modal testing and their corresponding modelled modes. Figure 50.3 shows the mode shapes for each of these modes. It should be noted that testing occurred only over the middle four bays of the floor. It is clear from the measurements that the first three modes of the floor have considerably lower frequencies than their modelled counterparts, although the mode shapes are quite similar. These large discrepancies can potentially be explained by some combination of two major uncertainties. First, the structural drawings that were available did not contain
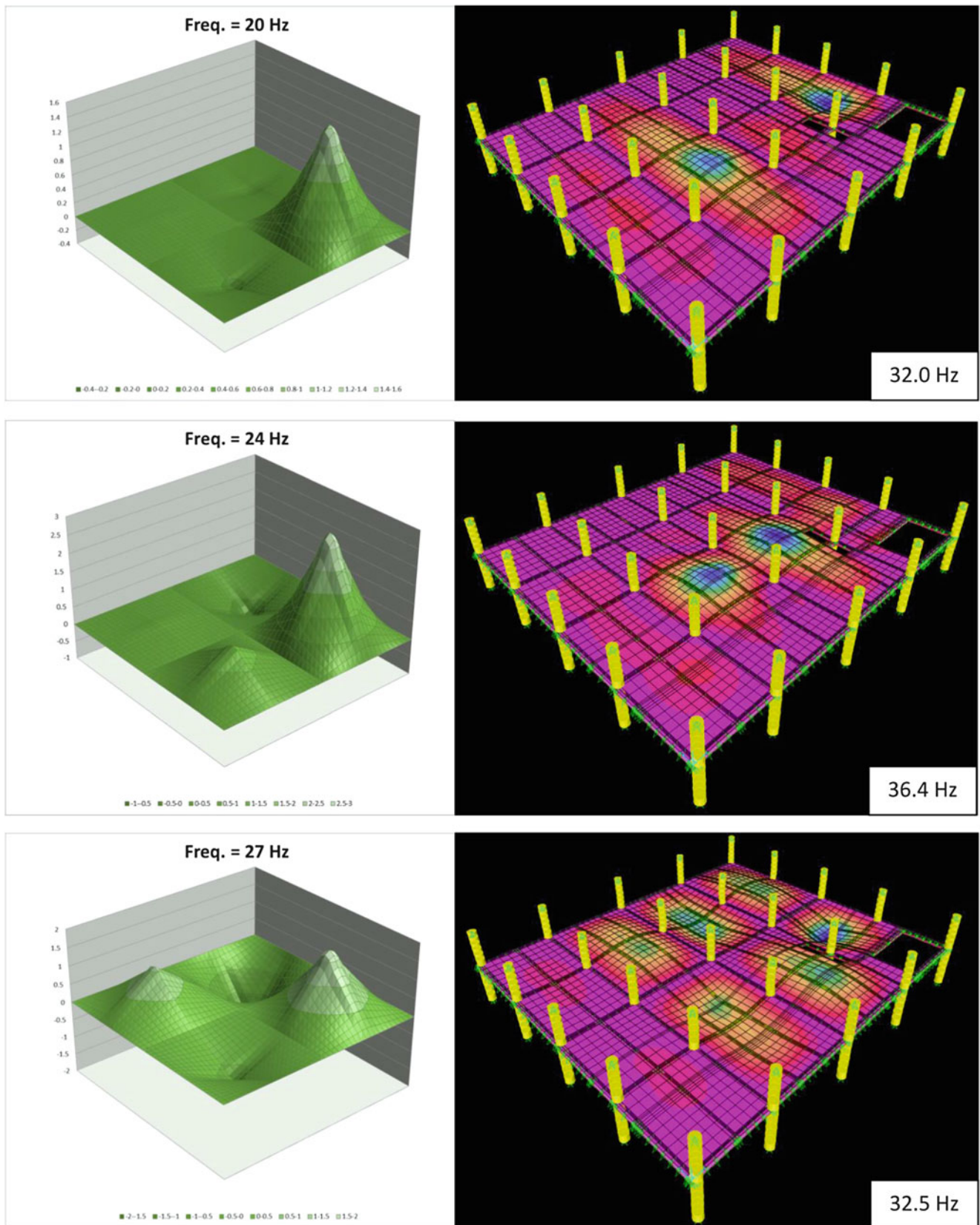
Fig. 50.3 First three measured and corresponding modelled mode shapes

any material properties, and the quality of concrete may have been significantly different than that which was assumed in our model. Second, 90 years of heavy use of the building has likely significantly altered the original dynamic properties of the building. The conclusion to be drawn is that when presented with a similar scenario, it is essential to perform modal testing of the building in order to calibrate any predictive modelling that is required.

Nofootfall-induced vibration measurements were taken due to limited time on-site.

50.4   Case Study #2 – Large Private Residence

The building used for Case Study #2 was constructed in 2013. The floor was 50 mm of concrete on a plywood form, which was supported by built-up engineered wood and steel I-beams. During construction it had been noted that the floor was particularly lively when construction workers walked across the living room and kitchen. The vibrations had also lead to significant cracking in the concrete topping, which had been polished and was intended to be the final finished floor. Further, cutlery and plateware in the kitchen were constantly rattling when occupants walked anywhere in the living room. The main span of the living room was a total of 10.4 m long, which is unusually large for a lightweight residential construction. A layout of the areas of concern can be found in Fig. 50.4.
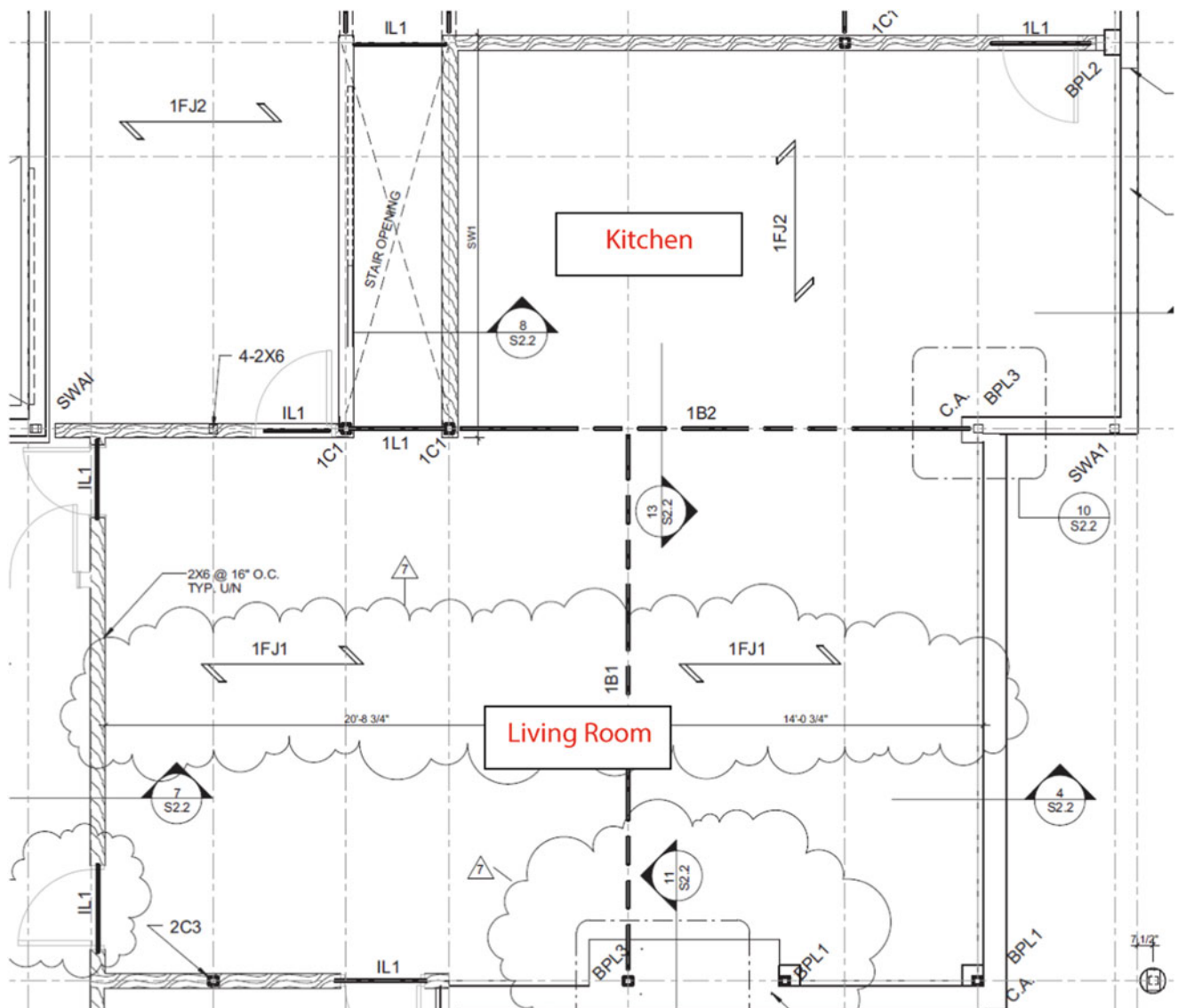

Fig. 50.4   Structural drawings of the area of concern in Structure #2
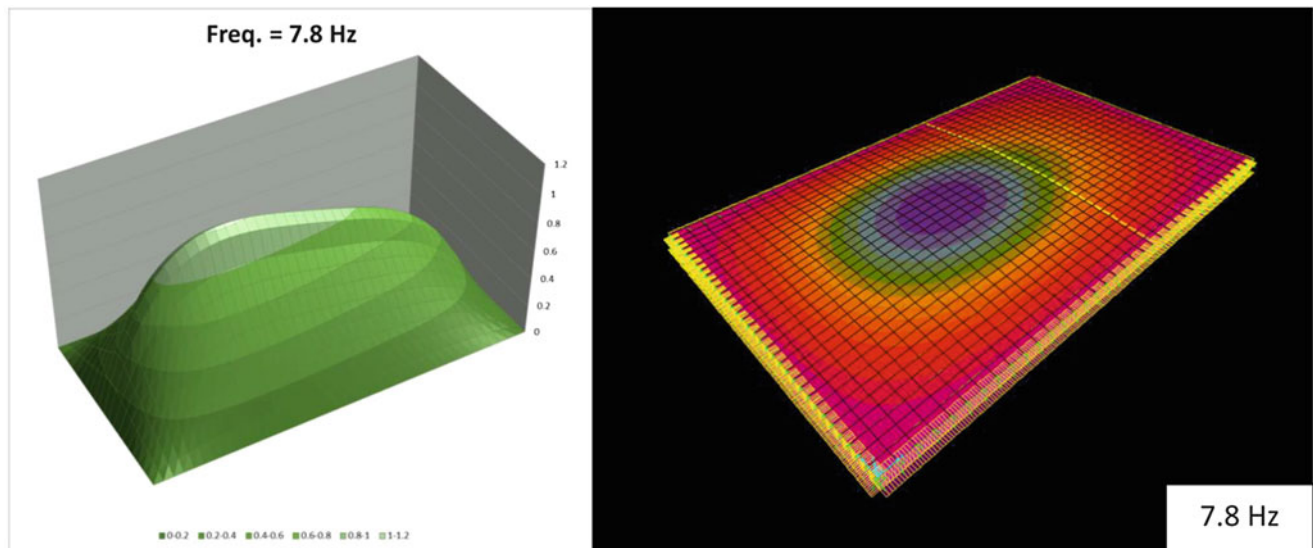
Fig. 50.5 First measured and corresponding modelled mode shape

A structural finite element model of the living room area was developed using SAP 2000. It was assumed that majority of the perimeter of the living room was pinned, as it was attached to either the top of the foundation wall, or connected to the top of load-bearing partitions. The properties of the engineered wood I-beams were obtained by contacting the manufacturer who provided material and section properties.

A four-channel simultaneous vibration measurement data acquisition system was used to quantify the existing performance of the floor. Four 1,000 mV/g Bruel & Kjaer (B&K) Type 4,508 accelerometers connected to a B&K Nexus Type 2,693 signal conditioner were used to measure floor vibrations at four measurements locations in the living room. The 4-channel simultaneous vibration acceleration time histories were recorded using an iOtech Wavebook 516 analogue to digital converter with a sampling rate of 200 Hz and a 100-Hz anti-aliasing low-pass filter. Time domain data was processed using 1,024-point (5 s) FFT windows, yielding a frequency resolution of 0.2 Hz.

A series of heel-drop and walking tests were conducted to determine the natural frequency of the floor. One mode at 7.8 Hz was identified, which was in the range of interest for footfall-induced vibration. This modal frequency and shape corresponded exactly to the modelled mode (see Fig. 50.5). It should be noted that as with Structure #1, the floor was modelled without superimposed dead load, as the floor surface was bare, and there were minimal services (e.g., plumbing, ducts, etc.) mounted under the floor.

The methodology proposed by The Steel Construction Institute (SCI P354) [4] was then used to verify the measured footfall-induced response of the floor. This method assumes that the response of each mode is either resonant or impulsive, depending on the associated floor frequency. Empirically determined frequency-dependent dynamic load factors are used to excite the floor along probable walking paths as determined from the architectural drawings. The loading conditions are then used to develop a time series response for each mode. The time series responses for each mode are then linearly superimposed to produce a total floor response at any receptor point on the floor. A range of realistic walking frequencies and walking paths can be considered to determine the governing floor response. Spectral analysis can be performed on the predicted time-series responses to express the floor behavior in a format appropriate for comparison with the relevant criteria, in this case, the VC curves described in Sect. 50.2.

Figure 50.6 shows the rms velocity response that was measured on the floor (L10) for a single walker having a weight of 76 kg (as per the SCI recommendations), walking at constant pace of 1.95 Hz, which is the 4th sub-harmonic of the first mode frequency of the floor. This figure also shows the predicted response of the floor using the same walking pathway, walker weight and walking pace. From this figure it can be seen that the SCI method predicted remarkably similar responses to the measured values, both in magnitude and frequency response.

This case study indicates that despite the SCI method being intended for a steel-concrete composite floor construction, it can produce accurate response predictions for a floor constructed of a combination of engineered wood, steel and concrete. It should also be noted that as this structure was new, the dynamic properties of the materials used were clearly more comparable to those assumed in the model.
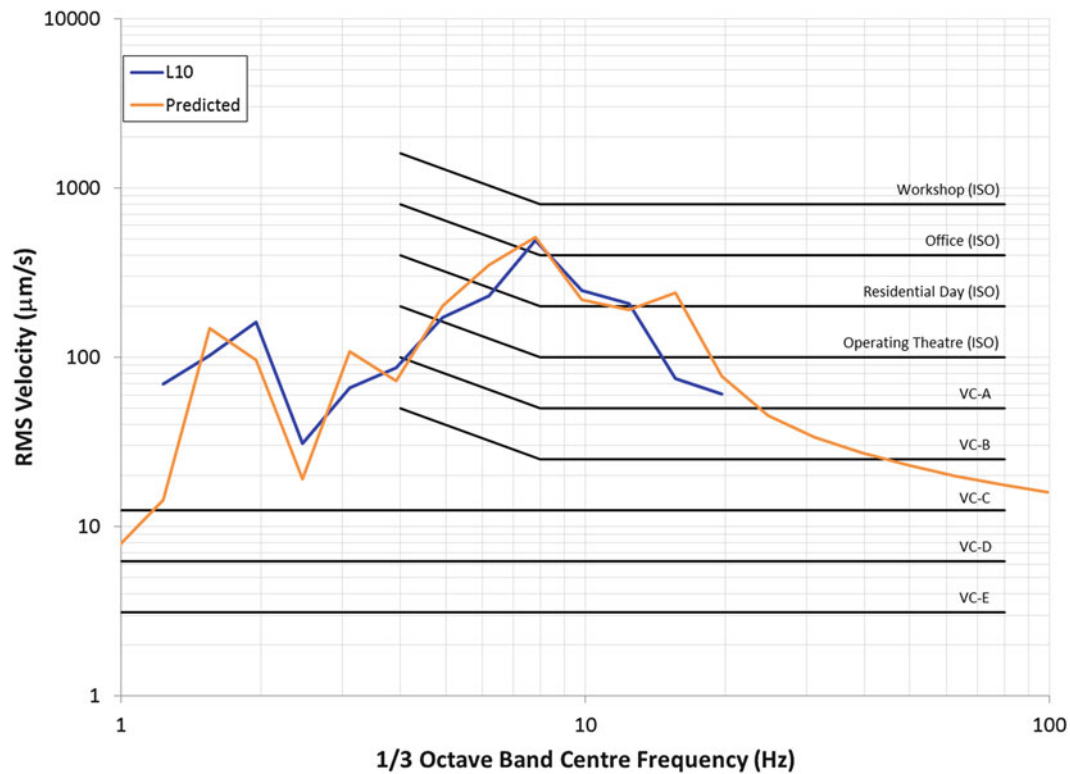
Fig. 50.6 Measured and prediction footfall-induced vibrations of Structure #2

50.5 Conclusions

Two case studies have been presented to compare measurements to modelling of unusual structures. The first was a 90-year old concrete building, and the second was newly built wood/steel/concrete hybrid structure. In both cases the floors were bare and had minimal dead loads from services mounted below the floors, which provided an opportunity to focus on the effects of the dynamic property assumptions in the models. The following conclusions have been made:

1. When modelling an older building which has seen heavy use, material assumptions based on commonly-used modern material properties are not valid, and models need to be calibrated based on in-situ field testing.
2. Despite the SCI method being intended for a steel-concrete composite floor construction, it can produce accurate response predictions for a floor constructed of a combination of engineered wood, steel and concrete.
3. When modelling a newer building which has seen almost no use, material assumptions based on commonly-used modern material properties are expected to be valid.

References

1. BS 6472 (1992) Guide to evaluation of human exposure to vibration in buildings (1 Hz to 80 Hz), British Standards Institution, London, United Kingdom
2. Amick H, Gendreau M, Busch T, Gordon C (2005) Evolving criteria for research facilities: I – vibration. In: Proceeding of SPIE conference 5933: buildings for nanoscale research and beyond, San Diego. July 31–August 1 2005
3. ISO 2631–2 (1989) Evaluation of human exposure to whole-body vibration-part 2: human exposure to continuous and shock-induced vibrations in buildings (1 to 80 Hz). International Standard, ISO 2631–2, Geneva, Switzerland
4. Smith AL, Hicks SJ, Devine PJ (2009) Design of floors for vibration: a new approach – revised edition (SCI P354). Steel Construction Institute, Ascot

Chapter 51
Predicting and Mitigating Ground-Borne Vibration Transmission to Elevated Floor Structures

Julia M. Graham

Abstract Ground-borne vibration from road and rail sources is often a critical consideration for the functionality of research and healthcare facilities. Sensitive equipment can be isolated individually, but when improved vibration performance of the overall structure is required vibration must be mitigated before it enters the structure. To accomplish this, more comprehensive analysis methods must be considered. In the current case study a 12-storey hospital building containing microsurgical and surgical suites is under construction 15 m from a busy commuter and freight rail line. A neighbouring building located at a similar distance from the rail line was measured to have clearly perceptible vibration levels on elevated floors. In order to determine the vibration mitigation required for the new building, an extensive measurement plan was conducted to determine vertical and lateral soil propagation characteristics, a foundation model was constructed to determine soil-structure interaction properties and a finite element model of the building structure was constructed to determine vibration propagation to all floors in the building. The study shows how careful analysis and testing can lead to informed evaluation of various mitigation strategies to combat a very serious problem.

Keywords Ground-borne vibration • Railway • Isolation • Barriers • Numerical model

51.1 Introduction

The case study building is a new hospital building located in Florida. For confidentiality reasons it cannot be named and will be referred to as the "new building". The new building will house vibration-sensitive operating suites and is located 15 m from a busy rail line. Initial vibration measurements indicated that expected vertical vibrations on elevated floors would exceed the required criteria and require significant mitigation efforts.

To accurately predict vibrations on elevated floors, an extensive vibration survey and modeling plan was developed. Vertical and lateral vibrations were measured at ten locations for a period of 22.5 h to capture as many train pass-bys as reasonably possible and to determine the attenuation characteristics of the soil. The measured vibrations were then used as inputs to a soil-structure interaction model and the outputs from this were used as inputs to a finite element method model of the new building structure.

The predicted results for the new building exceed the acceptable criterion requiring mitigation. A bentonite slurry wall capable of attenuating vibration levels down to the required criteria was designed. This paper discusses the slurry wall design along with alternate mitigation options.

51.2 Description of Project

The new building is a 12-storey concrete structure with most bays being approximately 9×9 m. It will house surgical suites and patient bedrooms on Levels 3–12 and micro-surgical suites on Level 2. Levels 1 and 3–12 have 300 mm slabs with no beams. Level 2 has a 300 mm slab supported on 600 mm beams to increase its stiffness. The new building is supported on a 1.5 m thick mat foundation. The soil in-situ is comprised of sands, silting sands, clay, and silty to clayey sands with shear wave velocities ranging from 55 to 360 m/s.

J.M. Graham, M.A.Sc. (✉)
Rowan Williams Davies & Irwin Inc, 650 Woodlawn Road West, Guelph, ON N1K 1B8, Canada
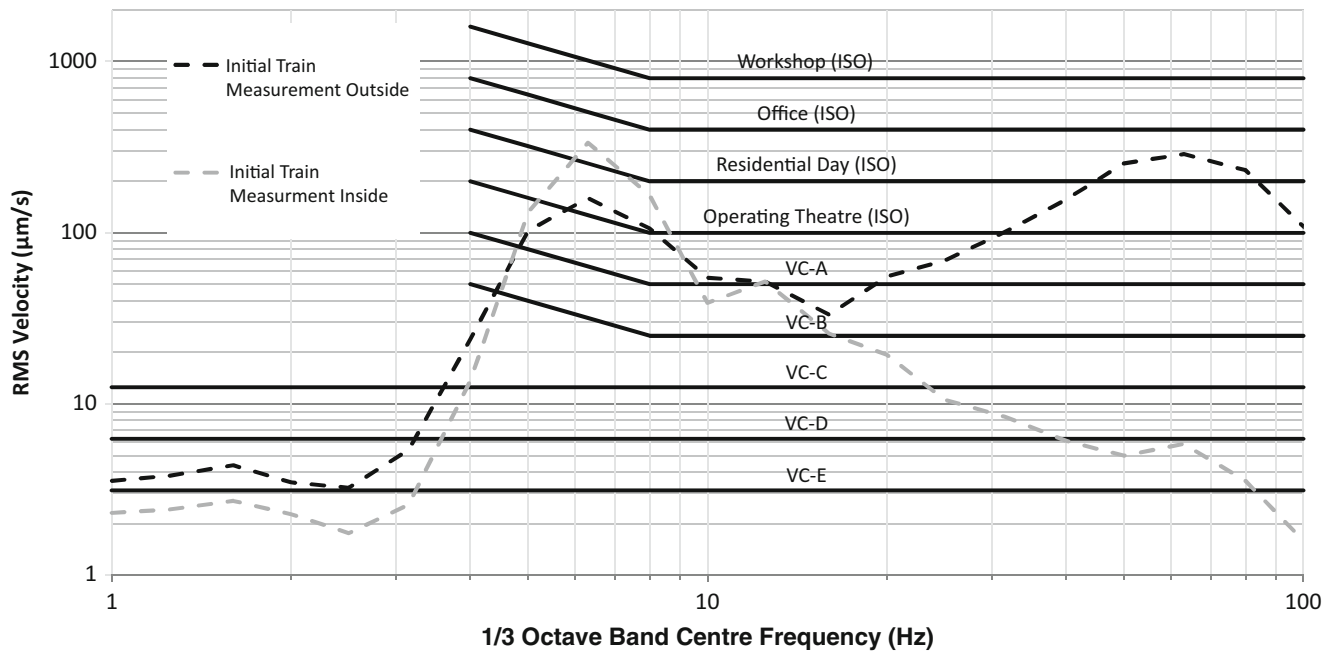e-mail: Julia.Graham@rwdi.com

Fig. 51.1 Initial L_{10} vertical velocities of freight train pass-by measurement at new building site and within existing building

For this project the predicted and measured vibration levels are assessed against the industry-standard Vibration Criteria (VC) curves. VC curves are generic vibration limits which were developed to provide frequency-dependent sensitivities for wide classes of equipment, and are used extensively in design for healthcare and research facilities [1]. The curves were originally based on the ISO 2631–2 (1989) [2] base curve for human response to whole body vibration, which is an approximation of the threshold of human perception, but have since evolved. The ISO base curve is often referred to as the ISO-Operating Room criterion. The VC curves are specified as root mean square (RMS) velocities in one-third octave bands. In the new building Levels 3–12 were required to achieve the ISO-Operating room criterion and Level 2 was required to achieve the VC-B criterion which is 25 % of the magnitude of the ISO-Operating criterion. These criterion levels are shown in Fig. 51.1 along with measurements taken at the site as discussed below.

The new building is located 15 m from a rail line which carries both freight and passenger trains. Figure 51.2 shows a plan view of the site. Medical staff working in an existing hospital building (shown in Fig. 51.2 just north of the new building) noted that floor vibrations were distinctly perceptible during train pass-bys. Initial vibration measurements were conducted in March of 2012 to assess the site conditions and determine the vibration levels in the existing building. Figure 51.1 shows vibration levels measured on the ground 10 m from the rail line and inside the existing building, on Level 2, approximately 30 m from the rail line. The data is processed into one-third octaves recorded during the 84-s train pass-by using 4-s windows. The presented results are the L_{10} velocity levels (defined as the one-third octave RMS velocity levels exceeded 10 % of the time during the train pass-by). Note that the measurement inside the building is actually higher than that outside the building at 6.3 Hz. This frequency is close to the natural frequency of the floor, thus the response is being amplified. Although the existing building was a steel structure, and thus was not directly comparable to the new concrete building, the large exceedance of the criteria inside the new building warranted a more extensive measurement plan as described below.

51.3   Description of Vibration Measurements

Vibration specialists from RWDI obtained vibration measurements at the site on January 23rd and 24th, 2013. Measurements were taken at three test pits as shown in Fig. 51.2. Each of the test pits was 6.1 m deep which is the depth of the new building's foundation. Vertical and lateral vibration measurements were taken at the base of each pit and vertical and lateral vibration measurements were also taken at the ground surface near Pits 1 and 3.
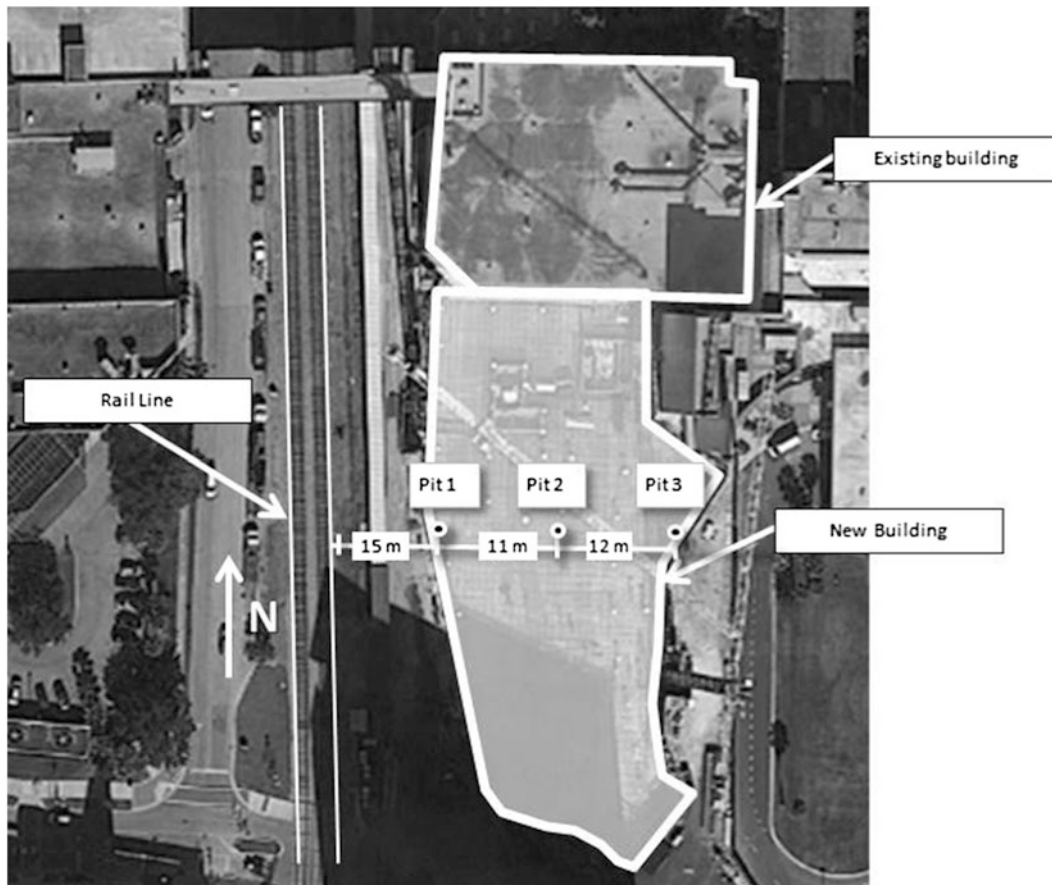
Fig. 51.2 Project site plan and measurement locations

The sensors at the base of the test pits were below the water table and dewatering pumps were required to run continuously during the measurements. The dewatering pumps were located on vibration isolating pads; however, vibration from the pumps was still noticeable in the measurements and the measurements collected at Pit 2 (located closest to the pumps) could not be used.

Vibration measurements were recorded using PCB model 393A03 and 3393B31 accelerometers, model VO626A01 velocity transducers, and a 40-channel LMS SCADAS Mobile real-time analyzer. The sensors at the bottoms of the test pits were fixed to 0.6-m-long angle irons which had been retrofitted to act as triaxial mounts. The angle irons were driven into the ground. The sensors on the ground surface were fixed to triaxial plates secured to steel spikes driven into the ground.

Measurements were recorded continuously for 22.5 h from 6:30 pm on January 23rd to 4:00 pm on January 24th, 2013. During that time, four passenger trains and eight freight trains passed by.

The time-history recordings of each train pass-by were separated from the ambient data. The one-third octave RMS velocity spectra for each measurement recorded during a train pass-by were determined using 4-s windows. The data presented here represent the L_{10} velocity levels from the train pass-bys. Although both vertical and lateral vibrations were recorded, this paper will focus only on vertical vibrations as these drove the necessary mitigation.

51.4   Vibration Measurement Results

Figure 51.3 shows the measured L_{10} vertical velocity spectra recorded during the pass-by of the largest freight train, where "largest" refers to the train inducing the highest levels of vibration. Figure 51.3a shows the measured spectra at the top and bottom of Pit 1. Figure 51.3b shows the measured spectra at the bottoms of Pits 1 and 3. Figure 51.3a shows some
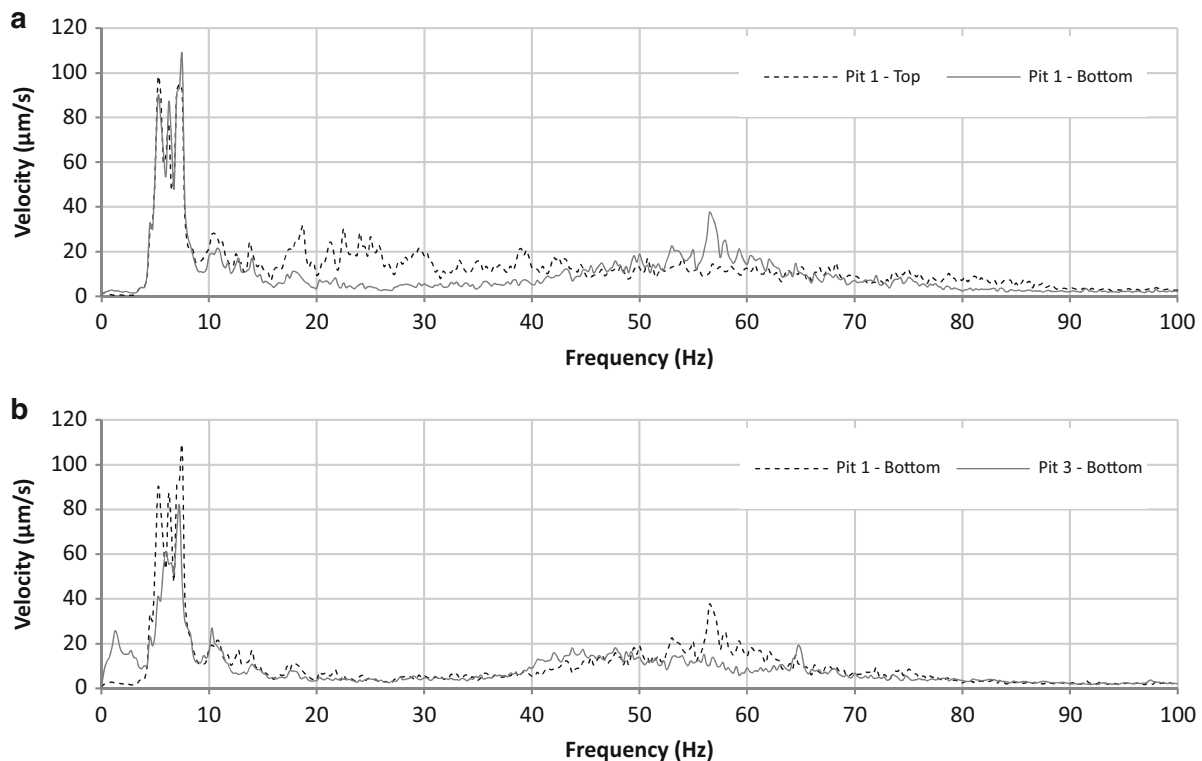
Fig. 51.3 Measured L_{10} vertical velocity spectra recorded during largest freight train pass-by (**a**) at the top and bottom of Pit 1, and (**b**) at the bottoms of Pits 1 and 3

attenuation in velocities between approximately 15 and 45 Hz. However, the highest levels of vibration, at 5–8 Hz, show little attenuation with vertical distance. It is noted that the vibrations measured at the bottom of the pit exceed those at the top between 50 and 60 Hz. This is believed to be attributable to an underground utility source rather than to train-induced vibration, as these vibration levels were present in the absence of trains as well and it is known that utilities run in the vicinity of the measurements. Figure 51.3b shows that there is very little attenuation in the horizontal direction. The plot shows some attenuation at 50–60 Hz, but as mentioned above, these vibrations are thought to be attributable to underground utilities and therefore, this decrease may be the result of proximity to the utility.

Measurements recorded during other train passes show similar results. Because of the low levels of attenuation across the plan of the building, measurements obtained at the base of Pit 1 were used in the analysis to predict vibration levels on elevated floors within the building. Figure 51.4 shows the L_{10} vertical velocity spectra in one-third octaves recorded at the base of Pit 1 during the pass-bys of the largest freight train (labeled "heavy freight train") and largest passenger train, along with the VC curves. Only two of the eight measured freight trains induced high levels of vibration at frequencies below 10 Hz as shown in Figs. 51.3 and 51.4. The other freight trains, along with the passenger trains, induced highest levels of vibration between 50 and 60 Hz. Figure 51.4 also shows vibration induced by a "typical" freight train, in which the highest levels are at 60 Hz.

Train vibration normally causes highest levels of vibration between 40 and 80 Hz. The high level of vibration observed at lower frequencies is believed to be attributable to a phenomenon known as "hanging ties" in which the rail ties become uncoupled from the supporting ballast. When the ties are excited by a heavy train they can pulse relative to the ballast creating a low-frequency vibration source.

Vibrations measured at the site exceed the VC-B criterion for all measured trains and exceed the ISO-Operating Theatre criterion for the heavy freight trains. It was expected that propagation of vibration through the building foundation and structure would attenuate some of the vibration. To predict the vibrations expected on elevated floors of the building, a numerical model of the building was created as discussed below.
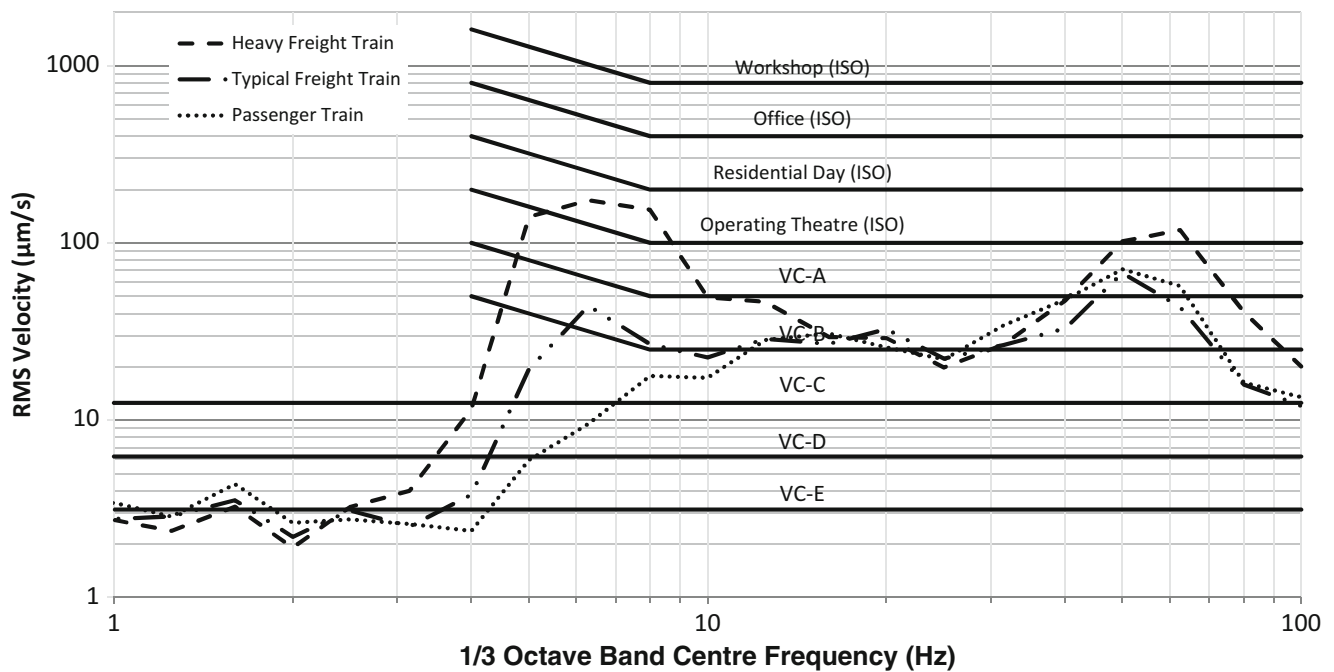
Fig. 51.4 L_{10} vertical velocities recorded at the base of Pit 1 during three train pass-bys

51.5 Description of Numerical Model

A model of the mat foundation and soil properties was created using the soil-structure interaction software Dyna 5.4 [3]. The foundation was modeled as a rigid 1.5 m thick slab resting on a half-space foundation. Soil properties were based on the geotechnical investigation. The model was used to determine the amount of attenuation expected from the kinematic interaction of the soil with the structure. The model was also used to determine the dynamic soil spring constants and damping values.

A finite element method (FEM) model of the entire new building structure was created in the structural analysis software SAP2000 [4]. Figure 51.5 shows the FEM model. The model included the mat foundation and dynamic soil spring constants and damping values obtained from the Dyna model. Base accelerations predicted after the expected attenuation from the soil-structure interaction were used as the dynamic inputs to the FEM model. Response vibrations were predicted on the elevated levels for comparison to criteria.

51.6 Results from Numerical Model

Figures 51.6 and 51.7 show the vertical vibration levels predicted on Levels 2 and 12 respectively. The vibrations predicted on Level 2 are expected to exceed the required VC-B criterion at several frequencies due to the heavy freight train. Vibrations induced by typical freight and passenger trains are expected to meet the required criterion. The vibrations levels predicted on Level 12 are higher than those predicted on Level 2 due to the lighter and more flexible construction of Level 12. However, Level 12 has a more lenient criterion and the vibration levels predicted on Level 12 are expected to achieve the required criterion. Figure 51.8 shows the vertical vibration levels predicted on Level 2 along with the data measured at Test Pit 1. This figure shows that the building and soil-structure interaction generally serve to decrease the expected vibrations across all frequencies but that there is a relative increase at the natural frequency of the floor at 16 Hz.

The large exceedance of criterion at low frequencies was especially troublesome, given the difficulty of attenuating vibration at these frequencies. Several mitigation options considered are discussed below.

Fig. 51.5 Finite element method
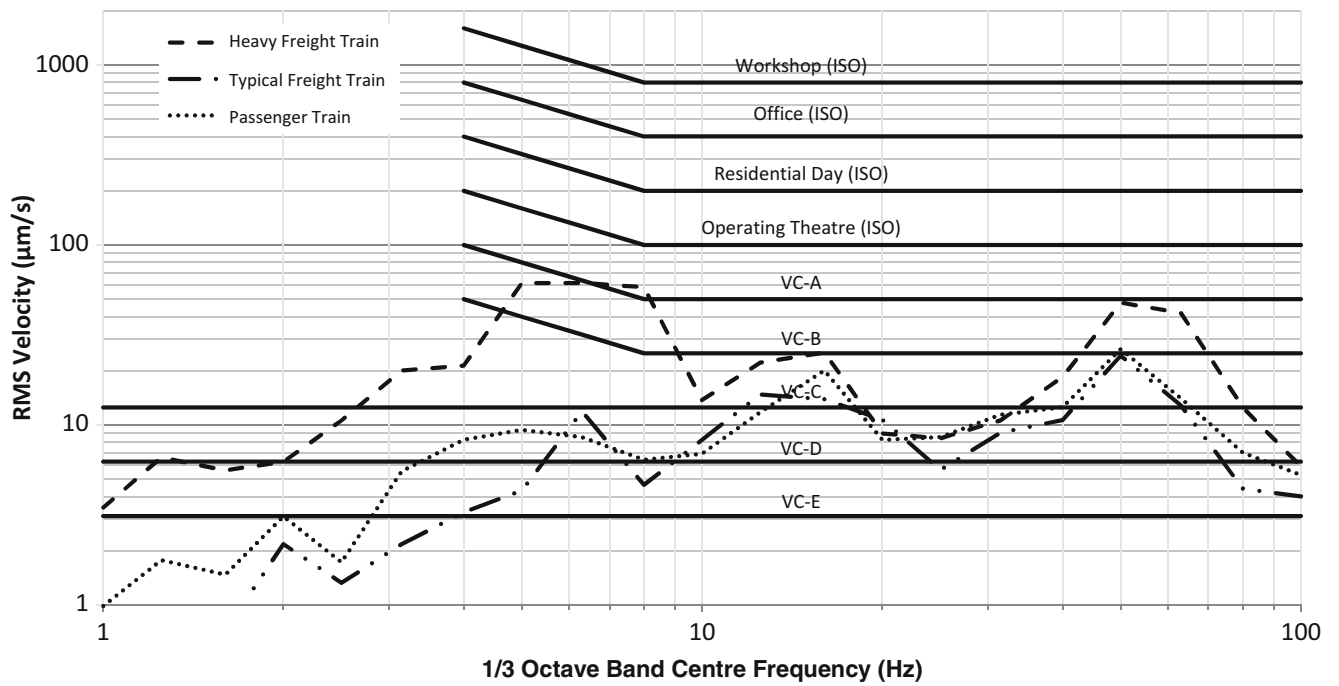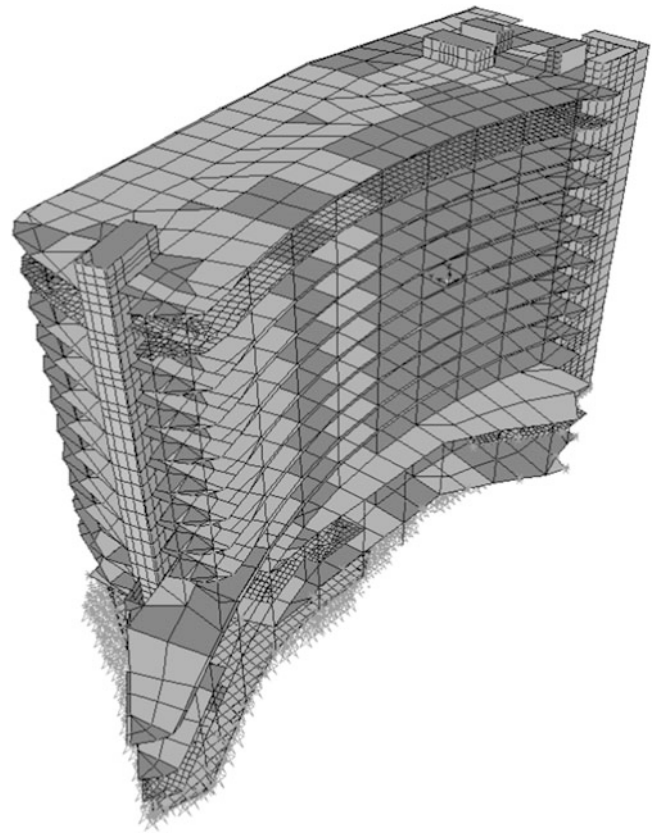model of the new building
structure

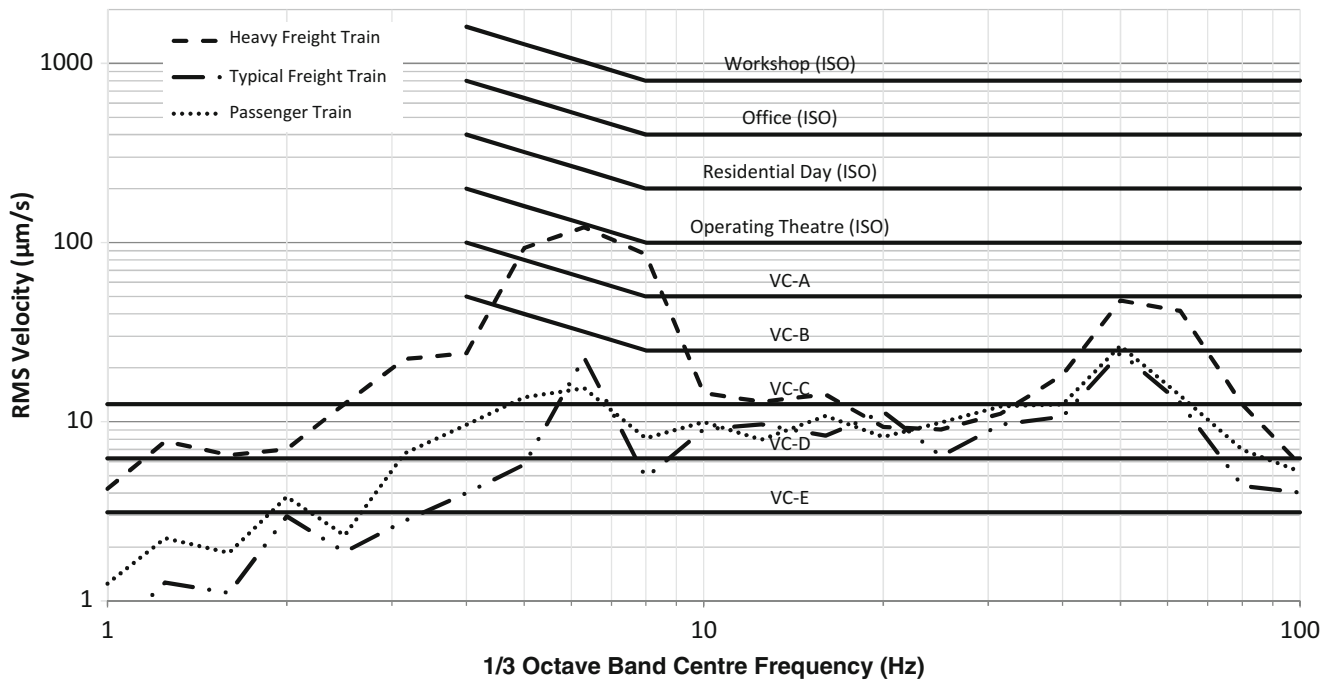**Fig. 51.6** L_{10} vertical velocities predicted on Level 2 due to three train pass-bys

Fig. 51.7 L_{10} vertical velocities predicted on Level 12 due to three train pass-bys
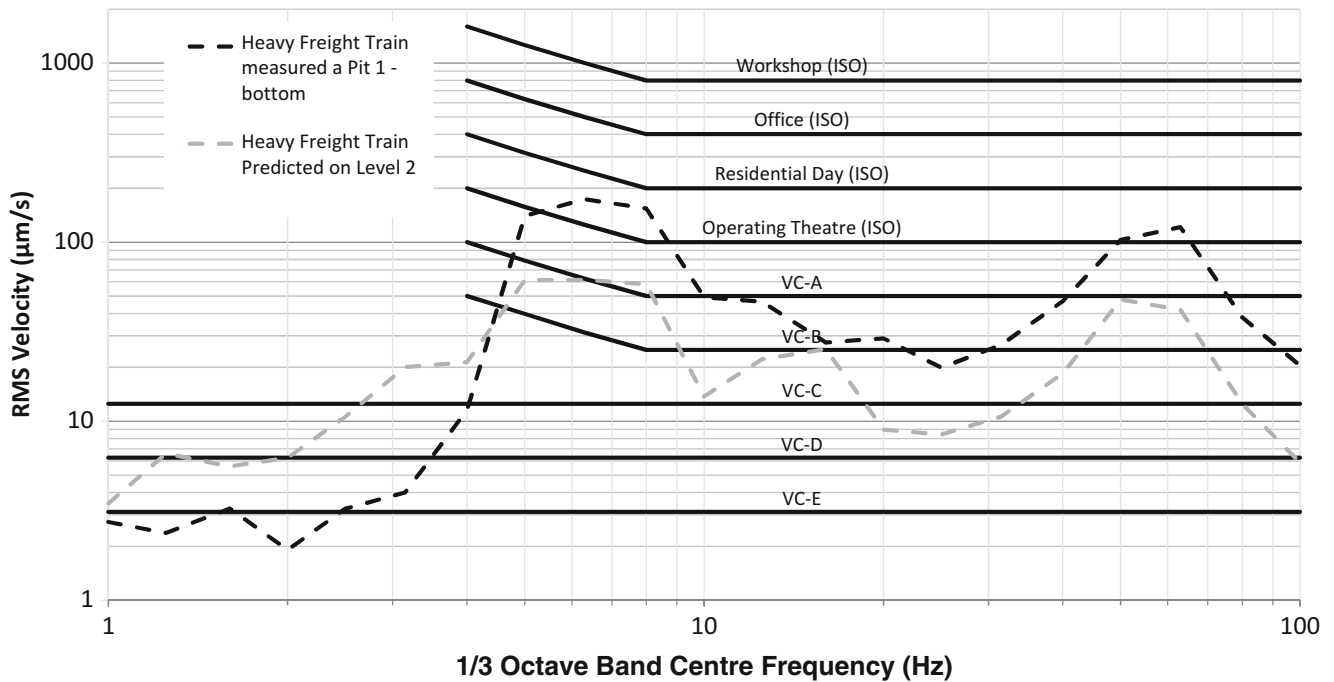

Fig. 51.8 L_{10} vertical velocities measured at the base of Pit 1 and predicted on Level 2 due to the heavy freight train pass-by

51.7 Vibration Mitigation Options

From an analytical perspective the most attractive mitigation option was rail isolation. Rail vibration can be isolated at its source by a number of methods including resilient fasteners, ballast mats, resiliently supported ties, and floating slabs. In the current case, the ballast mats and resiliently supported ties were the most feasible as the tracks were not supported on a concrete foundation. Although these resiliently supported ties work best above 15 Hz and ballast mats work best above
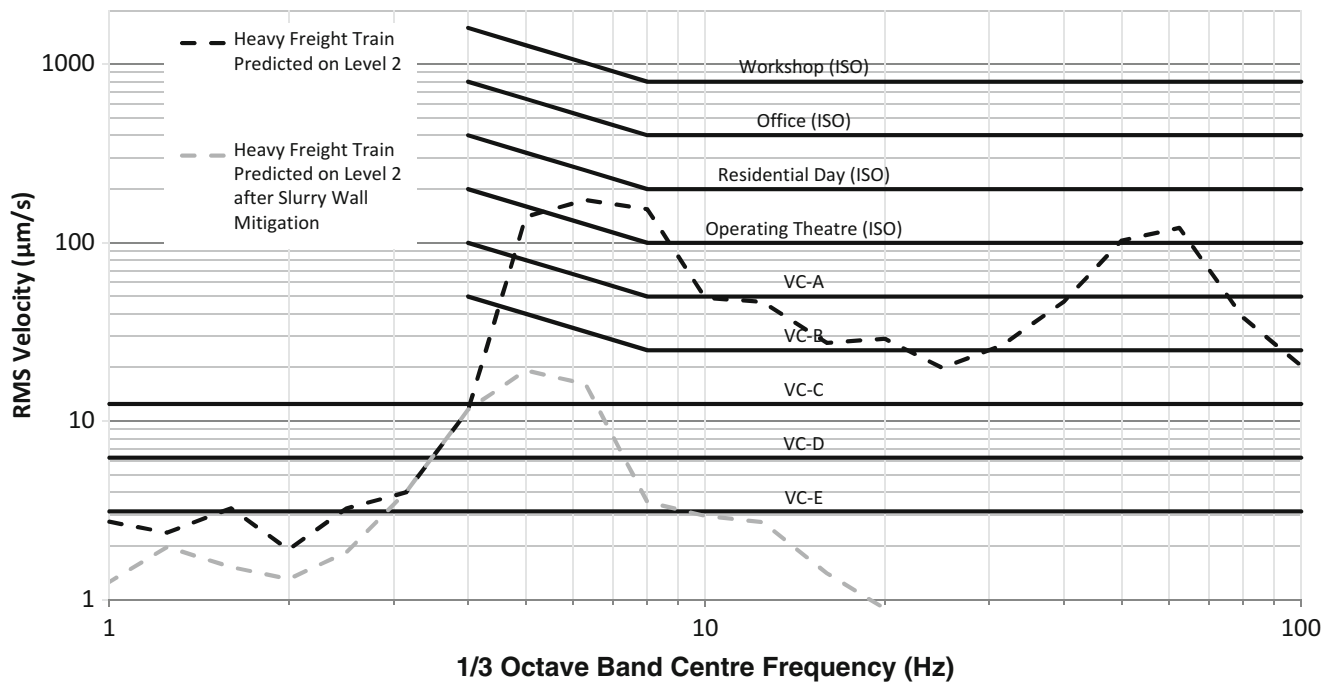
Fig. 51.9 L$_{10}$ vertical velocities predicted on Level 2 due to the heavy freight train pass-by before and after slurry wall mitigation

25 Hz [5], track improvements would be performed when the isolating system was installed which would likely mitigate the hanging ties, thus improving the low-frequency vibrations as well. Unfortunately the rail authority was unwilling to work with the hospital to develop a solution, thus rail isolation was not an option.

Base isolation of the structure and local isolation of floor slabs supporting micro-surgical suites were also considered. However, due to the high low-frequency content of the vibration, base isolation would not mitigate the critical frequencies.

The selected isolation option was a bentonite slurry wall. Slurry walls can reduce vibration magnitudes to less than 20 % of the levels on the incident side of the wall [6]; however the depth of the wall is critical. Usually the slurry wall is required to have a depth equal or greater than the Rayleigh wave length of the source [6, 7]. Slurry wall mitigation options were modeled in the finite element analysis (FEA) software Abaqus [8]. It was found that a 20 m deep, 0.61 m thick slurry wall located 20 m from the track would be required to attenuate the vibrations to an acceptable level. Figure 51.9 shows the vertical vibration predicted on Level 2 both before and after the slurry wall mitigation.

At the time of this writing the mitigation plan is under review. The hospital owner considers the large slurry wall infeasible due to space constraints between the new building and the rail tracks. The owner is in negotiations with the rail authority to permit rail isolation. Predictions of vibration expected on Level 2, if rail isolation is performed, will likely be the next phase in this project.

51.8 Conclusions

A new hospital building is to be located in close proximity to a busy rail line. The hospital is required to achieve stringent vibration criteria on most of the elevated floors. An initial vibration survey suggested that the vibration levels in the new building would likely exceed the criterion. A more extensive vibration measurement plan was executed in order to determine expected vibration levels at the foundation level of the new building and to estimate the vibration propagation characteristics of the soil.

The results of the vibration survey were used in conjunction with numerical models of the mat foundation and soil properties and of the building structure. Results from the models show that Level 2, which houses micro-surgical suites and has the most stringent vibration criterion, is expected to exceed the required criterion. High levels of vibration exist at low frequencies (between 5 and 9 Hz), making mitigation challenging. A bentonite slurry wall has been designed to mitigate the vibrations to required levels. However, the slurry wall is required to be impractically large. The building owner is currently in negotiations with the rail authority to permit rail isolation as an alternate mitigation strategy.

References

1. Amick H, Gendreau M, Busch T, Gordon C (2005) Evolving criteria for research facilities: I – Vibration. In: Proceeding of SPIE conference 5933: buildings for nanoscale research and beyond, San Diego, July 31 to August 1
2. ISO 2631–2 (1989) Evaluation of human exposure to whole-body vibration-part 2: human exposure to continuous and shock-induced vibrations in buildings (1 to 80 Hz), International Standard, ISO 2631–2
3. Dyna 5.4 [Software], El Naggar MH, El-Hifnawi L, El Marsafawi H, Sheta M, Geotechnical Research Centre/The University of Western Ontario, Copyright 2006
4. SAP2000 Plus (Version 15.2.1) [Software], Computers and Structures, Inc., Berkeley. Copyright 1976–2012
5. Transit Noise and Vibration Impact Assessment, Federal Transit Administration, May 2006
6. Ahmad S, Al-Hussaini TM (1991) Simplified design for vibration screening by open and in-filled trenches. J Geotech Eng 11(1), January 1991
7. Massarsch KR (2004) Mitigation of traffic-induced ground vibrations. Keynote Lecture. In: The 11th international conference on soil dynamics and earthquake engineering (ICSDEE) and the third international conference on earthquake geotechnical engineering (ICEGE). Berkeley Proceedings vol 1, pp 22–31, 7–9 Jan 2004
8. Abaqus (Version 6.9-1) [Software] Dassault Systems Corp, Providence

Chapter 52
Mitigation of Wind-Induced Vibration of the Pool-Deck Fence of a Condominium

S.A. Smith, W.D. Zhu, and C.M. Hou

Abstract On days with high wind speeds, it was observed that the pool-deck fence of an oceanfront condominium experiences large amplitude vibration, which can cause welds holding pickets to fail, resulting in impact noise. This work investigates the cause of the wind-induced vibration of the fence and presents a method to mitigate it. The fence was modelled using commercial finite element (FE) software, which was validated by modal testing. The FE model was used as the base for simulating various design modifications to the fence. After review of results from wind pressure measurements, modal testing, and FE model simulation, the primary mechanisms generating the vibration were identified to be vortex-induced vibration and buffeting. Due to design constraints, there are limited modification options. Increasing the geometric stiffness of the fence was selected as the mitigation technique and a modified design was proposed for the fence. The modified fence was installed and tested, and results indicated that vibration occurred less frequently. On-site monitoring of the fence by the owner indicated reduced vibration.

Keywords Fence vibration • Vortex-induced vibration • Buffeting • Modal testing • Finite element modeling • Vibration mitigation

52.1 Introduction

Wind storms cause flow-induced forces on structures and their vibrations. Flow-induced force and vibration can have many benefits, e.g., plant seed dispersion [1] and energy generation from energy harvesting skins [2]. However, wind-induced force and vibration also have adverse effects; wind has caused some of the most discussed structural failures in engineering, e.g., the failure of the Tacoma Narrows Bridge in Washington on November 7, 1940 under a wind speed of 68 km/h, and the collapse of the Ferrybridge Cooling Tower in the United Kingdoms in 1965 under wind speeds ranging from 122 to 167 km/h [3]. Wind can induce small vibration leading to gradual degradation and eventual failure, or large vibration leading to sudden degradation and failure.

On windy days, the fence surrounding the pool of an oceanfront condominium in Maryland was subjected to large amplitude vibration, which caused welds holding pickets to the fence to fail. The broken welds allowed the pickets to generate impact noise, which prompted owners of the building to contact the authors to mitigate the wind-induced vibration. The pool-deck fence is comprised of 13 sections of varying lengths and shapes; a section can be straight or have an L-shape. A typical section of the fence is shown in Fig. 52.1, which is part of section S2 shown in Fig. 52.2. The top-view schematic of the whole fence, with each section having a unique number, is shown in Fig. 52.2.

The fence is made of five main components: plazas, snap rails, punch rails, pickets, and posts; and peripheral components: L-beams. The side view schematic of a typical section with the location and size of each component, is shown in Fig. 52.3. An end view of a plaza, snap rail, and punch rail can be seen in Fig. 52.4. The components are made of Aluminum 6005-T5 or Aluminum 6063-T5/T52, with varying thicknesses between 0.238 and 0.635 cm. The pickets are welded to the punch rails on two sides of the picket in the out-of-plane direction, the out-of-plane direction is shown in Fig. 52.3. The top punch rails are attached to the post by U-brackets, while the middle and bottom punch rails are attached by L-brackets; the brackets are attached to the posts via bolts. The snap rails and plazas are held in place by clips along their bottom edge and those along the top edge of the punch rails, as seen in Fig. 52.4.

The vibration of the fence was noticed between mid-Autumn and mid-Spring, during which the average wind speed is higher than the rest of the year, according to the National Oceanic and Atmospheric Administration (NOAA; http://www.

_____

S.A. Smith • W.D. Zhu (✉) • C.M. Hou
Department of Mechanical Engineering, University of Maryland, Baltimore County, Baltimore, MD 21250, USA
e-mail: wzhu@umbc.edu

Fig. 52.1 A typical fence section, which is part of section S2 of the fence
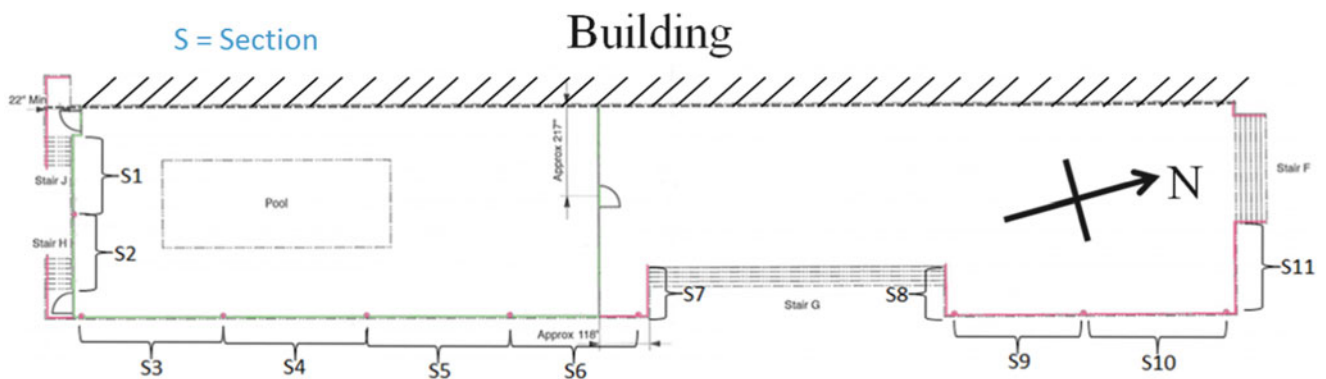

Fig. 52.2 Top-view schematic of the pool-deck fence with sections numbered

weatherspark.com/averages/31185/Ocean-City-Maryland-United-States). Upon inspection of the fence, some of the picket welds were broken, resulting in larger vibration and noise.

The objective of this work is to identify the source of the flow-induced force and vibration and methods to mitigate them. There are three flow-induced vibration mechanisms investigated: vortex-induced vibration, buffeting, and galloping. After identifying the source of vibration from experimental and finite element (FE) results, a design was proposed to the owner based on the design constraints. A new fence, based on the suggestions, was installed, tested, and monitored to verify that the vibration was successfully mitigated. The focus of this work is on fence section S2, shown in Figs. 52.1 and 52.2, all later references to the fence refer to this section. Section 52.2 was selected because it suffers the most from wind-induced vibration.

52.2 Investigation of Vibration Generation

A combination of FE modeling and experimental testing of the fence dynamic characteristics and wind property was used to investigate and identify the potential wind-induced vibration mechanisms. Three main wind-induced vibration mechanisms are studied; they are vortex-induced vibration, buffeting, and galloping.
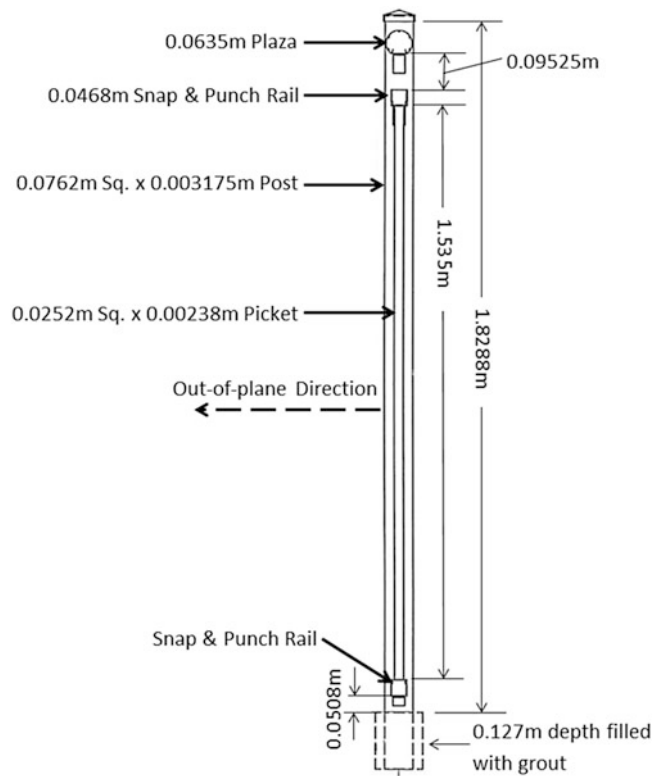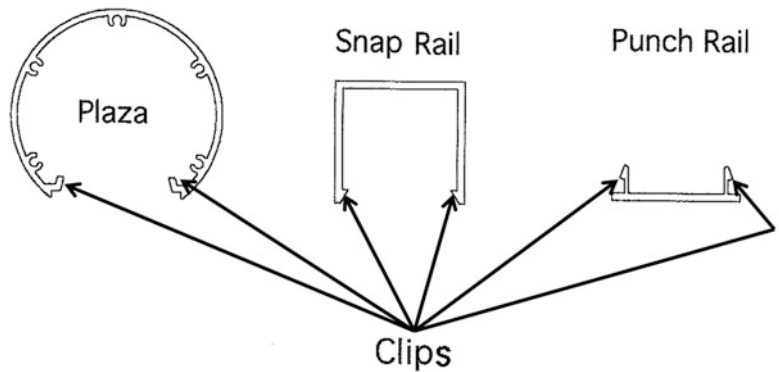
Fig. 52.3 Side-view schematic
of a typical section

Fig. 52.4 End view of a plaza,
snap rail, and punch rail with the
locations of the clips indicated

52.2.1 FE Model

52.2.1.1 FE Model of the Fence

A FE model was created to gain an understanding of the fence's natural frequencies, using a combination of linear tetrahedral solid elements (C3D4) and linear hexahedral solid elements (C3D8R). The model was created using ABAQUS 6.9EF according to the dimensions provided by the owner. The fence is made from aluminum alloys, which have the same relative material properties; modulus of elasticity within the range of $65 - 73$ GPa, Poisson's ratio of 0.33, and a density of $2700 \, \mathrm{kg/m^3}$. The boundaries for the bottom of the posts are set to be fixed, as the posts are cemented in the pool decking at the bottom. "Tie" constraints were used to simulate the welded joints and bolt joints. The model of the fence can be seen in Fig. 52.5a and an enlarged view to indicate the individual components, in Fig. 52.5b. The first seven natural frequencies of the fence from the FE simulation are listed in Table 52.1.

Fig. 52.5 (**a**) FE model of the fence and (**b**) an enlarged view with component indicators
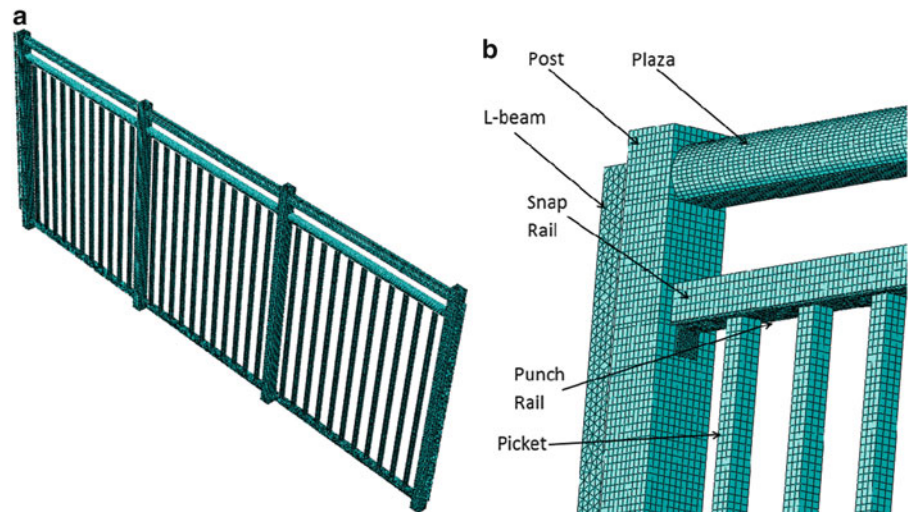

Table 52.1 Natural frequencies of the pool fence from FE modeling and experimental testing

Mode	FE (Hz)	Experiment (Hz)	Difference (%)
1	9.4955	8.788	8.05
2	11.171	10.236	9.13
3	14.240	13.506	5.43
4	17.661	16.445	7.39
5	25.577	26.147	−2.18
6	27.803	27.826	−0.08
7	29.560	29.397	0.55

52.2.1.2 Modal Testing on the Fence

Modal testing was performed on the fence to verify the FE model. The roving sensor method with multiple input locations was used. A PCB 086D05 impact hammer was used to excite the structure in the out-of-plane direction, shown in Fig. 52.3. The response of the structure was measured by 12 PCB TLD356A17 tri-axial accelerometers and gathered by an LMS 36-channel spectrum analyzer. The response of the fence was measured at the locations indicated on the geometry built in LMS TEST.LAB and the locations of excitation are indicated on the FE model shown in Fig. 52.6. The mass-loading effect from the accelerometers can be neglected, since their combined mass is much smaller than that of the fence. Three multiple random impact tests were performed and averaged at each excitation point to ensure repeatable, coherent results. Multiple random impact testing was used to improve the signal-to-noise ratio as well as average out any slight non-linearities [4]. LMS TEST.LAB 9B was used to extract the natural frequencies and mode shapes from the measured frequency response functions (FRF). The first seven natural frequencies are listed in Table 52.1. The maximum difference between the FE model and experimental natural frequencies is 9.13 %. During testing it was evident that there was damage caused by wind on the fence, which caused the stiffness of the structure to be reduced, resulting in the frequency difference. The difference in frequencies produces confidence in using the FE model as the groundwork for future modifications. The first four mode shapes from the experimental results and FE simulation are shown in Fig. 52.7. In the mode shapes from TEST.LAB one can see the left corner of the fence was not measured due to a physical constraint and were removed from the shape; however, the overall shape of the mode matched that of the FE model.

52.2.2 Vortex-Induced Vibration

52.2.2.1 Vortex-Induced Vibration Phenomenon

Vortex-induced vibration can be observed when fluid flow passes over a structure that is much longer in one direction than in the others, known as bluff bodies, e.g., chimneys, wind turbine towers, power-transmission lines, and cables of a cable-stayed bridge. Vortices are created by the boundary layers of the bluff body separating from the body creating a wake. The flow in the
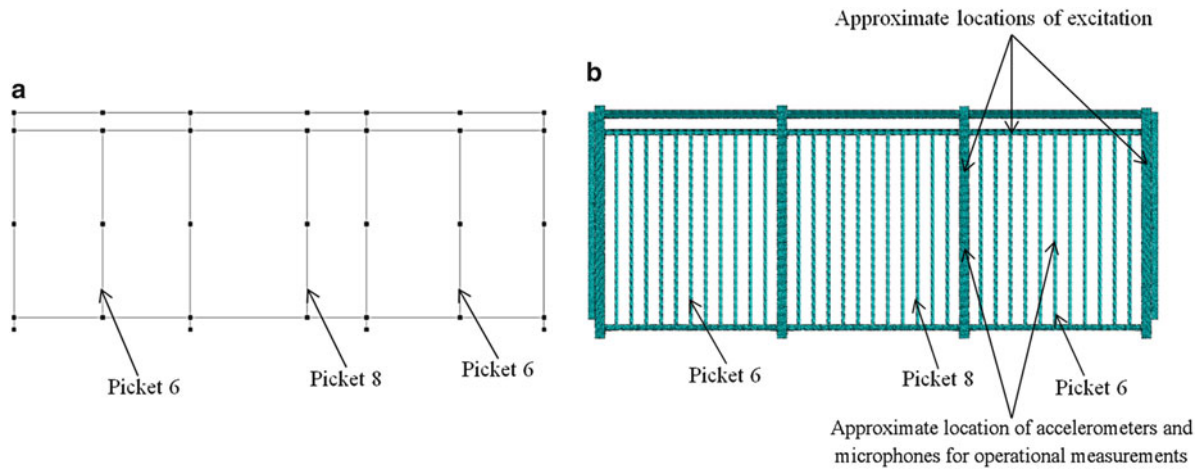
Fig. 52.6 Location of measurement points in (**a**) LMS TEST.LAB and (**b**) locations of excitation on FE model, as well as locations of accelerometers and microphones for operation measurements

layer after the separation point is moving much faster than the fluid in the wake region. This gradient causes the layers to roll into the wake creating the vortices, which interact with the body causing the surface pressure to fluctuate [5, 6]. The pressure fluctuations occur at frequencies governed by the type of fluid flow. The type of flow around the body is determined by the dimensional-less parameter, called the Reynolds number, Eq. (52.1):

$$R_E = \frac{UD}{\nu} \tag{52.1}$$

where U is the mean free stream velocity, D is the width of the frontal area of the body, and ν is the kinematic viscosity of the fluid. At Reynolds numbers (R_E) below 300 vortices are shed though the force caused by the pressure fluctuation is low. The range of R_E that correspond to the pressure fluctuation which cause most of the structural excitations is between 300 and 1.5×10^5, in this region the vortices are shed periodically [7]. The frequency at which vortices are shed is calculated using the Strouhal relation, Eq. (52.2):

$$f_o = \frac{S_T U}{D} \tag{52.2}$$

where f_o is the vortex shedding frequency, and S_T is the Strouhal number. Since R_E determines the type of flow around a body effecting vortex shedding, this causes S_T to be a function of R_E in subsonic flows. Strouhal number is relatively constant in the R_E range of 10^3 to 10^5 for any bluff body geometry [5, 8, 9]. For a square with sharp corners cross-section S_T is approximately 0.13–0.133 [5, 7–10]. Due to the relatively constant nature of S_T with R_E, the frequency at which the vortices are shed will change with the flow's mean velocity.

Vortex shedding of a bluff body can be observed by measuring the Power Spectral Density (PSD) of the pressure fluctuations behind the bluff body. The PSD of the pressure fluctuation behind a properly welded picket in an average wind speed of 5.56 m/s, using a PCB 378B02 condenser microphone can be seen in Fig. 52.8. The microphone was placed at the mid-height of the picket and 0.03 m away horizontally. With $U = 5.56$ m/s, $D = 0.0254$ m, and $S_T = 0.13$, the shedding frequency is calculated to be 28.5 Hz using Eq. (52.2), the calculated frequency is in agreement with the measurement in Fig. 52.8. The measured wind speed used in the calculation is a mean value; the actual speed fluctuates around this mean value due to turbulence and wind gusts. The fluctuations result in a band of dominant frequencies of vortex shedding from the picket. The structure will not have a large response if the vortex shedding frequency is well outside the natural frequency of the structure.

Fig. 52.7 Mode Shapes from
(*left*) experimental results and
(*right*) FE simulation

Mode 1

Mode 2

Mode 3

Mode 4
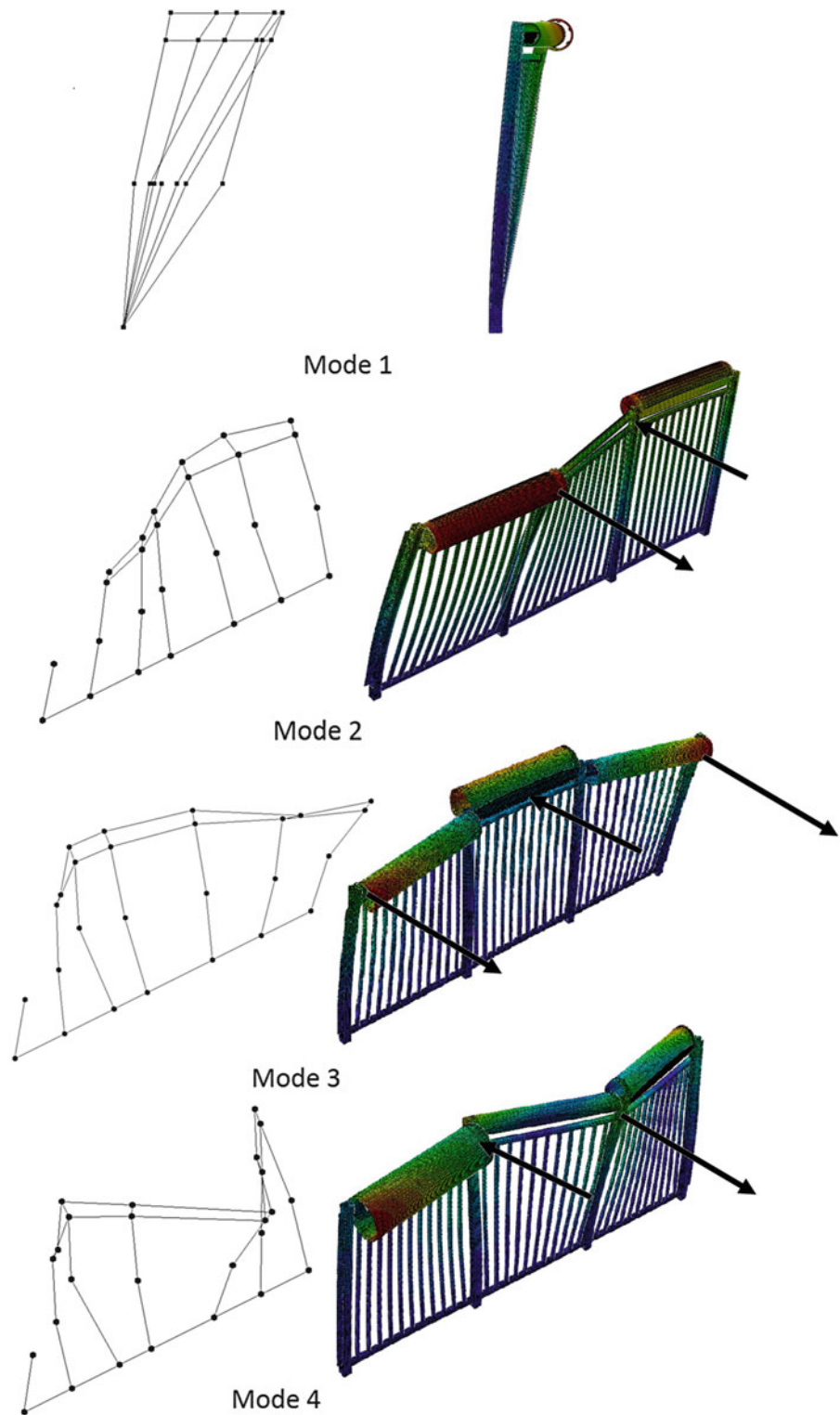
There is a band of frequencies synchronizing the structure's natural and shedding frequencies. If the structural damping is relatively low for the resonant mode, the vibration leads to limited amplitude instability. This event is known as *lock-in, wake capture,* or *synchronization [5, 7, 9, 11]. Lock-in* leads to a larger range of velocities that can lead to fatigue failure. The critical velocity U_v at which *lock-in* can occur is obtained from Eq. (52.2) as:

$$U_v = \frac{f_n D}{S_T} \tag{52.3}$$

where f_n is the natural frequencies of the structure. The range of velocities that *lock-in* occurs is called the *lock-in* band, the band is within 20 % of U_v [12].

During the *lock-in* phenomenon the vibration of the structure asserts a force on the fluid; this assertion leads to the production of aero-acoustic tones at the shedding frequency. In winds with the velocity of 15 m/s the turbulent effect is greater, causing the vortex shedding to be weakened from the reduction of the load's span-wise correlation. The high wind speeds, over 15 m/s, will net a smaller excitation force even during *lock-in* [6].

52.2.2.2 The Role of Vortex-Induced Vibration

Due to the small frontal width of the pickets, they are the most susceptible component to vortex-induced vibration. The fence as a whole was investigated to ensure the modes are picket modes. A picket mode is defined as a mode where the amplitude of vibration is much larger than that of the other components. The first three picket mode natural frequencies and damping ratios are listed in Table 52.2, which correspond to modes 5 through 7 in Table 52.1. The average damping ratio of the three modes is 0.0063.

From Table 52.2 it can be seen that large vibration of the picket will occur if the vortex shedding frequencies are between 26.147 and 29.397 Hz; Fig. 52.9 shows the first picket mode. The critical *lock-in* velocity from Eq. (52.3), with $D = 0.0254$ m, $S_T = 0.13$, and $f_n = 26.147$ to 29.397 Hz, ranges from 5.11 to 5.74 m/s. Wind data from NOAA indicates that wind speeds in this range are possible during the spring, fall and winter seasons. When the wind speed is in the *lock-in* range of the critical velocity, large vibration can occur, which leads to aero-acoustic humming and welded joint fatigue failure. When the welds fail impact noise and larger vibration can occur. Therefore, vortex-induced vibration is a major component of the structural vibration.
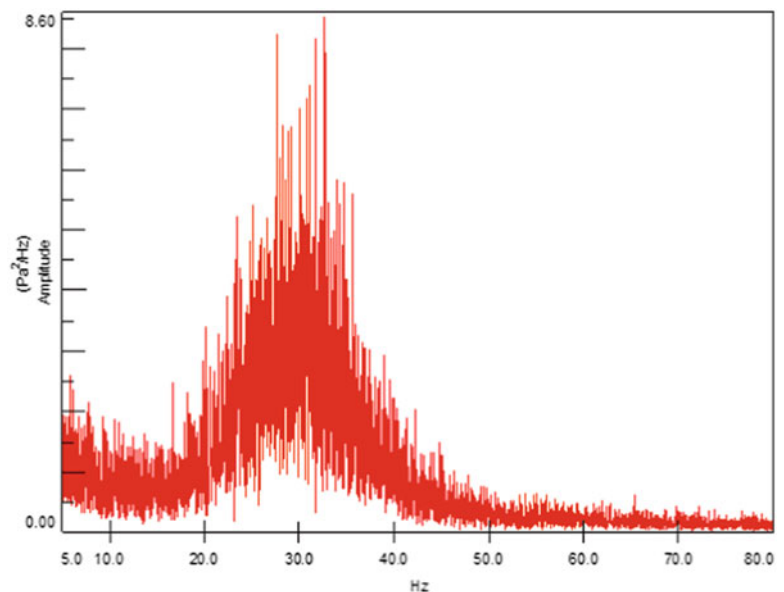

Fig. 52.8 The PSD of pressure fluctuation behind a properly welded picket with the average wind speed of 5.56 m/s

Table 52.2 First three picket mode natural frequencies along with damping ratios from analysis

Picket mode number	Natural frequency (Hz)	Damping ratio (%)
1	26.147	0.43
2	27.826	0.67
3	29.397	0.77

Fig. 52.9 Mode shape of the first picket mode from (*left*) experimental results and (*right*) FE simulation
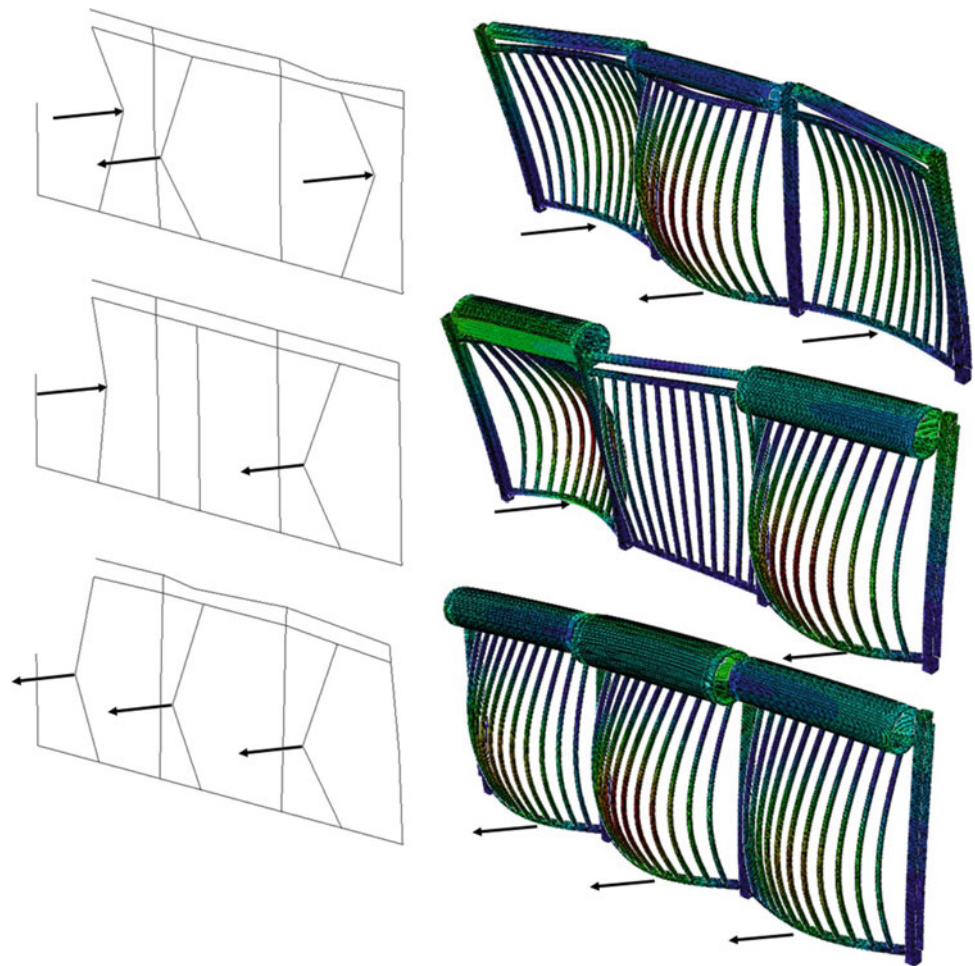
52.2.3 Buffeting Vibration

52.2.3.1 Buffeting Phenomenon

Buffeting of a structure occurs when turbulent eddies flow past or impinge upon the structure. Eddies are created from the viscous effects of surrounding structures and the surface roughness of the surrounding ground. The structure under wind loading has a mean deflection, caused by the mean wind velocity, and a fluctuating deflection caused by the turbulent eddies [11]. The deflection typically increases with wind velocity. When the pressure fluctuation caused by the eddies are in the narrow band of frequencies around the structure's natural frequency, large amplitude vibration can occur [6].

52.2.3.2 Wind Pressure Measurement

To gain a qualitative understanding of the wind pressure fluctuations, a PCB 378B02 free-field condenser microphone was used to measure the PSD of the wind pressure around the railing. The microphone has a measurement range of 5 to 20,000 Hz with ±1 dB accuracy; the use of this microphone is considered appropriate for the current application because the first natural frequency of the fence is above 8.5 Hz. The microphone was placed on top of a tripod and directed towards the approaching wind to measure the pressure fluctuations. To reduce interference from the railing, the microphone was placed 2.3 m from the railing. A Honeywell TE821W weather station was implemented to measure the average wind speed and direction. The measurements were taken at the North-East and South-East sides of the pool, and the results were similar. The PSD measured in the North-East location is shown in Fig. 52.10 in logarithmic scale (a) and linear scale (b). The figure is a zoomed in section of a 130 Hz band, of wind with the average speed of 4.44 m/s. The PSD figures show an approximately monotonically decreasing trend with increasing frequency; which is what is expected from the literature [11].
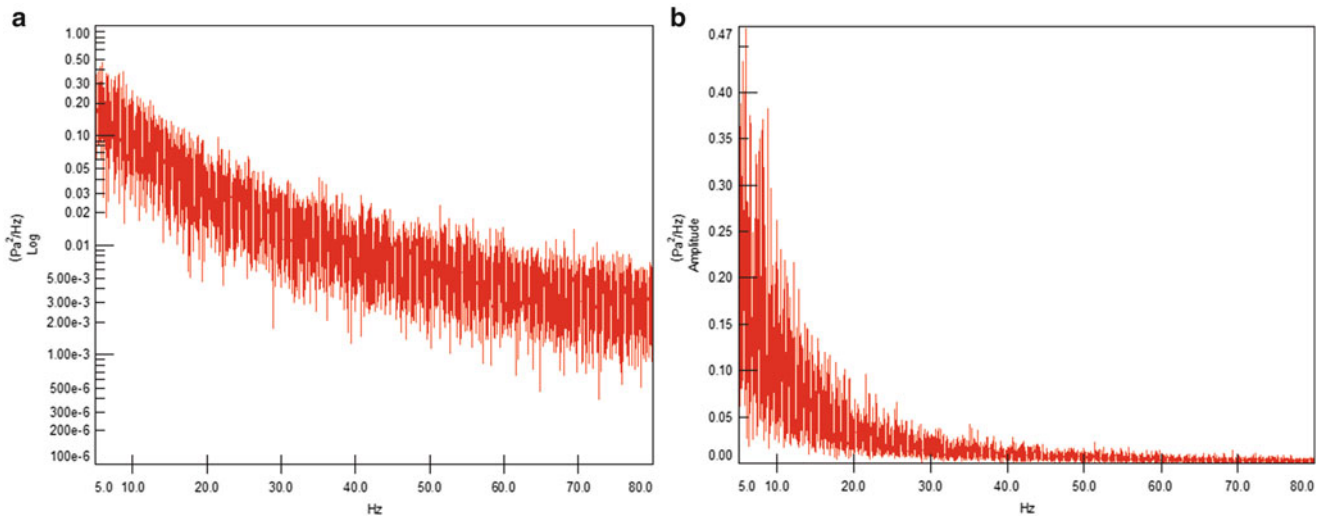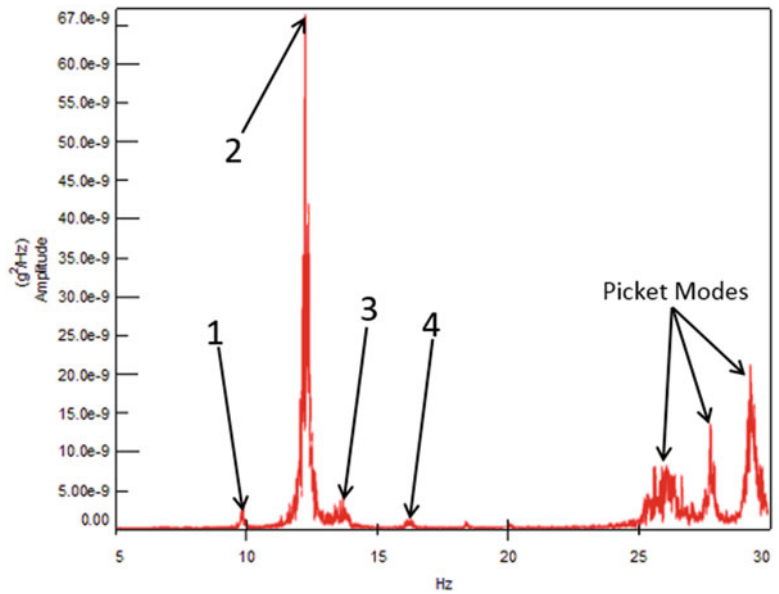
Fig. 52.10 PSD measurement of a 4.44 m/s wind to study the turbulent component, (**a**) in logarithmic scale and (**b**) linear scale

Fig. 52.11 PSD of fence response in operating conditions with fence modes indicated

52.2.3.3 Role of Buffeting

The response of the fence was measured in operating conditions to gain an understanding of the buffeting phenomenon. The response of the fence in Sect. 52.2.1.2 was measured using two PCB U352C66 uni-axial accelerometers. The accelerometers were attached along one of the posts and picket, shown in Fig. 52.6, in the in-plane and out-of-plane directions. The PSD of the out-of-plane response of the fence in a wind of 5.91 m/s is shown in Fig. 52.11. The PSD shows one dominant peak around the second natural frequency, as well as peaks around the natural frequencies of the pickets. Based on the measurements of the wind and the structure, the structure can be excited from the turbulent effects of the wind. Prolonged exposure to buffeting can lead to fatigue failure of the welded joints, further increasing the vibration of the fence.

52.2.4 Galloping Vibration

52.2.4.1 Galloping Phenomenon

During the galloping phenomenon the aerodynamic excitation force is dependent on the motion of the structure [9]. During the oscillation of the structure, the orientation of the structure changes, this oscillation causes the orientation of the flow's force to oscillate. If the oscillation of the force increases the vibration of the structure, the structure is aerodynamically unstable [5]. The instability caused by galloping occurs in any non-circular bluff body in which an unfavorable flow direction can develop negative aerodynamic damping. The galloping phenomenon is exemplified by the large-amplitude vibration of ice coated power transmission lines. Ice on the line changes the cross-section to a D-profile; the profile then acts similarly to that of an airfoil [9].

The condition for the galloping phenomenon to occur is called the Glauert-Den Hartog criterion [7, 13]:

$$\frac{\partial C_{F_y}}{\partial \alpha} = -\left(\frac{\partial C_L}{\partial \alpha} + C_D\right) > 0 \tag{52.4}$$

where C_L and C_D are the lift and drag coefficients, respectively, C_{F_y} is the transverse force coefficient, and α is the perceived angle of attack of the wind. Galloping can occur when C_{F_y} increases with the change of α. The transverse force coefficient for typical cross-sections can be found in [5]; for a square cross-section in turbulent flows the coefficient is 3.5. The onset of the galloping phenomenon occurs at a critical velocity U_{crit}, which is dependent on the structural damping [9]:

$$U_{crit} = \frac{8\pi m \zeta_y f_n}{\rho D} / \frac{\partial C_{F_y}}{\partial \alpha} \tag{52.5}$$

where m is the mass per unit length of the structure, ζ_y is the damping coefficient, f_n is the natural frequency of the structure in hertz, ρ is the density of the fluid, and D is the width of the frontal area of the body. Galloping can occur in wind velocities greater than U_{crit}, while vortex-induced vibration can only occur in a *lock-in* band of velocities. When the wind velocity is equal to or exceeds the critical velocity, and the damping of the structure is low energy can be inputted into the structure. When a structure is affected by the galloping phenomenon, the amplitude of vibration can be one to ten times that of the frontal area width. The amplitude of vibration in galloping increases with velocity [11].

52.2.4.2 The Role of Galloping

The critical velocity for galloping to occur is usually much higher than the *lock-in* velocity for vortex-induced vibration. However, if the structure has a low structural damping or mass density, U_{crit} could be close to or lower than U_{lock}. The pickets are investigated because the pickets have lower localized natural frequencies, from FE model investigation, than the plazas, and square cross-section have a higher $\partial C_{F_y}/\partial \alpha$ than a D-shape. Using $m = 0.707\,\text{kg/m}$, the average damping from Sect. 52.2.2.2 $\zeta = 0.00623$, $\rho = 1.293\,\text{kg/m}^3$, $D = 0.0254\,\text{m}$, the average picket natural frequencies $f_n = 27.79\,\text{Hz}$, and $\partial C_{F_y}/\partial \alpha = 3.5$, the velocity at which galloping can occur, using Eq. (52.5), is 26.76 m/s which is approximately five times that of U_{lock} for vortex-induced vibration. The critical velocity calculated is unlikely to occur at the condominiums location according to NOAA (http://www.weatherspark.com/averages/31185/Ocean-City-Maryland-United-States); indicating that galloping is not a main component of wind-induced vibration.

52.3 Wind-Induced Vibration Mitigation

52.3.1 Mitigation Techniques

Vibration mitigation needs to be performed on the fence to reduce the effect of vortex-induced vibration and buffeting, since the galloping phenomenon has a low probability of occurrence. There are mitigation techniques that are shared between vortex-induced vibration and buffeting; the shared techniques include [6, 14, 15]: attenuating or eliminating the source of excitation; increasing the structural stiffness; increasing (possibly decreasing) the structure's natural frequency; adding tuned mass dampers; or deploying filters to avoid excessive excitation from wind. Vortex-induced vibration has more techniques for

Table 52.3 The frequencies and frequency change to the original fence for the first mode and first picket mode for two simulations from each group

Group number	Modification number	First mode (Hz)	Percent change (%)	First picket mode (Hz)	Percent change (%)
1	1	10.125	15.21	22.454	−14.12
	2	13.715	56.07	35.079	34.16
2	1	7.547	−14.11	34.876	33.38
	2	15.504	76.42	33.588	28.46
3	1	16.253	84.95	34.893	33.45
	2	18.428	109.70	61.475	135.11

mitigation, they include: modifying the structure so that the shedding frequency lies well below the natural frequency of the structure, streamlining the cross-section to minimize flow separation from the structure, attenuate/ control vortex shedding by using a concave trailing edge to trap the vortices or by beveling the trailing edge to de-phase the transverse separation [6], or adding vortex suppression devices. There are two groups of vortex suppression devices; devices that do not increase the cross-section of the body more than 1.3 times the original size, e.g., helical strakes, perforated shrouds, and axial slates; and devices that rotate or increase the cross-section more than 1.3 times, e.g., pivoted guide vanes, streamlined fairings, splitters, ribbons, and spoiler plates [5].

The technique(s) to be selected have to consider design constraints set by the location, fence contractor, and building owner. The owner would prefer that the overall geometry of the fence to be changed as little as possible. The limiting of the geometry shape eliminates changing components to a more aerodynamic shape. The fence has a coating that can only be finished at the factory, any mitigation applications cannot destroy the coating on-site. Adding suppression devices cannot be implemented because the coating could be destroyed and the devices can be unsightly. A design constraint of having a pleasant looking fence eliminated the possibility of adding external vibration dampers. Due to the corrosive nature of salt water the material of the fence cannot be changed to steel. Any modification must have a reasonable cost which changing from aluminum to stainless steel does not meet, also tuned mass dampers are impractical due to their higher cost. The last constraint deals with security of the area; the top of the fence must be 1.83 m above the pool deck, and any additional horizontal members must be 1.14 m above the pool deck.

With the constraint imposed by the owner and contractor considered, the best option for mitigating wind-induced vibration is to increase the stiffness of the structure. Increasing the stiffness is the most effective way of reducing vibration excitation from turbulent/ vortex shedding effects; with the structure stiff enough the structural natural frequencies can fall outside the range at which wind excitation force is significant. The modifications of the fence need to reduce the vibration from vortex shedding and buffeting at a reasonable cost.

The first natural frequency of the structure is aimed at being increased as much as possible given the height of the structure. From the wind measurement in Fig. 52.10, it is noticed that the wind has an exponential decay of:

$$PSD(\mathrm{Pa}^2/\mathrm{Hz}) = 0.4239 * e^{-0.1042 * f} \tag{52.6}$$

which results in a 40.6 % decrease of power by shifting the first mode's natural frequency of 8.788 Hz by 5 to 13.788 Hz. At higher frequencies the response of the structure from wind excitation is lower due to the decrease of energy input from the pressure fluctuations.

Twenty-five different modifications were modeled to increase the structure's stiffness. The modifications are easier to describe in three different groups. In each group, the horizontal members are bolted to "U" or "L" brackets, which are welded to the posts. In Group 1 the pickets are modeled as having the two out-of-plane sides welded at the top and all sides at the bottom; the group tested changing the posts and pickets from box tubes to solid squares of the same dimension, adding a horizontal member with the same dimension as the pickets 1.14 m above the ground, and then changing the horizontal member to a solid square. In Group 2 the pickets are modeled as having all four sides at the top and bottom welded; the group tested changing the post's size and whether a box tube or solid post increased the stiffness of the structure. In Group 3 the pickets are modeled the same as in Group 2; the group tested different configurations of the plaza and horizontal members. The frequency and change in frequency from the original fence's first mode and first picket mode, for two simulations from each group can be found in Table 52.3.

Fig. 52.12 A typical modified fence section

Group 1's initial modification has the post's thickness changed from 0.003175 m to 0.00635 m, the pickets are changed to solid, and a 0.0254 m × 0.0254 m × 0.00238 m horizontal member is added. The modification increases the first mode's frequency and decreases the picket mode's. The picket mode being decreased is from the mass increase, from it becoming solid, is much more than the stiffness it adds. The second modification is similar to the first except the post is modified to be solid. All of the frequencies are increased from the change of posts, however the increase of the first mode still falls inside a relatively high power range for the wind and the increase for the picket mode only increases the wind velocity to 6.85 ms which has the same likelihood to occur as the original velocity of 5.11 m/s.

Group 2's first modification changes the post from a 0.0762 m × 0.0762 m × 0.003175 m to 0.0508 m × 0.0508 m × 0.00635 m box beam, the snap rails are changed to 0.00075 m × 0.01905 m × 0.003175 m, and the pickets are changed to 0.0254 m ⊘ ×0.003175 cylindrical tube. The change of the post reduced the structural stiffness resulting in a decrease of the first mode's frequency. The second modification the post is modified to a 0.0508 m × 0.1016 m × 0.00635 m box beam, with the same channel from the initial modification, the pickets are modeled as the original pickets. The first mode is increased enough that the power input is decreased by 50.3 %; however the first picket mode is still within a range that wind speed has a high probability to occur.

In Group 3 the channel from the second group is kept. In the first modification the heights of the posts were reduced from 1.88 to 1.83 m, the posts are also solid 0.0508 m × 0.1016 m members; the top of the plaza is leveled with the top of the post, a 0.0254 m × 0.1016 m × 0.002667 m member is added 1.143 m above the ground, and the pickets are solid 0.0254 m × 0.0254 m members. The frequencies of both modes increase, though the picket frequency is not increased enough for the *lock-in* velocity to be raised much higher than the original. The final fence modification has the pickets changed from a solid member to a box tube of the same dimensions with a thickness of 0.00238 m, and a 0.003175 m × 0.1016 m flat piece is added to the bottom of the channel. This modification gave the best results of all that were simulated; the first mode's frequency is increased causing the power to be 63.4 % less than the original, and the increase of the first picket mode causes the *lock-in* velocity to be 12.01 m/s, which according to NOAA has a low probability of occurring. The last modification was proposed to the owner and contractor as a way to reduce the vibration of the fence. A new fence was installed according to the modifications proposed, as shown in Fig. 52.12.

52.3.2 Experimental Testing on Modified Fence

To verify the modifications from FE simulation, modal testing was conducted on the modified fence using a PCB 086D05 impact hammer and PCB TLD356A17 tri-axial accelerometers; multiple impact roving hammer testing technique with nine reference points was used. When the authors arrived to test the modified structure, they noticed the fence was modified even more; the plaza, channels, and the added horizontal member were all changed to 0.0508 m × 0.1016 m × 0.002667 m

Table 52.4 Natural frequencies of the modified pool fence from FE and experimental results

Mode	Experiment (Hz)	FE (Hz)	Error (%)
1	15.804	16.025	1.40
2	18.472	18.926	2.46
3	22.806	24.325	6.66
4	28.906	31.679	9.59
5	57.574	56.894	−1.18
6	58.046	57.508	−0.93
7	60.208	57.738	−4.10
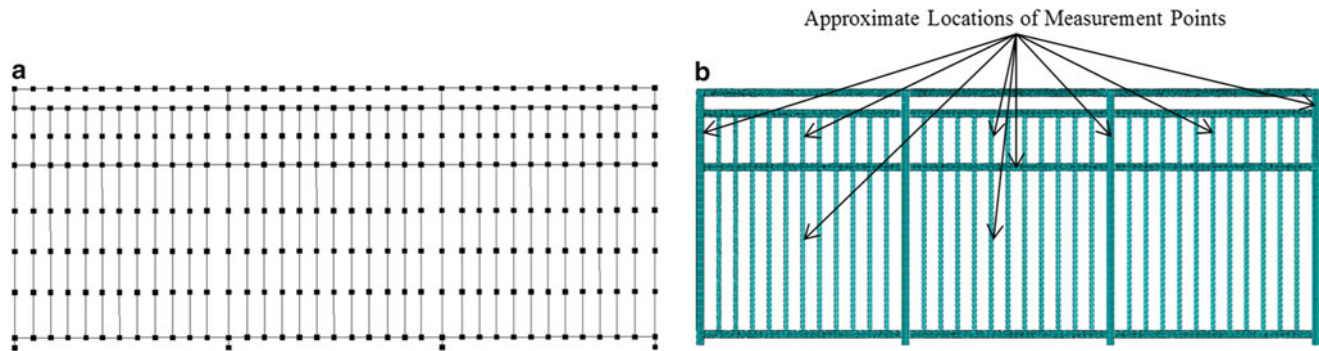
Fig. 52.13 Location of excitation points in (**a**) LMS TEST.LAB, and approximate locations of measurements (**b**) on FE model

box tubes attached to the posts via "U" brackets and the horizontal member that was added 1.143 m above the ground was actually 1.143 m above the lowest horizontal member of the fence. The change in this location of the horizontal member was discovered after further study of building codes. The frequencies of the re-modified fence can be found in Table 52.4. The structure was hit and measured at preselected locations shown in Fig. 52.13; the excitation points are shown on the left and the measurement locations are shown on the right. The first seven natural frequencies from the experiment are listed in Table 52.4. The additional modifications result in a slight decrease in the natural frequencies originally predicted; however, the frequencies are still in a region that the power from the wind is lower or the load's span-wise correlation is reduced. The experimental natural frequencies are all within 10 % of the FE simulation results. The mode shapes for the first 4 mode shapes is shown in Fig. 52.14, and the mode shapes for the first three picket modes, modes 5 through 7 in Table 52.4, can be seen in Fig. 52.15, corresponds to a *lock-in* velocity of 11.25 m/s, which according to NOAA is not likely to occur.

After the installation and testing of the fence, the fence was monitored by the building's engineer, who reported that no significant vibration has been observed for the first 6 months of the installation. On-site monitoring and experimental testing confirm that the modifications have resolved the vibration issue.

52.4 Conclusion

After investigating the cause of high amplitude vibration, vortex-induced vibration and buffeting were identified as the main phenomenon. Based on design constraints imposed, stiffening of the structure was selected as the best option to mitigate the vibration. Several different modifications of the original fence were investigated through FE simulations. The predicted response of the modified railing from FE simulation was determined to be accurate through experimental testing. On-site monitoring has confirmed that the vibration response of the fence has been mitigated.

Fig. 52.14 The (*left*) experimental and (*right*) FE mode shapes of the first four modes of the modified fence
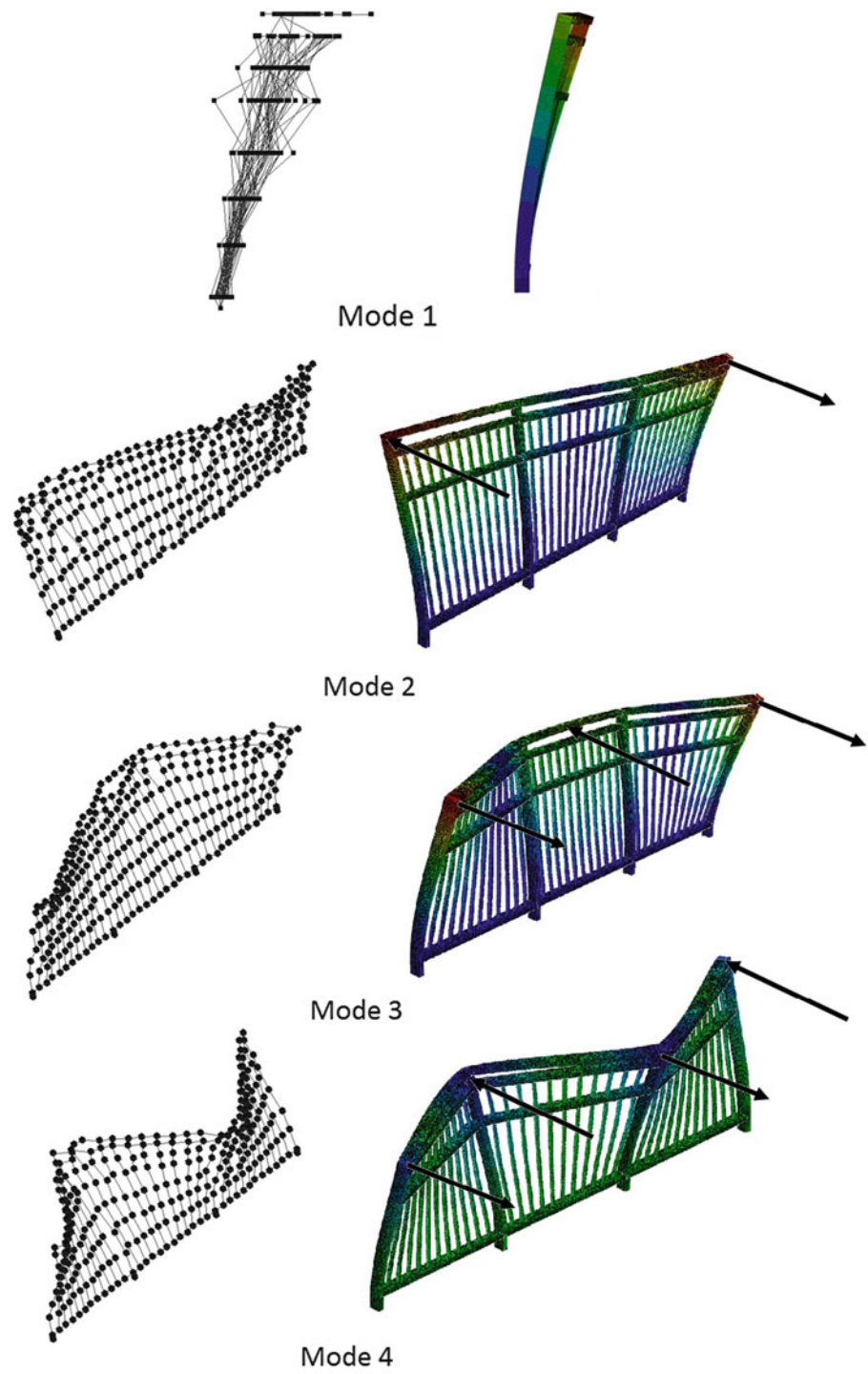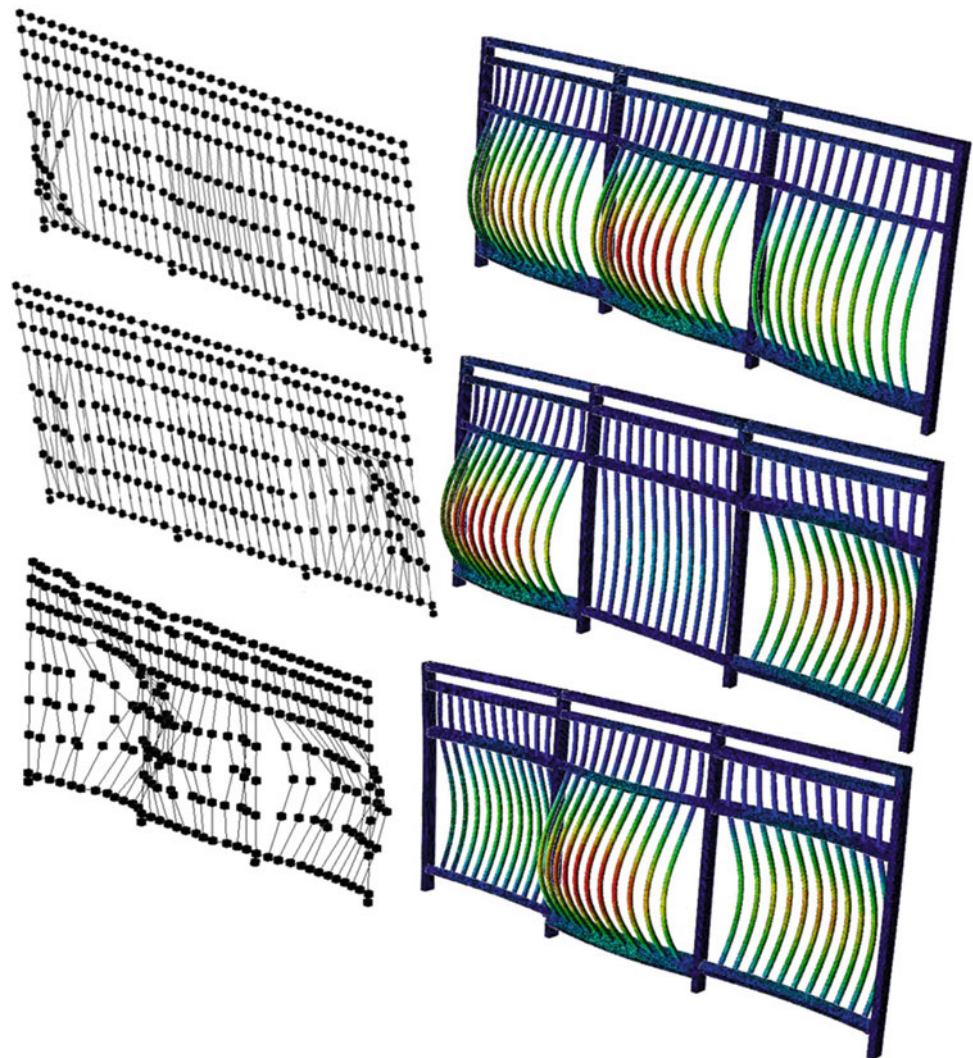

Mode 1

Mode 2

Mode 3

Mode 4

Fig. 52.15 The (*left*) experimental and (*right*) FE picket mode shapes

References

1. de Langre E (2008) Effects of wind on plants. Annu Rev Fluid Mech 40:141–168
2. Sodano HA, Inman DJ, Park G (2005) Comparison of piezoelectric energy harvesting devices for recharging batteries. J Intell Mater Syst Struct 16(10):799–807
3. Holmes JD (2007) Wind loading of structures, 2nd edn. Taylor, New York
4. Zhu WD, Zheng NA, Wong CN (2007) A stochastic model for the random impact series method in modal testing. ASME J Vib Acoust 129:265–275
5. Blevins R (1990) Flow-induced vibrations, 2nd edn. Van Nostrand, New York
6. Naudascher E, Rockwell D (1994) Flow-induced vibrations: an engineering guide. Balkema, Brookfield
7. Paidoussis MP, Price SJ, de Langre E (2011) Fluid-structure interactions: cross-flow-induced instabilities. Cambridge, New York
8. Okajima A (1982) Strouhal numbers of rectangular cylinders. J Fluid Mech 123:379–398
9. Bachmann H, Ammann W, et al. (1995) Vibration problems in structures: practical guidelines. Basel, Boston
10. Bearman PW (1987) Experiments on flow-induced vibration of a square-section cylinder. J Fluids Struct 1:19–34
11. Simiu E, Scanlan RH (1996) Wind effects on structures: fundamentals and applications to design. Wiley, New York
12. Giosan I, Eng P (2013) Vortex shedding induced loads on free standing structures. In Structural vortex shedding response estimation methodology and finite element simulation. Valmont West Coast Engineering. http://www.wceng-fea.com/vortex_shedding.pdf. Accessed Aug 2013
13. Den Hartog JP (1940) Mechanical vibrations, 2nd edn. McGraw-Hill, New York
14. Zdravkovich MM (1981) Review and classification of various aerodynamic and hydrodynamic means for suppressing vortex shedding. J Wind Eng Ind Aerodyn 7:145–189
15. Mahmoodi P (1969) Structural dampers. J Struct Div: Proc Am Soc Civ Eng 95:1661–72

Chapter 53
Isolating a Scanning Electron Microscope from Chiller Unit Vibrations

B.R. Barben and L.M. Hanagan

Abstract Although a scanning electron microscope (SEM) has very low tolerance to being disturbed by vibration, it requires a chiller for operation. Isolating the SEM from its associated chiller vibration takes careful consideration. This paper presents a case study of the performance of several slab-on-grade configurations. These configurations were specifically constructed to support various water chiller units and other service equipment as well as various vibration sensitive microscopes in a high performance research facility. In this study, the slabs are subjected to shaker-induced harmonic loading similar to that of a water chiller unit used to cool a SEM. The actual performance will be discussed in the context of generic design criteria for sensitive equipment and the SEM manufacturer-specified design criteria.

Keywords Slab on grade • Vibration sensitive equipment • Chiller vibrations • High performance research facility • Vibration criteria

53.1 Introduction

The concept of vibrations impacting the performance of vibration sensitive equipment, such as scanning electron microscopes and transmission electron microscopes, is nothing new. With the increase of nanotechnology research, universities and other agencies are investing significant space and financial resources in providing facilities to house sensitive instruments. Typically, vibration serviceability is related to human discomfort when subjected to vibrations; however, in facilities that contain electron microscopes, vibration serviceability is governed by instrument sensitivity. Electron microscopes are affected by vibrations that are periodic, random, or transient in nature. As laboratory equipment is introduced into a facility, vibration amplitudes generally increase relative to those of the unoccupied completed building [1]. The service equipment (e.g. water chillers, uninterrupted power systems, etc.), which are required for the operation of various electron microscopes, cause one form of periodic vibration that can affect the performance of electron microscopes. These unavoidable disturbances are often the source of the largest vibration levels to which the equipment could be exposed. The work described in this paper uses experimental techniques to first quantify the harmonic disturbance from an associated water chiller unit. Then, using shaker-induced harmonic loading similar to that of the water chiller unit, various slab on grade configurations are studied with respect to vibration transmission. Specifically, the vibration amplitudes of the corresponding configurations are compared to the generic design criteria and the equipment manufacturer-specified design criteria. The primary goal of this research is to assess vibration transmission caused by the water chiller as a function of slab on grade detailing. To accomplish the primary goal, an existing high performance research facility was utilized as a case study.

This paper begins with a brief overview of the commonly used generic vibration criteria for vibration sensitive equipment which is followed by vibration design criteria and room layout specified by the manufacturers of the equipment found in the case study facility. An overview of the design strategies for this facility as well as specific equipment layouts implemented for the quiet laboratory spaces are also provided. Following the layouts, the experimental testing procedure quantifying and replicating the chiller vibration is discussed. The actual performance of the design strategies are then compared with respect to the generic design criteria and the equipment manufacturer-specified design vibration criteria.

—————————————

B.R. Barben (✉) • L.M. Hanagan
Department of Architectural Engineering, The Pennsylvania State University, University Park, PA 16802, USA
e-mail: bbarben@psu.edu

53.2 Background

53.2.1 Generic Vibration Criteria

Numerous types of vibration criteria may exist; however the most prevalently referenced vibration criteria found in the literature and vibration design guides [2, 3] are the generic vibration criteria. The generic vibration criteria, commonly used throughout the world in the design and evaluation of high performance facilities (typically identified as the BBN or VC curves), were developed during the early 1980s by Eric Ungar and Colin Gordon [1]. Naturally, over the course of two decades, the original curves were modified and expanded to accommodate a wide range of instruments and tools used in the microelectronics, medical and biopharmaceutical industry. The generic vibration criteria consists of seven curves, all below the threshold of human perception, VC-A to VC-G, with VC-A being the least stringent and VC-G being the most stringent. These curves are expressed in root-mean-squared (RMS) velocity in one-third octave band frequencies from 1 up to 80 Hz. The modern VC curves are given in Fig. 53.1. The corresponding numeric values of the VC curves are given in Table 53.1 in US customary and metric units, with metric in parentheses.

53.2.2 Manufacturer Design Vibration Criteria and Suggested Layout

Another form of vibration criteria are the equipment manufacturer-specified design vibration criteria. These design vibration criteria can be expressed in many forms and can vary from manufacturer to manufacturer as well as instrument to instrument. The most common forms include: the units (displacement vs. velocity vs. acceleration), as a function of the domain (time domain vs. frequency domain). Additionally, the unit amplitude (peak to peak vs. peak vs. RMS) and the spectrum type
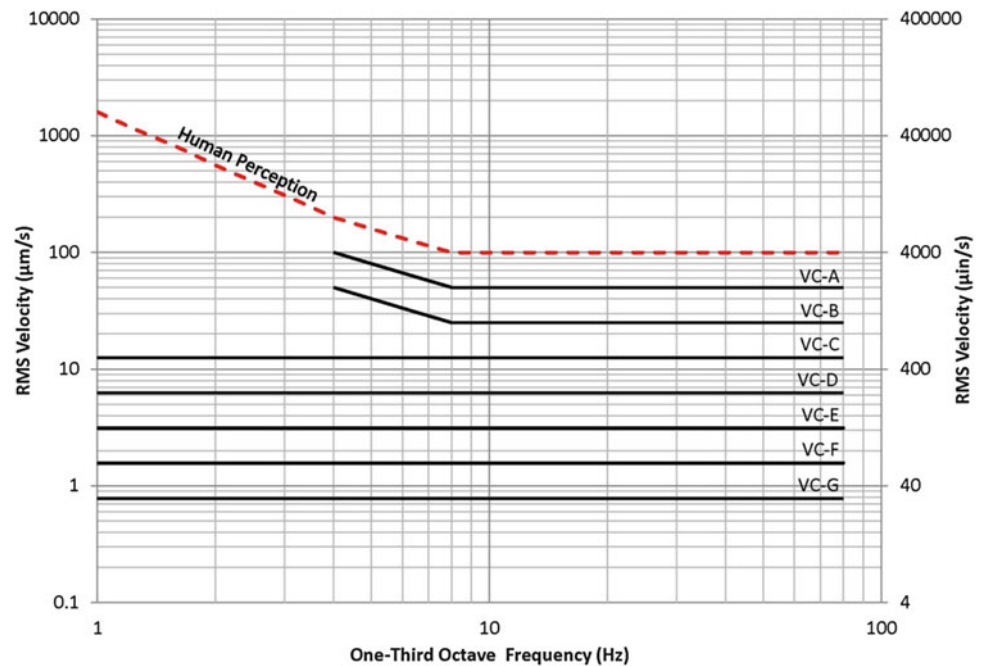

Fig. 53.1 Modern vibration criteria [4]

Table 53.1 Numeric values of the VC curves [4]

Frequency (Hz)	VC-A μin/s (μm/s)	VC-B μin/s (μm/s)	VC-C μin/s (μm/s)	VC-D μin/s (μm/s)	VC-E μin/s (μm/s)	VC-F μin/s (μm/s)	VC-G μin/s (μm/s)
1			500 (12.5)	250 (6.25)	125 (3.13)	62.5 (1.56)	31.25 (0.781)
4	4,000 (100)	2,000 (50)	500 (12.5)	250 (6.25)	125 (3.13)	62.5 (1.56)	31.25 (0.781)
8	2,000 (50)	1,000 (25)	500 (12.5)	250 (6.25)	125 (3.13)	62.5 (1.56)	31.25 (0.781)
80	2,000 (50)	1,000 (25)	500 (12.5)	250 (6.25)	125 (3.13)	62.5 (1.56)	31.25 (0.781)

Fig. 53.2 Vibration specifications for various electron microscopes
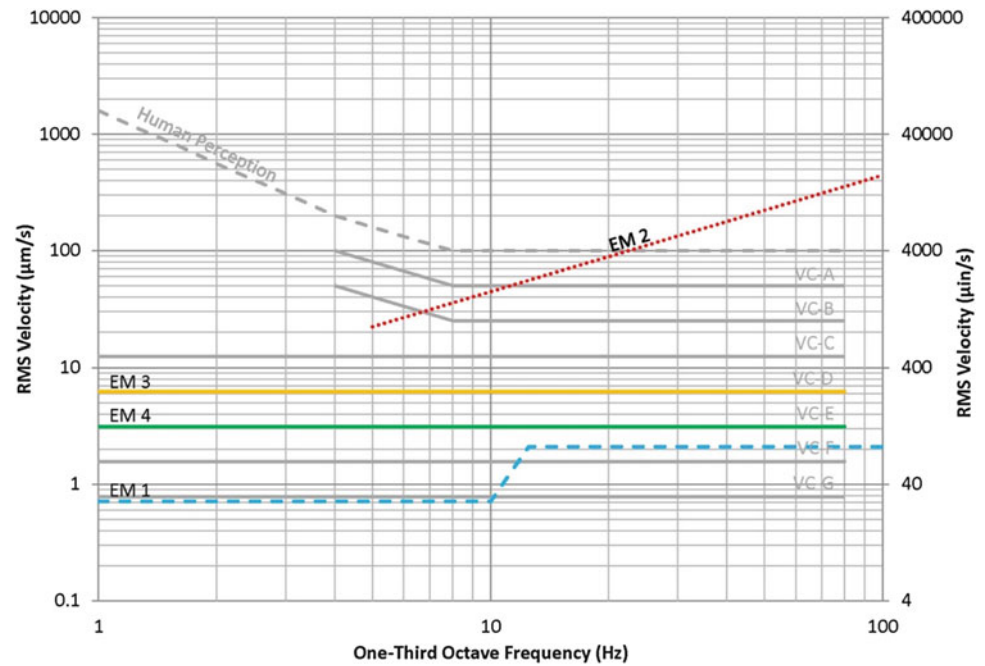
(one-third octave bands vs. constant vs. power spectral density) can also vary in manufacturer equipment specifications [1]. To illustrate the differences between design vibration criteria, vibration specifications are provided for four different electron microscopes as shown in Fig. 53.2. For reference, the associated VC curve for these microscopes is typically VC-D which corresponds to a 250 μin/s (6.25 μm/s) RMS velocity over a 1–80 Hz one-third octave band frequency range [1].

One electron microscope manufacturer, FEI, expresses their equipment's threshold in terms of RMS acceleration, measured in one-third octave bands, over a frequency range of 1–500 Hz. FEI also provides specifications for vertical vibrations as well as horizontal vibrations. To compare a FEI Nova Nano's vertical vibration specifications to that of the VC curves, the specifications are presented in RMS velocity as shown in Fig. 53.2 as EM 1. Another electron microscope manufacturer, JEOL Ltd., originally specified displacement based design vibration criteria for their microscopes; however, over the years, their vibration criteria evolved into a hybrid criteria with a displacement based criterion at lower frequencies and an acceleration based criterion at higher frequencies. An example of the original displacement based design vibration criteria presented in RMS velocity is given as EM 2 in Fig. 53.2. The JEOL JSM 6490's threshold is in terms of peak to peak displacement for sine waves with frequencies of 5 Hz and over. Although the authors of this paper were unable to obtain an example of the actual hybrid design vibration criteria for a JEOL JEM 1200 EXII and JEOL JEM 2010, an equivalent VC curve criteria of VC-D and VC-E, as shown in Fig. 53.2 as EM 3 (JEOL JEM 1200 EXII) and EM 4 (JEOL JEM 2010) respectively, were provided by the manufacturer in a phone call.

In addition to specifying their equipment's design vibration criteria, manufacturers will also provide installation and service requirements for their equipment. These requirements are often related to floor space, power, room and cooling water temperature. SEMs require specific quality and flow of cooling water for proper operation. If the facility that houses a SEM cannot achieve specific water conditions, a closed-circuit water cooler or chiller must be used. Some manufacturers recommend always using a closed-circuit water cooler. In addition to recommending a water chiller, some manufacturers will suggest a specific water chiller manufacturer, models and placement relative to the SEM. For example, FEI requires that the chiller be placed at least 5 ft (1.5 m) from the SEM to prevent electromagnetic interference. They also recommend that the chiller not be placed in the same room as the SEM, but in an adjacent room to prevent vibrations from the chiller affecting the SEM.

53.3 Overall Description of Case Study Building

The facility used in this case study is a 275,600 ft^2 (25,604 m^2) state of the art high performance research facility which includes multiple low-vibration laboratory environments. Located 20 ft (6.1 m) below grade in the basement of this research facility, 6,300 ft^2 (585.3 m^2) are dedicated to low-vibration laboratories for organic and inorganic material characterization.

These spaces are referred to as "quiet labs" and are shielded from vibrations and acoustic and electromagnetic noise. There are two classes of quiet labs, ultra-quiet labs and typical quiet labs, both are situated on 24 in. (610 mm) thick isolated slabs on grade and contain a variety of electron microscopy, electron spectroscopy and optical microscopy equipment. Additionally, both classes of labs were designed to meet a vibration criterion of VC-E or 125 μin/s (3.125 μm/s) from 2 to 200 Hz. The difference between the two classes of quiet labs is based on the level of isolation, with the ultra-quiet labs having a higher level of isolation. The quiet labs are isolated from the surrounding corridors and the ultra-quiet labs are additionally isolated from each other. The isolation features are more fully described below.

53.4 Quiet Labs

The laboratories are arranged in groups of five with one group consisting of five typical quiet labs and two groups of five ultra-quiet labs. The five typical quiet labs are situated on one isolated slab on grade whereas each individual ultra-quiet lab is situated on its own isolated slab on grade. The laboratory slabs on grade, all 24 in. (610 mm) thick are separated from the other slabs on grade by a 2 in. (50.8 mm) neoprene isolation joint. The group of labs are surrounded by a double wall with a 2 in. (50.8 mm) air gap at the slab isolation joint. The outer wall, which is supported on the 12 in. (305 mm) thick perimeter corridor slabs, is an 8 in. (203 mm) concrete masonry unit (CMU) wall. Bearing on the laboratory slabs on grade are the inner walls which are comprised of 6 in. (152 mm) metal studs, 6 in. (152 mm) of acoustic batt insulation between the studs and two layers of 5/8 in. (15.9 mm) gypsum wall board. Between each of the typical quiet labs is a single 6 in. (152 mm) metal stud wall. The laboratory walls between the ultra-quiet labs are similar to the typical quiet lab walls, however there is a double 6 in. (152 mm) metal stud wall with a 2 in. (50.8 mm) air gap at the slab isolation joint. Only the typical quiet labs, as shown in Fig. 53.3, are situated above a grid of pile caps which are connected to grade beams ranging in sizes of 24 in. (610 mm) by 24 in. (610 mm) to 36 in. (914 mm) by 36 in. (914 mm). Figure 53.3 overlays the foundation plan over basement architectural plan. The height difference between the bottom of these slabs and the top of the pile caps and grade beams is 12 in. (305 mm). The service corridors, which contain various service equipment (e.g. water chillers, uninterrupted power systems, etc.) required for the operation of the various electron microscopy, electron spectroscopy and optical microscopy equipment housed in the facility, are situated on 12 in. (305 mm) thick slabs on grade. Two service corridors are utilized, one service corridor is located between the group of typical quiet labs and a group of ultra-quiet labs and the other corridor is located between a group of ultra-quiet labs and regular research areas. An example of the location of a service corridor is shown in Fig. 53.3.
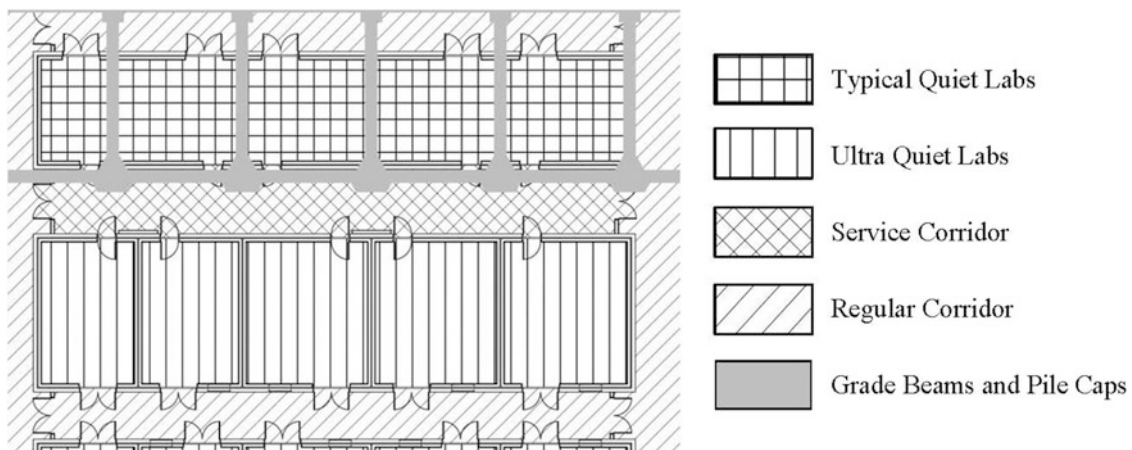

Fig. 53.3 Foundation plan overlaid on architectural plan

53.5   Experimental Testing

53.5.1   *Ambient Conditions*

Although the service corridors contain various pieces of service equipment, one water chiller unit, specifically a Haskris R050, was selected to study the effect of chiller induced vibration. Ambient conditions were measured near this unit to determine the amplitude and forcing frequency caused by the largest harmonic disturbance on the service corridor slab on grade. The Haskris R050 unit measures 18 in. (457 mm) wide by 27 in. (686 mm) deep by 34 in. (864 mm) high. The unit is in contact with the slab on grade at the four corners of the unit via the unit's support legs. The support legs are spaced 14 in. (356 mm) side to side and 23 in. (584 mm) front to back. The CMU wall is 17.25 in. (438 mm) from the Haskris R050's back two back support legs. One PCB 393B31 accelerometer, with a sensitivity of 10.0 V/g, was placed at a back support point to measure the harmonic vibration generated by the Haskris R050. Additionally, a PCB 393B31 accelerometer was placed on top of the unit at its center to assure this unit was causing the largest measured harmonic disturbance.

The measured response data was collected and processed by a Siglab model 20–42 dynamic signal analyzer. The response data was measured with a maximum resolvable frequency of 200 Hz and a frequency resolution of 0.125 Hz. The 200 Hz frequency was selected since a frequency range of 2–200 Hz was utilized for the vibration design criteria for facility. In fast Fourier transform (FFT) based frequency analysis, the basic assumption is that the vibration is periodic in nature and windowing can ensure a periodic nature. Windowing multiplies the time-domain data by a window function before the FFT is performed [5]. When analyzing vibration data, care must be taken to select the proper window for the desired results. Since the intent is to determine the periodic amplitude of the vibrations from the Haskris R050, a Flattop window is selected. The Flattop window is specifically designed to minimize amplitude error thus ensuring maximum harmonic amplitude accuracy [5]. The RMS acceleration spectra are plotted in Fig. 53.4. The orange dotted line is the measured response from the accelerometer that was placed on top of the unit at its center. The purple solid line is the response of slab from the accelerometer placed near the support leg. The spectral peaks occurred at 59.625 Hz with amplitudes of 51,370 μg (503,938 μm/s^2) and 69 μg (676 μm/s^2) for the top of the chiller and the slab by the support, respectively. From Fig. 53.4, it can be observed that, within the 200 Hz bandwidth, the greatest harmonic acceleration of the chiller at 59.625 Hz causes the greatest harmonic acceleration of the slab at the same frequency.

To convert the steady-state acceleration to steady-state velocity, the steady-state acceleration is divided by 2π and the frequency. To convert the constant bandwidths to one-third octave bandwidths, the constant (or narrow) bandwidths can be merged by simply adding the mean-square vibration vector quantities for the constant bandwidths [6]. These two conversions are necessary to compare the measured test data to that of the VC and manufacturer-specified design criteria. The conversion
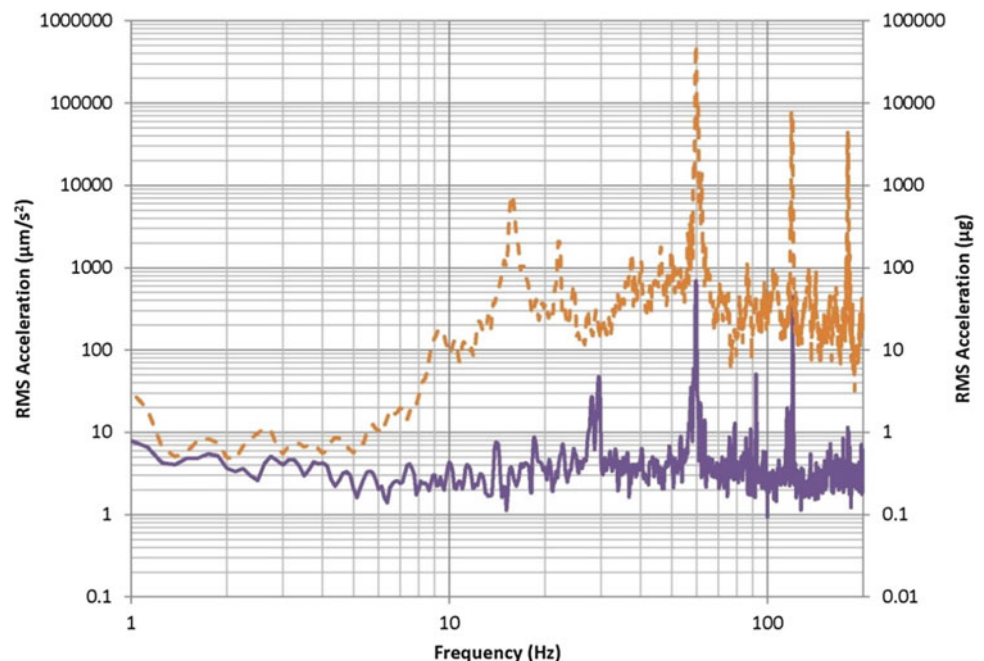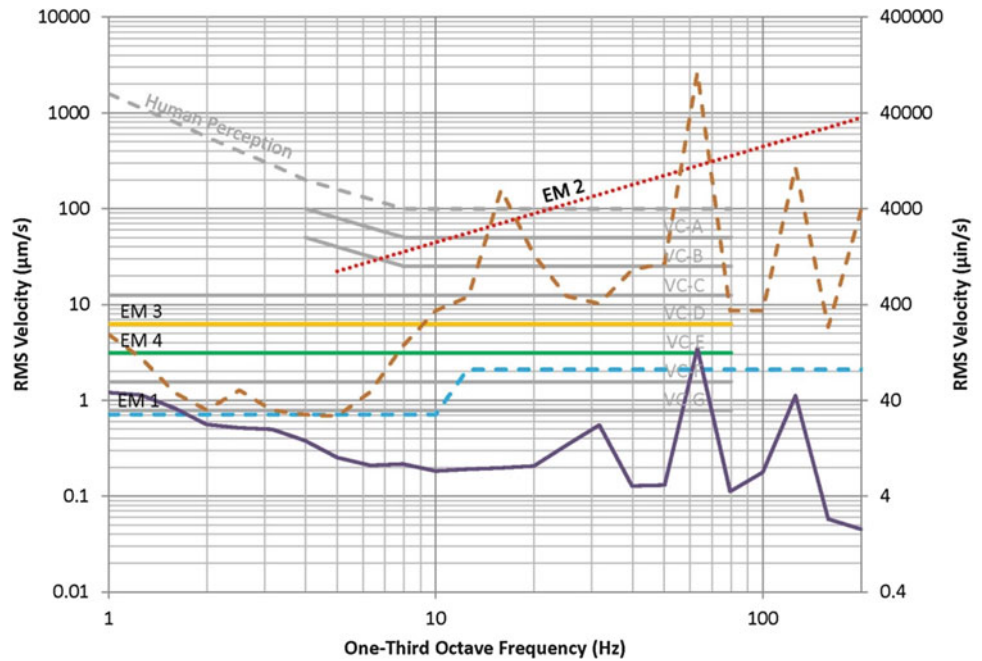

Fig. 53.4 Narrow band RMS acceleration spectra

Fig. 53.5 Ambient one-third octave RMS velocity with respect to vibration criteria RMS

for a narrow bandwidth spectrum to a wider bandwidth spectrum is given by Eq. (53.1). It should be noted that Eq. (53.1) is an approximation and assumes an idealized rectangular filter.

$$X_{1/3}^2 = \sum_{0.89f_c}^{1.12f_c} X_n^2 \tag{53.1}$$

Where,

X_n^2 = Narrow bandwidth mean-square vector quantity

$X_{1/3}^2$ = One-third octave mean-square vector quantity

f_c = One-third octave band center frequency

The converted one-third octave RMS velocity spectra from Fig. 53.4 are given in Fig. 53.5. The spectral peaks occurred at the 63 Hz one-third octave band with amplitudes of 105,265 μin/s (2,674 μm/s) and 140 μin/s (3.6 μm/s) for the top of the chiller (orange dashed) and the (solid purple) slab near the rear support of the chiller, respectively.

53.5.2 Shaker-Induced Conditions

Given that the periodic amplitude and forcing frequency for the Haskris R050 have been determined, a harmonic or steady-state vibration can be generated at that same periodic amplitude. Four PCB 393B31 accelerometers were placed at various locations to measure the response due to the steady-state vibration generated by an APS Dynamics model 400 electromagnetic shaker. Utilizing the shaker, the slabs on grade can be subjected to harmonic forces similar to that of the Haskris R050. A custom designed force plate, with four contact points, was used to measure the force output from the shaker. The shaker was placed on the force plate and located at four different locations, given in Fig. 53.6, while the accelerometers were placed at varying distances, noted in Figs. 53.7 and 53.8, from the force plate's contact points. The shaker and accelerometer locations were selected to provide a comparison of vibration amplitudes vs. distance from the excitation for four distinct conditions. These conditions will be described more thoroughly in conjunction with the observations that can be made from the data collected.

The measured response data was collected and processed by a Siglab model 20–42 dynamic signal analyzer. The response data was measured with the same maximum resolvable frequency of 200 Hz and a frequency resolution of 0.125 Hz. A constant force was provided by the shaker at a forcing frequency of 68 Hz. The 68 Hz frequency was selected to be in the same octave band but distinguishable from the chiller's 59.625 Hz forcing frequency and non-additive to its amplitude
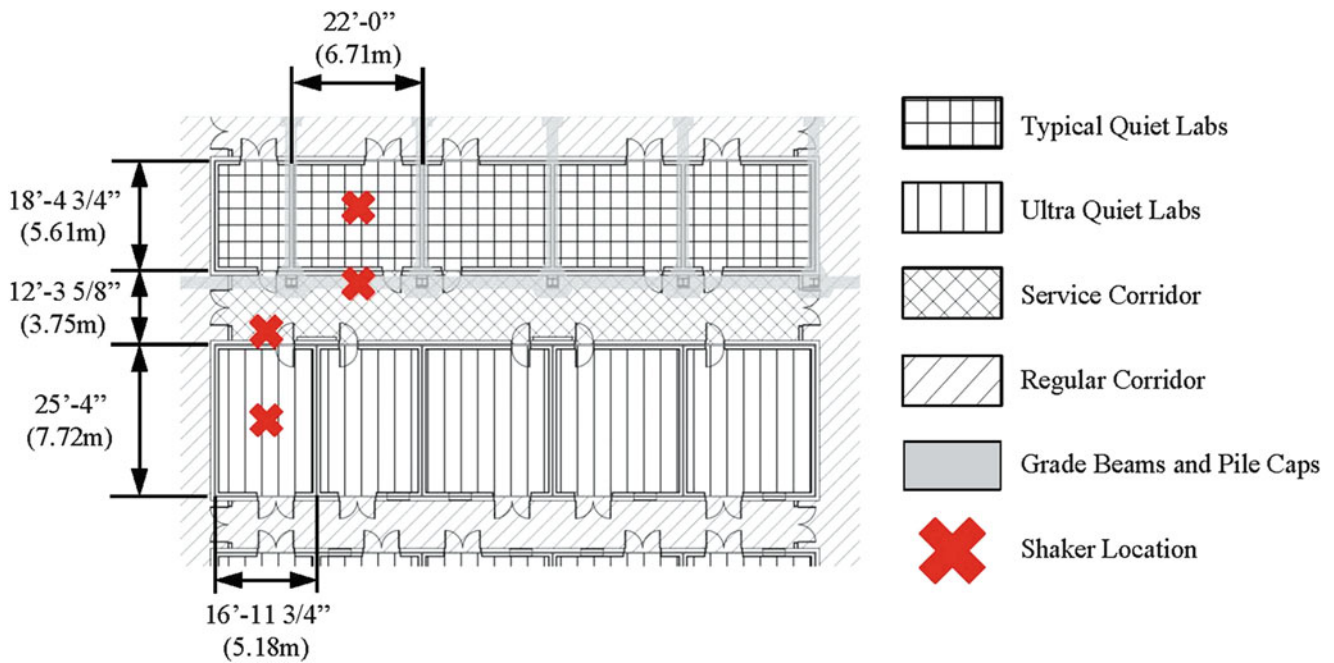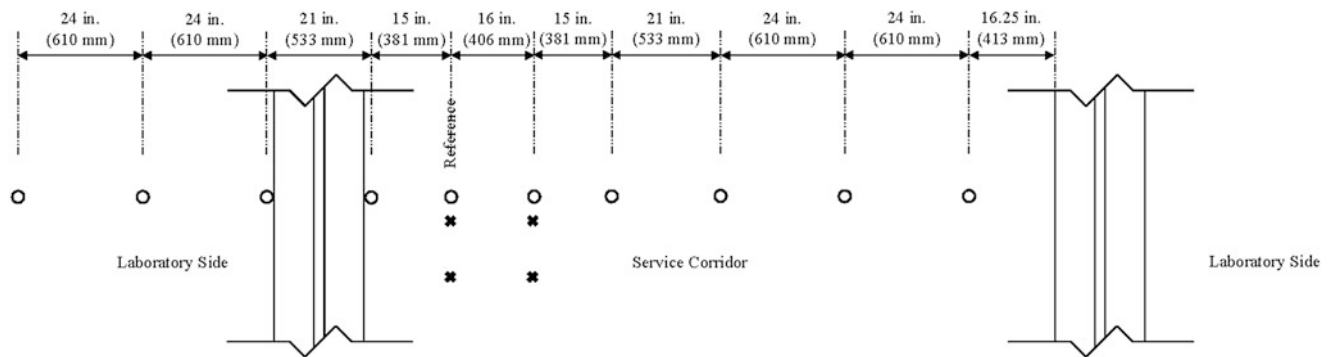
Fig. 53.6 Shaker locations

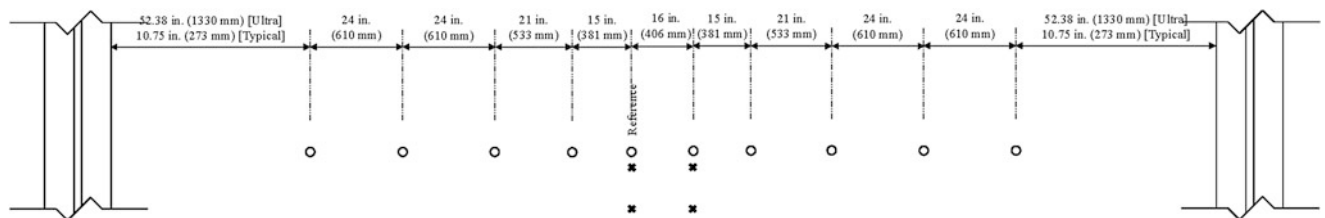**Fig. 53.7** Shaker testing layout in service corridor

Fig. 53.8 Shaker testing layout in laboratory

in the narrow band. Using Eq. (53.1), the narrow band vibration spectrum content from the 68 Hz shaker force will be converted to the one-third octave band with a center frequency of 63 Hz for comparison to the vibration criteria curves.

A total of ten measurements were taken at each shaker location. The testing configurations for the shaker in service corridor and in the laboratories are given in Figs. 53.7 and 53.8, respectively. The locations noted with a circle represent accelerometer placement. The excitation location in the service corridor, with the four legs of the force plate noted with an X in Fig. 53.7, was selected to be consistent with the rear support location of actual chiller with respect to the wall. This location is noted as reference in Fig. 53.7. The next accelerometer location was 15 in. (381 mm) away at the face of the support corridor wall. The third accelerometer was located next to the wall on the laboratory side. A fourth and fifth
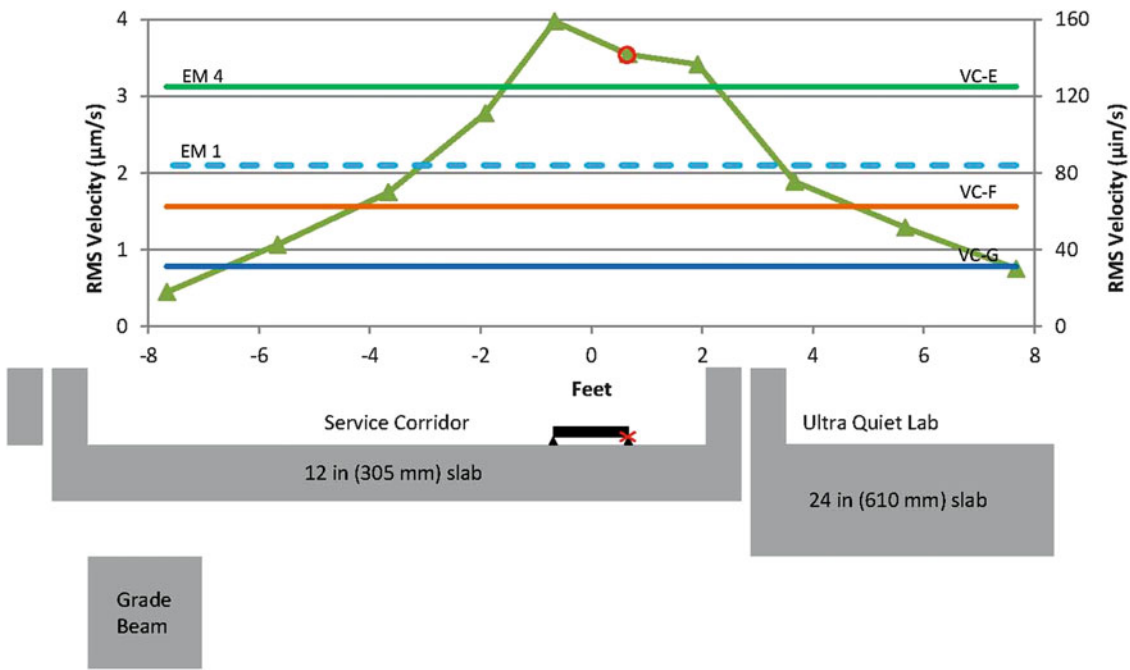
Fig. 53.9 Response from shaker testing in service corridor into ultra quiet lab
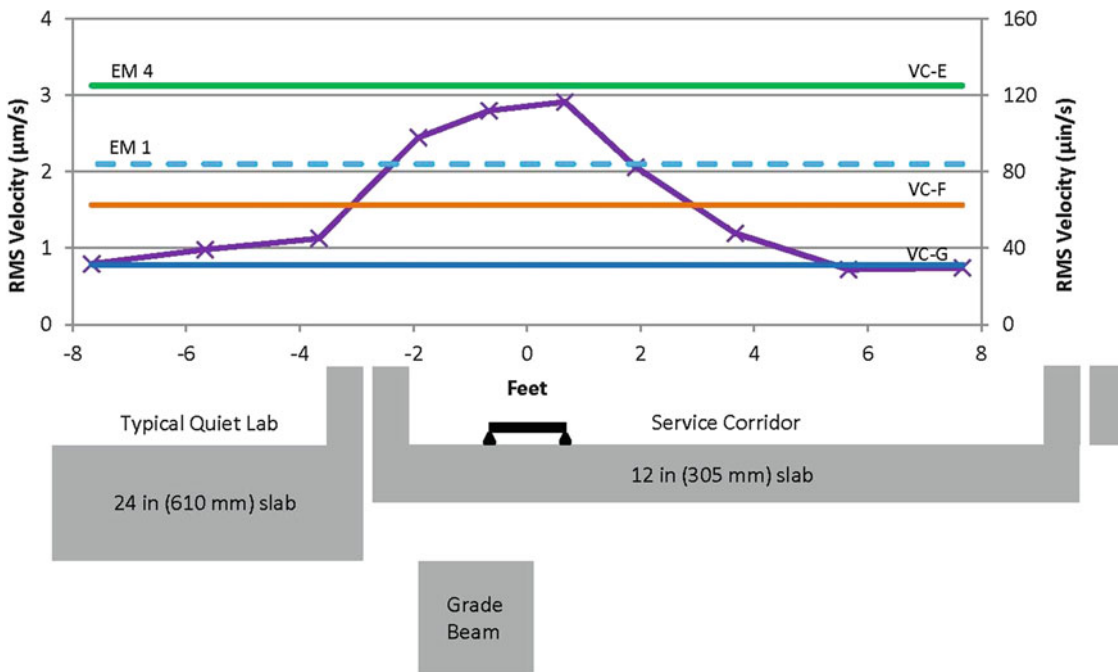

Fig. 53.10 Response from shaker testing in service corridor into typical quiet lab

accelerometer were placed at 2 ft. (0.61 m) increments away from the excitation. These five locations were then dimensionally mirrored on the service corridor side of the force place. The measurements within the labs utilized the same distances between accelerometers for consistency. The responses, in RMS velocity at the 63 Hz one-third octave band, due to the shaker testing with respect to generic and specific criteria are given in Figs. 53.9, 53.10, 53.11, and 53.12. The next section discusses observations made from the data.
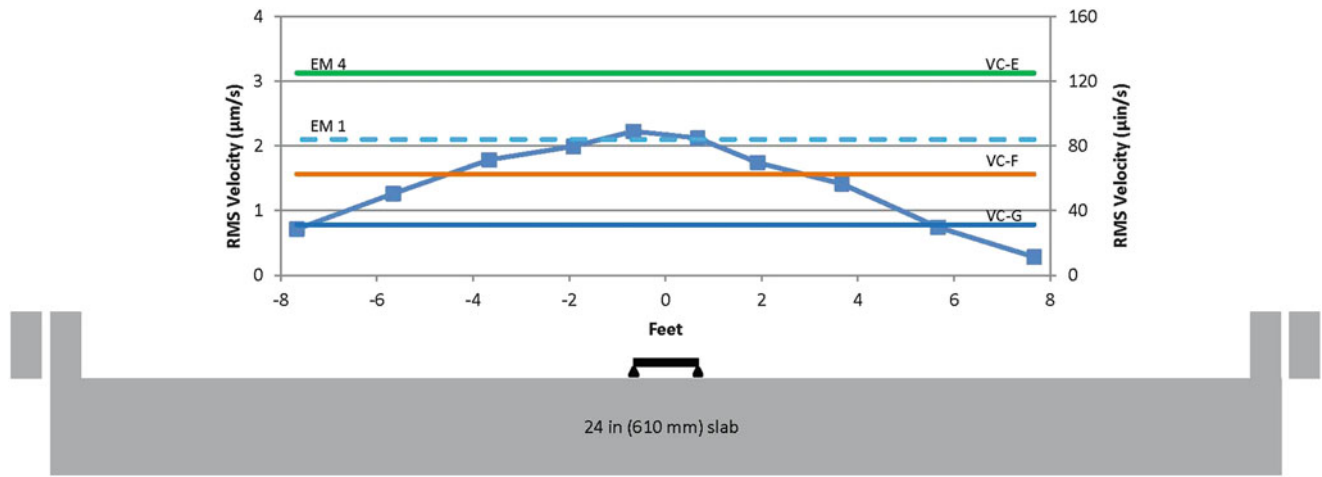
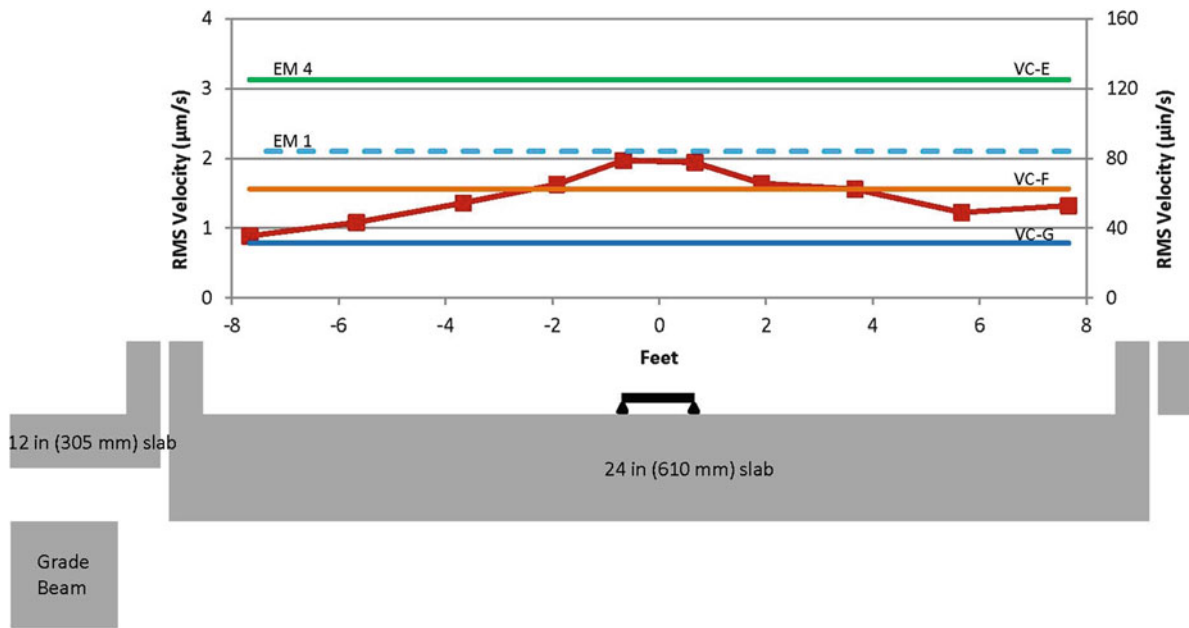**Fig. 53.11** Response from shaker testing in ultra quiet lab

Fig. 53.12 Response from shaker testing in typical quiet lab

53.6 Observations

53.6.1 Ambient Conditions

From the measurements taken in the case study facility, plotted in Fig. 53.5, it was shown that a Haskris R050 chiller causes a peak slab disturbance of 140 μin/s (3.6 μm/s) at 63 Hz near the base of one chiller support leg. This velocity amplitude is between the VC-D and VC-E limits for the general criteria and exceeds the limits for EM1 and EM 4. This demonstrates that this particular chiller, required for microscope operation, is capable of creating vibrations that exceed the VC-E criterion and some manufacturer criteria on the 12 in. (305 mm) slab. Since colocation is not probable, vibration levels under different slab conditions and various distances are of interest.

53.6.2 Shaker-Induced Conditions

The green triangles in Fig. 53.9 plot the maximum measured amplitudes at 63 Hz relative to accelerometer position for the shaker induced vibration. The graphic under the graph shows the slab conditions at the measurement locations. For this measurement, the accelerometer location for the ambient condition was reused, marked as an x, to demonstrate that the shaker excitation is creating a disturbance similar to the chiller. The red circle represents the level measured in the ambient condition. From this graph, it can be seen that vibration amplitudes decrease with distance from the source of vibration. This makes sense since vibration amplitudes attenuate with distance from the excitation source. Closer inspection reveals that at 3 ft. (0.91 m) to the right of force plate, inside the ultra quiet lab, the measured level drops below the VC-E general criteria curve and all manufacturer limits investigated. This is not a surprising result as this was one goal of the design recommendations for the ultra quiet lab. At 3 ft. (0.91 m) to the left of the force plate, in the service corridor, the level is actually lower than the ultra quiet lab measurement. The expectation was that the isolation joint between the service corridor and the ultra quiet lab would reduce the level of vibration transmission; however, this was not the case.

The purple X's in Fig. 53.10 plot maximum amplitudes caused by the same shaker induced force across the isolation joint for the typical quiet lab as demonstrated by the graphic below the graph. The amplitudes measured near the force plate legs are lower than those measured on the other side of the service corridor. This may be attributed to different sub-slab conditions caused by the grade beam. This is also true of the levels 3 ft. (0.91 m) away. It appears that the grade beam is positively affecting the levels vibration. At three of the four points 7 ft. (2.1 m) away from the shaker, there is little difference between the levels of the various conditions represented by Figs. 53.9 and 53.10 with all values close to the VC-G criteria line. The exception is a lower level over the grade beam.

Figures 53.11 and 53.12 plot maximum amplitudes due to shaker induced excitation on the 24 in. (610 mm) slabs. Though the levels near the disturbance are much lower than those on the 12 in. (305 mm) slab, the change in level vs. distance is much less. The levels recorded in both labs meet the VC-E general criteria. For all four conditions tested, the VC-F criterion is met for chiller vibrations at a distance of 5 ft (1.5 m) away from the source, as recommended by one manufacturer.

53.7 Conclusions

For this case study, slab thickness and distance from the source of vibration were found to be the strongest factors affecting the level of vibration measured from a shaker induced simulation of chiller vibration. At measurements near the vibration source, the measured amplitudes were significantly smaller on the 24 in. (610 mm) slab than those on the 12 in. (305 mm) slab. At distances 5 ft (1.5 m) away from the source, the difference between levels measured on 12 in. (305 mm) and 24 in. (610 mm) slabs were much less than those measured near the source. The presence of a grade beam below the slab was also a factor that resulted in lower vibration levels than similar conditions without a grade beam below. The isolation joint did not seem to have a strong reduction effect on vibration transmission.

References

1. Gordon CG (1999) Generic criteria for vibration-sensitive equipment. Proc SPIE Int Soc Opt Eng 3786:22–33
2. Murray TM, Allen DE, Ungar EE (1997) Floor vibrations due to human activity, vol 11, Steel design guide series. American Institute of Steel Construction (AISC), Chicago
3. Smith AL, Hicks SJ, Devine PJ (2007) Design of floors for vibration: a new approach, vol P354, The Steel Construction Institute publication. The Steel Construction Institute (SCI), Ascot
4. Institute of Environmental Sciences (IEST) (2005) Appendix C in recommended practice RP-012. Considerations in clean room design. IES-RP-CC012.2. Institute of Environmental Sciences, Rolling Meadows
5. McConnell KG (1995) Vibration testing: theory and practice. Wiley, New York
6. Vér IL, Beranek LL (2006) Noise and vibration control engineering: principles and applications. Wiley, Hoboken

Chapter 54
Dynamic Characteristics of Double Layer Beam with Respect to Different Boundary Conditions

Jongsuh Lee, Semyung Wang, Jongnam Kim, and Jaehu Ryu

Abstract Beam is one of the most commonly used object to verify the vibration theory since its analytic solutions have been well derived. For a double layer beam case, however, there are difficulties to estimate dynamic behavior of the layered beam with the derived analytic solutions for a single layer beam. This study is regarding investigations of dynamic characteristic changes of double layer beams with respect to various boundary conditions.

Keywords Laboratory • Beam vibration • Double layer • Boundary condition

54.1 Introduction

When new analysis/control algorithms for vibration are developed, a beam or plate has been used to verify the developed algorithms. When new analysis/control algorithms for vibration are developed, a beam or plate has been used to verify the developed algorithms. It is because a beam and plate are easy to implement in experiment and the analytic and numerical solutions for dynamic behavior of these structure already have been well derived [3, 4]. In many vibration textbooks, solutions for the dynamic behavior of a beam and plate have been well introduced and well explained with respect to variety boundary conditions. These solutions, however, are for a single layer beam and plate, therefore, there will be many difficulties to analyze a laminated beam or plate with the derived analytic and numerical solutions for a simple beam and plate. It is because there will occur the stick/slip/slap phenomena at the interface of each layer. The layered structure has not been well introduced in analytical and numerical way as compared to the many number of uses in real mechanical structure.

This paper will show experimental results of vibration behavior for a double layer beam with respect to different boundary conditions and it will find a trend of the vibration behavior for each boundary condition.

54.2 Experiments

The trend of dynamic behavior for a double layer beam with respect to different boundary conditions will be confirmed by frequency response functions (FRFs). Each single layer beam composing of the double layer is introduced in Fig. 54.1.

Figure 54.1 shows beams used in experiments. Each beam has 30 cm length and 6 cm width. As shown in the figure, each beam has different thickness. Each thickness of these beams from top to bottom is 8, 5 and 3 mm, respectively. In this paper, to compare the dynamic behavior of a double layer beam with a single beam which has the same thickness to the double layer beam, for the 8 mm case the experiment has been performed on a single layer beam. On the other hand, for the 5 and 3 mm cases, these two beams are laminated and the experiments have been performed. We made holes on the both sides of beams to implement several boundary conditions to the double layer beam (Fig. 54.2). In order to take into account the same effect by holes to the single beam, we make the same size holes to the single beam (8 mm) at the same locations.

Figure 54.2 shows every experimental configuration and boundary condition for the single layer beam and the double layer beams. Every experiment to identify the FRFs has been conducted on the free-free condition. The used hammer and accelerometer are 2,302–10 series of Endevco co. and 4,393 series of B&K Co., respectively. Each layer of double beam has been measured at seven different nodes so that each double beam has been measured at 14 nodes. While the single beam has been measured at seven nodes at only one side. Figure 54.2a shows the experimental configuration for the single layer beam.

_____

J. Lee • S. Wang (✉) • J. Kim • J. Ryu
Gwangju Institute of Science and Technology (GIST), Gwangju 500-712, Republic of Korea
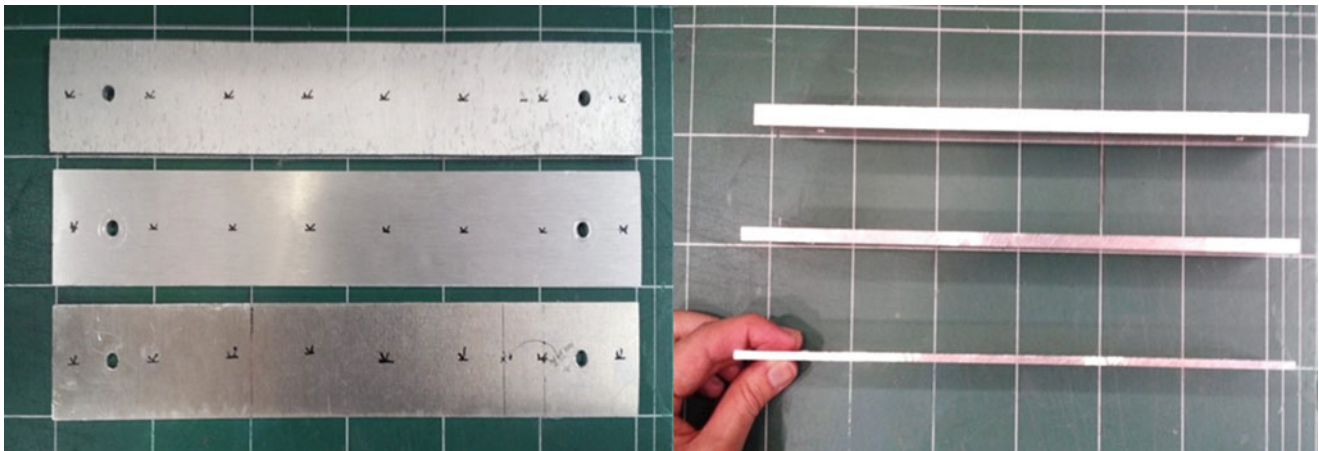e-mail: smwang@gist.ac.kr

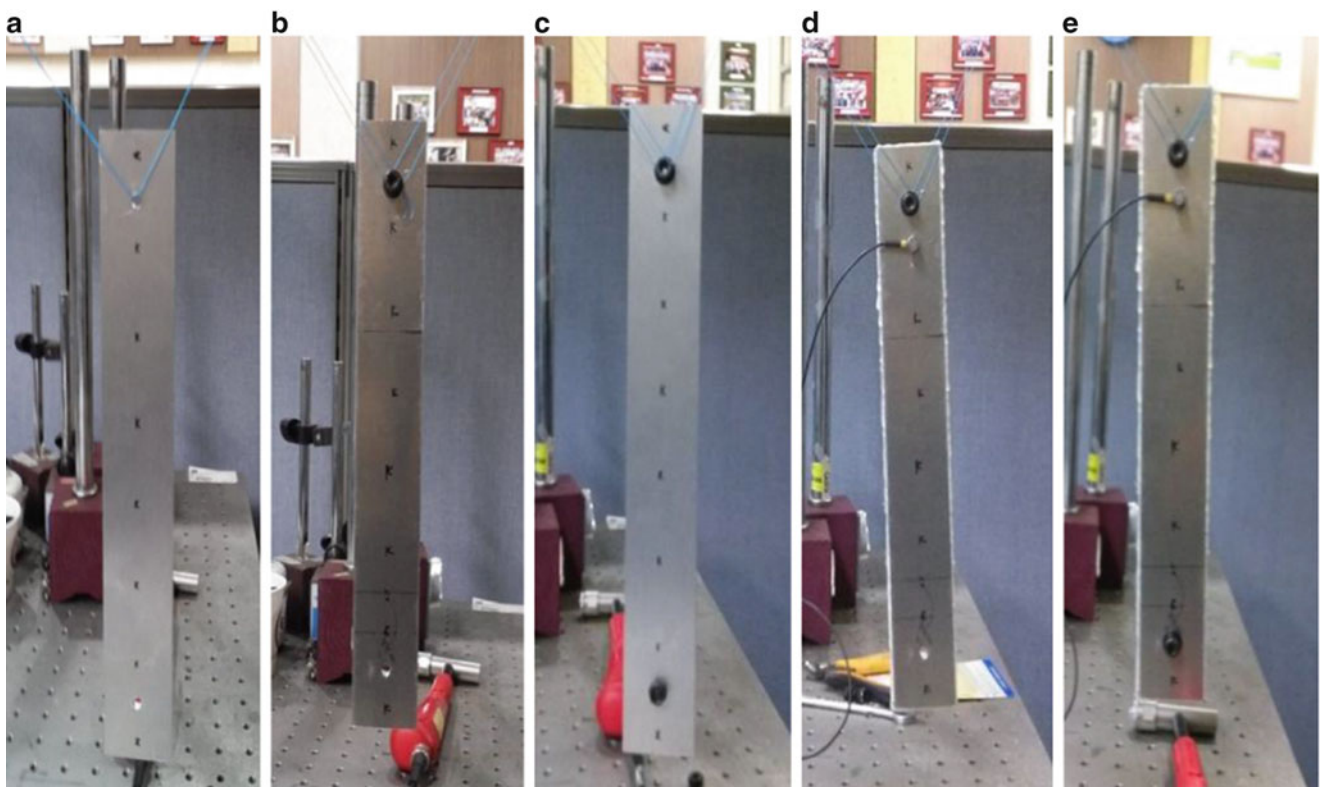**Fig. 54.1** Three different thickness of beams, from top to bottom 8, 5 and 3 mm

Fig. 54.2 Five different boundary condition of beams (**a**) 8 mm single beam, (**b**) double beam (5 + 3 mm) of 1 side bolt without glue, (**c**) double beam (5 + 3 mm) of 2 side bolts without glue, (**d**) double beam (5 + 3 mm) of 1 side bolt with glue at each edge and (**e**) double beam (5 + 3 mm) of 2 side bolts with glue at each edge

Figure 54.2b shows the experimental configuration for the double layer beam that is bolted to each layer at only one side hole. Figure 54.2c shows the experimental configuration for the double layer beam that is bolted at the both side holes. Figure 54.2d shows the experimental configuration for the double layer beam that is bolted at one side hole and it has been glued by silicon glue onto every edge. And Fig. 54.2d show the experimental configuration for the double layer beam that is bolted at the both side holes and it has been glued by silicon glue onto every edge. Every boundary condition performed in this paper has been chosen to identify vibration transmission trend with respect to increasing adhesive force that is applied to the interface of each layer. We have implemented boundary conditions from Figure (b) to (d) in increasing way of adhesive force.
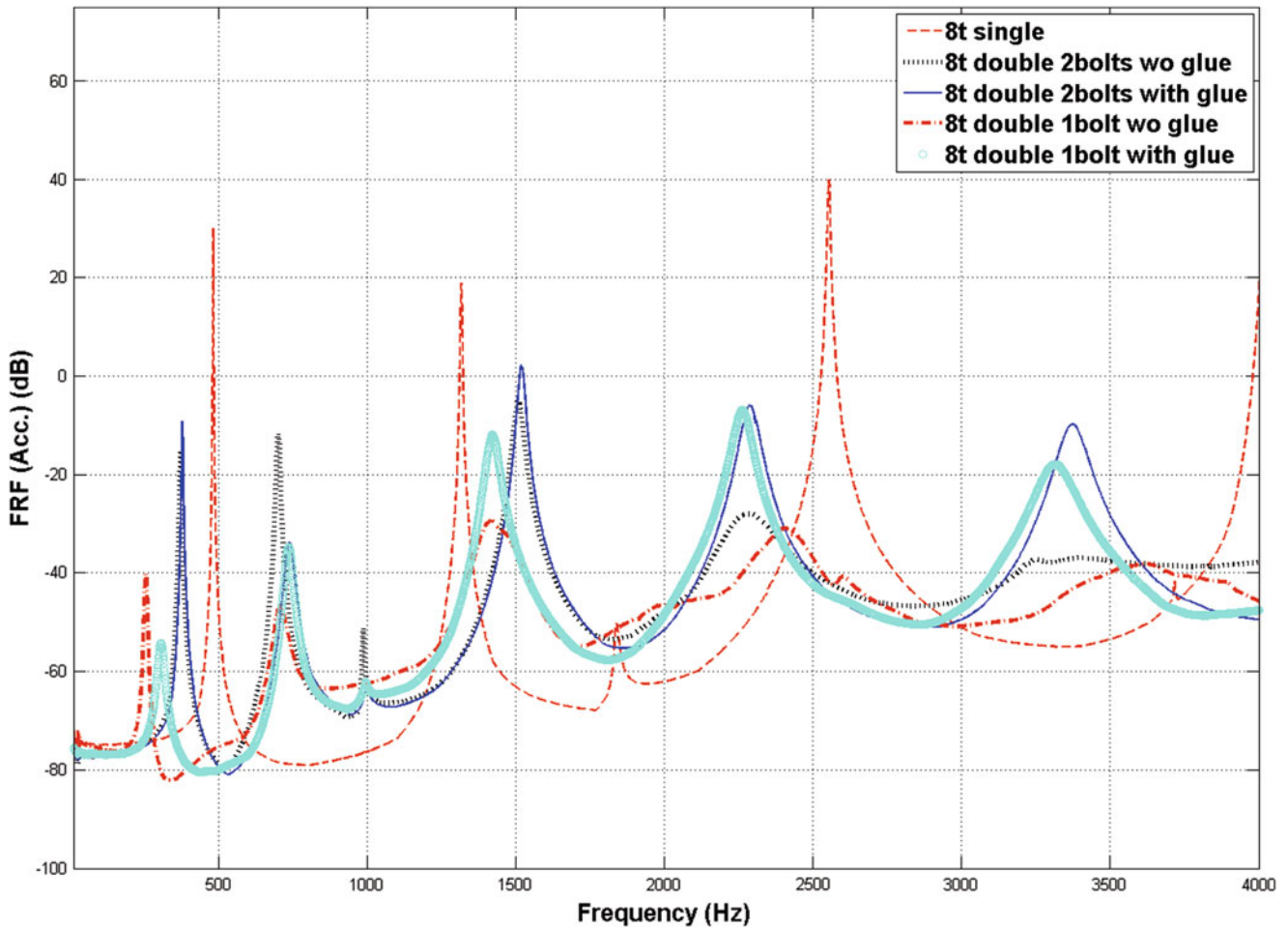
Fig. 54.3 Frequency response function results for each beam; single beam (−−), double beam of 2 side bolts without glue (¨), double beam of 2 side bolts with glue (—), double beam of 1 side bolt without glue (−•−), double beam of 1 side bolt with glue (o)

Figure 54.3 shows averaged FRFs at ever node for each boundary condition. As shown in this figure, it is confirmed that resonance frequencies of the single layer beam (−−) show higher as compared to the cases of double layer beams. Therefore, it can be conclude that a double layer structure shows better performance than a single layer structure from an aspect of reducing transmitted vibration energy. For the double layer beams, the bolted case at one side hole without glue (−•−) show the best vibration reduction performance, whereas the both side bolted case with glue (—) shows the worst performance. These results are because of the adhesive force at the interface of layers, the higher adhesive force results in the higher transmissibility of vibration. The same trend of this result has been identified into the other boundary conditions. It means that the vibration transmissibility increases in the order of Fig. 54.2b–e (i.e., in the order of increasing adhesive force). It is because the stiffness of a multi-layer structure increases when adhesive force increases. It can also be deduced from the result of the double layer that is bolted at the both side with glue (—), in which resonance frequencies are higher than those of the other double layer cases.

In summaries, it can be concluded that a double layer structure is better than a single layer structure in the aspect of reduction of the transmitted vibration from inner to outer of a mechanical structure and, for multi-layer structures, the lower adhesive force in the interface of multi-layers shows the better performance.

54.3 Conclusion

In this paper, vibration experiments have been carried out with a double layer beam under variety boundary conditions to analyze dynamic transmission characteristics of a multi-layer structure. The obtained experimental results are compared to the single layer beam whose thickness is the same to the double layer. In addition, each different boundary conditions for a double layer is classified with adhesive force to the interface. This classification is used to find a certain trend with respect to variation of adhesive force.

References

1. Fanson JL, Caughey TK (1990) Positive position feedback control for large space structure. AIAA 28:717–724
2. Kim S-M, Pietrzko S, Brennan M (2008) Active vibration isolation using an electrical damper or an electrical dynamic absorber. IEEE Trans Control Syst Technol 16:242–254
3. Inman DJ (2001) Engineering vibration. Prentice-Hall, Englewood Cliffs
4. Meirovitch L (2001) Fundamentals of vibrations. McGraw-Hill International Edition, Singapore

Chapter 55
Evaluation of an Automatic Selection Methodology of Model Parameters from Stability Diagrams on a Damage Building

Boroschek K. Rubén and Bilbao N. Joaquín

Abstract Automatic selection of modal parameters from stability diagrams is a requirement for automatic SHM systems and damage assessment. In the present article we describe and apply a methodology of an automatic modal selection based on data recorded continuously for 5 years in a building structure located in Chile. The building has been subjected to more than 1,700 earthquakes. Environmental conditions and noisy signals are present on the data and identified modal parameters. The methodology considers soft and hard discriminants between real and spurious modes. Evaluation of the methodologies is done based on the effectiveness of the discriminants and the computational cost of its evaluation. Results indicate that the parameters should be selected based on the number and type of sensors, noise level on the data, modal properties and damage characteristics of the structure.

Keywords Structural health monitoring • Modal analysis • Stabilization diagrams • Modal validation criteria • Structural dynamics

55.1 Introduction

Automatic determination of modal parameters is a requirement for remote and continuous structural health monitoring. The most used tool for parametric system identification methods is the interpretation of stabilization diagrams. An automated interpretation of the stability diagram is described and applied in this paper.

All parametric system identification methods require the model order to be initially defined. The model order is an integer value that equals the number of eigenvalues present in the model, and in theory, the double of modes to be defined by the identification method. Based on the empirical observation of numerous modal identification problems, the physical modes appear at nearly the same frequency when the model order is over-specified, while the spurious modes do not. From this perspective, the stabilization diagram is used, which can be roughly defined as a plot of model order vs. eigenfrequencies for a wide range of model orders.

The interpretation of such diagrams is often not straightforward, and additional criteria may be necessary to implement and analyze, hence requiring a high amount of user interaction and judgement by the analyst, justifying the need of the automatization of this procedure.

In order to obtain the stabilization diagram, considering an operational modal analysis framework, covariance driven stochastic subspace identification (SSI-COV) [1] is used.

The goal of this work is to present and evaluate a methodology of an automatic modal selection based on the interpretation of such diagrams by applying it on a building structure which vibrations and environmental conditions has been continuously measured from 2009.

The organization of the text is as follows. The automatic interpretation method is described in detail on Sect. 55.2. Section 55.3 presents the main properties of the damage building studied with the results of the implementation of the automatic interpretation method for the 2009–2014 years span. Finally, Sect. 55.4 concludes the paper.

B.K. Rubén (✉) • B.N. Joaquín
Department of Civil Engineering, University of Chile, Av. Blanco Encalada 2002, Santiago, Chile
e-mail: rborosch@ing.uchile.cl; jbilbao@ing.uchile.cl

55.2 Automatic Interpretation of Stabilization Diagrams

The method used to automatically interpret the stabilization diagrams is heavily based on the work developed by Reynders et al. [2] and a modification of the final stage. The procedure can be summarized as follows:

Stage 1: All the modes are assigned into a cluster of (possibly) physical modes or a cluster of spurious modes. The classification of these modes is made using k-means clustering (k = 2) on "soft" single-mode validation criteria. Later a hard validation is performed on the resulting (possibly) physical cluster.
Stage 2: Similar modes are grouped together based on the distance between them (as a function of the eigenvalues and MAC values). The clustering method used to form sets of similar modes is an agglomerative hierarchical algorithm with a cut-off distance determined directly from the result of the first stage.
Stage 3: The sets of similar modes are classified as physical or spurious using k-means clustering (k = 2) upon the number of elements containing each set. The sets of similar modes that are classified as physical are used in the next stage.
Stage 4: A single mode is chosen from each (physical) set. A density based clustering method (DBSCAN) is used in this stage.

Notice that the described method is independent of any user-defined parameter to be adjusted, ensuring a fully automated analysis.

55.2.1 Single-Mode Validation Criteria

Soft and hard single-mode validation criteria which can be applied to stochastic subspace identification algorithms are presented in the present section. The soft validation criteria are categorized in distance, mode shape and energy criteria, and in order to give the same weight for each criteria (for the k-means clustering method), they are normalized in the range [0,1].

55.2.1.1 Distance Validation Criteria

Four distance criteria can be used in the first stage based on the eigenfrequencies f_i^k, damping ratios β_i^k, continuous-time eigenvalue λ_{ci}^k and mode shape ϕ_i^k. The superscript is associated to the model order and the subscript to each mode identified by each model order.

Note that the continuous-time eigenvalue is (theoretically) a function of the eigenfrequency and damping ratio (see, for example, [3]):

$$\lambda_{ci} = -\beta \left(2\pi f_i \right) \pm j \left(2\pi f_i \right) \sqrt{1 - \beta_i^2} \tag{55.1}$$

The eigenfrequencies $d(f_i^k)$, damping ratios $d(\beta_i^k)$, and continuous-time eigenvalue $d(\lambda_i^k)$ distance criteria are defined by:

$$d \left(\chi_i^k \right) = \min \left(\frac{\left| \chi_i^k - \chi_j^{k-1} \right|}{\max \left(\left| \chi_i^k \right|, \left| \chi_j^{k-1} \right| \right)} \right) \tag{55.2}$$

Where χ_i^k represents generically f_i^k, β_i^k or λ_{ci}^k. In words, this parameter corresponds to the minimum of the (normalized) distance between the mode in analysis and the modes associated to the next inferior model order. In the case of physical stable mode, this parameter would take a low value (limited to 0) given the probability of encountering a similar mode in the next inferior model order, and a high value for spurious unstable mode (limited to 1).

For the distance criteria associated to the mode shape ϕ_i^k, the modal assurance criteria (MAC) value is used:

$$MAC \left(\phi_i, \phi_j \right) = \frac{\left| \phi_i^* \phi_j \right|^2}{\phi_i{}_2^2 \phi_j{}_2^2} \tag{55.3}$$

The distance criteria as a function of the MAC value of the mode shape ϕ_i^k is then defined as:

$$MAC_d\left(\phi_i^k\right) = \max\left(MAC\left(\phi_i^k, \phi_j^{k-1}\right)\right) \tag{55.4}$$

Analogous to the other distance criteria, this value corresponds to the maximum of the MAC values between the mode in analysis and the modes associated to the next inferior model order. The observations are similar to the other distance criteria, considering high MAC value (limited to 1) to correlated (similar) mode shapes, and low MAC values (limited to 0) to spurious ones.

55.2.1.2 Mode Shape Validation Criteria

Two validation criteria based upon the mode shape complexity are exposed: the modal phase collinearity (MPC) and the mean phase deviation (MPD). For proportionally damped structures the mode shapes lie in a straight line in the complex plane, and as such the mode shape is considered as a real or monophasic vector. Both criteria aims to quantify the degree of monophasic behavior of the mode shape vector, but given that this is not always the case, they should be used with care.

The MPC value is defined as [4]:

$$MPC\left(\phi_j\right) = \left[\frac{2\lambda_1}{\lambda_1 + \lambda_2} - 1\right]^2 \tag{55.5}$$

Where λ_1 and λ_2 are the maximum and minimum eigenvalue (respectively) of the covariance matrix S_{cov} between the real and imaginary part of the mode shape:

$$S_{cov} = \begin{bmatrix} Re(\phi_i)^T Re\left(\phi_i\right) & Re(\phi_i)^T Im\left(\phi_i\right) \\ Re(\phi_i)^T Im\left(\phi_i\right) & Im(\phi_i)^T Im\left(\phi_i\right) \end{bmatrix} \tag{55.6}$$

If the covariance matrix contains only one eigenvalue different from zero MPC would take a value equal to 1 (perfect collinearity), in any other case the collinearity would be imperfect, so two non-negative eigenvalues would be present diminishing the MPC value. The limit in which the real and imaginary part presents no collinearity, the eigenvalues would be equivalent ($\lambda_1 = \lambda_2$) so MPC would take a value of zero.

The MPD of the mode shape is determined by [2]:

$$MPD\left(\phi_j\right) = \frac{\sum_{o=1}^{n} w_o \arccos \left| \frac{Re(\phi_{jo})V_{22} - Im(\phi_{jo})V_{12}}{\sqrt{V_{12}^2 + V_{22}^2}|\phi_{jo}|} \right|}{\sum_{o=1}^{n} w_o}, \quad \sum_{o=1}^{n} w_o \neq 0 \tag{55.7}$$

Where the subscript o is used to define each element of the mode shape vector, w_o are weighting factors that are chosen equal to $|\phi_{jo}|$ (to provide higher weight to higher amplitude mode shape elements), and V_{22}, V_{12} are the (2,2) and (1,2) element of the V matrix determined from the singular value decomposition of the matrix formed by the real and imaginary part of the mode shape vector:

$$USV^t = \left[Re\left(\phi_j\right) \ Im\left(\phi_j\right) \right] \tag{55.8}$$

Finally, given that for the appropriate use of the k-means algorithm associated with the validation criteria, this value is normalized by 45°. Hence, if the mean phase is wide (limited by 45°) then MPD would take a value near unity, and in case of equal phase for each element of the mode shape vector, the MPD would take a value of zero.

55.2.1.3 Energy Validation Criteria

Two energy validation criteria are exposed: modal transfer norm (MTN) and the contribution of each mode to the measured response (CMM). Both aims to measure the energy associated to each mode.

The MTN is defined as the maximum of the set of singular values of the modal decomposition of the positive power spectral density evaluated at each eigenfrequency $S_{yy,j}^{+}\left(\omega_j\right)$ [1, 5]:

$$MTN(j) = \max \sigma \left(S_{yy,j}^{+}\left(\omega_j\right)\right) \tag{55.9}$$

Where $\sigma\left(\cdot\right)$ represents the set of singular values. This criterion measures the error that is made when the mode j is removed from the model; therefore high values would usually represent physical modes, and near zero values spurious ones. In order to limit the given value to the range [0,1], this criterion is normalized by the maximum value for each model order.

The CMM is defined as [6]:

$$CMM(j) = \frac{1}{l}\sum \mathbf{\Delta}_{m_j} \tag{55.10}$$

Where $\mathbf{\Delta}_{mj}$ is a vector formed by the diagonal elements of the matrix $\left(Y^{m_j}Y^{T}\right)$, where Y is the extended output matrix and Y^{m_j} is the extended modal estimated output matrix:

$$Y = [y_1\ y_2 \ldots y_N],\ Y^{m_i} = \left[y_1^{m_i}\ y_2^{m_i} \ldots y_N^{m_i}\right] \tag{55.11}$$

The extended output matrix Y is formed directly from the output signals of the structure, and the extended modal estimated output matrix is determined from the innovation (Kalman filter) model in modal form. For more details refer to [6].

The CMM is, as implied by its name, the contribution of each mode to the total (measured) response. As seen in [6], the CMM values are limited by the quantity of noise present in the signal; therefore, in order to give the appropriate weight for its use in the k-means clustering method, this criterion is normalized by the maximum value for each model order.

55.2.1.4 Hard Validation Criteria

Hard validation criteria are binary values representing the results of a test (if it passes the test it is assigned a value of 1, and if it does not, it gets a value of 0). According to Reynders [2] five hard validation criteria are used:

1. Presence of negative or high damping ratios ($\beta_i > 0\,[\%]$, $\beta_i < 20\,[\%]$). Given that structures are always stable, damping ratios of physical modes should always be positive, and given that high damping ratios are unlikely to occur, its value is limited to 20[%].
2. Presence of complex conjugate pairs. For every physical mode of a structure with continuous-time eigenvalue λ_{c_i} and mode shape ϕ_i, a second mode with conjugate properties (for each property) should also be present. Hence the presence of complex conjugate pairs for λ_{ci} and ϕ_i (independently) indicates a (possibly) physical mode.
3. Frequency limit. A limit in the eigenfrequency value is applied in order to limit the search of physical mode to a range of interest. For the analyzed structure only frequencies under 10 [Hz] are considered relevant.

55.2.2 First Stage

The first stage of the automatic interpretation method consists of two parts: the k-means clustering method is applied as a function of the soft validation criteria, and then the compliance of all of the hard validation criteria are verified. The resultant set of modes is the result of this stage (those who are classified as physical modes by the clustering method, and at the same time meets all of the hard criteria).

The k-means (k = 2) clustering algorithm minimizes the sum of the squared Euclidian distance between each mode defined by a point $p_i \in \mathbb{R}^{n_{sv}}$ formed by the values taken by each mode for the soft validation criteria. The implementation of this algorithm is shown in [2].

55.2.3 Second Stage

The second stage groups together similar modes (the set of modes that results from the previous stage) by means of an agglomerative hierarchical clustering (details of its implementation is shown on [2]). The distance function between modes considered in this clustering algorithm is defined as:

$$d(i, j) = \frac{\left|\lambda_{c_i} - \lambda_{c_j}\right|}{\max\left(\left|\lambda_{c_i}\right|, \left|\lambda_{c_j}\right|\right)} + 1 - MAC\left(\phi_i, \phi_j\right) \tag{55.12}$$

The cut-off distance used to limit the formation of groups is defined as:

$$\widetilde{d} = \mu_{s1} + 2\sigma_{s1} \tag{55.13}$$

Where μ_{s1} and σ_{s1} are the mean and standard deviation of the vector s_1 formed by the soft validation criteria of continuous-time eigenvalue distance and MAC distance of the set of modes that meets the conditions of stage one:

$$s_1 = d(\lambda)_1 + 1 - dMAC(\phi)_1 \tag{55.14}$$

The assignation of each mode into a set of similar modes is the result of this stage.

55.2.4 Third Stage

Based upon the stabilization property of physical modes, the number of elements of a group (defined in the previous stage) should be larger for physical (stable) modes than spurious (unstable) modes. From this perspective 2-means clustering algorithm is applied as a function of the number of elements of each group (details in [2]) in order to classify each group of similar modes as physical or spurious.

Given that the number of groups determined could be all physical, an additional number of empty groups are created equal to the number of groups that has at least a fifth of the number of elements present in the larger group.

In consequence, the k-means clustering algorithm is applied as a function of the number of elements of the groups determined from the previous stage and the empty groups created. The groups classified as groups of physical modes are the result of this stage.

55.2.5 Fourth Stage

The fourth and final stage aims to define a representative element of each group (or stable mode) formed in the previous stage. Reynders et al. [2] presented three possible ways to find this element: from the mode with the median damping value, highest MPC value or lowest MPD value. Due to some anomalous values, obtained with these three methods, a new method to determine this mode was introduced.

The methodology objective is to detect the densest cluster for each group on the frequency v/s damping plane by means of the density-based spatial clustering algorithm (DBSCAN, [7]). The DBSCAN algorithm depends on two parameters which can be roughly defined as: the minimum number of elements k required for a cluster to be considered as such (instead of noise) and the maximum distance ϵ for any given element to seek close elements. In order to maintain the automatic feature of the interpretation method, k will be considered as 1 and the distance ϵ will be defined as the necessary distance to get k elements given a uniform distribution of the elements [8]:

$$\epsilon = \sqrt{\frac{Vk\Gamma\left[\frac{n}{2} + 1\right]}{m\sqrt{\pi^n}}} \tag{55.15}$$

The methodology used to detect the representative element for each group is the following:

1. Each mode is classified using DBSCAN from the frequency-damping plane.
2. Every mode that is not assigned to the biggest cluster formed (as a function of the number of elements present in it) is discarded.
3. Steps 1 and 2 are repeated until no more clusters are formed (only noise would be present). The representative mode will be the one closest to the mean (frequency and damping) of the final cluster determined.

The previous methodology ensures the choosing of a mode centered on the densest cluster. This stage will result in the construction of a set of representative modes of the structure in study, therefore finalizing the process.

55.3 Case Study

The automatic interpretation method is applied to the "Torre Central" building located in the Mathematics and Physics Sciences Faculty of the University of Chile, Santiago, Chile. The structure is a nine floor building with two basements, has an approximate height of 30.2 [m] above ground level, structured based on shear walls 35 [cm] thick and slabs 25 [cm] thick. Eight uniaxial accelerometers are present, two on the basement, and three on the third and eighth floor. Also environmental sensors are present on the structure.

The records used for the identification of the structure are 15 min length from June of 2009 to July of 2014 with a resampled frequency rate to 25 [Hz] (from a variable original frequency rate between 100 and 200 [Hz]). Channels located on the basement where omitted from the identification process given that those would most likely represent the behavior of the soil and foundation than the structure and its vibration modes. In consequence only six channels where used.

The identification of the structure (construction of the stability diagrams) is made using the SSI-COV algorithm [1] considering the fast multi-order computation algorithm of the system matrices developed by Dölher et al. [9].

The Fig. 55.1 shows an example of the initial stabilization diagram and the resulting diagram following the full application of the automated interpretation process. Note that to lower the computational costs only 51 model orders are computed in the range [50,150]. The lower limit is established so as to ensure the presence of all stable modes.

The recording system presented high level of noise and low number of sensors. This affected considerably the results and the effectiveness of the different criteria. This is a real case of instrumentation so it is considered an interesting validation example.

Despite the noise present, all of the hard validation criteria contribute heavily to the efficient discrimination between physical and spurious modes.

The difference between the centroids for each soft criterion of stage 1 is shown in Fig. 55.2. Therefore the value shown in this figure represents the importance or the weight that each criterion holds on the discrimination between spurious and physical modes The negative value observed on the distance criteria for the poles $d(\lambda_c)$ implies that the physical centroid for this criterion is closest to the ideal spurious value and inversely for the spurious centroid, hence illustrating the poor quality of this criterion.
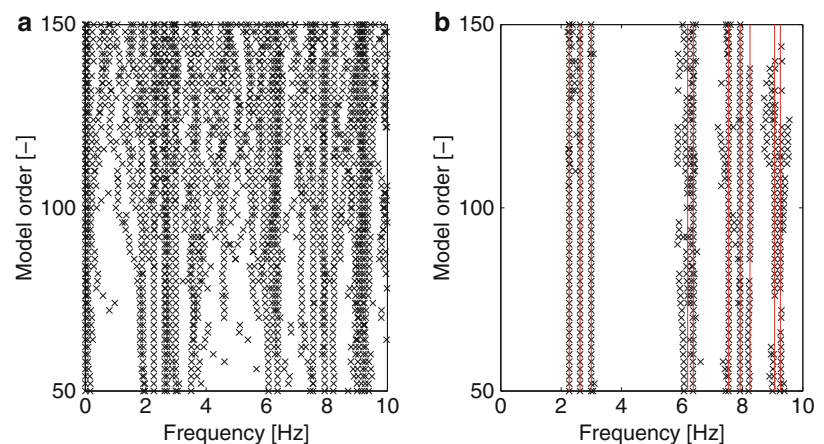

Fig. 55.1 Stabilization diagram (**a**) initial condition, (**b**) processed diagram

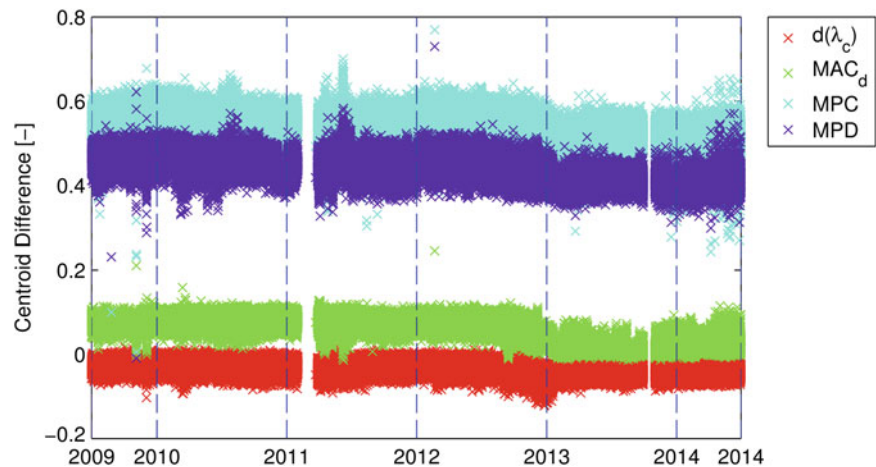**Fig. 55.2** Centroid difference of soft validation criteria (2009–2014)
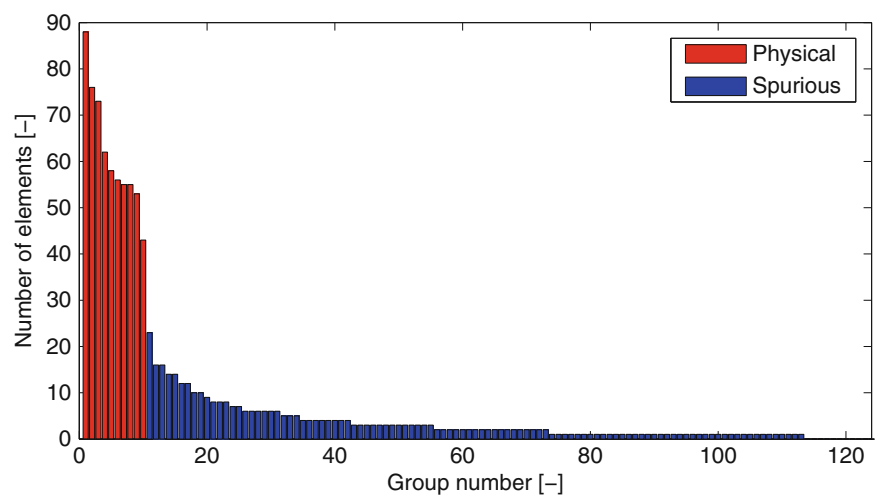

Fig. 55.3 Stage three k-means clustering

The high values of the mode shape distance criteria in comparison to the other ones indicates its strong efficiency on discriminating between spurious and physical modes.

A high value indicates a good indicator for physical modes.

The high level of noise of the system resulted in poor quality indicators for the energy based criteria. Although filtering of some of the noise is possible and could improve the efficiency of these criteria, the computation effort associated of implementing the alternative data-driven stochastic subspace identification (SSI-DATA) algorithm [1] (necessary for the application of these criteria) in addition to the higher computational effort associated to obtain these values, justifies in this case the omission of them from the analysis.

Figure 55.3 shows an example of the k-means algorithm of stage three. Note that the efficiency of this algorithm is determined by the quality of the groups formed in stage two, and it has been observed that low quality signals results in an increase of the number of elements of spurious modes, hence diminishing the discrimination provided by this stage. In spite of this statement, k-means clustering as a function of the number of elements proves to be an efficient way of distinguishing between physical stable modes and spurious stable modes when good quality signals are used.

Finally Fig. 55.4 shows an example of the representative element selection made by the density-based approach (stage four) on the frequency v/s damping plane. From this figure a lower dispersion of the first three modes is observed followed by an increase of this dispersion for higher frequency modes. The selection methodology effectiveness can also be observed from the location of the selected modes.

The results obtained from the 4 year analysis shows that relatively stable spurious modes (high number of elements inside the determined groups) can be encountered when low quality signals are used, and thus increasing the importance to effectively distinguish similar modes (stage two). The quality of the results obtained from stage three and four are a direct consequence of the efficiency of this stage, which in turn depends on the results of the first stage in terms of detecting and clearing the highest possible amount of spurious modes and the lowest possible amount of physical ones.

Fig. 55.4 Stage four mode selection
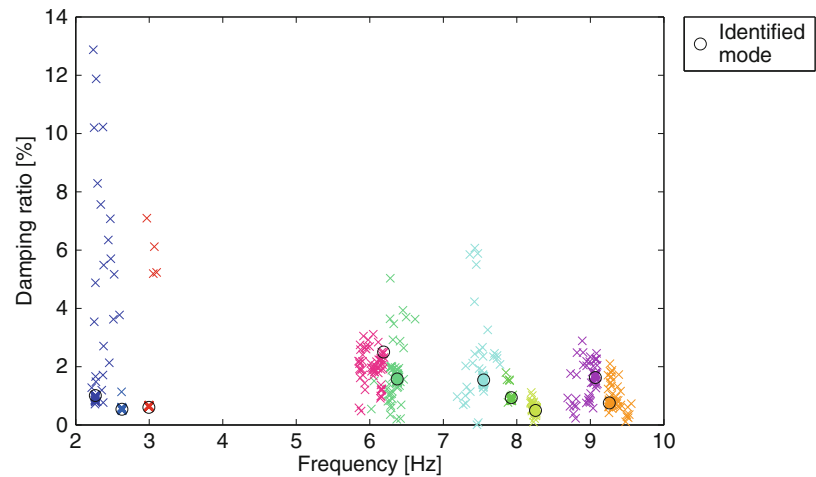
55.4 Conclusions

A fully automated interpretation of stabilization diagrams was evaluated over 15 min's records in the span of 4 years of a damage building. Hard and soft single-mode validation criteria where applied and results indicate the efficiency of the use of hard and mode shape validation criteria, and the dependency of the identified modes on the number and quality of the channels used.

High noise levels observed on the results due to noisy signals and excitation characteristics (due to colored noise, seismic events and other non-white noise solicitations on the structure) limited the applicability or benefit from some of the selected criteria.

The mean computational time required for the SSI-COV identification algorithm is approximately 1.6[s] and the time required for the automated interpretation process is approximately 1[s] (on a Intel(R) Core(TM) i7 2,640 M CPU @ 2.80 GHz processor, 8.00 GB ram) in lieu of the high quantity of processes involved, which proves to be a time-efficient method.

References

1. Reynders E, De Roeck G (2008) Reference-based combined deterministic-stochastic subspace identification for experimental and operational modal analysis. Mech Syst Signal Process 22:617–637
2. Reynders E, Houbrechts J, De Roeck G (2012) Fully automated (operational) modal analysis. Mech Syst Signal Process 29:228–250
3. Veletsos AS, Ventura CE (1986) Modal analysis of non-classically damped linear systems. Earthq Eng Struct Dyn 14:217–243
4. Pappa R, Elliott K, Schenk A (1992) A consistent-mode indicator for the eigensystem realization algorithm, Report NASA TM-107067, National Aeronautics and Space Administration
5. Reynders E, Pintelon R, De Roeck G (2008) Uncertainty bounds on modal parameters obtained from stochastic subspace identification. Mech Syst Signal Process 22:948–969
6. Cara F, Juan J, Alarcón E, Reynders E, De Roeck G (2013) Modal contribution and state space order selection in operational modal analysis. Mech Syst Signal Process 38:276–298
7. Ester M, Kriegel HP, Sander J, Xu X (1996) A density-based algorithm for discovering clusters in large spatial databases with noise. In: Proceedings of 2nd international conference on knowledge discovery and data mining, pp 226–331
8. Daszykowski M, Walczak B, Massart D (2002) Looking for natural patterns in analytical data. Part 2. Tracing local density with OPTICS. J Chem Inform Model 42:500–507
9. Döhler M, Mevel L (2012) Fast multi-order computation of system matrices in subspace-based system identification. Control Eng Pract 20: 882–894

Chapter 56
Original Expression of Tension of a Cable

Mathieu Babaz, Louis Jezequel, and Patrick Perrard

Abstract A new approach of cable dynamics is presented in this paper. It is based on the exact expression of tension coming from continuum mechanics, while the previous elastic models of cables in open literature considered an approximation of small strain which reduced the cable to a spring. The equations of a mass suspended to an elastic cable are derived on the basis of this new formulation, and numerically calculated. A comparison with the classical approach is presented.

Keywords Cable • Nonlinear • Dynamic • Oscillations • Tension

56.1 Introduction

Cables are present in many engineering fields such as bridges, elevators, cranes and ropeways. Due to their specific geometry and structure, they exhibit nonlinear properties which have an impact on their dynamic behavior through parametric resonance, leading to noise and vibrations. For example, the performance of a crane may be highly reduced and the transport of people in elevators can be uncomfortable when oscillations are not under control. Consequently, cables have always been of particular interest for industrials and researchers, leading to many different models depending on the applications.

An inelastic assumption was made by Rohrs [1] in 1851 to have an approximation of the natural frequencies of a suspended cable hanging freely under its own weight. He used the assumption of a sag to span ratio lower than 1:8, which simplifies the analysis since the shape of the cable can then be approximated by a parabola. In 1868, Routh [2] found the analytical solutions of the same problem, but they didn't reproduce the spectrum for the classical taut string.

An explanation was given by Irvine and Caughey [3] in 1974 who showed that it was the introduction of elasticity in the model of the cable which allowed the sagged cable model of Rohrs to pass smoothly to the taut string model in the limit of a vanishing cable sag. This transition had already been made in the models of Simpson [4] in 1966 and Soler [5] in 1970.

Thanks to these models, elastic cable systems with small sag lying on horizontal or inclined supports, such as taut structural cables and overhead transmission lines, were studied in statics and dynamics (see [3, 6, 7]). Numerical methods were proposed to extend the analysis to cables with arbitrary sag, like in suspension bridge cables [8] and skyline logging cables [9].

Then, a transport speed was introduced in order to model a cable travelling between two supports. In 1972, Simpson [10] analyzed the linear in-plane vibrations of an elastic cable with small sag moving through two fixed eyelets at the same elevation. He obtained analytical solutions for the eigenfrequencies and eigenmodes, with two main conclusions: the inclusion of cable transport speed leads to complex vibration modes, and two natural frequencies are repeated for some speeds. Triantafyllou, who extended this problem to arbitrary sags of cables and inclined eyelets [11], showed that the repeated frequencies became distinct due to the inclination of eyelets. To go further, Perkins and Mote [12] calculated in 1987 the out-of-plane motions which had not been considered previously, thanks to simplifications for the strain in the cable and a discretization of the linear equations by the Galerkin method.

On the same problem, Miroshnik [13] and Renezeder [14] used an inelastic cable model. The first one added the gravitational force and a viscous force acting tangentially on the cable, while the second one replaced eyelets by pulleys and introduced a bending stiffness of the cable, to be closer to the application of ropeways.

M. Babaz (✉) • L. Jezequel • P. Perrard
Laboratoire de Tribologie et Dynamique des Systemes, Ecole Centrale de Lyon, Ecully 69134, France
e-mail: babaz.m@gmail.com

Therefore, many models of cables were considered in the past, with more or less parameters taken into account, depending on the applications and the phenomena to characterize. However, a simplification is always made on the relation between tension T and elongation r:

$$T = k.r + T_0 \tag{56.1}$$

$$k = \frac{ES}{l} \tag{56.2}$$

$$r = l - l_0 \tag{56.3}$$

E is the Young's modulus of the cable, S the equivalent section, T_0 the tension of the cable in the prestressed configuration when $r = 0$, l_0 its length when $T = T_0$ and l its actual length under tension T.

This expression comes from a linearly elastic constitutive law.

It was used in many cases due to its simplicity, since it allows considering the cable as a mere spring with a rigidity k. For example, the problem of a mass suspended to a cable is commonly modeled as a swinging spring supporting a mass, which is a classical one to study nonlinear oscillations.

However, the above formulae are based on an approximation of small strain (elongation lower that 1 %) while it is not always the case, due to dynamic phenomena or when the length of the cable becomes very small. That is why a new approach has been sought to determine the relation between tension and elongation. It uses the basics of continuum mechanics, focusing on the most general expressions of stress and strain, valid even with large strain. This generalization has led to the following formula:

$$\dot{T} = \frac{ES}{l}\dot{r} \tag{56.4}$$

This last equation reveals a hyperelasticity of the cable. Indeed the speed of evolution of the strain is independent of the level of stress in the cable.

This behavior comes from the hypothesis that the cable has no inertia, which prevents the effects of waves because they can't propagate. This representation is valid under the assumption that the speed of evolution of the strain is much smaller than the speed of longitudinal waves in the cable, which is generally the case in the usual applications.

In what follows, the new way of modeling a cable is used on a few examples based on the problem of a mass suspended to a cable, which is already rich in terms of dynamic phenomena despite its apparent simplicity. The equations of motion are first derived. Then, numerical applications are implemented and an analysis of the results is made, highlighting the nonlinearities of the dynamics behavior.

56.2 Equations of Motion

The system which is considered is a mass suspended to a cable which is wound around a drive pulley at its top. An elongation and a swinging movement of the cable around the axis of the drive pulley are possible so the system has two degrees of freedom. An illustration is shown on Fig. 56.1.
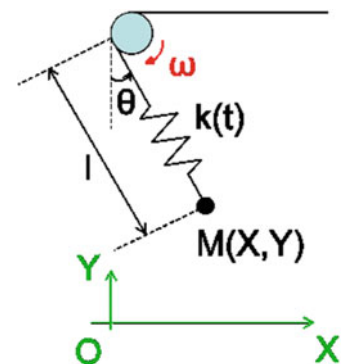

Fig. 56.1 Model of a mass of a mass suspended to an elastic cable

The length l(t) of the cable at time t from its original value l_0 depends on its instantaneous elongation r(t) and the change of length $\int_0^t V_m(t)dt$ accumulated since $t = 0$:

$$l(t) = l_0 - \int_0^t V_m(t)dt + r(t) \tag{56.5}$$

To get the equations of motion, the Fundamental Principle of Dynamics is applied on mass M:

$$\begin{cases} -T \sin \theta = M\ddot{X} \\ T \cos \theta - Mg = M\ddot{Y} \end{cases} \tag{56.6}$$

After derivation and substitution of $\dot{T}$ using (56.3), the following equations are finally obtained:

$$\begin{cases} \dddot{l} - 5\dot{\theta}^2\dot{l} + \frac{ES}{M}\frac{\dot{r}}{l} - g\dot{\theta}\sin\theta - 3\dot{\theta}\ddot{\theta}l = 0 \\ \ddot{\theta} + 2\dot{\theta}\frac{\dot{l}}{l} + \frac{g}{l}\sin\theta = 0 \end{cases} \tag{56.7}$$

$$l = l_0 - \int_0^t V_m(t)\,dt + r \tag{56.8}$$

The coupling between r and is clearly visible in this system of equations.

With the classical expression of tension (56.1) the equation of motion with respect to is the same, but the equation for the elongation r is the following one:

$$\ddot{l} - \dot{\theta}^2\dot{l} + \frac{ES}{M}\frac{r}{l} - g\cos\theta + \frac{T_0}{M} = 0 \tag{56.9}$$

56.3   Numerical Applications

In this section the equations of motion are applied with $V_m(t) = cte = V$, i.e. the drive pulley has a constant rotation speed. The example of $V > 0$ is computed, so that the length of the cable is decreasing linearly until the mass M reaches the drive pulley.

A comparison is made between the results obtained by using the exact expression of tension and the classical expression of tension. The trajectory of the mass M is plotted for these two cases on Fig. 56.2.

The differences between the exact and the classical formulations are significant, even after a few swinging oscillations. When the approximation corresponding to the classical expression of tension is used, a divergence is observed when the mass M approaches the drive pulley, while the exact tension gives more stable results. This is due to the length of the cable which becomes very small after some time, leading to a strain higher than 1 % which is the limit of the model of small strain and classical expression of tension (56.1). It can be seen on Fig. 56.3 where the strain overpasses 1 % when the length of the cable is lower than 4.4 m (in this example).

Therefore the new formulation of tension introduced in this paper is quite relevant considering the results of this application. The classical approximation of the cable as a linear spring may give unrealistic results so it might be quite dangerous to use it.

Fig. 56.2 Trajectory of mass M calculated with the exact expression of tension (*full line*) and the classical one (*dotted line*)
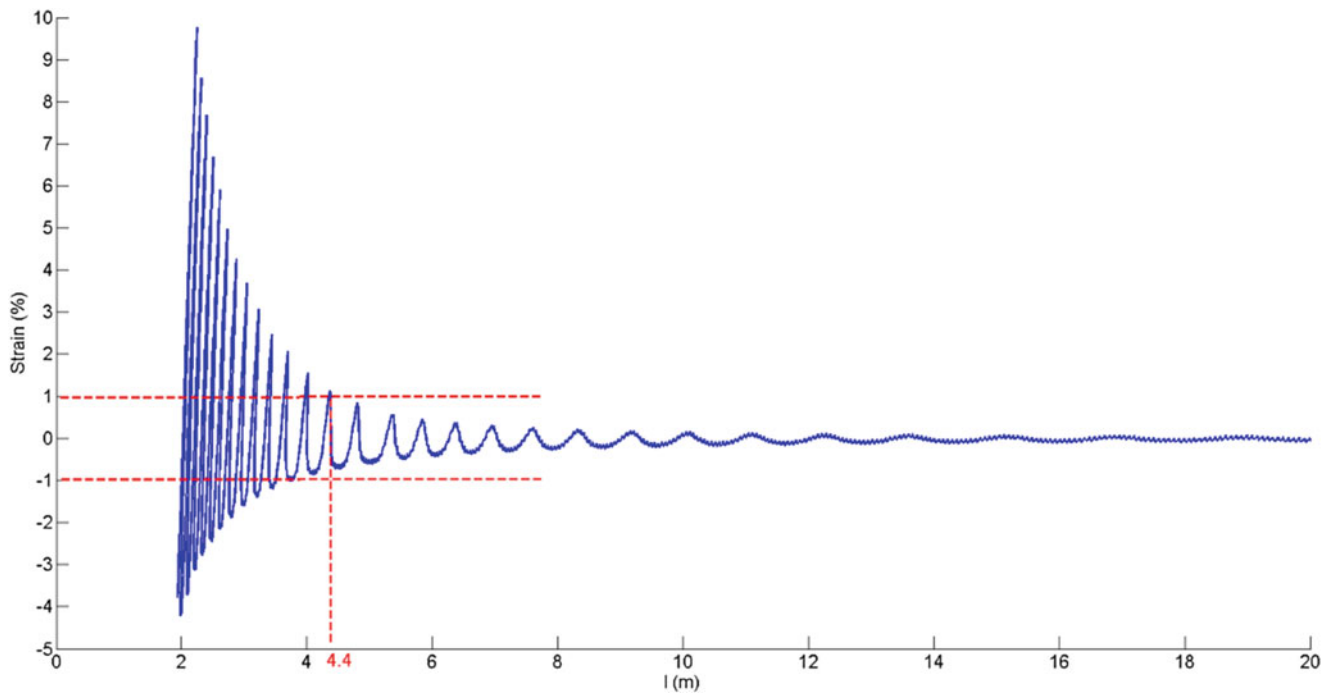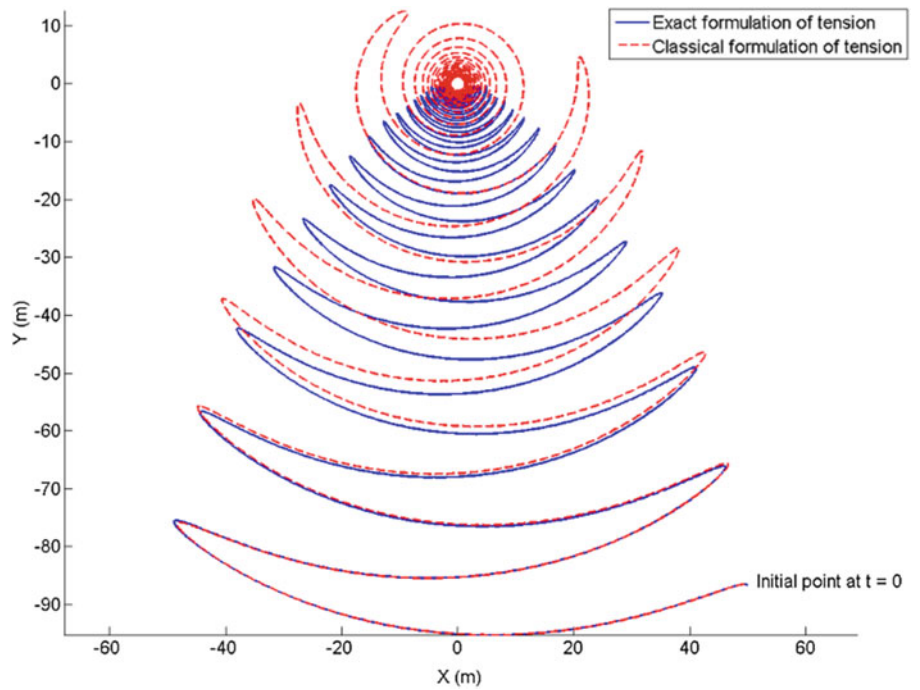

Fig. 56.3 Strain of cable with respect to its length calculated with the exact expression of tension

56.4 Conclusions

Even if many models of cables were developed in the past, some assumptions were made to simplify the expression of the tension, based on small strains and considering the cable as a linear spring. This article takes an original formulation of the tension as a starting point, which is more general and applicable to problems without the restriction of small strains.

The calculations made on the system of a mass suspended to a cable with a variable cable length give many openings to other applications, simple or more complex, since they show that this new approach is richer than the approximated one.

Indeed the equations of motion and therefore the numerical results are different from the classical ones when dynamic phenomena tend to change significantly the length of the cable, which reaches high levels of strain. In this case the amplitudes of the oscillations can be overestimated with the approximated expression of tension, reaching a divergence in some cases.

Therefore, the new formulation of tension presented in this article could be of high interest for industrials who wish to improve their models to simulate the dynamics of the cables they use.

References

1. Rohrs JH (1851) On the oscillations of a suspension cable. Trans Camb Philos Soc 9:379–398
2. Routh EJ (1892) Advanced rigid dynamics, 5th edn. Macmillan, New York
3. Irvine HM, Caughey TK (1974) The linear theory of free vibrations of a suspended cable. Proc R Soc Lond A 341:299–315
4. Simpson A (1966) Determination of the inplane natural frequencies of multispan transmission lines by a transfer matrix method. Proc Inst Electr Eng 113:870–878
5. Soler AI (1970) Dynamic response of single cables with initial sag. J Franklin Inst 290:377–387
6. Irvine HM (1978) Free vibrations of inclined cables. Am Soc Civ Eng J Struct Div 104:343–347
7. Triantafyllou MS (1984) The dynamics of taut inclined cables. Q J Mech Appl Math 37:421–440
8. West HH, Geschwindner LF, Suhoski JE (1975) Natural vibrations of suspension cables. Am Soc Civ Eng J Struct Div 101:2277–2291
9. Carson WW, Emery AF (1976) An energy method determination of large cable dynamics. Am Soc Mech Eng J Appl Mech 43:330–334
10. Simpson A (1972) On the oscillatory motions of translating elastic cables. J Sound Vib 20:177–189
11. Triantafyllou MS (1985) The dynamics of translating cables. J Sound Vib 103:171–182
12. Perkins NC, Mote CD (1987) Three-dimensional vibration of travelling elastic cables. J Sound Vib 114:325–340
13. Miroshnik R (2001) The phenomenon of steady-state string motion. J Appl Mech 68:568–574
14. Renezeder HC (2006) On the dynamics of an axially moving cable with application to ropeways. Ph.D. thesis, Technischen Universitat Wien